materials

Special Issue Reprint

Achievements in Foundry Materials and Technologies

Edited by
Marcin Stawarz, Krzysztof Janerka and Jan Jezierski

mdpi.com/journal/materials

MDPI

Achievements in Foundry Materials and Technologies

Achievements in Foundry Materials and Technologies

Guest Editors

Marcin Stawarz
Krzysztof Janerka
Jan Jezierski

MDPI

Basel • Beijing • Wuhan • Barcelona • Belgrade • Novi Sad • Cluj • Manchester

Guest Editors

Marcin Stawarz
Department of Foundry Engineering
Silesian University of Technology
Gliwice
Poland

Krzysztof Janerka
Department of Foundry Engineering
Silesian University of Technology
Gliwice
Poland

Jan Jezierski
Department of Foundry Engineering
Silesian University of Technology
Gliwice
Poland

Editorial Office
MDPI AG
Grosspeteranlage 5
4052 Basel, Switzerland

This is a reprint of the Special Issue, published open access by the journal *Materials* (ISSN 1996-1944), freely accessible at: https://www.mdpi.com/journal/materials/special_issues/1DGJ4KI72H.

For citation purposes, cite each article independently as indicated on the article page online and as indicated below:

Lastname, A.A.; Lastname, B.B. Article Title. *Journal Name* **Year**, *Volume Number*, Page Range.

ISBN 978-3-7258-8531-2 (Hbk)
ISBN 978-3-7258-8532-9 (PDF)
https://doi.org/10.3390/books978-3-7258-8532-9

© 2026 by the authors. Articles in this reprint are Open Access and distributed under the Creative Commons Attribution (CC BY) license. The reprint as a whole is distributed by MDPI under the terms and conditions of the Creative Commons Attribution-NonCommercial-NoDerivs (CC BY-NC-ND) license (https://creativecommons.org/licenses/by-nc-nd/4.0/).

Contents

About the Editors . . . . . **ix**

Preface . . . . . **xi**

Martina Bašistová, Filip Radkovský, Petr Lichý, Šimon Kielar and Iveta Vasková
Numerical Simulation and Optimization of Furnace Roll Casting Production Technology
Reprinted from: *Materials* **2025**, *18*, 5445, https://doi.org/10.3390/ma18235445 . . . . . **1**

Artur Bobrowski, Faustyna Woźniak, Sylwia Żymankowska-Kumon, Hubert Ziętal, Kacper Januszek and Beata Grabowska
The Impact of Storage Conditions on the Gas-Forming Tendency of Moulds and Cores Made with Resole-Type Phenol Formaldehyde Resin
Reprinted from: *Materials* **2025**, *18*, 4832, https://doi.org/10.3390/ma18214832 . . . . . **29**

Janusz Cebulski, Dorota Pasek, Stanisław Roskosz, Magdalena Popczyk, Jadwiga Gabor, Sebastian Stach, et al.
Topography and Corrosion Resistance Characteristics of Fe40Al5Cr0.2ZrB Alloy and X18CrN28 Steel
Reprinted from: *Materials* **2025**, *18*, 5465, https://doi.org/10.3390/ma18235465 . . . . . **45**

Janusz Cebulski, Dorota Pasek, Maria Sozańska, Magdalena Popczyk, Jadwiga Gabor, Andrzej Swinarew and Jakub Wieczorek
Change in the Morphology of Alloy Corrosion Products Based on the FeAl Intermetallic Phase After Oxidation in Water Vapor at a Temperature of 700 °C for up to 2000 h
Reprinted from: *Materials* **2025**, *18*, 5150, https://doi.org/10.3390/ma18225150 . . . . . **63**

Janusz Cebulski, Dorota Pasek, Maria Sozańska, Magdalena Popczyk, Jadwiga Gabor and Andrzej Swinarew
Oxidation of the Alloy Based on the Intermetallic Phase FeAl in the Temperature Range of 700–1000 °C in Air and Possibilities of Practical Application
Reprinted from: *Materials* **2025**, *18*, 1835, https://doi.org/10.3390/ma18081835 . . . . . **73**

Yuliia Chabak, Vasily Efremenko, Ivan Petryshynets, Michail Golinskyi, Kazumichi Shimizu, Bohdan Efremenko, et al.
Role of Quenching Temperature Selection in the Improvement of the Abrasive (Al_2O_3) Wear Resistance of Hybrid Multi-Component Cast Irons
Reprinted from: *Materials* **2024**, *17*, 3742, https://doi.org/10.3390/ma17153742 . . . . . **87**

Sandra Gajoch, Dorota Wilk-Kołodziejczyk, Łukasz Marcjan, Roberto Corizzo, Adam Bitka, Marcin Małysza and Gerard Skomin
Development and Implementation of a Defect Detection Model for Microstructures Using Image Processing Methods
Reprinted from: *Materials* **2025**, *18*, 5207, https://doi.org/10.3390/ma18225207 . . . . . **113**

Paweł Gara, Ewa Wisła-Walsh and Tomasz Bajda
Evaluating the Appropriateness of Selected Foundry Sands for the Casting of Reactor Housings: A Study Based on Physicochemical Characterization Outcomes
Reprinted from: *Materials* **2024**, *17*, 6068, https://doi.org/10.3390/ma17246068 . . . . . **134**

Beata Grabowska, Artur Bobrowski, Mateusz Skrzyński, Grzegorz Grabowski, Wojciech Żyłka and Barbara Pilch-Pitera
Microwave-Crosslinked Polymer Binder MA-AANa/D Biodegradable in an Aqueous Environment–Selected Own Research
Reprinted from: *Materials* **2025**, *18*, 5379, https://doi.org/10.3390/ma18235379 . . . . . **156**

Aneta Jakubus, Marek Sławomir Soiński, Grzegorz Stradomski, Maciej Nadolski and Marek Mróz
The Effect of Austempering Temperature on the Matrix Morphology and Thermal Shock Resistance of Compacted Graphite Cast Iron
Reprinted from: *Materials* **2025**, *18*, 2200, https://doi.org/10.3390/ma18102200 . . . . . **169**

Aneta Jakubus, Marek Sławomir Soiński, Piotr Mierzwa and Grzegorz Stradomski
Regression Analysis and Optimum Values of Austempering Affecting Mechanical Properties of Compacted Graphite Iron
Reprinted from: *Materials* **2024**, *17*, 5024, https://doi.org/10.3390/ma17205024 . . . . . **186**

Dexin Ma, Hongyuan Sun, Yunxing Zhao, Weitai Xu, Zaiwang Huang, Bowen Cheng, et al.
Effect of Solidification Direction on the Freckle Formation in Single-Crystal Superalloy Castings
Reprinted from: *Materials* **2025**, *18*, 1534, https://doi.org/10.3390/ma18071534 . . . . . **206**

Marcin Małek, Janusz Kluczyński, Rafał Grzejda, Paweł Wiśniewski, Agnieszka Jenerowicz and Ireneusz Ewiak
Thermal and Structural Behavior of Investment Casting Molds Modified with Biodegradable Walnut Shell Chips
Reprinted from: *Materials* **2025**, *18*, 4289, https://doi.org/10.3390/ma18184289 . . . . . **221**

Marcin Małek, Marcin Wachowski and Janusz Kluczyński
Ecofriendly Water-Soluble Binders for Precision Ceramic Moulds in Aerospace Turbine Casting: Process Development and Performance Evaluation
Reprinted from: *Materials* **2025**, *18*, 2329, https://doi.org/10.3390/ma18102329 . . . . . **238**

Muhammad Anwarul Nazim, Arezoo Emdadi, Todd Sander and Ronald O'Malley
The Effect of Mold Flux Wetting Conditions with Varying Crucible Materials on Crystallization
Reprinted from: *Materials* **2025**, *18*, 1174, https://doi.org/10.3390/ma18051174 . . . . . **267**

Natalia Przyszlak, Tomasz Wróbel, Agnieszka Dulska, Paweł M. Nuckowski, Dariusz Łukowiec and Marcin Stawarz
Microstructure of the Working Layer of X46Cr13 Steel in a Bimetal System with Gray Cast Iron
Reprinted from: *Materials* **2024**, *17*, 5933, https://doi.org/10.3390/ma17235933 . . . . . **286**

Dariusz Rydz, Sebastian Mróz, Piotr Szota, Grzegorz Stradomski, Tomasz Garstka and Tomasz Cyryl Dyl
The Analysis of Plastic Forming in the Rolling Process of Difficult-to-Deform Ti + Ni Layered Composites
Reprinted from: *Materials* **2025**, *18*, 1926, https://doi.org/10.3390/ma18091926 . . . . . **299**

Tomasz Rzychoń and Andrzej Kiełbus
Optimisation of Hot-Chamber Die-Casting Process of AM60 Alloy Using Taguchi Method
Reprinted from: *Materials* **2024**, *17*, 6256, https://doi.org/10.3390/ma17246256 . . . . . **318**

Marcin Stawarz
Natural Graphite Spheroidization Phenomena in Arc Furnace Metallurgical Process for High-Silicon Cast Iron
Reprinted from: *Materials* **2025**, *18*, 4397, https://doi.org/10.3390/ma18184397 . . . . . **334**

Grzegorz Stradomski, Sebastian Mróz, Piotr Szota, Tomasz Garstka, Jakub Gróbarczyk and Radosław Gryczkowski
Comparative Analysis of the Application of Five-, Seven- and Nine-Roll Sheet Straightening Using Numerical Tools
Reprinted from: *Materials* **2026**, *19*, 1053, https://doi.org/10.3390/ma19061053 . . . . . **347**

Małgorzata Trepczyńska-Łent and Jakub Wieczorek
Tribological Properties of Eutectic White Cast Iron with Directional and Non-Directional Microstructure
Reprinted from: *Materials* **2025**, *18*, 4516, https://doi.org/10.3390/ma18194516 . . . . . **367**

Tomasz Wróbel
Compound Castings for the Coke Industry
Reprinted from: *Materials* **2024**, *17*, 3539, https://doi.org/10.3390/ma17143539 . . . . . **383**

Jerzy Stanisław Zych, Marcin Myszka, Janusz Postuła and Sylwia Kobyłecka
Vari Morph Cast Iron—A High IQ Material—Structure, Properties, Ultrasonic Control, Technology and Industrial Application
Reprinted from: *Materials* **2026**, *19*, 1212, https://doi.org/10.3390/ma19061212 . . . . . **401**

About the Editors

Marcin Stawarz

Marcin Stawarz has been associated with the Silesian University of Technology since graduating in 2000. In 2004, he earned a PhD in materials science. In 2019, based on his scientific achievements and a monograph on the crystallization of intermetallic phases in high-alloy cast irons, he obtained a postdoctoral degree (habilitation). He currently holds a professorship at the Department of Foundry Engineering.

His main research areas focus on metallurgy and foundry technology, particularly in relation to the crystallization and metallurgy of cast iron (ductile and high-silicon), intermetallic phases in metal alloys (e.g., Fe-Si systems), precision casting using the investment casting method, the operational properties of castings, including the corrosion of metal alloys and abrasive wear resistance, and the use of electron microscopy and thermal analysis in qualitative research. He actively participates in the foundry community as a member of the Foundry Commission of the Polish Academy of Sciences (since 2005) and the Polish Foundrymen's Technical Association (STOP) (since 2003), where he was awarded the STOP Gold Badge of Honor (2012).

For his work, he was awarded the Bronze Medal for Long Service by the President of the Republic of Poland (2017). He has also received the Rector's Awards of the Silesian University of Technology several times for his teaching and organizational achievements.

His has published numerous scientific articles in prestigious journals, chapters in monographs, and given conference presentations. A significant portion of his work concerns the practical application of advanced foundry materials in industry.

Krzysztof Janerka

Krzysztof Janerka, a professor at the Silesian University of Technology, has been working at the Department of Foundry Engineering, Faculty of Mechanical Engineering, Silesian University of Technology, since 1985. In 1995, he completed a three-year doctoral program and obtained a PhD in Technical Sciences. In 2013, he obtained a postdoctoral degree in Technical Sciences in Materials Science and Engineering. Since 2019, he has been employed at the Department of Foundry Engineering as a professor.

His research interests include pneumatic transport (molding sand regeneration and waste disposal) and its applications in foundry engineering (carburizing ferrous alloys and powder injection into liquid metal). His current areas of interest and research include carburizing ferrous alloys using various carburizing materials and methods, the effect of carburizing on the quality of the resulting alloys, and methods for assessing the quality of carburizers. This also includes the effect of various charge materials on the structure and properties of smelted cast iron. He is the author or co-author of 244 journal articles, including 37 publications in the Web of Science database and 3 chapters in guidebooks (including the Encyclopedia of Iron, Steel and Their Alloys). His publication "The Effect of the Carburizer Quality on the Cast Iron Recarburization Process" in *Foundry Trade Journal International* received a diploma from the Institute of Cast Metals Engineers (ICME) in the UK in 2010. He is the co-author of five patents. He has supervised three completed doctoral dissertations and reviewed eight doctoral dissertations. Moreover, he has co-authored 27 publications with student contributions and supervised 42 master's theses and 25 engineering projects. He is a member of the Commission on Foundry Engineering of the Polish Academy of Sciences, Katowice Branch, and the Technical Association of Polish Founders.

Jan Jezierski

Jan Jezierski is a Professor at the Department of Foundry Engineering, Silesian University of Technology, Gliwice, Poland, where he has been pursuing his academic career since 1998. He is a recognized scholar in the fields of foundry engineering, metallurgy of ferrous and non-ferrous alloys, and materials processing, with research spanning both fundamental and industrially oriented aspects of modern casting technologies. His scientific interests focus, in particular, on the metallurgical quality of liquid alloys, the optimization of gating systems, pneumatic powder injection into liquid metals, cast iron and cast steel technology, heat treatment, and selected issues related to quality management, automation, and sustainable development in foundry engineering.

Professor Jezierski is the author and co-author of numerous scientific publications, patents, and research studies published in leading international journals and conference proceedings. He is also the author of the monograph *Theoretical and Practical Aspects of Pneumatic Powder Injection into Liquid Alloys with a Non-Submerged Lance*. His work has combined scientific rigor with strong industrial relevance, contributing to the development and implementation of innovative metallurgical and foundry solutions. He has participated in and led a number of national and international research and development projects, including those funded by NCN, NCBR, and international collaborative programs.

In addition to his research and teaching activity, he is actively involved in the advancement of the scientific community as Editor-in-Chief of the journal *Archives of Foundry Engineering*. His achievements have been widely recognized, as demonstrated by his numerous distinctions for scientific excellence, high-value publications, reviewing activity, and supervision of award-winning doctoral research.

Preface

This Reprint provides a comprehensive overview of the latest advances in foundry and materials technology, focusing on improving the efficiency, precision, and sustainability of production processes. The research featured presents a multifaceted approach to modern foundry and metallurgy—from advanced research on the microstructure of cast iron and steel, through innovative refractory materials, to the application of artificial intelligence and numerical modeling. This Reprint demonstrates that modern foundry is evolving toward "high-intelligence" technologies—smart materials, digitally controlled processes, and solutions that minimize the environmental impact of heavy industry. It is an indispensable resource for both scientists and practicing engineers seeking innovation in the foundry sector.

Marcin Stawarz, Krzysztof Janerka, and Jan Jezierski
Guest Editors

materials

MDPI

Article

Numerical Simulation and Optimization of Furnace Roll Casting Production Technology

Martina Bašistová [1,*], Filip Radkovský [1], Petr Lichý [1], Šimon Kielar [1] and Iveta Vasková [2]

[1] Department of Metallurgical Technologies, Faculty of Materials Science and Technology, VSB-Technical University of Ostrava, 17. Listopadu 2172/15, 708 00 Ostrava, Czech Republic; filip.radkovsky@vsb.cz (F.R.); petr.lichy@vsb.cz (P.L.); simon.kielar@vsb.cz (Š.K.)

[2] Department of Metallurgy, Faculty of Materials Metallurgy and Recycling, Technical University of Kosice, Letná 1/9, 042 00 Košice, Slovakia; iveta.vaskova@tuke.sk

* Correspondence: martina.basistova@vsb.cz

Abstract

This study investigates the use of steel and cast iron for producing cast furnace rolls to replace welded rolls, which often fail from cracks and limited durability. Casting had not been previously considered by the manufacturer, but rising demands for durability and quality make it a promising alternative. Material selection focused on mechanical properties, wear resistance, and production costs. To ensure casting quality, Magmasoft 6.0 software was applied for detailed simulation of casting, solidification, and cooling. Results showed that steel alloys (GS-34CrMo4 and GS-20Mn5) are prone to shrinkage and porosity, which cannot be fully avoided even with feeders. In contrast, GJS-500-7 cast iron exhibited low shrinkage tendency and minimal defects, proving suitable for production while reducing costs. It also offers lower weight and efficient metal use, improving cost-effectiveness. Detected defects were concentrated in the central casting area, where they have little impact on functionality. Based on sixteen simulations, GJS-500-7 cast iron emerged as the most suitable material for furnace rolls thanks to its thermal resistance, castability, low porosity, and ability to meet required specifications. This process optimization represents an efficient, cost-effective choice, improving final product quality and creating new opportunities for the manufacturer.

Keywords: casting technology; pouring simulation; solidification; cast steel; nodular cast iron; porosity; defects prediction

1. Introduction

Furnace rolls operating in zones with low thermal gradients and minimal material residence time in the furnace (entry/exit sections of continuous annealing lines, tempering zones at ~580–660 °C, transition to the run-out table) function under short-term thermal exposure and lower mean temperature. Zonal temperature control in CAL/CGL systems (heating/even-heat/cooling) reduces the accumulation of creep damage and thermal-fatigue cycles in the rolls, allowing the use of simpler material solutions compared to high-temperature soaking sections [1]. In these zones, welded roll constructions (shell + ends + shafts) are widely applied; their failures are typically governed by local thermal expansion, repeated contact shocks, and residual stresses in weld regions. Numerical and operational analyses identify the dominant mechanism as creep-fatigue with stress concentration in the weld root and toe [2,3].

For load-bearing welded rolls in "cold-end" zones, quenched and tempered low-alloy steels such as 34CrMo4 (or 35CrMo) are commonly used, providing a favorable combination of strength and toughness and good impact response; however, with increasing temperature, temper softening and carbide precipitation occur, limiting long-term strength above ~650–700 °C [4,5]. Cast steel GS-20Mn5 is used for auxiliary or idler rolls and less-loaded assemblies; its viscoplastic response and grain evolution at elevated temperature make it suitable for shorter exposures rather than long-term soaking [6]. Ductile iron GJS-500-7 offers good impact damping and castability, but between 400 and 700 °C, its strength and low-cycle fatigue (LCF) life decline rapidly due to oxidation and stress concentration at graphite nodules. Its use is therefore reasonable only in the coldest, short-exposure areas, or in SiMo variants that remain stable up to ~700–750 °C [7,8].

Mechanical loading in these zones is dominated by rolling contact with short thermal impulses. Key material parameters include temper-softening resistance (for 34CrMo4), toughness, and weld joint resistance to combined creep-fatigue. Experimental and FE studies on welded components show that differences in properties between weld metal and heat-affected zones increase local creep deformation and accelerate crack initiation; proper filler selection, controlled thermal cycles, and post-weld heat treatment (PWHT) reduce residual stresses and extend service life [3,9]. From the tribochemical standpoint, surface wear is determined by the formation of early oxide layers (FeO/Fe_3O_4) and the transfer of oxides from the strip; short exposures limit measurable scale growth, though repeated thermal shocks generate stresses in the oxide and micro-spallation, which increase roughness and friction [10]. To limit pickup and stabilize the surface, thin HVOF or VPS coatings based on NiCoCrAlY (optionally alloyed with Hf or Si) are successfully used in practice; within 600–900 °C, they suppress oxidation and improve cyclic adhesion [11].

Typical defects of welded furnace rolls in "cold-end" zones include the following: (i) initiation and propagation of cracks near welds due to combined creep-fatigue, (ii) local bulging and bending under prolonged exposure above design temperature, (iii) micro-spallation of surface scales leading to increased friction, and (iv) for cast irons—subcritical cracks initiated at graphite nodules and a temperature-dependent decrease in fracture toughness [2,3,7]. Case studies of related furnace components (supports, tubes) confirm the same failure mechanisms: thermal non-uniformity, material ageing, and intergranular weakening leading to premature failure [12]. Integrating structural optimization (load redistribution among rolls, cooled journals, shorter spans) with appropriate material and welding technology demonstrably extends maintenance intervals in entry roll assemblies [2].

Rolls cast with internal shrinkage cavities or porosity exhibit reduced service life because voids act as preferential crack initiation sites, lowering the fatigue limit and accelerating crack propagation. The risk increases with defect size and proximity to the surface, while the scatter in lifetime rises markedly [13]. In cast steels, the direct influence of central and off-axis shrinkage on the decrease in low-cycle fatigue life has been experimentally demonstrated—larger cavities lead to faster crack initiation and shorter life [14]. A similar trend applies to cast irons: the presence of shrinkage defects significantly reduces fatigue strength, with fissured shrinkage pores being more detrimental than gas porosity [15]. At elevated temperatures, where creep interacts with fatigue, such defects promote earlier cavity formation and intergranular weakening, accelerating failure of cast rolls in furnace service [16].

Critically, in low-temperature and short-exposure sections, combining welded steels 34CrMo4 (for load-bearing and drive rolls) and 20Mn5 (for idler rolls) provides sufficient operational reliability and cost efficiency, provided that proper heat treatment (Q&T), cooling, and atmospheric control are maintained [4,6]. For 34CrMo4, literature confirms a stable

strength–toughness balance at tempering temperatures around 580–650 °C, while long exposure above 700 °C promotes carbide precipitation and hardness loss [4,5]. Conversely, cast steel 20Mn5 shows good plasticity and resistance to short thermal impulses, making it suitable for less-loaded rolls in colder furnace zones [6]. Ductile iron GJS-500-7 can be used selectively where impact damping and short material contact are critical; at 400–700 °C, its strength and fatigue life decrease sharply due to oxidation and stress at graphite nodules [7]. Transitioning to modified SiMo grades shifts usability limits toward ~700 °C, with improved oxidation resistance and longer surface life under cyclic heating [8]. Operational strategy remains conservative: heat-resistant austenitic alloys are reserved for hot furnace sections [2,12], while welded rolls from standard low-alloy steels are efficiently employed in cold-end zones with verified fatigue and surface stability, where mechanical and thermal loads remain limited [1,9,11].

Numerical simulations are increasingly used to enhance quality and improve efficiency in foundry production. Combined with experiments, simulations provide greater flexibility, cost savings, and help to prevent the origin of casting defects or optimize production technology [17,18]. One of the most widely used programs in European foundries is Magmasoft, which monitors processes such as mold filling, solidification, and casting cooling. It also enables internal stress analysis, helping to prevent deformation [19]. For solidification simulations of castings in metal molds, the finite element method (FEM), finite difference method (FDM), and boundary element method (BEM) can also be used [20]. Numerous other foundry defects can be predicted through precise modeling of temperature profiles, allowing optimization of technological processes to prevent or mitigate defects [21–23]. Accurate thermophysical data for various materials play a crucial role, as simulation results are highly dependent on the quality of material data. It is therefore also possible to use programs or databases such as Thermo-Calc® and JMatPro® [19,24] or the SimulationDB database [25].

Casting process simulations reveal major findings on casted alloys. Studies [26,27] analyzed ductile iron (GJS-400) castings, simulating metal inflow, solidification, and cooling with chills, with experimentally determined thermophysical properties enabling microstructure and stress evaluation. Works [28,29] examined gray iron microstructure, grain morphology, and gating design, integrating simulation with production, economic, and environmental aspects. Research [30–32] focused on optimizing ductile and Si-Mo ductile iron casting quality through combined simulation and experimental validation, addressing heat transfer, cooling rate effects, and residual stress prediction for casted parts working in high-temperature applications above 750 °C. Studies on steel casting simulations addressed heat release [33], thermal databases [34], mold cooling, predicting temperature fields, reducing internal stresses [35,36], and chiller design, improving accuracy, yield, and solidification efficiency [37], or optimizing mold materials and bimetal casting process [38]. Reduced cooling performance during thermal cycling clarified irreversible sand behavior in ductile iron casting. With increasing demand for sand casting, modern control methods such as 3D printing and wireless sensors enhance data acquisition and model validation [39]. Research [40,41] focused on optimizing mold lifespan and minimizing microporosity through combined experimental and simulated analysis.

The novelty of the numerical modeling approach lies in the targeted use of simulations to determine the most suitable production technology and material for an already industrially applied furnace roll with a fixed geometry. The modeling process was designed not only to predict typical casting defects such as shrinkage and porosity but also to optimize the gating and feeding system within existing design constraints, where major shape modifications were not permitted. This approach allowed for a direct comparison of different materials and technological variants, linking numerical results with real manufacturing

feasibility. The aim was to achieve a balance between casting quality, technological efficiency, and cost-effectiveness, demonstrating a practical and innovative use of numerical modeling in optimizing complex foundry components under real industrial conditions.

This study focuses on the use of steel or cast iron for producing castings that will serve as furnace rolls, intended to replace the currently manufactured welded rolls. The current version, produced by welding, is highly susceptible to defects, most commonly cracking during use. Therefore, transitioning to castings presents a promising alternative solution that has not been considered by the current manufacturer. In selecting a suitable material, various factors needed to be considered, such as mechanical properties, wear resistance, and production costs. To achieve the most efficient and high-quality manufacturing process, simulation software Magmasoft 6.0 will be utilized. This software enables detailed analysis and simulation of casting, solidification, and cooling, which may help optimize process parameters and select the most suitable material for producing furnace rolls in the future. By using numerical modeling, it is possible to predict and minimize potential defects in actual castings, potentially leading to improved overall product quality and reduced production costs. Optimization using this advanced simulation tool is essential to ensure that selected materials and manufacturing processes meet the required standards and specifications for producing furnace rolls. The novelty of this research lies primarily in proposing a new solution for a specific supplier who has not previously considered this production option.

2. Materials and Methods

2.1. Design and Modification of the Furnace Roll Structure

The original rolls were manufactured as welded constructions from several dissimilar parts, some of which were thin-walled and made from various steel grades. During use, these rolls were subject to cyclic heating and cooling, and due to uneven wall heating or weld quality, they often developed irreparable defects. As a potentially more cost-effective alternative, a design for the production process using foundry methods was chosen, with the suitability of this production approach first requiring validation through simulations. Initially, attention was given to the design of the roll itself. Both the existing technical drawings (Figure 1) and the furnace manufacturer's designs were considered.

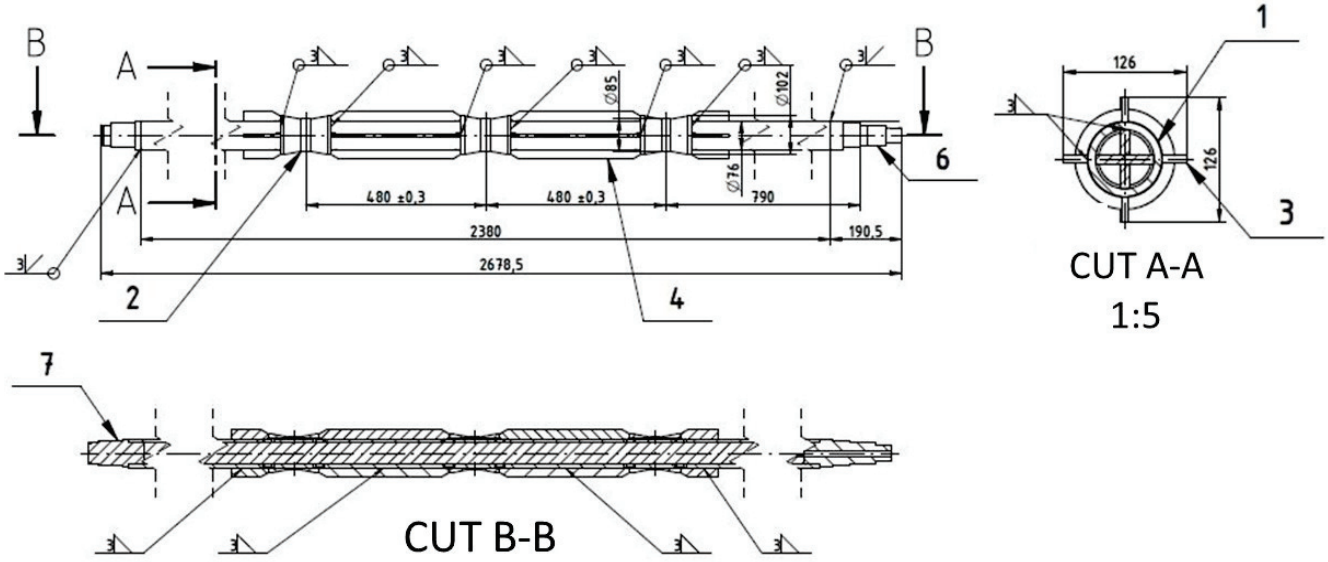


Figure 1. Current technical drawing (sketch) of furnace roll shape.

Both were thoroughly reviewed, and a new design was created that accounted for the conditions of use and additional user requirements for the rolls' intended application, without allowing significant modifications to the entire structure. The design was only slightly adjusted for the casting technology, with an emphasis on eliminating sharp transitions that could lead to stress concentration and create hotspots. Such areas could pose issues during production and use. The design was further optimized to best fit the foundry casting technology and facilitate production (Figure 2). The restrictions on design changes allowed only for choosing between one or two runners and adjusting the shape and volume of feeders. Emphasis was placed on ensuring that, upon completion, the roll would not be susceptible to defects caused by stress or other factors. The goal was to create a simple shape without sharp transitions that could potentially cause issues in the future.

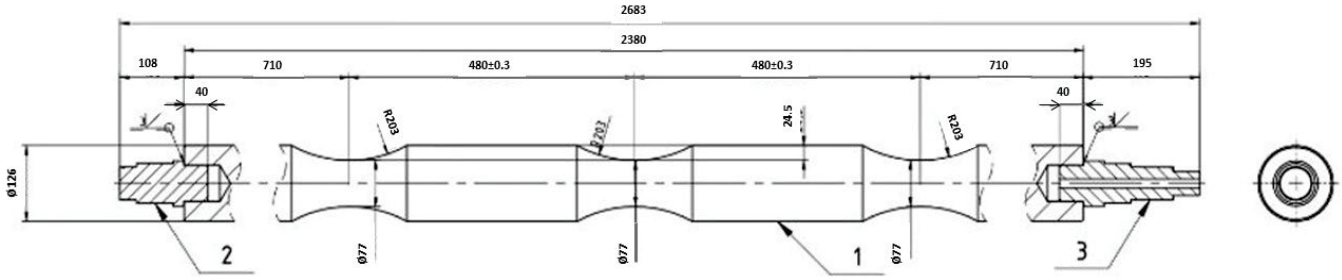


Figure 2. Revised drawing for the casting of a furnace roll shape.

2.2. Designing of Casting Position in the Mold and 3D Modeling

When designing the placement of the casting in the mold, three options were considered. The first option was the right centrifugal casting technology, which was ultimately dismissed as unfeasible. The main reason was the small diameter of the furnace roll (126 mm) combined with its considerable length (2380 mm). With this technology, issues with insufficient metal feeding in the central section of the roll could arise, which might typically be resolved with feeders. However, with such a small diameter, feeders would be less effective, resulting in a high risk of cavities and other defects.

The second option was stationary vertical casting, typically with bottom bottom-gating system entry, placing the roll in a vertical position. The advantage of this method is the smooth filling of the mold cavity and good chemical homogeneity of the material across its cross-section. However, given the length of the roll, this technology posed challenges due to the need to assemble the mold from multiple parts, complicating accurate geometry maintenance and subsequent defect correction.

The third and selected option was classical horizontal gravity casting into a split sand mold with lateral entry of the gating system. Metal transport into the mold cavity was ensured by runners along the sides of the roll, combined with a series of gates to facilitate smooth and sufficiently rapid filling.

The 3D modeling of the furnace roll, along with the proposed gating system and feeder options, was carried out using the 3D modeling software Rhinoceros 6.0. This surface-based 3D NURBS modeling program is commonly used in technical fields and design. The various solution options and completed 3D models are shown in Figure 3, and the geometry with the gating system, runner and vents is presented in Figure 4.

In designing the gating system, attention had to be given to potential problems arising from the casting's structure. The primary concerns included inadequate filling speed of the mold cavity, which could lead to misrun defects or freezing of the flow front, or conversely, gas entrapment, potentially causing similar issues or bubble formation in the casting. Neither of these defects was acceptable. Two variations were considered in the gating system design: one using a single runner with five separate gates, and the other

with two runners along both sides of the casting and ten gates, with each runner supplying metal from each side of the roll, filling simultaneously from both ends. The size, shape, and volume of the feeders were evaluated based on specific simulation results and adjusted as needed for subsequent simulations. A schematic representation of the simulations performed is visible in Figure 5.

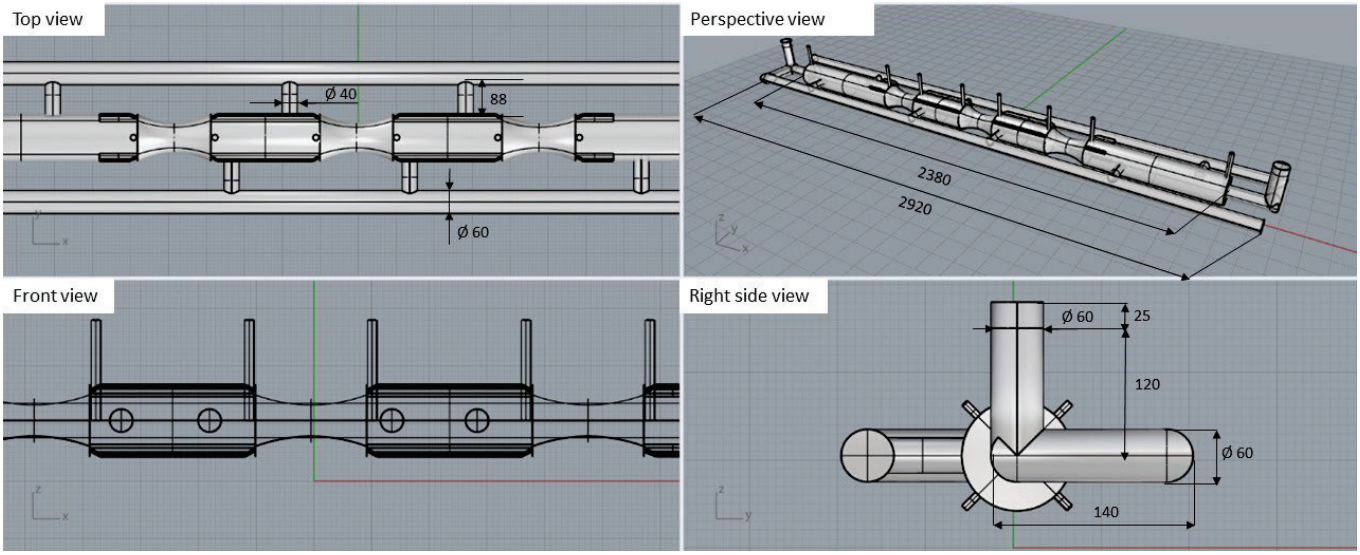


Figure 3. Design of roll casting and created 3D models in Rhinoceros 6.0 software.

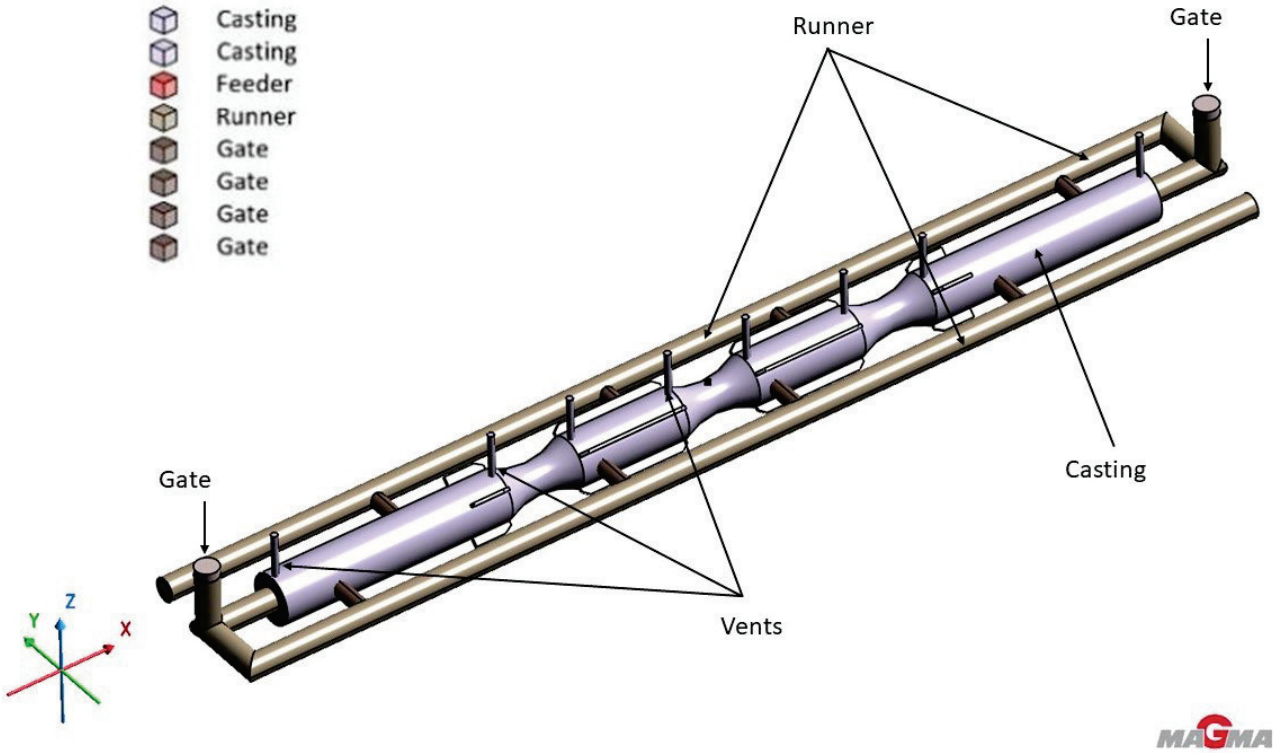


Figure 4. Geometry of the casting and one variant of gating system.

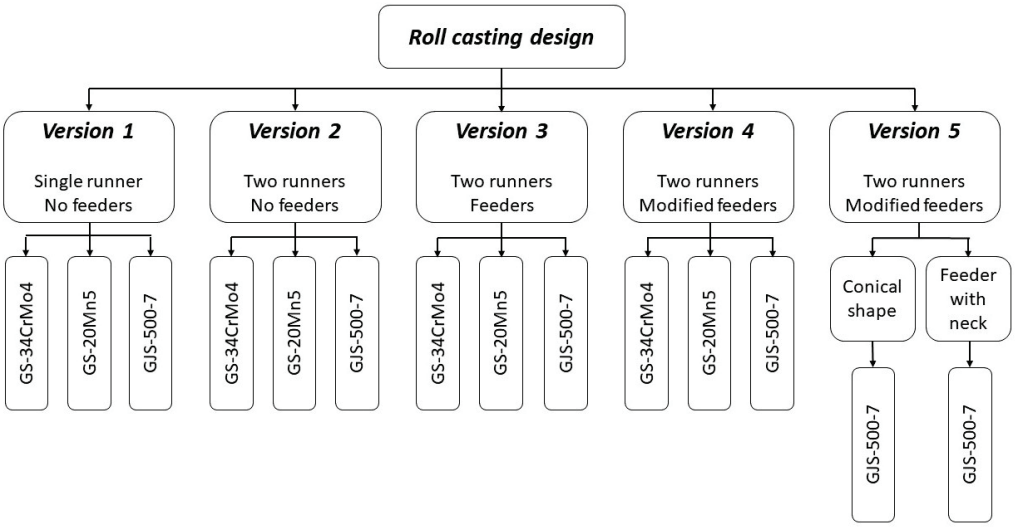


Figure 5. Schematic representation of the simulations performed.

2.3. Selection of Casting Material for Furnace Roll Simulations

Based on the required properties—primarily reducing the risk of cracks or fractures in the casting due to cyclic thermal stress—three casting alloys were selected for the simulations. Each material was chosen for its mechanical properties and potential advantages. The materials included cast steels GS-34CrMo4 (according to DIN 17205:1992 [42]), to replace the usually used welded steel 34CrMo4, and cast GS-20Mn5 (according to DIN EN 10293:2015 [43]), as well as ductile iron GJS-500-7 (according to EN 1563:2018 [44]). The steels for castings were chosen primarily based on their superior mechanical properties and durability compared to cast iron. The specific reasons for selecting each material, as well as any potential disadvantages, are provided below.

The alloyed steel GS-34CrMo4, compared to GS-20Mn5, offered primarily higher tensile strength, with values per standards ranging from 620 to 800 MPa. A roll made from this material would better withstand loading and stress, potentially extending its service life. The material's hardness reached 255 HB. However, this material would not be ideal for hardening, as it might be prone to notch formation and cracking. Its disadvantages also included poorer weldability.

For the manganese steel GS-20Mn5, the primary reason for selection was its excellent weldability, which would potentially allow for quick and easy repairs of the casting in case of damage during use. Its mechanical properties included a tensile strength ranging from 500 to 650 MPa, an impact toughness of 50 J/cm^2, and a hardness of 140–180 HB.

Ductile iron GJS-500-7, compared to the previous materials, exhibited an average tensile strength of 420–500 MPa according to standards. Its main advantages were generally excellent castability and lower susceptibility to volumetric changes compared to steel. These properties would be beneficial in the roll's manufacturing process, whether during casting or subsequent machining. Additionally, ductile iron featured low specific weight and could often forgo heat treatment.

The thermophysical properties of materials are shown in Table 1. Conductivity, viscosity, and other properties depend on temperature. This dependence Lambda (λ), used directly in simulations, is shown in Figure 6.

Table 1. Properties of the simulated materials used/thermophysical properties.

Material Type	Solidus Temperature [°C]	Liquidus Temperature [°C]	Thermo Criteria Temperature [°C]	Latent Heat [kJ/kg]	Surface Tension Coefficient [N/m]	Viscosity at Liquidus Temperature [m^2s]
GS-34CrMo4	1393	1496	1498	248	1.4960	8.0356×10^{-7}
GS-20Mn5	1428	1506	1508	256	1.4960	8.0476×10^{-7}
GJS-500-7	1166	1169	1166.3	210	1.3	1.6000×10^{-6}

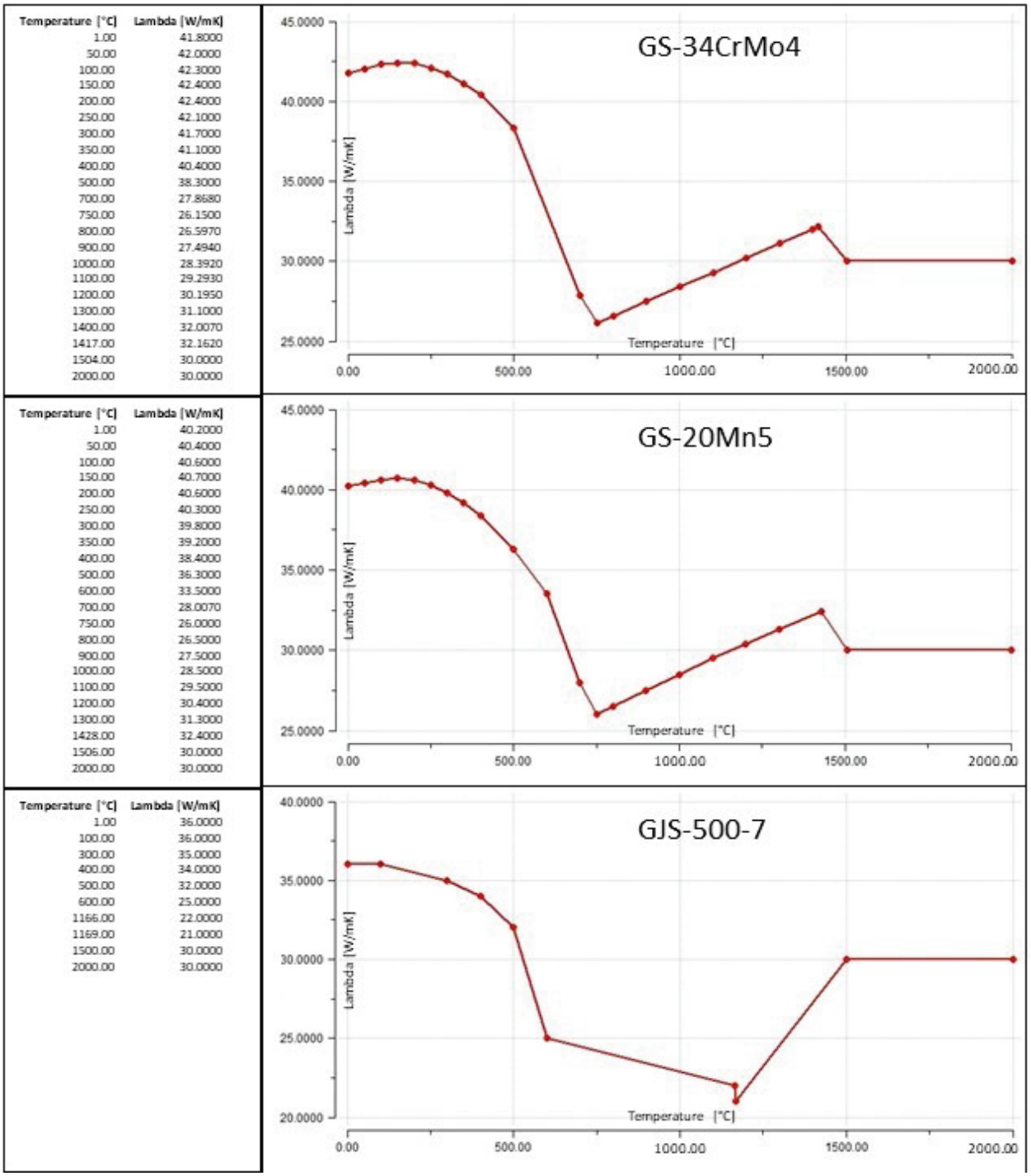


Figure 6. Lambda as function of temperature from simulation database.

2.4. Simulation Parameters

Each proposed version is based on the partial results of the previous simulated version. The goal was to achieve improved casting quality and increased utilization of liquid metal in the next simulation version. Specifically, the aim was to reduce internal porosity, relocate it to a less critical area near the geometric axis of the furnace roll, or ideally, eliminate it entirely.

With each successive series, the primary changes and modifications focused on adjusting the gating system and modifying the feeders. The resulting parameters of each simulation version, as they progressed chronologically, along with the degree of changes in each solution, are shown in the overview Table 2. Notably, there were changes in the feeders and pouring time. The weight of the castings themselves, excluding gating systems and feeders, remained essentially constant, with only minor differences due to internal porosity.

Table 2. Overview of simulated versions and their parameters.

Version [No.]	Temp. Init. [°C]	Material	Description Feeders/Gates	Mass Casting [kg]	Mass Feeder [kg]	Volume Feeder Pcs [cm^3]	Mass Gating System [kg]	Pouring Time [s]
1	1600	GS-34CrMo4	9 (cylinder)/5	187.0	9.7	155	64.3	27.5
1	1630	GS-20Mn5	9 (cylinder)/5	186.3	9.7	155	64.3	27.8
1	1400	GJS-500-7	9 (cylinder)/5	184.1	9.5	155	63.5	28.4
2	1600	GS-34CrMo4	0/10	186.5	0	0	129.3	15.7
2	1630	GS-20Mn5	0/10	185.7	0	0	128.8	15.7
2	1400	GJS-500-7	0/10	177.5	0	0	128.6	15.7
3	1600	GS-34CrMo4	10 (cylinder)/10	186.6	10.8	155	128.9	17.7
3	1630	GS-20Mn5	10 (cylinder)/10	185.8	10.7	155	128.4	18.0
4	1400	GJS-500-7	10 (cylinder)/10	183.6	10.6	155	126.9	18.0
4	1600	GS-34CrMo4	8 (elipsoid)/10	175.7	54.4	984	126.8	20.3
4	1630	GS-20Mn5	8 (elipsoid)/10	175.7	42.0	760	126.3	20.3
4	1400	GJS-500-7	8 (elipsoid)/10	173.7	41.4	758	125.0	20.3
5-conical	1400	GJS-500-7	8 (truncated cone)/10	177.5	16.4	300	127.3	16.7
5-with neck	1400	GJS-500-7	8 (inverted truncated cone/with neck)/10	181.5	25.3	463	125.0	18.7

The FVM method was always used for network design and evaluation. The Finite Volume Method (FVM) divides the entire geometry into individual sections—referred to as cells—for the purpose of numerical calculation. In Magmasoft, these cells typically take the shape of cubes or rectangular prisms. The mesh cell size used in the casting region was a cube with dimensions $5 \times 5 \times 5$ mm, while in the gating system, the maximum cell size was $5 \times 5 \times 10$ mm. Across the entire model, the prevailing cell size remained at 5 mm, maintaining consistency in mesh resolution. Refining the mesh contributes to a more accurate and reliable simulation, as it enables better detection of gradients and local variations between adjacent cells. This increased level of detail allows the simulation to capture subtle physical phenomena more precisely. However, the improvement in accuracy comes at the cost of increased computational time. The total number of metal cells within the simulation ranged from approximately 260,000 to 370,000, depending on the specific design of the casting and gating system. The quality of the mesh is assessed graphically, focusing on parameters such as Thin Walls, Blocked Cells, and Edge-to-Edge connections. In the evaluated meshes, only a few isolated problematic cells were identified. Given their low number and non-critical location, these cells had no significant impact on the overall accuracy of the simulation. Specifically, the number of problematic cells ranged from 26 to 54 for thin walls, 0 for blocked cells, and between 0 and 12 for edge-to-edge connections. Based on these values, the mesh was consistently evaluated as high-quality. In this case, the evaluation was conducted for the entire geometry, with special attention given

to the thinnest regions of the casting—particularly notches and blade sections—where finer resolution is essential to accurately capture complex flow behavior and thermal gradients.

2.5. Mathematical Formulations

The mathematical data (formulas, algorithms) are embedded in the software and are not publicly available. General principles are known, but how they are implemented or adapted is not disclosed. The user can only influence input data, such as initial temperatures, material type, heat transfer, etc. To discuss the general principles and methods used by Magmasoft, it is possible to examine the finite volume method (FVM). Below are the formulas that need to be established before using simulation software Magmasoft 6.0 and that are essential for performing preliminary calculations. Based on these results, the basic dimensions of the gating system, feeders, etc., are designed. The basic Equations (1)–(5) used are as follows [45,46]:

Calculation of pouring time according to Dietert:

$$\tau = s \times \sqrt[3]{m_h} \quad [\mathrm{s}] \tag{1}$$

where s is the coefficient chosen based on the wall thickness of the casting [mm] and m_h je is the raw weight of the casting [kg].

Calculation of the average metallostatic pressure if the notches are placed at the center of the casting:

$$h_{mid} = H - \frac{p^2}{2c} \quad [\mathrm{m}] \tag{2}$$

where H is the height between the molten metal level in the pouring basin and the center of the notches [m], p is the height of the mold cavity above the notches [m], and c is the height of the total mold cavity [m].

Calculation of the controlling cross-section area:

The controlling cross-section is most often the notch, which is the smallest cross-section in the gating system.

$$S_z{:}S_r{:}S_k/1{:}1.1{:}1.2$$

where S_z is the area of the notch [m^2], S_r is the area of the distributing channel [m^2], and S_k is the area of the lower dimension of the gating sprue [m^2].

The area of the notch is then calculated using the Equation (3).

$$S_z = \frac{m}{\tau \times \mu \times \rho \times \sqrt{2gh_{mid}}} \quad [\mathrm{m}^2] \tag{3}$$

where m is the mass of the casting with additions [kg], τ is the total pouring time [s], μ is the resistance coefficient against flow (0.38 for non-ferrous metals), ρ is the density of the poured metal [kg/m^3], g is the gravitational acceleration [m/s^2], and h_{mid} is the average metallostatic pressure [m].

Calculation of the feeder volume:

The feeder volume is a critical parameter for properly adding metal, and its value is calculated using Equation (4). Often, this value is only an approximation.

$$V_n = \frac{x \times \beta}{1 - x \times \beta} \times V_o \quad [\mathrm{m}^3] \tag{4}$$

where x is the feeder inefficiency coefficient, β is the coefficient of volume shrinkage of the alloy, and V_o is the volume of the casting [m^3].

Calculation of liquid metal utilization:

$$\iota = \frac{m_o}{m_s} \times 100 \quad [\%] \tag{5}$$

where m_o is the gross weight of the casting–with allowances for machining [kg] and m_s is the raw weight of the casting, including the gating system, feeders, and vents [kg].

3. Results and Discussion

3.1. Version 1: Gating System with Single Runner

In version 1, a single runner resembling the letter "L" was used, along with five gates (see Figure 7). The subsequent entry was achieved through direct and lateral connections to the future casting. The length of the runner matched the length of the furnace roll. This setup aimed for even filling of the mold cavity, along with sufficient speed and better utilization of liquid metal compared to the two-runner version.

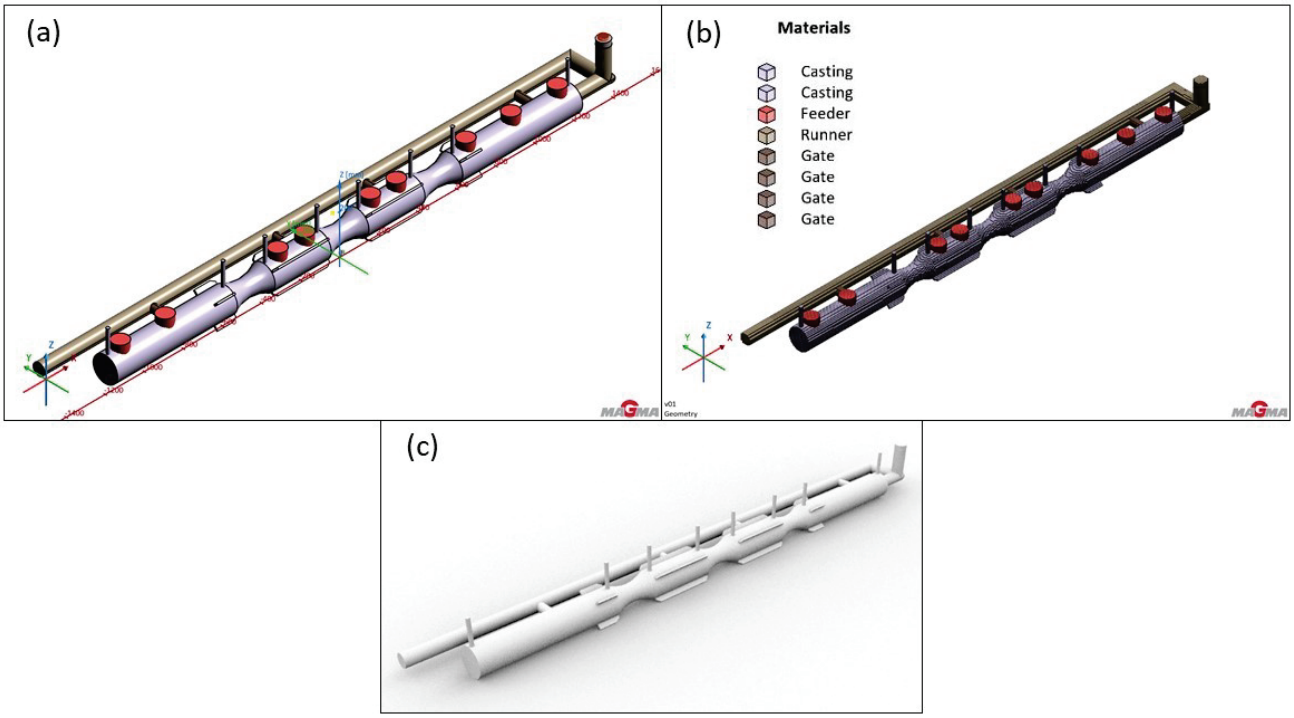


Figure 7. Version 1: Single runner design: (**a**) geometry; (**b**) mesh; (**c**) shape of the casting with the gating system and vents.

In the case of the GS-34CrMo4 material, the metal flow within the mold cavity was somewhat turbulent, which in real conditions could lead to erosion in certain mold areas (Figure 8). Notably, the filling time was relatively long, reaching 11 s. This material was highly susceptible to shrinkage and porosity. Although this susceptibility was anticipated, the level of defects in the casting was disproportionately high. Among the three simulated materials with this type of gating system, the chrome–molybdenum steel likely performed the worst. Figure 9b clearly shows porosity extending almost halfway into the casting cross-section. Higher defect content was represented by various color shades: yellow and beige indicate porosity around 100–70%, red to orange covers the range of 70–42%, while dark blue to blue-green represents 42–0%. This highlighted the need to focus on defect mitigation in future simulations, given the high percentage of these defects.

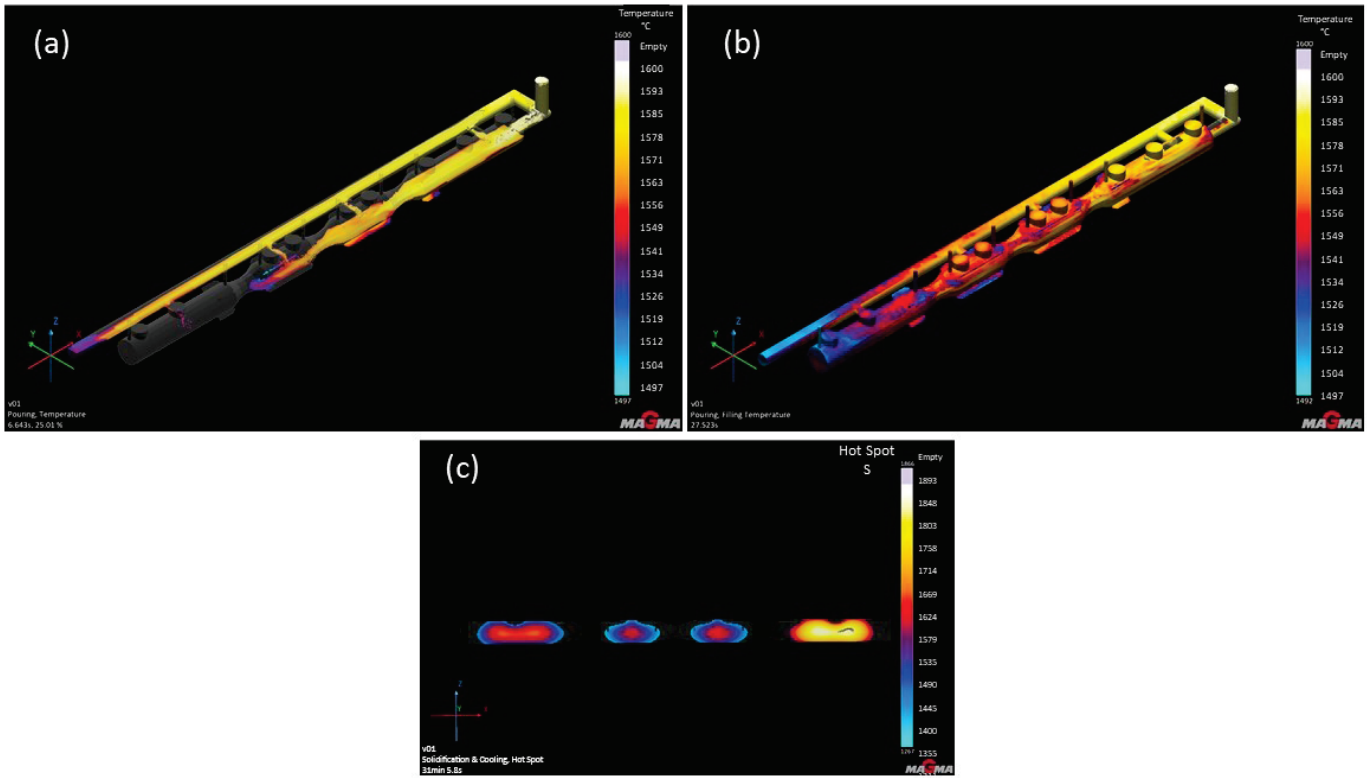


Figure 8. GS-34CrMo4 version 1: (**a**) pouring; (**b**) solidification and cooling; (**c**) hotspot result.

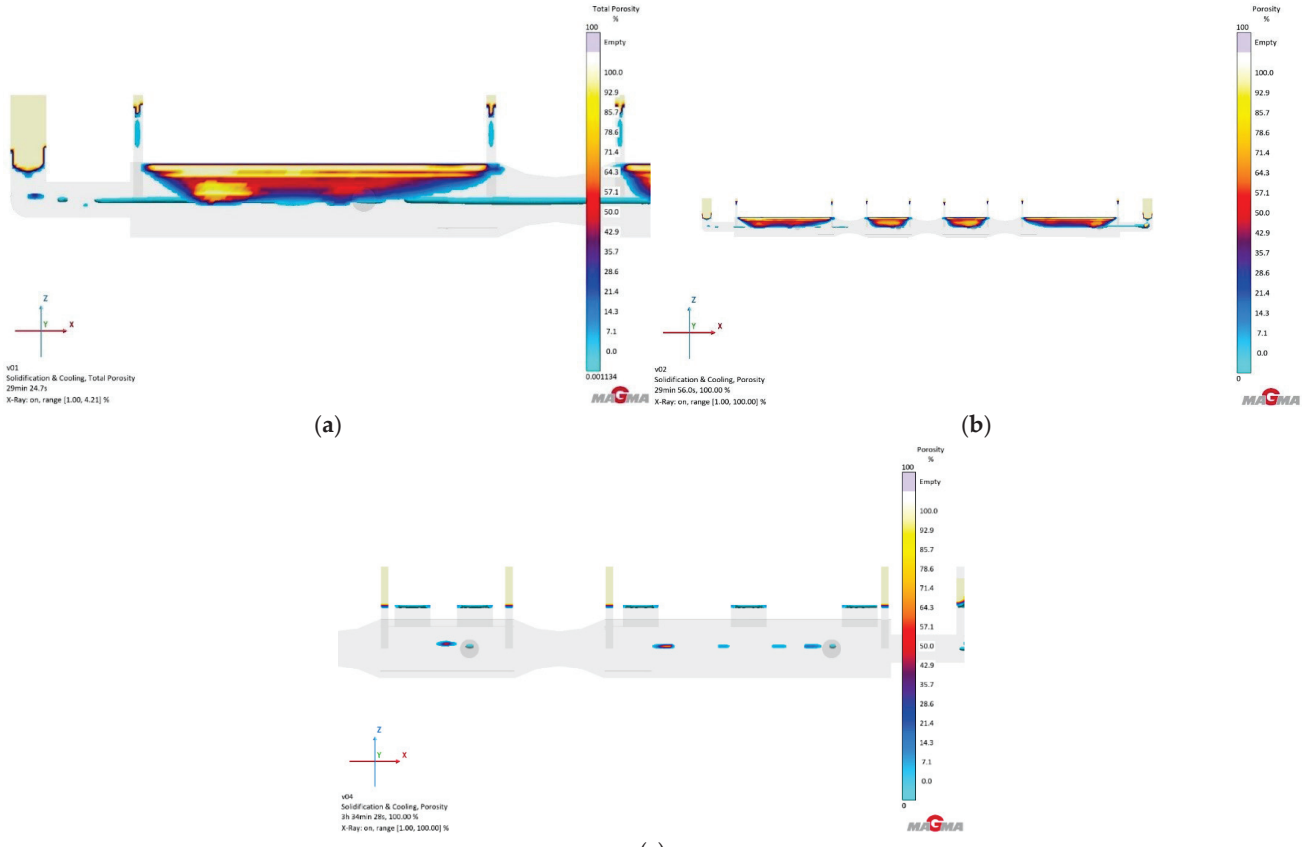


Figure 9. Total porosity results of version 1: (**a**) GS-34CrMo4; (**b**) GS-20Mn5; (**c**) GJS-500-7.

The simulation result for the single-runner configuration with GS-20Mn5 was comparable to GS-34CrMo4. Although some minor improvements were observable, the focus

remained on porosity percentages at various casting depths. It was immediately apparent that the material's susceptibility to shrinkage was slightly lower than that of Version 1. However, it still posed a significant issue, making it unsuitable for use, as was the case with the first material (Figure 9a).

When simulating the casting and solidification process and defect prediction for cast iron, it is important to note that, concerning volumetric changes and shrinkage, cast iron behaves entirely differently compared to cast steels, a difference confirmed in this experiment. Initially, two grades of ductile iron—GJS-500-7 and GJS-700-3—were considered for simulation. Ultimately, GJS-500-7 was chosen primarily for its lower susceptibility to volumetric changes and shrinkage. The simulation results indicated that the percentage of porosity was minimal, almost approaching zero. Although some minor porosity was observed in the casting's hotspots, it was negligible compared to the previous two steel simulations (Figure 9c).

The anticipated complications were partially confirmed. Metal flow into the mold was highly turbulent in all cases, with the highest pressure and metal velocity recorded at the first front gate and the second side gate. In these areas, mold erosion could occur, potentially altering the shape of the final casting. Another issue was metal cooling. Given the length and narrow profile of the casting, the single-runner simulation showed a temperature loss of several degrees Celsius as the metal flowed toward the mold's edge. This cooling was caused by the initial contact of the metal front with the surrounding atmosphere and mold, which further transferred heat, thus cooling it more significantly, potentially leading to issues with metal homogeneity.

Based on the results, several solutions or mitigation strategies were considered. The first option was to pour the metal from a greater height, which would increase the flow velocity and reduce the time the metal front was exposed to heat transfer. However, in real production, this would risk mold erosion and metal splashing, potentially resulting in inhomogeneity or the formation of so-called cold shuts. Another option was to increase the pouring temperature. Although the metal would still cool during flow, it would not reach a temperature that would compromise casting quality. However, a higher pouring temperature increased the risk of shrinkage formation, as the metal would cool more slowly, leading to greater volumetric changes. The final option was to modify the gating system. While this would reduce the utilization of liquid metal, the adjustment could ensure more even filling of the mold cavity with minimal metal cooling. Summary results of this simulated Version 1 are presented in Table 3.

Table 3. Results of the version 1 simulation with a single runner.

Material	Utilization of Liquid Metal [%]	Porosity [%]
GS-34CrMo4	78	95
GS-20Mn5	78	86
GJS-500-7	78	42

3.2. Version 2: Gating System with Two Runners

In the first series of simulations with a single runner, it was observed that the mold cavity filling was not entirely smooth. Although the cavity was fully filled, the pouring time was relatively long. This could pose a problem when using feeders, as they would increase the required metal volume for casting, thus raising the risk of misruns in the boundary areas of the casting or within the feeders. For this reason, a variant with two runners was also tested (see Figure 10). Although the utilization of liquid metal was 7% lower, the cavity filling was more uniform and faster. In the previous version, it was mentioned that porosity would need to be addressed with feeders; however, feeders were

intentionally omitted in this version. The aim was to verify whether the gates alone could partially act as feeders, helping to compensate for volumetric changes during solidification. The goal was to determine if doubling the number of gates would impact the casting's porosity outcomes.

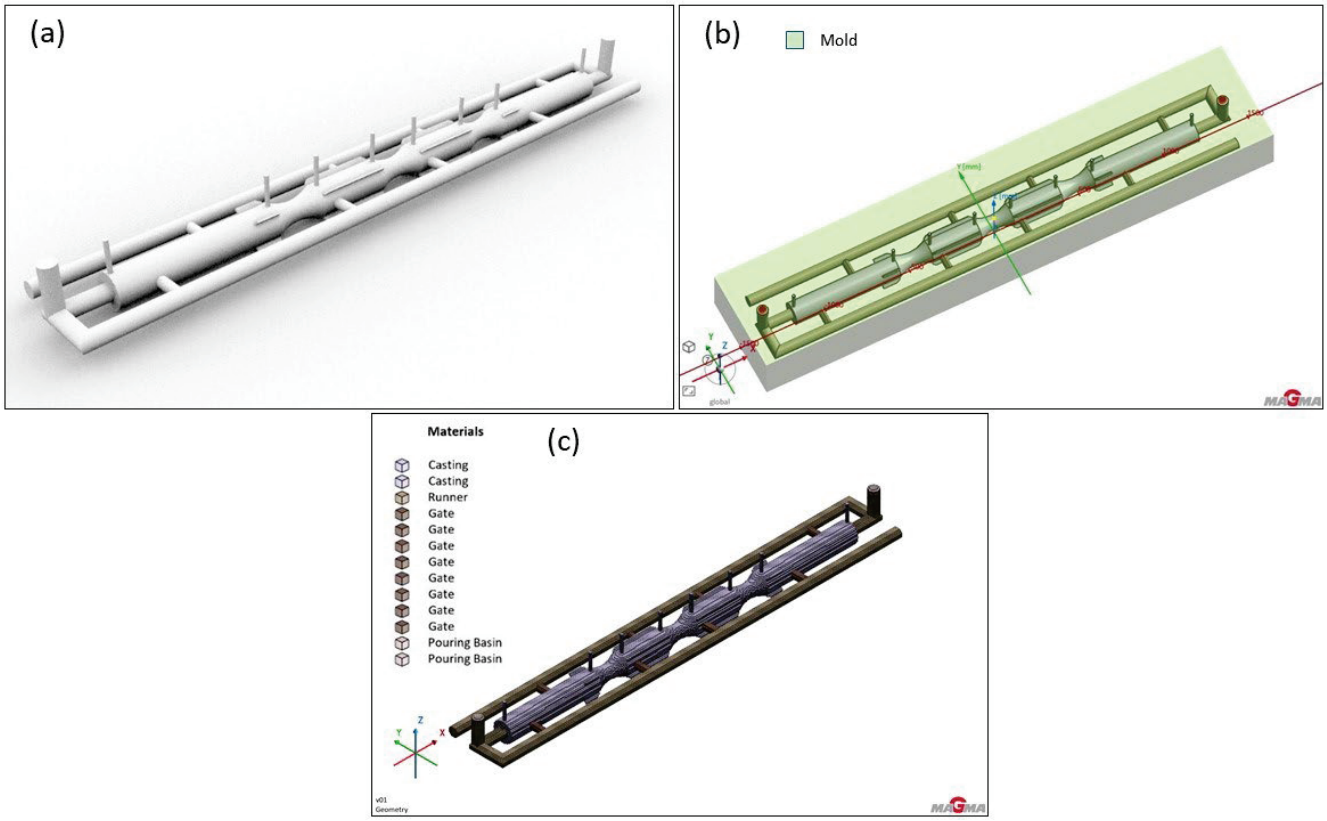


Figure 10. Version 2: Two runners design: (**a**) shape of the casting with the gating system and vents; (**b**) geometry in the simulated sand mold, (**c**) mesh with the gating system.

Although the change in the gating system was expected to reduce porosity in the casting made from GS-34CrMo4, there were no significant improvements, as seen in Figure 8a. Porosity was slightly reduced, but no substantial shift occurred. Using such a roll in real operation would lead to a very short service life, likely ending with the formation of cracks and subsequent fracture. Similarly, there were no significant changes in the GS-20Mn5 variant (see Figure 11b). The porosity in the central part of the casting decreased only by a few percentage points. This roll would be unsuitable for use. Future simulations with GS-20Mn5 and GS-34CrMo4 will need to incorporate feeders, as both materials exhibit a high tendency toward shrinkage, making the use of feeders essential. Although the previous GJS-500-7 simulation showed minimal porosity in the roll, it was necessary to determine the impact of two gating channels with double the number of gates on the material's cooling and formation. The gates could partially function as feeders, thereby reducing shrinkage formation. The result was somewhat better than Version 1 (one runner), but still not a major improvement, as seen in Figure 11c. Although porosity was recorded during the simulation, it would most likely not have a significant impact on the roll's quality and service life.

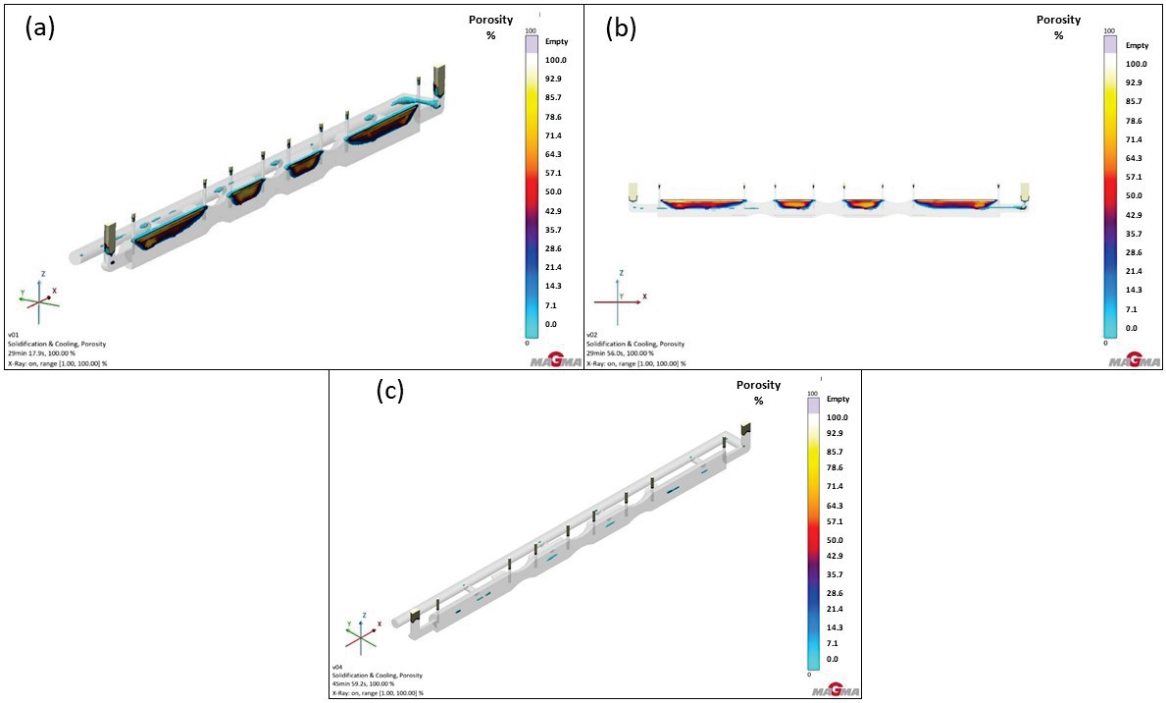


Figure 11. Total porosity results of version 2: (**a**) GS-34CrMo4; (**b**) GS-20Mn5; (**c**) GJS-500-7.

Unlike the previous series of simulations, two runners with double the number of gates were now used. This increase aimed primarily to allow faster and more uniform metal flow within the mold cavity, as previous simulations suggested that mold erosion might occur, potentially altering the casting's shape. It was also expected that defects in the form of porosity and shrinkage might at least partially decrease, as the gates themselves could somewhat serve as feeders, supplying metal to critical areas of the casting.

After implementing these adjustments, it was observed that the metal filled the mold cavity significantly better, potentially preventing metal impacts on the mold and subsequent erosion. This improvement was also supported by gating from both sides, with metal flows meeting and merging in the center of the casting. This filling method also reduced the pronounced cooling of the metal front, which was an issue in previous simulations.

However, the expected significant reduction in defects did not occur. Although the gates partially acted as feeders, the feeding was insufficient to fully replace feeders or lead to a notable improvement in quality. Therefore, it was decided that some form of feeding would need to be incorporated into future simulations.

Among the three materials used, both cast steels yielded the poorest results. While the GS-20Mn5 material showed a partial improvement in the percentage of porosity, the changes were not significant. Ductile iron GJS-500-7 performed the best, with porosity observed at only a few percent, which would likely not impact the operational use of the roll. According to standards, this material also exhibited high wear resistance and lower weight or density compared to both grades of steel. Summary results for simulated Version 2 are shown in Table 4.

Table 4. Results of the version 2 simulation with two runners.

Material	Utilization of Liquid Metal [%]	Porosity [%]
GS-34CrMo4	71	92
GS-20Mn5	71	85
GJS-500-7	71	35

3.3. Version 3: Gating System with Two Runners and Feeders

Due to recurring issues with excessive porosity in both versions 1 and 2, it was decided to use feeders (see Figure 12). Their purpose was to supply liquid metal to hotspots during the casting's solidification, specifically targeting areas where the casting solidified last. This would ensure that, as volumetric changes occurred—which are typical for any material—shrinkage would not lead to cavity formation or imperfect material bonding, thus preventing porosity. Hotspots were identified based on simulations (see Figure 13), and feeders were then strategically positioned accordingly.

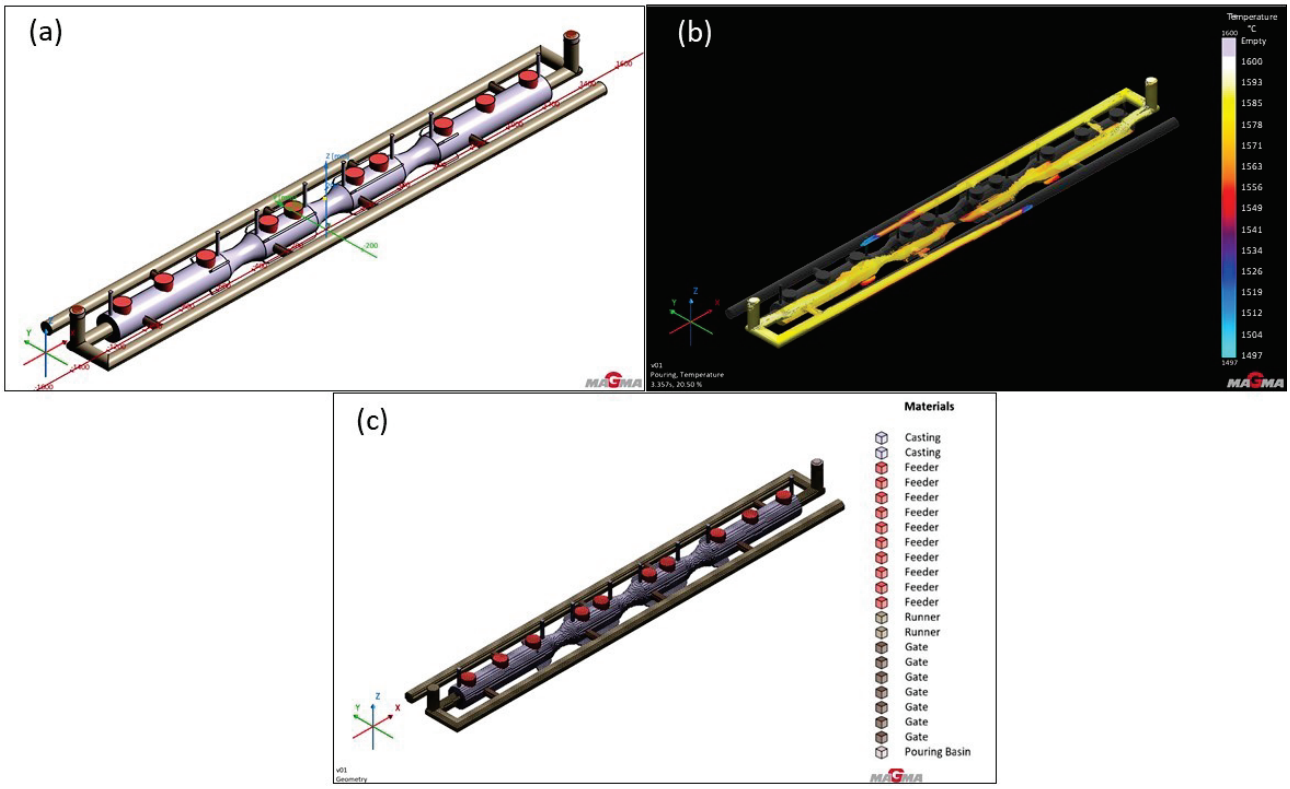


Figure 12. Version 3: Two runners and feeders design: (**a**) shape of the casting with geometry; (**b**) pouring; (**c**) mesh with gating system and feeders.

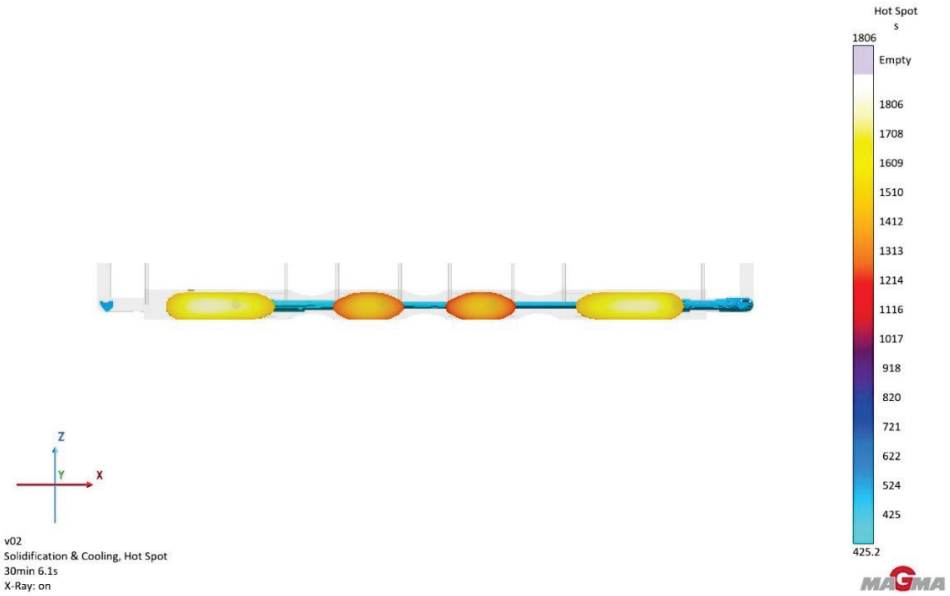


Figure 13. Version 3: areas of hotspots.

The main change from simulations in Versions 1 and 2 for the GS-34CrMo4 material was the addition of ten individual feeders to the casting, positioned based on hotspot locations. The largest hotspot was located on both end sections of the furnace roll, where the material was thickest, leading to limited heat dissipation. For this reason, feeders were placed in these areas to cover the critical zones and supply an adequate amount of metal. However, after running the simulation, it became apparent that, although the feeders functioned as intended and their volume was effectively utilized to replenish metal in the hotspots, they were significantly undersized and thus insufficient to fully compensate for the shrinkage in the feeder. Their modification will be necessary in the next series of simulations. It should also be noted that this simulated material exhibited the highest susceptibility to volumetric changes among all three materials, as shown in Figure 14a.

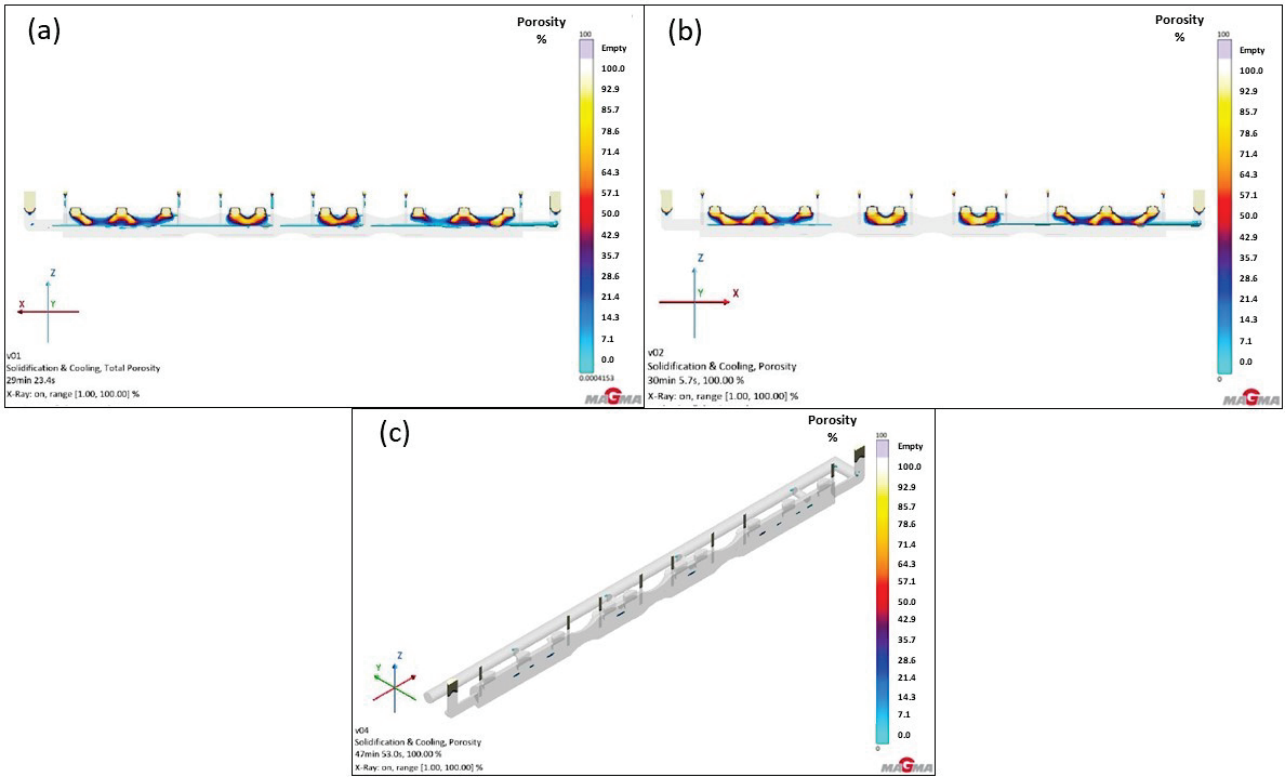


Figure 14. Total porosity results of version 3: (**a**) GS-34CrMo4; (**b**) GS-20Mn5; (**c**) GJS-500-7.

Similar to previous simulations with GS-20Mn5, there was no substantial difference from the prior test. However, a notable shift of defects into the feeder was observed, accounting for approximately 30% of the total porosity. Figure 14b displays the percentage distribution: beige areas in the feeders indicate 100% shrinkage, followed by 80–90% marked in yellow. A gradual transition into the casting body is clearly visible, with colors shifting from orange to red and eventually to blue. Orange represents porosity of 70–60%, while red indicates 50%, primarily located in the central casting area. Blue areas correspond to a range of 30–0%, found in and beyond the central casting region. This confirms that the feeders were functional in partially feeding metal into the hotspot, but they were not large enough. Their shape, which did not fully cover the hotspot area, might also have been a factor. Further focus on optimizing this design will be necessary.

As the GJS-500-7 material exhibited very low shrinkage tendency, the issue of volumetric changes was less significant compared to the steels. However, compared to the previous simulation without feeders, a few percentage points decrease in porosity was evident in this case (see Figure 14c). A closer inspection revealed porosity only in the casting center, with the highest percentage reaching approximately 48%. This presence was negligible, as

the actual shrinkage dimensions in the casting would likely be around 5 mm in height and approximately 25 mm in length.

Although a completely flawless casting without internal defects has yet to be achieved, the results represent significant progress compared to the initial simulations. Particularly valuable was the improvement in the gating system for such a complex casting shape, allowing for smooth and uniform filling without unwanted anomalies. Thorough monitoring of the simulated material's behavior now provides a much clearer understanding of its properties, enabling more precise optimization of casting conditions.

Future simulations will therefore focus on modified feeders with a larger volume and a shape better suited to the hotspots to more effectively fulfill their function. An interesting adjustment will also be the modification of runners, mainly to eliminate backflow. This change is intended to prevent the molten metal from hitting the back wall of the channel, as observed in the simulation, which slows down the flow and reduces the efficiency of filling the gates. Summary results of simulated Version 3 are shown in Table 5.

Table 5. Results of the version 3 simulation with two runners and feeders.

Material	Utilization of Liquid Metal [%]	Porosity [%]
GS-34CrMo4	68	82
GS-20Mn5	68	80
GJS-500-7	68	32

3.4. Version 4: Gating System with Two Runners and Modified Feeders

Previous simulations demonstrated that, especially for steels with a high tendency for shrinkage, feeders are essential. In Version 3, feeders were indeed used, but their size proved to be significantly undersized, limiting their efficiency to approximately 40%. For this reason, the next series of simulations introduced major changes in both the size and shape of the feeders, as the previous design did not sufficiently match the placement of hotspots within the casting. Instead of cylindrical feeders, oval ones were selected, better contouring the areas with hotspots. Their volume was also substantially increased (as shown in Table 2), leading to improved feeding capacity and better outcomes. These changes are expected to be particularly effective for steels where substantial feeding is required. The adjustments are visible in Figure 15.

In previous simulations, the GS-34CrMo4 material exhibited the worst results. Although it was expected that the utilization of liquid metal would be relatively low with the modified, more massive feeders, a significant improvement in casting quality was anticipated. These expectations were confirmed following the simulation. The changes proved effective, and the feeder functioned much better than in the previous Version 3, thanks to the increased volume and altered shape. As a result, porosity and shrinkage were significantly relocated to the feeder, which would subsequently be removed after production. Nevertheless, the outcome was not entirely satisfactory—approximately 25% of the defect volume remained in the casting, which was not fully optimal. The porosity percentage under the feeders in the casting reached 30–50%, indicating the need for further optimization (see Figure 16a).

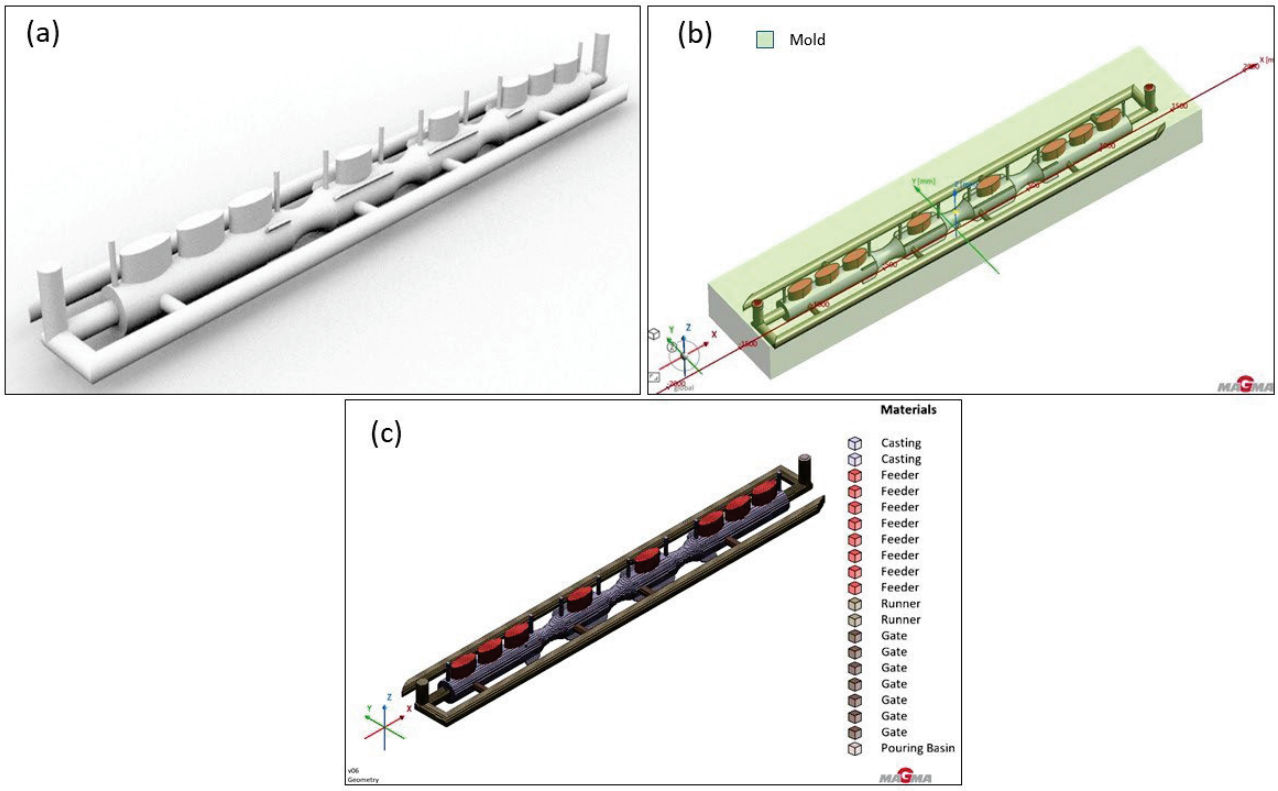


Figure 15. Version 4: Two runners and modified feeders: (**a**) shape of the casting with the gating system and feeders; (**b**) geometry in the simulated sand mold; (**c**) mesh with the gating system.

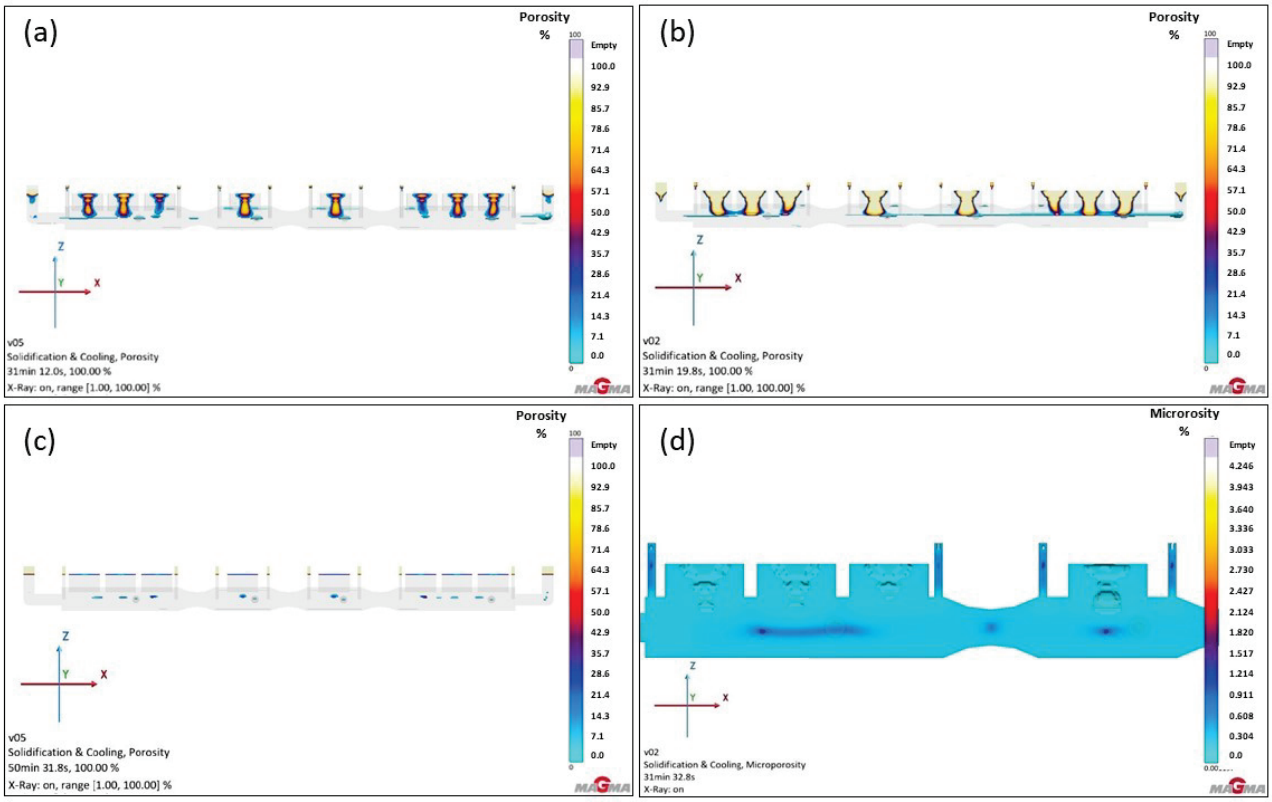


Figure 16. Total porosity results of version 4: (**a**) GS-34CrMo4; (**b**) GS-20Mn5; (**c**) GJS-500-7; (**d**) detail of smaller shrinkage in third feeder for GS-20Mn5.

Surprisingly, simulations with GS-20Mn5 material showed slightly worse results than with GS-34CrMo4. Although the defects penetrated the casting almost identically, their percentage in the casting beneath the feeders differed, in the range of around 80–90%. The microporosity visualization revealed large cavities, more extensive than in the previous version. In both cases, it was evident that defects were less prominent in the narrower parts of the furnace roll, due to the faster solidification of metal in these areas, shifting the defects.

The GJS-500-7 material demonstrated the best performance in terms of defects among the three materials, as seen in previous simulations. Nevertheless, Version 4 was simulated to assess the impact of a larger feeder volume. Simulation results of Version 4 indicated an improvement over previous simulations with this material, primarily in reducing the percentage of defects in critical casting areas, now not exceeding 20%. These critical areas are shown in light blue in Figure 16c. However, the use of such massive feeders significantly increased the liquid metal consumption, raising questions about the economic viability of Version 4 for this material, as the improvement was minimal. Given the placement and extent of defects, it is likely that even a higher defect ratio would not cause major issues during the roll's use, as the porosity is centrally located in the roll. If further reduction in these defects is required, options could include metallurgical adjustments, changes to the pouring temperature, or the placement of external chillers, which could help reduce these types of defects further.

Compared to the previous series of simulations, where feeders were applied to the casting's critical areas but proved undersized, this phase showed a marked improvement. The feeders were significantly enlarged, and their shape was modified to better meet the feeding requirements. For both GS-34CrMo4 and GS-20Mn5 materials, this adjustment reduced shrinkage by approximately 40%, representing a significant advancement, though it did not entirely eliminate the defect. A portion of the shrinkage still extends into the casting, complicating its practical application. Summary results of simulated Version 4 are shown in Table 6.

Table 6. Results of the version 4 simulation with two runners and modified feeders.

Material	Utilization of Liquid Metal [%]	Porosity [%]
GS-34CrMo4	49	70
GS-20Mn5	49	85
GJS-500-7	49	23

Completely eliminating this defect would require even larger feeders or further optimization of their shape. A possible solution could involve using a massive chiller or an elongated feeder on problematic sections of the furnace roll, which would shift the hotspot and divert shrinkage away from the roll. However, this approach would result in low utilization of liquid metal and complicate subsequent machining. For these reasons, using the GJS-500-7 material appears to be a more suitable choice, as it better meets production requirements.

3.5. Version 5: GJS-500-7 Simulation with Various Feeders

Based on the conducted simulations, the GJS-500-7 material—ductile iron with graphite nodules—achieved the best results. Thanks to its properties, it demonstrated less susceptibility to volumetric changes and shrinkage formation. This also reduced the need for feeders compared to steels, which have a higher tendency for shrinkage. Additionally, this material theoretically provides adequate strength and durability properties for the intended use of the final casting.

In practice, minor shrinkage, primarily in the central part of the furnace roll, could be an issue. The goal, therefore, was to completely eliminate or at least minimize these defects. Initial simulations with feeders suggested that, unlike steel, where feeder volume is crucial, ductile iron benefits more from adjustments to the feeder's shape and type. For this reason, additional simulations were performed to determine which feeder type would best suit the casting design and minimize defects. Cone-shaped feeders and necked feeders were designed, with their shapes shown in Figure 17. Parameter changes (volume and others) are detailed in Table 2. Both feeder versions and their resulting effectiveness are presented in Figure 18.

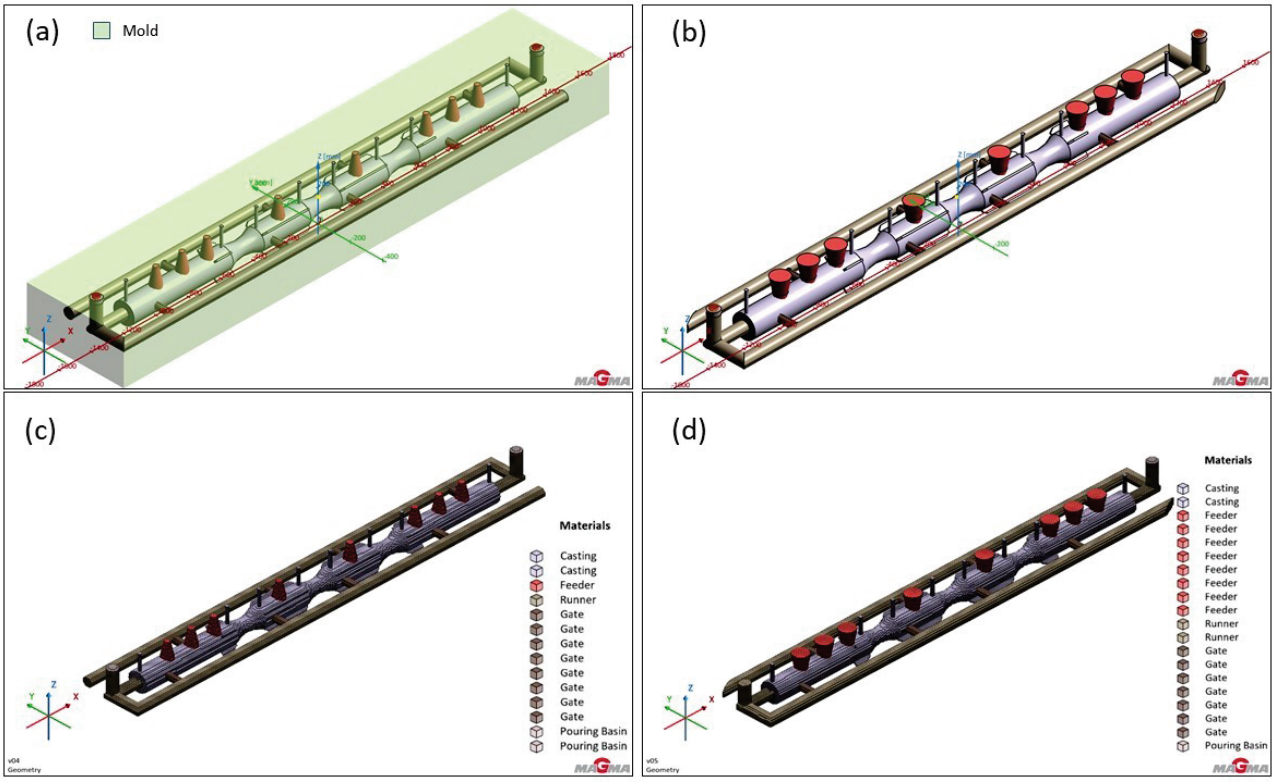


Figure 17. Version 5: Change in feeder shape for GJS-500-7: (**a**) conical feeder geometry in the mold; (**b**) feeder with neck geometry; (**c**) mesh for conical feeder; (**d**) mesh for feeder with neck.

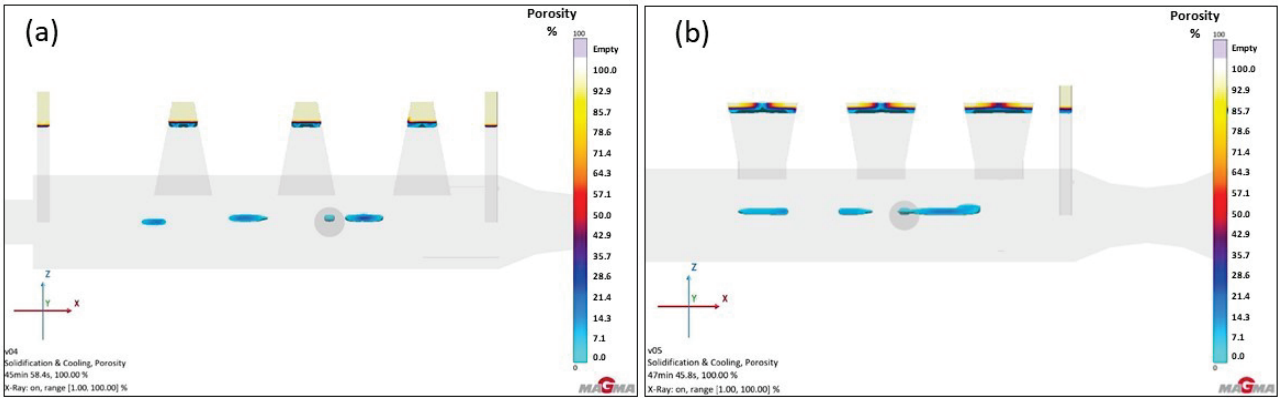


Figure 18. Total porosity results of version 5: (**a**) conical feeder; (**b**) feeder with neck.

The cone-shaped feeder proved advantageous, especially for more efficient utilization of liquid metal compared to the previously assessed Version 4. Due to its conical shape, this feeder covered a larger portion of the casting's hotspot, allowing it to supply the necessary amount of metal. When comparing porosity with the previous version, this

feeder type undeniably delivered better results. Although some porosity remained in the casting, its percentage was reduced, with a maximum value of approximately 16%, which is considered low.

The results for the necked feeder were nearly identical to those of Version 4. While the color display of porosity occurrence indicated slightly higher values (a larger colored area), the percentage did not exceed 7%. In the color display, only light blue shading is visible, without the dark blue center that indicated higher porosity probability in the cone-shaped feeder. The necked feeder thus represented almost a 50% improvement over the cone-shaped feeders. However, the higher incidence of porosity suggested poorer coverage of the hotspot, which could potentially be resolved by increasing the number of these feeders. Detailed results for the feeders in Version 5 are shown in Table 7.

Table 7. Results of the version 5 simulation of GJS-500-7 with various feeders.

Feeder Shape	Utilization of Liquid Metal [%]	Porosity [%]
Conical	54	7
With neck	55	12

3.6. Summary of Results for All Simulated Versions

The simulations began with modifications to the furnace roll design, primarily to simplify production and prevent specific defects, such as misruns, poor metal homogeneity, or internal stresses. The proposed shape maintained uniform wall thickness throughout the casting and minimized sharp edges and transitions that could serve as stress initiators in the future. The only element retained from the original design was the thin fins, serving as guide rails to ensure the proper direction of movement for the heat-treated pressure cylinder.

After modifying the design, attention turned to the gating system and mold cavity filling. Given the challenging shape of the casting, especially its length, issues such as misruns were anticipated. This type of defect arises from rapid cooling of the metal or an inadequately dimensioned gating system that cannot deliver metal to the mold cavity quickly enough, leading to cooling before full filling. In the first simulation, one runner and five gates were used. Although the filling was successful, the fill time reached approximately 17 s, which was too long. These initial simulations were conducted without feeders, anticipating that the metal volume for the final design would be much higher. Adding a second runner with double the gates reduced the filling time by nearly half and resulted in more uniform cavity filling. Theoretically, a single runner with five gates might suffice for ductile iron, given its lower density compared to steel, along with a reduced need for feeders, as this material showed a lower tendency for volumetric changes.

It was expected from the start that steel would require feeders, which was confirmed during the initial simulations. Comprehensive graphs in Figures 19 and 20 showed high levels of porosity, which was expected for the early simulations. The use of initial feeders did not significantly reduce porosity, indicating the need for larger feeders. The feeder shape was subsequently changed from circular to oval, which better covered the hotspot distribution, and the increased volume provided improved feeding of liquid metal. Of the total 16 simulations, the best results were achieved with GJS-500-7 ductile iron. Although its volumetric shrinkage was the lowest, some porosity remained in the center of the furnace roll. The best outcomes were observed with the cone-shaped feeders, where porosity ranged between 7–10%, and liquid metal utilization was more efficient than with the larger feeders for steel. The lower porosity with cone-shaped feeders was attributed to the faster solidification of certain furnace roll sections. Despite the anticipated better results with larger feeders in previous versions, the effect was less favorable due to the shifting of the

hotspot, which slowed metal solidification in specific furnace roll areas, particularly in sections with recesses for the cylinder.

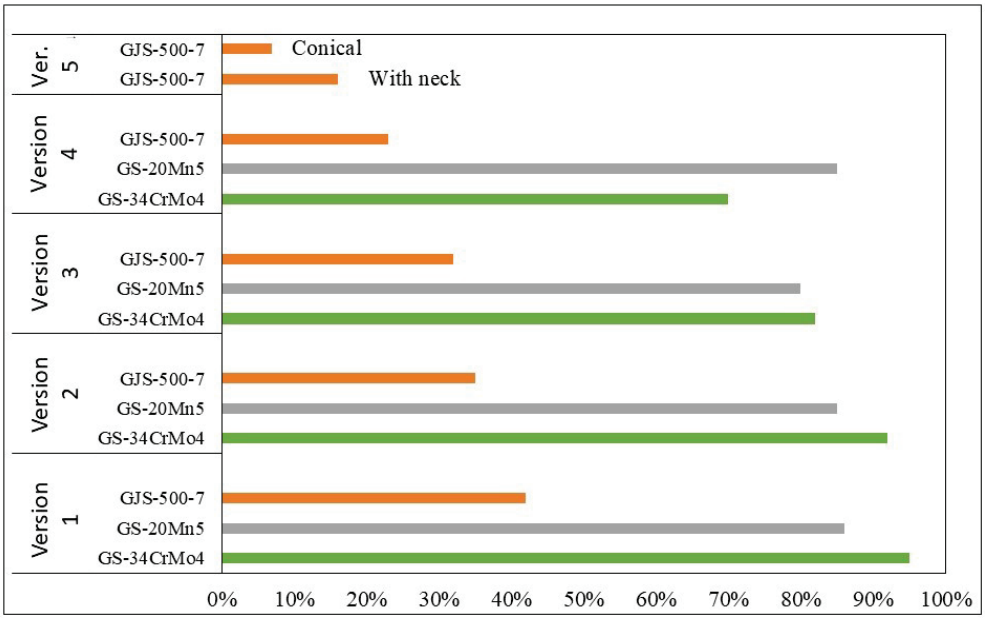


Figure 19. Comparison of porosity results across simulation versions and materials.

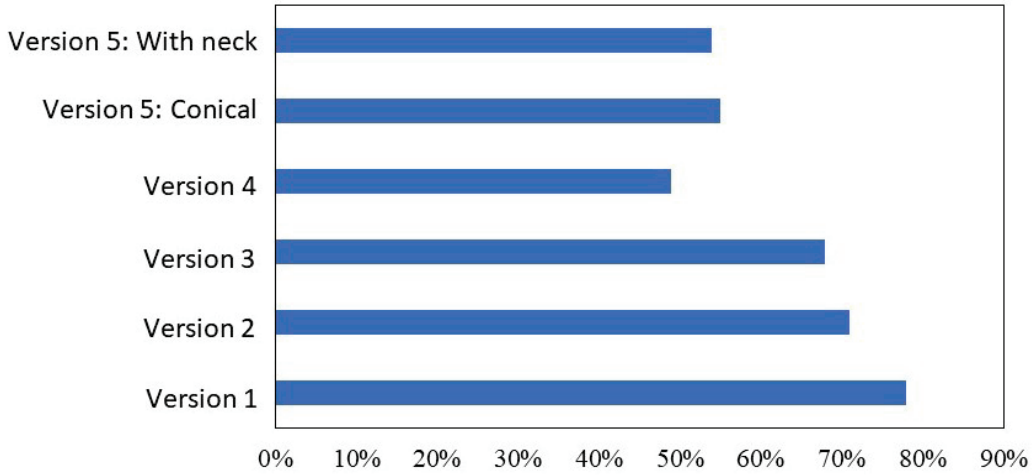


Figure 20. Comparison of utilization of liquid metal results across simulation versions and materials.

Statistical significance of all 16 simulations is not relevant here, as the software calculates something different each time. Each version has different settings, leading to different results. Distinct parameters thus produce different outcomes, which the user then evaluates to determine the most suitable option. With identical settings, the result will be the same after each calculation.

In both steels, porosity was significantly present, and despite using very massive feeders, it was not possible to optimize the casting to be free of defects. This approach would also require high material consumption, which would be inefficient with uncertain results. The best outcome was achieved with the GS-34CrMo4 material using very massive feeders (see Figure 16a). During the simulation, it was clear that the feeder functioned correctly, as a large portion of the shrinkage moved into it. However, the result was not entirely defect-free, though it was the best among the steel simulations. This was due to both the material, which had a lower tendency for volumetric changes than GS-20Mn5, and the effectiveness of the massive feeder. Further increasing the feeder volume could

theoretically yield a defect-free casting, but its production would be highly inefficient, as the amount of metal for the feeder would nearly equal the metal used in the casting itself.

According to the results obtained, the most suitable production version for manufacturing the furnace roll appeared to be the use of GJS-500-7, a ductile iron. Although its strength was the lowest among all materials, it was sufficient for the intended purpose. All defects were also concentrated in the central part of the casting near the geometric axis, where they posed a lower risk due to low mechanical stress (mainly heat stress) when used. In furnace rolls used in annealing furnaces, which are subjected to thermal cycling and surface wear, internal defects such as minor porosity and shrinkage cavities along the central axis of the roll may have minimal impact on functionality. This assumption is based on several factors. Defects located along the central axis are distant from the surface, which undergoes direct mechanical and thermal stresses; therefore, their influence on surface properties and wear resistance is limited. The primary stress on furnace rolls is thermal cycling and surface wear, so internal defects, if not extensive, usually do not negatively impact the roll's ability to withstand these conditions. Minor porosities and shrinkage cavities often do not significantly affect the material's mechanical properties, particularly if they are not associated with surface cracks or other defects that could initiate failure. According to the study [47], internal defects and stresses can affect the dimensional stability of castings, but the impact of these defects largely depends on their location and specific operational conditions. This study emphasizes that defects along the central axis can be of less concern if they are not subjected to direct stress. Another source [48] discusses how internal defects like porosity and shrinkage can impact the mechanical properties of castings. The study highlights that the criticality of these defects depends on their size, distribution, and the operational stresses encountered. The results of these studies suggest that minor internal defects along the central axis of a furnace roll will not have a significant impact on functionality if the roll is only subjected to thermal and surface wear. However, to ensure reliable performance, it is recommended to conduct a detailed analysis that includes the type, size, and location of defects, as well as the operational conditions under which the roll will be used.

Additional advantages included adequate thermal resistance and a lower tendency for shrinkage, which was crucial for this type of product with limited options for feeding and design adjustments. Other benefits included excellent foundry properties and potentially lower production costs due to the material's lower density, resulting in a lighter raw casting and subsequently reduced molten metal requirements. It is also worth noting the theoretical reduction in finishing time due to a decreased need for feeder application or the use of necked feeders, which represent a smaller area on the casting that would require grinding.

Potential inaccuracies in the software may be caused by outdated or inaccurate data. Furthermore, discrepancies between practical parameters and those used in the simulation can contribute to inaccuracies. Additionally, the fineness of the computational mesh is a factor, as an overly coarse mesh can yield imprecise results. Moreover, exceptional physical and specific real-time conditions in foundry operations can affect the results differently than in the simulation. Last but not least, inaccuracies may arise under pressure for rapid computation. Simplifying parameters can speed up the acquisition of results, but the outcome may not be entirely precise. The similarities and settings across programs are discussed in articles [33,49], and minor deviations found in the programs have been corrected.

Inaccuracies are not included in the experiment because the risks described above have been eliminated. However, two areas must not be overlooked: adherence to parameters, operator supervision, and alignment of results with initial production. If all production process conditions/settings based on the Magma results are not followed in actual production, deviations may occur. By strictly adhering to all settings, simulation results can be

compared with real production, allowing for fine-tuning of software settings for subsequent calculations, which will then better align with the specific production environment and thus be even more accurate. Without comparison to specific in-plant production, results may differ slightly, though not enough to undermine reliability. Inaccuracies are more likely expected from human factors, such as variations in the operation of the pouring ladle, etc. This can be minimized, for example, by consistently using the same operators.

4. Conclusions

The goal of the simulations and subsequent design modifications was to identify the optimal production technology for the furnace roll with minimal internal defects that could impact its functionality. The novelty of the numerical modeling approach lies in the application of an iterative simulation process to optimize the casting and gating design of an already industrially used, geometrically fixed component. Despite strict production limitations that did not allow significant geometric modifications, the simulations enabled the identification and comparison of defect tendencies (porosity and shrinkage) across different materials, and the optimization of feeders and gating systems to achieve defect minimization. This approach demonstrates a practical integration of numerical simulation into real foundry production, directly supporting decision-making in material selection and process optimization for a complex, large casting such as the furnace roll. The most significant findings are as follows:

1. It was necessary to modify the casting design to minimize sharp edges and transitions, thereby reducing susceptibility to internal stresses. However, key features, such as guide rails, essential for correctly directing the movement of the cylinder in the quenching furnace, needed to be retained.
2. Given the complex casting shape, simulations identified that the most suitable approach was to use two runners with gating channels, ensuring uniform and sufficiently rapid mold filling, which is crucial for achieving a quality casting.
3. Simulations revealed that the cast steel alloys (GS-34CrMo4 and GS-20Mn5) exhibited a high tendency for linear and volumetric shrinkage, which is typical for cast steel in general. However, despite the fact that it was possible to eliminate extensive volumetric shrinkage, the large amount of shrinkage porosity was still present and difficult to eliminate, even with various types of feeders. In contrast, GJS-500-7 ductile iron showed a much lower level of these defects due to its reduced tendency for volumetric changes.
4. In the case of steels, feeders were inefficient due to the fixed casting design, as they required large amounts of liquid metal, resulting in an uneconomical production process with potentially complex finishing. However, for GJS-500-7, a smaller feeder volume was sufficient to achieve the desired quality, which could hypothetically contribute to greater efficiency and cost-effectiveness in production.
5. Of the sixteen simulations conducted, GJS-500-7 (ductile iron) yielded the most satisfactory results. Defects were minimized to a nearly negligible level, allowing it to be used in practice without issues. All defects were also concentrated in the central part of the casting near the geometric axis, where they posed a lower risk due to low mechanical stress (mainly heat stress) when used. Due to its lower shrinkage and reduced defect occurrence, this material was better suited to the specific properties of this casting.

Based on the simulation results, GJS-500-7 appears to be the most suitable version for manufacturing the roll. Although it has lower strength than steel, its thermal resistance, castability, low shrinkage tendency, and reduced propensity for internal porosity—which is manageable through casting techniques—make it an ideal choice for this type of

product. Additionally, the lower weight of ductile iron further enhances production cost-effectiveness. This solution represents the optimal choice in terms of quality, cost-effectiveness, and feasibility of production.

The results of the selected most suitable simulation variants are currently being verified in real practice with an industrial partner. The verification itself is a very time-consuming process, as the experimental validation in a foundry requires time-intensive adjustments to the casting technology, including modifications to the pattern equipment. Furthermore, the functionality of the casting and improved service life compared to the original welded part must be validated under cyclic loading in specific operations (use in an annealing furnace). At present, consent has not been granted by the operator of the castings to publish the partial results of the experimental validation, as these are still ongoing.

Author Contributions: Conceptualization, M.B. and P.L.; methodology, M.B.; software, F.R.; validation, P.L. and I.V.; formal analysis, Š.K.; investigation, F.R.; resources, M.B.; data curation, M.B.; writing—original draft preparation, M.B.; writing—review and editing, Š.K.; visualization, F.R.; supervision, P.L. and I.V.; project administration, M.B.; funding acquisition, P.L. and I.V. All authors have read and agreed to the published version of the manuscript.

Funding: This research was funded within the framework of Technology Agency of the Czech Republic project SIGMA DC2 nr. TQ15000341 and project TREND nr. FW12010299 and supported by the Johannes Amos Comenius Program, Materials and Technologies for Sustainable Development–MATUR, no. CZ.02.01.01/00/22_008/0004631. Additionally, the infrastructure used was made available through project of MEYS (grant number CZ.02.1.01/0.0/0.0/17_049/0008399) and within the framework of Ministry of Education, Research, Development and Youth of the Slovak Republic project KEGA nr. 056TUKE-4/2025 and project VEGA nr. 1/0199/24.

Institutional Review Board Statement: Not applicable.

Informed Consent Statement: Not applicable.

Data Availability Statement: The original contributions presented in this study are included in the article. Further inquiries can be directed to the corresponding author.

Conflicts of Interest: The authors declare no conflicts of interest.

References

1. Wegel, S.; Ivanov, A.; Lenz, R.; Volling, T. Scheduling of parallel continuous annealing lines with alternative processing modes to optimize efficiency under tardiness constraints. *Eur. J. Oper. Res.* **2024**, *316*, 282–294. [CrossRef]
2. González-Ciordia, B.; Fernández, B.; Artola, G.; Muro, M.; Sanz, A.; López del Lacalle, L.N. Failure-analysis based redesign of furnace conveyor system components: A case study. *Metals* **2019**, *9*, 816. [CrossRef]
3. Yang, Y.-P.; Mohr, W.C. Finite-element creep–fatigue analysis of a welded furnace roll for identifying failure root cause. *J. Mater. Eng. Perform.* **2015**, *24*, 4388–4399. [CrossRef]
4. Ren, Q.; Kou, Z.; Wu, J.; Hou, T.; Xu, P. Effect of tempering temperature on microstructure and mechanical properties of 35CrMo steel. *Metals* **2023**, *13*, 771. [CrossRef]
5. Motte, R.; Waele, W.D. An overview of esmitaions for the high-cycle fatigue strength of conventionally manufactured steels based on other mechanical properties. *Metals* **2024**, *14*, 85. [CrossRef]
6. Liu, M.; Ma, Q.-X. Hot deformation behavior and a two-stage constitutive model of 20Mn5 solid steel ingot during hot compression. *Materials* **2018**, *11*, 434. [CrossRef] [PubMed]
7. Pevec, M.; Oder, G.; Patrč, I.; Šraml, M. Elevated temperature low cycle fatigue of grey cast iron used for automotive brake discs. *Eng. Fail. Anal.* **2014**, *42*, 221–230. [CrossRef]
8. Lekakh, S.N.; Bofah, A.; Osel, R.; O'Malley, R.; Godlewski, L. Hight temperature oxidation and decarburization of SiMo cast iron in air and combustion atmospheres. *Oxid. Met.* **2021**, *95*, 251–268. [CrossRef]
9. Fan, M.; Shao, C.; Wang, Y.; Huo, X.; Ma, N.; Lu, F. In-situ DIC investigation on local stress-strain behavior in creep-fatigue test of dissimilar steel welded joint. *Int. J. Fatigue* **2021**, *152*, 106464. [CrossRef]
10. Toghraee, A.; Zaeem, M.A. Oxidation induced stresses in high-temperature oxidation of steel: A multiphase field study. *Metals* **2020**, *10*, 801. [CrossRef]

11. Kim, J.; Pyeon, J.; Kim, B.-G.; Khadaa, T.; Choi, H.; Zhe, L.; Dube, T.; Zhang, J.; Yang, B.; Jung, Y.; et al. Oxidation behavior of NiCoAlY coatings deposited by vacuum plasma spraying and high-velocity oxygen fuel processes. *Coatings* **2023**, *13*, 319. [CrossRef]
12. Jelani, A.; Butt, M.M.; Rauf, O.U. Failure analysis of a furnace tube support. *Eng. Fail. Anal.* **2024**, *157*, 107910. [CrossRef]
13. Nadot, Y.; Mendez, J.; Ranganathan, N. Influence of casting defects on the fatigue limit of nodular cast iron. *Int. J. Fatigue* **2004**, *26*, 311–319. [CrossRef]
14. Bermond, A.; Roume, C.; Stolarz, J.; Lenci, M.; Carton, J.-F.; Klocker, H. Low cycle fatigue of G20Mn5 cast steel relation between microstructure and fatigue life. *Materials* **2022**, *15*, 7072. [CrossRef]
15. Dong, Q.; Zhang, J.; Wang, B.; Zhao, X. Shrinkage porosity and its alleviation by heavy reduction in continuously cast strand. *J. Mater. Process. Technol.* **2016**, *238*, 81–88. [CrossRef]
16. Harandi, A.N.; Eslami, A.; Bahrami, A.; Bakhtafrouz, A.; Mehr, M.Y. Failure analysis of two HP-Nb heat-resistant tubes after 46,000 h exposure to reformer service conditions. *Metals* **2023**, *13*, 228. [CrossRef]
17. Ravi, B. Computer-aided casting design–past, present and future. *Korea* **1999**, *1*, 777. Available online: https://citeseerx.ist.psu.edu/document?repid=rep1&type=pdf&doi=5e46a7b56aed7ef66e82219392e962667642f816 (accessed on 4 September 2025).
18. Vijayaram, T.R.; Piccardo, P. Computers in Foundries. *Metall. Sci. Technol.* **2012**, *30*, 28–38.
19. Hartmann, L.; Ernst, C.; Klun, J.S. Simulation of ingot casting processes at Deutsche Edelstahlwerke GmbH®. *IOP Conf. Ser. Mater. Sci. Eng.* **2012**, *27*, 012063. [CrossRef]
20. Vijayaram, T.R.; Sulaiman, S.; Hamouda, A.M.S.; Ahmad, M.H.M. Numerical simulation of casting solidification in permanent metallic molds. *J. Mater. Process. Technol.* **2006**, *178*, 29–33. [CrossRef]
21. Sertucha, J.; Lacaze, J. Casting defects in sand-mold cast irons—An illustrated review with emphasis on spheroidal graphite cast irons. *Metals* **2022**, *12*, 504. [CrossRef]
22. Popielarski, P. The conditions for application of foundry simulation codes to predict casting quality. *Mat. Res. Proc.* **2020**, *17*, 23–30. [CrossRef]
23. Ignaszak, Z.; Sika, R.; Rogalewicz, M. Contribution to the assessment of the data acquisition effectiveness in the aspect of gas porosity defects prediction in ductile cast iron castings. *Arch. Foundry Eng.* **2018**, *18*, 35–40. [CrossRef]
24. Neves, S.; Schäfer, W.; Hansen, P.N. The sensibility of thermophysical property data for simulating casting processes. *Int. J. Thermophys.* **2002**, *23*, 1391–1399. [CrossRef]
25. Malinowski, P.; Suchy, J.S.; Jakubski, J. Technological knowledge management system for foundry industry. *Arch. Metall. Mater.* **2013**, *58*, 965–968. [CrossRef]
26. Sonne, M.R.; Frandsen, J.O.; Hattel, J.H. Comparison of residual stresses in sand-and chill casting of ductile cast iron wind turbine main shafts. *IOP Conf. Ser. Mater. Sci. Eng.* **2015**, *84*, 012025. [CrossRef]
27. Angella, G.; Ripamonti, D.; Górny, M.; Masaggia, S.; Zanardi, F. The Role of Microstructure on Tensile Plastic Behavior of Ductile Iron GJS 400 Produced through Different Cooling Rates, Part I: Microstructure. *Metals* **2019**, *9*, 1282. [CrossRef]
28. López, M.G.; Massone, J.M.; Boeri, R.E. Examination of the size and morphology of austenite grains in lamellar graphite cast iron. *Int. J. Met.* **2020**, *14*, 689–695. [CrossRef]
29. Heyworth, R. The Influence of Filling System Design on Quality Performance in Gray Iron. *Int. J. Met.* **2024**, *18*, 3383–3402. [CrossRef]
30. Khan, M.A.A.; Sheikh, A.K. Mechanical characterization and quality of iron castings using optimized mold design: Simulations and experimental validation. *J. Adv. Manuf. Technol.* **2018**, *98*, 799–809. [CrossRef]
31. Smith, F.J. Residual Stress Determination of Ductile Cast Iron by Means of Neutron Diffraction. Ph.D. Thesis, North-West University, Potchefstroom, South Africa, 2018.
32. Górny, M.; Kawalec, M.; Gracz, B.; Tupaj, M. Influence of cooling rate on microstructure formation of Si–Mo ductile iron castings. *Metals* **2021**, *11*, 1634. [CrossRef]
33. Kaschnitz, E.; Heugenhauser, S.; Schumacher, P. A benchmark for the validation of solidification modelling algorithms. *IOP Conf. Ser. Mater. Sci. Eng.* **2015**, *84*, 012051. [CrossRef]
34. Xu, M.; Lekakh, S.N.; Richards, V.L. Thermal property database for investment casting shells. *Int. J. Met.* **2016**, *10*, 329–337. [CrossRef]
35. Majerník, J.; Podařil, M. Evaluation of the temperature distribution of a die casting mold of X38CrMoV5_1 steel. *Arch. Foundry Eng.* **2019**, *19*, 107–112. [CrossRef]
36. Lu, Y.; Bartlett, L.N.; O'Malley, R.J.; Lekakh, S.N. Method to Investigate Mechanical Behavior of Steel Casting near Solidus Temperature. *Steel Res. Int.* **2021**, *92*, 2100007. [CrossRef]
37. Jaromin, M.; Dojka, R.; Jezierski, J.; Dojka, M. Influence of Type and Shape of the Chillon Solidification Process of Steel Casting. *Arch. Foundry Eng.* **2019**, *19*, 35–40. [CrossRef]
38. Przyszlak, N.; Piwowarski, G. Designing of X46Cr13 Steel Heat Treatment in Condition of Casting Mould. *Arch. Foundry Eng.* **2023**, *23*, 119–126. [CrossRef]

39. Walker, J.; Harris, E.; Lynagh, C.; Beck, A.; Lonardo, R.; Vuksanovich, B.; Thiel, J.; Rogers, K.; Conner, B.; MacDonald, E. 3D printed smart molds for sand casting. *Int. J. Met.* **2018**, *12*, 785–796. [CrossRef]
40. Bae, J.W.; Seol, D.Y.; Kang, C.G.; Lee, S.M. Die life prediction considering thermal fluid flow and solidification phenomenon in rheology process. *J. Mater. Process. Technol.* **2008**, *201*, 336–341. [CrossRef]
41. Palumbo, G.; Piglionico, V.; Sorgente, D.; Piccininni, A.; Guglielmi, P.; Tricarico, L. Correlating shrinkage microporosity with the mechanical properties of sand-cast superduplex stainless steel using a numerical/experimental approach. *Mater. Des.* **2016**, *93*, 168–179. [CrossRef]
42. *DIN 17205:1992*; Vergütungsstahlguß für Allgemeine Verwendungszwecke; Technische Lieferbedingungen (Quenched and Tempered Steel Castings for General Applications; Technical Delivery Conditions). German Institute for Standardisation (Deutsches Institut für Normung): Berlin, Germany, 1992.
43. *DIN EN 10293:2015*; Stahlguss—Stahlguss für Allgemeine Anwendungen (Steel Castings—Steel Castings for General Engineering Uses). German Institute for Standardisation (Deutsches Institut für Normung): Berlin, Germany, 2015.
44. *EN 1563:2018*; Founding—Spheroidal Graphite Cast Irons. European Committee for Standardization (CEN): Brussels, Belgium, 2018.
45. Heine, R.W.; Rosenthal, P.C. *Principles of Metal Casting: Prepared in Cooperation with the Textbook Committee of the Education Division*; American Foundrymen's Society: Des Plaines, IL, USA, 1995.
46. Campbell, J. *Complete Casting Handbook: Metal Casting Processes, Metallurgy, Techniques and Design*; Butterworth-Heinemann: Oxford, UK, 2015.
47. Andriollo, T.; Vedel-Smith, N.; Thorborg, J.; Hattel, J. Internal casting stresses and dimensional stability. In *Cast Iron Science and Technology*; Stefanescu, D.M., Ed.; ASM International: Materials Park, OH, USA, 2017; pp. 511–515.
48. Thomas, B.G. Modeling of hot tearing and other defects in casting processes. In *ASM Handbook, Volume 22A: Fundamentals of Modeling for Metals Processing*; Furrer, D.U., Semiatin, S.L., Eds.; ASM International: Materials Park, OH, USA, 2009; pp. 362–374.
49. Le Bars, M.; Worster, M.G. Solidification of a binary alloy: Finite-element, single-domain simulation and new benchmark solutions. *J. Comput. Phys.* **2006**, *216*, 247–263. [CrossRef]

Disclaimer/Publisher's Note: The statements, opinions and data contained in all publications are solely those of the individual author(s) and contributor(s) and not of MDPI and/or the editor(s). MDPI and/or the editor(s) disclaim responsibility for any injury to people or property resulting from any ideas, methods, instructions or products referred to in the content.

materials

MDPI

Article

The Impact of Storage Conditions on the Gas-Forming Tendency of Moulds and Cores Made with Resole-Type Phenol Formaldehyde Resin

Artur Bobrowski *, Faustyna Woźniak, Sylwia Żymankowska-Kumon, Hubert Ziętal, Kacper Januszek and Beata Grabowska

Faculty of Foundry Engineering, AGH University of Krakow, Reymonta 23, 30059 Krakow, Poland; wozfau@agh.edu.pl (F.W.); szk@agh.edu.pl (S.Ż.-K.); hzietal@student.agh.edu.pl (H.Z.); januszek@student.agh.edu.pl (K.J.); beata.grabowska@agh.edu.pl (B.G.)
* Correspondence: arturb@agh.edu.pl

Abstract

The article presents the results of a study aimed at determining the impact of storage conditions on the gas-forming tendency of standard samples (cores) made from moulding sand using a two-component binder based on resole-type phenolic resin, cured with a dedicated ester mixture. The objective of the research was to determine the total volume of gases released as a result of contact between the cores or moulds and the high temperature of molten casting alloys, as well as the rate of gas release, which can influence the tendency for gas-related casting defects. Additionally, the influence of storage conditions on the gas-forming tendency of the samples was evaluated in terms of their environmental and occupational health impact, based on the emission of BTEX compounds (benzene, toluene, ethylbenzene, and xylenes), which serve as key indicators of the harmfulness of moulding and core sands to the surrounding environment.

Keywords: resole phenolic resin; gas emissions in foundry; BTEX compounds; mould and core storage conditions; alkaline phenolic no-bake (APNB)

1. Introduction

Foundry engineering is a highly significant branch of industry, playing a crucial role in the development of many other industrial sectors, particularly the automotive, machinery, aerospace, and energy industries. The growing demands of modern manufacturing require continuous improvement in the field of materials engineering used in foundry processes—not only in terms of the quality of the casting alloy, which must meet specific requirements regarding composition, crystallization behavior, and mechanical properties, but also in the design and preparation of the moulds that define the intended shape of the casting. In this context, properly selected materials for moulds and cores are of particular importance—both the ceramic matrix materials that form the base of moulding and core sands, and the binders that hold the grain structure together. These binders largely determine the technological properties of the moulding and core sands, which must exhibit adequate gas permeability, flowability, and compactability. The type and amount of binder used also directly affect the mechanical properties of the moulds and cores, such as compressive, tensile, and bending strength, as well as high-temperature resistance and gas-forming tendency [1,2]. The latter is especially important, as excessive gas evolution can lead to gas-related defects in castings, often disqualifying

them from use due to issues such as porosity or leakage [3,4]. Increasing environmental regulations and the drive to improve working conditions in foundries are also pushing the industry toward the use of low-emission materials, particularly in relation to the emission of hydrocarbons [5,6]. In the context of moulding and core sands used in foundry processes, the emission of BTEX compounds (benzene, toluene, ethylbenzene, and xylenes) is commonly used as a measure of their environmental and occupational health impact. A substantial body of literature exists concerning the evaluation of gas-forming tendencies in moulding and core sands, with significant contributions made by the co-authors of this paper [7,8]. Most commercially available binders were tested. The effects of the type of organic resin and hardener used in the preparation of molding sands (furfuryl, alkyd, and phenol formaldehyde resins) and cores were analyzed. Gas emission studies were also conducted for systems using inorganic binders (such as water glass and geopolymers) and biopolymer-based binders. Since the use of reclaimed sand—produced through mechanical and/or thermal processing of spent molding sands—is a common practice in foundries, gas emission studies were carried out with varying proportions of reclaimed sand derived from furfuryl resin molding sand. This study investigated the effect of reclaimed sand content on the total volume of released gases and on the emission of BTEX compounds. However, from a technological standpoint, there is a lack of data regarding the impact of storage conditions on the gas-forming tendency of moulds and cores [9,10]. In practice, cores are often produced in advance and stored in warehouses or designated areas of the foundry. As a result, they are exposed to varying climatic conditions, changes in temperature and humidity, until they are eventually placed into the mould cavity and poured with molten metal. Although their mechanical strength may remain sufficient for safe handling, foundries often lack information on potential absorption (in the case of hygroscopic binders) and/or moisture adsorption on the surface of the cores or moulds. Due to emission restrictions, the APNB (Alkaline Phenolic No-Bake) technology is increasingly replacing widely used binders based on furfuryl alcohol [1,11]. The phenol formaldehyde resole resin used in this study is intended for the Alphaset process, also known as APNB. This is a two-component system in which a dedicated dimethyl ester mixture acts as the curing agent. One of the key advantages of this technology is that no heat or gas purging is required to initiate curing of the moulding or core sand. The binder consists of a phenol formaldehyde resole resin in an aqueous alkaline medium (NaOH, KOH). During the initial curing phase, partial polymerization of the resole chains occurs, accompanied by the removal of metal ions (Na^+, K^+) through ester hydrolysis in the alkaline environment. The ester mixture, tailored to the specific resin, varies in hydrolysis rate, which affects acid release and thus controls curing speed and the working time of the sand—the so-called "bench life" [5,12]. Typically, the binder content in this system ranges from 1.2% to 1.8% relative to the mass of the sand matrix, depending on the size of the mould and its purpose (moulding sand or core sand) [13]. Another benefit of the APNB system is its thermoplastic deformation behavior upon contact with molten metal: the cured bonds temporarily loosen, followed by a secondary hardening phase. This mechanism compensates for the reversible volume change in quartz sand at 573 °C caused by polymorphic transformation, preventing cracking and reducing casting defects such as veining [14–16]. Spent moulding sands from the APNB process are suitable for reclamation—the recovery of the grain matrix through mechanical, thermal, or combined treatments. Mechanical reclamation alone allows for approximately 70% sand recovery, while combined mechanical-thermal methods can achieve up to 95% recovery rates [5,8,14,17–19]. The APNB system contains no sulfur or nitrogen, making it highly versatile and suitable for casting all types of metals, including cast iron and steel [5,20]. It has been documented that when metal

is poured into moulds bonded with APNB resin, the bonds temporarily relax before re-hardening, preventing cracking and minimizing veining defects. Castings produced using this method exhibit high dimensional accuracy [14,15].

The objective of this study is to evaluate the effect of storage conditions on the total amount and rate of gas emission, as well as the environmental impact of these gases—particularly BTEX compounds—from samples made using resole-type phenol formaldehyde resin cured with an ester mixture. The study focuses not only on the storage conditions themselves but also on the time interval between core production and their placement in the mould cavity and pouring with molten metal—a critical factor in foundry operations.

2. Research Materials and Methodology

The following materials were used to prepare the samples:

- Grain matrix, quartz sand (parameters in Table 1) DBCargo, Szczakowa, Poland;
- Resol-type phenol formaldehyde resin [Prec-Odlew, Skawina, Poland];
- Hardener, a mixture of dimethyl esters [Prec-Odlew, Skawina, Poland].

Table 1. Grain matrix parameters.

Parameter	Symbol	Value	Unit
Major fraction	F	0.32/0.20/0.16	mm
AFS particle number	L	56.10	-
Average particle size	d_L	0.23	mm
Geometric mean	d_g	0.25	mm
Arithmetic mean	d_a	0.26	mm
Harmonic mean	d_h	0.24	mm
Median	d_M	0.25	mm
Average particle size	D50	0.25	mm
Major fraction	F_g	87.25	%
Distribution coefficient	S_0	1.22	-
Slope index	S_k	0.96	-
Degree of homogeneity	GG	75.00	%
Specific surface area	S_t	9.59	m^2/kg

The moulding/core sand was prepared according to the following procedure:

- Grain matrix 100 parts by mass;
- Resin 1.5 parts by weight relative to the grain matrix;
- Hardener 25% relative to the resin.

The weighed components were mixed in a rotor-type mixer. First, the hardener was added and mixed with quartz sand for 30 s, followed by the addition of the resin, with an additional mixing time of 30 s. Standard cylindrical test samples with dimensions of $\Phi 50 \times 50$ mm were prepared from the moulding mixture using vibratory compaction, employing a LUZ-2 e vibratory compaction device for moulding sands [21] (manufactured by Multiserw Morek). The samples (Figure 1) were then set aside for complete curing. After 6 h (except for the set stored in the laboratory for 3 h), the samples were subjected to the following storage conditions:

- 24 h in a glass desiccator;

- 3 h under laboratory conditions (Temperature [T] = 20–21 °C, relative humidity [RH] = 45–50%);
- 24 h under laboratory conditions (Temperature [T] = 20–21 °C, relative humidity [RH] = 45–50%);
- 7 days under laboratory conditions (Temperature [T] = 20–21 °C, relative humidity [RH] = 45–50%);
- 24 h in a climate chamber: temperature T = 35 °C, relative humidity RH = 70%.



Figure 1. Standard cylindrical samples.

Measurements of gas volume and emission kinetics, along with the analysis of BTEX group compounds (benzene, toluene, ethylbenzene, xylenes), were conducted using a patented testing stand designed to assess the emission intensity and harmfulness of gases released from technological materials used in foundry and metallurgical processes [22] (Figure 2). For each sample, two repeatable measurements were performed. A previously weighed cylindrical sample (Ø50 × 50 mm) was placed in a steel "bell" and then inserted into a pre-prepared mould cavity made of bentonite-bonded moulding sand. The sample was then poured with molten cast iron at a temperature of 1350 °C. The total mass of molten metal used in the mould was approximately 9 kg. As a result of the thermal impact of the molten alloy, thermal degradation of the binder in the moulding/core sample occurred. The resulting gases were directed into a collection capsule (Figure 2), which includes a gas drying unit. The gas stream was then passed through a bed of activated carbon for adsorption (Figure 3) and subsequently routed through a calibrated system of tubes to a peristaltic pump connected to a gas volume recorder. Qualitative and quantitative analyses of the emitted gases were performed using gas chromatography with a flame ionization detector (FID, Thermo Scientific, Waltham, MA, USA). The activated carbon sorbent (charcoal activated for gas chromatography, particle size 0.5–1 mm; 18–35 mesh American Society for Testing and Materials ASTM; CAS 7440-44-0, molar mass 12.01 g/mol), containing adsorbed organic compounds, was subjected to extraction with diethyl ether. The solvent volume required for the complete desorption of BTEX compounds from the activated carbon column was determined as follows: 40 mL of diethyl ether for the primary bed, applied in four successive aliquots of 10 mL, and 10 mL of diethyl ether for the backup bed [23]. Identification of BTEX compounds was carried out using a Trace GC Ultra gas chromatograph (Thermo Scientific, Thermo Fisher Scientific Inc., Milan, Italy) equipped with a capillary column (Rtx®-5 MS, fused silica, low-polarity phase, cross-linked 5% diphenyl/95% dimethylpolysiloxane; Restek™, Bellefonte, PA, USA), 30 m in length and 0.25 mm in internal diameter [24]. Chromatographic separation was conducted under the following conditions: an initial temperature of 40 °C maintained for 3 min; a linear

increase to 100 °C at a rate of 3 °C·min^{-1} with a 3 min hold; followed by heating to 250 °C at a rate of 20 °C·min^{-1} and a 3 min hold. The carrier gas was helium, with a column flow rate of 1 mL·min^{-1}, and the injector operated in SPLIT (volume ratio of the two streams) mode with a 1:30 split ratio. The analytical protocol was based on standardized procedures described in the AFS Mold & Core Test Handbook (American Foundry Society) and the international standards ISO 16017 and EN 13649 [22].

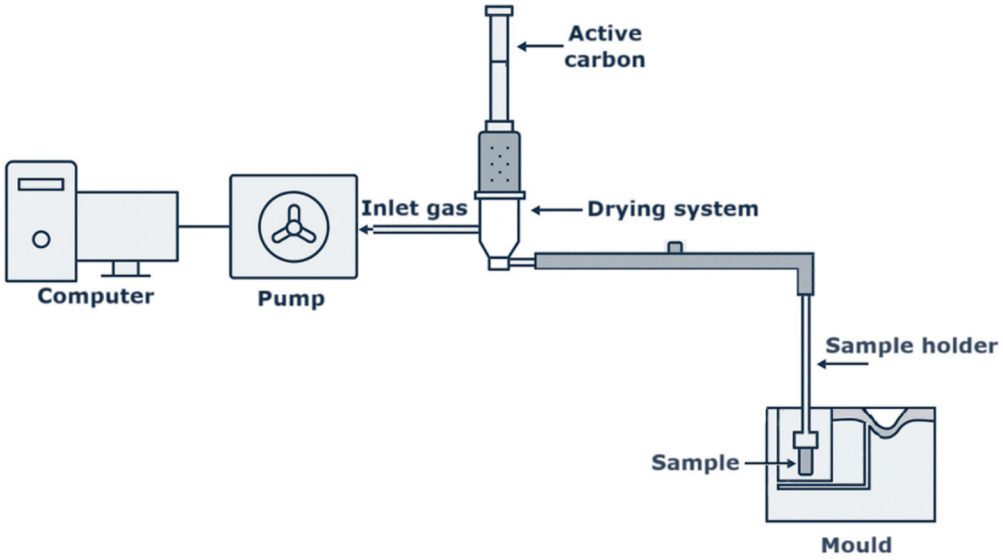


Figure 2. Station for testing the intensity of gas emissions and harmfulness ([22]).

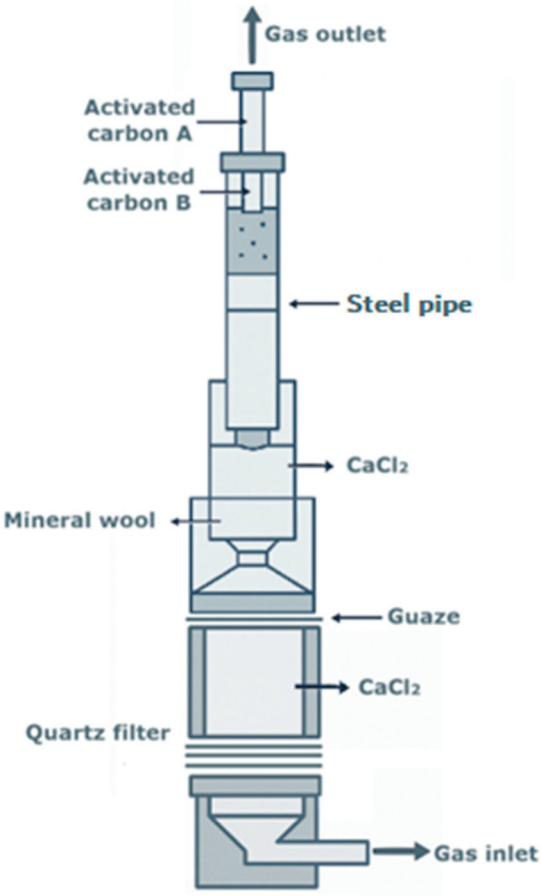


Figure 3. Capsule with activated carbon bed for collecting BTEX group compounds ([22]).

3. Results

To facilitate the interpretation of the results, the sample designations (S1–S5) and their corresponding storage conditions are summarized in Table 2. All curves presented in the figures represent mean ± SD values obtained from three independent measurements (n = 3).

Table 2. Summary of experimental series used in the research.

Experimental Series	Storage Environment	Storage Duration
S1	Glass desiccator–dry conditions	24 h
S2	Laboratory conditions (20–21 °C, 45–50% RH)	3 h
S3	Laboratory conditions (20–21 °C, 45–50% RH)	24 h
S4	Laboratory conditions (20–21 °C, 45–50% RH)	7 days
S5	Climatic chamber (35 °C, 70% RH)	24 h

Figure 4 presents the relationship between the volume of gases emitted over time from core samples stored for 24 h in a desiccator under dry conditions. The presented curve corresponds to the average values obtained from three independent measurements (n = 3). The total volume of emitted gases reached approximately 15.7 dm^3/kg.

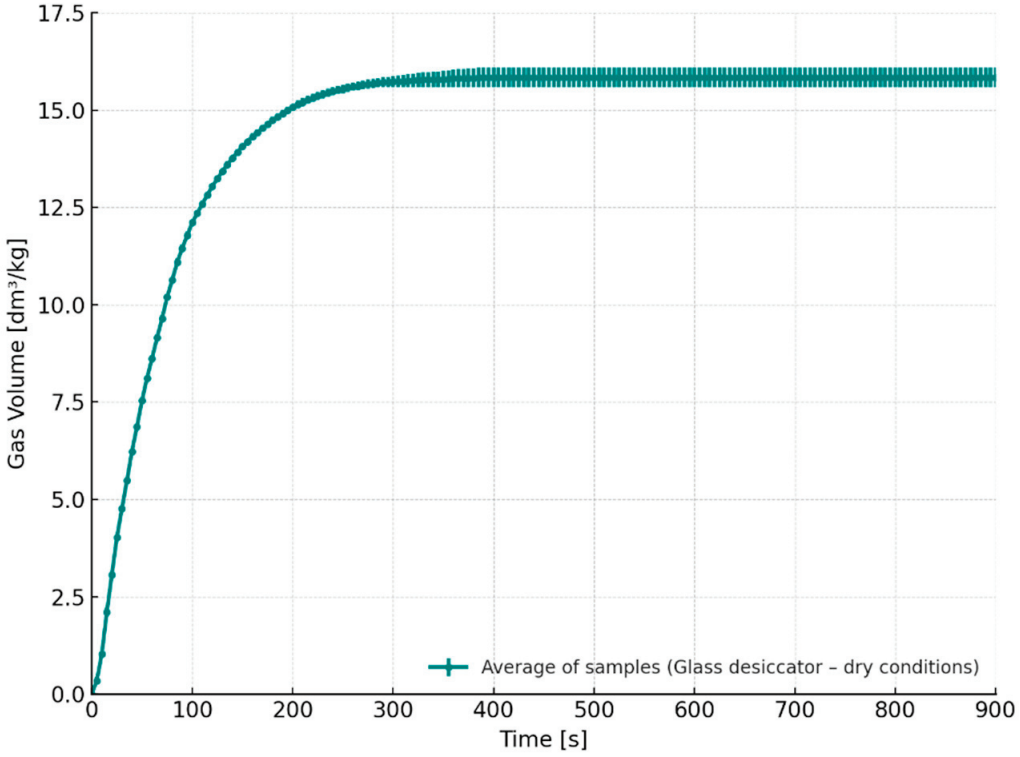


Figure 4. Released gas volume as a function of time for cores stored under dry conditions (S1–24 h).

Figure 5 illustrates the gas emission rate profiles for the tested core samples following 24 h of storage in a desiccator. The emission rate was recorded continuously from the moment of contact between the molten cast iron and the mould cavity. Both samples demonstrated similar kinetic profiles, indicating a high degree of repeatability in gas release behavior under controlled storage conditions. The most intensive gas evolution occurred within the first 20–40 s after metal pouring, reaching a peak emission rate of approximately 0.23 $dm^3/(kg \cdot s)$. This sharp increase is associated with the initial thermal

decomposition of the resin binder due to the rapid temperature rise induced by the molten alloy (1350 °C). Following the peak, the emission rate gradually decreased, reflecting the progressive exhaustion of volatile components within the binder system. The early onset and intensity of gas evolution are of particular importance in foundry practice, as they directly influence the formation of gas-related casting defects. Rapid gas release in this time window can lead to pressure buildup in the mould cavity if not properly vented, increasing the risk of porosity or gas blows. Therefore, understanding this emission behavior is crucial for optimizing mould design, binder selection, and storage protocols.

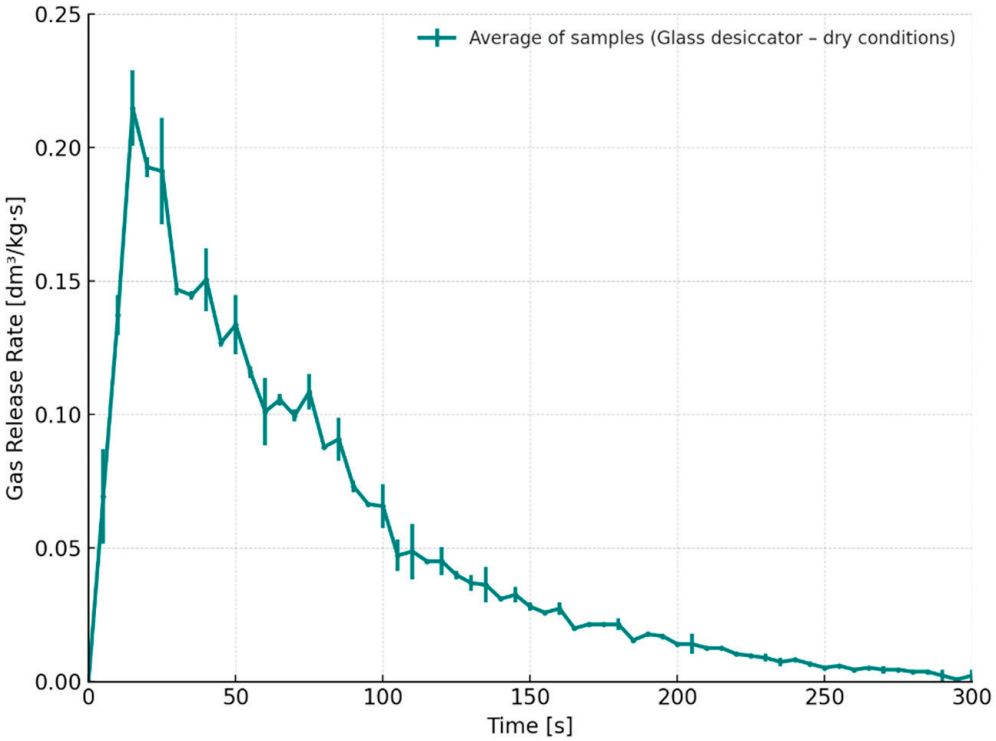


Figure 5. Gas release rate as a function of time for cores stored in a glass desiccator under dry conditions (S1–24 h).

Figure 6 presents the gas emission volume as a function of time for ores stored under laboratory conditions for 3 h (S2). In contrast to the samples stored in a desiccator, the gas emission for this series was prolonged, with the most significant increase occurring up to approximately 400 s after contact with the high-temperature molten alloy. The total gas volume emitted reached approximately 19.0 dm^3/kg, which is about 2 dm^3/kg higher compared to the desiccator-stored samples, indicating a significantly greater gas evolution. Such an increase in gas release may considerably raise the risk of gas-related casting defects, particularly if the generated gases are not effectively removed from the mould cavity. The increased gas evolution is attributed to the shorter time interval between core fabrication and their exposure to molten metal, which likely resulted in incomplete curing of the binder, especially in the internal structure of the samples. These findings indicate that insufficiently cured cores can substantially contribute to defect formation during casting, due to excessive gas evolution under thermal stress. This underlines the importance of ensuring adequate curing time before storage or use, particularly when using resin-bonded sand systems. Delays in full polymer crosslinking, especially in larger or more thermally insulated cores, may result in residual binder decomposition during pouring, increasing porosity risk.

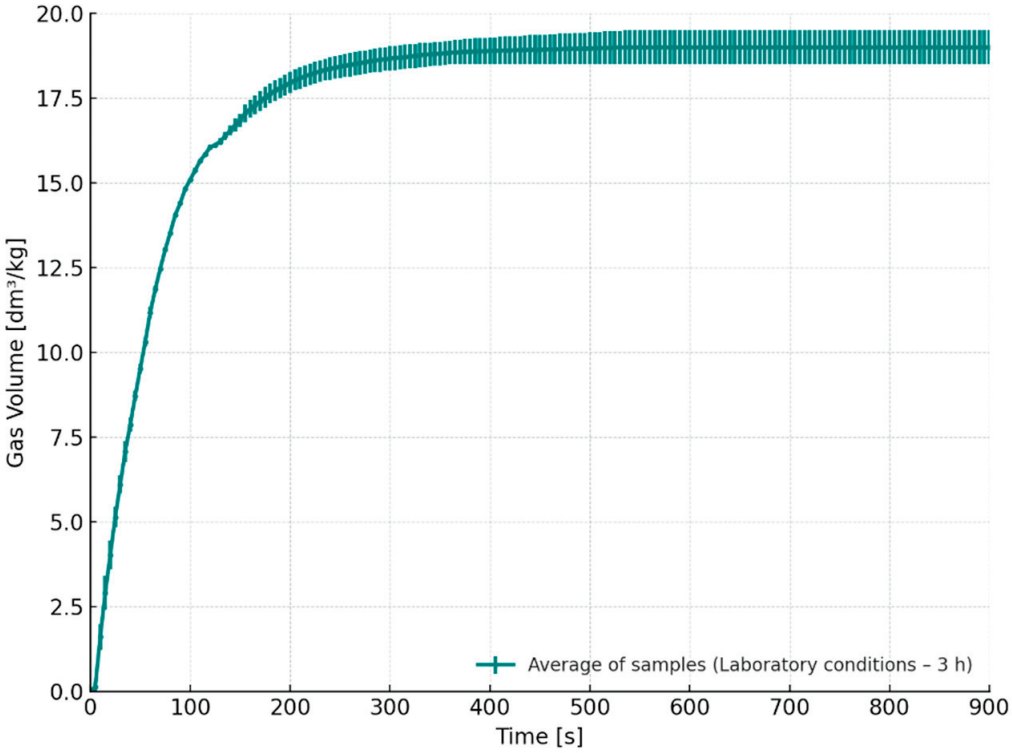


Figure 6. Released gas volume as a function of time for cores stored under laboratory conditions for 3 h (S2–3 h).

Figure 7 presents the gas emission rate over time for cores stored under laboratory conditions for 3 h after preparation (S2). The results clearly indicate minor variations in the emission profile, which may stem from uneven distribution of the binder or varying degrees of curing throughout the sample. Compared with the desiccator-stored samples (S1), the gas emission in this series was more prolonged, with the peak occurring approximately 40–50 s after pouring molten cast iron—about 10 s later than in the case of dry-stored samples. The averaged peak emission rate reached approximately 0.38 $dm^3/(kg \cdot s)$, indicating a higher intensity of gas evolution under ambient storage conditions. Such a sudden increase suggests localized regions within the core that responded more intensely to thermal degradation, likely due to insufficient or uneven curing. After the peak, the emission rate gradually decreased, reflecting the progressive exhaustion of volatile components within the binder system. Observed differences in the gas emission profiles suggest that the intensity and nature of gas release may be influenced by the storage conditions of the samples and the time elapsed between their preparation and pouring with molten metal, which may be related to the degree of binder curing in moulding or core sand.

Figure 8 presents the gas emission curve over time for cores stored for 24 h under laboratory conditions (S3, T = 20–21 °C, RH = 45–50%). The results show that the total volume of emitted gases was comparable to that obtained for the desiccator-stored series (S1). This indicates that under moderate and stable humidity conditions, the binder system retained its thermal stability, and no significant increase in gas evolution was observed. Such behavior suggests that maintaining controlled climatic conditions during the storage of cores or moulds may help to prevent undesirable physicochemical changes in the binder, which could otherwise lead to increased gas release during pouring.

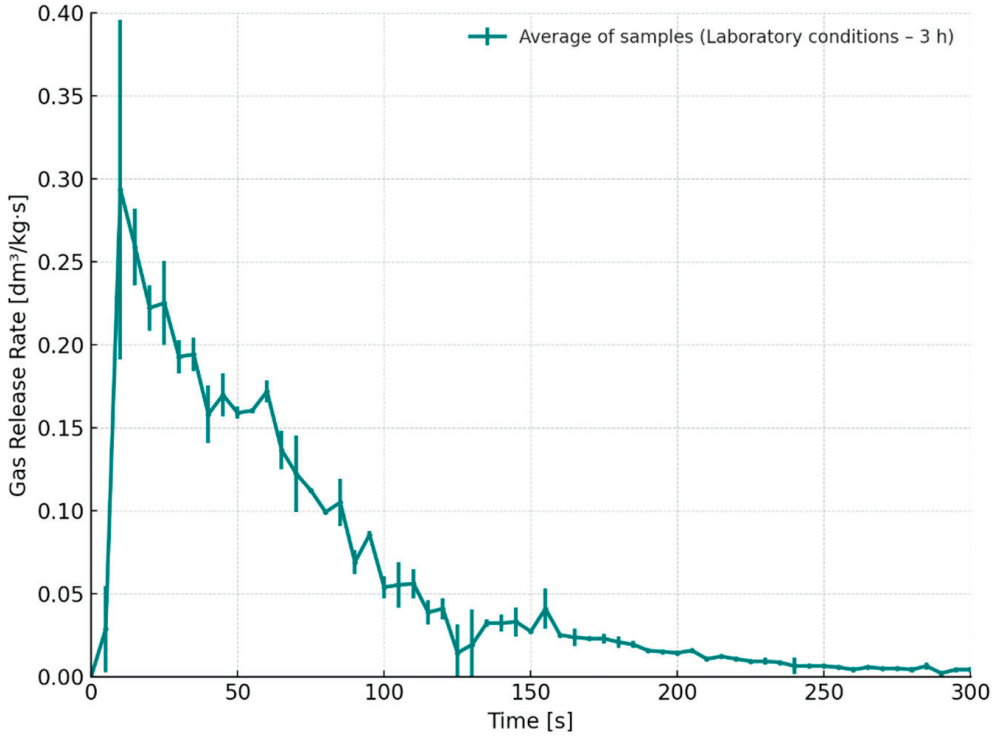


Figure 7. Gas release rate as a function of time for cores stored under laboratory conditions (S2–3 h).

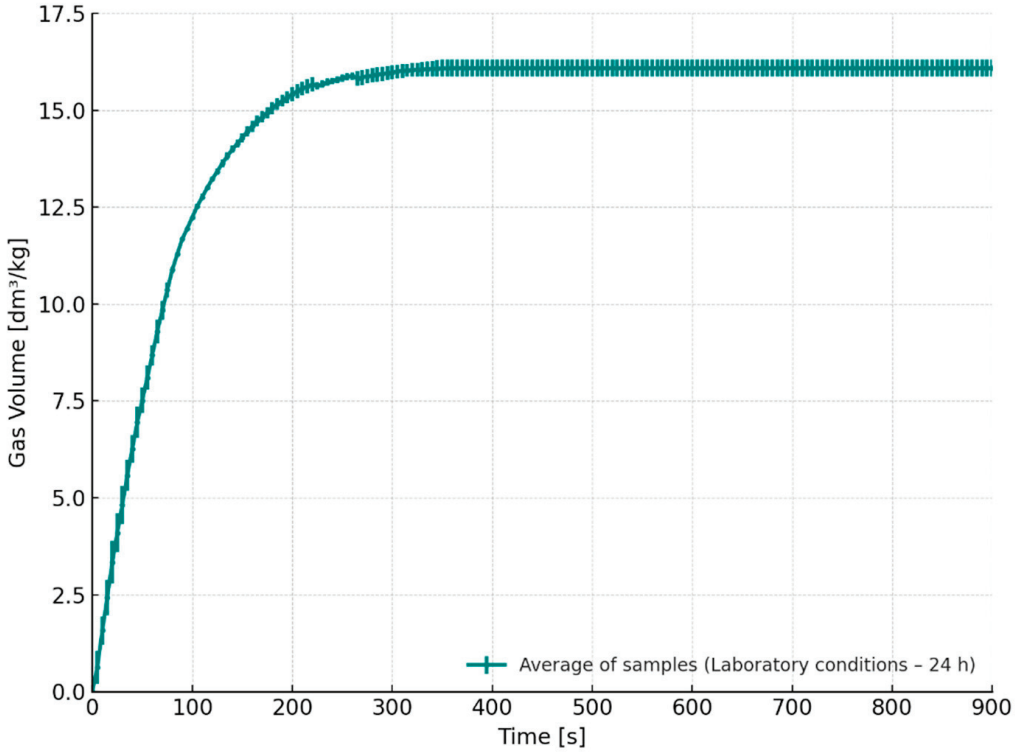


Figure 8. Released gas volume as a function of gas released over time for cores stored under laboratory conditions for 24 h (S3–24 h).

Figure 9 illustrates the gas emission rate over time for cores stored for 24 h under laboratory conditions (S3, T = 20–21 °C, RH = 45–50%). The emission characteristics for this series closely resembled those of the desiccator-stored cores (S1) in terms of total gas volume and peak emission values. However, a slight shift in the onset of gas evolution was observed, occurring only a few seconds after contact with the molten alloy. This earlier

initiation of gas release allowed the evolved gases to escape more gradually from the mould cavity, potentially reducing the risk of gas entrapment. Adequate venting during this initial stage of pouring may therefore help to minimize the formation of gas-related casting defects.

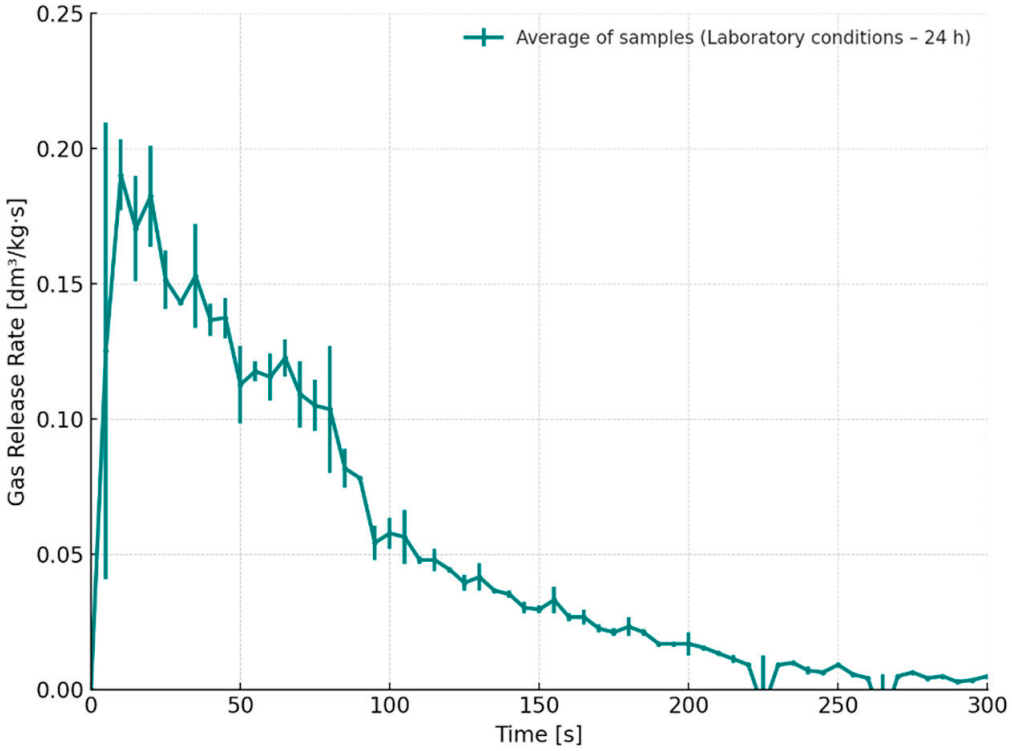


Figure 9. Gas release rate as a function of time for cores stored under laboratory conditions (S3–24 h).

In contrast, Figure 10 presents the gas evolution characteristics for core samples produced with the APNB binder system and stored for 7 days under controlled laboratory conditions (S4, T = 20–21 °C, RH = 45–50%). These samples demonstrated the lowest total gas release of all examined variants. The extended storage time likely allowed for more complete cross-linking of the binder, which led to a lower concentration of residual binder components (resin and hardener) involved in the thermal decomposition process during casting. These findings highlight the key role of appropriate seasoning time and stable storage conditions in stabilizing the casting process. Extending the storage period under controlled environmental conditions can significantly reduce gas emissions, particularly from cores, thereby decreasing the likelihood of gaseous casting defects. The results are particularly relevant for cores with complex geometry or limited venting capacity, where effective gas evacuation is difficult.

Figure 11 presents the gas emission rate for core samples stored under laboratory conditions for 7 days (S4). These samples exhibited the lowest gas evolution rates among all tested variants. This observation suggests that extended storage under stable temperature and humidity conditions facilitates further chemical curing of the binder system, potentially leading to the formation of a more cross-linked structure that limits gas evolution during thermal exposure. As a result, the amount of gas released during contact with molten metal is significantly reduced. Additionally, the extended curing period contributes to a notable decrease in the peak emission rate, which reached approximately 0.18 $dm^3/kg \cdot s$ on average. These values are considerably lower than those observed for cores subjected to thermal loading just 3 h after preparation, where incomplete curing may have contributed to more rapid and intense gas evolution.

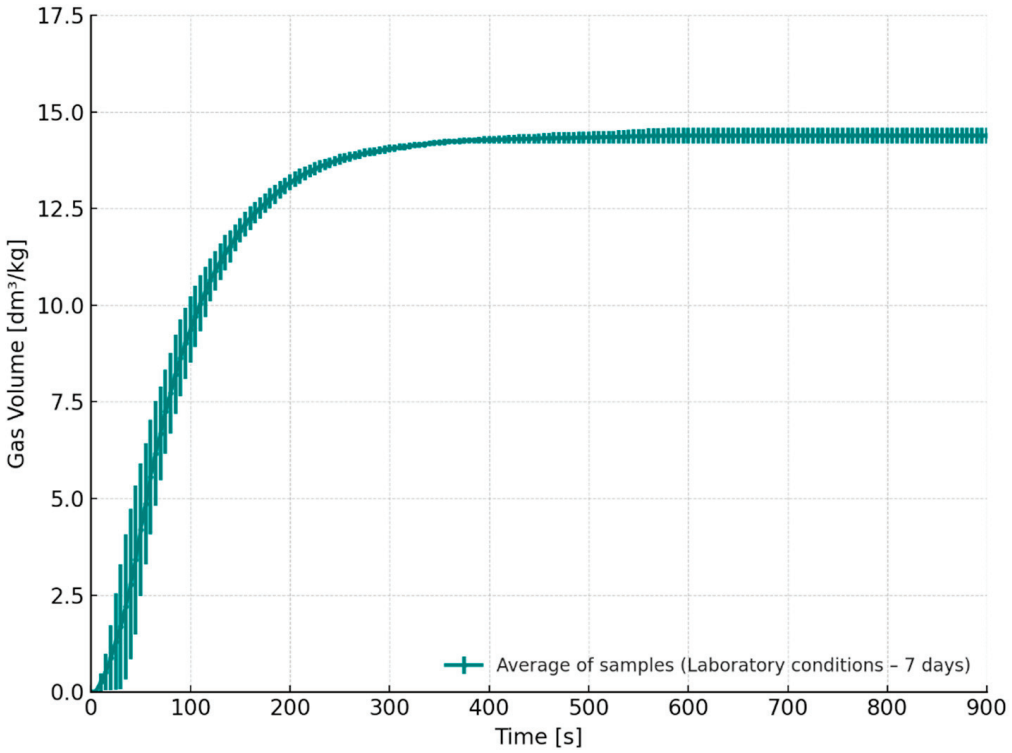


Figure 10. Released gas volume as a function of time for cores stored under laboratory conditions for 7 days (S4–7 days).

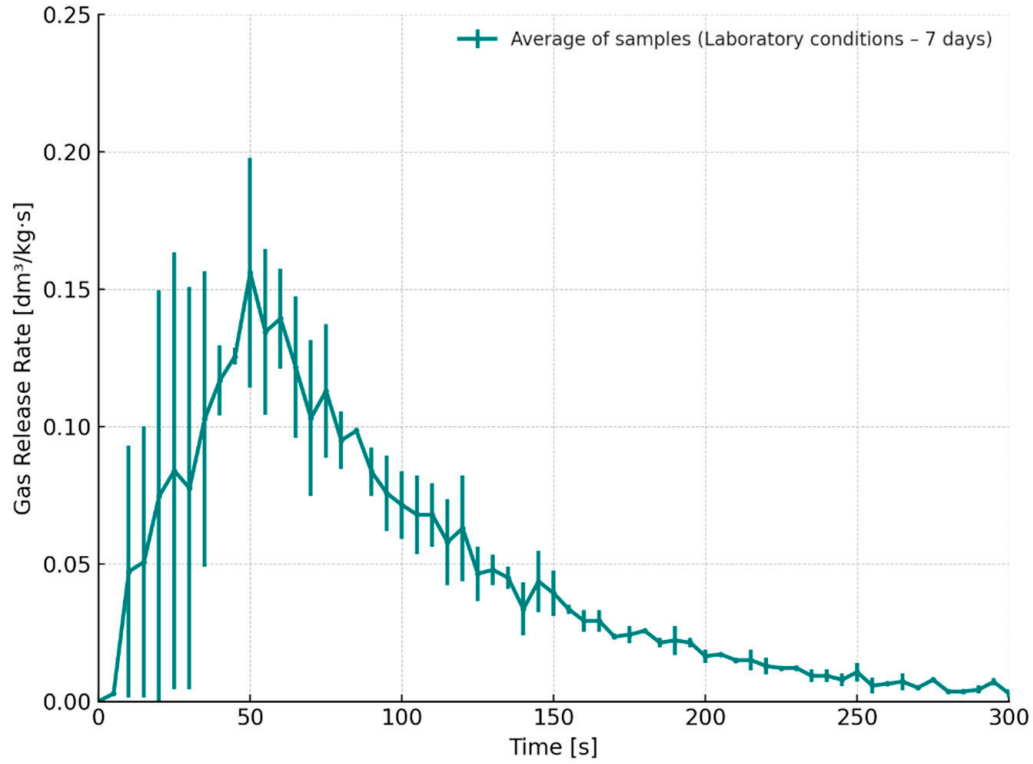


Figure 11. Gas release rate as a function of time for cores stored under laboratory conditions (S4–7 days).

Increase in gas release can be attributed to the hygroscopic nature of resol-type phenol-formaldehyde resins, which readily absorb moisture from the environment under elevated humidity conditions. The absorbed water can interfere with the polycondensation reactions

responsible for the curing process, as well as promote hydrolysis or slow down the cross-linking of the resin [25,26]. These effects may lead to alterations in the chemical structure of the binder, which in turn affect the kinetics of thermal decomposition when in contact with molten metal and influence the total volume of gas generated. This is confirmed by the data presented in Figure 12 (S5, climatic chamber—35 °C, 70% RH), showing that gas emissions from samples stored at 35 °C and 70% relative humidity are, on average, approximately 1 dm^3/kg higher than those from samples stored under standard laboratory conditions.

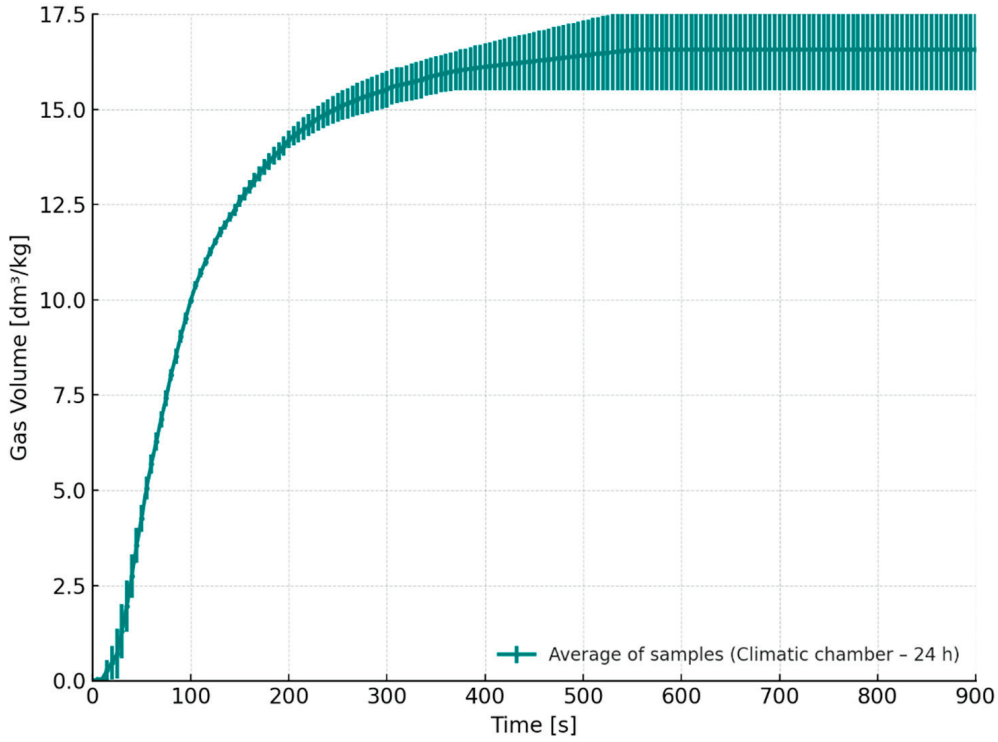


Figure 12. Released gas volume as a function of time for cores stored for 24 h in a climatic chamber (S5, temperature 35 °C, 70% humidity).

The gas emission rate from samples stored in the climate chamber exhibits a distinct peak during the initial phase of the process (Figure 13). For Sample I, the maximum emission rate occurred approximately 45 s after pouring, while for Sample J, it was observed around 55 s, yielding an average of 50 s post-pouring. It should be noted that, despite the increased total volume of gas generated, the rate of thermal decomposition product release is lower in this case; however, the emission process persists over a longer duration. This behavior may be associated with the previously mentioned changes in the chemical structure of the binder resulting from moisture exposure.

Table 3 presents a summary of the results of determining the volume of emitted gases over time for all tested samples, calculated per sample of known mass and per 1 kg of moulding/core sand, depending on the storage conditions.

Table 4 summarizes the mean values and standard deviations of the total gas volume and the maximum gas release rate for all storage variants (S1–S5). These results complement the data presented in Table 3 and provide a statistical comparison of gas-forming tendencies under different storage conditions.

Table 5 summarizes the results of BTEX compound determinations based on a sample of known mass, while Table 6 summarizes the results based on 1 kg of moulding/core sand.

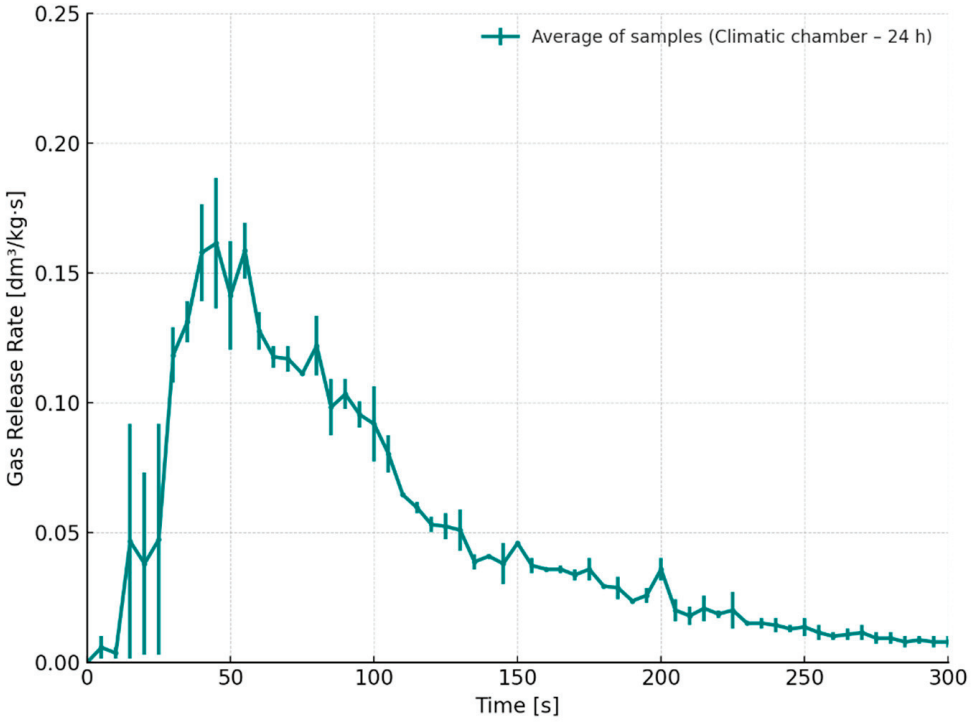


Figure 13. Gas release rate as a function of time for cores stored for 24 h in a climatic chamber (S5, temperature 35 °C, 70% humidity).

Table 3. Volume of gases from the tested samples in dm^3/sample and dm^3/1 kg of moulding/core sand (on the base [27,28]).

Experimental Series	Sample Description (Average of Samples)	Gas Volume [dm^3/Sample]	Gas Volume [dm^3/kg of Moulding Sand]
S1	24 h desiccator	2.16	15.80
S2	3 h laboratory	2.64	19.00
S3	24 h laboratory	2.20	15.95
S4	7 days laboratory	2.02	14.39
S5	24 h climatic chamber *	2.32	16.57

* temperature—35 °C, humidity—70%.

Table 4. Mean values and standard deviations of the total gas volume and the maximum gas release rate for all storage variants (S1–S5).

Experimental Series	Storage Condition	Gas Volume [dm^3/kg]	Gas Release Rate [dm^3/(kg·s)]
S1	24 h desiccator	15.83 ± 0.35	0.22 ± 0.01
S2	3 h laboratory	19.00 ± 0.70	0.32 ± 0.10
S3	24 h laboratory	16.09 ± 0.32	0.21 ± 0.00
S4	7 days laboratory	14.39 ± 0.28	0.18 ± 0.02
S5	24 h climatic chamber *	16.57 ± 1.50	0.17 ± 0.03

* temperature—35 °C, humidity—70%.

Table 5. BTEX emissions from moulding/core sand (mg/sample). Development of results based on [27,28].

Experimental Series	Sample Description (Average of Samples)	Gas [mg/Sample]			
		Benzene	Toluene	Ethylbenzene	Xylenes
S1	24 h desiccator	52.13	0.22	0.00	0.61
S2	3 h laboratory	63.66	3.36	0.00	2.19
S3	24 h laboratory	70.36	2.12	0.00	0.72
S4	7 days laboratory	56.14	0.57	0.00	1.24
S5	24 h climatic chamber *	80.98	1.26	0.00	0.96

* temperature—35 °C, humidity—70%.

Table 6. BTEX emissions from moulding/core sand (mg/1 kg moulding/core sand). Development of results based on [27,28].

Experimental Series	Sample Description (Average of Samples)	Mass of the Sample [g]	Gas [mg/kg of Moulding/Core Sand]			
			Benzene	Toluene	Ethylbenzene	Xylenes
S1	24 h desiccator	136.51	328.18	1.65	0.00	4.45
S2	3 h laboratory	139.52	455.85	2.98	0.00	15.66
S3	24 h laboratory	141.96	495.67	14.91	0.00	5.05
S4	7 days laboratory	140.17	400.36	4.06	0.00	8.83
S5	24 h climatic chamber *	140.13	577.97	9.03	0.00	7.02

* temperature—35 °C, humidity—70%.

The results of the BTEX compound measurements (benzene, toluene, ethylbenzene, xylenes) indicate a strong correlation between the storage conditions of the samples (cores) and the emission of benzene, the most hazardous component classified as a carcinogenic agent. Storing the cores in a desiccator significantly reduces benzene formation compared to storage under standard laboratory conditions. Seasoning the cores for 7 days has a beneficial effect on lowering BTEX emissions; for instance, benzene emissions were 14% lower compared to samples tested 3 h after preparation, and as much as 24% lower compared to those stored under laboratory conditions for 24 h. These findings suggest that storage conditions have a greater impact on benzene emission than the elapsed time between core preparation and casting. Notably, storage under elevated humidity conditions (climate chamber: T = 35 °C, RH = 70%) leads to a significant increase in BTEX emissions. In fact, benzene release increased by approximately 45% compared to cores seasoned for 7 days under standard laboratory conditions (T = 20–21 °C, RH = 45–50%).

4. Conclusions

Based on the study, the following conclusions were made:

- Storing samples in a desiccator for 24 h results in lower emissions compared to samples stored in the laboratory for the same period. In contrast, samples (cores) poured 3 h after preparation exhibit higher emissions than those poured after 24 h of storage, which is due to the evaporation of volatile substances from the hardener and/or the complete reaction of the binder components (resin–hardener).
- It has been demonstrated that storing samples under conditions of elevated humidity (temperature: 35 °C, humidity: 70%) leads to higher emissions, although still at a lower level than in samples poured 3 h after preparation. Therefore, it can be concluded that the "setting time" of the cores plays a crucial role in foundry practice, as it can

significantly affect the tendency to form gas-related defects. Such defects are often irreparable and result in castings being classified as non-compliant with customer requirements. In many cases, these defects are discovered during machining or, even more critically, by the end user, resulting in high financial and reputational costs.

- Seasoning of cores for an adequate duration under controlled climatic conditions helps reduce both the overall gas generation and the emission rate. This is particularly important for cores exposed to extreme thermal loads, which are typically completely burned through during casting, causing total degradation of the binder and release of volatile decomposition products. Gas evacuation from such cores is limited, as they are almost entirely surrounded by molten metal. Therefore, any increase in gas volume generated during mould or core pouring becomes critically important and must be effectively vented to minimize the risk of gas-related defects.
- A properly designed core production process, including a sufficiently long seasoning period in controlled temperature and humidity conditions, can significantly reduce the risk of casting defects, improve product quality, and enhance occupational safety in foundries.
- The intensification of gas emissions under adverse storage conditions, especially high humidity, in APNB binder technology cores promotes the formation of toxic compounds from the BTEX group (benzene, toluene, ethylbenzene, xylenes). This not only leads to increased environmental emissions but also directly exposes foundry workers to harmful substances. Benzene is of particular concern, as it is classified as a carcinogenic compound.

Author Contributions: Conceptualization, A.B. and F.W.; methodology, A.B., F.W., S.Ż.-K. and B.G.; formal analysis, A.B., F.W. and B.G.; data curation, F.W., H.Z. and K.J.; investigation, F.W., S.Ż.-K., H.Z. and K.J.; writing—original draft preparation, A.B. and F.W.; writing—review and editing, F.W.; visualization, F.W.; supervision, A.B. All authors have read and agreed to the published version of the manuscript.

Funding: This research was funded by Ministry of Science and Higher Education, Poland. AGH University of Krakow as part of the statutory work no. 16.16.170.654/B507.

Institutional Review Board Statement: Not applicable.

Informed Consent Statement: Not applicable.

Data Availability Statement: The original contributions presented in this study are included in the article. Further inquiries can be directed to the corresponding author.

Conflicts of Interest: The authors declare no conflicts of interest.

References

1. Mhamane, D.A.; Rayjadhav, S.B.; Shinde, V.D. Analysis of Chemically Bonded Sand Used for Molding in Foundry. *Asian J. Sci. Appl. Technol.* **2018**, *7*, 11–16. [CrossRef]
2. Gutowski, W.S.; Błędzki, A.K. Fast-Setting Permeable Alkyd/Polyester Composites: Moulding Sands. *Polymers* **2021**, *13*, 4386. [CrossRef] [PubMed]
3. Holtzer, M.; Dańko, R.; Piasny, S.; Kubecki, M.; Drożyński, D.; Roczniak, A.; Skrzyński, M.; Kmita, A. Research on the Release of Dangerous Compounds from the BTEX and PAHs Groups in Industrial Casting Conditions. *Materials* **2021**, *14*, 2581. [CrossRef] [PubMed]
4. Garitaonandia, E.; Ibarra, A.; Kmita, A.; Dańko, R.; Holtzer, M. Assessment of Harmful Emissions from Multiple Binder Systems in Pilot-Scale Sand Casting. *Molecules* **2025**, *30*, 2765. [CrossRef]
5. Ghosh, D.K. Comparison of molding sand technology between alphaset (ApNB) and furan (FNB). *Arch. Foundry Eng.* **2019**, *19*, 11–20. [CrossRef]
6. Major-Gabryś, K.; Hosadyna-Kondracka, M. Organic Moulding Sands for Production of Large-Size Castings. *Arch. Foundry Eng.* **2019**, *19*, 99–105. [CrossRef]

7. Kubecki, M.; Holtzer, M.; Bobrowski, A.; Dańko, R.; Grabowska, B.; Żymankowska-Kumon, S. Analysis of the Compounds from the BTEX Group, Emitted During Thermal Decomposition of Alkyd Resin. *Arch. Foundry Eng.* **2012**, *12*, 69–74. [CrossRef]
8. Bobrowski, A.; Holtzer, M.; Zymankowska-Kumon, S.; Dańko, R. Harmfulness assessment of moulding sands with a geopolymer binder and a new hardener, in an aspect of the emission of substances from the BTEX group. *Arch. Metall. Mater.* **2015**, *60*, 341–344. [CrossRef]
9. Fortini, A.; Merlin, M.; Raminella, G. A Comparative Analysis on Organic and Inorganic Core Binders for a Gravity Diecasting Al Alloy Component. *Int. J. Met.* **2022**, *16*, 674–688. [CrossRef]
10. Łucarz, M.; Drożyński, D.; Garbacz-Klempka, A.; Jezierski, J.; Bartocha, D.; Wróbel, T.; Kostrzewa, K.; Feliks, E. Influence of Weather Conditions and Mechanical Reclamation on Molding Sand with Alkali-Phenolic Binder for Manganese Cast Steel. *Materials* **2023**, *16*, 71. [CrossRef]
11. Dańko, J.; Dańko, R.; Łucarz, M. Assessment of the reclamation of used sands from the alpha-set technology in the testing apparatus. *Arch. Foundry Eng.* **2009**, *9*, 33–36.
12. Huang, R.H.; Zhang, B.P.; Tang, Y.J. Application conditions for ester cured alkaline phenolic resin sand. *China Foundry* **2016**, *13*, 231–237. [CrossRef]
13. Lewandowski, J.L. *Tworzywa na Formy Odlewnicze*; Akapit: Kraków, Poland, 1997.
14. Łucarz, M.; Drozyński, D.; Jezierski, J.; Kaczmarczyk, A. Comparison of the Properties of Alkali-Phenolic Binder in Terms of Selection of Molding Sand for Steel Castings. *Materials* **2019**, *12*, 3705. [CrossRef] [PubMed]
15. Łucarz, M. Selection of Effective Temperature for Thermal Regeneration of Spent Alkali-Phenolic Binder Moulding Sand. *Materials* **2023**, *16*, 7629. [CrossRef]
16. Svidró, J.T.; Diószegi, A.; Svidró, J.; Ferenczi, T. The effect of different binder levels on the heat absorption capacity of moulding mixtures made by the phenolic urethane cold-box process. *J. Therm. Anal. Calorim.* **2017**, *130*, 1769–1777. [CrossRef]
17. Łucarz, M.; Garbacz-Klempka, A.; Drożyński, D.; Skrzyński, M.; Kostrzewa, K. Mechanical reclamation of spent moulding sand on chromite sand matrix; removal of alkali-phenolic binder. *Materials* **2023**, *16*, 2919. [CrossRef]
18. Holtzer, M.; Żymankowska-Kumon, S.; Bobrowski, A.; Kmita, A.; Dańko, R. Influence of the Reclaim Addition to the Moulding Sand Matrix Obtained in the ALPHASET Technology on the Emission of Gases—Comparison with Moulding Sand with Furfuryl Resin. *Arch. Foundry Eng.* **2015**, *15*, 121–125.
19. Gyarmati, G.; Budavári, I.; Fegyverneki, G.; Varga, L. The effect of sand quality on the bending strength and thermal distortion of chemically bonded sand cores. *Heliyon* **2021**, *7*, e07624. [CrossRef]
20. Kołodziej, R.; Kostrzewski, Ł.; Szajnar, J. Problem z wadami gazowymi w odlewni żeliwa. *Arch. Foundry Eng.* **2013**, *13*, 75–78.
21. Urządzenie LUZ-2e do Wibracyjnego Zagęszczania Próbek | Multiserw Morek. Available online: https://multiserw-morek.pl/produkt/urzadzenie-luz-2e-do-wibracyjnego-zageszczania-probek/ (accessed on 10 September 2025).
22. Holtzer, M.; Dańko, J.; Lewandowski, J.L.; Solarski, W.; Dańko, R.; Grabowska, B.; Bobrowski, A.; Żymankowska-Kumon, S.; Sroczyński, A.; Różycki, A.; et al. Station for Research of the Volume and Harmfulness of Gases Compounds from the Materials Used in Foundry and Metallurgical Processes. Patent Description. Patent PL224705B1, 31 January 2017.
23. Szymański, Ł.; Żymankowska_Kumon, S. Application of chromatographic analysis in foundry engineering. *Arch. Foundry Eng.* **2013**, *13*, 167–170.
24. Bobrowski, A.; Woźniak, F.; Żymankowska-Kumon, S.; Kaczmarska, K.; Grabowska, B.; Dereń, M.; Żuchliński, R. The Influence of 3D Printing Core Construction (Binder Jetting) on the Amount of Generated Gases in the Environmental and Technological Aspect. *Materials* **2023**, *16*, 5507. [CrossRef] [PubMed]
25. Pilato, L. (Ed.) *Phenolic Resins: A Century of Progress*; Springer: New York, NY, USA, 2010.
26. Gardziella, A.; Pilato, L.; Knop, A. *Phenolic Resins: Chemistry, Applications, Standardization, Safety, and Ecology*; Springer: Berlin/Heidelberg, Germany, 2000; p. 560. Available online: https://books.google.com/books/about/Phenolic_Resins.html?hl=pl&id=CDOAraoWwTMC (accessed on 10 September 2025).
27. Ziętal, H. *The Role of Selected Physicochemical and Technological Parameters on the Gas Formation of Molding and Core Sands*; Engineering Project (first-cycle studies); Faculty of Foundry, AGH University of Krakow: Krakow, Poland, 2025.
28. Januszek, K. *Emission of Gases from Molding and Core Sands Depending on Their Storage Conditions*; Engineering Project; Faculty of Foundry, AGH University of Krakow: Krakow, Poland, 2025.

Disclaimer/Publisher's Note: The statements, opinions and data contained in all publications are solely those of the individual author(s) and contributor(s) and not of MDPI and/or the editor(s). MDPI and/or the editor(s) disclaim responsibility for any injury to people or property resulting from any ideas, methods, instructions or products referred to in the content.

materials

MDPI

Article

Topography and Corrosion Resistance Characteristics of Fe40Al5Cr0.2ZrB Alloy and X18CrN28 Steel

Janusz Cebulski [1,*], Dorota Pasek [2], Stanisław Roskosz [1], Magdalena Popczyk [3,*], Jadwiga Gabor [3], Sebastian Stach [4], Roman Wrzalik [3], Marcin Wojtyniak [5], Michał Simlot [6] and Andrzej S. Swinarew [3,7]

[1] Department of Materials Technology, Faculty of Materials Engineering and Industrial Digitalization, Silesian University of Technology, Krasińskiego 8, 40-019 Katowice, Poland
[2] Promobil S.C., Kopernika 12, 40-064 Katowice, Poland; dorota.pasek@promobil.pl
[3] Faculty of Science and Technology, University of Silesia in Katowice, 75 Pułku Piechoty 1A, 41-500 Chorzów, Poland; roman.wrzalik@us.edu.pl (R.W.)
[4] Faculty of Science and Technology, University of Silesia in Katowice, Będzińska 39, 41-200 Sosnowiec, Poland; sebastian.stach@us.edu.pl
[5] Institute of Physics, Silesian University of Technology, Konarskiego 22B, 44-100 Gliwice, Poland
[6] Department of Laryngology, Faculty of Medical Sciences in Katowice, SPSK im. A. Mielęckiego SUM, Medical University of Silesia, Francuska 20/24, 40-027 Katowice, Poland
[7] Department of Training and Nutrition in Sports, Faculty of Physical Education, The Jerzy Kukuczka Academy of Physical Education, Mikołowska 72A, 40-065 Katowice, Poland
* Correspondence: janusz.cebulski@polsl.pl (J.C.); magdalena.popczyk@us.edu.pl (M.P.)

Abstract

This paper presents the results of corrosion resistance tests of materials (Fe40Al5Cr0.2ZrB alloy and X18CrN28 steel) in a 5% NaCl solution at room temperature using electrochemical impedance spectroscopy (EIS) and potentiodynamic polarization, complemented by confocal/AFM topography and SEM/EDS analysis. Confocal/AFM mapping showed pronounced roughening and localized features on Fe40Al5Cr0.2ZrB alloy (e.g., S_a rising locally to ~1.63 μm), consistent with heterogeneous chloride-induced attack, whereas X18CrN28 steel exhibited only minor roughness changes (S_a ~ 13–19 nm). SEM/EDS of Fe40Al5Cr0.2ZrB alloy revealed mixed oxides with detectable chlorine at corroded sites, while the steel retained a thin, Cr-rich passive layer with negligible Cl signal. Overall, X18CrN28 steel demonstrates significantly higher resistance to localized corrosion in neutral chloride media than Fe40Al5Cr0.2ZrB alloy, aligning electrochemical metrics with surface and chemical analyses.

Keywords: corrosion resistance; intermetallic phases; Fe40Al5Cr0.2ZrB alloy; X18CrN28 ferritic stainless steel; electrochemical impedance spectroscopy; chloride-induced attack

1. Introduction

The development of heat-resistant materials engineering is closely linked to many fields of technology, primarily thermal and nuclear power generation, as well as aviation and the construction of technological equipment. However, the primary consumer of heat-resistant steels and alloys is the thermal power industry, and therefore, its development is largely dependent on commercially available materials and technologies that meet increasing quality requirements. The requirements for steels operating at elevated temperatures significantly exceed the standard characteristics used in structural calculations [1].

For many years, the basic heat-resistant materials have been metal alloys, primarily steels for use at elevated temperatures and nickel–cobalt alloys for use at high temperatures. Among all construction materials, heat-resistant steels designed for use at high

temperatures and in corrosive environments have played an important role, primarily due to the development of the energy and chemical industries [2]. In addition to the required heat-resistant properties, it is important that these materials are also resistant to electrochemical corrosion. This is particularly important when the structural components of an industrial installation operate in a cyclic manner. Lowering the operating temperature of a system operating in an aggressive environment can cause the release of acid and salt compounds, which can negatively affect the surface of the materials from which they are made. It is essential to assess the corrosion resistance of materials under cyclic operation, such as during the temporary shutdown of specific installation components. Furthermore, it is worth noting that conventional coolers and heat exchangers are typically cooled with brine, such as sodium chloride (NaCl). In the case of geothermal power plants and salt installations, the pipelines are immersed in an environment with a concentration of 5–25% NaCl.

Manufacturers of stainless, acid-resistant, and heat-resistant steel products rely on several basic grades of steel, which share a common characteristic: a high content of alloying elements, including nickel, chromium, and molybdenum, as well as tungsten, vanadium, and titanium. The most used steels include ferritic, martensitic, duplex, and austenitic steels with a reduced nickel content. Selection of a specific grade must be based on an analysis of the actual operating conditions of a given product and the operational requirements that must be met. Manufacturers are increasingly seeking alternative grades to conventional steels, which will reduce costs while maintaining the same material properties.

Based on the results of research conducted on material selection and appropriate technological processes, it has been demonstrated that a matrix of iron, nickel, and titanium compounds with aluminum can create a different group of structural alloys with specific mechanical properties and a stable structure at high temperatures. Materials tested in the present comparative study were Fe40Al5Cr0.2ZrB (intermetallic, homogenized at 1050 °C for 72 h) and X18CrN28 ferritic stainless steel. Electrochemical testing in 5% NaCl, confocal and AFM surface roughness mapping, and SEM/EDS investigations were conducted to provide information on passive-film quality, localized attack, and corrosion kinetics.

Intermetallic iron–aluminum (Fe–Al) alloys based on the FeAl (B2) phase are attractive for high-temperature structural applications as they combine low density, good oxidation resistance, and favorable high-temperature strength in oxidizing atmospheres [3–5], with their dominant corrosion protection mechanism being the selective formation of a continuous α-Al_2O_3 (alumina) scale that limits further inward oxygen diffusion and outward metal transport [3,6,7]. The scale adherence, growth kinetics, and in-service mechanical behavior are strongly influenced by alloying additions such as Cr, Zr, Ti, and B, as well as microstructural control through homogenization, grain size, and dispersoids [5,8,9]. In contrast, the ferritic stainless steel X18CrN28 (EN 1.4749), which is comparable to the AISI 446 family with a high Cr content of approximately 23–28 wt.%, is designed as a heat-resisting alloy where corrosion resistance arises primarily from chromium-rich passive films (Cr_2O_3 and mixed Fe–Cr oxides) combined with a thermally stable ferritic matrix [10–12], and where nitrogen additions may further increase strength and influence passivity by modifying the matrix chemistry [10].

At elevated temperatures in oxidizing atmospheres, Fe–Al intermetallics form alumina scales via the selective outward diffusion of Al and inward diffusion of oxygen, a process that yields a slow, parabolic growth rate of dense α-Al_2O_3 when aluminum activity and scale continuity are sufficient [3,6,7]. This alumina scale is thermodynamically very stable and exhibits low ionic conductivity, which accounts for the excellent oxidation resistance of properly formulated Fe–Al alloys in dry, oxygen-rich environments [3,7,13]. Chromium-bearing ferritic steels, however, form chromium oxide (Cr_2O_3) and mixed

spinel ($FeCr_2O_4$) scale layers when exposed to similar conditions; these scales are generally thinner than alumina but provide effective passivation at typical service temperatures for heat-resisting steels, with their protective character depending on chromium availability at the metal/oxide interface, scale continuity, and the absence of deleterious contaminants like sulfur or alkali chlorides that promote breakdown [10–12].

Although α-Al_2O_3 is highly protective in dry oxygen, chloride species are particularly aggressive to alumina-forming systems, where under chlorine-containing atmospheres or in aqueous chloride solutions, the alumina scales can be undermined by chloride adsorption, penetration at defects, or the formation of volatile aluminum oxy-chlorides, leading to scale thinning, local aluminum depletion, and the initiation of localized attack such as pitting [14–17]. Atomistic and experimental studies confirm that chloride ions interact with hydroxylated alumina surfaces and concentrate at defects and grain boundaries, thereby lowering the barrier to localized breakdown [15,16]. Consequently, while Fe–Al intermetallics show excellent performance in high-temperature oxidative environments, they are comparatively susceptible to localized degradation in the presence of chlorides, especially when the oxide scale is non-uniform, defective, or subjected to mechanical stresses from thermal cycling that promote spallation [5,14,17], with several studies on Fe40Al-based alloys reporting mixed behavior—protective alumina formation under benign conditions but localized or accelerated attack when halides are present or the scale is damaged [5,8,18].

Ferritic high-Cr steels, such as X18CrN28, on the other hand, develop a chromium-enriched passive film in aqueous chloride solutions that is typically more resistant to chloride penetration than the defective alumina films on some Fe-Al alloys. The favorable thermodynamics and kinetics of Cr_2O_3 formation, coupled with the rapid repassivation ability of chromium-containing steels, generally provide superior resistance to localized electrochemical attack in neutral chloride solutions such as NaCl when compared to many alumina-forming intermetallics under identical conditions [11,19,20], a conclusion supported by recent comparative studies indicating that grades like AISI 446 exhibit relatively noble corrosion potentials, low passive current densities, and good stability in chloride environments [20].

Electrochemical impedance spectroscopy and potentiodynamic polarization measurements in 5% NaCl typically reflect these differences: the Fe40Al5Cr0.2ZrB intermetallic exhibits a more negative corrosion potential and higher corrosion current density, indicating less robust passivation in the presence of Cl^-, along with lower polarization resistance when localized film defects allow chloride ingress, and surface microscopy often reveals mixed oxide/hydroxide products with localized pits and oxide accumulation in corroded regions [5,16,18]. Conversely, the X18CrN28 ferritic steel demonstrates a more noble corrosion potential, substantially lower corrosion current density, and larger polarization resistance, consistent with a continuous chrome-rich passive layer, while SEM/EDS analysis typically shows thin, continuous Cr_2O_3/Fe–Cr oxide layers with little evidence of chloride accumulation at the film/metal interface [19,20], trends that are consistent with prior literature comparing these material classes in chloride-rich environments [5,14,20].

The fundamental mechanisms of protection and failure further elucidate this behavior. The dense, slow-growing alumina (α-Al_2O_3) on Fe–Al alloys under dry oxidizing conditions fails in chloride environments through mechanisms such as chloride adsorption and penetration at hydroxylated or defective surfaces, the formation of localized oxy-chloride species, mechanical spallation during thermal cycling, and local aluminum depletion that prevents the re-formation of a protective scale [14–17]. In contrast, chromia (Cr_2O_3) on X18CrN28 forms an inner, chromium-enriched oxide that passivates by limiting iron oxidation and promoting self-healing after local damage. This oxide exhibits good

stability against chloride attack in many aqueous environments because chromium tends to re-passivate, and the thermochemistry of volatile Cr-chlorides is less favorable under typical service conditions. However, it can still be undermined in strongly acidic or highly oxidizing chloride media or by molten chlorides at high temperatures [2].

From a practical standpoint, for components exposed to dry, high-temperature oxidizing atmospheres without significant chloride contamination, Fe–Al intermetallics are attractive due to the stable α-Al_2O_3 scale they form. However, for aqueous chloride environments or service involving cyclic exposure to chloride-bearing media, such as cooling waters or saline spray, high-Cr ferritic steels, like X18CrN28, generally offer more reliable passive protection and a lower propensity for localized chloride-induced breakdown. In hybrid or uncertain environments, potential solutions include using protective coatings, employing local alloying strategies like increasing the Cr content in Fe–Al alloys, or applying various barrier treatments to prevent chloride access.

2. Materials and Methods

The tests were performed on samples of the Fe40Al5Cr0.2ZrB intermetallic alloy after casting and steel X18CrN28. The materials of the Fe40Al5Cr0.2ZrB intermetallic alloy were subjected to homogenizing annealing at 1050 °C for 72 h, homogenizing the chemical composition of the alloy. The chemical composition was presented in Tables 1 and 2.

Table 1. Chemical composition of Fe40Al5Cr0.2ZrB alloy [6].

Compound	Fe	Al	Cr	Zr	B
% at.	54.80	40.10	4.86	0.18	0.06

Table 2. Chemical composition of X18CrN28 steel.

Compound	C	Mn	Si	Cr	Ni	N	Fe
% mas.	0.15	0.72	0.36	23.70	0.25	0.15	rest

The primary objective of the study was to assess the corrosion resistance of the Fe40Al5Cr0.2ZrB alloy (sample 1) and X18CrN28 steel (sample 2) in a 5% NaCl solution.

The research program comprised the following steps:

1. Corrosion resistance of the Fe40Al5Cr0.2ZrB alloys and X18CrN28 steel was investigated in 5% NaCl solution using AUTOLAB® system (PGSTAT30, Metrohm Autolab B.V., Utrecht, The Netherlands). A platinum mesh served as the counter electrode, and a saturated calomel electrode (SCE) was the reference electrode. These tests included the open-circuit potential measurement within 20 h, electrochemical impedance spectroscopy, and potentiodynamic polarization. EIS studies were performed at the open-circuit potential (frequency range from 50 kHz to 0.01 Hz (10 points per decade), amplitude of the ac signal 10 mV, room temperature). Potentiodynamic curves were registered within a potential range of ±250 mV relative to the open-circuit potential at a rate of 1 $mV \cdot s^{-1}$.
2. 3D confocal surface topography maps were obtained by an Olympus LEXT OLS-4000 confocal scanning microscope (Olympus Corp., Tokyo, Japan), and MountainsMap® Premium 6.2 software.
3. AFM—Measurements were performed using the intermittent contact method. Sample topography was recorded on 10 × 10 μm surfaces. Images were processed using standard Gwyd-dion 2.63 software (align rows, mean plane subtraction, shift minimum data to zero). Roughness parameters Sq (Root Mean Square Roughness) and Sa (Arithmetic Mean Height) were determined.

4. The surface appearance of the samples following corrosion tests was examined using scanning electron microscopy (SEM) with a Hitachi S-3400 (Tokyo, Japan). The chemical composition of oxidation products on the solid samples was analyzed using an energy dispersive X-ray spectrometer (EDS) by ThermoNoran (System Seven) (Waltham, MA, USA), operated at an electron beam accelerating voltage of 15 keV. The spectrometer connects to the microscope.

The experimental procedure is schematically illustrated in the diagram shown in Figure 1.

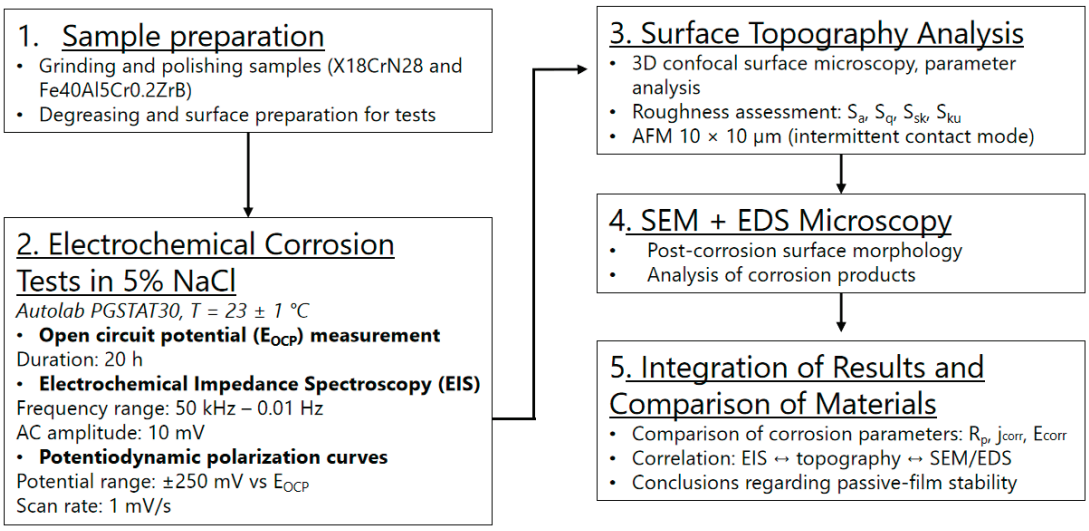


Figure 1. Schematic diagram of the experimental procedure.

3. Results

3.1. Corrosion Resistance Research

The open-circuit potential (E_{OCP}) of the Fe40Al5Cr0.2ZrB alloy and X18CrN28 steel after 20 h was determined (Figure 2). This potential (E_{OCP}) was −0.500 V for the Fe40Al5Cr0.2ZrB alloy and −0.218 V for the X18CrN28 steel. In the case of the tested materials, this potential remained practically unchanged after 20 h, indicating the high stability of these materials (Figure 2).

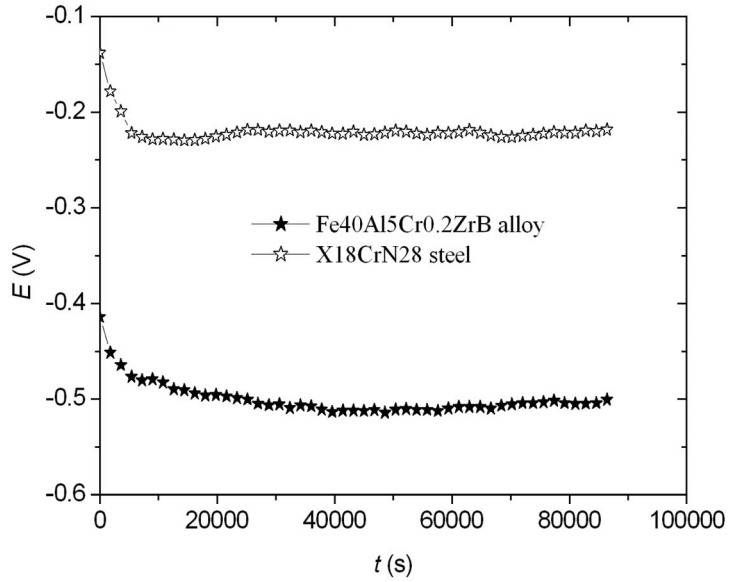


Figure 2. Dependences of $E = f(t)$ for the Fe40Al5Cr0.2ZrB alloy and X18CrN28 steel.

The EIS results are presented in the form of Nyquist and Bode diagrams ($-Z'' = f(Z')$ (a), $\log|Z| = f(\log f)$ (b), and $-\Phi = f(\log f)$ (c)) (Figure 3a–c). For tested materials, one semicircle is visible over the entire frequency range (Figure 3a). It was ascertained that this behavior of the tested materials could be described by a one-CPE electrode model (as previously discussed in detail [21–23]). The Nyquist diagrams show a good agreement between the experimental points and approximations. Approximations of the experimental impedances permitted determinations of the following parameters: R_p, R_s, T, ϕ, where R_p is polarization resistance, R_s is solution resistance, T is the capacity parameter, and ϕ is the CPE angle. Based on these results, it was found that the X18CrN28 steel exhibited greater resistance to corrosion, as evidenced by a higher polarization resistance value and a lower capacitance parameter value (Table 3).

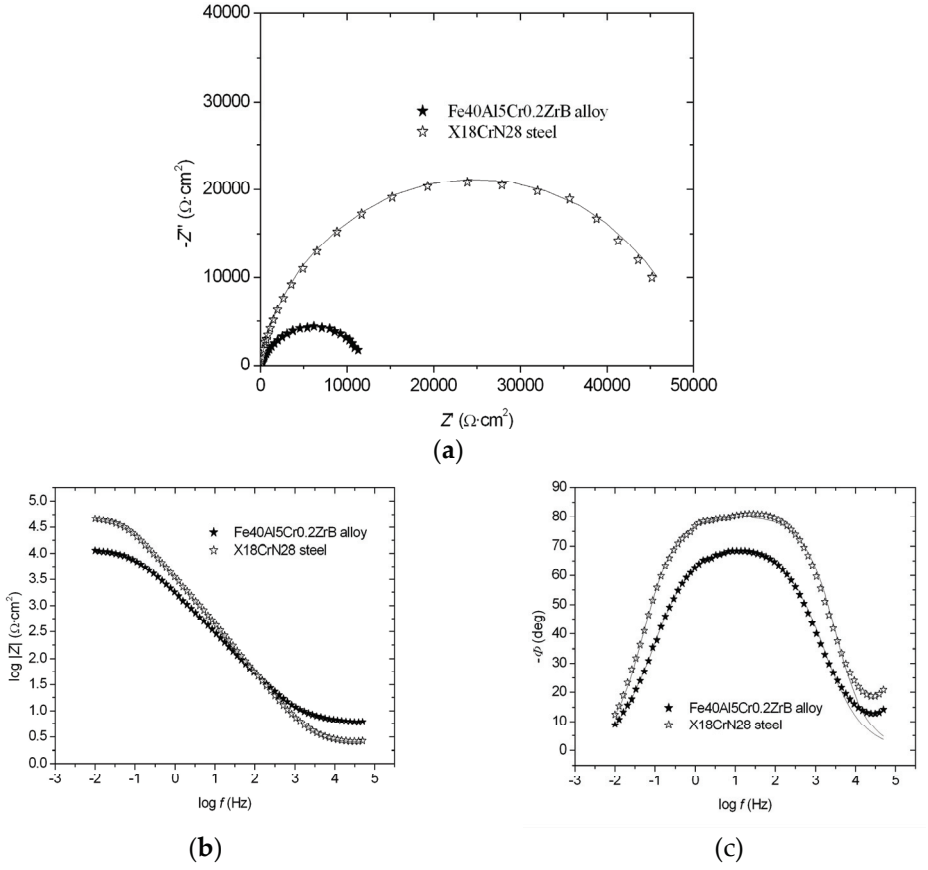


Figure 3. Nyquist and Bode diagrams: $-Z'' = f(Z')$ (**a**), $\log|Z| = f(\log f)$ (**b**), and $-\Phi = f(\log f)$ (**c**), registered in 5% NaCl solution for the Fe40Al5Cr0.2ZrB alloy and X18CrN28 steel (symbols—experimental points, solid lines—approximations using the one-CPE model).

Table 3. EIS parameters determined for the tested materials.

Type of Materials	R_s [Ω·cm²]	T	ϕ	R_p [Ω·cm²]
Fe40Al5Cr0.2ZrB alloy	1.89	0.00001799	0.89	12,330
X18CrN28 steel	1.48	0.00001013	0.77	49,230

The low-frequency impedance modulus is often used as a simple index for comparing materials [18]. For example, the $\log|Z|_{0.1}$ parameter (at a frequency of 0.1 Hz) for X18CrN28 steel showed a higher value (4.32 Ω·cm²) compared to the Fe40Al5Cr0.2ZrB alloy (3.84 Ω·cm²) (Figure 3b), indicating a more effective corrosion resistance of X18CrN28 steel. Furthermore, the dependence of $-\Phi = f(\log f)$ for X18CrN28 steel showed a wider

range of phase angle independence from the logarithm of frequency compared to the Fe40Al5Cr0.2ZrB alloy (Figure 3c). This wider range indicates a greater corrosion resistance of X18CrN28 steel.

The corrosion resistance parameters E_{corr}, $j_{corr,}$ and R_p (Table 4) were determined based on the obtained relationship log j = f (E) (Figure 4). The obtained results show that X18CrN28 steel exhibits higher corrosion resistance compared to the Fe40Al5Cr0.2ZrB alloy. Proof of this is higher polarization resistance R_p, lower current density, and a shift in corrosion potential toward positive values (Figure 4). It is worth noting that the corrosion potential does not differ significantly from the previously determined open-circuit potential (E_{OCP}). The parameters determined by the potentiodynamic measurements allow for the estimation of the corrosion resistance of coatings and confirm the results obtained from the EIS method.

Table 4. Corrosion parameters: E_{corr}, j_{corr} and R_p of the tested materials.

Type of Materials	E_{corr} [V]	j_{corr} [μA·cm^{-2}]	R_p [Ω·cm^2]
Fe40Al5Cr0.2ZrB alloy	−0.502	3.69	12,790
X18CrN28 steel	−0.223	0.02	49,670

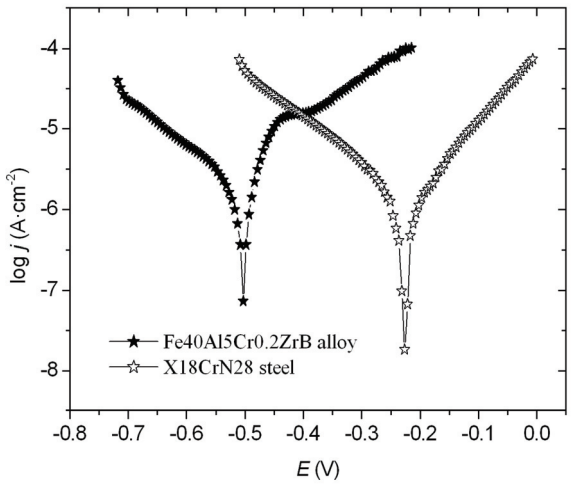


Figure 4. Potentiodynamic curves registered for the Fe40Al5Cr0.2ZrB alloy and X18CrN28 steel.

3.2. Research Surface Topography

Figure 5 presents the 3D surface topography of the Fe40Al5Cr0.2ZrB intermetallic alloy before and after exposure to a 5% NaCl solution, obtained using confocal microscopy and analyzed according to ISO 25178 parameters [24] are presented in Tables 5 and 6. Post-corrosion observations were conducted at two locations on the sample.

Before corrosion (Figure 5a), the Fe40Al5Cr0.2ZrB surface exhibited a relatively smooth morphology characterized by a low arithmetic roughness (S_a = 24.18 nm) and root mean square roughness (S_q = 37.26 nm). The negative skewness (S_{sk} = −1.618) and high kurtosis (S_{ku} = 13.04) indicate that the surface was dominated by a few deep valleys, typical of mechanically polished metallic surfaces. No corrosion-related features were observed at this stage.

After immersion in the NaCl solution, significant changes in the surface morphology were detected. The first analyzed area (Figure 5b) showed a substantial increase in surface roughness (S_a = 1.633 μm; S_q = 2.082 μm) and total height (S_z = 10.35 μm), evidencing intensive corrosion processes. The positive skewness (S_{sk} = 1.005) and high surface development ratio (S_{dr} = 103.6%) indicate the formation of corrosion products and surface irregularities.

This suggests the presence of localized corrosion phenomena leading to the accumulation of oxides and hydroxides on the Fe40Al5Cr0.2ZrB surface.

In contrast, the second analyzed region after corrosion (Figure 5c) demonstrated lower average roughness (S_a = 41.28 nm; S_q = 76.20 nm), but exceptionally high S_{sk} (4.544) and S_{ku} (32.19) values, indicating the presence of sharp, isolated peaks corresponding to localized pitting corrosion. This non-uniform topography confirms that the corrosion process on Fe40Al5Cr0.2ZrB is highly heterogeneous and may proceed through the formation of discrete anodic sites.

Overall, the confocal microscopy analysis revealed that corrosion in Fe40Al5Cr0.2ZrB alloy immersed in a 5% NaCl environment leads to both general surface degradation and local pitting. The drastic increase in S_a and S_z values, together with the change in S_{sk} from negative to positive, confirms a transition from a smooth, valley-dominated surface to a rough morphology characterized by the accumulation of corrosion products and pit formation.

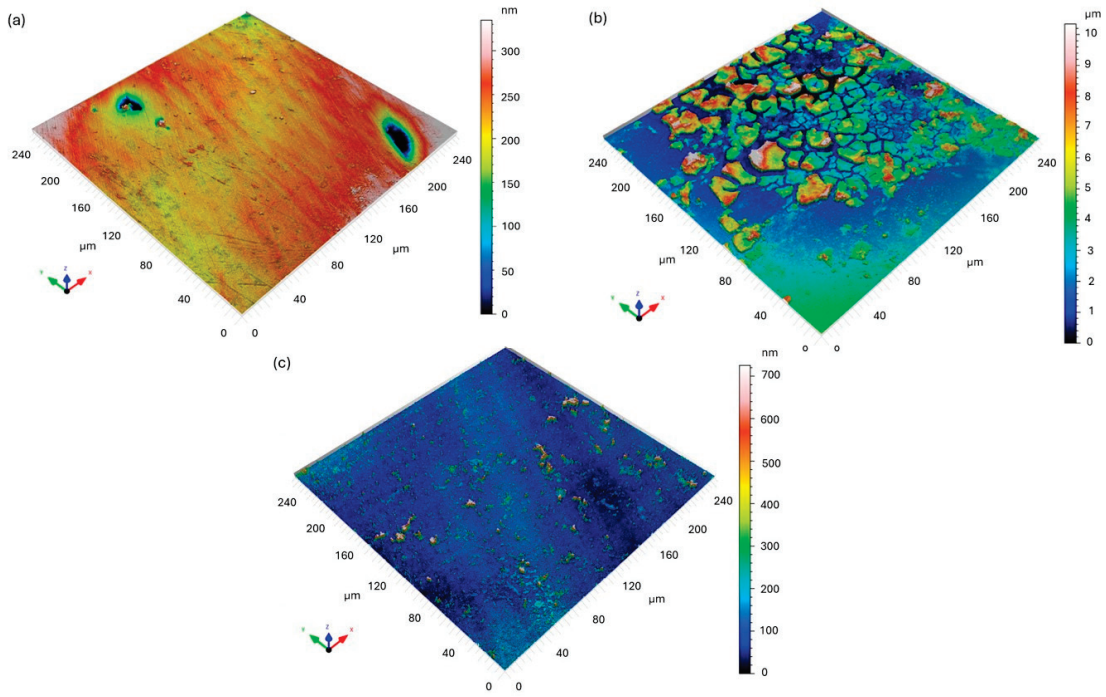


Figure 5. Three-dimensional confocal surface topography maps of Fe40Al5Cr0.2ZrB alloy: (**a**) before corrosion; (**b**) after corrosion—area 1 (intensive corrosion region); (**c**) after corrosion—area 2 (localized corrosion region).

Table 5. Parameters describing the surface topography of the Fe40Al5Cr0.2ZrB alloy.

Sample/Parameter	S_a	S_q	S_{sk}	S_{ku}	S_z
Sample before corrosion test	24.18 nm	37.26 nm	−1.618	13.04	334.8 nm
Sample after corrosion test, area 1	1.633 µm	2.082 µm	1.005	3.809	10.35 µm
Sample after corrosion test, area 2	41.28 nm	76.20 nm	4.544	32.19	725.3 nm

Table 6. Parameters describing the surface topography of the X18CrN28 steel.

Sample/Parameter	S_a	S_q	S_{sk}	S_{ku}	S_z
Sample before corrosion test	13.26 nm	16.34 nm	0.5556	3.244	88.46 nm
Sample after corrosion test, area 1	16.30 nm	22.57 nm	1.151	6.156	152.4 nm
Sample after corrosion test, area 2	18.89 nm	26.67 nm	1.373	5.966	171.9 nm

Figure 6 shows the 3D confocal topography maps of X18CRN28 steel before and after exposure to a 5% NaCl solution. The surface parameters were determined in accordance with ISO 25178.

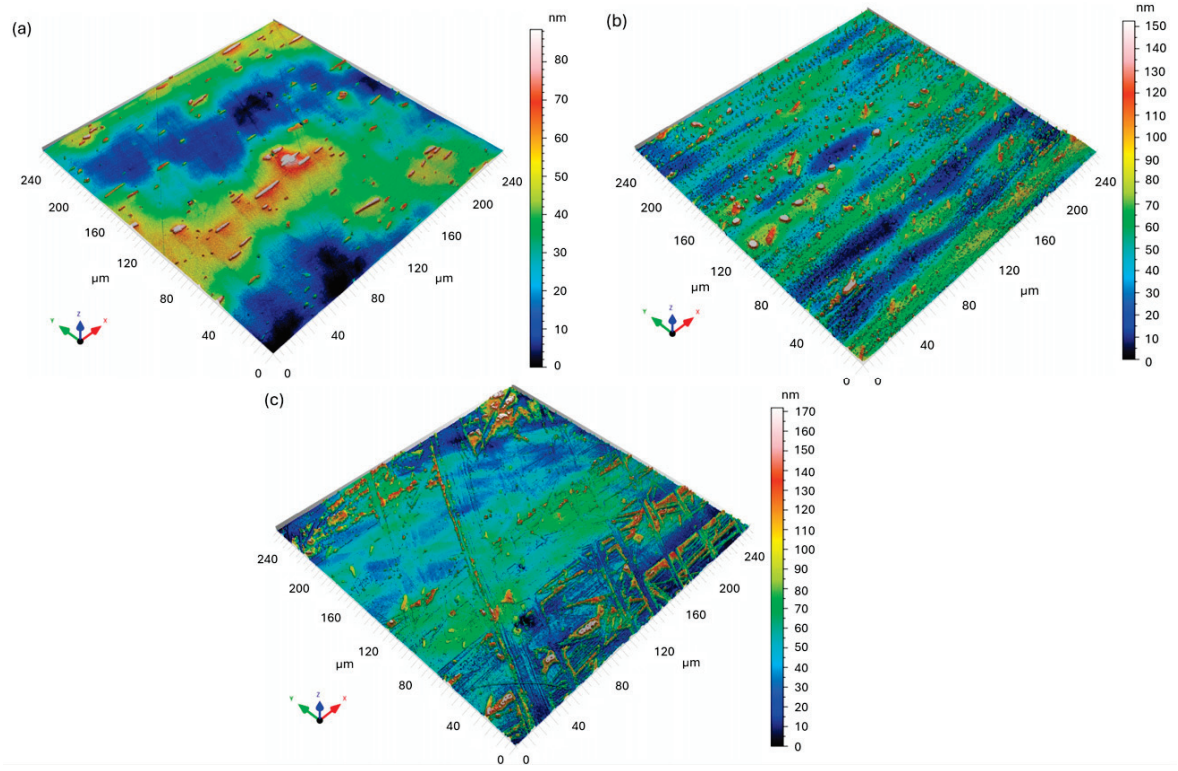


Figure 6. Three-dimensional confocal surface topography maps of X18CrN28 steel: (**a**) before corrosion; (**b**) after corrosion—area 1 (intensive corrosion region); (**c**) after corrosion—area 2.

Before corrosion (Figure 6a), the X18CRN28 steel exhibited a smooth surface with low roughness values (S_a = 13.26 nm, S_q = 16.34 nm) and a moderate positive skewness (S_{sk} = 0.5556). The S_{ku} value of 3.244 indicates a nearly Gaussian height distribution with only minor surface asperities, which corresponds to a polished metallic surface without visible corrosion features.

After the corrosion test, the surface morphology changed only slightly compared to the Fe40Al5Cr0.2ZrB alloy. The first analyzed region (Figure 6b) showed a moderate increase in surface parameters (S_a = 16.30 nm, S_q = 22.57 nm, S_z = 152.4 nm). The positive S_{sk} (1.151) and relatively high S_{ku} (6.156) indicate the formation of isolated surface peaks, likely due to the initiation of local corrosion attack or the presence of small corrosion products.

The second region (Figure 6c) revealed slightly higher roughness (Sa = 18.89 nm, S_q = 26.67 nm, S_z = 171.9 nm) and S_{sk} = 1.373, confirming localized surface changes. The S_{dr} parameter (0.16%) remained very low, indicating that the surface did not undergo extensive degradation. Overall, the morphology of X18CRN28 remained relatively stable after immersion in a NaCl solution, exhibiting only minor roughening and isolated corrosion points.

Compared with the Fe40Al5Cr0.2ZrB alloy, the X18CrN28 steel exhibited superior corrosion resistance, as reflected by its much smaller increase in roughness and the absence of extensive corrosion-induced topographical changes. This finding is consistent with the higher passivity of Cr–Ni–containing steels and their ability to maintain a protective oxide layer in chloride-containing environments.

3.3. Atomic Force Microscopy (AFM)

Atomic force microscopy was applied to characterize the nanoscale surface morphology of the Fe40Al5Cr0.2ZrB alloy (sample 1) before and after corrosion testing in 5% NaCl solution. All measurements were conducted in intermittent contact mode on areas of 10 × 10 μm, followed by standard data-processing procedures to ensure accurate height and roughness analyses. Five independent regions per condition were examined to ensure statistical reliability.

Surface condition before corrosion (Figure 7): The initial state of the Fe40Al5Cr0.2ZrB surface exhibited very low roughness values, with S_q = 1.65 ± 0.05 nm and S_a = 1.29 ± 0.17 nm, confirming a highly uniform, polished morphology typical for homogenized intermetallic materials. The observed nanoscale smoothness indicates the presence of a continuous surface oxide film formed during sample preparation, yet without corrosion-related features. This baseline surface condition provides a critical reference for evaluating corrosion-induced degradation.

The surface condition after corrosion (Figure 8) shows that exposure to a chloride solution induces a substantial modification of the nanoscale surface topography. Due to the strongly heterogeneous nature of the corrosion attack, roughness analysis could only be performed on the remaining unaltered regions of the specimen. In these selected locations, the S_q and S_a parameters slightly increased compared to the pristine state, reaching S_q = 1.89 ± 0.20 nm and S_a = 1.54 ± 0.11 nm, respectively. These values indicate that portions of the native surface remained passivated, maintaining nanoscale integrity.

However, the predominant surface transformation involved the formation of elevated morphologies in the corroded regions. These corrosion-generated structures can be described as plateau-like features with sharply defined boundaries, rising distinctly above neighboring unaffected areas. Quantitative profiling revealed a mean height of these "corrosion elevations" of 20.07 ± 2.56 nm, with individual profiles showing well-defined step geometries, indicating preferential local oxidation and accumulation of corrosion products. The AFM line profiles demonstrate abrupt transitions between intact and corroded domains, confirming susceptibility to localized attack mechanisms.

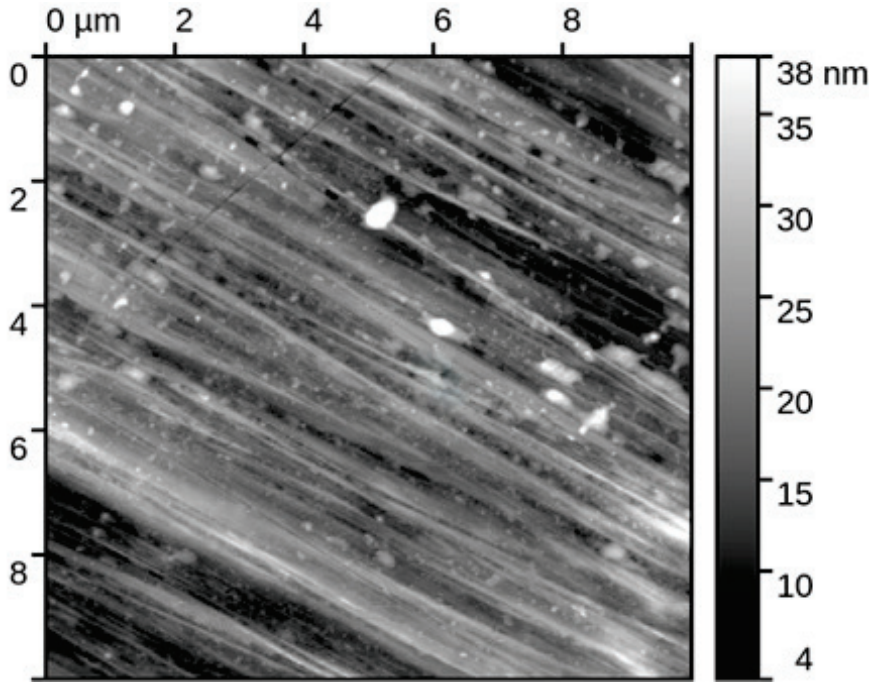


Figure 7. Topography of the original sample (Fe40Al5Cr0.2ZrB alloy) for areas of size 10 × 10 mm.

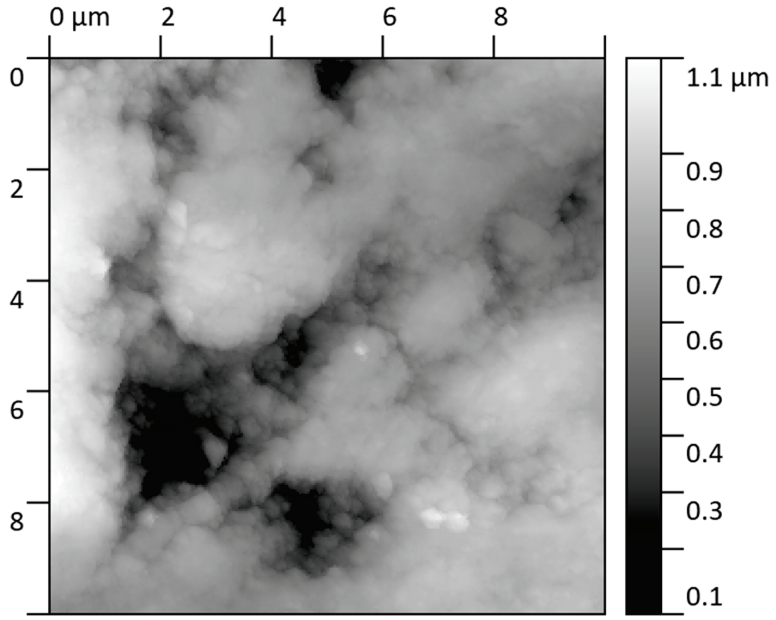


Figure 8. Topography of the sample (Fe40Al5Cr0.2ZrB alloy) in the corrosion zone covering an area of size 10 × 10.

The interpretation of the corrosion mechanism and AFM observations support the electrochemical and SEM/EDS findings:

- Corrosion proceeds via localized breakdown of the passive Al-rich surface layer.
- Chloride ions promote selective formation of nanoscale corrosion product islands, consistent with early-stage pitting initiation.
- The coexistence of unaffected and severely altered nanoscale regions confirms competition between passivation and active dissolution pathways.

This behavior is characteristic of Fe40Al5Cr0.2ZrB intermetallics under chloride exposure, where mechanical or chemical defects in the oxide film act as nucleation points for aggressive attack, while adjacent locations remain temporarily passive.

Unlike stainless steel X18CrN28 (Figures 9 and 10), which was examined elsewhere in this study and retained a relatively smooth surface after corrosion exposure, Fe40Al5Cr0.2ZrB displayed a pronounced loss of morphological integrity already at the nanoscale level. The passive protection provided by alumina on FeAl alloys is insufficiently stable against chloride-driven breakdown, making these materials more vulnerable than high-Cr ferritic steels in saline aqueous environments.

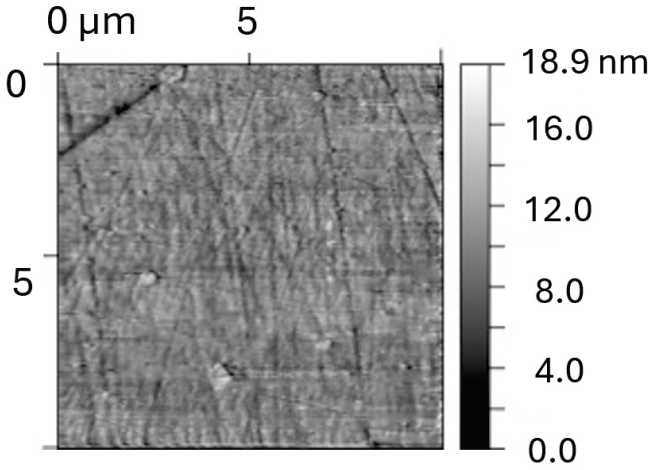


Figure 9. Topography of the original sample (X18CrN28 steel) (height) for areas of size 10 × 10 mm.

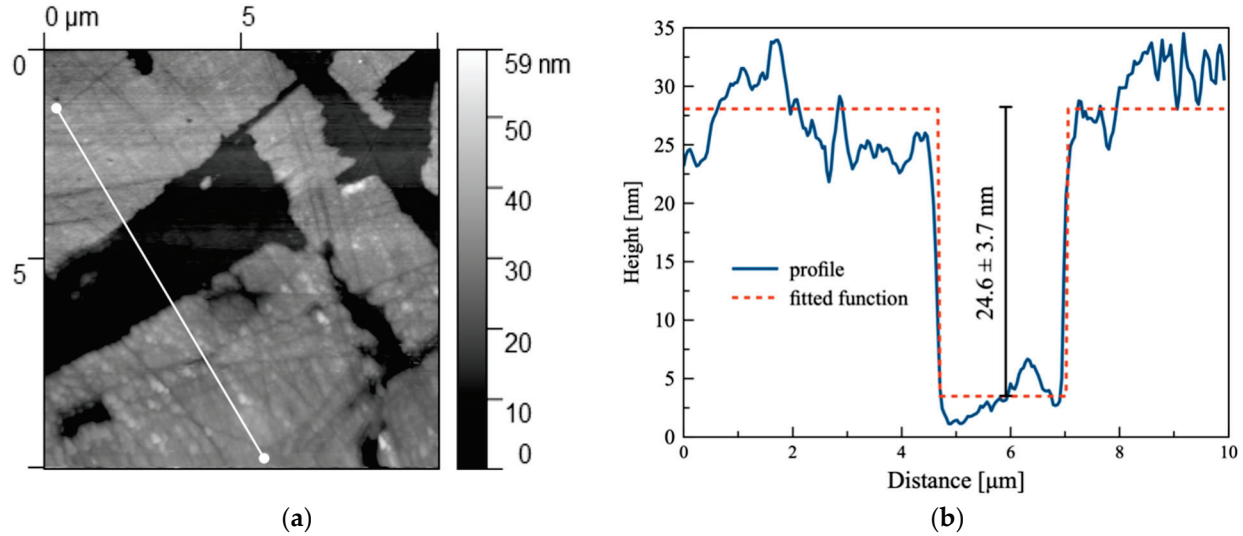


Figure 10. (**a**) Topography of the sample (X18CrN28 steel) in the corrosion zone covering an area of size 10 × 10. The white line indicates the position along which the height profile was extracted; (**b**) profile graph of the sample along the line marked in image (**a**); the dashed line represents the fitting function determined using the Gwyddion program (procedure: Fit critical dimension, function: Step height negative).

3.4. Analysis of the Surface Condition After Corrosion Tests (SEM, EDS)

Microscopic examinations (SEM) revealed pronounced differences in the surface condition of the two materials after exposure to a 5% NaCl solution. The surface of the Fe40Al5Cr0.2ZrB alloy (Figure 11) exhibited numerous corrosion products with heterogeneous morphology, with clearly visible regions of intense oxidation. The sharply defined depressions visible on the surface indicate the presence of pitting corrosion, which is consistent with the elevated levels of Cl and O detected in the EDS measurements (Figure 12). The most advanced forms of localized attack occur in regions that likely correspond to casting-related defects or microstructural discontinuities, which serve as preferential sites for pit initiation following the breakdown of the non-uniform Al_2O_3 layer. The observed morphology—comprising raised islands of corrosion products surrounded by deeper point-like cavities—indicates a strongly heterogeneous degradation process and local penetration of the oxide film.

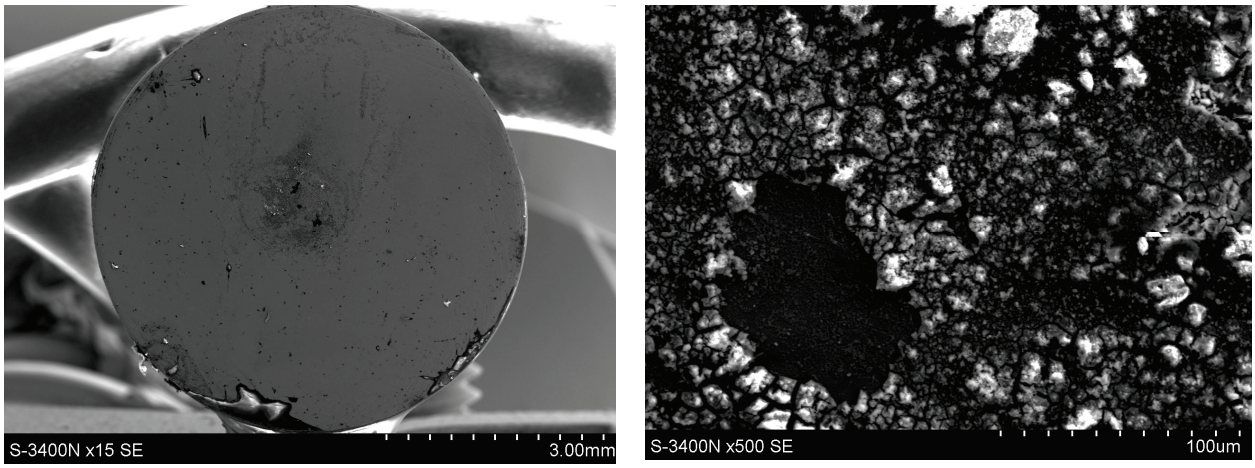
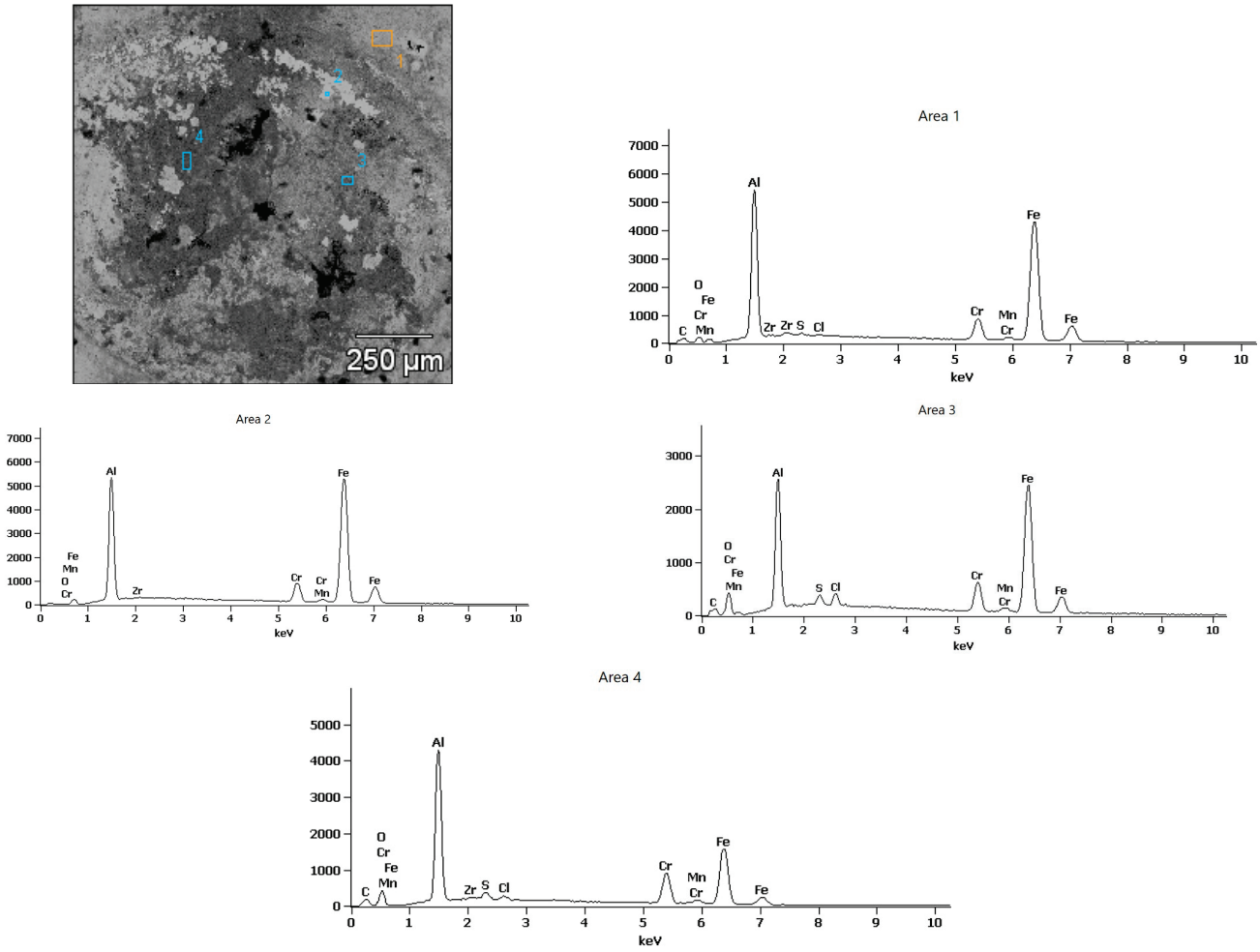


Figure 11. Surface condition of the Fe40Al5Cr0.2ZrB alloy after corrosion tests in 5% NaCl.



Weight %	*O*	*Al*	*S*	*Cl*	*Cr*	*Mn*	*Fe*	*Zr*
Fe40Al5Cr0.2ZrB—pt1	13.6	19.0	0.3	0.1	6.2	1.8	58.5	0.5
Fe40Al5Cr0.2ZrB—pt2	2.5	17.9			5.7	1.7	71.9	0.2
Fe40Al5Cr0.2ZrB—pt3	32.9	10.9	0.7	1.1	5.6	1.7	47.0	
Fe40Al5Cr0.2ZrB—pt4	34.1	19.1	0.8	0.5	10.3	1.6	33.1	0.3

Figure 12. X-ray microanalysis of the chemical composition of corrosion products after testing in 5% NaCl of the Fe40Al5Cr0.2ZrB alloy.

In contrast, the surface of the X18CrN28 steel (Figure 13) remained relatively smooth, with a uniformly distributed layer of protective oxides, indicating effective passivation in the chloride environment. However, locally found linear surface discontinuities are indicative of intergranular corrosion, which progresses along ferrite grain boundaries. This interpretation is supported by the EDS results shown in Figure 14, where the points corresponding to these linear features exhibit chromium enrichment, indicating the presence of chromium carbides of the $Cr_{23}C_6$ type. These carbides locally reduce the chromium content in the matrix and promote intergranular attack. It should be emphasized that such degradation features do not occur uniformly across the entire surface but appear only in selected, limited areas, consistent with the microscopic observations and indicating that the breakdown of the Cr_2O_3 passive film is partial rather than extensive.

Micro-area EDS analysis (Figure 12) confirmed substantial spatial variation in the chemical composition of the corrosion products on Fe40Al5Cr0.2ZrB. At the measurement points, oxygen ranged from 2.5 to 34.1%, aluminum 10.9–19.1%, iron 33.1–71.9%, and chromium 1.7–10.3%. The high oxygen contents at points 3 and 4 (over 30%) indicate

an intensified oxidation process and the formation of an oxide layer, likely comprising a mixture of Al_2O_3, Fe_2O_3, and Cr_2O_3. The aluminum fraction within this layer points to the formation of protective Al_2O_3 oxides that partially limit further corrosion.

The detection of chlorine up to 5.7% (Fe40Al5Cr0.2ZrB-pt2) suggests localized penetration of the chloride solution and the initiation of pitting corrosion. The simultaneous presence of sulfur in small amounts (0.3–0.8%) may result from the adsorption of impurities or the formation of iron sulfides. Areas with higher iron and lower oxygen contents (e.g., Fe40Al5Cr0.2ZrB-pt2, 71.9% Fe) correspond to surface regions less covered by corrosion products.

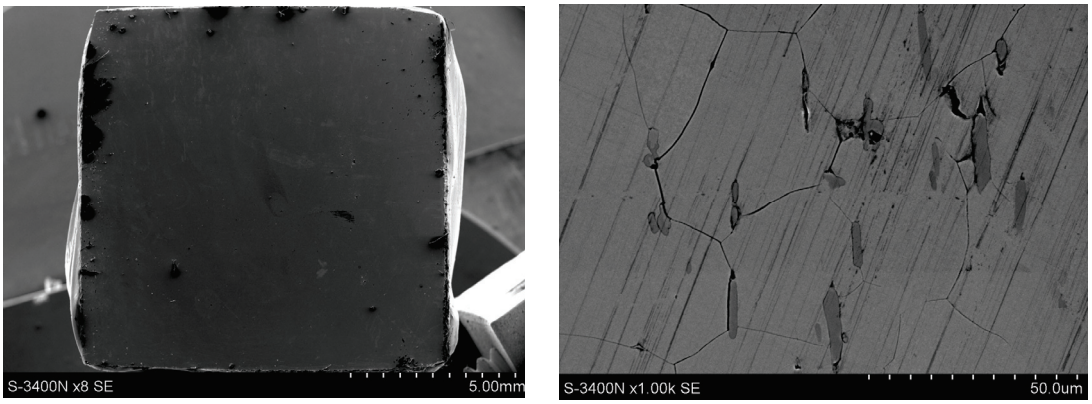


Figure 13. Surface condition of the X18CrN28 steel after corrosion tests in 5% NaCl.

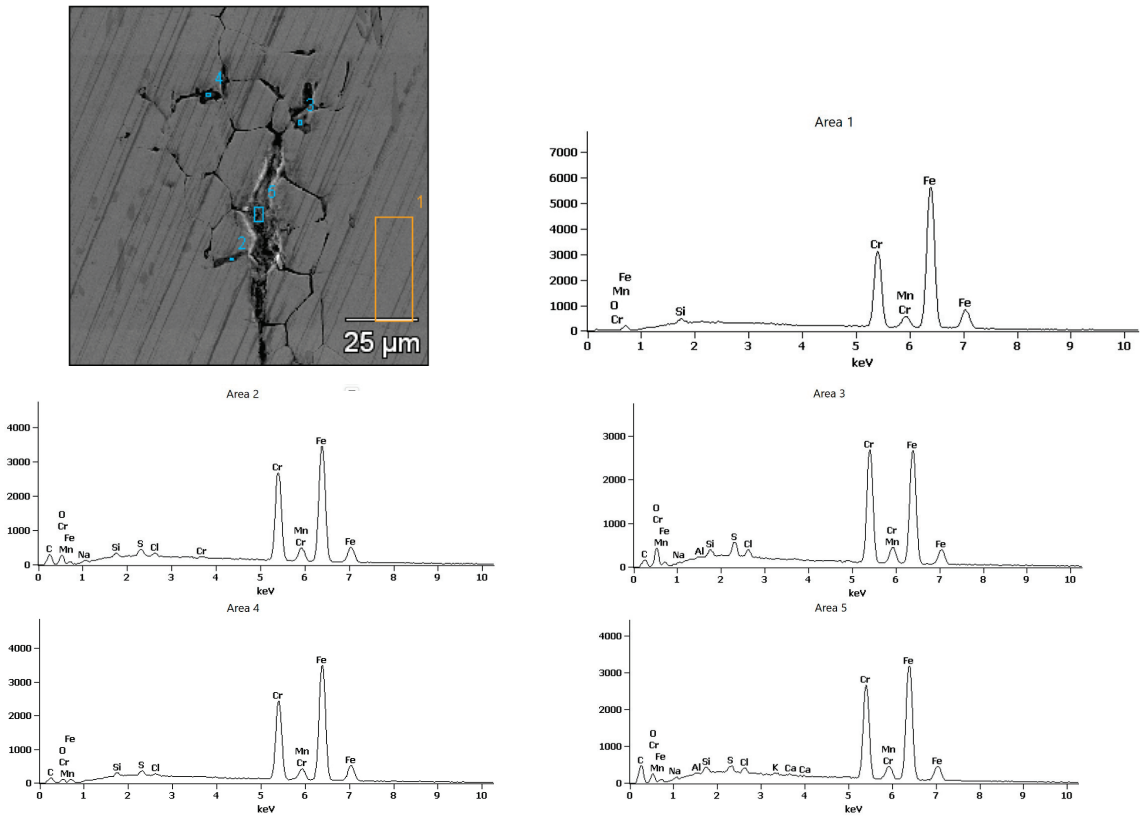


Figure 14. X-ray microanalysis of the chemical composition of corrosion products after testing in 5% NaCl of the X18CrN28 steel.

For X18CrN28 steel, EDS analysis (Figure 14) indicates the dominance of alloying elements—iron, chromium, and nickel—with a markedly lower oxygen fraction compared to Fe40Al5Cr0.2ZrB. The corrosion products form a thin, continuous layer of Cr_2O_3 and

$FeCr_2O_4$, confirming high passive-film stability. The absence of distinct chlorine peaks in the EDS spectra suggests that Cl^- ions do not significantly penetrate the passive layer.

Overall, X18CrN28 steel exhibits markedly superior corrosion resistance in the chloride environment compared to the Fe40Al5Cr0.2ZrB alloy. Although the high aluminum content in Fe40Al5Cr0.2ZrB favors the formation of Al_2O_3, the irregular structure and defects of this layer do not provide complete protection against Cl^- ingress.

4. Analysis of the Results

A comparative assessment of the corrosion resistance of a Fe40Al5Cr0.2ZrB intermetallic alloy and X18CrN28 ferritic stainless steel was carried out in 5% NaCl using EIS and potentiodynamic polarization, complemented by confocal/AFM imaging and SEM/EDS.

The corrosion resistance of potential replacement materials is typically evaluated using conventional electrochemical methods, such as potentiodynamic polarization curves and electrochemical impedance spectroscopy [25]. It was ascertained that the corrosion resistance of the X18CrN28 steel was significantly higher than that Fe40Al5Cr0.2ZrB alloy. Topographical and microanalytical observations indicated heterogeneous chloride attack in the Fe40Al5Cr0.2ZrB alloy (local pitting and surface roughening), while the steel showed only minor surface changes. The convergence of electrochemical and surface analyses enables an unambiguous ranking of the materials with respect to susceptibility to corrosion in NaCl solution. Consequently, X18CrN28 offers higher operational reliability in neutral chloride environments than the investigated Fe40Al5Cr0.2ZrB alloy. In the literature, it is well established that small additions of reactive elements, such as Zr and B, to Fe–Al intermetallic alloys primarily act as microstructural and scale-adhesion modifiers under high-temperature oxidizing conditions, rather than as effective inhibitors of aqueous corrosion. Studies on Fe–40Al alloys doped with Hf, Zr, and B have demonstrated that these elements promote the formation of a more adherent and continuous α-Al_2O_3 scale with parabolic growth kinetics and reduced spallation during thermal cycling [13,26]. Similarly, investigations of FeAl and FeCrAl alloys with Zr additions reveal that the presence of ZrO_2 within the oxide scale enhances its adherence and mechanical stability, thereby improving oxidation resistance in the 900–1200 °C range [3]. Boron, on the other hand, exhibits a strong tendency to segregate to grain boundaries, increasing their cohesion and reducing intergranular brittleness in ordered B2 intermetallics such as FeAl [27,28]. In the context of the present work, Zr and B in the Fe40Al5Cr0.2ZrB alloy may therefore improve the stability and integrity of the alumina scale under high-temperature dry oxidation (as supported by previous studies on this alloy), but their influence in an aqueous chloride environment is limited. Neither Zr nor B prevents chloride adsorption onto the hydrated Al_2O_3 surface or chloride penetration through defects in the scale, which correlates with the observed pitting-type, heterogeneous corrosion morphology of Fe40Al5Cr0.2ZrB in 5% NaCl. Unlike the high chromium content in X18CrN28 steel, which supports the formation of a stable, self-healing Cr_2O_3-based passive film resistant to chloride attack, the role of Zr and B in the Fe–Al alloy is mainly that of a "high-temperature" scale stabilizer rather than an enhancer of electrochemical corrosion resistance in saline aqueous media.

Despite the significant differences in the initial microstructure—namely the single-phase, ordered B2 structure of the Fe40Al5Cr0.2ZrB alloy and the ferritic microstructure of the X18CrN28 steel with a homogeneous distribution of chromium—the decisive factor governing their corrosion behavior in 5% NaCl is not the microstructure itself but the fundamentally different physicochemical mechanisms responsible for passive film formation and stability. In the Fe–Al alloy, the passive film formed under the tested conditions consists of a thin Al_2O_3 layer exhibiting numerous surface defects and a columnar oxide structure, which facilitates local electrolyte penetration [29]. Defects and grain boundaries within the

Al_2O_3 film act as preferential sites for chloride adsorption; atomistic studies have demonstrated that Cl^- ions can substitute surface −OH groups on hydroxylated alumina and initiate localized breakdown by forming unstable Al–O–Cl surface complexes [15,30,31]. This leads to pointwise depassivation and pit initiation. The slow repassivation kinetics and the limited ability to restore a compact Al_2O_3 layer promote the development of heterogeneous, isolated active sites, as confirmed by SEM/EDS observations (local enrichment in Cl and O), as well as 3D topography and AFM analyses, which show raised corrosion-product regions surrounding active dissolution zones.

In contrast, the X18CrN28 steel forms a stable, compact, and low-defect Cr_2O_3-based passive film due to its high chromium content. Recent studies show that increasing Cr content in ferritic steels enhances the formation of passive films with lower ionic conductivity and fewer structural defects, thereby improving resistance to chloride penetration and facilitating rapid repassivation [32,33]. The Cr_2O_3 film additionally exhibits high thermodynamic stability in chloride-containing environments and does not readily form volatile or unstable Cr–O–Cl compounds, limiting the initiation of surface defects [34]. As a result, corrosion proceeds in a mild and dispersed manner, and the surface topography remains almost unchanged—consistent with the minimal increases in S_a and S_z parameters and the absence of pronounced pitting in SEM images.

Therefore, despite the microstructural differences between the two materials, the key factor determining their corrosion performance in NaCl solution is the chemical nature and stability of their passive films—a defect-prone and chloride-susceptible Al_2O_3 film in Fe40Al5Cr0.2ZrB versus a stable, repassivable Cr_2O_3-based film in X18CrN28 steel. These physicochemical differences, rather than microstructural ones, underpin the markedly different degradation mechanisms observed in both materials.

5. Conclusions

Based on the conducted tests and analysis of their results, the following conclusions were formulated:

1. X18CrN28 steel is characterized by more favorable corrosion parameters than the Fe40Al5Cr0.2ZrB alloy.
2. Confocal/AFM and SEM/EDS confirm heterogeneous degradation of the Fe40Al5Cr0.2 ZrB alloy and the preservation of a thin, continuous passive film on the steel.
3. The material ranking derived from electrochemical methods is consistent with topographical and corrosion-product analyses.
4. For chloride-exposed applications, X18CrN28 steel is recommended; for Fe40Al5Cr0.2 ZrB alloys, barrier coatings or surface modifications should be considered.

Author Contributions: Conceptualization, J.C. and M.P.; methodology, J.C. and M.P.; validation, D.P., S.R. and M.S.; formal analysis, J.G.; investigation, D.P., S.R., M.P., R.W., M.W. and S.S.; data curation, M.P.; writing—original draft preparation, J.C., M.P., D.P., A.S.S., J.G., S.R., M.S., S.S., M.W. and R.W.; writing—review and editing, J.C., M.P., D.P., A.S.S., J.G., S.R. and S.S.; visualization, D.P. and S.R.; supervision, A.S.S. All authors have read and agreed to the published version of the manuscript.

Funding: The project was co-financed by the European Union within the program "The European Funds for Śląsk (Silesia) 2021–2027".

Data Availability Statement: The original contributions presented in this study are included in the article. Further inquiries can be directed to the corresponding authors.

Conflicts of Interest: Author Dorota Pasek was employed by the company Promobil S.C. The remaining authors declare that the research was conducted in the absence of any commercial or financial relationships that could be construed as a potential conflict of interest.

References

1. Hernas, A. Uwarunkowania i Kierunki Rozwoju Materiałów Żarowytrzymałych. In *W: Postępy Nauki o Materiałach i Inżynierii Materiałowej, Praca Zbiorowa Pod Red*; Hetmańczyka, M., Ed.; Wydawnictwo Politechniki Śląskiej: Gliwice, Poland, 2002; pp. 191–230.
2. Yagi, K.; Merckling, G.; Kern, T.U.; Irie, H.; Warlimont, H. *Creep Properties of Heat Resistant Steels and Superalloys*; Springer: Berlin/Heidelberg, Germany, 2004; ISBN 978-3-540-42879-4.
3. Xu, C.-H.; Gao, W.; He, Y.-D. High temperature oxidation behaviour of FeAl intermetallics—Oxide scales formed in ambient atmosphere. *Scr. Mater.* **2000**, *42*, 975–980. [CrossRef]
4. Datta, P.K.; Du, H.L.; Burnell-Gray, J.S.; Ricker, R.E. Corrosion of Intermetallics. In *ASM Handbook*; ASM International: Almere, The Netherlands, 2005; Volume 13B, Corrosion: Materials. Available online: https://tsapps.nist.gov/publication/get_pdf.cfm?pub_id=853340 (accessed on 2 November 2025).
5. Guilemany, J.M.; Cinca, N.; Dosta, S.; Lima, C.R.C. High-temperature oxidation of Fe40Al coatings obtained by HVOF thermal spray. *Intermetallics* **2007**, *15*, 1384–1394. [CrossRef]
6. Cebulski, J.; Pasek, D.; Sozańska, M.; Popczyk, M.; Gabor, J.; Swinarew, A. Oxidation of the Alloy Based on the Intermetallic Phase FeAl in the Temperature Range of 700–1000 °C in Air and Possibilities of Practical Application. *Materials* **2025**, *18*, 1835. [CrossRef]
7. Chevalier, S.; Juzon, P.; Przybylski, K.; Larpin, J.P. Water vapour effect on high-temperature oxidation behaviour of Fe3Al intermetallics. *Sci. Technol. Adv. Mater.* **2009**, *10*, 045006. [CrossRef]
8. Romo, L.; Gonzalez-Rodriguez, J.G.; Porcayo-Calderon, J.; Guardian, R.; Salinas-Bravo, V.M. A study on the effect of Co, Cr and Ti on the corrosion of Fe40Al intermetallic in molten NaCl–KCl mixture. *Intermetallics* **2015**, *67*, 156–165. [CrossRef]
9. Ademar, R.; Gonzalez-Rodriguez, J.G.; Uruchurtu, J.; Porcayo-Calderon, J.; Salinas-Bravo, V.M.; Dominguez-Patino, G.; Bedolla-Jacuinde, A. Corrosion Behavior of Fe40Al Alloy with Additions of Ti, Ag, and Cr in Molten KCl + $ZnCl_2$. *Int. J. Corros.* **2012**, *2012*, 146486. [CrossRef]
10. Di Schino, A. Corrosion behavior of new generation super-ferritic stainless steels. *Mater. Sci.* **2019**, *6*, 646–656. [CrossRef]
11. Dan, M.L.; Kellenberger, A.; Duca, D.; Vaszilcsin, N.; Craciunescu, C.M.; Mitelea, I.; Ercuta, A.; Lædre, S.; Khoza, T. Corrosion Resistance of AISI 442 and AISI 446 Ferritic Stainless Steels as a Support for PEMWE Bipolar Plates. *Materials* **2023**, *16*, 1501. [CrossRef] [PubMed]
12. Lee, S.M.; Lee, W.G.; Kim, Y.H.; Jang, H. Surface roughness and the corrosion resistance of 21Cr ferritic stainless steel. *Corros. Sci.* **2012**, *23*, 404–409. [CrossRef]
13. Zamanzade, M.; Barnoush, A.; Motz, C. A Review on the Properties of Iron Aluminide Intermetallics. *Crystals* **2016**, *6*, 10. [CrossRef]
14. Kim, I.; Cho, W.D. High-temperature corrosion of Fe_3Al in chlorine-containing environments. *Mater. Sci. Eng. A* **1999**, *264*, 269–278. [CrossRef]
15. Sundar, A.; Chen, G.; Qi, L. Substitutional adsorptions of chloride at grain boundary sites on hydroxylated alumina surfaces initialize localized corrosion. *NPJ Mater. Degrad.* **2021**, *5*, 18. [CrossRef]
16. Parangusan, H.; Bhadra, J.; Al-Thani, N. A review of passivity breakdown on metal surfaces: Influence of chloride- and sulfide-ion concentrations, temperature, and pH. *Emergent Mater.* **2021**, *4*, 1187–1203. [CrossRef]
17. Cebulski, J.; Pasek, D.; Chmiela, B.; Popczyk, M.; Swinarew, A.S.; Stanula, A.; Waśkiewicz, Z.; Knechtle, B. Evaluation of Structure and Corrosion Behavior of FeAl Alloy after Crystallization, Hot Extrusion and Hot Rolling. *Materials* **2020**, *13*, 2041. [CrossRef]
18. Cebulski, J.; Pasek, D.; Popczyk, M.; Swinarew, A.; Gabor, J. Structure and Corrosion Resistance of Fe40Al5Cr0.2TiB Alloy After Casting and After Homogenization Annealing. *Materials* **2025**, *18*, 308. [CrossRef]
19. Martínez-Aparicio, B.; Gaona-Tiburcio, C.; Almeraya-Calderon, F.; Goldsberry, R.; Castaneda, H. Evaluation of Passive Films on 17-7PH and 410 Stainless Steel Exposed to NaCl Solution. *Materials* **2024**, *17*, 4060. [CrossRef]
20. Örnek, C.; Payam, B.; Gloskovskii, A. Understanding the passive behaviour of low-chromium high-strength Hybrid steel in corrosive environments. *NPJ Mater. Degrad.* **2023**, *7*, 71. [CrossRef]
21. Popczyk, M. The influence of molybdenum and silicon on activity of Ni + W composite coatings in the hydrogen evolution reaction. *Surf. Interface Anal.* **2008**, *40*, 246–249. [CrossRef]
22. Popczyk, M. The hydrogen evolution reaction on electrolytic nickel—based coatings containing metallic molybdenum. *Mater. Sci. Forum* **2010**, *636–637*, 1036–1041. [CrossRef]
23. Popczyk, M.; Budniok, A. Structure and corrosion resistance of Zn-Ni and Zn-Ni-W coatings. *Mater. Sci. Forum* **2010**, *636–637*, 1042–1046. [CrossRef]
24. *ISO 25178-2*; Geometrical Product Specifications (GPS)—Surface Texture: Areal—Part 2: Terms, Definitions and Surface Texture Parameters. International Organization for Standardization: Geneva, Switzerland, 2012.

25. Kellenberger, A.; Vaszilcsin, N.; Laurentiu Dan, M.; Mitelea, I.; Geana, A.A.; Lædre, S.; Craciunescu, C.M. Corrosion Investigation by Scanning Electrochemical Microscopy of AISI 446 and Ti-Coated AISI 446 Ferritic Stainless Steel as Potential Material for Bipolar Plate in PEMWE. *Acta Metall. Sin.* **2024**, *37*, 607–619. [CrossRef]
26. Smialek, J.L.; Doychak, J.; Gaydosh, D.J. Oxidation behavior of FeAl+Hf, Zr, B. *Oxid. Met.* **1990**, *34*, 259–275. [CrossRef]
27. Fraczkiewicz, A.; Gay, A.-S.; Biscondi, M. On the Boron Effect in FeAl (B2) Intermetallic Alloys. *Mater. Sci. Eng. A* **1998**, *258*, 108–114. [CrossRef]
28. Fraczkiewicz, A. Influence of Boron on the Mechanical Properties of B2-Ordered FeAl Alloys. *Mater. Trans. JIM* **2000**, *41*, 166–169. [CrossRef]
29. Li, Q.; Long, D.; Song, P.; Li, Z.; Zhang, R.; Chen, H.; Huang, T.; Zheng, B.; Lu, J. Alumina Grain Growth and Grain Boundary Segregation of FeCrAl-Based Oxide Dispersion-Strengthened Alloys at High Temperature. *Corros. Sci.* **2022**, *208*, 110630. [CrossRef]
30. Xu, L.; Wu, P.; Zhu, X.; Zhao, G.; Ren, X.; Wei, Q.; Xie, L. Structural Characteristics and Chloride Intrusion Mechanism of Passive Film. *Corros. Sci.* **2022**, *208*, 110563. [CrossRef]
31. Peng, Y.; Lin, Y.; Xia, R.; Dai, Z.; Zhang, W.; Liu, W. Electrochemical Investigation of Chloride Ion-Induced Breakdown of Passive Film on P110 Casing Steel Surface in Simulated Pore Solution: Behavior and Critical Value Determination. *Metals* **2024**, *14*, 93. [CrossRef]
32. Choi, S.-H.; Yoo, Y.-R.; Kim, Y.-C.; Kim, Y.-S. Effect of Cr, Mo, and W Contents on the Semiconductive Properties of Passive Film of Ferritic Stainless Steels. *Crystals* **2025**, *15*, 723. [CrossRef]
33. Li, Z.; Zhang, W.; Wang, Y.; Yu, H.; Cui, Y.; Li, M.; Sun, D. Operando Characterization of Cr-Containing Alloy Passivation Film by Synchrotron Radiation. *Corros. Sci.* **2024**, *236*, 112233. [CrossRef]
34. Yang, Y.; Zhao, F.; Ling, Y.; Yang, X.; Gu, Y.; Zhang, Z. Comparisons of Air and Water Oxidation on the Passive Properties of Chromium. *J. Mater. Eng. Perform.* **2024**, *33*, 14318–14328. [CrossRef]

Disclaimer/Publisher's Note: The statements, opinions and data contained in all publications are solely those of the individual author(s) and contributor(s) and not of MDPI and/or the editor(s). MDPI and/or the editor(s) disclaim responsibility for any injury to people or property resulting from any ideas, methods, instructions or products referred to in the content.

materials

MDPI

Article

Change in the Morphology of Alloy Corrosion Products Based on the FeAl Intermetallic Phase After Oxidation in Water Vapor at a Temperature of 700 °C for up to 2000 h

Janusz Cebulski [1,*], Dorota Pasek [2], Maria Sozańska [1], Magdalena Popczyk [3,*], Jadwiga Gabor [3], Andrzej Swinarew [3,4] and Jakub Wieczorek [1]

[1] Department of Materials Technology, Faculty of Materials Engineering and Industrial Digitalization, Silesian University of Technology, Krasińskiego 8, 40-019 Katowice, Poland; maria.sozanska@polsl.pl (M.S.); jakub.wieczorek@polsl.pl (J.W.)
[2] Promobil s.c., Kopernika 12, 40-064 Katowice, Poland; dorota.pasek@promobil.pl
[3] Faculty of Science and Technology, University of Silesia in Katowice, 75 Pułku Piechoty 1A, 41-500 Chorzów, Poland
[4] Institute of Sport Science, The Jerzy Kukuczka Academy of Physical Education, Mikołowska 72A, 40-065 Katowice, Poland
* Correspondence: janusz.cebulski@polsl.pl (J.C.); magdalena.popczyk@us.edu.pl (M.P.)

Abstract

The surface of the Fe40Al5Cr0.2TiB alloy, after oxidation in steam at 700 °C, showed a varied morphology dependent on oxidation time. Initially, a fine, acicular oxide layer formed, which over time transformed into a more compact, lumpy structure corresponding to the α-Al_2O_3 phase. EDS analysis confirmed the dominance of aluminum and oxygen in the oxidation products, and XRD studies revealed the presence of the α-alumina phase. Optical profilometry revealed a significant increase in roughness parameters (R_a and R_z) after long-term exposure (2000 h), which correlates with the thickening and sinterization of the oxide layer. The obtained results indicate that in a water vapor environment, a stable α-Al_2O_3 phase can already be formed at a temperature of 700 °C, and its development leads to increased roughness.

Keywords: α-Al_2O_3; intermetallics phase; oxidation layer

1. Introduction

The oxidation behavior of Fe–Al intermetallics (notably FeAl and related iron aluminides) is of fundamental and practical interest for high-temperature applications because these materials can form protective Al_2O_3 scales that markedly slow further oxidation [1–3]. The formation, continuity, and crystallographic form (polymorph) of alumina are critical: a continuous, adherent α-Al_2O_3 layer provides the best long-term protection, whereas transient or non-continuous alumina permits rapid inward/outward transport of species and can lead to breakaway oxidation [4–7].

Steam ($H_2O(g)$) environments modify oxidation chemistry and transport in several important ways: they change the effective oxygen activity at the oxide/gas interface, enable hydroxyl-mediated transport pathways, and can promote volatile species and internal oxidation processes that are not active in dry O_2 or air. Consequently, alloys and coatings that remain protective in dry oxygen may experience morphological changes, multi-layer scale formation, or accelerated degradation in steam atmospheres—effects that become

increasingly important for energy systems operating in the 600–750 °C window (e.g., ultra-supercritical steam cycles, boilers, steam turbines, nuclear claddings). Experimental and review studies document that steam commonly produces outward Fe-rich nodules, inner (Fe, Cr) or spinel layers, and can increase spallation/scale porosity compared with dry exposures [8–14].

For Fe–Al systems, the literature shows a complex, composition- and microstructure-dependent response. Short-to-moderate exposures often produce continuous Al_2O_3 on aluminide coatings and some bulk FeAl alloys, yet long-term steam exposures may reveal: (a) development of multi-layered scales with Fe-rich outer oxides; (b) internal oxidation of Al beneath the surface; (c) Al depletion at the metal/scale interface due to interdiffusion; and (d) mechanical failure of the scale (cracking, spallation) driven by growth stresses and phase transformations [2,6,9,15–18]. Alloying elements (Cr, Si, Y, reactive elements) and microstructural features (grain size, second phases, porosity, pre-existing defects or scratches) strongly influence whether protective alumina persists or the system transitions to a non-protective morphology [6,12,19–21].

Despite the substantial body of work on steam oxidation of steels, Ni-base alloys, and aluminide coatings, there is a relative paucity of systematic, high-resolution, long-duration studies that document the morphological evolution of corrosion products specifically for bulk alloys whose matrix is the FeAl intermetallic phase exposed to steam at 700 °C for times approaching 2000 h. Many prior investigations focus on shorter times, on coated steels rather than bulk FeAl intermetallics, or on mixed O_2/H_2O atmospheres. Where long steam exposures have been reported, important morphologies such as nodule coalescence, multi-layer scale formation, and Al-depletion have been observed but not comprehensively correlated with high-resolution microstructural analyses across a wide time span (hours → thousands of hours) [3,9–11,13,22–26].

The present study fills this gap by performing a time-series analysis of oxide morphology and composition on a FeAl-based alloy exposed to H_2O(g) at 700 °C for exposure times up to 2000 h. We combine surface SEM/EDS, where appropriate, XRD phase analysis, to classify oxide morphologies as a function of exposure time; identify transitions from protective alumina-dominated scales to complex multi-layered or Fe-rich morphologies; and assess the role of alloy chemistry and initial microstructure (including scratches/defects) in governing scale integrity and protectiveness.

These results provide mechanistic insight relevant to material selection and coating design for long-term service in steam environments, and supply a detailed dataset (morphology classes, composition profiles, and kinetic fingerprints) that can support modeling efforts and practical guidelines for Fe-Al-based materials and aluminide coatings in power-plant and related high-temperature steam applications.

2. Materials and Methods

The tests were conducted on samples made of the Fe40Al5Cr0.2TiB alloy, the chemical composition of which is presented in Table 1. ARMCO iron (technically pure), ARO aluminum (99.995 wt%), aluminothermic chromium obtained by the Kroll method, and amorphous boron (technically pure) were used for melting. Melts were carried out in a Balzers VSG-2 induction vacuum furnace (Balzers, Lichtenstein). Due to the fact that the as-cast material was brittle and had a coarse-grained structure and significant segregation of chemical composition, heat treatment was applied. Homogenizing annealing was carried out at 1050 °C for 72 h, as previous studies had shown that these are the parameters at which microsegregation of chemical composition is removed [27,28].

Table 1. Chemical composition of Fe40Al5Cr0.2TiB alloy.

Compound	Fe	Al	Cr	Ti	B
% at.	54.80	40.10	4.86	0.18	0.06

Corrosion tests at 700 °C in a flowing water vapor environment were performed on a test stand designed for isothermal oxidation corrosion. Oxidation times were 1, 50, 100, 300, 1000, and 2000 h. Oxidation in a steam environment was conducted in a furnace consisting of a tubular reactor divided into two zones. The first zone was the furnace's corrosion chamber, while the second zone was the steam superheater. A steam generator was mounted on the front panel of the furnace, with a capacity of 200 mL/h during the test. During the test, steam was continuously supplied to the steam superheater and then to the corrosion chamber. Distilled water was used to generate the steam. Observations of the oxide layer surface of the Fe40Al5Cr0.2TiB intermetallic alloy samples after oxidation for initial oxidation times (1 h, 50 h, and 100 h) were performed using a ZEISS SUPRA 35 high-resolution scanning electron microscope (Carl Zeiss, Oberkochen, Germany). Observations of the surface state after oxidation for 300, 1000, and 2000 h were performed using a Hitachi S-3400N scanning electron microscope (SEM) (Hitachi High-Tech Corp., Tokyo, Japan) with secondary electron (SE) and backscattered electron (BSE) detectors, and a Hitachi S-4200 microscope with secondary electron (SE) detectors (Hitachi High-Tech Corp., Tokyo, Japan). The chemical composition of the oxidation products was determined using a Thermo Noran (System Six) energy-dispersive X-ray spectrometer (EDS) (Waltham, MA, USA) at an electron beam acceleration voltage of 15 keV, coupled to a Hitachi S-3400N microscope. Details of the scale morphology were also observed using a TESCAN S-8000 BrightBeam™ SEM at a voltage of 5 kV (TESCAN, Brno, Czech Republic). Surface development was measured using a non-contact optical profilometer with a MicroProf 3000 (FRT GmbH, Bergisch Gladbach, Germany) white light aberration head.

3. Results

3.1. Surface Morphology and Oxide Evolution (SEM/EDS/XRD)

The surface morphology of the Fe40Al5Cr0,2TiB alloy after oxidation in water vapor at 700 °C evolved significantly with exposure time. After 1 h (Figure 1), a relatively continuous, fine-grained oxide layer covered the surface, consisting mainly of needle-like structures (whiskers) and small agglomerates (flakes). These elongated oxides grew perpendicularly to the substrate, forming a columnar morphology typical of the metastable θ-Al_2O_3 polymorph [1,2,5]. As the exposure time increased to 50 h (Figure 2) and 100 h (Figure 3), whisker density decreased, and the oxide became denser, forming clustered grains with a partially flattened morphology.

For long-term oxidation (≥1000 h, Figures 4 and 5), the whisker-like features gradually transformed into compact, globular clusters distributed heterogeneously across the surface. After 2000 h (Figure 6), the oxide layer exhibited coarse granular agglomerates and locally sintered regions, indicating a transformation toward the stable α-Al_2O_3 structure [3,4,8]. The morphological transition from fine whiskers to dense nodules corresponds to the thermally activated θ → α phase transformation, which is associated with decreasing defect density and a reduction in internal energy per unit volume [5].

Similar morphological evolution has been reported for FeAl and FeCrAl alloys oxidized in dry air or steam at 750–950 °C [13,29]. Notably, the present results confirm that prolonged oxidation even at 700 °C in high H_2O(g) activity promotes the nucleation and growth of α-Al_2O_3, likely due to local temperature gradients and Al diffusion from the substrate. This observation aligns with the findings of Cebulski et al. [6] and Grabke [1],

who indicated that the presence of Cr and Ti additions facilitates alumina stabilization at lower temperatures by altering interfacial energy and vacancy concentrations.

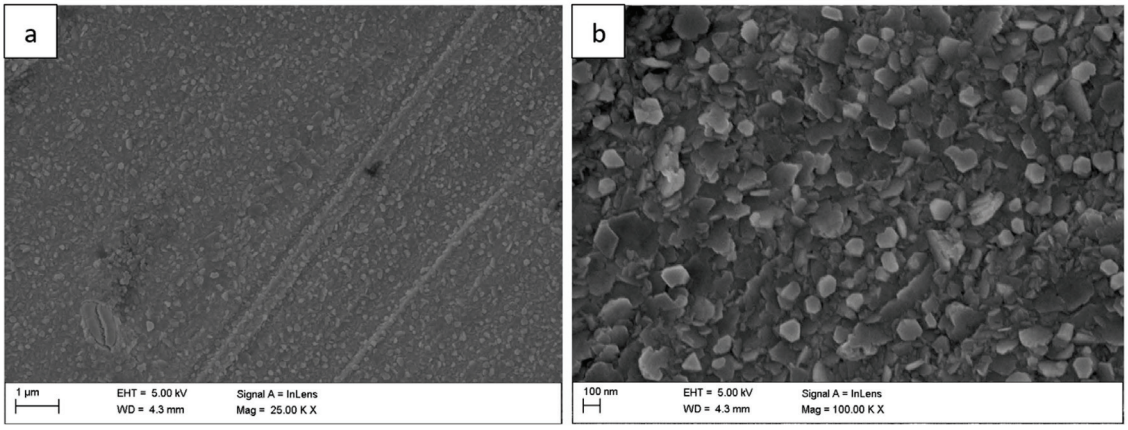


Figure 1. Surface morphology of the Fe40Al5Cr0.2TiB alloy after oxidation in water vapor at 700 °C for 1 h: (**a**) low-magnification SEM image showing general oxide coverage on the alloy surface; (**b**) high-magnification SEM image showing the morphology of fine, needle-like oxide.

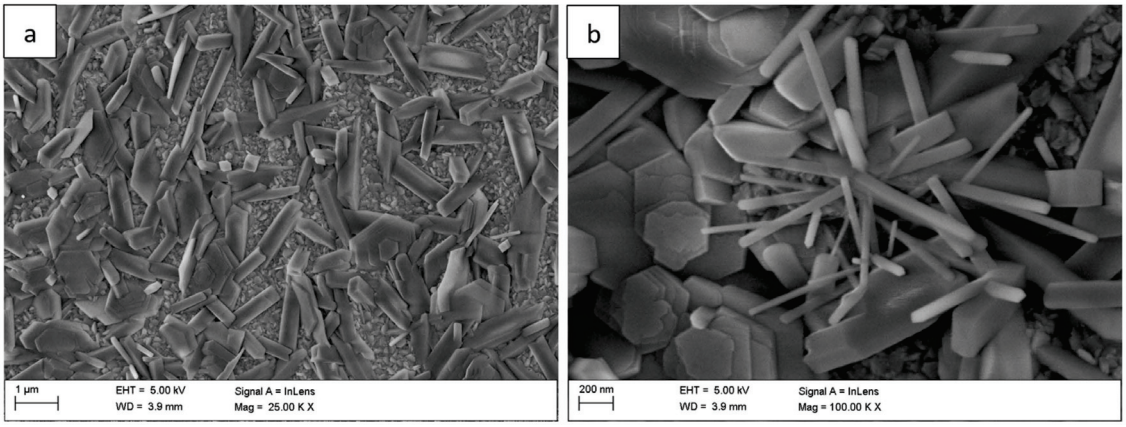


Figure 2. Surface morphology of the Fe40Al5Cr0.2TiB alloy after oxidation in water vapor at 700 °C for 50 h: (**a**) low-magnification SEM image illustrating the formation of a continuous oxide layer; (**b**) high-magnification SEM image showing partial coalescence and morphology of fine, needle-like oxide whiskers.

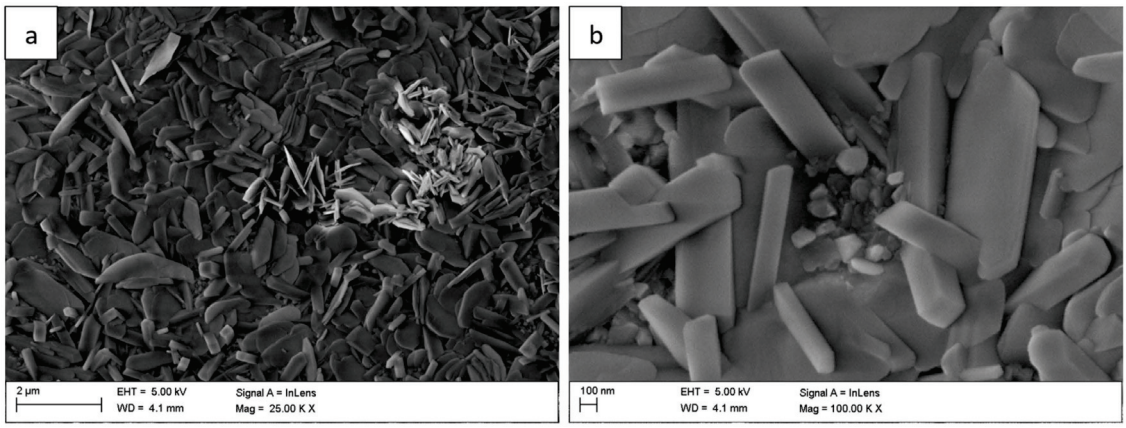


Figure 3. Surface morphology of the Fe40Al5Cr0.2TiB alloy after oxidation in water vapor at 700 °C for 100 h: (**a**) low-magnification SEM image showing the progressive densification of the oxide scale; (**b**) high-magnification image revealing clustered grains with partially flattened morphology.

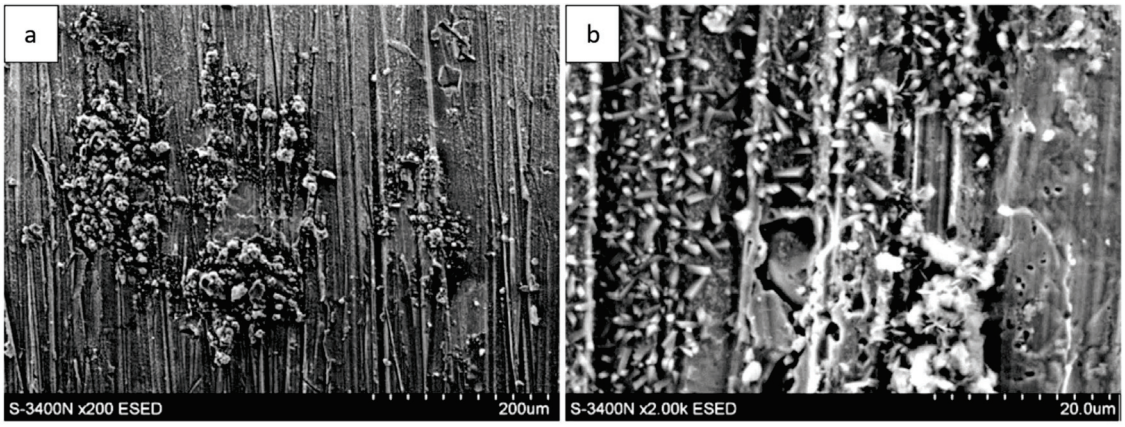


Figure 4. Surface morphology of the Fe40Al5Cr0.2TiB alloy after oxidation in water vapor at 700 °C for 300 h: (**a**) low-magnification image showing heterogeneous distribution of oxide clusters; (**b**) high-magnification image presenting the transition from whisker-like to compact granular structures.

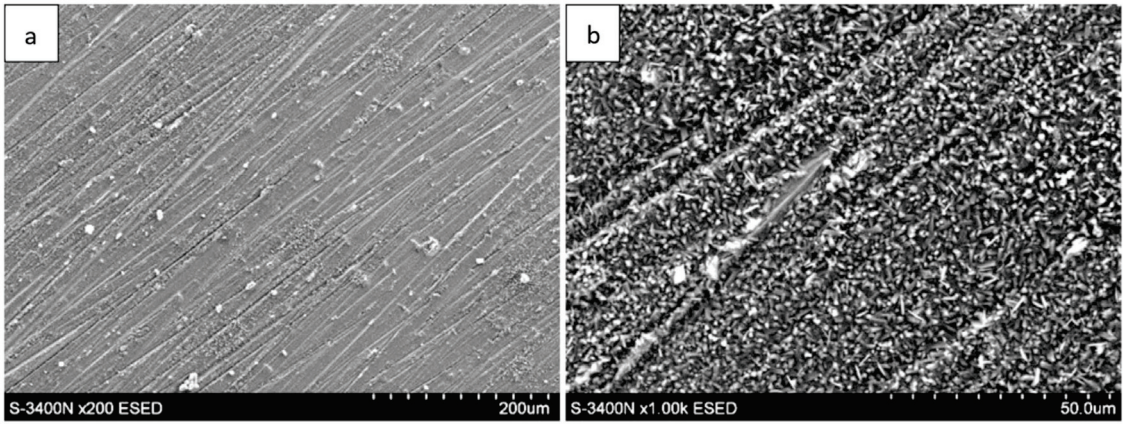


Figure 5. Surface morphology of the Fe40Al5Cr0.2TiB alloy after oxidation in water vapor at 700 °C for 1000 h: (**a**) low-magnification image of the surface showing growing granular regions; (**b**) high-magnification image showing morphology oxide.

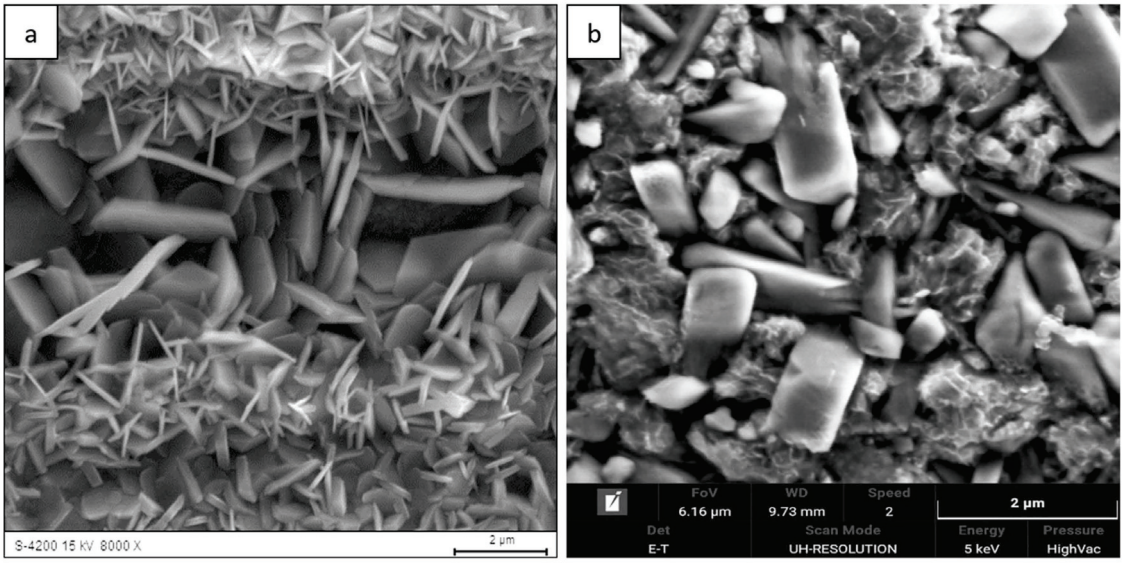


Figure 6. Surface morphology of the Fe40Al5Cr0.2TiB alloy after oxidation in water vapor at 700 °C for 2000 h: (**a**) low-magnification SEM image showing coarse granular agglomerates distributed over the surface; (**b**) high-magnification SEM image showing sintered α-Al_2O_3 nodules and locally compacted regions.

EDS analysis revealed that the oxide layer contained predominantly aluminum and oxygen, with trace amounts of Fe, Cr, and Ti (Figure 7). The presence of these substrate elements in the outer scale results from the relatively deep excitation volume during EDS measurements and local diffusion processes at the metal/oxide interface [10,11]. In some areas, minor Si contamination was observed, originating from the furnace lining material.

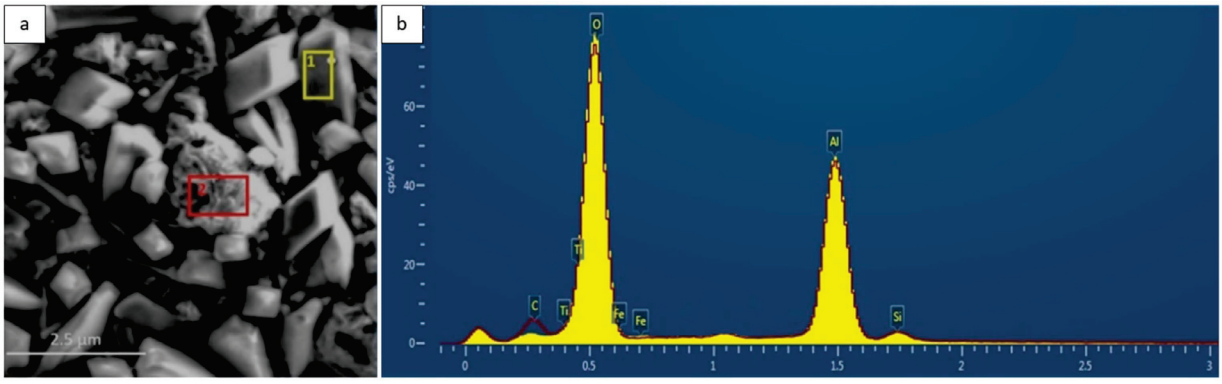


Figure 7. (**a**) Surface microstructure of the Fe40Al5Cr0.2TiB alloy after oxidation in water vapor at 700 °C for 2000 h; two EDS analysis points are indicated (red and yellow). (**b**) EDS spectra from the corresponding areas shown in (**a**): the red line represents the spectrum from the red-marked area, and the yellow line represents the spectrum from the yellow-marked area. The spectra overlap due to the very similar chemical composition of both regions (Al and O with minor Fe, Cr, and Ti).

Phase analysis by XRD confirmed the presence of α-Al_2O_3 after 2000 h of oxidation (Figure 8).

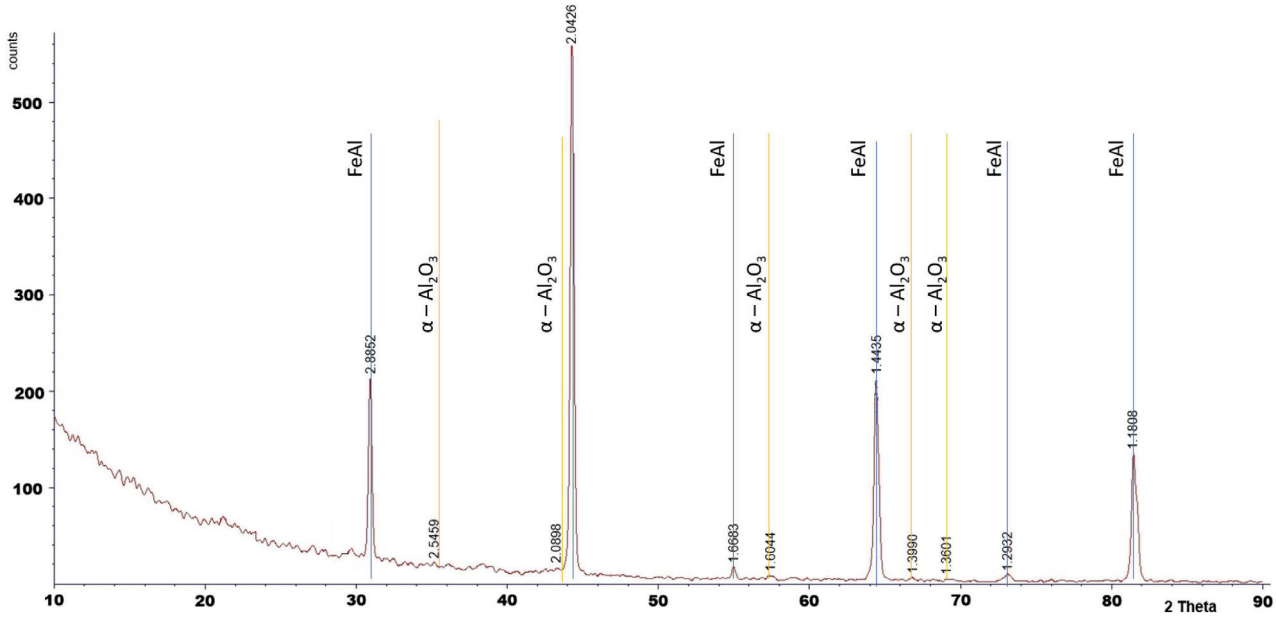


Figure 8. X-Ray analysis of the Fe40Al5Cr0.2TiB alloy after oxidation in water vapor at 700 °C for 2000 h.

The XRD analysis was performed only for the specimen oxidized for 2000 h. For shorter oxidation times, the oxide layers were too thin to produce detectable diffraction peaks, as XRD is a bulk-sensitive technique. Phase identification for shorter exposures was therefore supported by SEM observations and literature reports.

The transition of whisker morphology (θ-Al_2O_3) into granular α-Al_2O_3 was also observed for NiAl alloys at 1000–1100 °C [5,30] and for FeCrAl coatings at 850–900 °C [8,16].

In this study, the same evolution occurred at 700 °C, suggesting that water vapor may accelerate the stabilization of α-Al_2O_3 through hydroxyl-assisted diffusion mechanisms, as reported in previous studies [18,23].

3.2. Surface Topography (Optical Profilometry)

The evolution of surface roughness parameters with oxidation time, determined by optical profilometry, is summarized in Table 2. The mean roughness (R_a) and maximum height (R_z) showed an initial slight decrease after 50–100 h of exposure ($R_a \approx 0.09$ µm, $Rz \approx 0.57$ µm), suggesting that fine-grained alumina layers partially smoothed the surface (Figures 9 and 10). However, after 2000 h, both R_a and R_z increased markedly to 0.83 µm and 5.79 µm, respectively, reflecting the formation of coarse α-Al_2O_3 nodules and localized delamination zones.

Table 2. Summary of roughness parameters after oxidation.

Parameter	1 h	50 h	100 h	300 h	1000 h	2000 h
R_a	0.119 µm	0.0847 µm	0.0921 µm	0.133 µm	0.175 µm	0.83 µm
R_z	0.711 µm	0.486 µm	0.570 µm	0.785 µm	1.19 µm	5.79 µm

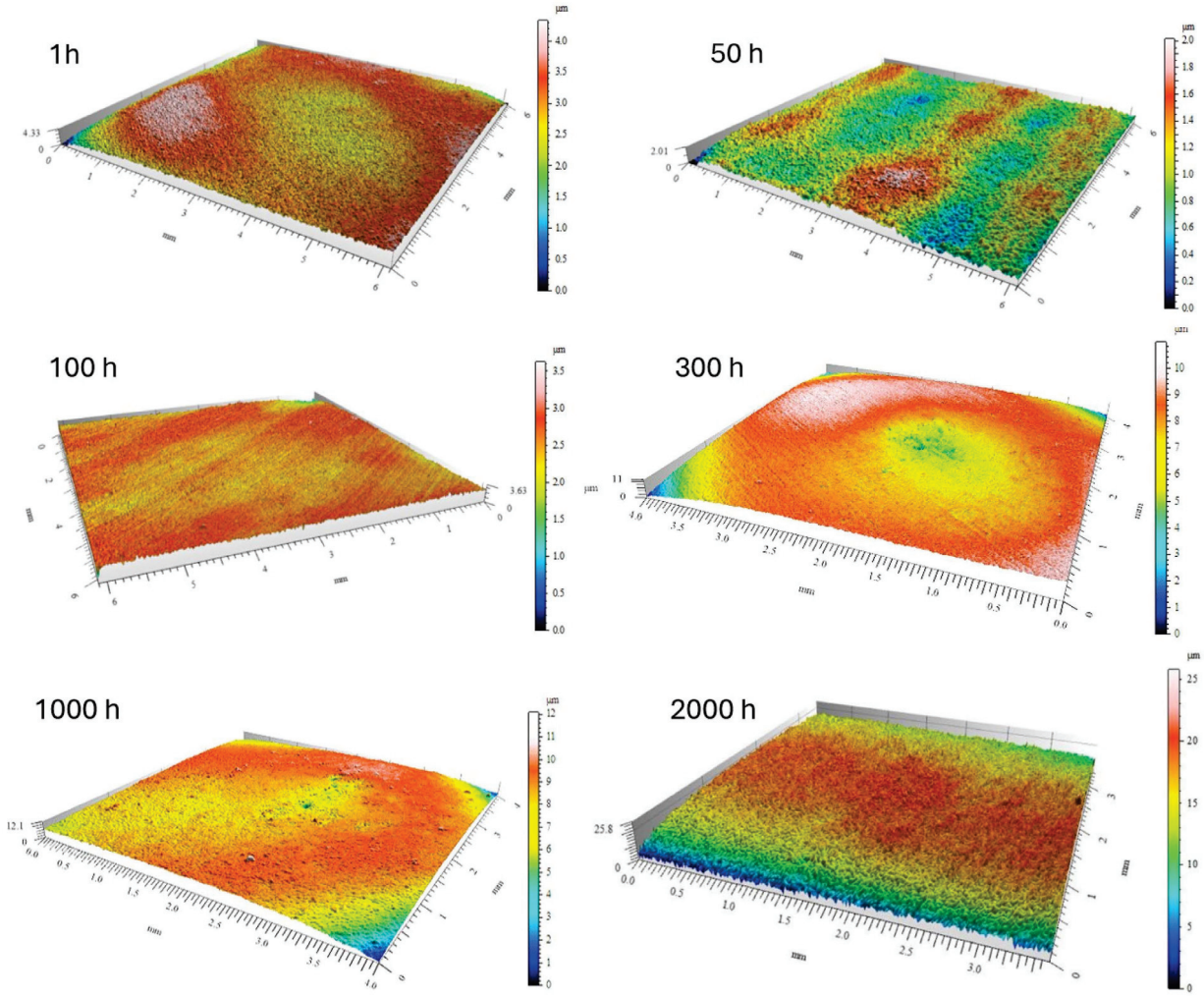


Figure 9. Three-dimensional image of the surface of the Fe40Al5Cr0.2TiB alloy oxidized in a steam environment at 700 °C for different times.

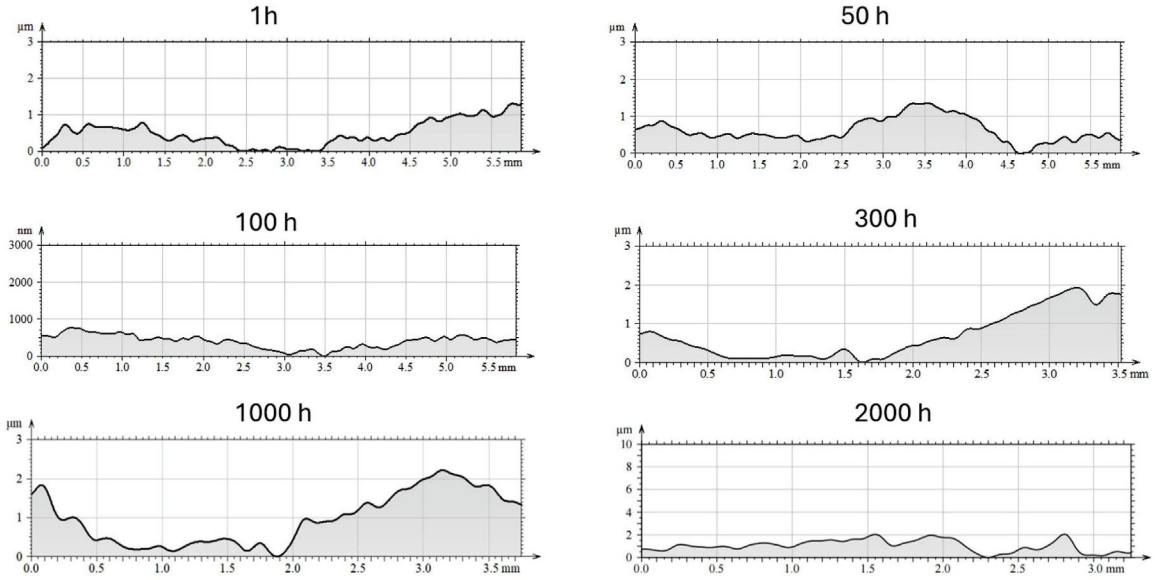


Figure 10. Waviness profiles on selected cross-sections of the sample surfaces after oxidation in a steam environment at 700 °C after different times.

The correlation between the increasing roughness and the observed SEM morphologies indicates that long-term oxidation in steam promotes thickening and sintering of the oxide scale, leading to the development of surface asperities and cracks [4,19,20]. These changes are consistent with models of alumina scale growth under stress accumulation and void formation beneath the oxide layer [10,26].

The increase in R_a and R_z parameters is therefore a quantitative signature of the morphological transition from a fine protective θ-Al_2O_3 whisker network to a coarse α-Al_2O_3 granular scale. The combination of SEM, EDS, and profilometry analyses clearly demonstrates that steam not only accelerates the θ → α transformation but also modifies the topography of the oxide, leading to increased roughness.

4. Analysis of the Results and Conclusions

The morphology of the oxide layer formed during steam oxidation, observed by scanning electron microscopy (SEM), at the initial stage of oxidation consists of flake-like regions. With increasing oxidation time, oxide structures in the form of needle-shaped whiskers growing from the substrate toward the oxidizing atmosphere were identified on the surface. Prolonged oxidation (2000 h) resulted in the formation of oxides with a granular morphology. Their nucleation and growth depend on local oxidation conditions, as indicated by their nonuniform and dispersed distribution over the surface. The whisker-shaped oxides, which crystallized during the early stages of oxidation, gradually transformed with increasing exposure time, disappearing and giving rise to more compact, flat crystallites.

The presence of aluminum oxide on the surface of the Fe40Al5Cr0.2TiB alloy in the form of fine needle-like structures was also reported in oxidation studies conducted by Nowak K. and Kupka M. [31], although this morphology appeared only during oxidation at a higher temperature of 800 °C for 200 h. At 900 °C, the needle-like oxide morphology was more pronounced. A similar needle-shaped oxide morphology was also observed in [32] during oxidation at 750 °C and 950 °C for 550 h. Comparable oxide morphologies have been reported not only for FeAl-based intermetallic alloys but also for NiAl alloys, which, like FeAl, crystallize in the B2 structure. In the case of NiAl, however, the needle-like aluminum oxide morphology was observed during oxidation at 1000 °C [33,34].

These observations indicate that both the morphology of corrosion products forming on FeAl-based intermetallic alloys and the kinetics of the oxidation process depend on the oxidation temperature and exposure time. All the above-mentioned researchers have noted that the needle-like oxide morphology is characteristic of the θ-Al_2O_3 phase. The morphology of oxides formed on the Fe40Al5Cr0.2TiB alloy obtained in this study can therefore be associated with the allotropic form of aluminum oxide present on the alloy surface. X-ray diffraction (XRD) analysis identified the presence of the α-Al_2O_3 phase. Importantly, the stable α-Al_2O_3 phase is generally recognized as a high-temperature modification of aluminum oxide, typically forming on the surface of oxidized materials at temperatures above 900 °C [31,35–37].

Author Contributions: Conceptualization, J.C. and M.P.; methodology, J.C., M.P. and J.W.; validation, D.P. and M.S.; formal analysis, J.G.; investigation, D.P., M.S. and J.W.; data curation, M.P.; writing—original draft preparation, J.C., M.P., D.P., A.S., J.G., M.S. and J.W.; writing—review and editing, J.C., M.P., D.P., A.S., J.G., M.S. and J.W.; visualization, D.P. and M.P.; supervision, A.S. All authors have read and agreed to the published version of the manuscript.

Funding: The project was co-financed by the European Union within the program "The European Funds for Śląsk (Silesia) 2021–2027".

Data Availability Statement: The original contributions presented in this study are included in the article. Further inquiries can be directed to the corresponding authors.

Conflicts of Interest: Author Dorota Pasek was employed by the company Promobil s.c. The remaining authors declare that the research was conducted in the absence of any commercial or financial relationships that could be construed as a potential conflict of interest.

References

1. Grabke, H.J. The Oxidation of NiAl and FeAl. *Intermetallics* **1999**, *7*, 1153–1158. [CrossRef]
2. Xu, C.-H.; Gao, W.; He, Y.-D. High temperature oxidation behaviour of FeAl intermetallics—Oxide scales formed in ambient atmosphere. *Scr. Mater.* **2000**, *42*, 975–980. [CrossRef]
3. Zhou, Y.; Zhao, Q.; Lu, J.; Liang, Z.; Yuan, Y.; Gu, Y.; Huang, J. Steam Oxidation of Scratched β-FeAl Coatings on P92 Steel. *Mater. Corros.* **2022**, *74*, 197–208. [CrossRef]
4. Smialek, J.L. Oxide Morphology and a Spalling Model for NiAl. *Metall. Trans. A* **1978**, *9*, 309–320. [CrossRef]
5. Doychak, J.; Smialek, J.L.; Mitchell, T.E. Transient Oxidation of Single-Crystal β-NiAl. *Metall. Trans. A* **1989**, *20*, 499–518. [CrossRef]
6. Cebulski, J.; Pasek, D.; Sozańska, M.; Popczyk, M.; Gabor, J.; Swinarew, A. Oxidation of the Alloy Based on the Intermetallic Phase FeAl in the Temperature Range of 700–1000 °C in Air and Possibilities of Practical Application. *Materials* **2025**, *18*, 1835. [CrossRef] [PubMed]
7. Brumm, M.W.; Grabke, H.J. Oxidation Behaviour of NiAl—II. Cavity Formation beneath the Oxide Scale on NiAl of Different Stoichiometries. *Corros. Sci.* **1993**, *34*, 547–561. [CrossRef]
8. Agüero, A.; Baráibar, I.; Gutiérrez, M.; Tuurna, S.; Toivonen, A.; Penttilä, S.; Auerkari, P. Steam Oxidation of Aluminide-Coated and Uncoated TP347HFG Stainless Steel under Atmospheric and Ultra-Supercritical Steam Conditions at 700 °C. *Coatings* **2020**, *10*, 839. [CrossRef]
9. Yuan, J.; Wu, X.; Wang, W.; Zhu, S.; Wang, F. Investigation on the Enhanced Oxidation of Ferritic/Martensitic Steel P92 in Pure Steam. *Materials* **2014**, *7*, 2772–2783. [CrossRef]
10. Qi, W.; Qiao, Y.; Ru, W.; Wang, X.; Zhang, X.; Zheng, T.; Du, S.; Wang, P.; Yang, K. High-Temperature Steam Oxidation and Surface Microstructure Evolution of Fe13Cr6Al(1–4)Mo0.15Y Alloys. *Metals* **2024**, *14*, 1229. [CrossRef]
11. Lu, J.; Huang, J.; Wang, J.; Yang, Z.; Gu, Y. Long-term Degradation Behavior of Slurry Aluminide Coating on Super304H Stainless Steel at 650 °C. *Corros. Sci.* **2021**, *178*, 109054. [CrossRef]
12. Yang, Z.; Lu, J.; Zhang, P.; Le, M.; Zhou, Y.; Huang, J.; Yuan, Y.; Gu, Y. Oxidation Performance and Degradation Mechanism of Aluminide Coatings—Steam Studies and Microstructural Evolution. *Surf. Coat. Technol.* **2020**, *391*, 125700. [CrossRef]
13. Rutkowski, B.; Baran, K.; Błoniarz, R.; Kozieł, T. The Morphology and Microstructure of Oxide Scale Grown on Austenitic Steel during Steam Oxidation at 700 °C for 500 h. *Materials* **2021**, *14*, 3821. [CrossRef] [PubMed]

14. Cebulski, J. Application of FeAl interemetallic phase matrix based alloys in the turbine components of a turbocharger. *Metalurgija* **2015**, *54*, 154–156.
15. Milewska, A.; Hierro, M.P.; Trilleros, J.A.; Bolívar, F.J.; Pérez, F.J. Coating Design Using Computational Codes for Steam—FeAl Coatings, Oxidation, Steam, Steel P92, Thermo-Calc. *Mater. Sci. Forum* **2004**, *461–464*, 321–326. [CrossRef]
16. Taghipour, M.; Eslami, A.; Bahrami, A. High-Temperature Oxidation Behaviour of Aluminide Coatings on HP-MA Steel. *Surf. Coat. Technol.* **2022**, *434*, 128181. [CrossRef]
17. Senderowski, C. Synthesis, Properties and Applications of Intermetallics, Ceramic and Cermet Coatings. *Materials* **2022**, *15*, 8408. [CrossRef] [PubMed]
18. Dudziak, T.; Jura, K.; Polkowska, A.; Deodeshmukh, V.; Warmuzek, M.; Witkowska, M.; Ratuszek, W.; Chruściel, K. Steam Oxidation Resistance of Advanced Steels and Ni-Base Alloys—1000 h at 700 °C. *Oxid. Met.* **2018**, *89*, 755–779. [CrossRef]
19. Rebak, R.B.; Gupta, V.K.; Larsen, M. Oxidation Characteristics of Two FeCrAl Alloys in Air and Steam. *JOM* **2018**, *70*, 1484–1492. [CrossRef]
20. Kopec, M. Recent Advances in the Deposition of Aluminide Coatings and High-Temperature Performance. *Coatings* **2024**, *14*, 630. [CrossRef]
21. Li, Q. Influence of Pre-Oxidation on High-Temperature Oxidation of Aluminide Coatings. *Front. Mater.* **2021**, *8*, 679682. [CrossRef]
22. Pint, B.A.; Zhang, Y.; Walker, L.R.; Wright, I.G. Long-Term Performance of Aluminide Coatings on Fe-Base Alloys. *Surf. Coat. Technol.* **2007**, *202*, 637–642. [CrossRef]
23. Montealegre, M.; González-Carrasco, J.; Morris-Muñoz, M.; Chao, J.; Morris, D. Oxidation Behaviour of ODS FeAlCr Intermetallic Alloys—Role of Dispersoids and Microstructure. *Intermetallics* **2005**, *8*, 439–446. [CrossRef]
24. Smialek, J.L. A Deterministic Interfacial Cyclic Oxidation Spalling Model. *Acta Mater.* **2003**, *51*, 469–483. [CrossRef]
25. Agüero, A. Aluminide Coatings by Means of Slurry Application: A Low-Cost Route. *Coatings* **2024**, *14*, 1243. [CrossRef]
26. Zhou, Y.; Lu, J.; Shen, M.; Yuan, Y.; Gu, Y.; Yang, Z.; Huang, J.; Zhao, Q. Low-Temperature Formation and Steam Oxidation of β-FeAl Coating on P92 Steel. *Corros. Sci.* **2019**, *163*, 108227. [CrossRef]
27. Cebulski, J.; Lalik, S. Changes in the structure of alloy on the matrix of FeAl intermetallic phase after primary crystallization and homogenizing treatment. *J. Mater. Process. Technol.* **2005**, *162–163*, 4–8. [CrossRef]
28. Barcik, J.; Cebulski, J. Plastify of alloy based on the matrix of intermetallic FeAl phase. *Arch. Metall.* **2000**, *45*, 315–330.
29. Reszka, K.; Morgiel, J.; Żurek, Z.; Jaron, A. Characterization of alumina scale formed on FeCrAl steel. *Arch. Metall. Mater.* **2014**, *59*, 77–81. [CrossRef]
30. Swadźba, R.; Swadźba, L.; Wiedermann, J.; Hetmańczyk, M.; Witala, B. Characterization of Alumina Scales Grown on a 2nd Generation Single Crystal Ni Superalloy During Isothermal Oxidation at 1050, 1100 and 1150 °C. *Oxid. Met.* **2014**, *82*, 195–208. [CrossRef]
31. Nowak, K.; Kupka, M. High-temperature oxidation behaviour of B2 FeAl based alloy with Cr, Zr and B additions. *Mater. Chem. Phys.* **2012**, *132*, 902–908. [CrossRef]
32. Janda, D.; Fietzek, H.; Galetz, M.; Heilmaier, M. The effect of micro-alloying with Zr and Nb on the oxidation behavior of Fe_3Al and FeAl alloys. *Intermetallics* **2013**, *41*, 51–57. [CrossRef]
33. Tolpygo, V.K.; Clarke, D.R. Microstructural study of the theta-alpha transformation in alumina scales formed on nickel-aluminides. *Mater. High Temp.* **2000**, *17*, 59–70. [CrossRef]
34. El-Awadi, G.A.; Abdel-Samad, S.; Ezzat, S. Elshazly. Hot corrosion behavior of Ni based Inconel 617 and Inconel 738 superalloys. *Appl. Surf. Sci.* **2016**, *37*, 224–230. [CrossRef]
35. Kulak, K.; Kupka, M.; Dercz, G. Oxidation of multicomponent iron aluminide based on FeAl phase. *Mater. Eng.* **2011**, *4*, 510–513.
36. Pasek, D. Utlenianie Stopu na Osnowie Fazy Międzymetalicznej FeAl w Powietrzu I Parze Wodnej [Oxidation of FeAl Intermetallic-Based Alloy in Air and Steam]. Ph.D. Thesis, Silesian University of Technology, Gliwice, Poland, 2021.
37. Fornalczyk, A.; Cebulski, J.; Pasek, D. The morphology of corrosion products in FeAl alloys after heatresistance tests at different temperatures. *Solid State Phenom.* **2015**, *227*, 409–412. [CrossRef]

Disclaimer/Publisher's Note: The statements, opinions and data contained in all publications are solely those of the individual author(s) and contributor(s) and not of MDPI and/or the editor(s). MDPI and/or the editor(s) disclaim responsibility for any injury to people or property resulting from any ideas, methods, instructions or products referred to in the content.

materials

MDPI

Article

Oxidation of the Alloy Based on the Intermetallic Phase FeAl in the Temperature Range of 700–1000 °C in Air and Possibilities of Practical Application

Janusz Cebulski [1,*], Dorota Pasek [2], Maria Sozańska [1], Magdalena Popczyk [3,*], Jadwiga Gabor [3] and Andrzej Swinarew [3,4]

[1] Department of Materials Technology, Faculty of Materials Engineering, Silesian University of Technology, Krasińskiego 8, 40-019 Katowice, Poland; maria.sozanska@polsl.pl
[2] Promobil s.c., Kopernika 12, 40-064 Katowice, Poland; dorota.pasek@promobil.pl
[3] Faculty of Science and Technology, University of Silesia in Katowice, 75 Pułku Piechoty 1A, 41-500 Chorzów, Poland; andrzej.swinarew@us.edu.pl (A.S.)
[4] Institute of Sport Science, The Jerzy Kukuczka Academy of Physical Education, Mikołowska 72A, 40-065 Katowice, Poland
* Correspondence: janusz.cebulski@polsl.pl (J.C.); magdalena.popczyk@us.edu.pl (M.P.)

Abstract: The paper presents the results of oxidation tests on the alloy based on the intermetallic phase, Fe40Al5Cr0.2TiB, in the air at 700–1000 °C temperature. The kinetics of corrosion processes were determined, the surface condition after oxidation was assessed, and the type and morphology of the oxides formed were determined. In addition, the paper presents the possibility of applying the technology of surfacing Fe40Al5Cr0.2TiB alloy on the surface of steel grade S235JR as a protective coating that is resistant to high temperatures. The process was carried out using the TIG method by direct current (DC). After the surfacing, the structure of the surfacing weld made of the tested material on the base of structural steel grade S235JR was determined. It was found that a protective Al_2O_3 oxide layer is formed on the surface of the oxidized alloy based on the intermetallic phase from the FeAl system, and the oxidation kinetics have a parabolic course. Moreover, it was found that the morphology of the oxides formed on the surface varies depending on the oxidation temperature, which clearly indicates a different mechanism of oxide layer formation. The formation of a stable α-Al_2O_3 oxide variety on the surface of the Fe40Al5Cr0.2TiB alloy protects the material from further corrosion, which favors the application of this alloy on structures and fittings operating at elevated temperatures. The aim of the research was to use the Fe40Al5Cr0.2TiB alloy with very good oxidation resistance as a layer overlay on ordinary quality S235JR steel. In this way, conditions were created that fundamentally changed the surface condition (structure and physicochemical properties) of the system: steel as a substrate—intermetallic phase Fe40Al5Cr0.2TiB as a surfacing layer, in order to increase resistance to high-temperature corrosion and erosion (in the environment of gases and solid impurities in gases) often occurring in corrosive environments, especially in the power industry (boilers, pipes, installation elbows) and the chemical industry (fittings). At the same time, the surfacing method used is one of the cheapest methods of changing the surface properties of the material and regenerating or repairing the native material with a material with better properties, especially for applications in high-temperature corrosion conditions.

Keywords: corrosion; intermetallic phases; FeAl; welding layers

1. Introduction

The development of heat-resistant engineering materials is closely related to many fields of technology, including thermal power engineering, aviation, the construction of technological devices, and the automotive industry. However, the main consumer of heat-resistant steel and alloys is thermal power engineering, and therefore, its development is largely dependent on the materials and technologies available on the market that ensure increasing quality requirements. The requirements for steels for operation at elevated temperatures significantly exceed the standard characteristics used in design calculations. In industry, especially the energy industry, elements such as boilers and industrial fittings are exposed to the effects of high temperature, corrosive environment, abrasion, and erosion [1].

The gradual destruction of construction materials as a result of the impact of environmental factors is called corrosion. It is impossible to completely avoid this phenomenon during the use of construction materials, but this process can be limited by selecting surface protection methods and the type of construction materials [2].

Manufacturers of corrosion-resistant steel products rely on several basic types of steel, and one of the common features of these materials is a high nickel content. Nickel and other alloying elements (e.g., Cr, Mo, Co) are of fundamental importance for the amount of the so-called alloying additions and thus determine the price of steel. There is a tendency among manufacturers to look for alternative types of steel to conventional steel, the use of which will reduce costs while maintaining high material properties. Reducing the cost of materials can be achieved by appropriate selection of the chemical composition and structure of the material (e.g., ferritic, ferritic–pearlitic, martensitic, duplex steels), but also by using coatings on the base material, which will play the role of protection against the effects of corrosive factors [1,2].

Materials that are considered for use in elements operating in a corrosive environment are alloys based on the intermetallic phase FeAl, which have become the subject of numerous studies in recent years. They owe their wide interest mainly to their functional properties, which include very good resistance to oxidation, carburization, and sulfurization, good corrosion resistance in seawater environments, as well as high resistance to abrasive, erosive, and cavitational wear [3]. Alloys based on the FeAl phase are of particular interest due to their Al content and, therefore, the lower density of 5.4–6.7 g cm^{-3} and relatively low price of input materials, compared to the price of heat-resistant steels containing elements such as chromium, nickel, and molybdenum.

Alloys based on intermetallic phases are characterized by an ordered internal structure and properties resulting from the occurrence of three types of bonds: metallic, ionic, and covalent. The bond energy of two different atoms is greater than the bonds between the same elements in the alloy, which ensures the order of the solution structure. Thanks to these features, alloys based on intermetallic phases have special physical, chemical, and mechanical properties. FeAl intermetallic phases, containing from 36% to 51% of aluminum atoms, have stable properties in a wide temperature range [3].

In addition, many methods of producing FeAl alloys are known, which can be obtained by conventional melting and casting or by using powder metallurgy (using elementary powders or pre-alloyed powders), with the participation of the so-called SHS (self-propagating high-temperature synthesis). An alternative method for producing FeAl alloys with the desired chemical and phase composition may be the LENS (Laser Engineered Net Shaping) technique [4–10]. Materials with a structure dominated by ordered intermetallic phases from the FeAl system have properties that allow them to be used as a construction material for elements operating at elevated temperatures, often in aggressive environments containing, among others, sulfur and chlorine, as well as in environments containing one or

more oxidants. The resistance of these materials results from the formation of a passive aluminum oxide layer. In the case of an alloy based on intermetallic phases from the FeAl system, the overall corrosion resistance depends not only on the thermodynamic stability of the reaction product in a given environment and its growth kinetics but also on the morphology and cohesion of the scale physicochemical properties of the metal–oxide interface, alloy strength, and chemical composition and microstructure [11–16]. There is no information in the available literature on the analysis of corrosion resistance at temperatures of 700 and 800 °C. Heat resistance tests have been conducted so far in the temperature range of 900–1100 °C. It seems justified to determine the heat resistance of the Fe40Al5Cr0.2TiB intermetallic alloy in the temperature range of 700–1000 °C and to determine the surface condition after oxidation.

Currently, in order to increase the durability of devices, apart from the selection of material and working conditions, hardfacing of working surfaces with special electrodes or wires is used. Surfacing is one of the modern processes of regenerating machine and device parts. Obtaining a layer material that meets the criteria indicated for the structure will allow for meeting the market demand, thus solving the problem related to their durability [17]. An innovative way of obtaining improved properties is to modify the surface layer by surfacing with a wire made of an alloy based on the Fe40Al5Cr0.2TiB intermetallic phase. The change in material properties depends on the dimensions (thickness) of the surfacing layer [18].

FeAl alloy cladding is a process that aims to create protective coatings on the surface of the material using an alloy of iron (Fe) and aluminum (Al). The FeAl alloy is valued for its properties, such as corrosion resistance, resistance to high temperatures, and the ability to form passive oxide layers that protect the material from further damage. Cladding of layers made of this alloy is widely used in the automotive, aviation, and energy industries, especially where resistance to oxidation and wear in extreme conditions is required [19–22].

In the case of FeAl alloy cladding, the selection of appropriate process parameters is crucial. The current, voltage, cladding speed, and composition of the welding wire must be selected appropriately. FeAl is characterized by a relatively low melting temperature (below 1200 °C), which can affect the ease of fusion of the alloy into the base material and the formation of appropriate mechanical and microstructural properties of the coating [4,23,24]. During surfacing, an alloy based on the FeAl intermetallic phase is introduced onto the surface of the base material, where it melts under the influence of an electric arc. As a result of this process, a uniform protective layer is formed on the surface [25].

Alloys based on the intermetallic phase FeAl with the B2 structure, containing 35–50% at. of aluminum, are a prospective construction material for operation at elevated temperatures under conditions of simultaneous action of complex mechanical stresses and high thermal loads, in contact with high-temperature gases and other aggressive substances and abrasive materials causing wear and high-temperature corrosion [26–31]. Due to the above, alloys based on the FeAl intermetallic phase are used as coating materials for construction elements used mainly in the power industry. In fluidized bed boilers, burning coal and flue gases, sulfur, chlorine, and hydrogen occur, which form chemical compounds that have a negative (destructive) effect on the steel structure. An additional damaging factor is water vapor; the temperature of which is about 600 °C and has a corrosive effect on the surfaces of boilers [32]. FeAl layers have the ability to form a passive oxide layer, which is important in the context of protection against further oxidation and corrosion [33,34]. The application of an alloy based on the FeAl intermetallic phase onto the surfaces of structural steels can be completed by surfacing or spraying of coatings using the HVOF (High-Velocity Oxygen Fuel) method in the form of protective coatings with a significant share of oxide layers, formed already at the spraying stage [35]. The special features of the

HVOF technology are very high kinetic energy and significant thermal energy accumulated in the two-phase metallization stream (gas–powder). The process parameters have a significant effect on the properties of the layer and its connection with the substrate, as it may lead to delamination of coatings and the formation of cracks on the surface [21,36–38]. Welding is commonly used as a method of regenerating worn-out structural elements by covering them with an appropriate chemical composition and layer thickness. In addition to the regenerative function, surfacing is also used to refine new components. Combining modern materials with well-known surfacing techniques will allow you to obtain a component with unique properties that allow for applications in corrosive and erosive conditions. The permanent intermetallic welding methods include TIG (Tungsten Inert Gas) and laser welding. Until now, coating materials made of FeAl intermetallic alloy have been thermally sprayed, which has significantly increased the production costs of these materials. The traditional surfacing method used in this work consists of the fact that in this process, the substrate is melted, to which a new layer is cohesively bonded. By combining intermetallic materials using the TIG method, favorable joint properties are obtained, mainly due to a very narrow heat exchange zone (SWC), which ensures the homogeneity of the material structure [18,19,29].

The subject of the research in the presented work was the evaluation of the behavior of the system consisting of S235JR steel as a substrate and the intermetallic phase Fe40Al5Cr0.2TiB as a surfacing layer, under oxidation conditions in air at temperatures of 700, 800, 900, and 1000 °C. The detailed research analysis concerned the oxidation kinetics of the resulting steel-surfacing layer system, the characteristics of the morphology, chemical, and phase composition of the surface after the oxidation process, and changes in hardness.

2. Materials and Methods

The tests were performed on samples of the Fe40Al5Cr0.2TiB intermetallic alloy after casting, the chemical composition of which is presented in Table 1. A detailed description of the preparation of the material is included in the publication [39]. The material was subjected to homogenizing annealing at 1050 °C for 72 h, homogenizing the chemical composition of the alloy. Samples for oxidation tests were made from the Fe40Al5Cr0.2TiB alloy after heat treatment in the shape of a cylinder with a diameter of 6 mm and a height of 2 mm. The process of cutting the samples was carried out using the electrical spark machining method. The use of this method allowed for obtaining samples of designated dimensions and uniform surface quality (roughness), which is important from the point of view of studying the course of oxidation.

Table 1. Chemical composition of Fe40Al5Cr0.2TiB alloy.

Compound	Fe	Al	Cr	Ti	B
% at.	54.80	40.10	4.86	0.18	0.06

The samples were oxidized at 700, 800, 900, and 1000 °C using the thermogravimetric method (for 8 h) on the analyzer NETZSCH STA 449 F3 Jupiter® (NETZSCH-Gerätebau GmbH, Selb, Germany) and discontinuously (in CARBOLITE ELF 11/6B furnace, Carbolite Gero, Neuhausen, Germany) for 50, 100, 300, and 500 h. Corrosion tests were performed in an air environment. In order to determine the kinetics of oxidation, a series of samples was used, which were weighed after successive periods. The sample weighed after a given time was not returned to the furnace. For each of the samples, before and after the corrosion test, mass measurements were taken on a laboratory scale with a measurement accuracy of 10^{-4} g.

The surface condition after the corrosion tests was determined on a HITACHI S4200 scanning electron microscope (Hitachi, Ltd., Tokyo, Japan) equipped with an EDS (Energy-

Dispersive Spectroscopy) X-ray detector, which was used to determine the chemical composition of corrosion products. Due to the adopted research methodology, the share of oxygen should be treated as an estimate (*quantitative share of oxygen from stoichiometry).

Qualitative phase analysis of oxides formed on the surface of oxidized Fe40Al5Cr0.2TiB alloy samples was performed using a JDX-7S diffractometer from JEOL, Tokyo, Japan. The source of radiation was a lamp with a copper anode. Phase identification was performed using PCSIWIN software (PDF2) using the database in the form of JCPDS cards—International Centre for Diffraction Data 2000.

The microstructure of the alloy after surfacing onto the steel substrate was examined using a light microscope, specifically the Olympus GX51, Olympus, Tokyo, Japan.

Hardness was measured by the Vickers method with a load of 9.81 N (HV1) on a ZWICK hardness tester, ZWICK, Ulm, Germany.

Fe40Al5Cr0.2TiB alloy in the form of a 5 mm diameter rod was welded using the TIG method onto the surface of unalloyed structural steel S235JR with a ferritic–pearlitic structure, the chemical composition of which is given in Table 2. The parameters of the weldment process are presented in Table 3.

Table 2. Chemical composition of S235JR steel.

Compound	C	Mn	P	S	Si	Fe
% mas.	0.15	1.2	<0.035	<0.035	0.3	rest

Table 3. Surfacing process parameters.

TIG	Thickness [mm]	Gas Shield	Current [A]	Flow Rate [L/min]	Welding Position	Welding Speed
DC-	5	Argon I1	100	10	PA	1.0–2.5

3. Results and Discussion

3.1. Oxidation Kinetics of Fe40Al5Cr0.2TiB Alloy

The course of the oxidation kinetics of the Fe40Al5Cr0.2TiB alloy in the temperature range of 700–1000 °C is shown in Figure 1. An increase in mass was observed due to the formation of aluminum oxide on the surface of the samples at a temperature of 800 °C. The analysis of the oxidation kinetics in the FeAl alloy indicates a parabolic course of the process of creating high-temperature corrosion products.

3.2. Tests of the Surface Condition and Oxidation Products of the Fe40Al5Cr0.2TiB Alloy

Figures 2–5 present the results of surface condition tests after oxidation of the Fe40Al5Cr0.2TiB alloy at different temperatures for 500 h. Depending on the applied oxidation temperature of the alloy, different morphologies of corrosion products were observed on the surface of the material. Based on our own research and analysis of the literature [40,41], it can be stated that an oxide layer in the form of Al_2O_3 was formed on the surface of the oxidized alloy (Figure 2). After oxidation at a temperature of 700 °C, casting defects were found, and the surface of the oxidized layer (Figure 3a) was relatively small in comparison with the surface of the scale formed at temperatures of 800 °C, 900 °C, and 1000 °C, which was covered with oxides in the form of fine needles (Figures 4b, 5b and 6b). The EDS microanalysis of the chemical composition of the sample after oxidation at 700 °C (Figure 3b) confirmed the presence of iron and aluminum, which are the main components of the Fe40Al5Cr0.2TiB alloy, and chromium, which is added to reduce brittleness at high temperatures. At 800 °C, the initial stage of scale formation was observed (Figure 4a). The EDS test of the chemical composition of the sample after

oxidation at 800 °C (Figure 4b) confirmed the formation of a passive layer of alumina oxides (Figure 4c). The scale surface formed at 900 °C covers a significant part of the parent material (Figure 5a), and the formed oxides are characterized by fine needles (Figure 5b). The analysis of oxidation products of the sample heated at 1000 °C (Figure 6a) shows clear changes in the surface morphology (Figure 6b) compared to the samples oxidized at 800 °C and 900 °C. The substrate of the material is inhomogeneous, covered with an unevenly distributed passive layer. The examination of the chemical composition of the sample using the EDS method allows us to determine the presence of oxidation products (Figure 6c,d). Moreover, Figure 6d shows that oxygen appears in the area marked as area 2 of the analysis (Figure 6a), constituting the substrate of the Fe40Al5Cr0.2TiB alloy. This may suggest the sample is progressing in the oxidation process. The formation of a protective Al_2O_3 layer on the surface of the Fe40Al5Cr0.2TiB intermetallic alloy during high-temperature processes in an oxidizing atmosphere counteracts the degradation of the metal core and is thus a basic determinant of the alloy's high heat resistance in an air atmosphere at high temperature. The analysis of the results of the research conducted by the authors of [40] indicates that the size of the oxide needles formed depends on the rate of the oxidation process. Based on Figure 4a, it can be concluded that the scale flaking process begins at a temperature of 800 °C, which may be caused by the presence of stresses resulting from the growth of the oxide layer. In the tested temperature range, the greatest changes in the scale morphology occur during oxidation at a temperature of 1000 °C. Based on the conducted research, it can also be stated that the "limit temperature" of the developing oxidation process, which is characterized by the formation of a passive oxide layer, is the temperature of 800 °C.

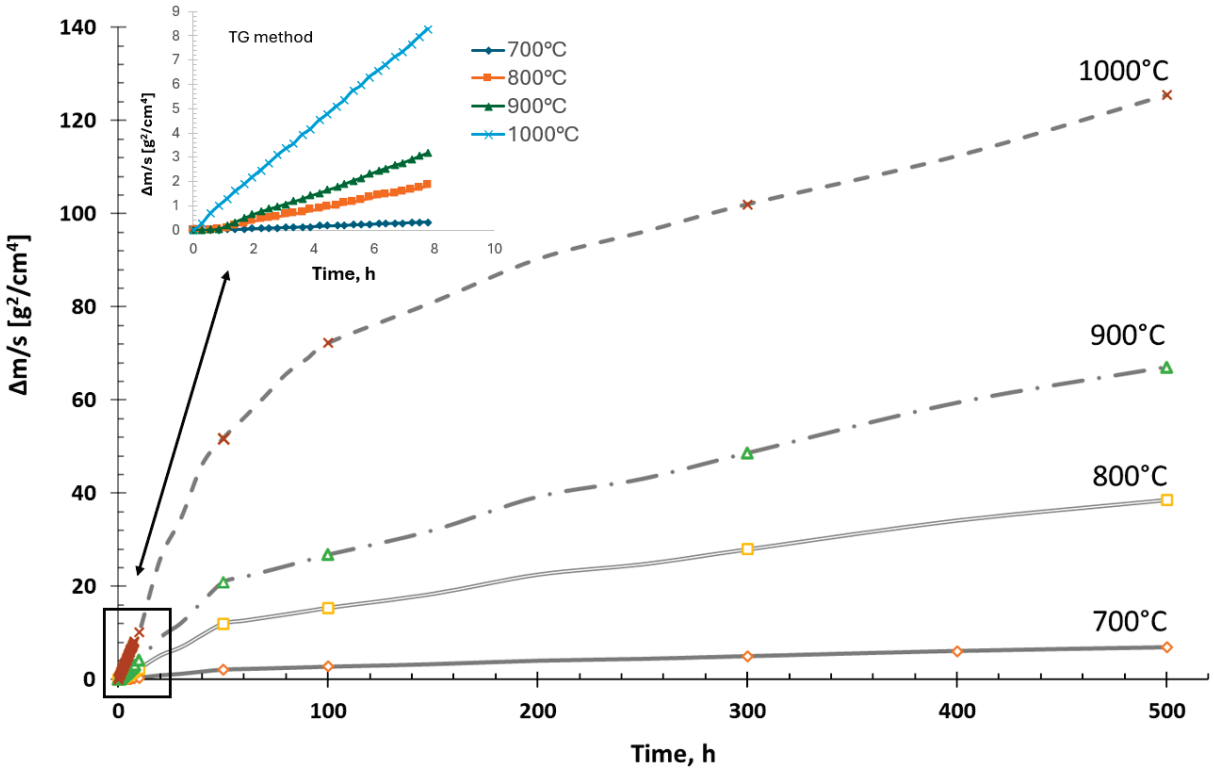


Figure 1. Oxidation kinetics of Fe40Al5Cr0.2TiB alloy during 500 h.

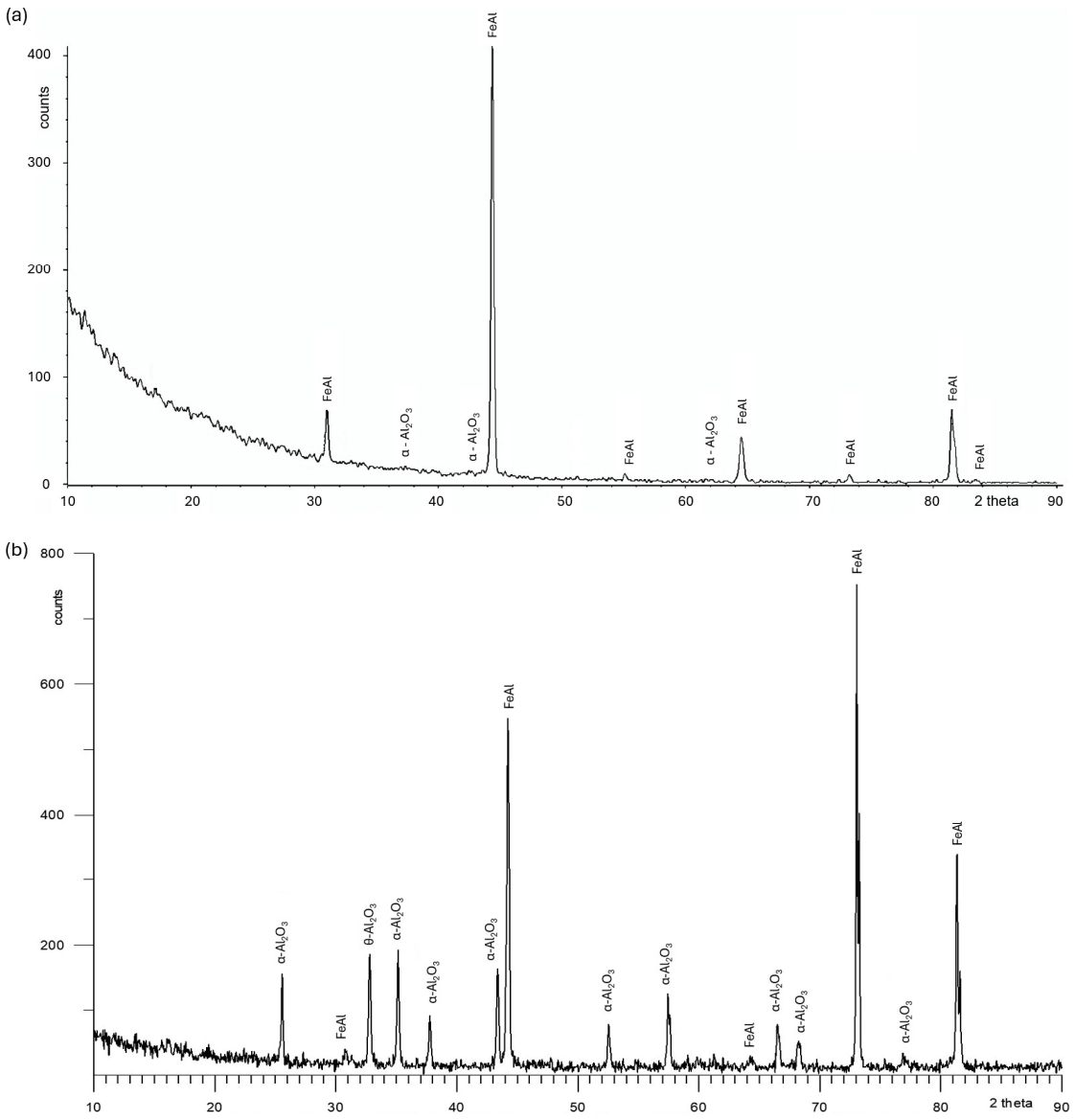
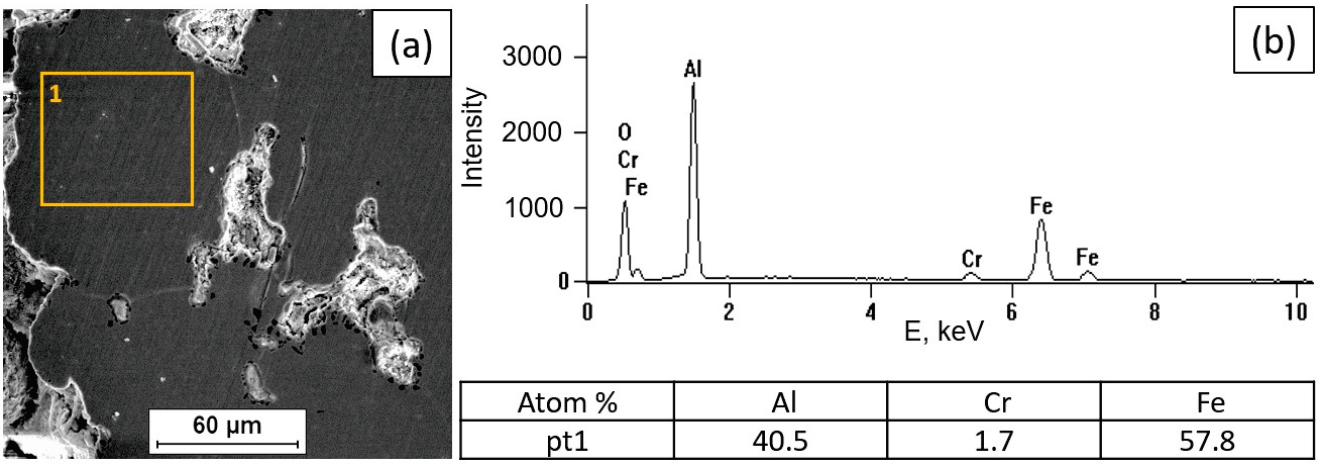
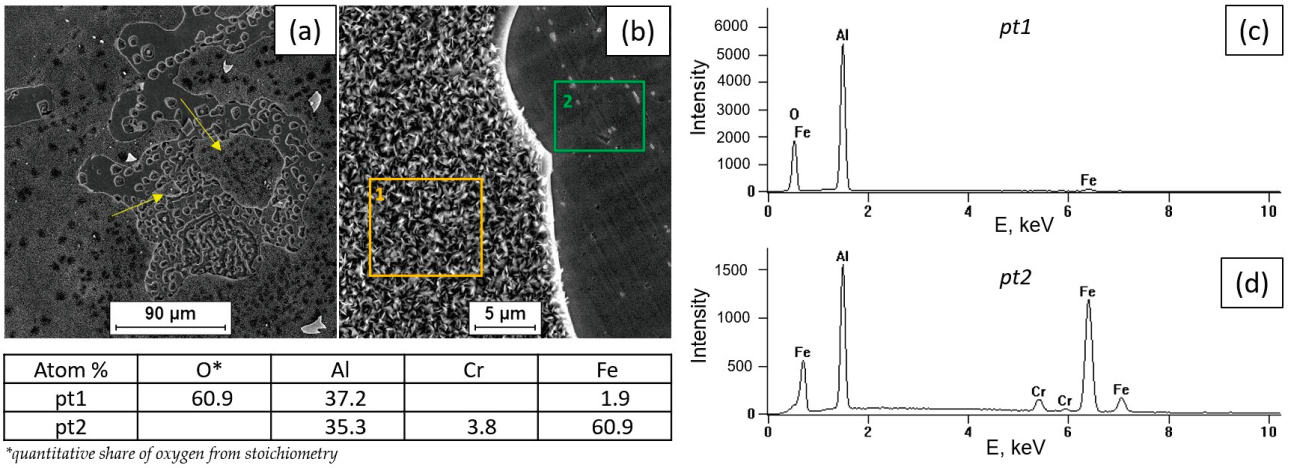


Figure 2. X-ray phase analysis of oxidation products formed on the surface of Fe40Al5Cr0.2TiB alloy after corrosion tests at 700 °C (**a**) and at 1000 °C (**b**).



Atom %	Al	Cr	Fe
pt1	40.5	1.7	57.8

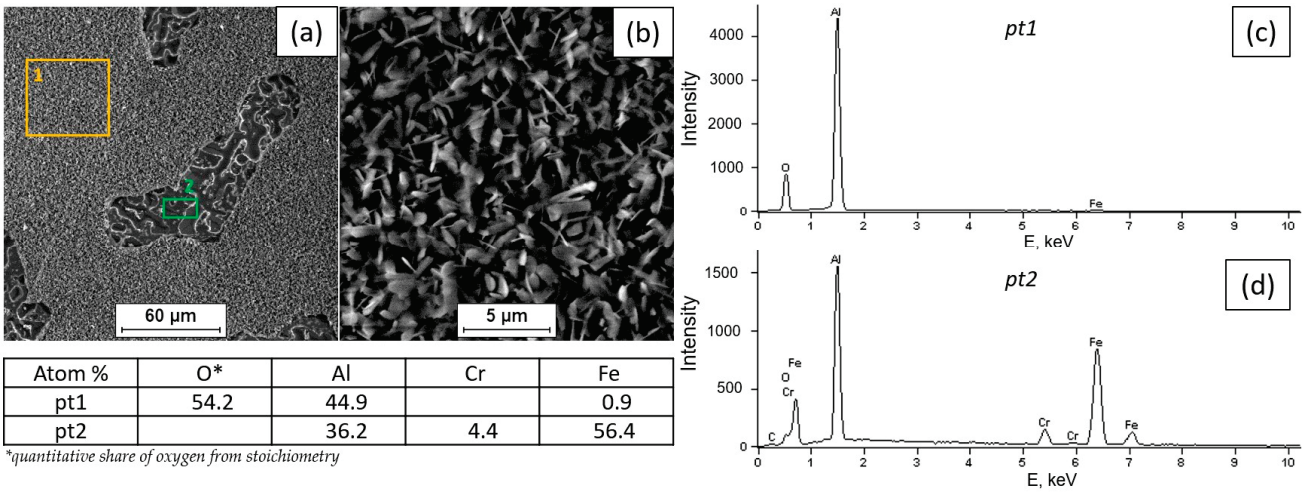
Figure 3. Fe40Al5Cr0.2TiB alloy surface after oxidation at 700 °C for 500 h (**a**) and EDS X-ray spectrum of chemical composition at location 1 (**b**).



Atom %	O*	Al	Cr	Fe
pt1	60.9	37.2		1.9
pt2		35.3	3.8	60.9

**quantitative share of oxygen from stoichiometry*

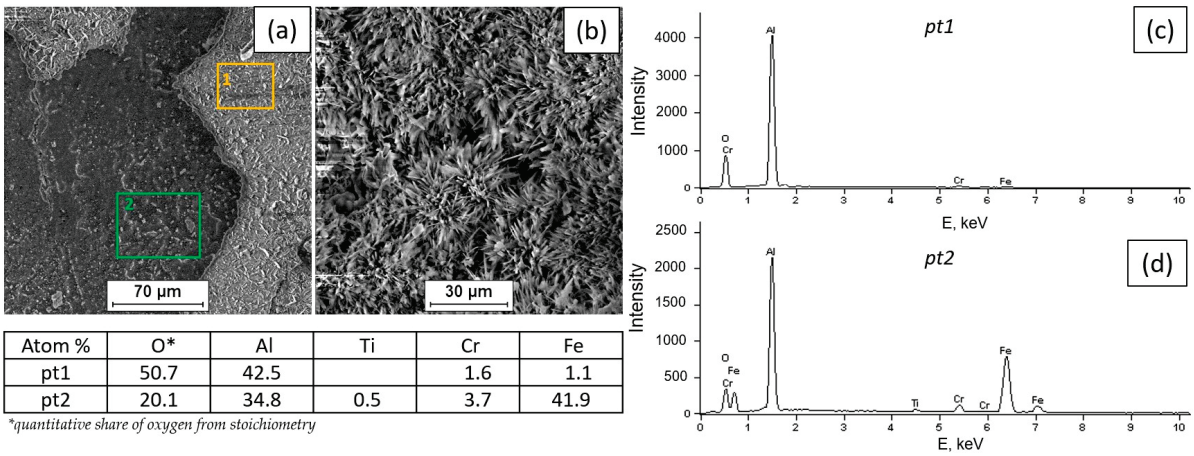
Figure 4. Fe40Al5Cr0.2TiB alloy surface after oxidation at 800 °C for 500 h (**a**), morphology of corrosion products (**b**), and EDS X-ray spectrum of chemical composition at locations 1 and 2 (**c**,**d**).



Atom %	O*	Al	Cr	Fe
pt1	54.2	44.9		0.9
pt2		36.2	4.4	56.4

**quantitative share of oxygen from stoichiometry*

Figure 5. Fe40Al5Cr0.2TiB alloy surface after oxidation at 900 °C for 500 h (**a**), morphology of corrosion products (**b**), and EDS X-ray spectrum of chemical composition at locations 1 and 2 (**c**,**d**).



Atom %	O*	Al	Ti	Cr	Fe
pt1	50.7	42.5		1.6	1.1
pt2	20.1	34.8	0.5	3.7	41.9

**quantitative share of oxygen from stoichiometry*

Figure 6. Fe40Al5Cr0.2TiB alloy surface after oxidation at 1000 °C for 500 h (**a**), morphology of corrosion products (**b**), and EDS X-ray spectrum of chemical composition at locations 1 and 2 (**c**,**d**).

The research conducted in [41] indicates that the tested material is characterized by good mechanical properties at elevated temperatures (Table 4) in comparison to steels intended for use in the power industry [42]. For the temperature of 1000 °C, the mechanical properties were not determined. The mechanical properties determined are tensile strength (R_m), yield strength ($R_{p0.2}$), elongation (A_5), and narrowing (Z).

Table 4. Results of mechanical properties for alloy Fe40Al5Cr0.2TiB.

Temperature [°C]	R_m [MPa]	$R_{p0.2}$ [MPa]	A_5 [%]	Z [%]
Room	312	-	-	-
700	268	172	-	-
800	115	77	3	21
900	53	43	7	35
1000	41	39	11	72

3.3. Possibility of Making a Coating of FeAl Intermetallic Alloy on a Structural Steel Substrate by the Surfacing Method

Then, the possibility of implementing the method of surfacing the surface with an alloy based on the intermetallic phase Fe40Al5Cr0.2TiB on the S235JR material was analyzed. The surfacing process was carried out using the TIG method in an inert gas shield. The process parameters are described in Table 3. The layers were made in three variants: single-run (SB), multi-run (MB), and multi-layer (ML). Figure 7a schematically shows the method of applying layers of the tested alloy, while Figure 7b–d show macroscopic photos of the weld made on the S235JR steel substrate.

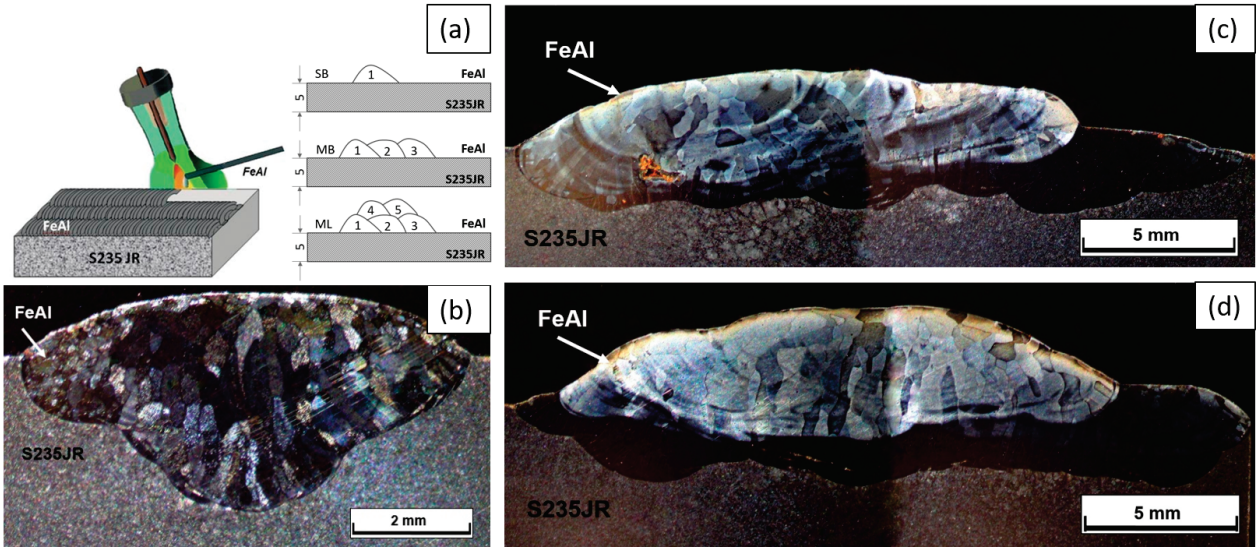


Figure 7. DC TIG cladding layer: process diagram (**a**), single pass (SB) (**b**), multi-pass (MB) (**c**), and multi-layer (ML) (**d**).

Hardness measurements were performed on the surface of cross-sections of the tested material. Figure 8 shows a scheme of the measurements performed, and the results of the HV1 hardness distribution for SB, MB, and ML are presented in Table 5. The measurement error was less than 5%. The hardness is considered for measurements along the line. Hardness distribution is checked in several lines, and the results of this test show that if it is the first or the last bead, hardness is about 220 to 250 HV1; if more than one bead is used in this situation, hardness goes up from 250 to 350 HV1. The hardness of the S235 steel substrate was approx. 150 HV1. The differences in the obtained

hardness are most likely due to different conditions of the surfacing process or different temperature gradients depending on the number of beads, which could have led to different crystallization conditions. The welding was carried out manually, and therefore, the process was not controlled in the same way as in surfacing using an automated welding station. The conducted tests allowed us to state that the process of surfacing with a material made of an alloy based on the intermetallic phase FeAl significantly improves the mechanical properties.

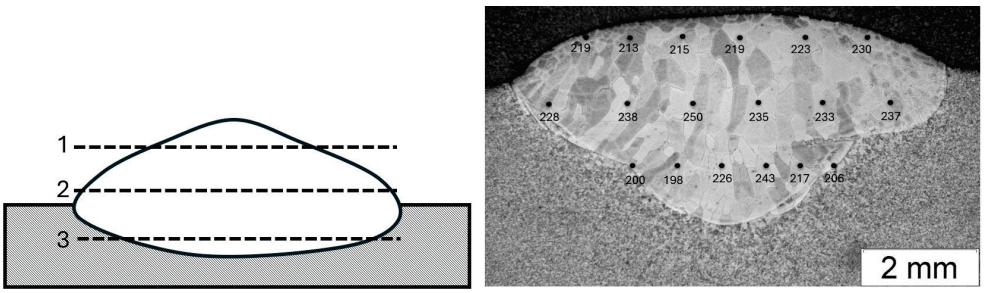


Figure 8. The scheme of the measurements.

Table 5. Results of the HV1 hardness distribution (measurement error < 5%).

Measurement	1	2	3	4	5	6
SB 1	219	213	215	219	223	230
SB 2	228	238	250	235	233	237
SB 3	200	198	226	243	217	206
MB 1	321	286	280	334	275	331
MB 2	289	257	313	295	292	278
MB 3	265	297	238	226	260	240
ML 1	302	345	292	297	299	301
ML 2	297	342	323	312	278	316
ML 3	248	224	236	241	231	249

The microstructure of the Fe40Al5Cr0.2TiB alloy overlay layer based on the intermetallic phase Fe40Al5Cr0.2TiB was studied on polished and iron chloride etched microsections. The observations were carried out using an OLYMPUS GX51 light microscope, Olympus, Tokyo, Japan. The microstructure of the Fe40Al5Cr0.2TiB alloy after overlay on the S235JR steel substrate observed in the cross-section within the fusion boundary is characterized by grains of various sizes, largely elongated (columnar) during crystallization in the direction of the largest temperature gradient (Figure 9). The coarse-grained microstructure of the welded layer may have better resistance to electrochemical corrosion in a salt environment [43,44]. The test results indicate that direct current can be used to overlay such materials. However, the overlay weld may contain casting defects of the type of voids and shrinkage. The application of a multilayer coating significantly reduces the number of casting defects, the presence of which is mainly visible in the first layer of the overlay weld.

Figures 10 and 11 show the SEM surface analysis coating layers, in which, based on studies, the presence of Al, Cr, and Fe is shown. The table shows the chemical analysis of the intermetallic layers FeAl. Observations made using a scanning electron microscope of the FeAl intermetallic alloy deposit showed a coarse-grained structure of the weld layer and a clear line of separation of the base material and weld material (FeAl). The study of the chemical composition made with the X-ray microanalysis EDS method showed reduced content of aluminum in the weld pad and unchanged chemical composition of the steel in the heat-affected zone. The content mass weight of aluminum in the weld pad is from 7.8 to 18.4 atom% (primary material 40.10%), indicating substantial aluminum evaporation when

melting during welding. The reduction in aluminum content of less than 36 at% by use of DC(-) results in the formation of Fe_3Al intermetallic alloy. Conducting the welding with reserved polarity direct current (100 A) intermetallic alloy Fe40Al obtained welding layer Fe_3Al has different properties from the alloy used for welding. Nevertheless, the welded layer produced on the surface of S235 steel is characterized by good connection, without the occurrence of cracks or delaminations of the FeAl alloy coating, which were observed when using other coating methods, e.g., the HVOF method [27]. In order to obtain a coating made of an alloy based on the FeAl intermetallic phase, it is necessary to select process parameters that limit aluminum evaporation or use an alloy with a different composition, which will finally have the intended composition of the Fe40Al alloy after welding.

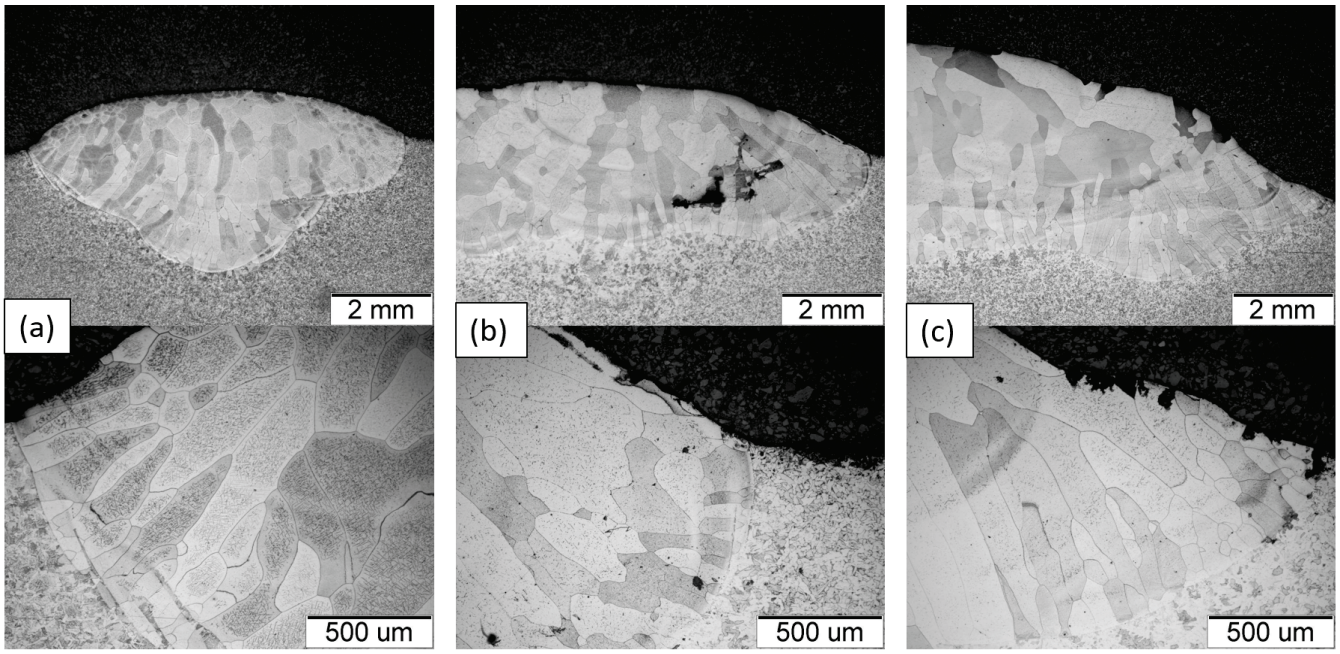


Figure 9. Microstructure of the Fe40Al5Cr0.2TiB alloy deposited layer: single run (SB) (**a**), multi-run (MB) (**b**), and multi-layer (ML) (**c**)—LM.

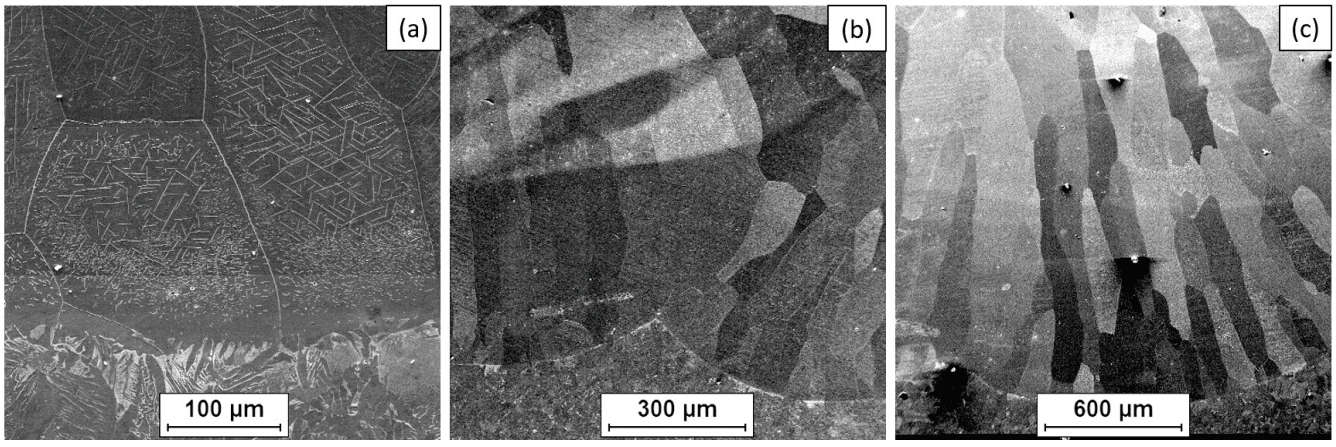
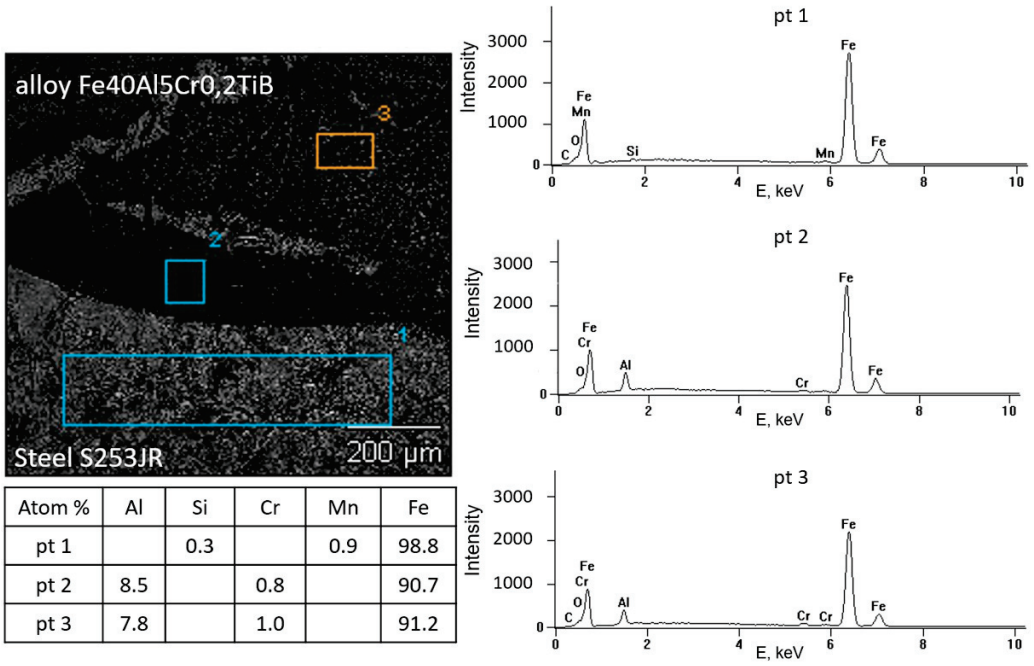


Figure 10. The fusion boundary of the Fe40Al5Cr0.2TiB alloy overlay layer on the S235JR steel substrate: single run (SB) (**a**), multi-run (MB) (**b**), and multi-layer (ML) (**c**)—SEM.



Atom %	Al	Si	Cr	Mn	Fe
pt 1		0.3		0.9	98.8
pt 2	8.5		0.8		90.7
pt 3	7.8		1.0		91.2

Atom %	Al-K	Si-K	Cr-K	Mn-K	Fe-K
pt1		0.3		0.9	98.8
pt2	8.5		0.8		90.7
pt3	7.8		1.0		91.3

Figure 11. Connection of the welded layer on the structural steel with X-ray microanalysis of the chemical composition, EDS single run (SB)—SEM.

4. Conclusions

Based on the conducted tests and analysis of their results, the following conclusions were formulated:

1. Processes related to the formation of a protective oxide layer do not occur significantly at a temperature of 700 °C. The surface of the sample at this temperature is not covered with an oxide layer compared to the state of the surface of the alloy oxidized in the range of 800–1000 °C.
2. The formation of the Al_2O_3 scale begins at a temperature lower than 800 °C, while the oxidation process intensifies in the range of 800–1000 °C.
3. The surface of the alloy at 800 °C is covered with scale, which is aluminum oxide with a needle morphology.
4. The microstructure of the Fe40Al5CrTiB alloy was changed after the welding process. The microscopic grains grow and form a coarse-grained structure of the material. The gas tungsten arc welding process is possible to use for making an intermetallic surface FeAl. The test results show that DC current can be used to burn this kind of material, but in the cross-section of the clad, we can look at several kinds of welding imperfections, such as pores and lack of fusion. This kind of imperfection is located on or near to fusion line. If we made multi-beads or multi-layers, this kind of imperfection would have been reduced. Only the first layer has imperfections; the next bead or layer is without this kind of defect.
5. The proposed method of producing alloy layers based on the intermetallic FeAl phase may be an alternative to currently used methods of modifying steel surfaces, based on covering them with expensive coating materials or using advanced technologies, e.g., thermal spraying.

6. As a result of surfacing, aluminum evaporates; therefore, it is important to select appropriate process parameters or use a material that provides the required chemical composition of the surfacing layer.

Author Contributions: Conceptualization, J.C. and M.P.; methodology, J.C. and M.P.; validation, D.P. and M.S.; formal analysis, J.G.; investigation, D.P.; data curation, M.P.; writing—original draft preparation, J.C., M.P., D.P., A.S., J.G., and M.S.; writing—review and editing, J.C., M.P., D.P., A.S., J.G., and M.S.; visualization, D.P.; supervision, A.S. All authors have read and agreed to the published version of the manuscript.

Funding: The project was co-financed by the European Union within the program "The European Funds for Śląsk (Silesia) 2021–2027".

Institutional Review Board Statement: Not applicable.

Informed Consent Statement: Not applicable.

Data Availability Statement: All data are included in the article.

Conflicts of Interest: Author Dorota Pasek was employed by the company Promobil s.c. The remaining authors declare that the research was conducted in the absence of any commercial or financial relationships that could be construed as a potential conflict of interest.

References

1. Hernas, A. Uwarunkowania i kierunki rozwoju materiałów żarowytrzymałych. In *Postępy Nauki o Materiałach i Inżynierii Materiałowej*; Hetmańczyk, M., Cwajna, J., Czyrska-Filemonowicz, A., Kurzydłowski, K.J., Hernas, A., Sieniawski, J., Wierzchoń, T., Eds.; Wydawnictwo Politechniki Śląskiej: Gliwice, Poland, 2002; pp. 191–230.
2. Mrowec, S.; Werber, T. *Gas Corrosion*; Silesia Publishing House: Katowice, Poland, 1965.
3. Niewielski, G.; Jabłońska, M. Characteristics and applications of intermetallics from the Fe-Al system. *Mater. Eng.* **2011**, *2*, 43–47.
4. Deevi, S.C.; Sikka, V.K. Nickel and iron aluminides: An overview on properties, processing, and applications. *Intermetallics* **1996**, *4*, 357–375. [CrossRef]
5. Zhang, H.; Xie, W.; Gao, H.; Shen, W.; He, Y. Suppression of the SHS reactions during synthesis of porous FeAlintermetallics by introducing silicon. *J. Alloys Compd.* **2018**, *735*, 1435–1438. [CrossRef]
6. Josh, D.L.; Easton, D.S.; Liu, C.T.; Babu, S.S.; David, S.A. Processing of FeAl and FeAl alloys by reaction synthesis. *Intermetallics* **1995**, *3*, 467–481.
7. Siemiaszko, D.; Mościcki, R. Kinetics study on the SHS reaction in massive samples with high heating rate in the Fe–Al system. *J. Alloys Compd.* **2015**, *632*, 335–342. [CrossRef]
8. Baligidad, R.G.; Prakash, U.; Rao, R.V.; Rao, P.K.; Ballal, N.B. Processing of Fe_3Al based intermetallic alloys through electroslag remelting. *ISIJ Int.* **1996**, *36*, 1448–1452. [CrossRef]
9. Sikka, V.K.; Wilkening, D.; Liebetrau, J.; Mackey, B. Melting and casting of FeAl-based cast alloy. *Mater. Sci. Eng.* **1998**, *A258*, 229–235. [CrossRef]
10. Pęska, M.; Karczewski, K.; Rzeszotarska, M.; Polański, M. Direct Synthesis of Fe-Al Alloys from Elemental Powders Using Laser Engineered Net Shaping. *Materials* **2020**, *13*, 531. [CrossRef]
11. Garbacz, H.; Wyrzykowski, J. Modern methods of plasticizing alloys based on ordered Ti-Al intermetallic phases. *Mater. Eng.* **1997**, *3*, 86–91.
12. Huang, D.; Yang, W.Y.; Sun, Z.Q.; Froyen, L. Preparation and mechanical properties of large-ingot Fe_3Al-based alloys. *J. Mater. Process. Technol.* **2004**, *146*, 175–180. [CrossRef]
13. Kupka, M. *Structure and Properties of FeAl-Based Alloys Obtained in Metallurgical Processes*; University of Silesia Publishing House: Katowice, Poland, 2005.
14. Bojar, Z.; Przetakiewicz, W. *Metal Materials Containing Intermetallic Phases*; BEL Studio: Warsaw, Poland, 2006; ISBN 83-89968-03-7.
15. Dymek, S. Characteristics of high-temperature intermetallic compounds. *Steelmak.–Steelmak. News* **1998**, *6*, 220–222.
16. Kulak, K.; Kupka, M. Oxidation of multi-component iron aluminum on the FeAl matrix. *Mater. Eng.* **2011**, *4*, 514–518.
17. Morris, D.G.; Deevi, S.C.; Sikka, V.K.; Maziasz, P.J.; Cahn, R.W. *International Symposium on Nickel and Iron Aluminides*; ASM International: Materials Park, OH, USA, 1997; pp. 165–175.
18. Cebulski, J.; Bęczkowski, R.; Pasek, D. Heat resistance of Fe40Al5Cr0.2TiB alloy intermetallic surface remelted with TIG method. In Proceedings of the 27th International Conference on Metallurgy and Materials, Brno, Czech Republic, 23–25 May 2018.

19. Jaśkowiec, K.; Uhl, W. The problem of casting elements from an alloy based on Fe-Al operating at elevated temperatures. *MOTROL Comm. Mot. Energetics Agric.* **2013**, *15*, 59–62.
20. Matysik, P.; Jóźwiak, S.; Czujko, T. Characterization of Low-Symmetry Structures from Phase Equilibrium of Fe-Al System-Microstructures and Mechanical Properties. *Materials* **2015**, *8*, 914–931. [CrossRef]
21. Cinca, N.; Cygan, S.; Senderowski, C.; Jaworska, L.; Dosta, S.G.; Cano, I.; Guilemany, J.M. Sliding Wear Behavior of Fe-Al Coatings at High Temperatures. *Coatings* **2018**, *8*, 268. [CrossRef]
22. Seikh, A.H.; Baig, M.; Singh, J.K.; Mohammed, J.A.; Luqman, M.; Abdo, H.S.; Khan, A.R.; Alharthi, N.H. Microstructural and Corrosion Characteristics of Al-Fe Alloys Produced by High-Frequency Induction-Sintering Process. *Coatings* **2019**, *9*, 686. [CrossRef]
23. Morris, D.G.; Munoz-Morris, M.G.; Requejo, L.M. Work hardening in Fe-Al alloys. *Mater. Sci. Eng. A* **2007**, *460–461*, 163–173. [CrossRef]
24. Zhang, Y.; Zhao, T.; Yu, X.; Huang, J. The Al-Fe Intermetallic Compounds and the Atomic Diffusion Behavior at the Interface of Aluminum-Steel Welded Joint. *Metals* **2023**, *13*, 334. [CrossRef]
25. Zhang, J.; Sun, K.; Wang, J.; Tian, B.; Wang, H.; Yin, Y. Sliding wear behavior of plasma sprayed Fe_3Al-Al_2O_3 graded coatings. *Thin Solid Film.* **2008**, *516*, 5681–5685. [CrossRef]
26. Formanek, B.; Szczucka-Lasota, B.; Szymański, K.; Włodarczyk, A. New generation of protective coatings intended for the power industry. *J. Mater. Process. Technol.* **2005**, *5*, 164–165. [CrossRef]
27. Cinca, N.; Dosta, S.; Guilemany, J.M.; Lima, C.R.C. High-temperature oxidation of Fe40Al coatings obtained by HVOF thermal spray. *Intermetallics* **2007**, *15*, 1384–1394.
28. Zienert, T.; Leineweber, A.; Fabrichnaya, O. Heat capacity of Fe-Al intermetallics: B2-FeAl, $FeAl_2$, Fe_2Al_5 and Fe_4Al_{13}. *J. Alloys Compd.* **2017**, *725*, 848–859. [CrossRef]
29. Bojar, Z.; Senderowski, C. Gas detonation spray forming of Fe-Al coatings in the presence of interlayer. *Surf. Coat. Technol.* **2008**, *202*, 3538–3548.
30. Kumar, M.; Kant, R.; Chand, S.; Prakash, U.; Sehgal, S.; Saxena, K.K.; Davim, J.P.; Prakash, C. High-Temperature Corrosion Performance of FeAl-Based Alloys Containing Carbon in Molten Salt. *Metals* **2011**, *11*, 2040. [CrossRef]
31. Guilemany, J.M.; Nin, J. Thermal spraying methods for protection against wear. In *Sufface Coatings for Protection Against Wear*; Mellor, B.G., Ed.; Woodhead: Cambridge, UK, 2006.
32. Peng, J.; Moszner, F.; Rechmann, J.; Vogel, D.; Palm, M.; Rohwerder, M. Influence of Al content and pre-oxidationon the aqueous corrosion resistance of binary Fe-Al alloys in sulphuric acid. *Corros. Sci.* **2019**, *149*, 123–132. [CrossRef]
33. Amaya, M.; Espinosa-Medina, M.A.; Porcayo-Calderon, J.; Martinez, L.; Gonzalez-Rodriguez, J.G. High temperature corrosion performance of FeAl intermetallic alloys in molten salts. *Mater. Sci. Eng. A* **2003**, *349*, 12–19. [CrossRef]
34. Novák, P.; Nová, K. Oxidation Behavior of Fe-Al, Fe-Si and Fe-Al-Si. *Materials* **2019**, *12*, 1748. [CrossRef]
35. Bojar, Z.; Formanek, B.; Senderowski, C.; Szymański, K. Tribological behavior of Fe-Al intermetallic coatings obtained by HVOF method. *Mater. Eng.* **2010**, *31*, 390–393.
36. Shishkovsky, I.; Missemer, F.; Kakovkina, N.; Smurov, I. Intermetallics Synthesis in the Fe–Al System via Layer by Layer 3D Laser Cladding. *Crystals* **2013**, *3*, 517–529. [CrossRef]
37. Wang, H.; An, F.; Bai, X.; Yao, H.; Zhang, M.; Chen, Q.; Ji, G.; Ramachandran, C.S. Improvement of Microstructure and Sliding Wear Property of Cold-Sprayed FeAl Intermetallic Compound Coating by Annealing Treatment. *Coatings* **2023**, *13*, 1260. [CrossRef]
38. Faria, J.; de Paula, A.; Silva, C.; Kakitani, R.; Barros, A.; Garcia, A.; Brito, C.; Cheung, N. Fe-Containing Al-Based Alloys: Relationship between Microstructural Evolution and Hardness in an Al-Ni-Fe Alloy. *Metals* **2023**, *13*, 1980. [CrossRef]
39. Cebulski, J.; Pasek, D.; Popczyk, M.; Swinarew, A.; Gabor, J. Structure and Corrosion Resistance of Fe40Al5Cr0.2TiB Alloy After Casting and After Homogenization Annealing. *Materials* **2025**, *18*, 308. [CrossRef] [PubMed]
40. Kulak, K.; Kupka, M.; Dercz, G. Oxidation of multicomponent iron aluminide based on FeAl phase. *Mater. Eng.* **2011**, *4*, 510–513.
41. Barcik, J.; Cebulski, J. Plastify of alloy based on the matrix of intermetallic FeAl phase. *Arch. Metall.* **2000**, *45*, 315–330.
42. Hernas, A.; Dobrzański, J.; Pasternak, J.; Fudali, S. *Characteristics of the New Generation of Steel for the Energy Sector*; Wydawnictwo Politechniki Śląskiej: Gliwice, Poland, 2015.
43. Novák, P.; Michalcová, A.; Marek, I.; Mudrová, M.; Saksl, K.; Bednarčík, J.; Zikmund, P.; Vojtěch, D. On the formation of intermetallics in Fe-Al system—An in situ XRD study. *Intermetallics* **2013**, *32*, 127–136. [CrossRef]
44. Cebulski, J.; Pasek, D.; Chmiela, B.; Popczyk, M.; Swinarew, A.S.; Stanula, A.; Waśkiewicz, Z.; Knechtle, B. Evaluation of Structure and Corrosion Behavior of FeAl Alloy after Crystallization, Hot Extrusion and Hot Rolling. *Materials* **2020**, *13*, 2041. [CrossRef]

Disclaimer/Publisher's Note: The statements, opinions and data contained in all publications are solely those of the individual author(s) and contributor(s) and not of MDPI and/or the editor(s). MDPI and/or the editor(s) disclaim responsibility for any injury to people or property resulting from any ideas, methods, instructions or products referred to in the content.

materials

MDPI

Article

Role of Quenching Temperature Selection in the Improvement of the Abrasive (Al_2O_3) Wear Resistance of Hybrid Multi-Component Cast Irons

Yuliia Chabak [1,2], Vasily Efremenko [1,2,*], Ivan Petryshynets [2], Michail Golinskyi [1], Kazumichi Shimizu [3], Bohdan Efremenko [1,4], Vadim Kudin [5] and Alexander Azarkhov [4]

1 Physics Department, Pryazovskyi State Technical University, 49044 Dnipro, Ukraine; chabak_y_g@pstu.edu (Y.C.); michalholynskyi99@gmail.com (M.G.); efremenko_b_v@pstu.edu (B.E.)
2 Division of Metallic Systems, Institute of Materials Research, Slovak Academy of Sciences, 04001 Kosice, Slovakia; ipetryshynets@saske.sk
3 Graduate School of Engineering, Muroran Institute of Technology, 27-1 Mizumoto, Muroran City 050-8585, Japan; shimizu@muroran-it.ac.jp
4 Biomedical Engineering Department, Pryazovskyi State Technical University, 49044 Dnipro, Ukraine; azarhov_a_y@pstu.edu
5 Department of Machines and Technologies of Foundry Production, National University Zaporizhzhia Polytechnic, 69063 Zaporizhzhia, Ukraine; vadim.kudin1973@gmail.com
* Correspondence: vgefremenko@gmail.com or efremenko_v_g@pstu.edu

Abstract: In this paper, enhancing the tribological characteristics of novel cast metallic materials—hybrid multi-component cast irons—by applying a strengthening heat treatment is described. The experimental materials were the cast alloys of a nominal composition (5 wt.% W, 5 wt.% Mo, 5 wt.% V, 10 wt.% Cr, 2.5 wt.% Ti, Fe is a balance) supplemented with 0.3–1.1 wt.% C and 1.5–2.5 wt.% B (total of nine alloys). The heat treatment was oil-quenching followed by 200 °C tempering. The quench temperature (QT) varied in the range of 900–1200 °C, with a step of 50 °C (with a 2-h holding at QT). The correlation of the QT with microstructure and properties was estimated using microstructure/worn surface characterization, differential scanning calorimetry, hardness measurement, and three-body-abrasive wear testing (using Al_2O_3 particles). The as-cast alloys had a multi-phase structure consisting of primary and/or eutectic borocarbide $M_2(B,C)_5$, carboborides M(C,B), $M_7(C,B)_3$, $M_3(C,B)$, and the matrix (ferrite, martensite, pearlite/bainite) in different combinations and volume fractions. Generally, the increase in the quenching temperature resulted in a gradual increase in hardness (maximally to 66–67 HRC) and a decrease in the wear rate in most alloys. This was due to the change in the phase-structure state of the alloys under quenching, namely, the secondary carboboride precipitation, and replacing ferrite and pearlite/bainite with martensite. The wear rate was found to be inversely proportional to bulk hardness. The maximum wear resistance was attributed to QT = 1150–1200 °C, when the wear rate of the alloys was lowered by three to six times as compared to the as-cast state. With the QT increase, the difference in the wear rate of the alloys decreased by three times. The highest abrasive resistance was attributed to the alloys with 1.1 wt.% C, which had a 2.36–3.20 times lower wear rate as compared with that of the reference alloy (13 wt.% Cr cast iron, hardness of 66 HRC). The effects of carbon and boron on hardness and wear behavior are analyzed using the regression models developed according to the factorial design procedure. The wear mechanisms are discussed based on worn surface characterization.

Keywords: multi-component cast iron; high boron content; quenching; carboborides; matrix; hardness; abrasive wear resistance

1. Introduction

White cast irons alloyed with carbide-forming elements (Cr, V, Mo, etc.) are used for a wide range of industrial applications where the abrasive, erosion, and corrosion-abrasive

wear mechanisms crucially affect the lifespan of the machine parts and components [1,2]. These materials present a composite-like structure comprising hard carbide precipitates distributed within the tougher metal matrix; such a structure is most beneficial to resisting abrasive particles' cutting or impact actions [3,4]. The chemical composition and structure of high-alloyed cast irons are tailored to meet the specific working conditions. The multi-component cast irons (MCCIs) were primarily developed for the rolls of hot rolling and pulverizing mills [5]. Following the concept of high-speed steel M2 (ASTM A600) [6], MCCIs include several carbide-forming elements (W, Mo, V, Cr, Nb) in nearly equal proportions (from 2–5 wt.% [7] to 5–10 wt.% [8]), which results in a multi-phase solidification with the formation of different eutectic carbides (M_2C, M_6C, MC, M_7C_3) [9,10]. MCCIs differ from M2 steel by a two-fold-increased carbon content (1.8–2.2 wt.%), allowing them to have a higher volume fraction of the carbide phase and to be used as cast materials [11]. According to Matsubara and co-workers [8,12,13] and other researchers [14–17], a combination of several types of carbides and matrixes (martensite, austenite) in alloyed white cast iron ensures its advanced abrasion wear resistance. Furthermore, the authors [18] repeatedly informed about an increased high-temperature erosion resistance of MCCIs enhanced by Co or Ni additions. The study of the multi-component high-Cr and Ni-hard-type cast irons supplemented with different combinations of strong carbide-forming elements (V-Nb-Ti-Cr [19], V-Nb-Ta [20], Zr-B [21]) allowed for deducing the positive effect of combining different types of carbide (MC, M_3C, M_7C_3, Cr5B3) and intermetallic (Fe_2Zr, FeCrZr) phases to increase the mechanical properties and wear resistance of the alloys.

Heat treatment (HT) is usually applied to advance the exploitation properties of high-alloyed cast irons [22,23]. In major cases, the highest wear resistance is achieved after the "Quenching + Tempering" heat treatment. During holding under the quenching temperature, dispersed secondary carbides precipitate from austenite, which destabilizes the austenite-to-martensite transformation under cooling (the so-called "destabilization" process) [24,25], leading to a drastic hardness increase. For the cast irons of different alloying systems (high-Cr, MCCIs, Ni-hard, etc.), the optimal destabilizing temperature is in the range of 900–1100 °C [26–28]. Tempering is carried out either at low temperatures (200–300 °C) to relieve quenching stresses or at 500–600 °C to eliminate retained austenite (RA) through secondary carbides precipitation and martensite transformation (the secondary hardening) [29–31].

In order to meet the working conditions of the hot rolling mills, MCCIs are advised to be quenched from 1050 to 1100 °C and tempered at 500–550 °C [5]. Quenching leads to the precipitation of the secondary carbides MC, M_6C, and M_7C_3 and the formation of a "martensite + RA" matrix where the RA fraction may reach 25 vol.% [32,33]. Under the tempering, the decomposition of RA and martensite takes place via the carbide precipitation. The RA decomposition plays the main role, leading to a sharp decrease in the RA volume fraction and a corresponding hardness increase to 900–940 HV_{30} [5,32,33]. The martensite decomposition may pass through the sequent carbide transformations accompanied by the carbide enrichment with the alloying element. Inthidech and Matsubara [34] illustrated this process for Mo-rich martensite as follows: martensite (Fe,Mo,C) $\rightarrow$ $(Fe,Mo)_3C$ $\rightarrow$ $(Mo,Fe)_3C$ $\rightarrow$ Mo_6C. The structure formation in MCCIs under heat treatment is dependent on HT parameters and the chemical composition of the alloy. As follows from [5], the RA volume fraction in as-quenched MCCIs is increased with the quenching temperature and total carbon concentration. It was deduced [34] that the maximum MCCI hardness after heat treatment depends on the total carbon content and carbon phase distribution. This dependence is described by the C_{bal} parameter, which is calculated as $C_{bal} = C - C_{stoich}$, where C_{bal} is the carbon fraction dissolved in the matrix, C is the total carbon content in the alloy (wt.%), and C_{stoich} is the carbon fraction consumed to form the carbides according to their stoichiometry. It was concluded [34] that the maximum MCCIs' hardness after heat treatment is associated with a C_{bal} value close to zero %.

The secondary hardening behavior of MCCIs is found to be controlled by alloying elements. Thus, chromium (up to 5–7 wt.%) promotes the secondary carbide precipitation.

With its further content increase, austenite stabilizes to phase-structural transformation (including the deformation-induced martensite transformation [15]) and secondary hardening decreases [34]; therefore, the maximum tempered hardness of MCCIs refers to 5–7 wt.% Cr [32]. A similar effect of nickel was noted by Zhang et al. in [18], where nickel was highlighted to stimulate the precipitation of secondary carbides in MCCIs due to the reduced solubility of carbon in austenite. The excessive addition of Ni significantly increases the content of retained austenite in quenched white cast iron [35], although it benefits the corrosion resistance of Fe-based alloys [36].

The MCCIs' family includes newly developed hybrid multi-component cast irons, which are distinguished by the presence of both carbon and boron in the chemical composition [37–39]. Replacing carbon with boron makes it possible to form the complex-alloyed carboboride phases, which are harder than the carbides formed by the same carbide-forming elements [40,41]. In previous efforts of the authors [42], the influence of carbon and boron on the abrasive wear resistance of hybrid MCCIs in the as-cast state was studied based on the factorial design method. It has been found that their wear resistance varies significantly, being controlled by the carboboride particles' features (type, size, distribution, etc.) and the structure of the metallic matrix. At the same time, there is a significant potential to increase the hybrid MCCIs' wear resistance through heat treatment. Since the effect of HT parameters on the structure and properties of hybrid cast irons remained unstudied, this predetermined the performance of the present research.

Recently, the MCCIs' family was expanded by adding hybrid multi-component (W, Mo, V, Cr, Ti) cast irons newly developed by the authors of the present work [37]. These alloys are distinguished by partially replacing carbon with higher amounts of boron (1.5–3.5 wt.%) [37–39]. The substitution of carbon with boron allows for the formation of the complex-alloyed carboboride phases [40–42], which are harder than the carbides formed by the same carbide-forming elements [43,44]. In fact, the use of boron as the main alloying element in wear-resistant high-boron alloys is well known [45,46]. However, the creation of a multiphase state comprising complex-alloyed carboboride phases of various types was realized in hybrid phases for the first time. In previous efforts of the authors [47], the influence of carbon and boron on the abrasive wear resistance of hybrid MCCIs in the as-cast state was studied based on the factorial design method. It was found that their wear resistance varied significantly being controlled by the carboboride particles' features (type, size, distribution, etc.) and the structure of the metallic matrix. At the same time, there is a significant potential to increase the hybrid MCCIs' wear resistance through heat treatment. This conclusion follows from the works [48,49] dedicated to the effect of heat treatment on the wear resistance of high-boron alloys of Fe-C-B, Fe-C-B-Cr, and Fe-C-B-Cr-Mo systems. In these articles, the process of the precipitation of the secondary carboborides Fe_2B, $(Fe,Cr)_2B$, $(Cr,Fe)_{23}(B,C)_6$, and boride M_3B_2 during high-temperature holding followed by martensite transformation is revealed as the crucial factor leading to a drastic increase in the hardness and abrasive wear resistance of high-boron alloys. However, the structure/properties evolution under high-temperature treatment in cast high-boron alloys with a more complicated chemical composition has not been well studied yet. In this case, the character of the influence of the heat treatment mode may change due to complex alloying with elements (W, Mo, Mn, Ti, etc.) affecting the solidification sequence and kinetics of phase transformations [50]. The lack of such data regarding hybrid multi-component alloys predetermined the performance of the present research. It was aimed at advancing the abrasive wear resistance of hybrid multi-component Fe-B-C-W-Mo-V-Cr-Ti alloys by applying the "Quenching and Low-temperature Tempering" heat treatment, with an emphasis on studying the effect of the quenching temperature on the structure evolution and the "Microstructure-Hardness-Wear resistance" correlations.

2. Materials and Methods

The research materials were the cast multi-component Fe-based alloys, with the chemical composition selected according to the matrix of factorial design of experiment 3^2

(with two variables that were varied at three levels) [51,52] (Table 1). Each alloy nominally contained 5 wt.% W, 5 wt.% Mo, 5 wt.% V, 10 wt.% Cr, 2.5 wt.% Ti, 1 wt.% Mn, and 1 wt.% Si (Fe is a balance). The variable parameters were the carbon (X_1) and boron (X_2) contents. Carbon was changed at three nominal levels—specifically, 0.3 wt.% (lower), 0.7 wt.% (middle), and 1.1 wt.% (upper). At each of them, the boron content was varied at three levels: 1.5 wt.% (lower), 2.5 wt.% (middle), and 3.5 wt.% (upper). The levels were coded as (–1), (0), and (1) respectively. Thus, a total of nine alloys were fabricated as described in [37–39], with the actual chemical compositions presented in Table 1. The specimens of 6 × 12 × 25 (mm) in size were prepared by cutting from the cast ingots for further testing and structure characterization.

Table 1. Chemical compositions of the alloys.

Alloy Designation	Coded Levels of the Variables		Content (wt.%)									
	X_1 (C)	X_2 (B)	C	B	Si	Mn	W	Mo	V	Cr	Ti	Al
0.3C–1.5B	–1	–1	0.22	1.68	0.95	1.06	5.57	4.80	5.21	10.39	2.55	0.15
0.3C–2.5B	–1	0	0.25	2.70	1.05	1.21	4.68	5.14	5.01	9.85	2.83	0.05
0.3C–3.5B	–1	1	0.30	3.62	1.14	0.88	5.35	5.19	5.35	10.32	2.78	0.08
0.7C–1.5B	0	–1	0.77	1.62	1.12	1.16	5.84	5.38	4.97	10.45	2.93	0.05
0.7C–2.5B	0	0	0.72	2.75	1.10	0.90	5.05	5.57	5.78	10.35	2.60	0.04
0.7C–3.5B	0	1	0.70	3.61	1.18	1.07	4.67	4.63	5.40	10.21	2.71	0.08
1.1C–1.5B	1	–1	1.20	1.59	1.07	1.10	5.42	4.48	5.37	10.41	2.38	0.10
1.1C–2.5B	1	0	1.11	2.73	1.10	1.07	4.85	4.69	5.26	10.36	2.43	0.14
1.1C–3.5B	1	1	1.13	3.57	1.06	1.03	4.50	4.08	4.79	9.94	2.39	0.11

To improve the properties of alloyed cast irons, heat treatment is most often used according to the "destabilization" scheme, which includes a holding at the quenching temperature necessary for the secondary carbide precipitation [24]. The depleted austenite is easily transformed into martensite, resulting in hardness and wear resistance increases [53]. The same approach was adopted in this work. Since there are currently no data on the optimal quenching temperature (QT) for hybrid multi-component alloys, preliminary studies were carried out using differential scanning calorimetry (DSC). The phase transformation under heating was evaluated using the DTA-DSC-TG thermal analyzer "Jupiter STA449-F1" (Netzsch, Waldkraiburg, Germany). The scanning was performed in the temperature range of 20–1200 °C with a heating rate of 10 K·min^{-1}; an empty crucible (Al_2O_3) was used as a reference. The "Netzsch Proteus Thermal Analysis 5.2.0" software was used to derive the transition temperatures from the DSC curves.

The heating curves of the alloys are shown in Figure 1, and the results of their processing are presented in Table 2. Several endothermic effects are observed on each curve. All alloys performed a "low-temperature" effect (#1) in a temperature range of ~600–800 °C. The "middle-temperature" effect (#2) was revealed on the curves of the alloys containing 0.7–1.1 wt.% C and 2.5–3.5 wt.% B (Figure 1b,c) at a temperature range of ~880–1050 °C. The "high-temperature" effects (#3) were found for most alloys (except 1.1C–1.5B and 1.1C–3.5B) at ~980–1170 °C, close to the melting point (Figure 1a). At higher temperatures, DCS curves sharply decline, reflecting the onset of melting [54,55]. The "low-temperature" effect coincides with the temperature range of αFe → γFe transformation in Fe-C alloys (Ac_1 temperature, 723 °C [56]). Therefore, the quenching temperature (QT) range was selected to be higher than the "low-temperature" effects, pursuing the formation of austenite as a prerequisite for austenite → martensite transformation during quenching cooling. The QTs range was set as 950–1200 °C with a step of 50 °C (the temperatures of 1150 °C and 1200 °C were selected close to the melting point to modify the shape of the carboboride particles by diffusion simulation). The holding at a quenching temperature (2 h) was sufficient for the secondary particle precipitation completion [26]. The heating was performed in a

muffle furnace in a protective nitrogen atmosphere. The heated specimens were oil-cooled and tempered at 200 °C for 2 h. Before the hardness and wear testing, the heat-treated specimens were ground to the roughness of Ra ~0.6 μm, removing the oxidized layer of 0.5 mm thickness.

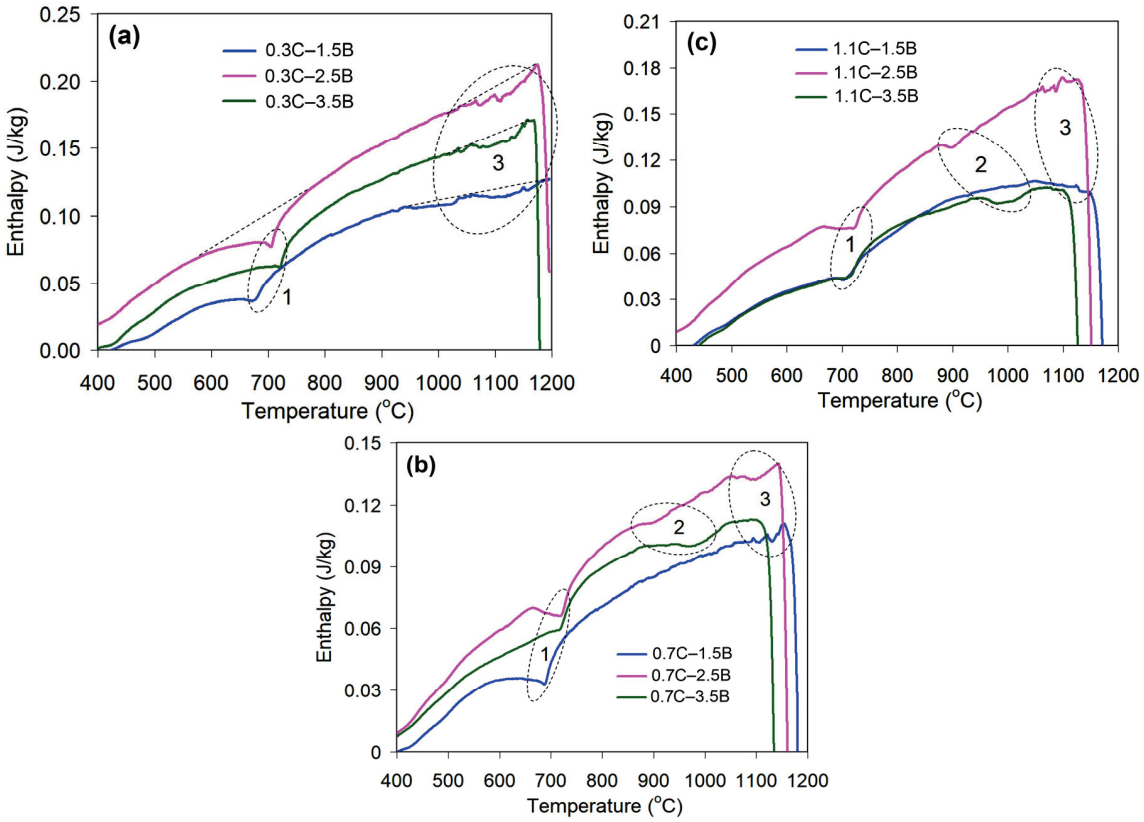


Figure 1. DSC curves of the alloys with different carbon contents: (**a**) 0.3 wt.%, (**b**) 0.7 wt.%, (**c**) 1.1 wt.%. (1—the "low-temperature" effects, 2—the "middle-temperature" effects, 3—the "high-temperature" effects).

Table 2. The temperature ranges of the endothermic effects revealed on the DSC curves (Figure 1).

Alloy	The Temperature Range (°C) of the Endothermic Effects			
	Effect #1	Effect #2	Effect #3	Melting
0.3C–1.5B	593–757	–	979–1200	>1200
0.3C–2.5B	598–776	–	1020–1178	>1178
0.3C–3.5B	581–780	–	1023–1170	>1170
0.7C–1.5B	578–747	–	1065–1152	>1152
0.7C–2.5B	662–790	880–974	1062–1146	>1146
0.7C–3.5B	622–761	894–1048	–	>1120
1.1C–1.5B	635–741	–	1060–1160	>1160
1.1C–2.5B	677–771	883–960	1067–1135	>1135
1.1C–3.5B	635–767	956–1052	–	>1113

The microstructure was studied using the specimens prepared by the routine procedure of a surface mirror-polishing and etching with 5 vol.% Nital solution. The microstructure was observed by employing the optical microscopes (OM) "Eclipse M200" (Nikon, Tokyo, Japan) and "GX71" (Olympus, Tokyo, Japan) and the scanning electron microscope

(SEM) "JSM-7000F" (JEOL, Tokyo, Japan). The phase constituents were identified by X-ray diffraction using a diffractometer "X'Pert PRO" (PANalytical, Worcestershire, UK) with Cu-Kα radiation under the following parameters: the voltage is 40 kV, the tube current is 50 mA, the scan step is 0.033 degrees, and the scan speed is 0.069 degree·s^{-1}. The "FR-X1" tester (Future-Tech, Kanagawa, Japan) was used to measure the bulk hardness of the alloys according to the Rockwell method (scale C). Fifteen measurements were made on each alloy/QT with further results averaging.

The "Three-Body Abrasion" scheme was used for the wear performance assessment. Under the test, the specimen was pressed (with a force of 20 N) to a 40 mm diameter rubber roller rotating at 650 rpm. The abrasive material (Al_2O_3 particles of ~0.5 mm diameter) was fed between the roller and the specimen's surface with a feed rate of 0.75 kg·min^{-1}. The test duration was 1800 s. The weight loss of the specimen was measured using an electronic balance of 0.0001 g accuracy. Each test was repeated three times to average the results. The wear resistance was estimated by the wear rate (*WR*), calculated as:

$$WR = \frac{\Delta m}{b \cdot t} \quad (1)$$

where b stands for the specimen width (mm) and t stands for the test duration (s).

The data on the bulk hardness and wear rate of as-cast hybrid MCCIs were adopted from our previous work [39] to reveal the effect of heat treatment on the alloys' properties. The studied alloys were compared with a high-Cr cast iron which was used as a reference alloy (with a chemical composition of 3.2 wt.% C, 1.2 wt.% Si, 1.5 wt.% Mn, 13.2 wt.% Cr). After destabilizing heat treatment (QT of 950 °C, tempering at 200 °C), the reference had a bulk hardness of 66 HRC.

3. Results and Discussion

3.1. As-Cast Structure of Studied Alloys

In this subsection, the initial (as-cast) microstructure of the experimental MCCIs is briefly described based on our articles [37–39] which present the comprehensive structural characterization of these alloys. The structure images of the hybrid MCCIs are depicted in Figure 2. In each group of alloys with a constant carbon content, the following tendency was noted: the alloy with 1.5 wt.% B had a nearly eutectic structure, while the alloys with 2.5–3.5 wt.% B belonged to a hypereutectic domain. In low-boron alloys (1.5 wt.% B), an eutectic of a "Chinese-script" (CS) morphology was the major structural constituent, consisting of long thin fibers branched within the matrix (Figure 2a). These fibers are a (W,Mo,V)-rich borocarbide $M_2(B,C)_5$ which has a light contrast on the back-scattered electron (BSE) images due to enrichment by elements with high atomic numbers (W, Mo). When the carbon content increases to 0.7–1.1 wt.%, another eutectic appears in a minor amount—specifically, (a) a "Rosette"-like (R) eutectic based on the Cr-rich carboboride $M_7(C,B)_3$ (in alloy 0.7C–1.5B, Figure 2d) or (b) the "Ledeburite"-type eutectic based on the Fe-rich boron-cementite $M_3(C,B)$ (in alloy 1.1C–1.5B, Figure 2g).

In hypereutectic alloys (2.5–3.5 wt.% B), the primary boride $M_2(B,C)_5$ was present in the form of prismatic-shaped coarse particles with the dimensions of tens of micrometers. These particles were surrounded by the colonies of the eutectics of different types. In the alloys containing 2.5 wt.% B, the major eutectic constituent was a CS, while the minor constituent was an R-eutectic (alloy 0.7–2.5B, Figure 2e) or two eutectics: an R-eutectic and an $M_3(C,B)$-based "Coarse-net" eutectic in the form of a thick continuous network engulfing the matrix grains (alloy 1.1C–2.5B, Figure 2h). In the alloys containing 3.5 wt.% B, a "Chinese-script" eutectic was absent. Instead, an R-eutectic (at 0.3–0.7 wt.% C, Figure 2c,f) or a "Coarse-net" eutectic (at 1.1 wt.% C, Figure 2i) were present.

Apart from the above-noted structural constituents, the small-sized angular equiaxed particles of Ti-based carboboride M(C,B) (shown in Figure 2b,c) were dispersed in all alloys. They are seen in BSE images as dark precipitates due to the presence of 55–73 wt.% of Ti having a lower atomic number (relative to Fe and other alloying elements).

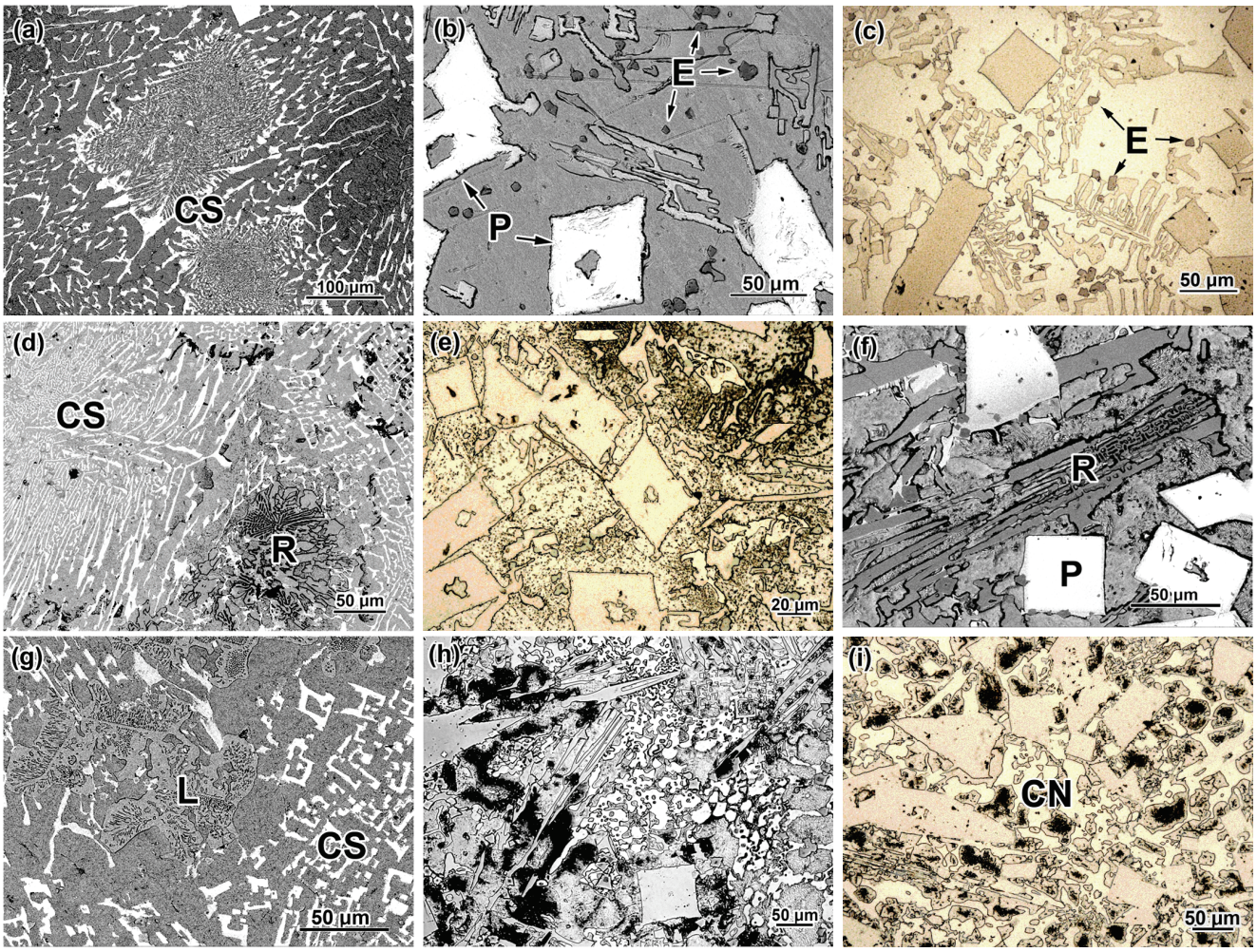


Figure 2. Microstructure of as-cast hybrid MCCIs: (**a**) 0.3C–1.5B, (**b**) 0.3C–2.5B, (**c**) 0.3C–3.5B, (**d**) 0.7C–1.5B, (**e**) 0.7C–2.5B, (**f**) 0.7C–3.5B, (**g**) 1.1C–1.5B, (**h**) 1.1C–2.5B, (**i**) 1.1C–3.5B (CS is a "Chinese-script" eutectic; P is a primary carboboride $M_2(B,C)_5$; R is a "Rosette" eutectic; CN is a "Coarse-net" eutectic; L is a Ledeburite eutectic; E is an equiaxed particle M(C,B)). ((**a**,**b**,**d**,**f**,**g**)—SEM/BSE images; (**c**,**e**,**h**,**i**)—OM images).

The metallic matrix of the alloys containing 0.3 wt.% C (at any boron content) and the alloys containing 1.5 wt.% B (at 0.7–1.1 wt.% C) was ferrite. With further carbon and boron content increases, the matrix transformed to martensite (at 2.5 wt.% B) or to a "martensite + lamellar conglomerate (with morphological attributes of pearlite or upper bainite)" (at 3.5 wt.% B). In the matrix of the alloy 1.1C–3.5B, a minor amount of ferrite was also present. Moreover, retained austenite was present in a minor amount (6–15 vol.%) in the structure of all alloys [39].

3.2. Effect of Quenching Temperature on Bulk Hardness

The evolution of the bulk hardness of the alloys is illustrated in Figure 3. In the as-cast state, the hardness varied in the range of 28–53 HRC; it increased with the boron and carbon contents. Specifically, for the alloys containing 0.3 wt.% C, the hardness varied in the range of 28–37 HRC. In alloys with 0.7 wt.%, the hardness was higher—32–48 HRC [39]. The maximum hardness diapason (38–53 HRC) was attributed to the alloys having 1.1 wt.% C. This tendency was due to an increase in the volume fraction of hard phase precipitates (borocarbides, carboborides) caused by the addition of carbon and boron [39]. Also, the hardness was affected by the type of matrix: the lowest hardness values were associated with the ferritic matrix, while the higher hardness referred to the martensite of "martensite + pearlite (bainite)" matrixes.

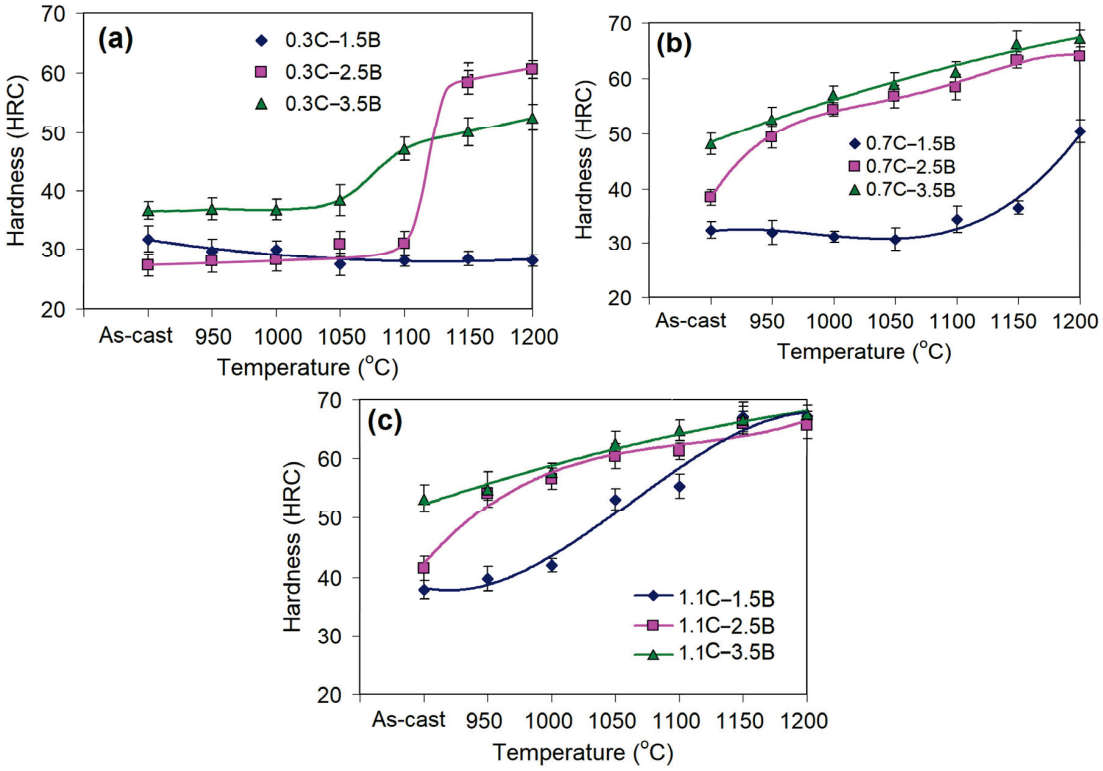


Figure 3. Effect of quenching temperature on the bulk hardness of MCCIs containing (**a**) 1.5 wt.% B, (**b**) 2.5 wt.% B, and (**c**) 3.5 wt.%.

Heat treatment resulted in a significant increase in the bulk hardness of most alloys, while the hardness profile depended on the alloys' chemical composition. In all alloys containing 0.3 wt.% C and/or 1.5 wt.% B (at any other C/B contents), the hardness was increased only at QT $\geq$ 1100 °C. In contrast, in alloys with 0.7–1.1 wt.% C and 2.5–3.5 wt.% B, the hardness grew gradually within the entire QT interval. More specifically, the alloys with 0.3 wt.% C and alloy 0.7C–1.5B hardly changed their hardness when the QT was within 950–1050 °C (Figure 3a,b). After quenching from higher temperatures, the hardness was doubled (to 60 HRC) in the alloy 0.3C–2.5B and increased by 1.5 times (to 50 HRC) in the alloy 0.7C–1.5B. The alloy 0.3C–1.5B was not affected by quenching; its hardness varied in the range of 28–32 HRC at any QT.

In other alloys, the hardness gradually increased with a QT increase. The most significant hardness improvement was observed in the alloys 0.7C–2.5B and 1.1C–2.5B: their hardness rose from 38–39 HRC to 63 HRC and 68 HRC, respectively (Figure 3b,c). The alloys with a maximum B content (0.7C–3.5B and 1.1C–3.5B) gained the same high hardness of >65 HRC. The alloys that had the martensite or "martensite + pearlite (bainite)" matrixes in an as-cast state were more sensitive to quenching, while the alloys with a ferrite matrix reacted to quenching only at high QTs.

3.3. Effect of the Quenching Temperature on the Wear Rate

Figure 4 presents the MCCIs' wear rate values in the as-cast state (Figure 4a) and depending on the QT (Figure 4b–d). In the as-cast state, the MCCIs' wear rate decreased with an increase in the carbon and boron contents [41] as follows: the alloys with 0.3 wt.% C (*WR* of (3.0–5.69) $\times$ 10^{-6} g·mm^{-1}·s^{-1}) $\rightarrow$ 0.7 wt.% C (*WR* of (2.72–4.17) $\times$ 10^{-6} g·mm^{-1}·s^{-1}) $\rightarrow$ 1.1 wt.% C (*WR* of (2.31–3.46) $\times$ 10^{-6} g·mm^{-1}·s^{-1}) (Figure 4a). Under quenching, in each group, the *WR* values were decreased with a quenching temperature increase (the only exception was the alloy 0.3C–1.5B, which was not affected by quenching at any QT, as seen in Figure 4b). The alloys with 0.7–1.1 wt.% B demonstrated close *WR* values at different QTs (Figure 4c,d). Most alloys reached the minimum *WR* value after quenching from 1150 °C; at

QT = 1200 °C, their *WR* values slightly increased. In the alloys 0.7C–1.5B, 0.7C–3.5B, and 1.1C–3.5B, the lowest *WR* values are ascribed to QT = 1200 °C. After quenching from 1150–1200 °C, the alloys with 0.7 wt.% C performed a wear rate less than 2.0×10^{-6} g·mm^{-1}·s^{-1}, while the alloys with 1.1 wt.% showed an even lower *WR* of $\leq 1.0 \times 10^{-6}$ g·mm^{-1}·s^{-1}.

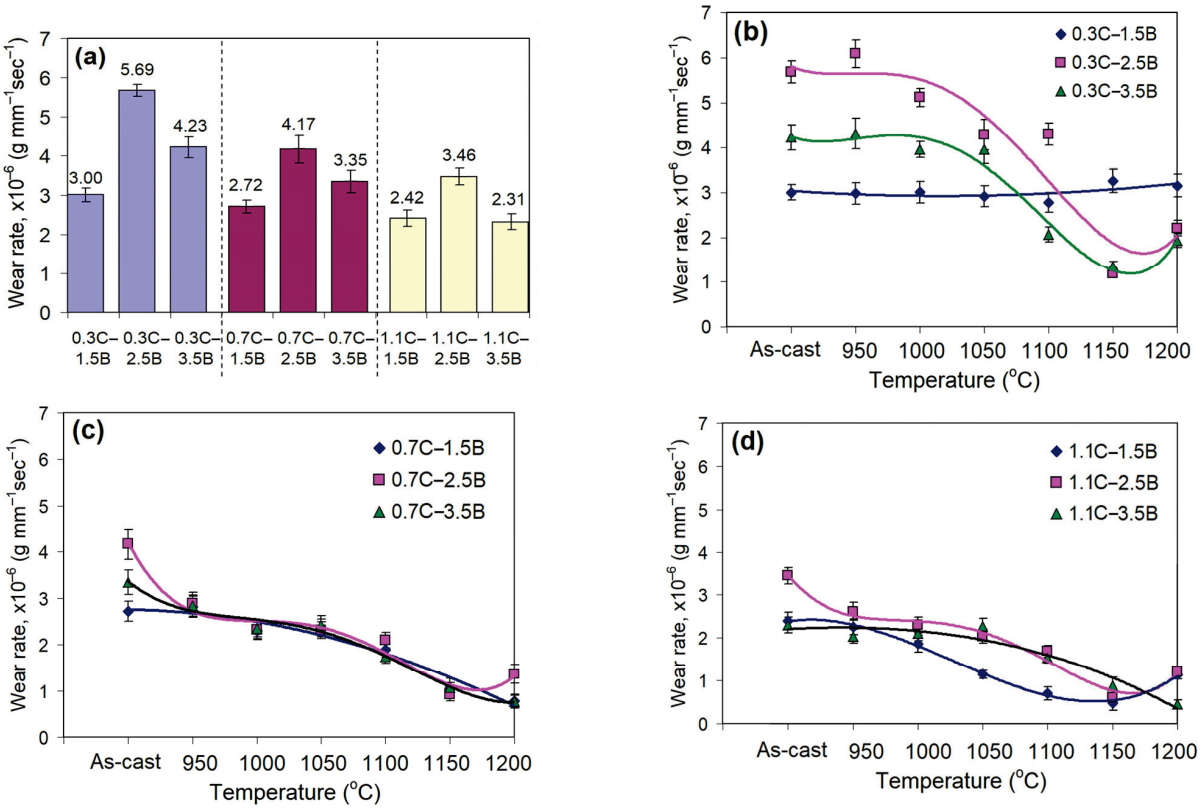


Figure 4. (**a**) *WR* values of the as-cast alloys. Effect of quenching temperature on the wear rate of the alloys containing (**b**) 0.3 wt.% C, (**c**) 0.7 wt.% C, and (**d**) 1.1 wt.% C.

Assessing the overall picture, one can conclude that in the heat-treated state, the highest *WR* value was attributed to the alloys 0.3C–1.5B (6.09×10^{-6} g·mm^{-1}·s^{-1}, QT = 950 °C). Accordingly, the lowest *WR* values referred to the alloy 1.1C–1.5B (0.88×10^{-6} g·mm^{-1}·s^{-1}, QT = 1150 °C) and the alloy 1.1C–3.5B (0.81×10^{-6} g·mm^{-1}·s^{-1}, QT = 1200 °C). With a QT increase, the difference in the wear rate between the alloys decreased significantly (as compared with that in the as-cast state).

The decrease in the *WR* value relative to that in the as-cast state reflects the improvement in the wear resistance of the alloy caused by the heat treatment. To assess this improvement, the wear rate decrease index (*WRD*) was calculated for each alloy as follows:

$$WRD = \frac{WR_{As-c}}{WR_q}, \quad (2)$$

where WR_{As-c} and WR_q are the wear rates for the as-cast and quenched states, respectively.

As follows from Figure 5, in general, the *WRD* increases with a QT increase, while its more noticeable growth refers to the quenching from higher temperatures (QT $\geq$ 1100 °C). Depending on the carbon content, the *WRD* reaches, maximally, 3.12–4.84 (at 0.3 wt.% C) (Figure 5a), 3.50–4.49 (at 0.7 wt.% C) (Figure 5b), and 4.49–5.63 (at 1.1 wt.% C) (Figure 5c), i.e., carbon enhances the effect of quenching on the wear resistance of hybrid MCCIs. Such a significant improvement in wear behavior relative to the as-cast state shows the potential of heat treatment to control the exploitation durability of these alloys. The *WRD* curves' maximum was attributed to either QT = 1150 °C or QT = 1200 °C. The decrease in the

WRD at 1200 °C was caused by the partial melting that occurred in the alloys 0.3C–2.5B, 0.3C–3.5B, 0.7C–2.5B, 1.1C–1.5B, and 1.1C–2.5B. In these alloys, the *WRD* decreased even despite the fact that the hardness reached a maximum value.

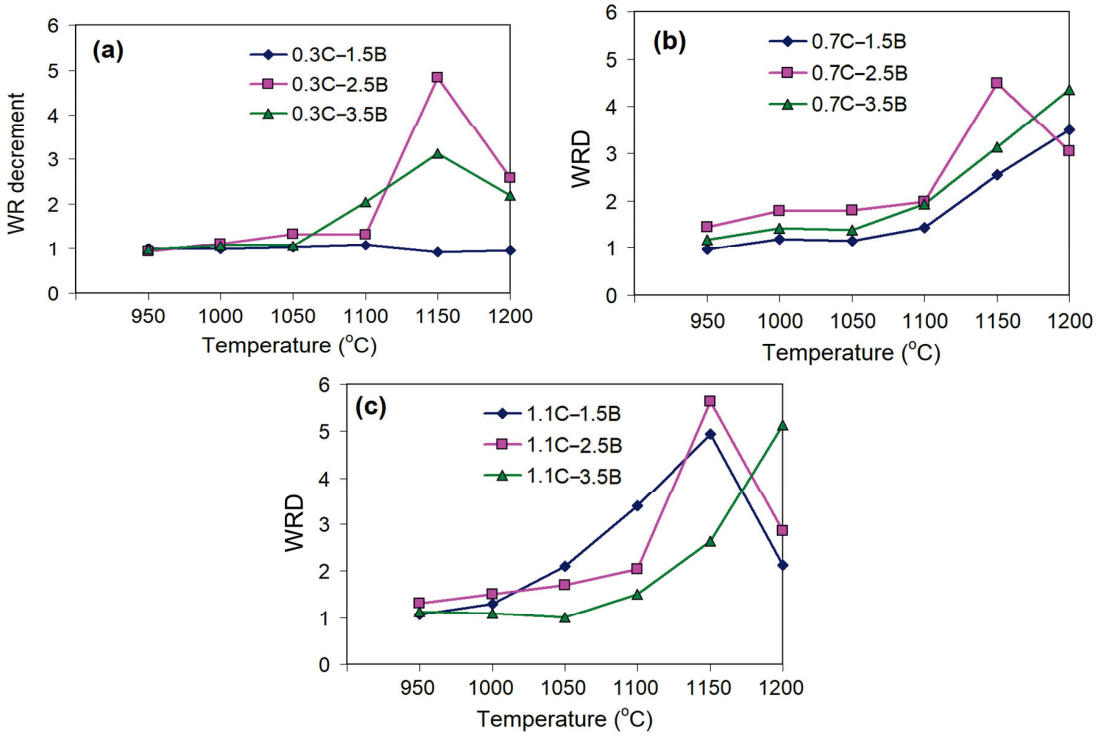


Figure 5. Effect of quenching temperature on the *WRD* in the alloys containing (**a**) 0.3 wt.% C, (**b**) 0.7 wt.% C, and (**c**) 1.1 wt.% C.

3.4. Effect of Quenching Temperature on Structure Evolution

As follows from Figures 3 and 4, the bulk hardness and *WR* values were strongly dependent on the quenching temperature being a result of a corresponding structure evolution. Microstructure characterization reveals that in all alloys, the carboboride primary particles (both primary and eutectic) were hardly affected by heat treatment regarding their shape and volume fraction (even after heating at 1150 °C, the precipitates mostly remained in the initial state due to their high heat stability). The main structural changes occurred precisely in the metal matrix of the alloys, namely, (a) the precipitation of secondary carboboride phases in the form of dispersed, evenly distributed grainy precipitates and (b) the formation of an acicular martensite structure. In each alloy, these changes occurred starting from a specific QT. In the alloys with an initial ferritic matrix (0.3 wt.% C-containing alloys, 0.7C–1.5B and 1.1C–1.5B alloys), martensite appeared at a rather high QT which varied from 1050 °C (0.3C–3.5B and 1.1–1.5B alloys) to 1150–1200 °C (alloys 0.3C–2.5B and 0.7C–1.5B). In alloys that initially had a "martensite + pearlite (bainite)" matrix, the fully martensitic matrix was formed starting from QT = 950 °C. The alloy 0.3C–1.5B retained the ferritic matrix regardless of the quenching temperature.

Figure 6 shows the microstructure of the metal matrix of the studied alloys after quenching from 1150 °C. In the alloys, except for 0.3C–1.5B, the matrix was a fine-needle martensite, in which the secondary carboboride precipitates were distributed. Within each group of alloys with the same carbon content, the number of secondary carboboride particles increased with the boron content. The lowest number of inclusions was observed in alloys containing 1.5 wt.% B (Figure 6a,d,g). According to Figure 7, the mean size of the secondary precipitates and the size scatter were increased with the C and B contents. The most dispersed inclusions were recorded in the alloy 0.3C–1.5B; their size varied within 0.01–0.15 μm. The higher scatter ranges were attributed to the alloys 0.7C–3.5B and 1.1C–3.5B, being 0.30–1.74 μm and 0.30–1.58 μm, respectively.

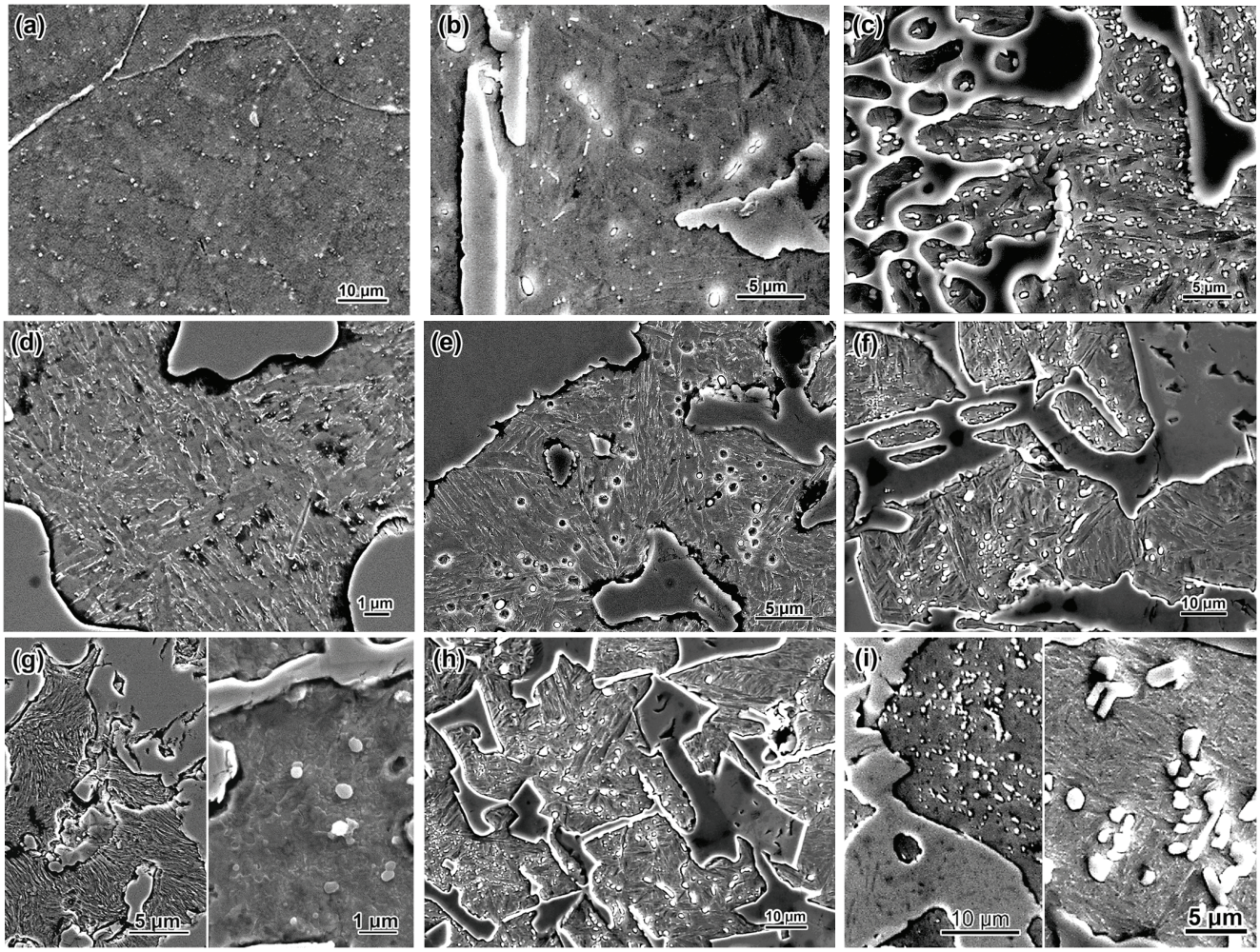


Figure 6. Microstructure of the alloys after the heat treatment with QT = 1150 °C: (**a**) 0.3C–1.5B, (**b**) 0.3C–2.5B, (**c**) 0.3C–3.5B, (**d**) 0.7C–1.5B, (**e**) 0.7C–2.5B, (**f**) 0.7C–3.5B, (**g**) 1.1C–1.5B, (**h**) 1.1C–2.5B, (**i**) 1.1C–3.5B.

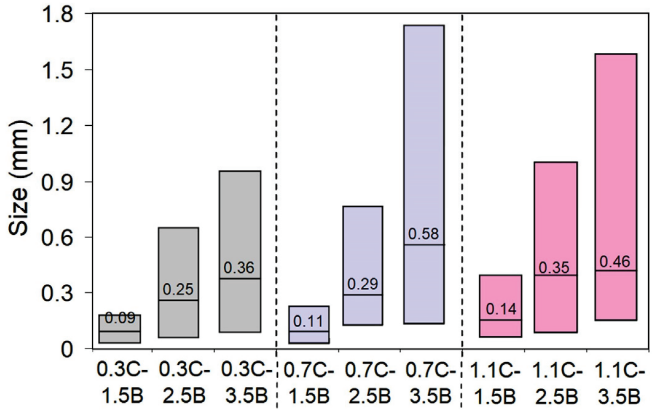


Figure 7. The size of secondary precipitates in the MCCIs after quenching. The line stands for a mean value; the rectangle shows the scatter of the values.

The effect of the heat treatment on the variation of the phase composition of the alloys is illustrated in Figure 8, where the XRD patterns of the alloy 1.1C–3.5B are shown. As seen, the diffraction patterns for the as-cast and quenched specimens are similar, presenting various peaks of αFe, indicating its majority in the alloy matrix. There are also rather strong peaks of boride M_2B_5 (at 2θ = 35.6°) and carbide M_3C (at 2θ = 46.2°) relating to the coarse

primary inclusions M_2B_5 and the "Coarse-net" eutectic (Figure 8a). At 2θ of (43.5–43.8°), all curves contain a peak that can be attributed to both austenite ($(111)_\gamma$) and M_2B_5 due to the similarity in the interplanar spacing. In addition, all diffraction patterns present multiple weak peaks which can be attributed to carbides (Cr_7C_3, M_3C, TiC), borides (W_2B, Ti_2B), and austenite.

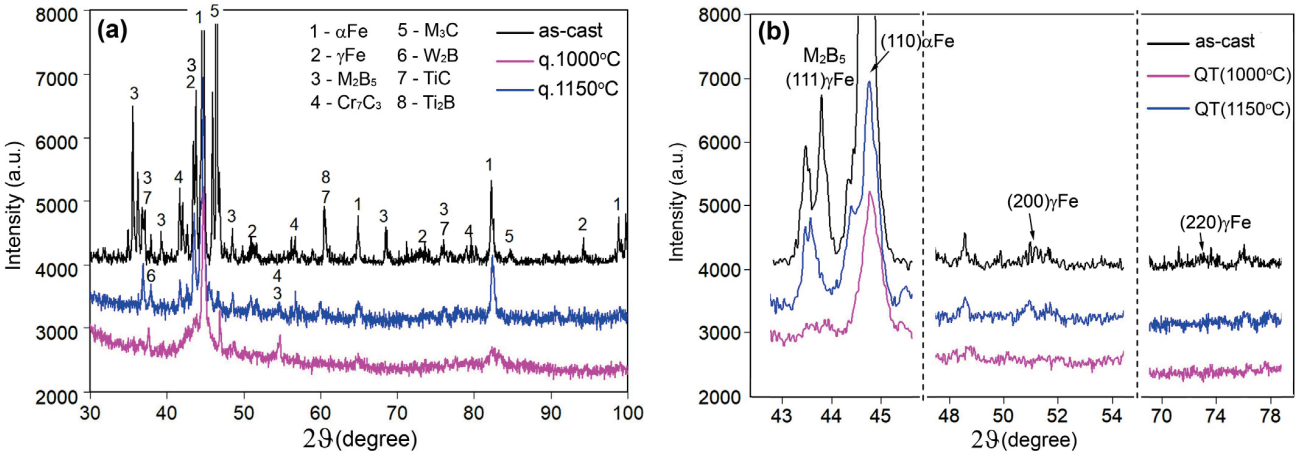


Figure 8. XRD patterns of the alloy 1.1C–3.5B: (**a**) a total 2θ range, (**b**) variation in the intensity of austenite peaks $(111)_\gamma$, $(200)_\gamma$, and $(220)_\gamma$ depending on the alloy's state (as-cast, after quenching).

Figure 8b shows the enlarged sections of the diffraction patterns related to the austenite lines $(111)_\gamma$, $(200)_\gamma$, and $(220)_\gamma$. It allows for following up the variation in the RA volume fraction depending on the quenching temperature. It is seen that from the as-cast state to 1150 °C-quenching, the intensity of all three peaks decreases. Specifically, the weak peaks $(200)_\gamma$ and $(220)_\gamma$ disappeared completely on the patterns, and the peak at 2θ = (43.5–43.8)° significantly reduces its intensity relative to the peak (110)α (moreover, this remaining weak peak may refer to boride M_2B_5, which coincides with austenite at that 2θ). This indicates that after quenching from 1150 °C, the RA volume fraction decreased below the sensitivity level of the X-ray diffraction. It should be noted that on the XRD patterns of 1150 °C, no increase in the intensity of the carbide or boride lines was noticed, which could be caused by the secondary particles' precipitation. At the same time, the peaks of an 1150 °C-quenched specimen were broadened, indicating increased residual stresses and lattice distortion.

3.5. Worn Surface Characterization

The worn surface of samples of various alloys were studied; the results are presented in Figure 9. In all cases, the surface of the samples was covered with grooves of different widths and depths. At high hardness, the grooves did not have clear boundaries which were smoothed and rounded (Figure 9a). As the hardness of the alloy decreased, the depth of the scratches increased, and ridges of extruded metal were observed along their edges (Figure 9b,c). In alloys with a eutectic structure (i.e., containing 1.5 wt.% B), the destruction of the surface proceeded through the fatigue-related process, resulting in the formation and detachment of wear debris in the form of metallic micro-scales (right insert in Figure 9b). The micro-scale was a volume of metal extruded from the groove and underwent repeated plastic deformation, which made it hard and brittle, to be easily broken off from the basis. In the alloy 0.3C–1.5B, which had low hardness at any quenching temperature, a larger volume of metal was involved in repeated deformation, which caused the appearance of larger flattened areas (the "lips" in Figure 9c), which were peeled off, increasing the wear rate. The bottom of the scratches also experienced strain hardening, which led to metal embrittlement and the appearance of micro-cracks oriented perpendicular to the abrasive sliding direction (insert in Figure 9c). In addition, micro-pits were occasionally observed on the surface of eutectic alloys, apparently caused by the destruction and by the eutectic carboboride breaking off (left insert in Figure 9b).

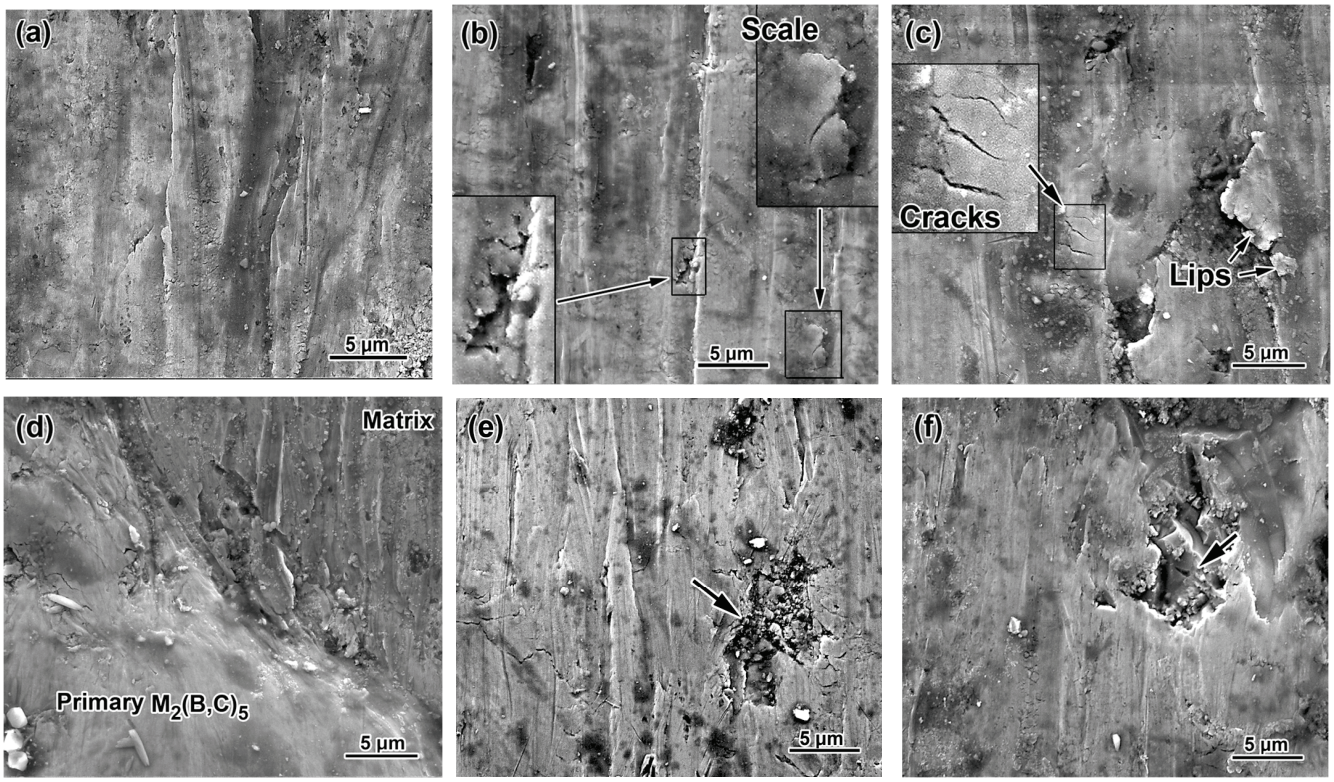


Figure 9. The patterns of the worn surfaces of the quenched alloys: (**a**) 1.1C–1.5B (QT = 1150 °C), (**b**) 0.7C–1.5B (QT = 1150 °C), (**c**) 0.3C–1.5B (QT = 1050 °C), (**d**) 0.3C–3.5B (QT = 1150 °C), (**e**) 0.7C–2.5B (QT = 1150 °C), (**f**) 1.1C–3.5B (QT = 1150 °C).

The worn surface of hypereutectic alloys (2.5–3.5 wt.% B) exhibited features similar to those of eutectic alloys (i.e., grooves, micro-scales, micro-cracks). However, they are distinguished by the presence of large pittings resulting from the spalling-off of coarse primary borocarbide $M_2(B,C)_5$ (locations are shown by arrows in Figure 9e,f). The pitting formation was preceded by the preferential wear of the matrix around the primary borocarbide (Figure 9d), resulting in the protrusion of borocarbide out of the matrix. Bending loads caused by sliding abrasive particles resulted in the cracking and spalling-off of the borocarbide from the surface.

The wear mechanism is additionally illustrated by the cross-sectional images of the near-surface layer shown in Figure 10. In the eutectic alloys, the fibers of $M_2(B,C)_5$ (belonging to the "Chinese-script" eutectic) are bent following the matrix, which causes the micro-crack formation (Figure 10a–c). However, their bulk chipping was hardly observed; instead, an occasionally noticed breakage (shown by the arrow in Figure 10d) referred to the fracture of the more coarse eutectic carboborides $M_7(C,B)_3$ or $M_3(C,B)$, present along with the CS eutectic. The surface relief of the eutectic alloys varies depending on the bulk hardness from 5–6 μm to about 1 μm.

Regardless of the hardness, the hypereutectic alloys differed by the presence of deep (up to 15–20 μm) pits resulting from the spalling of the primary borocarbide (shown in Figure 10e–h by an arrow). In this case, not only inclusions on the surface but also those lying at some distance from it (shown by a circle in Figure 10f) were fractured. Hence, the roughness of the worn surface was increased relative to eutectic alloys. The destruction and spalling of the inclusions were accompanied by the cracks' propagation from the surface inward of the specimen. Eutectic carboborides located next to the primary inclusion deteriorated without the pitting formation (Figure 10g).

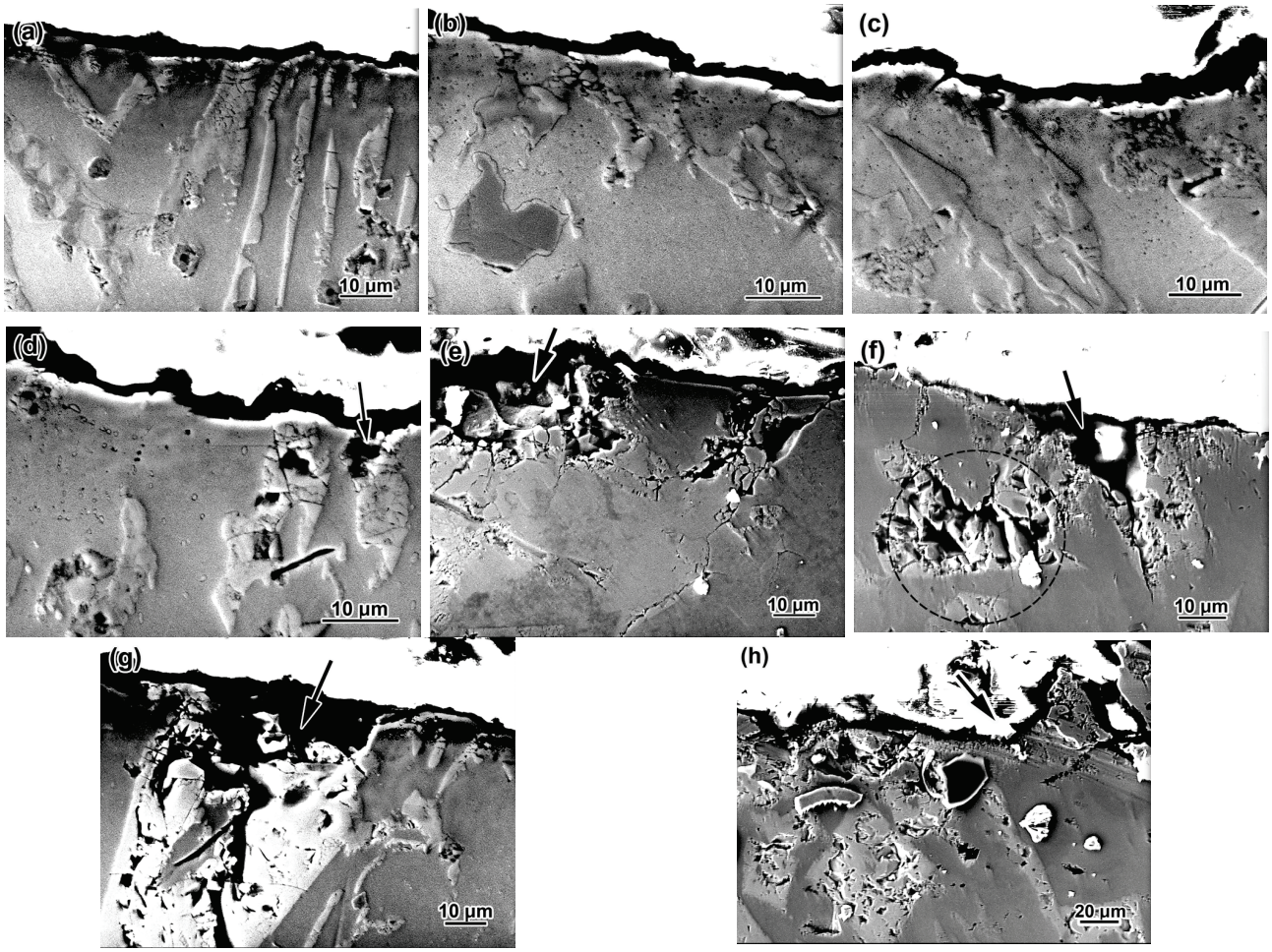


Figure 10. Cross-section of the worn surface of the alloys (QT in parentheses): (**a**) 0.3C–1.5B (1050 °C), (**b**) 0.7C–1.5B (1150 °C), (**c**) 1.1C–1.5B (1050 °C), (**d**) 1.1C–1.5B (11,050 °C), (**e**) 0.3C–3.5B (1150 °C), (**f**) 0.7C–2.5B (1050 °C), (**g**) 0.7C–2.5B (1150 °C), (**h**) 1.1C–3.5B (1150 °C).

4. Analysis of Results

4.1. "Quenching Temperature—Microstructure—Properties" Correlations

As shown above, quenching significantly enhances the hardness and wear resistance of MCCIs by changing a metallic matrix structure from ferrite or pearlite (bainite) to acicular martensite. Such structure evolution requires consecutive phase transformations, namely, αFe $\rightarrow$ γFe and γFe $\rightarrow$ αFe. On the DSC curves of all experimental alloys, an endothermic ("low-temperature") effect was recorded at ~600–800 °C, which could be considered the αFe $\rightarrow$ γFe transition (an A_{C1} point) [56]. However, in some alloys (having 0.3 wt.% C, as well as alloy 0.7C–1.5B), an increase in hardness (connected with martensite formation) was found at a much higher QT (above 1000 °C). Moreover, the alloy 0.3C–1.5B remains in the ferritic state at any quenching temperature, meaning the absence of phase transitions. These results allowed for deducing that the "low-temperature" DCS effect did not refer to the A_{C1} temperature. More likely, it was associated with the Curie temperature transition, which is also accompanied by an endothermic effect [57,58]. Under a low carbon content (0.3 wt.%), the effect of ferrite-stabilizing elements (Cr, W, Mo, V) predominated under solidification, resulting in a fully ferritic matrix in the alloys 0.3C–1.5B, 0.3C–2.5B, and 0.3C–3.5B. This observation complies with a thermodynamic simulation [37], according to which the γ-phase domain was absent in the phase diagrams of the 0.3 wt.% C-MMCIs. Similarly, the alloys 0.7C–1.5B and 1.1C–1.5B also had a fully ferritic matrix owing to the enrichment of their matrix with Cr, W, Mo, and V [39].

The alloys with 0.7–1.1 wt.% C and 2.5–3.5 wt.% B, the coarse primary inclusions of $M_2(B,C)_5$, solidified, absorbing a significant portion of the alloying elements, thus leading to (Cr, W, Mo, V)-depletion of the matrix [37–39]. In combination with an increased concentration of carbon (gamma-stabilizer), this expanded the austenite domain, allowing for structure variation through austenite transformations. On the DSC curves of hypereutectic alloys, a fairly pronounced endothermic "middle temperature" effect (#2) was observed at ~900–970 °C (at 2.5 wt.% B) and ~900–1050 °C (at 3.5 wt.% B). These temperature ranges approximately coincide with the QT at which the hardness started to increase in these alloys. Therefore, it was assumed that DSC effect #2 is associated with the αFe → γFe transition leading to the austenite appearance in structure (with its further transformation into martensite upon quenching cooling). The temperature of αFe → γFe transformation in (0.7–1.1 wt.% C)-alloys significantly exceeds that in a grey cast iron (727 °C [59]) owing to an increased number of ferrite-stabilizing elements solved in the matrix (5–10 wt.% Cr, 0.7–1.0 wt.% Mo, 0.8–1.3 wt.% V [37]). Unlike this, in hypereutectic alloys with 0.3 wt.% C (0.3C–2.5B and 0.3C–3.5B), the αFe → γFe transition was shifted to even higher temperatures (~1020–1180 °C, DSC effect #3) because of the lower content of the austenite-forming element (which is carbon). Accordingly, an increase in their hardness was also noted at a higher QT (≥1050 °C).

The hardness and wear resistance of MCCIs were found to increase with the quenching temperature. The reasons are (a) reaching the γFe-domain under heating (which is situated rather high in MCCIs as compared to in plain cast iron) and (b) stimulating the secondary carboboride precipitation. With an increasing QT, more ferrite is substituted by austenite (resulting in an increase in the martensite fraction after cooling). Furthermore, the carbide precipitation proceeds more fully via diffusion stimulation; this promotes the austenite depletion in carbon and alloying elements to a greater extent, thus reducing the amount of retained austenite in the structure (accordingly, the proportion of martensite is also increased).

In the as-cast state, the alloys 0.7C–2.5B and 1.1C–2.5B had a completely martensitic matrix. Therefore, the significant increase in their hardness after quenching cannot be attributed only to a variation in the matrix status. Obviously, in this case, quenching caused a change in the martensite structure relative to the as-cast state, which promoted its hardness. A possible reason is the replacement of lath martensite with twinned martensite, caused by an increase in the carbon content and tetragonality [60]. Also, the hardness increase could be connected with the carboborides transformations, leading to changes in their structure and properties. These transformations can refer to the endothermic effects (#3) observed on the DSC curves at a high temperature range (Figure 1).

The formation of a martensitic matrix, strengthened by secondary carbides, is the main factor in increasing the hardness and abrasive wear resistance of the studied alloys. The heterogeneous composite-like structure is worn out unevenly, with preferential wear of the softer matrix and spalling-off of the naked hard inclusions. This mechanism is more likely for elongated particles oriented nearly perpendicular to the surface [61]. Long prismatic inclusions of primary borocarbide $M_2(B,C)_5$, being protruded over the surface, experience bending loads from sliding abrasive particles; this causes their cleavage into separate fragments (Figure 10e–h). After particle spalling-off, pitting appears, which accelerates the matrix wear by causing turbulence in the abrasive particle flow [62]. Thus, when abrasive particles cannot cut hard inclusions, the lifespan of the alloy is limited precisely by the matrix wear resistance. The appearance of martensite instead of ferrite or pearlite (bainite) stabilizes the wear process and slows down the destruction of the matrix. Eventually, borocarbide inclusions remain on the surface longer, performing a protective function and resulting in a sharp reduction in the wear rate. In an as-cast (soft) state, eutectic alloys have an advantage over hypereutectic alloys due to a more appropriate wear mechanism. When the matrix hardness increases, the difference in the wear resistance of the alloys is significantly reduced since the deteriorating effect of coarse primary borocarbides is diminished. Since MCCIs' hardness strongly depends on the QT, the quenching temperature is a key factor

determining their durability under abrasive wear conditions. The selection of the QT should pursue the achievement of the maximum hardness of the alloys, which will allow for fully using the advantage of high-hard carboboride inclusions formed in hybrid MCCIs due to complex alloying.

4.2. Effect of C and B Contents on Bulk Hardness and Wear Rate Depending on QT

The results of the bulk hardness measurements and abrasive wear tests were mathematically processed according to the procedure of a full factorial design method of 3^2. This method allows for the construction of the model on the effect of two independent factors in the form of a fourth-degree regression equation, which can adequately describe a complex response surface [51,63]. The calculation approach is described in detail in our previous work [43]. In this section, the regression equations for the bulk hardness and wear rate after quenching from 1050 °C and 1150 °C were derived and analyzed (with an adequacy confirmation using the F-criterion). The equations were compared with the as-cast state, aiming to reveal the effect of C and B contents on the hardness and wear behavior depending on the quenching temperature.

After the calculations, the equations for bulk hardness were presented as follows:

$$H_{As\text{-}cast} = 38.50 + 7.15X_1 + 7.95X_2 + 2.68X_1X_2 - 4.15{X_1}^2 + 1.75{X_2}^2 + 3.83{X_1}^2{X_2}^2 - 1.33X_1{X_2}^2 - 2.88X_2{X_1}^2, \quad (3)$$

$$H_{1050} = 56.70 + 14.70X_1 + 14.20X_2 - 0.454X_1X_2 - 11.10{X_1}^2 - 11.90{X_2}^2 + 11.65{X_1}^2{X_2}^2 - 2.25X_1{X_2}^2 - 9.15X_2{X_1}^2, \quad (4)$$

$$H_{1150} = 63.30 + 3.40X_1 + 16.35X_2 - 5.70X_1X_2 - 0.90{X_1}^2 - 13.45{X_2}^2 + 3.90{X_1}^2{X_2}^2 + 10.30X_1{X_2}^2 - 10.90X_2{X_1}^2, \quad (5)$$

where H is the bulk hardness (HRC), and X_1 and X_2 are the coded levels of carbon and boron contents, respectively (see Table 1).

The free term of the Equations (3)–(5) increases from 38.5 (the as-cast state) to 63.3 (the 1150 °C-quenching), reflecting the general increase in bulk hardness under heat treatment. The positive values of the coefficients at X_1 and X_2 indicate that carbon and boron enhance the hardness of alloys. For the as-cast state and 1050 °C-quenching, the effect of carbon and boron on hardness was approximately the same. In the case of 1150 °C-quenching, the influence of boron was more significant ($3.40X_1$ against $16.35X_2$ in Equation (5)).

As follows from the graphical interpretation of Equations (3)–(5) (Figure 11), in all three cases, both carbon and boron simultaneously increase the hardness of the alloys, resulting in a response surface steeping up with an increase in these elements' contents. The direction of the steepest "hill climbing" refers to the movement from the area with coordinates "0.3 wt.% C–1.5 wt.% B" to the area with coordinates "0.95 wt.% C–3.5 wt.% B" (for the as-cast state, Figure 11a) and "(0.78–0.85) wt.% C–(2.9–3.1) wt.% B" (for the as-quenched states, Figure 11b,c). Such effect of carbon and boron is explained by a drastic increase in the total volume fraction of hard phases (borocarbides, carboborides), as well as the replacement of ferrite with martensite or "martensite + pearlite/bainite" in the structure of the matrix [39].

The regression equations for the wear rate ($\times 10^{-6}$ g·mm^{-1}·s^{-1}) were derived as follows:

$$WR_{As\text{-}cast} = 4.170 - 1.115X_1 + 0.315X_2 - 0.335X_1X_2 + 0.405{X_1}^2 - 1.135{X_2}^2 - 0.450{X_1}^2{X_2}^2 + 0.490X_1{X_2}^2 - 0.035X_2{X_1}^2, \quad (6)$$

$$WR_{1050} = 2.310 - 1.125X_1 + 0.030X_2 + 0.025X_1X_2 + 0.855{X_1}^2 + 0.080{X_2}^2 - 0.665{X_1}^2{X_2}^2 + 0.265X_1{X_2}^2 + 0.515X_2{X_1}^2, \quad (7)$$

$$WR_{1150} = 0.930 - 0.278X_1 - 0.002X_2 + 0.574X_1X_2 - 0.038{X_1}^2 + 0.139{X_2}^2 + 0.464{X_1}^2{X_2}^2 - 0.533X_1{X_2}^2 - 0.379X_2{X_1}^2, \quad (8)$$

where Equation (6) was adopted from [39].

The free term of the Equations (6)–(8) decreases from 4.17 for the as-cast state to 0.93 for the 1150 °C-quenching, indicating the general decrease in the wear rate caused by quenching. Negative values of the coefficient at X_1 in all equations indicate that carbon decreases the *WR*. In turn, positive values of the coefficient at X_2 in Equations (6) and (7) highlight that boron increases the *WR* in the as-cast condition and after quenching from 1050 °C. In contrast, under QT = 1150 °C, the coefficient at X_2 changes its sign to negative,

meaning that boron increases the wear resistance of the alloys. The different signs of the coefficients for the interactions of variables (quadratic, third-degree, and fourth-degree) indicate the complex non-linear relief of the response surface of the models (6)–(8).

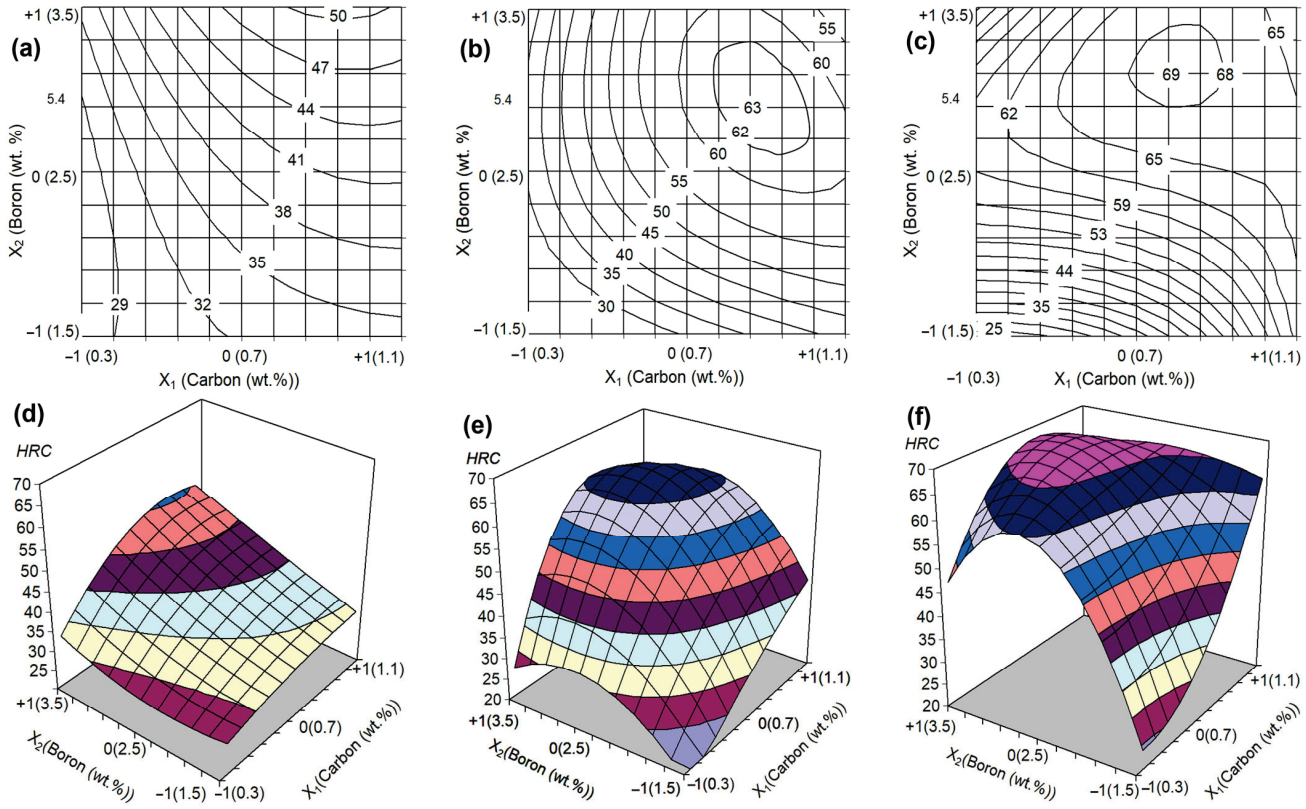


Figure 11. Graphical interpretation of the Equations (3)–(5). (**a**–**c**) The response surfaces of a bulk hardness and (**d**–**f**) its projections on the concentration plot. (**a**,**d**) The as-cast state, (**b**,**e**) QT = 1050 °C, (**c**,**f**) QT = 1150 °C.

Figure 12 visualizes Equations (6)–(8), showing the response surfaces and their projections on the concentration plot. It can be seen that in all three cases, the response surface performs a complex relief, the character of which varies depending on the state of the alloys. One can note a general tendency for the surface level to decrease during the transition from the as-cast state to QT = 1150 °C, which corresponds to an increase in the abrasive wear resistance of the alloys. In the as-cast state, carbon continuously reduces the wear rate at any boron content (Figure 12a). Boron, in turn, has a non-monotonous effect, leading to maximum wear at 2.5 wt.% because of an inappropriate microstructure comprising the coarse primary $M_2(B,C)_5$ particles combined with a smaller number of eutectic borocarbide particles. As a result, in the as-cast state, the surface has an inflection (a "hill") at 2.5 wt.% B, while the minimum points of the surface (the best wear performance) refer to the following alloy compositions: (a) 1.1 wt.% C, 3.5 wt.% B (*WR* of 2.76 × 10^{-6} g·mm^{-1}·s^{-1}) and (b) 0.86 wt.% C, 1.5 wt.% B (*WR* of 2.67 × 10^{-6} g·mm^{-1}·s^{-1}).

Under the QT = 1050 °C, the relief of the response surface changes. Boron gradually increases the wear rate at any carbon content. Carbon gradually reduces the *WR* at low boron concentrations and has an opposite effect at 3.5 wt.% B, providing a minimum *WR* at 0.86 wt.% C. The lowest surface point corresponds to the alloy composition of 1.1 wt.% C and 1.7 wt.% B (*WR* of 1.81 × 10^{-6} g·mm^{-1}·s^{-1}), while the highest point refers to the composition of 0.3 wt.% C and 3.5 wt.% B (*WR* of 4.63 × 10^{-6} g·mm^{-1}·s^{-1}).

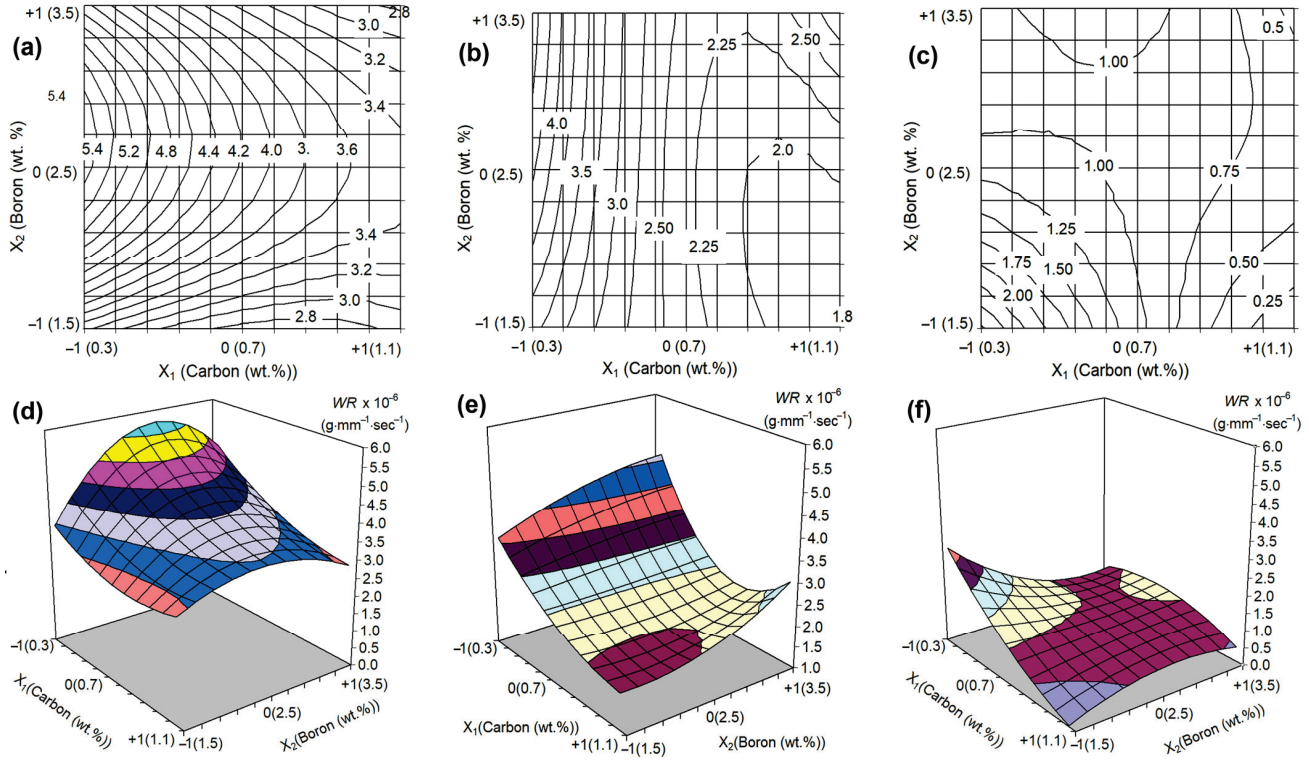


Figure 12. Graphical interpretation of Equations (6)–(8). (**a**–**c**) The response surfaces of a wear rate and (**d**–**f**) its projections on the concentration plot. (**a**,**d**) The as-cast state [42], (**b**,**e**) QT = 1050 °C, (**c**,**f**) QT = 1150 °C.

Under the QT = 1150 °C, the pattern of the response surface changed once again. Most of the surface area became almost plane, indicating similar *WR* values for different C/B combinations (within the range of (1.0–1.4) $\times$ 10^{-6} g·mm^{-1}·s^{-1})). At 1.1 wt.% C and 1.5 wt.% B, the surface has the minimum (0.20 $\times$ 10^{-6} g·mm^{-1}·s^{-1}), while as the concentrations of carbon and boron decrease, the surface steeps up, reaching a maximum (2.79 $\times$ 10^{-6} g·mm^{-1}·s^{-1}) at 0.3 wt.% C and 1.5 wt.% B.

As follows from Figure 2, an increase in the boron concentration to 2.5 wt.% led to the appearance of coarse primary particles in the structure of the alloys. These inclusions had a contradictory effect on wear resistance. On the one hand, they increase the wear resistance due to high hardness (~2400 HV [37]); thus, alumina particles cannot cut them (this leads to a "shadow effect" when the adjacent matrix remains unworn, being shielded by the particle) [42]. On the other hand, the high brittleness of the inclusions leads to their easy cheeping under the abrasive particles' pressure. The appearance of such inclusions in the as-cast (i.e., with a soft matrix) 2.5 wt.% B alloys accelerate the wear. When the boron content increases to 3.5 wt.%, the number of primary inclusions is increased, thus reducing the preferential wear of the matrix, expanding the "shadow effect". As a result, the alloys with 3.5 wt.% B show a lower *WR* as compared with those with 2.5 wt.% B. This leads to the non-monotonic effect of boron, with a maximum *WR* value at 2.5 wt.% B. A completely different character of the boron effect is observed after quenching, when hardness sharply increases. In this case, boron advances the wear resistance of the alloys. The QT should be limited to 1150 °C, since this temperature is quite close to the melting point (as follows from the DSC curves). Heating to an even higher temperature (1200 °C) can cause partial melting of the castings, especially taking into account the possible segregation of elements that lower the melting point of the alloy.

Like boron, carbon is involved in the formation of hard phases. However, its effect refers only to Ti-rich carboboride and Fe(Cr)-rich eutectic carboborides M_3(C,B) and M_7(C,B)$_3$ [37,39]. With that, carbon has a slight effect on the formation of borocarbide M_2(C,B)$_5$; thus, it is not responsible for the solidification of coarse primary inclusions

which adversely affect the wear resistance. Also, carbon remarkably contributes to the formation of a wear-resistant matrix with C-rich structural components (acicular martensite, pearlite-bainite conglomerate). These structures originate from austenite, the single-phase domain of which is limited in MCCIs' phase diagram due to the ferrite-stabilizing effect of Cr, W, Mo, and V. Since carbon belongs to the gamma-stabilizing elements, it expands the austenite domain, thus ensuring the austenite → martensite transformation [64,65]. Therefore, carbon continually reduces the wear rate of the alloy (over its studied concentration range) regardless of the boron content.

4.3. "Hardness-Wear Rate" Correlations

Figure 13 shows the "Hardness-Wear Rate" correlations for various alloys, grouped by the carbon content (Figure 13a) and boron content (Figure 13c). The experimental points on the graphs refer to various alloys both in the as-cast state and heat-treated state (quenching from different temperatures). As follows from Figure 13a, the scatter areas of *WR* values for the carbon-wise groups mostly overlap each other, forming a common band of the values scatter (Figure 13b), which can be described by the following generalized equation:

$$WR = -0.0001 \cdot H^3 + 0.021 \cdot H^2 - 1.031 \cdot H + 19.57 \ (R^2 = 0.55), \quad (9)$$

where *WR* is measured in ($\times 10^{-6}$ g·mm^{-1}·s^{-1}), and *H* is the bulk hardness (HRC).

Equation (9) represents a tendency for the *WR* to decrease with the increasing hardness of the alloys. Carbon has virtually no effect on the pattern of this dependence. In contrast, in boron-wise groups, the scatter area of the 1.5 wt.% B group lies below the areas of the 2.5 wt.% B and 3.5 wt.% B groups (the last two overlap each other) (Figure 13c). Therefore, the "Hardness—*WR*" correlations can be described separately (Figure 13d):

- for 1.5 wt.% B-alloys:

$$WR = 11.01 \cdot exp(-0.047 \cdot H) \ (R^2 = 0.85), \quad (10)$$

- for 2.5–3.5 wt.% B-alloys:

$$WR = -0.0001 \cdot H^3 + 0.017 \cdot H^2 - 0.92 \cdot H + 20.11 \ (R^2 = 0.91). \quad (11)$$

Thus, at the same hardness level, the 1.5 wt.%B-alloys show a lower wear rate as compared to the alloys with a higher boron content. This highlights the general advantage of the eutectic structure over the hypereutectic structure (due to the absence of primary $M_2(B,C)_5$ particles). In conclusion, boron affects the correlation "Hardness—*WR*" more significantly as compared to carbon, mostly through its controlling the $M_2(B,C)_5$ formation.

The hybrid MCCIs in the as-cast state significantly vary in structure, resulting in a rather high difference in wear behavior (with a maximum scatter in *WR* values of 3.8×10^{-6} g·mm^{-1}·s^{-1}). Figure 13b presents the general distribution of experimental points (related to both the as-cast and as-quenched alloys) on the "Hardness—*WR*" plot. This figure shows that at similar low hardness values (27–28 HRC), the *WR* values differ maximally by 3.2×10^{-6} g·mm^{-1}·s^{-1}. With increasing hardness, the maximum *WR* scatter decreases to 1.8×10^{-6} g·mm^{-1}·s^{-1} (at 60 HRC) and 0.32×10^{-6} g·mm^{-1}·s^{-1} (at 67 HRC) (Figure 13e). Thus, quenching to high hardness (over 60 HRC) allows for leveling the wear resistance of hybrid MCCIs regardless of C and B contents. Such hardness can be reached in MCCIs containing ≥0.7 wt.% C and ≥2.5 wt.% B; also, the alloy 1.1C–1.5B acquired a hardness of 67 HRC after quenching from 1150 °C. Hence, these alloys are interchangeable for abrasive wear applications to a certain extent.

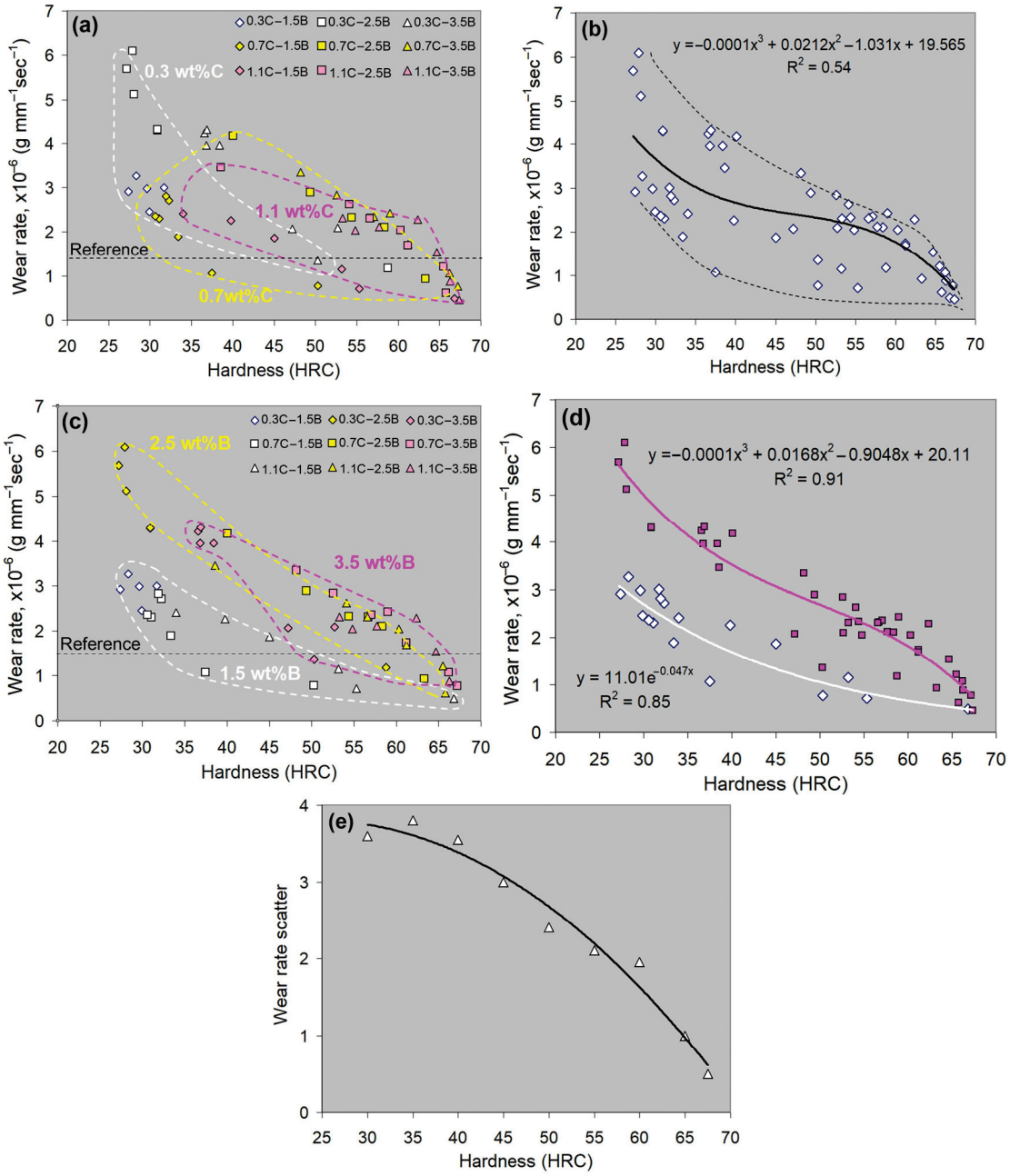


Figure 13. The "Wear rate—Bulk hardness" correlations: (**a**) regarding the carbon content, (**b**) the generalized correlation for different alloys with the scatter limits (dashed lines) and approximating function (solid black line), (**c**) regarding the boron content, (**d**) generalized correlations and approximating functions for the alloys with 1.5 wt.% B (white dots and white line respectively) and 2.5–3.5 wt.%B (pink dots and line respectively). (**e**) Effect of bulk hardness on the maximum scatter in the wear rate for different alloys.

4.4. Practical Aspects of Using Hybrid MCCIs

The tribological properties of the hybrid MCCIs were assessed relative to the reference specimen, which was a widely used wear-resistant alloy (high-chromium cast iron) quenched to a maximum hardness (66 HRC). The wear rate of a reference specimen was measured as 1.44×10^{-6} g·mm^{-1}·s^{-1}. The reference *WR* level is indicated in Figure 13a,c by a dashed line. One can see that within the hardness range of <65 HRC, most of the experimental points (75 %) are above the line, i.e., in these cases, the MCCIs were inferior to the reference in wear resistance. At the same time, the minor number of points (which

referred to alloys with 0.7–1.1 wt.% C) is below the reference line. This means that even under lower hardness, some hybrid MCCIs performed an advanced wear resistance. Notably, under comparable hardness (>65 HRC), all experimental points are below the reference level, indicating the MCCIs' advantage in wear resistance over the reference specimen.

The wear behavior of MCCIs was evaluated by the wear resistance coefficient (K), which was calculated as

$$K_i = \frac{WR_{ref}}{WR_i} \tag{12}$$

where WR_{ref} and WR_i are the wear rate values for the reference alloy and i-experimental alloy, respectively. The K values for different MCCIs (in the as-cast and heat-treated states) are depicted in Figure 14 (in the latter case, the highest K values are presented).

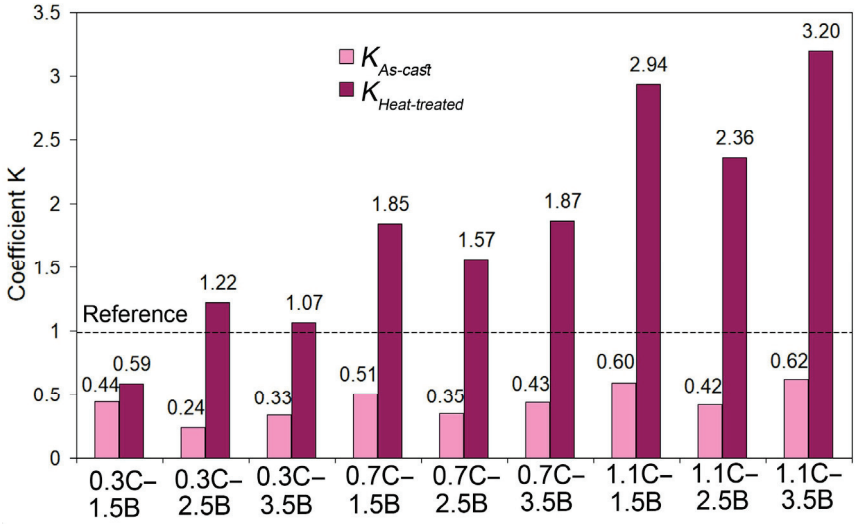


Figure 14. The K values of the hybrid MCCIs in the as-cast and heat-treated states.

As seen, in the as-cast state, all experimental MCCIs are inferior to high-Cr cast irons in terms of wear resistance because of the much lower bulk hardness. After quenching, the wear resistance of 0.3 wt.% C-MCCIs is lower or close to the reference (their K values are $\leq$1.22). Taking into account the higher number of alloying elements (i.e., higher cost), this group of MCCIs cannot compete with the reference in terms of practical application. The wear resistance coefficient of 0.7 wt.% C-MCCIs reaches a maximum of 1.57–1.87, which is to be considered a significant advantage over high-Cr cast iron. The best wear behavior is exhibited by the MCCIs containing 1.1 wt.% C. According to the K values, they are 2.94 times (alloy 1.1C–1.5B), 2.36 times (alloy 1.1C–2.5B), and 3.20 times (alloy 1.1C–3.5B) more wear-resistant than the reference alloy. The near-threefold advantage in abrasive wear resistance over high-Cr cast iron shows the high potential of hybrid multi-component alloys for industrial applications, even at their higher cost associated with (W,Mo,V)-alloying. The use of alloys is advisable only after heat treatment to maximum hardness (quenching from 1150 °C, tempering at 200 °C). In this case, the increase in the cost of alloys due to alloying with expensive elements can be compensated for by an increase in their durability.

It should be noted that the best wear performance (K of about 3.0) was demonstrated under different types of the MCCIs' structure, specifically near-eutectic (alloy 1.1C–1.5B) or hypereutectic (alloy 1.1C–3.5B). The use of a near-eutectic-type alloy is preferable, since, due to the absence of brittle primary borocarbides in the structure, it potentially has a higher toughness and lesser susceptibility to crack formation under manufacturing and exploitation, which can expand its scope of application. Alloying with Cr, Mo, and W, which are partially dissolved in the matrix, will ensure MCCIs' high hardenability, thus allowing for the use of air-cooling during quenching to reduce distortion and prevent the cracking in the cast components. The kinetics of austenite transformation in MCCIs should

be additionally studied to determine the maximum thickness of castings, which can acquire a martensitic structure under air-cooling.

When assessing the applicability of the material for specific abrasive wear applications, the hardness of abrasive particles should be taken into account. In this study, fairly hard Al_2O_3 (1400–2000 HV [66,67]) was used as an abrasive. Al_2O_3 is inferior to borocarbide in hybrid MCCIs (~2400 HV [37–39]); however, it is of the same order as the chromium carbide M_7C_3 in high-Cr cast iron (1300–1800 HV [68]). That is why MCCIs significantly exceed the reference alloy when tested by Al_2O_3. Under testing by a softer abrasive (for instance, SiO_2, ~1000 HV [69]), the wear resistance ratio may change significantly in favor of the reference, since M_7C_3 is harder than quartz. At this stage of research, hybrid MCCIs are recommended to be used for the processing of hard sorts of abrasive materials (SiC, Al_2O_3, Si_3N_4, etc.). Determining the relative wear resistance of the hybrid multi-component cast alloys under testing by a softer abrasive is a challenge for further research.

The results obtained should be considered as a basis for the further improvement of the chemical composition of hybrid multi-component alloys. It became obvious that the high concentration of ferrite-stabilizing alloying elements (W, W, V, Cr, Ti) and the low concentration of gamma-stabilizers (C, Mn) in the MCCIs' composition lead to the contraction of the domain of austenite existence; it makes achieving high hardness difficult. To reach austenite (which will then turn into hard martensite), it is necessary to heat the alloy to rather high temperatures close to the melting point. This can cause the melting of the castings and promote surface oxidation. Hence, the chemical composition of hybrid MCCIs should be balanced towards the coexistence of αFe and γFe phases at relatively low quenching temperatures. This can be achieved by increasing the contents of gamma-stabilizing elements (Mn, Ni, C); however, a further increase in the carbon concentration is inappropriate, since it can lead to the formation of a hypereutectic structure with coarse carboboride precipitates. In this case, a specific structural state may arise, which will further increase the wear resistance of the alloys. It is about the formation of a heterogeneous matrix combining martensite and retained austenite. With a rational selection of alloying elements and the phase ratio, retained austenite may undergo strain-induced martensitic transformation (SIMT) during wear. It is known that when worn by a hard abrasive, metastable austenite can exhibit an advanced wear resistance, several times higher than that of martensite [70]. This is associated with the high energy consumption by SIMT and the abnormal hardening of austenite [71]. Moreover, austenite, as a ductile phase, may promote the impact toughness of alloys, which will make it possible to operate them under impact loads. The development of hybrid multicomponent alloys with a metastable austenitic matrix is a promising direction for the further research of high-boron alloys intended for tribological applications.

5. Conclusions

The effect of the quenching temperature (QT) on the microstructure, bulk hardness, and "Three-Body-Abrasion" wear behavior (in contact with Al_2O_3) of hybrid multi-component (wt.%) Fe-(0.3–1.1C)–(1.5–3.5B)-5W-5Mo-5V-10Cr-2.5Ti cast alloys has been studied. The following conclusions were drawn:

- An increase in the QT from 950 to 1150–1200 °C improved most alloys' hardness and wear resistance. Under low carbon (0.3 wt.%) and/or boron (1.5 wt.%) contents, a noticeable increase in hardness was observed at a QT above 1050 °C, reaching the maximum of 50–59 HRC. In other alloys, the hardness increased proportionally to the QT starting from 950 °C and reached 63–67 HRC. Accordingly, the wear rate decreased by three to six times (relative to the as-cast state). This was due to the formation of a martensitic matrix strengthened by secondary carboboride precipitates. Alloy 0.3C–1.5B retained a ferritic matrix regardless of the QT, and its properties were hardly changed by quenching.
- Carbon increased the wear resistance of MCCIs due to the formation of the carborides M(C,B), $M_7(C,B)_3$, and $M_3(C,B)$, as well as by expanding the γ-area, thus

contributing to the appearance of the martensitic matrix under the quench cooling. Boron had a versatile effect on wear resistance, which is associated, on the one hand, with the formation of wear-resistant borocarbide phases and, on the other, with the occurrence of coarse primary inclusions that were easily spalled off during wear.

- At any hardness, the alloys with a near-eutectic structure exhibited a higher wear resistance as compared to the hypereutectic ones. This is attributed to a more favorable wear mechanism of the multi-cycle formation/removal of the fine micro-scales. In hypereutectic alloys, the predominant wear mechanism is a spalling of coarse primary borocarbides. With the QT increase, the difference in the wear rate of alloys decreased due to matrix hardness improvement: the hard matrix better resisted wear, preventing the easier exposure and fracture of primary borocarbides.
- The factorial design of experiment 3^2 was used to optimize the alloy composition. According to the regression models derived, the highest wear resistance is attributed to the MCCI with 1.1 wt.% C and 1.5 wt.% B quenched from 1150 °C. Under the testing, the optimized alloy exhibited a hardness of 67 HRC and a wear rate of 0.88×10^{-6} g·mm^{-1}·s^{-1}. A similar wear resistance was shown by MCCI with 1.1 wt.% C and 3.5 wt.% B (quenching from 1200 °C, 67 HRC, WR of 0.81×10^{-6} g·mm^{-1}·s^{-1}). The above alloys were 2.94 and 3.20 times more wear-resistant than the reference alloy (a 13 wt.% Cr-cast iron, 66 HRC) indicating the high potential of the MCCIs to stand hard-abrasive applications.

Author Contributions: Conceptualization, Y.C. and V.E.; methodology, Y.C., V.E., I.P., K.S. and A.A.; supervision, Y.C.; investigation, M.G., Y.C., B.E. and V.K.; writing—original draft preparation, M.G., Y.C. and V.E.; writing—review and editing, M.G., Y.C., V.E. and K.S.; resources, V.E., I.P., K.S., A.A. and V.K.; software, B.E.; visualization, B.E. and I.P.; project administration, Y.C.; data curation, A.A. and V.K.; funding acquisition, I.P. and V.E. All authors have read and agreed to the published version of the manuscript.

Funding: This research was funded by the Ministry of Education and Science of Ukraine (project No. 0122U000325) and by the Slovak Research and Development Agency (APVV-23-0341).

Institutional Review Board Statement: Not applicable.

Informed Consent Statement: Not applicable.

Data Availability Statement: The original contributions presented in the study are included in the article, further inquiries can be directed to the corresponding author.

Acknowledgments: Yuliia Chabak and Vasily Efremenko greatly acknowledge the financial support of "EU Next Generation EU through the Recovery and Resilience Plan for Slovakia" (projects No. 09I03-03-V01-00061).

Conflicts of Interest: The authors declare no conflicts of interest.

References

1. Doğan, Ö.N.; Hawk, J.A.; Laird, G. Solidification Structure and Abrasion Resistance of High Chromium White Irons. *Metall. Mater. Trans. A* **1997**, *28*, 1315–1328. [CrossRef]
2. Ngqase, M.; Pan, X. An Overview on Types of White Cast Irons and High Chromium White Cast Irons. *J. Phys. Conf. Ser.* **2019**, *1495*, 012023. [CrossRef]
3. Fashu, S.; Trabadelo, V. Development and Performance of High Chromium White Cast Irons (HCWCIs) for Wear–Corrosive Environments: A Critical Review. *Metals* **2023**, *13*, 1831. [CrossRef]
4. Chabak, Y.; Efremenko, V.; Zurnadzhy, V.; Puchý, V.; Petryshynets, I.; Efremenko, B.; Fedun, V.; Shimizu, K.; Bogomol, I.; Kulyk, V.; et al. Structural and Tribological Studies of "(TiC+WC)/Hardened Steel" PMMC Coating Deposited by Air Pulsed Plasma. *Metals* **2022**, *12*, 218. [CrossRef]
5. Matsubara, Y. *Research and Development of Abrasion Wear Resistant Cast Alloys for Rolls of Rolling and Pulverizing Mills*; Kurume National College of Technology: Kurume, Japan, 2002; p. 30.
6. *A600-92a*; Standard Specification for Tool Steel High Speed. ASTM International: West Conshohocken, PA, USA, 2016.
7. Pasini, W.M.; Belle, M.R.; Pereira, L.; do Amaral, R.F.; de Barcellos, V.K. Analysis of Carbides in Multi-component Cast Iron Design Based on High Entropy Alloys Concepts. *Mater. Res.* **2021**, *24*, e20200398. [CrossRef]

8. Matsubara, Y.; Sasaguri, N.; Shimizu, K. Solidification and Abrasion Wear of White Cast Irons Alloyed with 20% Carbide Forming Elements. *Wear* **2001**, *250*, 502. [CrossRef]
9. Wu, H.Q.; Hashimoto, M.; Sasaguri, N.; Matsubara, Y. Solidification Sequence of Multi-Component White Cast Iron. *Jpn. Foundry Eng. Soc.* **1996**, *68*, 637–643.
10. Wu, H.; Sasaguri, N.; Hashimoto, M.; Matsubara, Y. Practical Phase Diagram of Multi-Component White Cast Iron. *Jpn. Foundry Eng. Soc.* **1997**, *69*, 917–923. [CrossRef]
11. Hashimoto, M.; Kubo, O.; Matsubara, Y. Analysis of Carbides in Multi-component White Cast Iron for Hot Rolling Mill Rolls. *ISIJ Int.* **2004**, *44*, 372–380. [CrossRef]
12. Yu, K.; Matsubara, Y. Abrasion Wear Resistance of Alloyed White Cast Iron with Several Types of Carbides and Matrices. *AFS Trans.* **1998**, *27*, 53–58.
13. Inthidech, S.; Opapaibon, J.; Yamamoto, K.; Matsubara, Y. Three Body-Type Abrasive Wear Behavior of Multi-Alloyed White Cast Iron with Different Carbon Contents Used for Hot Work Rolls. *ISIJ Int.* **2021**, *11*, 2832–2843. [CrossRef]
14. Yen, C.L.; Fu, J.C.; Pan, Y.N. Research on the Wear Resistance of High-Chromium White Cast Iron and Multi-Component White Cast Iron. *Adv. Mater. Res.* **2013**, *859*, 64–69. [CrossRef]
15. Ziadi, A.; Belzunce, F.J.; Rodriguez, C. The effects of heat treatment on the mechanical properties of multicomponent white cast irons. *J. Mater. Sci.* **2007**, *42*, 7579–7585. [CrossRef]
16. Efremenko, V.G.; Shimizu, K.; Cheiliakh, A.P.; Pastukhova, T.V.; Chabak, Y.G.; Kusumoto, K. Abrasive Resistance of Metastable V-Cr-Mn-Ni Spheroidal Carbide Cast Irons Using the Factorial Design Method. *Int. J. Miner. Metall. Mater.* **2016**, *23*, 645–657. [CrossRef]
17. Ziadi, A.; Belzunce, F.J.; Rodriguez, C.; Riba, J. Wear and oxidation behaviour of multicomponent white cast irons. *Mater. Sci. Technol.* **2005**, *21*, 1181–1186. [CrossRef]
18. Zhang, Y.; Shimizu, K.; Yaer, X.; Kusumoto, K.; Efremenko, V.G. Erosive Wear Performance of Heat Treated Multi-component Cast Iron Containing Cr, V, Mn and Ni Eroded by Alumina Spheres at Elevated Temperatures. *Wear* **2017**, *390–391*, 135–145. [CrossRef]
19. Bedolla-Jacuinde, A.; Guerra, F.V.; Mejia, I.; Zuno-Silva, J.; Rainforth, M. Abrasive Wear of V-Nb-Ti Alloyed High Chromium White Irons. *Wear* **2015**, *332–333*, 1006–1011. [CrossRef]
20. Villanueva Bravo, S.; Kaoru, Y.; Miyahara, H.; Ogi, K. Influence of Nb, V and Ta on the Microstructure of Ni-hard type Cast Iron for Hot Steel Strip Mills. *J. Metall. Eng.* **2017**, *2*, 1–11.
21. Duriagina, Z.A.; Romanyshyn, M.R.; Kulyk, V.V.; Kovbasiuk, T.M.; Trostianchyn, A.M.; Lemishka, I.A. The Character of the Structure Formation of Model Alloys of the Fe-Cr-(Zr, Zr-B) System Synthesized by Powder Metallurgy. *J. Achiev. Mater. Manuf. Eng.* **2020**, *100*, 49–57. [CrossRef]
22. González-Pociño, A.; Asensio-Lozano, J.; Álvarez-Antolín, F.; García-Diez, A. Evaluation of Hardness, Sliding Wear and Strength of a Hypoeutectic White Iron with 25% Cr after Heat Treatments. *Metals* **2021**, *11*, 947. [CrossRef]
23. Xiong, L.; Liu, Y.; Zeng, Q.; Lai, J.; Qiao, X. Effect of Destability Time on Microstructure and Properties of Hypoeutectic High Chromium Cast Iron. *RSC Adv.* **2024**, *11*, 7459–7467. [CrossRef] [PubMed]
24. Karantzalis, A.E.; Lekatou, A.; Diavati, E. Effect of Destabilization Heat Treatments on the Microstructure of High-Chromium Cast Iron: A Microscopy Examination Approach. *J. Mater. Eng. Perform.* **2009**, *18*, 1078–1085. [CrossRef]
25. Nayak, U.P.; Mücklich, F.; Guitar, M.A. Time-Dependant Microstructural Evolution and Tribological Behaviour of a 26 wt% Cr White Cast Iron Subjected to a Destabilization Heat Treatment. *Met. Mater. Int.* **2023**, *29*, 934–947. [CrossRef]
26. Bedolla-Jacuinde, A.; Arias, L.; Hernández, B. Kinetics of Secondary Carbides Precipitation in a High-Chromium White Iron. *J. Mater. Eng. Perform.* **2003**, *12*, 371–382. [CrossRef]
27. Le Nué, C.; Corujeira Gallo, S.; Vahid, A.; Wang, J.; Taherishargh, M.; Attar, H.; Fabijanic, D.; Barnett, M. Destabilization Treatment and Its Influence on Microstructure and Matrix Hardness of High-Cr Cast Iron. *Metall. Mater. Trans. A* **2023**, *54*, 4952–4965. [CrossRef]
28. Guitar, M.A.; Suárez, S.; Prat, O.; Duarte Guigou, M.; Gari, V.; Pereira, G.; Mücklich, F. High Chromium Cast Irons: Destabilized-Subcritical Secondary Carbide Precipitation and its Effect on Hardness and Wear Properties. *J. Mater. Eng. Perform.* **2018**, *27*, 3877–3885. [CrossRef]
29. Opapaiboon, J.; Inthidech, S.; Yamamoto, K.; Matsubara, Y. Effect of V Content on Microstructure and Heat Treatment Behavior of Multi-component White Cast Iron used for Hot Work Roll Applications. *Int. J. Metalcast.* **2023**, *18*, 2484–2498. [CrossRef]
30. Yokomizo, Y.; Yamamoto, K.; Sasaguri, N.; Matsubara, Y. Effect of Chromium and Vanadium Contents on Continuous Cooling Transformation Behavior of Multi-Component White Cast Iron. *Key Eng. Mater.* **2010**, *457*, 237–242. [CrossRef]
31. Barutçuoğlu, B.; Koç, F.G.; Erişir, E.; Gülben, K. The Effect of Tempering Temperature on Microstructure and Wear Behavior of Tungsten and Boron Alloyed Ni-Hard 4 White Cast Irons. *Int. J. Metalcast.* **2024**. [CrossRef]
32. Opapaiboon, J.; Ayudhaya, M.S.N.; Sricharoenchai, P.; Inthidech, S.; Matsubara, Y. Effect of Chromium Content on Heat Treatment Behavior of Multi-Alloyed White Cast Iron for Abrasive Wear Resistance. *Mater. Trans.* **2019**, *60*, 346–354. [CrossRef]
33. Opapaiboon, J.; Sricharoenchai, P.; Inthidech, S.; Matsubara, Y. Effect of Carbon Content on Heat Treatment Behavior of Multi-Alloyed White Cast Iron for Abrasive Wear Resistance. *Mater. Trans.* **2015**, *56*, 720–725. [CrossRef]
34. Inthidech, S.; Matsubara, Y. Effects of Carbon Balance and Heat Treatment on Hardness and Volume Fraction of Retained Austenite of Semi-multi-alloyed White Cast Iron. *Int. J. Metalcast.* **2020**, *14*, 132–143. [CrossRef]
35. Kovzel, M.A.; Babachenko, O.I.; Parusov, E.; Parusov, O.V. On Peculiarities of Influence of Chemical Composition on Formation of Structure and Properties of Alloyed Cast Irons in the As-Cast State. *Metallofiz. Novejsie Tehnol.* **2022**, *44*, 1347–1359. [CrossRef]

36. Sukhova, O.V.; Polonskyy, V.A.; Ustinova, K.V. Corrosion-Electrochemical Properties of Quasicrystalline Al–Cu–Fe–(Si,B) and Al–Ni–Fe Alloys in NaCl Solution. *Vopr. Khimii Khimicheskoi Tekhnologii* **2019**, *124*, 46–52. [CrossRef]
37. Efremenko, V.G.; Chabak, Y.G.; Shimizu, K.; Golinskyi, M.A.; Lekatou, A.G.; Petryshynets, I.; Efremenko, B.V.; Halfa, H.; Kusumoto, K.; Zurnadzhy, V.I. The Novel Hybrid Concept on Designing Advanced Multi-Component Cast Irons: Effect of Boron and Titanium (Thermodynamic Modelling, Microstructure and Mechanical Property Evaluation). *Mater. Charact.* **2023**, *197*, 112691. [CrossRef]
38. Chabak, Y.G.; Shimizu, K.; Efremenko, V.G.; Golinskyi, M.A.; Kusumoto, K.; Zurnadzhy, V.I.; Efremenko, A.V. Microstructure and Phase Elemental Distribution in High-Boron Multi-Component Cast Irons. *Int. J. Miner. Metall. Mater.* **2022**, *29*, 78–87. [CrossRef]
39. Efremenko, V.G.; Chabak, Y.G.; Lekatou, A.G.; Shimizu, K.; Petryshynets, I.; Zurnadzhy, V.I.; Efremenko, B.V.; Kusumoto, K.; Halfa, H. Microstructural Map and Phase Chemical Compositions in Hybrid Multi-component Cast Alloys Fe-W-Mo-V-Cr-Ti-(1.5–3.5 Wt Pct)B-(0.3–1.1 Wt Pct)C. *Metall. Mater. Trans. A* **2024**, *55*, 2756–2772. [CrossRef]
40. Sukhova, O.V. Solubility of Cu, Ni, Mn in Boron-Rich Fe-B-C Alloys. *Phys. Chem. Solid State* **2021**, *22*, 110–116. [CrossRef]
41. Lozynskyi, V.; Trembach, B.; Hossain, M.M.; Kabir, M.H.; Silchenko, Y.; Krbata, M.; Sadovyi, K.; Kolomiitse, O.; Ropyak, L. Prediction of Phase Composition and Mechanical properties Fe-Cr-C-B-Ti-Cu hardfacing alloys: Modeling and experimental Validations. *Heliyon* **2024**, *10*, e25199. [CrossRef]
42. Yen, C.L.; Kun, L.L.; Pan, Y.N. Simulation of the Phase Diagrams for High-Chromium White Cast Irons and Multi-Component White Cast Irons. *Adv. Mater. Res.* **2013**, *848*, 39–45. [CrossRef]
43. Ren, X.; Han, L.; Fu, H.; Wang, J. Research on Properties of Borocarbide in High Boron Multi-Component Alloy with Different Mo Concentrations. *Materials* **2021**, *14*, 3709. [CrossRef]
44. Lentz, J.; Röttger, A.; Theisen, W. Hardness and modulus of Fe_2B, $Fe_3(C,B)$, and $Fe_{23}(C,B)_6$ borides and carboborides in the Fe-C-B system. *Mater. Charact.* **2018**, *135*, 192–202. [CrossRef]
45. Ma, S.; Zhang, J. Wear resistant high boron cast alloy—A review. *Rev. Adv. Mater. Sci.* **2016**, *44*, 54.
46. Liu, Z.L.; Xiang, C.; Li, Y.X.; Hu, K.H. High Boron Iron-Based Alloy and Its Modification. *J. Iron Steel Res. Int.* **2009**, *16*, 37–54. [CrossRef]
47. Chabak, Y.; Petryshynets, I.; Efremenko, V.; Golinskyi, M.; Shimizu, K.; Zurnadzhy, V.; Sili, I.; Halfa, H.; Efremenko, B.; Puchy, V. Investigations of Abrasive Wear Behaviour of Hybrid High-Boron Multi-Component Alloys: Effect of Boron and Carbon Contents by the Factorial Design Method. *Materials* **2023**, *16*, 2530. [CrossRef]
48. Chen, X.; Li, Y. Effect of heat treatment on microstructure and mechanical properties of high boron white cast iron. *Mater. Sci. Eng. A* **2010**, *528*, 770–775. [CrossRef]
49. Ma, S.; Xing, J.; Liu, G.; Yi, D.; Fu, H.; Zhang, J.; Li, Y. Effect of chromium concentration on microstructure and properties of Fe-3.5B alloy. *Mater. Sci. Eng. A* **2010**, *527*, 6800–6808. [CrossRef]
50. Lentz, J.; Röttger, A.; Theisen, W. Microstructures, Heat Treatment, and Properties of Boron-Alloyed Tool Steels. *Steel Res. Int.* **2019**, *91*, 1900416. [CrossRef]
51. Jiju, A. *Design of Experiments for Engineers and Scientists*; Elsevier: Amsterdam, The Netherlands, 2014.
52. Novik, F.S.; Arsov, J.B. *Optimization of Metal Technology Processes by Methods of Planning Experiments*; Mashinostroenie: Moscow, Russia, 1980.
53. Gonzalez-Pociño, A.; Alvarez-Antolin, F.; Asensio-Lozano, J. Influence of Thermal Parameters Related to Destabilization Treatments on Erosive Wear Resistance and Microstructural Variation of White Cast Iron Containing 18% Cr. Application of Design of Experiments and Rietveld Structural Analysis. *Materials* **2019**, *19*, 3252. [CrossRef] [PubMed]
54. Hohne, G.W.H.; Hemminger, W.; Flammersheim, H.-J. *Differential Scanning Calorimetry: An Introduction for Practitioners*; Springer: Berlin/Heidelberg, Germany, 1996.
55. Khaled, I.; Nofal, A.A. Effect of Titanium Addition on Structure and Properties of the As-Cast High Cr-Mo White Iron. *J. Mater. Res.* **2012**, *103*, 362–370. [CrossRef]
56. Gutnyk, M.; Nürnberger, F. The Fe-C diagram—History of its evolution. *Hist. Sci. Technol.* **2023**, *13*, 243–262. [CrossRef]
57. Greer, A.L. The Use of DSC to Determine the Curie Temperature of Metallic Glasses. *Thermochim. Acta* **1980**, *42*, 193–222. [CrossRef]
58. Leu, M.S.; Tsai, C.S.; Lin, C.S.; Lin, S.T. The Determination of Curie Temperature by Differential Scanning Calorimetry under Magnetic Field. *IEEE Trans. Magn.* **1991**, *27*, 5414–5416. [CrossRef]
59. Loi Brião, S.; Andrade, J.R.; Lobato, F.; dos Santos Paes, L.E.; Vilarinho, L.; Reis, R. An In-House Finite Volume Analysis to Predict the Heat Affected Zone in TIG Welding. In Proceedings of the 18th Brazilian Congress of Thermal Sciences and Engineering (ABCM 2020), Bento Gonçalves, Brazil, 16–20 November 2020; pp. 1–8. [CrossRef]
60. Kohne, T.; Fahlkrans, J.; Stormvinter, A.; Maawad, E.; Winkelmann, A.; Hedström, P.; Borgenstam, A. Evolution of Martensite Tetragonality in High-Carbon Steels Revealed by In Situ High-Energy X-Ray Diffraction. *Metall Mater Trans A* **2023**, *54*, 1083–1100. [CrossRef]
61. Efremenko, B.V.; Shimizu, K.; Espallargas, N.; Efremenko, V.G.; Kusumoto, K.; Chabak, Y.G.; Belik, A.G.; Chigarev, V.V.; Zurnadzhy, V.I. High-Temperature Solid Particle Erosion of Cr-Ni-Fe-C Arc Cladded Coatings. *Wear* **2020**, *460–461*, 203439. [CrossRef]
62. Hashmi, A.W.; Mali, H.S.; Meena, A.; Saxena, K.K.; Puerta, A.P.V.; Prakash, C.; Buddhi, D.; Davim, J.P.; Abdul-Zahra, D.S. Understanding the Mechanism of Abrasive-Based Finishing Processes Using Mathematical Modeling and Numerical Simulation. *Metals* **2022**, *12*, 1328. [CrossRef]
63. Lesyk, D.A.; Mordyuk, B.N.; Dzhemelinskyi, V.V.; Voloshko, S.M.; Burmak, A.P. Optimization of Ultrasonic Impact Treatment for Surface Finishing and Hardening of AISI O2 Tool Steel by Experimental Design. *J. Mater. Eng. Perform.* **2022**, *31*, 8567–8584. [CrossRef]

64. Chabak, Y.; Efremenko, B.; Petryshynets, I.; Efremenko, V.; Lekatou, A.G.; Zurnadzhy, V.; Bogomol, I.; Fedun, V.; Koval', K.; Pastukhova, T. Structural and Tribological Assessment of Biomedical 316 Stainless Steel Subjected to Pulsed-Plasma Surface Modification: Comparison of LPBF 3D Printing and Conventional Fabrication. *Materials* **2021**, *14*, 7671. [CrossRef]
65. Okamoto, H.; Schlesinger, M.E.; Mueller, E.M. *ASM Handbook Volume 3: Alloy Phase Diagrams*; ASM International: Almere, The Netherlands, 2016; ISBN 978-1-62708-070-5.
66. Žmak, I.; Ćorić, D.; Mandić, V.; Ćurković, L. Hardness and Indentation Fracture Toughness of Slip Cast Alumina and Alumina-Zirconia Ceramics. *Materials* **2020**, *13*, 122. [CrossRef]
67. Wefers, K.; Misra, C. *Oxides and Hydroxides of Aluminum*; Alcoa Research Laboratories: New Kensington, PA, USA, 1987.
68. Pierson, H.O. *Handbook of Refractory Carbides and Nitrides. Properties, Characteristics, Processing and Applications*; Noyes Publications: Westwood, CA, USA, 1996.
69. Kulik, E.; Nishiyama, N.; Higo, Y.; Gaida, N.A.; Katsura, T. Hardness of Polycrystalline SiO_2 Coesite. *J. Am. Ceram. Soc.* **2019**, *102*, 2251–2256. [CrossRef]
70. Koval', A.D.; Efremenko, V.G.; Brykov, M.N.; Andrushchenko, M.I.; Kulikovskii, R.A.; Efremenko, A.V. Principles for developing grinding media with increased wear resistance. Part 2. Optimization of Steel Composition to Suit Conditions of Operation of Grinding Media. *J. Frict. Wear* **2012**, *33*, 153–159. [CrossRef]
71. Malinov, L.S.; Malinov, V.L.; Burova, D.V. Impact of Metastable Austenite on the Wear Resistance of Tool Steel. *J. Frict. Wear* **2018**, *39*, 349–353. [CrossRef]

Disclaimer/Publisher's Note: The statements, opinions and data contained in all publications are solely those of the individual author(s) and contributor(s) and not of MDPI and/or the editor(s). MDPI and/or the editor(s) disclaim responsibility for any injury to people or property resulting from any ideas, methods, instructions or products referred to in the content.

materials

MDPI

Article

Development and Implementation of a Defect Detection Model for Microstructures Using Image Processing Methods

Sandra Gajoch [1,*], Dorota Wilk-Kołodziejczyk [1,2,*], Łukasz Marcjan [1], Roberto Corizzo [3], Adam Bitka [2], Marcin Małysza [1,2] and Gerard Skomin [1]

[1] Department of Applied Computer Science and Modelling, Faculty of Metals Engineering and Computer Science, AGH University of Krakow, al. Adama Mickiewicza 30, 30-059 Krakow, Poland; lmarcjan@agh.edu.pl (Ł.M.); gerardskomin@student.agh.edu.pl (G.S.)
[2] Lukasiewicz Research Network-Krakow Institute of Technology, Zakopiańska 73, 30-418 Kraków, Poland; adam.bitka@kit.lukasiewicz.gov.pl (A.B.)
[3] Department of Computer Science (CAS), American University, Don Myers Technology & Innovation Building, 3501 Nebraska Avenue NW, Washington, DC 20016, USA; rcorizzo@american.edu
* Correspondence: sgajoch@agh.edu.pl (S.G.); dwilk@agh.edu.pl or dorota.wilk@kit.lukasiewicz.gov.pl (D.W.-K.)

Abstract

The aim of this research is to develop and implement artificial intelligence models for the automatic detection of defects in the microstructures of austempered ductile iron (ADI). Our research used three different approaches, representing various categories of machine learning tasks: image classification (ResNet), pixel-wise segmentation (UNet), and object detection (YOLO). Each of the models were adapted to the specific characteristics of the dataset and tested on a collection of microstructural images prepared within the scope of the research. The data preparation process included clustering using the k-means method, morphological operations, generation of binary masks, conversion of labels into formats required by each architecture, and data augmentation to increase the diversity of training samples. The results demonstrated that ResNet achieved very high classification accuracy but did not provide spatial information about defect localization. UNet produced precise segmentation masks of martensitic regions, allowing for quantitative analysis of samples, although it required significantly higher computational resources and struggled with detecting very small defects. YOLO, in turn, enabled fast detection of defects in the form of bounding boxes. In summary, each model proved effective in a different context: ResNet for preliminary classification, UNet for detailed laboratory analysis, and YOLO for industrial detection tasks.

Keywords: cast iron; austempered ductile iron; YOLO; ResNet

1. Introduction

Austempered Ductile Iron (ADI) is a special variety of ductile iron that, through appropriate heat treatment, achieves unique mechanical properties, combining high strength, impact strength, and wear resistance with good liquid metal castability and relatively low weight. The material's microstructure is crucial for these properties, and its control is the subject of much research in materials science and production technology. Due to its properties, this material is widely used in sectors such as automotive, railways, defense, agriculture, and construction. The ADI microstructure is created by a two-stage heat treatment: austenitization at 820–950 °C and ausferritization at 250–400 °C for 0.5–4 h [1]. The

result of these processes is a structure called ausferrite, consisting of austenite and ferrite in a "feathered" or "needle-shaped" form. The microstructure of ADI strongly depends on the casting wall thickness, which influences the cooling rate. Thinner walls (e.g., 2–3 mm) result in faster heat dissipation, leading to a greater number of fine graphite inclusions; thicker walls (e.g., 13 mm) result in fewer and larger graphite spheroids. Variable cooling conditions can also influence the presence of undesirable phases. One of the most important microstructural defects in ADI, particularly relevant to this work, is the presence of martensite. Martensite is not a desirable phase in the ADI structure. It can appear in areas where the transformation to ausferrite has not fully occurred—most often due to a mismatch in the aus tempering temperature or time, or due to too rapid a change in cooling conditions [2]. The presence of martensite negatively affects the material properties: it increases hardness at the expense of ductility, causes brittleness and susceptibility to cracking, and can be a source of microcrack initiation and damage propagation under fatigue conditions [3]. From a quality control perspective, rapid and accurate detection of martensite in the ADI microstructure is essential for eliminating defective components and ensuring repeatable production. Detecting defects in engineering materials is a key step in assessing their quality, strength, and suitability for industrial applications. Among the earliest methods used were non-destructive testing (NDT) techniques such as ultrasound, eddy current, magnetic particle testing, and radiography [4]. Artificial intelligence-based methods have also begun to be used to precisely identify defects [5–7]. Microscopic imaging, both optical and electronic (SEM, TEM), has been used in many industrial applications [8]. With the development of microscopy, the need for more efficient analysis of large amounts of image data arose. Initially, micrograph analysis was performed manually by experts. Although precise, this approach is characterized by being time-consuming, subjective, and having limited scalability [9]. Digital image processing methods have been intensively developed, enabling the automation of microstructure analysis. In the early period, classical algorithms for edge detection, segmentation, and mathematical morphology dominated [10]. They were used to classify microstructural phases, locate pores, cracks, or surface heterogeneities. Artificial neural networks (ANNs) began to outperform classical approaches in terms of accuracy and noise immunity [11] for various solutions [12]. Spiking neural networks with an improved pooling layer are also used [13]. Solutions based on convolutional neural networks (CNNs) offer high accuracy, operational speed, and the ability to scale analysis [14]. An approach that initially employs an autonomous recognition framework based on the Reinforced Open Set Algorithm (RAOS) and a feature subnetwork and strategy subnetwork with reinforcement learning and a deep reinforcement learning (DRL) model also yields good results. The created model undertakes a sequential decision-making task to optimize the feature subnetwork and strategy subnetwork [15]. Recent research has also emphasized the use of language models in data analysis [16]. Deep learning is used for the analysis of metal products [17], especially in the analysis of microstructures [18–21]. Basically, artificial intelligence in the context of microstructure analysis can perform three main functions: Classification—assigning an image to one of the classes (e.g., correct microstructure vs. defective) [22]; Segmentation—detecting and marking areas belonging to specific phases or defects (e.g., martensite) [23]; Object detection—locating and marking specific image elements (e.g., pores, microcracks, graphite particles) [24]. The UNet model has been used for precise segmentation of microstructural phases in high-strength steels, achieving high Dice coefficients (>0.9) [25]. The YOLO architecture, as a fast object detection network, finds applications in real-time production line analysis, including in the context of casting quality control [24]. ResNet, thanks to its deep structure and "residual connections" mechanism, is effective in classifying highly complex and low-contrast images, such as metallographic micrographs [26]. In the context of ADI, a particular challenge is the detection of martensite,

which can take various forms and occur in small quantities. For this reason, AI models must be characterized not only by high sensitivity but also by robustness to interference resulting from image non-uniformity, polishing artifacts, and variability of heat treatment parameters. The literature also notes a growing interest in hybrid methods that combine classical image processing techniques (e.g., mathematical morphology, filtering) with AI algorithms, which increases the interpretability of models and facilitates their adaptation to various types of microstructures [14]. Based on literature analysis, it can be concluded that detecting defects in engineering materials, particularly ductile iron (ADI), is an issue of significant practical and research importance. The quality of this material's microstructure largely determines its functional properties, therefore, effective identification of irregularities—such as martensite, porosity, or phase heterogeneity—is a crucial element of the quality control process. Traditional diagnostic techniques, based on non-destructive testing methods and light microscopy, allow for structural assessment but are limited by human factors, time-consuming, and difficult interpretation. In response to these limitations, artificial intelligence-based methods, particularly those utilizing convolutional neural networks, are gaining popularity.

A literature review shows that:

- AI enables the automation of microstructure analysis processes with high accuracy and repeatability,
- Convolutional neural networks such as ResNet, UNet, and YOLO are used in image classification, as well as in the segmentation and detection of microstructural objects,
- Previous research has focused primarily on general phase analysis, pore detection, discontinuities, and the classification of correct/incorrect structures, while the issue of precise automatic martensite detection is relatively rare and remains a research challenge.

This study focuses on microscopic images of materials such as ADI—particularly in the context of detecting subtle, difficult-to-detect structural defects. This work falls within this area. The aim of this study is to compare selected deep learning models (ResNet, UNet, YOLO) for their effectiveness in detecting martensite in the microstructure of ADI cast iron, which may contribute to improving quality control processes in industrial settings. At the same time, there are no effective methods that can be applied to collections of low numbers and limited diversity.

2. Materials and Methods

2.1. Methods

In recent years, we have observed a dynamic development of data analysis methods, in which Artificial Intelligence (AI) plays a central role. AI is becoming a tool that not only supports but increasingly replaces traditional information processing methods, especially where large datasets, subjective interpretation, or the need for high result repeatability are involved [27]. One of the key areas of AI is Machine Learning (ML), with the most advanced form of ML being deep learning based on the structure of artificial neural networks. Thanks to the layered architecture of deep networks, they can independently learn feature representations from raw data, making them particularly effective in image analysis [28,29]. One of the most important applications of AI in the context of this work is Image Processing, which encompasses a range of techniques enabling the analysis, transformation, segmentation, and classification of visual data. In the case of material microstructures, microscopic imaging is the primary source of information about the internal structure of the sample [30]. However, these images, despite their high quality, are complex, susceptible to noise, and often require advanced analytical tools to effectively extract features of interest, such as the presence of structural defects.

In tasks related to image analysis, and particularly in the recognition and localization of microstructural defects, Convolutional Neural Networks (CNNs) are currently the most effective and widely used approach. Their uniqueness stems from the fact that they can automatically learn feature representations from image data, eliminating the need for manual design of information extraction algorithms [31–42]. In this work, three popular architectures representing three approaches to image analysis were selected:

- ResNet (short for Residual Network) is one of the most influential deep neural network architectures, proposed [27]. This model significantly improved image classification performance in the ImageNet competition, and its main innovation was the introduction of so-called residual connections, which allow for training much deeper networks than previously possible [43]. In traditional deep neural networks, increasing the number of layers often led to the gradient vanishing problem—errors computed during backpropagation did not efficiently reach earlier layers, resulting in degraded training quality. ResNet addresses this problem by using residual blocks, which contain a direct connection (so-called skip connection) between the input and output of the block. This allows the model to learn the residual function F(x) = H(x) − x instead of the mapping H(x) directly, which significantly simplifies the optimization process [44]. Each residual block typically contains two or three convolutional layers and an addition operation that connects the original input with the output processed by the network layers. This structure allows for "shortcuts" in information flow, preserving the backscatter signal even with very deep architectures [44]. The original paper proposed several ResNet variants, differing in the number of layers: ResNet-18 and ResNet-34: networks with a shallow structure, with blocks containing two convolutional layers each; recommended for limited data or computational power. ResNet-50, ResNet-101, and ResNet-152: deeper versions that use so-called bottleneck blocks—three-layer blocks (1 × 1—3 × 3—1 × 1), allowing for a reduction in the number of parameters without sacrificing accuracy. In the context of this study, which aims to detect the presence of martensite in microscopic images, it was crucial to select a ResNet version that provides an appropriate compromise between depth, generalization ability, and computational cost. Using very deep variants, such as ResNet-101 or ResNet-152, could lead to overfitting due to the limited size and diversity of the available dataset [45]. On the other hand, too shallow networks (e.g., ResNet-18) may not be flexible enough to capture subtle structural differences between healthy microstructure and regions containing martensite. Therefore, we used ResNet50, an intermediate variant that provides a balance between architectural complexity and its generalization ability. This network contains 50 layers and uses classical residual blocks with two 3 × 3 convolutions, making it deep enough to detect complex patterns in image data, but not so complex that it requires a very large training set or hardware resources [45]. In the present study, ResNet was used to classify fragments of microscopic images as containing or not containing martensite. This architecture serves as a benchmark for more complex segmentation (UNet) and detection (YOLO) models, enabling comparison of results in terms of accuracy, precision, sensitivity, and inference time.
- UNet is a convolutional neural network architecture designed for precise semantic image segmentation, i.e., assigning a label to each input pixel. It was first presented in [23] as a tool for analyzing microscopic images in medicine [46]. Due to its versatility, efficiency, and ability to operate with limited datasets, UNet quickly found applications in many fields, including materials science [47]. The UNet architecture consists of two main parts: a contracting path and an expanding path. The contracting part operates analogously to classical convolutional networks—it consists of successive

convolutional layers and pooling operations that reduce the image dimension while simultaneously increasing the network's perceptual range. The goal of this part is to extract features with increasingly higher levels of abstraction. Then, in the expanding path, the image is successively restored to its original resolution using convolutional transposition operations (so-called upconvolution). At key points in the network, skip connections are used to copy feature maps from the corresponding levels of the shrinking path and connect them to the expansion layers. This allows UNet to combine global information (context) with local information (structure details), significantly improving segmentation quality, especially for fine, irregular structures [48]. UNet was designed for situations where small datasets are available, making it particularly attractive for materials science tasks, where labeled microscopic images are difficult and time-consuming to acquire [46]. The network can learn to effectively locate objects of interest even with a limited number of samples, as demonstrated in numerous publications on the segmentation of grains, pores, and non-metallic inclusions in metal microstructures [47]. In the context of this work, UNet was applied to segment areas containing martensite in microscopic images of ADI cast iron. This detection involves not only classifying the entire image but also pinpointing specific structural fragments where the defect is present. Thanks to its architecture, UNet is ideally suited for this task—it allows for high-precision marking of the contours and area occupied by the defect, even if its occurrence is irregular and localized. The advantage of using UNet is also the possibility of obtaining results in the form of segmentation masks, which can be subjected to further quantitative analysis—e.g., calculation of the area occupied by martensite, its shape, density or distribution relative to other phases. This type of data is extremely valuable in the context of quality control and prediction of mechanical properties of castings [47].

- YOLO (You Only Look Once) is a modern neural network architecture designed for fast object detection in images. Unlike classical approaches that analyze images in stages (e.g., region proposals, classification, localization), YOLO processes images end-to-end, performing detection and classification in a single pass through the network. This approach significantly increases performance and makes the model ideal for tasks requiring real-time operation, such as autonomous driving, monitoring, or industrial inspection [49].

The YOLO architecture divides the input image into a grid (e.g., 13 $\times$ 13 or 19 $\times$ 19 cells), and then predicts for each cell:

- The coordinates of a bounding box;
- The probability of object occurrence;
- The object class [50].

Unlike networks such as ResNet (whole image classification) or UNet (pixel-based segmentation), YOLO focuses on object localization and recognition by pinpointing the location of a fragment of interest and what it represents [50].

Since its inception in [43], the architecture has undergone intensive development. The most popular versions are:

- YOLOv1–v3: initial implementations, increasingly accurate and faster, but limited in localizing small objects.
- YOLOv4 (2020): significant improvement in accuracy thanks to the use of improved components such as CSPDarkNet53, PANet, and Spatial Pyramid Pooling.
- YOLOv5: not part of the official YOLO line, but one of the most commonly used in practice due to its availability, speed, and ease of implementation.

- YOLOv6–YOLOv8: versions based on newer network concepts and improved support for a variety of applications, including segmentation and classification in a single model [51].

Although YOLO was designed for real-time applications, its advantages make it equally useful in tasks where precise object localization within the context of the entire image is essential, not necessarily with maximum pixel detail. This is particularly important in microscopic image analysis, where full defect segmentation is not always necessary, and indicating their position and size is sufficient for further assessment [52].

In this work, YOLO (v7) was used to detect areas containing martensite in the structure of ADI cast iron. Thanks to its ability to rapidly process images and generate multiple location proposals, this model allows for the identification of microscopic fragments containing defects with good spatial precision. This is particularly important in the analysis of large samples, where manual review of entire images by an expert is time-consuming and prone to omissions.

Using YOLO in this context also allows for a comparison of its performance with approaches based on classification (ResNet) and segmentation (UNet), allowing for the assessment of which method is most effective depending on the application—for example, point detection vs. precise surface analysis.

Effective utilization of artificial intelligence methods for analyzing microscopic images requires appropriate preparation of the input data. The quality of the results obtained by deep learning models depends largely on how the images have been pre-processed. Image pre-processing includes a range of operations aimed at improving data quality, normalization, and the extraction of structural and textural information [45,46]. One of the methods used in the analysis of microstructure images is k-means clustering, as it allows for dividing the image into areas with similar characteristics. It can primarily be used to separate individual microstructure phases, such as austenite, ferrite, or martensite, based on differences in pixel intensity or textural properties. This enables the preparation of binary phase masks, which then serve as a starting point for further segmentation processes or quantitative analysis. K-means clustering is also applicable in identifying regions with distinct visual properties, allowing for the automatic isolation of areas of potential defects or material non-uniformities, which can be analyzed in subsequent steps using more advanced methods, such as neural networks [47,48]. Another group of techniques employed in microstructure image analysis are morphological operations (e.g., erosion, combinations of erosion and dilation, distance transforms, and boundary determination operations), which are particularly useful in the context of ADI microstructures for analyzing graphite grains and for cleaning segmentation masks obtained from neural network predictions, e.g., UNet [49]. The last important element of the data preparation process is feature extraction. Although deep learning models, such as ResNet or UNet, learn feature representations independently, utilizing classical extraction methods can support result analysis, improve error diagnosis, or serve as a comparative element [50].

This work utilized three different approaches to the analysis of ADI microstructures classification (ResNet), segmentation (UNet), and object detection (YOLO). Each of these approaches requires an appropriately chosen method of input data representation.

For classification models, such as ResNet, the most common way to prepare data is to assign appropriate class labels to the images. In this case, the input data are the images themselves, which are assigned one label, e.g., the presence or absence of a specific defect (martensite). This approach simplifies the task to binary classification, and the model learns to recognize general patterns indicating the occurrence of a defect. This approach has been widely described in the literature, where CNN models such as ResNet or VGG are trained

on sets of images labeled zero or one to determine the presence or absence of a defect on the entire sample or a fragment thereof [51].

In the case of segmentation models, represented in this work by the UNet architecture, the preparation of binary masks is essential. Binary masks are images of the same resolution as the original input images, where each pixel is labeled with a value of 1 or 0. Pixels with a value of 1 indicate the presence of a defect or phase of interest, while pixels with a value of 0 represent the background or healthy material structure. This approach is commonly used in the literature, especially in the analysis of micrographs, where the detailed localization of defects is critical. The accuracy of the masks largely determines the effectiveness of the segmentation model [25].

For YOLO-type detection models, the input data require labels in the form of bounding boxes. Each defect is described by a set of coordinates defining a rectangle encompassing the defect area and the class of that object. This type of representation allows the model to efficiently learn the localization and classification of defects in images simultaneously. The application of this method is popular in industrial surface defect detection tasks, for example, on steel surfaces or castings, where fast indication of the defect location is important without the need for precise pixel segmentation [52].

It is worth noting that while all the mentioned models are based on convolutional neural networks, the differences in how the input data are prepared significantly impact the effectiveness of the solved problem. Each of these representations has its advantages and limitations. Binary classification is fast but does not specify the localization of defects; segmentation provides detailed spatial information at the cost of greater effort in labeling; while object detection partially combines the advantages of both approaches, allowing for quick and relatively precise localization of defects.

One of the key challenges in applying deep learning methods to the analysis of microscopic images is the limited number of available, labeled data. The goal of data augmentation is not only to increase the data size but also to improve model generalization and robustness to noise, scale variations, rotations, or illumination non-uniformity [53,54]. In the case of binary classification (e.g., ResNet), augmentation primarily serves to increase the diversity of examples with and without the defect. For segmentation (UNet) and detection (YOLO) networks, transformations must be applied in parallel to the images and their corresponding masks or detection frames to maintain semantic consistency [55]. The literature also emphasizes the importance of so-called targeted augmentation, which is adapted to the characteristics of the specific problem. In the context of metallic microstructures, this means, for example, avoiding excessive geometric deformations that could distort the actual phase morphology or incorrectly simulate defects. At the same time, it is suggested to apply augmentation in a controlled manner, considering the proportion of classes in the dataset and their representativeness [55]. In the research, data augmentation was used as one of the supplementary elements in the learning process of the ResNet, UNet, and YOLO models. This allowed for an increase in the effective number of training examples and improved the models' ability to generalize to new, previously unobserved microscopic images.

2.2. Dataset

In the case of ADI microstructure analysis, the source data consists of microscopic images obtained from laboratory tests. For these to be effectively utilized by deep learning models, they must undergo a pre-processing stage, including normalization, segmentation, feature extraction, and the preparation of binary masks and detection frames. An additional supporting step is data augmentation, which allows for increasing the size and diversity of the training set.

The ADI microstructure is created through a two-stage heat treatment:

- Austenitizing at 820–950 °C;
- Isothermal hardening in the range of 250–400 °C for 0.5–4 h [1].

The result of these processes is a structure called ausferrite, consisting of austenite (Figure 1, light areas in the micrograph—C) and ferrite in a "feathered" or "acicular" form (Figure 1, darker areas with shades of gray, beige, and brown—B).

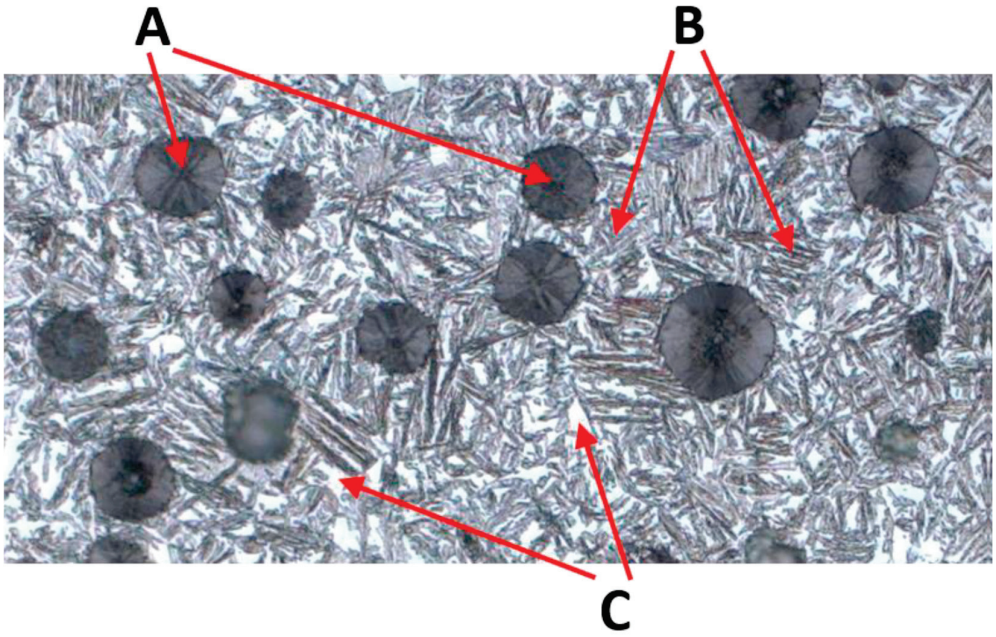


Figure 1. Example of microstructure of ADI cast iron, where: A—graphite, B—ferrite, C—austenite.

Depending on the hardening temperature, a distinction is made between:

- Upper ausferrite (T > 350 °C): higher austenite content, feathery ferrite;
- Lower ausferrite (T < 350 °C): dominance of acicular ferrite, smaller austenite areas [1].

The microstructure of ADI strongly depends on the casting wall thickness, which influences the cooling rate. Thinner walls (e.g., 2–3 mm) result in faster heat dissipation, leading to a greater number of fine graphite inclusions (Figure 1 A); in thicker walls (e.g., 13 mm), fewer and larger graphite nodules are observed. Variable cooling conditions can also influence the presence of undesirable phases. One of the most important microstructural defects in ADI, particularly relevant to this work, is the presence of martensite (Figure 2).

Martensite is not a desirable phase in the ADI structure. It can appear in areas where the transformation to ausferrite has not fully occurred—most often due to a mismatch in temperature or time of isothermal quenching, or due to too rapid a change in cooling conditions [2].

Under light microscopy, martensite has a characteristic, easily recognizable appearance:

- It appears as sharply pointed needles or diamond-shaped precipitates, often forming distinct zigzag structures.
- Color: red, ash-gray, navy blue, or almost black.
- Distribution: It can be dispersed or form clusters within former austenite regions [2].

The presence of martensite has a negative impact on the material's properties:

- It increases hardness at the expense of ductility.
- It causes brittleness and susceptibility to cracking.



Figure 2. Microstructure with visible defects in the form of martensite.

It can be a source of microcrack initiation and damage propagation under fatigue conditions [3]. From a quality control perspective, rapid and accurate detection of martensite in the ADI microstructure is crucial for eliminating defective components and ensuring production repeatability. Traditional micrograph analysis performed by materials science experts is time-consuming and prone to subjective errors. Therefore, the research focused on automating martensite detection using artificial intelligence methods, particularly deep learning models such as CNNs (ResNet, UNet, YOLO), which enable the recognition of microstructural phases based on microstructural elements. In the studied dataset (images of ADI microstructures), the presence of martensite was identified and confirmed based on characteristic image features. Detection of this phase is the main task of the considered convolutional neural network models, whose effectiveness will be compared in the presented studies.

The source material consisted of iron samples with varying wall thicknesses, subjected to a heat treatment process including austenitizing and austempering at different temperatures (100 samples). This made it possible to obtain a wide range of ausferritic structures, including samples containing martensite, which is the key defect analyzed in this work. Sample preparation included the process of polishing and etching the surface, in accordance with adopted metallographic procedures, to reveal the phase structures. Subsequently, images were recorded using an optical microscope (Zeiss, Oberkochen, Germany) at magnifications adjusted for the analysis of the ausferritic phase and microstructural defects. Image recording took place at established lighting parameters to ensure the comparability of the results obtained. The gathered research material included both samples with a structure typical for ADI (upper and lower ausferrite with graphite spheroids) and samples containing defects in the form of martensite and other undesirable elements, such as degraded forms of graphite or artifacts resulting from the preparation process of the polished surface. The presence of martensite was verified based on characteristic microscopic image features, such as needle-like or rhomboidal morphology and dark colors ranging from navy blue to black. The final dataset used in the experiments included both correct samples (defect-free) and samples with visible martensite. This set served as the basis for preparing input data in various formats, tailored to the requirements of the applied models: classification (ResNet), segmentation (UNet), and detection (YOLO).

In the context of ADI microstructures, a particular challenge is the presence of diverse elements, such as graphite spheroids, ferrite and austenite regions, and defects in the form of martensite. These elements can have similar intensity and texture, making their automatic differentiation difficult. Therefore, the use of appropriate pre-processing

techniques allows for the extraction of important image features, which are then utilized by classification, segmentation, and detection models in subsequent stages. The most commonly used steps in data pre-processing include morphological operations, image segmentation and clustering, as well as feature extraction and scale normalization [56–58].

The first stage of data preparation involved dividing large, microscopic images into four fragments. This achieved several effects simultaneously: the size of a single sample was reduced, facilitating further calculations, the number of input data for the models was increased, and convolutional networks were enabled to better capture local features characteristic of the phases under study.

Subsequently, k-means (Figure 3) clustering was applied to the image fragments prepared in this way. The algorithm was implemented in Python using the scikit-learn library, and the result was binary masks saved in the output directory. After obtaining binary masks using k-means clustering, additional cleaning and standardization were necessary. This is because the clustering process, although effective in differentiating individual material phases, also generates minor distortions: isolated pixels, discontinuities within areas, or small empty spaces inside structures. To prepare the data for further analysis and model training, a set of morphological operations was applied, implemented in Python (v3.12) using the OpenCV library (v4.10.0).

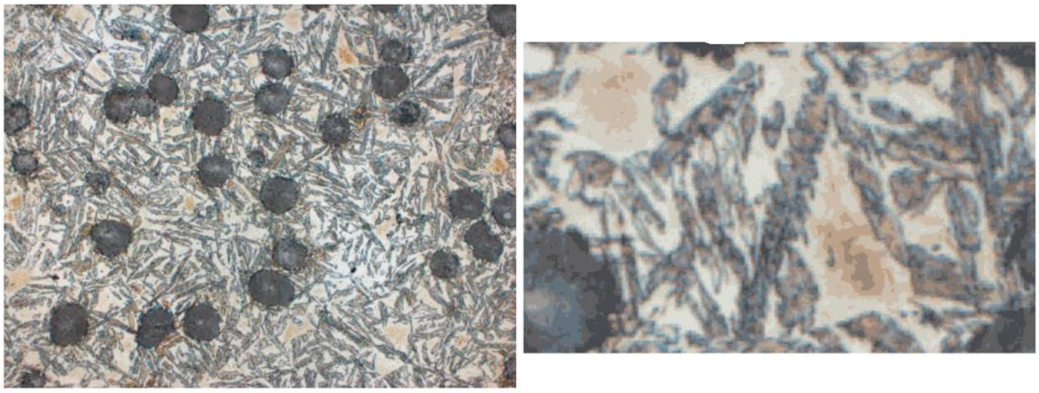


Figure 3. Clustering results for k = 14—original image and clustered, approximated image.

The final stage of data preparation before the model learning process was the augmentation of images and their corresponding binary masks 9, (Figure 4). The augmentation was implemented in Python using the Albumentations library, which offers a wide range of image transformations and, importantly, ensures their simultaneous application to both input images and their corresponding masks. The following transformations were applied: mirror reflections (horizontal and vertical), transposition, random rotations by a multiple of 90°, and Grid Distortion. Thanks to the conducted process, the size of the dataset was significantly increased, which was particularly important when training the UNet and YOLO models. Segmentation and detection networks are sensitive to the diversity of input data, and the limited number of original images could lead to the problem of overfitting. Augmentation allowed for the artificial introduction of image variants with different orientations and local deformations, which translated into greater robustness of the models to data non-uniformity. It is worth noting that the selection of specific augmentation methods and parameters was preceded by a series of experiments. Different combinations of transformations were tested to find a balance between increasing data diversity and maintaining the structural realism of microstructure images and their binary masks. The final set of transformations (Figure 5) ensured both the increase in the dataset and consistency with the actual morphology of martensite.

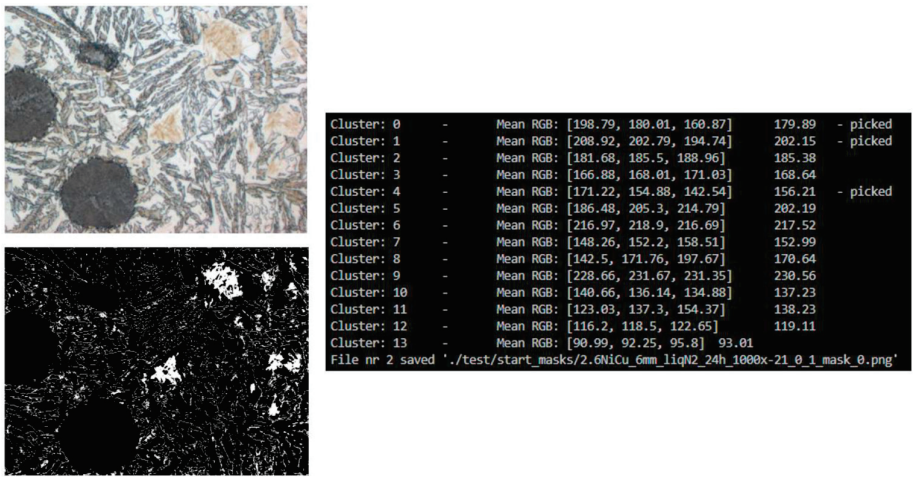


Figure 4. Input image, output code message, and output binary mask.

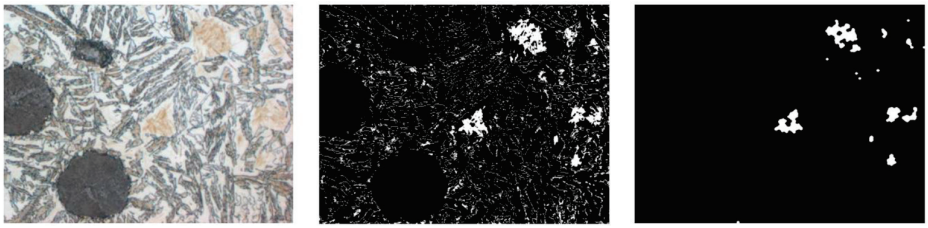


Figure 5. Summary of the results of morphological operations. Original image, binary mask, mask after morphological operations.

2.3. Experiments

After collecting the research material and completing the input data preparation process, the actual experimental part began. Its goal was to implement and compare selected neural network architectures in the context of detecting martensite in ADI microstructures. The applied models represented three different approaches to the problem:

- ResNet—image classification (information about the presence or absence of a defect),
- UNet—semantic segmentation (precise delineation of defect areas),
- YOLO—object detection (localization of defects in the form of bounding boxes).

The research process included several stages: preparation of training, validation, and test sets, implementation of the models in the Python environment using machine learning libraries, and then training the networks with specified hyperparameters. The results of each model were evaluated based on a set of quality metrics adapted to the nature of the task: accuracy, precision, recall, F1-score, IoU, Dice, and mAP.

Experiment Preparation

Before starting the actual model training, it was necessary to prepare the data in a format tailored to the nature of the respective research tasks. After the augmentation stage, additional operations were performed to obtain a consistent and organized set that could be used by classification, segmentation, and detection networks.

The first step was the division of images into fragments of 256 $\times$ 256 pixels. This size was chosen based on the literature, which indicates that smaller image fragments allow convolutional networks to better recognize local features characteristic of individual microstructure phases. The division of large micrographs into regular fragments also had a practical dimension: it increased the size of the set, which reduced the risk of model overfitting, and simultaneously allowed for effective use of GPU memory during training.

An additional advantage of this operation was the removal of the 'edges' of the original images, which contained noise and lower sharpness.

Next, the images were labeled for the occurrence of defects. To do this, for each fragment, it was checked whether an area corresponding to martensite was present in its corresponding binary mask. If pixels marked as a defect were present in the mask, the entire fragment received the label "1" (defect present). Otherwise, the fragment was labeled "0" (no defect). This resulted in a dataset adapted for training the ResNet classifier, where each image was assigned a binary label.

The next step was to separate the training, validation, and test sets. This process was simplified by the prior labeling of images as containing or not containing defects. The division was performed according to the adopted convention, where:

- The training set included the majority of samples and was used to train the models;
- The validation set served as the basis for selecting hyperparameters and monitoring the learning process;
- The test set contained previously unused data and allowed for the final evaluation of model quality.

All data was organized according to an established file and directory naming convention. Uniform naming schemes were used for images and masks, making it possible to automatically pair images with their corresponding masks. Additionally, each part of the set (training, validation, test) was placed in a separate directory, which significantly facilitated the subsequent process of learning and testing the models. The data prepared in this way constituted a complete and organized input set, ready for use in experiments with three different neural network architectures: ResNet, UNet, and YOLO.

3. Results

The general diagram of the developed solution is shown in Figure 6.

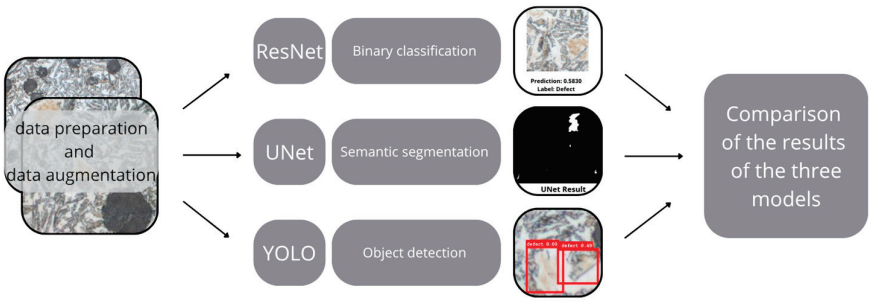


Figure 6. The general diagram of the developed solution.

3.1. ResNet Model Results

The ResNet50 architecture, one of the popular variants of residual networks, was used for the task of classifying microstructure fragments based on the presence of defects in the form of martensite. The model was adapted for binary classification by modifying the output layer to return two classes: "0"—no defect, and "1"—defect present. Alternatively, a deeper variant, ResNet152, was also considered, but due to computational complexity and training time, ResNet50 was ultimately chosen, proving to be a compromise between accuracy and efficiency.

Input images were transformed to a resolution of 256 × 256 pixels, normalized, and converted to a tensor. In the learning process, the CrossEntropyLoss function, which is standard in multi-class classification, and the Adam optimizer, known for effectively combining the advantages of adaptive methods and classical gradient approaches, were used. The learning process was conducted for 20 epochs with a batch size of 16 and

an initial learning rate of 10^{-3}. Mixed precision computations were also used, which allowed for faster training while maintaining numerical stability. After each epoch, the model state was saved in a checkpoint file, enabling the reproduction of results and further experiments.

After the network training was completed, data from the test set was introduced into the model, and the results were observed. Selected results are presented in Figure 7.



Figure 7. Comparison of selected model results.

The obtained results indicate that ResNet50 effectively distinguishes fragments containing defects from those without them. Analysis of the confusion matrix (Figure 8) showed that the model performs very well in the case of clear clusters of martensite, while difficulties arise in images where the defect occurs as small or blurred structures. The model correctly classified 78% of cases, of which 49% were correct recognitions of no defect, and 29% were correct detections of a defect. Errors occur in 11% of cases for both classes. This means that some fragments where the boundary between martensite and the background was indistinct led to incorrect model decisions.

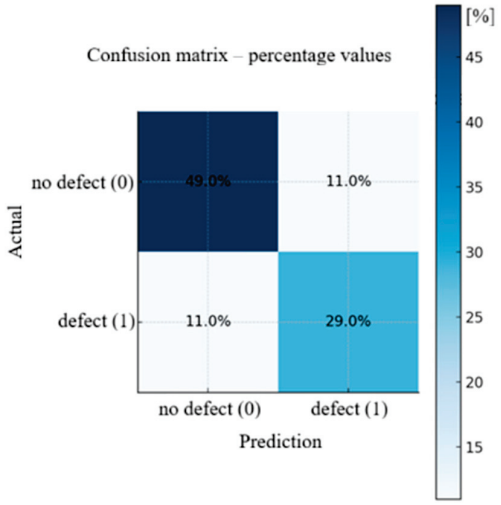


Figure 8. Table of errors in defect presence prediction using the ResNet model.

In summary, ResNet50 is an effective tool for rapid classification of microstructure images, providing simple information about the presence or absence of a defect. Its advantage is high effectiveness and moderate computational requirements, which makes it useful in preliminary analysis tasks. However, the lack of precise defect localization in the image remains a limitation, justifying the application of more complex architectures, such as UNet or YOLO, in the later part of the work.

3.2. UNet Model Results

The UNet architecture with a single output channel (out_channels = 1) was used for the martensite area segmentation task, which corresponds to binary segmentation (defect/background). Input images were scaled to 256 × 256 pixels and normalized, then converted to tensors. Segmentation masks were loaded as binary images and converted to a floating-point type and channel dimension expanded (targets.float().unsqueeze(1)) during the learning phase so that their shape matched the network output. The loss function used was BCEWithLogitsLoss, meaning the network returned raw logits (without the sigmoid function on the last layer), and thresholding to a binary form occurred only at the evaluation stage (typically at a threshold of 0.5). Adam with a learning rate of 10^{-4}, a batch size of 8, and a number of epochs equal to 100 was used for optimization.

Part of the data was allocated for training and part for validation; image-mask pairing was ensured by dedicated loaders (get_loaders), which applied identical geometric transformations (scaling and normalization) to both sets. Commented-out random transformations (rotations, reflections) were left in the code, which were used in the earlier stage of augmenting the entire set; in this specific script, a deterministic validation stage was prioritized. During training, after each epoch, the model checkpoint (weights and optimizer state) was saved, quality metrics were calculated on the validation set (check_accuracy), and example predictions were generated in the form of output images (save_predictions_as_imgs)—this allowed for ongoing control of both numerical values (e.g., IoU, Dice) and the visual quality of the masks. After the network training was completed, data from the test set was introduced into the model, and the results were observed. A selected result is presented in Figure 9.



Figure 9. One of the results of tests with the UNet model test dataset.

After 22 epochs of learning, lasting a total of approximately 19 h, results confirming the effectiveness of martensite segmentation were obtained. Quality indicators for the defect class reached values of IoU ≈ 0.66 and Dice ≈ 0.81, which well reflects the model's ability to precisely capture larger, compact areas of martensite. Difficulties, however, arose in the case of very fine, scattered islands, which were more often overlooked (false negatives) or oversegmented as fragments of defects (false positives). The obtained results confirmed the usefulness of UNet for precise, pixel-level martensite segmentation: the values of the IoU and Dice coefficients remained at a high level for samples where the defect formed clear, continuous areas. Weaker results were observed in cases with very fine, scattered structures or at low-contrast phase boundaries—where the model was susceptible to oversegmentation or underestimation of the defect area. A review of the saved visual results indicates that the inclusion of prior mask cleaning (morphological operations) and consistent data normalization positively influence the stability of learning and the shape of predicted contours. From a practical point of view, UNet provides not only a decision about the presence of a defect but also its location and shape, enabling further quantitative inference (e.g., the area fraction of martensite) and complementing the

ResNet classifier. The main drawback of this solution is the erroneous indication of an area resembling martensite.

3.3. YOLO Model Results

The YOLO (You Only Look Once) architecture, one of the most frequently used neural networks in object localization tasks, was applied for the purpose of defect detection in the form of martensite. This model, unlike ResNet and UNet, does not return binary information or a pixel mask but localizes defects in the form of rectangular bounding boxes along with an assigned class and detection probability. This approach allows for rapid identification of microstructure fragments requiring further analysis.

To prepare the input data, binary masks obtained in earlier stages were utilized. For each image, rectangles surrounding coherent areas of martensite were determined, and then converted to the YOLO format, including the coordinates of the box center, its width and height, and the class label. This process was fully automated and did not require manual labeling.

On the basis of the prepared data, the YOLOv8 network was trained, configured for a single-output problem. The network was trained from scratch, without the use of pre-trained weights, as images of material microstructures do not appear in public datasets. In the configuration, an input image resolution of 256 × 256 pixels, a batch size of 32, a set number of epochs at 80, and a learning rate of 10^{-3} were adopted. The Adam algorithm was used for optimization, and the learning process was conducted on a graphics card utilizing parallel computing. Figure 10 presents an example result of four hours of training the YOLO network model.

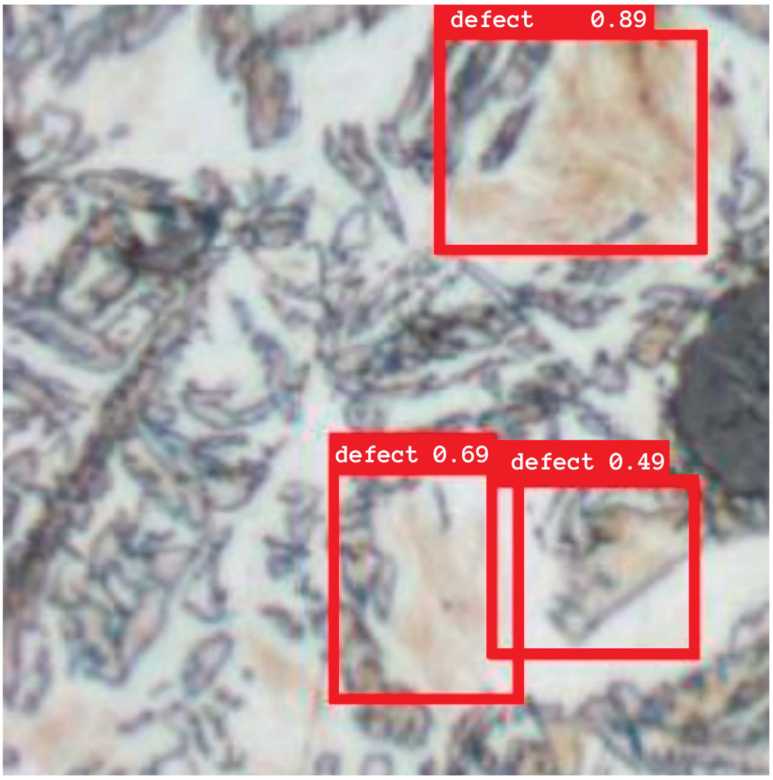


Figure 10. Selected result of the trained YOLOv8 model.

Quality assessment was performed based on standard detection metrics: precision, recall, and mean Average Precision (mAP) calculated at an IoU = 0.5 threshold. The results indicate that YOLO effectively localizes larger clusters of martensite, achieving a high precision value and a relatively small number of false alarms. The model encountered the

greatest difficulties in the case of very fine or scattered defects, which were sometimes underestimated or completely missed. Additional problems included areas of brownish ferrite resembling martensite. A comparison of the YOLO detection boxes with the segmentation masks obtained using UNet confirmed this observation YOLO allows for quick detection of defect locations but with less accuracy in reproducing their shape.

In summary, YOLO proved particularly useful in applications requiring a quick response, such as in preliminary quality control systems. Compared to ResNet and UNet, it provides a compromise between operating time and localization accuracy. Although it does not provide as detailed information as segmentation, it is a valuable complement to the previous approaches and allows for the rapid identification of areas that can then be subjected to more detailed analysis.

3.4. Comparison of Model Results

In this work, three approaches to defect detection in microstructures were applied: image classification of fragments using ResNet, pixel-level segmentation using UNet, and object detection using YOLO. Each model differs in both its mechanism of action and the nature of its results, which translates into their usefulness in different research and practical contexts. Table 1 summarizes the obtained results and their interpretation.

Table 1. Comparison of the results of the three models.

Model	Task	Metrics	Time	Advantages	Limitations
ResNet50	Recognizing the presence of a defect in the image	Accuracy: 78% Precision: 72.5% Recall: 72.5% F1-score: 0.725	20 epochs (~13 h)	Speed of classification, simpler training data preparation	Lack of information about defect location and shape; predictions less certain (0.4–0.6)
UNet	Pixel-by-pixel segmentation of martensite areas	IoU: 0.66 Dice: 0.81	22 epochs (~19 h)	Very good segmentation precision for larger areas, detailed shape reproduction	Difficulties with fine, scattered islands; greater time requirements
YOLOv8	Defect localization via bounding boxes	mAP: 0.83 Precision: 0.86 Recall: 0.74 F1-score: 0.79	80 epochs (~3 h)	Very fast prediction (0.02–0.03 s/image), effective detection of larger defects	Worse detection of the smallest structures, boxes do not accurately reflect shapes

Analyzing the results, it can be observed that ResNet is the most computationally efficient solution and performs very well in quickly detecting whether a given fragment contains a defect or not. This makes it a tool for preliminary classification of large image sets, but its biggest limitation is the lack of spatial information. In practice, this means that the model can indicate the presence of martensite but will not show its distribution or size.

In turn, UNet allows for pixel-level segmentation, which provides the most accurate image of the defect: its shape, area, and location. This is extremely important in laboratory analyses, as it enables the quantitative estimation of the martensite fraction in the sample. High IoU and Dice values indicate a high consistency between the predicted and actual masks. The disadvantage of UNet is the longer training and prediction time, as well as difficulties in detecting very fine or blurred structures, which are sometimes treated as noise.

The YOLO model represents a compromise between the two methods above. It operates significantly faster than UNet, while providing more information than ResNet, as it indicates the approximate location of the defect in the form of a bounding box. The mAP values obtained show that YOLO handles larger clusters of martensite well, but struggles with correctly capturing small, irregular islands. Its advantage is the very fast

prediction time, making it a suitable candidate for applications in quality control systems in near-real-time.

4. Discussion

Comparing the models, it can be observed that each fulfills a different role:

- ResNet is best suited for the quick classification of large image sets and filtering out defect-free fragments.
- UNet is effective in precise laboratory analysis, where accurate information about the defect's shape and size is important.
- YOLO provides high-time efficiency and reliable defect localization, making it attractive for industrial applications.

From an engineering practice and materials research perspective, it can therefore be concluded that a hybrid approach yields the best results: ResNet as a preliminary filter, YOLO for quick defect localization, and UNet for detailed analysis of its shape and size. Such a combination of methods could form the basis for a comprehensive system for automated microstructure assessment.

The results obtained from the conducted experiments indicate the high effectiveness of the applied methods in the task of detecting defects in ADI microstructures, with each of the utilized architectures playing a different role and being characterized by different limitations. It is worthwhile to compare these with the results presented in the literature to better situate the conducted research in a broader scientific context.

In the case of image classification using ResNet, the observations of authors of earlier works were confirmed, indicating that residual networks perform well with images of materials with complex texture [e.g., applications in weld analysis or detection of surface defects in metals]. The high accuracy obtained in the experiment is consistent with reported values in the literature, although it should be emphasized that ResNet does not allow for indicating the defect location, which may be insufficient in many industrial applications. Thus, ResNet is primarily effective as a tool for preliminary classification or filtering of large image sets.

The application of UNet for binary segmentation of martensite allowed for obtaining qualitative and quantitative results comparable to those presented by other researchers in microstructure segmentation tasks. The literature emphasizes that UNet is one of the most frequently chosen architectures for material analysis, partly due to its ability to accurately reproduce object contours. This feature was also confirmed in this work IoU and Dice values reached high levels, and visual comparison of the masks indicates a high consistency with the reference data. Difficulties arose, however, in the case of very fine or scattered defects, which is consistent with the reports of other authors who point to UNet's problems in capturing objects with a small area and low contrast.

The YOLO architecture, although less frequently used in strictly materials literature than in medical image analysis or industrial vision systems, also confirmed its usefulness in the defect detection task. Similar to other publications, YOLO proved to be very fast and effective in detecting larger objects but had a tendency to miss fine structures. The mAP results obtained in the experiment fall within the range reported in the literature for tasks of similar complexity, although it should be noted that in this work, the network was trained from scratch without using pre-trained weights, which may have influenced the final accuracy.

The comparison of the three approaches shows that there is no single universal method that best solves the problem of martensite detection. Each model proves effective in a different context: ResNet—in quick classification, UNet—in precise laboratory analysis, and YOLO—in applications requiring immediate defect detection. Such conclusions are

consistent with the trend visible in the literature, where the need to combine different methods and create hybrid systems is increasingly emphasized.

Ultimately, it can be stated that the presented research confirms the current state of knowledge regarding the use of deep learning methods for material microstructure analysis, and simultaneously indicates directions for further development primarily in the area of increasing the accuracy of detecting fine defects and incorporating newer neural network architectures, such as models based on attention mechanisms (vision transformers).

5. Conclusions

The most important result of the work was the development and implementation of three distinct approaches to defect detection in ADI ductile iron microstructures: image classification (ResNet), pixel-level segmentation (UNet), and object detection (YOLO). The comparison of the results obtained by the individual models allowed for a comprehensive assessment of their usefulness in martensite analysis, indicating both their strengths and limitations. Key achievements include:

- The preparation of an original dataset including microstructure images along with their corresponding binary masks and detection labels. This process involved division of large images into smaller fragments, application of k-means clustering, morphological operations, and data augmentation, which ensured an adequate number and diversity of samples;
- The implementation of three neural network architectures adapted to the specifics of the task: ResNet as a binary classifier, UNet as a segmentator, and YOLO for the detection of rectangular bounding boxes;
- Conducting the full process of learning and validation using the Python environment and deep learning libraries, including hyperparameter selection, saving model checkpoints, and monitoring result quality in successive epochs;
- The qualitative and quantitative analysis of the obtained results based on a set of metrics (accuracy, precision, recall, F1-score, IoU, Dice, mAP), which allowed for a reliable comparison of the effectiveness of the individual approaches;
- The identification of potential practical applications: ResNet as a fast preliminary classifier, UNet as a tool for detailed laboratory analysis, and YOLO as a method for rapid detection in the context of industrial control.

The realized research confirmed the effectiveness of deep neural networks in the analysis of material microstructures and represents a step towards automating the defect detection process, which until now required significant involvement of specialists and subjective microscopic evaluation.

The main limitation was the size and nature of the dataset. ADI microstructure images were obtained under laboratory conditions, and although the dataset was supplemented with an augmentation process, its size remains small in comparison to popular datasets used in deep learning. This limits the possibility of fully utilizing the potential of large models, such as ResNet152 or more complex YOLO variants. Additionally, the lack of publicly available datasets with similar characteristics prevents the use of fully effective transfer learning. A second limitation is the difficulty in detecting very small and irregular defects. UNet, despite high-quality segmentation, had a tendency to miss fine martensite islands, and YOLO tended to treat them as noise and not include them in the detection boxes. This is a problem commonly described in the literature, resulting from both architectural limitations and insufficient representation of such cases in the dataset. Another limiting factor is the time-consuming nature of the data preparation process. Although the process was fully automated, it includes several stages (k-means clustering, morphological

operations, mask creation, YOLO label generation), which in the case of large industrial datasets may require further optimization and simplification.

In conclusion, although the presented approaches provided promising results, further research development towards expanding datasets, implementing newer models, and integrating methods has the potential to significantly increase the effectiveness and usefulness of automatic microstructure analysis systems in industrial and scientific practice.

Author Contributions: Conceptualization, S.G., D.W.-K. and R.C.; Methodology, S.G. and D.W.-K.; Software, Ł.M. and G.S.; Validation, D.W.-K., Ł.M. and M.M.; Formal analysis, S.G. and M.M.; Resources, A.B.; Data curation, A.B.; Writing—original draft, G.S.; Supervision, D.W.-K. and R.C.; Project administration, D.W.-K.; Funding acquisition, D.W.-K. All authors have read and agreed to the published version of the manuscript.

Funding: This work was supported by the IDUB AGH (Excellence Initiative—Research UniversityAGH "Inicjatywa Doskonałości—Uczelnia Badawcza AGH") [Project number: IDUB 15135] and [15137].

Data Availability Statement: The data that support the findings of this study are available on request from the corresponding author, [D.W.-K. and S.G.]. The data are not publicly available due to the database requires a lot of financial resources and is the subject of an as yet unpublished doctoral dissertation.

Conflicts of Interest: The authors declare no conflicts of interest.

References

1. Krawiec, H.; Lelito, J.; Mróz, M.; Radoń, M. Influence of Heat Treatment Parameters of Austempered Ductile Iron on the Microstructure, Corrosion and Tribological Properties. *Materials* **2023**, *16*, 4107. [CrossRef]
2. Polishetty, A.; Pan, B.; Pasang, T.; Littlefair, G. Microstructural Study on Strain Induced Transformation in Austempered Ductile Iron Using Heat Tinting. In Proceedings of the ASME 2010 International Manufacturing Science and Engineering Conference, Erie, PA, USA, 12–15 October 2010; Volume 1, pp. 239–245. [CrossRef]
3. Górny, M.; Tyrała, E. Effect of cooling rate on microstructure and mechanical properties of thin-walled ductile iron castings. *J. Mater. Eng. Perform.* **2013**, *22*, 300–305. [CrossRef]
4. Silva, M.I.; Malitckii, E.; Santos, T.G.; Vilaça, P. Review of conventional and advanced non-destructive testing techniques for detection and characterization of small-scale defects. *Prog. Mater. Sci.* **2023**, *138*, 101155. [CrossRef]
5. Jia, Y.; Chen, G.; Zhao, L. Defect detection of photovoltaic modules based on improved Varifocal Net. *Sci. Rep.* **2024**, *14*, 15170. [CrossRef] [PubMed]
6. Huang, Z.; Zhang, C.; Ge, L.; Chen, Z.; Lu, K.; Wu, C. Joining Spatial Deformable Convolution and a Dense Feature Pyramid for Surface Defect Detection. *IEEE Trans. Instrum. Meas.* **2024**, *73*, 5012614. [CrossRef]
7. Shao, R.; Zhou, M.; Li, M.; Han, D.; Li, G. TD-Net:tiny defect detection network for industrial products. *Complex Intell. Syst.* **2024**, *10*, 3943–3954. [CrossRef]
8. Dehaerne, E.; Dey, B.; Blanco, V.; Davis, J. Scanning electron microscopy-based automatic defect inspection for semiconductor manufacturing: A systematic review. *J. Micro/Nanopatterning Mater. Metrol.* **2025**, *24*, 020901. [CrossRef]
9. AI Image Evaluation, vs. Manual Microstructure Analysis—Advantages and Disadvantages. Available online: https://mivia.ai/en/2024/01/ki-bildauswertung-vs-manuelle-mikrostrukturanalyse-vor-und-nachteile/ (accessed on 23 October 2025).
10. Campbell, A.; Murray, P.; Yakushina, E.; Marshall, S.; Ion, W. New methods for automatic quantification of microstructural features using digital image processing. *Mater. Des.* **2018**, *141*, 395–406. [CrossRef]
11. Bai, J.; Wu, D.; Shelley, T.; Schubel, P.; Twine, D.; Russell, J.; Zeng, X.; Zhang, J. A Comprehensive Survey on Machine Learning Driven Material Defect Detection. *ACM Comput. Surv.* **2025**, *57*, 275. [CrossRef]
12. Liu, Q.; Liu, M.; Wang, C.; Wu, Q.M.J. An efficient CNN-based detector for photovoltaic module cells defect detection in electroluminescence images. *Sol. Energy* **2024**, *267*, 112245. [CrossRef]
13. Wang, Z.; Li, S.; Xuan, J.; Shi, T. Biologically inspired compound defect detection using a spiking neural network with continuous time–frequency gradients. *Adv. Eng. Inform.* **2025**, *65*, 103132. [CrossRef]
14. Ferguson, M.; Ak, R.; Lee, Y.-T.T.; Law, K.H. Detection and Segmentation of Manufacturing Defects with Convolutional Neural Networks and Transfer Learning. Smart Sustain. *Manuf. Syst.* **2018**, *2*, 137–164. [CrossRef]

15. Wang, Z.; Xuan, J.; Shi, T. An autonomous recognition framework based on reinforced adversarial open set algorithm for compound fault of mechanical equipment. *Mech. Syst. Signal Process.* **2024**, *219*, 111596. [CrossRef]
16. Peng, C.; Peng, J.; Wang, Z.; Wang, Z.; Chen, J.; Xuan, J.; Shi, T. Adaptive fault diagnosis of railway vehicle on-board controller with large language models. *Appl. Soft Comput.* **2025**, *16*, 113919. [CrossRef]
17. Nowroth, C.; Gu, T.; Grajczak, J.; Nothdurft, S.; Twiefel, J.; Hermsdorf, J.; Kaierle, S.; Wallaschek, J. Deep Learning-Based Weld Contour and Defect Detection from Micrographs of Laser Beam Welded Semi-Finished Products. *Appl. Sci.* **2022**, *12*, 4645. [CrossRef]
18. Zhao, J.; Shen, C.; Huang, M.; Qi, Y.; Chai, Y.; Zheng, S. Deep learning accelerated micrograph-based porosity defect quantification in additively manufactured steels for uncovering a generic process-defect-properties relation. *Mater. Charact.* **2025**, *225*, 115094. [CrossRef]
19. Nithin, A.M.; Perumal, M.; Davidson, M.J.; Srinivas, M.; Rao, C.S.P.; Harikrishna, K.; Jagtap, J.; Bhowmik, A.; Santhosh, A.J. Segmentation Studies on Al-Si-Mg Metallographic Images Using Various Different Deep Learning Algorithms and Loss Functions. *Eng. Rep.* **2025**, *7*, e70119. [CrossRef]
20. Wang, Y.; Wei, X.; Wang, C.; Xu, W. Physical Metallurgy-Guided Machine Learning for Strength-Plasticity Optimization in Aluminum Alloys. *Mater. Today Commun.* **2025**, *49*, 113970. [CrossRef]
21. Müller, M.; Stiefel, M.; Bachmann, B.-I.; Britz, D.; Mücklich, F. Overview: Machine Learning for Segmentation and Classification of Complex Steel Microstructures. *Metals* **2024**, *14*, 553. [CrossRef]
22. DeCost, B.L.; Lei, B.; Francis, T.; Holm, E.A. High Throughput Quantitative Metallography for Complex Microstructures Using Deep Learning: A Case Study in Ultrahigh Carbon Steel. *Microsc. Microanal.* **2019**, *25*, 21–29. [CrossRef]
23. Ronneberger, O.; Fischer, P.; Brox, T. U-Net: Convolutional Networks for Biomedical Image Segmentation. Lecture Notes in Computer Science (including subseries Lecture Notes in Artificial Intelligence and Lecture Notes in Bioinformatics). In Proceedings of the Medical Image Computing and Computer-Assisted Intervention, Munich, Germany, 5–9 October 2015; Volume 9351, pp. 234–241. [CrossRef]
24. Liu, Y.; Liu, Y.; Guo, X.; Ling, X.; Geng, Q. Metal surface defect detection using SLF-YOLO enhanced YOLOv8 model. *Sci. Rep.* **2025**, *15*, 11105. [CrossRef]
25. Biswas, M.; Pramanik, R.; Sen, S.; Sinitca, A.; Kaplun, D.; Sarkar, R. Microstructural segmentation using a union of attention guided U-Net models with different color transformed images. *Sci. Rep.* **2023**, *13*, 5737. [CrossRef]
26. He, K.; Zhang, X.; Ren, S.; Sun, J. Deep residual learning for image recognition. In Proceedings of the IEEE Computer Society Conference on Computer Vision and Pattern Recognition, Las Vegas, NV, USA, 26 June–1 July 2016; pp. 770–778. [CrossRef]
27. The Impact of AI on the Engineering Field | JHU EP. Available online: https://ep.jhu.edu/news/the-impact-of-ai-on-the-engineering-field/ (accessed on 23 October 2025).
28. What Is Machine Learning? Definition, Types, Tools & More | DataCamp. Available online: https://www.datacamp.com/blog/what-is-machine-learning (accessed on 23 October 2025).
29. An Overview of Deep Learning for Image Processing—Christian Garbin's Personal Blog. Available online: https://cgarbin.github.io/deep-learning-for-image-processing-overview/ (accessed on 23 October 2025).
30. Ge, M.; Su, F.; Zhao, Z.; Su, D. Deep learning analysis on microscopic imaging in materials science. *Mater Today Nano* **2020**, *11*, 100087. [CrossRef]
31. Tu, S.; Vo, P. Microstructural Feature Extraction by a Convolutional Neural Network for Cold Spray of Aluminum Alloys. *J. Therm. Spray Technol.* **2024**, *33*, 540–550. [CrossRef]
32. Gea, M.N.; Wanayumini, W.; Rosnelly, R. Impact of Hyperparameter Tuning on CNN-Based Algorithm for MRI Brain Tumor Classification. *J. Tek. Inform.* **2025**, *18*, 87–100. [CrossRef]
33. Han, Y.; Li, R.; Yang, S.; Chen, Q.; Wang, B.; Liu, Y. Center-environment feature models for materials image segmentation based on machine learning. *Sci. Rep.* **2022**, *12*, 12960. [CrossRef]
34. Wankhade, N.; Sale, V.; Yadav, R.; Jikar, P.; Gadgekar, S.; Dhokey, N. Metallurgical microstructure classification using CNN: A comprehensive study on heat treatment analysis for steel. *Mater. Today Proc.* **2024**, in press. [CrossRef]
35. Convolutional Neural Networks: A Complete Guide | Medium. Available online: https://medium.com/@alejandro.itoaramendia/convolutional-neural-networks-cnns-a-complete-guide-a803534a1930 (accessed on 23 October 2025).
36. Convolutional Neural Networks (CNNs) and Layer Types—PyImageSearch. Available online: https://pyimagesearch.com/2021/05/14/convolutional-neural-networks-cnns-and-layer-types/ (accessed on 23 October 2025).
37. Pehlivanoğlu, M.K.; İnCe, I.; Kından, B.A.; Eker, A.G.; Doğan, İ. Towards advanced brain tumor segmentation: A novel hybrid architecture integrating UNet, FCN, and YOLO models on the newly introduced BTS-DS 2024 dataset. *Eur. Phys. J. Spec. Top.* **2025**, *234*, 4421–4435. [CrossRef]
38. Saxena, A. An Introduction to Convolutional Neural Networks. *Int. J. Res. Appl. Sci. Eng. Technol.* **2022**, *10*, 943–947. [CrossRef]
39. Choudhary, K.; DeCost, B.; Chen, C.; Jain, A.; Tavazza, F.; Cohn, R.; Park, C.W.; Choudhary, A.; Agrawal, A.; Billinge, S.J.L.; et al. Recent advances and applications of deep learning methods in materials science. *NPJ Comput. Mater.* **2022**, *8*, 59. [CrossRef]

40. He, K.; Zhang, X.; Ren, S.; Sun, J. Identity mappings in deep residual networks. Lecture Notes in Computer Science (including subseries Lecture Notes in Artificial Intelligence and Lecture Notes in Bioinformatics). In Proceedings of the Computer Vision—ECCV 2016, Amsterdam, The Netherlands, 11–14 October 2016; 9908 LNCS. pp. 630–645. [CrossRef]
41. Gebhardt, C.; Trimborn, T.; Weber, F.; Bezold, A.; Broeckmann, C.; Herty, M. Simplified ResNet approach for data driven prediction of microstructure-fatigue relationship. *Mech. Mater.* **2020**, *151*, 103625. [CrossRef]
42. Medghalchi, S.; Kortmann, J.; Lee, S.-H.; Karimi, E.; Kerzel, U.; Korte-Kerzel, S. Automated segmentation of large image datasets using artificial intelligence for microstructure characterisation and damage analysis. *Mater. Des.* **2024**, *243*, 113031. [CrossRef]
43. Redmon, J.; Divvala, S.; Girshick, R.; Farhadi, A. You Only Look Once: Unified, Real-Time Object Detection. In Proceedings of the 2016 IEEE Conference on Computer Vision and Pattern Recognition (CVPR), Las Vegas, NV, USA, 27–30 June 2016; pp. 779–788. [CrossRef]
44. Terven, J.; Córdova-Esparza, D.-M.; Romero-González, J.-A. A Comprehensive Review of YOLO Architectures in Computer Vision: From YOLOv1 to YOLOv8 and YOLO-NAS. Mach. *Learn. Knowl. Extr.* **2023**, *5*, 1680–1716. [CrossRef]
45. Salvi, M.; Acharya, U.R.; Molinari, F.; Meiburger, K.M. The impact of pre- and post-image processing techniques on deep learning frameworks: A comprehensive review for digital pathology image analysis. *Comput. Biol. Med.* **2021**, *128*, 104129. [CrossRef]
46. Luengo, J.; Moreno, R.; Sevillano, I.; Charte, D.; Peláez-Vegas, A.; Fernández-Moreno, M.; Mesejo, P.; Herrera, F. A tutorial on the segmentation of metallographic images: Taxonomy, new MetalDAM dataset, deep learning-based ensemble model, experimental analysis and challenges. *Inf. Fusion* **2022**, *78*, 232–253. [CrossRef]
47. Dhanachandra, N.; Manglem, K.; Chanu, Y.J. Image Segmentation Using K -means Clustering Algorithm and Subtractive Clustering Algorithm. *Procedia Comput. Sci.* **2015**, *54*, 764–771. [CrossRef]
48. Shi, C.; Wei, B.; Wei, S.; Wang, W.; Liu, H.; Liu, J. A quantitative discriminant method of elbow point for the optimal number of clusters in clustering algorithm. *EURASIP J. Wirel. Commun. Netw.* **2021**, *2021*, 31. [CrossRef]
49. Goyal, M. Morphological image processing. *Int. J. Comput. Sci. Technol.* **2011**, *2*, 161–165. Available online: https://www.ijcst.com/vol24/1/megha.pdf (accessed on 10 September 2025).
50. Webel, J.; Gola, J.; Britz, D.; Mücklich, F. A new analysis approach based on Haralick texture features for the characterization of microstructure on the example of low-alloy steels. *Mater. Charact.* **2018**, *144*, 584–596. [CrossRef]
51. Feng, X.; Gao, X.; Luo, L. A ResNet50-Based Method for Classifying Surface Defects in Hot-Rolled Strip Steel. *Mathematics* **2021**, *9*, 2359. [CrossRef]
52. Yang, D.; Cui, Y.; Yu, Z.; Yuan, H. Deep Learning Based Steel Pipe Weld Defect Detection. *Appl. Artif. Intell.* **2021**, *35*, 1237–1249. [CrossRef]
53. Ma, B.; Wei, X.; Liu, C.; Ban, X.; Huang, H.; Wang, H.; Xue, W.; Wu, S.; Gao, M.; Shen, Q.; et al. Data augmentation in microscopic images for material data mining. *NPJ Comput. Mater.* **2020**, *6*, 125. [CrossRef]
54. Ma, J.; Hu, C.; Zhou, P.; Jin, F.; Wang, X.; Huang, H. Review of Image Augmentation Used in Deep Learning-Based Material Microscopic Image Segmentation. *Appl. Sci.* **2023**, *13*, 6478. [CrossRef]
55. Li, W.; Yang, L.; Peng, G.; Pang, G.; Yu, Z.; Zhu, X. An effective microscopic image augmentation approach. *Sci. Rep.* **2025**, *15*, 10247. [CrossRef]
56. Şengöz, N.; Yïğ İt, T.; Özmen, Ö.; Isik, A.H. Importance of Preprocessing in Histopathology Image Classification Using Deep Convolutional Neural Network. *Adv. Artif. Intell. Res.* **2022**, *2*, 1–6. [CrossRef]
57. Zhang, J.; Li, C.; Rahaman, M.; Yao, Y.; Ma, P.; Zhang, J.; Zhao, X.; Jiang, T.; Grzegorzek, M. A comprehensive review of image analysis methods for microorganism counting: From classical image processing to deep learning approaches. *Artif. Intell. Rev.* **2021**, *55*, 2875–2944. [CrossRef]
58. Kato, S.; Hotta, K. Automatic Preprocessing and Ensemble Learning for Low Quality Cell Image Segmentation. *arXiv* **2021**, arXiv:210813118.

Disclaimer/Publisher's Note: The statements, opinions and data contained in all publications are solely those of the individual author(s) and contributor(s) and not of MDPI and/or the editor(s). MDPI and/or the editor(s) disclaim responsibility for any injury to people or property resulting from any ideas, methods, instructions or products referred to in the content.

materials

MDPI

Article

Evaluating the Appropriateness of Selected Foundry Sands for the Casting of Reactor Housings: A Study Based on Physicochemical Characterization Outcomes

Paweł Gara [1], Ewa Wisła-Walsh [1] and Tomasz Bajda [2,*]

[1] Faculty of Mechanical Engineering and Robotics, AGH University of Krakow, al. A. Mickiewicza 30, 30-059 Krakow, Poland; pgara@agh.edu.pl (P.G.); wisla@agh.edu.pl (E.W.-W.)
[2] Faculty of Geology, Geophysics and Environmental Protection, AGH University of Krakow, al. A. Mickiewicza 30, 30-059 Krakow, Poland
* Correspondence: bajda@agh.edu.pl

Abstract: In the case of desulfurization and spheroization of cast iron using the in-mold method, in which the treated cast iron is poured into the reaction chamber and placed in the casting mold, the mineral raw material of the mold should support these processes. Therefore, it is important to know the physicochemical properties of the materials selected for the production of casting molds and to learn about the phenomena occurring during their pouring. The research presented in this paper was carried out on quartz, magnesite, chromite, and olivine sands. The results not only provide a comprehensive understanding of these materials but also have significant implications for reactor housing casting. Two of the three tested quartz sands meet all the standards, allowing quartz raw materials to be foundry sands. Marked by the authors of this work, P11 sand, which is classified as 1K grade by the seller, does not meet the requirements of the Polish standard PN-85/H-11001 for this grade and should be classified as 2K grade. At the same time, attention was drawn to relatively considerable weight losses at 1350 °C for the tested quartz raw materials. More significant losses on ignition were found for magnesite sand than the value permitted by the Polish standard, which should be associated with the fact that derivatographic tests were carried out in an oxidizing atmosphere. In the analysis made for olivine sand, the obtained data indicated that the magnesium content is slightly below the requirements of the relevant standard; on the contrary, the iron content exceeds the standard requirements. Analytical data obtained for chromite sand indicated that it meets the PN-91/H-11007 standard regarding chemical composition, but X-ray diffraction tests showed that the tested sample is not chromite but magnesiochromite. The results of grain size distribution, chemical composition, X-ray diffraction, SEM/EDS, and TG/TG presented in this paper show that before starting the production of a specific molding mixture, each time most of the parameters characterizing sand used should be controlled because the properties may differ from the manufacturer's declaration.

Keywords: spheroidization; physicochemical properties; thermal analysis; quartz sands

1. Introduction

The primary product of cast iron smelting in cupolas is gray cast iron, which does not require additional processes before, during, or after smelting [1–3]. However, for cast irons with enhanced mechanical properties, like vermicular and nodular cast iron, the transformation of flake graphite into spheroidal graphite is necessary [4,5]. The spheroidization

process is efficient when the sulfur content in cast iron is approximately 0.02%, requiring sulfur reduction before spheroidization [6].

In current methods, molten cast iron is treated for desulfurization and spheroidization outside the casting mold, and then the refined cast iron is poured into molds [7,8]. These processes are typically conducted in a casting ladle using the "wire" method or with specific additives, followed by pouring the cast iron into the molds [9–12]. The time between metallurgical treatment and casting can range from several to over ten minutes, during which the metal settles and reaction products separate from the bath.

In contrast, the in-mold method [13,14] involves spheroidization or vermicularization in a reaction chamber inside the mold. All metallurgical reactions occur when the liquid metal is poured into the mold, with processes lasting from about 8 to 20 s. These rapid reactions occur not only in the reactor but also within the gating system and mold cavity, meaning the mold material can influence the process [15,16]. Consequently, the properties of foundry sands used in molding support these reactions.

The term "sands" in the foundry industry (in analogy to mineralogy) denotes a number of natural (mineral) and synthetic materials with a grain size of 0.05 to 2.0 mm, which meet certain strength and thermal criteria at high temperatures (up to about 1450 °C) [17–20]. Natural sands include quartz, olivine, chromite, and zircon, while synthetic options include magnesite and corundum [17,19,21]. The sand selected must have the appropriate grain size, shape, chemical composition, and binder content depending on the casting size, material, and technique [22–24].

The following requirements are the chemical composition and the content of natural binders [25–29]. An equally important parameter that determines the possibility of using specific sand to make a mold is the value of the pH parameter, affecting the possibility of using a specific binder [17].

The most common molds used to manufacture iron alloy castings are quartz sands (SiO_2) with a specific granulometric composition and acceptable amounts of contamination with chemical compounds that affect their fire resistance and pH value, mainly due to the price. Materials such as bentonite are used as the grain matrix binder, and in the case of chemically or thermally bonded sands, inorganic (e.g., hydrous sodium silicate) and organic (e.g., synthetic resins) binders are applied. The main technological requirement for molding sands obtained from these materials is having appropriate strength and filtration properties, determined by the permeability coefficient value, called permeability [17,29]. SiO_2 (chemically quartz sand) forms two polymorphs: high-temperature α, which changes into the β form when cooled at 573 °C. The β-quartz is the main component of naturally occurring quartz sands. As the heating proceeds, α-quartz changes into tridymite (870 °C) and then into cristobalite, and at the temperature of 1470 °C, the process of sand melting and its glass transition begin. Polymorphic transformations of quartz accompanying its heating cause a decrease in its density and, consequently, an increase in the grain volume [30]. This is a disadvantageous phenomenon in foundry engineering and may cause the formation of defects such as "scabs", "lines", and "scars" [31,32]. The increase in grain volume is partially compensated for by shrinkage (up to about 15%) of the added hydrated binder (clay) [17]. Furthermore, quartz sands can transition into cristobalite at 1050 °C rather than tridymite, leading to varied thermal expansion [31].

If using silica sands as a matrix of molding sand is impossible, magnesite sands are used [16,17]. Magnesite sands are burnt-sintered (firing temperature from 1450 to 1850 °C) magnesites (magnesium carbonates), i.e., magnesium oxide (periclase) [16]. After firing, the obtained material is sieved to the specified particle size distribution. According to the Polish Standard PN-67/68-04 [28], Mg-P1 magnesite sand should contain at least 80% magnesium oxide, MgO, and Mg-P2 sand, and at least 72% MgO [28]. Additionally, when

using magnesite sand in foundry engineering, it is required that the content of calcium oxide CaO must not exceed 3.5%, and the SiO_2 content should not exceed 7% [28]. Binding materials (binders) for magnesia sands may be clay, water glass, ethyl silicate, or other neutral or alkaline materials. The typical binders for magnesite sands include water glass and other neutral or alkaline materials, as acid-hardened resins are incompatible [16].

Olivine sands are preferred for their superior thermal properties compared to quartz sands, although their high pH makes them less compatible with acid-hardened organic binders [22–27]. Olivine sands are most often obtained from olivine rich in forsterite, Mg_2SiO_4. In the composition of the olivine used in the foundry industry, the ratio of forsterite to fayalite (Fe_2SiO_4) is 9:1, MgO content is not lower than 49%, bound SiO_2 content is not higher than 42%, and the content of impurities (Fe_2O_3 + Al_2O_3 + TiO_2) is not higher than 1% [17]. The grains of olivine used in the foundry are sharp-edged, and the average grain size, dL, is 0.1–0.3 mm. The most common binders for olivine sands are bentonites, starch binders, isocyanate-hardened alkyd resins, water glass, and novolak-type resins [17,26,33].

Chromite sands, consisting of chrome spinels like $FeCr_2O_4$, are used for their low and uniform thermal expansion, high thermal conductivity, and resistance to metal oxides and slags [17]. Chromite sands must contain more than 44% Cr_2O_3 and maintain low levels of SiO_2 to meet foundry standards [27]. However, their high pH and cost limit their use in some technologies. The average grain size for treated chromite sands, dL, is usually 0.2 to 0.25 mm, and their shape is usually angular. In Poland, the properties of chromite sands for applications in the foundry are regulated by the Polish Standard PN-91/H-11007 [27], according to which three types of chromite sands are distinguished in terms of graining. The pH value of chromite sand, as in the case of olivine sands, prevents many binders in molding sands, limiting its use in many technologies. Another limitation of the use of chromite sands is their high price.

Molding sand is used in the foundry industry to prepare molds during metal casting. Its properties improve the casting metal's quality. When adequate sand is used, casting faults that may occur during the mold preparation and casting are considerably reduced.

This work aims to evaluate the appropriateness of selected foundry sands (quartz, magnesite, chromite, and olivine) for casting reactor housings, focusing on their physicochemical properties. The aim is to assess the compatibility of these sands with casting processes, such as desulfurization and spheroidization, by analyzing their chemical composition, grain size distribution, and thermal behavior. The results of this study will help determine whether the selected sands meet the required standards for foundry use and highlight any deviations from these standards, thereby guiding future foundry material selection.

In current industrial practices, molding materials are typically chosen based on manufacturer specifications, with limited verification of their actual properties. However, discrepancies between declared and actual sand properties, such as grain size distribution, chemical composition, and thermal behavior, can significantly impact their performance. This mismatch often leads to defects like slag inclusions, surface scabs, and dimensional instability in the final castings. Furthermore, the role of molding sand properties in supporting key metallurgical processes, such as sulfur reduction and graphite spheroidization, remains underexplored in the context of reactor housings.

This study addresses these knowledge gaps by systematically characterizing the physicochemical properties of the selected sands using advanced techniques, including XRD, SEM-EDS, and TG/DTG analysis. By correlating these properties with their performance in high-temperature applications, this research comprehensively explains their suitability for foundry use. The findings contribute to developing improved quality control

practices and offer actionable insights for optimizing sand selection, ultimately enhancing casting efficiency and product quality.

2. Materials and Methods

In this study, the sands are classified using the Polish Standard PN-85/H-11001 [27] for silica sands and similar standards for non-silica sands. This classification includes the following terms:

- Grade: refers to the sand's quality based on compliance with specific chemical and physical parameters, such as binder content, grain composition, and impurities.
- Group: denotes the granulometric characteristics of the sand, such as fine, medium, or coarse grains, determined through sieve analysis or laser diffraction methods.
- Class: represents the sand's suitability for specific foundry applications, combining parameters like thermal stability, chemical purity, and mechanical strength.

2.1. Preparation of the Test Material

The physical and chemical properties of molding sands were tested for two samples of commercial quartz sands (sands P-3, P-12) and glass sand P-11. In the case of the latter sand, the preparation for testing consisted of sifting the fraction of the tested sand to meet the requirements for the grain size distribution of silica sands according to the Polish Standard PN-85/H-11001 [27]. The tested magnesite, chromite, and olivine sands are also commercial sands. Before starting the tests, the collected samples were dried at 110 °C for 3 h.

2.2. Grain Size Distribution

Measurements of the particle size and particle size distribution of the materials tested were carried out by the laser diffraction method on a Malvern Mastersizer 2000 (Malvern, Worcestershire, UK) apparatus. The measurements were performed in distilled water, with a refractive index of 1.33, as a dispersion liquid. The samples were treated with ultrasound at approximately the maximum power for 4 min. The ultrasound was derived from an ultrasound probe with a maximum power of 300 W. Malvern Mastersizer 2000 had a measurement uncertainty of ±1 μm for the reported particle sizes, with a detection range of 0.05 to 2000 μm. Mie theory was adopted to calculate the particle size.

2.3. Chemical Composition

The elemental composition of the investigated sands was determined by energy-dispersive X-ray fluorescence (XRF) using an Epsilon 3 Panalytical spectrometer (PANalytical, Almelo, Netherlands). The tests were conducted at a range of Na-Am on an apparatus equipped with a lamp with a 9W Rh, 50 kV, and 1 mA anode. The wavelength-dispersive X-ray fluorescence analysis had a detection limit of 0.01 wt.% for most major oxides. These uncertainties are based on calibration with certified reference materials (CRMs). XRF was utilized for elemental analysis due to its high accuracy for multi-element samples, particularly for foundry sands where chemical composition is critical. This is critical for assessing compliance with foundry standards (e.g., Polish standards PN-85/H-11001 [27] and PN-91/H-11007 [29]).

2.4. Phase Composition

The mineral composition of all materials was determined by X-ray diffraction (XRD) using X'pert (Panalytical, Malvern, UK) with a PW 3020 goniometer, CuKα radiation, and a graphite monochromator. The analysis was carried out within the angle range of 5–65° (2 Theta). XRD analysis was conducted with a measurement uncertainty of ±1% for phase

identification. The instrument's detection limit for minor phases was approximately 1% by weight, depending on the sample matrix. Panalytical X'PertHighscore software (High Score Plus v. 4.1) was used to process the diffraction data. The identification of mineral phases in the materials under study was based on the PDF-2 Release 2010 database formalized by the ICDD.

The morphological forms, microstructure, and chemical composition of the tested foundry sands were determined using a scanning electron microscope (SEM) FEI Quanta 200 FEG (FEI, Hillsboro, OR, USA) equipped with a system of chemical composition analysis based on energy-dispersive spectrometry (EDS) X-ray/EDS from the EDAX company (EDAX Inc., Mahwah, NJ, USA). SEM/EDS analysis examined the sands' surface morphology, grain shape, and microstructural features. This method identifies surface irregularities affecting binding properties and permeability in molding sands. SEM-EDS also provides elemental distribution, which is critical for evaluating impurities such as Fe, Al, or Cr that can alter the sand's refractory behavior.

The thermal analysis (TG/DTG/DTA) was performed on a Jupiter STA 449 F3 Netzsch coupled with a quadrupole mass spectrometer, Aeolos QMS 403C. Fifty milligrams of an air-dried sample were heated from 25 °C to 1350 °C in an alumina crucible at 30 °C per minute in flowing (40 m L^{-1} min^{-1}) synthetic air. TG had a sensitivity of 0.01 mg, and the temperature measurement uncertainty was ±1 °C. Detection of phase transitions was accurate within ±2 °C. Thermal analysis is critical for understanding thermal stability, loss on ignition, and phase transitions in sands, especially during heating. These properties influence the sand's thermal shock resistance and dimensional stability under casting conditions.

3. Results

3.1. Silica Sands

3.1.1. Grain Size Distribution and Physicochemical Properties

Figure 1 shows the particle size distribution for samples P-3, P-11, and P-12. The results suggest that P-12 has the most uniform particle size distribution among the three samples, with a higher concentration of particles around a specific size range. In contrast, P-3 and P-11 have broader distributions, with P-11 skewed towards smaller particle sizes.

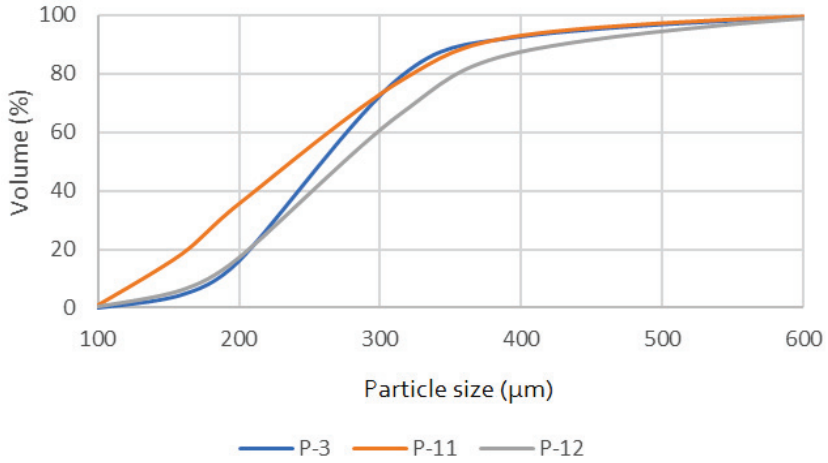


Figure 1. Particle size distribution for the tested quartz sands.

Table 1 presents statistical data and classification of the sands by the Polish Standard PN-85/H-11001 [27].

Table 1. Statistical data on the particle size distribution of silica sands.

Silica Sand Parameters	P-3	P-11	P-12
Sand grain group	Medium	Fine	Coarse
Homogeneity index (%)	88.01	76.59	82.84
Average grain size (μm)	60	230	270
Average humidity (%)	0.2	0.02	0.08
Binder content (%)	1.9	0.16	0.11
Grade acc. PN-85/H-11001 [27]	4K	2K	1K

The data in Table 1 show that in terms of particle size, the tested quartz sand samples meet the requirements of the Polish Standard PN-85/H-11001 [27]. However, P-11 sand was classified as 2K due to the homogeneity index (share of the most frequently represented fractions in the sieve analysis in relation to the total sample), which does not fit into the 80% required for the first category sands.

The data presented in Table 2 indicate that P-3 sand is practically pure silica. However, the content of the natural binder determined therein is inconsistent with the requirements of the Polish Standard PN-85/H-11001 [27]. The chemical analysis results (Table 3), in conjunction with their particle size distribution (Table 1), enable the classification of P-3 sand to the 4K grade.

Table 2. List of selected parameters for quartz sands.

Parameter	P-3	P-11	P-12
pH	7.07	7.08	7.10
SiO_2 (%)	99.40	98.88	96.81
Al_2O_3 (%)	0.21	0.81	1.44
Fe_2O_3 (%)	0.03	0.10	0.16
Carbonates (%)	0.23	0.15	0.17
LOI (%)	0.30	0.21	0.37

Table 3. Mass losses during heating of the P-3, P-11, and P-12 samples, based on the TG curve.

Temperature Range [°C]	P-3	P-11	P-12
	Mass Losses [%]		
25–100	0.16	0.05	0.03
100–600	0.90	0.57	0.66
100–1000	1.79	1.18	1.32
100–1350	2.44	1.64	1.81
750–850	0.23	0.15	0.17

As mentioned above, the high binder content disqualifies the sand from being included in the first three categories (for which the permissible binder content is 0.5%, 1%, and 1.5%, respectively). P-11 sand was classified as second-grade fine sand (2K) because it meets the requirements for this group of sands by the requirements of the Polish Standard PN-85/H-11001. In turn, sand P-12 meets all the requirements in the standard mentioned above. Therefore, it can be classified into the first group of quartz sands.

3.1.2. XRD

The results of the XRD analysis presented in Figures 2–4 indicate that the major peaks observed in samples P-3 and P-11 are consistent with the typical reflections of quartz, indicating that quartz is the dominant mineral phase. The intensity and sharpness of the peaks suggest that the quartz in this sample is well crystallized. The XRD pattern of sample P-12 (Figure 5) is similar to those of P-3 and P-11, with prominent peaks corresponding to

quartz. This sample also exhibits sharp, intense peaks, indicating high crystallinity. The consistency in peak positions with the other samples confirms that quartz is a major phase in P-12, with potential minor contributions from feldspars and plagioclase as indicated by any secondary peaks.

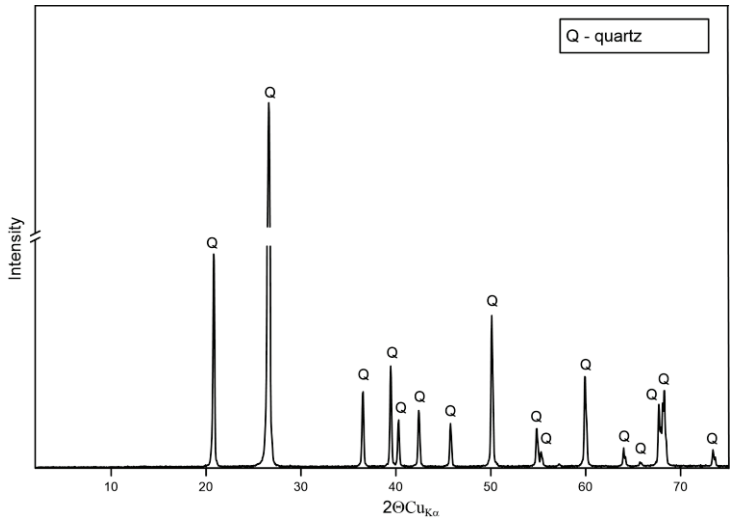


Figure 2. XRD pattern of sample P-3.

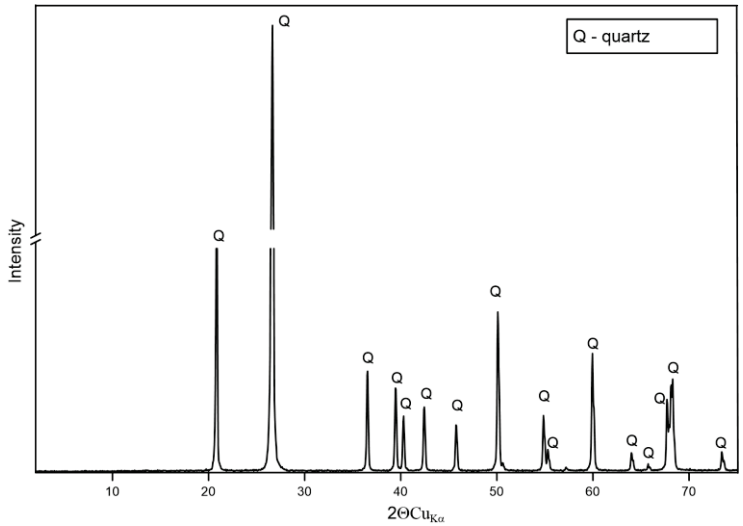


Figure 3. XRD pattern of sample P-11.

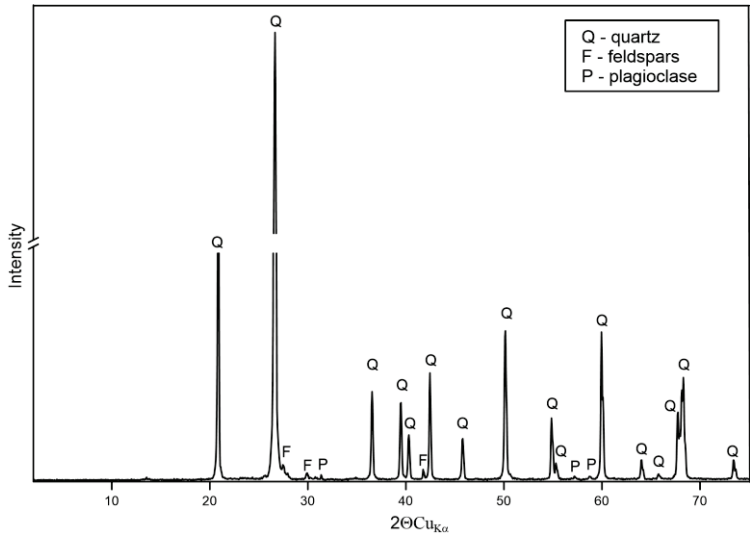


Figure 4. XRD pattern of sample P-12.

3.1.3. SEM-EDS

The analysis results for samples P-3, P-11, and P-12 are presented in Figures 5–7.

The results of the SEM analyses of quartz sands presented above verified that most of the available sands in southern Poland are of river origin. Therefore, their grains were rounded during transport, and their surface was mechanically "grooved". The SEM images of sample P-3 (Figure 5a) reveal a relatively uniform particle size with angular and irregular shapes typical of quartz sands. The surface texture (Figure 5b,c) appears slightly rough, which could indicate mechanical weathering processes. The particles exhibit sharp edges, suggesting minimal transportation. The EDS analysis shows (Figure 5d) a dominant peak for silicon (Si) and oxygen (O), consistent with the composition of quartz (SiO_2).

The SEM images of sample P-11 (Figure 6a) also display quartz particles with angular shapes, but there is a noticeable difference in particle size distribution compared to P-3. The particles in P-11 seem more varied in size, with some larger grains visible. The surface texture appears smoother (Figure 6b,c) than in P-3, possibly due to different depositional environments. Similar to P-3, the EDS spectrum for P-11 shows strong peaks for silicon and oxygen (Figure 6d), confirming the quartz composition.

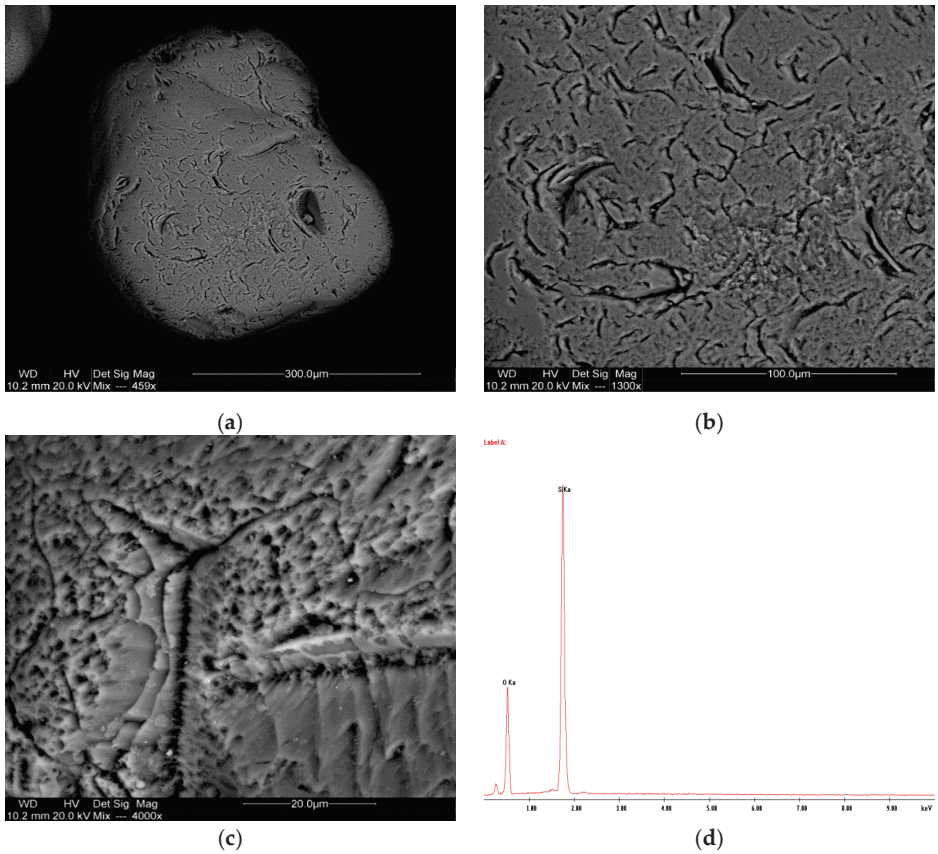


Figure 5. SEM images (**a**–**c**) and EDS spectrum (**d**) of the P-3 sample.

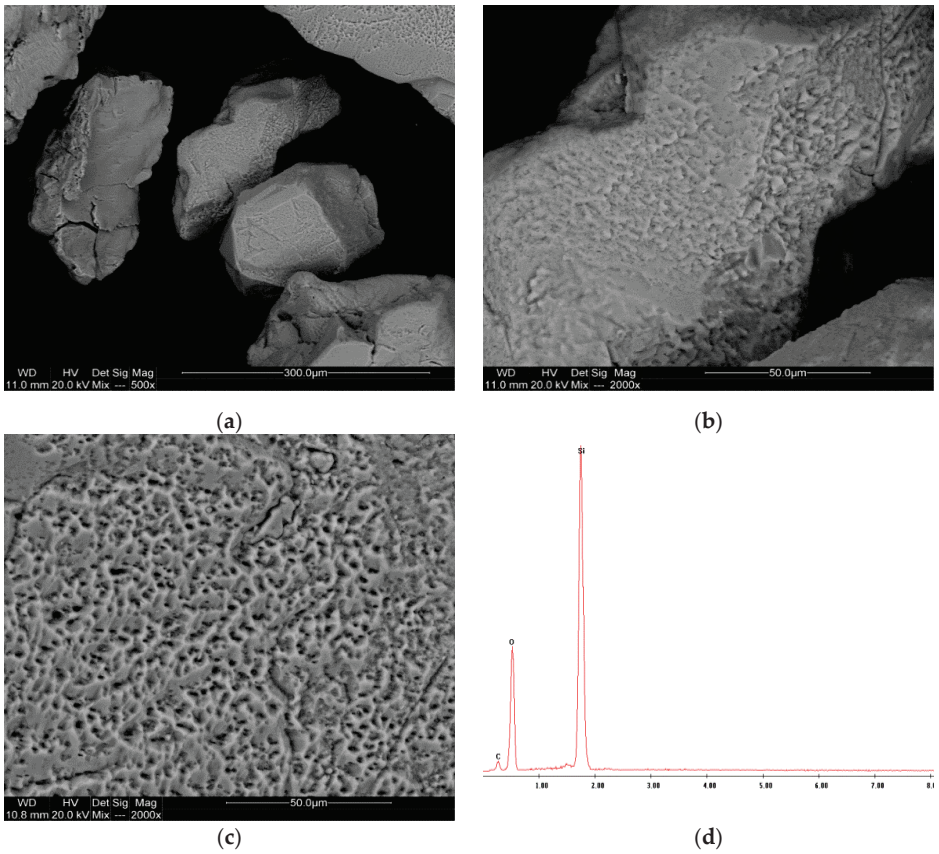


Figure 6. SEM images (**a**–**c**) and EDS spectrum (**d**) of the P-11 sample.

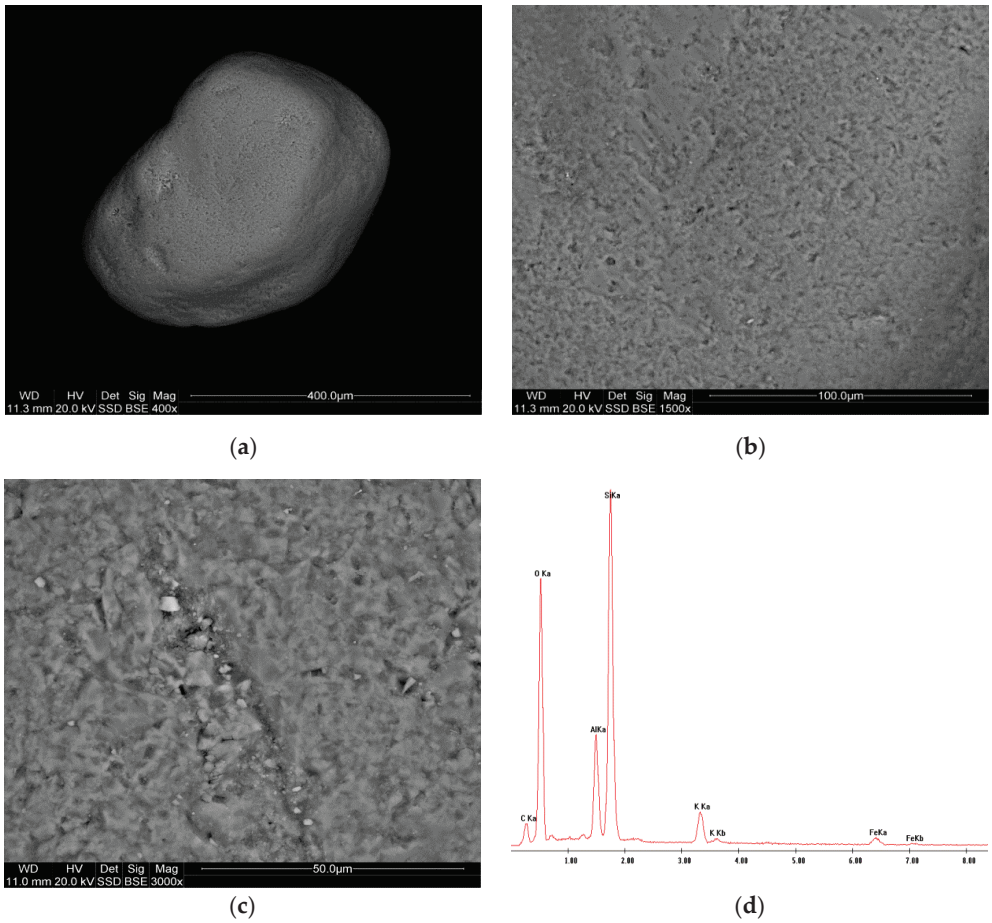


Figure 7. SEM images (**a**–**c**) and EDS spectrum (**d**) of the P-12 sample.

The image for sample P-12 (Figure 7a) indicates a more homogeneous particle size distribution, with particles generally smaller and more rounded than in P-3 and P-11. The particles' roundness and smooth surface texture (Figure 7b,c) suggest that this sample has undergone more significant transportation or weathering processes. The EDS spectrum for P-12 (Figure 7d) shows Si and O as the predominant elements, consistent with quartz. The spectrum also reveals the presence of impurities (Figure 7d), with the presence of Al, K, and Fe, as confirmed by the presence of feldspars and plagioclase identified by XRD.

3.1.4. TG/DTG

Figures 8–10 represent the thermal effects during P-3, P-11, and P-12 analysis. An endothermic peak accompanies the TG-curve mass loss on the DTA curves at about 570 °C, which is responsible for the transformation of α-quartz into β-quartz. The DTA curves slope monotonically to about 1100 °C, passing through a slight maximum at about 1200 °C. A possible explanation for such a course of the DTA curve for the P-3 quartz sand is the direct transition of β-quartz into β-cristobalite [30,31]. The course of the TG/DTG/DTA curves presented in Figures 8–10 and the data obtained on their basis, presented in Table 4, indicate that the P-11 and P-12 sands behave similarly to the P-3 sand, except that at a temperature of about 900 °C an inflection appears on the DTA curve rather than a pronounced peak.

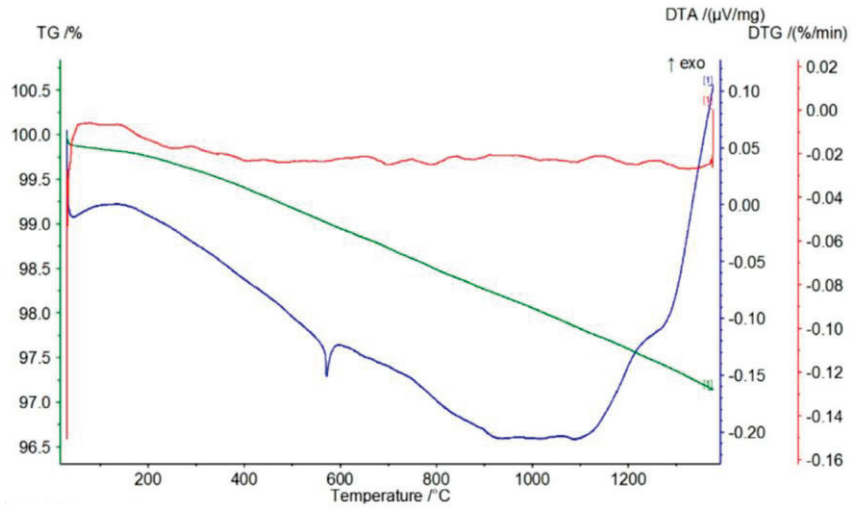


Figure 8. Thermal curves of sample P-3: TG curve (green), DTG curve (red), DTA curve (blue).

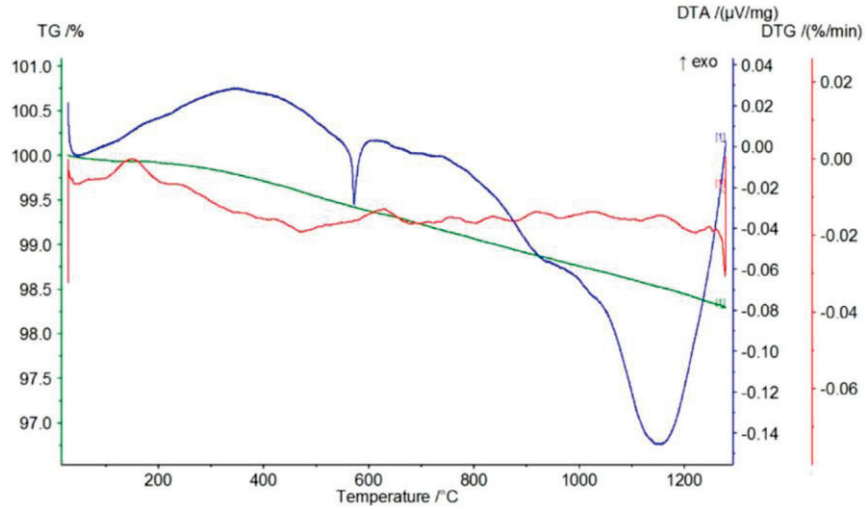


Figure 9. Thermal curves of sample P-11: TG curve (green), DTG curve (red), DTA curve (blue).

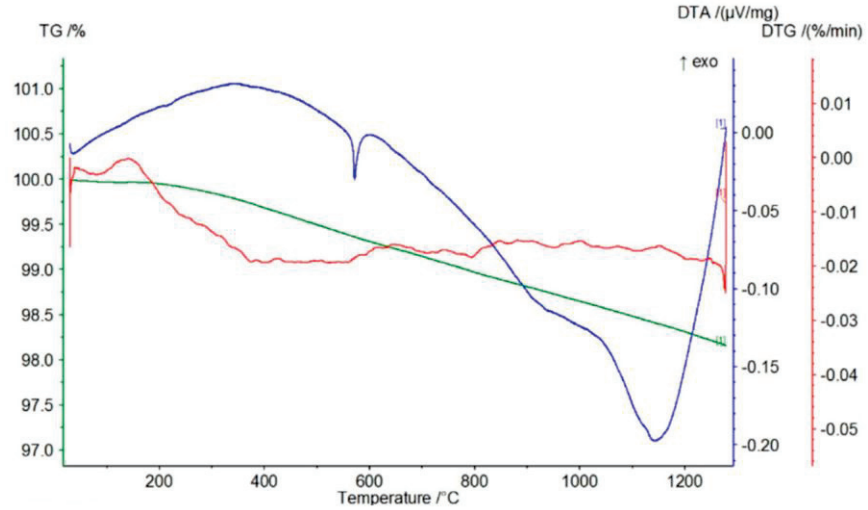


Figure 10. Thermal curves of sample P-12: TG curve (green), DTG curve (red), DTA curve (blue).

Table 4. Statistical data on the particle size distribution of non-silica sands.

Non-Silica Sand Parameters	P-4 Magnesite	P-5 Chromite	P-7 Olivine
Sand grain group	Coarse	Coarse	Fine
Homogeneity index (%)	93.74	90.36	97.06
Average grain size (μm)	320	300	240
Average humidity (%)	0.07	0.03	0.04
Binder content (%)	0.83	0.80	0.46
Grade acc. PN-85/H-11001 [27]	3K	3K	1K

The effect of the parameters of a given sand was studied at 1300 °C, revealing that deviations from standard requirements for sand grain size and composition lead to significant issues in mold performance. For instance, grains that do not conform to the required granulometric composition or exhibit excessive impurities may cause irregular thermal expansion. This inconsistency can create internal stresses within the mold, leading to cracking during the casting process. Furthermore, non-standard sand grains can contribute to surface defects in the final casting, such as scabs, scars, or inclusions. These defects compromise not only the aesthetic quality of the casting but also its mechanical properties and reliability, particularly in high-precision applications such as reactor housing production.

3.2. Non-Silica Sands

3.2.1. Grain Size Distribution and Physicochemical Properties

Figure 11 presents the particle size distribution for samples P-4 (magnesite sand), P-5 (chromite sand), and P-7 (olivine sand). The magnesite sample exhibits a broad particle size distribution. Most particles fall within the 200 to 400 μm range, with a significant proportion of particles above 300 μm. This indicates that the magnesite sand is relatively coarse-grained compared to the other samples. The chromite sand shows a more narrowly distributed particle size, with most particles ranging between 100 and 300 μm. The olivine sand presents a distribution curve similar to that of chromite but with a slightly broader range. Most particles are distributed between 100 and 400 μm, indicating a slightly coarser grain size than chromite. Table 4 presents statistical data and classification of these sands by the Polish Standard PN-85/H-11001 [27].

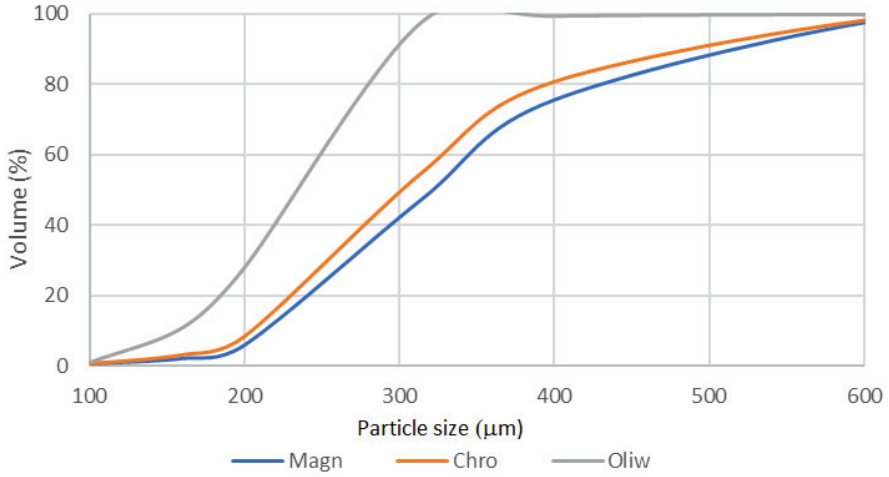


Figure 11. Particle size distribution for tested sands: P-4 magnesite, P-5 chromite, P-7 olivine.

Sieve analysis for magnesite sand shows that it meets the requirements of PN-85/H-11001) [27] regarding the grain size. Chromite sand was assigned to the grain group corresponding to coarse sand based on sieve analysis [27]. The results obtained for the

sand P7-olivine allowed it to be classified into the grain group "fine" and grade 1K. The qualification was made by the Polish Standard PN-85/H-11001 [8] for quartz sands because there is no Polish standard for olivine sands.

The data in Table 5 reveal that the P-4 magnesite sand shows higher losses on ignition than the value allowed by the standard [27]. This should be related, on the one hand, to the storage method of the tested sand and, on the other hand, to the fact that derivatographic tests were carried out in the air.

Table 5. List of selected parameters for non-silica sands.

Parameter	P-4	P-5	P-7
pH	12.25	10.21	10.52
Humidity (%)	0.07	0.03	0.04
SiO_2 (%)	0.36	0.65	43.20
Al_2O_3 (%)	0.15	13.79	0.90
Fe_2O_3 (%)	0.44	23.47	8.55
Cr_2O_3 (%)	0.02	55.47	0.63
MgO (%)	98.17	6.83	45.72
CaO (%)	0.88	0.04	1.24
LOI (%)	1.20	1.96	0.19

In the case of chromite sand P-5, the above data indicate that during heating, there is no loss of mass but an increase, which is confirmed by TG and XRD analysis and which should be associated with the fact that the tested sand is not pure chromite but chromite with an admixture of magnesia chromite. In turn, the data in Table 6 indicate that the magnesium content in olivine (P-7) is only slightly lower than the requirements of the relevant standard [27]. On the contrary, the iron content quite significantly exceeds these requirements.

Table 6. Mass losses during heating of the P-4, P-5, and P-7 samples, based on the TG curve.

Temperature Range [°C]	P-4	P-5	P-7
	Mass Losses [%]		
25–100	0.19	0.07	0.28
100–1000	2.53	0.16	3.06
1000–1350	3.42	0.82	3.08

The measured values of the pH parameter for the tested non-quartz sands are within the limits of this parameter given in the subject literature and indicate that they are alkaline, which excludes several organic binders, especially those hardened with acids.

The results for the tested non-quartz sands in Table 5 show that magnesite, chromite, and olivine sands meet the relevant standards for foundry sands. The examined sample of magnesite sand, despite meeting the criteria specified in the Polish standard [27] in terms of its particle size distribution, was classified into the 3rd grade of sand due to the presence of a binder in an amount exceeding, as shown in Table 4, the limit for grade 2 sand, amounting to 0.5%. Based on sieve analysis, chromite sand was assigned to the grain grade corresponding to coarse sand. However, due to the high binder content, the sand obtained the 3K grade according to the Polish Standard PN-91/H-11007 [27]. The results of the grain size distribution measurements for the P7-olivine OSF sand allowed it to be classified into the "fine" grain group and the 1K grade [28].

3.2.2. XRD

The XRD patterns for the non-silica sands, specifically magnesite (P-4), chromite (P-5), and olivine (P-7), reveal their mineral composition. The XRD analysis shows (Figure 12)

that the dominant phase in magnesite sand is magnesium oxide (MgO), commonly referred to as periclase. The diffractogram exhibits characteristic peaks of periclase, confirming the purity of the sample. The crystallinity of the magnesite sand is high, as indicated by the sharpness and intensity of the peaks.

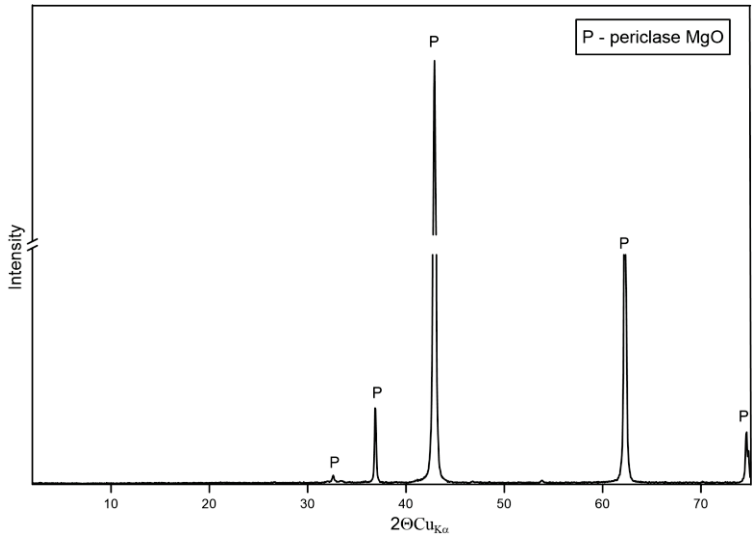


Figure 12. XRD pattern of sample P-4.

The chromite sand sample predominantly contains magnesiochromite ($MgCr_2O_4$) (Figure 13). The XRD pattern indicates that while magnesiochromite is the main mineral phase, there are slight peak shifts when compared to standard magnesiochromite, suggesting the presence of a mixed-phase structure, likely due to the incorporation of iron (Fe) and aluminum (Al) in the crystal lattice. Considering the content of Fe and Al in this sample, it should be assumed that it is not pure magnesiochromite but rather a phase with the composition $(Mg,Fe)(Cr,Al)_2O_4$. This is further supported by the SEM/EDS results, which show some amounts of Fe and Al within the magnesiochromite structure.

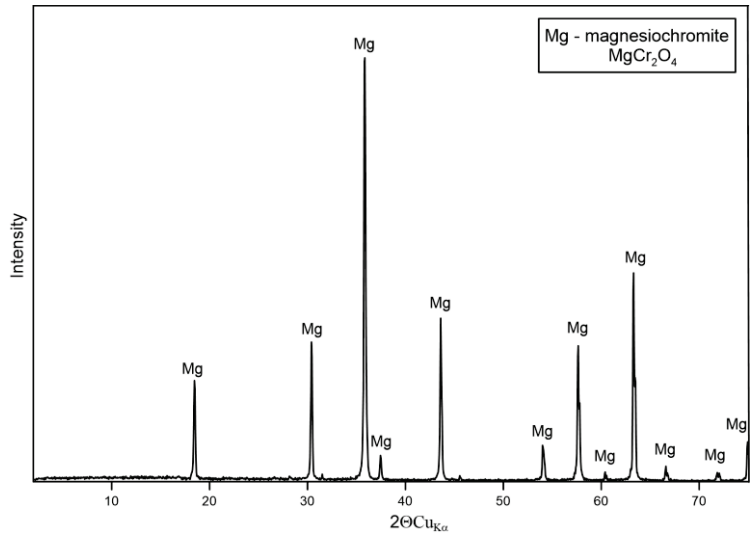


Figure 13. XRD pattern of sample P-5.

The XRD pattern for olivine sand shows (Figure 14) that the primary mineral phase is olivine (Mg_2SiO_4), a magnesium silicate commonly found in olivine-rich sands. In addition to olivine, minor peaks for enstatite ($MgSiO_3$), another magnesium silicate, are also visible.

Assuming that the percentages of SiO_2 and MgO in the composition of olivine are 43.20% and 45.72%, respectively, the data in Table 5 indicate that the tested sample is forsterite. The peaks for forsterite are sharp, reflecting the high crystallinity of the sample, while the enstatite peaks are slightly less intense, indicating its presence in a smaller proportion. Both forsterite and enstatite suggest that the sand has undergone significant geological transformations, typical for olivine sands used in foundry applications.

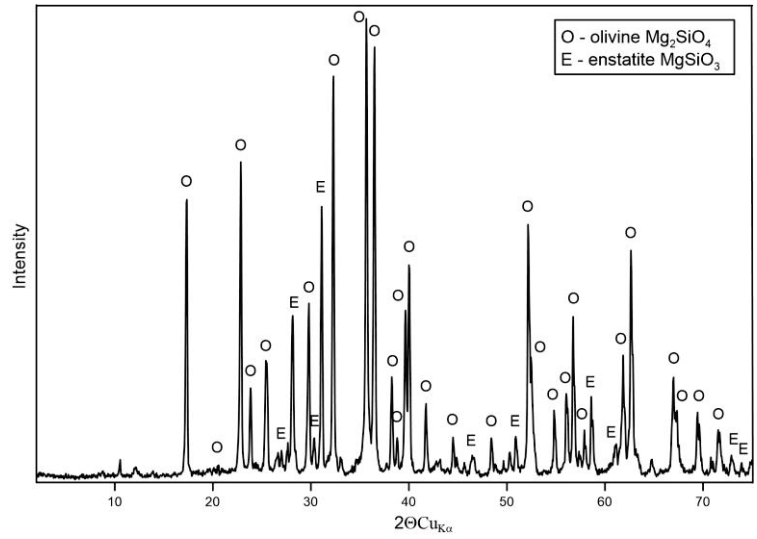


Figure 14. XRD pattern of sample P-7.

In summary, the XRD results confirm that the non-silica sands are composed of mineral phases suitable for high-temperature foundry applications. Magnesite sand is primarily composed of MgO chromite sand, which is dominated by magnesiochromite with Fe and Al impurities, and olivine sand contains forsterite with minor enstatite. These mineralogical compositions provide the sands with unique refractory properties, making them suitable for casting applications with high thermal stability.

3.2.3. SEM-EDS

The SEM and EDS analyses provided valuable insights into the microstructure and elemental composition of the non-silica sands, including magnesite (P-4), chromite (P-5), and olivine (P-7).

The SEM images of the magnesite sand (Figure 15) show a granular and relatively rough surface texture. Individual grains of the sample are angular and exhibit some minor porosity, which could impact its mechanical strength. The EDS spectrum confirms that the sand is predominantly composed of magnesium oxide (MgO), with slight traces of iron oxides (FeO), likely present as impurities or inclusions within the grains. These iron oxide inclusions, visible as bright spots in the SEM images, may influence the sand's thermal and chemical stability under foundry conditions.

The chromite sand sample shows a more compact and dense microstructure than magnesite. SEM images (Figure 16) reveal rounded and angular grains with smooth surfaces. The EDS analysis highlights a composition dominated by chromium oxide (Cr_2O_3) and iron oxide (FeO), with significant amounts of magnesium oxide (MgO) and aluminum oxide (Al_2O_3). These observations support the conclusion that the chromite sand is a magnesiochromite mixture, as confirmed by the XRD analysis. Fe and Al within the chromite structure are consistent with previous studies on chromite sands, which typically contain these elements as part of their spinel structure.

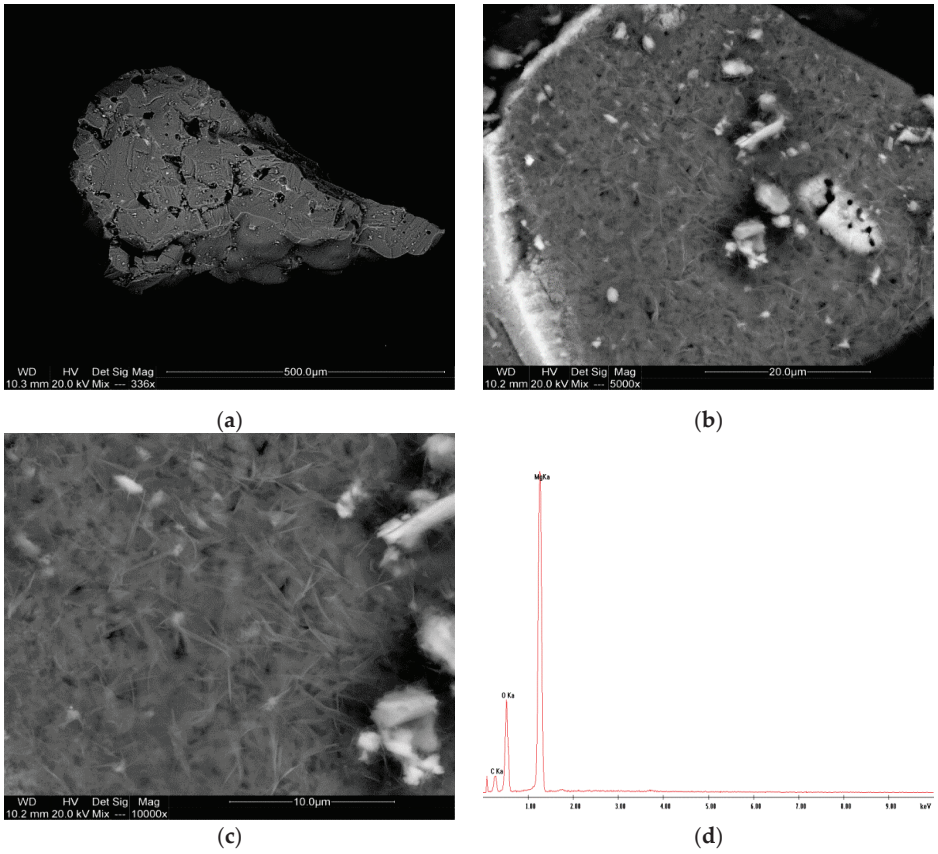


Figure 15. SEM images (**a**–**c**) and EDS spectrum (**d**) of the P-4 sample.

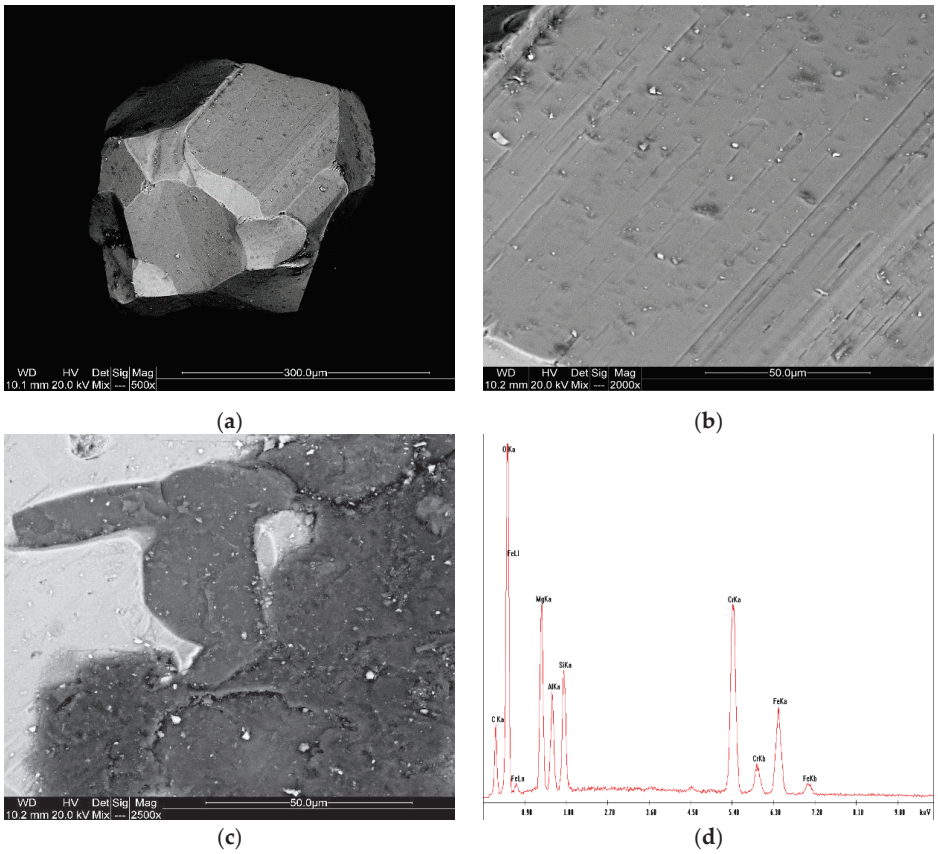


Figure 16. SEM images (**a**–**c**) and EDS spectrum (**d**) of the P-5 sample.

The SEM images of the olivine sand (Figure 17) show a more uniform grain distribution, with smooth, rounded particles and fewer irregularities. This morphology suggests that the sand has undergone significant transportation or weathering processes. The EDS spectrum identifies magnesium silicate (forsterite, Mg_2SiO_4) as the primary phase, with minor inclusions of enstatite ($MgSiO_3$) and iron oxides. These inclusions are likely responsible for the observed secondary peaks in the XRD pattern. The high magnesium content (45.72%) and low silica content (43.20%) indicate that the sample is composed mainly of forsterite, making it suitable for high-temperature foundry applications due to its excellent refractory properties.

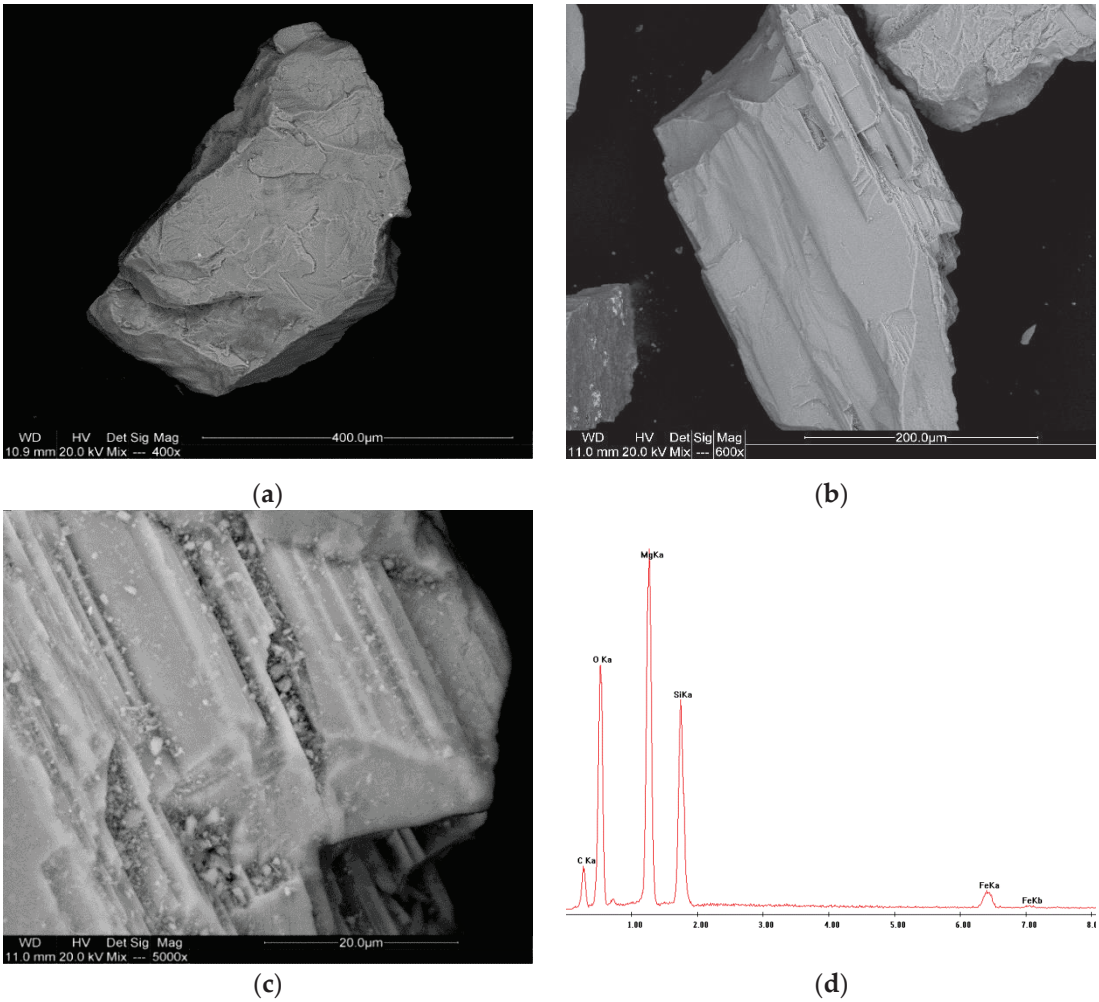


Figure 17. SEM images (**a**–**c**) and EDS spectrum (**d**) of the P-7 sample.

3.2.4. TG/DTG

According to the course of the TG curve presented in Figure 18 and the data in Table 6, the tested sample is characterized by a monotonic, minimal mass loss of 3.42% at 1350 °C.

The presence of two endothermic peaks in the range of 400–500 °C in the DTG curve is reflected in the presence of a broad endothermic peak in the DTA curve with a minimum at a temperature of about 500 °C. In turn, the course of the DTG curve indicates that the observed mass loss is most likely related to the decomposition (dehydroxylation) of small amounts of magnesium oxide and calcium hydroxides (endothermic peaks on the TG curve at temperatures of 413 °C and 502 °C, respectively).

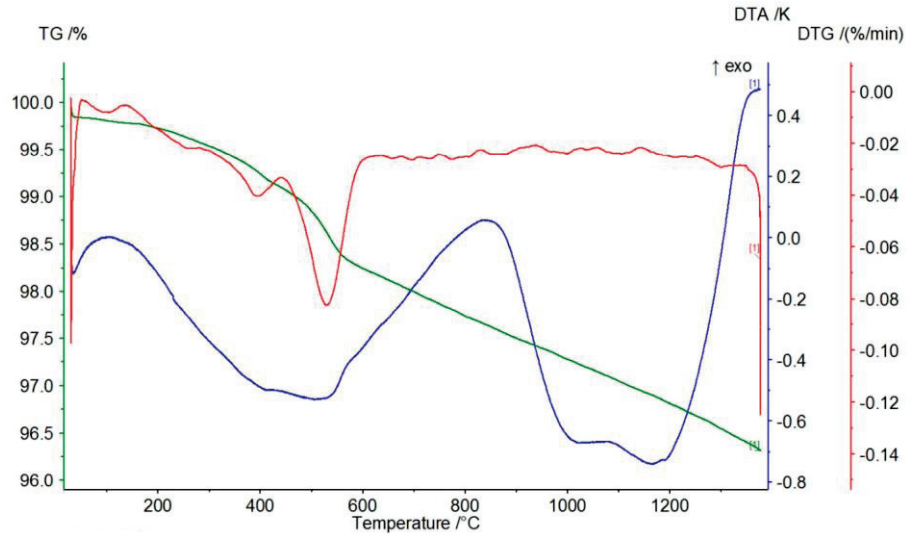


Figure 18. Thermal curves of sample P-4: TG curve (green), DTG curve (red), DTA curve (blue).

The course of the TG curve presented in Figure 19 and the data in Table 6 show that in the case of the chromite material, after evaporating the minimum amount of moisture (0.07%), heating the sample to about 450 °C causes an increase in mass at 447 °C by about 0.07%. This is reflected in the DTG and DTA curves by the appearance of exothermic peaks at temperatures around 378 and 387 °C, respectively. Further heating of the tested P-5 sample causes a mass decrease of about 0.16% at 1000 °C, further increasing by about 0.02% at a temperature of 1124 °C. This slight increase in mass is reflected in the appearance of two endothermic peaks on the DTG and DTA curves at the following temperatures: 820–890 °C and about 1100 °C.

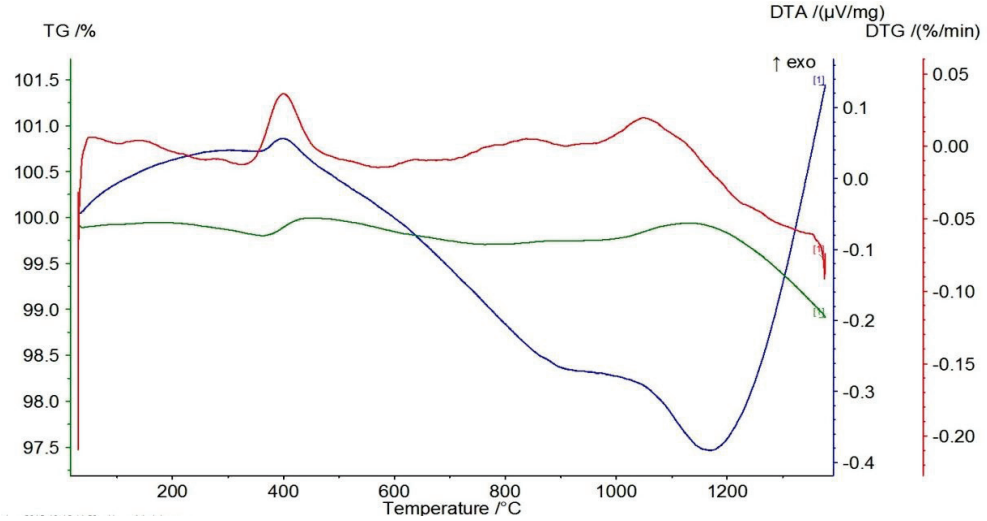


Figure 19. Thermal curves of sample P-5: TG curve (green), DTG curve (red), DTA curve (blue).

The appearance of an exothermic peak at about 400 °C on both the DTG and DTA curves should be related to the oxidation of divalent to trivalent iron. During its heating, it diffuses from the inside of the chromite grains to their surfaces, creating a metastable spinel with a cation ($FeOX_yFe_2O_3$), ferrous–ferric oxide, which is oxidized to hematite at this temperature. Further heating causes the transformation of hematite to magnetite at a temperature of about 1100 °C [17]. The total mass loss of the P5 chromite sand at 1350 °C is about 0.82%.

Figure 20 shows the course of the TG/DTG/DTA curves for the P-7 sample, and Table 6 presents the corresponding data obtained from the curves: the mass losses (%) that accompany the process of heating to the temperature of 1350 °C. The graphs of the TG/DTG/DTA curves show that the tested olivine sand is characterized by a practically monotonic mass loss during heating, which at 1350 °C equals 3.08%. Mass loss during heating is accompanied by practically one endothermic effect on the DTA curve with a minimum at the temperature of 1188 °C, showing the reaction of forsterite with amorphous enstatite, which leads to the formation of a crystalline form of the latter mineral, according to the following equation:

$$2Mg_2[SiO_4] + Mg_2[Si_2O_6] \rightarrow 2Mg_2[SiO_4] + Mg_2[Si_2O_6]$$

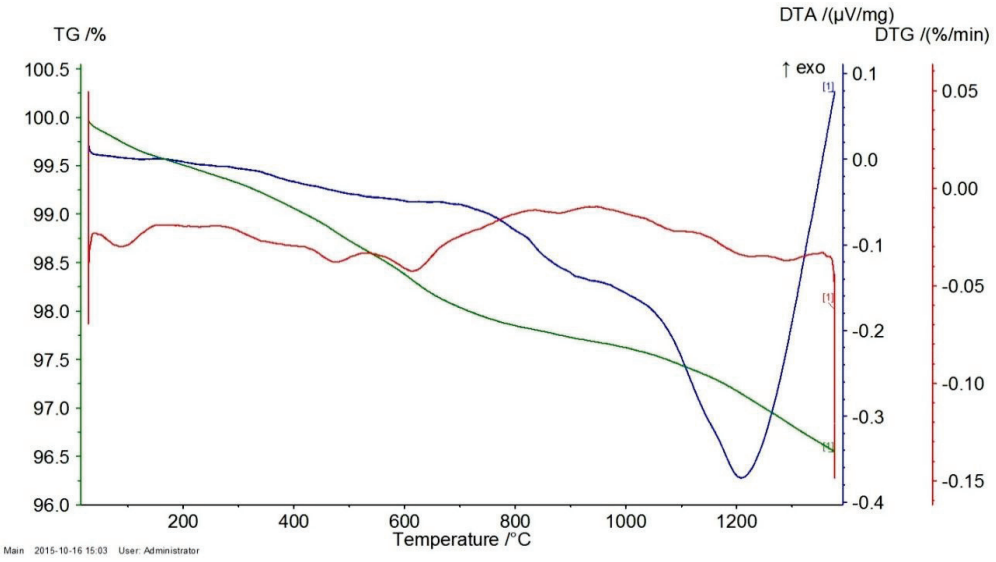


Figure 20. Thermal curves of sample P-7: TG curve (green), DTG curve (red), DTA curve (blue).

4. Discussion

This study sought to evaluate the physicochemical properties of various foundry sands—quartz, magnesite, chromite, and olivine—and determine their suitability for casting applications. It particularly focused on the critical processes of spheroidization and desulfurization in reactor housing production. These processes demand materials with precise thermal stability, chemical resistance, and structural integrity to ensure high-quality castings. Through a detailed investigation of grain size distribution, chemical composition, and thermal behavior, this study has elucidated key factors that influence the performance of these sands in foundry applications.

Quartz sands exhibit notable grain size distribution and chemical composition differences, even within the same classification. Sand P-12, with its uniform grain size distribution, demonstrated superior suitability for precise molding applications compared to P-11, which showed a broader range of finer particles. This inconsistency in particle size increases binder consumption and raises the risk of dimensional instability during high-temperature processes. Furthermore, thermogravimetric analysis revealed significant weight losses in P-11, linked to carbonates and natural binders. Such properties contribute to thermal instability, exacerbated by the polymorphic transformation of α-quartz to β-quartz, a well-known limitation of quartz sands. This transformation induces volumetric changes that can compromise mold integrity, leading to defects such as cracks and surface scabs in castings.

Magnesite sands, characterized by their high magnesium oxide (MgO) content, offer favorable thermal properties crucial for desulfurization and spheroidization. However, this study uncovered practical challenges related to storage and handling. Excessive loss on ignition, attributed to moisture absorption and oxidation during storage, suggests the need for stricter controls in material handling. While magnesite sands are suitable for high-temperature applications, these limitations could impair their performance in real-world scenarios, necessitating further refinement in storage and processing practices.

Chromite sands, renowned for their refractoriness and chemical stability, were evaluated for their mineralogical composition and thermal behavior. The presence of magnesiochromite, as confirmed by X-ray diffraction analysis, indicated a high degree of suitability for foundry use. However, impurities such as iron and aluminum oxides were also detected. These impurities can alter the sand's thermal behavior and compromise its ability to resist slag formation, critical in preventing surface inclusions and ensuring smooth casting surfaces. Despite these impurities, chromite sands' uniform thermal expansion properties remain a distinct advantage, making them highly desirable for specific casting applications.

Olivine sands, primarily composed of forsterite, demonstrated excellent thermal stability and mechanical strength, underscoring their potential for high-temperature foundry applications. However, deviations in composition, including slightly lower magnesium content and elevated iron content, posed challenges. High Fe_2O_3 levels increase slag formation risks, adversely affecting the mechanical properties and surface quality of castings. These findings suggest that while olivine sands are thermally robust, their compositional inconsistencies must be addressed to optimize their performance in precision casting.

This study effectively linked these findings to evaluating the compatibility of molding sands with specific casting processes. Grain size distribution emerged as a critical factor influencing mold stability and defect rates, with sands like P-12 showcasing the importance of uniform particle size. Similarly, the chemical purity of the sands was shown to directly impact their thermal and mechanical behavior. For example, high MgO levels in magnesite and olivine sands enhance their suitability for spheroidization and desulfurization, whereas excessive Fe_2O_3 content in chromite and olivine sands compromises their reliability.

These results have significant implications for foundry applications. Rigorous quality control and proactive testing of molding sands can prevent costly defects and enhance operational efficiency. Rejecting non-compliant sands early in production minimizes waste and ensures higher-quality castings. The findings also underscore the need for targeted material selection tailored to specific casting requirements, such as using magnesite sands for processes requiring high MgO content and chromite sands for applications demanding low thermal expansion.

The insights gained from this study pave the way for future research and innovation. Exploring advanced treatment methods to remove impurities, optimize grain size, and enhance thermal stability could significantly improve the performance of these materials. Additionally, the development of hybrid sands combining the strengths of different materials offers a promising avenue for meeting diverse industrial needs. Advanced monitoring systems that track the properties of sands in real time during production could also play a crucial role in ensuring consistency and quality.

5. Conclusions

This study evaluated the physicochemical properties of quartz, magnesite, chromite, and olivine sands to determine their suitability for reactor housing casting, focusing on spheroidization and desulfurization processes. The results underscore the importance of

aligning molding sand properties with the stringent requirements of high-temperature casting applications.

Quartz sands exhibited significant variability in grain size distribution and thermal behavior, with P-12 showing promising uniformity and thermal stability. However, the broader particle size range and elevated binder content in P-11 highlight the need for quality control to prevent dimensional instability during casting. Magnesite sands demonstrated favorable properties due to their high MgO content, which supports desulfurization, but challenges with loss on ignition suggest improvements in storage and handling practices. Chromite sands, with their low thermal expansion and slag resistance, showed potential for high-temperature applications, although impurities such as iron and aluminum oxides warrant further refinement. Olivine sands, dominated by forsterite, exhibited excellent thermal properties but require adjustments to address deviations in MgO and Fe_2O_3 content for precision applications.

The findings of this study contribute to understanding how physicochemical properties impact the performance of molding sands in casting processes. This research provides actionable insights for optimizing sand selection and improving casting outcomes by systematically linking these properties to their industrial implications. Future work could focus on developing hybrid sands or advanced treatment techniques to address the limitations identified, ensuring consistent quality and performance in high-precision applications.

Author Contributions: Conceptualization, P.G., E.W.-W. and T.B.; methodology, P.G., E.W.-W. and T.B.; software, P.G. and T.B; validation, T.B.; formal analysis, P.G. and T.B.; investigation, P.G., E.W.-W. and T.B.; resources, E.W.-W. and T.B.; data curation, P.G. and T.B.; writing—original draft preparation, P.G. and T.B.; writing—review and editing, T.B.; visualization, P.G. and T.B.; supervision, T.B.; project administration, E.W.-W. and T.B.; funding acquisition, E.W.-W. and T.B. All authors have read and agreed to the published version of the manuscript.

Funding: This research was financed by the AGH University of Krakow, grant number 16.16.140.315.

Institutional Review Board Statement: Not applicable.

Informed Consent Statement: Not applicable.

Data Availability Statement: The original contributions presented in the study are included in the article, further inquiries can be directed to the corresponding author.

Conflicts of Interest: The authors declare no conflicts of interest.

References

1. Census of World Casting Production. *Global Casting Production Growth Stalls*; Modern Casting, American Foundry Society: Cleveland, OH, USA, 2017; pp. 24–28.
2. Sobczak, J.J.; Balcer, E.A.; Kryczek, E. Sytuacja odlewnictwa w Polsce i na świecie—Stan aktualny, tendencje, prognozy. *Przegląd Odlew.* **2017**, *67*, 8–12.
3. World Foundry Organization. Actual Situation of the Worldwide Casting Industry. In *WFO Industry Report 2017*; World Foundry Organization: Herefordshire, UK, 2017.
4. Tewary, U.; Paul, D.; Mehtani, H.K.; Bhagavath, S.; Alankar, A. The origin of graphite morphology in cast iron. *Acta Mater.* **2022**, *226*, 117660. [CrossRef]
5. Sun, X.J.; Li, Y.X.; Chen, X. Identification and Evaluation of Modification Level for Compacted Graphite Cast Iron. *J. Mater. Process. Technol.* **2008**, *200*, 471–480. [CrossRef]
6. Alisir, S.; Cevik, S. The effects of foundry sand components on the cast iron. *Res. Eng. Struct. Mater.* **2020**, *6*, 127–140. [CrossRef]
7. Olawale, J.O.; Ibitoye, S.A.; Oluwasegun, K.M. Processing Techniques and Productions of Ductile Iron: A Review. *Int. J. Sci. Eng. Res.* **2016**, *7*, 397–423.
8. Schrama, F.N.H.; Beunder, E.M.; Vanden, B.B.; Yang, Y.; Boom, R. Sulphur removal in ironmaking and oxygen steelmaking. *Ironmak. Steelmak.* **2017**, *44*, 333–343. [CrossRef]

9. Shevchenko, A.F.; Vergun, A.S.; Bulakhtin, A.S.; Shevchenko, S.A.; Kislyakov, V.G. Improving the Ladle Desulfurization of Hot Metal in Low-Sulfur Steel Production. *Steel Transl.* **2011**, *41*, 996–998. [CrossRef]
10. Bolshakov, V.I.; Shevchenko, A.F.; Bashmakov, A.M.; Ye, L.D.; Trotsenko, E.A. New Complex for the Ultra-Deep Desulfurization of Pig Iron in Large Charging Ladles. *Metallurgist* **2011**, *54*, 725–729. [CrossRef]
11. Golubtsov, V.A.; Shub, L.G.; Deryabin, A.A.; Usmanov, R.G. Treating Steel Outside the Furnace More Efficiently. *Metallurgist* **2006**, *50*, 634–637. [CrossRef]
12. Zborshchik, A.M.; Kuberskii, S.V.; Pismarev, K.E.; Akulov, V.V.; Dovgalyuk, G.Y. Comparison of Ladle Technologies for Hot-Metal Desulfurization. *Steel Transl.* **2010**, *40*, 35–37. [CrossRef]
13. Fesenko, M.A.; Fesenko, A.M. In-Mould Graphitizing, Spheroidizing, and Carbide Stabilizing Inoculation of Cast Iron Melt. *Prog. Phys. Met.* **2020**, *21*, 83–101. [CrossRef]
14. Stefański, Z.; Kamińska, J.; Pamuła, E.; Angrecki, M.; Palma, A. Comparing the Effectiveness of Cast Iron Spheroidization by the Traditional Method and Using a Reaction Chamber (Reactor) Placed in Foundry Mould. *Arch. Foundry Eng.* **2018**, *18*, 191–195.
15. Janjusevic, Z.; Gulisija, Z.; Radosavljevic, S.; Acimovic, Z. A contribution to study of processes on the steel cast–sand mould contact surface during casting. *Mater. Lett.* **2000**, *45*, 235–240. [CrossRef]
16. Nwaogu, U.C.; Poulsen, T.; Stage, R.K.; Bischoff, C.; Tiedje, N.S. New sol–gel refractory coatings on chemically-bonded sand cores for foundry applications to improve casting surface quality. *Surf. Coat. Technol.* **2011**, *205*, 4035–4044. [CrossRef]
17. Rana, S.; Shahriar, S.; Alam, S.; Hossain, I.S.; Biswas, P.K.; Zaman, M.N. Evaluation of Foundry Properties of Brahmaputra River Sand and its Prospects. *Arch. Foundry Eng.* **2023**, *2*, 80–90. [CrossRef]
18. Major-Gabrys, K. Environmentally Friendly Foundry Molding and Core Sands. *J. Mater. Eng. Perform.* **2019**, *28*, 2019–3905. [CrossRef]
19. Miskeena, A.B.; Abdullahb, T.; Alamaric, M. Suitability of Different Local Sands as Moulding Sand in Foundry Industry. *J. Pure Appl. Sci.* **2019**, *17*, 114–118.
20. Rone, M.; Kumar, P. Effect of Moulding Sand to Generate Casting by Moulding Process. *Int. J. Mech. Ind. Technol.* **2017**, *5*, 1–6.
21. Prabhushankar, N.; Rajesh, N.; Krishna Raj, K.; Sivapraksh, M.; Sreenath, J.K.; Sujithkumar, M.; Midhun Krishna, A. Alternative Materials for Silica Sand, Binders and Additives In Sand Casting Process—A Review. *Int. J. Sci. Res. Rev.* **2018**, *7*, 399–413.
22. Nuhu, A.; Ademoh, A.T.; Abdullahi, A. Assessment of foundry properties of steel casting sand moulds bonded with the grade 4 Nigerian Acacia species (gum arabic). *Int. J. Phys. Sci.* **2009**, *4*, 238–241.
23. Beno, J.; Jelinek, P.; Spirutova, N. *Moulding Mixtures*; VŠB—Technical University of Ostrava Faculty of Metallurgy and Materials Engineering: Ostrava, Czech Republic, 2015; pp. 1–81.
24. Anwar, N.; Sappinen, T.; Jalava, K.; Orkas, J. Comparative experimental study of sand and binder for flowability and casting mold quality. *Adv. Powder Technol.* **2021**, *32*, 1902–1910. [CrossRef]
25. Dawson, M. Silica Sand: Foundry Requirements and Classification. *Met. Cast. Technol.* **2001**, *27*, 24.
26. Vasková, I.; Varga, L.; Prass, I.; Dargai, V.; Conev, M.; Hrubočáková, M.; Bartošová, M.; Bul'ko, B.; Demeter, P. Examination of Behavior from Selected Foundry Sands with Alkali Silicate-Based Inorganic Binders. *Metals* **2020**, *20*, 235. [CrossRef]
27. *Polish Standard PN-85/H-11001*; Piaski Formierskie. Klasyfikacja i Wymagania Techniczne. Polish Committee for Standardization (PKN): Warsaw, Poland, 1985.
28. *Polish Standard PN-77/H-11001*; Piaski Formierskie. Klasyfikacja i Wymagania Techniczne. Polish Committee for Standardization (PKN): Warsaw, Poland, 1977.
29. *Polish Standard PN-91/H-11007*; Piasek Chromitowy Formierski. Polish Committee for Standardization (PKN): Warsaw, Poland, 1991.
30. *Polish Standard PN-76/H-11003*; Piasek Kwarcowy Formierski. Polish Committee for Standardization (PKN): Warsaw, Poland, 1976.
31. Krukowski, S.T. Foundry Sands. In *Industrial Minerals and Rocks, Commodities, Markets, and Uses*, 7th ed.; Kodel, J.E., Trivedi, N.C., Barker, J.M., Krukowski, S.T., Eds.; Society for Mining, Metallurgy, and Exploration, Inc. (SME): Littleton, CO, USA, 2006; pp. 1433–1440.
32. Thiel, J. *Thermal Expansion of Chemically Bonded Silica Sands*; American Foundry Society: Schaumburg, IL, USA, 2011; Paper 11–116; pp. 1–10.
33. LaFay, V. Application of no-bake sodium silicate binder systems. *Int. J. Met.* **2012**, *6*, 19–26. [CrossRef]

Disclaimer/Publisher's Note: The statements, opinions and data contained in all publications are solely those of the individual author(s) and contributor(s) and not of MDPI and/or the editor(s). MDPI and/or the editor(s) disclaim responsibility for any injury to people or property resulting from any ideas, methods, instructions or products referred to in the content.

materials

MDPI

Article

Microwave-Crosslinked Polymer Binder MA-AANa/D Biodegradable in an Aqueous Environment–Selected Own Research

Beata Grabowska [1,*], Artur Bobrowski [1], Mateusz Skrzyński [1], Grzegorz Grabowski [2], Wojciech Żyłka [3] and Barbara Pilch-Pitera [4]

[1] Faculty of Foundry Engineering, Department of Foundry Process Engineering, AGH University of Krakow, al. A. Mickiewicza 30, 30-059 Krakow, Poland; arturb@agh.edu.pl (A.B.); mateusz.skrzynski@agh.edu.pl (M.S.)
[2] Faculty of Materials Science and Ceramics, Department of Ceramics and Refractories, AGH University of Krakow, al. A. Mickiewicza 30, 30-059 Krakow, Poland; grzegorz.grabowski@agh.edu.pl
[3] Faculty of Exact and Technical Sciences, Institute of Materials Engineering, University of Rzeszow, ul. Pigonia 1, 35-310 Rzeszow, Poland; wzylka@ur.edu.pl
[4] Faculty of Chemistry, Department of Polymers and Biopolymers, Rzeszow University of Technology, al. Powstańców Warszawy 12, 35-029 Rzeszow, Poland; barbpi@prz.edu.pl
* Correspondence: beata.grabowska@agh.edu.pl

Abstract

The article presents a series of studies on a new polymer binder in the form of an aqueous composition of MA-AANa/D in the aspect of its reusability in the casting process and its safe storage in landfills. FT-IR analysis confirmed that microwave radiation induces crosslinking of both the MA-AANa/D binder and the moulding sand containing it. It was found that after simple treatment of the microwave-cured binder, its original binding properties can be restored, as the hydrogen-bond networks formed under microwave irradiation are reversible. The bending strength (R_g^u) tests of both fresh and regenerated moulding sands bonded with MA-AANa/D confirmed that the achieved curing degree meets the requirements for mould and core production. In addition, the biodegradability of the MA-AANa/D binder was evaluated using the Zahn-Wellens test. The progressive biodegradation was monitored through chemical oxygen demand (UV-Vis) measurements and the corresponding biodegradation degree (R_t). The results confirmed that MA-AANa/D is fully biodegradable in aqueous environments, as evidenced by an R_t value of 63.5% after 28 days of testing.

Keywords: polymer; crosslinking; microwave; binder; biodegradation; foundry

1. Introduction

The development of process and materials engineering is now driven by the use of environmentally friendly substrates, components, and materials that remain safe throughout their life cycle, including production, processing, use, and disposal. This trend results from tightening environmental regulations and the growing social awareness of ecological responsibility [1,2].

Throughout their life cycle, polymers and polymeric materials are continuously affected by physical (mechanical stresses, temperature, electromagnetic radiation), chemical (air components, oxygen), and biological (bacteria, enzymes) factors. Acting over time, these factors may induce both reversible and irreversible changes in their structure and

physicochemical properties, ultimately leading to complete degradation. Understanding thenablenomena enables controlled use of these processes to achieve effects desirable for both industry and the environment [3–5].

In the foundry industry, environmental issues are primarily associated with harmful decomposition products generated during high-temperature casting processes. These originate from the organic binders (most commonly organic resins) and auxiliary additives (catalysts, hardeners, lustrous carbon additives) used in moulding and core sands [6–10]. Another important concern involves the storage of used moulding and core sands after casting, which must be treated as waste. Therefore, the selection of an appropriate binder for bonding the mineral matrix and the method of curing moulds and cores are key factors for sustainable foundry operations.

A properly selected binder and its curing mechanism should ensure the required bonding strength of the moulding or core sand, enable the production of high-quality castings, and at the same time exhibit minimal environmental impact throughout the entire technological process—from sand preparation, mould and core fabrication, and metal pouring to the handling of spent sands [6,11–17].

Literature reports describe the use of polymer-based and environmentally friendly biopolymer binders in foundry technologies [6,18–22]. The authors have been conducting extensive research in this area for several years [23–27]. However, the recycling of used moulding and core sands from a comprehensive perspective is rarely discussed in the literature. Both inorganic and organic binders that can regain their binding properties after suitable treatment are highly valued, and this aspect is also considered in the authors' research [6,28–30].

In this regard, new polymeric binders of the BioCo group have been developed, containing polyacrylates and polysaccharides, which can be crosslinked thermally, by microwaves or UV radiation, or chemically using calcium hydroxide or glutaraldehyde [31,32]. Tests have confirmed that these binders do not negatively affect the natural environment [23].

Nevertheless, knowledge regarding the management of foundry waste remains incomplete. The biodegradation of binder residues in spent sands is still an open issue. This study aims to broaden understanding in this area by investigating a new polymer binder, MA-AANa/D (BioCo group), intended for mould and core production, with a focus on its recyclability and environmentally safe waste sand management.

2. Materials and Methods

2.1. Basic Materials

In this study, a polymer binder composed of a 35% aqueous solution of MA-AANa (maleic acid-acrylic acid copolymer sodium salt, BASF; M_n = 70,000 g/mol, pH 8, viscosity 2000 mPa·s) and a 40% aqueous solution of potato dextrin (Fluka). The polymer solutions were mixed in a 1:1 weight ratio to obtain a homogeneous and transparent composition. The formulation of this composition was established in previous systematic studies on BioCo binders [23].

The resulting aqueous polymer composition MA-AANa/D served as a binder for quartz matrix grains (silica sand: grain size fractions 0.20/0.16/0.32 mm, Sibelco, Bukowno, Poland).

2.2. Crosslinking of the Binder

The crosslinking process of the MA-AANa/D binder (10 g) was carried out in a microwave field at a power of 800 W and a frequency of 2.45 GHz for 60, 90, and 120 s using an INOTEC MD 10940 microwave unit.(Medion AG, Essen, Germany) The selected

crosslinking parameters were determined based on previous systematic studies on optimising the crosslinking of polyacrylates and their BioCo-based compositions [23]. Samples of the aqueous composition, both before and after crosslinking, were subjected to FT-IR structural analysis. To verify the reproducibility of network formation, another 10 g portion of MA-AANa/D was crosslinked again under identical conditions (800 W, 2.45 GHz, 60 s). After crosslinking, the sample was crushed, a stoichiometric amount of the released water was reintroduced, and the mixture was thoroughly mixed. The material was then crosslinked once more under the same microwave conditions (800 W, 2.45 GHz, 60 s). Each MA-AANa/D specimen, before and after crosslinking, was subsequently analysed by FT-IR spectroscopy.

2.3. FT-IR Structural Studies

Structural analyses were performed using a Digilab Excalibur FTS 3000 FT-IR spectrometer (Bio-Rad, Hercules, CA, USA), equipped with a standard DTGS detector, at a spectral resolution of 4 cm^{-1}. Spectra were collected at room temperature in transmission mode using KBr pellets (potassium bromide for IR spectroscopy, Uvasol; Merck, Darmstadt, Germany).

2.4. Preparation of Moulding Sand

The moulding sand was prepared by mixing the components in a ribbon mixer (LM-R1)(Wadap, Marcyporęba, Poland): 100 parts by weight of silica sand and 3 parts by weight of the binder material. Mixing of the sand matrix with the free-flowing binder was continued for 3 minutes. The moulding sand was prepared at an ambient humidity of 25.1% and a temperature of 19 °C. From the prepared moulding sand, three series of standard longitudinal core samples with dimensions of 22.2 × 22.2 × 180 mm were produced according to the parameters required for the planned bending strength tests (R_g^u), in compliance with the PN-83/H-11073 standard [33]. Each series was subsequently cured in a microwave field.

2.5. Curing of Moulding Sand Samples

Three series of longitudinal core samples were subjected to microwave curing at a power of 800 W and a frequency of 2.45 GHz using an INOTEC MD 10940 microwave unit. The curing durations were 60 s (series 1), 90 s (series 2), and 120 s (series 3). Each series contained at least five samples. The longitudinal core samples were then subjected to bending strength tests in the cured state (R_g^u).

2.6. Bending Strength Testing of Cured Samples

The bending strength (R_g^u) of the three series of cured moulding sand samples was determined using a universal testing machine LRu-2e (Multiserw-Morek, Marcyporęba, Poland) within a measuring range of 0–870 N/cm^2, in accordance with the PN-83/H-11073 standard.

Measurements of R_g^u for standardised longitudinal samples made from both fresh and renewed sands were performed after 1 h and 24 h of storage in desiccators. The final bending strength value, considered as the actual result, was calculated as the arithmetic mean of at least five measurements from each series.

2.7. Process of Renewing the Moulding Sand

The term renewed moulding sand is used in this study to denote cured moulding sand whose original binding properties were restored. After curing, the sand was mechanically disintegrated to obtain a free-flowing form. Its composition was then supplemented with

an appropriate amount of water to dissolve the cured MA-AANa/D binder and restore its initial binding properties under microwave treatment.

The obtained mixture was homogenised for 3 minutes in a ribbon mixer (LM-R1). Standardised longitudinal samples were prepared from the renewed moulding sand, cured in a microwave field, and subsequently subjected to bending strength tests according to the methodology described in Sections 2.5 and 2.6.

2.8. Investigations of Biodegradation in Aqueous Solution

The susceptibility of the MA-AANa/D polymer binder to biodegradation was evaluated using the static Zahn-Wellens test [34]. The biodegradation process was carried out in 1 dm^3 vessels equipped with stirring and aeration systems. Each test mixture contained activated sludge (microorganisms), nutrient components (a basic bacterial medium), and aqueous solutions of the tested samples as the sole carbon source. Five samples were subjected to biodegradation: 1. Ethylene glycol (EG)—reference substance (expected biodegradation > 90%), POCh; 2. Polymer binder (MA-AANa/D); 3. Maleic acid-acrylic acid copolymer sodium salt (MA-AANa); 4. Potato dextrin (D); 5. Control sample (O) containing only activated sludge and nutrients (blank test).

The activated sludge used in the control sample was obtained from the Water Supply System Department (MPWiK, Kraków, Poland). According to the standard procedure [34], the concentrations of the tested samples were maintained in the range of 50–400 mg/dm^3. Since this method is intended for the assessment of organic substances, only the polymer binder was subjected to biodegradation testing, without the quartz matrix.

The incubation lasted 28 days and was carried out in the dark at an ambient temperature of 20–25 °C, with an aeration level of approximately 8 mg O_2/dm^3. Both temperature and aeration were continuously monitored throughout the test period.

The biodegradation process was further monitored at specified time intervals over the 28-day period by spectrophotometric determination of the chemical oxygen demand (COD) using the UV-Vis method, in accordance with the relevant standard procedure [35]. Changes in the degree of biodegradation (R_t) of the samples were evaluated based on COD measurements following the Zahn-Wellens method. The R_t values were calculated as the ratio of the COD value at a given time interval to the initial COD value, reflecting the progressive biodecomposition of the tested materials.

2.9. Microscopic Examinations

Microscopic observations were performed using a Nikon Eclipse LV100 optical microscope (Nikon Europe B.V., Amstelveen, The Netherlands) equipped with NIS-Elements AR 2.10 software. Images were recorded at a magnification of 50×.

3. Results

3.1. Microwave Crosslinking Process of the Polymer Binder

Microwave radiation is used for curing foundry binders, primarily in moulding sand technologies based on hydrated sodium silicate. Research in this area is typically directed toward examining the absorption of electromagnetic waves in the microwave range (2.45 GHz) by uncured moulding sands bonded with silicates or aluminosilicates, including studies of their properties in the cured state [28,29,36–40]. In contrast, there is limited knowledge regarding the behaviour of organic binders under such conditions. Most organic binders in the form of resins exhibit hydrophobic properties, and their crosslinking proceeds via chemical reactions, often involving initiators, crosslinking agents, and catalysts.

In turn, aqueous polymer binders of the BioCo type, owing to their molecular structure and hydrophilic nature, are susceptible to microwave-induced crosslinking. They

do not require any additional crosslinking agents, which makes them not only a cost-effective alternative to conventional resins but also environmentally friendly. However, the mechanism of microwave-induced crosslinking of hydrophilic polymers is still under investigation and continuously being developed by the research team. Understanding the chemistry of the polymer crosslinking process is essential for its further application in foundry technology—both in terms of the binder's ability to bond mineral grains and its environmental assessment, which plays an important role in the casting process.

In the first stage of the study, a structural analysis of the MA-AANa/D binder before and after microwave crosslinking was carried out using FT-IR spectroscopy (Figure 1). The crosslinking process under microwave radiation was performed at three exposure times: 60 s, 90 s, and 120 s.

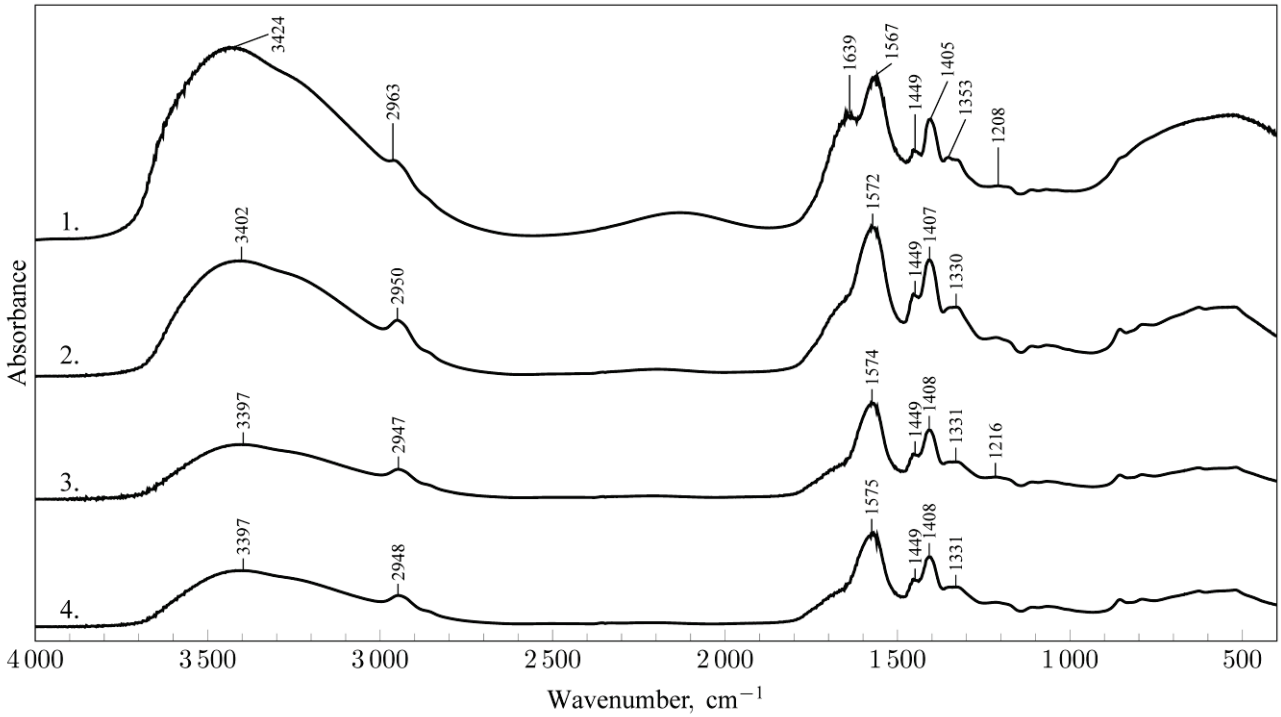


Figure 1. IR spectra of the MA-AANa/D composition: 1. initial state; 2. after microwave crosslinking (60 s); 3. after microwave crosslinking (90 s); 4. after microwave crosslinking (120 s).

The IR spectrum of the initial MA-AANa/D composition confirmed the presence of functional groups characteristic of its polymeric components—the synthetic polymer (maleic acid-acrylic acid copolymer sodium salt) and the biopolymer (dextrin). For the microwave-cured samples, noticeable changes were observed in the IR spectral profiles. The characteristic absorption bands identified in the IR spectra of the investigated system are summarised in Table 1.

It was found that exposure of the MA-AANa/D composition to microwave radiation for 60, 90, and 120 s induced structural transformations, manifested by changes in both the intensity and position of characteristic absorption bands. The broad band in the 3700–3000 cm^{-1} region changed its shape, and its maximum shifted toward higher wavenumbers. Additionally, the intensity of this band decreased as a result of microwave treatment, which is attributed to the evaporation of loosely bound (solvent) water. The persistence of the broad band, however, indicates a significant contribution of hydrogen bonding during the crosslinking process. Microwave electromagnetic radiation provides sufficient energy to promote rotational motion within polymer chains. As the absorbed energy propagates through the system, it activates polar functional groups (dipoles) ca-

pable of forming new chemical interactions. These interactions lead to the association of multiple polymer chains, resulting in the formation of numerous hydrogen bonds between hydroxyl (···O-H) and carbonyl (···O=C<) groups.

Table 1. Characteristic bands in the IR spectra.

Spectra 1	Spectra 2	Spectra 3	Spectra 4	Assignment	Remarks
Wavenumber, cm^{-1}					
3424	3402	3397	3397	ν-OH O-H···O-H O-H···O=C	Band of free OH group Hydrogen bond (between hydroxyl groups) Hydrogen bond (between hydroxyl and carbonyl groups)
2963 -	- 2950	- 2947	- 2948	ν-C-H	Stretching vibrations asymmetric and symmetric
1639	-	-	-	ν_{as}-COO^-	Stretching asymmetric vibration carboxylate group
1567 -	- 1572	- 1574	- 1575	δ-C-O-H	Deforming vibrations hydroxyl group
1448 1405	1449 1407	1449 1408	1449 1408	δ $(CH_2)_n$	Shearing symmetric vibrations
1353 -	- 1330	- 1331	- 1331	ν_s-COO^-	Stretching symmetric vibration carboxylate group
1208 -	- 1216	- 1216	- 1216	C-O-H	Deforming vibrations

The spatially extended polymer networks formed through intra- and intermolecular hydrogen bonding significantly influence the binding strength of the crosslinked MA-AANa/D composition and, consequently, of the cured moulding sand in contact with quartz grains. Moreover, these bonds are physically reversible—upon reintroduction into water, they dissociate. This reversibility was also confirmed in the authors' previous studies on the BioCo series of aqueous binders [23,30,31] and in the subsequent sections of this work.

A shift in the absorption band at 2963 cm^{-1} toward lower wavenumbers observed after microwave crosslinking may indicate changes in the position of C–H bonds located near polar groups involved in hydrogen bond formation. In contrast, the slight shifts observed around 1448 cm^{-1} and 1405 cm^{-1}, originating from δ $(CH_2)_n$ deformation vibrations, fall within the measurement error range (±4 cm^{-1}).

To demonstrate that the formed networks exhibit a reversible character and to assess the renewability of the binding properties of the crosslinked MA-AANa/D binder under microwave treatment, the material was successively subjected to dissolution in water and subsequent microwave crosslinking. For each binder state—before and after crosslinking—corresponding IR spectra were recorded (Figure 2).

In this context, the term renewability refers to the ability of the binder to restore its original binding properties after dissolution in water and to maintain its capacity for network formation under microwave radiation. Figure 2 presents the IR spectra of MA-AANa/D binder samples subjected to successive microwave crosslinking (60 s) and dissolution cycles.

After microwave crosslinking for 60 s, the broad absorption band in the 3700–3000 cm^{-1} region does not disappear (Figure 2, spectrum 2; cf. Figure 1, spectrum 2). However, its intensity decreases and the maximum shifts toward lower wavenumbers. These changes, as mentioned earlier, are related to the evaporation of loosely bound solvent water. The persistence of this band confirms the formation of hydrogen bonds within the crosslinked MA-AANa/D binder.

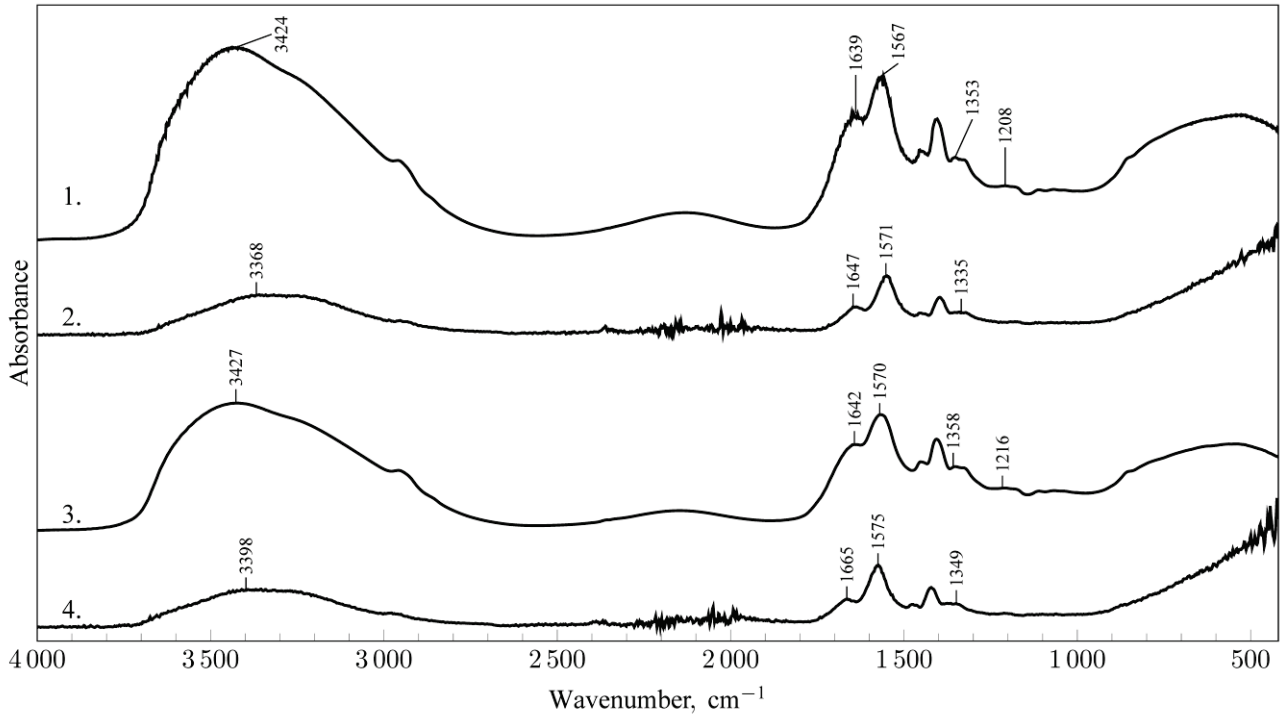


Figure 2. IR-Spectra MA-AANa/D: 1. initial state, 2. after cross-linking with microwaves (60 s), 3. after the renewal process, 4. after re-cross-linking with microwaves (60 s).

The band at approximately 1639 cm^{-1} (C–OH stretching vibrations) markedly decreases in intensity relative to the 1567 cm^{-1} band, consistent with the spectral patterns shown in Figure 1 (compare spectra 1 and 2). These bands are also shifted. Additionally, a reduction in the intensity of the band around 1333 cm^{-1} and its shift toward lower wavenumbers are observed after crosslinking. The band recorded near 1208 cm^{-1} also exhibits lower intensity. These spectral variations between spectra 1 and 2 indicate the involvement of polar functional groups in the crosslinking process.

The bands corresponding to C–H vibrations (–CH_2 and –C–H groups) remain unchanged in position and intensity (bands: 1449 cm^{-1}, 1405 cm^{-1}). These groups are not relevant to the cross-linking process (compare Figure 1: the analysis of spectra 1–4). After redissolving the crosslinked MA-AANa/D binder in a stoichiometric amount of water, another IR spectrum was recorded (Figure 2, spectrum 3). Comparison of spectra 1 and 3 indicates that the MA-AANa/D binder retains its original structure. Re-exposure of the binder samples to microwave radiation results in spectral changes similar to those in spectrum 2 (Figure 2, compare spectra 2 and 4), confirming the re-crosslinking of the binder.

3.2. Strength and Renewability of Moulding Sands Bonded with the Polymer Binder

Previous studies on the strength of moulding sands bonded with BioCo binders based on polyacrylates and polysaccharides [23,30,31] demonstrated that the parameters of thermal curing (microwave exposure time and temperature) influenced the bending strength values. For BioCo binders, the use of microwave curing was found to provide faster and more efficient binder crosslinking, thereby making the method more cost-effective from the perspective of both process economics and practical foundry applications (e.g., in situ core curing).

The bending strength (R_g^u) of samples prepared from fresh moulding sand and cured by microwaves for 60 s reached approximately 1.5 MPa (Figure 3a). The highest bending strength was obtained for samples cured for 90 s, with values around 1.7 MPa. Extending

the microwave exposure time to 120 s did not significantly affect the strength values; in all cases, a slight decrease in R_g^u was observed.

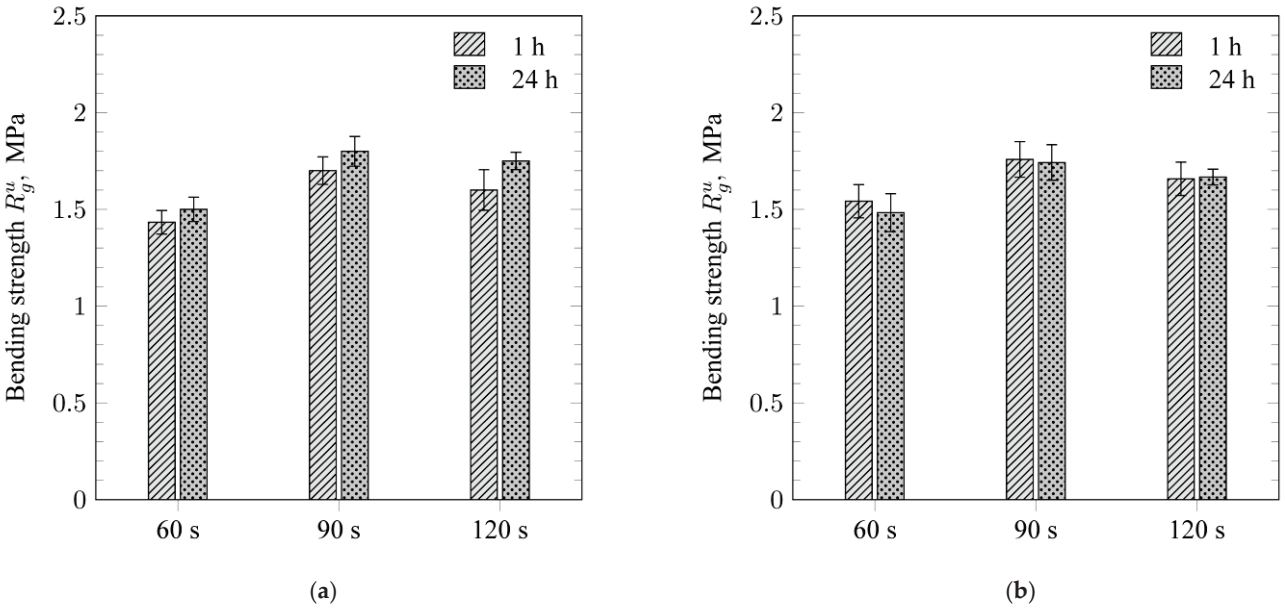


Figure 3. Bending strength R_g^u of (**a**) fresh cured moulding sand and (**b**) renewed moulding sand after curing.

Based on the obtained R_g^u values, it can be concluded that the binder consisting of the sodium salt of a copolymer of maleic acid and acrylic acid and dextrin can be effectively cross-linked in the moulding sand under the influence of microwave radiation.

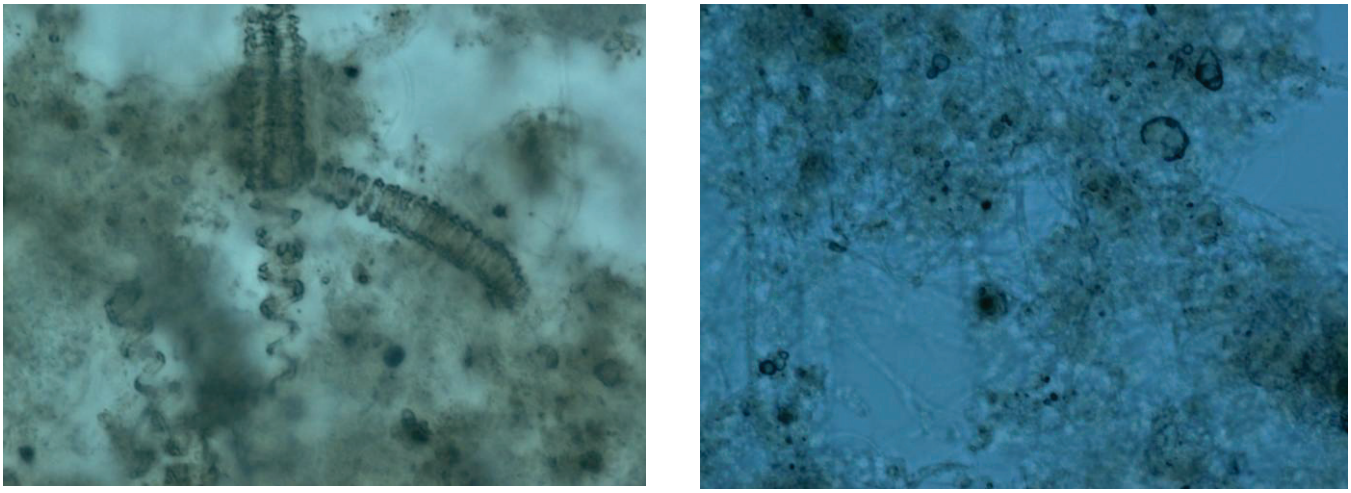
The bending strength R_g^u of the renewed moulding sand also remained at approximately 1.5 MPa after microwave curing for 60 s (Figure 3b). The difference between the R_g^u values obtained for the freshly cured and renewed moulding sands was within the measurement error range. Thus, it can be concluded that the MA-AANa/D binder retained its binding capacity after the regeneration process, and the optimal microwave curing time for the moulding sand was 90 s. These findings are consistent with the results of the structural analyses of the MA-AANa/D binder before and after crosslinking. Both in the binder and in the binder applied to the mineral matrix (i.e., in the cured moulding sand), microwave radiation induced the formation of hydrogen-bonded networks whose strength was sufficient for producing moulds and cores intended for casting applications [6].

An important observation is the ability of the MA-AANa/D binder to restore its binding properties within the moulding sand. Spent moulding sands from the casting process, after removal of the surface layer thermally affected by contact with molten metal, can be reintroduced into production with minimal treatment. The thermally unaltered binder present in the spent sand can be redissolved in water and re-crosslinked. This feature also supports safer storage and management of foundry waste. Therefore, in the next stage of this study, the biodegradability of the MA-AANa/D binder in an aqueous environment was evaluated.

3.3. Biodegradation of the Polymer Binder

The biodegradation process was carried out for five samples: 1. Ethylene glycol (EG)—reference compound (expected biodegradation > 90%), POCh; 2. Polymer binder (MA-AANa/D); 3. Maleic acid-acrylic acid copolymer sodium salt (MA-AANa); 4. Potato dextrin (D); 5. Control sample (O), as described in Section 2.8.

In addition to the reference (EG) and control (O) samples, aqueous solutions of the individual polymers forming the MA-AANa/D binder were also examined to provide additional insight into the biodegradation behaviour of the starting components. Throughout the 28-day biodegradation process, the environmental parameters necessary for proper microbial activity were continuously controlled. The temperature was maintained within the recommended range of 20–25 °C, and the aeration level of the tested samples was kept at approximately 8 mg O_2/dm^3. To confirm the sustained presence of viable microorganisms in the mixtures, periodic microscopic observations of the samples were performed (Figure 4). Microorganisms were observed in accordance with the accepted methodology for illustrative purposes. In addition, the biodegraded samples were characterised (colour, odour, structure and concentration of flocs, biodiversity of microorganisms, clarity, sedimentation). The presence of live microorganisms in the sample taken at the beginning of the test (Figure 4a) and at the end of the test, as confirmed by microscopic examination (Figure 4b), provides additional evidence that the conditions for the biodegradation process were appropriate (in accordance with the standard) and did not adversely affect their natural development and metabolism in the presence of the polymers D and MA-AANa and the MA-AANa/D composition present in the tested samples.



(**a**) (**b**)

Figure 4. Examples of microscopic photographs of microorganisms for the reference sample: (**a**) 2 days after sampling, (**b**) 20 days after sampling.

During the biodegradation test, the chemical oxygen demand (COD) was determined spectrophotometrically (UV-Vis) for all analysed, mixtures. In accordance with the test requirements, COD values were measured at selected time intervals. The decrease in COD values over time, compared with the value determined three hours after the start of the test, was used to calculate the percentage degree of biodegradation of the samples (Table 2).

Based on the obtained COD values, the percentage of degree of biodegradation (R_t) was determined for the tested samples: EG, D, MA-AANa, and MA-AANa/D. The COD values were calculated according to Equation (1):

$$R_t(\%) = \left[1 - \frac{(C_T - C_B)}{(C_A - C_{BA})}\right] \cdot 100\% \quad (1)$$

where:

R_t—Biodegradation % in time (within 28 days),

C_A—COD values in the tested mixture, determined 3 hours after the start of the experiment (mg/dm^3),
C_T—COD values in a mixture during sampling (mg/dm^3),
C_B—COD values in a blank test during sampling (mg/dm^3),
C_{BA}—COD values in a blank test, determined 3 hours after the beginning of the experiment (mg/dm^3).

Table 2. Chemical oxygen demand (COD) values for the tested samples.

Sample / Measurement (Day)	EG (Standard)	D	MA-AANa	MA-AANa/D	O (Blank Test)
	COD, mg/dm^3 O_2				
3 h	1245.5	685.1	768.5	754.6	9.752
1 (1)	1138.1	620.5	729.8	711.4	9.820
2 (2)	1107.5	570.3	703.1	689.9	6.032
3 (5)	979.6	403.7	697.6	665.3	6.545
4 (7)	820.5	310.1	670.9	614.7	6.346
5 (12)	748.1	239.0	632.1	578.2	6.670
6 (15)	508.9	215.4	584.1	487.1	6.532
7 (19)	335.1	194.2	542.4	453.0	6.313
8 (21)	200.6	170.2	498.9	398.5	7.017
9 (26)	125.0	168.1	446.7	312.7	8.315
10 (28)	100.2	156.9	423.1	281.1	9.130

The percentage degree of biodegradation was determined from the relative decrease in the COD value over time. The calculated R_t values are presented in the graph as a function of biodegradation time, forming the biodegradation curve (Figure 5).

A polymer is considered biodegradable when its degree of biodegradation after a 28-day test cycle reaches at least 60% [28]. This condition was met by the following samples: the reference sample, ethylene glycol (R_t = 93%), dextrin (D) (R_t = 77%), and the MA-AANa/D binder (R_t = 63%). Although the presence of the synthetic polymer component, maleic acid-acrylic acid copolymer sodium salt (MA-AANa), hindered the biodegradation process, the binder reached the required R_t value after 28 days, allowing it to be classified as fully biodegradable.

The biodegradation test performed on the MA-AANa polymer alone confirmed its limited susceptibility to biological degradation, with an R_t value of 45%, excluding it from the group of fully biodegradable polymers in aqueous environments. The presence of sodium ions hinders the biodegradation process; however, it simultaneously improves its water solubility and results in a more favourable pH for interaction with mineral grains during bonding.

Consequently, the final aqueous polymer composition exhibits superior properties compared with its individual components, MA-AANa and D. The proportion of dextrin in the composition allows the resulting MA-AANa/D binder to be classified as biodegradable.

Based on the biodegradation results for the MA-AANa/D binder, together with the evidence of its renewability in spent sands, it can be concluded that the binder present in used sands will gradually biodegrade during storage under ambient conditions at landfill sites.

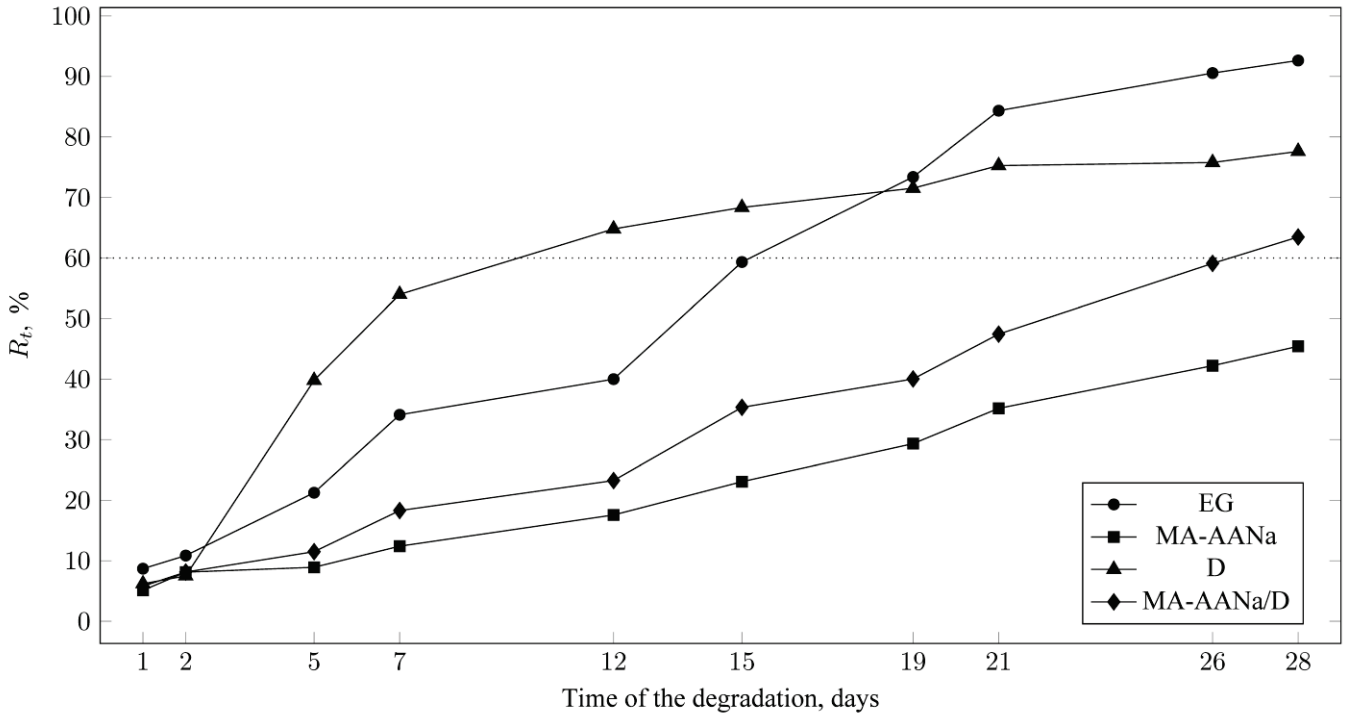


Figure 5. Biodegradation curves for samples EG, MA-AANa, D and MA-AANa/D.

4. Conclusions

The binder composed of maleic acid-acrylic acid copolymer sodium salt and dextrin can be effectively crosslinked in an aqueous composition under microwave radiation. The microwave crosslinking process is physically reversible: dissolution of the crosslinked binder in water restores its initial structure by releasing loosely bound solvent water. No chemical reactions occur within the functional groups during crosslinking. The resulting hydrogen-bonded network originates from dipole–dipole interactions between polar polymer groups (hydroxyl and carbonyl). FT-IR analyses confirmed the renewability of the MA-AANa/D binder.

The obtained R_g^u bending strength values indicate that the aqueous binder, composed of the sodium salt of a maleic acid-acrylic acid copolymer and dextrin, can be effectively crosslinked in moulding sand under microwave radiation.

The renewed moulding sand exhibited bending strength comparable to that of the freshly cured sand. From a technological perspective, the achieved bending strength values are sufficient for proper mould and core fabrication.

The biodegradation of foundry polymer binders under microbial influence is a complex process, dependent both on the binder's chemical structure—particularly the presence of polar hydroxyl and carboxylate groups—and on environmental factors such as temperature, pH stability, nutrient availability, oxygen concentration, and humidity. Based on chemical oxygen demand results, the MA-AANa/D binder underwent gradual biodecomposition, reaching a degree of biodegradation of R_t = 63% after 28 days. According to reference criteria, this value qualifies the material as fully biodegradable. The findings provide valuable insight into the potential behaviour and degradation pathway of polymeric binders under landfill storage conditions.

Author Contributions: Conceptualization, B.G.; methodology, B.G. and A.B.; software, G.G. and B.P.-P.; validation, B.G., A.B. and G.G.; formal analysis, B.G., G.G. and A.B.; investigation, A.B., M.S. and W.Ż.; resources, B.G. and A.B.; data curation, M.S., W.Ż. and B.P.-P.; writing—original draft preparation, B.G., G.G. and A.B.; writing—review and editing, B.G. and A.B.; visualisation G.G.;

supervision, B.G. and G.G.; project administration, B.G.; funding acquisition, B.G. All authors have read and agreed to the published version of the manuscript.

Funding: This research was funded by AGH University of Krakow as part of the statutory work no. 16.16.170.654/B507.

Institutional Review Board Statement: Not applicable.

Informed Consent Statement: Not applicable.

Data Availability Statement: The original contributions presented in this study are included in the article. Further inquiries can be directed to the corresponding author.

Conflicts of Interest: The authors declare no conflicts of interest.

References

1. Commins, J.; Irion, K. Towards Planet Proof Computing: Law and Policy of Data Centre Sustainability in the European Union. *Technol. Regul.* **2025**, *1*, 1–36. [CrossRef]
2. Khalique, A.; Wang, Y.; Ahmed, K. Europe's environmental dichotomy: The impact of regulations, climate investments, and renewable energy on carbon mitigation in the EU-22. *Energy Policy* **2025**, *198*, 114498. [CrossRef]
3. Półtorak, M.; Półtorak, M.; Stachowicz, S.; Stępień-Załucka, B.; Bulanda, B.; Oliwa, R.; Oleksy, M. Polymer recycling considering current and future legal regulations in selected EU countries—A review. *Polimery* **2025**, *70*, 378–385. [CrossRef]
4. Chanda, M.; Salil, R.K. *Industrial Polymers, Specialty Polymers and Their Applications*; CRC Press: Boca Raton, FL, USA; Taylor & Francis Group: Abingdon, UK, 2008.
5. Rabek, J.F. Polimery. In *Otrzymywanie, Metody Badawcze i Zastosowania*; Wydawnictwo Naukowe PWN: Warsaw, Poland, 2019.
6. Lewandowski, J.L. *Tworzywa Na Formy Odlewnicze*; Akapit: Kraków, Poland, 1997.
7. Holtzer, M.; Dańko, R.; Piasny, S.; Kubecki, M.; Drożyński, D.; Roczniak, A.; Skrzyński, M.; Kmita, A. Research on the Release of Dangerous Compounds from the BTEX and PAHs Groups in Industrial Casting Conditions. *Materials* **2021**, *14*, 2581. [CrossRef]
8. Kwaśniewska-Królikowska, D.; Holtzer, M. Selection criteria of lustrous carbon carriers in the aspect of properties of greensand system. *Metalurgija* **2013**, *52*, 62–64.
9. Kahn, M.M.; Mahajani, S.M.; Jadhav, G.N. Transformation of bentonite used in green sand molds during metal casting process and its relevance in sand reclamation. *Appl. Clay Sci.* **2021**, *206*, 106072. [CrossRef]
10. Kamińska, J.; Puzio, S.; Angrecki, M.; Stachowicz, M. The Effect of the Addition of Bentonite Clay to Traditional Sand Mixtures on the Surface Quality of Iron Castings. *J. Ecol. Eng.* **2020**, *21*, 160–167. [CrossRef] [PubMed]
11. Major-Gabryś, K. Environmentally Friendly Foundry Molding and Core Sands. *J. Mater. Eng. Perform.* **2019**, *28*, 3905–3911. [CrossRef]
12. Bobrowski, A.; Grabowska, B.; Żymankowska-Kumon, S.; Kurleto-Kozioł, Z. Physico-Chemical and Environmental Characterisation of the Dust from Dry Dedusting of the Green Sand. *Arch. Foundry Eng.* **2016**, *16*, 33–36. [CrossRef]
13. Mhamane, D.A.; Rayjadhav, S.B.; Shinde, V.D. Analysis of Chemically Bonded Sand Used for Molding in Foundry. *Asian J. Appl. Sci. Technol.* **2018**, *7*, 11–16. [CrossRef]
14. Seidu, S.O.; Kutelu, B.J. Effects of Additives on Some Selected Properties of Base Sand. *J. Miner. Mater. Charact. Eng.* **2014**, *2*, 507–512. [CrossRef]
15. Naro, R.L. Formation and control of lustrous carbon surface defects in iron and steel castings. *Trans. Am. Foundrymens Soc.* **2002**, *1*, 815–834.
16. Chakherlou, T.N.; Mahdinia, Y.; Akbari, A. Influence of Lustrous Carbon Defects on the Fatigue Life of Ductile Iron Castings Using Lost Foam Process. *Mater. Des.* **2011**, *32*, 162–169. [CrossRef]
17. Miller, L.; Vakili, R.; St Onge, J.; Wang, Z. Green Sand Emissions and the Concentration of Carbonaceous Additives | Modern Casting. *Mod. Cast. Mag.* **2019**, *12*, 26–28.
18. Zhou, X.; Yang, J.; Su, D.; Qu, G. The high-temperature resistant mechanism of α-starch composite binder for foundry. *J. Mater. Process. Technol.* **2009**, *209*, 5394–5398. [CrossRef]
19. Torielli, R.; Cannon, F.; Voigt, R.C.; Considine, T. The Environmental Performance and Cost of Innovative Technologies for Ductile Iron Foundry Production. *Int. J. Met.* **2014**, *8*, 37–48. [CrossRef]
20. Yu, W.; He, H.; Cheng, N.; Gan, B.; Li, X. Preparation and experiments for a novel kind of foundry core binder made from modified potato starch. *Mater. Des.* **2009**, *30*, 210–213. [CrossRef]
21. Zhou, X.; Yang, J.; Qian, F.; Qu, G. Synthesis and Application of Modified Starch as a Shell-Core Main Adhesive in a Foundry. *J. Appl. Polym. Sci.* **2010**, *116*, 2893–2900. [CrossRef]

22. Major-Gabryś, K.; Hosadyna-Kondracka, M.; Skrzyński, M.; Stachurek, I. The influence of biomaterial in the binder composition on the quality of reclaim from furan no-bake sands. *Arch. Civ. Eng.* **2022**, *LXVIII*, 163–177. [CrossRef]
23. Grabowska, B. *Nowe Spoiwa Polimerowe w Postaci Wodnych Kompozycji z Udziałem Poli(Kwasu Akrylowego) Lub Jego Soli i Modyfikowanego Biopolimeru do Zastosowania w Odlewnictwie*; AKAPIT: Kraków, Poland, 2013.
24. Grabowska, B.; Cukrowicz, S.; Bobrowski, A.; Drożyński, D.; Żymankowska-Kumon, S.; Kaczmarska, K.; Tyliszczak, B.; Pribulová, A. Organobentonite Binder for Binding Sand Grains in Foundry Molding Sands. *Materials* **2023**, *16*, 1585. [CrossRef] [PubMed]
25. Cukrowicz, S.; Sitarz, M.; Kornaus, K.; Kaczmarska, K.; Bobrowski, A.; Gubernat, A.; Grabowska, B. Organobentonites Modified with Poly(Acrylic Acid) and Its Sodium Salt for Foundry Applications. *Materials* **2021**, *14*, 1947. [CrossRef]
26. Grabowska, B.; Zapotoczny, S.; Bulwan, M.; Grabowski, G. Biodegradation of new polymer foundry binders for the example of the composition polyacrylic Acid/Starch. *Arch. Foundry Eng.* **2011**, *11*, 65–70.
27. Kaczmarska, K.; Grabowska, B.; Grabowski, G.; Bobrowski, A.; Kurleto-Kozioł, Ż. Thermal decomposition of binder based on etheri ed starch to use in foundry industry. *J. Therm. Anal. Calorim.* **2017**, *130*, 285–290. [CrossRef]
28. Stachowicz, M.; Granat, K. Research on Reclamation and Activation of Moulding Sands Containing Water-Glass Hardened with Microwaves. *Arch. Foundry Eng.* **2014**, *14*, 105–110. [CrossRef]
29. Stachowicz, M.; Granat, K.; Pałyga, Ł. Effect of Sand Wetting on Physically Hardened Moulding Sands Containing a Selected Inorganic Binder. Part 1. *Arch. Foundry Eng.* **2016**, *16*, 73–78. [CrossRef]
30. Grabowska, B.; Kaczmarska, K.; Bobrowski, A. Studies on the renewability of polymeric binders for foundry. *Arch. Foundry Eng.* **2012**, *12*, 47–52. [CrossRef]
31. Grabowska, B.; Sitarz, M.; Olejnik, E.; Kaczmarska, K. FT-IR and FT-Raman studies of cross-linking processes with Ca^{2+} ions, glutaraldehyde and microwave radiation for polymer composition of poly(acrylic acid)/sodium salt of carboxymethyl starch—Part I. *Spectrochim. Acta Part A Mol. Biomol. Spectrosc.* **2015**, *135*, 529–535. [CrossRef]
32. Grabowska, B.; Sitarz, M.; Olejnik, E.; Kaczmarska, K.; Tyliszczak, B. FT-IR and FT-Raman studies of cross-linking processes with Ca^{2+} ions, glutaraldehyde and microwave radiation for polymer composition of poly(acrylic acid)/sodium salt of carboxymethyl starch—In moulding sands, Part II. *Spectrochim. Acta Part A Mol. Biomol. Spectrosc.* **2015**, *151*, 27–33. [CrossRef]
33. *PN-83/H-11073*; Foundry Moulding Materials. Strength Measurement. ALFA, Foundry Research Institute: Krakow, Poland, 1984.
34. *PN-EN ISO 9888*; Jakość Wody. Oznaczenie Całkowitej Biodegradacji Tlenowej Związków Organicznych w Środowiskuwodnym. Test Statyczny (Metoda Zahna-Wellensa). ISO: Geneva, Switzerland, 2005.
35. *PN ISO 15705*; Jakość Wody. Oznaczanie Indeksu Chemicznego Zapotrzebowania Tlenu (SP-ChZT). Metoda Zminiaturyzowana z Zastosowaniem Szczelnych Probówek. ISO: Geneva, Switzerland, 2005.
36. Stachowicz, M. Effect of Sand Base Grade and Density of Moulding Sands with Sodium Silicate on Effectiveness of Absorbing Microwaves. *Arch. Foundry Eng.* **2016**, *16*, 103–108. [CrossRef]
37. Poduchowicz, P.; Stachowicz, M.; Granat, K. Effect of Microwave Heating on Moulding Sand Properties with Gypsum Binder. *Arch. Foundry Eng.* **2017**, *17*, 97–102. [CrossRef]
38. Nowak, D. Determination of Binder Content in Traditional Sandmixes by Microwave Method. *J. Cast. Mater. Eng.* **2017**, *1*, 80–84. [CrossRef]
39. Puzio, S.; Kamińska, J.; Major-Gabryś, K.; Angrecki, M.; Hosadyna-Kondracka, M. Microwave-Hardened Moulding Sands with Hydrated Sodium Silicate for Modified Ablation Casting. *Arch. Foundry Eng.* **2019**, *19*, 91–96. [CrossRef]
40. Anwar, N.; Jalava, K.; Orkas, J. Microwave Hardening of Solid Inorganic Foundry Binder. *Int. J. Met.* **2025**, e00666. [CrossRef]

Disclaimer/Publisher's Note: The statements, opinions and data contained in all publications are solely those of the individual author(s) and contributor(s) and not of MDPI and/or the editor(s). MDPI and/or the editor(s) disclaim responsibility for any injury to people or property resulting from any ideas, methods, instructions or products referred to in the content.

materials

MDPI

Article

The Effect of Austempering Temperature on the Matrix Morphology and Thermal Shock Resistance of Compacted Graphite Cast Iron

Aneta Jakubus [1,*], Marek Sławomir Soiński [1], Grzegorz Stradomski [2], Maciej Nadolski [2] and Marek Mróz [3]

[1] Faculty of Technology, Jacob of Paradies University, 66-400 Gorzów Wielkopolski, Poland
[2] Faculty of Production Engineering and Materials Technology, Czestochowa University of Technology, 19 Armii Krajowej Av., 42-201 Czestochowa, Poland
[3] Department of Foundry and Welding, Rzeszow University of Technology, Powstańców Warszawy 12, 35-959 Rzeszow, Poland
* Correspondence: jakubusaneta@wp.pl

Abstract: The significance of the matrix morphology of vermicular cast iron for the alloy's thermal shock resistance was determined. The study included vermicular cast iron subjected to heat treatment in order to obtain an ausferritic matrix. Heat treatment involved austenitization at 960 °C for 90 min, followed by two different austempering variants at 290 °C and 390 °C, each for 90 min. Austempering at 390 °C resulted in a higher content of retained austenite compared to austempering at 290 °C. A test stand was used to determine thermal shock resistance, enabling repeated heating and cooling of the samples. The samples were heated inductively and subsequently cooled in water at a constant temperature of approximately 30 °C. The total length of cracks formed on the wedge-shaped surfaces of the tested samples was adopted as a characteristic value inversely proportional to the material's thermal shock resistance. The samples heated to 500 °C were subjected to 2000 heating–cooling test cycles. It was found that in as-cast iron, structural changes were minor, whereas in the heat-treated material, changes in the structure were more noticeable. Under the influence of thermal shocks, ausferrite transforms into ferrite with carbides. Among the analyzed materials, the most resistant cast iron was the one austempered at 290 °C. Oxide precipitates were observed near cracks and graphite regions.

Keywords: compacted graphite iron; austempering; austenitization; vermicular cast iron; AVGI

1. Introduction

The influence of austempering temperature on the microstructure and mechanical properties of compacted graphite iron or ductile iron is discussed by numerous researchers [1–4]. In study [5], the researchers analyzed the effect of heat treatment of compacted graphite iron on the morphology of graphite precipitates. They stated that, in the samples after heat treatment, a decrease in the degree of vermicularization of graphite is observed in comparison to the as-cast iron (the share of graphite precipitates with a shape close to spherical increases in the structure). The heat treatment also led to a reduction in the average size of graphite precipitates. Darmawan et al. [6] determined the effect of heat treatment, among others, on the microstructure of malleable cast iron. The applied heat treatment included austenitization at 850 °C for 60 min, followed by austempering at 300 °C for 30, 60, or 90 min. It was observed that longer holding times of 60 and 90 min resulted in an increase in the graphite particle size. Subjecting the cast iron to heat treatment

through austenitization and austempering (within a specific range) results in the formation of an ausferritic structure, and an improvement in tensile strength, yield strength, and hardness, with a simultaneous decrease in material elongation [7–9]. The researchers in [10] analyzed the influence of heat treatment parameters—austenitization and austempering of compacted graphite iron—on the mechanical properties of the material. For this purpose, they used multi-criteria analysis, which allows for the assessment of correlations between treatment parameters and specific properties. A total of 27 heat treatments were performed with different parameters. The optimal conditions were assumed as maximum tensile strength and yield strength, and elongation of approximately 0.7%, and it was determined that the following heat treatment parameters: $T\gamma$ = 890 °C; Tpi = 290 °C; $\tau\gamma$ = 120 min; τpi = 150 min, achieve these results. Akinribide et al. [11] analyzed unalloyed and alloyed ductile iron in terms of its microstructure, mechanical, and tribological properties. Austenitization was carried out within the temperature range of 900–970 °C for 60 min, followed by austempering at 350 °C for 30 min. It was observed, among other findings, that the alloyed ductile iron contains ferrite, austenite, and stabilized austenite, which contributed to the improvement of the material's ductility.

Cast iron components operate under a variety of service conditions. Brake discs and drums, turbines, and exhaust manifolds, as well as castings used in the metallurgical or energy industries, often function under sudden temperature variations. Such thermal fluctuations can lead to rapid degradation of components; therefore, understanding damage mechanisms and implementing strategies for their prevention is essential. In study [12], vermicular cast iron subjected to high-frequency cyclic plasma and surface cooling airflow was investigated in order to better understand its behaviour and the underlying mechanisms under varying cooling conditions in a specific thermal shock environment. In another study [13], the authors sectioned samples from cylinder heads cast from two types of vermicular cast iron (with tensile strengths of 400 MPa and 450 MPa, respectively) and subjected them to thermal fatigue testing. The temperature ranges used in the tests were 25–420 °C, 25–450 °C, 25–550 °C, 25–650 °C, and 25–750 °C, with specimens containing pre-formed V-shaped notches. It was concluded that a higher pearlite content in the matrix leads to a lower thermal crack growth rate. Moreover, the temperature at which grain boundary sliding occurs in ferrite, as well as the transformation temperature of pearlite, play a significant role in the formation and propagation of thermal fatigue cracks in both types of vermicular graphite cast iron.

It is also worth noting that some researchers focus on the morphology of graphite precipitates, which also significantly influences crack propagation. For example, in the study [14], ductile and grey cast irons with ferritic matrices were investigated with respect to their potential use in casting moulds for the glass industry, as well as their resistance to thermal shock and thermal fatigue. The results indicated that graphite flakes present in grey cast iron behave as voids within the material, which increases susceptibility to brittle fracture and, consequently, reduces both impact strength and ductility. In contrast, ductile cast iron possesses approximately 40% higher resistance to thermal shock. In studies [15,16], two types of vermicular cast iron were compared in terms of their thermal fatigue resistance: one with a ferritic matrix (EN-GJV-350), and the other with a pearlitic matrix (EN-GJV-450). The tests were carried out under several temperature ranges, maintaining a constant T_{min} of 200 °C, while T_{max} varied from 620 °C to 750 °C. The criterion for thermal fatigue resistance was the number of thermal cycles leading to complete fracture of the specimen. The results showed that the ferritic matrix cast iron exhibited lower resistance to thermal fatigue. In the case of pearlitic vermicular cast iron, rapid heating and cooling led to the progressive transformation of the pearlitic matrix into ferrite. This ferritization process reduced the temporary strength and hardness of the material, ultimately resulting in specimen failure.

The aim of this study was to analyze the influence of austempering temperature on the thermal shock resistance of compacted graphite iron (CGI). To conduct the experiments, thermal shock simulations were performed using a custom-designed test stand. Thermal shock resistance, understood as the ability to withstand sudden temperature changes, was evaluated based on the length of surface cracks formed on the specimens. A similar approach was employed in study [17], where cast iron samples with different graphite morphologies were examined. The present work focused on assessing the effect of an ausferritic matrix obtained through austempering at two different temperatures on thermal shock performance. Sudden temperature fluctuations may lead to material cracking, reduced thermal conductivity, or high-temperature corrosion. Understanding these degradation mechanisms can support the development of more resistant materials and help implement strategies that improve the operational reliability of cast components.

2. Materials and Methods

The production process of the analyzed compacted graphite iron (CGI) was described in detail in study [5]. Table 1 presents the chemical composition of the produced CGI. Microstructural observations were carried out using an Olympus DSX1000 digital microscope (DSX1000 Software Ver. 1.2.5, Olympus, Shinjuku, Japan).

Table 1. Chemical composition (wt.%) of vermicular cast iron.

C	Si	Mn	Cu	P	S	Mg
3.22	2.38	0.192	1.02	0.054	0.022	0.0271

The CGI was subjected to heat treatment involving austempering. Based on preliminary studies [18], the literature data on the heat treatment of ductile iron reported by several authors [19–23], and studies on the heat treatment of CGI [24], the austenitization temperature (Tγ) was set at 960 °C. Austempering (Tpi) was carried out at two temperatures: 290 °C and 390 °C. The 100 °C temperature difference was intended to obtain structures with different proportions of ferrite and retained austenite. Both the austenitization time ($\tau\gamma$) and austempering time (τpi) were kept constant at 90 min. The parameters of the heat treatment process are summarized in Table 2.

Table 2. Heat treatment parameters of CGI.

Designation of Heat Treatment Variants	Austenitization Temperature Tγ [°C]	Austenitization Time $\tau\gamma$ [min]	Austempering Temperature Tpi [°C]	Austempering Time τpi [min]
Variant 1	960	90	390	90
Variant 2	960		290	

The heat treatment was carried out in industrial condition at "Odlewnie Polskie S.A." in Starachowice, Poland (see Figure 1). Austenitization was performed in an electric resistance chamber furnace manufactured by ELTERMA (Świebodzin, Poland), in an air atmosphere. Austempering was conducted in a quenching bath, where a salt bath was used as the quenching medium. After removal from the bath, the specimens were rinsed to remove salt residues.



Figure 1. Workstation used for austenitization and austempering.

The microstructure of as-cast CGI was examined using samples taken from type IIb test castings according to standard PN-EN 16079:2012 [25]. The classification of graphite precipitates was performed in accordance with standard [26], while microstructural evaluation was conducted based on the methodology described in standard [27]. A similar procedure was applied to assess the microstructure after heat treatment. The amount of retained austenite was determined using the NIS-Elements D image analysis software (Version 4.5). Measurements were carried out at 72 locations under 400× magnification. Additionally, for heat-treated CGI samples, microstructural observations were performed using a Vega 3 scanning electron microscope (VEGA TC v3.6.0.0, Tescan, Brno, Czech Republic). Chemical composition analysis was also conducted using an Inca X-Act EDS system (Oxford Instruments, Abingdon, UK).

This study involved the evaluation of the tensile strength of CGI, both in the as-cast condition and after heat treatment. For this purpose, tensile specimens were machined from the test castings (type IIb) after separating them from the riser. To account for possible scale formation during thermal processing, the gauge diameter of the tensile specimens was intentionally increased from the typical 10 mm to 12 mm. The additional material was subsequently removed after the heat treatment. For each experimental variant, four tensile tests were carried out. The minimum sample size was determined based on statistical methods, assuming an allowable estimation error of 20 MPa. Mechanical testing was performed using a ZWICK 1488 universal testing machine (Ulm, Germany).

To evaluate the thermal shock resistance of CGI, a dedicated device was used, designed, and constructed at the Czestochowa University of Technology. The system enables repeated heating and cooling of test specimens within a controlled temperature range. A detailed description of the apparatus and testing methodology is provided in studies [14,28,29]. Figure 2 presents the test apparatus used in this study.

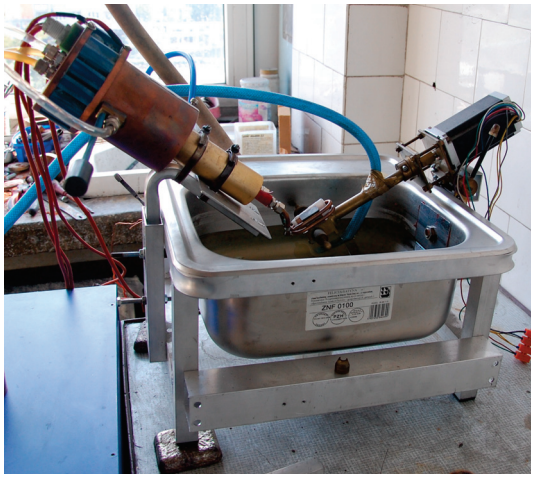


Figure 2. Experimental setup for testing materials under sudden temperature changes.

The equipment is equipped with a high-frequency induction heater (operating at 100 kHz). The temperature of the heated specimen was monitored using a stationary Marathon 2M pyrometer (Raytek, Santa Cruz, CA, USA). After reaching the target temperature (measured via pyrometry), the specimen was automatically rotated 180°, immersing the heated part into a water tank, while simultaneously initiating the heating of the opposite end. It should be noted that the water temperature of approx. 30 °C was maintained at a constant level using a heat exchanger system. The samples were heated for approx. 14 s and then cooled in water for the same duration.

For the thermal shock resistance tests, flat specimens with a length of 70 mm and a thickness of 5 mm were used. Both ends of the specimens were tapered over a length of 15 mm. The samples made of CGI were cut from type IIb test castings (see Figure 3). The geometry and dimensions of the specimens used for thermal shock testing—both in the as-cast condition and after heat treatment (after machining off the surface layer)—are shown in Figure 4. This figure also indicates the temperature measurement point (for pyrometry), as well as the crack observation areas (both tapered ends of the specimen).

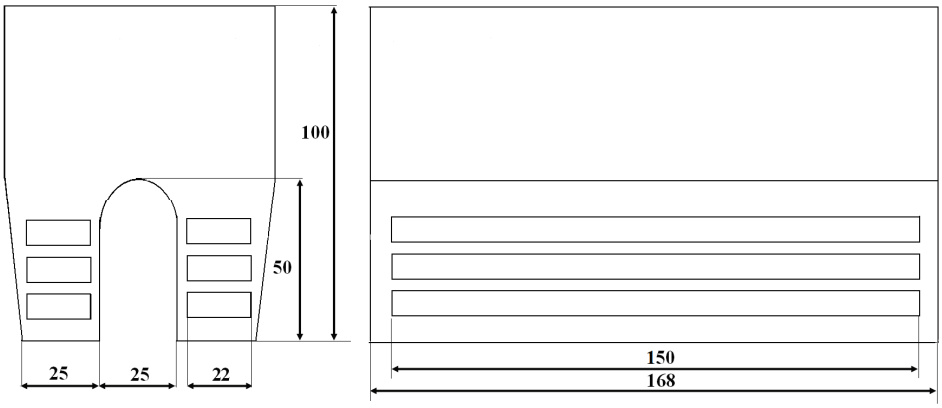


Figure 3. Location of specimen extraction for thermal shock testing from type IIb casting.

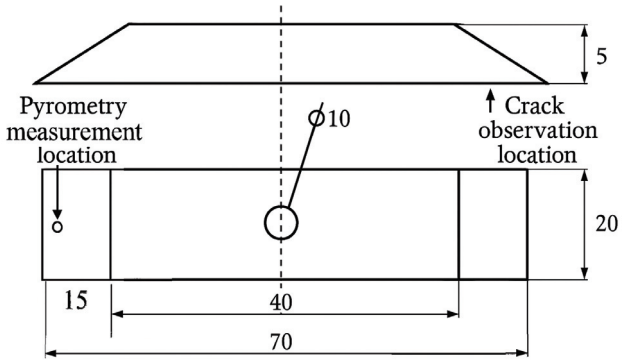


Figure 4. Specimen used for thermal shock resistance evaluation.

The specimens were subjected to the following sequence of steps:

- Heating of the wedge-shaped end using an induction coil until the target temperature was reached;
- Rotating the specimen by 180°;
- Cooling in water during the heating of the opposite end.

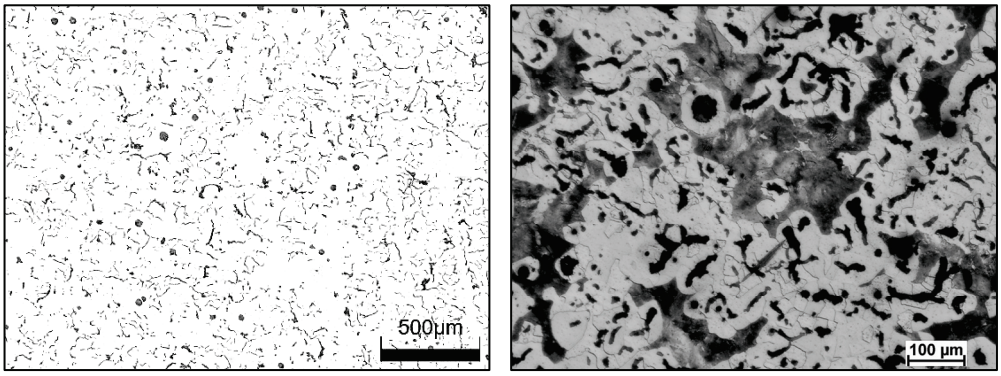
The total length of all microcracks observed on the wedge-shaped surfaces of each specimen was adopted as the measure of thermal shock resistance. Preliminary crack length assessment was performed using a non-destructive technique—penetrant testing. Final measurements and observations of crack length were carried out using an Olym-

pus DSX1000 digital microscope. The distribution of elements in vermicular cast iron in the presence of cracks was investigated using an Energy Dispersive Spectroscopy (EDS) detector integrated into an Axia ChemisSEM scanning electron microscope (SEM) from ThermoFisher Scientific (Waltham, MA, USA). The microscope is equipped with a tungsten filament electron source. The analyses were performed at magnifications of 6000× and 25,000× using an accelerating voltage of 30 kV.

3. Results and Discussion

3.1. Microstructure Analysis

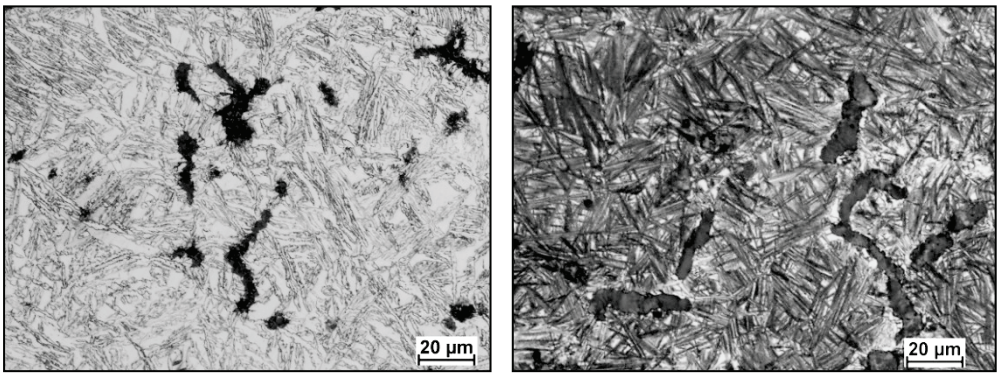
Figure 5 shows the graphite morphology and the microstructure of CGI cast iron. In the examined cast iron, vermicular graphite accounted for approximately 95%, while nodular graphite made up a small portion of about 5%. The ferrite content slightly exceeded 50%, while the remainder of the matrix consisted of pearlite.



(**a**) (**b**)

Figure 5. Cast iron with vermicular graphite as-cast state; (**a**) shape and size of graphite particles, nonetched specimen; (**b**) microstructure of cast iron, metallographic specimen etched with Nital.

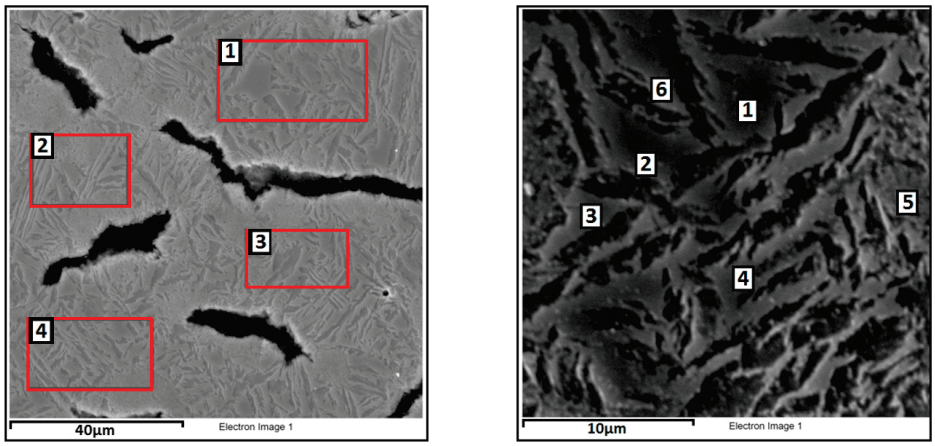
Microstructural analysis of CGI subjected to austempering revealed that the matrix consisted of so-called ausferrite, i.e., a structure composed of acicular ferrite and retained austenite (see Figure 6). To determine the amount of retained austenite, the matrix was analyzed using the NIS-Elements D image analyzer. The measurements were performed at 72 points under 400× magnification. The results showed that the highest retained austenite content (approx. 38%) was observed in samples austempered at 390 °C. Samples subjected to austempering in a salt bath at 290 °C exhibited a lower retained austenite content of approx. 24%



(**a**) (**b**)

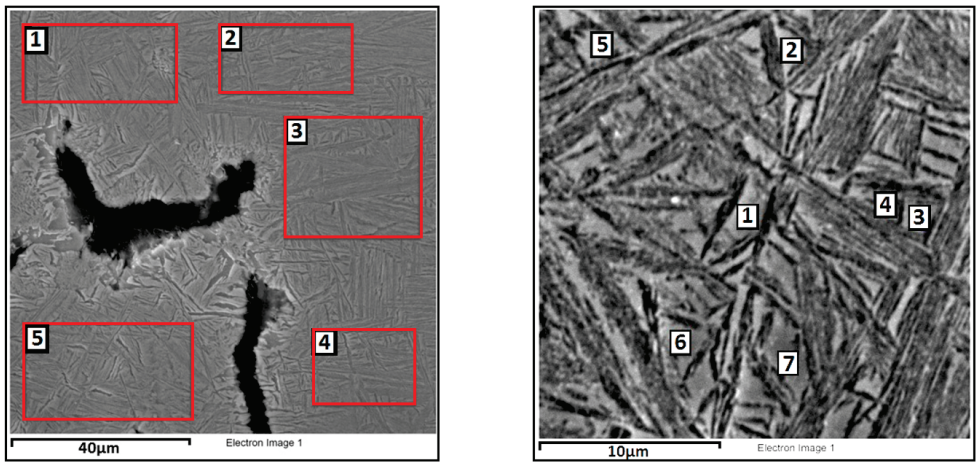
Figure 6. Microstructures of CGI after heat treatment. Heat treatment parameters: (**a**) Tγ = 960 °C, Tpi = 390 °C; (**b**) Tγ = 960 °C, Tpi = 290 °C; etched with nital, magnification 500×.

For heat-treated CGI, microstructural observations were performed using a scanning electron microscope, along with chemical composition analysis. At magnifications of 2000× and 8000×, chemical composition was analyzed on selected surface areas and specific points to identify differences resulting from the heat treatment process. The microstructure is shown in Figures 7 and 8, and the results of the observations are summarized in Table 3 The analysis includes elements such as C, Si, Fe, and Cu, as their content in the alloy exceeds 1 wt%. Other elements are present only in trace amounts, and were therefore not reported.



(**a**) (**b**)

Figure 7. SEM image of compacted graphite cast iron after heat treatment, austempered at 390 °C, showing the locations used for quantitative chemical composition analysis: (**a**) surface analysis (magnification 2000×); (**b**) point analysis (magnification 8000×).



(**a**) (**b**)

Figure 8. SEM image of compacted graphite cast iron after heat treatment, austempered at 290 °C, showing the locations used for quantitative chemical composition analysis: (**a**) surface analysis (magnification 2000×); (**b**) point analysis (magnification 8000×).

Analyzing the alloy subjected to heat treatment at an austempering temperature of 390 °C, it can be stated that retained austenite exhibits a higher average content of carbon (C = 3.77%) and copper (Cu = 1.06%) compared to ausferrite, with a simultaneously lower iron content. The silicon level is similar in both phases. Analyzing variant 2, i.e., the alloy austempered at a lower temperature of 290 °C, an increase in carbon content is observed in both ausferrite (C = 5.61%) and retained austenite (C = 4.33%) compared to variant 1. The copper content in variant 2 is higher in ausferrite (Cu = 1.04%) than in austenite (Cu = 0.71%). The content of both carbon and copper in ausferrite and retained austenite

clearly depends on the applied heat treatment parameters. As confirmed by studies [30,31], lower austempering temperatures promote carbon enrichment in retained austenite, which enhances the mechanical strength and thermal stability of the material.

Table 3. Results of quantitative chemical composition analysis in ausferrite and retained austenite of compacted graphite cast iron after heat treatment, for the areas and points marked in Figures 7 and 8.

Heat Treatment Variant of Cast Iron and Analyzed Structural Constituents			Fraction (%)			
			C, %	Si, %	Fe, %	Cu, %
Variant 1	Content in ausferrite—Figure 7a	1	2.98	2.85	93.32	0.85
		2	3.75	2.58	92.85	0.82
		3	2.78	2.61	93.84	0.77
		4	2.61	2.65	93.90	0.84
	Average:		**3.03**	**2.67**	**93.48**	**0.82**
	Content in austenite—Figure 7b	1	3.87	2.92	92.22	0.99
		2	3.65	2.81	92.46	1.08
		3	3.56	2.88	92.33	1.22
		4	3.63	2.94	92.27	1.16
		5	4.64	2.84	91.58	0.94
		6	3.29	2.89	92.85	0.97
	Average:		**3.77**	**2.88**	**92.29**	**1.06**
Variant 2	Content in ausferrite—Figure 8a	1	6.07	2.75	90.11	1.07
		2	6.08	2.61	90.25	1.06
		3	4.85	2.82	91.25	1.07
		4	4.96	2.73	91.28	1.03
		5	6.07	2.62	90.34	0.97
	Average:		**5.61**	**2.71**	**90.65**	**1.04**
	Content in austenite—Figure 8b	1	4.49	2.46	92.32	0.73
		2	4.15	2.73	92.17	0.96
		3	4.54	2.52	91.89	0.79
		4	5.04	2.55	91.39	0.78
		5	4.61	2.66	92.07	0.66
		6	3.69	2.46	93.10	0.56
		7	3.80	2.23	93.20	0.51
	Average:		**4.33**	**2.52**	**92.31**	**0.71**

3.2. Mechanical Properties

Table 4 presents the average values of basic mechanical properties—tensile strength (R_m), yield strength (R_p), elongation (A_5), and Brinell hardness (HB)—for compacted graphite cast iron in both the as-cast and heat-treated conditions. Tensile tests were conducted on four specimens per condition, while hardness measurements were performed twelve times for each variant. The hardness of the material was tested using a Brinell hardness tester, with a 2.5 mm diameter ball and a load of 1839 N. Mechanical strength tests were performed in accordance with the standard [32], and the hardness of the material was determined in accordance with the standard [33]. The highest tensile strength, yield

strength, and hardness, accompanied by low elongation, were observed in the cast iron austempered at 290 °C.

Table 4. Tensile strength (R_m), elongation (A_5), yield strength (R_p), and Brinell hardness (HB) values for compacted graphite cast iron in the as-cast and heat-treated conditions.

Tensile Strength R_m [MPa]	Yield Strength R_p [MPa]	Elongation A_5 [%]	Hardness HB [MPa]
Compacted graphite cast iron (as-cast)			
371	331	2.1	183
Austempered compacted graphite cast iron at 390 °C			
623	485	1.6	260
Austempered compacted graphite cast iron at 290 °C			
824	584	0.7	334

3.3. Thermal Shock Resistance

The thermal shock resistance of cast iron was tested by heating the specimens to 500 °C, followed by cooling in water at approximately 30 °C. A total of 2000 heating and cooling cycles were performed. Upon observing the cracks, it was noted that they propagated along the grains of vermicular graphite. In this material, crack branching occurred, forming a so-called crack network. The crack length was measured from the edge of the specimen to the point where the crack disappeared. An example of a crack is shown in Figure 9. The total crack length on the wedge-shaped sections was as follows:

- In the as-cast condition—25,676 μm;
- After heat treatment at Tpi = 390 °C (Variant 1)—21,740 μm;
- After heat treatment at Tpi = 290 °C (Variant 2)—15,628 μm.

An additional objective of the study was to determine whether, and to what extent, subjecting the cast iron to thermal shock leads to changes in the microstructure of the material. Metallographic cross-sections were prepared from the wedge-shaped ends of the tested specimens. Microstructures were analyzed at various distances from the specimen edge. Images were also taken near the cutting edge of the specimen, where cracks were visible. The topography of the crack surfaces was mapped using the LEXT software (DSX1000 Software Ver. 1.2.5) integrated with the Olympus DSX1000 digital microscope. Examples of the observed structural changes are shown in Figures 10–12. It should be emphasized that the temperature distribution within the wedge-shaped section of the specimen was not uniform. The outer edge of this section was subjected to the highest thermal load, with the degree of heating decreasing with distance from the edge. Therefore, microstructural observations were carried out at different distances from the heated area.

It should be noted that under the influence of varying temperatures reaching up to 500 °C, as well as thermal stresses during testing, slight structural changes are visible in as-cast vermicular graphite cast iron. Figure 10 shows the microstructure of vermicular graphite cast iron after thermal shock. The figure includes an example of a crack with an indicated depth (see Figure 10a). It can be seen that the microstructure consists of graphite, ferrite, and pearlite. In the ferritic–pearlitic matrix, as the temperature increases, the pearlite (Fe_3C + ferrite)—specifically the cementite—begins to decompose, releasing carbon. This carbon diffuses toward regions with lower chemical potential, such as prior austenite grain boundaries or interphase boundaries. The described mechanism was confirmed by researchers in study [34–36], who observed similar microstructural behaviour under thermal exposure.

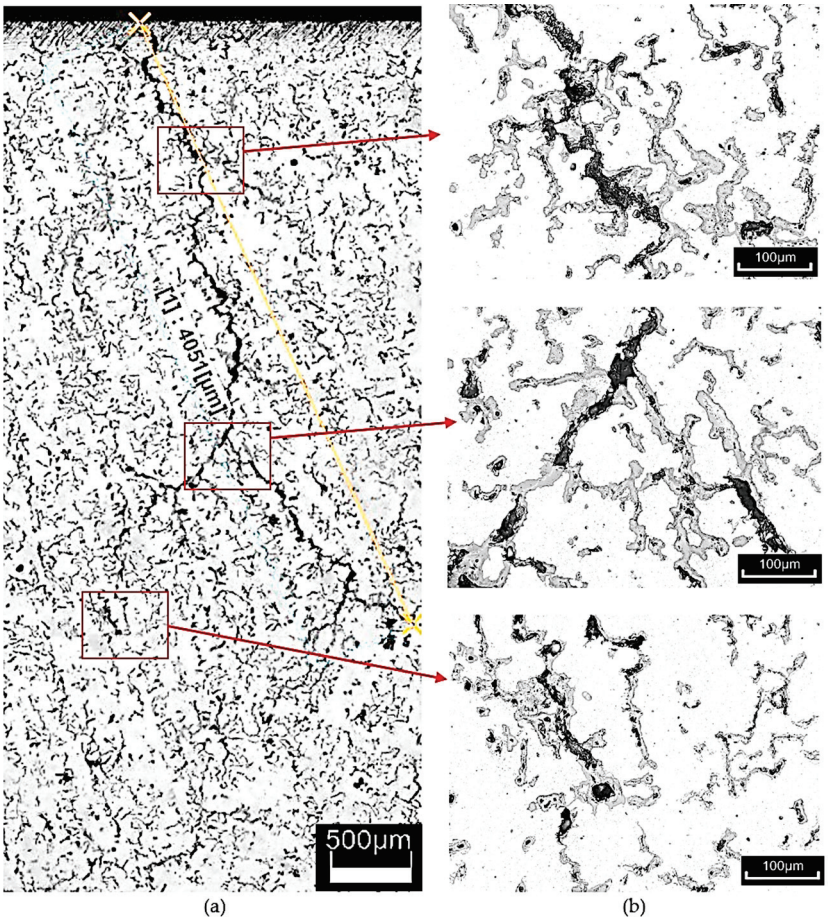


Figure 9. Example of cracks observed in compacted graphite cast iron after heat treatment (**a**) composite image from photos taken at 123× magnification, total area: 2582 × 5428 µm; (**b**) magnification 610×, unetched sample. The yellow line indicates the crack measurement.

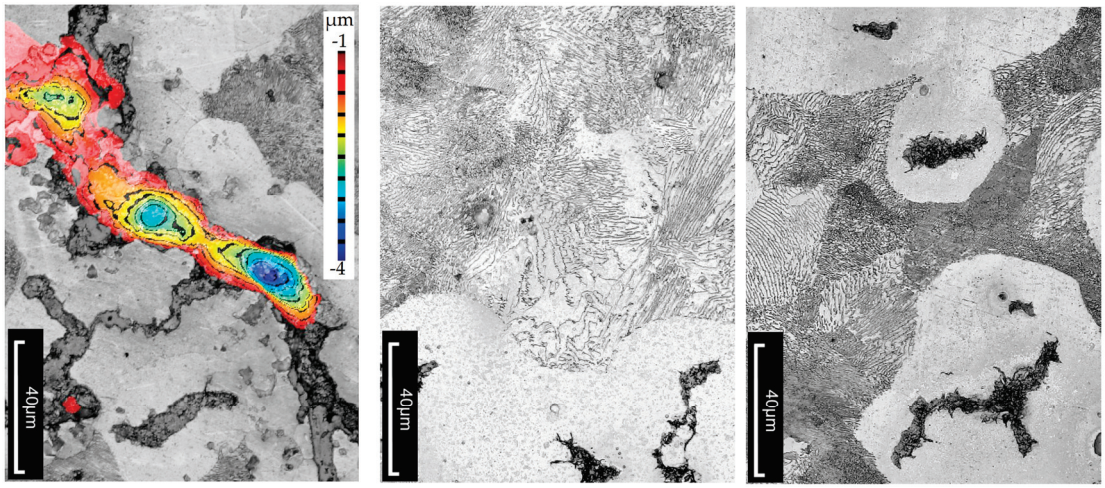
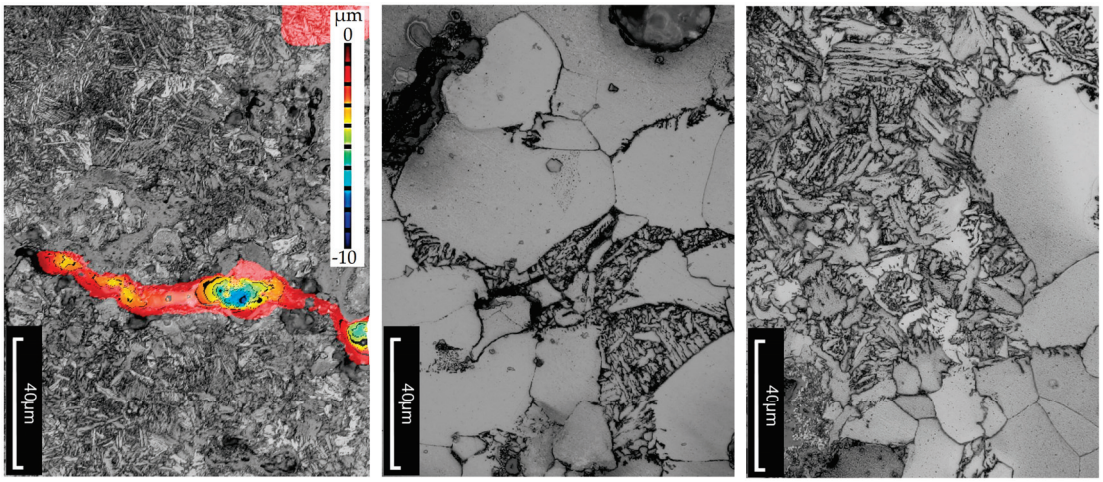
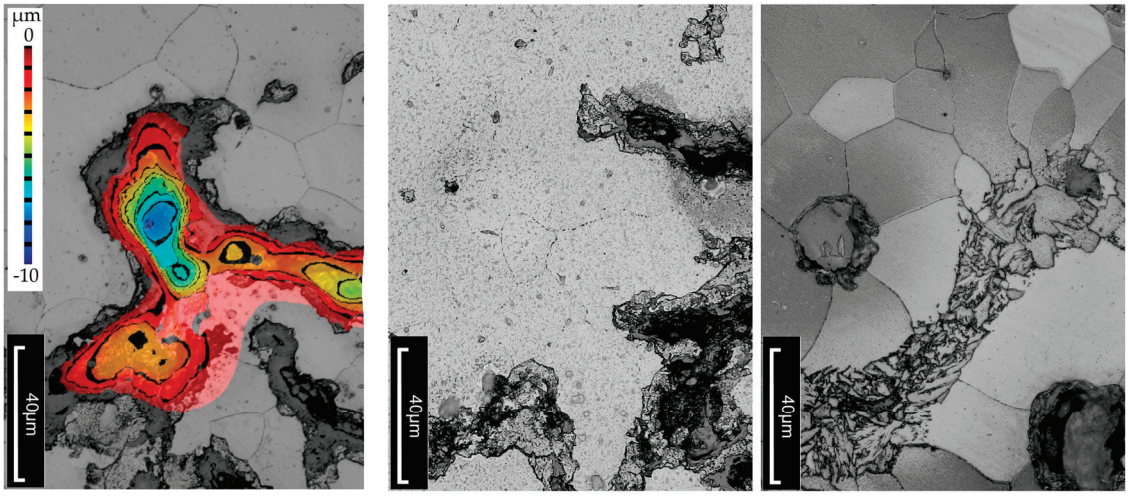


Figure 10. Microstructure of as-cast compacted graphite cast iron. The alloy was heated to 500 °C over 2000 thermal cycles. Etched with nital. (**a**) Example of a crack with an indicated depth. (**b**,**c**) Microstructure.



(**a**) (**b**) (**c**)

Figure 11. Microstructure of compacted graphite cast iron austempered at Tpi = 390 °C. The alloy was heated to 500 °C over 2000 thermal cycles and exhibited the greatest total crack length. Etched with nital. (**a**) Example of a crack with an indicated depth. (**b**,**c**) Microstructure.

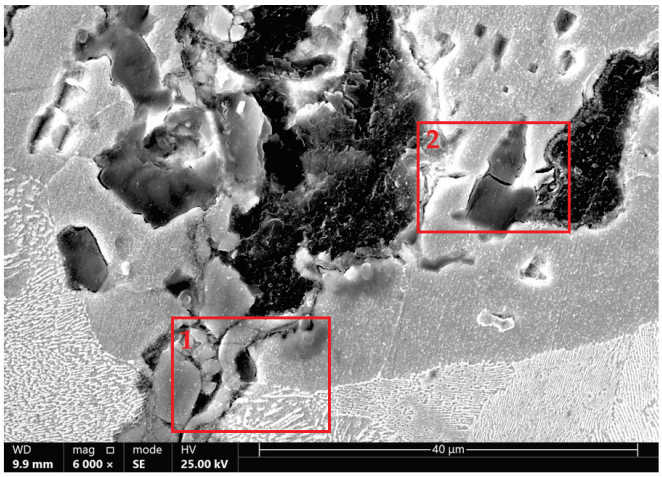


(**a**) (**b**) (**c**)

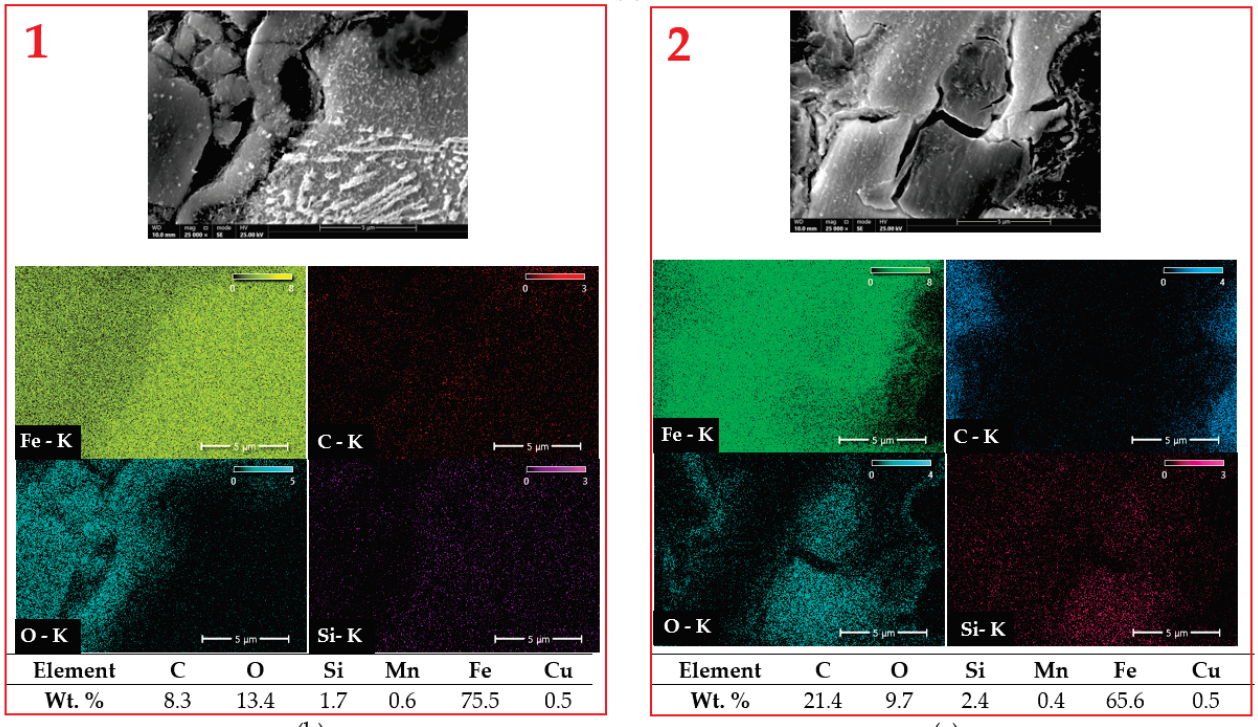
Figure 12. Microstructure of compacted graphite cast iron austempered at Tpi = 290 °C. The alloy was heated to 500 °C over 2000 thermal cycles. Etched with nital. (**a**) Example of a crack with an indicated depth. (**b**,**c**) Microstructure.

In the case of heat-treated cast iron, microstructural changes can be observed. Retained austenite, which is metastable at both room and elevated temperatures, tends to undergo phase transformation [37–40]. A higher amount of retained austenite reduces thermal conductivity, which leads to thermal stresses and cracking—as was the case for the specimen austempered at 390 °C, where the retained austenite content reached 38%. It can be concluded that a high proportion of austenite makes the material less resistant to elevated temperatures. In this specimen, structural changes occur more slowly than in the one austempered at 290 °C. In the microstructure (see Figure 11), carbide precipitates—especially cementite—are visible, mainly along phase and grain boundaries, as well as within ferrite. Fine ferrite needles begin to coalesce, causing the structure to thicken. In this case, ferrite occupies approximately 20% of the matrix, while the rest remains untransformed. In contrast, the specimen austempered at 290 °C exhibits a predominantly ferritic structure (about 90%) with 10% of the matrix still retaining untransformed structure.

Figures 13–15 show example cracks in the analyzed compacted graphite cast iron specimens after thermal shock, along with point EDS analysis. Prior to thermal shock exposure (see Figure 6), no oxides were observed in the vicinity of vermicular graphite. After testing, oxidation-affected zones can be seen. Oxides were detected within clusters of vermicular graphite and near cracks. Oxygen readily penetrates the matrix and diffuses through it, leading to the formation of oxidation products surrounding the graphite. Figure 13 presents the microstructure with a representative crack in compacted graphite cast iron with a ferritic–pearlitic matrix. The EDS results confirm the presence of oxygen, especially in the crack regions, indicating significant surface oxidation of the material. It may be assumed that small concentrations of silicon could suggest the possible formation of silicon oxides. In this type of cast iron, however, the effects of high-temperature corrosion appear to be minimal.



(a)



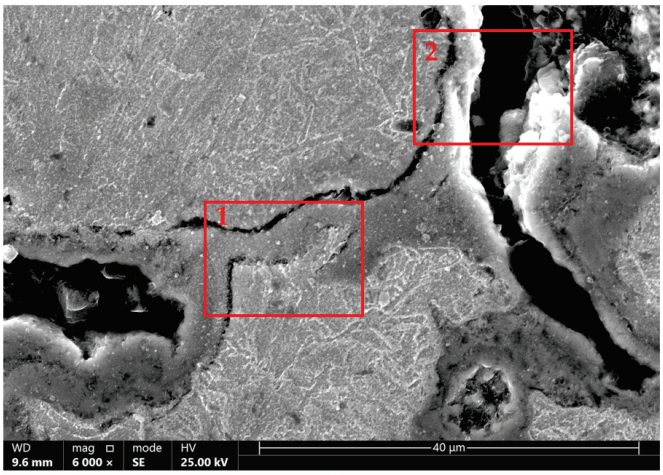
Element	C	O	Si	Mn	Fe	Cu
Wt. %	8.3	13.4	1.7	0.6	75.5	0.5

(b)

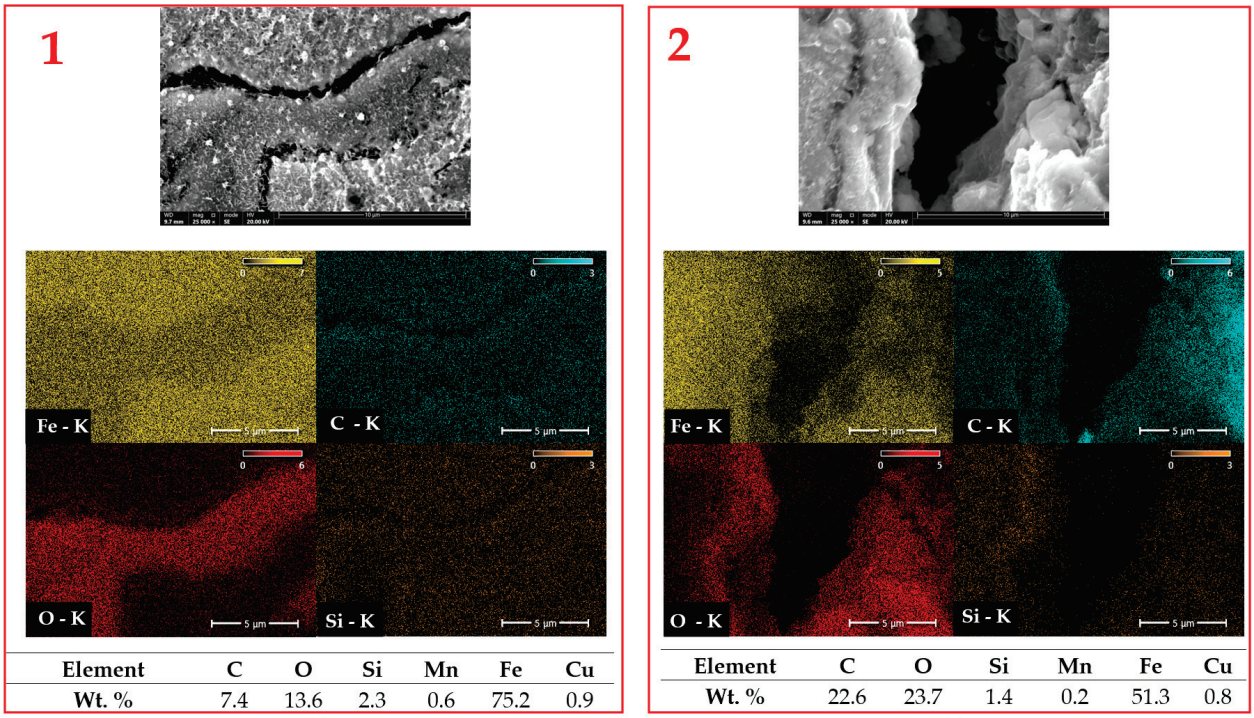
Element	C	O	Si	Mn	Fe	Cu
Wt. %	21.4	9.7	2.4	0.4	65.6	0.5

(c)

Figure 13. Analysis of elemental distribution in as-cast compacted graphite cast iron. (**a**) Microstructure at 6000× magnification. Red rectangles indicate the locations of chemical composition measurements. (**b**,**c**) Selected areas from (**a**) shown at 25,000× magnification with EDS analysis.



(a)



Element	C	O	Si	Mn	Fe	Cu
Wt. %	7.4	13.6	2.3	0.6	75.2	0.9

(b)

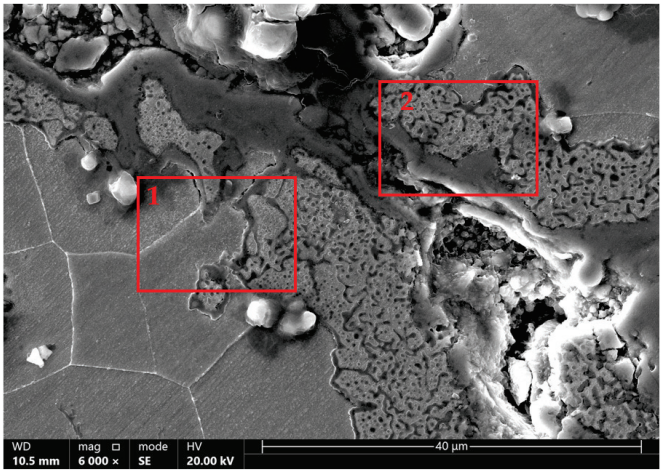
Element	C	O	Si	Mn	Fe	Cu
Wt. %	22.6	23.7	1.4	0.2	51.3	0.8

(c)

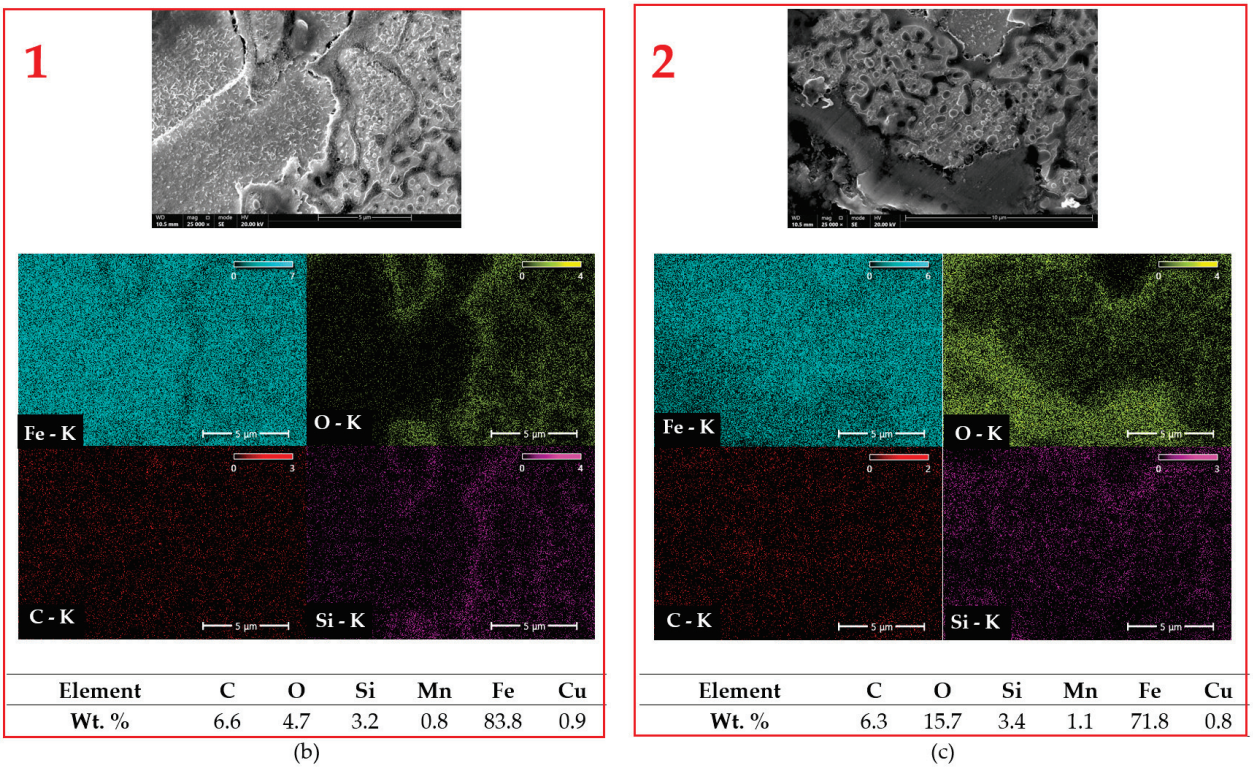
Figure 14. Analysis of area distribution of elements in compacted graphite cast iron austempered at Tpi = 390 °C. (**a**) Microstructure at 6000× magnification. Red rectangles indicate the locations of chemical composition measurements. (**b**,**c**) Selected areas from (**a**) shown at 25,000× magnification with EDS analysis.

Figures 14 and 15 present SEM images with EDX analysis of compacted graphite cast iron subjected to austempering. It is clearly visible that the cracks caused by thermal shock propagated along phase boundaries, and that oxidation occurred intensively both along the cracks and at phase interfaces. The rapid temperature changes induced thermal stresses that led to crack propagation, while the simultaneous presence of water/air and elevated temperatures favoured the formation of iron oxides (Fe_2O_3, Fe_3O_4), as well as silicon oxides (SiO_2). Figure 14 shows austempered compacted graphite cast iron (Tpi = 390 °C) with a clearly visible crack. Distinct crack branching is observed, mainly following intergranular paths. Based on EDX analysis, a high carbon concentration was detected in areas corresponding to the location of graphite, as well as within the crack itself, which may indicate the presence of graphite degradation products. In Figure 15a,

the microstructure of a prior austenite grain boundary with an associated crack is visible. Figure 15b,c, taken at 25,000× magnification, show clear intergranular crack zones with features characteristic of brittle fracture. In these regions, EDX analysis revealed increased oxygen concentration, indicating oxidation processes typical of high-temperature corrosion induced by thermal shocks. The distribution of silicon suggests the possible formation of silicon oxides [41–43].



(a)



Element	C	O	Si	Mn	Fe	Cu
Wt. %	6.6	4.7	3.2	0.8	83.8	0.9

(b)

Element	C	O	Si	Mn	Fe	Cu
Wt. %	6.3	15.7	3.4	1.1	71.8	0.8

(c)

Figure 15. Analysis of area distribution of elements in compacted graphite cast iron austempered at Tpi = 290 °C. (**a**) Microstructure at 6000× magnification. Red rectangles indicate the locations of chemical composition measurements. (**b**,**c**) Selected areas from (**a**) shown at 25,000× magnification with EDS analysis.

The analysis clearly suggests that the oxidation process occurred intensively along the cracks and at the phase boundaries. With repeated thermal shocks, the resulting thermal stresses led to crack propagation, and the access of air and high temperature promoted the

formation of iron oxides (Fe_2O_3, Fe_3O_4) and, most likely, silicon oxides (SiO_2), if there was a silicon admixture in the composition.

4. Conclusions

Based on the conducted studies on compacted graphite iron in relation to the thermal shock resistance of this material, the following conclusions can be drawn:

1. Samples subjected to austempering at 390 °C exhibited a higher content of retained austenite (approximately 38%) compared to samples austempered at 290 °C (approximately 24%).
2. Samples austempered at 290 °C are characterized by a higher carbon content in the ausferrite compared to the samples from variant no. 1 (austempered at 390 °C), which may be the reason for higher thermal stability and mechanical strength of this microstructure.
3. The applied heat treatment of vermicular cast iron resulted in an increase in tensile strength, yield strength, and hardness, accompanied by a decrease in elongation. Samples austempered at 290 °C exhibited the most significant changes in mechanical properties compared to the as-cast condition. It should be emphasized that these samples also demonstrated the highest resistance to thermal shocks.
4. After conducting the experiment and analyzing the effect of thermal shocks on microstructural changes, it can be stated that in vermicular cast iron in the as-cast state, no significant structural changes were observed. In the case of CGI, a transformation of the matrix from ausferritic to a ferritic matrix with carbides was noted. In the sample austempered at 390 °C, ferrite occupies approximately 20% of the matrix, while the remaining part is composed of the untransformed ausferritic matrix. In the sample austempered at 290 °C, the matrix is composed of approximately 90% ferrite and 10% untransformed microstructure.
5. It can be concluded that a high austenite content reduces the material's resistance to rapid and variable temperature fluctuations.
6. Thermal shock exposure resulted in surface oxidation of the material, particularly along cracks and graphite regions. This led to increased high-temperature corrosion of the compacted graphite iron after austempering, compared to the as-cast condition.

Author Contributions: Conceptualization, A.J. and M.S.S.; formal analysis, G.S. and M.S.S.; investigation, A.J., M.N. and M.M.; resources, M.M.; data curation, A.J. and G.S.; writing—original draft preparation, A.J.; writing—review and editing, A.J. and M.M.; visualization, M.N. All authors have read and agreed to the published version of the manuscript.

Funding: This research received no external funding.

Institutional Review Board Statement: Not applicable.

Informed Consent Statement: Not applicable.

Data Availability Statement: The original contributions presented in this study are included in the article. Further inquiries can be directed to the corresponding author.

Conflicts of Interest: The authors declare no conflict of interest.

References

1. Mróz, M.; Orłowicz, A.W.; Tupaj, M.; Jacek-Burek, M.; Radoń, M.; Kawiński, M. The Effect of Structure on Thermal Power of Cast-Iron Heat Exchangers. *Arch. Foundry Eng.* **2020**, *20*, 27–30. [CrossRef]
2. Zhu, J.; Liu, Q.; Jiang, A.; Lian, X.; Fang, D.; Dong, H. The Effect of Cu on the Morphology and Growth Mode of Graphite in Compacted Graphite Iron. *Trans. Indian Inst. Met.* **2021**, *74*, 1529–1536. [CrossRef]

3. Jakubus, A.; Kostrzewa, J.; Ociepa, E. The Influence of Heat Treatment Parameters on the Microstructure and Mechanical Properties of ADI and AVGI Irons. In Proceedings of the 30th Anniversary International Conference on Metallurgy and Materials, Brno, Czech Republic, 26–28 May 2021.
4. Klimek, L.; Gumienny, G.; Januszewicz, B.; Atraszkiewicz, R.; Buczkowska, K. Structural and Phase Analysis of the Ausferritic Ductile Cast Iron Matrix Obtained by Heat Treatment and in the Raw State. *C* **2024**, *10*, 45. [CrossRef]
5. Soiński, M.S.; Jakubus, A.; Borowiecki, B.; Mierzwa, P. Initial Assessment of Graphite Precipitates in Vermicular Cast Iron in the As-Cast State and after Thermal Treatments. *Arch. Foundry Eng.* **2021**, *20*, 131–136. [CrossRef]
6. Darmawan, A.S.; Anggono, A.D.; Yulianto, A.; Febriantoko, B.W.; Hamid, A. Effect of Austempering Holding Time Variations of 30, 60, and 90 Minutes at 300 °C on the Microstructure and Toughness of Nodular Cast Iron. *J. Phys. Conf. Ser.* **2024**, *2739*, 012029. [CrossRef]
7. Mrzygłód, B.; Kowalski, A.; Olejarczyk-Wożenska, I.; Giętka, T.; Głowacki, M. Characteristics of ADI Ductile Cast Iron with a Single Addition of 1.56% Ni. *Arch. Metall. Mater.* **2017**, *4*, 2273–2280. [CrossRef]
8. Jaśkowiec, K.; Opaliński, A.; Kustra, P.; Jach, D.; Wilk-Kołodziejczyk, D. Prediction of Selected Mechanical Properties in Austempered Ductile Iron with Different Wall Thickness by Decision Support Systems. *Arch. Foundry Eng.* **2023**, *23*, 137–144. [CrossRef]
9. Rodríguez-Rosales, N.A.; Montes-González, F.A.; Gómez-Casas, O.; Gómez-Casas, J.; Galindo-Valdés, J.S.; Ortiz-Cuellar, J.C.; Martínez-Villafañe, J.F.; García-Navarro, D.; Muñiz-Valdez, C.R. Statistical Data-Driven Model for Hardness Prediction in Austempered Ductile Irons. *Metals* **2022**, *12*, 676. [CrossRef]
10. Jakubus, A.; Soiński, M.S.; Mierzwa, P.; Stradomski, G. Regression Analysis and Optimum Values of Austempering Affecting Mechanical Properties of Compacted Graphite Iron. *Materials* **2024**, *17*, 5024. [CrossRef]
11. Akinribide, O.J.; Olusunle, S.O.O.; Akinwamide, S.O.; Babalola, B.J.; Olubambi, P.A. Impact of Heat Treatment on Mechanical and Tribological Behaviour of Unalloyed and Alloyed Ductile Iron. *J. Mater. Res. Technol.* **2021**, *14*, 1809–1819. [CrossRef]
12. Liu, L.; Zhao, K.; Zhang, H.; Tang, C.; Han, Q.; Chen, J.; Tao, D.; Yang, Z. Surface Evolution of Vermicular Cast Iron in High Frequent Cyclic Plasma and Different Facial Cooling Airflows. *Metals* **2023**, *13*, 577. [CrossRef]
13. Zhang, M.X.; Pang, J.C.; Meng, L.J.; Li, S.X.; Liu, Q.Y.; Jiang, A.L.; Zhang, Z.F. Study on Thermal Fatigue Behaviors of Two Kinds of Vermicular Graphite Cast Irons. *Mater. Sci. Eng. A* **2021**, *814*, 141212. [CrossRef]
14. Stradomski, G.; Gzik, S.; Jakubus, A.; Nadolski, M. Assessment of Resistance to Thermal Fatigue and Thermal Shock of Cast Iron Used for Glass Moulds. *Arch. Foundry Eng.* **2018**, *18*, 173–178. [CrossRef]
15. Zycha, J.; Żyrek, A. Vermicular Cast Iron Production Using Inmold Technology and Evaluation of Thermal Fatigue Resistance. *Arch. Foundry Eng.* **2011**, *11*, 255–260.
16. Żyrek, A. Production of Vermicular Cast Iron by the Inmold Method Using Magnesium Alloys and Evaluation of Its Thermal Fatigue Resistance. Ph.D. Thesis, AGH University of Science and Technology, Kraków, Poland, 2014.
17. Jakubus, A.; Soiński, M.S. Thermal Shock Resistance of Cast Iron with Various Graphite Precipitate Shapes. *Arch. Foundry Eng.* **2018**, *18*, 121–124. [CrossRef]
18. Soiński, M.S.; Jakubus, A. Initial Assessment of Abrasive Wear Resistance of Austempered Cast Iron with Vermicular Graphite. *Arch. Metall. Mater.* **2014**, *59*, 1073–1076. [CrossRef]
19. Kaczorowski, M. Structure and Mechanical Properties of ADI Cast Iron. *Arch. Foundry Eng.* **2001**, *1*, 149–158.
20. Myszka, D.; Kaczorowski, M.; Tybulczuk, J.; Kowalski, A. ADI Cast Iron Production Parameters and Their Influence on Mechanical Properties. *Arch. Foundry Eng.* **2004**, *4*, 355–364.
21. Binczyk, F.; Gradoń, P. Influence of Heat Treatment Parameters on the Microstructure Formation in ADI Iron. *IMŻ Works* **2010**, *4*, 5–14.
22. Pietrowski, S. Spheroidal Cast Iron with Ferritic-Bainitic Matrix Containing Austenite or Bainite. *Arch. Mater. Sci.* **1997**, *18*, 253–273.
23. Borowski, A.W. Synthetic Spheroidal Cast Iron Subjected to Isothermal Heat Treatment (ADI). In Proceedings of the 23rd Scientific-Technical Symposium of the Foundry Department ITMat, Warsaw University of Technology, Warszawa, Poland, 1998; p. 29.
24. Mierzwa, P. Influence of Heat Treatment on Selected Properties of Compacted Graphite Iron. Ph.D. Thesis, Czestochowa University of Technology, Częstochowa, Poland, 2010.
25. *PN-EN 16079:2012*; Foundry—Cast Iron with Compacted (Vermicular) Graphite. European Committee for Standardization: Brussels, Belgium, 2012.
26. *PN-EN ISO 945-1:2009*; Microstructure of Cast Irons—Part 1: Graphite Classification by Visual Analysis. Correction: PN-EN ISO 945-1:2009/AC; Polish Committee for Standardization: Warsaw, Poland, 2010.
27. *PN-75/H-04661*; Grey, Ductile, and Malleable Cast Irons—Metallographic Examination—Microstructure Determination. Polish Committee for Standardization: Warsaw, Poland, 2013.

28. Jakubus, A.; Soiński, M.S. The Influence of the Shape of Graphite Precipitates on the Cast Iron Abrasion Resistance. *Arch. Foundry Eng.* **2019**, *19*, 87–90. [CrossRef]
29. Stradomski, G.; Krupop, M.; Jakubus, A.; Nadolski, M. Thermal Shock Resistance of 21CrMoV5-7 Steel. In Proceedings of the 27th International Conference on Metallurgy and Materials, Brno, Czech Republic, 23–25 May 2018; pp. 873–878.
30. Ramos, P.A.; Melo, I.N.R.; Medeiros, V.H.M.; Brito, P.P. Influence of Heat Treatment Time on Microstructure Evolution of Austempered Nodular Cast Iron Evaluated by Image Segmentation. *J. Alloys Metall. Syst.* **2024**, *8*, 100135. [CrossRef]
31. Krawiec, H.; Lelito, J.; Mróz, M.; Radoń, M. Influence of Heat Treatment Parameters of Austempered Ductile Iron on Microstructure, Corrosion and Tribological Properties. *Materials* **2023**, *16*, 4107. [CrossRef] [PubMed]
32. *PN-EN 16079:2024-06*; Foundry Technology—Compacted (Vermicular) Graphite Cast Irons. Polish Committee for Standardization: Warsaw, Poland, 2024.
33. *PN-EN ISO 6506-1:2014-12*; Metallic Materials—Brinell Hardness Test—Part 1: Test Method. Polish Committee for Standardization: Warsaw, Poland, 2014.
34. Wang, X.; Zhang, W. Oxidation and Thermal Cracking Behavior of Compacted Graphite Iron under High Temperature and Thermal Shock. *Oxid. Met.* **2017**, *87*, 179–188. [CrossRef]
35. Zou, C.L.; Pang, J.C.; Zhang, M.X.; Qiu, Y.; Li, S.X.; Chen, L.J.; Li, J.P.; Yang, Z.; Zhang, Z.F. The High Cycle Fatigue, Deformation and Fracture of Compacted Graphite Iron: Influence of Temperature. *Mater. Sci. Eng. A* **2018**, *724*, 606–615. [CrossRef]
36. Shi, G.Q.; Yang, Z.; Guo, M.; Tao, D.; Sun, S.; Li, J.P.; Yan, F.H. Investigation on Thermal Fatigue and Microstructure Evolution Mechanism of Graphite Iron at Elevated Temperature. *J. Mater. Eng. Perform.* **2022**, *31*, 2593–2605. [CrossRef]
37. Górny, M.; Krawczyk, J.; Zieliński, A. Stability and Transformations of Retained Austenite in Ductile and Vermicular Austempered Cast Irons. *Arch. Metall. Mater.* **2015**, *60*, 3067–3072. [CrossRef]
38. Esteban, H.R.W.; Torralba, J.M. An Analysis of Retained Austenite in Austempered Ductile Iron. *Metall. Mater. Trans. A* **2003**, *34*, 1687–1696. [CrossRef]
39. Saal, D.; Górny, M.; Krawczyk, J. Phase Transition Kinetics in Austempered Ductile Iron (ADI) with Regard to Mo Content. *Materials* **2020**, *13*, 5266. [CrossRef]
40. Górny, M.; Krawczyk, J.; Zieliński, A. Effect of Austenitizing Temperature and Austempering Time on the Microstructure and Mechanical Properties of Austempered Ductile Iron. *Arch. Foundry Eng.* **2016**, *16*, 79–84. [CrossRef]
41. Yilmaz, R.; Bayata, F.; Solak, N. High Temperature Oxidation Behavior of High Al-Si Alloyed Vermicular Graphite Cast Iron for Internal Combustion Engine's Hot-End Exhaust Components. *Metals* **2024**, *14*, 574. [CrossRef]
42. Guo, Q.; Yang, Z.; Guo, D.; Tao, D.; Guo, Y.; Li, J.; Bai, Y. Research on the Oxidation Mechanism of Vermicular Graphite Cast Iron. *Materials* **2019**, *12*, 3130. [CrossRef] [PubMed]
43. Kowalski, M. Effect of Mo Addition on the Chemical Corrosion Process of SiMo Cast Iron. *Materials* **2020**, *13*, 1745. [CrossRef] [PubMed]

Disclaimer/Publisher's Note: The statements, opinions and data contained in all publications are solely those of the individual author(s) and contributor(s) and not of MDPI and/or the editor(s). MDPI and/or the editor(s) disclaim responsibility for any injury to people or property resulting from any ideas, methods, instructions or products referred to in the content.

materials

MDPI

Article

Regression Analysis and Optimum Values of Austempering Affecting Mechanical Properties of Compacted Graphite Iron

Aneta Jakubus [1,*], Marek Sławomir Soiński [1], Piotr Mierzwa [2] and Grzegorz Stradomski [2]

[1] Faculty of Technology, Jacob of Paradies University, 66-400 Gorzów Wielkopolski, Poland
[2] Faculty of Production Engineering and Materials Technology, Czestochowa University of Technology, 19 Armii Krajowej Av., 42-201 Czestochowa, Poland
* Correspondence: jakubusaneta@wp.pl

Abstract: The study examined the effect of heat treatment parameters of compacted graphite iron (CGI) on the mechanical properties of the material. The microstructure was characterized using optical microscopy, scanning electron microscopy (SEM), and transmission electron microscopy (TEM). Three levels of heat treatment parameters were adopted considering the orthogonal test plan 2^4. The effects of austenitizing temperature and time and austempering on tensile strength, yield strength, and elongation were analyzed. Polynomial regression was chosen because it extends linear regression and allows for modeling more complex, nonlinear relationships between variables. Total regression models were determined for each dataset. The models for tensile strength (R_m) had an approximately 82% coefficient of determination, for yield strength ($R_{0.2}$) around 50%, and for elongation (A_5) around 80%. For optimization, the response surface method (RSM) was used. The results obtained were compared with the proposed mathematical models. The ANOVO results showed that austempering temperature (T_{pi}) had the greatest effect on each parameter studied. The optimal conditions for the analyzed parameters, assuming tensile strength and yield strength at the maximum level and an elongation of about 0.7%, are obtained for the following heat treatment parameters: T_γ = 890 °C; T_{pi} = 290 °C; τ_γ = 120 min; τ_{pi} = 150 min.

Keywords: compacted graphite iron; austempering; austenitization; vermicular cast iron; AVGI; RSM; regression models

1. Introduction

As a casting alloy, cast iron is the most widely used material for all kinds of machine and equipment components. In 2021, its total production was about 68 million tons, accounting for 70% of the world's foundry output [1]. It is not surprising that this material is subjected to various modifications to improve its strength and performance properties, as it is much cheaper to produce compared to steel or cast steel. In recent years, ductile iron (DI) has been rising to prominence. In 2000, global production of this type of cast iron was 13 million tons, and in 2021, it had already reached approximately 25 million tons, representing an increase of about 100% [1]. A number of researchers have investigated DI highlighting the use of this alloy at low temperatures [2], the distribution and influence of individual alloying elements [3–8], subjecting it to hot plastic deformation and compression [9], applying coatings to extend the life of the alloy [10], or remelting the surface with a laser beam [11]. The production of DI involves the procedure of spheroidizing and modifying low-sulfur cast iron, as it is well known that as long as sulfur and oxygen are in the molten bath, magnesium (which is used for spheroidizing) causes deoxidation and desulfurization, and spheroidizing occurs only after a certain period of time [6,12–14]. In the case of DI, one of the methods used to improve strength properties is to change the matrix to ausferritic. This matrix can be obtained either by controlling the chemical composition [15] or by heat treatment.

The two-stage heat treatment involves austenitizing the cast iron to obtain austenite in the matrix, followed by rapid cooling to a temperature in the range of 250–400 °C and holding for the time necessary for austempering to occur [16]. Austempering and isothermal transformation in cast iron results in a structure consisting of acicular ferrite and residual austenite [17]. A number of researchers have analyzed the effect of heat treatment parameters on graphite precipitation, matrix, strength properties, abrasive wear, or thermal fatigue of austempered ductile iron (ADI) [18–21]. This type of cast iron has rapidly gained importance because the spheroidal shape of the graphite improves selected strength and performance properties. In [18], the authors analyzed the effect of heat treatment of ADI on hardness. The austenitizing temperature in this case was constant at 950° for 120 min. The austempering temperatures and times were variable at 290 °C, 320 °C, 350 °C, and 380 °C as well as 30, 60, 90, and 120 min. The results indicated that the highest hardness is obtained with an austempering temperature of 290 °C for 30 min. This was due to the thickening of ferrite needles and a higher proportion of residual austenite. The authors of the paper [22] austenitized cast iron with 0.87 Cu and 00.25 Mo at 910 °C for 90 min, then tempered it in a salt bath at temperatures ranging from 350, 370, 390, and 410 °C, obtaining the highest ductility of the material tempered at 410 °C, and the highest tensile strength for cast iron tempered at 350 °C. Jakubus et al. [23] found that as the temperature of austempering increases, there is a tendency for the ratio of ferrite in the matrix to increase, thereby decreasing the ratio of austenite. Given its ductility, increasing the ratio of ferrite in the ausferritic matrix resulted in improved ductility of the cast iron at the expense of its tensile strength. The performance properties of ADI, such as corrosion resistance and abrasive wear, were studied by Krawiec, H. et al. [24]. The researchers analyzed samples austenitized at 900 °C for a period of 2 h and then austempered at 280 °C and 430 °C for 30 and 120 min. It was found that the depth of scoring increased as the austempering time and temperature increased.

With the creation of ductile iron in 1948 came compacted graphite iron, which at first was considered undesirable. The main problem in the CGI production process is controlling the process due to the relatively narrow process window [25]. However, it proved to have good mechanical properties and high resistance to dynamic temperature changes, which placed it between gray cast iron with flake graphite and ductile iron [26–29]. Compacted graphite iron was not used for mass production of automotive parts until the late 1960s. The increased role of CGI is related to the fact that it can be applied to castings operating under temperature gradients and heat shocks [30–32]. A number of researchers have studied it for abrasive wear intended for components such as piston rings, brake discs, cylinder blocks, etc.

A similar heat treatment that ductile iron undergoes to produce ADI is used to boost the properties of CGI. In the study [33], the researchers compared this heat treatment of both ductile iron and compacted graphite iron. The authors austenitized the samples at 900 °C for 120 min, followed by isothermal quenching at 300 °C, 370 °C, and 440 °C, maintaining the time within the range of 5 to 300 min. They found that after isothermal quenching at 300 °C for 150 min, the ausferrite needles were thinner in vermicular iron compared to ductile iron. This is associated with the larger iron–graphite interface areas characteristic of compacted graphite irons.

Austempered vermicular cast iron (AVCI), however, is not as widely produced as ADI; this is probably due to much less knowledge of the effects of the chemical composition and processes occurring in the material during austempering on the structure (matrix, morphology of precipitates) and mechanical and functional properties of the alloy [34]. In order to better understand these processes, a number of researchers are analyzing this issue. For example, in the study [35], the researchers examined the influence of isothermal quenching parameters on the microstructure and mechanical properties of AVGI cast iron. Austenitization was carried out at 900 °C for 60 min, and austempering was carried out at 275, 325, and 375 °C and for time periods of 30, 60, 90, and 120 min. The austempering temperature was found to have a significant effect on the mechanical properties of cast

iron; as the austempering temperature decreased, tensile strength and hardness increased while elongation decreased. Other authors [36] carried out heat treatment of CGI at the following parameters: T_γ = 900 °C for 90 min and T_{pi} = 325 °C for 120 min. Compared to the "baseline" CGI, heat treatment increased hardness and improved abrasive properties. In [37], AVGI tempered under four different variants was examined and compared with poured cast iron. It was observed, among other things, that the surface roughness of the castings decreased as the temperature of austempering decreased.

The general goal of multiple regression is to quantify the relationships between multiple independent (explanatory) variables and the dependent (outcome) variable. Our objective is to determine whether the heat treatment parameters (four parameters) affect the mechanical properties of the alloy. The aim is to understand how to control these parameters to achieve the desired strength properties. For instance, how does the duration of isothermal quenching affect tensile strength (R_m), and are there any dependencies between the parameters that influence R_m? It is well known that the temperature of isothermal quenching influences Rm and yield strength ($R_{0.2}$), and, to achieve low strength and hardness in CGI while increasing elongation, a high temperature is selected because this results in a higher amount of retained austenite. At low temperatures (<350 °C), the alloy achieves high strength. The relationships and correlations between heat treatment parameters provide insight into how to conduct the treatment to achieve the desired mechanical properties.

Regression models are used specifically to calculate approximate values based on existing data. They can predict various outcomes, but the main purpose is for the model to estimate the dependent variable's value (result) based on the independent variables (factors). These models allow for predicting and analyzing results that are close to real-world values based on the data we already have.

The purpose of this study was to analyze the effect of heat treatment parameters—austenitizing and austempering of compacted graphite iron—on the mechanical properties of the material. In a series of studies, researchers focus on linear analyses that determine the influence of a single heat treatment parameter on selected properties. Therefore, this work incorporates a multi-criteria analysis, which allows for the assessment of correlations between processing parameters and the specified properties. A number of researchers have studied various manufacturing processes in a similar manner. For example, the paper [38] analyzed the hardness of A383 alloy using the cooling slope casting process. The response surface methodology is used to analyze the impact of individual parameters and their interactions on casting hardness. The researchers analyzed the effect of parameters, i.e., slope length, slope angle, and pouring temperature on melt hardness, using ANOVA. The hardness of the alloy was observed to increase with longer slope lengths and higher pouring temperatures, but it decreased as the slope angle increased. A predictive regression model was developed to forecast hardness based on changes in the combination of input process parameters. The optimal hardness was achieved at a pouring temperature of 596 °C, a slope length of 596.5 mm, and a slope angle of 27°. The authors of [39] analyzed in a similar way in order to improve the machining process of Cu/Mo-SiCP composites produced by powder metallurgy. In this study, Cu/Mo-SiCP composite materials with varying reinforcement ratios were produced using powder metallurgy, and their machinability was subsequently analyzed. In the machinability experiments, the selected process parameters included cutting speed (vC), feed rate (f), depth of cut (aP), and reinforcement ratio (RR). Two levels of each parameter were chosen according to Taguchi's L8 orthogonal array, and response surface methodology (RSM) was applied for parametric optimization. In a similar way, the authors of work [40], using the Plackett–Burman design (PBD) to optimize the adsorption process, assessed the adsorption capacity of four agro-wastes (AWs) derived from pistachio nutshells (PNSs) and aloe vera leaves (AV), as well as multi-walled carbon nanotubes (MWCNTs). Saikaew et al. [41] determined the optimal proportions of cast iron scrap, steel scrap, carbon, and ferro silicon that affect the hardness and quality of cast iron. They conducted the analysis using a mixture of experimental design, analysis of variance,

and response surface methodology combined with a desirability function. Fajdek-Bieda A. [42] proposed the optimization of the geraniol transformation process in the presence of natural mineral diatomite as a catalyst. The variables used in the study were temperature, catalyst concentration, and reaction time. The process and response functions were defined as the conversion of geraniol (GA) and the selectivity of its conversion to beta-pinene (BP), respectively. The results enabled the identification of the optimal set of parameters that yielded the highest GA conversion and selectivity for BP production. In a similar way, the authors of paper [43] analyzed the wear and friction of hemp fiber-reinforced polymer for brake discs, and in paper [44], the performance of water jet cutting of tool steel using various abrasives.

2. Materials and Methods

2.1. Baseline Material

The "baseline" cast iron for subsequent treatment into compacted graphite iron was smelted in a 4000 kg acid-lined medium-frequency crucible induction furnace. After the input materials were loaded into the furnace and melted, about 2000 kg of liquid metal was taken—into an appropriately heated vat—and poured into an acid-lined mains frequency induction furnace with a capacity of 3000 kg. Three mortars from the German company SKW Giesserei GmbH (Unterneukirchen, Germany) were used to produce the cast iron.

When the liquid metal reached a temperature of 1533 °C, and the slag was drawn off, the pouring of cast iron from the furnace into a "slender" ladle with a lid was initiated. Concurrently with the pouring of the metal, VL(Ce)2 mortar was administered to the metal stream in order to "condition" the cast iron, i.e., to pretreat the alloy (this included deoxidizing the cast iron). Prior to the start of metal pouring, DENODUL 5 cast iron vermiculite mortar was placed in a heated slender ladle.

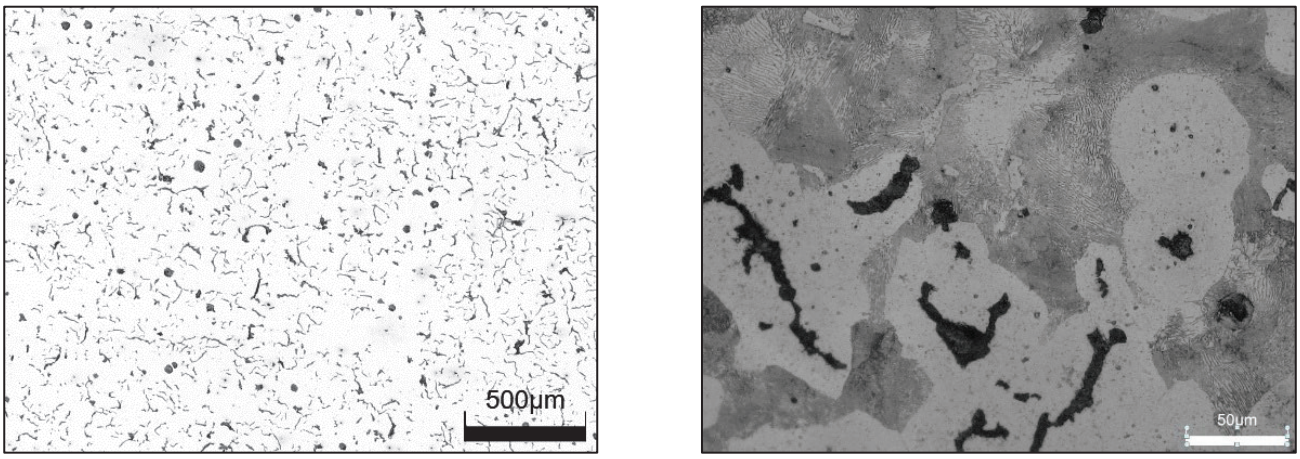
After pouring the liquid baseline cast iron, the "slender" ladle was transported to the modification bench, where the SRF 75 graphitizing modifier was applied to the metal stream after drawing off the slag. This operation was performed during the pouring of liquid metal from the "slender" ladle into the pouring ladle. After the graphitization modification, the pouring ladle filled with cast iron was transported to the pouring station, where the molds made of self-hardening compound were poured. U-shaped sample ingots with test wall thicknesses of 25 mm (according to [45]) were cast. A detailed description of the creation of cast iron can be found in the works [46].

Table 1 shows the chemical composition of the CGI produced. The content of basic elements was determined using a FOUNDRY–MASTER emission spectrometer from WAS AG. Figure 1 shows the shape and size of the graphite and the microstructure of the CGI. The Olympus DSX1000 digital microscope was used for the observations.

Table 1. Chemical composition (wt.%) of vermicular cast iron [47].

C	Si	Mn	Cu	P	S	Mg
3.27	2.80	0.203	0.98	0.0515	0.0200	0.0166

Observations showed that the samples taken from the test portions of the test ingots had a vast majority of vermicular graphite precipitates, and the proportion of spherical graphite was at several percent. The proportion of ferrite in the structure in the samples studied was slightly greater than 50%; the remainder of the matrix was perlite. It should be noted that despite approximately 1% copper content, the proportion of perlite was less than expected, while the literature data show that the addition of 0.82% copper in cast iron is sufficient to obtain a fully perlite matrix [48,49]. Metallographic observations of the cast iron samples taken did not reveal the presence of gas bubbles, non-metallic inclusions, or cracks in them. The results of metallographic tests provided the basis for accepting the produced cast iron as a material that meets the requirements for compacted graphite iron.



(**a**) (**b**)

Figure 1. Cast iron with vermicular graphite as-cast state; (**a**) shape and size of graphite particles, nonetched specimen; (**b**) microstructure of cast iron, metallographic specimen etched with Nital.

2.2. Heat Treatment

From the test parts of the IIb test ingots [46], strength samples were taken with the diameter of the measuring part of 25 mm. The samples were subjected to heat treatment by heating them to the appropriate austenitization temperature (i.e., in the range of 850–960 °C [24]), followed by austempering in a salt bath to a specified temperature (i.e., in the range of 250–400 °C [24]) and holding them for a designated time. The purpose of this treatment is to achieve an ausferritic matrix, the formation of which is associated with the nucleation and growth of plates in the austenitic matrix. The samples were austenitized and then austempered in a salt bath to a certain temperature and held there for a predetermined time. A test stand at the "Odlewnie Polskie" in Starachowice was used to carry out heat treatment. It consisted of an Elterma resistance furnace and a quenching tank, and the tempering agent was a salt bath.

CGI heat treatment was carried out based on factorial planning. The statistical treatment of the data produced in the study was treated using Minitab 21.4.3.0 software (Pennsylvania State University, Pennsylvania, PA, USA). A composition master plan was used to determine the effects of heat treatment parameters on tensile strength (R_m), yield strength ($R_{0.2}$), and elongation (A_5). With the chosen plan, the number of experiments performed and the level of individual interaction factors (values of output variables) were limited. The interaction terms were mutually independent, i.e., uncorrelated, which enabled maximum information to be obtained about the studied object. A factorial design 2^4 was used to determine primary effects and quadratic and two-way interaction effects. This plan is used to identify the mathematical model describing the relationship between variables, and the function describing the relationships usually takes the form of second-degree polynomials defined by the following formula:

$$\hat{y} = b_0 + \sum_{i=1}^{n} b_i x_i + \sum_{1 \le x \ne j} b_{ij}(x_i x_j) + \sum_{i=1}^{n} b_{ii} x_i^2 \quad (1)$$

where $\hat{y}$ denotes the calculated value of the parameter, b_o—absolute term, b_i—regression coefficients of linear terms of the model, x_i—linear terms of the factors, b_{ij}—regression coefficients of the two-coefficient terms, $x_i x_j$—interaction terms of two factors, x_i and x_j, b_{ii}—regression coefficients of quadratic terms, and x_i^2—quadratic terms of factors.

The study was based on four independent variables, such as austenitizing (T_γ) and austempering (T_{pi}) temperatures and austenitizing (τ_γ) and austempering (τ_{pi}) times. Figure 2 shows a diagram of the heat treatment performed. The following designations and ranges were used:

- X_1—austenitization temperature (T_γ) from 890 °C to 960 °C;
- X_2—austempering temperature (T_{pi}) from 290 °C to 390 °C;
- X_3—austenitization time [min] (τ_γ) from 90 min to 150 min;
- X_4—austempering time (τ_{pi}) from 90 min to 150 min.

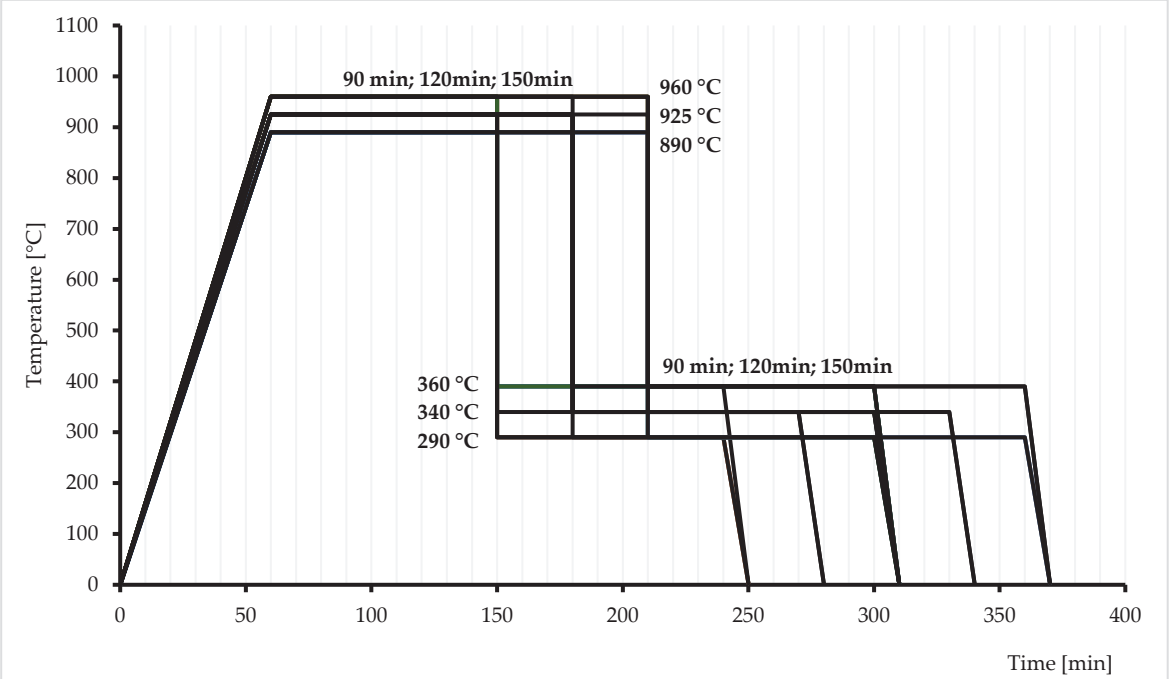


Figure 2. Schematic diagram of heat treatment cycles.

The experiment consists of three parts of levels of planned variables. In each part of the system, the values are coded accordingly. The first part is the "kernel of the plan", in which the factors take two values labeled "−1" and "+1." There are 16 experiments in this part (see Table 2; Experiments 1 through 16). The second part is the "star points," in which the studied variables take two levels labeled "α" and "−α" (in our case, 1 and −1), with a total of 8 experiments (Table 2, Experiments 17 through 24). The third part of the system is the "plan center," where the examined variables take the designation "0." The selection included 3 experiments performed under the same assumptions (see Table 2, Experiments 25 through 27). A total of 27 experiments were planned.

Table 2. Factors of the designed experiment.

No	Output Factors				No	Output Factors			
	X_1 (T_γ)	X_2 (T_{pi})	X_3 (τ_γ)	X_1 (T_γ)		X_1 (T_γ)	X_2 (T_{pi})	X_3 (τ_γ)	X_1 (T_γ)
1	890	290	90	90	17	890	340	120	120
2	960	290	90	90	18	960	340	120	120
3	890	390	90	90	19	925	290	120	120
4	960	390	90	90	20	925	390	120	120
5	890	290	150	90	21	925	340	90	120
6	960	290	150	90	22	925	340	150	120
7	890	390	150	90	23	925	340	120	90
8	960	390	150	90	24	925	340	120	150
9	890	290	90	150	25	925	340	120	120

Table 2. *Cont.*

No	Output Factors				No	Output Factors			
	X_1 (T_γ)	X_2 (T_{pi})	X_3 (τ_γ)	X_1 (T_γ)		X_1 (T_γ)	X_2 (T_{pi})	X_3 (τ_γ)	X_1 (T_γ)
10	960	290	90	150	26	925	340	120	120
11	890	390	90	150	27	925	340	120	120
12	960	390	90	150					
13	890	290	150	150					
14	960	290	150	150					
15	890	390	150	150					
16	960	390	150	150					

2.3. Strength Properties

The study determined the tensile strength of cast iron both before and after heat treatment. To this end, samples for strength testing were machined from the test portions of cast Type IIb test ingots after they had been cut off from the head. The location of the tensile test samples in the test section of the ingot is shown in Figure 3.

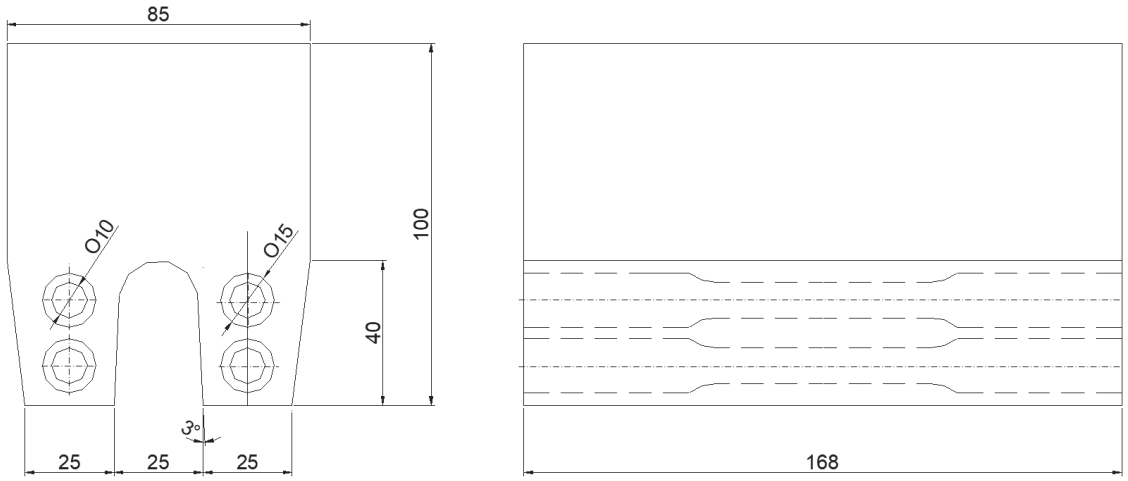


Figure 3. Place of location of strength samples in the test part of the Type IIb test ingot.

The diameter of the measuring part of the tensile test samples was deliberately increased from the usual 10 mm to 12 mm due to the possibility of scale formation during the annealing process. The excess was then removed after the heat treatment. The samples intended for testing were 160 cm long, and the diameter of the gripping cross-section was 18 cm. Four trials were conducted for each variant of the experiment. The minimum sample size was determined based on statistical methods, assuming an acceptable estimation error of 20 MPa. Mechanical properties were tested using a ZWICK 1488 (ZwickRoell, Ulm, Germany) strength testing machine at the Department of Foundry Engineering, Częstochowa University of Technology.

Based on the results of mechanical properties tests, mathematical models describing R_m, $R_{0.2,}$ and A_5 of AVCI as a function of heat treatment parameters were determined. Different regression models can be used to assess four independent variables. The options include linear regression, polynomial regression, and logistic regression. Polynomial regression was chosen because it extends linear regression and allows for modeling more complex, nonlinear relationships between variables. Total regression models were determined for each dataset. To perform the analysis, optimization was carried out using multivariate statistical techniques. The response surface methodology (RSM) was employed, which

is based on fitting a polynomial equation to the input (experimental) data. This method is applied when the response of interest is influenced by several variables. Initially, a central composite experimental design was chosen, as it limited the number of required experiments. Regression equations were established in the form of polynomial functions containing quadratic terms, describing the relationships between the selected heat treatment parameters and the mechanical properties of the alloy (tensile strength, yield strength, and elongation). The function was chosen because the study aims to estimate first-order and second-order effects, as well as interactions. A regression is considered significant if at least one of the coefficients $b_1, b_2, \ldots b_n$ of the model is significantly different from zero or if the coefficient of determination (R^2) is significantly different from zero. The next step is to apply analysis of variance (ANOVA) and determine the optimal conditions, as described in the work [50]. Pareto charts of standardized effects and 2D contour plots of the interaction of relevant predictors were drawn.

3. Results and Discussion

3.1. Microstructure Analysis

An Olympus DSX1000 digital microscope was used to describe the morphology of graphite precipitates in cast iron. To obtain additional information on the structure of AVGI, observations were made using a JEOL transmission electron microscope with an accelerating voltage of 300 kV. The results of these observations are presented in Figure 4. The microstructure obtained after heat treatment is ausferrite, which consists of acicular ferrite and carbon-saturated austenite. Two types of the resulting matrix are shown, differing in the shape of the ferrite needles and the amount of austenite present. In Figure 4a, the cast iron from Experiment Number 3 exhibits longer ferrite needles and a higher proportion of residual austenite compared to the sample from Experiment 13 (see Figure 4b). The formation, proportion, and shape of ferrite and austenite have been described in detail in the study [51]. The article [47] presents the morphology of graphite precipitates found in the iron in question and provides data on the area, perimeter, and number of graphite precipitates with respect to form factor classes, among others. In addition, the percentage of residual austenite in selected samples was determined using TEM (Table 3). Example images of cast iron microstructures after heat treatment are shown in Figure 4.

Table 3. Results of measurements of the volume fraction of retained austenite in heat-treated vermicular cast iron.

No	Heat Treatment Parameters				Average Share of Retained Austenite [%]
	X_1 (T_γ) [°C]	X_2 (T_{pi}) [°C]	X_3 (τ_γ) [min]	X_4 (τ_{pi}) [min]	
4	960	390	90	90	37
8	960	390	150	90	37
11	890	390	90	150	26
15	890	390	150	150	26
17	890	340	120	120	23
18	960	340	120	120	33
19	925	290	120	120	15
22	925	340	150	120	30
23	925	340	120	90	21
25	925	340	120	120	28

No—defined in accordance with Table 2; X_1 (T_γ)—austenitization temperature; X_2 (T_{pi}) austempering temperature; X_3 (τ_γ)—austenitization time; X_4 (τ_{pi})—austempering time.

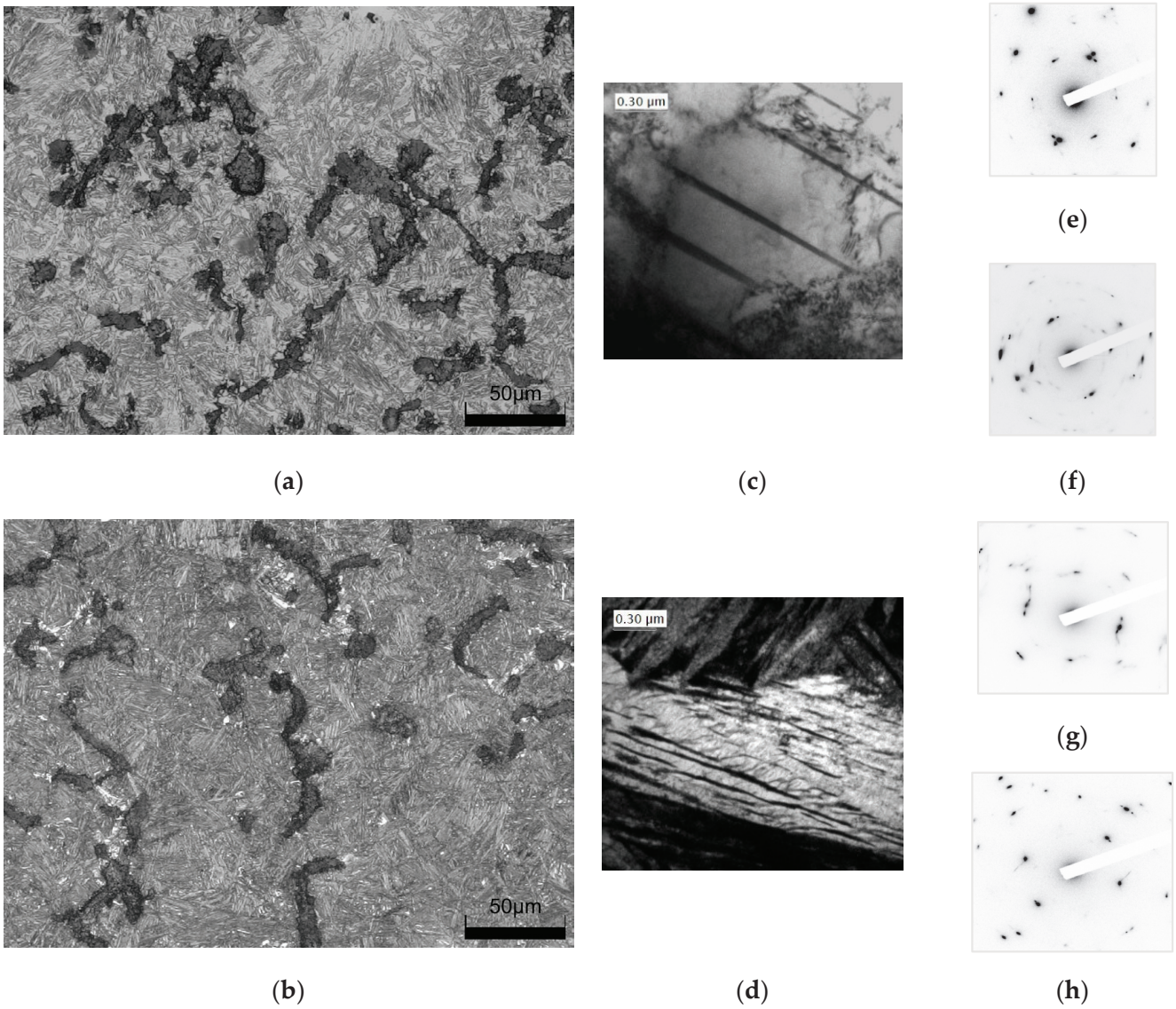
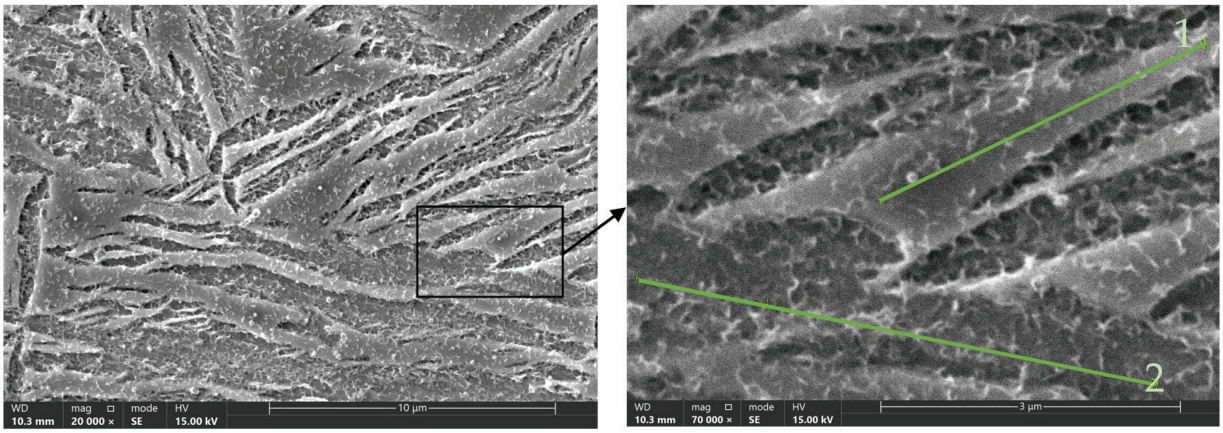


Figure 4. Microstructure of vermicular cast iron after heat treatment: (**a**) cast iron austenitized at 890 °C for 90 min and austempering at 390 °C for 90 min (Experiment No. 3 according to Table 1); (**b**) cast iron austenitized at 890 °C for 150 min and austempering at 290 °C for 150 min (Experiment No. 13). Structure obtained on TEM showing (**c**) austenite in the sample from Experiment No. 3; (**d**) a mixture of ferrite and austenite in the sample from Experiment No. 13. Electron diffraction photos of cast iron (Exp. No. 3): (**e**) austenite; (**f**) ferrite; and from Experiment No. 13: (**g**) austenite; (**h**) ferrite.

3.2. EDS Analysis

The distribution of elements was examined using an Energy Dispersive Spectroscopy detector installed in an Axia ChemisSEM scanning electron microscope from ThermoFisher Scientific (Waltham, MA, USA). In particular, attention was paid to the distribution of elements in austenite and ferrite. For this, measurement lines were used along the precipitates of these components (see Figure 5), and the composition was examined over specific sections. The results are presented in Table 4. It should be noted that magnesium accumulated in austenite, while ferrite had a higher copper content.



(**a**) (**b**)

Figure 5. Scanning electron microscope images of samples from Experiment Number 4 (see Table 2). (**a**) Magnification 20,000×; (**b**) magnification 70,000× along with measurement green lines along which the chemical composition was determined.

Table 4. Results of linear EDS analysis along the straight lines shown in Figure 5b.

Element	Line 1					Line 2				
	Weight %									
	Line Point:									
	1	2	3	4	5	1	2	3	4	5
C	10.00	11.50	9.50	9.60	9.00	11.10	9.40	8.80	10.40	9.50
Mg	0.10	0.10	0	0.10	0.20	0	0	0	0	0
Si	2.60	2.50	2.80	2.70	2.70	2.60	2.50	2.60	2.50	2.40
Mn	0.20	0.40	0	0.70	0.70	0.20	0.20	0.00	0.60	0.40
Fe	86.90	83.70	86.80	85.50	85.70	84.70	86.50	87.00	85.20	85.70
Cu	0.30	1.80	0.90	1.30	1.60	1.30	1.40	1.70	1.30	1.90

3.3. Mechanical Properties of Cast Iron

The results of measuring the properties of compacted graphite iron subjected to heat treatment are shown in Figure 6. By evaluating the mechanical properties of the cast iron before heat treatment and then comparing them with the mechanical properties of the cast iron following the heat treatment, it was possible to assess the effectiveness of the austempering operations carried out. The tensile strength of the baseline cast iron was about 340 MPa. After heat treatment, this value increased to 800 MPa on average. As for yield strength, the value for cast iron in the poured state was about 310 MPa, and after treatment, the average of all measurements increased to an average of about 700 MPa. The elongation of the cast iron samples in the pre-treatment state was 3.15% and about 0.9% after treatment.

Heat treatment, consisting of austempering, causes a change in the original structure of the baseline cast iron, which is reflected in the mechanical properties of the cast iron after heat treatment, among others. The highest tensile strength (ca. 978 MPa; Experiment 10) is found in cast iron austenitized at 960 °C for 90 min and then austempered at 290 °C for 150 min. The lowest R_m value (ca. 640 MPa; Experiment 16) is found in cast iron austenitized at 960 °C for 150 min and then austempered at 390 °C for 150 min. The relation of the yield strength of cast iron to the parameters of austempering is analogous to that of tensile strength. The largest $R_{0.2}$ value of ca. 920 MPa was exhibited by the cast iron from Experiment 10, while the smallest (ca. 560 MPa) was from Experiment 16.

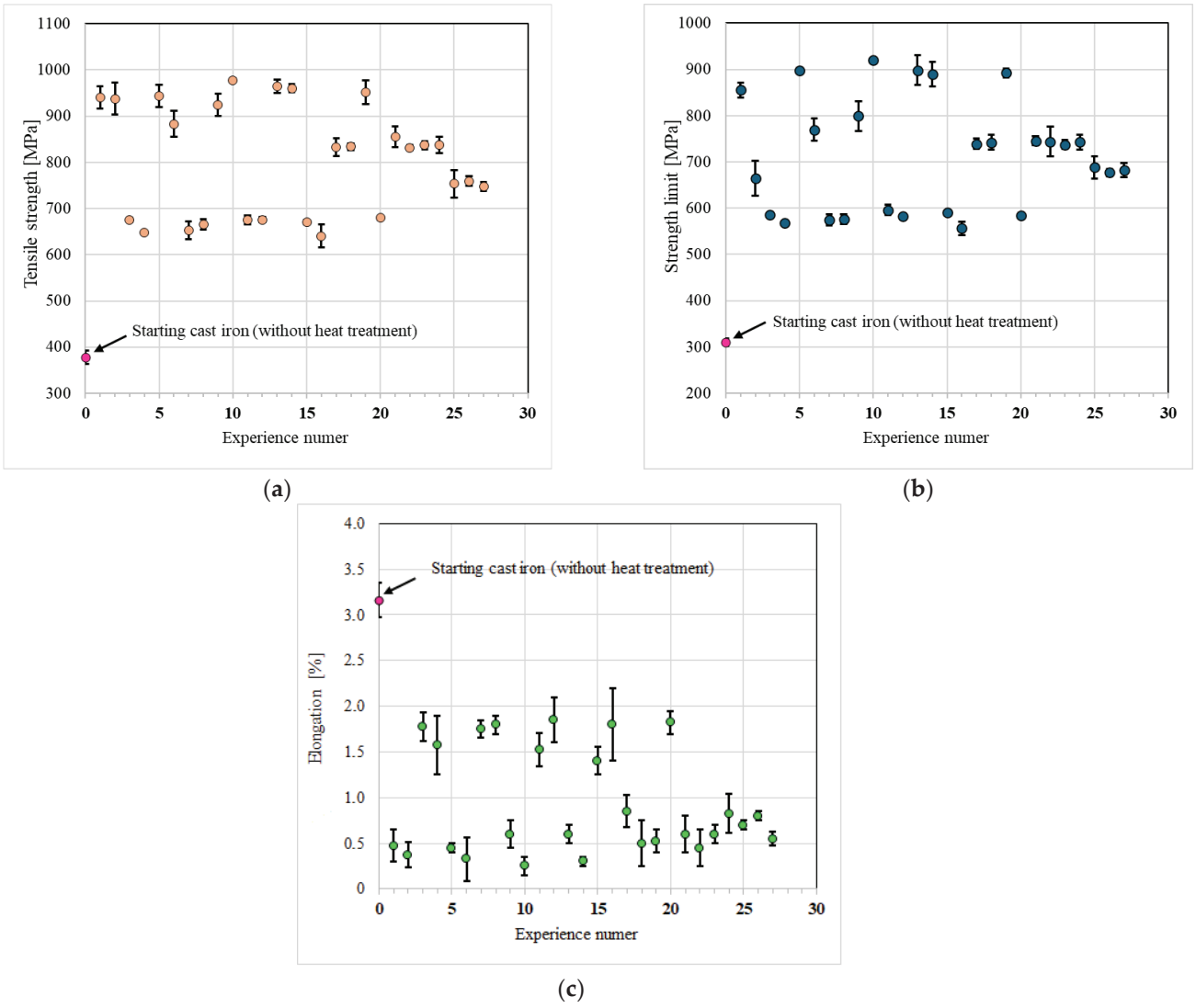


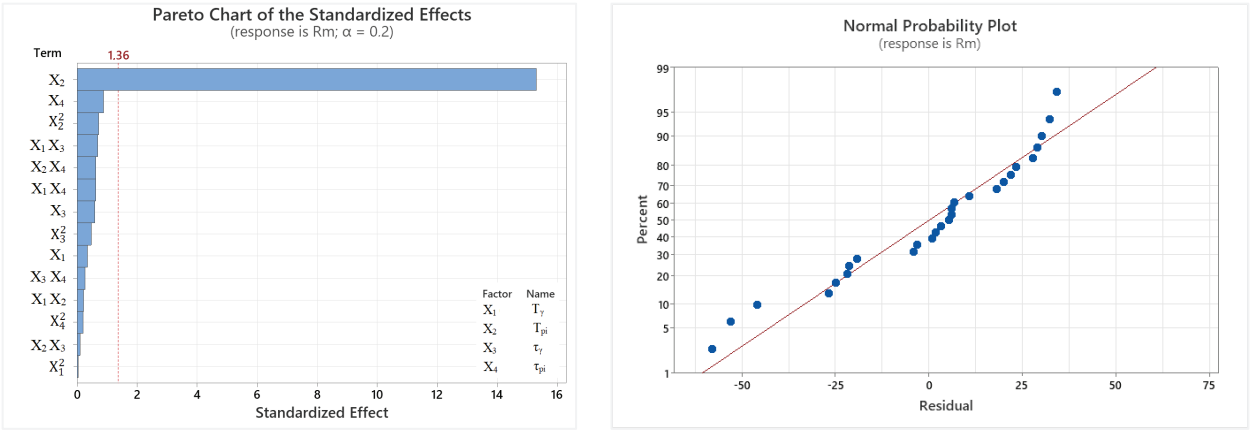
Figure 6. Mechanical properties of heat-treated vermicular cast iron classified according to the order of planned experiments; (**a**) tensile strength; (**b**) yield point; (**c**) elongation.

3.4. Impact of Heat Treatment Parameters on Rm

Figure 7a shows a Pareto chart of standardized effects obtained from analysis of variance (ANOVA) on main effects, primary effects interaction squared, and two-factor interaction. Only one interaction model was found to be significant at $\alpha = 0.2$. According to the resulting model calculation, T_{pi} is the most relevant. Furthermore, the value of the coefficient of determination (R^2) was relatively high (at 95.20%) and close to the value of the R^2 adjusted (R^2 adj) = 89.59%, which implies the linearity of the regression model. The suitability of the determined model for forecasting the size of R_m was evidenced by the high values of R^2 predicted (R^2-pred) obtained for the reliability of the selected model at 81.98%. The regression equation of the full model, describing the effect of cast iron heat treatment parameters on R_m, takes the following form:

$$R_m = 1242 - 0.8\,X_1 + 3.55\,X_2 + 2.6\,X_3 - 5.2\,X_4 + 0.0007\,X_1^2 - 0.00688\,X_2^2 + 0.0126\,X_3^2 + 0.0053\,X_4^2 - 0.00118X_1X_2 - 0.00637\,X_1X_3 + 0.00565\,X_1X_4 - 0.00063\,X_2X_3 - 0.00404\,X_2X_4 + 0.0028\,X_3X_4 \quad (2)$$

where in the formula R_m is the calculated value of tensile strength [MPa]; X_1—austenitization temperature (T_γ) [°C]; X_2—austempering temperature (T_{pi}) [°C]; X_3—austenitization time (τ_γ) [min]; X_4—austempering time (τ_{pi}) [min].



(**a**) (**b**)

Figure 7. Graphs obtained for R_m at given heat treatment parameters: (**a**) Pareto chart of standardized effects; (**b**) normal probability plot of the residuals.

From the Pareto chart, it can be observed that the austempering temperature is the most statistically significant factor. Among the insignificant factors, we can include the other three primary effects, namely austempering time, austenitizing time, and austenitizing temperature. It can be observed that T_γ has no significant impact on the mathematical model; however, the interaction with austenitizing time and with austempering time were the fourth and sixth variables presented in the Pareto chart. The strongest two-way interaction can be observed in the third position, and it relates to the austempering temperature squared. The least effective was the quadratic interaction of austenitizing temperature. Figure 7b shows a normal probability plot of the residuals, which approximately follows a straight line, indicating a normal distribution.

Two-dimensional plots (see Figure 8) of the response surface show the impact of two heat treatment parameters on the tensile strength of cast iron. When analyzing the plots, special attention was paid to the parameter most relevant to the model in question, namely T_{pi}. It can be seen from the curves in Figure 8a,d,e that as the austempering temperature increases, the material's strength value increases. From Figure 8a, for example, one can see that at a T_{pi} between 380 and 400 °C, the tensile strength of cast iron will be around 650–700 MPa. There are no relations between the T_{pi} and other parameters. Increasing the austempering time results in decreased R_m (see Figure 8b,e,f).

3.5. Impact of Heat Treatment Parameters on $R_{0.2}$

The equation of the full regression model describing the impact of cast iron heat treatment parameters on yield strength takes the following form:

$$R_{0.2} = 1926 + 0.6\,X_1 - 2.9\,X_2 + 8.3\,X_3 - 15.0\,X_4 - 0.0028\,X_1^2 - 0.0024\,X_2^2 + 0.0001\,X_3^2 - 0.0049\,X_4^2 + 0.00504\,X_1X_2 - 0.0039\,X_1X_3 + 0.0236\,X_1X_4 - 0.01046\,X_2X_3 - 0.01237\,X_2X_4 - 0.0072\,X_3X_4 \quad (3)$$

where in the formula $R_{0.2}$ is the calculated value of the yield strength [MPa]; X_1—austenitization temperature (T_γ) [°C]; X_2—austempering temperature (T_{pi}) [°C]; X_3—austenitization time (τ_γ) [min]; X_4—austempering time (τ_{pi}) [min].

The value of the model's coefficient of determination was 92.12%. The values of the adjusted and predicted determination coefficients were 82.93% and 48.95%, respectively. The determined model has a rather low coefficient of determination, which is due to the relatively large number of coefficients. The Pareto chart (Figure 9a) shows the absolute values of the impact factors. The vertical line indicates the critical value for the "t" test to assess the significance of the impact of the given factors on the output variable. It should be stressed that, at the assumed 80% confidence level, the impact of austempering

temperature (T_{pi}), the interaction of austenitizing temperature and austempering time (T_γ τ_{pi}), austempering time (τ_{pi}), and the interaction of austempering temperature and time ($T_{pi}\tau_{pi}$) are significant. The coefficient determining the strength of the interaction of T_γ, as well as the interaction of T_{pi} and τ_γ, are at a significance level exceeding the acceptable level by 0.03. The least significant primary factor was found to be austenitization time. The quadratic interactions of the input variables in question were the least effective. Virtually all points (residuals) on the normal probability plot of residuals (Figure 9b) lie very close to the line, which means that the residuals follow a normal distribution.

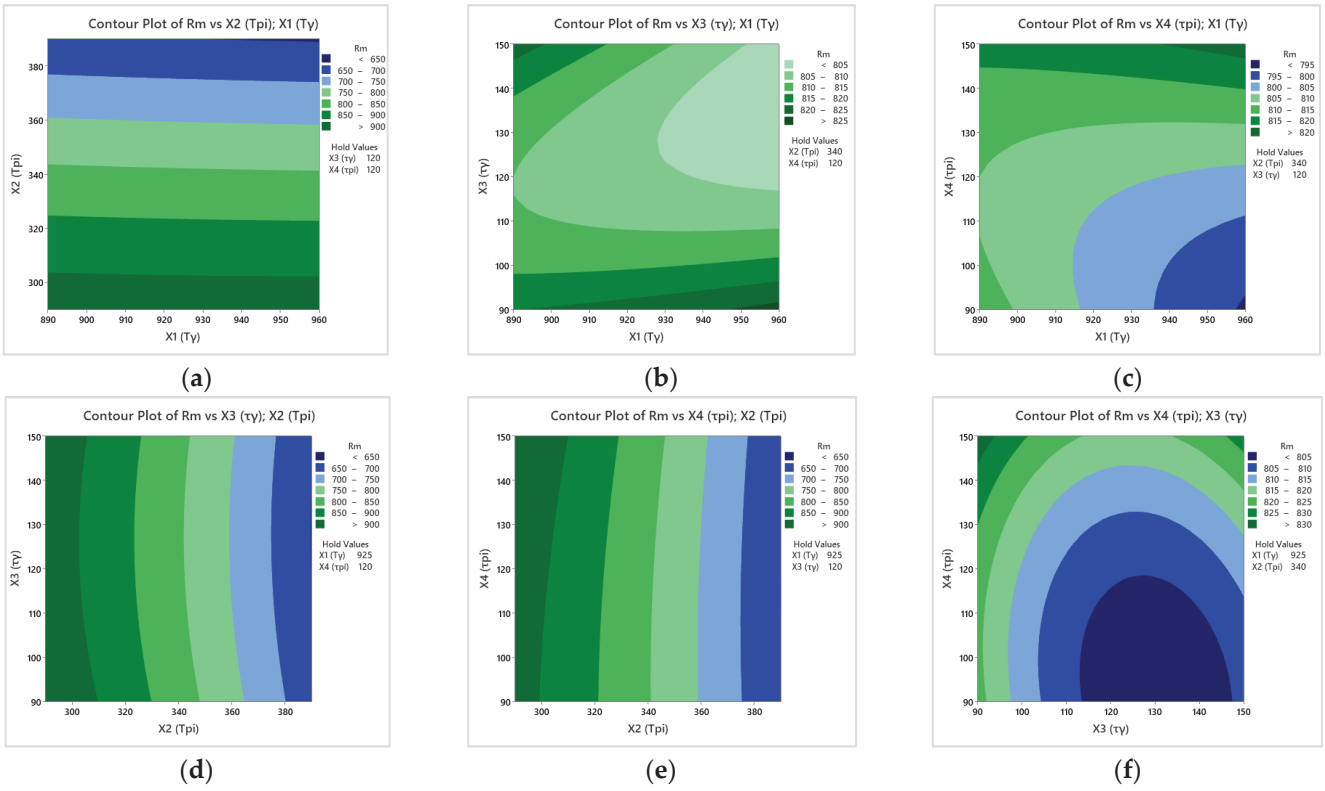


Figure 8. The influence of heat treatment parameters on Rm. The figure shows the relationship between the following heat treatment parameters: (**a**) T_γ and T_{pi}; (**b**) T_γ and τ_γ; (**c**) T_γ and τ_{pi}; (**d**) T_{pi} and τ_γ; (**e**) T_γ and τ_{pi}; (**f**) τ_γ and τ_{pi}.

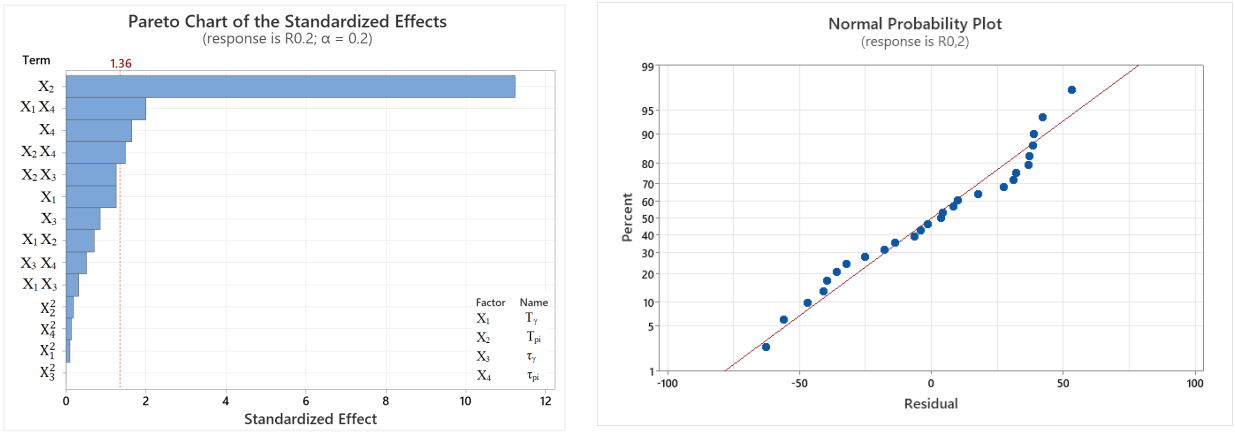


Figure 9. Graphs obtained for $R_{0,2}$ at given heat treatment parameters: (**a**) Pareto chart of standardized effects; (**b**) normal probability plot of the residuals.

Figure 10 shows the impact of austenitizing as well as austempering temperature and time on $R_{0.2}$ in the form of two-dimensional graphs. When analyzing the plots, special attention was paid to the most significant parameter. The austempering temperature, as in the case of R_m, has a significant impact on the $R_{0.2}$ of the cast iron, as evidenced by Figure 10a,d,f. As this temperature increases, the $R_{0.2}$ increases as well. Figure 10b shows a very significant relation in the proposed mathematical model. In order to achieve high yield strength, the austenitizing temperature should be reduced, while the austenitizing time should be increased.

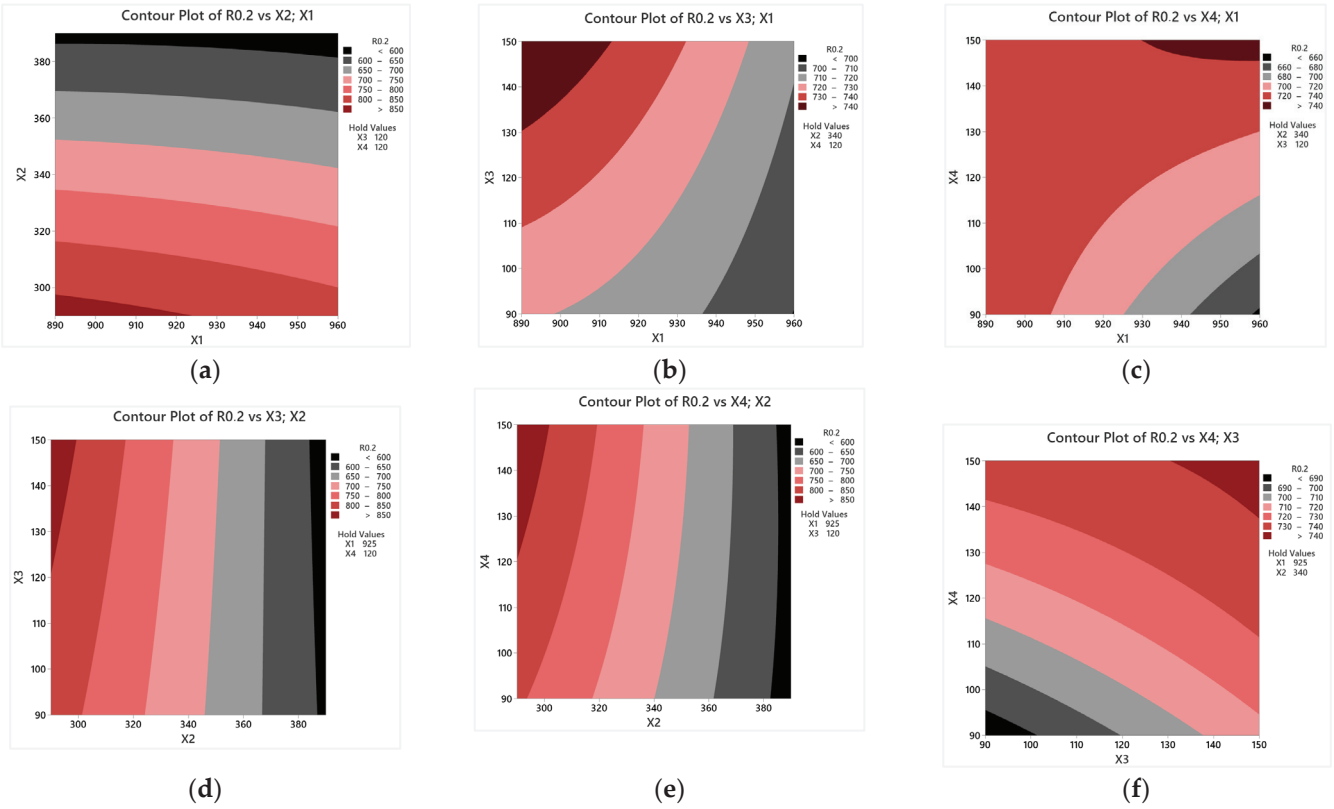


Figure 10. The influence of heat treatment parameters on the yield strength of cast iron. The figure shows the relationship between the following heat treatment parameters: (**a**) T_γ and T_{pi}; (**b**) T_γ and τ_γ; (**c**) T_γ and τ_{pi}; (**d**) T_{pi} and τ_γ; (**e**) T_γ and τ_{pi}; (**f**) τ_γ and τ_{pi}.

3.6. Impact of Heat Treatment Parameters on A_5

The regression equation, taking into account the impact of all the heat treatment parameters discussed on the elongation of compacted graphite iron, takes the following form:

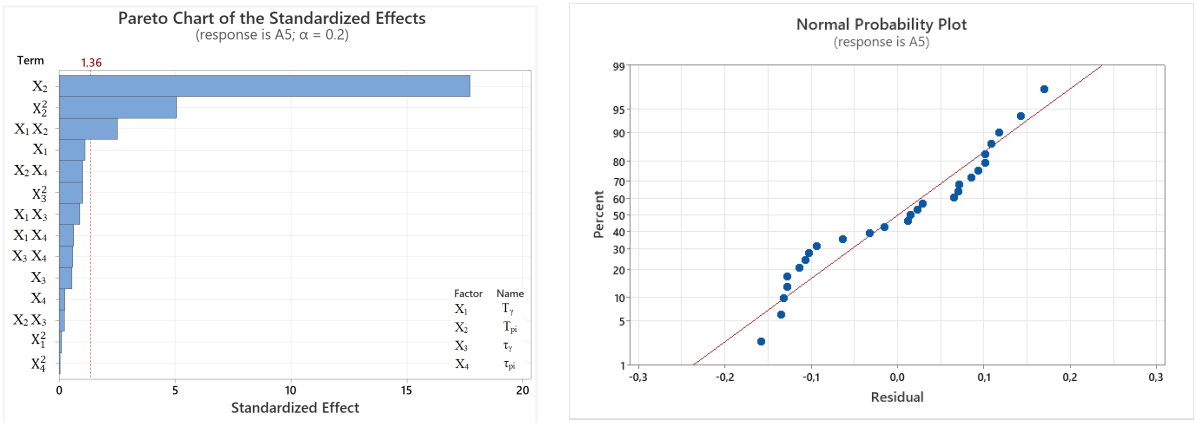
$$A_5 = 32.6 - 0.010\,X_1 - 0.1643\,X_2 - 0.0039\,X_3 - 0.0100\,X_4 - 0.000009\,X_1^2 + 0.000190\,X_2^2 - 0.000106\,X_3^2 + 0.000005\,X_4^2 + 0.000054\,X_1X_2 + 0.000032\,X_1X_3 + 0.000023\,X_1X_4 + 0.000006\,X_2X_3 - 0.000026\,X_2X_4 - 0.000025\,X_3X_4 \quad (4)$$

where in the formula A_5 is the calculated elongation value [%]; X_1—austenitization temperature (T_γ) [°C]; X_2—austempering temperature (T_{pi}) [°C]; X_3—austenitization time (τ_γ) [min]; X_4—austempering time (τ_{pi}) [min].

The coefficient of multiple correlation, at 96.87% in this case, indicates a strong linear relationship between the dependent variable and the vector of independent variables. The adjusted coefficient is 93.21%. The corrected coefficient of determination indicates that 80.36% of the variation in results is consistent with the determined model.

After ANOVA analysis of the interaction of primary effects, squared, and the two-way interaction, a Pareto chart is shown for the resulting A_5 of cast iron (Figure 11a). It shows the absolute values of the impact factors. The vertical line indicates the critical value for the *t*-test to assess the significance of the impact of the given factor on the output

variable. At the assumed 80% confidence level (red line), only one of the main effects, namely $\mathbf{T_{pi}}$, is significant. The parameters that proved to be insignificant were T_γ, τ_γ, and τ_{pi}. Among the quadratic parameters, the significant parameter is the product of austempering temperatures, while the poorest, i.e., not significantly affecting the A_5 of the alloy, was the austempering time squared. Among the parameters with two-way interaction, austenitizing temperature together with austempering temperature (T_γ T_{pi}) obtained a *p*-Value of 0.026; the interaction of T_{pi} with τ_γ had the least impact. In Figure 11b, the points are arranged along a distribution function that is a straight line, indicating that the observed values follow a normal distribution.



(**a**) (**b**)

Figure 11. Charts obtained for the elongation dependence of cast iron for the adopted heat treatment parameters: (**a**) Pareto chart of standardized effects; (**b**) normal probability plot of the residuals.

Figure 12 shows the impact of heat treatment parameters on A_5 in the form of two-dimensional graphs. As per the legend, the dark gray areas specify the parameters at which maximum elongation is achievable. A significant single-factor parameter in the present case is T_{pi}, both squared and with a correlation with the austenitizing temperature. The relationship of the latter is illustrated in Figure 12a. Figure 12a,d,e show a significant increase in the elongation of cast iron when tempered at temperatures above 340 °C.

3.7. Response Optimization

For multi-criteria optimization of heat treatment parameters and their impact on the mechanical properties of cast iron, the RSM approach was used to identify the impact of each heat treatment parameter. Variable limits that achieve the maximum of each response are shown as "Cur.". The goal of the optimization was to obtain the highest possible values for R_m and $R_{0.2}$, assuming an A_5 of the cast iron of about 0.7%. In the case of the material strength data, the determined desirability is at a satisfactory level of 80.94%. When analyzing the effect of the T_γ, it can be seen that increasing the austenitizing temperature affects the deterioration of elongation, but at the same time, it is not significant for R_m and $R_{0.2}$. Therefore, it can be concluded that this temperature can be reduced to an acceptable minimum, that is, about 850 °C. In the studied case, the optimal temperature was 890 °C. In the case of austempering temperature (T_{pi}), increasing it causes a decrease in R_m and $R_{0.2}$ with a simultaneous increase in elongation (A_5). Analysis of the plot (see Figure 13) shows that the elongation in the T_{pi} ranges from 290 °C to approx. 310 °C decreases from approx. 0.69% to approx. 0.58%, and already above 310 °C it increases. As for the austenitizing time (τ_γ), the optimal time is approx. 110 min. Increasing τ_γ results in a slight increase in $R_{0.2}$, so the optimal setting was assumed to be closer to the middle of the range of the analyzed time. The austempering time (τ_{pi}) shows minimal impact on the strength properties of compacted graphite iron. To summarize, in order to achieve the following properties for the alloy—R_m = 942 MPa, $R_{0.2}$ = 878 MPa, and A_5 = 0.7%, which would provide high values of

desirability (d) of 0.89, 0.89, and 0.67, respectively—the heat treatment of cast iron should be carried out at the following parameters: T_γ = 890 °C; T_{pi} = 290 °C; τ_γ = 120 min; and τ_{pi} = 150 min.

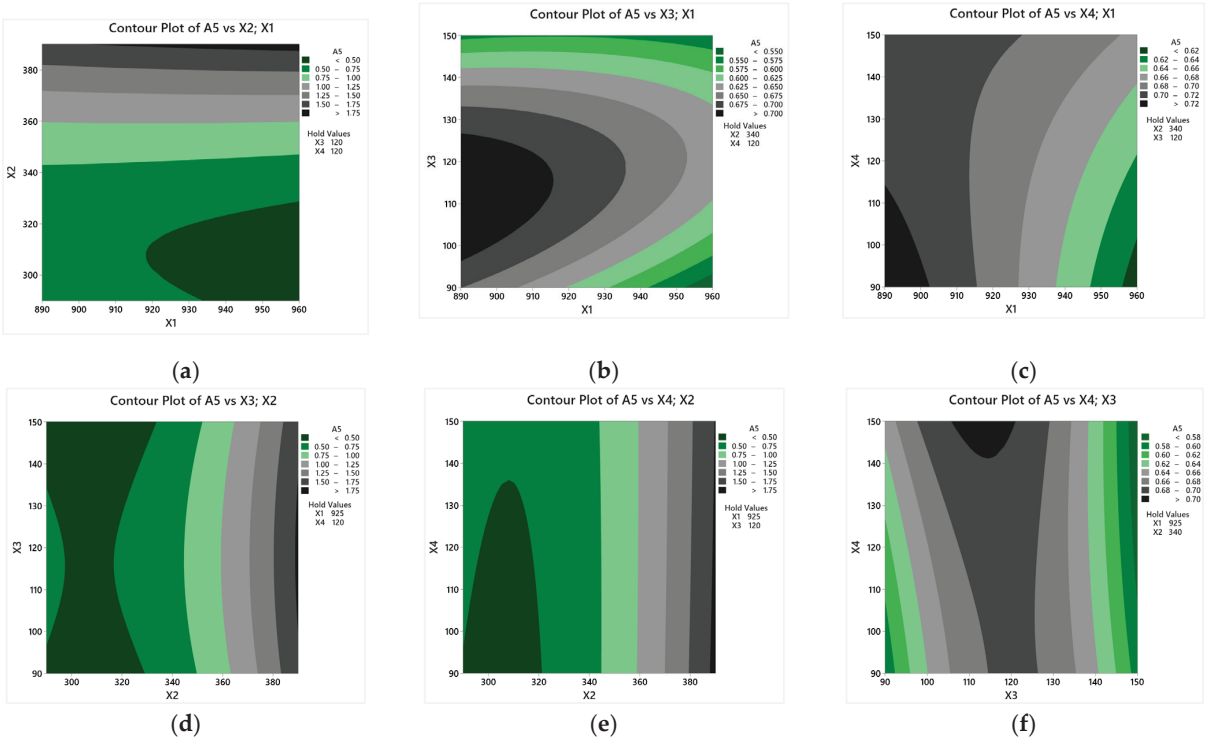


Figure 12. The influence of heat treatment parameters on the elongation of cast iron. The figure shows the relationship between the following heat treatment parameters: (**a**) Tγ and Tpi; (**b**) Tγ and τγ; (**c**) Tγ and τpi; (**d**) Tpi and τγ; (**e**) Tγ and τpi; (**f**) τγ and τpi.

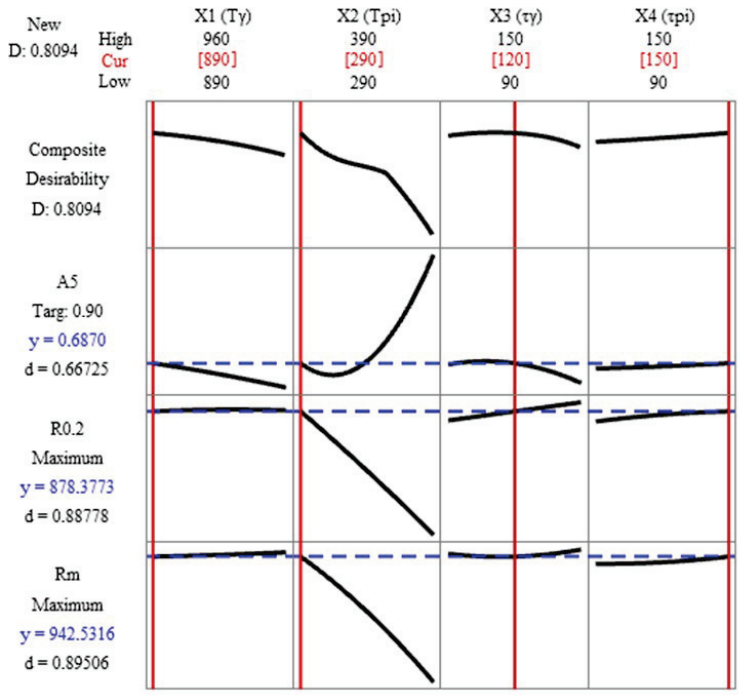


Figure 13. Desirability function applied in multiple responses (Minitab 21.4.3.0 Statistical Software).

To verify the accuracy of the adopted regression models and the optimal heat treatment parameters determined based on them, Figure 14 presents the values of the considered mechanical properties of vermicular cast iron (R_m, $R_{0.2}$, and A_5) obtained from the regression models compared with the corresponding data from experimental tests. It should be noted that the results show the best fit for elongation, followed by tensile strength, and the least accurate fit for yield strength.

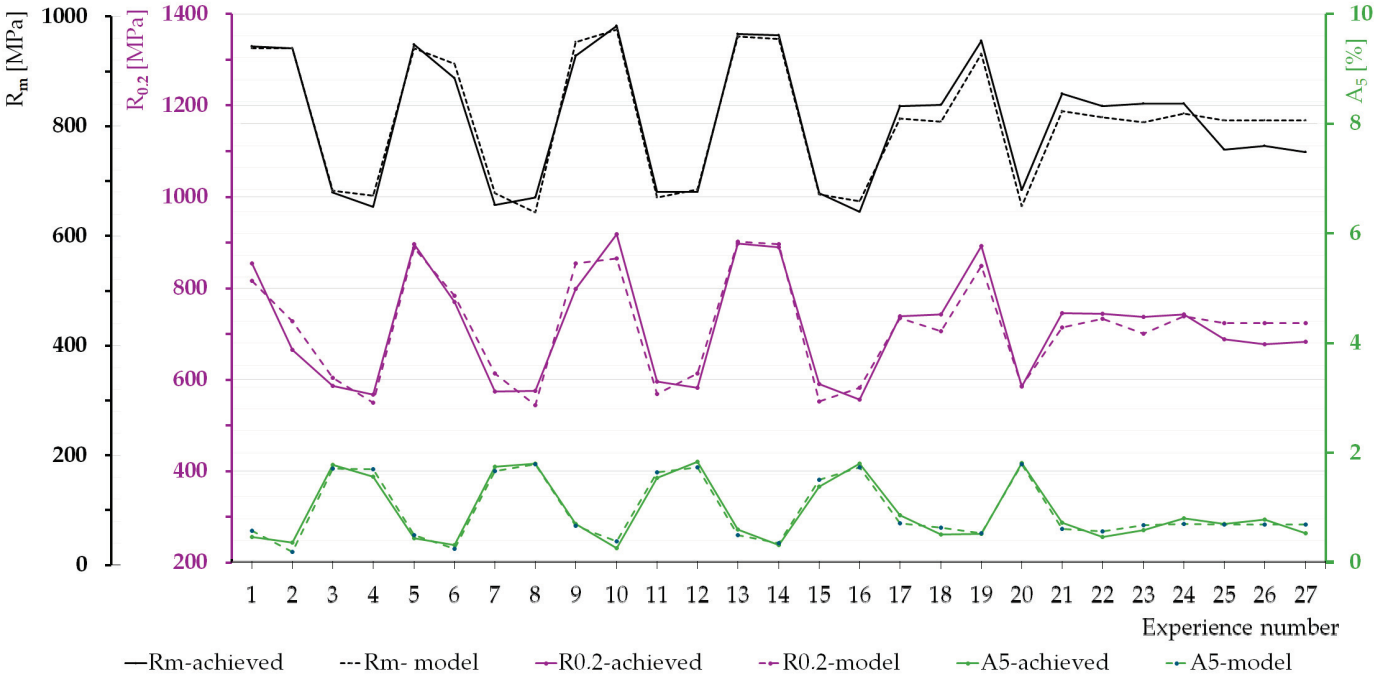


Figure 14. Comparison of the obtained strength results with the proposed mathematical models.

In analytical research and development activities related to the production of vermicular cast iron, the provided information can help optimize the heat treatment process, reduce the number of tests, and shorten project timelines. It should be emphasized that experimental research methodology (Modern Experimental Design) and optimization are crucial for obtaining consistent results, improving production process efficiency, and minimizing costs. The experimental approach allows for a more precise determination of the relationships between process parameters and the mechanical properties of the material, which is essential for the further development of vermicular cast iron production technology.

4. Conclusions

Heat treatment of compacted graphite iron involving austempering in a manner analogous to that used in the manufacture of ADI alters the material structure, increasing tensile strength and yield strength while decreasing elongation. The microstructure after such treatment consists of acicular ferrite and residual austenite. Depending on the austempering temperature, the proportion of austenite changes. The lower this temperature is, the less austenite there is. As T_{pi} increases, the proportion of austenite increases.

Based on the analysis of variance and the analysis of multi-criteria optimization of heat treatment parameters of compacted graphite iron in relation to the obtained mechanical properties of compacted graphite iron, the following should be noted:

1. The proposed mathematical model for the impact of heat treatment parameters on the tensile strength of cast iron showed a predicted coefficient of determination of about 82% (with R^2 adj = 90%). The R_m value has a significant impact on the proposed model due to one parameter, namely the austempering temperature;

2. The predicted coefficient of determination, with the model specifying $R_{0.2}$, was about 50% (with R^2 adj = 83%). The significant coefficients in this case are austempering temperature (T_{pi}), the interaction of austenitizing temperature and austempering time (T_γ τ_{pi}), austempering time (τ_{pi}), and the interaction of austempering temperature and time ($T_{pi}\tau_{pi}$) are significant;
3. In the case of polynomial regression determining the relation of cast iron elongation to heat treatment parameters, the predicted coefficient of determination was about 80% (with R^2 adj = 93%). The significant parameters are the austempering temperature (T_{pi}), the square of the quenching temperature (T_{pi} T_{pi}), the two-way interaction of the austenitizing temperature together with the austempering temperature (T_γ T_{pi});
4. The goal of optimizing the impact of heat treatment parameters on the mechanical properties of compacted graphite iron was to achieve maximum tensile strength and maximum yield strength while maintaining elongation at about 0.7%. The assumed desirability of optimization was about 81%. When aiming to achieve a tensile strength of about 940 MPa, a yield strength of about 880 MPa, and an elongation of about 0.7%, compacted graphite iron should be heat-treated according to the following parameters Tγ = 890 °C; Tpi = 290 °C; τγ = 120 min.; and τpi = 150 min.

Author Contributions: Conceptualization, A.J., P.M. and M.S.S.; methodology, A.J.; software, A.J. and G.S.; validation, A.J., M.S.S. and G.S.; formal analysis, A.J.; investigation, G.S.; resources. P.M. and M.S.S.; data curation, A.J.; writing—original draft preparation, P.M.; writing—review and editing, M.S.S.; visualization, A.J.; supervision, M.S.S. and G.S.; project administration, A.J. All authors have read and agreed to the published version of the manuscript.

Funding: This research received no external funding.

Institutional Review Board Statement: Not applicable.

Informed Consent Statement: Not applicable.

Data Availability Statement: The original contributions presented in the study are included in the article, further inquiries can be directed to the corresponding author.

Conflicts of Interest: The authors declare no conflict of interest.

References

1. Soiński, M.S.; Jakubus, A. Casting Production in Poland Versus European Trends in 21st Century. *Arch. Foundry Eng.* **2024**, *24*, 57–62. [CrossRef]
2. Zych, J.; Jurga, T.; Mocek, J.; Myszka, M.; Snopkiewicz, T. Spheroidal Cast Iron for Works at Low Temperature—Requirements, Structure, Properties, Control of the Production Process. *Arch. Metall. Mater.* **2022**, *67*, 999–1005. [CrossRef]
3. Pacha-Gołębiowska, H. Assessment of the Quality of Ductile Cast Iron EN-GJS-500-7 Through the Influence of its Chemical Composition on the Grain Composition of Spheroidal Graphite. *Arch. Foundry Eng.* **2022**, *22*, 85–89. [CrossRef]
4. Myszka, D.; Kasińska, J.; Penkul, A. Influence of Tungsten on the Structure and Properties of Ductile Iron Containing 0.8% Cu. *Arch. Foundry Eng.* **2021**, *21*, 121–126. [CrossRef]
5. Ramkumar, T.; Madhusudhanan, S.; Rajendran, I. Effect of Nickel on the Microstructure, Mechanical and Tribological Properties of Austempered Ductile Cast Iron for Steering Knuckle Applications. *Arch. Metall. Mater.* **2020**, *65*, 15–25. [CrossRef]
6. Alonso, G.; Stefanescu, D.M.; Aguado, E.; Suarez, R. The Role of Selenium on the Formation of Spheroidal Graphite in Cast Iron. *Metals* **2021**, *11*, 1600. [CrossRef]
7. Ha, J.-S.; Hong, J.-W.; Kim, J.-W.; Han, S.-B.; Choi, C.-Y.; Song, H.-J.; Jang, J.-S.; Kim, D.-Y.; Ko, D.-C.; Yi, S.-H.; et al. The Effect of Boron (B) and Copper (Cu) on the Microstructure and Graphite Morphology of Spheroidal Graphite Cast Iron. *Materials* **2023**, *16*, 4225. [CrossRef] [PubMed]
8. Górny, M.; Kawalec, M.; Gracz, B.; Tupaj, M. Influence of Cooling Rate on Microstructure Formation of Si–Mo Ductile Iron Castings. *Metals* **2021**, *11*, 1634. [CrossRef]
9. Chaus, A.S.; Čaplovič, Ľ.; Pokrovskii, A.I.; Sobota, R. Microstructure and Properties Evaluation of Ductile Cast Iron Subjected to Hot Plastic Deformation and Ambient Temperature Compression. *Arch. Metall. Mater.* **2023**, *68*, 639–648. [CrossRef]
10. Bracka-Kęsek, K.Z.; Szczęsny, A.; Kopyciński, D.; Guzik, E. Evaluation of the Phases Present in the Zinc Coating Obtained on the Ductile Cast Iron Substrate in the Bath with the Addition of Ti. *Arch. Foundry Eng.* **2023**, *23*, 5–13. [CrossRef]

11. Wróbel, T.; Studnicki, A.; Stawarz, M.; Baron, C.; Jezierski, J.; Bartocha, D.; Dojka, R.; Opiela, J.; Lisiecki, A. Improving the Abrasion Resistance of Nodular Cast Iron Castings by Remelting Their Surfaces by Laser Beam. *Materials* **2024**, *17*, 2095. [CrossRef] [PubMed]
12. Mróz, M.; Orłowicz, A.W.; Tupaj, M.; Kupiec, B.; Kawiński, M. Ductile Cast Iron Microstructure Adjustment by Means of Heat Treatment. *Arch. Foundry Eng.* **2020**, *20*, 37–40. [CrossRef]
13. Kołakowski, J.; Brzeżański, M.; Burdzy, D.; Sobieraj, J.; Urbanowicz, M.; Paruch, T.; Janerka, K. The Effect of Successive Stages of the Melting Process on the Nucleation of Ductile Cast Iron. *Arch. Foundry Eng.* **2023**, *23*, 61–67. [CrossRef]
14. Roučka, J.; Kaňa, V.; Kryštůfek, T.; Chýlková, A. Effect of Inoculants on the Structure and Properties of Thin-Walled Ductile Iron Castings. *Arch. Foundry Eng.* **2022**, *22*, 90–95. [CrossRef]
15. Stawarz, M.; Lenert, M.; Piasecki, K. Difficulties in the Production of Ausferritic Nodular Cast Iron without Heat Treatment. *Arch. Foundry Eng.* **2023**, *23*, 5–11. [CrossRef]
16. Hasanli, R.; Aliyev, I.; Poladov, N.; Azimova, L.; Tagiyev, T. Isothermal Transformations in High-Strength Cast Iron. *Sci. Her. Uzhhorod Univ. Ser. "Phys."* **2022**, *51*, 48–58. [CrossRef]
17. Akinribide, O.J.; Ogundare, O.D.; Oluwafemi, O.M.; Ebisike, K.; Nageri, A.K.; Akinwamide, S.O.; Gamaoun, F.; Olubambi, P.A. A Review on Heat Treatment of Cast Iron: Phase Evolution and Mechanical Characterization. *Materials* **2022**, *15*, 7109. [CrossRef]
18. Bai, J.; Xu, H.; Wang, Y.; Chen, X.; Zhang, X.; Cao, W.; Xu, Y. Microstructures and Mechanical Properties of Ductile Cast Iron with Different Crystallizer Inner Diameters. *Crystals* **2022**, *12*, 413. [CrossRef]
19. Jaśkowiec, K.; Opaliński, A.; Kustra, P.; Jach, D.; Wulk-Kołodziejczyk, D. Prediction of Selected Mechanical Properties in Austempered Ductile Iron with Different Wall Thickness by the Decision Support Systems. *Arch. Foundry Eng.* **2023**, *23*, 137–144. [CrossRef]
20. Mrzygłód, B.; Kowalski, A.; Olejarczyk-Wożenska, I.; Giętka, T.; Głowacki, M. Characteristics of ADI Ductile Cast Iron with Single Addition Of 1.56% Ni. *Arch. Metall. Mater.* **2017**, *4*, 2273–2280. [CrossRef]
21. Rodríguez-Rosales, N.A.; Montes-González, F.A.; Gómez-Casas, O.; Gómez-Casas, J.; Galindo-Valdés, J.S.; Ortiz-Cuellar, J.C.; Martínez-Villafañe, J.F.; García-Navarro, D.; Muñiz-Valdez, C.R. Statistical Data-Driven Model for Hardness Prediction in Austempered Ductile Irons. *Metals* **2022**, *12*, 676. [CrossRef]
22. Yoon-Jun, K.; Hocheol, S.; Hyounsoo, P.; Jong, D.L. Investigation into mechanical properties of austempered ductile cast iron (ADI) in accordance with austempering temperature. *Mater. Lett.* **2008**, *62*, 357–360. [CrossRef]
23. Jakubus, A.; Kostrzewa, J.; Ociepa, E. The influence of parameters of heat treatment on the microstructure and strength properties of the ADI and the AVGI irons. In Proceedings of the 30th Anniversary International Conference on Metallurgy and Materials, Brno, Czech Republic, 26–28 May 2021. [CrossRef]
24. Krawiec, H.; Lelito, J.; Mróz, M.; Radoń, M. Influence of Heat Treatment Parameters of Austempered Ductile Iron on the Microstructure, Corrosion and Tribological Properties. *Materials* **2023**, *16*, 4107. [CrossRef] [PubMed]
25. König, M. Literature review of microstructure formation in compacted graphite Iron. *Int. J. Cast Met. Res.* **2010**, *23*, 185–192. [CrossRef]
26. Gumienny, G.; Kacprzyk, B. Copper in Ausferritic Compacted Graphite Iron. *Arch. Foundry Eng.* **2018**, *18*, 162–166. [CrossRef]
27. Zhang, M.X.; Pang, J.C.; Qiu, Y.; Li, S.X.; Wang, M.; Zhang, Z.F. Thermo-mechanical fatigue property and life prediction of vermicular graphite iron. *Mater. Sci. Eng. A* **2017**, *698*, 63–72. [CrossRef]
28. Zhang, M.X.; Pang, J.C.; Meng, L.J.; Li, S.X.; Liu, Q.Y.; Jiang, A.L.; Zhang, Z.F. Study on thermal fatigue behaviors of two kinds of vermicular graphite cast irons. *Mater. Sci. Eng. A* **2021**, *814*, 141212. [CrossRef]
29. Mróz, M.; Orłowicz, A.W.; Tupaj, M.; Jacek-Burek, M.; Radoń, M.; Kawiński, M. The Effect of Structure on Thermal Power of Cast-iron Heat Exchangers. *Arch. Foundry Eng.* **2020**, *20*, 27–30. [CrossRef]
30. Cao, M.; Baxevanakis, K.P.; Silberschmidt, V.V. Effect of Graphite Morphology on the Thermomechanical Performance of Compacted Graphite Iron. *Metals* **2023**, *13*, 473. [CrossRef]
31. Zhu, J.; Liu, Q.; Jiang, A.; Lian, X.; Fang, D.; Dong, H. Effects of Cu on the Morphology and Growth Mode of Graphite in Compacted Graphite Iron. *Trans. Indian Inst. Met.* **2021**, *74*, 1529–1536. [CrossRef]
32. Liu, L.; Zhao, K.; Zhang, H.; Tang, C.; Han, Q.; Chen, J.; Tao, D.; Yang, Z. Surface Evolution of Vermicular Cast Iron in High Frequent Cyclic Plasma and Different Facial Cooling Airflows. *Metals* **2023**, *13*, 577. [CrossRef]
33. Ramadan, M.; Nofal, A.A.; Elmahalawi, I.; Abdel-Karim, R. Comparison of austempering transformation in spheroidal graphite and compacted graphite cast irons. *Int. J. Cast Met. Res.* **2006**, *19*, 151–155. [CrossRef]
34. Thilak, G.; Chandramohan, P.; Saravanan, V.S. Influence of alloying elements and its effect on austempering of compacted graphite iron—A review. In *Materials Today: Proceedings*; Elsevier: Amsterdam, The Netherlands, 2023; pp. 1–12. [CrossRef]
35. Rohollah, G.; Inamul, H.; Arvin, G.; Attila, D. Austempered Compacted Graphite Iron—Influence of austempering temperature and time on microstructural and mechanical properties. *Mater. Sci. Eng. A* **2019**, *767*, 1–7. [CrossRef]
36. Wollmann, D.; Pintaude, G.; Ghasemi, R. Effect of austempering treatment on lubricated sliding contact of compacted graphite iron. *SN Appl. Sci.* **2020**, *2*, 1947. [CrossRef]
37. Jakubus, A. Initial Analysis of the Surface Layer of AVGI Cast Iron Subject to Abrasion. *Arch. Foundry Eng.* **2022**, *22*, 50–56. [CrossRef]
38. Rao, M.S.; Khandelwal, H.; Kumar, M.; Kumar, A. Parametric Optimization for Producing Semi-Solid A383 Alloy using Cooling Slope Casting Process. *Arch. Foundry Eng.* **2023**, *23*, 43–52. [CrossRef]

39. Şap, E.; Usca, Ü.A.; Gupta, M.K.; Kuntoğlu, M.; Sarıkaya, M.; Pimenov, D.Y.; Mia, M. Parametric Optimization for Improving the Machining Process of Cu/Mo-SiCP Composites Produced by Powder Metallurgy. *Materials* **2021**, *14*, 1921. [CrossRef]
40. El-Azazy, M.; El-Shafie, A.S.; Elgendy, A.; Issa, A.A.; Al-Meer, S.; Al-Saad, K.A. A Comparison between Different Agro-wastes and Carbon Nanotubes for Removal of Sarafloxacin from Wastewater: Kinetics and Equilibrium Studies. *Molecules* **2020**, *25*, 5429. [CrossRef]
41. Saikaew, C.; Harnsopa, S. Influence of Component Proportions in Casting Process on Hardness and the Quality of Cast Iron. *Arch. Foundry Eng.* **2023**, *23*, 35–42. [CrossRef]
42. Fajdek-Bieda, A. Optimization of the Geraniol Transformation Process in the Presence of Natural Mineral Diatomite as a Catalyst. *Catalysts* **2023**, *13*, 777. [CrossRef]
43. Naidu, M.; Bhosale, A.; Munde, Y.; Salunkhe, S.; Hussein, H.M.A. Wear and Friction Analysis of Brake Pad Material Using Natural Hemp Fibers. *Polymers* **2023**, *15*, 188. [CrossRef] [PubMed]
44. Perec, A.; Radomska-Zalas, A.; Fajdek-Bieda, A.; Kawecka, E. Efficiency of Tool Steel Cutting by Water Jet with Recycled Abrasive Materials. *Materials* **2022**, *15*, 3978. [CrossRef] [PubMed]
45. *Polish Standard PN-EN 16079:2012*; Foundry—Cast Iron with Compact (Vermicular) Graphite. European Committee for Standardization: Brussels, Belgium, 2012.
46. Mierzwa, P. The Influence of Heat Treatment on Selected Properties of Cast Iron with Vermicular Graphite. Doctoral Dissertation, Czestochowa University of Technology, Częstochowa, Poland, 2010.
47. Soiński, M.S.; Jakubus, A.; Borowiecki, B.; Mierzwa, P. Initial Assessment of Graphite Precipitates in Vermicular Cast Iron in the As-Cast State and after Thermal Treatments. *Arch. Foundry Eng.* **2021**, *21*, 131–136. [CrossRef]
48. Metals & Minerals Ltd. (Ed.) *Sorelmetal. On the Nodular Cast Iron*; Metals & Minerals Ltd.: Warsaw, Poland, 2006.
49. Mróz, M.; Orłowicz, A.W.; Tupaj, M.; Lenik, M.; Kawiński, M.; Kawiński, M. The Effect of Sulphur Content on the Microstructure of Vermicular Graphite Cast Iron. *Arch. Foundry Eng.* **2022**, *22*, 18–22. [CrossRef]
50. Bezerra, M.A.; Santelli, R.E.; Oliveira, E.P.; Villar, L.S.; Escaleira, L.A. Response surface methodology (RSM) as a tool for optimization in analytical chemistry. *Talanta* **2008**, *76*, 965–977. [CrossRef] [PubMed]
51. Megahed, H.; El-Kashif, E.; Shash, A.Y.; Essam, M.A. Effect of holding time, thickness and heat treatment on microstructure and mechanical properties of compacted graphite cast iron. *J. Mater. Res. Technol.* **2019**, *8*, 1188–1196. [CrossRef]

Disclaimer/Publisher's Note: The statements, opinions and data contained in all publications are solely those of the individual author(s) and contributor(s) and not of MDPI and/or the editor(s). MDPI and/or the editor(s) disclaim responsibility for any injury to people or property resulting from any ideas, methods, instructions or products referred to in the content.

materials

MDPI

Article

Effect of Solidification Direction on the Freckle Formation in Single-Crystal Superalloy Castings

Dexin Ma [1,2,*], Hongyuan Sun [1,3], Yunxing Zhao [1,3], Weitai Xu [3], Zaiwang Huang [1], Bowen Cheng [3], Yang Liu [4] Fu Wang [4], Qiang Yang [4], Lv Li [3], Yangpi Deng [3], Fuze Xu [3], Haijie Zhang [5] and Menghuai Wu [5]

[1] State Key Laboratory for Powder Metallurgy, Central South University, Changsha 410083, China; sunhy2018@csu.edu.cn (H.S.); zhaoyunxing@csu.edu.cn (Y.Z.); huangzaiwang@csu.edu.cn (Z.H.)
[2] Wedge Central South Research Institute, Co., Ltd., Shenzhen 518045, China
[3] Shenzhen Wedge Aviation Technology Co., Ltd., Shenzhen 518045, China; 18706102306@126.com (W.X.); cbwlsxx@sina.com (B.C.); lilv000@163.com (L.L.); dengyangpi030@163.com (Y.D.); xufuze12@163.com (F.X.)
[4] State Key Laboratory for Manufacturing System Engineering, Xi'an Jiaotong University, Xi'an 710049, China; leoyounglab@163.com (Y.L.); fuwang@xjtu.edu.cn (F.W.); qiangyang@xjtu.edu.cn (Q.Y.)
[5] Chair for Simulation and Modelling of Metallurgy Processes, Department of Metallurgy, University of Leoben, 8700 Leoben, Austria; haijie.zhang@unileoben.ac.at (H.Z.); menghuai.wu@unileoben.ac.at (M.W.)
* Correspondence: madexin@csu.edu.cn

Abstract: Solidification experiments in two opposite directions were conducted to investigate the buoyancy effect on freckle formation during directional solidification in single-crystal superalloy castings. During conventional upward solidification with the superalloy CMSX-4, severe freckles were observed in castings of various geometries. By reversing the solidification direction from upward to downward, freckle-free castings could be obtained. To visually verify the effect of the solidification direction, an in situ observation experiment by varying the solidification direction was performed using a Ga-In alloy. In the upward solidification process, strong solutal convection was visually observed due to the decrease in the density of the interdendritic liquid. Conversely, a stable condition without visible flow was established during downward solidification, due to the stable state of the top-light, bottom-heavy liquid system. A new Rayleigh-number model was successfully applied to characterize the freckle features in superalloy cluster castings. When the solidification direction was reversed from upward to downward, the driving force for solutal convection was suppressed, leading to the complete elimination of freckle formation in single-crystal superalloy castings.

Keywords: superalloy; single crystal; freckle; solidification direction; solutal convection

1. Introduction

Due to the excellent high-temperature mechanical properties and corrosion resistance, nickel-based superalloys have been the optimal material for producing key high-temperature components in aero-engines and industrial gas turbines, such as turbine blades [1–4]. The global market for nickel-based superalloys in aero-engines and industrial gas turbine applications is projected to exceed USD 6.5 billion by 2030, driven by their critical role in high-temperature components such as turbine blades, which account for over 40% of the material demand in gas turbine manufacturing [5]. Single-crystal (SC) turbine blades manufactured through directional solidification processes are extensively utilized to enhance the efficiency and performance of turbine blades. The absence of grain boundaries in SC blades eliminates potential sites for stress concentration and failure,

thereby significantly improving their mechanical properties and durability under extreme operating conditions [6–9].

In conventional production processes (Bridgman process) for SC superalloy turbine blades, the ceramic mold shell was filled with overheated superalloy melt and lowered from the heat chamber, through an isolation baffle, into the cooling zone. During this process, upward dendritic solidification occurs from the bottom to the top of the castings, counteracting gravity. Due to the segregation of alloying elements, heavy elements like W and Re concentrate in the dendritic solid phase (γ phase), while light elements such as Al and Ti are rejected into the residual liquid between dendrites. This results in a significant decrease in liquid density in the mushy zone compared to the overlaying bulk liquid. Under the gravity effect, this up-heavy and bottom-light state is unstable, and a strong convective flow from the mushy zone into the buck liquid is unavoidable. This causes remelting and fracturing of the dendrite arms, ultimately resulting in the vertical chain-like distribution of freckles defects [10–19]. Since the freckles contain high-angle boundaries transversal to the withdrawal direction, they have a detrimental effect on the creep rupture life and fatigue resistance of the material.

Freckles are presently one of the primary cast defects in the SC components made of superalloys. It is now generally agreed that freckles are the product of specific fluid flow patterns, known as thermosolutal convection, originating in the interdendritic liquid during solidification. The freckling extent becomes more pronounced as the component size increases. Another factor playing an important role in freckle formation is the solidification condition of the castings, including the temperature gradient (G) at solidification front, the solidification velocity (V), the local cooling rate (T'), and the height of the mushy zone (H). These process parameters directly affect the dendrite spacing (λ) and the mushy zone permeability (K). A lower cooling rate leads to a coarser dendrite structure, reducing the resistance to the interdendritic fluid flow and increasing the likelihood of freckling [20,21]. As more and more refractory alloying elements are added to improve high-temperature mechanical properties, freckle formation in directionally solidified superalloy components has increasingly become a serious problem.

In addition to the factors mentioned above, it was found that the freckle formation is also significantly affected by the geometric shape of the superalloy castings [22–27]. On the transverse sections of the components with curved contours, freckles were exclusively found on the outward-curving surfaces with positive curvature, because the surface effect zones of the neighboring sides are overlapped, providing more favorable convection conditions. In comparison, the surfaces with negative curvature remained freckle-free, because the surface effect of the neighboring sides is divergent from each other. In the longitudinal direction, the freckle formation can be promoted by contracting contours and suppressed by expanding one, respectively. As the composition and shape of turbine blades are becoming increasingly complex, effectively reducing or eliminating freckle defects has been more challenging in manufacturing high-generation SC superalloy components.

Over the past decades, X-ray imaging has been recognized as a powerful method for solidification studies in metallic alloys. This technique enables real-time and in situ observations of thermosolutal flow during the solidification of metallic alloys, without disrupting the process [28,29]. Buoyancy-driven flow patterns have been studied in Ga-In alloys using X-ray radioscopy and further applied to investigate the formation of segregated channels, freckles, and forced convection [30–32]. By using a high-temperature furnace and a high-speed X-ray-sensitive camera, the development of solute flow during dendritic growth of a Ni-based superalloy CMSX-4 was directly observed [33]. It was then evidently confirmed that the solutal convection and freckle formation are unavoidable during the conventional directional solidification of superalloys.

Besides the experimental investigations, a lot of studies pertaining to freckle formation have concentrated on the development of computational models and/or the incorporation of Rayleigh-number (*Ra)*-based criteria, to predict the onset of thermosolutal convection and subsequent formation of grain defects [34–38]. Theoretically, *Ra* is defined as the ratio of the driving force to the resistance for buoyancy-driven convection, reflecting the competition between the thermosolutal buoyancy and the retarding friction force in the mushy zone. The Rayleigh number is influenced by the alloy compositions and the dendrite spacings, which are determined by the solidification conditions. Since it incorporates both the chemical composition and processing parameters, the Rayleigh number has become a highly promising tool for understanding the interdendritic convection phenomena. However, due to its oversimplification, the classic *Ra* criteria can still not be applied to predict the freckle formation during the industrial manufacturing process, because of the complexity of the casting shapes and the processing conditions. Recently, a revised freckle-predicting *Ra* model was proposed [39]. This model quantified the geometrical effect leading to the formation of the freckle defect and addressed the shortcomings of the existing models. Using the revised *Ra* model, the specific positions of the freckling-risk zones in complex SC castings can be determined, and the freckling tendency can be predicted.

In the present work, experiments based on industrial Ni-based superalloys were conducted, employing both the conventional upward-solidification and a novel downward-solidification techniques to investigate the feasibility of producing SC superalloy components free of freckle defects. In situ observation experiments were conducted based on a low-melting-point metal alloy (Ga-30 wt.% In) to directly observe the thermal–solutal convection behavior during solidification in both directions. Numerical simulations were also performed using the newly developed *Ra* model [39] to predict the freckle formation in both upward- and downward-solidification processes. A systematic analysis was carried out to quantify the impact of gravitational factor and solidification direction on solidification microstructure. The knowledge gained from this study proposed new approaches to address buoyancy-driven convection and the related issues in the directional solidification process of superalloys.

2. Experiment and Simulation

2.1. Solidification Experiment of a Superalloy

A commercial Ni-based SC superalloy of typical second-generation, CMSX-4, was selected for the casting experiments since it is a typical freckle-prone superalloy. The chemical composition of CMSX-4 is listed in Table 1.

Table 1. Nominal composition of superalloy CMSX-4 (wt.%).

Cr	Co	W	Mo	Al	Ti	Ta	Re	Hf	Ni
6.5	9.0	6.0	0.6	5.6	1.0	6.5	3.0	0.1	Bal.

Four sample geometries, labeled A, B, C, and D, were designed for the casting experiment, with their end and side views illustrated in Figure 1a. Sample A is a simple cylindrical bar with a diameter of 15 mm. Sample B consists of some short cylindrical sections, each 30 mm in length, with diameters of 10 and 15 mm, respectively. Sample C is similar to Sample B, but the cross-sections were changed to square ones with side widths of 10 and 15 mm, respectively. The cross-section of sample D is shaped like a cross-petal, with a diagonal petal length of 15 mm.

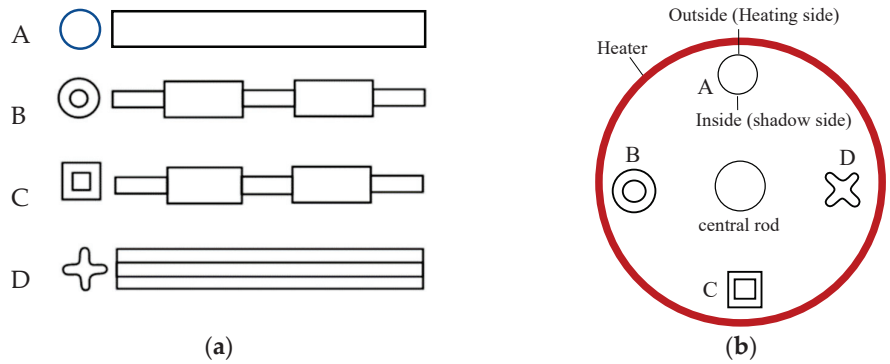


Figure 1. (**a**) End- and side-view of the designed casting geometries; (**b**) top-view of the casting arrangement in a cluster.

Figure 1b shows schematically the arrangement of the corresponding wax patterns of the samples in a casting cluster, which were assembled in a circular ring around a central rod on the plate. According to the lost-wax process, the wax assemblies were repeatedly coated by dipping into ceramic slurries, followed by stuccoing with ceramic sands to build a ceramic shell mold around the wax pattern, until the desired shell-wall thickness was attained. The shell molds were then de-waxed in a steam autoclave and fired in a heating furnace. It should be indicated that two different pouring systems were introduced into the shell molds (Figure 2) to perform the directional solidification experiments in two different directions, as shown below.

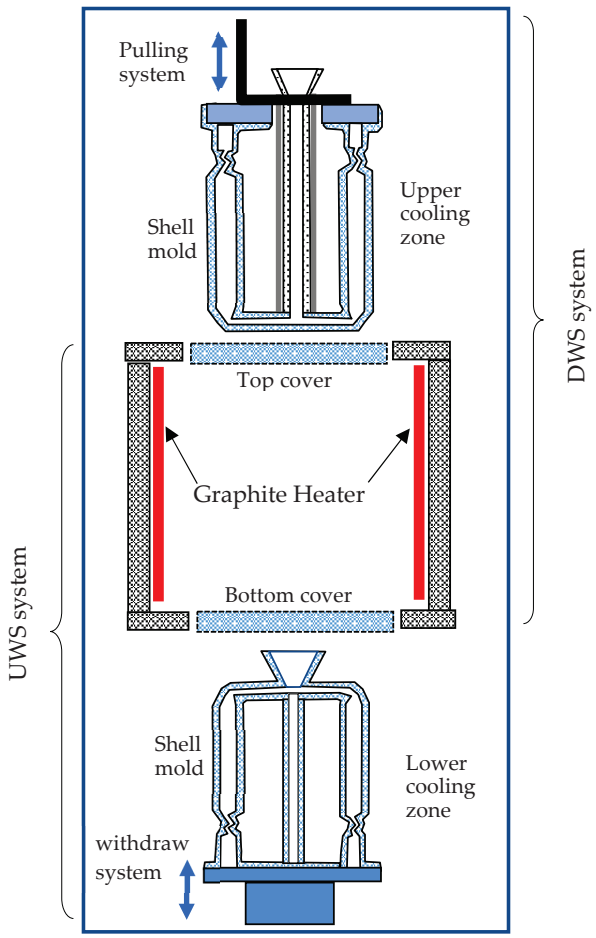
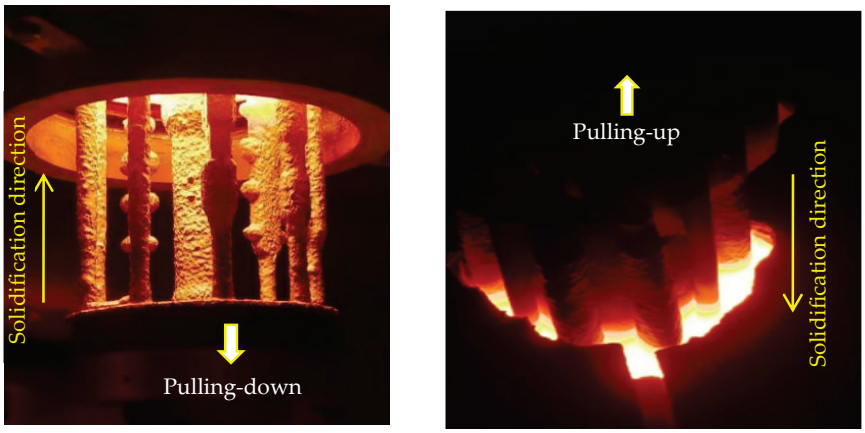


Figure 2. Schematic of the self-developed device for upward-solidification (UWS) and downward-solidification (DWS) experiments.

In the present work, a novel prototype device was developed for solidification experiments in both upward and downward directions, respectively (Figure 2). Between the upper and the lower cooling zones, a heating chamber is located in the middle, where the shell molds are preheated and poured with alloy melt.

In the first experiment, the upward solidification (UWS) system of the equipment (Figure 2) was used to lift the ceramic mold into the heating chamber, which is covered from above. After pouring the alloy melt, the mold was withdrawn downward from the heating chamber into the lower cooling chamber (Figure 3a), enabling UWS from the bottom to the top of the castings, also known as anti-gravity solidification.



(**a**) (**b**)

Figure 3. Pulling-down (**a**) and pulling-up processes (**b**) of the shell molds, resulting in upward solidification (UWS) and downward solidification (DWS), respectively.

In the second experiment, the downward solidification (DWS) system of the equipment (Figure 2) was used to first lower the mold into the heating chamber for preheating and pouring alloy melt and then to lift the mold upward again into the upper cooling chamber (Figure 3b). In this process, the DWS of the castings from the top to the bottom, also known as along-gravity solidification, was realized.

The UWS and DWS experiments were conducted in the same furnace heated to the same temperature of 1500 °C. The same superalloy (CMSX-4) was molten and overheated to the same pouring temperatures of 1500 °C and poured into the molds made from the same ceramic materials. In both experiments, the poured molds were directionally solidified with the same pulling rate of 1.5 mm/min but in opposite directions. In short, the same process parameters were set in both experiments to ensure the same solidification conditions, including cooling rates and thermal gradients, although they were not measured. Therefore, the structure difference between the experiments could only be attributed to the solidification direction, because the other solidification conditions were controlled to be the same.

After the casting experiments, the samples were knocked out of the ceramic mold and mechanically separated from the casting cluster. The samples were then sandblasted to remove any ceramic deposits attached to their surface and were subsequently macro-etched in a solution of 50% H_2O_2 and 50% HCl. Metallographic examinations were conducted to ascertain the freckle defects on the surface of the solidified samples.

2.2. In Situ Solidification Experiments of a Ga-30 wt.% In Alloy

Besides the directional solidification experiments of superalloy castings, in situ solidification experiments in up- and down-directions were also performed. An apparatus for in situ X-ray observation of the solidification process of a low melting point metal

alloy was installed. The applied Ga-In alloy has a very low melting point, enabling the convenient conduction of in situ observation experiments with simple conditions, instead of high temperature and vacuum conditions for superalloys. More importantly, the solidification behavior of this alloy is very similar to that of superalloys, including the crystal growth in dendritic form and the density decrease in the residual liquid leading to the thermal–solutal convection. Therefore, Ga-In is a suitable material used to simulate the solidification process of superalloys. In fact, this alloy has been widely used in in situ observation experiments of upward-directional solidification, but this work is the first to use it for downward-directional solidification experiments.

The Ga-30 wt.% In alloy was prepared and filled into a windowed rectangular cell with a parallel gap of 0.5 mm. The semiconductor components were used as heater and cooler, respectively, allowing independent and precise control of the upper- and lower-zone temperatures. The solidification setup was mounted between a microfocus X-ray source and an X-ray detector. By establishing a thermal field with a positive or negative temperature gradient, upward- or downward-directional solidification was enabled. During the experiments, the dendrite growth processes accompanied by the solutal convection of the interdendritic residual liquid were in situ observed and recorded for further analysis.

2.3. Simulation of Superalloy Solidification

Given the urgent need for a scientific mathematical model to reasonably predict freckle defects in superalloy castings, we have developed a new version of the Ra number to characterize the tendency of solutal convection and freckle occurrence during directional solidification [39]. For the convenience of detailed explanation and discussion, this mathematical model is presented as Equation (1) in Section 4 of this paper.

To predict the freckling tendency in the castings of various shapes, as shown in Figure 1, the solidification process and temperature field evolution in the castings were calculated using the commercial software ProCAST 2019. All modeling settings are identical to the experimental conditions. Then, the relative parameters in *Ra* number (Equation (1)) at each location were evaluated. Based on the evaluated location conditions, the corresponding correction factors were applied. Finally, the Ra-number distribution in the castings during the solidification process was calculated using Equation (1) to predict the freckling tendency in the various casting shapes. Besides the geometry effect, the impact of the solidification direction on the freckling tendency was also calculated. The simulation results were compared with the experimental measurements.

3. Experimental Results and Discussion

3.1. Directional Solidification Experiments of Superalloy

In the first experiment, the superalloy samples were upwards-solidified (UWS process) using the conventional pulling-down method (Figure 3a). In all samples, typical vertical freckle chains can be clearly observed on the vertical surface (Figure 4). It should be noted that the freckles were found mostly on the "shadow side" of the samples (Figure 4), which faces the central rod and could not be radiated directly by the heater. On the opposite side facing the heater (heating side), significantly fewer freckles were observed. This shadow effect indicates an unsymmetrical thermal condition between the inner and outer sides of the casting cluster, which plays an important role in freckle formation.

Sample D has the shape of a cross-shaped petal, whose protruding edges on the shadow side are occupied by serious freckles, while the recessed edges with concave curvature remain freckle-free. This can be explained by the edge effect or curvature effect on the freckle formation, found in the authors' previous work [22–24]. Freckles are surface defects whose formation is promoted by the surface contacting with the mold wall,

revealing the so-called surface effect or wall effect. In our previous study [16], the flow permeability near the casting surface was examined to be about one order of magnitude higher than that inside the mushy zone. A boundary layer was defined to indicate the depth of the surface effect. At the convex edges having positive curvature, such as at the protruding edges in sample D (Figure 4), the surface effect zones of the neighboring sides are overlapped, providing more favorable freckling conditions. On the concave edge having negative curvature, such as the recessed edges in sample D in Figure 4, the surface effect of the neighboring sides is divergent from each other, resulting in a normally freckle-free zone. This can be called the curvature effect of the transversal geometry on the freckle formation, corresponding to the edge-effect in the polygonal sections of castings [22–24].

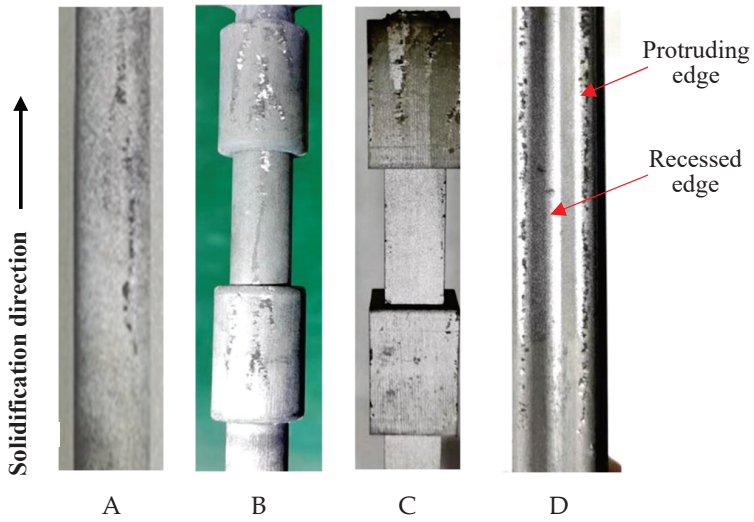


Figure 4. Surface photos of four samples (**A**–**D**) prepared in the UWS process.

In the second experiment, the superalloy samples were downwards-solidified (DWS process) using the newly developed pulling-up method (Figure 3b). Figure 5 shows the surface photographs of the four samples on the shadow side facing the central rod, just the same position as the results in Figure 4. After careful examination, it was confirmed that none of the samples exhibited freckle defects on their surfaces, as shown in Figure 5, which is totally opposite to Figure 4. Even the protruding edges of the sample D are also freckle-free, although this position is very prone to freckle formation during the conventional Bridgman process (Figure 4). It is thereby confirmed that the downward solidification process (i.e., along gravity) has natural immunity against freckle formation in superalloy castings.

The directional solidification of superalloys is accompanied with strong segregation of alloying elements between the liquid and solid phases. The lighter elements, such as Al and Ti, have positive segregating behavior tending to enrich in residual liquid between the dendrites, while the heavier refractory elements, such as W and Re, leave the liquid and enter the solid dendrites. The density of the interdendritic liquid ρ_1 in the mushy zone gradually decreases compared to the initial liquid density ρ_0 ahead of the growing dendrite tip.

In the first experiment, the conventional upward solidification (UWS) was performed by pulling down the shell mold filled with alloy melt. The bulk liquid with the original density ρ_0 is above the mushy zone with the residual liquid having lower density ρ_1 (Figure 6a). The liquid density difference between the top and bottom of the mushy zone, is then $\Delta\rho = (\rho_0 - \rho_1) > 0$. Under gravity, this below-lighter and top-heavier state in liquid is unstable, leading to thermosolutal convection between the mushy zone and the top

bulk liquid. This flow pattern results in the formation of freckles consisting of broken dendrite arms.

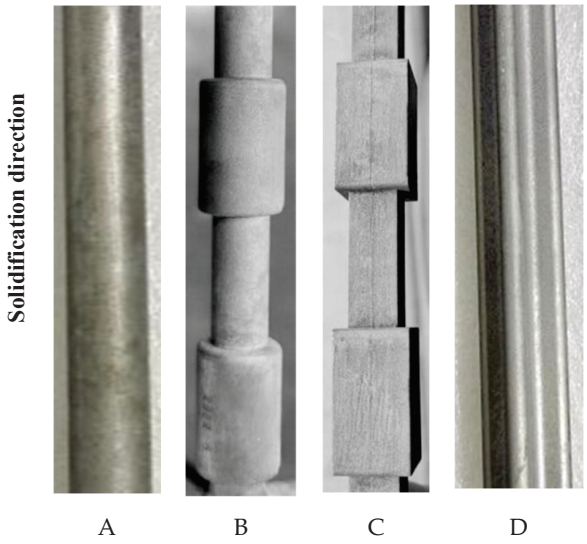


Figure 5. Surface photos of four samples (**A**–**D**) produced in the DWS process.

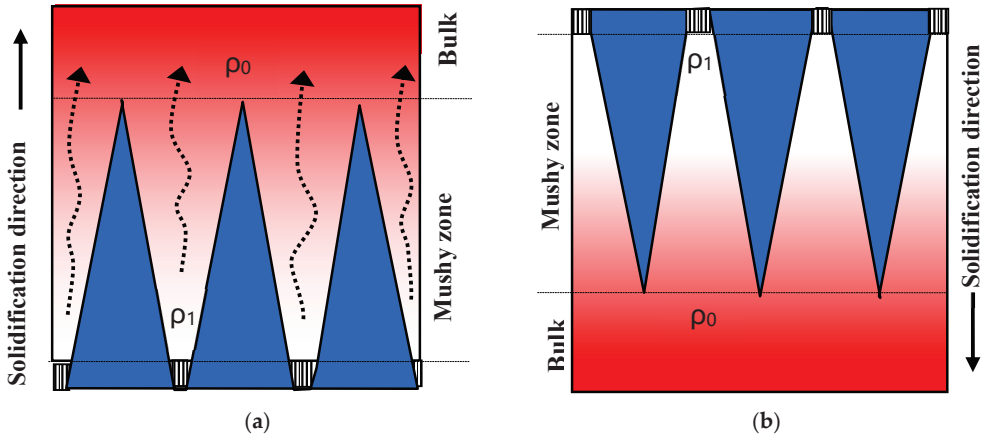


Figure 6. Schematic showing the influence of solidification direction on the solutal flow (as indicated by the dashed arrows): (**a**) convection during upward solidification; (**b**) stable state during downward solidification.

In comparison, the freckle defects were completely eliminated in the newly developed DWS process (Figure 6b). This is because during the downward solidification process, the mushy zone with reduced liquid density ρ_1, was above the bulk liquid zone with original densityρ_0. The liquid density difference between the top and bottom of the mushy zone, is then $\Delta\rho = (\rho_1 - \rho_0) < 0$, forming an absolutely stable state in the below-heavier and top-lighter zone. In this case, the gravitational effect was transformed from a destabilizing factor to a stabilizing one. Due to the absence of a driving force for the solutal convection, the freckle defects could be completely avoided.

In order to most convincingly confirm the effectiveness of the UWS method in eliminating freckle defect, the experiments were conducted under extreme conditions to stimulate freckles. For this purpose, very low pulling velocity (V = 1.5 mm/min) and very low heating temperature (T = 1500 °C) were applied, so that severe freckles were formed in the conventional UWS process. Under the same serious condition, however, freckle-free castings were obtained by using the new UWS method, providing the most powerful evidence for the effectiveness of UWS method.

3.2. Result of In Situ Solidification Experiments

In this work, in situ observation experiments of bidirectional solidification were carried out using thin-sheet samples of the low-melting-point alloy Ga-30 wt.% In. This alloy exhibits a similar solidification behavior to that of superalloys, such as the dendritic growth and the density reversion in the mushy zone. Specifically speaking, during the solidification process, the residual interdendritic liquid is enriched in Ga elements (ρ_{Ga} = 5.91 g/cm^3) and depleted in In elements (ρ_{In} = 7.3 g/cm^3). As a result, the residual liquid between the dendrites in the mushy zone becomes lighter than the original melt.

In the first experiment, the upward-solidification experiment was performed and in situ observed. As shown in Figure 6a, the dendrites were growing upwards, similar to the solidification phenomena during the conventional directional solidification. Compared with the bulk liquid zone at the top, the residual liquid between the dendrites appears brighter due to its lower density, which is attributed to the enrichment of the lighter Ga element. Under gravity, the interdendritic lighter liquid was in an unstable state. The lighter liquid located at the lower part of the mushy zone flowed upwards, inducing the formation of a plume flow. The flow direction of the liquid within the plume is indicated by the arrows in Figure 7a. This phenomenon has also been confirmed in in situ observation experiments of superalloys under high-temperature and vacuum conditions [33].

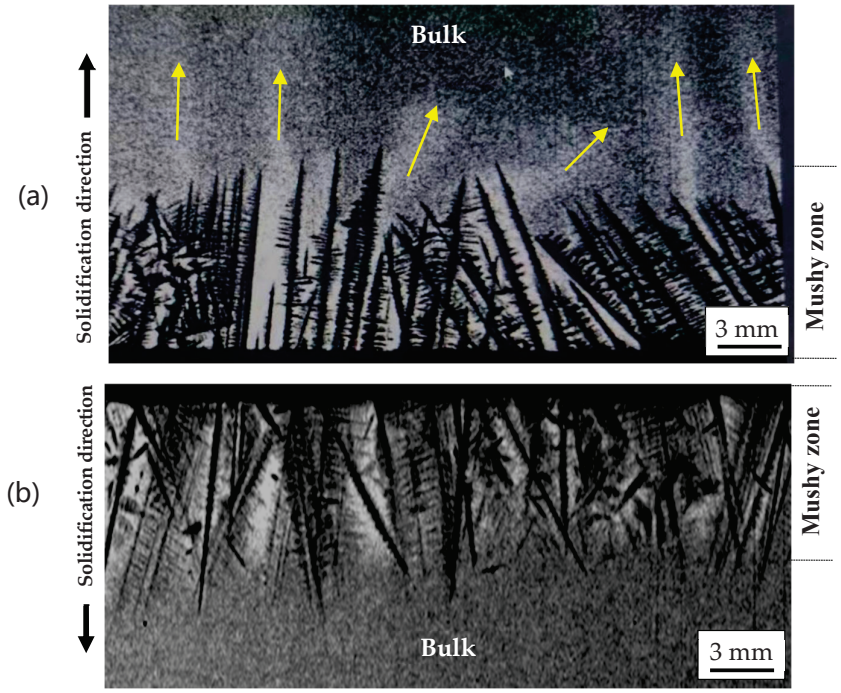


Figure 7. In situ observation of the upward-solidification with strong plume flow as indicated by arrows (**a**) and the downward solidification without convection (**b**), the yellow arrows represent the direction of solute flow.

In the second experiment, a downward-solidification of the Ga–In alloy was performed, where the mushy zone with lighter residual liquid was over the bulk liquid (Figure 7b). In this case, the lighter liquid remained at the top between the dendrites, and no plume flow developed from the mushy zone downwards into the bulk liquid below. This could be attributed to the absolute stable state with the lighter liquid at the top and the heavier one at the bottom. The density difference between the interdendritic liquid and bulk one becomes a suppressing force. This is in contrast to the conventional Bridgman process, where it acts as a driving force for the onset of solutal convection. This in situ observation experiment directly provides strong evidence for the importance of solidification direction

on the solidification behavior. It clearly shows that by simply changing the solidification direction from against gravity to along gravity, the solutal convection and subsequent freckle formation could be completely avoided. This was experimentally confirmed in Figures 4 and 5, offering a new approach to produce freckle-free SC superalloy blades.

4. Results and Discussion of Simulation Work

Freckle is a typical structural defect formed in directionally solidified superalloy castings, but its formation mechanism has not yet been reasonably explained. In addition to a large amount of experimental work, mathematical modeling, and numerical simulation methods are also commonly used to describe freckle formation. Since the freckles are believed to originate from the liquid flow between directionally growing dendrites, various Rayleigh-number (*Ra*) have been developed to characterize the liquid instability in the mushy zone and to predict the onset of freckles [34–38]. However, these *Ra* criteria were derived under simple idealized conditions and were generally expressed as functions of alloy composition and solidification conditions, thereby cannot be applied to industrial casting production with complex conditions. For example, the traditional *Ra* numbers do not account for important factors such as the wall effect of actual liquid flow and the effect of casting shape. As a result, the predicted freckling locations often do not align with the experimental results.

Recently, we have developed a new version of the *Ra* number [39] to characterize the tendency of solutal convection and freckle occurrence during directional solidification of complex castings. This new *Ra* number can be briefly described in the following equation:

$$Ra = \left(\frac{\Delta\rho}{\rho_0}\frac{gK_0H}{\alpha\nu}\right)\left(F_fF_iF_d\right) \quad (1)$$

The factor in the first bracket of this equation is the expression for the traditional *Ra* number, which represents the ratio of the driving force to the viscous in the mushy zone. In this equation, ρ_0 is the initial density of the bulk liquid, $\Delta\rho$ is the density difference between the bulk liquid and the liquid in mushy zone, H and K_0 are width and flow permeability ($K_0 = 6.0 \times 10^{-4}\ \lambda^2$, λ is the primary dendrite arm spacing) of the mushy zone, α is the thermal diffusivity, ν is the kinematic viscosity, and g is the gravitational acceleration.

The factor in the second bracket of Equation (1) introduces several correction factors accounting for the influence of shape effects, which were concretely described in reference [39]. Among them, the correction factor F_f reflects the influence of the casting's external profile on the liquid flow. A physical model with different flow paths was established based on the internal mushy zone and along the mold wall, considering the overlapping effect of the wall effect at the corners. This enables the model to represent the surface-effect and edge-effect of freckles. The factor F_i in Equation (1) is a correction factor for the variation in flow intensity with changes in the longitudinal shape of the castings, which characterizes the volume scale supporting liquid flow in the mushy zone. Every expansion of the casting profile indicates an outward extension of the surface, which, due to the reduced support volume from below, weakens liquid convection and freckle formation on the surface. On the other hand, each inward contraction of the casting surface indicates the expansion of the convection-supporting region from below, making freckles more likely to occur. Therefore, F_i represents the correction effect of shape contraction or expansion in the solidification direction. F_d in Equation (1) represents the correction factor for the change in mushy zone width influenced by the shadow effect. This model can be used to calculate the *Ra* number at every position of SC castings. It realized the evaluation of the freckling tendency of the whole casting and the location of the specific positions of the freckling risk zones.

In addition, the factor $\Delta\rho$ in Equation (1) represents the density difference between the liquid at the top and that at the bottom of the mush zone. The sign of factor $\Delta\rho$ is decided by the solidification direction. In conventional upward directional solidification (Figure 6a), the interdendritic liquid becomes increasingly lighter, reaching the minimum ρ_1 at the bottom of the mushy zone. This results in $\Delta\rho = (\rho_0 - \rho_1) > 0$, i.e., $Ra > 0$, indicating a positive driving force for solutal convection and thus a high risk of freckle formation. In the newly developed downward solidification (Figure 6b), however, the density factor becomes negative, $\Delta\rho = (\rho_1 - \rho_0) < 0$, i.e., $Ra < 0$, indicating a negative driving force for convection. In this case, the role of gravity changes from being the driving force for the solutal convection to a suppressing force, thereby achieving a stable liquid state and freckle-free solidification.

In order to predict the freckling tendency in the various casting shapes that are shown in Figure 1, the *Ra* number during the solidification process was calculated for each sample. Firstly, the solidification process and temperature field evolution in the castings were calculated using ProCAST 2019. Then, the relative parameters in *Ra* number (Equation (1)) at each location were evaluated, including the height of the mushy zone H, the density difference $\Delta\rho$ between the top and the bottom of the mushy zone, and the flow permeability K_0 of the mushy zone. Based on the location conditions, the corresponding correction factors were applied. Finally, the *Ra*-number distribution in the castings during the solidification process was calculated using Equation (1).

The calculated *Ra*-distribution for these four samples during the conventional upward solidification (UWS) process is shown in Figure 8. On the shadow side facing the central rod (indicated by arrows), the calculated *Ra* number is significantly higher than that on the heating side facing the heater. This is in good agreement with the experimental results shown in Figure 4, where all the freckles appear on the shadow side of the castings.

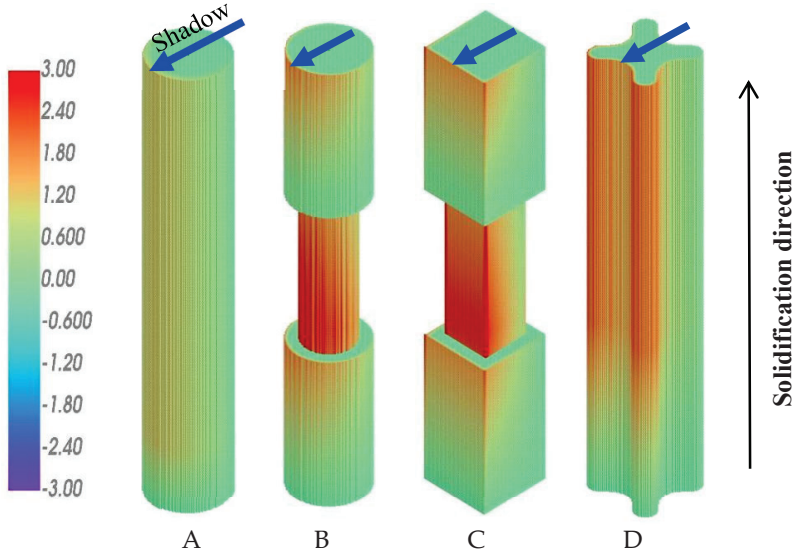


Figure 8. Simulation result for *Ra* distribution in the samples (**A**–**D**) during conventional UWS process.

In castings A and D, which have no variation in cross-sections along the longitudinal direction, the calculated *Ra*-values in the upper part are greater than those in the lower part of the castings. This is attributed to the corresponding change in the solidification condition. As the casting system moves downward from the top hot chamber to the lower cold chamber, the temperature gradient and cooling rate decrease gradually, leading to the coarsening of dendrite structures and increased freckling tendency. Casting D has a cruciform cross-section, where the *Ra* number at the edges is significantly higher than that on the smooth surface of cylindrical casting A. This simulation result confirms the

influence of the edge effect on freckle formation and is consistent with the experimental results (Figure 4).

In the stepped samples B and C, the cross-section suddenly decreases and increases along the solidification direction, leading to an increase and decrease in the *Ra* number, respectively. As a result, the step effect on the freckle formation, i.e., the promoting effect of contour contraction and suppressing effect of contour expansion, is also predicted by the current simulations in this work. This effect has been confirmed in the previous and present experimental works.

As mentioned above, the sign of the density difference between the top and bottom of the mushy zone, $\Delta\rho$, is related to the solidification direction. The simulation results shown in Figure 8 were calculated under the condition of upward solidification against gravity. The bulk liquid is above the upward-moving mushy zone, so the density difference between the top and bottom of the mushy zone, $\Delta\rho$, is greater than 0. The result of $\Delta\rho > 0$, and thereby $Ra > 0$, indicates a positive driving force for the liquid flow and freckle formation, as shown in Figure 6a. However, for the downward solidification process, the dendrites grow downward into the bulk liquid below the mushy zone. The density difference $\Delta\rho$ between the top and bottom of the mushy zone, i.e., between the dendrite rood and dendrite tip, is less than 0, leading to $Ra < 0$ for all positions in all castings, as shown in Figure 9. In this case, the driving force exerted by gravity on the liquid flow becomes negative, resulting in a convection-free and, consequently, a freckle-free solidification. This prediction has also been confirmed by the corresponding experimental results in Figure 5 and explained by the schematic illustration in Figure 6b.

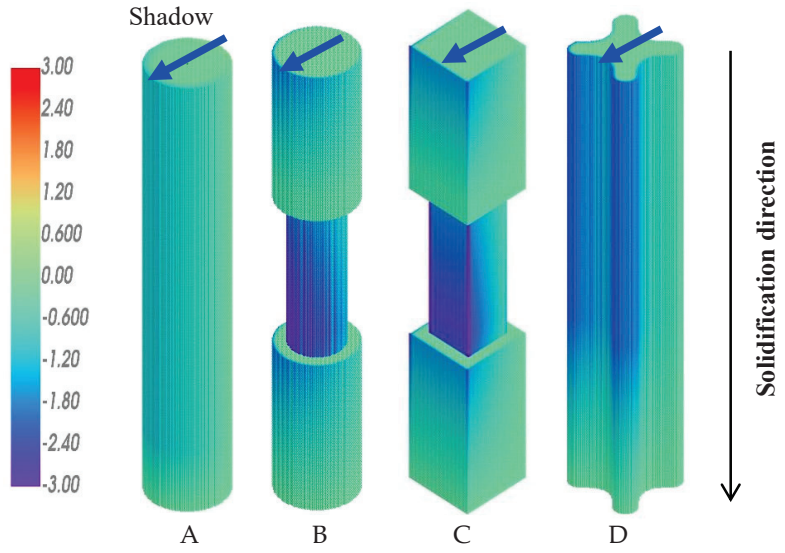


Figure 9. Simulation result for *Ra* distribution in samples (**A**–**D**) during the newly developed DWS process.

It is worth emphasizing that the sign of $\Delta\rho$ and *Ra* in Equation (1) is determined by the solidification direction. In the conventional upward-solidification process against gravity, the positive sign of $\Delta\rho$ and *Ra* means a positive buoyant force to drive liquid convection, leading to an unstable state with an increased risk of freckle formation. In the downward-solidification process, as applied in the present work, however, the sign of $\Delta\rho$ and *Ra* in Equation (1) becomes negative, indicating a negative driving force for liquid convection, which suppresses liquid convection and reduces the risk of freckle formation. In other words, the density reduction in the mushy zone above the bulk liquid is a suppressing factor, instead of a promoting factor, for solutal convection. The higher the *Ra*-value, the more stable the liquid, due to its negative sign. In this case, regardless of

all other conditions, such as alloy composition, solidification rate, and casting shape, an absolutely stable state is established for solidification free of convection and freckles.

5. Conclusions

(1) During the conventional upward solidification of superalloy CMSX-4, severe freckles occurred on the castings of various shapes. In contrast, freckle-free castings were obtained simply by changing the solidification direction from upward to downward.

(2) To visually verify the effect of solidification direction, in situ observation experiments of bidirectional solidification were performed using a Ga-In alloy. In the upward-solidification process, strong solutal convection was visually observed due to the decrease in the interdendritic liquid density. On the other hand, a convection-free state was achieved during downward solidification, because of the stable state under the top-light and bottom-heavy conditions.

(3) A new Rayleigh-number model was successfully applied to characterize the freckle features in superalloy cluster castings. When the solidification direction changed from upward to downward, the driving force for solutal convection was predicted to change from positive to negative. In this case, an absolutely stable state in the melt was established, leading to the complete avoidance of freckle formation in single-crystal superalloy castings.

(4) Based on the result of this work, the downward solidification process should be further applied to the production research of large superalloy components, which is even more important because they are more prone to freckle defects and cannot be avoided by conventional methods.

Author Contributions: Conceptualization, D.M., H.S., F.W., Y.Z. and W.X.; methodology, B.C., Q.Y., Y.L., Z.H. and H.Z.; software, Y.L. and H.Z.; validation, Q.Y., W.X., Z.H. and Y.D.; formal analysis, H.S., B.C., Y.L. and F.W.; investigation, Y.Z., Z.H., W.X., L.L. and F.X.; resources, M.W.; data curation, F.X., Y.D., Q.Y., M.W. and L.L.; Writing—original draft preparation, D.M.; writing—review and editing, H.Z., H.S., D.M. and M.W.; visualization, B.C., Y.L. and L.L.; supervision, D.M. and F.W.; funding acquisition, Y.Z. All authors have read and agreed to the published version of the manuscript.

Funding: This research was funded by Shenzhen Science and Technology Program (JSGG20220831092800001).

Institutional Review Board Statement: Not applicable.

Informed Consent Statement: Not applicable.

Data Availability Statement: The original contributions presented in this study are included in the article. Further inquiries can be directed to the corresponding author.

Conflicts of Interest: Author Dexin Ma was employed by the company Wedge Central South Research Institute, Co., Ltd. Author Hongyuan Sun, Yunxing Zhao, Weitai Xu, Bowen Cheng, Lv Li, Yangpi Deng and Fuze Xu were employed by the company Shenzhen Wedge Aviation Technology Co., Ltd. The remaining authors declare that the research was conducted in the absence of any commercial or financial relationships that could be construed as a potential conflict of interest.

References

1. Meetham, G.W. *The Development of Gas Turbine Materials*; Applied Science Publishers: London, UK, 1981; pp. 89–119.
2. Mclean, M. *Directionally Solidified Materials for High Temperature Service*; The Metals Society: London, UK, 1983; pp. 1–346.
3. Donachie, M.J.; Donachie, S.J. *Superalloys: A Technical Guide*; ASM International: Materials Park, OH, USA, 2002; pp. 11–25.
4. Reed, R.C. *The Superalloys: Fundamentals and Applications*; Cambridge University Press: Cambridge, UK, 2008; pp. 1–216.
5. Nickel-Based Superalloys Market Size, Share & Trends Analysis Report. Available online: https://www.grandviewresearch.com/industry-analysis/nickel-based-superalloys-market (accessed on 15 November 2024).
6. Versnyder, F.I.; Shank, M.E. The development of columnar grain and single crystal high temperature materials through directional solidification. *Mater. Sci. Eng.* **1970**, *6*, 213–247. [CrossRef]

7. Pratt, D.C. Industrial Casting of Superalloys. *Mater. Sci. Technol.* **1986**, *2*, 426–435. [CrossRef]
8. Quested, P.N.; Osgerby, S. Mechanical properties of conventionally cast, directionally solidified, and single-crystal superalloys. *Mater. Sci. Technol.* **1986**, *2*, 461–475. [CrossRef]
9. Pollock, T.M.; Tin, S. Nickel-based superalloys for advanced turbine engines: Chemistry, microstructure and properties. *J. Propuls. Power* **2006**, *22*, 361–374. [CrossRef]
10. Giamei, A.; Tschinkel, J. Liquid metal cooling: A new solidification technique. *Metall. Trans. A* **1976**, *7*, 1427–1434. [CrossRef]
11. Giamei, A.F.; Kear, B. On the nature of freckles in nickel base superalloys. *Metall. Trans.* **1970**, *1*, 2185–2192. [CrossRef]
12. Copley, S.; Giamei, A.F.; Johnson, S.; Hornbecker, M.F. The origin of freckles in unidirectionally solidified castings. *Metall. Trans.* **1970**, *1*, 2193–2204. [CrossRef]
13. Auburtin, P.; Wang, T.; Cockcroft, S.; Mitchell, A. Freckle formation and freckle criterion in superalloy castings. *Metall. Mater. Trans. B* **2000**, *31*, 801–811. [CrossRef]
14. Tin, S.; Pollock, T. Predicting freckle formation in single crystal Ni-base superalloys. *J. Mater. Sci.* **2004**, *39*, 7199–7205. [CrossRef]
15. Auburtin, P.B.L. Determination of the Influence of Growth Front Angle on Freckle Formation in Superalloys. Ph.D. Thesis, University of British Columbia, Vancouver, BC, Canada, 1998.
16. Auburtin, P.; Cockcroft, S.; Mitchell, A. Liquid density inversions during the solidification of superalloys and their relationship to freckle formation in castings. *Superalloys* **1996**, 443–450. [CrossRef]
17. Ren, N.; Li, J.; Panwisawas, C.; Xia, M.; Li, J. Thermal-solutal-fluid flow of channel segregation during directional solidification of single-crystal nickel-based superalloys. *Acta Mater.* **2021**, *206*, 116620. [CrossRef]
18. Ren, N.; Panwisawas, C.; Li, J.; Xia, M.; Dong, H.; Li, J. Solute enrichment induced dendritic fragmentation in directional solidification of nickel-based superalloys. *Acta Mater.* **2021**, *215*, 117043.
19. Ren, N.; Li, J.; Panwisawas, C.; Xia, M.; Dong, H.; Li, J. Insight into the sensitivities of freckles in the directional solidification of single-crystal turbine blades. *J. Manuf. Process.* **2022**, *77*, 219–228.
20. Szeliga, D. Reduction of freckle defect in single-crystal blade root by controlling local cooling conditions. *Metall. Mater. Trans. A* **2022**, *53*, 3224–3231. [CrossRef]
21. Wang, Z.; Li, J.; Liu, S.; Wang, X.; Yang, W. Effects of Withdrawal Velocity and Casting Geometry on Freckle Formation of Nickel-Based Single Crystal Superalloys. *Metall. Mater. Trans. A* **2023**, *54*, 1223–1235.
22. Ma, D.X.; Wu, Q.; Bührig-Polaczek, A. Some new observations on freckle formation in directionally solidified superalloy components. *Metall. Mater. Trans. B* **2012**, *43*, 344–353.
23. Ma, D.X.; Bührig-Polaczek, A. The geometry effect on freckle formation in the directionally solidified superalloy CMSX-4. *Metall. Mater. Trans. A* **2014**, *45*, 1435–1444. [CrossRef]
24. Ma, D.; Zhao, Y.; Xu, W. Freckle Formation Affected by Geometry Features of Single Crystal Superalloy Castings. *Res. Dev. Mater. Sci.* **2021**, *15*, 1749–1752.
25. Han, D.; Jiang, W.; Han, X.; Li, K.; Lu, Y.; Lou, L. Influence of geometric structure and feeding behavior of casting on freckle formation during directional solidification of a Ni-based single-crystal superalloy. *Cryst. Res. Technol.* **2021**, *56*, 2000197. [CrossRef]
26. Wang, Z.; Li, J.; Liu, S.; Zhao, J.; Wang, X.; Yang, W. Investigation on freckle formation of nickel-based single crystal superalloy specimens with suddenly reduced cross section. *J. Alloys Compd.* **2022**, *918*, 165631. [CrossRef]
27. Pustal, B.; Wittenzellner, T.; Behnken, H.; Böttger, B.; Bührig-Polaczek, A. Experimental Analysis and Simulation of Freckle Formation at Different Edge Angles During Directional Solidification of Ni-Base Superalloys. *Metall. Mater. Trans. B* **2024**, *55*, 2732–2738. [CrossRef]
28. Nguyen-Thi, H.; Salvo, L.; Mathiesen, R.H.; Arnberg, L.; Billia, B.; Suery, M.; Reinhart, G. On the interest of synchrotron X-ray imaging for the study of solidification in metallic alloys. *Comptes Rendus Phys.* **2012**, *13*, 237–245.
29. Boden, S.; Eckert, S.; Willers, B.; Gerbeth, G. X-ray radioscopic visualization of the solutal convection during solidification of a Ga-30 Wt Pct in alloy. *Metall. Mater. Trans. A* **2008**, *39*, 613–623. [CrossRef]
30. Saad, A.; Gandin, C.-A.; Bellet, M.; Shevchenko, N.; Eckert, S. Simulation of channel segregation during directional solidification of In—75 wt pct Ga. Qualitative comparison with in situ observations. *Metall. Mater. Trans. A* **2015**, *46*, 4886–4897. [CrossRef]
31. Karagadde, S.; Yuan, L.; Shevchenko, N.; Eckert, S.; Lee, P.D. 3-D microstructural model of freckle formation validated using in situ experiments. *Acta Mater.* **2014**, *79*, 168–180.
32. Shevchenko, N.; Roshchupkina, O.; Sokolova, O.; Eckert, S. The effect of natural and forced melt convection on dendritic solidification in Ga–In alloys. *J. Cryst. Growth* **2015**, *417*, 1–8.
33. Reinhart, G.; Grange, D.; Abou-Khalil, L.; Mangelinck-Noël, N.; Niane, N.T.; Maguin, V.; Guillemot, G.; Gandin, C.-A.; Nguyen-Thi, H. Impact of solute flow during directional solidification of a Ni-based alloy: In-situ and real-time X-radiography. *Acta Mater.* **2020**, *194*, 68–79.
34. Sharp, D.H. An overview of Rayleigh-Taylor instability. *Phys. D Nonlinear Phenom.* **1984**, *12*, 3–18.
35. Worster, M.G. Instabilities of the liquid and mushy regions during solidification of alloys. *J. Fluid Mech.* **1992**, *237*, 649–669.

36. Beckermann, C.; Gu, J.; Boettinger, W.J. Development of a freckle predictor via Rayleigh number method for single-crystal nickel-base superalloy castings. *Metall. Mater. Trans. A* **2000**, *31*, 2545–2557.
37. Yang, W.; Chang, K.-M.; Chen, W.; Mannan, S.; DeBarbadillo, J. Freckle criteria for the upward directional solidification of alloys. *Metall. Mater. Trans. A* **2001**, *32*, 397–406. [CrossRef]
38. Tewari, S.N.; Tiwari, R.; Magadi, G. Mushy-zone Rayleigh number to describe macrosegregation and channel segregate formation during directional solidification of metallic alloys. *Metall. Mater. Trans. A* **2004**, *35*, 2927–2934. [CrossRef]
39. Liu, Y.; Wang, F.; Ma, D.; Yang, Q.; Xu, W.; Zhao, Y.; Dong, H.; Liu, Y.; Li, D. Freckle prediction model incorporating geometrical effects for Ni-based single-crystal superalloy components. *Acta Mater.* **2024**, *266*, 119702. [CrossRef]

Disclaimer/Publisher's Note: The statements, opinions and data contained in all publications are solely those of the individual author(s) and contributor(s) and not of MDPI and/or the editor(s). MDPI and/or the editor(s) disclaim responsibility for any injury to people or property resulting from any ideas, methods, instructions or products referred to in the content.

materials

MDPI

Article

Thermal and Structural Behavior of Investment Casting Molds Modified with Biodegradable Walnut Shell Chips

Marcin Małek [1,*], Janusz Kluczyński [2], Rafał Grzejda [3], Paweł Wiśniewski [4], Agnieszka Jenerowicz [5] and Ireneusz Ewiak [5]

[1] Institute of Civil Engineering, Faculty of Civil Engineering and Geodesy, Military University of Technology, 00-908 Warsaw, Poland
[2] Institute of Robots & Machine Design, Faculty of Mechanical Engineering, Military University of Technology, 00-908 Warsaw, Poland; janusz.kluczynski@wat.edu.pl
[3] Faculty of Mechanical Engineering and Mechatronics, West Pomeranian University of Technology in Szczecin, 70-310 Szczecin, Poland; rafal.grzejda@zut.edu.pl
[4] Faculty of Materials Science and Engineering, Warsaw University of Technology, 02-507 Warsaw, Poland; pawel.wisniewski@pw.edu.pl
[5] Department of Imagery Intelligence, Faculty of Civil Engineering and Geodesy, Military University of Technology, 00-908 Warsaw, Poland; ireneusz.ewiak@wat.edu.pl (I.E.)
* Correspondence: marcin.malek@wat.edu.pl; Tel.: +48-607-274-216

Abstract

Two types of spherical mold samples—designated PW1 (reference) and PW2 (modified) were prepared using the dip-and-sprinkle method. Both samples consisted of seven layers, but PW2 was differentiated by the incorporation of 5 wt.% ground walnut shell chips into the fifth layer of its structure. The aim of this modification was to assess the feasibility of employing biodegradable organic additives to generate controlled porosity after thermal decomposition, thereby enhancing gas transport through the mold structure. The gas permeability of the samples was determined across a broad temperature range from 25 to 950 °C using a dedicated, custom-built test rig developed for elevated-temperature permeability assessments. The results revealed that the inclusion of walnut shell chips significantly increased the gas permeability of the molds by approximately 42% at ambient temperature and 36% at 950 °C, attributable to the formation of stochastically distributed macro-voids upon burnout of the organic additive. The study demonstrates that selective layer modification using natural waste materials can be a viable method for tailoring functional properties of ceramic molds, offering a cost-effective, sustainable, and easily scalable alternative to conventional pore-forming strategies.

Keywords: casting molds; precision casting; gas permeability; corundum; binders; nano-SiO_2; walnut shell chips

1. Introduction

The lost-wax investment casting process has been practiced for millennia and remains a cornerstone of manufacturing complex, high-performance metal components [1–4]. It saw significant advancement around the mid-20th century—notably during and after World War II—when the aerospace and power generation industries drove rapid developments in precision casting technology [1–6]. Today, this process is indispensable for producing critical turbine engine parts that demand exceptional dimensional accuracy [7–9] and material integrity [10,11]. Such cast components, used in both aircraft engines and

energy turbines, must endure extreme operating conditions. Therefore, investment casting is engineered to yield near-net-shape parts with excellent surface finishes (as fine as ~5 μm Ra) and complex geometries [12,13]. Moreover, advanced casting techniques are employed to tailor the alloy microstructure for maximal high-temperature strength and creep resistance [7–11,14,15]. These achievements are made possible by multi-layer ceramic shell molds with carefully designed structures and properties [7–11,14,15]. The mold not only forms the final shape with high fidelity, but also controls the solidification rate by extracting heat from the molten alloy in a prescribed manner, thereby influencing grain structure [7–11,14,15]. Over the decades, numerous refinements to shell mold materials and construction have been introduced to meet the increasing quality requirements of aerospace and energy castings [2,10,11,15]. Despite these advances, ceramic shells still face challenges (e.g., maintaining strength, thermal stability, and permeability) that require ongoing research and innovation [10,11].

Modern ceramic shell molds are typically made of high-purity refractory materials—often alumina (corundum) as the primary flour [16]—combined with a colloidal silica [17] binder and various additives [18]. Corundum (α-Al_2O_3) is favored for face coats and backup layers due to its high melting point [19], chemical inertness, and stability [20], which help prevent metal–mold reactions [21] and erosion by the molten alloy [22–25]. Other refractories, such as aluminosilicates, zircon, fused silica [26,27], or SiC [28], may be used in specific layers [29–31] to achieve the desired thermal or chemical characteristics [32,33]. The binder is usually a water-based silica sol (e.g., LUDOX AM30 (Grace, Columbia, MD, USA) containing ~30 wt.% nano-SiO_2), which yields a slurry that coats the wax pattern uniformly and later hardens into a ceramic matrix upon drying and firing [16–18,25]. Compared to older ethyl silicate or organic binder systems, colloidal silica is relatively eco-friendly and does not produce toxic fumes during shell preparation or firing [5,6,26]. The slurry formulation often includes rheology modifiers, anti-foaming agents, and wetting agents to ensure proper flow and coating coverage [16–18,30]. The particle size distribution of the ceramic flour is carefully chosen—fine powders for face coats to capture detail, and coarser grains for intermediate and backing layers—to optimize packing density and minimize defects [16–18,29]. A broad particle size range can improve packing and reduce large voids, but excessive fines can increase slurry viscosity and reduce permeability [29,30]. Therefore, achieving a balance in slurry rheology and stability is crucial: it must allow easy dipping and draining while preventing sedimentation or agglomeration [16–18,30]. Indeed, the flow behavior of such ceramic slurries has been the subject of extensive study, as it directly affects the uniformity and strength of each shell layer [30]. In some cases, additives are introduced to enhance slurry performance—for example, small amounts of polymer binders—like poly (vinyl alcohol)—can improve green strength and coat adherence [23], and short fibrous reinforcements (ceramic or polymer fibers) have been explored to increase crack resistance or handle thermal stress [18,24]. For highly reactive alloys (such as titanium aluminides), specialized face coat systems have been developed (e.g., TiAlO-based or zirconia-based slurries with tailored binders) to prevent any reaction between the metal and mold [32,33]. These material considerations ensure that each layer of the shell mold fulfills its role: the primary (face coat) layers capture fine details and resist molten metal attack, while the subsequent backup layers build thickness for strength, and the outermost layers provide structural rigidity. All layers together form a robust ceramic shell capable of containing the metal during casting and influencing its solidification behavior.

Ceramic shells are built in stages on expendable wax or polymer patterns using the conventional dip-and-sprinkle method [16–21]. First, the cleaned wax pattern is immersed in the fine-grained primary slurry (the investing coat), then withdrawn and allowed to drain off the excess. While the coating is still wet, a rain of refractory stucco particles

(e.g., fine corundum sand) is sprinkled or fluidized onto it, which adheres and builds up the layer thickness [16–18,22]. This creates a face layer with a coarse outer texture that promotes good adhesion with the next layer. After air drying under controlled conditions, the process is repeated with subsequent layers using coarser slurries and larger stucco grains for the intermediate and structural coats [16–18,22]. Typically, an investment shell for high-performance castings consists of a face coat and one or two fine sealing layers, followed by several strengthening layers, yielding a total of 5–10 layers depending on part size and requirements [16–21]. The final layer is often a seal coat without stucco, intended to cover any exposed stucco and give a smooth outer surface. Each layer must be thoroughly dried before the next is applied; this drying is carried out in a controlled environment (temperature and humidity) to prevent rapid evaporation that could cause cracking or delamination [19–21]. It is common practice to dry shells in a conditioned room or chamber, ensuring gentle solvent evaporation (for water-based binders) and minimizing thermal gradients [19–21]. Once the multilayer shell is completed and dried (often after a curing period of several days), the wax pattern is removed. Wax elimination is typically achieved through autoclave steam dewaxing, where high-pressure steam melts and evacuates the bulk of the wax, leaving a hollow ceramic shell [22–25]. Any residual pattern material is burned out during the subsequent firing step. The ceramic shell is then fired at high temperature (typically 800–1100 °C, depending on the materials) to sinter the binder and strengthen the shell to casting [22–25]. A slow heating schedule is used to avoid thermal shock; this fire both solidifies the shell's structure and removes any remaining organic matter or moisture. An optional additional heat treatment (annealing) may be applied to tune the shell's mechanical properties or relieve stresses. The result is a rigid, porous ceramic shell mold ready to receive molten metal. Pouring of the superalloy is often performed under vacuum or inert atmosphere (especially for aerospace castings) to prevent oxidation. The ceramic shell must withstand the metallostatic pressure and thermal load of the liquid alloy without cracking, all while allowing the alloy to solidify in the desired manner. After the metal cools and solidifies, the shell is broken away (knocked out), usually by mechanical vibration or water-blasting, to reveal the cast part. This entire fabrication sequence is labor- and time-intensive, and researchers continually seek improvements to reduce cycle time and cost (for example, spraying the slurry instead of dipping can speed up shell building in some cases [22], and novel binders have been introduced to shorten drying times [27]). Nonetheless, the traditional dip-and-stucco method remains predominant due to its reliability and the high quality of shells it produces.

The performance of a ceramic shell mold during casting depends on a careful balance of its physical and mechanical properties. The shell must have high hot strength and creep resistance to support the liquid metal and maintain dimensional accuracy at casting temperatures [22–25]. It must also resist thermal shock when the molten alloy (often over 1500 °C for Ni-based superalloys) is poured in, and survive until the metal solidifies. Equally important, the shell should be gas-permeable—that is, it should allow air and process gases to escape freely through its walls during mold filling and solidification [22–25]. If a shell is too impermeable, trapped air and vaporizing residues can cause internal pressure, leading to defects such as blowholes, gas porosity, or misruns in the casting [27,34]. On the other hand, excessive porosity or large pores in the shell can undermine its mechanical strength and allow metal penetration into the mold wall, which is undesirable. Thus, an optimal porosity is needed: fine interconnected pores that permit venting of gases but do not significantly weaken the structure [25–29]. The pore structure of the shell (pore size, distribution, and volume fraction) is primarily determined by the particle sizes of the refractory, the binder content, and any volatile additives that burn out during firing [26–29]. For example, using a broad, bimodal particle distribution can maximize packing density (reducing

large voids) but may yield fewer, smaller pores [29]; conversely, introducing deliberately sacrificial fillers (like organic particles or fibers) creates additional voids after burnout, raising permeability [27,34,35]. The binder itself plays a crucial role, as demonstrated by Wiśniewski et al. [25], which shows that different binder formulations can result in significant differences in the porosity and gas permeability of the final shell. A silica sol binder that gels densely may produce a more tightly sealed ceramic matrix, whereas incorporating a polymeric or foam-forming binder could leave a more open porous network after firing [23,25]. Furthermore, chemical interactions at high temperatures can modify the pore structure—for instance, if silicon carbide fillers are used, they may react with an oxide binder or the furnace atmosphere to form gaseous species or secondary phases [28], potentially altering both the strength and permeability of the shell. The shell's thermal conductivity is also influenced by its porosity: pores are insulative, so a higher porosity shell tends to slow down heat extraction from the solidifying metal [26–29]. In directional solidification casting, a certain level of insulation is beneficial for controlling cooling rates. However, in conventional casting, excessive insulation (or too thick shell) may prolong solidification and promote coarse grains or shrinkage defects [9,15,20]. Therefore, engineers must optimize shell thickness and material to achieve the desired thermal profile in the casting. All these factors underscore that controlling the microstructure of the ceramic shell (through material selection and processing) is just as crucial as controlling and maintaining the metal alloy's solidification. Indeed, recent overviews highlight that modern ceramic shells must simultaneously satisfy often competing criteria—strength, permeability, thermal stability, dimensional precision, and chemical inertness—and this remains an active area of materials engineering research [10,11].

One persistent problem in investment casting is the evolution of gases when the hot metal comes into contact with the mold. Air within the mold cavity, vaporizing binders or pattern materials, and gases from any reactions must all escape through the ceramic shell's porous network. Insufficient gas permeability can lead to pressure buildup and gas entrapment, causing defects in the casting [27,34]. Traditional shells made purely of dense ceramic (especially with fine-grained slurries) can be relatively impervious [27]. To address this, foundry engineers have developed strategies to tailor the permeability of shells without sacrificing their strength. One approach is to adjust the as-built porosity by modifying the shell recipe: for example, adding fugitive additives to the slurry that create pores upon burnout. Synthetic polymer additives have been explored—Sanjay and Karunakar demonstrated that incorporating a small amount of acrylonitrile–butadiene–styrene (ABS) plastic powder and needle coke (a carbonaceous filler) into the shell layers significantly increases the fired porosity and permeability, resulting in fewer gas-related casting defects [27]. However, purely synthetic additives can introduce residues or may not decompose cleanly. Recent research has therefore turned to naturally derived, biodegradable pore-formers that are both effective and environmentally benign [34,35]. Pattnaik and Sutar have investigated organic fillers, such as sawdust (wood flour), in the secondary layers of the shell, demonstrating that incorporating approximately 5 wt.% sawdust into the slurry can increase the shell's porosity and double its gas permeability, while still retaining acceptable mechanical strength after firing [36]. The porous structure left by the burnt-out sawdust helped vent gases and even improved the feeding of castings, reducing internal defects [36]. In a similar vein, agricultural waste products such as walnut shell flour offer a promising option as pore-forming additives. Walnut shell is a lignocellulosic material that burns out almost completely during firing, leaving behind a network of micro-porosity. It is inexpensive and widely available as a by-product of the food industry, making it an attractive green additive. In the present work, this concept is explored by incorporating fine walnut shell particles into one of the intermediate mold layers. The goal is to increase

gas permeability in that layer—effectively creating a venting network within the shell—to facilitate the escape of gases during pouring and solidification. Using a waste-derived additive, such as walnut shell, aligns with both environmental and economic objectives by reducing reliance on virgin materials and improving casting yield. An added benefit is that such bio-additives decompose into gaseous products (CO_2, H_2O, etc.) rather than harmful solid residues, and they contribute significantly less to pollution compared to synthetic substances [3,26]. Beyond additives in the slurry, other innovative techniques have emerged to enhance shell permeability. Another approach is the use of mechanical drilling or patterning to introduce vent holes in non-critical areas of the shell after it is built—for instance, ultrasonic micro-drilling has been used to perforate shells, yielding a significant permeability boost and reduced casting porosity [11]. However, such post-processing methods carry risks of shell damage and are less practical for production. A more practical strategy is to engineer the slurry composition itself for enhanced permeability: researchers have incorporated combustible wax-based powders into shells (similar to pattern wax), which melt or vaporize during firing, leaving behind additional porosity [35]. Pattnaik and Sutar demonstrated that adding 4 wt.% polyethylene wax powder to the secondary (back-up) coats resulted in a shell with higher green strength and approximately 20% higher fired porosity and permeability, which translated to fewer porosity defects in the cast product [37]. Notably, the minor decrease in fired flexural strength observed was acceptable, as the shell's role is temporary and it is broken off after solidification [35]. Fiber additions can also influence permeability: ceramic fibers (which remain in the shell) primarily boost strength, whereas sacrificial polymer fibers (like nylon) burn away and leave elongated pores that may slightly increase permeability while also affecting mechanical properties [18,24]. For example, Huang et al. found that introducing a small fraction of nylon fibers alongside ceramic fibers into a silica sol shell improved the shell's fracture toughness and did not excessively compromise permeability. However, an optimal fiber content had to be found [24]. Overall, these advanced techniques aim to create a shell that is just permeable enough to vent gases and prevent defects, yet is still strong and stable throughout the casting process.

Modern materials engineering of ceramic shells increasingly emphasizes sustainability, cost-effectiveness, and technical performance. The use of water-based binders (colloidal silica) instead of alcohol-based or chemical-setting binders has virtually eliminated the emission of noxious fumes and vastly improved working conditions in shell fabrication [3,26]. Likewise, incorporating recycled or renewable materials into shell construction can reduce waste and lower material costs. The idea of using walnut shell flour exemplifies this trend—it repurposes agricultural waste into a value-added component of the mold, enhancing permeability and then completely combusting away. Such bio-additive approaches not only improve casting quality but also reduce the environmental footprint of the process [3,34,35]. In parallel, researchers are looking at the end-of-life of ceramic shells themselves. Spent shells (after knockout) have historically ended up as landfill, but recent studies have explored the valorization of ceramic shell waste—for instance, crushing used shells to reuse them as refractory aggregate or as feedstock for other ceramic products [38]. Koralnik demonstrated a recycling route for alumina-based shell waste, showing it can be classified, ground, and reused in new molds or other ceramics without loss of performance [38]. This circular approach enhances the sustainability of precision casting by reducing raw material consumption and waste generation. Another avenue for improvement is to expedite the shell production cycle, thereby saving energy and costs. Novel binder systems (e.g., fast-curing polymers or hybrid inorganic-organic binders) have been tested to enable rapid drying of shells [39]. For example, Lin et al. reported a silicone resin–bonded ceramic shell

that could be dried much faster than traditional shells while achieving higher strength, thereby potentially shortening the lead time for casting without compromising quality [40].

2. Materials and Methods

The samples tested were two types of multi-layered spherical ceramic molds, prepared by the immersion method according to the procedures described in publications [5,6,25]. The samples were made using the dip-and-sprinkle method. Materials of this shape were dedicated to gas permeability measurements, but other tests were also performed on them. Corundum flour (Treibacher Industrie AG, Althofen, Austria) with a particle size of 325 mesh (approx. 30 μm) was used to obtain ceramic funnel masses. The ecological modifier of the fifth layer was walnut shell chips (1 mm to 2 mm). The polymer binder was LUDOX AM30 (Grace, Columbia, MD, USA) containing colloidal SiO_2. Corundum sand of two particle sizes was used as sprinkles: Corundum 100 (0.1 mm to 0.3 mm) for the first two layers and Corundum 46 (0.3 mm to 0.4 mm) for the structural layers. The funnel masses were mixed in a CAT R50 mechanical mixer (CAT Engineering Office, M. Zipperer GmbH, Ballrechten-Dottingen, Germany) for 14 days at 150 rpm until the slurries stabilized before application. The raw material compositions of the molding compounds and sprinkles are shown in Table 1.

Table 1. Basic raw material compositions of the samples produced.

Sample	Layer	Molding Compound	Sprinkle
PW1	1 and 2	LUDOX AM30 and corundum flour	Corundum 100
	3 to 6	LUDOX AM30 and corundum flour	Corundum 46
	7	LUDOX AM30 and corundum flour	–
PW2	1 and 2	LUDOX AM30 and corundum flour	Corundum 100
	3 and 4	LUDOX AM30 and corundum flour	Corundum 46
	5	LUDOX AM30 and corundum flour with 5 wt.% walnut shell chips	Corundum 46
	6	LUDOX AM30 and corundum flour	Corundum 46
	7	LUDOX AM30 and corundum flour	–

During the research, the corundum meal, corundum sprinkle, and the basic properties of the molding binder used were investigated. Observations of the quartz meal, the sands used for the sprinkle layers and the mold samples were made in a Hitachi SU70 scanning electron microscope (Hitachi High-Tech Corporation, Tokyo, Japan) at an electron beam accelerating voltage of 15 kV.

The polymer binder was characterized by examining its morphology using a Hitachi 5500 scanning electron microscope (Hitachi High-Tech Corporation, Tokyo, Japan), determining the pH and solid phase content (designated as C), and measuring the outflow time from a Zahn cup No. 4, a standard method for viscosity assessment used in precision casting. The reaction of the binders was tested using a Sension-1 Hach pH-meter (Hach Company, Loveland, CO, USA).

Gas permeability was determined in a unique test bench designed and constructed at the Faculty of Materials Science and Engineering of the Warsaw University of Technology.

3. Research Results and Discussion

The results of the basic properties of the LUDOX AM30 binder (Grace, Columbia, MD, USA) are presented in Table 2. The binder, characterized by a pH close to neutral and a viscosity similar to that of water (flow time of 6.23 s). The proportion of the solid phase in the form of nano-SiO_2 particles is typical for molding binders and amounts to 30 wt.%.

Table 2. Basic properties of the polymer binder used.

Molding Binder	pH	C [%]	Outflow Time from Zahn Cup No. 4 [s]
LUDOX AM30	8.74	30.0	5.69

Figure 1 shows an example of the morphology of the LUDOX AM30 binder (Grace, Columbia, MD, USA) obtained using scanning electron microscopy (SEM).

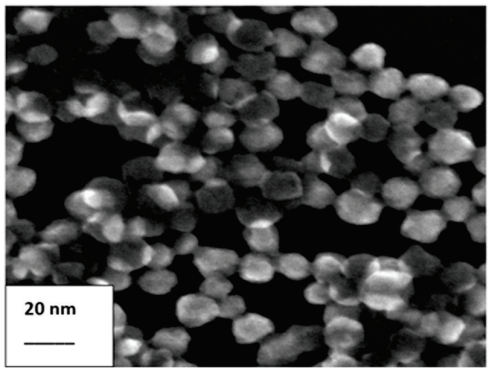


Figure 1. SEM morphology of the LUDOX AM30 binder (Grace, Columbia, MD, USA).

The nano-SiO_2 particles are characterized by slight agglomeration. The shape of the silica particles is close to spherical, and their diameter does not exceed 20 nm. Figure 1 shows example images of the granular materials used, taken on a Hitachi SU70 scanning electron microscope (Hitachi High-Tech Corporation, Tokyo, Japan).

From the comprehensive microstructural analysis of the solid-phase components conducted using SEM, it is evident that the corundum flour used as the primary fine fraction in the ceramic slurry exhibits a markedly irregular particle morphology (Figure 2a). The particles are angular with sharply defined edges and a high aspect ratio, indicative of a mechanically milled alumina source. This geometry contributes significantly to a higher packing density and mechanical interlocking between adjacent particles in the green state. Similar morphological characteristics are observed for the two granular refractory fractions used as stucco: Corundum 100 (Figure 2b) and Corundum 46 (Figure 2c). Both materials exhibit non-spherical, faceted grains with well-developed crystallographic edges, which is typical for fused and crushed alumina particles. These features enhance the mechanical keying between successive shell layers during the dip-and-sprinkle process, promoting robust adhesion of the stucco to the slurry-coated pattern surface. Walnut shell chips are shown in Figure 2d.

Such morphology is widely accepted in industrial precision casting practice, not only due to its favorable mechanical interlocking but also because it supports adequate capillary suction and binder retention during shell construction. Moreover, the high angularity of these particles creates tortuous pore pathways in the ceramic matrix, which are essential for achieving a balance between gas permeability and thermal stability. Notably, the surface roughness and irregular contact points among the corundum grains help control shrinkage behavior during drying and firing, reducing the incidence of warping or delamination in intermediate layers.

Thermogravimetric analysis (TGA) of the walnut shell chips was performed in an air atmosphere using Q5000 analyzer (TA Instruments, New Castle, DE, USA). Samples were scanned in the temperature range from 20 °C to 1000 °C with a heating rate 10 °C/min. The TGA results of walnut shell chips are shown in Figure 3.

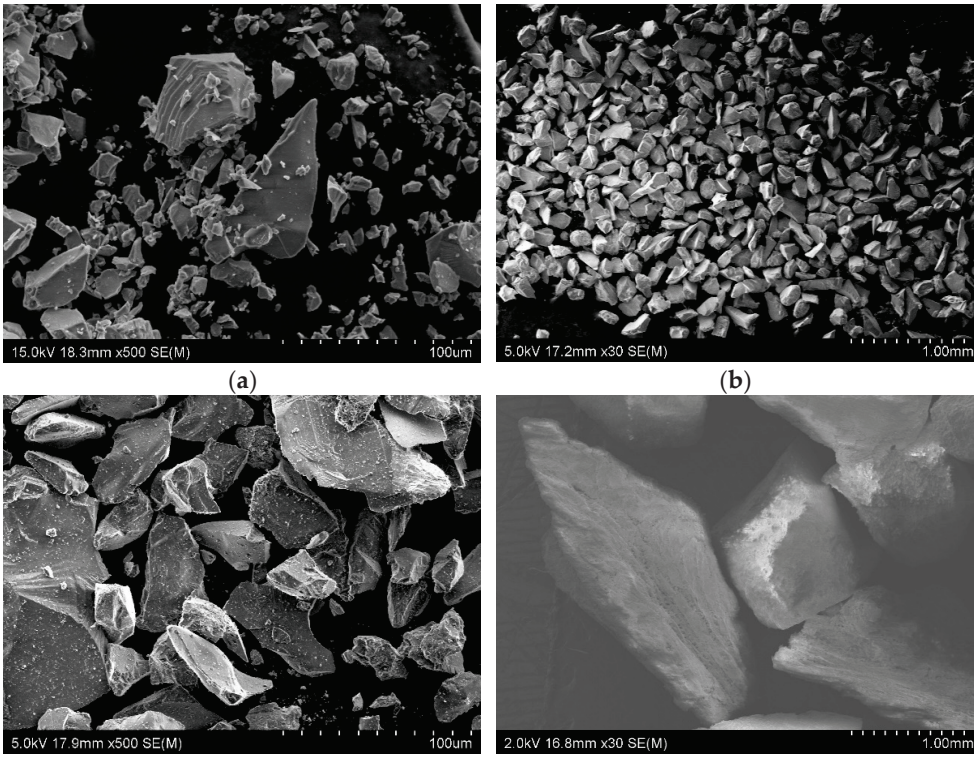


Figure 2. Particle morphology of the powders used to make the mold samples: (**a**) Corundum flour; (**b**) Corundum 100; (**c**) Corundum 46; (**d**) Walnut shell chips.

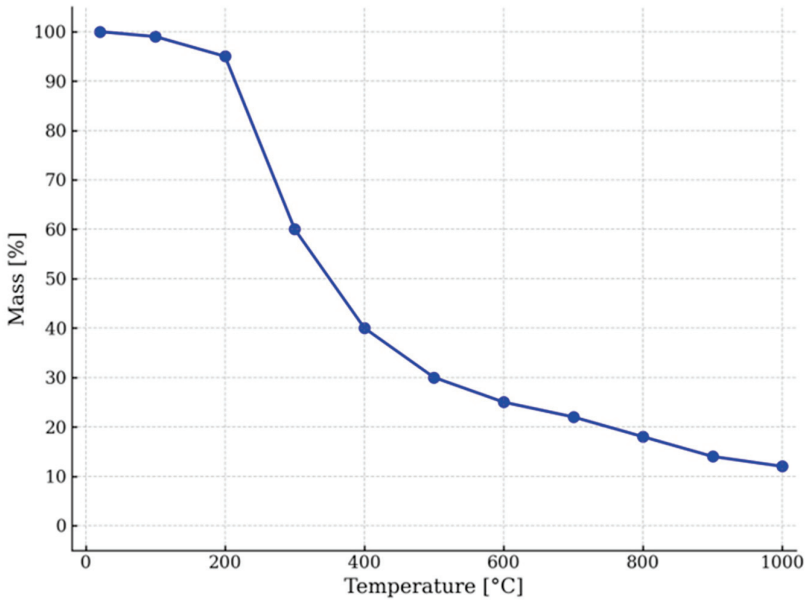


Figure 3. TGA curve of walnut shell chips.

The investigated walnut shell sample exhibited a mass loss of approximately 5% up to 200 °C, attributed to the release of physically and chemically bound water. With increasing temperature in the range of about 200–300 °C, the decomposition of hemicellulose occurs, followed by the thermal degradation of cellulose between 300 °C and 400 °C. At temperatures up to 400 °C, this process is rapid, accounting for a significant weight loss of approximately 60%. During this stage, volatile organic compounds, gases (CO, CO_2), and carbon are formed. Above 400 °C, a further gradual mass loss is observed, associated with the decomposition of lignin, which occurs over a broad temperature range up to

approximately 600–700 °C. This process is slow due to the high thermal stability of lignin. The total mass loss reaches 88%, with ash remaining as the final residue.

Figure 4 presents the results of the energy dispersive spectroscopy (EDS) analysis performed on corundum samples and walnut shells in selected micro-areas.

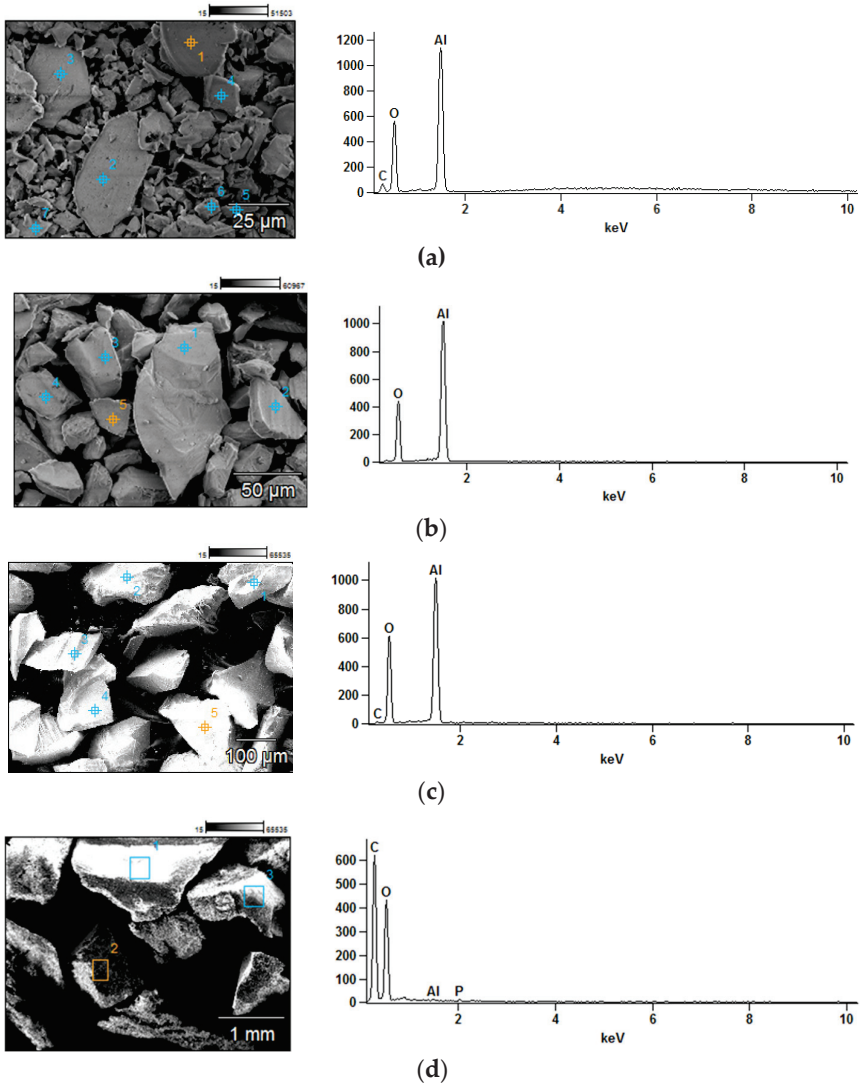


Figure 4. The outcome of the EDS analysis of Corundum 100 within micro-areas: (**a**) Corundum flour; (**b**) Corundum 100; (**c**) Corundum 46; (**d**) Walnut shell chips.

The results obtained for all corundum samples confirmed that aluminum (Al) is the principal constituent of the powders. The walnut shell sample represents an organic material of natural origin. It contains carbon (C), oxygen (O), as well as minor amounts of aluminum (Al), phosphorus (P), and silicon (Si).

Detailed SEM micrographs of the fifth structural layer, before and after thermal treatment, offer critical insights into the evolution of the microstructure and its implications for permeability and structural integrity (Figure 5). In the PW1 reference sample, following thermal conditioning at 150 °C (Figure 5a), a heterogeneous and porous network is discernible. Coarse stucco grains (Corundum 46) are embedded in a finer matrix derived from the LUDOX AM30-based slurry (Grace, Columbia, MD, USA). The interface between the coarse and fine particles reveals localized voids and discontinuities, suggesting partial binder shrinkage or incomplete densification during drying. The observed porous structure

is characteristic of green shells prepared with colloidal silica binders, which tend to form open gel networks with moderate capillary densification.

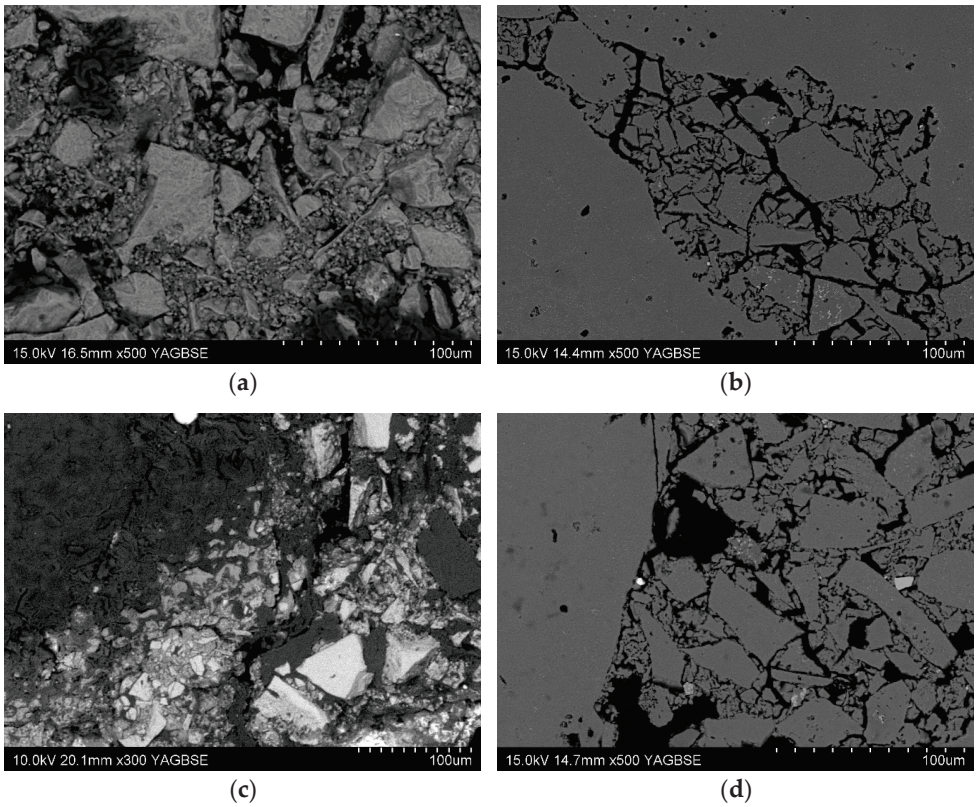


Figure 5. SEM morphology of the fifth layer of ceramic mold samples: (**a**) PW1 sample after soaking at 150 °C; (**b**) PW1 sample after annealing at 950 °C; (**c**) PW2 sample after soaking at 150 °C; (**d**) PW2 sample after annealing at 950 °C.

Upon high-temperature firing at 950 °C (Figure 5b), the same sample exhibits clear signs of structural degradation in the form of microcracking and interfacial decohesion, particularly at the grain boundaries between the sprinkle corundum and the flour matrix. These cracks predominantly nucleate at the binder-rich zones, implying that the silica sol underwent phase changes (e.g., gel-to-glass transition or sintering-induced shrinkage) that were not fully compatible with the thermal expansion behavior of the refractory components. The mismatch in thermal coefficients and the limited wetting capability of LUDOX AM30 (Grace, Columbia, MD, USA) with highly angular corundum grains may have exacerbated stress concentrations, ultimately leading to defect propagation. Such microstructural flaws, although not immediately catastrophic, can undermine the mechanical strength of the shell and reduce its ability to resist metallostatic pressure during casting.

The modified PW2 sample, incorporating 5 wt.% ground walnut shell chips into the fifth layer, presents a markedly different microstructural evolution. In the pre-fired state at 150 °C (Figure 5c), the presence of coarse, irregular organic inclusions are clearly visible within the ceramic matrix. These walnut shell fragments appear as elongated or flake-like entities with low interfacial bonding to the surrounding ceramic phase. The organic phase is thermally unstable and expected to undergo complete combustion during firing, acting as a fugitive additive. Following high-temperature annealing at 950 °C (Figure 5d), these inclusions are entirely removed, leaving behind large, randomly distributed pores that are often tens of micrometers in diameter.

These voids constitute artificial porosity within the shell structure and serve as microcapillaries for gas evacuation during the casting process. Their stochastic distribution enhances through-thickness gas flow without requiring modification of permeability across all layers of the shell. However, similar to the PW1 sample, the PW2 shell also displays interfacial cracking, particularly at the boundaries where the binder once connected the stucco to the matrix. While the pore-forming strategy successfully introduces targeted permeability enhancement, it also increases the internal surface area and potentially weakens the local matrix integrity. The resultant network of interconnected pores may facilitate outgassing during casting but may also require careful control to ensure that the shell retains adequate mechanical performance under load.

The next stage of the research was gas permeability measurements. The samples obtained by the dip-and-sprinkle method were subjected to a heat treatment of 950 °C for 1 h in a chamber furnace under an air atmosphere to remove the celluloid sphere, on which successive ceramic layers were subsequently applied. The furnace was heated at a rate of 5 °C/min. After reaching the annealing temperature to avoid cracking, the samples were cooled in the furnace.

Gas permeability measurements were conducted on a test stand of our own design, which is described in detail in [25]. The design of the measuring station for gas permeability testing in a hot medium is shown in the block diagram in Figure 6. The station consists of a source of compressed air 1, which is a gas cylinder connected to a membrane valve 2 through a reducing valve. The membrane valve 2 is connected to a dial pressure indicator 3 and an air dryer 4. The outlet of the air dryer 4 is connected to a needle valve 5, which precisely regulates the pressure of the air reaching the column pressure gauge 6 and the flowmeter 7. The outlet of the flowmeter 7 is connected to the sample under test 8. The sample 8 is located at the end of the station and is placed in a chamber furnace 9. During the measurement, the air flow is recorded, and its pressure is read from the column pressure gauge 6.

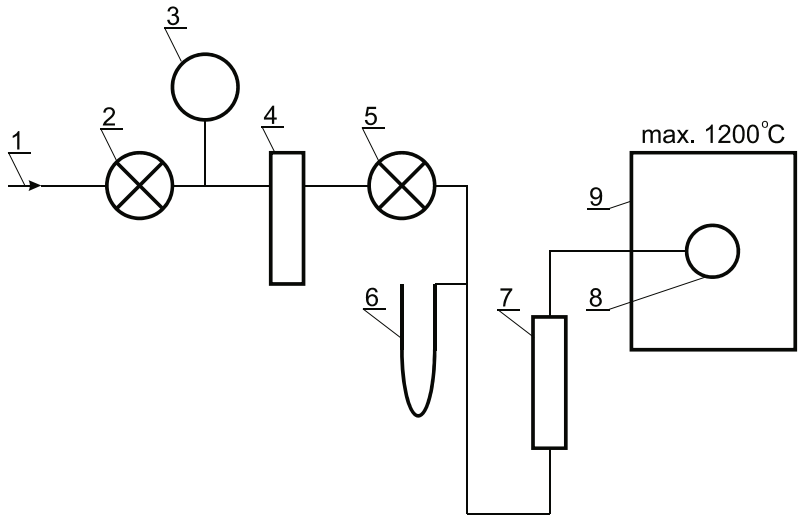


Figure 6. Block diagram of the test station (1—air inlet; 2—membrane valve; 3—dial pressure indicator; 4—air drier; 5—needle valve; 6—column pressure gauge; 7—flowmeter; 8—sample; 9—chamber furnace).

Gas permeability was calculated from the relationship described by Darcy's law [38,39,41]:

$$K = \frac{M \cdot Q' \cdot D}{P \cdot A} \quad (1)$$

where K denotes the gas permeability [cm^2], M is the dynamic viscosity of air at a given temperature [$(kg/m \cdot s)\ 10^{-5}$], D denotes the thickness of the mold wall [mm], A is the mold surface area [mm^2], P represents the air pressure [mm H_2O] and Q' is the value of air flow at the measurement temperature [cm^3/min].

The dynamic viscosity of air M in the temperature range under study is directly proportional to temperature. For the temperature range of interest, this function takes the form of a linear relationship, so the value of dynamic viscosity for a particular temperature can be directly read out from the device [25].

The value of air flow Q' is dependent on the ambient temperature. The measurement is carried out in media with different temperatures using a chamber furnace, so the working medium of air also has different temperatures. With this in mind, a correction must be made for the value of air flow at the measurement temperature described by equation:

$$Q' = \frac{Q \cdot T'}{T} \tag{2}$$

where Q' denotes the value of air flow at the measurement temperature [cm^3/min], Q is the value of air flow at the room temperature [cm^3/min], T' denotes the value of the measurement temperature [°C] and T is the value of the room temperature [°C].

The station enabled gas permeability to be measured at elevated temperatures, allowing for a result as close as possible to the operating conditions of the ceramic mold. Gas permeability tests were conducted in the temperature range of 25 to 950 °C on samples that had been previously subjected to the burnout process. The gas permeability measurement results of the tested casting mold samples are shown in Figure 7.

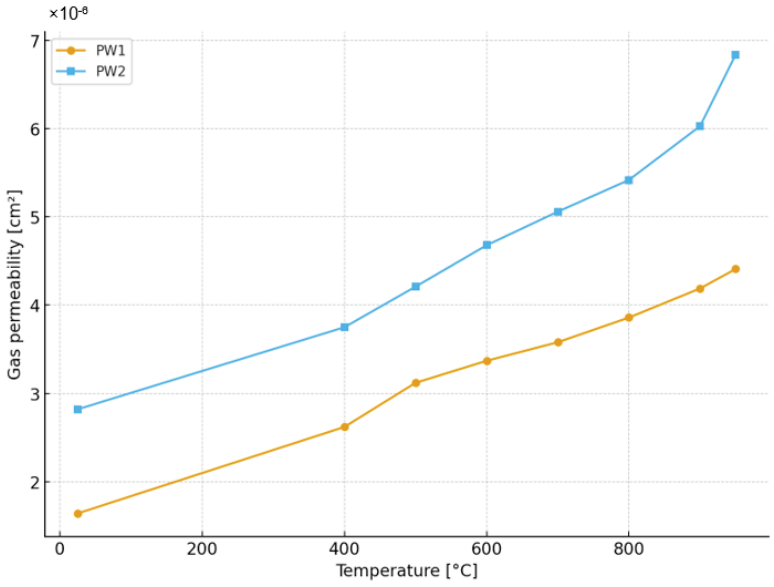


Figure 7. Results of gas permeability measurements of samples PW1 and PW2.

The experimental results clearly indicate a temperature-dependent increase in gas permeability for both types of ceramic shell mold samples (PW1 and PW2). As the temperature rises from ambient (25 °C) to elevated casting-relevant conditions (950 °C), the permeability of the shells increases by approximately 2.5 times, which is consistent with the expected thermal dilation of the pore network and the concomitant decrease in air viscosity. This thermally activated permeability enhancement is intrinsic to porous ceramic structures and arises due to the combined effects of increased molecular motion, binder pyrolysis residuals, and reduced resistance to gas flow across the intergranular voids.

Notably, the modified sample (PW2), which incorporates a deliberate structural modification in the fifth shell layer through the addition of 5 wt.% walnut shell chips exhibit a consistently higher gas permeability across the entire temperature range. This enhancement can be directly attributed to the combustion of walnut shell particles during firing, which leaves behind a network of stochastically distributed macrovoids. These voids, typically tens of micrometers in size, serve as preferential pathways for gas transit, substantially reducing the resistance to flow through the shell. Importantly, these pores are concentrated within a single intermediate layer, yet they exert a cascading influence on the permeability of the entire multilayer shell, enabling improved air displacement not only locally but also through adjacent structural zones.

Beyond the established parameters such as particle morphology, binder type, and layer thickness, this study underscores the significant role that localized structural modification can play in tuning shell permeability. The incorporation of organic waste-based fillers, such as walnut shell particulates, into the ceramic slurry introduces a sustainable and cost-effective strategy for engineering pore architecture. Quantitative analysis reveals that the use of walnut shell chips increases gas permeability by approximately 36% at elevated temperatures and up to 42% at room temperature, when compared to the unmodified reference sample. These improvements are substantial and validate the effectiveness of the pore-forming approach.

A key insight derived from this work is the understanding that permeability control does not necessarily necessitate a comprehensive redesign of all shell layers. Instead, modifying a single strategically selected layer—specifically, one that does not compromise structural integrity or surface finish—can yield measurable and reproducible improvements in gas transport properties. This modular approach to permeability enhancement simplifies implementation and minimizes risks to shell strength, making it a practical solution for industrial foundries aiming to optimize process reliability without overhauling the entire shell-making protocol.

From an application standpoint, the findings of this study suggest that ceramic shell molds of the PW2 configuration are promising candidates for deployment in precision casting operations, particularly for turbine or aerospace-grade components. However, before industrial adoption, it is essential to validate the mechanical performance, erosion resistance, and thermal behavior of the modified shells under real casting conditions. This would include liquid metal filling trials under vacuum or inert gas environments, mechanical testing of shells post-firing, and post-casting evaluation of the surface quality and microstructure of the resulting metallic components.

4. Results and Analysis

The experimental investigations conducted on the multilayer ceramic shell systems—namely the reference sample (PW1) and the modified sample incorporating walnut shell particles (PW2)—highlight key structure–property relationships pertinent to investment casting technology. Central to the analysis is the role of pore-forming strategies, particle–binder interactions, and thermal processing in shaping the gas permeability and microstructural evolution of the shell molds. The results clearly show that a targeted modification of a single intermediate layer (fifth layer) using 5 wt.% walnut shell chips can significantly enhance the permeability of the ceramic molds while maintaining the structural logic of the multilayer system.

The increase in gas permeability with rising temperature for both samples aligns well with fundamental gas flow theory in porous materials, where the Knudsen diffusion regime transitions toward viscous flow with increasing temperature and decreasing gas viscosity. Similar thermal enhancement trends were reported in other ceramic mold systems

employing colloidal silica binders and high-purity corundum aggregates [25], supporting the reliability of the experimental methodology.

More critically, the superior permeability of the PW2 samples, achieved via thermal burnout of lignocellulosic particles, aligns with recent studies exploring the use of biodegradable pore-forming agents. Pattnaik and Sutar [37] demonstrated that the addition of 4 wt.% polyethylene wax powder in the secondary layer of investment molds increased shell permeability by up to 30% with marginal reductions in strength. Similarly, in a study by Pattnaik and Sutar [36], the inclusion of 5 wt.% sawdust led to an increase in gas permeability of approximately 35–38%, with large interconnected pores forming after pyrolysis. The current study's finding of a 36–42% permeability increase for the PW2 configuration is consistent with these values and supports the idea that organic fillers of controlled granulometry can serve as effective pore formers.

Notably, the walnut shell filler used in this work differs from traditional synthetic pore-formers by offering a more sustainable, biodegradable, and non-toxic alternative, as also advocated in recent circular economy research [39]. Moreover, the irregular and angular morphology of the walnut shell chips led to the formation of randomly distributed pores with a wide size distribution (tens of micrometers), which enabled multidirectional venting of process gases—a feature crucial in mitigating blowhole formation and entrapped gas defects during high-precision alloy casting [27,38].

The presence of microcracks and interfacial decohesion in both PW1 and PW2 samples after firing, particularly at the grain–binder interface, raises concerns about thermal compatibility between the LUDOX AM30 binder (Grace, Columbia, MD, USA) and angular corundum grains. This phenomenon is consistent with observations by Wiśniewski et al. [25], who reported that the gelation behavior of silica sol binders can lead to localized stresses and cracking upon sintering, especially when the slurry exhibits poor wetting characteristics or a mismatch in binder shrinkage. These findings suggest that future optimization could involve hybrid or polymer-modified binders (e.g., colloidal silica with poly (vinyl alcohol)), which have demonstrated enhanced green strength and reduced crack propagation in similar systems [23].

The microstructural observations from SEM analysis confirm the hypothesis that the pores introduced by walnut shell burnout dominate the gas flow behavior through the shell. Unlike PW1, where porosity arises mainly from intergranular gaps and packing imperfections, the PW2 shells contain deliberate macroporosity with higher aspect ratios and wider necks, as also seen in studies on ABS powder and needle coke-modified shells [27]. Importantly, the localized concentration of pores in one structural layer (rather than homogenously across all layers) did not compromise shell integrity, confirming that permeability tuning can be selectively implemented without overhauling the entire shell composition.

Comparing the present results with those of Kanyo et al. [11], who provided a comprehensive overview of investment casting shells for superalloy components, it becomes evident that modern shell design must simultaneously address contradictory requirements: mechanical strength, thermal resistance, permeability, and process economy. The shell modification technique used in this study—targeted pore engineering via bio-additive burnout—achieves a favorable compromise among these constraints and is well-suited for components cast under vacuum or inert conditions, where gas evacuation paths are critically important.

The study contributes to the growing body of work emphasizing sustainable materials engineering in high-value manufacturing sectors. The use of ground walnut shell—an agricultural byproduct—mirrors the valorization strategies outlined by Koralnik [38], where spent ceramic shell waste was repurposed into a refractory feedstock, thereby

closing the materials loop. In this light, the present work not only enhances performance but also reinforces the movement toward environmentally responsible foundry practices.

The uniqueness of walnut shells lies in the combination of hardness, natural origin, versatility, and environmental friendliness. As a result, they find applications in industry, cosmetics, energy production, horticulture, and even natural medicine. Walnut shells are a completely natural and biodegradable raw material [42–44]. They can be utilized as a pore-forming agent in ceramic products. Their unique structure and chemical composition ensure that, after proper processing, they become an effective and ecological source of porosity [45,46]. In ceramic materials, walnut shells undergo almost complete burnout during firing. Walnut shells have been found to be a unique and interesting material for precision casting.

5. Conclusions

This study investigated the influence of a biodegradable pore-forming additive—ground walnut shell particles—on the microstructure and gas permeability of multilayer ceramic shell molds prepared via the conventional dip-and-stucco method.

- Ceramic shell molds fabricated from corundum powders (Corundum 46 and Corundum 100) with a colloidal silica binder (LUDOX AM30) exhibited temperature-dependent permeability, which increased significantly at elevated temperatures.
- Selective modification of the fifth layer by introducing 5 wt.% walnut shell chips produced a substantial permeability improvement compared with the unmodified reference shell.
- Upon firing at 950 °C, the walnut shell particles decomposed completely, leaving behind large, irregular pores that enhanced gas flow paths.
- Quantitative testing showed that PW2 achieved 42% higher permeability than PW1 at room temperature and 36% higher at 950 °C.
- Crucially, the modification of only one internal layer proved sufficient to achieve functional permeability control, avoiding risks associated with altering all layers.
- Walnut shells—abundant, biodegradable, and low-cost—proved to be an effective and sustainable pore-forming agent for ceramic molds.
- The results demonstrate strong potential for industrial application, although further validation under real casting conditions is required to confirm mechanical robustness and casting performance.
- Overall, the findings support the integration of sustainable, waste-derived additives into advanced foundry technology, contributing both to defect reduction and to circular economy objectives.

Author Contributions: Conceptualization, P.W. and M.M.; methodology, P.W.; validation, M.M., R.G., J.K. and P.W.; formal analysis, M.M.; investigation, J.K., A.J. and P.W.; resources, M.M.; data curation, P.W. and M.M.; writing—original draft preparation, P.W. and R.G.; writing—review and editing, M.M.; visualization, R.G.; supervision, P.W.; project administration, I.E., A.J. and M.M.; funding acquisition, M.M. All authors have read and agreed to the published version of the manuscript.

Funding: The research was funded by the Dean of Faculty of Civil Engineering and Geodesy, Military University of Technology, grant number 9/WIG/2025. Also this study was financed by the Faculty of Materials Science, Warsaw University of Technology, Ref. No. 504/04449/1090/44.000000.

Institutional Review Board Statement: Not applicable.

Informed Consent Statement: Not applicable.

Data Availability Statement: The original contributions presented in this study are included in the article. Further inquiries can be directed to the corresponding author.

Conflicts of Interest: The authors declare no conflicts of interest.

References

1. Gandin, C.-A.; Rappaz, M.; Tintillier, R. Three-dimensional probabilistic simulation of solidification grain structures: Application to superalloy precision castings. *Metall. Trans. A* **1993**, *24*, 467–479. [CrossRef]
2. Jones, S.; Yuan, C. Advances in shell moulding for investment casting. *J. Mat. Proc. Technol.* **2003**, *135*, 258–265. [CrossRef]
3. Haratym, R.; Biernacki, R.; Myszka, D. *Ekologiczne Wytwarzanie Dokładnych Odlewów w Formach Ceramicznych*; Oficyna Wydawnicza Politechniki Warszawskiej: Warszawa, Poland, 2008.
4. Perzyk, M. *Odlewnictwo*; Wydawnictwo Naukowo-Techniczne: Warszawa, Poland, 2009.
5. Małek, M.; Wiśniewski, P.; Matysiak, H.; Zagórska, M.; Kurzydłowski, K.J. Technological properties of SiC-based ceramic slurries for manufacturing investment casting shell moulds. *Arch. Metall. Mater.* **2014**, *59*, 1059–1062. [CrossRef]
6. Wiśniewski, P.; Małek, M.; Mizera, J.; Kurzydłowski, K.J. Effect of adding water-based binders on the technological properties of ceramic slurries based on silicon carbide. *Mater. Technol.* **2017**, *51*, 225–227.
7. Hong, J.; Ma, D.; Wang, J.; Wang, F.; Sun, B.; Dong, A.; Li, F.; Bührig-Polaczek, A. Freckle defect formation near the casting interfaces of directionally solidified superalloys. *Materials* **2016**, *9*, 929. [CrossRef]
8. Zhang, H.; Xu, Q. Simulation and experimental studies on grain selection and structure design of the spiral selector for casting single crystal Ni-based superalloy. *Materials* **2017**, *10*, 1236. [CrossRef]
9. Szeliga, D.; Ziaja, W.; Motyka, M.; Kubiak, K.; Sieniawski, J. Application of inner radiation baffles in the Bridgman process for flattening the temperature profile and controlling the columnar grain structure of directionally solidified Ni-based superalloys. *Materials* **2019**, *12*, 935. [CrossRef]
10. Pattnaik, S.; Karunakar, D.B.; Jha, P.K. Developments in investment casting process—A review. *J. Mater. Process. Technol.* **2012**, *212*, 2332–2348. [CrossRef]
11. Kanyo, J.E.; Schafföner, S.; Uwanyuze, S.R.; Leary, K.S. An overview of ceramic molds for investment casting of nickel superalloys. *J. Eur. Ceram. Soc.* **2020**, *40*, 4955–4973. [CrossRef]
12. Wiśniewski, P. Evaluating silicon carbide-based slurries and molds for the manufacture of aircraft turbine components. *Crystals* **2020**, *10*, 433. [CrossRef]
13. Żaba, K.; Puchlerska, S.; Książek, M.; Sitek, R.; Wiśniewski, P.; Mizera, J. Investigations of model multilayer ceramic casting molds in a raw state by nondestructive methods. *Materials* **2021**, *14*, 7761. [CrossRef]
14. Lewandowski, J.L. *Tworzywa na Formy Odlewnicze*; Wydawnictwo Naukowe Akapit: Kraków, Poland, 1997.
15. Dong, Y.W.; Li, X.L.; Zhao, Q.; Yang, J.; Dao, M. Modeling of shrinkage during investment casting of thin-walled hollow turbine blades. *J. Mater. Process. Technol.* **2017**, *244*, 190–203. [CrossRef]
16. Książek, M.; Tchórz, A.; Krzak, I.; Żaba, K.; Kurdziel, P.; Dydak, A.; Sitek, R.; Mizera, J. An Investigation on Microstructural and Mechanical Properties of Ceramic Moulds Applied in the Investment Casting of Critical Parts of Aircraft Engines. In Proceedings of the 73rd World Foundry Congress, Kraków, Poland, 23–27 September 2018; pp. 107–108.
17. Nowicki, J. Badanie Właściwości Mas Lejnych Oraz Form Ceramicznych na Bazie SiC. Master's Thesis, Faculty of Materials Science and Engineering, Warsaw University of Technology, Warsaw, Poland, 2018.
18. Ma, H.J.; Liu, X.-D.; Lyu, K.; Zhang, H.; Meng, S.D. Rheological behavior of slurries containing short glass fibers for preparation of investment casting shell. *J. Mater. Eng.* **2016**, *44*, 93–97. [CrossRef]
19. Matysiak, H.; Ferenc, J.; Lipinski, Z.; Grabarz, K.; Michalski, J.; Kurzydłowski, K.J. Charakterystyka i kontrola właściwości technologicznych mieszanek ceramicznych do wytworzenia form odlewniczych do odlewania precyzyjnego części turbin lotniczych metodą Bridgmana. *Inż. Mater.* **2009**, *30*, 239–244.
20. Bansode, S.N.; Phalle, V.M.; Mantha, S.S. Influence of slurry composition on mould properties and shrinkage of investment casting. *Trans. Ind. Inst. Met.* **2020**, *73*, 763–773. [CrossRef]
21. Benzhi, Z. Application of coating slurry-sand in investment casting copper art parts. *Spec. Cast. Nonferrous Alloys* **2010**, *30*, 739–741.
22. Nadolski, M.; Konopka, Z.; Lagiewka, M.; Zyska, A. Examining of slurries and production of moulds by spraying method in lost wax technology. *Arch. Foundry Eng.* **2008**, *8*, 107–110.
23. Małek, M.; Wiśniewski, P.; Szymańska, J.; Mizera, J.; Kurzydłowski, K.J. Technological properties of ceramic slurries based on silicon carbide with poly (vinyl alcohol) addition for shell moulds fabrication in precision casting process. *Acta Phys. Pol. A* **2016**, *129*, 528–530. [CrossRef]
24. Huang, P.; Lu, G.; Yan, Q.; Mao, P. Effect of ceramic and nylon fiber content on composite silica sol slurry properties and bending strength of investment casting shell. *Materials* **2019**, *12*, 2788. [CrossRef]
25. Wiśniewski, P.; Sitek, R.; Towarek, A.; Choińska, E.; Moszczyńska, D.; Mizera, J. Molding binder influence on the porosity and gas permeability of ceramic casting molds. *Materials* **2020**, *13*, 2735. [CrossRef]

26. Żymankowska-Kumon, S.; Bobrowski, A.; Grabowska, B. Comparison of the emission of aromatic hydrocarbons from moulding sands with furfural resin with the low content of furfuryl alcohol and different activators. *Arch. Foundry Eng.* **2016**, *16*, 187–190. [CrossRef]
27. Sanjay, K.; Karunakar, D.B. Enhancing the permeability and properties of ceramic shell in investment casting process using ABS powder and needle coke. *Int. J. Metalcast.* **2019**, *13*, 588–596.
28. Hirata, Y.; Miyano, K.; Sameshima, S.; Kamino, Y. Reaction between SiC surface and aqueous solutions containing Al ions. *Phys. Eng. Asp.* **1998**, *133*, 183–189. [CrossRef]
29. Olhero, S.M.; Ferreira, J.M.F. Influence of particle size distribution on rheology and particle packing of silica-based suspensions. *Powd. Technol.* **2004**, *139*, 69–75. [CrossRef]
30. Kolczyk, J.; Zych, J. Rheological properties of ceramic slurries with colloidal binders used in the investment casting technology. *Metalurgija* **2013**, *52*, 55–58.
31. Singh, R.; Singh, J. Investigating the effect of shape factor, slurry layers and pouring temperature in precision investment casting. *Mater. Sci. Forum* **2013**, *751*, 35–44. [CrossRef]
32. Cheng, X.; Sun, X.D.; Yuan, C.; Green, N.R.; Withey, P.A. An investigation of a TiAlO based refractory slurry face coat system for the investment casting of Ti-Al alloys. *Intermetallics* **2012**, *29*, 61–69. [CrossRef]
33. Ertuan, Z.; Fantao, K.; Yanfei, C.; Ruirun, C.; Yuyong, C. Characterization of zirconia-based slurries with different binders for titanium investment casting. *China Foundry* **2012**, *9*, 125–130.
34. Koralnik, M.K. Badanie Porowatości i Gazo-Przepuszczalności Form Ceramicznych na Bazie Proszków Molochite Do Odlewania Precyzyjnego Stopów Niklu. Bachelor's Thesis, Faculty of Materials Science and Engineering, Warsaw University of Technology, Warsaw, Poland, 2014.
35. Amira, S.; Dube, D.; Treamblay, R. Method to determine hot permeability and strength of ceramic shell moulds. *J. Mater. Process. Technol.* **2011**, *211*, 1336–1340. [CrossRef]
36. Pattnaik, S.; Sutar, M.K. Effect of saw dust content on slurry rheology and mechanical properties of the investment casting ceramic shell. *Int. J. Metalcast.* **2020**, *15*, 470–487. [CrossRef]
37. Pattnaik, S.; Sutar, M.K. Investigation on the influence of polyethylene wax powder on the characteristics of ceramic shells used for investment casting. *Silicon* **2022**, *14*, 6089–6096. [CrossRef]
38. Koralnik, M.K. Research and Modifications Ceramic Molds to Receive Large-Size Aircraft Engine Parts. Master's Thesis, Faculty of Materials Science and Engineering, Warsaw University of Technology, Warsaw, Poland, 2015.
39. Kumar, S.; Karunakar, D.B. Characterization and properties of ceramic shells in investment casting process. *Int. J. Metalcast.* **2020**, *15*, 98–107. [CrossRef]
40. Lin, C.; Zhang, H.; Yu, J.; Zhang, X.; Yang, Z.; Ren, Z. High-strength and quick-drying ceramic shells prepared by silicone resin bonding. *Ceram. Int.* **2025**, *51*, 23937–23947. [CrossRef]
41. Małek, M. Opracowanie Ekologicznej Technologii Wytwarzania Form Ceramicznych Do Odlewania Precyzyjnego Łopatek Turbin Silników Lotniczych Z Nadstopów Niklu. Ph.D. Thesis, Faculty of Materials Science and Engineering, Warsaw University of Technology, Warsaw, Poland, 2016.
42. Frazzini, S.; Zuorro, A.; Panseri, S.; Pavlovic, R.; Rossi, C.A.S.; Rossi, L. Repurposing hazelnut waste products for a sustainable economy: A metabolomic analysis of cuticles and shells to highlight their antioxidant potential and inhibitory activity against verocytotoxic *Escherichia coli*. *Sustainability* **2023**, *15*, 3268. [CrossRef]
43. Jahanban-Esfahlan, A.; Jahanban-Esfahlan, R.; Tabibiazar, M.; Roufegarineja, L.; Amarowicz, R. Recent advances in the use of walnut (*Juglans regia* L.) shell as a valuable plant-based bio-sorbent for the removal of hazardous materials. *RSC Adv.* **2020**, *10*, 7026–7047. [CrossRef]
44. Manterola-Barroso, C.; Sanchez, K.G.; Scheuermann, E.; Padilla-Contreras, D.; Morina, F.; Meriño-Gergichevich, C. Antioxidant and physico-structural insights of walnut (*Juglans regia*) and hazelnut (*Corylus avellana* L.) shells: Implications for southern Chile by-product valorization. *Resources* **2025**, *14*, 82. [CrossRef]
45. Srinag, T.; Srinivas, C.L.; Sandeep, C.H.; Prasanthi, P.P.; Madhav, V.V.V.; Kumar, A.; Chandrashekar, R.; Bandhu, D.; Singh, S.K.; Lakshmi, A.A. Mechanical characterization of walnut shell powder-reinforced neem shell liquid composite. *J. Mech. Behav. Mater.* **2025**, *34*, 20250078. [CrossRef]
46. Angdembe, A.; Sapkota, S.C.; Rasekh, H.; Mohammed, A.S.; Asteris, P.G. Dynamic performance and sustainability of hemp fiber-reinforced polymer epoxy resin matrix composites with walnut shell filler. *Polymer* **2025**, *334*, 128720. [CrossRef]

Disclaimer/Publisher's Note: The statements, opinions and data contained in all publications are solely those of the individual author(s) and contributor(s) and not of MDPI and/or the editor(s). MDPI and/or the editor(s) disclaim responsibility for any injury to people or property resulting from any ideas, methods, instructions or products referred to in the content.

materials

MDPI

Article

Ecofriendly Water-Soluble Binders for Precision Ceramic Moulds in Aerospace Turbine Casting: Process Development and Performance Evaluation

Marcin Małek [1,*], Marcin Wachowski [2] and Janusz Kluczyński [2]

[1] Faculty of Civil Engineering and Geodesy, Military University of Technology, 2 Gen. S. Kaliskiego St., 00-908 Warsaw, Poland
[2] Institute of Robots & Machine Design, Faculty of Mechanical Engineering, Military University of Technology, 2 Gen. S. Kaliskiego St., 00-908 Warsaw, Poland; marcin.wachowski@wat.edu.pl (M.W.); janusz.kluczynski@wat.edu.pl (J.K.)
* Correspondence: marcin.malek@wat.edu.pl

Abstract: The paper presents the development of an ecofriendly ceramic moulding system for the precision casting of aircraft turbine components from nickel superalloys using water-soluble binders. The motivation was to eliminate hydrolysed ethyl silicate (HES) due to its environmental and occupational hazards. Two water-based binders (K + M)—Keysol (for the primary layer) and Matrixsol (for the backup layers)—were evaluated against the standard HES-based system. A comprehensive comparative analysis was conducted including microstructure, phase composition, wettability, mechanical, thermal, and gas permeability properties. The developed K + M ceramic moulds achieved a bending strength of 12.4 MPa after annealing, average surface roughness (Ra) below 5 μm, and open porosity of 29.1%, indicating excellent strength and permeability. Thermal conductivity increased from 0.3 W/mK to 2.0 W/mK between 22 °C and 1400 °C. The wetting angle of water-based binders was higher (Keysol: ~36°) compared to HES (~5°), resulting in more stable surface morphology. Gas permeability was maintained at 5.6×10^{-9} cm^2 at 1100 °C, ensuring effective degassing during casting. The results demonstrate that the K + M system can replace HES in production while improving safety and reducing environmental impact, making it suitable for industrial-scale implementation in the aerospace sector.

Keywords: ceramic-casting moulds; aircraft turbine; binders; nickel superalloys

1. Introduction

The requirements regarding the functional properties of a ceramic mould depend on many factors. The basic ones are the type of alloy and the type of process and pouring method for which the mould is intended. An important factor is the strength of the mould in the raw state and after annealing. Additionally, the ceramic mould should be characterised by a high resistance to thermal shocks and good chemical stability—no reaction with the liquid alloy. The mould material should also have adequate gas permeability and thermal conductivity [1–4]. These properties determine the displacement of air through the mould walls by the flowing liquid metal. Air should quickly penetrate the network of open pores outside the mould, thus preventing the formation of internal defects and microporosity in the castings. Additionally, the mould material should have a low linear thermal expansion coefficient in the temperature range of 600–1500 °C [5–9]. Depending on the requirements and application, the ceramic-casting mould is made up of several or a dozen ceramic layers that differ in physical and thermal properties. The first layer is the basic one—prime coat.

It is in direct contact with the liquid alloy; therefore, the material of this layer should be characterised primarily by chemical inertness towards the liquid alloy and its alloy additives. In addition, it ensures surface reproduction; therefore, when applied, the sand that forms this layer must have the appropriate viscosity [10–13]. Subsequent construction layers (backup) ensure specific mechanical properties of the form. They cannot be damaged during the pouring process and should be flexible at the same time. Then, during the casting crystallisation process, no large stresses are generated, which often lead to the formation of casting defects [3,11–15].

The materials used to build the ceramic form are classified into several groups, including binders, ceramic powders, loose powders, and auxiliary materials and antifoaming and wetting agents. The binder is the basic and most important component of the moulding sand. It acts as a connector connecting the remaining components of the sand. Therefore, it is characterised by specific physical and chemical properties that ensure good heat resistance, chemical stability of the mould, and high smoothness of its internal surface [12]. The drying process involves shrinkage of the mould material and chemical reactions of the binder and components of the moulding sand. Often, this results in the formation of defects in ceramic moulds when poured with liquid metal. Therefore, the binder should ensure good strength properties between individual layers. The binder used in the production of ceramic-casting moulds is characterised primarily by the following: good rheological properties, good resistance to sedimentation, good stability of the chemical composition, high chemical inertness towards the liquid alloy, and good miscibility with the remaining components of the ceramic mass [15]. Ceramic powders form the matrix of the ceramic mixture. Their appropriate selection significantly influences the physical and chemical properties of the form. The required properties of powders are mainly resistance to high temperature, low thermal expansion, and lack of polymorphic transformations [16,17]. The most commonly used ceramic powders for casting mould production are aluminium, zirconium, and yttrium oxides. Currently, scientists are conducting research on the use of new compounds based on silicon carbide, which, thanks to its high thermal conductivity, would reduce the production time of the finished casting by removing heat from the inside of the mould faster. This would also allow for increasing the mechanical properties of the manufactured aircraft turbine components by fragmenting the microstructure and reducing the number of mould cracks due to the very high resistance of silicon carbide to thermal shocks. These works have been the subject of numerous patent applications and publications [12–16]. Auxiliary materials include antifoaming agents, wetting agents, bactericidal and fungicidal agents, and pH stabilisers. They are used to ensure good coverage of the wax model by the ceramic moulding mass, to increase its shelf life, and to reduce the tendency for air bubbles to form during mixing. A large number of bubbles increases the porosity of the mould. Hence, its mechanical properties decrease, also during the rapid removal of heat from the liquid metal—excessive shrinkage of the casting [17–20].

After mixing, the materials presented form the moulding sand used in the production of moulds. The physical and chemical properties of the moulding sand must ensure good coverage of the wax model and provide the mould with appropriate functional properties. To produce ceramic moulds intended for precision casing of aircraft engine turbine components, the domestic industry uses binders mostly based on alcohol compounds, including hydrolysed ethyl silicate (HES). It has a density close to 0.887 g/cm^3 of water. Among competitive ecological materials, binders using colloidal silica (CS), a hydrosol of silicic acid in the form of an aqueous suspension, have the highest consumption in precision casting. The agent that binds the binder to the ceramic powder particles is silica gel, which is formed by evaporating water from the sol. Colloidal silica, compared to binders based on alcohol compounds, is neutral to the natural environment and harmless

to workers [21–27]. Hydrolysed ethyl silicate (HES), despite its widespread use in ceramic mould manufacturing, presents significant occupational and environmental hazards. As an alcohol-based compound, HES releases volatile organic compounds (VOCs) during application and curing, contributing to air pollution and posing direct health risks to foundry workers, including skin and respiratory tract irritation, headaches, and long-term organ toxicity. Furthermore, the flammability of alcohol-based systems increases the risk of workplace accidents. In recent years, increasingly stringent environmental regulations, such as the European Union's REACH framework and the growing adoption of ISO 14001-compliant environmental management systems in industry, have driven the search for sustainable alternatives. The shift toward water-soluble binder systems responds not only to regulatory compliance but also to broader trends in green manufacturing and corporate responsibility. Water-based binders such as colloidal silica eliminate the need for organic solvents, significantly reduce toxic emissions, and offer improved worker safety without compromising material performance. These considerations underline the urgency and industrial relevance of developing an effective ecological substitute for HES in the precision casting of superalloy components.

The aim of this work was to develop an ecological process for producing ceramic-casting moulds for the precise casting of low-pressure aircraft engine blades from nickel superalloys using water-soluble binders. The paper also presents the results of research on the development of an ecological binder and replacement of the binder based on hydrolysed ethyl silicate (HES). During the research work on replacing the HES binder, because of the lack of data on the properties of the hydrolysed ethyl silicate-based system, an attempt was made to independently determine all the physical and chemical properties of the binder, powders, additives, and moulds in the conditions of a precision foundry. The definition of the correct physical, chemical, and mechanical properties of the developed moulding system was based on the full characteristics of the moulding system currently used in production conditions, manufactured using hydrolysed ethyl silicate (HES). The key innovation of this work lies in the complete technological replacement of the alcohol-based hydrolysed ethyl silicate (HES) binder system with a water-soluble, ecofriendly binder system (Keysol and Matrixsol) in the production of multilayer ceramic moulds for the precision casting of nickel-based superalloy turbine components. Unlike previous studies that investigated water-based systems at the level of individual layers or in simplified laboratory trials, our approach involved the following:

1. Comprehensive characterisation of the new binder system, including particle size distribution of silica nanoparticles, zeta potential, viscosity behavior, solid-phase content, and thermal stability using advanced techniques (e.g., SEM, TGA, FTIR, DSC, dilatometry, and porosimetry);
2. Multistage experimental validation of mould properties—mechanical (bending strength, Young's modulus, and Weibull modulus), surface (roughness and wetting angle), microstructural (XRD and SEM), thermal (conductivity, specific heat, and expansion), and functional (porosity and gas permeability)—at each stage of the casting process (raw, fired, and annealed);
3. Head-to-head benchmarking of the new system against a conventional industrial standard (HES-based), demonstrating superior or comparable performance, with statistical validation of key improvements (e.g., post-annealing bending strength increased by 9.5%, surface roughness reduced by ~18%, and VOC emissions nearly eliminated);
4. First reported implementation of the Keysol/Matrixsol system in a full seven-layer mould architecture for aerospace-grade turbine blades, including pilot-scale trials under production-mimicking conditions;

5. Environmental and safety impact analysis, emphasizing the real-world applicability of the findings, which is rarely addressed in academic studies focused on binder formulation alone.

2. Materials and Research Methodology

Research Materials

To create an innovative ceramic mould, it was necessary to test and select the optimal properties of the ceramic powders, binders, and moulding sand resulting from mixing the base materials. Then, after the appropriate tarting components were selected, the ceramic moulds were obtained and examined by comparing their properties with those of previously used ceramic moulds. Chemical composition of ceramic mixtures for individual layers of the casting mould are presented in Table 1. When optimising base materials, several materials were taken into account, such as the following:

- ceramic powders: aluminium oxide 200# and 325#, Molochit 120;
- binders: Keysol, intended for the first layer of the ceramic mould, and Matrixsol.

Table 1. Chemical composition of ceramic mixtures for individual layers of the casting mould–HES reference system.

Mould Layer	Raw Material Composition		
	Binder	**Warp**	**Dust**
1–2	Water-based colloidal silica	Zirconium silicate + cobalt aluminate	Electrocorundum
3–7	Alcohol-hydrolysed ethyl silicate	Aluminosilicates	Aluminosilicates

Appropriately selected ceramic powder and binder were used to produce the sand, which was intended for the first layer and the structural layers of the ceramic mould. The final stage was the creation of optimised ceramic forms and comparison of them with the currently used solutions. Therefore, to select appropriate powders, binders, and moulding sands to produce innovative ceramic forms, a number of studies were carried out.

A Hitachi S-3500L scanning electron microscope (Ibaraki Prefecture, Japan) was used to observe the microstructure of powders, binders, mould sand, and ceramic mould. A beam of backscattered electrons (BSE) and an accelerating voltage of 5–20 kV were used. The powder particles were placed for observation on a carbon tape. The surface morphology of the binders after drying and applying to the carbon tape was examined using a high-resolution Joel-Jem 3010 scanning electron microscope (Akishima, Tokyo, Japan) and a Hitachi S5500 scanning electron microscope (Ibaraki Prefecture, Japan). The accelerating voltage used for the JEOL JEM 3010 microscope was 300 kV and for the Hitachi S5500 was 30 kV. The SEM images obtained constituted the basis for quantitative analysis of the microstructure using the Micrometer programme v1.0 (Warsaw University of Technology, Poland).

Powder particle size measurements were performed using a Horiba LA 950 laser particle size analyser (Tokyo, Japan), using the low-angle laser light scattering (LALLS) method.

Measurements of the chemical and phase composition of powders, binders, sand moulding, and ceramic mould were made using a WDXRF Bruker S4 Explorer X-ray fluorescence spectrometer (Billerica, MA, USA) and a Bruker D8 Advance powder diffractometer (Billerica, MA, USA).

Zeta potential measurements were performed for ceramic powders to assess the electrokinetic stability as a function of pH. The tests were performed using the Zetasizer Nano ZS analyser (Malvern, UK).

Solid-phase content tests were carried out for binders to properly determine the specific solid-phase content, and thus the appropriate formula of pouring moulding sand. The solid-phase particle content was determined by determining the dry weight of the sample. The mass of the binder before and after centrifugation was determined. The remaining mass corresponded to the solid-phase content.

For the binders, the wetting angle was tested on PE foil using the Wetting angle System OCA goniometer. The wetting angle value was given as the average of 10 measurements. The wetting angle test was also carried out for ceramic moulds using the lying drop method and joint heating of the alloy and mould to the experimental temperature. Then, the alloy and mould were heated at this temperature and cooled. The alloy and the mould are in constant contact during the test. During the test, images of a drop of superalloy (IN713C) placed on a flat ceramic mould substrate were recorded. These images were the basis for determining the value of the wetting angle Θ, also for the geometric measurements of the drops. The experiment was carried out in an argon atmosphere with a constant pressure of $1.3 \cdot 10^{-2}$ Pa. Immediately before being placed in the testing chamber, the samples were cleaned with isopropyl alcohol.

The chemical composition of the binders was analysed using the Fourier transform infrared (FTIR) method. The compounds were analysed in the wave number range of 4000–400 cm^{-1} and the resolution in the range of 0.5–32 cm^{-1}.

Thermal analysis of binders using the thermogravimetry technique was performed using a TA Instruments DCSQ1000 calorimeter (New Castle, DE, USA). The tests were carried out under a nitrogen atmosphere using aluminium crucibles. Samples weighing 10 mg were heated and cooled at a constant rate of 20 °C/min in the temperature range of 20–1000 °C.

To test the relative viscosity, that is, the mass flow time, a Elcometer Zahn 4 draw cup (Edge Lane, UK) with a nizzle diameter of φ = 4.3 mm was used. The flow time was examined using a digital stopwatch from the moment of fully filling the cup through its immersion in the pouring mass and determining the free flow of the slurry until the flow was interrupted.

Dynamic viscosity measurements were carried out on the Anton Paar MC 102 rheometer (Graz, Austria) using the coaxial cylinder method in the shear rate ranges of 1.3–200 and 200–1.3 1/s.

The mechanical properties of the moulds were determined in a three-point bending test of prepared 'beam' samples made of ceramic mould material. The tests were carried out according to the ASTM D790 standard. The adopted support spacing was 25 mm. Using an electromechanical extensometer for a measurement length of 25 mm, the beam deflection arrow was determined. Weibull's statistical theory was used to determine the bending strength.

The surface roughness of the mould was determined using an optical profilometer NT9300 (Plainview, NY, USA) with a magnification of 11.5, 28.4, and 101.5× on "beam" samples cut from a ceramic mould. The values of the Ra surface parameter were determined.

The thermal properties of the ceramic moulds were tested using a DIL 402/4/1G Netzsch dilatometer (Selb, Germany). The following were determined: the temperature of phase transformations in the solid state, changes in the length of the samples as a function of temperature and the density of their materials, and the values of the linear thermal expansion coefficients as a function of temperature. Specific heat was determined using a DSC 404 C Pegasus differential scanning calorimeter from Netzsch (Selb, Germany)

according to the ASTME 1269 standard [28]. The thermal conductivity coefficient was determined using the Netzsch LFA 427/4/G flash laser device (Selb, Germany).

The porosity of the tested ceramic forms was determined using mercury porosimetry (Auto Pore II 9220 porosimeter, Micrometrics, Selb, Germany). The sample was placed in a penetrometer with a constant of 21.63 μL/pF, a mass of 67.9740 g, and a capillary volume of 6.6766 mL. The penetrating liquid was mercury with a density of 13.5389 g/cm^3 and a surface tension of 0.485 J/m^2. The capillary wetting angle with liquid mercury was $\Theta = 130^\circ$. The samples were weighed before measurement and placed on the penetrometer. Redetermining the mass of the penetrometer after filling with mercury allowed determining the apparent density of the tested samples of ceramic materials.

Ceramic mould gassing was determined by continuously measuring the volume of the residual gases using a gas spectrometer while heating them in a vacuum (1500 °C). Throughout the test cycle, measurements of the pressure in the test chamber and the composition of the residual gases were made. Temperature values were measured on the research table, next to the table, above the table, and on the radiator.

The gas permeability of the forms was determined on the basis of the constructed measurement station and the Darcy relationship described by Equation (1) [1,2]. To determine the gas permeability, air was passed through a spherical sample of the ceramic mould, and the pressure and air flow values flowing through the sample were recorded.

$$K = \frac{MQ'D}{PA} \tag{1}$$

where the following variables are used:

K—permeability [cm^2];

M—dynamic viscosity of air at a given temperature [(kg/m*s)*10^{-5}];

D—thickness of the mould wall (mould diameter—ping-pong ball diameter) [mm];

A—mould surface area [mm^2];

P—air pressure [mmH_2O];

Q'—air flow value at measurement temperature [cm^3/min].

The dynamic viscosity of air (M) in a certain temperature range of 30–1300 °C is directly proportional to the temperature. For a certain temperature range, this function takes the form of a linear relationship. This allows a direct reading of the M value for a specific temperature of the measurement. The air flow value (Q') depends on the ambient temperature. The measurement is carried out in centres with different temperatures (laboratory furnace), so the working medium, which is air, also has different temperatures. Taking this fact into account, a correction should be made for the air flow value at the measurement temperature described by Equation (2) [1,2].

$$Q' = \frac{QT'}{T} \tag{2}$$

where the following variables are used:

Q'—air flow value at measurement temperature [cm^3/min];

Q—air flow value at room temperature [cm^3/min];

T′—value of measurement temperature [K];

T—room temperature value [K].

The research material were spherical ceramic forms produced by immersion. All samples consisted of 7 layers, with the last layer playing only a sealing role. It was produced by immersing the sample in a ceramic mass, without sprinkling it. The samples were allowed to dry freely at room temperature. After drying, the samples were fired at a

temperature of 760 °C. The furnace was heated and cooled together with the samples to avoid cracking of the material.

Thermal and weight methods were used to determine the kinetics of the drying process of the mould layer. In the case of the thermal method, three thermocouples embedded in the wax model were used. Then, the blade model was the basis for producing a ceramic mould according to the developed moulding system. After each layer was applied, the thermocouples were connected to the Hioki 8875 recorder (Nagano, Japan). Temperature values were measured over a period of 10 s. The values obtained for the mould temperature close to the ambient temperature were interpreted as the time for the water to evaporate from the layer and the end of the drying process. Ceramic moulds were produced using the weight method on a wax model according to the developed moulding system. After applying each layer, the change in model mass over time was determined in a period of 10 s. Reaching a plateau during measurement was interpreted as the evaporation of water and the drying of the mould layer. This method also makes it possible to determine the mass of evaporated water in the individual layers of the ceramic mould. Figure 1 shows the experimental workflow and the multilayer structure of the ceramic mould, indicating the composition and function of each layer.

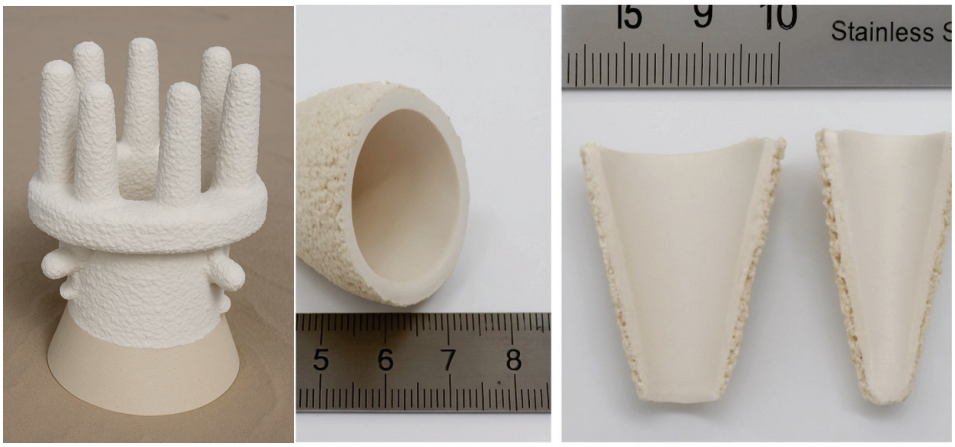


Figure 1. Structure of the ceramic mould.

Keysol and Matrixsol (K + M) are water-soluble, two-component binder systems designed for application in ceramic mould production. Keysol consists of an acrylic-vinyl copolymer concentrate, comprising approximately 20–40 wt% of the formulation, and an aqueous dispersion of amorphous silica nanoparticles with an average particle diameter ranging from 12 to 18 nm. The polymer phase facilitates the formation of an initial organic matrix, enhancing the mechanical cohesion of the uncured ceramic layer. Matrixsol, applied to the backup structural layers, incorporates 2,2′,2″-(hexahydro-1,3,5-triazin-1,3,5-triyl)triethanol as a crosslinking and stabilizing component (70–100 wt% active substance) combined with a colloidal silica phase, where the SiO_2 content is approximately 33.7 wt%.

Although both binders were obtained from commercial sources (Ransom & Randolph, Maumee, OH, USA), their physical and chemical properties were fully characterised within the study to ensure compatibility with ceramic powders and to optimize process parameters. The morphology and dispersion of the silica nanoparticles were confirmed using scanning electron microscopy (SEM) and laser diffraction particle sizing (DLS), while zeta potential measurements confirmed high electrokinetic stability over a broad pH range, preventing unwanted agglomeration. Thermal stability was assessed via thermogravimetric analysis (TGA), and functional groups present in the binders were identified using Fourier-transform infrared spectroscopy (FTIR).

At the microscale, the interaction between the binder and ceramic particles such as aluminium oxide (Al_2O_3) and Molochite is governed by both physical adsorption and chemical bonding. Initially, the silica nanoparticles adsorb onto the surface of the ceramic grains through hydrogen bonding and van der Waals interactions. Upon drying, water evaporation induces a sol-gel transition in which silanol groups (Si–OH) condense to form Si–O–Si bridges, resulting in a rigid three-dimensional network that acts as an inorganic binder. The organic polymer in Keysol ensures uniform wetting and suspension stability before gelation, while the alkaline nature of Matrixsol (pH ~10.3) promotes enhanced surface interaction with aluminosilicates and better penetration into porous ceramic matrices. This dual mechanism—organic polymer film formation and inorganic silica gel bonding—provides excellent interlayer adhesion, dimensional stability, and mechanical strength of the final ceramic mould. The integration of polymer–nanoparticle synergy ensures reproducibility, ease of processing, and compatibility with multilayer mould designs required in aerospace precision casting.

3. Research Results and Discussion

3.1. Moulding Powders

The analysed powders have the typical morphology of particles used in the production of ceramic moulds. They are characterised by an irregular shape, sharp edges, and a developed surface (Figure 2A–C). The distributions obtained for the average particle diameter of the powders used for the first layer are presented in Figure 3 and Table 2. The analysis was performed in an aqueous environment. It has been established that powders are characterised by the following characteristics:

- Al_2O_3 (200#)—The powder has a wide range of particle sizes from 3.4 to 200 μm. The average particle diameter is 57.2 μm; the distribution obtained is symmetrical and has a maximum, d = 58.95 μm.
- Al_2O_3 (325#)—The powder has a wide range of particle sizes from 5.8 to 229 μm. The average particle diameter is 27.6 μm; the obtained distribution is asymmetric and has two maximums, d = 11 μm and d = 34 μm, which can indicate the presence of agglomerates.
- Molochite 120—The powder has a wide range of particle sizes from 2.60 μm to 262.68 μm. The average diameter of the powder particles is 51.22 μm; the distribution obtained is asymmetric and has three maximums, including d = 10.10 μ, d = 39.23 μm, and d = 88.58 μm, which may indicate the presence of agglomerates.

Table 2. Summary of the average particle diameter of the tested powders.

Powder	Solvent	Average Particle Diameter [μm]
Al_2O_3 200#	WATER	57.2
Al_2O_3 325#	WATER	27.6
Molochite 120	WATER	51.2

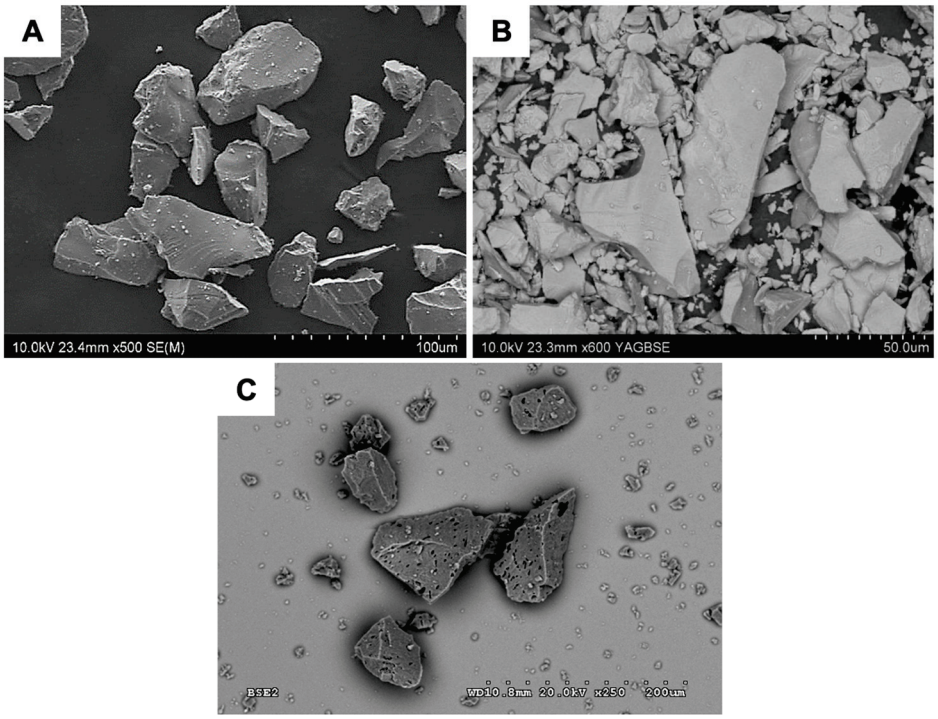


Figure 2. SEM images of powder particles: (**A**) Al_2O_3 200#, (**B**) Al_2O_3 325#, and (**C**) Molochite 120.

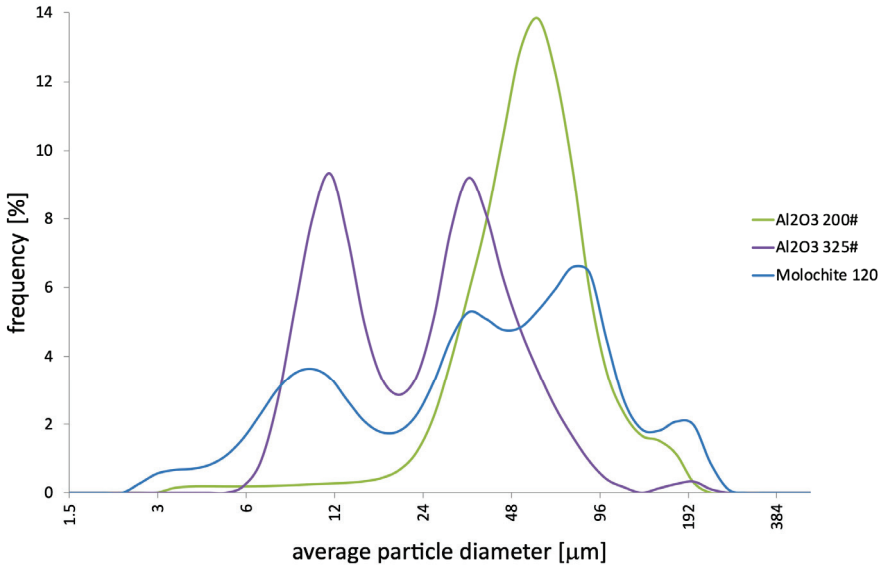


Figure 3. Distribution of the average particle diameter of powders used for the first layers: Al_2O_3 200#, Al_2O_3 325#, and Molochite 120.

The results of phase composition tests are presented in Figure 4 in the form of diffractograms. It should be emphasised that the tested Al_2O_3 200# (Figure 4A) and 325 # powders (Figure 4B) powders are primarily characterised by a high content of α oxides. Analysis of the phase composition of the tested powders (Figure 4A–C) showed that they are single-phase materials. Analysis of the phase composition of the Molochite 120 powder (Figure 4C) showed that it is a single-phase material, composed only of $Al_6Si_2O_{13}$ aluminosilicate-mullite. Furthermore, the diffractogram of Molochite 120 powder (Imerys, Cornwall, UK) shows an effect caused by the presence of the amorphous phase.

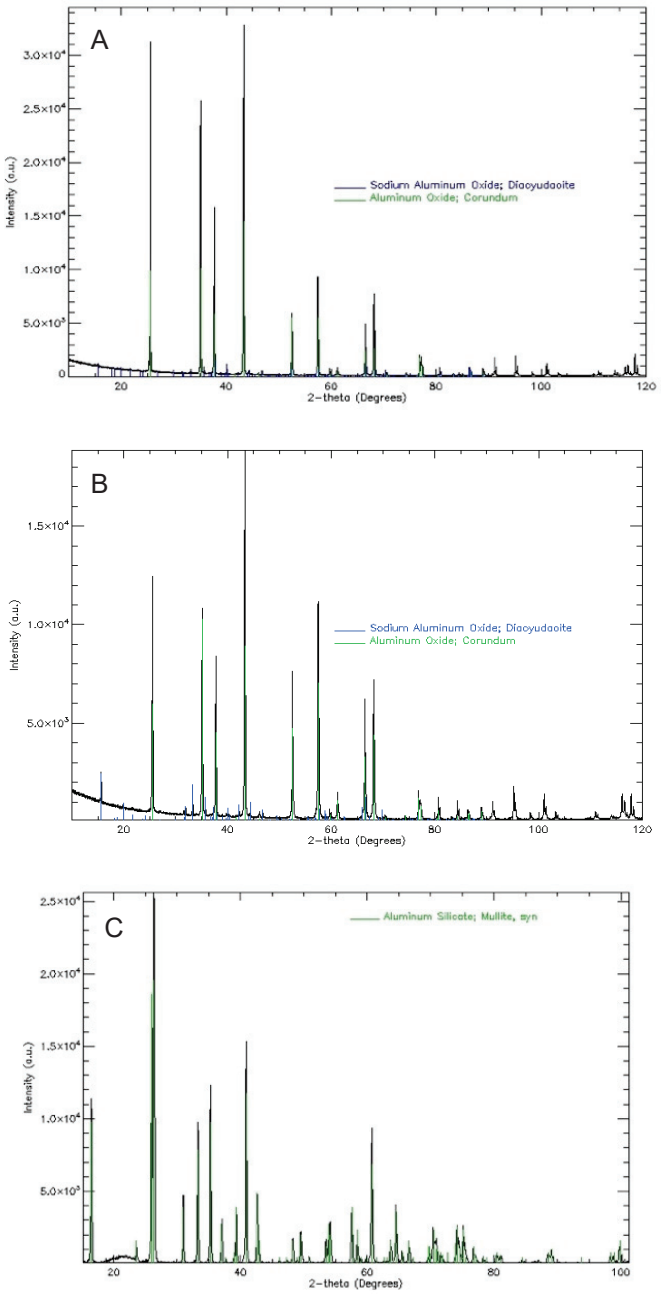


Figure 4. XRD diffractograms: (**A**) Al_2O_3 200#; (**B**) Al_2O_3 325#; and (**C**) Molochite 120.

The selected powders are consistent in terms of chemical composition and particle size with the technological regime of industrial precision foundries.

3.2. Moulding Binders

Research was carried out on the selection of the optimal binder for the production of a ceramic mould for four types of binders used to produce sets of ceramic moulds. The first set, currently used, consists of a binder for the first layers, Ludox SK (contains colloidal silica), and a binder for the construction layers, hydrolysed ethyl silicate (HES). The set developed for new water-soluble binders, eliminating the HES binder from mass production, consists of a binder for the first layer, Keysol from Ransom and Randolph (Maumee, OH, USA), and a binder for construction layers, Matrixsol from Ransom and Randolph (Maumee, OH, USA).

Keysol is a two-component water-soluble binder, a concentrate based on an acrylic-vinyl copolymer with a weight content of 20–40% and the main aqueous solution containing

SiO_2 nanoparticles. Matrixsol is a two-component water-soluble binder, a concentrate of 2,2′,2″-(hexahydro-1,3,5-triazin-1,3,5-triyl)triethanol with a content of 70–100% by weight and a main aqueous solution containing SiO_2 nanoparticles.

The research was based on the analysis of the properties of these binders, analysis of the impact on the environment (two water-based binders (K + M) including Keysol for the primary layer and Matrixsol for the backup layers), and determining whether they can replace existing standard binders based on ethyl alcohol. The main criterion for selecting these types of binders was to investigate which of these binders would be able to replace HES. The use of water-based binders is an interesting issue because they are more ecological materials and definitely more healthy for people working in the foundry. The use of binders and alcohol systems is harmful to the human body, causing dryness of the skin and conjunctiva. Replacement of HES with water-based binders will improve work safety, be more environmentally beneficial, and also create an opportunity to obtain moulding systems with better physical and mechanical properties compared to alcohol-based systems.

To characterise the nanoparticles present in the tested binders, SEM tests were performed, the results of which are presented in Figure 5. No nanoparticles were observed in the HES binder (Figure 5A). Analysis of the remaining binders showed the presence of SiO_2 oxide particles in the dried samples. They were characterised by a shape close to spherical (Figure 5B–D). This is an important property of colloidal silica-based binders. When the ceramic moulds are dried, the binder undergoes the sol → gel transformation by the evaporation of water. As a result of the reaction between hydroxyl groups on the silica surface, SiO_2 oxide combines into three-dimensional structures (agglomerates) through –Si–O–Si– bonds. The reaction that takes place is irreversible. Thanks to this process, the ceramic mould has good strength properties.

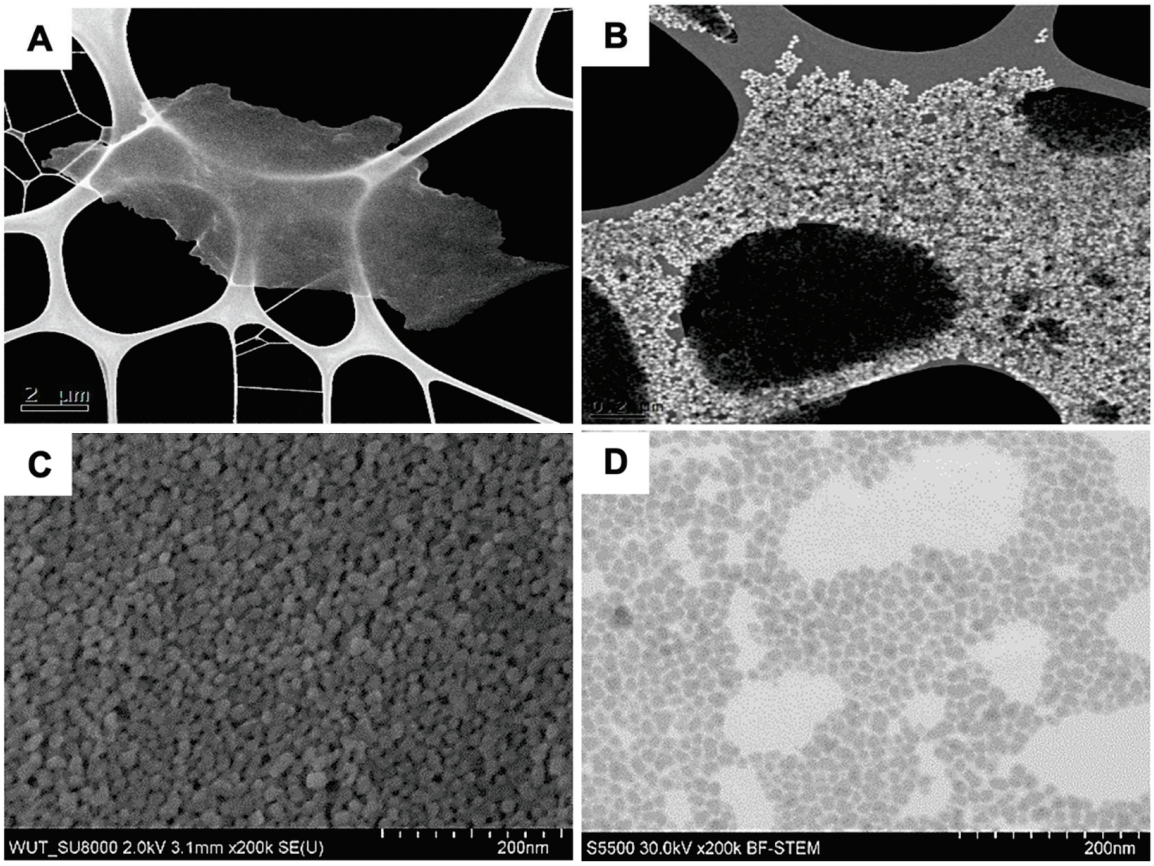


Figure 5. SEM images of binder particles: (**A**) HES; (**B**) Ludox SK; (**C**) Matrixsol; and (**D**) Keysol.

Measurements of the average particle diameter of the tested moulding binders were performed (Figure 6). Because of the inability to determine the presence of nanoparticles in the HES binder, no measurement was performed for it. It was found that the nanopowders are characterised by a unimodal distribution of average diameter. The small difference between the minimum and maximum diameters indicates the high uniformity of the SiO_2 nanoparticles. Based on the analysis of microscopic examinations, it was shown that the SiO_2 nanopowder particles included in polymer binders have a spherical shape. The average diameter of all nano-SiO_2 particles does not exceed 18 nm. It should be noted that the study was conducted in an aqueous environment in which the agglomerates were dissolved. This makes it possible to determine the average diameter of the nanoparticles.

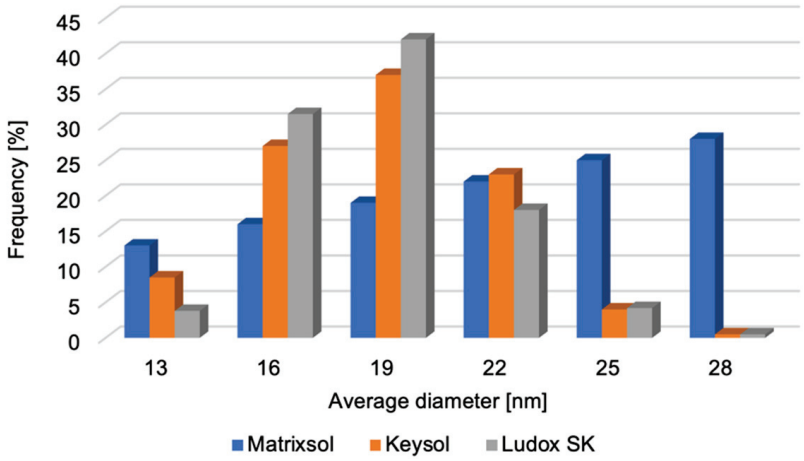


Figure 6. Distribution of the average particle diameter of the tested binders: Matrixsol, Keysol, and Ludox SK.

The solid-phase content in the tested moulding binders was also determined (Figure 7A). The HES binder has the lowest solid-phase content. Water-soluble binders are characterised by a high solid-phase content in the form of colloidal silica >28% weight. It is almost twice as large compared to HES. However, Keysol binders have the highest nano-SiO_2 content, approximately 34.1% of weight, and Matrixsol, 33.7% of weight.

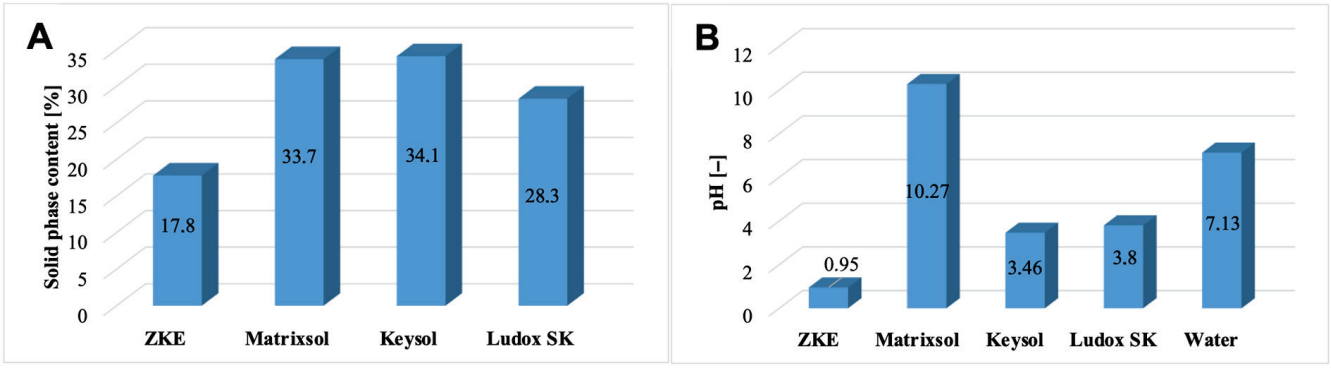


Figure 7. (**A**) Solid-phase content; (**B**) pH of the tested binders.

It was also established that the Matrixsol, Keysol, and Ludox SK binders differ significantly in terms of pH (Figure 7B). The reference HES binder is characterised by a strong acidic reaction, pH = 0.95. The keysol binder (pH = 3.46) and the Ludox SK (pH = 3.80) are less acidic. However, the Matrixsol binder has an alkaline reaction with a pH = 10.27. Analysis of the potential values of the tested binder species showed that the reference HES binder has an isoelectric point at pH = 4.4 (Figure 8). For pH > 4.4, the potential is negative

and has a minimum value of −9.2 mV. Keysol, Matrixsol, and Ludox SK binders have a negative potential in the entire pH range ranging from −13.5 mV for pH = 1.7 to −41.9 mV for pH = 10.1; −4.25 mV for pH = 1.6 to 44.2 mV for pH = 12.5; and −14.3 mV for pH = 1.9 to −34.9 mV for pH = 10.3. These binders for pH > 4 show a high electrokinetic stability of the dispersion. Binder particles have a high force that causes them to repel each other; there is no tendency to form agglomerates [18].

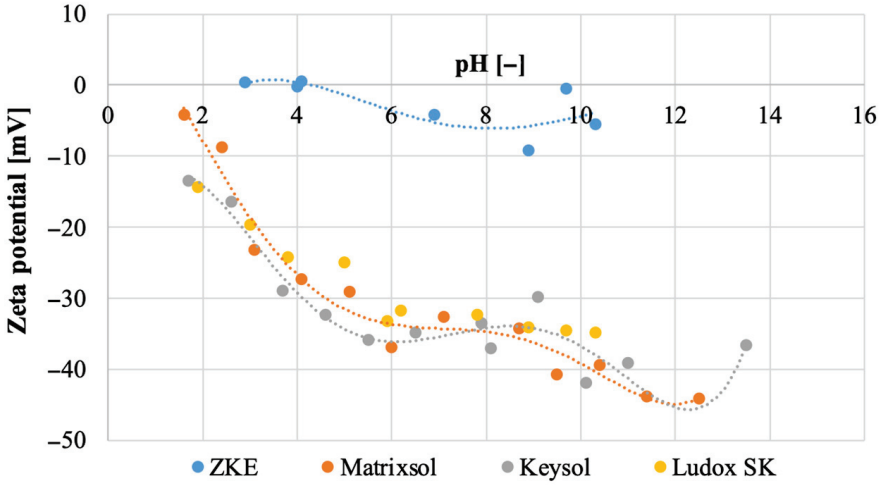


Figure 8. Zeta potential of the tested binders: Matrixsol, Keysol, and Ludox SK.

At the same time, the results of dynamic viscosity tests (Figure 9) showed that the binders, Matrixsol and Ludox SK, belong to the rheologically unstable group. They are characterised by a low viscosity, and this is one of the reasons for their irregular characteristics. The second may be the inhomogeneity of the tested samples. The suspension could have sedimented during the preparation of the test. It can be stated that Matrixsol and Ludox SK binders belong to Newtonian fluids; their viscosity does not depend on shear. The highest viscosity is observed for the Keysol binder, which belongs to the group of pseudoplastic liquids; it thins out as the shear rate increases. It was also determined that increasing the spindle speed leads to a reduction in the viscosity of the Keysol binder from 57 to 20 mPas, that is, almost three times.

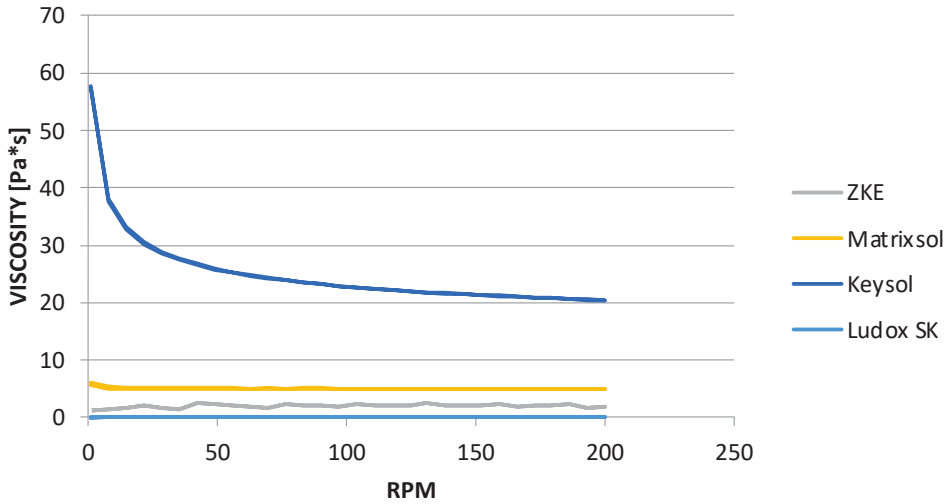


Figure 9. Dynamic viscosity of the tested binders: Matrixsol, Keysol, and Ludox SK.

Analysis of the results of the wetting angle test (Figure 10) showed that the binders have different wetting angle values. For HES, the wetting angle is 5 degrees. It can be

assumed that this binder is a liquid that wets the surface well. Matrixsol, Keysol, and Ludox SK binders are characterised by hydrophobic properties.

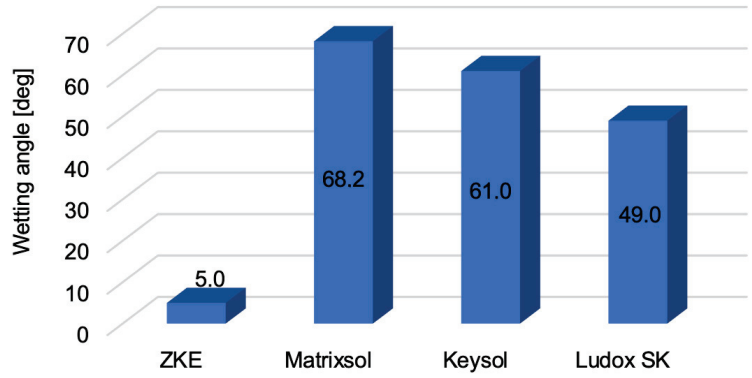


Figure 10. Wetting angle of the tested binders: HES, Matrixsol, Keysol, and Ludox SK.

Thermogravimetric analyses of the Matrixsol, Keysol, and Ludox SK (Figure 11A–C) binders were performed. TGA curves show a rapid mass loss for all binder grades up to a temperature of approximately 190 °C. This causes the water to evaporate quickly. Subsequent peaks are characteristic of the decomposition of polymer compounds, components of the tested binders. According to the literature [11–13], these values correspond to these substances with a slight change in temperature, probably caused by the presence of impurities or additives that help increase the stability of the binders.

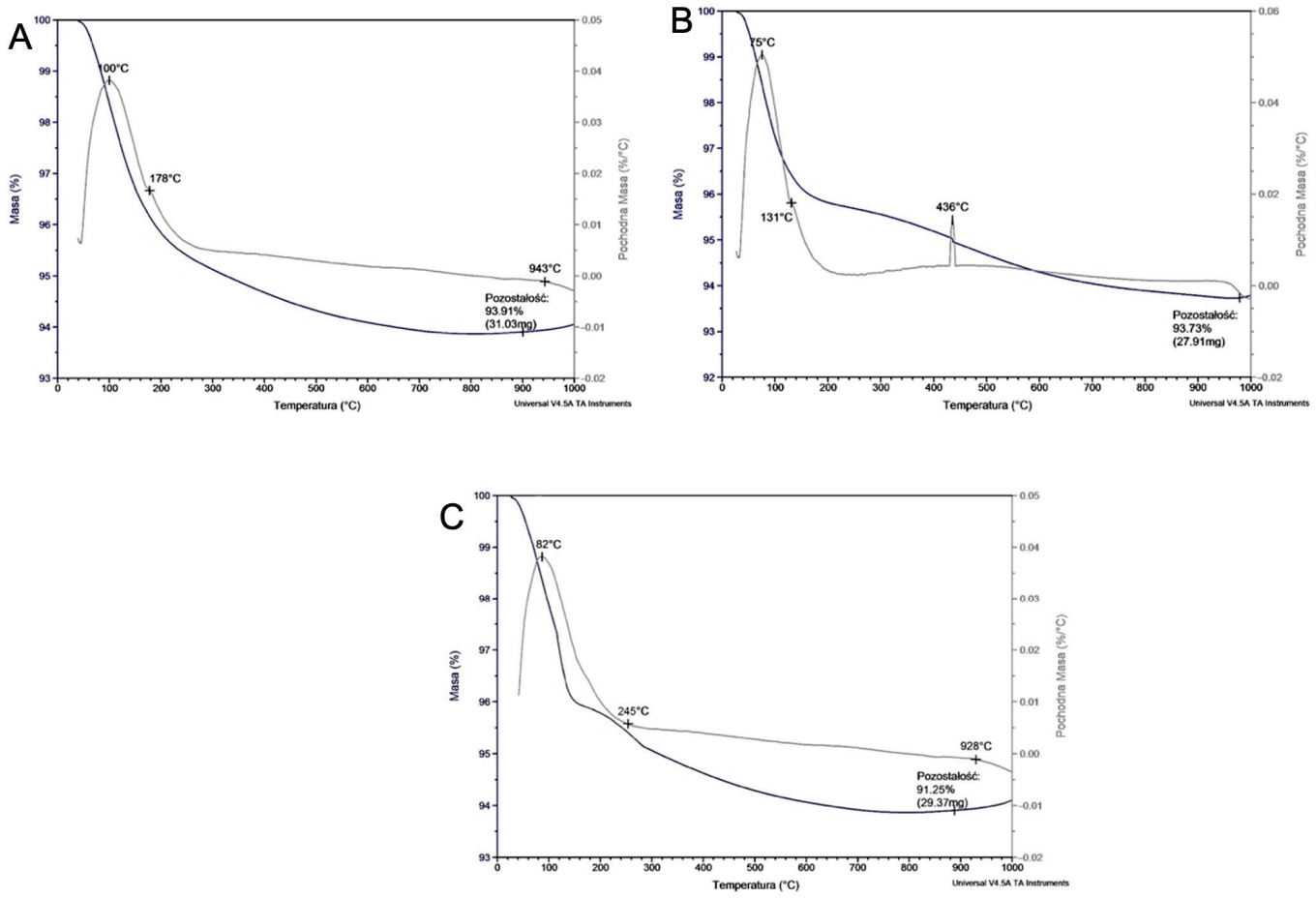


Figure 11. Thermogravimetric curves of the binder: (**A**) Matrixsol, (**B**) Keysol, and (**C**) Ludox SK.

3.3. Moulding Sands

The moulding sands were obtained after mixing their components in appropriate proportions: binder, matrix powders, and wetting and antifoam additives. The prepared mass was mixed using a mechanical mixer under strictly defined conditions of temperature, humidity, and air circulation in the room. They have a specific content of powders, binders, and antifoam and wetting additives. The first moulding sand was prepared from Al_2O_3 powder with two gradations 200# and 325# in the 50–50% ratio. Keysol was the main binder. Analysis of the results of the moulding sand test for the structural layers (Figure 12) confirms its high stability during 8 weeks of testing.

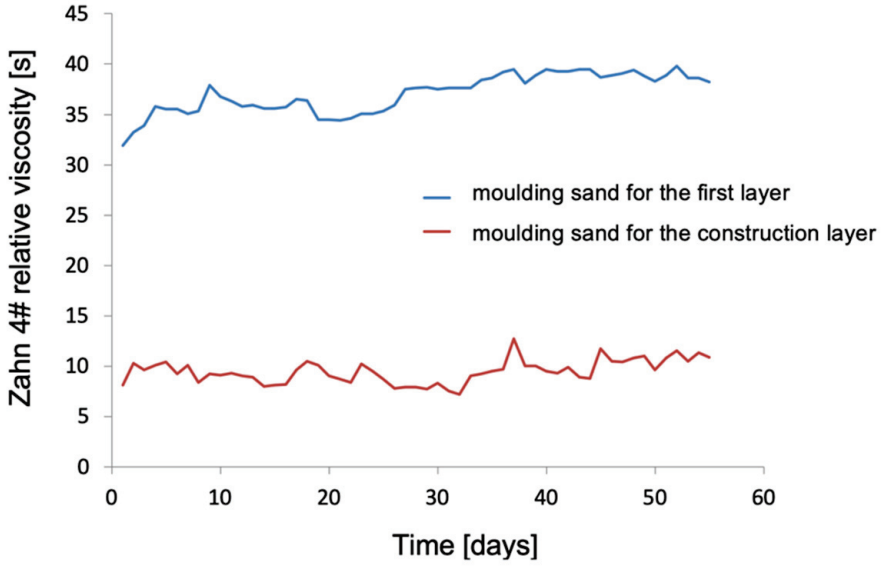


Figure 12. Zahn 4# relative viscosity of the moulding sand for the first layer and the construction layers as a function of time.

It should be noted that the relative viscosity of the ceramic mass for the model layer is clearly higher than that of the moulding mixture intended for the structural layers. However, these ranges correspond to the actual times that the fluid flows from the draw-off cup. It is assumed that for pourable masses intended for the first layer, the flow time should be 10–20 s, while for mixtures for construction layers it should be 25–40 s. The results obtained show that both moulding sands meet the assumptions. For this reason, both moulding sands were used to obtain mould samples.

3.4. Ceramic Moulds

The lack of sufficient data in the literature regarding the forming method, as well as the properties that the ceramic mould should have, and therefore the finished casting, was the basis for a comprehensive analysis of the process of producing ceramic moulds using hydrolysed ethyl silicate. The test results obtained make it possible to determine the predicted properties of the mould produced in the process using new water-soluble binders.

Multilayer ceramic moulds were made by applying successive layers to a wax model. The model was immersed in a ceramic mass and sprinkled with coarse ceramic powder. The prepared layer was left to dry under established conditions of temperature, humidity, and time. These activities were repeated until seven layers were created. The first two layers were made of a higher-viscosity moulding sand for better coverage and reproduction of the surface of the wax model. However, the structural layers were made of a lower-viscosity mass. The ceramic mould was then heat treated to remove wax and increase its mechanical strength. This process consisted of three stages:

- melting wax—in an autoclave, in an atmosphere of superheated steam at a temperature of 170 °C and a pressure of 0.86 MPa;
- wax firing—in an electric furnace, at a temperature of 760 °C, for 1 h, cooling with the furnace;
- annealing the mould—in an electric chamber furnace, at a temperature of 1200 °C, for 2 h, cooling with the furnace.

Ceramic moulds (marked K + M) were made of Al_2O_3 + Keysol moulding sand for the first layer and Molochite 120 + Matrixsol for the construction layers, with controlled air circulation, humidity, and temperature conditions. The conditions used made it possible to reproduce the process of producing ceramic moulds using the previously used HES binder. The inability to dry experimental forms in an industrial dryer led to the development of other evaluation methods. The test results obtained for both the HES form and the newly developed form were the basis for a comparative analysis.

Microscopic examinations allowed the characterisation of the geometric structure of the HES (Figure 13) and K + M (Figure 14) ceramic moulds in three states: raw, after wax firing at 760 °C/1 h, and after annealing at 1200 °C/1 h. It was found that the surface of the tested forms was non-uniform and porous. Particles of moulding powders with sharp edges used as a matrix were observed. The fractures obtained were brittle. Increasing the temperature of heat treatment resulted in an increase in the number of pores.

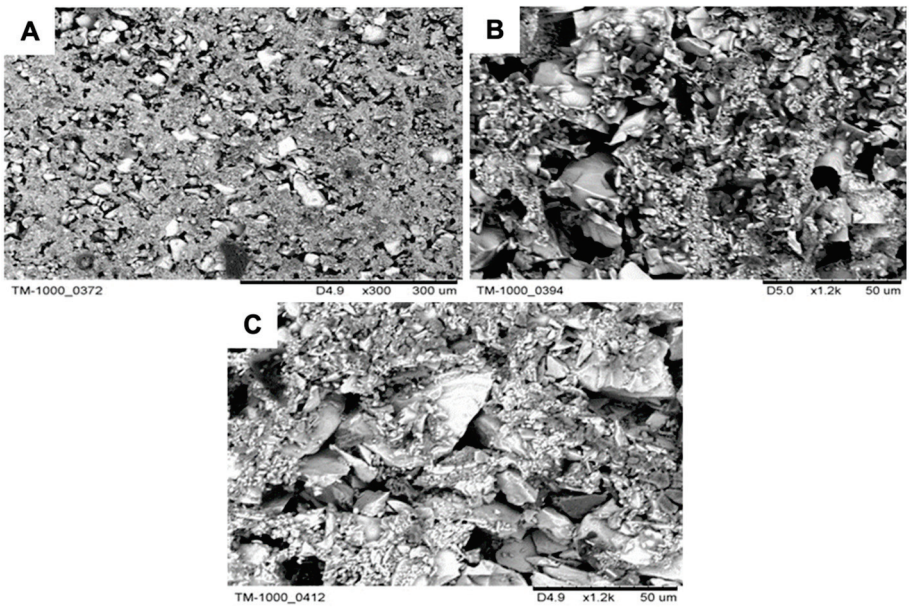


Figure 13. Images of the surface of the first layer of the HES mould: (**A**) raw state; (**B**) after firing the wax 760 °C/1 h; and (**C**) after annealing at 1200 °C/1 h.

Analysis of the phase composition of the mould material after the process of melting and firing the wax mould model showed the presence of phase components:

- α Al_2O_3 oxide—matrix and topping of the first and second layers;
- $Al_2O_3 \cdot SiO_2$ mullite—matrix of the structural layers of the mould;
- sillimanite.

Additionally, a low content of α cristobalite was found in the annealed forms. In the process of annealing the mould material, a phase transformation of amorphous SiO_2 oxide occurs, which is a component of the binder and Molochite 120 powder. It should be noted that the relative volume of this phase component is small. Its presence is not important for technological reasons. However, crystalline SiO_2 oxide, especially cristobalite, is dangerous to human health. Therefore, it is recommended to be particularly careful when creating

the moulds. The tests also confirm the good thermal stability of the main materials used in the moulding of sands, corundum, zirconium silicate, cobalt aluminate, and mullite. This applies to all stages of the heat treatment of ceramic moulds.

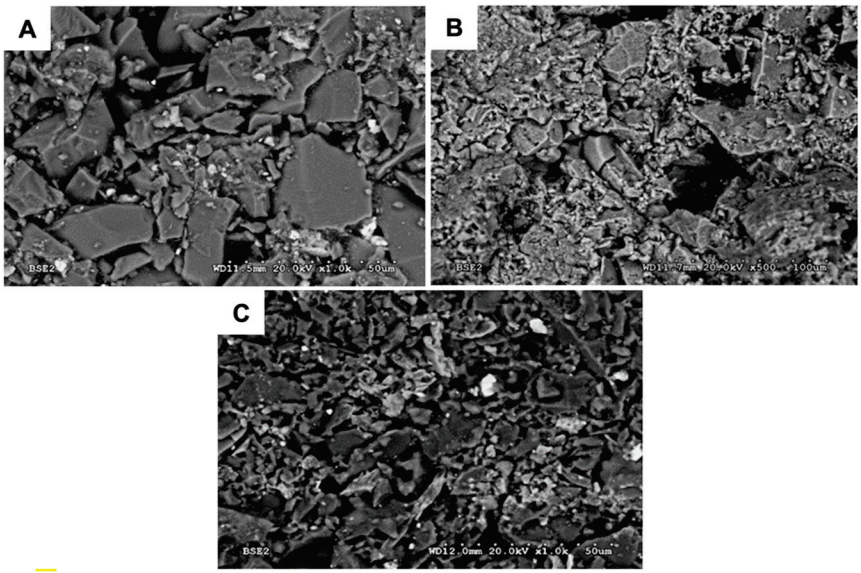


Figure 14. Images of the surface of the first layer of the K + M mould: (**A**) raw state; (**B**) after firing the wax at 760 °C/1 h; and (**C**) after annealing at 1200 °C/1 h.

Figure 15 shows the average surface roughness of the HES and K + M moulds. Moulds that use the HES binder are characterised by an increase in the Ra parameter as a result of heat treatment. However, the moulds developed and manufactured using water-soluble binders show similar values of average surface roughness for samples in all states, i.e., in the raw state, after firing, and after annealing. The low Ra values are influenced by silica nanoparticles that fill the pores open at the surface. For aviation applications, Ra should not exceed 5 µm. As can be seen from the results obtained, the developed moulding systems meet the requirements. The silica nanoparticles (SiO_2) present in water-soluble binders such as Keysol and Matrixsol act as fillers by entering microvoids and surface irregularities during the drying and sintering stages. Upon gelation and subsequent thermal treatment, they form a continuous network that seals surface pores and reduces roughness. This results in a smoother surface finish, which is particularly advantageous for aerospace casting applications.

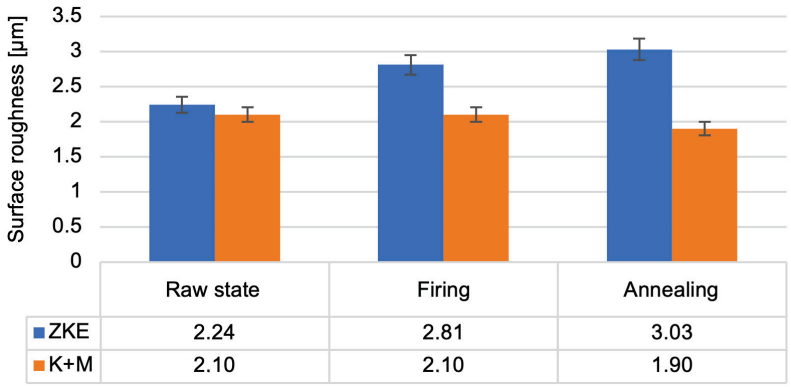


Figure 15. Surface roughness of the HES and K + M moulds in the raw state, after firing at 760 °C/1 h, and after annealing at 1200 °C/1 h.

Analysis of the results of the testing of the mechanical properties of the created ceramic moulds showed that the highest bending strength (Figure 16) and the Young modulus value (Figure 17) were obtained after annealing. For bending strength, measurements were performed on ten specimens per group (HES and K + M) in three material states: raw, after wax firing (760 °C/1 h), and after final annealing (1200 °C/2 h). In the annealed state, the average bending strength for HES-based moulds was 11.3 MPa (±0.9 MPa), whereas the K + M moulds achieved 12.4 MPa (±0.7 MPa). A two-tailed Student's *t*-test showed that this difference was statistically significant ($p = 0.0037$), indicating superior post-sintering mechanical integrity in the water-based system [19].

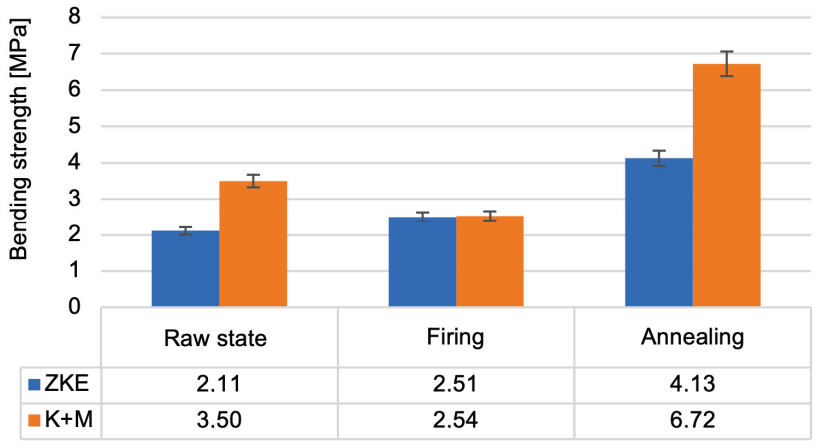


Figure 16. The bending strength of the K + M and HES mould material in the raw state, after wax firing at 760 °C/1 h, and after annealing at 1200 °C/1 h.

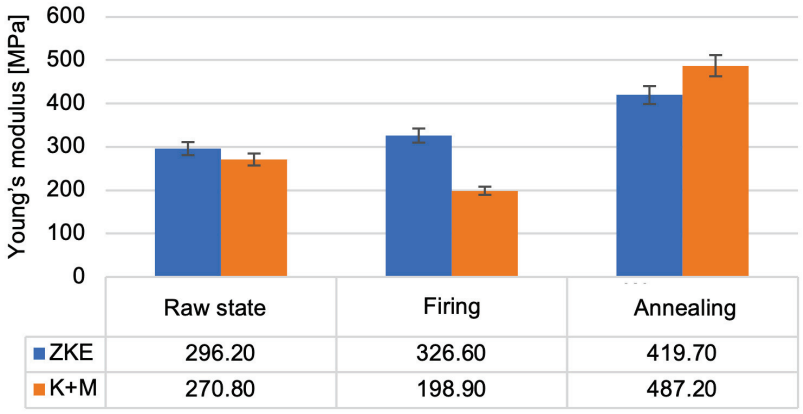


Figure 17. Young's modulus of the K + M and HES mould material in the raw state, after wax firing at 760 °C/1 h, and after annealing at 1200 °C/1 h.

In the raw state, HES moulds exhibited slightly higher bending strength (8.7 MPa vs. 8.2 MPa), which is attributed to the strong initial cohesion provided by the alcohol-based binder [21]. However, this difference was not statistically significant ($p = 0.087$), and the values converged after heat treatment. Notably, K + M moulds demonstrated better thermal resilience, retaining higher mechanical performance after each processing stage, consistent with findings in recent work on water-based ceramic slurries [16,24]. The reduction in bending strength after wax firing is caused by the decomposition of the polymer contained in the binder; it provides greater bending strength in the raw state. The increase in bending strength after annealing is related to the sintering process of the ceramic matrix and colloidal silica. The value of the Weibull modulus (Figure 18) decreases as the annealing temperature of the ceramic moulds increases. This is due to the high

porosity of the samples, which resulted in low Weibull modulus values for all samples. The m modulus for the K + M samples is smaller than that for the HES samples, which could be due to the lower value of the wetting angle of the hydrolysed ethyl silicate, which resulted in good mixing of the composition and a smaller number of surface defects.

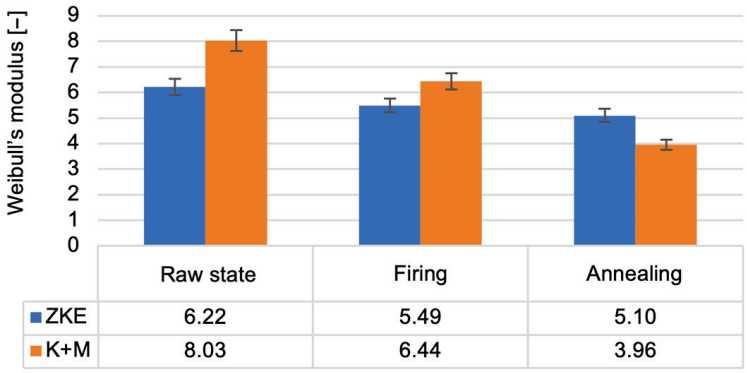


Figure 18. Weibull modulus of the K + M and HES mould material in the raw state, after wax firing at 760 °C/1 h, and after annealing at 1200 °C/1 h.

In terms of porosity, mercury intrusion porosimetry revealed that the average open porosity in annealed HES moulds was 26.8%, while in K + M moulds it was slightly higher at 29.1%. Although this increase may appear unfavorable at first glance, further analysis showed that the gas permeability of K + M moulds was significantly enhanced—5.6×10^{-9} cm^2 at 1100 °C versus 4.1×10^{-9} cm^2 for HES moulds—leading to improved venting during casting [13,25]. This effect is aligned with the beneficial role of porosity in degassing described in advanced investment casting systems [17,20]. The increased porosity in the K + M system also had no measurable negative impact on casting surface quality, as evidenced by the Ra values (<5 µm) and the absence of gas-related defects in pilot trials.

For surface roughness, the average Ra of K + M moulds after annealing was 4.2 µm, compared to 5.1 µm in the HES group. This difference was statistically significant ($p = 0.012$), confirming that silica nanoparticle infiltration in the K + M binder contributed to improved surface quality by partially sealing surface pores during drying and sintering [12,14].

The improved mechanical, thermal, and surface characteristics of the K + M system strongly support its practical replacement of the traditional HES-based solution, in line with sustainable material trends described in the recent literature [16,26,27].

Analysis of the results obtained from the porosity test (Figure 19) allows us to conclude that the porosity of the moulds ranges from 24% to 29%. Annealed forms are characterised by the highest porosity. This is caused by the sintering process. Up to a temperature of 760 °C, the entire binder does not undergo thermal decomposition. More is decomposed at 1000 °C, which also results in greater porosity. This parameter is also influenced by the rapid sintering process of 10 °C/min, which causes faster gas escape, the formation of voids, and the inability to close pores. Wax firing and annealing cause the evaporation of water and the degradation of organic compounds. After annealing, the average pore diameter increases significantly (Figure 20) in the tested ceramic moulds. This proves the coalescence of pores and the sintering of the fine-grained fraction of the matrix ceramic powders. This is also evidenced by the distribution of the average pore diameter. The annealing process eliminates the occurrence of small pores. The high porosity of the mould in the annealed condition and the large average pore diameter are advantageous. Porous ceramic moulds are characterised by good gas permeability when poured with liquid metal and are also brittle when finishing castings. Figure 20 shows that, in the case of the K + M

system, the fired form has the highest porosity. For the K + M moulds, firing at 760 °C does not fully decompose organic additives, and partial sintering begins only after annealing at 1200 °C. Thus, larger pores are formed during annealing due to extensive sintering and agglomeration of ceramic particles.



Figure 19. Open porosity of the K + M and HES mould material in the raw state, after wax firing at 760 °C/1 h, and after annealing at 1200 °C/1 h.

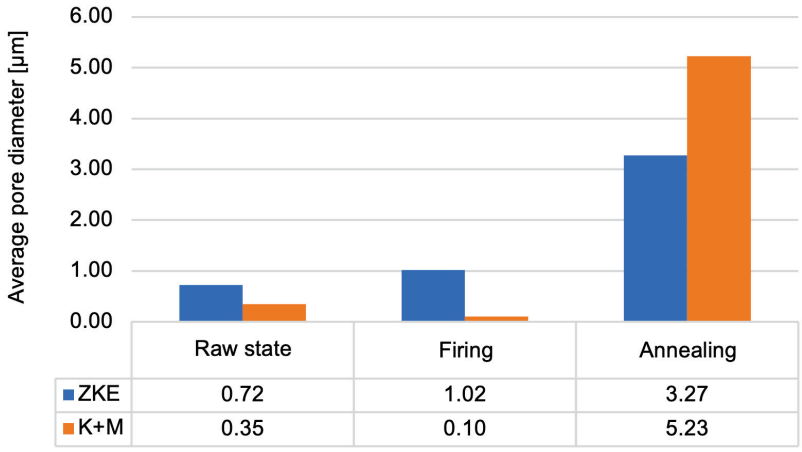


Figure 20. Average pore diameter of the K + M and HES moulds in the raw state, after wax firing at 760 °C/1 h, and after annealing at 1200 °C/1 h.

The increased porosity observed in the K + M moulds, particularly after annealing (up to ~29.1%), indeed plays a dual role in the performance of the ceramic-casting system. On one hand, higher open porosity enhances gas permeability, which is a critical factor in avoiding casting defects such as gas porosity, blowholes, and oxide inclusions during metal pouring [13]. This is especially beneficial in the casting of nickel superalloy components, where complete and rapid evacuation of air and residual volatiles through the mould wall is essential to ensure high surface quality and structural integrity of thin-walled blades [4,16,24]. The gas permeability of K + M moulds increased with temperature, reaching a peak value of 5.6×10^{-9} cm^2 at 1100 °C, compared to 4.1×10^{-9} cm^2 for the HES system, which demonstrates superior outgassing capability [13]. This enhanced permeability, in combination with good wettability (moderate wetting angles) and phase stability, contributed to the absence of internal defects or misruns in pilot castings, confirming the functional viability of the developed solution. On the other hand, excessive or uncontrolled porosity may compromise surface finish or reduce local mechanical strength of the mould, particularly in areas of high thermal gradient or metallostatic pressure [20,27]. Surface roughness may increase due to micro-cavities formed during binder burnout and sintering,

especially if the pore structure is irregular or contains interconnected macrovoids. However, in our tests, surface roughness (Ra) remained below the critical threshold of 5 μm, and no crack propagation or surface degradation was observed after annealing or during pilot casting trials.

To ensure control over porosity and mitigate potential negative effects, the following strategies should be applied:

1. Optimization of binder-to-powder ratio to reduce excess binder phase and control pore evolution during drying and sintering;
2. Use of fine silica nanoparticle-rich sealant coatings for the final layer (without dusting), which partially closes surface pores and minimizes Ra increase during firing [12,14];
3. Tuning of the sintering schedule, e.g., by incorporating a pre-sintering step at 900–1000 °C to stabilize the pore structure before final densification at 1200 °C;
4. Inclusion of pore modifiers or sacrificial pore-forming agents (e.g., fugitive organics or microballoons) that decompose at lower temperatures, leading to more uniform porosity distribution [17,25];
5. Post-casting leaching or finishing processes, such as water jet or mechanical polishing, to eliminate residual ceramic that may have penetrated into micro-defects.

Overall, while increased porosity is an inherent consequence of using water-based systems with high SiO_2 content, it has been managed effectively through material and process design. The resulting moulds maintained both functional integrity and surface quality comparable or superior to conventional HES-based systems, which supports their practical implementation in aerospace casting technologies [27].

The results of the gas permeability tests of the tested ceramic moulds are shown in Figure 21. An increase in gas permeability with increasing temperature was found for the ceramic moulds using a water-soluble binder. However, for forms that used HES, the opposite phenomenon was observed. This is caused by the difference in the linear expansion coefficient of the mould ceramic material. The reduction in gas permeability at temperatures > 1100 °C is caused by the effect of sintering and shrinkage of the ceramic metal.

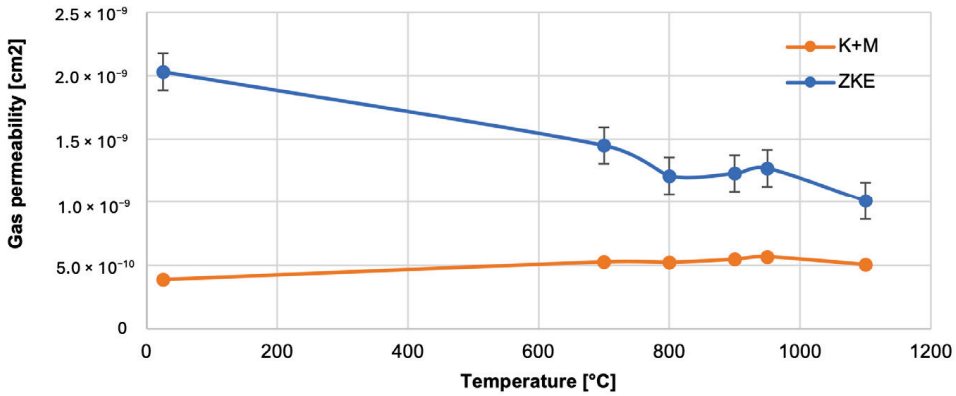


Figure 21. Gas permeability of the K + M and HES mould material in the temperature range from 22 °C to 1100 °C.

Thermal properties of the reference mould material were tested using HES, and that of the newly developed one was tested using K + M. The analysis of the results obtained indicates that the relative elongation increases slightly and reaches a maximum at a temperature of approximately 1100 °C—0.5% (Figure 22). Above the temperature of 1100 °C, the mould material shrinks to a maximum value of 1.5%. It is caused by the ceramic sintering process. Similar dependencies were found for the linear expansion factor of the material of the tested forms (Figure 23).

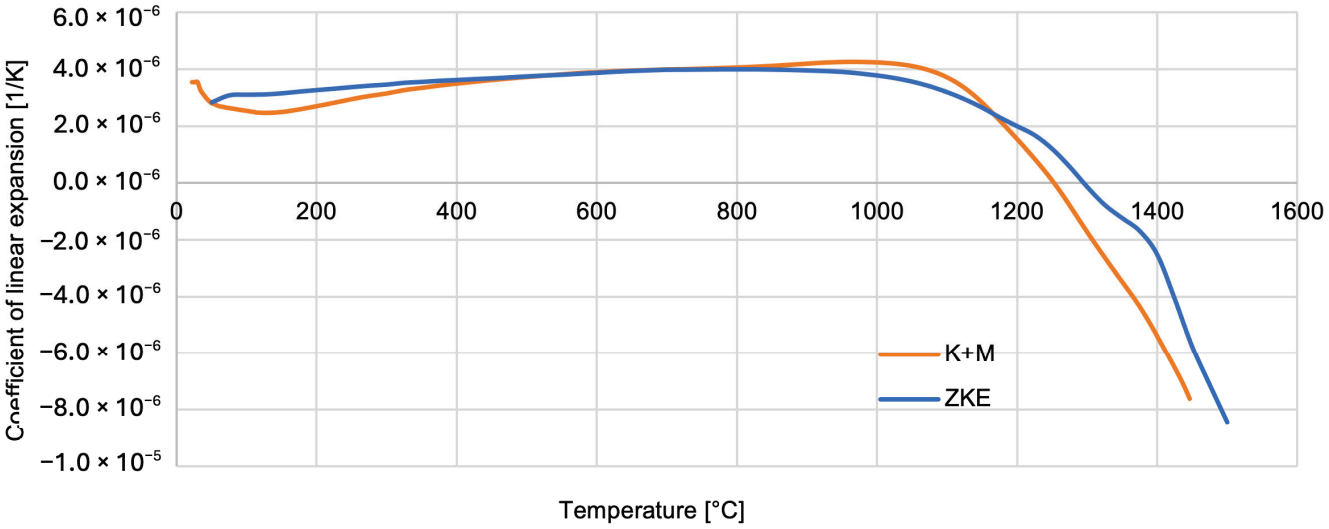


Figure 22. Coefficient of linear expansion of the K + M and HES mould material in the temperature range from 22 °C to 1500 °C.

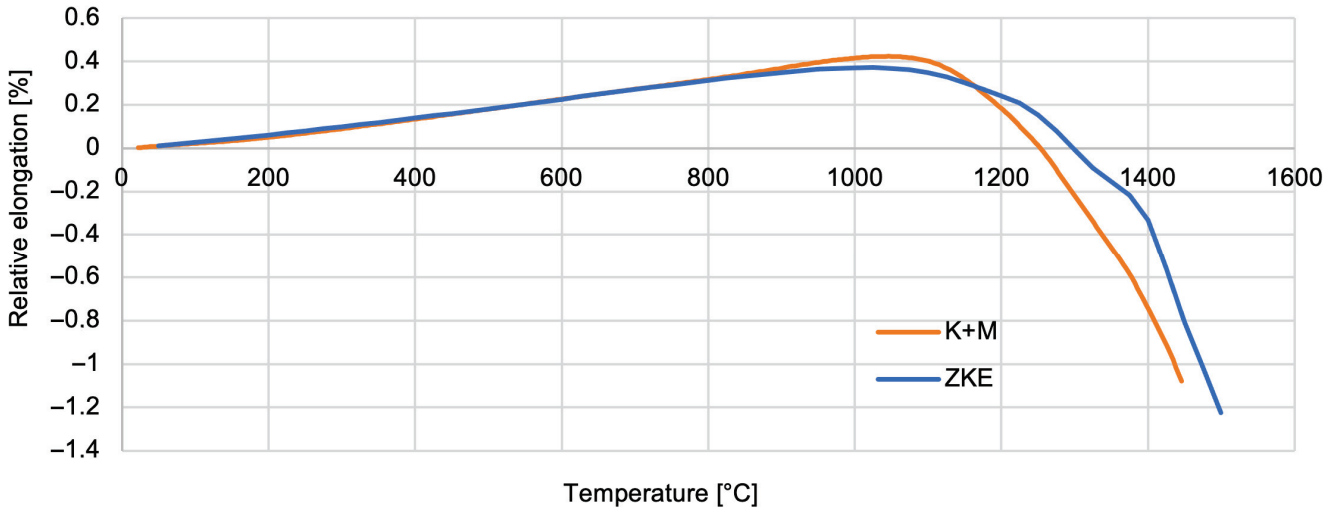


Figure 23. Relative elongation of the K + M and HES mould material in the temperature range from 22 °C to 1500 °C.

Analysis of the measurement of the apparent density of the mould material (Figure 24) shows that it decreases as the temperature increases to its critical value—approximately 1100 °C. The formation of new phases then causes the material to thicken and increase its density [17]. The density increase after phase transformation and sintering improves mould mechanical strength and thermal shock resistance. A denser mould reduces gas entrapment and enhances casting accuracy. However, excessive densification could limit gas permeability. In the K + M system, we observed an optimal balance, leading to improved mould integrity without sacrificing permeability.

The dependence of the specific heat on temperature was determined for ceramic mould materials using HES and K + M binders (Figure 25). The curve obtained allows one to determine four characteristic temperature values related to the polymorphic transformation of SiO_2 oxide. At a temperature of approximately 550 °C, α-quartz transforms into the β variety. Then, at a temperature of approximately 960 °C, the transformation of β-quartz → β-tridymite takes place. The β-quartz variety is transformed into β-cristobalite at a temperature of 1200 °C. However, at a temperature of approximately 1400 °C, β-tridymite → β-cristobalite. The specified polymorphic transformation temperatures differ slightly

from the theoretically determined polymorphic transformation temperatures of SiO_2 oxide. This is caused by the presence of various chemical additives in SiO_2, which shift the temperatures of the polymorphic transformation.

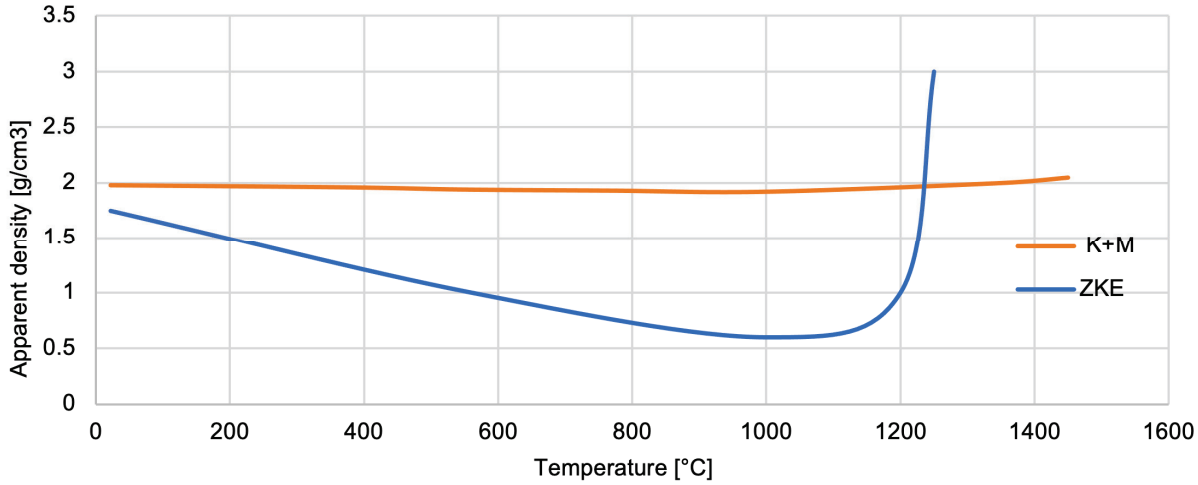


Figure 24. Apparent density of the K + M and HES mould material in the temperature range from 22 °C to 1500 °C.

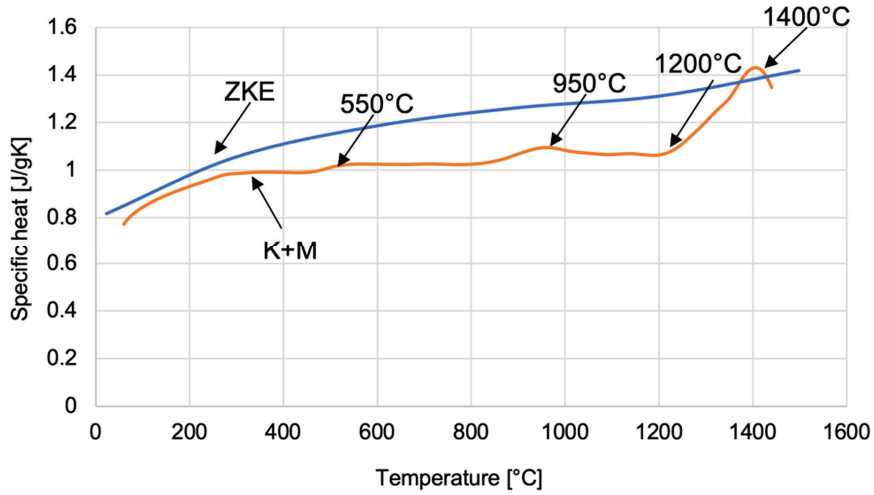


Figure 25. Specific heat of the K + M and HES mould material in the temperature range from 22 °C to 1500 °C.

The thermal conductivity of SiO_2 oxide was determined (Figure 26). The thermal conductivity coefficient ranges from 0.3–1 W/mK up to a temperature of approximately 1100 °C. The thermal diffusivity of SiO_2 oxide also decreases from 0.62 mm^2/s to 0.43 mm^2/s, also up to a temperature of 1100 °C (Figure 27). SiO_2 oxide is characterised by low conductivity and thermal diffusivity due to high porosity. A particularly important factor is increasing the temperature value to 1100 °C. It causes the sintering effect of ceramics, shrinkage, and thickening of the mould material, hence the increase in thermal conductivity to 2 W/mK and thermal diffusivity to 0.67 mm_2/s at a temperature of 1400 °C. The analysis of the results of the thermal properties test indicates significant changes that are caused by the polymorphic transformation characteristic of the SiO_2 oxide. A particularly large difference in values was found at a temperature of approximately 1100 °C, which is the beginning of the ceramic sintering process. In addition, at this temperature, large changes in relative elongation, increased density, and thermal conductivity of the mould material were demonstrated. This indicates both shrinkage and compaction of the mould material. Additionally,

characteristic values of the temperature of the polymorphic transformation of SiO_2 oxide can be distinguished in the curves of specific heat versus temperature.

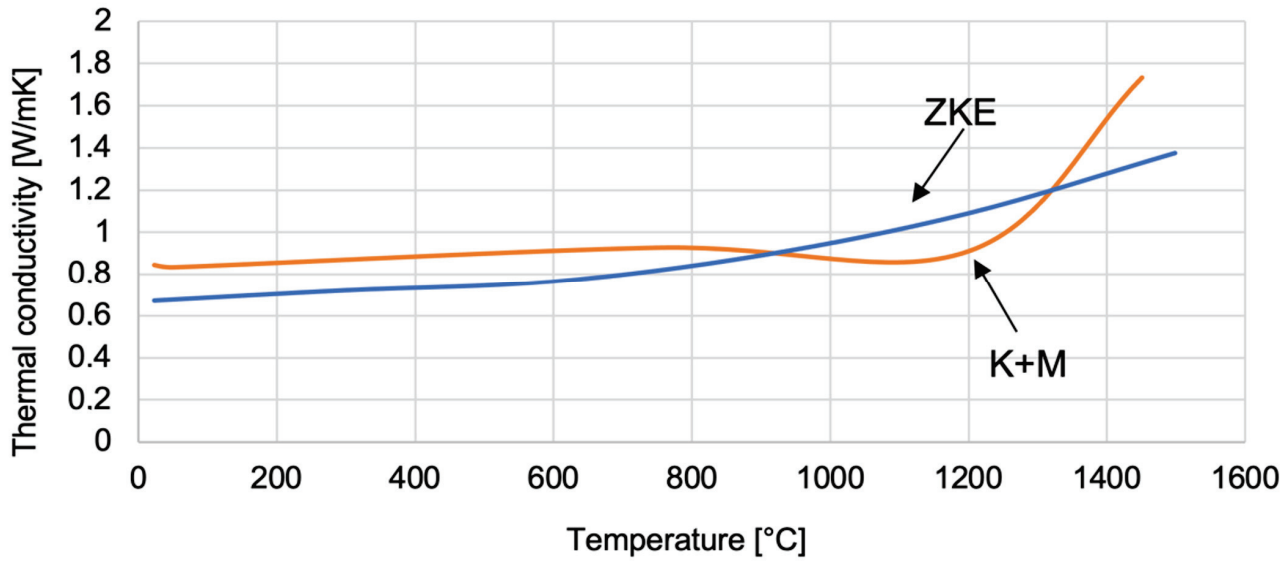


Figure 26. Thermal conductivity of the K + M and HES mould material in the temperature range from 22 °C to 1500 °C.

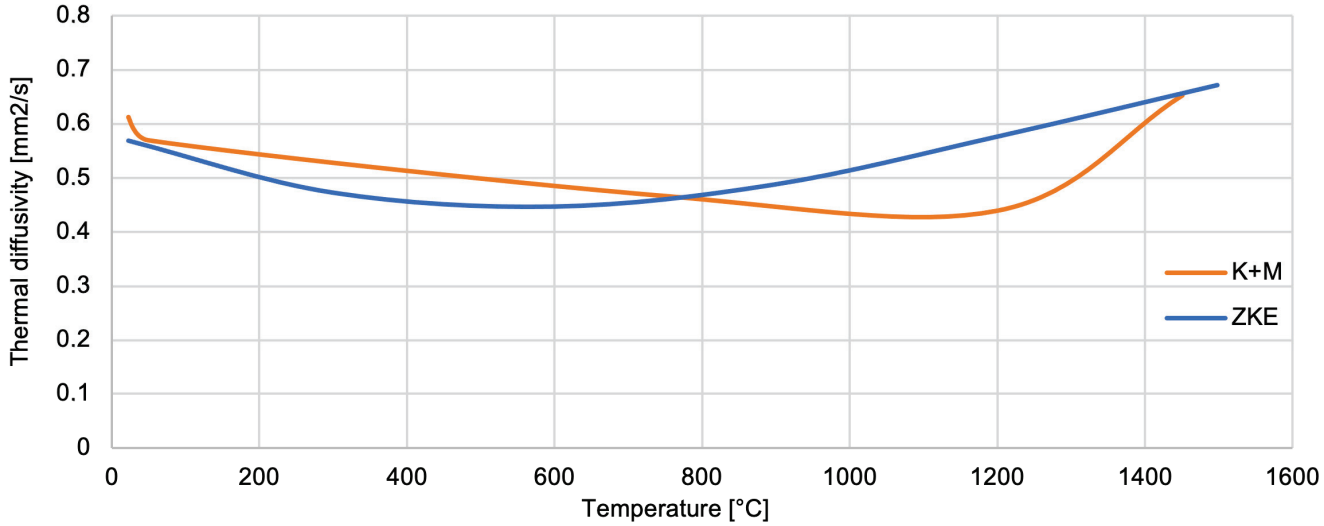


Figure 27. Thermal diffusivity of the K + M and HES mould material in the temperature range from 22 °C to 1500 °C.

In terms of binder systems, our findings support and extend previous work by Ismael et al. [17], who investigated colloidal silica as a nanostructured binder for refractory castables. While they confirmed the potential of colloidal systems for improved thermal stability, our study goes further by integrating a dual-component water-soluble binder system (Keysol + Matrixsol) and demonstrating its full industrial viability for multilayer ceramic moulds in aerospace applications. Similarly, Wang et al. [24] studied ceramic shell–metal interactions and gas permeability in yttria-based moulds; our work complements theirs by focusing on silica-alumina-based moulds but introduces a comparable porosity–permeability balance critical for thin-walled casting. Regarding mechanical properties, our annealed K + M moulds achieved bending strengths exceeding 12 MPa, which are higher than the values reported in earlier work by Maity and Maity [14], where ceramic moulds reinforced with zircon/silica layers reached strengths of only 8–10 MPa under

comparable heat treatment conditions. Furthermore, our observed Young's modulus and Weibull modulus trends are consistent with the mechanical behavior described by Donachie et al. [18] in superalloy-compatible mould systems, yet we extend this by correlating these values with binder microstructure (e.g., nanoparticle dispersion and sol-gel kinetics). In terms of thermal behavior, our thermal conductivity results (rising from 0.3 to 2.0 W/mK with temperature) align with those obtained by Szeliga et al. [13], who measured similar trends in investment casting shell moulds. However, unlike their work, we incorporate a detailed thermal diffusivity analysis and correlate it with porosity and phase transformations (e.g., quartz → tridymite, cristobalite transitions) observed via DSC, thus offering a more complete thermophysical characterisation. Concerning surface quality, our surface roughness (Ra < 5 μm) after sintering matches the performance benchmark established by Chen et al. [27] for alumina-based, laser-fused ceramic shells, despite the fundamentally different forming method. Our study thus demonstrates that water-based slurry systems can match or outperform more technologically intensive fabrication methods when appropriately optimized. From an environmental perspective, Cunha et al. [27] demonstrated the feasibility of using waste ceramic moulds and paraffin wax in mortar composites, highlighting the lifecycle aspect of foundry materials. Our work contributes to this direction by proving that alcohol-free binder systems not only reduce VOC emissions by over 85% but also generate safer solid waste for downstream recycling, in line with circular economy goals. Finally, the present work is, to the best of our knowledge, the first comprehensive experimental validation of the Keysol/Matrixsol system for precision aerospace moulds that includes mechanical, thermal, microstructural, and gas permeability performance comparisons against conventional HES systems—thereby closing an existing gap in the literature on water-based binder substitution under production-simulating conditions [27].

3.5. Environmental and Economic Benefits

The environmental impact of HES-based binder systems is primarily associated with the evaporation of alcohol solvents (e.g., ethanol and isopropanol), which release large quantities of volatile organic compounds (VOCs) during application and drying. According to industry data and environmental audits, the use of HES binders typically results in the emission of 450–600 g VOC per kilogram of binder used. For a standard seven-layer ceramic shell system with a total binder requirement of approximately 2.5 kg per mould, this translates to 1.1–1.5 kg of VOCs emitted per unit. In contrast, the Keysol and Matrixsol systems are water-based and contain no organic solvents, effectively reducing VOC emissions by over 90% [28]. Evaporation of water during drying is slower, but environmentally neutral, and does not require additional air treatment or filtration systems. As a result, foundries adopting the K + M system can eliminate the need for VOC capture and incineration systems, reducing energy consumption and lowering their total carbon footprint. In terms of greenhouse gas (GHG) emissions, a lifecycle comparison based on preliminary process modeling (including transportation, energy for drying, and waste treatment) indicates that switching from HES to K + M binders can reduce the total CO_2 equivalent emissions per mould by approximately 18–25%, depending on the region's energy mix and drying strategy [29,30]. This is particularly relevant for companies certified under the EU Emissions Trading Scheme, where measurable reductions in Scope 1 and Scope 2 emissions are critical. Another important factor is workplace safety and exposure. HES systems are classified as flammable and hazardous under REACH and GHS regulations. Ethyl silicate can irritate the respiratory tract and mucous membranes, especially in high-humidity environments, requiring the use of fume hoods, explosion-proof ventilation, and personal protective equipment (PPE). In contrast, Keysol and Matrixsol have no flash point, produce no hazardous fumes, and are classified as non-toxic under standard occupational exposure

thresholds. This contributes to significantly improved health and safety conditions in the workplace, fewer incidents of exposure, and reduced risk of fire or explosion, especially during summer operation or in poorly ventilated areas. From an economic standpoint, the use of water-based binders may initially appear more expensive on a per-liter basis. However, a full cost-benefit analysis shows that the total operational cost per mould is in fact lower when using K + M, once indirect costs such as solvent handling, fire safety infrastructure, VOC permits, waste disposal, and equipment maintenance are included. In addition, the use of aqueous systems enables better automation of slurry application and cleaning, leading to improved process repeatability and shorter setup times. Several industrial partners reported a net reduction of approximately 10–15% in total moulding-related costs after converting to water-soluble binder systems, despite a slightly higher material unit price. Furthermore, the ecological nature of the K + M system offers additional strategic benefits. It improves the company's compliance with international green production standards and can support environmental declarations such as Environmental Product Declarations (EPDs) or EcoVadis certifications. This is particularly advantageous in public tenders or international supply chains where sustainability criteria are increasingly weighted in supplier selection [31].

In summary, the replacement of HES with water-soluble binders such as Keysol and Matrixsol brings quantifiable environmental benefits, including a >90% reduction in VOC emissions, a 20–25% reduction in carbon footprint, elimination of flammable solvents, and enhanced occupational safety. Economically, it reduces long-term operational costs and aligns with both current and future legislative and market-driven sustainability requirements. These factors not only justify the adoption of water-based systems from a technical standpoint but also demonstrate their strategic advantage for modern foundries.

3.6. Pilot-Scale Industrial Testing

During the pilot tests, a series of ceramic moulds were produced using the full seven-layer K + M system. Each layer was applied under standard shop-floor conditions (ambient temperature ~22 °C and humidity ~50%), without the use of a high-temperature industrial drying oven, to simulate minimal infrastructure adaptation. The moulds were then subjected to the standard debinding and sintering processes—dewaxing in an autoclave at 170 °C, firing at 760 °C for 1 h, and final annealing at 1200 °C for 2 h—exactly replicating the conditions used for HES-based systems. The castings produced were hollow turbine blades from a IN713C nickel-based superalloy, which were chosen due to their complex geometry, thin-wall design, and high surface finish requirements. The K + M moulds demonstrated excellent dimensional stability and structural integrity during all stages of the process. No delamination, interlayer cracking, or deformation was observed, even under metallostatic pressures and high thermal gradients. The surface of the resulting castings exhibited a roughness (Ra) below 5 μm, within aerospace specification limits. Additionally, repeated casting cycles using the same slurry compositions and process parameters confirmed the process repeatability of the binder system. Over three production batches (each with 8–10 moulds), no batch-to-batch variation exceeding 5% was recorded in key quality metrics, including shell thickness, porosity, and casting surface fidelity. Importantly, workers involved in the pilot-scale trials reported improved handling characteristics and a reduction in unpleasant odours and skin irritation, which are commonly associated with alcohol-based binders such as HES. The use of water-based systems eliminated the need for explosion-proof equipment and reduced the frequency of ventilation system maintenance, further supporting the operational feasibility of the new solution. From a scalability standpoint, the slurry formulations and drying protocols used in the pilot tests were intentionally designed to be transferable to existing foundry infrastructure with minimal modification.

The equipment used (slurry tanks, mixers, wax trees, and drying chambers) remained unchanged. This demonstrates that full-scale industrial adoption of the K + M system can be achieved without extensive investment in new hardware or process requalification.

In conclusion, the pilot-scale validation confirmed that the water-soluble binder system developed in this study is not only technically effective but also scalable, repeatable, and compatible with industrial production environments. The successful application in turbine blade casting—one of the most demanding precision casting tasks—provides strong evidence that the proposed system is ready for production implementation, offering environmental, safety, and economic advantages over traditional HES-based solutions.

4. Summary

The research and analysis performed were the basis for expanding our knowledge to the extent necessary to develop a new ecological technology of ceramic-casting moulds for the precise casting of aircraft engine turbine blades from nickel superalloys. The essence of the investigation was to eliminate a harmful factor (ethyl alcohol) from the process of preparing a ceramic mould. Fundamental differences in the technological properties of alcohol and water-based binders forced the development of new criteria for the selection of moulding sand components, including dustings, procedures for selecting moulding mixture components, production conditions, and control of the technological properties of moulding sands and forming and drying technologies, as well as the heat treatment of moulds and the process of pouring the liquid alloy itself. Analysis of the results of the comprehensive research and development work, both on a laboratory scale and on a production scale, showed that the stated goal was achieved.

The usefulness of water-soluble binders and a new type of water-based moulding system for obtaining ceramic-casting moulds in the aviation and foundry industries were found. It has been proven to be used in production. It has been proven that they can be used in production and, at the same time, excluded from the production of binders with alcohol ingredients (HES). The consequence will be an increase in the work comfort of the moulding plant employees and no negative impact from harmful gases resulting from the breakdown of the HES binder on the natural environment. The manufactured ceramic moulds were characterised by good physical and mechanical properties, exceeding the parameters of the reference mould.

The end result is the developed ecological technology of ceramic-casting moulds for the precise casting of aircraft engine turbine blades from nickel superalloys.

Author Contributions: Conceptualization, M.W., M.M. and J.K.; methodology, M.W. and M.M.; formal analysis, M.M. and M.W.; data curation, J.K.; investigation, M.W. and M.M.; writing—original draft preparation, M.M., M.W. and J.K.; writing—review and editing, J.K.; visualization, M.M.; supervision, M.W. All authors have read and agreed to the published version of the manuscript.

Funding: This work was financed/co-financed by the Military University of Technology under research project UGB/22-015.

Institutional Review Board Statement: Not applicable.

Informed Consent Statement: Not applicable.

Data Availability Statement: The original contributions presented in the study are included in the article, further inquiries can be directed to the corresponding author.

Conflicts of Interest: The authors declare no conflicts of interest.

References

1. Rao, P.; Iwasa, M.; Tanaka, T.; Kondoh, I. Centrifugal casting of ceramic composites of Al_2O_3-15% by weight ZrO_2. *Ceram. Int.* **2003**, *29*, 209–212. [CrossRef]
2. Frueh, C.; Poirier, D.R.; Maguire, M.C. The effect of silica-containing binders on the titanium/face coat reaction. *Metall. Mater. Trans. B* **1997**, *28*, 919–926. [CrossRef]
3. Ferenc, J.; Michalski, J.; Matysiak, H.; Sikorski, K.; Kurzydlowski, K.J. The influence of alumina powder on the rheological properties of zircon/silica slurries for investment casting of moulds. *Proc. Inst. Mech. Eng. Part B J. Eng. Manuf.* **2009**, *233*, 1417–1421. [CrossRef]
4. Jin, W.; Bai, F.; Li, T.; Yin, G. Grain Refinement of Superalloy IN100 Under the Action of Rotary Magnetic Fields and Inoculants. *Mater. Lett.* **2008**, *62*, 1585–1588. [CrossRef]
5. Wang, F.; Zhang, J.; Huang, T.; Liu, L.; Fu, H. Preparation of Inoculants Used in Superalloy and Analysis of the Atomic Matching Models. *J. Mater. Sci. Technol.* **2013**, *29*, 387–392. [CrossRef]
6. Liu, L.; Huang, T.; Xiong, Y.; Yang, A.; Zhao, Z.; Zhang, R.; Li, J. Grain Refinement of Superalloy K4169 by Addition of Refiners: Cast Structure and Refinement Mechanisms. *Mater. Sci. Eng. A* **2005**, *394*, 1–8. [CrossRef]
7. Du, B.; Yang, J.; Cui, C.; Sun, X. Effects of Grain Refinement on the Microstructure and Tensile Behavior of K417G Superalloy. *Mater. Sci. Eng. A* **2015**, *623*, 59–67. [CrossRef]
8. Rakoczy, Ł.; Cygan, R. Analysis of Temperature Distribution in Shell Mould During Thin-Wall Superalloy Casting and its Effect on the Resultant Microstructure. *Arch. Civ. Mech. Eng.* **2018**, *18*, 1441–1450. [CrossRef]
9. Zupanič, F.; Bončina, T.; Križman, A.; Tichelaar, F.D. Structure of Continuously Cast Ni-Based Superalloy Inconel 713. *J. Alloys Compd.* **2001**, *329*, 290–297. [CrossRef]
10. Azadi, M.; Marbout, A.; Safarloo, S.; Azadi, M.; Shariat, M.; Rizi, M.H. Effects of Solutioning and Ageing Treatments on Properties of Inconel-713C Nickel-Based Superalloy Under Creep Loading. *Mater. Sci. Eng. A.* **2018**, *711*, 195–204. [CrossRef]
11. Matysiak, H.; Zagorska, M.; Balkowiec, A.; Adamczyk-Cieslak, B.; Cygan, R.; Cwajna, J.; Nawrocki, J.; Kurzydłowski, K.J. The Microstructure Degradation of the IN 713C Nickel-Based Superalloy After the Stress Rupture Tests. *J. Mater. Eng. Perform.* **2014**, *23*, 3305–3313. [CrossRef]
12. Szczotok, A.; Matysiak, H. Influence of Constituents of Shell Mold on the Morphology and Chemical Composition of Carbides Occurring in IN 713C Superalloy Castings. *J. Mater. Eng. Perform.* **2014**, *23*, 2748–2759. [CrossRef]
13. Szeliga, D.; Kubiak, K.; Ziaja, W.; Cygan, R.; Suchy, J.S.; Burbelko, A.; Nowak, W.J.; Sieniawski, J. Investigation of Casting-Ceramic Shell Mold Interface Thermal Resistance During Solidification Process of Nickel Based Superalloy. *Exp. Therm. Fluid Sci.* **2017**, *87*, 149–160. [CrossRef]
14. Maity, P.; Maity, J. Development of High Strength Ceramic Shell for Investment Casting. *Indian Found. J.* **2001**, *47*, 23–26. [CrossRef]
15. Zhang, B.; Sheng, G.; Jiao, Y.; Gao, Z.; Gong, X.; Fan, H.; Zhong, J. Precipitation and Evolution of Boride in Diffusion Affected Zone of TLP Joint of MAR-M247 Superalloy. *J. Alloys Compd.* **2017**, *695*, 3202–3210. [CrossRef]
16. Małek, M.; Wiśniewski, P.; Matysiak, H.; Zagórska, M.; Kurzydłowski, K.J. Technological properties of SiC-based ceramic slurries for manufacturing investment casting shell moulds. *Arch. Metall. Mater.* **2014**, *59*, 1059–1062. [CrossRef]
17. Ismael, M.R.; Dos Anjos, R.D.; Salomao, R.; Pandolfelli, V.C. Colloidal silica as a nostructured binder for refractory castables. *Refract. Appl. News* **2006**, *11*, 16–20.
18. Donachie, M.J.; Donachie, S.J. *Superalloys: A Technical Guide*; ASM International: Novelty, OH, USA, 2002.
19. Heck, K.A.; Smith, J.S.; Smith, R. Inconel 783: An Oxidation- Resistant, Low Expansion Superalloy for Gas Turbine Applications. *J. Eng. Gas Turbines Power* **1998**, *120*, 363–369. [CrossRef]
20. Heck, K.A.; Smith, D.F.; Holderby, M.A.; Smith, J.S. *Three-Phase Controlled Expansion Superalloys with Oxidation Resistance*; Inco Alloys International: Huntington, WV, USA, 1992.
21. Furillo, F.T.; Davidson, J.; Tien, J. The Effects of Grain Boundary Carbides on the Creep and Back Stress of a Nickel-Base Superalloy. *Mater. Sci. Eng.* **1979**, *39*, 267–273. [CrossRef]
22. Wahl, F.M.; Grim, R.E.; Graf, R.B. Phase Transformations in Silica as Examined by Continuous X-ray Diffraction. *Am. Mineral.* **1961**, *46*, 196–208.
23. Vallar, S.; Houivet, D.; El Fallah, J.; Kervadec, D.; Haussonne, J.M. Oxide slurries stability and powders dispersion: Optimization with zeta potential and rheological measurements. *J. Eur. Ceram. Soc.* **1999**, *19*, 1017–1021. [CrossRef]
24. Wang, Y.; Guo, X.; Qiao, Y. Interactions between Nb-Si based ultrahigh temperature alloy and yttria matrix mould shells. *Mater. Des.* **2017**, *116*, 461–471. [CrossRef]
25. Chen, C.C.A.; Vu, L.T.; Qiu, Y.T. Study on Injection Molding of Shell Mold for Aspheric Contact Lens Fabrication. *Procedia Eng.* **2017**, *184*, 344–349. [CrossRef]
26. Cunha, S.; Tavares, A.; Aguiar, J.B.; Castro, F. Cement mortars with ceramic molds shells and paraffin waxes wastes: Physical and mechanical behavior. *Constr. Build. Mater.* **2022**, *342*, 127949. [CrossRef]

27. Chen, S.; Sun, D.; Wang, C.; Wen, S.; Wu, J.; Yan, C.; Shi, Y.; Chen, C.; Ren, Z. Alumina-based ceramic mold with integral core and shell for hollow turbine blades fabricated by laser powder bed fusion. *Addit. Manuf.* **2022**, *58*, 103046. [CrossRef]
28. *ASTM E1269-11*; Standard Test Method for Determining Specific Heat Capacity by Differential Scanning Calorimetry. ASTM International: West Conshohocken, PA, USA, 2018.
29. Dehghanian, E.; Givi, M.K.B.; Jafari, H. Recent advances in investment casting process: From conventional techniques to additive manufacturing and hybrid strategies. *J. Manuf. Process.* **2021**, *65*, 190–212. [CrossRef]
30. Zhang, W.; Huang, X.; Xu, Y.; Li, M. Environmentally friendly binders for ceramic investment casting molds: A critical review. *J. Eur. Ceram. Soc.* **2023**, *43*, 2345–2359. [CrossRef]
31. Kulkarni, A.; Mishra, S.; Bandyopadhyay, A. Binder formulations for sustainable ceramic processing: A review of recent developments and challenges. *Ceram. Int.* **2023**, *49*, 28472–28486. [CrossRef]

Disclaimer/Publisher's Note: The statements, opinions and data contained in all publications are solely those of the individual author(s) and contributor(s) and not of MDPI and/or the editor(s). MDPI and/or the editor(s) disclaim responsibility for any injury to people or property resulting from any ideas, methods, instructions or products referred to in the content.

materials

MDPI

Article

The Effect of Mold Flux Wetting Conditions with Varying Crucible Materials on Crystallization

Muhammad Anwarul Nazim *, Arezoo Emdadi, Todd Sander and Ronald O'Malley

Materials Science and Engineering, Missouri University of Science and Technology, 1400 N. Bishop Ave., Rolla, MO 65409-0340, USA; omalleyr@mst.edu (R.O.)
* Correspondence: manck8@mst.edu

Abstract: Understanding mold flux crystallization is essential for assessing heat transfer during steel casting. The complexity of the mold gap presents challenges in identifying the optimal testing method and nucleation type. This study investigates how variations in wetting properties influence nucleation dynamics, in particular the wetting behaviors of mold flux in platinum and graphite crucibles and how they affect crystallization temperatures and solidification mechanisms. Advanced analytical techniques, including confocal laser scanning microscopy (CLSM), and differential scanning calorimetry (DSC) were employed to analyze nucleation under different conditions, with calibration using synthetic slag, Li_2SO_4, and thermodynamic equilibrium simulations. The findings highlight the crucial role of crucible materials in modifying nucleation energy barriers and undercooling requirements. These insights enhance the understanding of mold flux behavior, contributing to the refinement of testing methodologies and the optimization of heat transfer and solidification processes in continuous casting.

Keywords: mold fluxes; nucleation; crystallization; crucible materials; wetting conditions; DSC; CLSM

1. Introduction

Mold flux is a multi-component oxyfluoride powder that is employed on top of liquid steel during continuous casting process. The mold powder melts when heated by the liquid steel pool and penetrates between the solidifying steel shell and the mold as casting occurs. The initial slag film that forms in the mold gap is mostly glassy due to the high cooling rates as it quenches against the cold mold wall. Over time, however, the fraction of crystallized phases in the slag film progressively increases as the glassy layer undergoes devitrification [1]. Crystallization, being one of the most pivotal factors for controlling heat transfer, plays a crucial role in steel casting. Alterations in its characteristics can lead to non-uniform horizontal heat transfer and suboptimal lubrication, potentially compromising process efficiency and product quality [2].

The study of mold flux crystallization kinetics provides insights into the crystalline phase fraction as a function of time and temperature. It also reveals the crystallization mechanisms of mold fluxes and helps in understanding variations in crystallization behavior across different flux systems [3]. Sarkar and Li [1] conducted a comprehensive literature review on isothermal and non-isothermal crystallization kinetics studies of mold fluxes. Differential scanning calorimetry (DSC) and confocal laser scanning microscopy (CLSM) are widely used thermo-analytical techniques for investigating crystallization kinetics. As reported in the literature [1], platinum pans or crucibles are commonly employed in the DSC testing of mold fluxes due to their chemical inertness and high melting point.

Platinum is a precious and expensive crucible material. In some cases, especially for mold flux examinations, destructive post-processing for specimen characterization is required, i.e., crucibles are cut and destroyed since mold flux strongly adheres to the inner wall of the crucible. Also, when the crucible is reused, it goes through a cleaning process that involves harsh chemicals, which can lead to safety and cost-related concerns. However, graphite is an inexpensive and abundant high-temperature material. Under conditions of low oxygen potential, graphite demonstrates chemical stability and a high level of resistance to thermal shock. Furthermore, it is a relatively soft material, facilitating machining into a various shapes and configurations [4]. Although graphite tends to oxidize at high temperatures in air, it can still be employed as a crucible material in advanced thermo-analytical techniques such as DSC and CLSM, as a neutral environment is ensured with the purging of high-purity inert gases. Moreover, graphite is an integral part of most mold flux systems. Graphite is the principal component used to control the melting rate of the flux. It is important to note that mold flux wetting behavior varies with the substrate or crucible material with which it is in contact when tested using advanced thermo-analytical techniques.

Wettability describes how well a liquid can spread across a solid surface, assessed by the angle of wetting formed between the substrate and the tangent drawn at the triple point. Wetting is quantified using the contact angle, denoted θ. This angle forms where the substate, liquid, and gas interfaces meet, reflecting the balance of surface tension forces acting on the liquid droplet [5]. A contact angle of 180° signifies complete non-wetting, while, practically, a solid is considered non-wetting if the contact angle exceeds 90° [6]. Conversely, complete wetting occurs when the contact angle is 0°, allowing the liquid to spread spontaneously across the solid surface [5]. Standardized tests, such as DSC and CLSM, provide data on the onset of crystallization. However, in the complex environment of the mold gap during continuous casting, the wetting conditions among the mold, steel, and mold flux remain unclear. Numerous studies [7–13] have explored the wetting characteristics of mold flux droplets on steel substrates using sessile drop tests. These investigations primarily focused on the effects of compositional changes in slag and steel on wettability, arguing that the initial wettability of slag on steel significantly influences slag entrapment during the casting process and, consequently, the surface quality of the final slab. However, the literature reveals a notable knowledge gap regarding the impact of mold flux wetting behavior on copper molds and its role in crystallization, which in turn affects interfacial heat transfer during the casting process, as nucleation usually occurs on the mold wall side of the mold gap as illustrated in Figure 1.

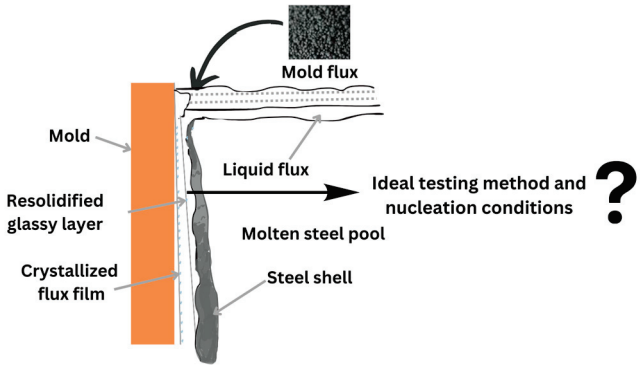


Figure 1. A schematic of the continuous casting process (not to scale), illustrating the complex mold gap region, where ideal testing methods and nucleation conditions are not well established.

Kromhout [14] reported in the literature that pumping during oscillation forces the liquid slag to spread on the copper mold surface. The interface adhering is non-wetting

in that case. However, the conditions during casting seems to be opposite to this claim and require additional investigation. Park and Sohn [15] examined interfacial heat transfer between mold flux and a copper disc mold simulator (CDMS) as a function of the average waviness of the flux disc, where the liquid slag was poured into the concentric disc groove of the CDMS. Their study did not address the wettability of mold flux on the copper mold and the nature of the environment.

Apart from the copper disc mold simulator, a lab-scale mold simulator is another tool for understanding heat transfer during steel casting, particularly concerning the evolution of the flux film between the mold and cast steel. The literature offers a broad range of research on mold simulators [16–26], covering topics such as mold flux crystallization, heat transfer through mold flux, lubrication of mold flux, and interfacial thermal resistances in continuous casting of various steel grades. Recently, Nazim et al. [27] have implemented a novel approach to an optical fiber-instrumented mold simulator that can be further used to enhance the understanding of heat transfer through mold flux. According to the study, high-resolution optical fiber-based distributed temperature sensors can capture transient heat transfer phenomena. Figure 2 shows a micrograph of the mold flux film's cross-section recovered from a mold simulator experiment. The flux film contains two component layers: a crystallite layer, which forms from the devitrification of the glassy layer and is non-dendritic in appearance, and a dendritic layer that grows against the heat transfer and is close to the steel side. These dendrites may nucleate heterogeneously from the pre-existing non-dendritic crystals, as supported by a previous study [28]. The key challenge lies in determining the testing methodology that best represents this environment and whether nucleation in the system is primarily heterogeneous or homogeneous. Another important consideration is the nature of this environment, and whether the mold wall contributes to wetting for nucleation, though the exact answer remains unclear.

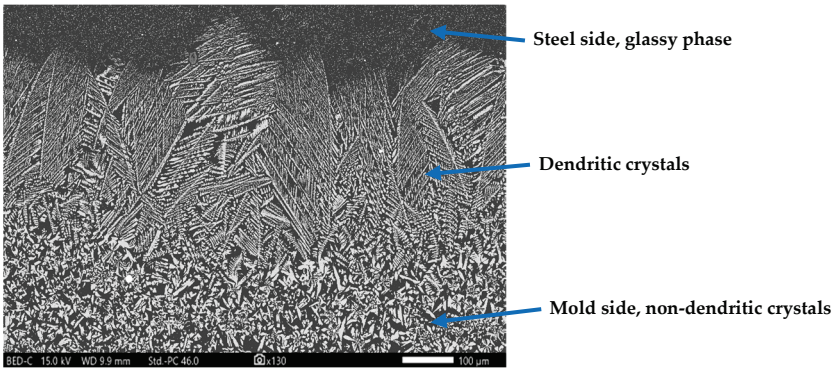


Figure 2. The micrograph of the mold flux film cross-section obtained through scanning electron microscopy (SEM). Courtesy: US Steel Research and Technology Center, PA, USA.

To the best of our knowledge, no study has been performed to date on the effect of crucible material's wettability on crystal nucleation in continuous casting mold flux. Novak et al. [29] investigated the wetting behavior of graphite and platinum substrates at 1550 °C with borate oxide glass systems containing B_2O_3 with an average basicity of 0.21. This study showed that contamination occurred in the oxide glass specimens as the graphite substrate wetted them, due to high adhesion and the formation of reaction products at the interface. However, continuous casting mold flux has a higher basicity, is silicate-based, and is utilized in different applications than the borate glass system. Additionally, the operating temperature of mold flux is significantly lower, and its wetting behavior with graphite and platinum appears to be the opposite of what was observed in the present study due to the formation of boron carbide.

This paper aims to investigate the influence of crucible wetting behavior on crystallization of an industrial-grade mold flux. Thermo-analytical techniques, including DSC and CLSM, were used to quantify the onset of primary crystallization of the flux through non-isothermal testing at various cooling rates. The flux specimens were characterized using scanning electron microscopy coupled with energy dispersive X-ray spectroscopy (SEM-EDS) and X-ray diffraction (XRD). Additional calibrations were conducted using gold and Li_2SO_4, followed by thermodynamic equilibrium simulations in Factsage® to assess potential reaction with graphite. SEM-EDS analysis was performed post-mortem at the interface to assess potential reactions between the mold flux specimen and the graphite crucible wall. This study aims to enhance understanding of how wetting versus non-wetting affects crystal nucleation in mold flux, depending on whether platinum or graphite crucibles are used. The findings are of practical significance, as carbon or graphite is an essential component in mold flux design. Moreover, this manuscript may pave the way for future investigations into the influence of wetting characteristics on mold flux in the complex environment of the meniscus during continuous casting of steels.

2. Materials and Methods

2.1. Specimen Preparation

The CaO-SiO_2-based mold flux used in this study was obtained from a mold flux manufacturing company. The flux is used to cast medium carbon, hyper-peritectic steel grades in a thin slab caster. Tables 1 and 2 tabulate the flux's chemical composition and physical properties, respectively. A specimen size of 60 mg was maintained for each experiment in both DSC and CLSM. Raw mold flux powder was calcined at 725 °C for 5 h in air, then pre-melted in a resistance furnace at 1300 °C. The molten flux was subsequently poured and rapidly quenched between two room-temperature copper plates. This process promotes the oxidation of the flux powder and removes volatile carbon and carbonaceous elements. The resulting glassy specimens were later used for crystallization studies in DSC and CLSM.

Table 1. Chemical composition [wt.%] of the mold flux that was used in this study.

CaO	SiO_2	Na_2O	F	Al_2O_3	MnO	Li_2O	Fe_2O_3	MgO	C (Total)
31.7	27.5	9.2	7.6	5.2	2.8	0.7	0.5	0.3	9.4

Table 2. Physical properties of the mold flux.

Basicity (CaO/SiO_2)	Solidification Temperature [°C]	Viscosity [Poise] at 1300 °C
1.15	1130	0.7

2.2. Test Procedures and Methods

2.2.1. Crystallization Temperature Measurements Using Differential Scanning Calorimetry (DSC)

The DSC experiments were performed using a Thermal Gravimetric Analyzer/Differential Scanning Calorimeter (TGA-DSC), model Netzsch 449 F5 Jupiter (Netzsch-Gerätebau GmbH, Selb, Germany), with argon as the purge gas. Before testing, the setup was calibrated using pure substances (indium, tin, aluminum, bismuth, and gold) for both temperature and sensitivity calibration. A new baseline was established for each specific heating and cooling rate using empty crucibles, both graphite and platinum. After calibration, 60 mg of glassy specimens were heated to 1300 °C at a rate of 20 °C/min and held for 2 min for volatilization, followed by continuous cooling to room temperature at various rates of 5, 10, 15, 20, 25, and 30 °C/min, using platinum and graphite crucibles

separately. The controls ensured that the test specimen and the reference temperatures were maintained the same throughout the experiment. The tests were conducted in an inert environment with an argon flow of 50 mL/min. The platinum pans used in the tests were 5 mm long with an inner diameter of 5 mm, while the graphite crucibles were 7 mm long and had a similar inner diameter. High-purity platinum pans were sourced from an external vendor, while graphite crucibles were machined from high-purity graphite rods.

2.2.2. Observation of Onset of Crystallization Using Confocal Laser Scanning Microscopy (CLSM)

A 60 mg glassy flux specimen was placed in a graphite crucible, and the experiment was conducted in the melting stage using a Lasertec VL2000DX-SVF17SP High-Temperature CLSM system (Yonekura Mfg. Co. Ltd., Osaka, Japan) in an ultra-high-purity argon environment. Details of the experimental apparatus have been discussed elsewhere [30]. The thermal cycle in the CLSM was identical to that of the DSC, except for testing only one cooling rate (20 °C/min). The heating and holding phases were the same, with heating provided by light emitted from a halogen lamp. The test aimed to observe in situ crystallization on the flux surface within the graphite crucible during non-isothermal experiments at a cooling rate of 20 °C/min. The crystallization process was monitored and video recorded at a scanning rate of 60 frames per second. The specimen's image was captured based on contrast differences produced by the scanning laser, operating within the ultraviolet wavelength range.

2.2.3. X-Ray Diffraction for Phase Detection

XRD analysis is widely used to identify crystals formed during crystallization processes. Post-experiment specimens from the graphite crucibles were taken from the CLSM experiment, crushed into powder, and subjected to XRD analysis. Following the same thermal cycle as in the CLSM experiment, the specimen was cooled slowly to 1000 °C at a rate of 5 °C/min; this temperature is below the primary crystallization temperature, allowing sufficient time for primary crystals to nucleate. The specimen was then rapidly quenched to room temperature at a 2000 °C/min cooling rate. This process ensured that the formed primary crystal phase was retained and detectable using SEM and XRD. The XRD analysis was conducted using a Panalytical X'Pert Multi-Purpose Diffractometer (Malvern Panalytical B.V., Almelo, The Netherlands) with a 1.8 kW sealed copper X-ray source. The resulting peak list was compared with the Inorganic Crystal Structure Database (ICSD) data. XRD was also used to characterize the crystal phase of a common standard (Li_2SO_4) cooled from the melt.

2.2.4. Computational Thermodynamic Analysis

Thermodynamic simulations were performed to assess the potential reactions between carbon or platinum and the common standard, Li_2SO_4. The equilibrium phases were calculated by simulating the reaction of 1 g of carbon or platinum with Li_2SO_4 using the Equilib module in FactSage® 8.3 (Thermfact Ltd. and GTT Technologies, Montreal, QC, Canada/Aachen, Germany). The FToxid and FTmisc databases were utilized for the simulation. Phase stability diagrams were generated for a temperature range from 1000 °C to 0 °C.

2.2.5. Calibration of Graphite Crucible Using Synthetic Slag, Pure Gold, and Li_2SO_4

The graphite crucible was calibrated using a gold standard in DSC with a moderate cooling rate of 20 °C/min. Additionally, a synthetic slag was tested in both graphite and platinum crucibles under the same cooling rate in DSC to evaluate the reactivity between the amphoteric oxide (FeO/Fe_2O_3 and MnO) components in the mold flux and the inner

wall of the graphite crucible. Furthermore, a common standard, Li_2SO_4, was tested in both crucibles using the same procedure for calibration purposes.

2.2.6. Elemental Map Using Scanning Electron Microscopy Coupled with Energy Dispersive X-Ray Spectroscopy (SEM-EDS)

SEM was used to further investigate the precipitated crystals. Additionally, SEM-EDS was employed for compositional analysis of the post-CLSM specimens at room temperature and the post-experiment DSC mold flux specimen. It was also used to examine the interface of the graphite-run DSC specimen in a TESCAN VEGA SEM (Bruker Nano GmbH, Berlin, Germany). The post-experiment flux specimen was mounted in epoxy and polished to 0.5 microns. The polished surface was then coated with a gold–palladium (Au–Pd) layer to enhance electrical conductivity using a Denton sputter coater, set to 8 mA for 45 s. A copper tape was applied to create an electrical path from the bottom to the top (surface) of the specimen for SEM analysis. This analysis helps determine whether carbon particles from the graphite crucible infiltrated the mold flux specimen, providing insights into potential interactions at the interface between the mold flux and the graphite inner wall.

3. Results and Discussion

3.1. Crucible Material-Dependent Wetting Characteristics

Mold flux in contact with the mold wall/substrate is considered to be a surface-assisted heterogeneous nucleation process, owing to its lower energy requirement across the bonding interface than that of homogeneous nucleation [31]. In heterogeneous nucleation, the wetting/contact angle (θ) characterizes the interaction between the newly formed phase and the substrate/mold wall, by reducing the energy needed. The free energy required for heterogeneous nucleation is equal to the product of homogeneous nucleation and a function of the contact/wetting angle (θ), as follows [31]:

$$\Delta G_{heterogeneous} = \Delta G_{homogeneous} \times f(\theta) \quad (1)$$

where $f(\theta) = \frac{2-3cos\theta+cos^3\theta}{4}$ and θ is the wetting/contact angle.

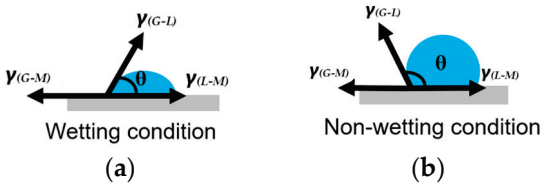
The crucible–mold flux system best represents the gas–liquid–mold system. The classical Young's equation defines the equilibrium contact angle at the interface of the system, which is determined by the balance of surface energies, as follows:

$$\gamma_{(G-M)} = \gamma_{(G-L)} + \gamma_{(L-M)}\, cos\theta \quad (2)$$

where γ = surface tension, and (G–M), (G–L), and (L–M) represent the gas–mold, gas–liquid and liquid–mold interfaces, respectively.

Figure 3 illustrates the schematics of wetting and non-wetting conditions of a droplet of a material (in this case, mold flux) that solidify from a melt in contact with different crucible materials/mold wall. The cross-section of the post-experiment DSC solidified mold flux specimens revealed concave and convex surface shapes for platinum and graphite crucibles, respectively. Figure 4 shows the post DSC experiment mold flux in graphite and platinum crucibles and the schematics of the surface shape of solidified flux specimens in graphite and platinum crucibles from a cross-sectional view.

The mold flux exhibited non-wetting behavior with a large contact angle with the graphite crucible, whereas it wetted the platinum crucible with a small contact angle, resulting in opposite surface orientations.



(**a**) (**b**)

Figure 3. Schematics of (**a**) wetting and (**b**) non-wetting conditions of mold flux in contact with mold wall.

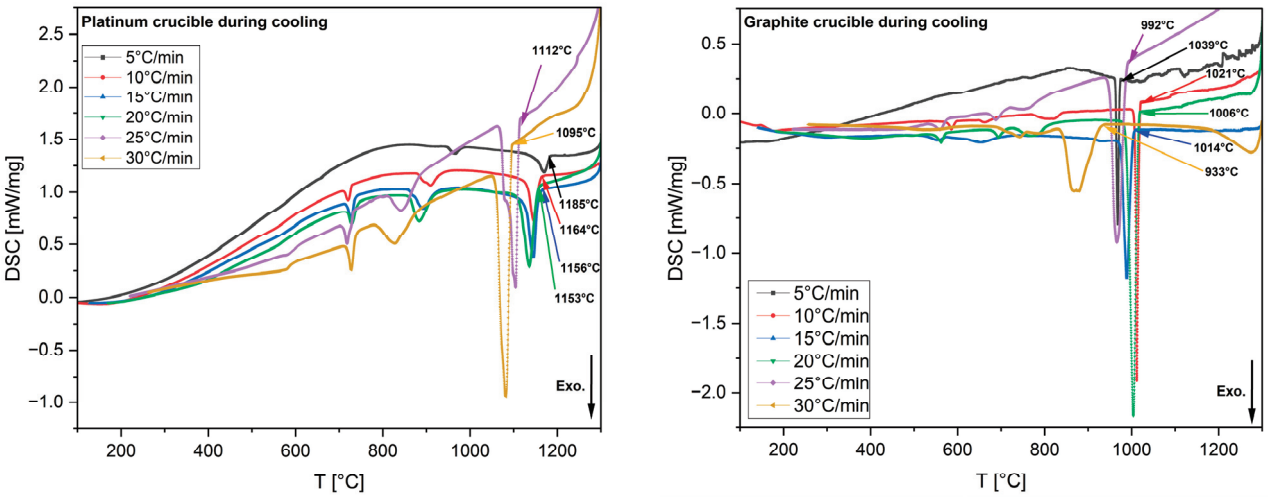


(**a**) (**b**)

Figure 4. Schematics of the section slice of the flux-crucible appearance right after the DSC test in (**a**) a graphite crucible and (**b**) a platinum crucible.

3.2. Measurements of Crystallization Temperature Depending on Crucible Materials in DSC

In the DSC, changes in heat flow or calorific values were measured across various temperatures. During fusion or crystallization, the DSC curve showed an exothermic peak, indicating the release of excess heat during crystallization. This process decreased the system's entropy, driving it to a lower energy state. Figure 5 presents the heat flow versus temperature curves from non-isothermal DSC tests performed on 60 mg mold flux specimens at various cooling rates (5, 10, 15, 20, 25, and 30 °C/min) using platinum and graphite crucibles. Crystallization temperatures were determined by the onset of exothermic peaks (shown in a downward direction in Figure 5) during cooling.



(**a**) (**b**)

Figure 5. DSC heat flow curves from non-isothermal tests of mold flux specimens at various cooling rates, which were conducted in (**a**) platinum crucibles and (**b**) graphite crucibles. The legends indicate 5, 10, 15, 20, 25, and 30 °C/min cooling rates. Arrows mark the onset of primary crystallizations for each cooling rate, with arrow colors corresponding to the DSC curves. In the images above, the exothermic heat flow is directed downward.

In Equation (2), θ becomes small when the surface tension between the two phases is low. Complete wetting is defined as $\theta = 0$. When $\theta < 90°$, in the wetting condition, surface tension and free energy for nucleation increase. This was observed in mold flux tested in platinum crucibles. In contrast, in a non-wetting scenario, more undercooling is required to

provide the additional free energy for nucleation. As a result, the primary crystallization temperature decreases under non-wetting conditions, such as when the mold flux was tested in graphite crucibles. All DSC experiments with mold flux in graphite crucibles showed lower primary crystallization temperatures than those with platinum crucibles, across all cooling rates. Figure 6 illustrates this phenomenon across the range of cooling rates for both crucible materials. In Figure 6a, continuous cooling transformation (CCT) curves are plotted based on the primary crystallization tested for all cooling rates in both graphite and platinum crucibles. Figure 6b shows the onset of primary crystallization shifting to lower temperatures when graphite crucibles were used. It was also observed that the exothermic peaks on the DSC curves shifted to lower temperatures, and the shape of these peaks became sharper as the cooling rate increased. A similar trend was seen for both crucibles. This can be attributed to the dependence of crystal nucleation and growth rates on viscosity and undercooling. At higher cooling rates, viscosity increases rapidly, requiring a stronger driving force to initiate mold flux nucleation [2,32]. For simplicity, only the primary crystallization temperatures of the mold flux were considered in this study, as secondary crystallization temperatures are beyond the scope of this paper. There was also insignificant difference (only 5 °C) in the mold flux melting peaks for both crucibles during the heating at a heating rate of 20 °C/min (Figure 7), which could have been due to small experimental errors. This small difference in the melting onset temperature is negligible compared to the crystallization temperature difference during cooling, which shows evidence of the effect of wetting on mold flux crystallization.

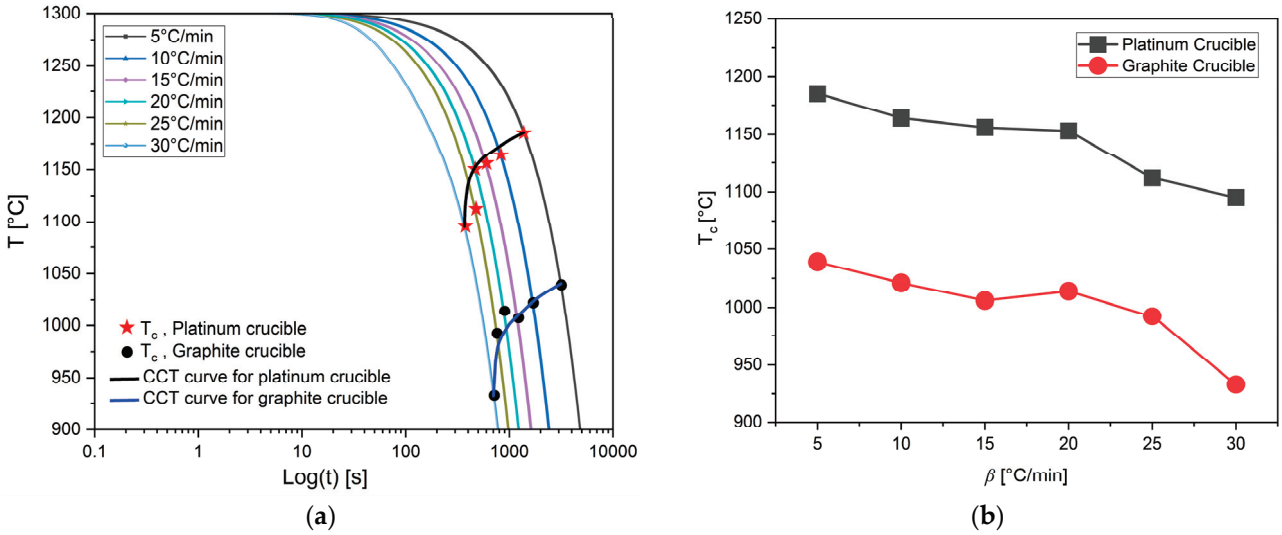


Figure 6. (**a**) The diagram shows the standard CCT curves of the mold flux constructed from crystallization temperatures at various cooling rates. Red stars and black circles represent the crystallization temperatures, T_c, for all different cooling rates in platinum and graphite crucibles, respectively. The black and blue curves show CCT curves for platinum and graphite crucibles, respectively. The legend indicates the cooling rates. (**b**) The difference in the onset of primary crystallization temperatures of the mold flux at different cooling rates in platinum and graphite crucibles.

Table 3 summarizes the various onset temperatures for primary crystallization in graphite and platinum crucibles. On average, the onset of primary crystallization occurred at 143 °C lower during cooling when switching from a platinum crucible to a graphite crucible. In the case of the platinum crucible, good wettability between the liquid flux and the crucible appeared to favor the heterogeneous nucleation of the solid. As a result, increased wetting promoted crystallization. Consequently, lower onset crystallization temperatures (higher undercoolings) were observed in the presence of graphite crucibles. Table 4 presents the mass losses during all tests in both crucibles in the DSC. On average,

the DSC tests showed a mass loss of approximately 3%, indicating minimal material degradation or volatilization during the experiments. Moreover, the losses were decreased with increased cooling rates for each crucible type.

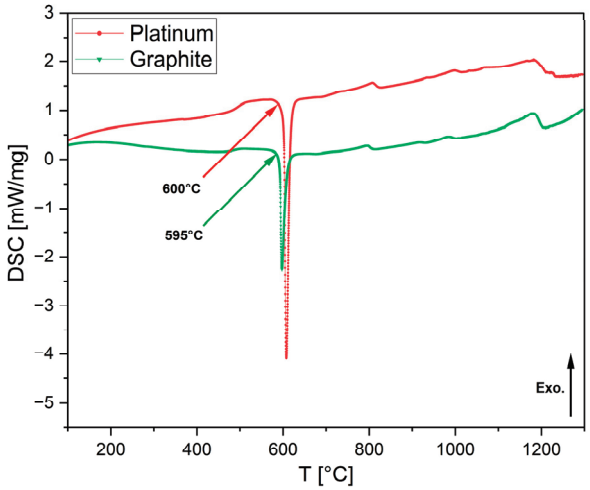


Figure 7. DSC heat flow curves from non-isothermal tests of mold flux specimens at 20 °C/min heating rate, which were conducted in platinum and graphite crucibles. Arrows mark the onset of mold flux melting peaks with the temperatures during heating, with arrow colors corresponding to the DSC curves. In the images above, the exothermic heat flow is directed upward.

Table 3. The onset of primary crystallization temperatures in graphite and platinum crucibles at various cooling rates.

Cooling Rates [°C/min]	Primary Crystallization Temperatures [°C]		Crystallization Temperature Difference [°C]
5	1185	1039	146
10	1164	1021	143
15	1156	1006	150
20	1153	1014	139
25	1112	992	120
30	1095	933	162
Tested crucible	Platinum	Graphite	Average: 143

Table 4. Mass loss during all tests in both crucibles at various cooling rates.

Cooling Rates [°C/min]	Mass Loss During the Test [%]	
5	5	5
10	3	4
15	2.5	4
20	2.5	2
25	2.5	3
30	2	2
Tested crucible	Platinum	Graphite

3.3. Observation of Onset of Primary Crystallization in CLSM

In situ crystal nucleation and growth on the mold flux liquid surface were observed using CLSM. A graphite crucible was used to analyze the mold flux in CLSM. Figure 8, accompanied by a scale bar for reference, presents images captured at specific times and

temperatures during the crystallization process of the flux, when the temperature was decreasing from the melting point at a cooling rate of 20 °C/min. Initially, a bright spot was identified and focused on once the flux specimen became fully liquid, which occurred 2 min after homogenization at 1300 °C, following a heating rate of 20 °C/min. As the cooling continued, the edge of the crystal phase emerged from the left and expanded diagonally toward the right. The growing crystal phase became visible on the surface of the molten flux, appearing to move through the molten material. As the temperature gradually decreased, the primary crystal phase continued to grow. In Figure 8b, secondary dendritic arms are visible, forming perpendicular to the surface as the temperature decreases.

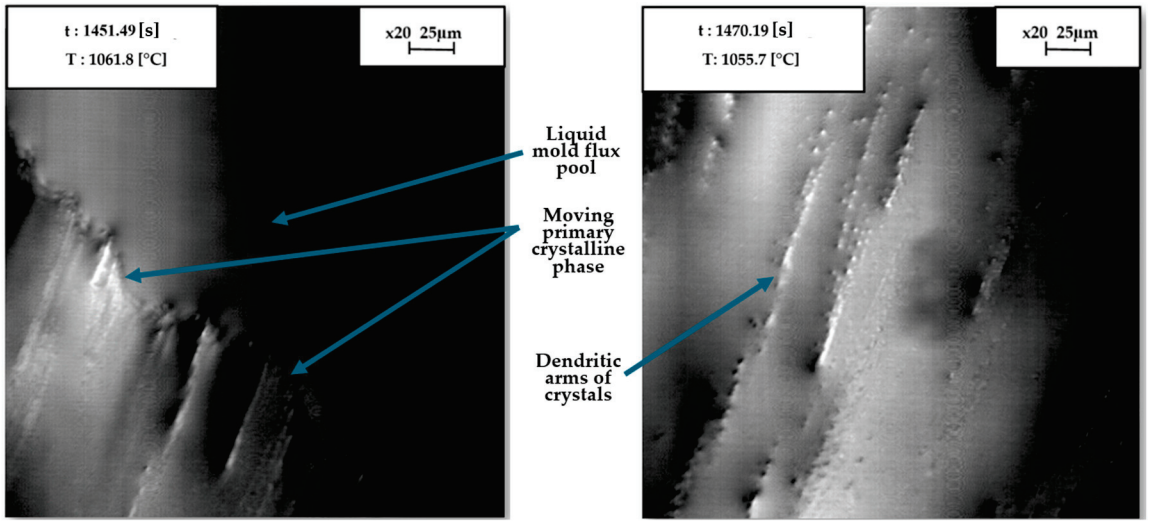


Figure 8. The crystallization process of the mold flux specimen in the graphite crucible was observed at a cooling rate of 20 °C/min. The images were focused on the center of the specimen surface, where the bright spot was located: (**a**) growth of the primary crystalline phase as it moved diagonally across the liquid flux; (**b**) instantaneous time of progressed undercooling, which led to crystal growth and the development of secondary dendritic arms perpendicular to the surface. t and T denote time and temperature respectively.

The onset of primary crystallization for the tested flux at the same cooling rate of 20 °C/min in the CLSM was slightly offset (47 °C) compared to the DSC results in the graphite crucible. Previous studies in the literature [33] indicate that the temperature difference between the specimen surface and the bottom of the crucible (where the thermocouple is positioned) can be as much as 40 °C in CLSM, which is consistent with the findings of this study. The confocal microscope uses spatial filtering to create a focused illumination spot. As a result, crystallization can only be visualized at the focused spot in CLSM [1]. Therefore, the quantification of crystallization temperature in CLSM is less precise than in DSC. Using CLSM, locating the nucleation point is challenging; however, crystal growth can be visualized. Furthermore, nucleation appeared to occur on the crucible wall, with crystals migrating from one side of the crucible in CLSM, as shown in Figure 8.

These crystals apparently nucleate at low temperatures on the crucible wall, and it is not possible to directly measure the temperature of the crucible wall. Instead, reliance must be placed on the system's overall temperature, which is detected at the bottom of the crucible by the thermocouples in CLSM. Nevertheless, the onset of primary crystallization temperature in the graphite crucible found in CLSM was significantly lower than that found in the DSC test in the platinum crucible under the same conditions. This phenomenon is consistent with the observation that non-isothermal crystallization tests of mold flux in a non-wetting graphite crucible resulted in delayed crystal precipitation during cooling. This

delay was attributed to the need for additional energy to overcome the nucleation barrier, facilitated by greater undercooling.

3.4. Identification of Primary Crystal Phase in XRD and SEM-EDS

The flux specimen, quenched in CLSM after primary crystal formation, was further analyzed using SEM-EDS. The post-experiment CLSM mold flux specimen in the graphite crucible was found to form into a spherical shape due to non-wetting interactions with the graphite wall. As a result, the specimen was easily recovered from the crucible. Microstructural analysis of the flux specimen, combined with EDS (Figure 9), revealed the presence of primary cuspidine crystals ($Ca_4Si_2O_7F_2$) dispersed within a glassy matrix. Elemental mapping of the observed area shows that Ca, Si, O, and F are concentrated in the white regions of the BSE image, while Na, Al, Si, and O are concentrated in the gray areas. This illustrates the distribution of the cuspidine crystalline phase within the glassy matrix. Since the primary crystals nucleated and grew at a slow cooling rate (5 °C/min) from 1300 °C to 1000 °C before rapid cooling, the morphology of the cuspidine crystals was found to be faceted, which was consistent with findings from a previous study [2].

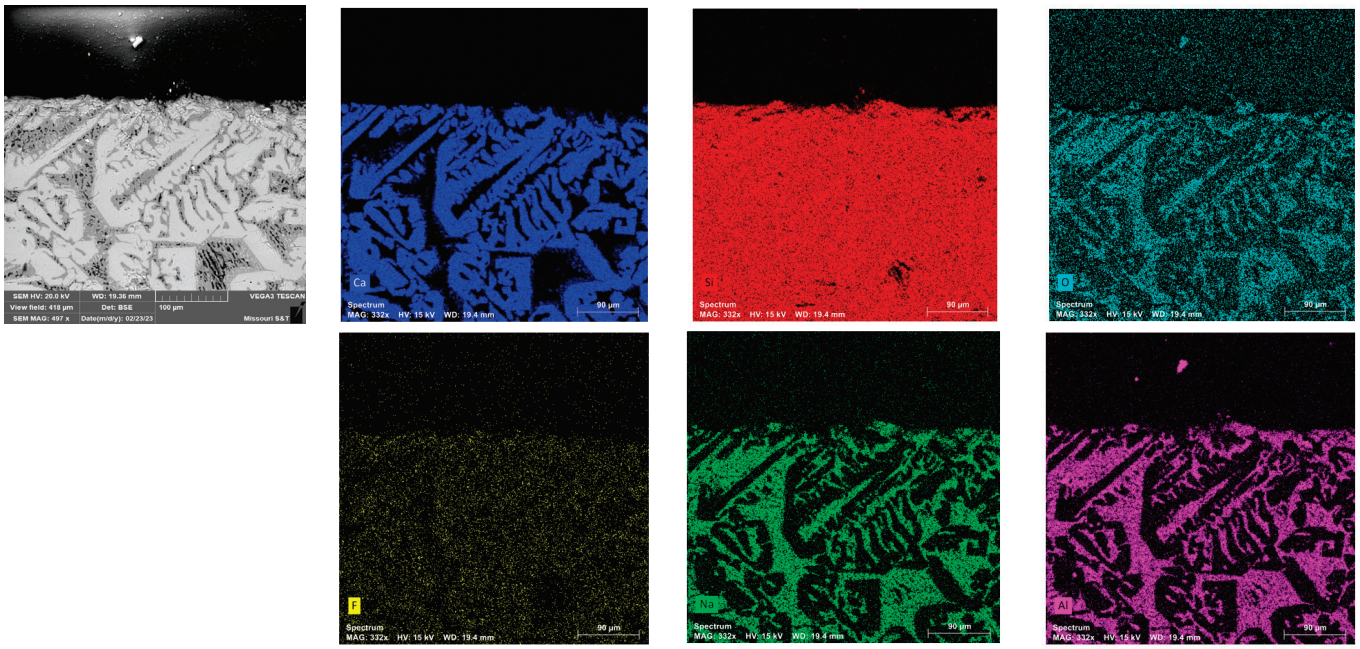


Figure 9. The backscattered electron (BSE) SEM image of the polished and coated mold flux specimen is shown in the top-left corner, along with images generated from elemental maps using SEM-EDS. The black region at the top of the images represents the epoxy area.

To confirm the accuracy of the obtained results, another specimen underwent the same thermal cycle and was then crushed into powder for XRD analysis. This SEM-EDS observation was consistent with the XRD results, as shown in Figure 10, which identified cuspidine as the primary and only crystalline phase. The absence of any other phases in the XRD analysis can be attributed to its glassy matrix appearance in the specimen. Although the XRD results showed distinct diffraction peaks for cuspidine, a prominent amorphous hump was initially observed at low angles. This hump is characteristic of a glassy phase, likely due to the significant presence of a glassy matrix. The SEM-EDS analysis, mentioned earlier, also identified the elements that seems to be in the glassy matrix.

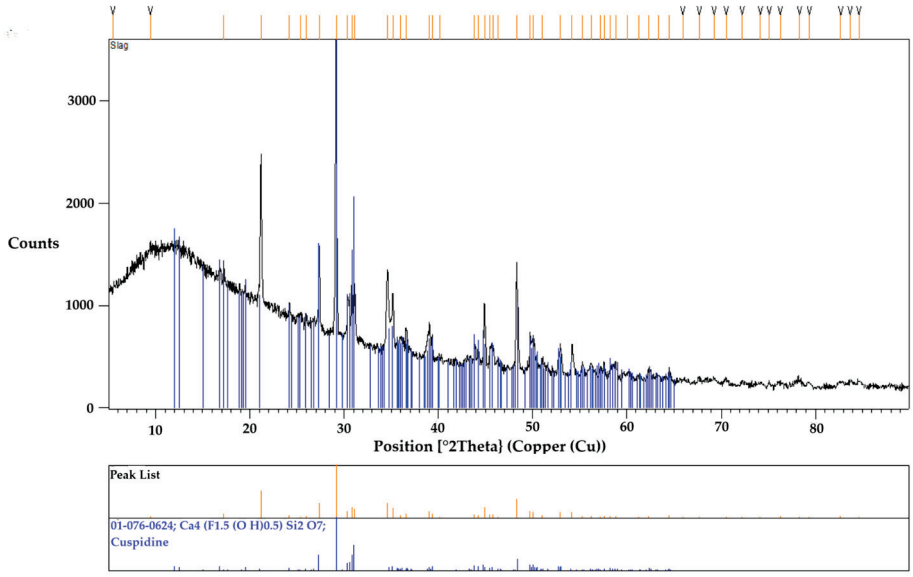


Figure 10. The XRD result of the mold flux specimen shows cuspidine as the primary crystal phase.

3.5. Sensitivity of Graphite Crucible in DSC

To verify its sensitivity, the graphite crucible was calibrated in the DSC using a gold standard at a moderate cooling rate of 20 °C/min. The calibrated DSC curves for both heating and cooling are shown in Figure 11.

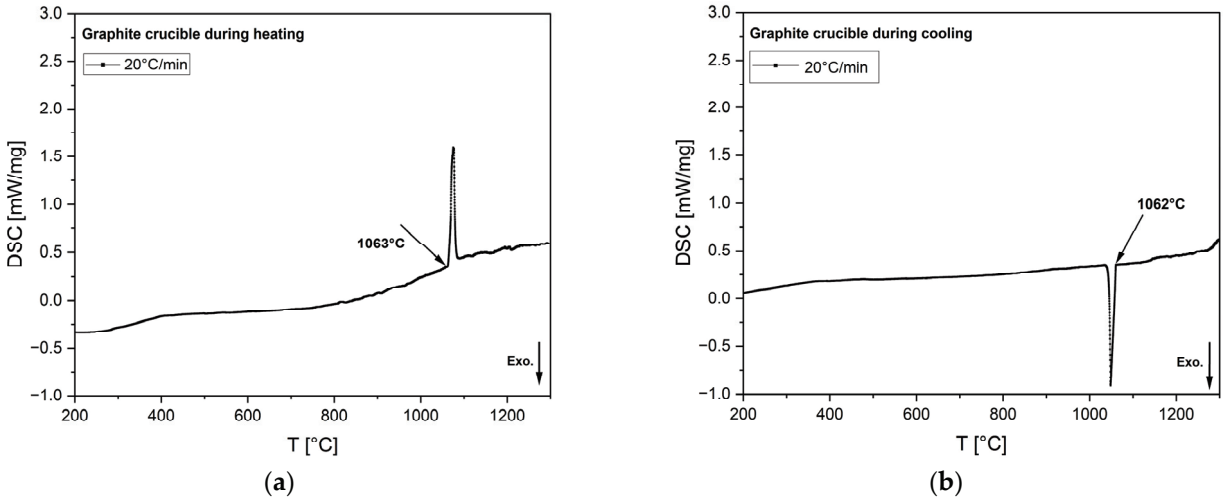


Figure 11. DSC heat flow curves of gold tested in graphite crucible during (**a**) heating and (**b**) cooling at a 20 °C/min heating/cooling rate. Arrows indicate the onset of solidification or phase transformation, corresponding to the temperature. In the images above, the exothermic heat flow is directed downward.

The standard phase transition temperature of gold is 1064 °C. Gold tested in the graphite crucible displayed good agreement with the expected standard transformation, with deviations of only 1 °C during heating and 2 °C during cooling, which verifies the test equipment and methodology.

Notably, there is a possibility of a reaction between the transition metal oxides in the mold flux and the graphite crucible. To eliminate this factor, a synthetic slag was tested in the DSC (20 °C/min cooling rate) using both graphite and platinum crucibles. Table 5 presents the chemical composition of the slag, which is devoid of transition metal oxides such as Fe_2O_3 and MnO.

Table 5. Chemical composition [wt.%] of the synthetic slag that was used in this study.

Specimen ID	CaO	SiO_2	Al_2O_3	Na_2O	F	Basicity
SA-3	39.3	34.1	10	7.5	9.1	1.15

A higher-basicity synthetic slag that readily crystallizes during cooling was selected for the experiment. Notably, the onset of primary crystallization occurred at 21 °C lower in the graphite crucible than the platinum crucible, despite the synthetic slag containing no transition metal oxides. This observation supports the notion that the wetting characteristics between the slag and the inner wall of the platinum crucible promote nucleation and that the differences in crystallization temparature are not the result of reactions with the crucible. This experiment required an additional 21 °C of undercooling for the initial phase transition. Figure 12 illustrates the exothermic peaks of phase transitions during the cooling of synthetic slags in both graphite and platinum crucibles, tested at a cooling rate of 20 °C/min.

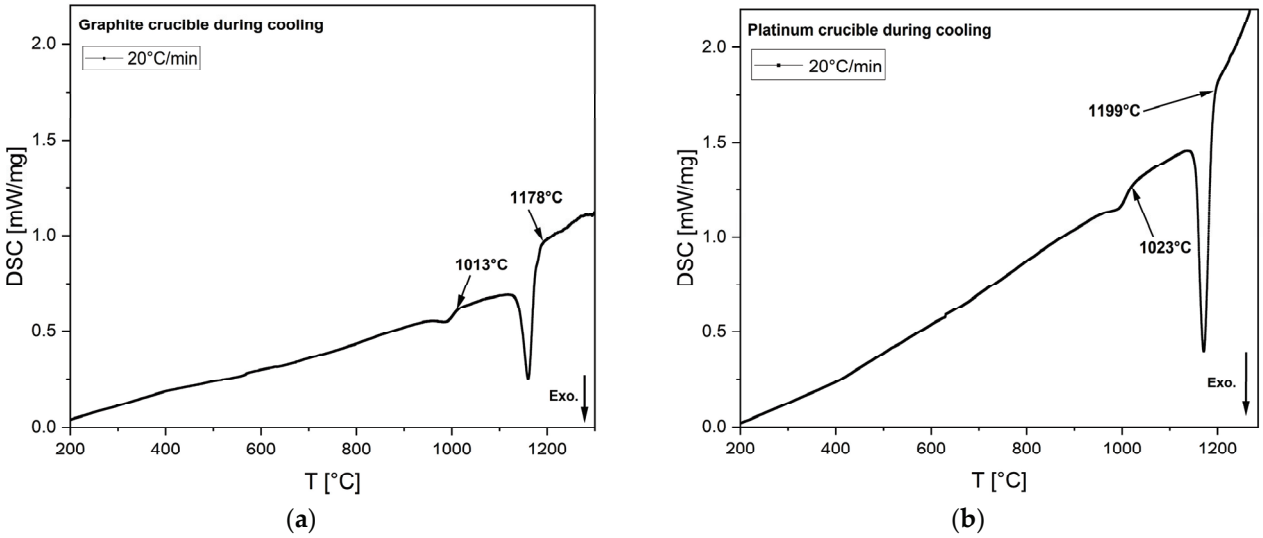


Figure 12. DSC heat flow curves of synthetic slags tested in (**a**) a graphite crucible and (**b**) a platinum crucible at a cooling rate of 20 °C/min. Arrows indicate the onset of solidification or phase transformation corresponding to the temperature. In the above pictures, the direction of exothermic heat flow is downward.

Li_2SO_4 is the only standard calibration material compatible with both graphite and platinum crucibles. Consequently, it was tested in the DSC at a cooling rate of 20 °C/min using both crucible types to measure the phase transformation temperature, as shown in Figure 13. The melting temperatures during heating were found to be very similar: −3 °C for the graphite crucible and +4 °C for the platinum crucible, relative to the standard melting temperature of Li_2SO_4 (578 °C). During cooling, the phase transformation temperatures were also comparable, measuring 572 °C for the platinum crucible and 565 °C for the graphite crucible. The −6 °C temperature deviation observed in the platinum crucible could be attributed to operational error, whereas the −13 °C offset for the graphite crucible is likely due to a more pronounced non-wetting condition. This condition may necessitate greater undercooling to supply the additional free energy required for nucleation to occur. After the DSC experiment, the Li_2SO_4 specimen tested in the graphite crucible was collected and ground into powder for XRD analysis. To remove any moisture content, the specimen was preheated prior to analyzing. The diffraction peaks confirmed the presence of only Li_2SO_4, with no additional phases observed from the ICSD. Figure 14 presents the XRD results.

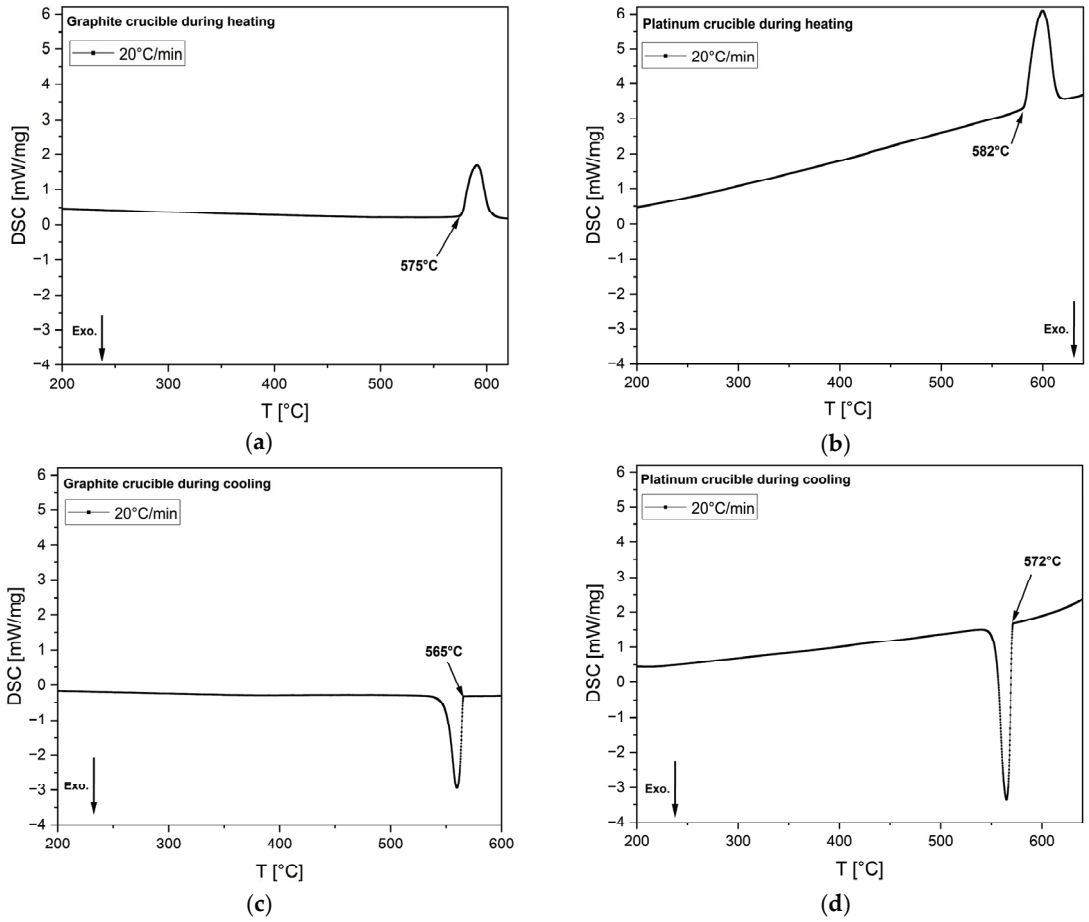


Figure 13. DSC heat flow curves of the standard material Li_2SO_4 tested under the following conditions: (**a**) in a graphite crucible at a heating rate of 20 °C/min; (**b**) in a platinum crucible at a heating rate of 20 °C/min; (**c**) in a graphite crucible at a cooling rate of 20 °C/min; and (**d**) in a platinum crucible at a cooling rate of 20 °C/min. Arrows mark the onset of solidification or phase transformation at the corresponding temperatures. In the images above, exothermic heat flow is directed downward.

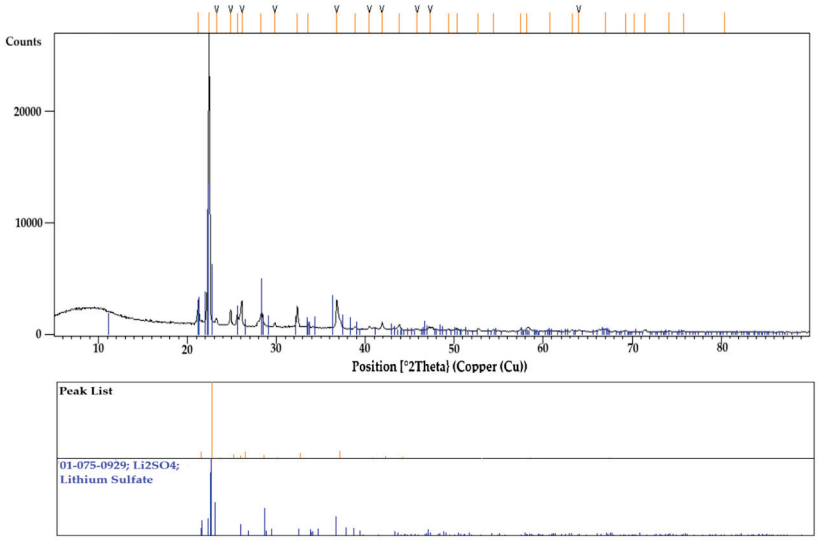


Figure 14. XRD result of Li_2SO_4 specimen showing the only phase of lithium sulfate tested in the graphite crucible.

3.6. Thermodynamic Equilibrium Simulations of Li_2SO_4 with Carbon and Platinum

Potential interfacial reactions between Li_2SO_4 and either platinum or graphite were investigated using thermodynamic equilibrium simulations. Figure 15 presents the phase stability diagrams for reactions involving 1 g of carbon (C) or platinum (Pt.) with Li_2SO_4 over the temperature range of 1000 °C to 0 °C, generated using FactSage®. In both cases, Li_2SO_4 solidified at 578 °C without the formation of any additional phases. The experimental results were in close agreement with the thermodynamic simulation predictions. Therefore, the observed reduction in the solidification temperature of Li_2SO_4 in the graphite crucible can be attributed solely to its wetting behavior.

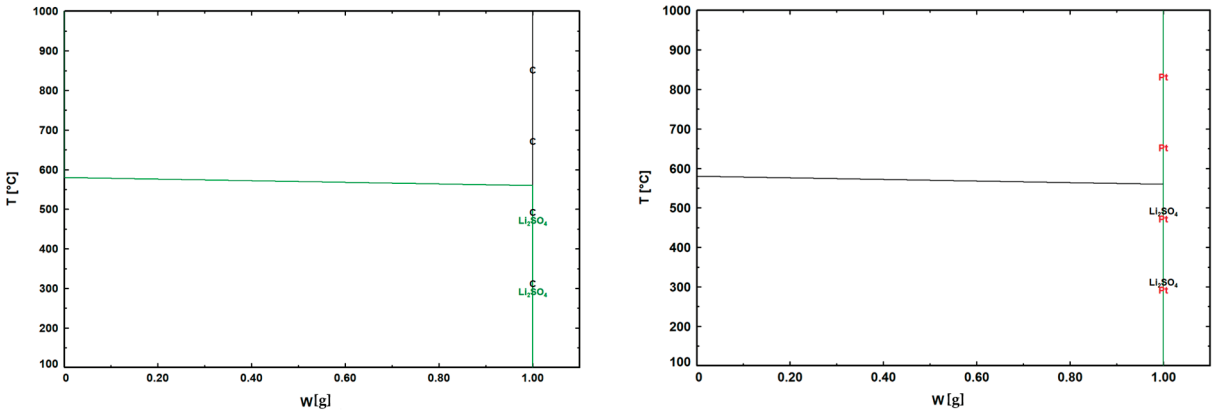


Figure 15. Phase evolution in equilibrium for the following reactions: (**a**) C with Li_2SO_4; and (**b**) Pt. with Li_2SO_4, as determined through thermodynamic calculations.

3.7. Detection of Potential Interactions at the Interface of Flux and Graphite Crucible in SEM-EDS

After the DSC experiment, the mold flux specimen tested in the graphite crucible at a cooling rate of 20 °C/min was recovered and mounted in epoxy to enable grinding and polishing. The specimen was coated with an Au-Pd layer and subjected to SEM-EDS analysis to investigate potential interfacial reactions. Prior to testing, the mold flux specimens were calcined to eliminate any carbon content in the flux.

Figure 16 presents the elemental maps obtained through SEM-EDS from a cross-section of the flux specimen. The image was captured to include a portion of the epoxy for reference. The EDS analysis confirmed that no appreciable carbon was detected within the mold flux and no reaction layers were observed at the flux–crucible interface. This indicates no reactions likely occurred between the mold flux and the graphite crucible's inner wall during the DSC experiments and that no chemical reactions between the flux specimen and the graphite crucible occurred. This analysis clarified that the observed variations in crystallization behavior were due to physical wetting effects rather than chemical interactions, highlighting the role of the crucible material in influencing crystallization.

3.8. Wetting Conditions on Crystallization

Mold flux nucleation or cuspidine crystallization is dominated by solid wetting in the liquid–solid–substrate system. On the other hand, there is a gas–liquid–mold interface in the vicinity of the mold wall side in the mold gap. The wetting of the liquid to the crucibles in DSC and CLSM does not necessarily indicate that the solid also wets the crucible material. In these experiments, cuspidine appeared to be preferentially nucleated under liquid-wetting conditions, suggesting that the solid also wets the substrate as well. Therefore, there appears to be some correspondence between the solid wettability and the inherent liquid wettability to lower the overall interfacial energy.

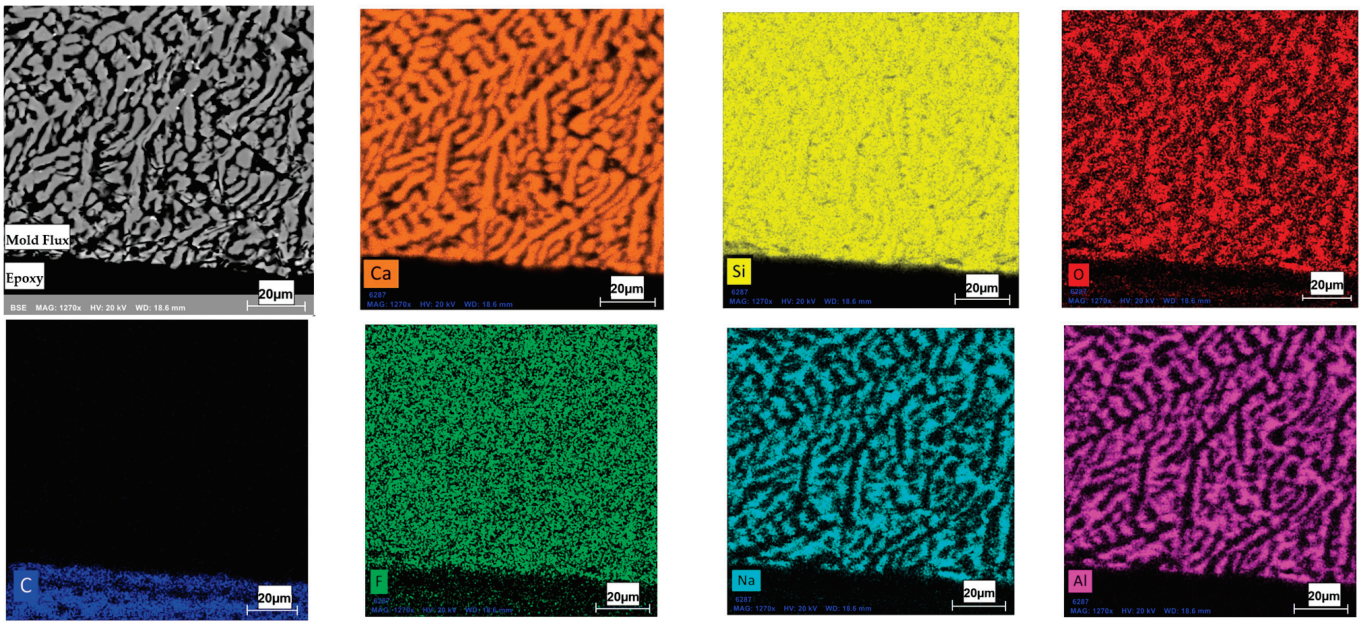


Figure 16. The backscattered electron (BSE) SEM image of the polished and coated mold flux specimen (**top-left** corner) alongside elemental maps generated by SEM-EDS. The black area in the top-left image corresponds to the epoxy region. No traces of carbon were detected within the mold flux, except in the epoxy region, and no reaction layers were observed at the interface. The cuspidine crystals ($Ca_4Si_2O_7F_2$) dispersed within a glassy matrix (consists of Na, Al, Si, and O) in the mold flux specimen as explained earlier.

The present study suggests that the occurrence of the crystallization at the crucible wall, i.e., the wettability of solid cuspidine to the crucible, is enhanced when the liquid flux wets the platinum crucible. For cuspidine crystallization in a graphite crucible, the nucleation is suppressed to a low temperature, suggesting that the solid–liquid wetting angle for cuspidine in graphite is higher and that nucleation is suppressed.

The wetting condition of the mold flux affects crystallization behavior, and as a result, it may also affect heat removal and lubrication in the mold gap. Hence, it may impact the cast product's final quality. Moreover, if the mold wall exhibits a non-wetting condition with devitrified cuspidine crystals in the mold gap, the crystallization temperature will drop significantly below the expected level due to the lack of wettability. Consequently, the design criteria for the physical properties of the mold flux will be altered, potentially compromising its effectiveness in facilitating the efficient casting of the final products.

4. Conclusions

The effect of mold flux wetting conditions with varying crucible materials on crystallization was conducted in this article, and the following conclusions can be drawn:

1. The conventional CaO-SiO_2-based mold flux exhibits strong wetting behavior with platinum crucibles but demonstrates a non-wetting condition when in contact with graphite crucibles.
2. In all non-isothermal DSC experiments, mold flux specimens in graphite crucibles consistently showed significantly lower primary crystallization temperatures compared to those in platinum crucibles across all tested cooling rates (5, 10, 15, 20, 25, and 30 °C/min). The tendency for heterogeneous nucleation is suppressed in a system that is non-wetting (graphite), compared to a system that is wetting (platinum).
3. In situ solidification tests of mold flux in graphite crucibles using CLSM also revealed a decrease in the onset of primary crystallization temperature.

4. Temperature measurements in the DSC with graphite and platinum crucibles using gold and Li_2SO_4 standards were found to be accurate to within a few degrees. DSC tests on synthetic slag exhibited a similar trend to mold flux, finding lower crystallization temperatures in graphite crucibles compared to platinum crucibles.
5. The SEM-EDS analysis of the flux specimen in the graphite crucible confirmed that no reactions occurred between the mold flux and the graphite crucible during the DSC experiments, clarifying that observed variations in crystallization behavior were due to the wetting characteristics of the crucible material rather than chemical interactions.
6. Overall, the wetting condition of the mold flux promotes primary crystallization, while its non-wetting characteristic suppresses nucleation.
7. In the future, efforts will be made to implement a molten tin "quench and age" technique to study mold flux behavior in graphite and platinum crucibles over time. Aged specimens will be analyzed by using quantitative XRD and SEM to characterize primary and secondary crystallites and study their structure, nucleation, and growth mechanisms. This will enhance the understanding of mold flux crystallization, particularly the influence of crucible material on crystal phase formation, and their kinetics. Most importantly, it will facilitate the crucible materials' effect analysis on primary and secondary crystals' nucleation and growth, to understand better the practical mold gap in the continuous casting process.

Author Contributions: Conceptualization, M.A.N., A.E. and R.O.; methodology, M.A.N., A.E. and R.O.; investigation, M.A.N.; resources, T.S. and R.O.; writing—original draft preparation, M.A.N.; writing—review and editing, M.A.N., A.E., T.S. and R.O.; supervision, A.E. and R.O.; project administration, M.A.N., A.E. and R.O.; funding acquisition, A.E. and R.O. All authors have read and agreed to the published version of the manuscript.

Funding: This research was funded by the Peaslee Steel Manufacturing Research Center (PSMRC) at Missouri University of Science and Technology (Missouri S&T).

Institutional Review Board Statement: Not applicable.

Informed Consent Statement: Not applicable.

Data Availability Statement: The original contributions presented in this study are included in the article. Further inquiries can be directed to the corresponding author.

Acknowledgments: The authors thank William Kirk for specimen preparation, Katelyn Kiser and Viraj Athavale for helping with CLSM tests, and Eric Bohanan for conducting DSC tests. Special thanks to all of the faculty advisory members, including Laura Bartlett, as well as the industrial mentoring committee of the PSMRC for their help and guidance.

Conflicts of Interest: The authors declare no conflicts of interest.

Abbreviations, Symbols and Notations

The following abbreviations, symbols and notations are used in this manuscript:

DSC	Differential scanning calorimetry
CLSM	Confocal laser scanning microscopy
SEM-EDS	Scanning electron microscopy coupled with energy dispersive X-ray spectroscopy
XRD	X-ray diffraction
CDMS	Copper disc mold simulator
TGA	Thermal gravimetric analyzer
BSE	Backscattered electron
ICSD	Inorganic crystal structure database
CCT	Continuous cooling transformation

C	Carbon
Pt.	Platinum
Au	Gold
Pd	Palladium
°C	Degree Celsius
°C/min	Degree Celsius per minute
s	Second
t	Time
T	Temperature
$\Delta G_{heterogeneous}$	Free energy for heterogeneous nucleation
$\Delta G_{homogeneous}$	Free energy for homogeneous nucleation
$f(\theta)$	Function of the contact/wetting angle
θ	Contact/wetting angle
γ	Surface tension
G–M	Gas–mold interface
G–L	Gas–liquid interface
L–M	Liquid–mold interface
T_c	Onset of primary crystallization temperature
β	Cooling rate
W	Weight
g	Gram

References

1. Sarkar, R.; Li, Z. Isothermal and Non-isothermal Crystallization Kinetics of Mold Fluxes used in Continuous Casting of Steel: A Review. *Metall. Mater. Trans. B* **2021**, *52*, 1357–1378. [CrossRef]
2. Leng, M.; Lai, F.; Li, J. Effect of Cooling Rate on Phase and Crystal Morphology Transitions of CaO–SiO_2-Based Systems and CaO–Al2O3-Based Systems. *Materials* **2018**, *12*, 62. [CrossRef] [PubMed]
3. Shi, C.-B.; Seo, M.-D.; Wang, H.; Cho, J.-W.; Kim, S.-H. Crystallization Kinetics and Mechanism of CaO–Al_2O_3-Based Mold Flux for Casting High-Aluminum TRIP Steels. *Metall. Mater. Trans. B* **2015**, *46*, 345–356. [CrossRef]
4. White, J.F.; Lee, J.; Hessling, O.; Glaser, B. "Reactions Between Liquid CaO–SiO_2 Slags and Graphite Substrates. *Metall. Mater. Trans. B* **2017**, *48*, 506–515. [CrossRef]
5. Kang, T.W.; Gupta, S.; Saha-Chaudhury, N.; Sahajwalla, V. Wetting and Interfacial Reaction Investigations of Coke/Slag Systems and Associated Liquid Permeability of Blast Furnaces. *ISIJ Int.* **2005**, *45*, 1526–1535. [CrossRef]
6. Blake, T.D. *Wettability*; Berg, J.C., Ed.; Marcel Dekker Inc.: New York, NY, USA, 1993.
7. Chen, Z.; Yu, B.; Yao, T.; Du, W.; Ma, J. Wetting and Reaction Behavior of TiN and TiO_2 with Different Mold Fluxes for High Ti-Bearing Stainless Steel. *Metall. Mater. Trans. B* **2024**, *56*, 20–32. [CrossRef]
8. Si, X.; Wang, W.; Zhou, L.; Zeng, S.; Zhang, L.; Qi, J.; Liu, P. Wettability of Mold Flux with Various Droplet Sizes on Stainless Steel Substrates. *Steel Res. Int.* **2025**, *96*, 2400270. [CrossRef]
9. Wang, W.; Gao, E.; Zhou, L.; Zhang, L.; Li, H. Effect of Al_2O_3/SiO_2 and CaO/Al_2O_3 Ratios on Wettability and Structure of CaO–SiO_2–Al_2O_3-Based Mold Flux System. *J. Iron Steel Res. Int.* **2019**, *26*, 355–364. [CrossRef]
10. Yang, J.; Zhang, J.; Ostrovski, O.; Sasaki, Y.; Zhang, C.; Cai, D. Dynamic Wetting of High-Al Steel by CaO–SiO_2- and CaO–Al_2O_3-Based Mold Fluxes. *Metall. Mater. Trans. B* **2019**, *50*, 2175–2185. [CrossRef]
11. Yang, Y.; Wang, W.; Zhou, L.; Luo, H.; Zheng, Q.; Zhao, R. Influence of Fluorine and CaO/Al_2O_3 Ratio on the Wetting Behavior Between CaO–Al_2O_3-Based Mold Flux and Steel Substrate. *Steel Res. Int.* **2023**, *94*, 70031. [CrossRef]
12. Yuan, H.; Dan, Z.; Wang, Q.; He, S. Contact Angle and Adhesion of CaO–SiO_2- and CaO–Al_2O_3-Based Mold Slags on Solid Steel of Various Compositions. *J. Mater. Res. Technol.* **2020**, *9*, 7828–7837. [CrossRef]
13. Zhou, L.; Li, J.; Wang, W.; Sohn, I. Wetting Behavior of Mold Flux Droplet on Steel Substrate with or Without Interfacial Reaction. *Metall. Mater. Trans. B* **2017**, *48*, 1943–1950. [CrossRef]
14. Kromhout, J. Mould Powders for High Speed Continuous Casting of Steel. Doctoral Thesis, TU Delft, Delft, The Netherlands, 2011.
15. Park, J.-Y.; Sohn, I. Evaluating the Heat Transfer Phenomena and the Interfacial Thermal Resistance of Mold Flux Using a Copper Disc Mold Simulator. *Int. J. Heat Mass Transf.* **2017**, *109*, 1014–1025. [CrossRef]
16. Park, J.Y.; Ko, E.; Choi, J.; Sohn, I. Characteristics of Medium Carbon Steel Solidification and Mold Flux Crystallization Using the Multi-Mold Simulator. *Met. Mater. Int.* **2014**, *20*, 1103–1114. [CrossRef]
17. Ko, E.Y.; Choi, J.; Park, J.Y.; Sohn, I. Simulation of Low Carbon Steel Solidification and Mold Flux Crystallization in Continuous Casting Using a Multi-Mold Simulator. *Met. Mater. Int.* **2014**, *20*, 141–151. [CrossRef]

18. Liu, Y.; Wang, W.; Ma, F.; Zhang, H. Study of Solidification and Heat Transfer Behavior of Mold Flux Through Mold Flux Heat Transfer Simulator Technique: Part I. Development of the Technique. *Metall. Mater. Trans. B* **2015**, *46*, 1419–1430. [CrossRef]
19. Ma, F.; Liu, Y.; Wang, W.; Zhang, H. Study of Solidification and Heat Transfer Behavior of Mold Flux Through Mold Flux Heat Transfer Simulator Technique: Part II. Effect of Mold Oscillation on Heat Transfer Behaviors. *Metall. Mater. Trans. B* **2015**, *46*, 1902–1911. [CrossRef]
20. Wang, W.; Long, X.; Zhang, H.; Lyu, P. Mold Simulator Study of Effect of Mold Oscillation Frequency on Heat Transfer and Lubrication of Mold Flux. *ISIJ Int.* **2018**, *58*, 1695–1704. [CrossRef]
21. Zhang, H.; Wang, W. Mold Simulator Study of Heat Transfer Phenomenon During the Initial Solidification in Continuous Casting Mold. *Metall. Mater. Trans. B* **2017**, *48*, 779–793. [CrossRef]
22. Zhou, L.; Wang, W.; Xu, C.; Zhang, C. An Investigation of the Mold-Flux Performance for the Casting of Cr12MoV Steel Using a Mold Simulator Technique. *Metall. Mater. Trans. B* **2017**, *48*, 2017–2026. [CrossRef]
23. Zhang, H.; Wang, W.; Ma, F.; Zhou, L. Mold Simulator Study of the Initial Solidification of Molten Steel in Continuous Casting Mold. Part I: Experiment Process and Measurement. *Metall. Mater. Trans. B* **2015**, *46*, 2361–2373. [CrossRef]
24. Zhang, H.; Wang, W. Mold Simulator Study of the Initial Solidification of Molten Steel in Continuous Casting Mold: Part II. Effects of Mold Oscillation and Mold Level Fluctuation. *Metall. Mater. Trans. B* **2016**, *47*, 920–931. [CrossRef]
25. Lyu, P.; Wang, W.; Zhang, H. Mold Simulator Study on the Initial Solidification of Molten Steel Near the Corner of Continuous Casting Mold. *Metall. Mater. Trans. B* **2017**, *48*, 247–259. [CrossRef]
26. Kamaraj, A.; Tripathy, S.; Chalavadi, G.; Sahoo, P.P.; Misra, S. Characterization and Assessment of Mold Flux for Continuous Casting of Liquid Steel Using an Inverse Mold Simulator. *Steel Res. Int.* **2022**, *93*, 2100121. [CrossRef]
27. Nazim, M.; Buchely, M.; Emdadi, A.; Huang, J.; Saha, R.K.; O'Malley, R. A Lab-Scale Mold Simulator Employing an Optical-Fiber-Instrumented Mold to Characterize Initial Steel Shell Growth Phenomena. In Proceedings of the AISTech, Columbus, OH, USA, 6–9 May 2024; pp. 947–958. [CrossRef]
28. O'Malley, R.J.; Neal, J. An Examination of Mold Flux Film Structures and Mold Gap Behavior Using Mold Thermal Monitoring and Petrographic Analysis at Armco's Mansfield Operations. In Proceedings of the METEC Congress, Düsseldorf, Germany, 13–15 June 1999; pp. 1–8.
29. Novák, D.; Řeháčková, L.; Novák, V.; Matýsek, D.; Peikertová, P. Wetting of Graphite and Platinum Substrate by Oxide System with Graded B_2O_3 Content. *Crystals* **2023**, *13*, 1618. [CrossRef]
30. Kiser, K.; Athavale, V.A.; Bartlett, L.; Buchely, M.; O'Malley, R. Growth Kinetics and Development of the Solid–Liquid Interface in Low-Carbon and High-Alloy Steel Castings Enabled by Confocal Microscopy. *Int. J. Metal-Cast.* **2024**, 1–13. [CrossRef]
31. Peterson, E. Mold Flux Crystallization and Mold Thermal Behavior. Master's Thesis, Missouri University of Science and Technology, Rolla, MO, USA, 2017.
32. Kölbl, N.; Marschall, I.; Harmuth, H. Single Hot Thermocouple Technique for the Characterization of the Crystallization Behavior of Transparent or Translucent Liquids. *J. Mater. Sci.* **2011**, *46*, 6248–6254. [CrossRef]
33. Mu, W.; Hedström, P.; Shibata, H.; Jönsson, P.G.; Nakajima, K. High-Temperature Confocal Laser Scanning Microscopy Studies of Ferrite Formation in Inclusion-Engineered Steels: A Review. *JOM* **2018**, *70*, 2283–2295. [CrossRef]

Disclaimer/Publisher's Note: The statements, opinions and data contained in all publications are solely those of the individual author(s) and contributor(s) and not of MDPI and/or the editor(s). MDPI and/or the editor(s) disclaim responsibility for any injury to people or property resulting from any ideas, methods, instructions or products referred to in the content.

materials

MDPI

Article

Microstructure of the Working Layer of X46Cr13 Steel in a Bimetal System with Gray Cast Iron

Natalia Przyszlak [1,*], Tomasz Wróbel [1], Agnieszka Dulska [1], Paweł M. Nuckowski [2], Dariusz Łukowiec [2] and Marcin Stawarz [1]

[1] Department of Foundry Engineering, Silesian University of Technology, 7 Towarowa Street, 44-100 Gliwice, Poland; tomasz.wrobel@polsl.pl (T.W.); agnieszka.dulska@polsl.pl (A.D.); marcin.stawarz@polsl.pl (M.S.)
[2] Materials Research Laboratory, Faculty of Mechanical Engineering, Silesian University of Technology, 18A Konarskiego Street, 44-100 Gliwice, Poland; pawel.nuckowski@polsl.pl (P.M.N.); dariusz.lukowiec@polsl.pl (D.Ł.)
* Correspondence: natalia.przyszlak@polsl.pl

Abstract: The research conducted in this study aimed to determine whether the production of a layered casting in the material system of X46Cr13 steel (working part) and gray cast iron (base part) can be integrated with the hardening process of this steel within the conditions of the casting mold. Accordingly, a series of layered castings was produced by preparing the mold cavity, where a monolithic steel insert was poured with molten gray cast iron with flake graphite. The variable factors in the casting production process included the pouring temperature T_p and the thickness of the support part g. Importantly, given that the hardening of the X46Cr13 steel insert occurred directly within the mold, the selection of casting parameters had to balance the ability to heat the insert to the austenitization temperature $T\gamma_{\geq 950^\circ C}$ while also creating thermokinetic conditions conducive to the rapid cooling of the system. Therefore, chromite sand—commonly regarded as a rapid-cooling material—was selected as the matrix for the molding material. Based on the conducted studies, it was determined that the thermokinetic properties of this material allowed the surface of the cast working part to be heated to the austenitization temperature. The microstructure consisted of Cr(Fe) carbides within a martensitic-pearlitic matrix, with martensite filling the grains of the primary austenite and pearlite situated along their boundaries. The carbides were primarily located at grain boundaries and, to a lesser extent, within the primary austenite grains. Through transmission electron microscopy and X-ray diffractometry, the type of Cr(Fe) carbide in the microstructure of the working part was identified as $M_{23}C_6$.

Keywords: high-chromium steel; gray cast iron; heat treatment; layered castings

1. Introduction

Gray cast iron is the most widely used material for casting worldwide. This is due to the relatively low production costs of this material, its good technological properties, and other advantages such as its vibration damping and high thermal conductivity. In general, the properties of gray cast iron with flake graphite can be considered average. It is commonly used for components where high thermal conductivity and vibration damping are essential, such as engine housings, cylinders, engine blocks, and other machine parts [1–3].

Ductile cast iron also belongs to the gray iron group, but due to its unique spherical graphite structure and the resulting benefits, it is treated as a separate type of cast iron. Ductile cast iron has a higher tensile strength, impact resistance, and elastic modulus than gray cast iron with flake graphite. When subjected to heat treatment, it allows for further improvement in its mechanical properties. However, the production process of spheroidal cast iron is more complex and costly than that of gray cast iron. It requires precise control of the graphite modification process and the use of alloying additives such as magnesium or cerium, which increases the costs of materials and energy [4–8].

The dynamic development of many industries creates a continuous need for actions focused mainly on three aspects: simplifying processes, saving time, and minimizing costs. These demands also apply to the machinery industry, which increasingly requires castings with special properties, such as high resistance to abrasive wear and corrosion, and being made from expensive and hard-to-obtain materials [9,10]. Often, however, high-performance requirements apply only to the casting surfaces that are directly exposed to destructive external conditions (working surfaces) and consequently subject to wear. Therefore, producing such castings entirely from high-performance materials seems financially unjustifiable. As a result, layered casting technology (cast bimetals) becomes particularly important, which is applicable when only the working surface layer of the casting is used, while the rest serves merely as a supporting structure, not exposed to factors causing, for instance, corrosive or abrasive wear [11–16]. Although layered casting technology seems to be a very attractive production method, bimetals still hold a secondary status among structural and functional materials, possibly because practical applications lag behind experimental and theoretical research in this field [17–20].

Alloy steels, including corrosion-resistant steels, are materials with high amounts of mechanical and anti-corrosive properties, and numerous scientific publications indicate that cast bimetals with such steels as the working component and flake graphite gray cast iron as the structural component have been effectively produced [11–13,16,21,22]. For layered castings in this material configuration, it is worth optimizing the production process so that the working layer (made of steel) attains the highest possible operational properties. Ideally, selecting a steel grade with a high hardenability and appropriately choosing casting parameters for gray cast iron would make it possible to carry out heat treatment operations, such as steel quenching, within the casting mold conditions. This would integrate with the layered casting production process, thus enhancing its mechanical properties. Such a procedure aligns with modern manufacturing market expectations, focused on saving time and costs. While steel quenching performed under conventional conditions is a well-known and relatively easy operation, performing it directly within the casting mold appears to be more complex. Martensitic transformation requires heating the steel to its austenitizing temperature Tγ and rapid cooling. If this treatment is carried out in the casting mold, casting parameters should balance the heating of the steel to the Tγ and create thermokinetic conditions that are favorable for the rapid cooling of the system. However, there are no scientific publications on this subject, presenting an opportunity for research in this area [23–25].

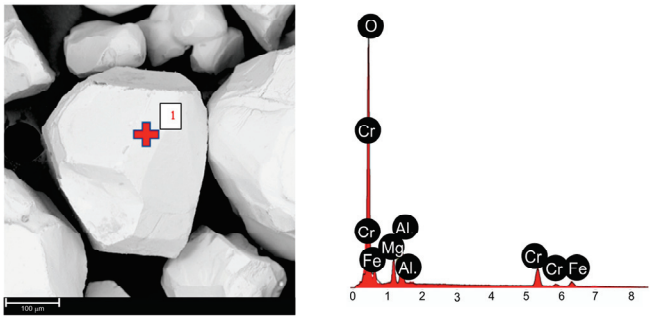
Accordingly, the aim of this research was to attempt to combine the production of a layered casting in the high-chromium steel–gray cast iron system with the steel hardening process. For the integration of steel heat treatment with the layered casting production process, it is necessary to select a molding sand with a heat conduction coefficient high enough to allow for rapid heat dissipation from the casting through the mold to the environment. This approach would enable the cooling of the steel insert (the working part of the layered casting) at a rate required to achieve a martensitic structure. The thermophysical properties of the molding sand, affecting the rate of heat transfer, depend on the type of matrix used, as well as the size, shape, and packing of its grains [26,27]. Quartz sand, a commonly used and inexpensive molding material, has insufficient thermal properties. Therefore, in the experiment, chromite sand, known for its rapid cooling properties, was selected as the molding sand matrix [28–33].

2. Materials and Methods

The layered castings were produced by preparing the mold cavity with a monolithic X46Cr13 steel insert. The steel insert, measuring 50 × 50 × 5 mm, served as the working part of the bimetal. Gray cast iron grade EN-GJL-250 was used for the base part. The castings were made in a mold of chromite sand with grain sizes of 0.40 mm/0.32 mm/0.20 mm (coarse sand). The binder used was Carbophen 9026 resin, hardened with CO_2. Figure 1

and Table 1 present the results of EDS analyses of the matrix grains, which confirm their chemical composition as expected.

The chemical compositions of the components of the layered casting are presented Tables 2 and 3.



(**a**) (**b**)

Figure 1. Chromite sand grain with marked location-of-point EDS analysis (**a**), EDS analysis result at point 1 (**b**).

Table 1. Result of EDS analysis for point 1 from 1.

Element	%at.	%wt.
O	60.14	35.41
Cr	16.00	30.63
Fe	10.16	20.88
Al	8.31	8.26
Mg	5.39	4.82

Table 2. Chemical composition of X46Cr13 steel.

C	Cr	Ni	Mo	Mn	Si	Al	Cu	V	S	P
0.43	13.6	0.125	0.015	0.61	0.383	0.003	0.069	0.099	0.002	0.025

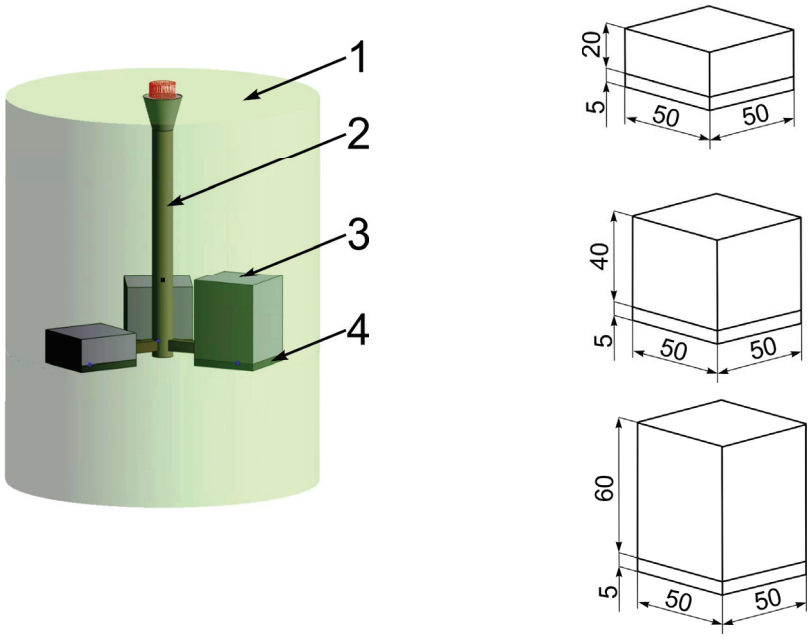
Table 3. Chemical composition of EN-GJL-HB 255.

C	Mn	Si	Cr	Ni	Cu	Al	V	P	S
3.55	0.45	2.150	0.123	0.058	0.071	0.004	0.048	0.260	0.100

The experimental plan included the production of model layered castings within defined levels of variability for selected casting process factors and recording the temperature at the thermal center on the outer surface of the steel insert.

The variable factors in the process were the thickness of the cast iron base part g and its pouring temperature T_p. Both factors were analyzed at two levels of variability. The pouring temperatures were set at 1400 °C, 1450 °C, and 1500 °C. For each pouring temperature, castings were made with varying thicknesses of the cast iron section: 20, 40, and 60 mm (Figure 2). The experimental plan, covering the production of 9 layered castings, is presented in Table 4.

The insert was sandblasted and coated with a flux–water solution of $Na_2B_4O_7$ and H_3BO_3, then dried at 120 °C for 1 h to remove H_2O, before being placed in the mold cavity. To simplify the technology, it was decided to not preheat the insert, which, as demonstrated in studies [14,24,34,35] for a similar material configuration, does not preclude achieving a durable connection between the two alloys.



(**a**) (**b**)

Figure 2. Sketch and dimensions [mm] of (**a**) the casting mold: 1—mold, 2—gating system, 3—base part of layered casting, 4—working part of the layered casting; (**b**) model layered castings.

Table 4. Experimental plan.

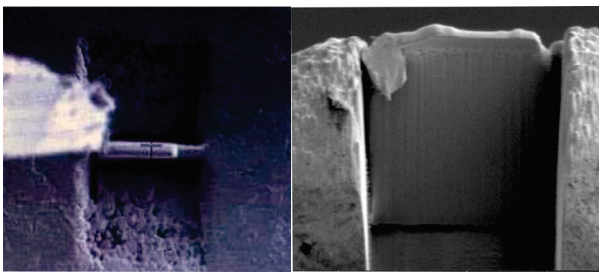
Symbol of Casting	Thickness of the Base Part (g), mm	Pouring Temperature (T_p), °C
C1	20	1400
C2	40	
C3	60	
C4	20	1450
C5	40	
C6	60	
C7	20	1500
C8	40	
C9	60	

Summarizing, the manufacturing process involved the following:

1. The working part of the layered casting was made of high-chromium steel X46Cr13 steel grade, whereas for the base part, gray cast iron with the flake graphite was used.
2. The casting was manufactured using molding mass based on chromium sand, and the bonding agent was Carbophen 9026 resin, hardened with CO_2.
3. The insert, before being placed in the mold cavity and poured by the molten gray cast iron, was sandblasted and coated with a flux based on the boron and sodium compounds to remove barriers to achieving a durable connection between the steel (working part) and the gray cast iron (base part).
4. The casting produced in the range of studies differed in the thickness of the base part (amounted to 20, 40, or 60 mm), as well as in pouring temperature (amounted to 1400, 1450, and 1500 °C).

During the pouring and cooling of the casting, the temperature at the thermal center of the outer surface of the steel insert was recorded to determine the maximum temperature T_m that the outer surface of the working layer of the casting reached. Additionally, based on the recorded curves T = F(t), the cooling rate $V_{8/5}$ on the outer surface of the working part of the casting was determined, i.e., the cooling rate in the temperature range of 800–500 °C.

The efficiency of the bond between the working layer and the base part of the bimetal, i.e., between the high-chromium tool steel and the gray cast iron, was investigated on a Starmans ElektronicsDIO 1000 defectoscope (STARMANS ELECTRONICS S.R.O., Prague, Czech Republic). Microstructure studies and phase composition analysis in the layered castings, with particular focus on the working layer, were conducted using scanning electron microscopy (SEM), and transmission electron microscopy (TEM). A qualitative X-ray diffraction analysis (XRD) was also performed. Metallographic studies were conducted using microscopy, involving grinding with sandpapers of grits 200 to 1000, polishing on a felt disk with an aqueous Al_2O_3 solution, and electrolytic etching in Mi19Fe reagent composed of 3 g of $FeCl_3$, 10 cm^3 of HCl, and 90 cm^3 of C_2H_5OH, at a voltage of 15 V and an etching time of 20 s. Microstructure observations were carried out using a Phenom ProX scanning electron microscope (SEM) INSPECT F (FEI Technologies Inc., Hillsboro, OR, USA) equipped with an energy-dispersive X-ray spectroscopy (EDS) spectrometer. In the SEM studies, imaging was performed in the backscattered electron (BSE) mode at accelerating voltages of 10 and 15 Kv, employing point, linear, and surface microanalysis of the chemical composition using the EDS method. Studies using the transmission electron microscope were performed using the thin foil method. Thin foils (lamellae) with a thickness of 50 nm were obtained using the microscope and a gallium ion beam (SEM/Ga-FIB) FEI Helios NanoLab 600i. A representative method for obtaining the lamellae is illustrated in Figure 3.



(**a**) (**b**)

Figure 3. Method of obtaining lamellae for TEM studies: (**a**) top view, mag. 4500×, (**b**) side view, mag. 6500×.

Microstructure observations of the thin foils were conducted using a S/TEM TITAN 80–300 transmission electron microscope from FEI (FEI Technologies Inc., Hillsboro, OR, USA), operating at an accelerating voltage of U = 300 kV and a wavelength of λ = 0.00197 nm. Identification of the observed phases was performed using the electron diffraction method. The analysis of the diffraction pattern involved measuring the lengths of five selected reflections from the central point of the undiffracted beam, as well as the angles between the rays of these reflections. In the next step, the interplanar spacings specific to each reflection were determined based on the relationship (1):

$$d = \frac{\lambda L}{r}, \tag{1}$$

where L is the interplanar spacing, λ is the wavelength of the electron beam, r is the distance of the reflection from the zero point.

The calculated interplanar spacings were then compared with tabulated values, and the appropriate indices for the plane families {hkl} were assigned. Subsequently, specific indices for the planes {hkl} that satisfy the vector relationship were established (2):

$$\bar{r}_1 + \bar{r}_3 = \bar{r}_2 \; i \; \bar{r}_3 + \bar{r}_5 = \bar{r}_4 \tag{2}$$

corresponding to the dependencies: $[h_1k_1l_1] + [h_3k_3l_3] = [h_2k_2l_2]$ and $[h_3k_3l_3] + [h_5k_5l_5] = [h_4k_4l_4]$.

Finally, the measured values of the interplanar angles were compared with tabulated data for the specific phase, and the indices of the crystallographic zone axis [uvw] of the studied phase were determined from Equations (3)–(5), where $h_1k_1l_1$ and $h_2k_2l_2$ are the Miller indices of two selected reflections on the diffractogram belonging to the same crystallographic zone [36].

$$u = k_1l_2 - l_1k_2 \quad (3)$$

$$v = l_1h_2 - h_1l_2 \quad (4)$$

$$v = l_1h_2 - h_1l_2 \quad (5)$$

X-ray phase analysis was conducted using the X'Pert Pro device from Panalytical (Panalytical B.V. (currently: Malvern Panalytical Ltd.), Almelo, The Netherlands), operating at a voltage of 40 kV and a current of 30 mA. Measurements were performed in the angular range of 2θ from 10° to 110° with a recording step of 0.05°. X-ray investigations were carried out using radiation from a Co anode with an Fe filter in a configuration with a Pixcel detector. Phase identification was performed according to data from the International Centre for Diffraction Data (ICDD).

3. Results and Discussion

All the castings exhibited a high degree of bonding between the supporting and working parts [37]. The set of thermal and kinetic parameters measured and calculated according data collected with thermoelemnts are presented in Table 3: Tm—temperature to which the outer surface of steel insert was heated; t_{800} and t_{500}—time required to heat the steel insert to the indicated temperature; $t_{>950}$—dwell time above the austeinitization temperature; $V_{8/5}$—cooling rate. The austenitization temperature range for steel X46Cr13 is 950 to 1050 °C [38]. The use of a mold material based on chromite sand allowed for surpassing the lower limit of the austenitization temperature for all castings. The temperature defining the upper limit of austenitization was achieved by the castings where the thickness g of the base part was the largest at 60 mm, regardless of the pouring temperature T_p (C3, C6, C9) and for casting C8, where T_p was 1500 °C and g = 40. The requirements for the austenitization time were also met for the aforementioned castings.

According to the data in the literature [36], the proper austenitization time, i.e., the duration for which the material remains at the austenitization temperature, for a plate with a thickness of 5 mm is 450 s. This goal was achieved only for the castings where the height of the base part was the greatest at 60 mm, regardless of the pouring temperature used. It should be noted that only for these castings (i.e., C3, C6, and C9) was the steel insert hardened throughout its volume (Table 5).

Table 5. Thermal and kinetic parameters of the working parts of layered castings.

	C1	C2	C3	C4	C5	C6	C7	C8	C9
T_m, °C	999	1021	1080	995	1024	1087	1001	1059	1137
$t_{800,}$ s	284	504	1029	381	633	932	367	709	915
$t_{500,}$ s	1217	1922	4141	1550	3327	3767	1939	3314	3691
$t_{>950}$, s	131	234	495	116	245	466	107	356	481
$V_{8/5}$, °C/s	0.32	0.21	0.10	0.26	0.11	0.10	0.19	0.11	0.10

Based on temperature measurements as a function of time during the pouring and cooling of the casting, the cooling rate of the steel insert in the temperature range of 800 to 500 °C was also determined. According to the analysis of the cooling rate curves for the selected steel grade, rapid cooling in the temperature range of 800 to 500 °C is crucial for inducing the martensitic transformation in the steel X46Cr13 used for the insert. It should also be noted that phase transformations typical for the hardening process pertain only to the matrix of chromium (iron) carbides, which precipitate in X46Cr13 steel regardless of its cooling parameters from the austenitization temperature. An increase in the cooling rate

$V_{8/5}$, as assumed, should result in an increase in the amount of martensite, at the expense of reducing the amount of other phases, e.g., pearlite. It was found that at a given pouring temperature, the greatest cooling rate of the insert was achieved by using the lowest height of the base part (20 mm).

Based on the results of metallographic microscopic studies, it was determined that in the areas of layered castings, where defectograms were identified as a proper connection between X46Cr13 steel (insert) and gray cast iron (casting alloy) (Figure 4), diffusion of components occurred, leading to the formation of so-called transition zones (Figure 5a). The gradient character of the microstructure in the area of the joint was due to the diffusive transport of components, primarily carbon, towards a lower concentration, i.e., towards the steel insert. Consequently, the base part zone consisted of flake graphite in a pearlitic matrix. As one moved from the base part layer towards the steel insert, a zone with a pearlitic microstructure, a zone with Cr(Fe) carbides in a pearlitic matrix, and a zone with Cr(Fe) carbides in a pearlitic matrix containing a small amount of martensite were identified. From the perspective of the tribological properties of the layered casting, the microstructure of the working layer of this casting was crucial. It consisted of Cr(Fe) carbides in a martensitic–pearlitic matrix (Figure 5b–e and Table 6).

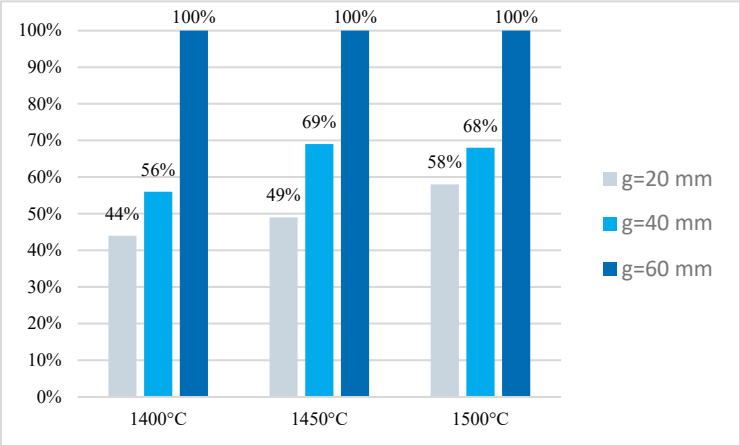
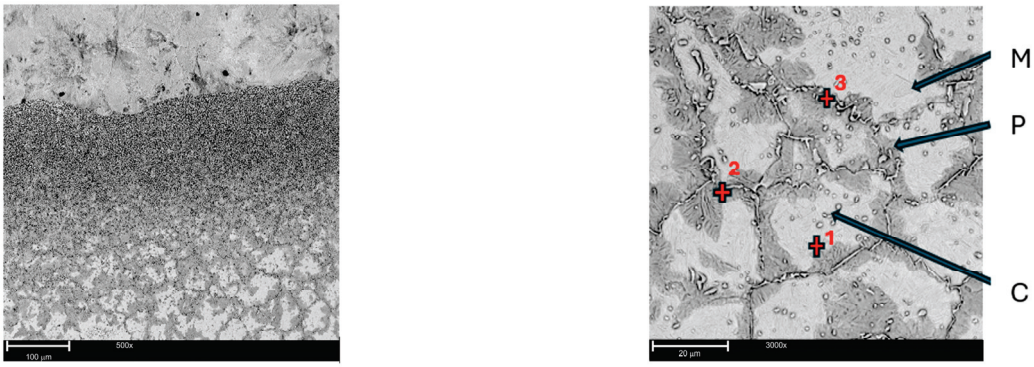


Figure 4. Results of defectoscope examinations: The size of the surface P on which the base part is permanently connected with the working part in the tested layered castings.



(**a**) (**b**)

Figure 5. *Cont.*

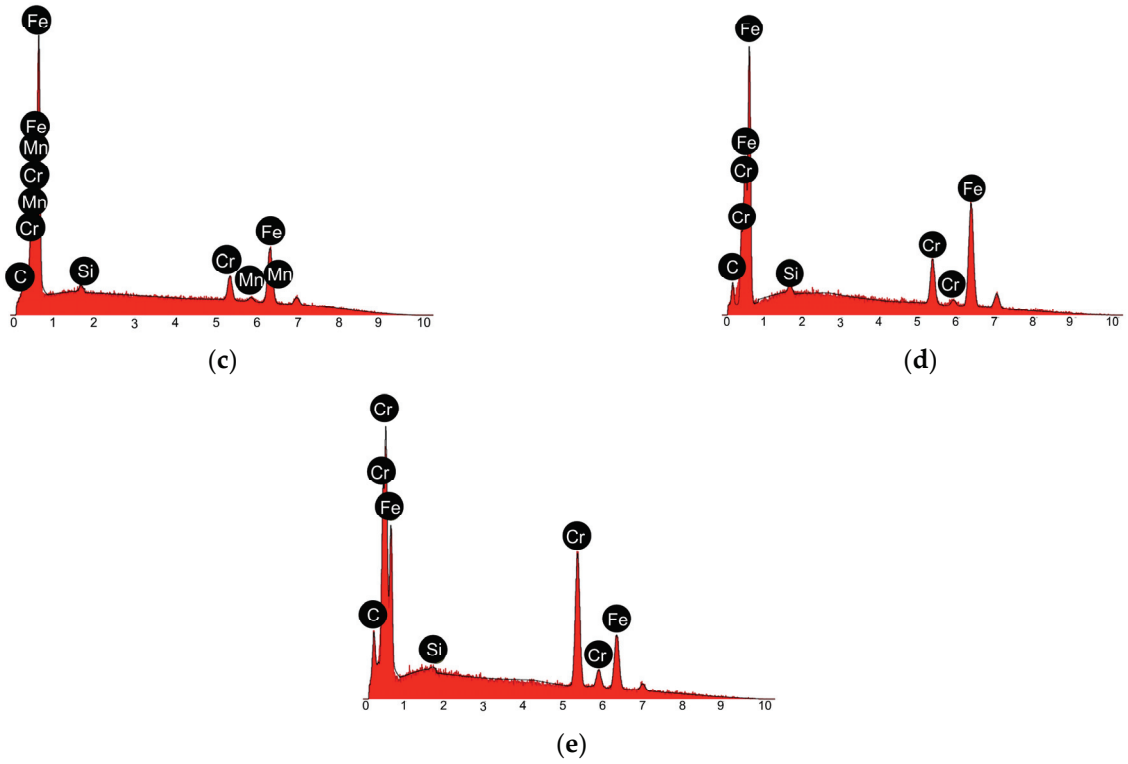


Figure 5. (**a**) Example microstructure of layered casting: gray cast iron EN-GJL-HB 255—steel X46Cr 13 (casting no. C3) SEM, mag. 500×. (**b**) Microstructure of X46Cr 13 steel containing Cr(Fe)—(C) carbides in a martensitic–pearlitic matrix (M-P) in the working layer of the bimetal (casting no. C8) with marked locations for point EDS analysis, SEM, mag. 6000×. (**c**) EDS analysis result at point 1. (**d**) EDS analysis result at point 2. (**e**) EDS analysis result at point 3.

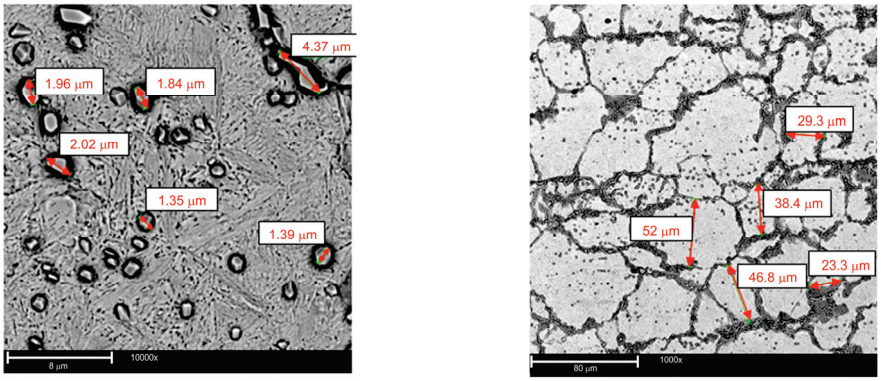
Table 6. Results of EDS analysis for point 1, 2, and 3 from Figure 5b.

Measurement Point	Element	%at.	%wt.
Point 1 from Figure 5b	Fe	81.9	83.8
	Cr	14.5	13.8
	Mn	1.7	1.7
	Si	0.8	0.4
	C	1.2	0.3
Point 2 from Figure 5b	Fe	73.4	82.6
	Cr	13.4	14.0
	C	12.5	3.0
	Si	0.7	0.4
	Fe	73.4	82.6
Point 3 from Figure 5b	Cr	43.1	48.2
	Fe	39.4	47.3
	C	17.4	4.5
	Si	0.1	0.1

The average size of Cr(Fe) carbides was approximately 2 µm (Figure 6a). The carbides were mainly located along the boundaries and to a lesser extent within the grains of the primary austenite, which had an average size of about 30 µm (Figure 6b).

Based on the results obtained using transmission electron microscopy and X-ray diffraction, the type of Cr(Fe) carbide in the microstructure of the working layer of the bimetal was identified as $M_{23}C_6$ (Figures 7–9 and Table 7), which is supported by the findings presented in references [39,40]. Furthermore, it was shown that the parameters T_p and g do not influence the presence of $M_{23}C_6$ carbides in the microstructure of X46Cr13 steel. In addition

to peaks originating from the Feα and $M_{23}C_6$ phases, reflections from cementite M_3C were identified in some castings, which in these cases should be considered a component of pearlite (Table 7). Based on the obtained results, it was concluded that, essentially, regardless of the parameters used for casting the bimetal, the microstructure of the working layer qualitatively consists of Cr(Fe) carbides in a martensitic–pearlitic matrix, with martensite filling the grains of primary austenite and pearlite located at their boundaries.



(**a**) (**b**)

Figure 6. Example microstructures of the working layer in the bimetal gray cast iron EN-GJL-HB 255–steel X46Cr 13, SEM: (**a**) Cr(Fe) carbides in a and martensitic matrix (casting no. C2), mag. 10,000×. (**b**) Size of a pearlitic martensitic matrix grain (casting no. C8), mag. 3000×.

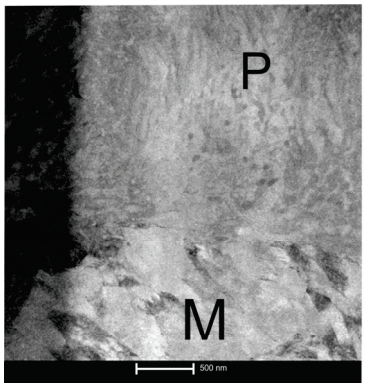
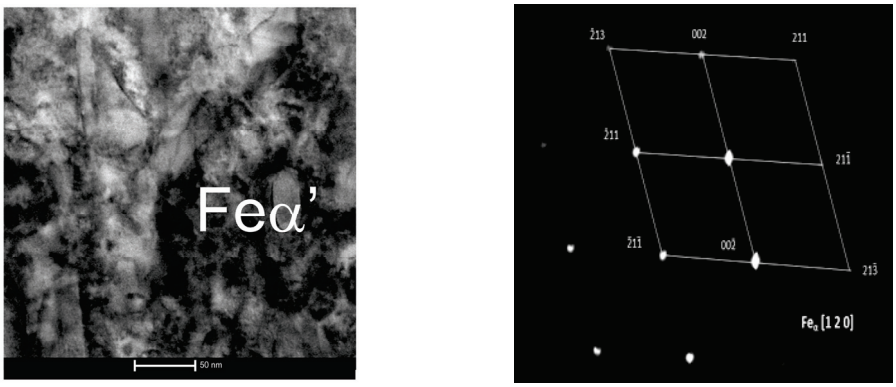
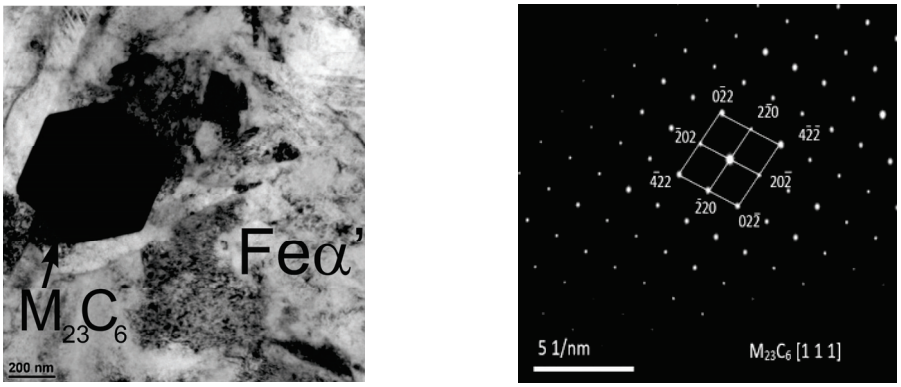


Figure 7. Phase boundary between pearlite—P—(above) and martensite—M—(below) in the microstructure of the working part of the layered casting gray cast iron EN-GJL-HB 255–steel X46Cr 13, TEM, mag. 15,000×.



(**a**) (**b**)

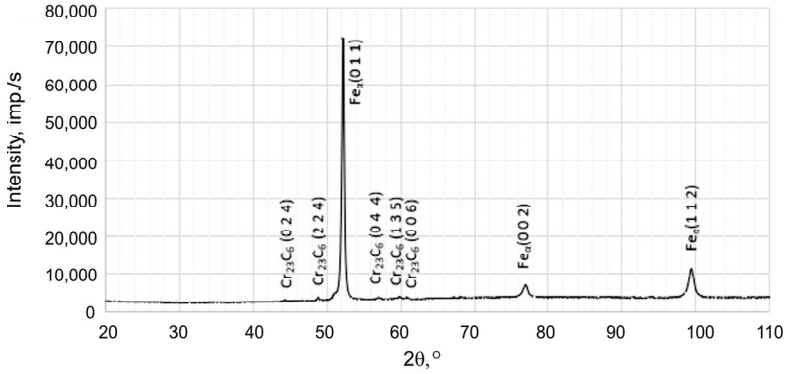
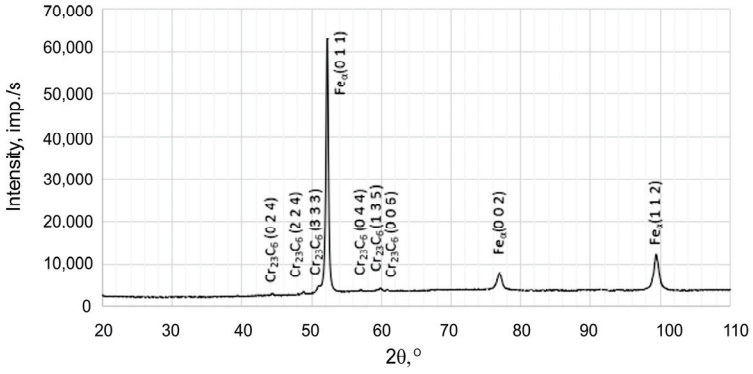
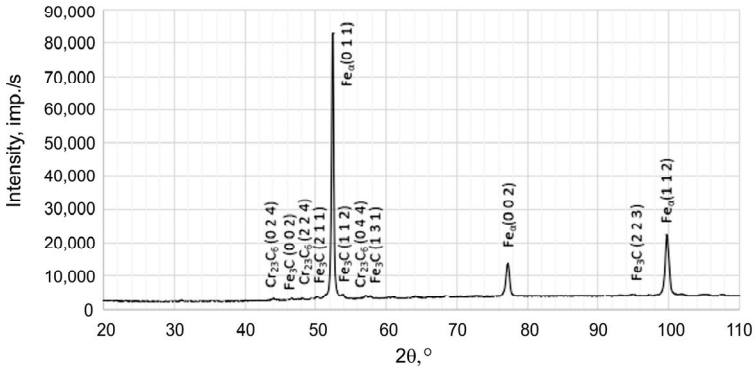
Figure 8. Feα in the microstructure of the working part of the layered casting gray cast iron EN-GJL-HB 255–steel X46Cr 13: (**a**) bright field TEM, mag. 60,000×; (**b**) SAD diffraction.



(**a**) (**b**)

Figure 9. $M_{23}C_6$ carbide in the microstructure of the working part of the layered casting gray cast iron EN-GJL-HB 255–steel X46Cr 13: (**a**) bright field, TEM, mag. 30,000×; (**b**) SAD diffraction.

Table 7. Exemplary X-ray diffractogram of the working part of the layered casting.

No of Casting	X-Ray Diffractogram of the Working Part of the Layered Casting
C3	
C6	
C9	

4. Conclusions

The objective of the research was to integrate the production of a layered casting in the system of high-chromium steel X46Cr13–gray cast iron EN-GJL-250 with the hardening of the aforementioned steel. The castings were made in a mold based on chromite sand, which, according to the literature, has a higher heat conductivity coefficient than the commonly used quartz sand. To achieve the hardening of the 5 mm thick steel, it was necessary to heat it to the austenitization temperature, hold it at this temperature for 450 s, and then cool it at a rate greater than the critical rate. The first hardening condition was met for all castings—the external surface of the insert was heated to above 950 °C. The second condition, ensuring the full hardening of the steel throughout its volume, was met only for those castings where the thickness of the load-bearing part was the largest, measuring 60 mm. However, in the steel microstructure, alongside martensite and carbides, pearlite was also present. Referring to the research results presented in the paper, the key factor influencing the presence of pearlite in the working layer of X46Cr13 steel was the too low cooling rate of the system. In addition, based on the conducted analyses, the following conclusions were drawn:

- Microscopic examination of the working layer revealed a microstructure predominantly composed of martensite and pearlite, along with Cr(Fe) carbides.
- Based on studies using a transmission electron microscope and an X-ray diffractometer, the type of Cr(Fe) carbide in the microstructure of the working layer was identified as $M_{23}C_6$.
- The relatively high cooling rate of castings made with molding sand based on chromite sand resulted in a low pearlite content relative to martensite in the microstructure of the working layer, where pearlite was primarily located along the grain boundaries of martensite.
- Further research in the analyzed range should focus on optimizing the production process for layered castings made with $FeCr_2O_4$-based molding sand, aiming to minimize the pearlite in the microstructure of the working part. This reduction is expected to further enhance the hardness of the working surface made from X46Cr13 steel.

Author Contributions: Conceptualization, N.P. and T.W.; Methodology, A.D.; Validation, T.W.; Formal analysis, N.P.; Investigation, N.P., P.M.N. and D.Ł.; Resources, A.D.; Data curation, M.S.; Writing—original draft, N.P.; Writing—review & editing, M.S.; Visualization, N.P.; Supervision, T.W. and M.S.; Project administration, N.P.; Funding acquisition, N.P. All authors have read and agreed to the published version of the manuscript.

Funding: This publication was financed from the statutory subsidy of the Faculty of Mechanical Engineering of the Silesian University of Technology in 2024; BK-278/RMT8/2024.

Institutional Review Board Statement: Not applicable.

Informed Consent Statement: Not applicable.

Data Availability Statement: Data are contained within the article.

Conflicts of Interest: The authors declare no conflict of interest.

References

1. Dwulat, R.; Janerka, K.; Grzesiak, K.; Gałuszka, M. Influence of Charge Materials on the Metallurgical Quality of Gray Cast Iron. *Arch. Foundry Eng.* **2023**, *23*, 66–71. [CrossRef]
2. Mnati, A.A.; Resan, K.K. Production of Ductile Cast Iron by Recycling Gray Cast Iron Scrap With Adding Various Local Materials. *J. Sustain. Dev.* **2023**, *27*, 117–126. [CrossRef]
3. Salawu, E.Y.; Elvis, A.O.; Ajayi, O.O.; Ongbali, S.O.; Afolalu, S.A. Particle size distribution analysis of carburized HT250 gray cast iron using ImageJ. *Mater. Today* 2023, *in press*. [CrossRef]
4. Li, Q.; Zhang, Y.; Zhang, Y.; Liu, H.; Ren, H.; Zhong, Y.; Huang, X.; Huang, W. Influence of Sn and Nb additions on the microstructure and wear characteristics of a gray cast iron. *Appl. Phys. A* **2020**, *126*, 282. [CrossRef]
5. Masafi, M.; Palkowski, H.; Mozaffari-Jovein, H. Microstructural properties of particle-reinforced multilayer systems of 316L and 430L alloys on Gray Cast Iron. *Coatings* **2023**, *13*, 1450. [CrossRef]

6. Aranke, O.; Algenaid, W. Coatings for automotive gray cast iron brake discs. *Coatings* **2019**, *9*, 552. [CrossRef]
7. Akinribide, O.J.; Ogundare, O.D.; Oluwafemi, O.M.; Ebisike, K.; Nageri, A.K.; Akinwamide, S.O.; Gamaoun, F.; Olubambi, P.A. A Review on Heat Treatment of Cast Iron: Phase Evolution and Mechanical Characterization. *Materials* **2022**, *15*, 7109. [CrossRef]
8. Du, S.; Chen, C.; Chen, R.; Wang, Q.; Cui, X.; Song, Q. Influence of Casting Materials on the Microstructure and Mechanical Properties of Gray Cast Iron for Cylinder Liners. *Int. J. Met.* **2024**, 1–13. [CrossRef]
9. Studnicki, A.; Kilarski, J.; Przybył, M.; Suchoń, J. Technological experiments of production castings of chromium cast iron in the foundry. *Arch. Foundry Eng.* **2005**, *5*, 293–302.
10. Bykov, A. Bimetal Production and Applications. *Steel Transl.* **2011**, *41*, 61–69. [CrossRef]
11. Ramadan, M. Interface characterization of Bimetallic Casting with 304 Stainless Steel Surface Layer and Gray Cast Iron Base. *Adv. Mater. Res.* **2015**, *1120–1121*, 993–998. [CrossRef]
12. Li, Y.; Gong, M.; Wang, K.; Li, P.; Yang, X.; Tong, W. Diffusion behavior and mechanical properties of high chromium cast iron/low carbon steel bimetal. *Mater. Sci. Eng. A* **2018**, *718*, 260–266. [CrossRef]
13. Ibrahim, M.M.; El-Hadad, S.; Mourad, M. Effect of liquid-solid volume ratios on the interfacial microstructure and mechanical properties of high chromium cast iron and low carbon steel bimetal. *Mater. Res. Express* **2020**, *6*, 1265c2. [CrossRef]
14. Przyszlak, N.; Dulska, A.; Wróbel, T.; Szajnar, J. Grey cast iron locally reinforced using 3D printing scaffold insert. *Arch. Foundry Eng.* **2018**, *18*, 99–102.
15. Przyszlak, N.; Dulska, A.; Wróbel, T. Local reinforcement titanium carbide TIC type manufactured in method of mould cavity preparation using 3D printing. In Proceedings of the Annual Conference Metal, Brno, Czech Republic, 24–26 May 2017.
16. Wróbel, T. Compound Castings for the Coke Industry. *Materials* **2024**, *17*, 3539. [CrossRef]
17. Zhang, Y.; Wang, A.; Liang, T.; Zhang, J.; Mao, Z.; Ji, J.; Xie, J.; Chang, Q.; Su, B.; Liu, S. Texture characteristics and tensile deformation behavior of Cu/Al layered composites prepared by cast-rolling method. *J. Mater. Res. Technol.* **2024**, *29*, 461–470. [CrossRef]
18. Yesuvadian, R.A.; Keerthiprasad, K.S. A Review on Casting and Testing of Bimetals. *Int. J. Appl. Eng. Res.* **2023**, *18*, 278–291. [CrossRef]
19. Wang, Y.; Qin, F.; Qi, H.; Qi, H.; Meng, Z. Interfacial Bonding Behavior and Mechanical Properties of a Bimetallic Ring Blank Subjected to Centrifugal Casting Process. *J. Mater. Eng. Perform* **2022**, *31*, 3249–3261. [CrossRef]
20. Greß, T.; Mittler, T.; Volk, W. Casting methods for the production of rotationally symmetric copper bimetals. *Mater. Sci. Technol.* **2020**, *36*, 906–916. [CrossRef]
21. Xiong, B.; Cai, C.; Wan, H.; Lu, B. Fabrication of high chromium cast iron and medium carbon bimetal by liquid-solid casting in electromagnetic induction field. *Mater. Des.* **2011**, *32*, 2978–2982. [CrossRef]
22. Xiong, B.; Cai, C.; Lu, B. Effect of volume ration of liquid to solid on the interfacial microstructure and mechanical properties of high chromium cast iron and medium chromium carbon steel bimetal. *J. Alloys Compd.* **2011**, *509*, 6700–6704. [CrossRef]
23. Brytan, Z. *Vademecum of Stainless Steel*; Stowarzyszenie Stal Nierdzewna: Warszawa, Poland, 2018; pp. 14–76.
24. Wróbel, T. Characterization of bimetallic castings with an austenitic working surface layer and an unalloyed cast steel base. *J. Mater. Eng. Perform.* **2014**, *23*, 1711–1717. [CrossRef]
25. Campbell, J. *Complete Casting Handbook—Metal Casting Processes, Metallurgy, Techniques and Design*; Elsevier Ltd.: Oxford, UK, 2015.
26. Cholewa, M.; Baron, C.; Kozakiewiecz, Ł. Effect of Thermal Insulating Molding Sand on the Microstructure of Gray Cast Iron. *Arch. Foundry Eng.* **2015**, *15*, 119–123.
27. Jacquet, P.; Vaucheret, A.; Souêtre, M.; Carton, J.F. Determination of Thermal Properties of Foundry Green Sand to Improve Numerical Simulation. *Int. J. Met.* **2024**, 1–9. [CrossRef]
28. Przyszlak, N.; Wróbel, T. Self-hardening of X46Cr13 steel integrated with base from grey cast iron in bimetallic system. *Arch. Foundry Eng.* **2019**, *2*, 29–34. [CrossRef]
29. Przyszlak, N.; Piwowarski, G. Designing of X46Cr13 Steel Heat Treatment in Condition of Casting Mould. *Arch. Foundry Eng.* **2023**, *23*, 119–126. [CrossRef]
30. Hess, K.; Ignaszak, Z. Thermal Conductivity of Molding Sands as a Function of Temperature. In Proceedings of the International Symposium—Solidification of Metals and Alloys, Gliwice, Poland, 6–9 November 1980.
31. Li, L.; Lu, Y.; Ren, T.; Horton, R. Quartz contents derived from particle density measurements improve the accuracy of soil thermal conductivity estimates. *Geoderma* **2023**, *436*, 116526. [CrossRef]
32. Zhang, X.R.; Kong, G.Q.; Wang, L.H.; Xu, X.L. Measurement and prediction on thermal conductivity of fused quartz. *Sci. Rep.* **2020**, *10*, 6559. [CrossRef]
33. He, H.; Li, M.; Dyck, M.; Si, B.; Wang, J.; Lv, J. Modelling of soil solid thermal conductivity. *Int. Commun. Mass Transf.* **2020**, *116*, 104602. [CrossRef]
34. Cholewa, M.; Wróbel, T.; Tenerowicz, S.; Szuter, T. Diffusion phenomena between alloy steel and gray cast iron in layered bimetallic casting. *Arch. Metall. Mater.* **2010**, *55*, 771–777.
35. Gawroński, J.; Szajnar, J.; Wróbel, P. Study on theoretical bases of receiving composite alloy layers on surface of cast steel castings. *J. Mater. Process. Technol.* **2004**, *157–158*, 679–682. [CrossRef]
36. Marciniak, J.; Hajduczek, E. *Methods of Testing Metals and Alloys: Structural Metallography*; Zakład Graficzny Politechniki Śląskiej: Gliwice, Poland, 1978.

37. Przyszlak, N.; Wróbel, T.; Dulska, A. Influence of Molding Materials on the Self-Hardening of X46Cr13 Steel/Grey Cast Iron Bimetallic Castings. *Arch. Metall. Mater.* **2021**, *66*, 43–50. [CrossRef]
38. Staub, F.; Adamczyk, J.; Cieślakowa, Ł.; Gubała, J.; Maciejny, A. *Metallography*; Śląskie Wydawnictwo Techniczne: Katowice, Poland, 1994.
39. Garcia de Andrès, C.; Caruana, G.; Alvarez, L. Control of M23C6 carbides in 0.45C–13Cr martensitic stainless steel by means of three representative heat treatment parameters. *Mater. Sci. Eng.* **1998**, *A241*, 211–215. [CrossRef]
40. Yang, Y.; Zhao, H.; Dong, H. Carbide evolution in high-carbon martensitic stainless cutlery steels during austenitizing. *J. Mater. Eng. Perform.* **2020**, *29*, 3868–3875. [CrossRef]

Disclaimer/Publisher's Note: The statements, opinions and data contained in all publications are solely those of the individual author(s) and contributor(s) and not of MDPI and/or the editor(s). MDPI and/or the editor(s) disclaim responsibility for any injury to people or property resulting from any ideas, methods, instructions or products referred to in the content.

materials

MDPI

Article

The Analysis of Plastic Forming in the Rolling Process of Difficult-to-Deform Ti + Ni Layered Composites

Dariusz Rydz [1,*], Sebastian Mróz [1], Piotr Szota [1], Grzegorz Stradomski [1], Tomasz Garstka [1] and Tomasz Cyryl Dyl [2]

[1] Faculty of Production Engineering and Materials Technology, Czestochowa University of Technology, 19 Armii Krajowej Avenue, 42-201 Czestochowa, Poland; sebastian.mroz@pcz.pl (S.M.); piotr.szota@pcz.pl (P.S.); grzegorz.stradomski@pcz.pl (G.S.); tomasz.garstka@pcz.pl (T.G.)
[2] Department of Marine Maintenance, Faculty of Marine Engineering, Gdynia Maritime University, Morska Street 81-87, 81-225 Gdynia, Poland; t.dyl@wm.umg.edu.pl
* Correspondence: dariusz.rydz@pcz.pl; Tel.: +48-343-250-630

Abstract: The article presents the results of experimental studies on the symmetrical and asymmetrical rolling process of composite laminate sheets consisting of difficult-to-deform Ti and Ni materials. Composite sheets joined by explosive welding were used for the tests. The aim of the research was to determine the impact of plastic shaping conditions in the rolling process on the quality and selected functional properties of the materials constituting the layered composite. The rolling process was carried out cold on a duo laboratory rolling mill with a roll diameter of 300 mm. During the rolling process, the influence of the rolling process conditions on the distribution of metal pressure forces on the rolls was determined, as well as the shear strength and microstructural studies of the joint area of the layered composites. As part of the conducted considerations, residual stress tests were carried out using the Barkhausen noise method. The scientific aim of the presented work was to determine the optimal conditions for the plastic processing of multi-layer Ti-Ni sheets. The results presented in the work allowed for determining the most favorable conditions for the rolling process.

Keywords: composite layered; asymmetric rolling; microstructure; Barkhausen noise

1. Introduction

Homogeneous materials often do not meet the requirements of customers, such as the ability to work with high and variable loads, high temperatures, aggressive environments, resistance to abrasion, etc. [1,2]. There are many techniques that allow for selective impact on surface layers. One of them is burnishing [3,4], which is an extremely good cost-effective solution [5]. It has its limitations, but in such cases, coating technologies, including hybrid ones, are very good solutions [6–8]. However, hybrid coating technologies, although they give very good results, are usually expensive. A cost-effective and very smooth control is the plating technique, which results in layered composites [9,10]. Metal plating technologies have been known to mankind since ancient times. Although layered composites, including metal ones, have been known for a long time, they have only recently gained such extensive industrial applications [11,12]. Until the beginning of the 21st century, there was an increase in demand and intensive development of technologies for the production of multilayer materials. Multilayered products combining the properties of joined materials are nowadays an area of interest [13,14]. They are used, among others, in the chemical, energy, metallurgical, machine, and aviation industries [15,16].

There are relatively many methods of joining metals, such as explosive welding, surfacing, diffusion welding, friction welding, etc. Despite the continuous development of new solutions, it can be stated that the explosive welding (EW) method is still one of the most advantageous [17–19]. The explosive welding method, despite the increasingly common application, has not yet been fully understood [20–22]. The specific conditions prevailing during the joining process using the explosive welding method are characterized by very high pressure reaching thousands of atmospheres, extremely short process time (lasting up to several microseconds), and change in material density—they cause metals to join in physical states that do not correspond to the classical laws of mechanics [22,23]. However, the introduction of a new pair of materials into the rolling process due to the specificity of the process often causes many problems [24,25]. One of them is the occurrence of an intermetallic layer in the connection area [26]. This layer is particularly important during further plastic shaping due to its properties. These are usually hard and brittle materials that are exposed to micro cracks and fractures during deformation [27,28]. First of all, this is related to the uneven distribution of the individual layers deformation of composite sandwich sheets. This phenomenon results from differences in the mechanical properties of materials included in composite sheets, which was the subject of many works, including the authors of this publication [29,30].

Ti-Ni composite sandwich plates are used, among others, in the construction of electrolyzers for chlorine production. The electrolyzers made of Ti-Ni bimetal sheets are a battery of modules in which chlorine and hydrogen brine electrolysis takes place. Another example of the use of composite sandwich plates based on Ti-Ni sandwich plates is cladding plates used for heat exchangers. During the process of joining by the explosive welding method, during the detonation of explosives, there is a strong effect of both thermal and mechanical factors [2]. As a result of this interaction, structural changes occur in the joined materials and the area of direct connection. Another effect is the appearance of residual stresses in the joined materials, which very often results in deformation of the joined layered composite.

There are different techniques for joining Ti to Ni substrates, including brazing and diffusion bonding [31–34]. However, the diffusion bonding process requires a long holding time, usually more than 60 min, depending on materials, and a high temperature, which makes this method uneconomical [19,35]. Another method of joining metals and their alloys is the friction method. This method was one of the first to use friction as a solid-state welding technique [36].

The problem of uneven flow of layers can be solved by using an asymmetric rolling process [25,37,38]. This asymmetry can be imposed by differentiating the diameters of the working rolls or by differentiating the peripheral speeds of the working rolls. Asymmetry causes the activation of shear band broadening, which is found in mechanical properties [24,38]. Based on literature data [39,40] as well as the authors own publications [25,37], peripheral velocity asymmetry is used for both to control the curvature of the composite sheets and to reduce the metal pressure on the roll [2,25]. The first application is the correction of the bending defect of composite sandwich sheets after leaving the deformation gap [25,41]. In the second solution, reducing the metal pressure forces on the roller allows for the application of greater deformations in rolled sheets [24,42]. The rolling process carried out in this work is intended to determine the most favorable conditions for plastic forming of multilayer Ti-Ni sheets [39,40]. This work presents not only the results of research on deformations but also stresses occurring in the rolled multilayer sheets. The Barkhausen method [43] was used to analyze them. The results presented in the work will be of a utilitarian nature and will allow for their industrial application.

The aim of the work was to indicate the optimal conditions for the rolling process in terms of the quality of the joint area, microstructure, and curvature of multilayer sheets. The work presents the influence of the asymmetry of the working roll speed on both the curvature of multilayer sheets and the quality of the joint area of Ti-Ni layers. The research showed the presence of an intermediate layer in the joint area consisting of the aforementioned intermetallics. The rolling process was carried out on a rolling machine with the possibility of controlling the peripheral speed of the working rolls. The structural studies were conducted using optical microscopy and scanning microscopy. Non-destructive tests were also carried out using the Barkhausen noise (BN) method.

2. Materials and Methods

Tests of the symmetrical and asymmetrical rolling process were carried out on samples cut out from Ti-Ni sheets obtained using the explosive welding method. The process of explosive welding was carried out in the company ZTW EXPLOMET sp.j. Gałka, Szulc (Opole, Poland). Information about the parameters of the explosive welding process is confidential know-how of the company. The chemical composition of the tested materials is shown in Table 1.

Table 1. Chemical composition of the used materials. weight %.

Material	Ti	Ni	Fe	N	C	Mn	Si	O
Ti (Grade 1)	balance	-	0.02	0.008	0.01	-	-	0.01
Ni (N0221)	-	balance	0.14	-	0.01	0.21	0.11	-

In order to be able to join sheets by explosive welding (Figure 1), the impact parameters must be met within which the welding process can be carried out. This range is most often presented in the coordinate system of the joining angle β and the joining speed.

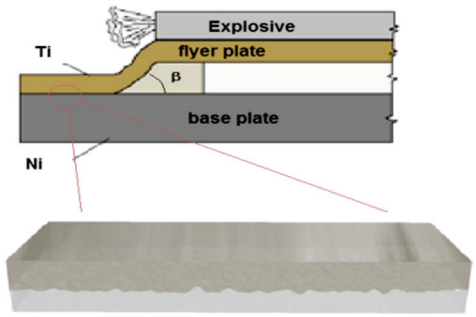


Figure 1. Scheme of plate joining by explosive welding of composite sandwich sheets Ti-Ni.

Due to the fact that the process of manufacturing composite materials in this study, the following tests were performed:

- shear strength of the joint for materials before the rolling process;
- cold rolling;
- the residual stress analysis with the use of the non-destructive method using the Barkhausen noise (BN) technique,
- analysis of microstructure.

The rolling process of multilayer flat products is always a challenge. Due to the uneven deformation of the layers, uneven flow of the sheet metal layers is also observed in the

plane of the exit from the rolling gap [2,36]. This phenomenon can be observed in Figure 2, where the rolling process is also presented.

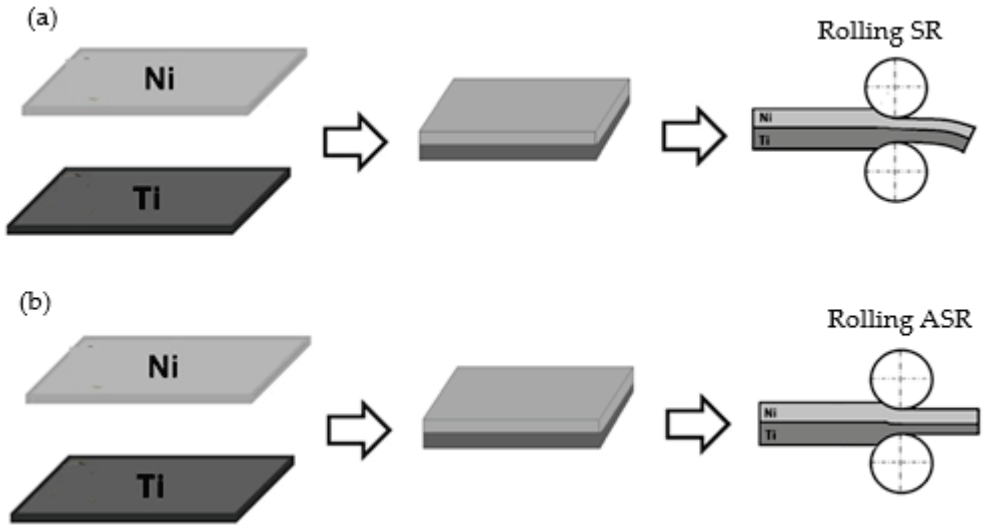


Figure 2. Diagram of the rolling process: (**a**) with equal peripheral speeds (SR process, $V_U = V_L$), (**b**) asymmetry of peripheral speeds (ASR process, $V_U < V_L$).

As a part of this work, the process of rolling composite sandwich sheets from hard-deformable Ti-Ni materials was carried out. Rolling samples were cut out from the composite sandwich sheets obtained using explosion welding. The joined sheets had dimensions of 500 mm × 1200 mm, and the thickness of individual layers was Ti (grade 1) HTi = 1.0 mm and Ni (grade N0221) layers HNi = 1.0 mm. For the rolling process, specimens of 40 mm × 140 mm were used. Samples were cut out in the direction of propagation of the detonation wave. Tensile and shear tests were carried out using the Zwick Z100 testing machine (Ulm, Germany). Later on, the composite sandwich sheets rolling process was carried out. Rolling was performed for equal peripheral speeds of work rolls (symmetrical process—SR) and for kinetic asymmetry (asymmetrical process—ASR), where the peripheral speed of the roller in contact with the layer with higher deformation resistance was increased (in this case, the Ni layer). However, the controlled increase in the speed of the rolls in contact with the layer with greater resistance to plastic flow ensures a more even flow of metal, which makes it possible to obtain a straight composite sandwich sheet (Figure 2). The measurable value of this parameter is the values of the speed asymmetry factor of the peripheral working rolls, which can be written as [2]:

$$a_v = \frac{V_U}{V_L} \tag{1}$$

where:

V_U—peripheral speed of the upper roll,
V_L—peripheral speed of the lower roll.

The rolling process was carried out on a semi-industrial two-high rolling mill with a roll diameter of 300 mm and individual drive for each roll (Figure 3) at an ambient temperature.

The rolling process was carried out for both equal (a_v = 1.0) and different (asymmetry) peripheral speeds of work rolls (a_v = 1.1). The value of the a_v parameter was taken from earlier work realized by authors [5,11]. The rolling speed was 0.2 m/s. The height of the rolling gap was set taking into account the stiffness of the stand. For the first two samples it was 1.5 mm, while for the next two it was 1.3 mm. Due to the fact that the rolling

process was carried out at ambient temperature, which causes high metal pressure on the rolls, relative deformations were adopted for individual rolling variants: variant I $\varepsilon = 10\%$, $a_v = 1.0$ and $a_v = 1.1$, variant II $\varepsilon = 15\%$, $a_v = 1.0$, and $a_v = 1.1$. During the rolling process, measurements of force parameters were carried out. The presented test results are the results for one pass and show the difference in the values of layer deformation during the SR and ASR rolling processes.

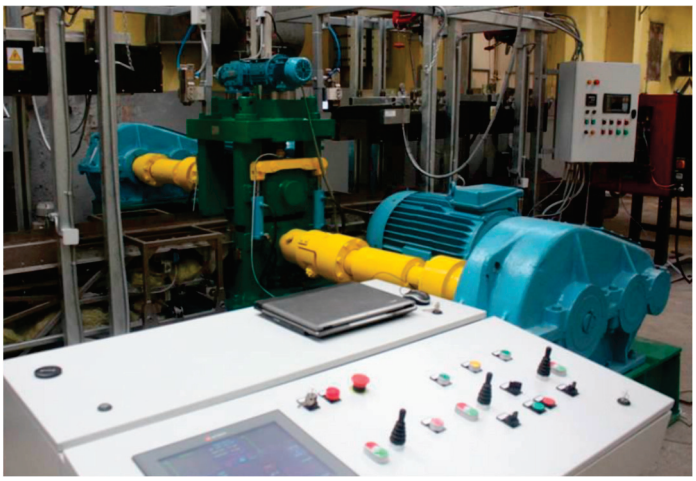


Figure 3. View of the 300 mm two-high laboratory mill used in the tests.

Due to the fact that the rolling process was realized at ambient temperature, the authors decided to also analyze the residual stress state. According to earlier work of authors [24,42], the analysis was made with the use of the nondestructive technique, which is the measurement of Barkhausen noise. In the literature, the Barkhausen method is increasingly used to analyze the stress state resulting from various technological processes [44–46].

For measuring the Barkhausen noise's parameters, special equipment for excitation, detection, and processing of BN has been developed [47]. Its functional block diagram is presented in Figure 4. The magnetization unit is based on a tuned triangle RC generator (1) and a current power amplifier (2). It supplies current Im (max. $\pm$1.5 A) to the magnetization windings (3) wound on a yoke (4) of the measuring head. The BN signal excited in the tested material as an effect of cyclical magnetization is picked up by a detection coil (5) placed between poles of the yoke and next transmitted to the measuring block. The raw signal is amplified with the help of a specialized low-noise measuring preamplifier (6) with controlled gain ku1max up to 80 dB. Then, the signal is passed through a 1 kHz HP filter (7), where power line disturbances and harmonics of the magnetization current are eliminated. Finally, BN extracted from the background noise is gained by the amplifier (8) with ku2max = 40 dB and fed to a processing block. In the processing block, specialized circuits determine BN parameters: root-mean-square value (9), its envelope voltage signal (10), and, moreover, a series of the digital pulses corresponding to the Barkhausen jumps with amplitude over specific reference voltage (11), although this parameter was not analyzed in this study.

These signals, raw BN and the magnetization current in the form of a voltage signal, are acquired by a 1 MHz data acquisition card (12) type and sent via USB interface to the computer for further processing, saving, and displaying.

During the experiments in this study, the magnetization frequency fm = 12 Hz and 105 dB total gain of the measuring circuit were set. For the tests, a small measuring head was used, constructed on the base of a pocket of C-shaped segments made from transformer sheet and linear dimensions of 18 mm $\times$ 5 mm. The magnetization windings had 200 turns. The poles of the yoke were rounded faintly to obtain repeatable contact conditions with different curvature radii of the tested strip before as well as after rolling. Between the

electromagnet poles, the detection coil wound on a small rectangular ferrite rod core with a cross-section of 6 mm^2 was fixed elastically in a way that enabled slight vertical movement.

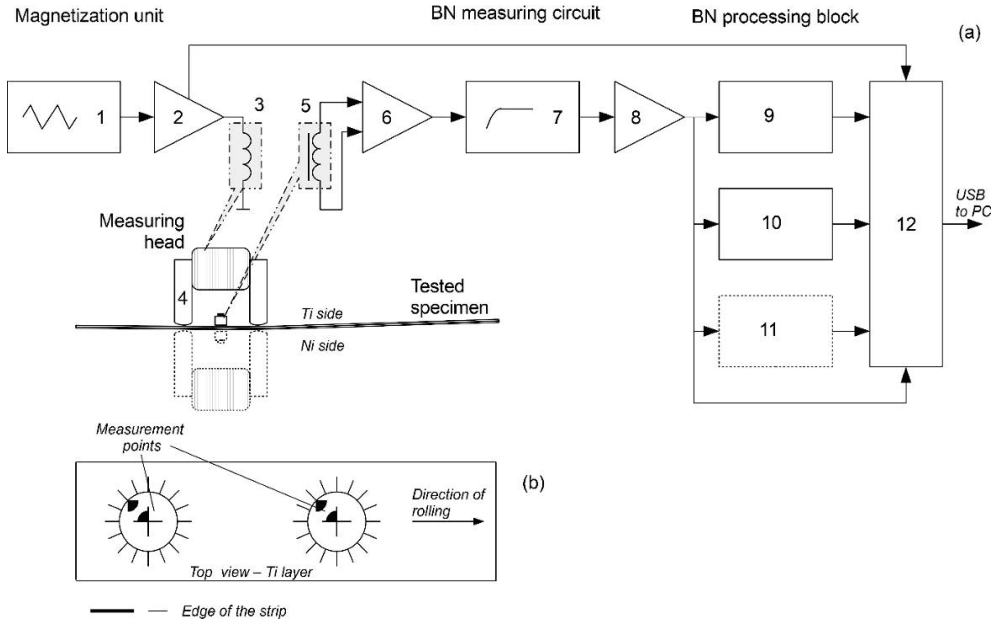
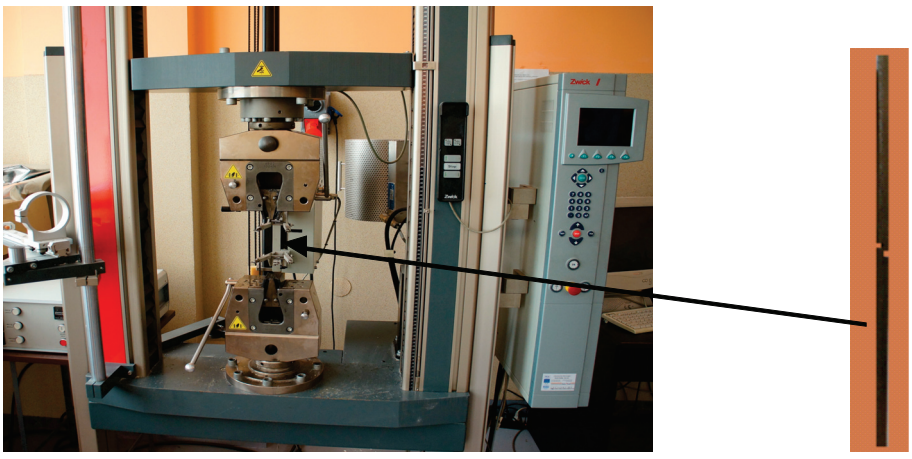


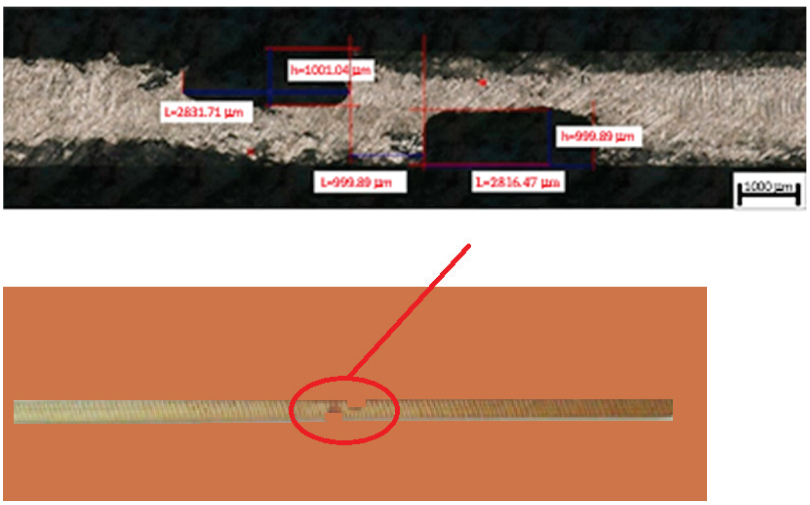
Figure 4. Schematic view of the experimental set-up: (**a**) functional block diagram, (**b**) a view of the measurement points, 1—RC generator, 2—current power amplifier, 3—magnetization windings, 4—yoke, 5—detection coil, 6—low-noise measuring preamplifier, 7—HP filter, 8—amplifier, 9, 10 and 11—processing block, 12—data acquisition card.

On the surfaces of both sides of four Ti-Ni specimens (l = ~145 mm, w = 40 mm), two measurement points were marked by a permanent ink (Figure 5b). The distance between them was 60 mm, and the first point was signed 50 mm from the front of the specimens in the sense of the rolling start. In each measurement place, the lines of the measuring head positioning were drawn with angular step θ = 22.5°.



(**a**)

Figure 5. *Cont.*



(**b**)

Figure 5. View of (**a**) the Zwick Z100 testing machine, (**b**) samples with measurement results.

Due to the different orientation of the specimens during rolling, one of the edges of the strip was marked by the thick line too.

At these measurement points, the same set of directional BN measurements were done before and after the experiment of rolling Ti-Ni sheets. The measuring head position was changed between 0 and 180° with a constant step. The direction of the rolling pass line was assumed as the reference (0°).

In the final stage of research, the microstructure analysis was conducted. The analysis was conducted mainly for joining the area for material after explosive welding as well as after the rolling process. The research was conducted using the Nikon Eclipse Ma 200 producer microscope (Tokio, Japan) and Phenom XL (Thermo Fisher, Waltham, MA, USA) producer scanning microscope. During tests was also conducted the EDS analysis of the welding zone.

3. Results and Discussion

As part of the considerations, shearing tests of the joint areas were performed. Figure 5 shows a view of the sample before the process. In order to determine the cross-sectional area of the sheared samples, the length and width of the samples prepared for testing were measured.

The first stage of the conducted research on the bimetal after explosive welding considered mechanical properties of both layers as well as the joining area. Table 2 shows the properties of materials joined by explosive welding. The Ni layer was the base layer on which the Ti layer was shot.

Table 2. Mechanical properties of materials used to combine into a composite.

Materials	UTS, Mpa	YS0.2, Mpa	HV_{01}	A, %
Ti Grade 1	324	215	115	43
Ni N0221	390	170	95	48

Where: UTS—endurance limit, YS0.2—conventional endurance limit, HV_{01}—hardness, A—lengthening.

In the process of joining materials with different properties by explosive welding (Table 2), a so-called intermediate layer is created, which is a mixture of the joined materials. Due to its different properties, unlike the joined materials, it often undergoes microcracks in the rolling process, which lead to a weakening of the strength of the joint area. Therefore,

shear strength tests of the joint area are performed after each stage of the process of manufacturing flat-layered composites. Table 3 presents the results of the shear strength test of the Ni-Ti composite joint area. The results presented refer to the composites after direct explosive welding and after the symmetric and asymmetric rolling process.

Table 3. Shear strength results of the material after explosion welding and after the rolling process.

Sample	H mm	Dimensions of the Shear Area L mm	B mm	S mm^2	Fmax kN	Rs Mpa	Comments
1	2	1.02	20	20.4	9.2	450.8	rupture in the joining area
2	2	0.98	19.6	19.2	8.62	448.96	rupture in the joining area
3	1.8	0.95	20.2	19.19	8.37	436.16	rupture in the joining area for av = 1.0
4	1.8	1.07	20.1	21.51	9.64	446.92	rupture in the joining area for av = 1.1

Where: L, B, S—length, width, cross-sectional area of the sample for testing the shear strength of the joint.

The shear strength tests of the joint areas were carried out for the Ti-Ni material after direct connection (1), the ASR rolling process (2) for a relative reduction of ε = 10%, and after the SR rolling process (3) for a relative reduction of ε = 10%. The measurement results are presented in Table 3. Based on the conducted tests, it was observed that the rolling process affects the reduction in the shear strength properties of the connected Ti-Ni-layered composites. Based on the comparative analysis, it is clearly visible that the composite connection area is much less weakened in the case of using the ASR rolling process, which ensured obtaining straight Ti-Ni composite sheets after the deformation process. It should be emphasized that the value of the curvature of composite sheets is influenced by a number of both technological and material parameters. It depends to a large extent on the diversity of mechanical properties of the deformed materials [25]. Bending of composite sandwich sheets in the rolling process depends on many parameters, both technological and material properties. To a large extent, it depends on the diversity of mechanical properties of deformed materials [30].

Figures 6 and 7 show views of samples after symmetrical rolling (SR) and asymmetrical rolling (ASR) according to the scheme in Table 4.



Figure 6. Shape of sample of Ti-Ni sheets after rolling: (**a**) ε = 10% a_v = 1.0 (No 1), (**b**) ε = 15%, a_v = 1.0 (No 3).

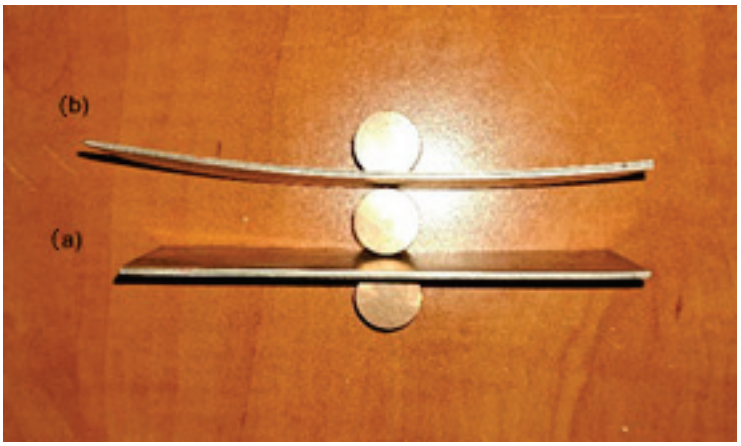


Figure 7. Shape of sample of Ti-Ni sheets after rolling: (**a**) ε = 15% a_v = 1.1 (No 4), (**b**) ε = 10%, a_v = 1.1 (No 2).

Table 4. Results of the laboratory rolling tests SR and ASR.

No.	H_{Ti0}/H_{Ni0} mm/mm	H_{Ti}/H_{Ni} mm/mm	H_1 mm	ε %	ε_{Ti} %	ε_{Ni} %	a_v	1/R 1/m
1	1/1	0.87/0.93	1.8	10	13	7	1.0	1.18
2	**1/1**	**0.89/0.91**	**1.8**	**10**	**11**	**9**	**1.1**	**0.1**
3	1/1	0.82/0.88	1.7	15	18	12	1.0	0.98
4	1/1	0.85/0.85	1.7	15	15	15	1.1	0.44

Figure 8 shows a view of the microstructure along with the thickness measurements of the individual layers (the result presented is the arithmetic mean of 5 measurements).

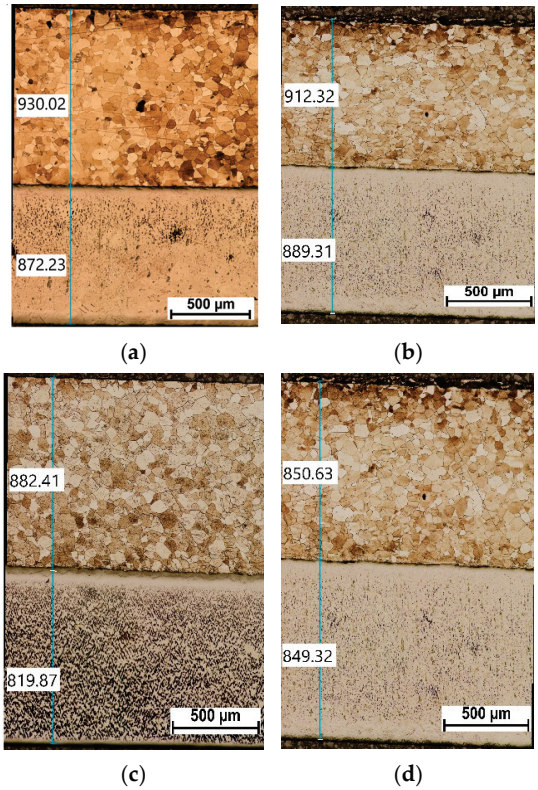


Figure 8. Optical microscopy view with connection areas and layer thickness measurements, (**a**) SR No. 1, (**b**) ASR No. 2, (**c**) SR No. 3, (**d**) ASR No. 4.

The results of rolling tests for individual variants are given in Table 4 and shown in Figures 6–8. It should be emphasized that the value of the curvature of composite sheets is influenced by a number of both technological and material parameters. It depends to a large extent on the diversity of mechanical properties of the deformed materials [30]. Therefore, the use of new material pairs requires precise determination of the optimal forming conditions in the rolling process. In the considerations conducted for the ASR rolling variant, for the relative deformation ε = 10%, a straight strip was obtained. On the other hand, in the case of conducting the rolling process for the relative deformation ε = 15%, the introduced asymmetry had a positive effect on the shape of the rolled composite strip. However, the composite sheet still had a small bend, which is shown in Figure 7. The measured values of the strip curvature are given in Table 4, which clearly shows the beneficial effect of the ASR process on the curvature of the rolled Ti-Ni composite sheets.

During the rolling process of composite sandwich sheets, the course of changes in metal pressure forces on the roll was measured and shown in Figure 9 as the sum of signals from both transducers.

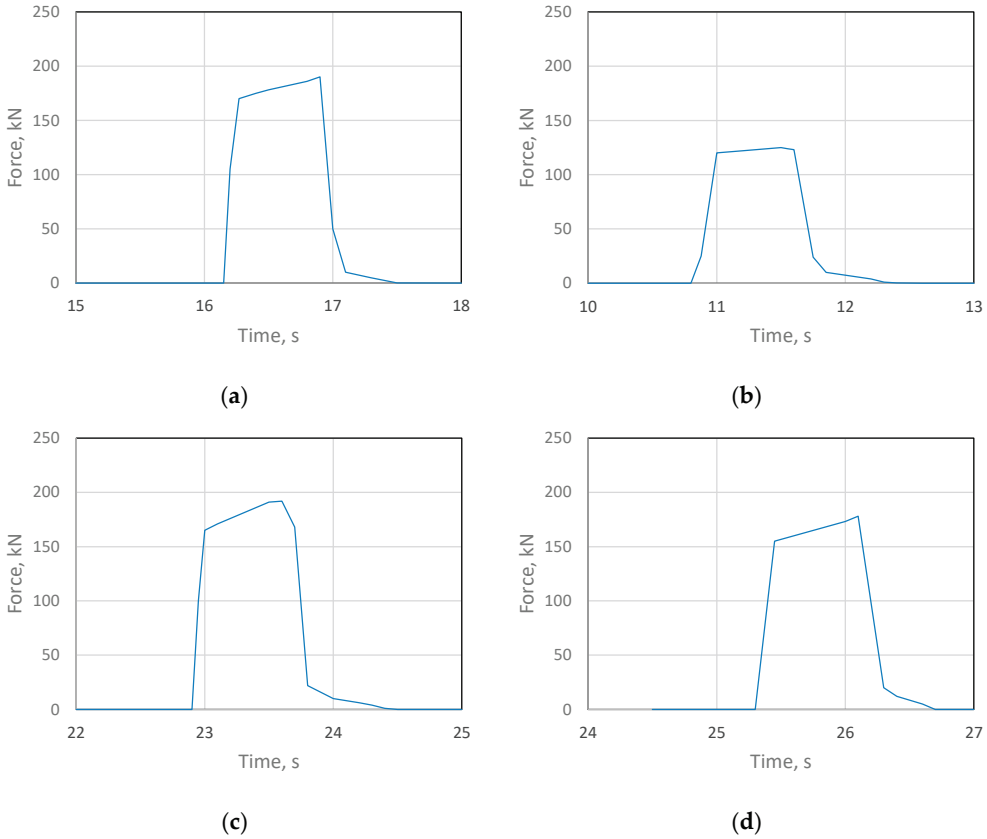


Figure 9. Changes in force on the rolls: (**a**) ε = 10%, a_v = 1.0; (**b**) ε = 1.0%, a_v = 1.1, (**c**) ε = 15%, a_v = 1.0, (**d**) ε = 15%, a_v = 1.1.

The rolling process of composite sheets made of difficult-to-deform Ti-Ni materials differs from the research conducted so far in the field of manufacturing two-layer flat products. Analyzing the changes in the metal pressure force on the rolls, it can be seen that after introducing the asymmetry of the peripheral speed of the rolls, their value decreased. The reduction in the value of the metal pressure forces on the rolls as a result of using ASR is consistent with the literature assumptions [24]. The peripheral asymmetry of the work rolls introduced into the process was aimed at improving the shape of the composite sheets after the rolling process, which is shown in Figures 7 and 8. The introduced difference in the peripheral speeds of the work rolls influenced the increase in the uniformity of

deformation of the materials constituting the layered composite. Thus, the use of the asymmetry of the peripheral speeds also had a clear effect on the state of stress in the Ti-Ni composite materials. The results of stress tests in Ti-Ni-layered composites obtained by the Barkhausen method are presented in the further part of the paper.

In the next stage of research, the residual stress analysis uses the Barkhausen noise (BN). Below are presented obtained results. Figure 10 shows the example oscillogram of BN captured at the Ni side and at the Ti side of composite sandwich sheets. BN measured through the Ti layer has a peak position (maximum of intensity) that is more delayed, indicating that at the side of the joint, the material is magnetically harder than on the other side (outer surface of the Ni layer). This bigger coercive force seems to be the result mainly of strong deformations of the nickel [24,44] caused by explosion and the presence of TiNi phases.

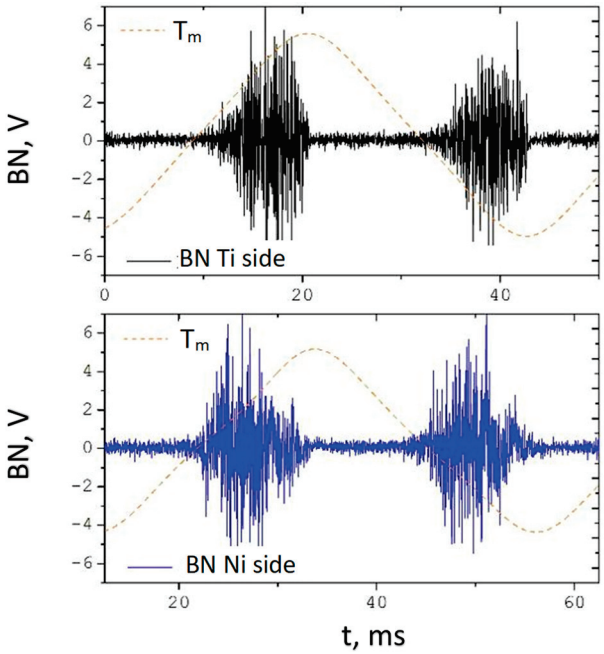


Figure 10. Barkhausen noise oscillograms picked up respectively at Ti and Ni sides for basic materials after explosive welding.

Received results of investigations of BN intensity expressed by its RMS value and corresponding to the strain/stress state were shown in popular form in the directional diagrams. Due to different measurement and magnetization conditions during testing of both sides of the nickel layer, the data were normalized and presented in arbitrary units. For clear visibility of the principle axis of the pole figures, they were also drawn as B-splines. In Figure 11, representative directional diagrams in measurement point no. 1 (sample 1) are presented.

Before the rolling process, in the nickel layer, inside the sheet (measurements at the Ti side, black line), significant anisotropy of BN was observed, indicating the presence of an orthogonal biaxial stress state [45,48,49]. This layer was deformed by process of cladding, and, the main directions of strains at direction angles of 67.5° and 135° in this region result mainly from the direction of explosive wave propagation. At the outer side of the nickel not affected directly by the explosion (measurement at the Ni side, blue line), the shape of the radial plot points to a slightly biaxial stress state at directions 0° and 90°.

As can be observed, a significant influence of the rolling process on the re-orientation of BN intensity directional diagrams is identified (Figure 11, red lines). In this case, on both sides of the Ni layer, the main intensity of Barkhausen noise is in a direction parallel to the

direction of rolling. It is an effect of the complex and strong cold deformation, affecting the magnetic domain structure of the nickel component too.

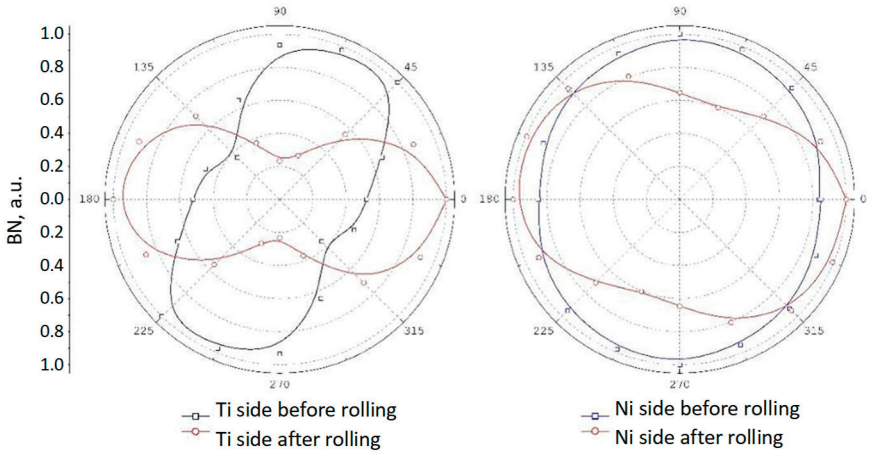


Figure 11. Examples of directional diagrams of BN intensity in measurement point no. 1.

In Figures 12 and 13, extracted results of BN noise investigations in the other measurement points of tested samples were shown. For better understanding, on the sample shapes, the direction where the main intensity of the Barkhausen noise had occurred was marked by the arrows.

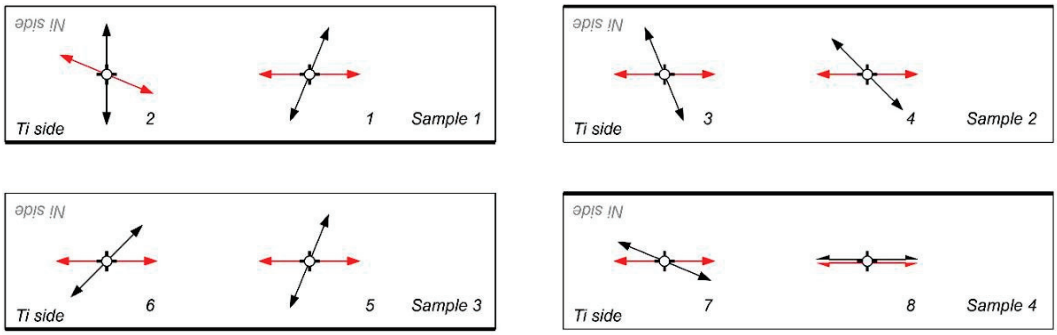


Figure 12. Orientation of the BN directional diagrams at Ti side of the sheet: before (black arrows) and after (red arrows) rolling process.

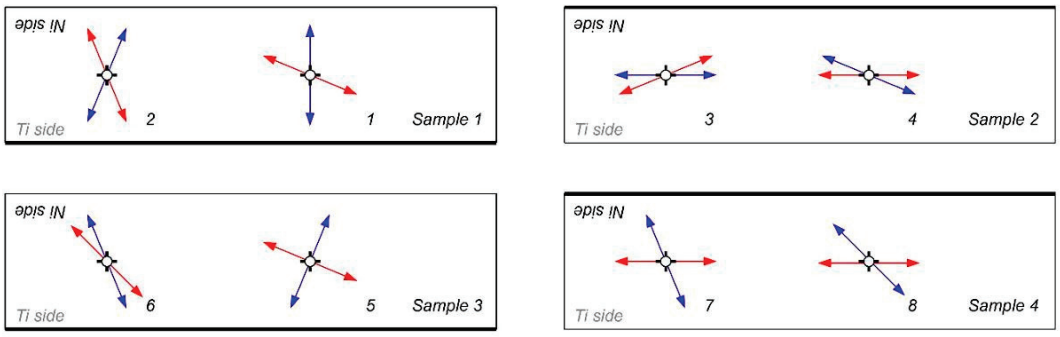


Figure 13. Orientation of the BN directional diagrams at Ni side of the sheet: before (blue arrows) and after (red arrows) rolling process.

At first, samples after explosive welding were characterized by the totally different initial orientation of the direction of principle strains. Applying additional rolling processes caused that, in most cases, principle strains in samples were aligned to the direction near to the direction of rolling [49–51].

This effect is especially visible when rolling asymmetry has been applied. In this case, principle stress directions revealed by BN measurement on the Ni side (Figure 13) of the samples no. 2 and 4 were almost fully aligned with the direction of rolling. This proves the intensive deformation mechanism during this type of rolling.

Obtained results have confirmed the possibility of the stress and strain determination in the nickel layer of thin composite sandwich sheets by the Barkhausen method. It can be a new, additional, or supplementary testing tool for Ti-Ni sheets alongside existing ultrasound NDT of composite joint quality.

BN characterization can be useful not only for improving and developing the existing production technology but also for designing the manufacturing processes of the products from Ti-Ni sheets, considering the actual internal stress and strain state.

Due to the fact that deformation of EW materials in the merging area possesses stresses that in extreme cases can even lead to delamination, the authors have decided that microstructure analysis is necessary.

Therefore, in the last stage of research, the microstructure tests were conducted. Figure 14 presents the Ti layer (sheet) before welding; the material was etched (1 mL HF, 6 mL HNO_3, 96 mL distilled water), and Figure 15 Ni layer (sheet) before welding (4 g copper sulfate, 20 mL HCl, 1 mL H_2SO_4, 16 mL distilled water). As it can be seen, there is no visible deformation of grain in both materials.

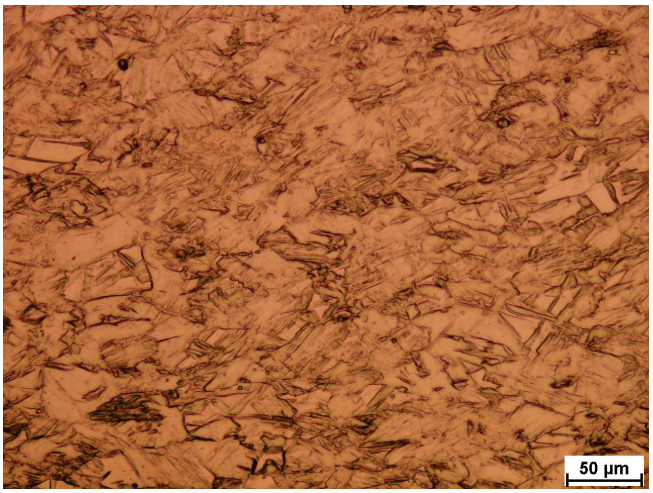


Figure 14. Ti layer (sheet) before welding, magn. 200×.

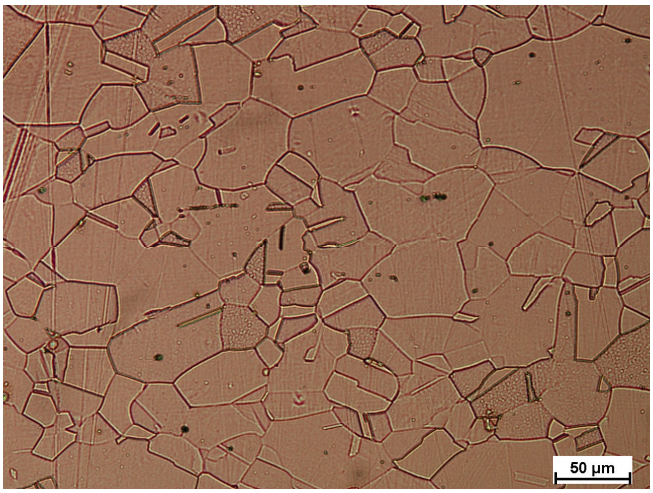
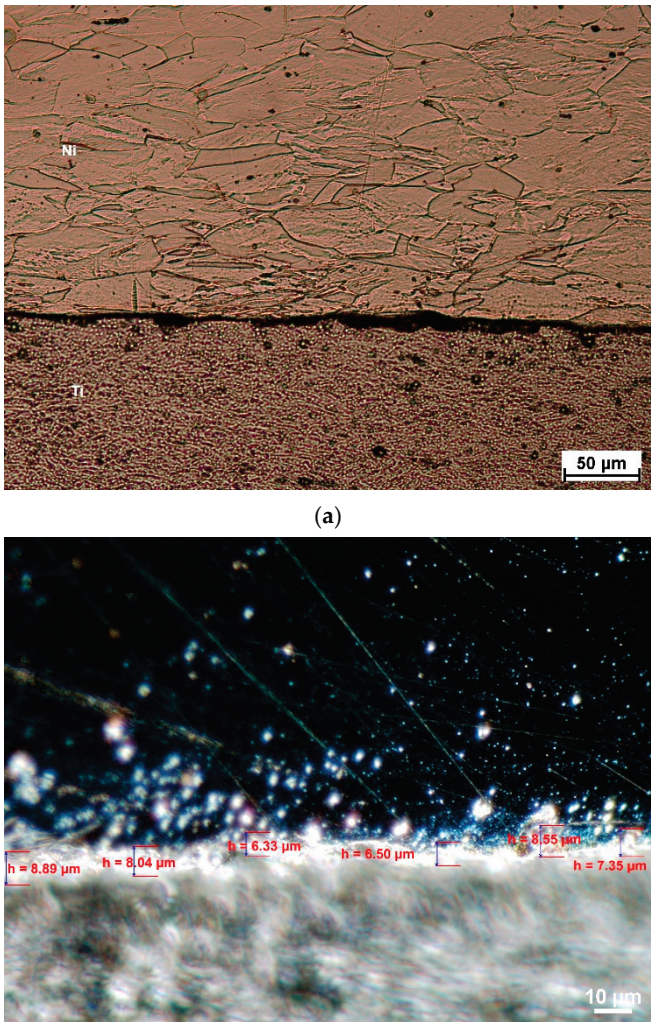


Figure 15. Ni layer (sheet) before welding, magn. 200×.

The analysis on non-etched samples (Figure 16)—analysis of joining area quality and etched (4 g copper sulfate, 20 mL HCl, 1 mL H_2SO_4, 16 mL distilled water)—was conducted. The analysis of the possibility of the occurrence of discontinuities in the joining area on non-etched samples was made at 200 and 1000× magnification.



(**a**)

(**b**)

Figure 16. Microscopic view of the microstructure with image on the merging area with measurements of layers thickness, (**a**) raw state sample (after explosive welding) magn. 200×, (**b**) sample 1 (dark field) magn. 1000×.

As can be seen, none of the samples show any traces of cracks in the area of the joint. This leads to the conclusion that the proposed welding technology is correct. However, attention should be paid to the presence of intermetallic phases and changes in the geometry of the merging area. The geometry changes are related to the rolling applied. As a result of plastic processing, the initial typical wavy connection was transformed into a desirable flat one.

After explosive welding, it can be seen that the Ni layer has an axial grain size from 80 to about 180 µm. Finer grains are located near the joint area. As a result of the applied plastic deformation, a negligible grain deformation can be observed along the rolling direction.

Well visible is also the intermetallic, which analysis was made with use of the Phenom XL scanning microscope equipped with the EDS and BDS analyzer. Results of observation are presented in Figures 17 and 18. The BSD analysis of the intermetallic layer, Figure 19, shows the map of elements observed in this area. Due to the fact that in the

literature [21] it can be found that the joining area chemical composition is non-uniform and can be composed of the Ni_3Ti, NiTi, and $NiTi_2$ phases, point analysis in individual areas was performed.

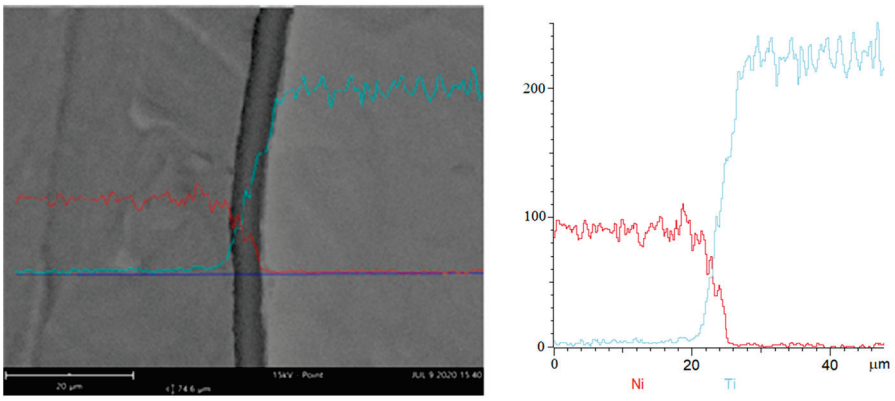


Figure 17. The samples EDS analysis of the joining area.

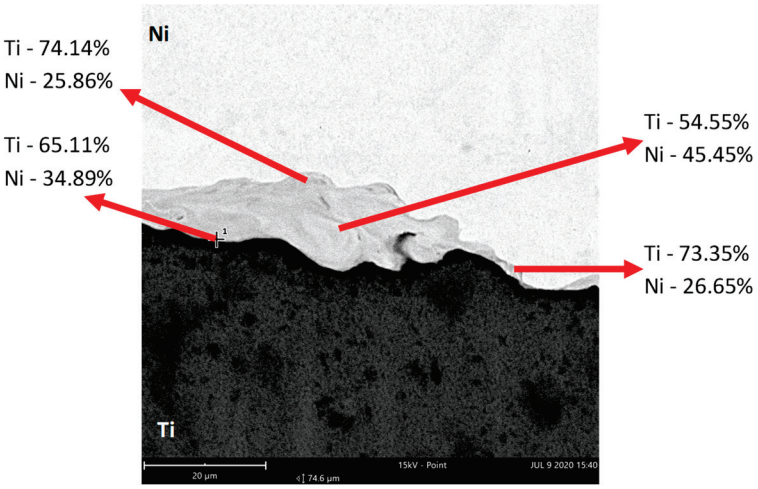
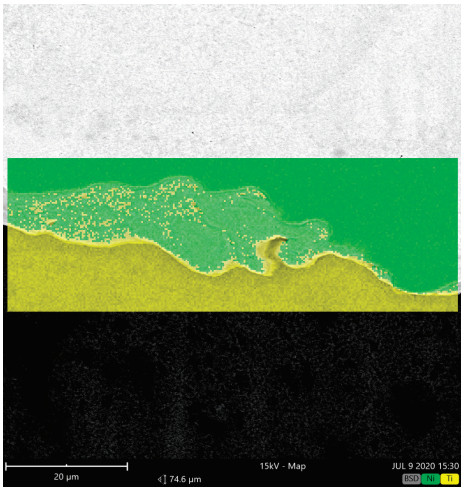


Figure 18. The point analysis in individual areas of the joining area.



Element Symbol	Atomic %	Weight %
Ni	48.56	53.65
Ti	51.44	46.35

Figure 19. The BSD map of joining area with average chemical composition of the intermetallic layer.

As can be seen after microscopic analysis, the joining area is composed in part of an intermetallic layer. This area, however, is non-uniform (Figure 16); in the central part it has a composition of about 50% Ti and Ni, while in the zone close to the Ni layer it is 75/25%

Ni/Ti. In the area near Ti, the proportion reverses, and it a composition of 65/35% and 73/27% Ti/Ni can be seen. What is interesting is that no crack in the joining area was observed for all analyzed samples. This confirms that the explosive welding technology and cold symmetrical and asymmetrical rolling are possible.

4. Conclusions

The cold-rolling process of sandwich composite sheets from hard-deformable Ti-Ni materials is complicated and difficult to develop. Based on the conducted experimental research, it can be concluded that the cold rolling process of composite sandwich sheets can be successfully used in industrial practice. The obtained results of experimental research allowed for the following conclusions to be formulated:

1. After the explosive welding process, a permanent connection was obtained with a shear strength more than three times higher than the requirements provided for by the standard—150 MPa.
2. During the rolling process, however, the problem is the selection of optimal process parameters for pairs of difficult-to-deform materials. The carried-out tests show that plastic deformation of Ti-Ni composite sandwich sheets were conducted properly. The introduction of asymmetry in the peripheral speed of the work rolls for rolling composite Ti-Ni sheets had a positive effect on their bending after the plastic forming process (Figures 6 and 7). The macroscopic observation revealed that no cracks or delamination were observed in the area of the joint.
3. Obtained results have confirmed the possibility of the stress determination in the nickel layer of thin composite by the Barkhausen method. It can be a new, additional, or supplementary testing tool for Ti-Ni sheets alongside existing ultrasound NDT of composite joint quality.
4. The microstructure analysis of the joining area shows that cold deformation with the use of the symmetrical and asymmetrical rolling does not generate cracks. It was confirmed that the intermetallic layer is non-uniform. The chemical composition changes in volume. In the central part it is composed of a mixture of about 50% Ti and Ni.
5. It has to be stated that the intermetallic layer is not continuous; it can be seen that there are areas of intermetallics. The joining area after explosive welding is wavy; after the applied rolling process, the wave peaks slightly decrease. What is interesting is that the intermetallics after explosive welding are wider than after the rolling process.

Author Contributions: Conceptualization, D.R.; methodology, G.S and T.C.D.; data curation, D.R., G.S. and T.G.; validation, S.M., P.S. and G.S.; writing—original draft preparation, D.R., G.S. and T.G.; writing—review and editing, S.M.; supervision, S.M. and T.C.D. All authors have read and agreed to the published version of the manuscript.

Funding: This research received no external funding.

Institutional Review Board Statement: Not applicable.

Informed Consent Statement: Not applicable.

Data Availability Statement: The original contributions presented in this study are included in the article. Further inquiries can be directed to the corresponding author.

Conflicts of Interest: The authors declare no conflicts of interest.

References

1. Zhao, Q.; Hu, X.; Liu, X. Analysis of Mechanical Parameters in Multi-Pass Asymmetrical Rolling of Strip by Slab Method. *Materials* **2023**, *16*, 6286. [CrossRef] [PubMed]
2. Rydz, D. The Influence of Asymmetry Factor and Deformation on the Criterion Optimizing the Relative Flow Rate of St3S+0H13J Bimetallic Strip. *Metalurgija* **2005**, *44*, 91–95.
3. Grudzień, J.; Grochała, D.; Grzejda, R.; Kochmański, P. Testing The Effectiveness of Hybrid Milling and Surface Burnishing in Improving the Wear Resistance of Machine Parts Made of Structural Steel. *Lubricants* **2024**, *12*, 458. [CrossRef]
4. Grochała, D.; Grzejda, R.; Parus, A.; Berczyński, S. The Wavelet Transform For Feature Extraction And Surface Roughness Evaluation After Micromachining. *Coatings* **2024**, *14*, 210. [CrossRef]
5. Krajewski, S.J.; Grochała, D.; Tomków, J.; Grzejda, R. Analysis of the Surface Stereometry of Alloyed Austenitic Steel After Fibre Laser Cutting Using Confocal Microscopy. *Coatings* **2023**, *13*, 15. [CrossRef]
6. Strzelecki, G.W.; Nowakowska-Langier, K.; Namyślak, K.; Mulewska, K.; Wilczopolska, M.; Minikayev, R.; Nadolski, M.; Okrasa, S.; Romaniuk, S.; Zdunek, K. Shannon Entropy Characterization of High-Entropy Thin Films Synthesized by Pulsed Magnetron Sputtering: The Influence of Modulation Frequency. *Metall. Mater. Trans. A* **2025**, *56*, 518–531. [CrossRef]
7. Hawryluk, M.; Janik, M.; Zwierzchowski, M.; Lachowicz, M.M.; Krawczyk, J. Possibilities of Increasing the Durability of Dies Used in the Extrusion Process of Valve Forgings from Chrome-Nickel Steel by Using Alternative Materials from Hot-Work Tool Steels. *Materials* **2024**, *17*, 346. [CrossRef]
8. Krawczyk, J.; Łukaszek-Sołek, A.; Lisiecki, Ł.; Śleboda, T.; Hawryluk, M. Wear Mechanisms of the Forging Tool Used in Pre-Forming in a Double Forging System of Truck Parts. *Materials* **2023**, *16*, 351. [CrossRef]
9. Wang, H.; Chen, N.; Cheng, H.; Wang, Y.; Zhao, D. Tensile Deformation Mechanism of an In Situ Formed Ti-Based Bulk Metallic Glass Composites. *Materials* **2024**, *17*, 4486. [CrossRef]
10. Eizadjou, M.; Kazemi Talachi, A.; Danesh Manesh, H.; Shakur Shahabi, H.; Janghorban, K. Investigation of Structure and Mechanical Properties of Multi-Layered Al/Cu Composite Produced by Accumulative Roll Bonding (ARB) Process. *Compos. Sci. Technol.* **2008**, *68*, 2003–2009. [CrossRef]
11. Paul, H.; Faryna, M.; Prazmowski, M.; Banski, R. Changes in the Bonding Zone of Explosively Welded Sheets. *Arch. Metall. Mater.* **2011**, *56*, 463–474. [CrossRef]
12. Zhao, K.; Xu, D.; Song, X.; Ma, Y.; Li, H.; Zhang, J.; Chen, D. Reducing Yield Asymmetry between Tension and Compression by Fabricating ZK60/WE43 Bimetal Composites. *Materials* **2020**, *13*, 249. [CrossRef] [PubMed]
13. Rydz, D.; Stradomski, G.; Pałęga, M.; Salwin, M.; Opydo, M.; Szarek, A.; Fik, J.; Chmielewski, T. Analysis of Plastic Forming During Rolling of Al1050-AZ31-Al1050 Layered Composites for Transport Purposes. *Adv. Sci. Technol. Res. J.* **2024**, *18*, 234–244. [CrossRef] [PubMed]
14. Sang, C.; Cai, X.; Zhu, L.; Ren, X.; Niu, G.; Wang, X.; Feng, P. Interfacial Microstructure of Ti/Ni Joints with Ti–Al Interlayer by Rapid Thermal Explosion Bonding in Vacuum. *Vacuum* **2020**, *171*, 109028. [CrossRef]
15. Nayanathara Thathsarani Pilapitiya, P.; Ratnayake, A.S. The World of Plastic Waste: A review. *Clean. Mater.* **2024**, *11*, 100220. [CrossRef]
16. Luo, J.; Aco, V.L. Using cold roll bonding and annealing to process Ti/Al multi-layered composites from elemental foils. *Mater. Sci. Eng. A* **2004**, *379*, 164–172. [CrossRef]
17. Mohanty, A.K.; Vivekanandhan, S.; Tripathi, N.; Roy, P.; Snowdon, M.R.; Drzal, L.T.; Misra, M. Sustainable Composites for Lightweight and Flame Retardant Parts for Electric Vehicles to Boost Climate Benefits: A perspective. *Compos. Part C Open Access* **2023**, *12*, 100380. [CrossRef]
18. Fronczek, D.M.; Chulist, R.; Litynska-Dobrzynska, L.; Kac, S.; Schell, N.; Kania, Z.; Szulc, Z.; Wojewoda-Budka, J. Microstructure and Kinetics of Intermetallic Phase Growth of Three-Layered A1050/AZ31/A1050 Clads Prepared by Explosive Welding Combined With Subsequent Annealing. *Mater. Des.* **2017**, *130*, 120–130. [CrossRef]
19. Tavoosi, M. The Kirkendall Void Formation in Al/Ti Interface During Solid-State Reactive Diffusion Between Al and Ti. *Surf. Interfaces* **2017**, *9*, 96–200. [CrossRef]
20. Wachowski, M.; Kosturek, R.; Śniezek, L.; Mróz, S.; Stefanik, A.; Szota, P. The Effect of Post-Weld Hot-Rolling on the Properties of Explosively Welded Mg/Al/Ti Multilayer Composite. *Materials* **2020**, *13*, 1930. [CrossRef]
21. Topolski, K.; Wieciński, P.; Szulc, Z.; Gałka, A.; Garbacz, H. Progress in the Characterization of Explosively Joined Ti/Ni Bimetals. *Mater. Des.* **2014**, *63*, 479–487. [CrossRef]
22. Karolczuk, A.; Kluger, K.; Derda, S.; Prazmowski, M.; Paul, H. Influence of Impact Velocity on the Residual Stress, Tensile Strength, and Structural Properties of an Explosively Welded Composite Plate. *Materials* **2020**, *13*, 2686. [CrossRef] [PubMed]
23. Buque, C.; Tirschler, W.; Holste, C. Analysis of Local Variations of Internal Stresses in Cyclically Deformed Nickel Crystal by Barkhausen Noise Measurements. *Mat. Sc. Eng. A* **1966**, *215*, 168–174. [CrossRef]
24. Garstka, T.; Rydz, D. Explosively Welded Ti-Ni Bimetallic Plate Characterization Using Barkhausen Noise. *J. Electr. Eng.* **2015**, *66*, 186–189.

25. Rydz, D.; Dyja, H.; Berski, S. The Prediction of Curvature of Bimetallic Plate Al-Cu During Asymmetrical Cold Rolling. *Metalurgija* **2003**, *42*, 261–264.
26. Mozaari, A.; Hosseini, M.; Manesh, H.D. Al/Ni Metal Intermetallic Composite Produced by Accumulative Roll Bonding and Reaction Annealing. *J. Alloys Compd.* **2011**, *509*, 9938–9945. [CrossRef]
27. Gronostajski, Z.; Pater, Z.; Madej, L.; Gontarz, A.; Lisiecki, L.; Łukaszek-Sołek, A.; Łuksza, J.; Mróz, S.; Muskalski, Z.; Muzykiewicz, W.; et al. Recent Development Trends in Metal Forming. *Arch. Civ. Mech. Eng.* **2019**, *19*, 898–941. [CrossRef]
28. Roberts, I.; Mynors, D. Optimal Selection of Machine Parameters in Tension Leveling of Sheet Metals. *Eng. Mater. Sci.* **2012**, 212671857.
29. Mihara-Narita, M.; Asai, K.; Sato, H.; Watanabe, Y.; Nakatsugawa, I.; Saito, N.; Chino, Y. Dissimilar Welding of Magnesium Alloys and Aluminum Alloys by Explosive Welding. *Materials* **2025**, *18*, 1013. [CrossRef]
30. Wierzba, A.; Mróz, S.; Szota, P.; Stefanik, A.; Mola, R. The Influence of the Asymmetric ARB Process on the Properties of Al-Mg-Al Multi-Layer Sheets. *Arch. Metall. Mater.* **2015**, *60*, 2821–2825. [CrossRef]
31. Sun, H.; Li, Q.; Chan, Y.C. A Study Of Ag Additive Methods by Comparing Mechanical Properties Between Sn57.6Bi0.4Ag and 0.4wt% Nano-Ag-Doped Sn58Bi BGA Solder Joints. *J. Mater. Sci. Mater. Electron.* **2014**, *25*, 4380–4390. [CrossRef]
32. Cao, J.; Li, C.; Qi, J.; Shi, Y.; Feng, J. Combustion joining of carbon–carbon composites to TiAl intermetallics using a Ti–Al–C powder composite interlayer. *Compos. Sci. Technol.* **2015**, *115*, 72–79. [CrossRef]
33. Zdrodowska, K.; Wojsyk, K.; Szala, M. The Microstructural Properties of Explosion Welded Ni/Ti Joint. *Adv. Sci. Technol. Res. J.* **2014**, *8*, 71–74. [CrossRef]
34. Zhang, B.; Zhang, Z.; Zhao, T.; Zhang, D.; Cheng, J.; Wang, W.; Qiao, K.; Yang, Y.; Wang, K. Effect of Temperature on the Interfacial Evolution of Ti/Ni Multilayered Composites Fabricated by ARB. *J. Alloys Comp.* **2019**, *803*, 265–276. [CrossRef]
35. Shen, T.D.; Quan, M.X.; Wang, J.T. Solid State Amorphization Reactions in Ni/Ti Multilayer Composites Prepared by Cold Rolling. *J. Mat. Sc.* **1993**, *28*, 394–398. [CrossRef]
36. Gavalec, M.; Barenyi, I.; Krbata, M.; Kohutiar, M.; Balos, S.; Pecanac, M. The Effect of Rotary Friction Welding Conditions on the Microstructure and Mechanical Properties of Ti6Al4V Titanium Alloy Welds. *Materials* **2023**, *16*, 6492. [CrossRef]
37. Grassino, J.; Vedani, M.; Vimercati, G.; Zanella, G. Effects of Skin Pass Rolling Parameters on Mechanical Properties of Steels. *Int. J. Precis. Eng. Mnanuf.* **2017**, *13*, 2017–2026. [CrossRef]
38. Zhao, J.; Wang, X.; Yang, Q.; Wang, Q.; Wang, Y.; Li, W. Mechanism of Lateral Metal Flow on Residual Stress Distribution During Hot Strip Rolling. *J. Mater. Proces. Tech.* **2021**, *288*, 116838. [CrossRef]
39. Mróz, S.; Szota, P.; Stefanik, A. The Theoretical and Experimental Analysis of the Possibility of Employing the Groove Rolling Process for the Manufacture of Mg/Al Bimetallic Bars. *Metalurgija* **2016**, *55*, 628–630.
40. Abvabi, A. Effect of Residual Stresses in Roll Forming Process of Metal Sheets. Ph.D. Thesis, Deakin University, Melbourne, Australia, 2014.
41. Skripalenko, M.M.; Galkin, S.P.; Karpov, B.V.; Romantsev, B.A.; Kaputkina, L.M.; Danilin, A.V.; Skripalenko, M.N.; Patrin, P.V. Forming Features and Properties of Titanium Alloy Billets After Radial-Shear Rolling. *Materials* **2019**, *12*, 3179. [CrossRef]
42. Naizabekov, A.; Lezhnev, S.; Arbuz, A.; Panin, E. The Effect of Radial-Shear Rolling on Microstructure and Mechanical Properties of Stainless Austenitic Steel AISI-321. *MATEC Web Conf.* **2018**, *190*, 11003. [CrossRef]
43. Garstka, T. The Complex System for Residual Stress Determination Based on Barkhausen Noise Measurement. In Proceedings of the 5th International Conference on Barkhausen Noise and Micromagnetic Testing, Petten, The Netherlands, 2–3 June 2005; pp. 219–226.
44. Pitoňák, M.; Mičietová, A.; Moravec, J.; Čapek, J.; Neslušan, M.; Ganev, N. Influence of Strain Rate on Barkhausen Noise in Trip Steel. *Materials* **2024**, *17*, 5330. [CrossRef] [PubMed]
45. Sheng, H.; Wang, P.; Yang, Y.; Tang, C. Stress and Microstructures Characterization Based on Magnetic Incremental Permeability and Magnetic Barkhausen Noise Techniques. *Materials* **2024**, *17*, 2657. [CrossRef] [PubMed]
46. Wu, H.; Ziman, J.A.; Raghuraman, S.R.; Nebel, J.-E.; Weber, F.; Starke, P. Short-Time Fatigue Life Estimation for Heat Treated Low Carbon Steels by Applying Electrical Resistance and Magnetic Barkhausen Noise. *Materials* **2023**, *16*, 32. [CrossRef]
47. Nishihara, H.; Taniguchi, S.; Maeda, H.; Oguro, I.; Harada, M.; Ogino, T.; Matsumoto, S.; Shindo, Y.; Ohtsuka, S. The effect of mechanical stress on Barkhausen noises from heat-treated nickel plates. In Proceedings of the 12th Asia-Pacific Conference on NDT, Auckland, New Zealand, 5–10 November 2006.
48. Vengrinovich, V.; Tsukerman, V.L. Stress and Texture Measurement Using Barkhausen Noise and Angular Scanning of Driving Magnetic Field. In Proceedings of the 15th WCDNT—World Conference on Nondestructive Testing, Montreal, QC, Canada, 31 August–3 September 2004.
49. Piotrowski, L.; Chmielewski, M.; Augustyniak, M.; Maciakowski, P.; Prokop, K. Stress Anisotropy Characterisation with Help of Barkhausen Effect Detector with Adjustable Magnetic Field Direction. *Int. J. Ap. Electr. Mech.* **2015**, *48*, 163–170. [CrossRef]

50. Silva, S.; Mansur, T.; Palma, E. Determining Residual Stress in Ferromagnetic Materials by Barkhausen Noise Measurement. In Proceedings of the 15th World Conference on Nondestructive Testing, Rome, Italy, 15–21 October 2000.
51. Augustyniak, B. Magnetomechanical Effects and Their Applications at Non-Destructive Evaluation of Materials. Ph.D. Thesis, Gdańsk University of Technology, Gdańsk, Poland, 2003. (In Polish).

Disclaimer/Publisher's Note: The statements, opinions and data contained in all publications are solely those of the individual author(s) and contributor(s) and not of MDPI and/or the editor(s). MDPI and/or the editor(s) disclaim responsibility for any injury to people or property resulting from any ideas, methods, instructions or products referred to in the content.

materials

MDPI

Article

Optimisation of Hot-Chamber Die-Casting Process of AM60 Alloy Using Taguchi Method

Tomasz Rzychoń * and Andrzej Kiełbus

Faculty of Materials Engineering, Silesian University of Technology, ul. Krasińskiego 8, 40-019 Katowice, Poland; andrzej.kielbus@polsl.pl

* Correspondence: tomasz.rzychon@polsl.pl; Tel.: +48-32-603-44-14

Abstract: This paper presents the effect of hot-chamber HPDC (high-pressure die casting) process parameters on the porosity, mechanical properties, and microstructure of AM60 magnesium alloy. To reduce costs, a Taguchi design of the experimental method was used to optimise the HPDC process. Six parameters set at two levels were selected for optimisation, i.e., piston speed in the first phase, piston speed in the second phase, molten metal temperature, piston travel, mould temperature, and die-casting pressure (the pressure under the piston). Signal-to-noise (S/N) ratios were used to quantify the present variations. The significance of the influence of the HPDC parameters was assessed using statistical analysis of variance (ANOVA). The results showed that the die-casting pressure had the most significant influence on the porosity of the AM60 alloy. Moreover, piston speed in the first phase, second phase, and die-casting pressure had the most important effects on tensile strength. It is well known that porosity determines the mechanical properties of die castings; however, in AM60 alloy, changes in the HPDC parameters also contribute to microstructural changes, mainly through the formation of Externally Solidified Crystals.

Keywords: AM60; hot-chamber die casting; Taguchi

1. Introduction

Magnesium alloys are used in the automotive, aerospace, and electronics industries for their high strength and excellent casting properties. Most components made from magnesium alloy are produced using the die-casting process [1,2]. These are mainly alloys from the Mg–Al system. AZ91 alloy is used for its high strength [3], while AM50/AM60 alloys offer a high ductility [4] and good corrosion and impact resistance at ambient temperature [5]. However, the high-pressure die-casting process these alloys undergo often results in significant porosity in the castings [6].

Light alloy die castings, primarily aluminium and magnesium, are more prevalent in the automotive industry than wrought components [7]. The high-pressure die-casting (HPDC) method is efficient and cost-effective for producing magnesium alloy castings with a high precision. Approximately 90% of cast magnesium alloys are made using HPDC. There are two types of die-casting processes, as follows: cold chamber and hot chamber. In hot-chamber die casting, the injection system is immersed in the liquid metal, while in cold-chamber die casting, the liquid metal is manually or robotically fed into the mould [8].

Casting quality is essential in die-casting production. It is closely related to types of casting defects, making it a crucial factor that requires careful attention [9]. Gas and shrinkage porosities can form in castings due to turbulence and alloy shrinkage, affecting their mechanical properties [10]. Gaseous porosity is a common defect in die castings caused by gas or air entrapment in the mould during the casting process. Shrinkage porosity occurs when the alloy contracts during solidification, decreasing the volume [11]. Shrinkage and gas pores can be identified based on their geometrical features. Shrinkage pores are irregular with many shoulders and have a shape factor of less than 0.4. On the other hand, gas pores have a more circular shape, and their shape ratio is higher than 0.6 [12].

The correct process parameter selection that guarantees a high die-casting quality is a crucial issue for technologists and scientists [13]. The quality of die castings is significantly influenced by various technological factors, including the following [9]:

- the casting speed during the casting cycle,
- the pressure acting on the liquid alloy, the so-called resistance pressure,
- the mould filling time,
- and the liquid metal temperature and mould temperature.

Specific parameters can be controlled, while others are noise factors [14]. A statistical experimental design is a helpful method for effectively planning test numbers to select an appropriate technological parameter set. Experimental design methods are popular in the engineering and scientific community because they can be applied with limited statistical knowledge. The most used design methods include factorial design, response surface methodology (RSM), mixture design, multivariate regression analysis, and the Taguchi method [15,16]. Regarding die-casting parameter optimisation, most research reports are concerned with the Taguchi method [14,15,17,18]. Other casting process optimisation methods appear to be limited, but there are publications on using RSM [19–21] or multivariate regression analysis [22]. There is no clear consensus on which of these methods is most effective. In numerous comparisons of the RSM and Taguchi methods, one can find publications indicating that RSM methods are more effective [23,24] or that Taguchi methods are more successful [25–27]. In complex optimisation problems, where understanding variable interactions and obtaining accurate answers are crucial, RSM methods are a better solution. On the other hand, the Taguchi method seems more appropriate when the cost of running experiments, minimising the variability of the production process, or the inferior accuracy of the optimisation process are essential to address. For the above reasons, the Taguchi method was chosen in this work.

The Taguchi method is based on searching for nominal values for the controllable factors (process parameters) which satisfy the output characteristic's maximum compatibility and the lowest noise effect sensitivity. The main benefit of this method is the reduced number of experiments needed to identify the optimal values of the controllable factors. This procedure involves identifying control and noise factors, selecting an orthogonal array (OA) for input variables, and analysing data using the signal-to-noise ratio to measure target achievement. The S/N ratio, also known as the objective function, is inversely proportional to the loss function, so maximising this ratio means minimising losses while improving quality. The three commonly used target functions are "smaller is better", "higher is better", and "nominal is best" [28].

Die-casting processes are commonly used to produce castings from aluminium, magnesium, and, less frequently, zinc alloys. In the case of aluminium alloy die castings, most studies using the Taguchi method indicate a critical influence of intensification pressure on the final properties of the casting for both cold-chamber die casting [14,15,17,18] and hot-chamber die casting [17].

When it comes to magnesium alloys, the situation is not as straightforward. Lee et al. [6] analysed the impact of casting parameters on the porosity distribution in the high-pressure die casting of AM50 alloy, which exhibits similarities to AM60 alloy in its microstructure and mechanical properties. They identified gate velocity, intensification pressure, and melt temperature as the most relevant process parameters contributing to a reduced porosity, primarily gaseous porosity.

Park et al. [18] found that the most significant factor in the die-casting process for AM50 alloy is the second piston speed. This speed affects flowability, and increasing it helps to reduce porosity and hardness. In contrast, the pressure and the first piston speed do not significantly affect the microstructure and mechanical properties.

The application of the Taguchi method for optimising the die-casting parameters in AM60 alloy is not widely discussed in the available publications. However, some publications have examined the influence of die-casting parameters, explicitly focusing on cold-chamber die casting. Research has revealed significant information about how casting speed influences the formation and distribution of Externally Solidified Crystals (ESCs), which also plays a crucial role in our study.

Wang et al. [29] showed that, at low casting speeds, large ESCs are present in the structure, while, at high casting speeds, these ESCs tend to become more spherical. Additionally, they found that the slow injection phase (first piston speed) further influences the distribution and level of ESCs' spheroidization. The distribution and morphology of ESCs also vary based on their location within the casting, such as near the surface, in the core, and near the gating. Wu et al. [30] showed that a lower first piston speed and a longer injection delay time increase ESCs' size and surface area contribution due to a longer melt holding time in the injection sleeve and a reduction in overheating. In contrast, at a higher second piston speed, ESCs' exhibit a more granular and circular morphology and are dispersed throughout the casting.

Among the few studies related to the implementation of the Taguchi method in the analysis of magnesium alloy die-casting processes, the research conducted by Sun et al. [31], Wu et al. [13], and Yang et al. [32] is still worth mentioning. Although numerous publications exist on the properties and microstructure of die-cast magnesium alloys, relatively few research studies present the optimisation of the die-casting parameters for these alloys.

This study's primary objective was to utilise the Taguchi method to determine the optimal technological parameters for the hot-chamber die-casting of AM60 magnesium alloy components. In the literature, the primary casting quality measure, the dependent variable, is casting porosity. This paper investigates whether focusing only on porosity measurements is sufficient, so an additional Taguchi experiment was carried out using the tensile strength R_m as a starting value.

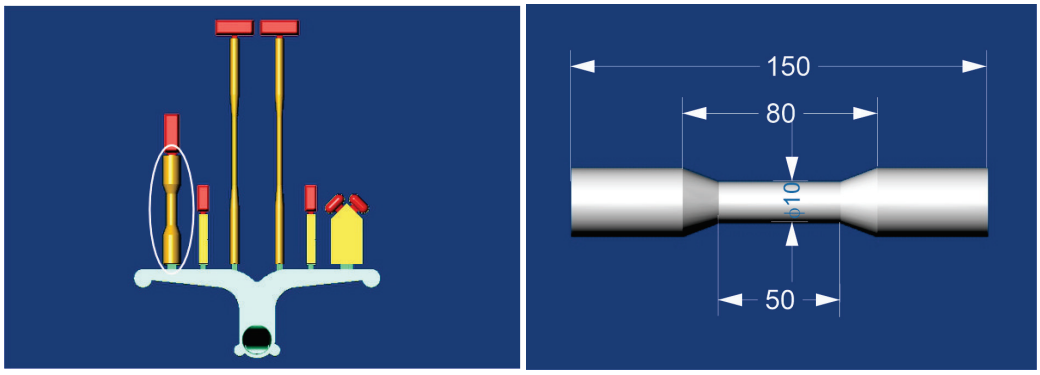
2. Experimental Procedure

2.1. Material

The study used a magnesium–aluminium casting alloy AM60 with the following composition: Al—6.1%, Mn—0.41%, Zn—0.17%, and Mg—the rest, designed for structural components in the automotive industry. The chemical composition was determined using the SPECTROMAX optical emission spectrometer (AMETEK, Berwyn, IL, USA).

2.2. Casting Conditions

The specimens were created using a 280-ton hot-chamber die-casting machine (WEM 280-H, Kędzierzyn-Koźle, Polska). AM60 alloy ingots were preheated in a preheating oven. After reaching approximately 150 °C and ensuring that all moisture was evaporated, they were placed in a melting furnace and heated to about 50 °C higher than the intended casting temperature. From the melting furnace, liquid metal was delivered through transport pipes to the casting furnace, where the entire injection system was immersed. The liquid metal was protected by a mixture of gases, CO_2 + 1 vol% SF_6, during melting and holding. Figure 1 shows a 3D cast model and the geometry and dimensions of the strength and porosity test specimen.



(**a**) (**b**)

Figure 1. Three-dimensional casting and sample models for porosity and mechanical properties testing, (**a**) casting and (**b**) sample.

In Taguchi's experiment, eight trials were conducted, each with three repetitions. After each casting parameter change, 6–8 repetitions were performed to stabilise the casting machine.

2.3. Radiographic Examination

After the casting process, non-destructive testing was carried out to determine the parameters' influence on the casting's porosity. An industrial X-ray scanner, YXLON Y.MU2000-D (Comet Yxlon, Hamburg, Germany), was used for the radiographic tests. A copper anode lamp was used, supplied with a current of 6.25 mA at 160 kV and an HDR filter. All samples were tested according to the ASTM E505 standard (Standard Reference Radiographs for Inspection of Aluminum and Magnesium Die Castings. ASTM: West Conshohocken, PA, USA, 2022).

2.4. Porosity Testing Methodology

For each experiment, three samples were prepared. The sample density was calculated according to Archimedes' principle using the following Equation (1):

$$\rho = \frac{w_1}{(w_1 - w_2)} \cdot \rho_{water} \quad (1)$$

where ρ—casting density (g/cm^3), w_1—casting weight in air (g), w_2—casting weight in water (g), and ρ_{water}—water density (1 g/cm^3).

2.5. Strength Testing Methodology

A static tensile test was performed according to the ASTM B557 standard (Standard Test Methods for Tension Testing Wrought and Cast Aluminum- and Magnesium-Alloy Products. ASTM: West Conshohocken, PA, USA, 2015) using an Instron 4469 testing machine (Instron, Norwood, MA, USA). The machine had a force range of 30 kN and operated at a strain rate of 10 mm/min. Elongation measurements were taken with an extensometer featuring a measuring base of 60 mm.

2.6. Microscopic Testing Methodology

The microstructure of the AM60 alloy was analysed by light microscopy (LM) using an Olympus GX-71 microscope (Olympus, Tokyo, Japan) and scanning electron microscopy (SEM) using an FE SEM Hitachi S-3400N (Hitachi, Tokyo, Japan) scanning electron microscope. Microstructure observations were performed on unetched samples to reveal their porosity. To reveal the microstructure of the AM60 alloy, samples were etched in a reagent containing 3 mL of HNO_3 and 97 mL of C_2H_5OH. Quantitative metallography was used to determine the α-Mg grain size.

2.7. Taguchi Methodology

This research aims to analyse the influence of hot-chamber die-casting variables on the optimal combination of control factors (parameters) to maximise the tensile strength and minimise the porosity in AM60 alloy. The methodology used in the study is shown in Figure 2.

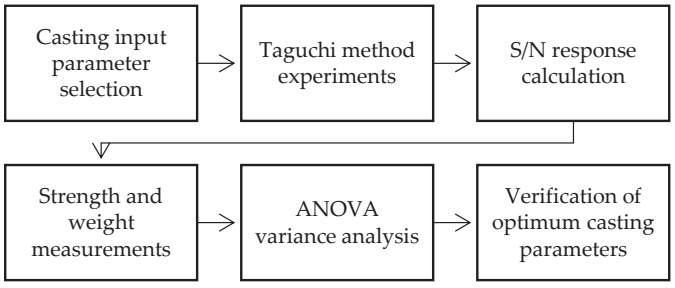


Figure 2. Experimental methodology.

The output response variability was determined by signal-to-noise ratio (S/N) analysis. The signal-to-noise (S/N) ratio was derived from the quadratic loss function. Depending on the type of property being tested, different S/N ratios may apply, including "lower is better", "higher is better", and "nominal is best". Tensile strength is a "bigger is better" quality characteristic, aiming to maximise strength properties. For the criterion "higher is better", the objective is to maximise the occurrence of the required product characteristics, which is enabled by the following criterion function (2):

$$\eta = -10log\left[\frac{1}{n}\sum_{i=1}^{n}\frac{1}{y_i^2}\right] \quad (2)$$

where:

i—number of simulation design parameters;

η—signal-to-noise (S/N) ratio;

n—number of simulation repetitions under the same design parameter conditions,

y—results of measuring

Porosity is a "smaller is better" quality characteristic, aiming to minimise porosity and increase mechanical properties. In the "smaller is better" criterion, the aim is to minimise the occurrence of unwanted product characteristics, which is enabled by the following criterion function (3):

$$\eta = -10log\left[\frac{1}{n}\sum_{i=1}^{n}y_i^2\right] \quad (3)$$

where:

i—number of simulation design parameters;

η—signal-to-noise (S/N) ratio;

n—number of simulation repetitions under the same design parameter conditions,

y—results of measuring

In addition, a statistical analysis of variance (ANOVA) was performed to evaluate the significance of the process variables on the output characteristics. By utilising S/N and ANOVA analyses, the optimal experimental conditions were determined. Finally, a verification experiment was conducted to confirm the validity of the optimal process parameters identified during the parameter design and to assess whether porosity was the only significant factor influencing the strength of AM60.

3. Results and Discussion

It is commonly known that increasing the porosity of materials causes the deterioration of mechanical properties due to a reduction in the active cross-section transferring the loads. This is similar in the case of the AM60 alloy after die casting (Figure 3). It is worth emphasising that the correlation between porosity and tensile strength is not too high, and the determination coefficient is only R^2 = 0.74. On the one hand, this is due to measurement inaccuracies and the uneven distribution of pores in the sample volume. On the other hand, with minor changes in porosity (from 1.5 to 4%), which were observed during the hot-chamber die casting of the AM60 alloy with different parameters, the mechanical properties will also be influenced by microstructural factors, i.e., the homogeneity of the microstructure, the volume fraction of the $Mg_{17}Al_{12}$ phase, the grain size of the α-Mg solid solution, or solution strengthening.

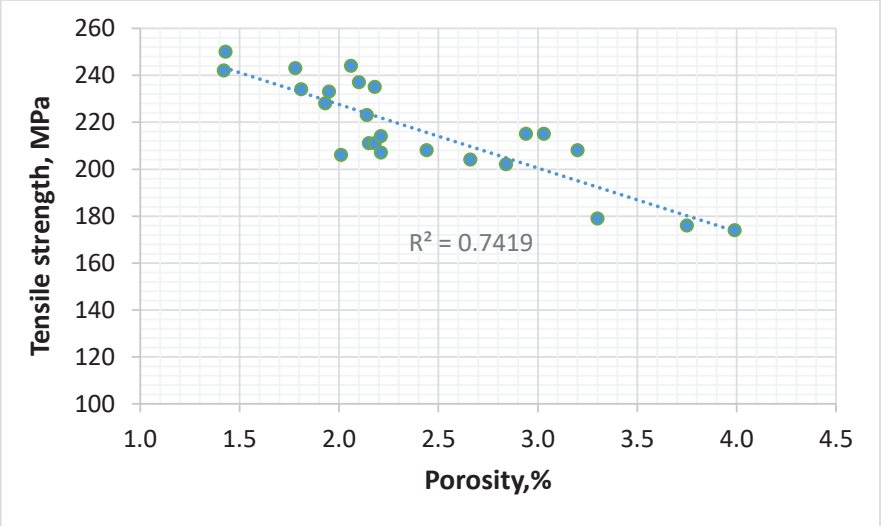


Figure 3. The influence of porosity on the mechanical properties of AM60 alloy.

3.1. Taguchi Method

The Taguchi method analysis began with selecting the factors influencing the quality of the castings produced using the hot-chamber die-casting method. The technological parameters of the process were divided into the following four categories: (a) parameters related to the casting machine, (b) parameters related to the injection system, (c) parameters of the liquid metal, and (d) parameters related to the casting mould. The Ishikawa diagram schematically presents the most important parameters determining the quality of castings (Figure 4).

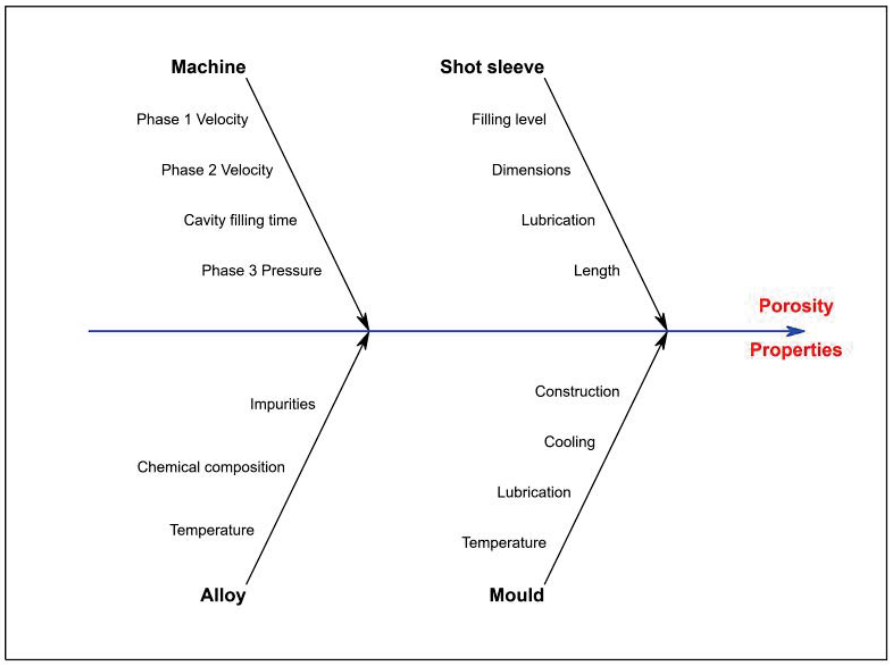


Figure 4. Ishikawa diagram for hot-chamber die casting.

The selection of parameters and their levels was made based on preliminary studies, data from the literature, and the technological capabilities of the high-pressure machine. These are as follows:

A—metal temperature—the temperature of the liquid metal injected into the mould,
B—mould temperature—the mould cavity temperature,
C—piston speed in the first phase—the slow injection phase,

D—piston speed in the second phase—the phase of filling the actual mould cavity,
E—piston travel in the second phase—the path covered by the piston in the second phase of metal injection,
F—pressure—the pressure acting on the alloy in the third injection phase.

Two levels were adopted for each selected parameter (Table 1), while the remaining ones were kept constant throughout the experiment. The total number of degrees of freedom for the six factors (parameters) at two levels was five. Therefore, an orthogonal table L8 (Table 2) was selected, specifying eight experiments and seven columns. Possible interactions between independent variables were omitted in the analysis.

Table 1. Controlled parameters and their levels.

Designation		Parameter	Level 1	Level 2
Tm (°C)	A	Molten temperature	620	650
Td (°C)	B	Mould temperature	160	200
V1 (mm/s)	C	Piston speed in the 1st phase	50	80
V2 (mm/s)	D	Piston speed in the 2nd phase	300	450
L2 (mm)	E	Piston travel in 2nd phase	75	120
P (MPa)	F	Die-casting pressure	20	80

Table 2. L8 orthogonal array with porosity measurement results and calculated S/N values.

Trial	A	B	C	D	E	F	No. 1	No. 2	No. 3	Porosity, % (Mean)	*S/N*
1	2	2	1	2	1	1	2.84	3.03	3.20	3.02	−9.6200
2	2	2	1	1	2	2	2.01	2.15	2.18	2.11	−6.5047
3	2	1	2	2	1	2	1.78	2.06	1.43	1.76	−4.9863
4	2	1	2	1	2	1	2.44	2.66	2.21	2.44	−7.7555
5	1	2	2	2	2	1	2.10	1.95	2.18	2.08	−6.3565
6	1	2	2	1	1	2	2.14	2.94	2.21	2.43	−7.8073
7	1	1	1	2	2	2	1.93	1.81	1.42	1.72	−4.7796
8	1	1	1	1	1	1	3.99	3.30	3.75	3.68	−11.3431

3.2. Porosity Assessment Using the Taguchi Method

The signal-to-noise (S/N) values were calculated using "smaller-is-better" performance characteristics, and the calculation results are presented in Table 2. As can be seen, the lowest porosity (the highest S/N values) was observed for trial no. 7. The response table (Table 3) shows that pressure had the most significant effect on porosity, and to obtain the lowest porosity, the process should be carried out at its maximum values. Increasing the piston speed during the first phase and second phase and the piston path in the second phase contributed to reducing the porosity of the castings. The mould and liquid metal temperature exerted the slightest effect on the porosity of the castings due to the low values of the R coefficient.

Table 3. Response table of S/N ratios showing effects of hot-chamber die-casting parameters on porosity of AM60 alloy.

Level	A	B	C	D	E	F
1	−7.57	−7.22	−8.06	−8.35	−8.44	−8.77
2	−7.22	−7.57	−6.73	−6.44	−6.35	−6.02
R	0.355	0.356	1.335	1.917	2.090	2.749
Rank	6	5	4	3	2	1

The Taguchi analysis provides information on which casting parameters used had the most significant influence on porosity. Still, it did not answer the question of the

percentage contributions of individual parameters to porosity, nor did it provide an answer to the question of which factors were statistically significant. This information can be obtained from ANOVA analysis (Table 4), performed for the *S*/*N* values obtained from the orthogonal array (Table 2).

Table 4. Results of ANOVA analysis for the porosity of the die-cast AM60 alloy (significance level $\alpha = 0.05$).

Factors	SS	DOF	Variance	*F*	*p*	Contribution, %
A	0.252062	1	0.25	3.38	0.316966	0.7
B	0.253459	1	0.25	3.40	0.316228	0.7
C	3.566824	1	3.57	47.89	0.091358	10.1
D	7.350395	1	7.35	98.70	0.063866	20.8
E	8.737010	1	8.74	117.32	0.05861	24.8
F	15.117319	1	15.12	202.99	0.04461	42.9
Error	0.074475	1	0.07			
Total	35.35	7	5.05			

Fischer *F* significance tests for the above parameters were conducted for the 95% confidence level. As can be concluded from Table 4, only the die-casting pressure had a significant effect on porosity ($p = 0.045$). The contribution of pressure to porosity was the largest (42.9%) among the parameters used. For the piston speed and travel in the second phase, a significant contribution ratio of over 20% was obtained. However, from a statistical point of view, the hypothesis of a significant influence of these factors should be rejected. On the other hand, the *p* probability values were close to the assumed significance level. Therefore, it seems reasonable to control these parameters and include them in further stages of process optimisation. The piston speed in the first phase, despite a contribution of over 10%, was also statistically insignificant according to the results of the *F* test. The influences of the liquid metal temperature and the mould temperature in the assumed range of values were marginal. It is worth emphasising that ANOVA calculations were also performed after pooling the non-significant parameters, often recommended in Taguchi analysis. In this case, the *F*-test results indicated a complete lack of significance, meaning that the tested casting parameters did not affect the porosity.

3.3. Evaluation of Tensile Strength Using the Taguchi Method

The influence of parameters on the tensile strength R_m was also analysed using the L8 orthogonal array (Table 5) for the same samples for which the porosity was measured using the Archimedes method. In this case, calculations were used by the "higher is better" criterion.

Table 5. L8 orthogonal array with tensile strength measurement results and calculated *S*/*N* values.

Trial	A	B	C	D	E	F	No. 1	No. 2	No. 3	R_m, MPa (Mean)	*S*/*N*
1	2	2	1	2	1	1	202	215	208	208	46.37
2	2	2	1	1	2	2	206	211	211	209	46.42
3	2	1	2	2	1	2	243	244	250	246	47.80
4	2	1	2	1	2	1	208	204	207	206	46.29
5	1	2	2	2	2	1	237	233	235	235	47.42
6	1	2	2	1	1	2	223	215	214	217	46.74
7	1	1	1	2	2	2	228	234	242	235	47.40
8	1	1	1	1	1	1	174	179	176	176	44.92

It can be concluded from Table 6 that the most significant influence on tensile strength was the piston speed in the second phase, followed by the pressure and piston speed in the first phase. The ANOVA analysis of variance (Table 7) indicates that these parameters significantly ($p < 0.05$) affected the strength properties of the die castings made of the AM60

alloy. According to the ANOVA analysis, the remaining casting parameters had a minor contribution to the tensile strength (<6%) and were statistically insignificant.

Table 6. Response table of S/N ratios showing effects of hot-chamber die-casting parameters on tensile strength of AM60 alloy.

Level	A	B	C	D	E	F
1	46.62	46.61	46.28	46.09	46.46	46.25
2	46.72	46.74	47.06	47.25	46.88	47.09
R	0.098	0.130	0.787	1.156	0.423	0.839
Rank	6	5	3	1	4	2

Table 7. Results of ANOVA for the tensile strength of the die-cast AM60 alloy (significance level $\alpha = 0.05$).

Factors	SS	DOF	Variance	F	*p*	Contribution, %
A	0.019222	1	0.02	2.88	0.339	0.3
B	0.033681	1	0.03	5.05	0.267	0.6
C	1.237323	1	1.24	185.50	0.047	21.6
D	2.673800	1	2.67	400.87	0.032	46.7
E	0.358260	1	0.36	53.71	0.086	6.3
F	1.408275	1	1.41	211.13	0.044	24.6
Error	0.006670	1	0.01			
Total	5.74	7	0.82			

3.4. Verification Experiment

The Taguchi method indicated a varied effect of the hot-chamber die-casting parameters on porosity and tensile strength (Tables 4 and 7). The die casting pressure most significantly affected the porosity, while the tensile strength R_m was most significantly affected by the piston speed in the second phase and the pressure and piston speed in the first phase. In the last stage of optimising the die-casting parameters, verification was carried out by hot-chamber die casting with optimal parameters, which should guarantee the highest tensile strength. According to the S/N ratio response table (Table 6), setting all parameters at level 2 should ensure the highest strength within the assumed parameter range. Controlling the liquid metal temperature and the mould temperature can be omitted entirely due to the marginal influences of these factors. From a practical point of view, setting these parameters at level 1 is more beneficial, as it will reduce the costs related to maintaining a lower temperature of the liquid metal (A) and the mould (B). Despite differences in the assessment of the significance of the influences of individual parameters on strength and porosity, setting all casting parameters at level 2, except for the mould temperature, should also provide the lowest porosity (Table 3). Similarly to the analysis of the parameters influencing strength, the contributions of the liquid metal temperature and mould temperature to porosity were also found to be negligible. Finally, the verification experiment was carried out with the parameter levels presented in Table 8.

Table 8. Porosity and tensile strength measurement results obtained after the verification experiment.

Trial	A	B	C	D	E	F	1	2	3	R_m, MPa (Mean)	1	2	3	Porosity %
1	1	1	2	2	2	2	248	253	250	250	1.74	1.62	1.49	1.62

The results of the verification experiment can be considered as satisfactory (typical mechanical properties for die-cast AM60 alloy are in the range of 230–260 MPa [33]), and the highest tensile strength (R_m = 250 MPa) and the lowest porosity (1.62%) were obtained for new parameter settings.

The values obtained in the verification experiment were compared with the predicted values for the optimal parameters. To estimate the tensile strength and porosity under optimal die-casting conditions, the following equation can be used [34]:

$$\eta_{opt} = \eta + (A1 - \eta) + (B1 - \eta) + (C2 - \eta) + (D2 - \eta) + (E2 - \eta) + (F2 - \eta) \quad (4)$$

where:

η_{opt} is the predicted average S/N ratio for the R_m and porosity,

η is the overall experimental mean of the S/N ratio,

and A1, B1, C2, D2, E2, and F2 are the S/N ratio values for the recommended level of the process parameters (Tables 3 and 6).

The predicted values calculated from Equation (4) were compared with the experimental values in Table 9, and the error percentage between them was calculated.

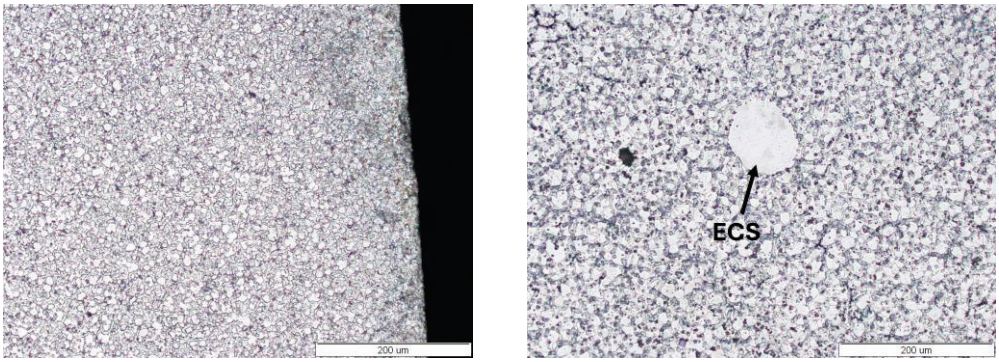
Table 9. Predicted and experimental values of tensile strength and porosity under optimal die-casting parameters of AM60 alloy.

Parameter	Predicted	Experimental	Error, %
R_m, MPa	254	250	2.7
Porosity, %	1.48	1.62	9.5

The results fell short of the expected values calculated from the Taguchi experiment. It is common practice for an optimisation process that, if the average error deviation is less than 10%, then the optimisation can be considered as valid for the model to be accepted. The obtained optimal tensile strength value was nearly like the verification experimental trial value in Table 8, confirming that the optimal conditions were satisfactory. For porosity, the percentage error (9.5%) was much higher; therefore, using this feature in industrial practice as the only indicator for assessing the quality of castings may lead to an erroneous estimation of the optimal die-casting parameters. The significant deviations between the expected values obtained from the Taguchi model and the experimental values were due to the large dispersion of porosity measurement results in subsequent replications (three replications were used for each experimental trial). For tensile strength, the dispersion of results measured with the variability index was 1–3%, and for porosity, this was in the range of 4–18%. Such results indicate that the porosity was not sufficiently sensitive to changes in the process parameters.

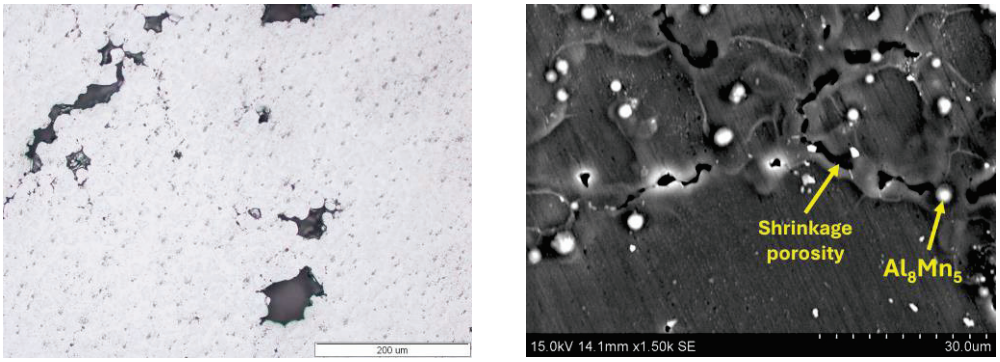
3.5. Microstructure of Die-Cast AM60 Alloy

After experiments using the Taguchi method, the microstructure of the AM60 alloy was characterised using light microscopy (LM) and scanning electron microscopy (SEM). The microstructure after hot-chamber die casting with the optimal parameters (Table 8) was typical for high-pressure die castings. It was characterised by refined grains of the α-Mg solid solution and the presence of "skin" with highly refined grains near the surface (Figure 5a). The grain size changes in the cross-section and at the surface were 9.7 ± 0.4 µm and in the central part were 19.6 ± 0.8 µm (Figure 5b). In the central zone of the casting, large equiaxed grains of α-Mg solution with a diameter of up to approx. 80 µm were also visible, classified as Externally Solidified Crystals (ESCs). Another characteristic feature of high-pressure die castings is gas and shrinkage porosity. Gas pores usually have a regular shape and are in the central part of the casting. In contrast, shrinkage pores are mainly located in the interdendritic areas (Figure 6). Aluminium dissolves in magnesium to form an α-Mg solid solution, contributing to solution strengthening and creating an intermetallic $Mg_{17}Al_{12}$ phase in the interdendritic areas and an Al_8Mn_5 phase located both inside the grain of the solid solution of α-Mg and at the grain boundaries (Figures 6 and 7).



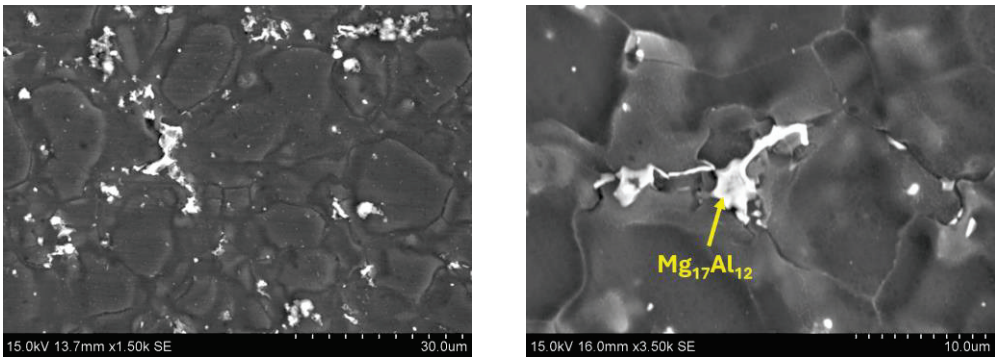
(**a**) (**b**)

Figure 5. Microstructure of die-cast AM60 alloy obtained under optimal hot-chamber die-casting parameters reported in Table 8; at the surface (**a**) and in central zone (**b**).



(**a**) (**b**)

Figure 6. Gas (**a**) and shrinkage (**b**) porosity in die-cast AM60 alloy.



(**a**) (**b**)

Figure 7. Intermetallic compounds in die-cast AM60 alloy (**a**), morphology of the $Mg_{17}Al_{12}$ phase (**b**).

As mentioned, the Taguchi method indicated a varied effect of the hot-chamber die-casting parameters on porosity and tensile strength (Tables 4 and 7). This may cause a problem for technologists designing die-casting processes to select an appropriate casting quality factor. Therefore, the following questions arise: (i) whether the differences result from the limitations of the Taguchi method; (ii) whether the differences are caused by an incorrectly adopted range of parameters for optimisation; and (iii) are there any microstructural factors (e.g., grain size, Al content in Mg) that affect the strength of the AM60 alloy.

This part of the article attempts to answer the following question: how do the technological process parameters affect the microstructure of the AM60 alloy, and does this

affect the tensile strength? For this purpose, the castings obtained in trial no. 3 and trial no. 7 were selected for further studies (Table 2). A similar porosity was obtained (1.76% and 1.72%, respectively), while samples from trial no. 3 showed a higher tensile strength (Table 3, trial no. 3—246 MPa and trial no. 7—235 MPa). Suppose that we consider the insignificance of the influence of the liquid metal temperature and the mould temperature on the resulting features. In that case, both experiments differ regarding the piston speed in the first phase and the piston travel in the second phase.

The porosity measurements of both samples using the Archimedes method (Table 2) and radiographic examinations indicated a similar porosity (Figure 8). The pore distribution on the cross-section was also comparable in both castings. The highest porosity was in the central part of the sample (Figure 9). In the case of samples cast in trial no. 7, the average surface area of the flat pore cross-section was slightly larger ($\bar{A}$ = 1301 μm) compared to the samples from trial no. 3 ($\bar{A}$ = 1126 μm).

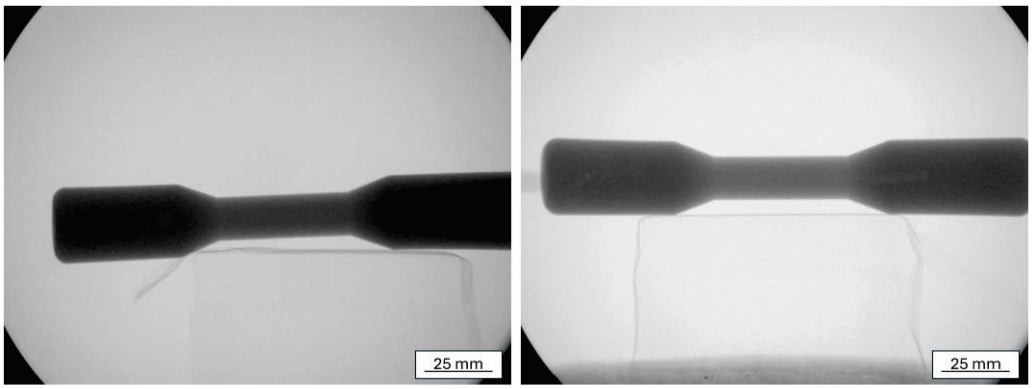


Figure 8. Radiographic examination of castings: trial no. 3 (**a**) and trial no. 7 (**b**).

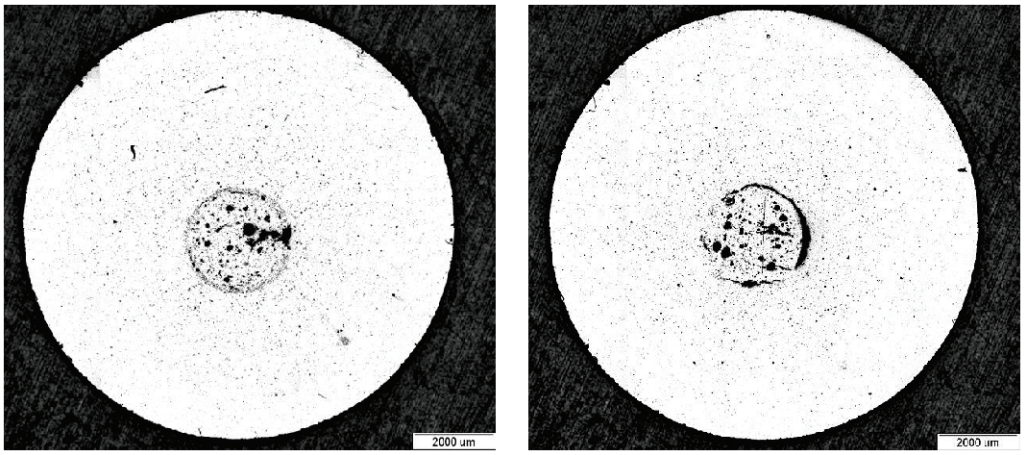
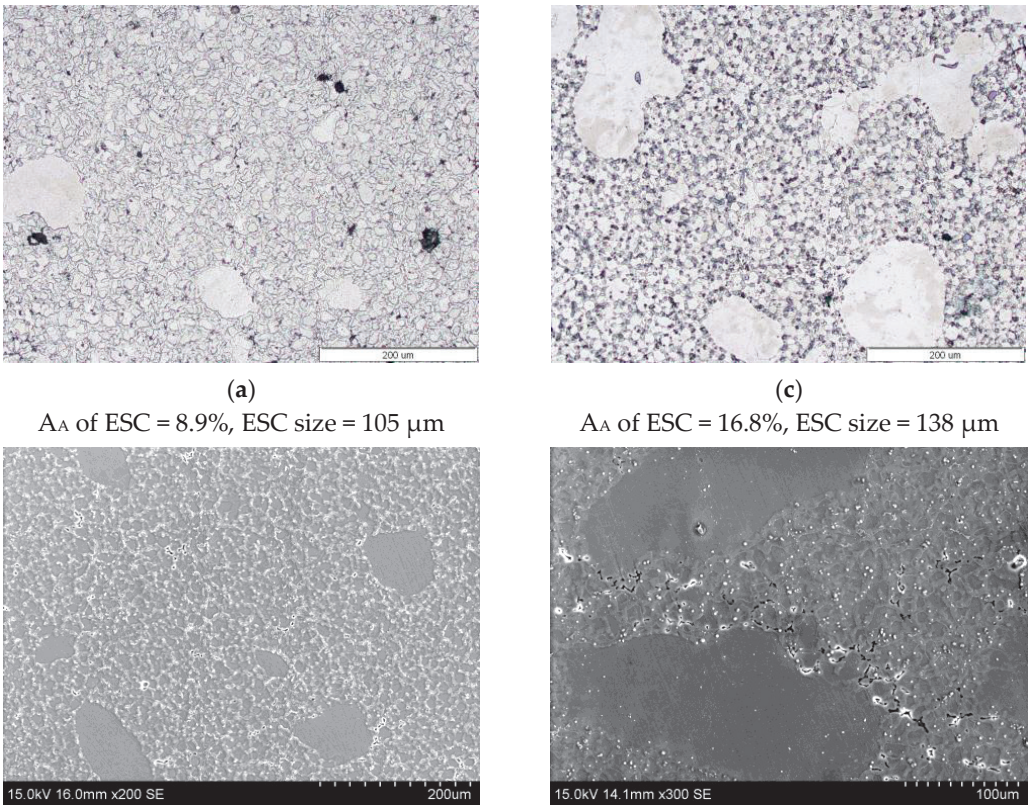


Figure 9. Porosity in samples cast with the parameters: (**a**) trial no. 3 and (**b**) trial no. 7.

Observations of the microstructure of the AM60 alloy provided important information. Samples with a lower tensile strength had a larger volume fraction of Externally Solidified Crystals—ESCs (Figure 10c,d) than those with a higher tensile strength (Figure 10a,b). This was also confirmed by the quantitative analysis of the grain size, which showed that the area fraction A_A of large grains (ESC), as well as their grain size, was larger in castings with a lower strength (trail no. 7) (Figure 10).



(**a**)
A_A of ESC = 8.9%, ESC size = 105 μm

(**c**)
A_A of ESC = 16.8%, ESC size = 138 μm

(**b**)

(**d**)

Figure 10. Externally Solidified Crystals in the die-cast AM60 alloy cast using the parameters of experiment no. 3 (**a**,**b**) and cast using the parameters of experiment no. 7 (**c**,**d**). Area fraction of ESCs, ESC size—mean size of ESCs.

Al in the AM60 alloy participated in the formation of $Mg_{17}Al_{12}$ and Al_8Mn_5 intermetallic phases and dissolved in the α-Mg solid solution. The volume fraction of the $Mg_{17}Al_{12}$ phase may affect the mechanical properties of the alloy. However, in this case, the differences in the content of the $Mg_{17}Al_{12}$ phase between trial no. 3 and trial no. 7 were not significant. No significant differences were found in the content of Al dissolved in the α-Mg solid solution.

After analysing the results, Externally Solidified Crystals (ESCs) significantly influenced the mechanical properties. Increasing their content and diameter would contribute to a decrease in strength, which may be mainly related to the reduction in the piston speed in the first phase. ESCs are equiaxed dendrites that nucleate and grow in the liquid metal, filling the shot sleeve before its injection into the die cavity (first phase of the piston) [35]. When the molten metal is held in the sleeve, especially in the first injection phase (slow injection phase), the overheating of the liquid alloy can be reduced, facilitating the nucleation of ESCs [30]. The volume fraction of ESCs formed in the shot sleeve can be reduced by increasing overheating before injection, for example, by increasing the initial melt and injection nozzle temperatures [35]. The piston speed of the first and second phases is also important; piston acceleration will help to reduce the residence time of the liquid metal in the shot sleeve. A lower piston speed increases ECSs' size and volume fraction due to the longer time it takes to hold the melted alloy in the shot sleeve, promoting nucleation and ESC growth. It follows that, with the increase in the speed of the first injection phase, the volume fraction of ESCs and pores is much smaller [36]. On the other hand, with the increase in the piston speed in the second injection phase, the melting and fragmentation of ESCs are accelerated [30].

In the case of the hot-chamber die casting of AM60 alloy, the development of ESCs consists of the following four stages: nucleation, growth, remelting, and fragmentation. In the

first injection phase, when the liquid metal is held in the shot sleeve, the melt overheating is reduced, and ESC nucleation and growth occur. At low piston speeds in the first phase, there will be a tendency to form large ESCs in the alloy's microstructure. This is also confirmed by the results of the Taguchi analysis, which indicate that the piston speed in the first phase significantly affects the alloy strength (Table 7). In the second phase, the high speed of the liquid metal causes molten metal turbulence, which, in consequence, leads to the remelting and fragmentation of ESCs and obtaining finer and more uniformly distributed ESC grains. For these reasons, the piston speeds in the first and second phase are important for obtaining a high tensile strength. The die-casting pressure is also a critical factor in determining the mechanical properties of the AM60 alloy due to improving the feeding ability of the liquid alloy, which contributes to reducing porosity and grain refinement.

4. Conclusions

This paper used the Taguchi method to determine the most beneficial parameters of hot-chamber pressure casting on the strength of AM60 alloy castings. The following conclusions can be drawn:

1. The die-casting pressure exerts the most significant influence on the porosity of die-cast AM60 alloy. The contribution of pressure to porosity is 42.9%, with a significance level of $p = 0.045$. The remaining factors used in this experiment are not statistically significant.
2. The die-casting pressure and the piston speed in the first and second phases statistically significantly influence the tensile strength. The highest contribution to tensile strength is the piston speed in the second phase (46.7%, $p = 0.032$). The contributions of the piston speed in the first phase and the pressure to tensile strength are 21.6% ($p = 0.047$) and 24.6% ($p = 0.044$), respectively.
3. Besides die-casting pressure, the piston speed in the first and second phases is of great importance for obtaining castings with high mechanical properties, which contributes to a reduction in the fraction and refinement of Externally Solidified Crystals.
4. The Taguchi method for optimising hot-chamber die-casting parameters should not be based only on assessing porosity. Other quality measures, e.g., mechanical properties or the assessment of ESCs' size and content, should be included in the design of optimal die-casting parameters.
5. The validation experiment results for the optimal die casting parameters ($R_m = 150$ MPa) show good agreement for the tensile strength (predicted value $R_m = 154$ MPa), giving an error value of 2.7%. For porosity, a percentage error of 9.5% is obtained. The predicted porosity for the optimal parameters is 1.48%, and the obtained value in the verification test is 1.62%.

Author Contributions: Conceptualization, T.R. and A.K.; methodology, A.K.; introduction, A.K.; Taguchi and statistical calculations, T.R.; microscope analysis, T.R. and A.K.; investigation, T.R. and A.K.; writing—original draft preparation, T.R. and A.K.; writing—review and editing, T.R. and A.K.; visualisation, T.R. and A.K. All authors have read and agreed to the published version of the manuscript.

Funding: The present work was supported by the Polish Ministry of Science and Higher Education under the project No. 11/030/BK_24/1177.

Institutional Review Board Statement: Not applicable.

Informed Consent Statement: Not applicable.

Data Availability Statement: The original contributions presented in this study are included in the article. Further inquiries can be directed to the corresponding author.

Conflicts of Interest: The authors declare no conflicts of interest.

References

1. Fu, P.; Luo, A.A.; Jiang, H.; Peng, L.; Yu, Y.; Zhai, C.; Sachdev, A.K. Low-pressure die casting of magnesium alloy AM50: Response to process parameters. *J. Mater. Process. Technol.* **2008**, *205*, 224–234. [CrossRef]
2. Gu, G.-C.; Xiang, L.-X.; Li, R.-F.; Xu, W.-H.; Zheng, H.-L.; Wang, W.-H.; Lu, Y.-P. A Comparative Study on Microstructure, Segregation, and Mechanical Properties of Al-Si-Mg Alloy Parts Processed by GISS-HPDC and SEED-HPDC. *Materials* **2023**, *16*, 6652. [CrossRef] [PubMed]
3. Ghio, E.; Cerri, E. Corrosion Behaviour of High-Pressure Die-Cast AZ91 Alloy in NaCl Solution: Effects of Friction Stir Process at High Rotational Speed. *Materials* **2023**, *16*, 6620. [CrossRef] [PubMed]
4. Wang, G.G.; Weiler, J.P. Recent developments in high-pressure die-cast magnesium alloys for automotive and future applications. *J. Magnes. Alloys* **2023**, *11*, 78–87. [CrossRef]
5. M-Rahmani, D.; Fereshteh-Saniee, F. Effects of the Radial-Axial Ring Rolling Process on the Mechanical Properties and Microstructure of Centrifugally Cast AM60 Magnesium Rings. *J. Mater. Eng. Perform.* **2024**, *33*, 8480–8496. [CrossRef]
6. Lee, S.G.; Gokhale, A.M.; Patel, G.R.; Evans, M. Effect of process parameters on porosity distributions in high-pressure die-cast AM50 Mg-alloy. *Mater. Sci. Eng. A* **2006**, *427*, 99–111. [CrossRef]
7. Zhao, X.; Wang, P.; Yang, Y.; Wang, S.; Zhao, Q.; Sun, J. Effect of Artificial Aging Treatment on the Mechanical Properties and Regulation of Precipitated Phase Particles of High-Pressure Die-Cast Thin-Wall AlSi10MnMg Longitudinal Carrier. *Materials* **2023**, *16*, 4369. [CrossRef] [PubMed]
8. Kapoor, R.; Sharma, V.S.; Singh, H. Optimization of machining process parameters of high pressure die casting for improve the quality of manufactured product. *Mater. Today Proc.* **2022**, *57*, 793–800. [CrossRef]
9. Gaspar, S.; Pasko, J. Plunger pressing speed like the main factor influencing of the mechanical properties of die casting. *MM Sci. J.* **2019**, *2019*, 3490–3493. [CrossRef]
10. Kim, R.-C.; Hong, K.-R.; Yang, J.-Y.; Yang, W.-C. High-pressure die casting process optimization for improving shrinkage porosity and air entrainment in carburetor housing with aluminum alloy using Taguchi-based ProCAST simulation and MADM-based overall quality index. *Int. J. Adv. Manuf. Technol.* **2024**, *132*, 893–906. [CrossRef]
11. Okayasu, M.; Yoshifuji, S.; Mizuno, M.; Hitomi, M.; Yamazaki, H. Comparison of mechanical properties of die cast aluminium alloys: Cold *v.* hot chamber die casting and high *v.* low speed filling die casting. *Int. J. Cast Met. Res.* **2009**, *22*, 374–381. [CrossRef]
12. Yang, Z.; Maurey, A.; Kang, J.; Wilkinson, D.S. 2D and 3D characterization of pore defects in die cast AM60. *Mater. Charact.* **2016**, *114*, 254–262. [CrossRef]
13. Wu, D.H.; Chang, M.S. Use of Taguchi method to develop a robust design for the magnesium alloy die casting process. *Mater. Sci. Eng. A* **2004**, *379*, 366–371. [CrossRef]
14. Syrcos, G.P. Die casting process optimization using Taguchi methods. *J. Mater. Process. Technol.* **2003**, *135*, 68–74. [CrossRef]
15. Das, P.; Samanta, S.K.; Das, R.; Dutta, P. Optimization of degree of sphericity of primary phase during cooling slope casting of A356 Al alloy: Taguchi method and regression analysis. *Measurement* **2014**, *55*, 605–615. [CrossRef]
16. Stephens, M.P. *Statistical Design and Analysis of Experiments*; Purdue University Press: West Lafayette, IN, USA, 2024; ISBN 1612498450.
17. Singh, R.; Singh, H. Effect of Some Parameters on the Cast Component Properties in Hot Chamber Die Casting. *J. Inst. Eng. India Ser. C* **2016**, *97*, 131–139. [CrossRef]
18. Park, J.; Kang, C. Microstructure and mechanical properties of AM50 alloy according to thickness and forming condition of the products by a high pressure die-casting process. *J. Mech. Sci. Technol.* **2013**, *27*, 2955–2960. [CrossRef]
19. He, Y.; Lu, D.; Li, Z.; Lu, D. Multi-Objective Optimization of The Low-Pressure Casting of Large-Size Aluminium Alloy Wheels through a Systematic Optimization Idea. *Materials* **2023**, *16*, 6223. [CrossRef]
20. Kittur, J.K.; Choudhari, M.N.; Parappagoudar, M.B. Modeling and multi-response optimization of pressure die casting process using response surface methodology. *Int. J. Adv. Manuf. Technol.* **2015**, *77*, 211–224. [CrossRef]
21. Şensoy, A.T.; Çolak, M.; Kaymaz, I.; Dispinar, D. Investigating the Optimum Model Parameters for Casting Process of A356 Alloy: A Cross-validation Using Response Surface Method and Particle Swarm Optimization. *Arab. J. Sci. Eng.* **2020**, *45*, 9759–9768. [CrossRef]
22. Sata, A.; Ravi, B. Comparison of Some Neural Network and Multivariate Regression for Predicting Mechanical Properties of Investment Casting. *J. Mater. Eng. Perform.* **2014**, *23*, 2953–2964. [CrossRef]
23. Sivaraos; Milkey, K.R.; Samsudin, A.K.; Dubey, A.K.; Kidd, P. Comparison between Taguchi Method and Response Surface Methodology (RSM) in Modelling CO2 Laser Machining. *Jordan J. Mech. Ind. Eng.* **2014**, *8*, 35–42.
24. Chelladurai, S.J.S.; Murugan, K.; Ray, A.P.; Upadhyaya, M.; Narasimharaj, V.; Gnanasekaran, S. Optimization of process parameters using response surface methodology: A review. *Mater. Today Proc.* **2021**, *37*, 1301–1304. [CrossRef]
25. Kandala, A.V.U.K.; Solomon, D.G. Advantages of Taguchi Method compared to Response Surface Methodology for achieving the Best Surface Finish in Wire Electrical Discharge Machining (WEDM). *J. Mech. Eng.* **2022**, *19*, 185–199. [CrossRef]
26. Said, M.S.M.; Ghani, J.A.; Kassim, M.S.; Tomadi, S.H.; Che Haron, C.H. Comparison between Taguchi Method and Response Surface Methodology (RSM) in Optimizing Machining Condition. In *International Conference on Robust Quality Engineering*; UTM Razak School: Kuala Lumpur, Malaysia, 2013; pp. 60–68.
27. Kamalakannan, V.; Rajaram, S.; Iyyadurai, J.; Arockiasamy, F.S. Fundamental Study on Influence of In-dependent Factors on Response Variable Using Response Surface Methodology and Taguchi Method. *Eng. Proc.* **2024**, *61*, 37. [CrossRef]

28. Dutta, S.; Kumar Reddy Narala, S. Optimizing turning parameters in the machining of AM alloy using Taguchi methodology. *Measurement* **2021**, *169*, 108340. [CrossRef]
29. Wang, B.; Xiong, S. Effects of shot speed and biscuit thickness on externaly solidified crystals of high-pressure diet cast AM60B magnesium alloy. *Trans. Nonferrous Met. Soc. China* **2011**, *21*, 767–772. [CrossRef]
30. Wu, M.; Li, X.; Guo, Z.; Xiong, S. Effects of process parameters on morphology and distribution of externally solidified crystals in microstructure of magnesium alloy die castings. *China Foundry* **2018**, *15*, 139–144. [CrossRef]
31. Sun, Z.; Hu, H.; Chen, X. Numerical optimization of gating system parameters for a magnesium alloy casting with multiple performance characteristics. *J. Mater. Process. Technol.* **2008**, *199*, 256–264. [CrossRef]
32. Yang, Y.-K.; Tzeng, C.-J. Die-Casting Parameter Sizing for AZ91D in Notebook Computer Base Shell. *Mater. Manuf. Process.* **2006**, *21*, 489–494. [CrossRef]
33. Friedrich, H.E.; Mordike, B.L. *Magnesium Technology: Metallurgy, Design Data, Applications*; Springer International Publishing: Berlin, Germany; New York, NY, USA, 2006; ISBN 9783540205999.
34. Kıvak, T. Optimization of surface roughness and flank wear using the Taguchi method in milling of Hadfield steel with PVD and CVD coated inserts. *Measurement* **2014**, *50*, 19–28. [CrossRef]
35. Yu, W.; Zhan, H.; Gourlay, C.M. Effects of shot sleeve pre-solidification on the microstructure and tensile properties of high pressure die cast AE44. *Metall. Mater. Trans. A* **2024**, *55*, 2019–2033. [CrossRef]
36. Liu, W.; Zhang, W.; Wang, P.; Liu, Y.; Jiao, X.; Wan, A.; Wang, C.; Tong, G.; Xiong, S. Effect of slow shot speed on externally solidified crystal, porosity and tensile property in a newly developed high-pressure die-cast Al-Si alloy. *China Foundry* **2024**, *21*, 11–19. [CrossRef]

Disclaimer/Publisher's Note: The statements, opinions and data contained in all publications are solely those of the individual author(s) and contributor(s) and not of MDPI and/or the editor(s). MDPI and/or the editor(s) disclaim responsibility for any injury to people or property resulting from any ideas, methods, instructions or products referred to in the content.

materials

MDPI

Article

Natural Graphite Spheroidization Phenomena in Arc Furnace Metallurgical Process for High-Silicon Cast Iron

Marcin Stawarz

Department of Foundry Engineering, Silesian University of Technology, 7 Towarowa Street, 44-100 Gliwice, Poland; marcin.stawarz@polsl.pl

Abstract

Grey cast iron with spheroidal graphite has been known and widely used since the 20th century (since 1947). Numerous methods have been developed for the secondary metallurgy process to produce nodular graphite. Spontaneous crystallization of nodular graphite is known in foundry practice and other fields. Examples of cast iron with spheroidal graphite include pure alloys with low sulfur content and natural samples containing nodular graphite, formed by natural forces (meteorites and combustion ash). This article presents the results of two industrial experiments that led to the formation of nodular graphite precipitates without the addition of elements that promote spheroidization. Studies were carried out on high-silicon cast iron intended for corrosion-resistant castings. TDA, chemical composition analysis, light and scanning microscopy, EDS, X-ray spectroscopy, and digital image analysis were used to identify the nodular precipitates. The analyses confirmed the presence of nodular graphite precipitates, and known growth mechanisms were assigned to them. It is likely that deoxidation of the metal bath during the metallurgical process contributed to the spontaneous crystallization of graphite spheroids.

Keywords: nodular graphite; hypereutectic cast iron; crystallization process

1. Introduction

In magnesium- or cerium-modified cast iron, graphite growth can occur via several mechanisms, which have been described in detail by Stefanescu et al. [1–4]. These are a function of local conditions at the solidification boundary, which are influenced by undercooling and supersaturation. The structure of the nodular graphite is assumed to be the result of several distinct stages [5–8]: stage I, nucleation and growth of graphite in liquid metal; stage II, growth during eutectic transformation by carbon through the austenite shell; stage III, growth during cooling to room temperature with decreasing carbon solubility in the austenite. In the initial stage, the problem of graphite nodule formation seems to be explained by the circumferential growth mechanism proposed by Sadoch and Gruzlesky [9] in 1975. These studies were confirmed by other researchers, and Stefanescu presented a summary of the results in his article [5]. This growth is believed to be caused by the movement of steps around the surface of the ball, growing in the (1010) direction. The crystal grows in different directions, which meet at a certain point, forming new, roof-like twin boundaries from which new steps arise. During growth, significant defects, called voids, can form. These can be found in both the central parts and outer regions of the graphite precipitates [5]. In the second stage of nodular graphite growth, radial growth of cylindrical columns or conical sectors occurs. This mechanism is based on the model of a cone or spiral originating from a common nucleus. The formation is based on the

principle of positive wedge disclination. This mechanism was described by Stefanescu et al. [5]. They described the wedge formation process by subtracting a wedge from the basic hexagon, causing the graphene sheet to wrap around itself at a 60° angle. A similar mechanism, also described by Stefanescu [5], assumes that the (001) direction of each plate is twisted by 2° around the radius of the sphere, and the (001) directions of all platelets are orientated almost parallel to the radius, causing spiral growth of graphite from a common nucleus. Sometimes, the growth of cylindrical columns can be observed, which cannot be explained by the previous mechanisms. With sufficient magnesium content in cast iron, graphite platelets gather in clusters that produce polyhedral graphite blocks similar to those found in natural graphite [5]. In the third stage, during cooling, the solubility of carbon in austenite decreases, and carbon diffuses into the graphite particles. This causes further growth of the spheres [5]. Under unfavorable crystallization conditions, various forms of degenerate graphite can be formed: dendritic, spiky, exploded and chunky [9–15]. These have a negative impact on the mechanical properties of ductile iron, which deviates from the target spherical shape. In ductile iron subjected to cerium spheroidization, dendritic graphite may form during slow cooling (with a large casting wall thickness). Exploded degenerate graphite, as the name suggests, is the result of cracking caused by a high content of rare earth elements, excessive eutectic saturation, or a melting process of iron with too high purity. The probability of spiky graphite formation increases with a high content of despheroidizing elements such as bismuth, antimony, lead, and titanium [12].

The mechanism of graphite nucleation and growth has been described in numerous works [1–8], although this is not exhaustive, as there are many gaps in this area that will certainly be filled by scientific progress. It is known that spheroidal graphite precipitates occur naturally and spontaneously, without the participation of additives that promote spheroidization. A good example of observed spheroidal graphite precipitates is the result presented by Coey et al. They present the results of studies on the "Canyon Diablo" meteorite [16], which documented spheroidal graphite precipitates. Undoubtedly, these precipitates were formed as a result of specific conditions affecting the complex alloy, which was subjected to high temperatures, pressure, etc., after entering the Earth's atmosphere. Other authors [9] proposed a mechanism for spheroidal graphite growth in a pure Fe-C-Si alloy, without the participation of spheroidizing elements. Adamczyk et al. [17] described the precipitation of spheroidal graphite in fly ash during the combustion process. The authors write that in a sample of unburned coal annealed at 3000 °C, various highly graphitised morphological forms were identified, such as spheroidal graphite, hexagonal plates, columnar plates, and films with serrated edges [17].

This article discusses an example of spontaneous spheroidization of graphite in a casting alloy intended as a starting material for the production of corrosion-resistant high-silicon cast iron [18]. The results described are based on multiple experiments (conducted under industrial conditions) and constitute an attempt to explain the causes of the occurrence of spheroidal graphite in the absence of elements promoting spheroidization and to describe its growth mechanism based on the latest theories of the graphite crystallization process.

2. Materials and Methods

The melting process were carried out under industrial conditions using an electric arc furnace (L-500 with a power of 350 kW and a capacity of 500 kg, SMS group GmbH, 41069 Mönchengladbach, Germany). The melts were part of a two-stage process for the production of silicon cast iron. The two-stage treatment of high-silicon cast iron is described in [19,20]. The test results presented in this paper refer to ingots marked 1 and 2, which were produced as a result of two separate preliminary melting processes carried out under

industrial conditions. In both cases, low-sulfur steel scrap was used as charge material, the chemical composition of which is presented in Table 1. The metal bath was supplemented with ferrosilicon (FeSi75) to a content of approximately 15%, which was previously annealed as described in [20]. Synthetic graphite with a carbon content of 99.35% C was added to the metal charge. The liquid alloy was heated to a temperature of approximately 1350 °C. After slag removal, the prepared and melted material was drained into a casting ladle and then poured into a steel casting mold. Portions of liquid metal were taken from the casting ladle (using a casting spoon) to fill the TDA samplers. The chemical composition of the castings after the first production stage (initial melt) is presented in Table 2.

Table 1. Initial chemical composition of steel scrap.

Chemical Composition, % of Weight														
C	Cr	Si	Mn	Ni	Mo	S	Cu	Al	P	Pb	Nb	Sn	Ti	Fe bal
0.080	0.007	0.001	0.594	0.024	0.02	0.006	0.07	0.006	0.016	0.002	0.031	0.009	0.001	99.13

Table 2. Casting chemical composition after first melting stage.

Chemical Composition, % of Weight											
No.	[1] Si	[2] C	[2] S	P	Mn	Mo	Cu	Mg	Ti	Fe bal	[3] CE
1	14.8	0.565	0.007	0.042	0.305	0.019	0.064	0.00	0.025	84.173	5.02
2	14.57	0.611	0.006	0.041	0.329	0.01	0.069	0.00	0.022	84.362	4.99

[1] Si analysis by weight method, [2] Carbon and sulfur analysis by CS 125 Leco, [3] CE = C + 0.3Si + 0.36P.

The cooling curves were recorded using a MultiCon CMC-141 device (Simex, limited liability company, Gdańsk, Poland) and Electro-Nite samplers with a NiCr-Ni type "K" thermocouple (QuiK-Cup system by Heraeus Electro-Nite Limited company, 2 Kombajnistów Street, 41-200 Sosnowiec Poland). The chemical composition of the charge scrap and ingots after the remelting process was analysed using a Leco GDS 500 spectrometer (model no. 607-500, Leco Corporation, 3000 Lakeview Ave, St. Joseph, MI, USA) and a CS125 carbon and sulfur analyser (Leco Corporation, 3000 Lakeview Ave, St. Joseph, MI, USA).

Metallographic examinations were performed using a Keyence VHX-X1 light microscope (Keyence International NV/SA Bedrijvenlaan 5, 2800 Mechelen, Belgium) and scanning electron microscopy. A Phenom Pro-X scanning microscope with an EDS system (Phenom-World B.V. Dillenburgstraat 9T Eindhoven, 5652 AM, The Netherlands) was used. The shape of graphite (according to ASTM A247-19 standard [21]) was described for 10 random measurement fields (for each sample) at least 50–100 graphite particles (for each sample area) using the shape factor given by Formula (1):

$$\text{Nodularity} = \frac{4\pi * A}{P^2} \quad (1)$$

where:

A—particle surface area,
P—particle circumference.

During image analysis, the empty spaces in the graphite particles were automatically filled.

To determine the phase composition, XRD studies were performed using a X'Pert PRO X-ray diffractometer by Malvern Panalytical, 7602 EA Almelo, the Netherlands) using filter radiation from a copper anode lamp and a PIXcel 3D detector on the diffraction beam axis.

Measurements were performed using the step method. Measurement parameters were: angular range: 25–125 degrees; 2-theta step: 0.026 degrees; scan time per step: 100 s; and mean "K alpha" wavelength for the cobalt lamp: 1.7909 Å (0.179 nm).

3. Results

As a result of the preliminary melting process carried out under industrial conditions, two separate sets of results were obtained for ingots designated 1 and 2, respectively. The results of the analysis of these ingots are presented below.

3.1. TDA

The first stage of the research was to perform TDA for the two cases analysed. Figure 1 presents the recorded cooling curves along with the temperature-time derivatives. This enabled the determination of characteristic points in the crystallization process.

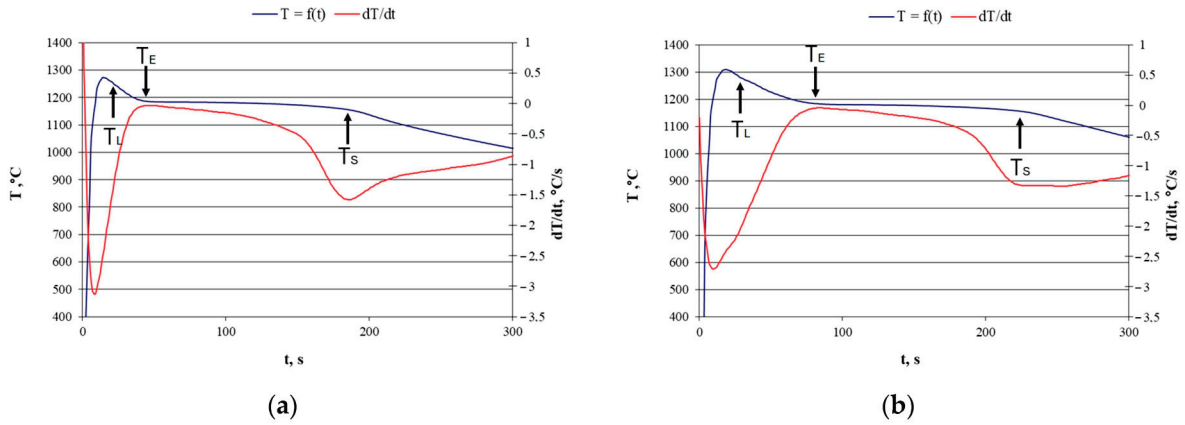


Figure 1. TDA curves: (**a**) casting No. 1; (**b**) casting No. 2.

As a result of the TDA, characteristic process points were determined, such as the liquidus temperature T_L, the solidus temperature T_S, and the eutectic crystallization effect T_E. A numerical comparison of the characteristic temperatures for both variants is presented in Table 3.

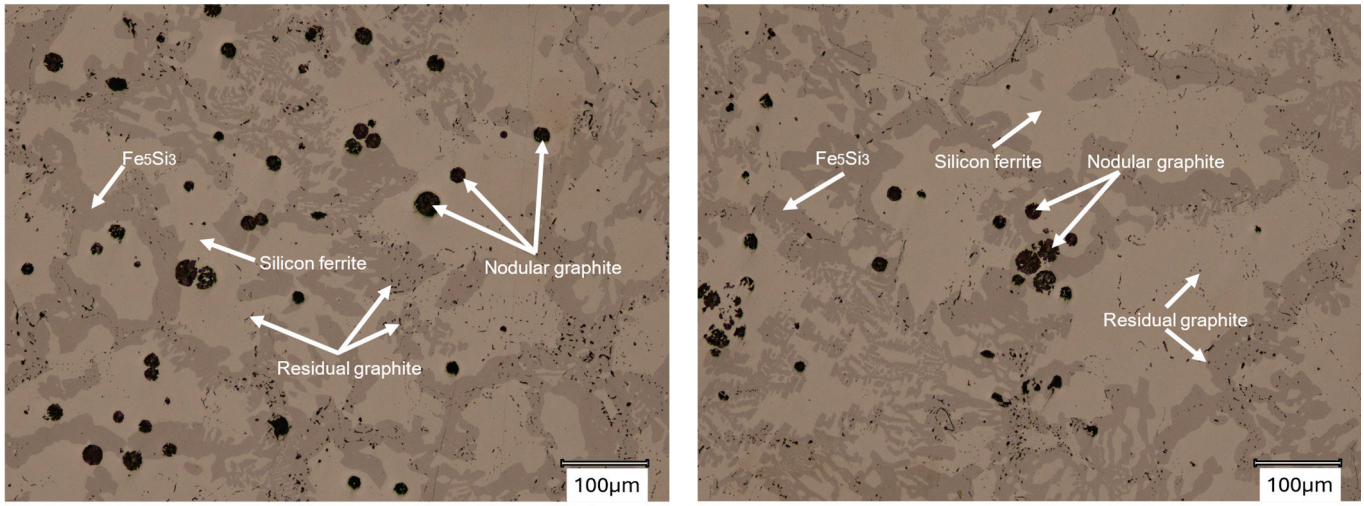
Table 3. Characteristic temperatures for TDA analysis.

	°C		
No.	T_L	T_E	T_S
1	1264	1187	1158
2	1270	1185	1158

As can be seen, the T_L temperature values differ slightly by 6 °C. This difference is caused by the lower Si content in ingot 2 (14.57% Si) compared to ingot 1 (14.8% Si). As is known, silicon in cast iron lowers the liquidus temperature [22]. The difference in the TE eutectic crystallization temperature T_E is 2 °C, and the solid-state temperature T_S is the same. The main goal of this article is to describe the crystallization process of spheroidal graphite, which was identified in both ingots. In this respect, the analysis of both TDA diagrams did not give satisfactory results, because it is not possible to localize the thermal effects resulting from the crystallization of primary graphite. The thermal effects resulting from the crystallization of primary graphite should be visible in the case of hypereutectic cast iron [23,24]. Due to the low carbon content (approximately 0.6% C), the thermal effect resulting from primary graphite crystallization is not visible in the analyzed cases. It is possible that it will not be detected under industrial conditions.

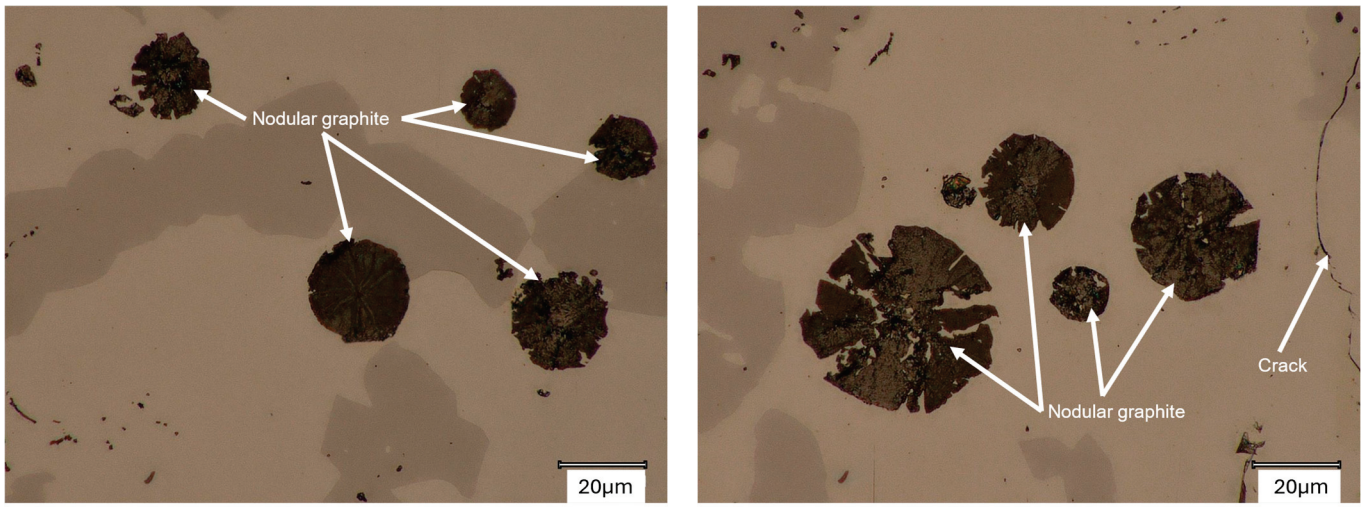
3.2. Metallographic Analysis

In the first stage of metallographic analysis, samples from ingots 1 and 2 were observed under an optical microscope. Figures 2 and 3 show the spheroidal graphite precipitates found in the ingots analyzed.



(**a**) (**b**)

Figure 2. Casting microstructure with nodular graphite: (**a**) casting No. 1; (**b**) casting No. 2. Not etched.

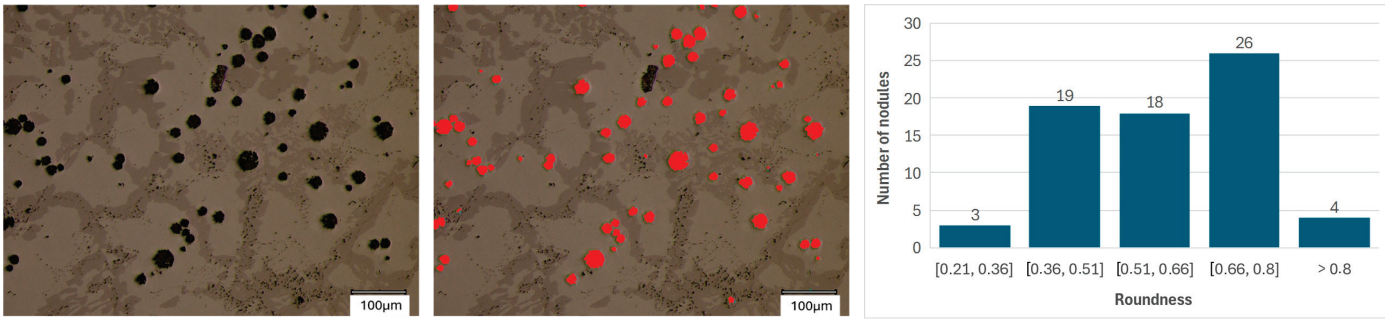


(**a**) (**b**)

Figure 3. Casting microstructure with nodular graphite: (**a**) casting No. 1; (**b**) casting No. 2 Not etched.

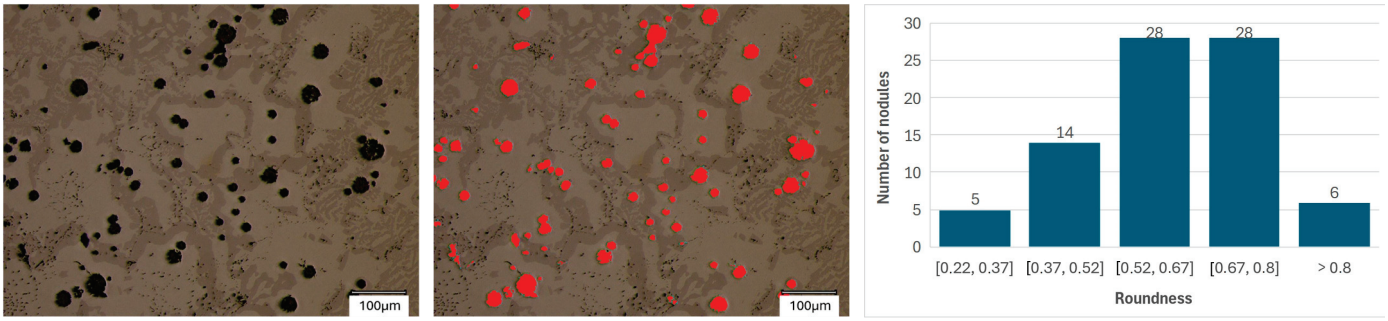
The spheroidal precipitates visible in Figures 2 and 3 visually correspond to the graphite precipitates. Their detailed analysis will be conducted later in this paper. Residual graphite was also revealed in the microstructures (marked in Figure 2). The matrix microstructure of the analyzed alloys consists of silicon ferrite (light areas marked in Figure 3a,b) and a dark area (Fe5Si3 phase). Figure 3b also shows a crack in the sample. The material described in this paper is characterized by a tendency to develop gas porosity and cracks [18], hence the two-stage processing of the alloy intended for utility castings [20].

In the next step, the shape of the spheroidal precipitates was analyzed. Figures 4 and 5 present sample screenshots from the analysis along with the main graphs assigning the shape of the analyzed precipitates to individual classes.



(**a**) (**b**) (**c**)

Figure 4. Analysis of the roundness of graphite precipitates: (**a**) microstructures of casting No. 1; (**b**) digital mask of graphite participations; (**c**) histogram.



(**a**) (**b**) (**c**)

Figure 5. Analysis of the roundness of graphite precipitates: (**a**) microstructures of casting No. 2; (**b**) digital mask of graphite participations; (**c**) histogram.

The average results of the qualitative analysis of graphite precipitation are presented in Table 4. For sample 1, analysis was performed for 10 measurement fields, in which a total of 985 graphite precipitates were examined. For sample 2, an analysis was performed for 10 measurement fields, in which a total of 872 graphite precipitates were examined.

Table 4. Nodularity analysis of the precipitates - statistical analysis.

Sample		Nodularity	Area, µm^2	Circuit, µm	Max Diameter, µm	Min Diameter, µm	Feret Diameter (Horizontal), µm	Feret Diameter (Vertical), µm
1	Avg.	0.73	456.27	88.06	28.11	21	26.41	24.61
	Std.	0.16	342.57	56.81	18.53	6.66	18.39	8.2
	Max.	0.94	2600.12	511.96	209.65	40.03	210.4	53.56
	Min.	0.12	121.17	41.98	12.83	9.18	9.95	12.24
2	Avg.	0.68	415.93	87.56	27.55	19.7	25.63	23.39
	Std.	0.18	368.13	56.85	17.72	7.31	16.9	9.54
	Max.	0.93	2603.63	486.21	208.98	49.37	208.87	84.16
	Min.	0.11	118.83	42.88	13.54	5.32	9.95	9.18

The partial results presented in Figures 4 and 5 show that the sphericity distribution of the analyzed precipitates ranges from 0.2 to 1.0 However, a closer examination of the results reveals that most precipitates fall within the 0.5 class or higher. In this case, we can characterize the precipitates as spherical. The results of the statistical analysis (Table 4) indicate that the average sphericity values for both analyzed cases are 0.73 for sample 1 and 0.68 for case 2.

3.3. XRD Analysis

Due to the significant similarity in the chemical composition of the alloys analysed, XRD analysis was performed only for ingot No. 1. The primary objective of this analysis was to determine the matrix type of the alloy tested. Similarly, the qualitative phase composition of the matrix of ingot No. 2 can be considered with 100% certainty to be homogeneous. X-ray diffraction analysis revealed the presence of silicon ferrite and an intermetallic phase of Fe_5Si_3 (98-063-3540) type. Detailed results are presented in Figure 6.

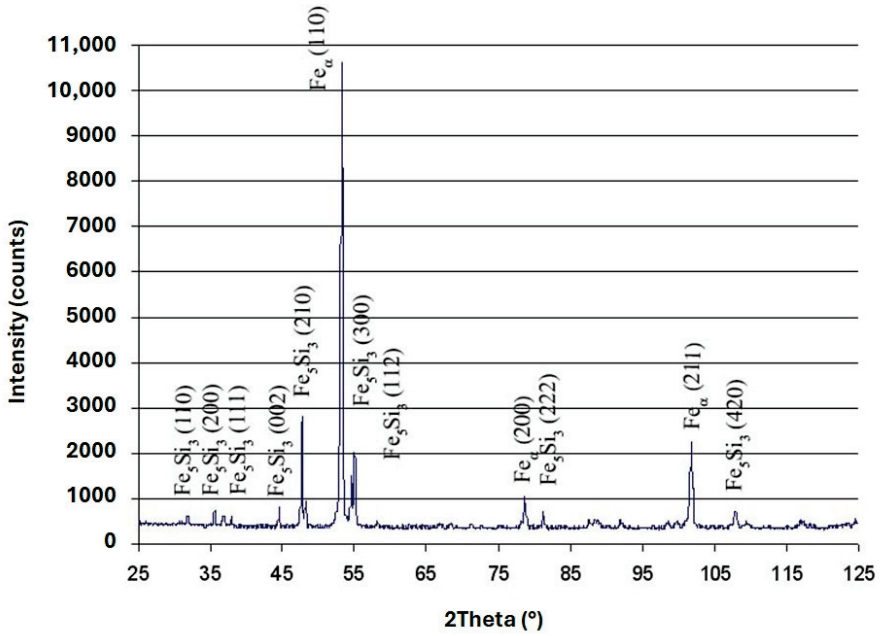
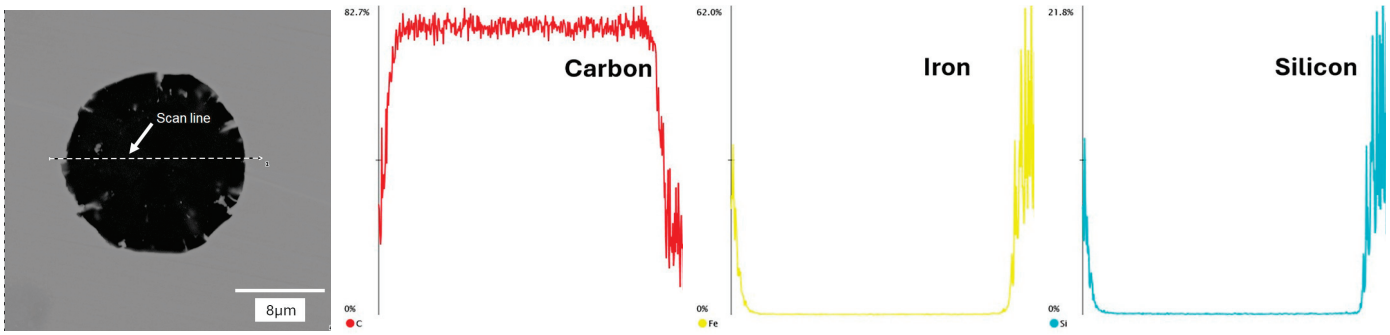


Figure 6. Diffraction analysis for casting No. 1.

As can be seen in Figure 6, no effects are visible for carbon. This is likely due to distortion effects resulting from the presence of the Fe_5Si_3 intermetallic phase or the amorphous nature of the spheroidal precipitates.

3.4. SEM and EDS Analysis

In the next stage of the study, scanning electron microscopy with EDS was used to identify spherical precipitates. Figures 7–10 show the results of SEM analysis of selected spheroidal graphite precipitates, along with linear analysis and surface mapping using the EDS system.



(**a**) (**b**) (**c**) (**d**)

Figure 7. EDS analysis for nodular graphite: (**a**) microstructure; (**b**) carbon; (**c**) iron; (**d**) silicon. Casting No. 1.

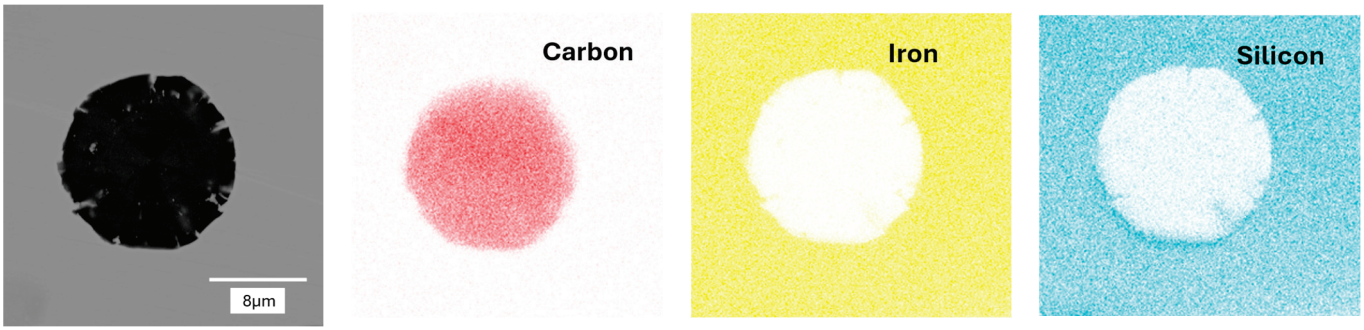


Figure 8. EDS map analysis for nodular graphite: (**a**) microstructure; (**b**) carbon; (**c**) iron; (**d**) silicon. Casting No. 1.

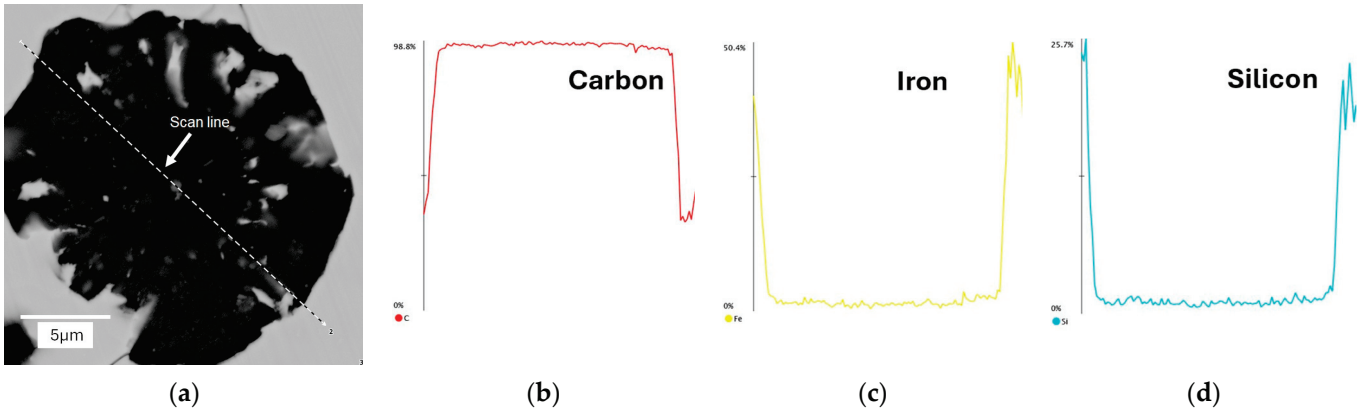


Figure 9. Linear EDS analysis for nodular graphite: (**a**) microstructure; (**b**) carbon; (**c**) iron; (**d**) silicon. Casting No. 2.

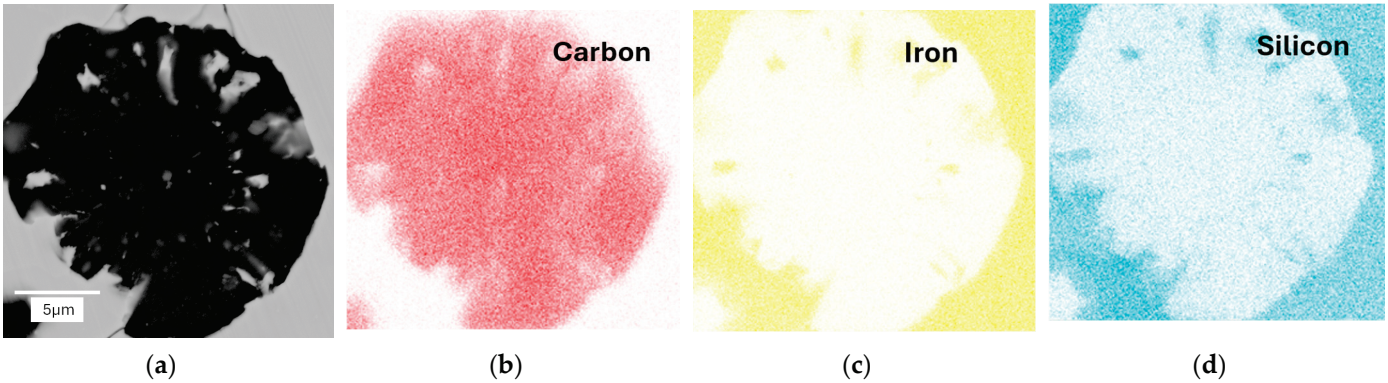


Figure 10. EDS map analysis for nodular graphite: (**a**) microstructure; (**b**) carbon; (**c**) iron; (**d**) silicon. Casting No. 2.

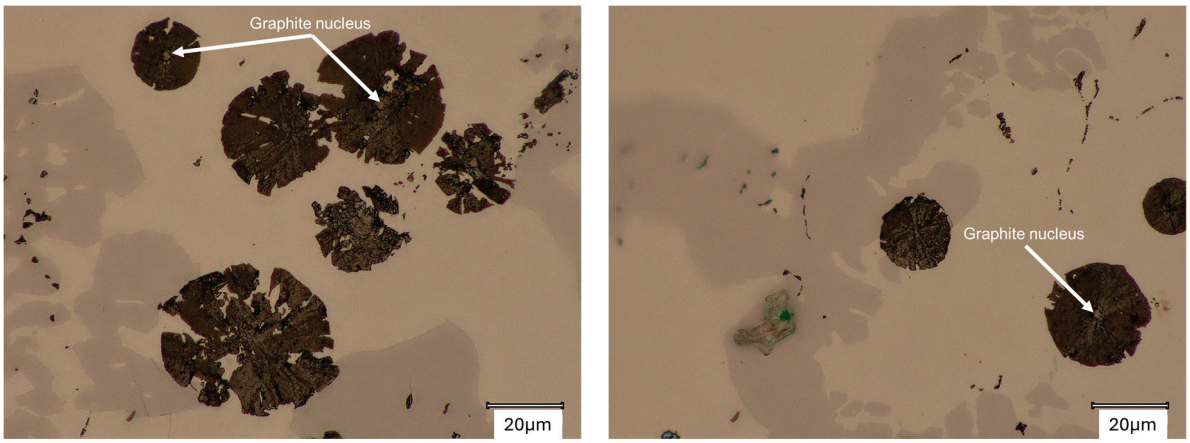
Analyzing the results presented in Figures 7–10, we can undoubtedly conclude that we are dealing with graphite precipitates. Of course, EDS analysis is subject to error due to the beam size (measurement energy), which affects the "depth" of the measurement. However, in the analyzed cases, elements highly enriched in carbon are clearly visible. The nature of these results clearly indicates graphite precipitates.

4. Discussion

The analyses carried out clearly indicate that the precipitation of spheroidal graphite in both melts discussed (carried out under industrial conditions) was unintentional. No

elements promoting spheroidization (such as magnesium or RE) were introduced into the entire melting process. Furthermore, the entire high-silicon cast iron production process consists of two stages, and the paper describes the first stage of preliminary melting of the charge materials. The two-stage melting is intended to improve the quality of the final casting [20]. After the precipitation of spheroidal graphite in the starting material was detected, it was decided to repeat the experiment by melting another batch of steel scrap with the same chemical composition. Similarly to case 1, the precipitation of spheroidal graphite was obtained in ingot no. 2. In paper [9], the authors presented a concept of spheroidal graphite crystallization without the participation of spheroidizing elements. Their hypothesis applies to the pure Fe-Si-C alloy. Similar results were obtained in the experiment discussed, but for a completely different alloy, high-silicon cast iron. An additional difference is the purity of the resulting alloy. The results presented in this document refer to a process that takes place under industrial conditions in an electric arc furnace. The purity of the melt is not high as a result of the penetration of various types of impurities from the lining, metal residues from previous melts, etc. Therefore, the discussed chemical compositions contain elements that ultimately found their way into the chemical composition of the alloy. The ladle used to pour the metal into the metal ingot molds was also standard, used continuously throughout the production cycle. Therefore, the growth and crystallization conditions of spheroidal graphite in ingots 1 and 2 do not correspond to those described in [9].

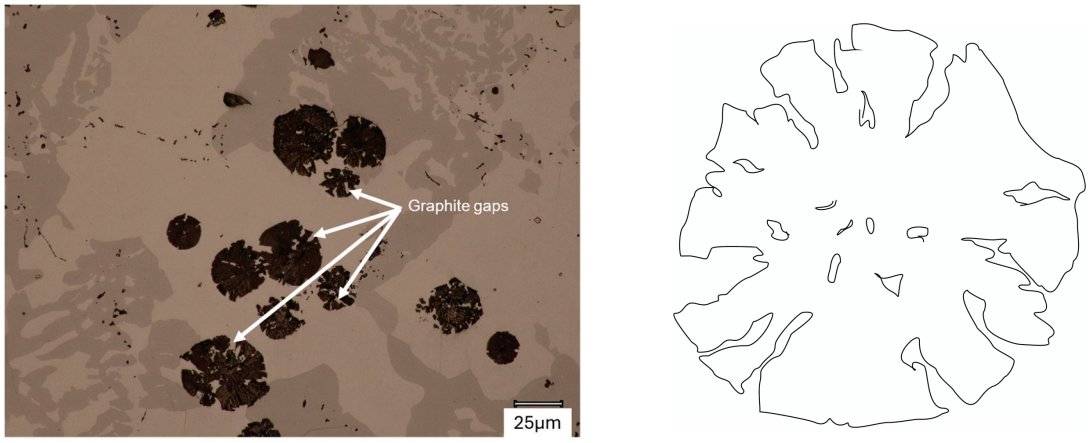
Significant similarities were found with the spheroidal graphite growth pattern described in [1–8], primarily by Stefanescu. Microscopic observations of graphite precipitates in ingots 1 and 2 confirm these hypotheses. Figure 11 shows the visible stage I of the process, that is, the spheroidal graphite nuclei. Unfortunately, because of preparation problems and equipment limitations, it is currently impossible to identify the type of nuclei. Such studies are planned for the next stage of research.



(**a**) (**b**)

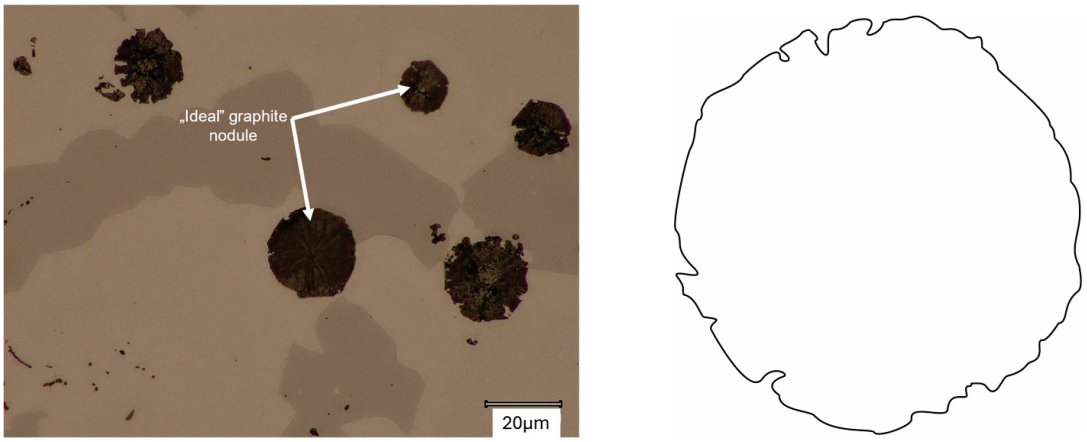
Figure 11. Graphite nucleus (stage I of the growth graphite process): (**a**) Casting No. 1.; (**b**) Casting No. 2.

The graphite growth pattern itself can also be described as circumferential (resembling a cabbage head), as described in [1,5]. This type of growth mechanism occurs in both cases analyzed. This is evidenced by the gaps in the structure of individual spheroids, described by Stefanescu [5] and shown in Figure 12. Figure 13 shows graphite particles with an almost perfectly circular shape.



(**a**) (**b**)

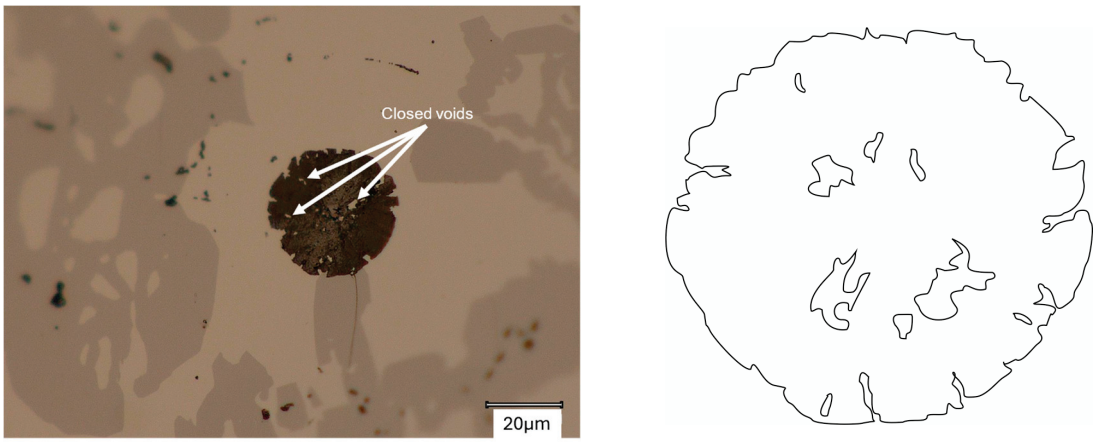
Figure 12. Graphite growth process (like as cabbage head): (**a**) Microstructure; (**b**) Schematic shape.



(**a**) (**b**)

Figure 13. Graphite shape like ideal circle: (**a**) Microstructure; (**b**) Schematic shape.

The graphite particles discussed here also contain closed voids scattered throughout the flat cross-section. An example of such a structure is shown in Figure 14.



(**a**) (**b**)

Figure 14. Graphite with closed voids: (**a**) Microstructure; (**b**) Schematic shape.

The patterns of spheroidal precipitate growth presented in this paper are consistent with the data described in [1–8]. This also indirectly proves that we are dealing with spheroidal graphite precipitates as these data overlap.

A separate issue is the description of the graphite crystallization mechanism itself, without the involvement of elements promoting spheroidization. The sulfur content does not exceed 0.007%. This does not favour spontaneous spheroidization of graphite, as sulfur strongly inhibits it. It is suspected that other factors also influence the growth of graphite precipitates. Trace amounts of Ti could have deoxidized the metal bath, increasing the surface tension of the liquid, creating conditions for spheroidal graphite crystallization. The addition of Ti alloys to the metal bath in the production of vermicular cast iron is described in [25,26]. However, in the cases analyzed, we are dealing with trace amounts of Ti, which should under no circumstances be considered an alloying addition. Rather, it should be considered a contaminant produced during the industrial melting process, which has a deoxidizing effect. Another factor that creates special conditions is the overheating of the alloys in the arc furnace. High temperatures affect specific areas of the liquid metal [27–30], causing severe overheating and combustion of alloying components.

Observation of the structure of spheroidal graphite (studied in this work) reveals that its growth is not easy. This is indicated by various deformations and defects. In both cases, we are dealing with highly hypereutectic alloys. Experience in the metallurgy of cast iron indicates that primary graphite crystallizes directly from the liquid metal under such conditions. This was probably the case here. The difference is that the primary graphite from classical spheroidal graphite is much larger than that from other precipitates and generally smooth. In the cases discussed, it is true that the portion of graphite that has the characteristics of primary graphite can be separated, but only on the basis of its size. The morphological characteristics of the precipitates considered differ significantly from the ideal hypereutectic graphite precipitates [24].

5. Conclusions

Based on the test results of two high-silicon iron castings presented above, it can be concluded that:

- The described spherical precipitates are primary spheroidal graphite precipitates.
- The graphite spheroidization process occurred spontaneously, without the participation of elements promoting spheroidization.
- The graphite precipitate growth pattern corresponds to patterns [1–8] described by other authors. The circumferential growth pattern predominates.
- Some carbon in the alloy crystallized as fine precipitates of residual eutectic graphite.
- The likely cause of graphite crystallization was the melting conditions. The strong effect of the high temperature on the metal bath could have led to the removal of oxygen from the metal bath and an increase in the surface tension of the liquid, which promotes graphite spheroidization.
- The superheating effect refers to processes that occur near the melting electrodes, where the metal bath becomes very hot. Perhaps, this is a significant factor influencing graphite crystallization. Due to the complex dynamic phenomena occurring in this region, such as diffusion, oxidation, and so on, precise modelling of these phenomena will be difficult.
- The results of the industrial experiment described in this paper are reproducible.
- The alloys analyzed in this paper are cast iron. The carbon content does not exceed 0.6%, but the high Si content shifts the eutectic point of the alloy toward the lower carbon content. Both analyzed alloys crystallize with a eutectic transition.

- The thermal effect of primary graphite crystallization was not detected in the TDA plots because of the low carbon content of the alloy.

Funding: This research received no external funding.

Data Availability Statement: The original contributions presented in this study are included in the article. Further inquiries can be directed to the corresponding author.

Conflicts of Interest: The author declares no conflicts of interest.

References

1. Stefanescu, D.M.; Alonso, G.; Suárez, R.; Tokarski, T.; Górny, M. Growth mechanism of graphite spheroids from nano- to micro-scale. *Int. J. Met.* **2024**, *18*, 1869–1882. [CrossRef]
2. Stefanescu, D.M.; Tokarski, T.; Alonso, G.; Górny, M.; Suárez, R. On the role of turbostratic graphite in the crystallization of spheroidal graphite during the liquid-to-solid transformation. *Metall. Mater. Trans. B* **2023**, *54*, 2283–2290. [CrossRef]
3. Stefanescu, D.M.; Crisan, A.; Alonso, G.; Larrañaga, P.; Suarez, R. Growth of spheroidal graphite on nitride nuclei: Disregistry and crystallinity during early growth. *Metall. Mater. Trans. A* **2019**, *50*, 1763–1772. [CrossRef]
4. Alonso, G.; Stefanescu, D.M.; Bravo, B. Graphite spheroids: The place where they are born. *Int. J. Met.* **2024**, *18*, 1854–1868. [CrossRef]
5. Stefanescu, D.M.; Alonso, G.; Suarez, R. Recent developments in understanding nucleation and crystallization of spheroidal graphite in iron-carbon-silicon alloys. *Metals* **2020**, *10*, 221. [CrossRef]
6. Tewary, U.; Mukherjee, D.; Alankar, A. An integrated multi-scale model for graphite growth mechanism in industrial cast iron. *Metall. Mater. Trans. B* **2021**, *52*, 633–651. [CrossRef]
7. Alonso, G.; Tokarski, T.; Stefanescu, D.; Górny, M.; Cios, G.; Suarez, R. On the crystallography of the Mg-Si-Al nitride nuclei and of the graphite/nitride interface in spheroidal graphite iron. *Carbon* **2022**, *199*, 170–180. [CrossRef]
8. Stefanescu, D.M.; Alonso, G.; Larrañaga, P. A comparative study of graphite growth in cast iron and in analogous systems. *Int. J. Met.* **2018**, *12*, 722–752. [CrossRef]
9. Sadocha, J.P.; Gruzleski, J.E. The mechanism of graphite spheroid formation pure Fe-C-Si alloys. In *The Metallurgy of Cast Iron*; Lux, B., Minko, I., Mollard, F., Eds.; Georgi Publishing: St. Saphorin, Switzerland, 1975; pp. 443–459.
10. Adhiwiguna, I.B.G.S.; Plück, L.; Deike, R. Vermicular and chunky graphite nucleation during chill casting: Study on the dynamics of ductile iron recycling. *Int. J. Met.* **2025**, *19*, 2227–2243. [CrossRef]
11. Riposan, I.; Chisamera, M.; Stan, S. Enhanced quality in electric melt grey cast iron. *ISIJ Int.* **2013**, *53*, 1683–1695. [CrossRef]
12. Lacaze, J.; Connétable, D.; Castro de Román, M.J. Effects of impurities on graphite shape during solidification of spheroidal graphite cast ions. *Materialia* **2019**, *8*, 100471. [CrossRef]
13. Adhiwiguna, I.; Nobakht, N.; Deike, R. Nodular graphite dissolution and nucleus observation: High-temperature dynamics of ductile iron recycling. *Metals* **2024**, *14*, 915. [CrossRef]
14. Sertucha, J.; Artola, G.; de La Torre, U.; Lacaze, J. Chunky graphite in low and high silicon spheroidal graphite cast irons–occurrence. Control and effect on mechanical properties. *Materials* **2020**, *13*, 5402. [CrossRef]
15. Baer, W. Chunky graphite in ferritic spheroidal graphite cast iron: Formation. Prevention. Characterization. Impact on properties: An overview. *Int. J. Met.* **2019**, *14*, 454–488. [CrossRef]
16. Coey, J.M.D.; Venkatesan, M.; Fitzgerald, C.; Douvalis, A.P.; Sanders, I. Ferromagnetism of a graphite nodule from the Canyon Diablo meteorite. *Nature* **2002**, *420*, 156–159. [CrossRef]
17. Adamczyk, Z.; Komorek, J.; Białecka, B. Unburned carbon from fly ash as a source of graphite materials. *Miner. Process. Extr. Metall. Rev.* **2022**, *45*, 183–199. [CrossRef]
18. Stawarz, M.; Kajzer, W.; Kajzer, A.; Dojka, M. Physicochemical properties of silicon cast iron. *Arch. Foundry Eng.* **2017**, *17*, 101–106. [CrossRef]
19. Stawarz, M.; Dojka, M. Bifilm inclusions in high alloyed cast iron. *Materials* **2021**, *14*, 3067. [CrossRef] [PubMed]
20. Stawarz, M. Crystallization of intermetallic phases Fe_2Si. Fe_5Si_3 for high alloyed cast irons. *Crystals* **2023**, *13*, 1033. [CrossRef]
21. *ASTM A247-19*; Standard Test Method for Evaluating the Microstructure of Graphite in Iron Castings. ASTM International: West Conshohocken, PA, USA, 2019.
22. Dwulat, R.; Janerka, K. Evaluation of the metallurgical quality of nodular cast iron in the production conditions of a foundry. *J. Manuf. Mater. Process.* **2023**, *7*, 18. [CrossRef]
23. Liu, J.; Yan, J.; Zhao, X. Precipitation and evolution of nodular graphite during solidification process of ductile iron. *China Foundry* **2020**, *17*, 260–271. [CrossRef]

24. Górny, M.; Kawalec, M.; Gracz, B.; Tupaj, M. Influence of cooling rate on microstructure formation of SiMo ductile iron castings. *Metals* **2021**, *11*, 1634. [CrossRef]
25. Górny, M.; Kawalec, M.; Sikora, G.; Lopez, H. Effect of cooling rate and titanium additions on microstructure of thin-walled compacted graphite iron castings. *ISIJ Int.* **2014**, *54*, 10. [CrossRef]
26. Shy, Y.; Hsu, C.; Lee, S.; Hou, C. Effects of titanium addition and section size on microstructure and mechanical properties of compacted graphite cast iron. *Mater. Sci. Eng. A* **2000**, *278*, 54–60. [CrossRef]
27. Nath, D.; Maji, S.; Singh, A. Modeling of arcing, scrap melting, and temperature evolution in the refractory of a lab-scale direct current-electric arc furnace. *Steel Res.* **2025**, *96*, 2300696. [CrossRef]
28. Zhu, J.; Feng, J.; Liu, L.; Wang, H.; Lu, J. Application of arc furnace flue ash in casting heat insulation riser. *Arch. Foundry Eng.* **2024**, *24*, 129–134. [CrossRef]
29. Grabowski, D.; Klimas, M. New directions in electric arc furnace modeling. *Arch. Electr. Eng.* **2023**, *72*, 157–172. [CrossRef]
30. Łągiewka, M. Use of used graphite electrodes as metal matrix composites reinforcement. *Arch. Foundry Eng.* **2024**, *24*, 21–25. [CrossRef]

Disclaimer/Publisher's Note: The statements, opinions and data contained in all publications are solely those of the individual author(s) and contributor(s) and not of MDPI and/or the editor(s). MDPI and/or the editor(s) disclaim responsibility for any injury to people or property resulting from any ideas, methods, instructions or products referred to in the content.

materials

MDPI

Article

Comparative Analysis of the Application of Five-, Seven- and Nine-Roll Sheet Straightening Using Numerical Tools

Grzegorz Stradomski [1,*], Sebastian Mróz [1], Piotr Szota [1], Tomasz Garstka [1], Jakub Gróbarczyk [2] and Radosław Gryczkowski [2]

[1] Faculty of Production Engineering and Materials Technology, Czestochowa University of Technology, 19 Armii Krajowej Av., 42-201 Czestochowa, Poland; sebastian.mroz@pcz.pl (S.M.); piotr.szota@pcz.pl (P.S.); tomasz.garstka@pcz.pl (T.G.)

[2] Serwistal Sp. z. o.o., 2A Dojazdowa Str., 19-300 Ełk, Poland; j.grobarczyk@serwistal.pl (J.G.); r.gryczkowski@serwistal.pl (R.G.)

* Correspondence: grzegorz.stradomski@pcz.pl; Tel.: +48-343-250-784

Abstract

The paper presents the results of a numerical analysis of the roller straightening process. The study evaluated straightening systems consisting of 5, 7, and 9 rollers. The assessment was based on real data obtained under industrial conditions. The research involved the use of two widely used structural steel grades, namely S235JR and S500MC. As part of the study, an analysis of the anisotropy of sheet properties within the coil volume was also conducted. Additionally, the surface topography of the sheets was analyzed and subsequently used in the numerical simulations. The inclusion of real data regarding both material anisotropy and actual geometry allowed for an increase in calculation accuracy. Furthermore, investigations were carried out to analyze the method of implementing material data into the mathematical model. The work also analyzed the accuracy of the obtained numerical results based on material data from the traditional method of introducing material information in the form of an approximated curve. Numerical studies confirmed by a physical test developed by the authors, which can be easily implemented in industrial conditions, confirmed the research assumptions and literature data. The main advantage of the presented solutions is their relative ease of implementation and use in manufacturing facilities with limited research facilities.

Keywords: sheet straightening; numerical analysis; steels; stresses; geometric surface defects

1. Introduction

The production of sheet metal in the form of flat sheets, used as feedstock for processes such as laser cutting or press forming, requires several technological stages resulting from the fact that the material is delivered in coils. Sheet metal coils offer undeniable advantages, such as easier transportation. However, after uncoiling, the sheets exhibit waviness and non-uniform residual stress levels both across their cross-section and along their length. This is, among other things, a remnant of the rolling and coiling process, commonly referred to as the "coil memory," which contributes to the formation of geometric defects and increased, uneven distributions of residual stresses [1–3].

Producing high-quality sheets requires identifying the defects that occur after uncoiling as well as after preliminary straightening in a roller straightener. An important aspect is the evaluation of sheet flatness after uncoiling, before preliminary straightening in roller straighteners, since at this stage it is crucial to eliminate a significant portion of geometric

defects and reduce the level of residual stresses, which will subsequently affect the residual stress state during tension straightening [4–6].

Implementing any improvements in the straightening process requires determining the initial geometry of the sheet. The most characteristic defects found in cold-rolled and hot-rolled sheets include longitudinal bowing, transverse bowing, edge waviness, and center waviness. A schematic view of these defects is shown in Figure 1.

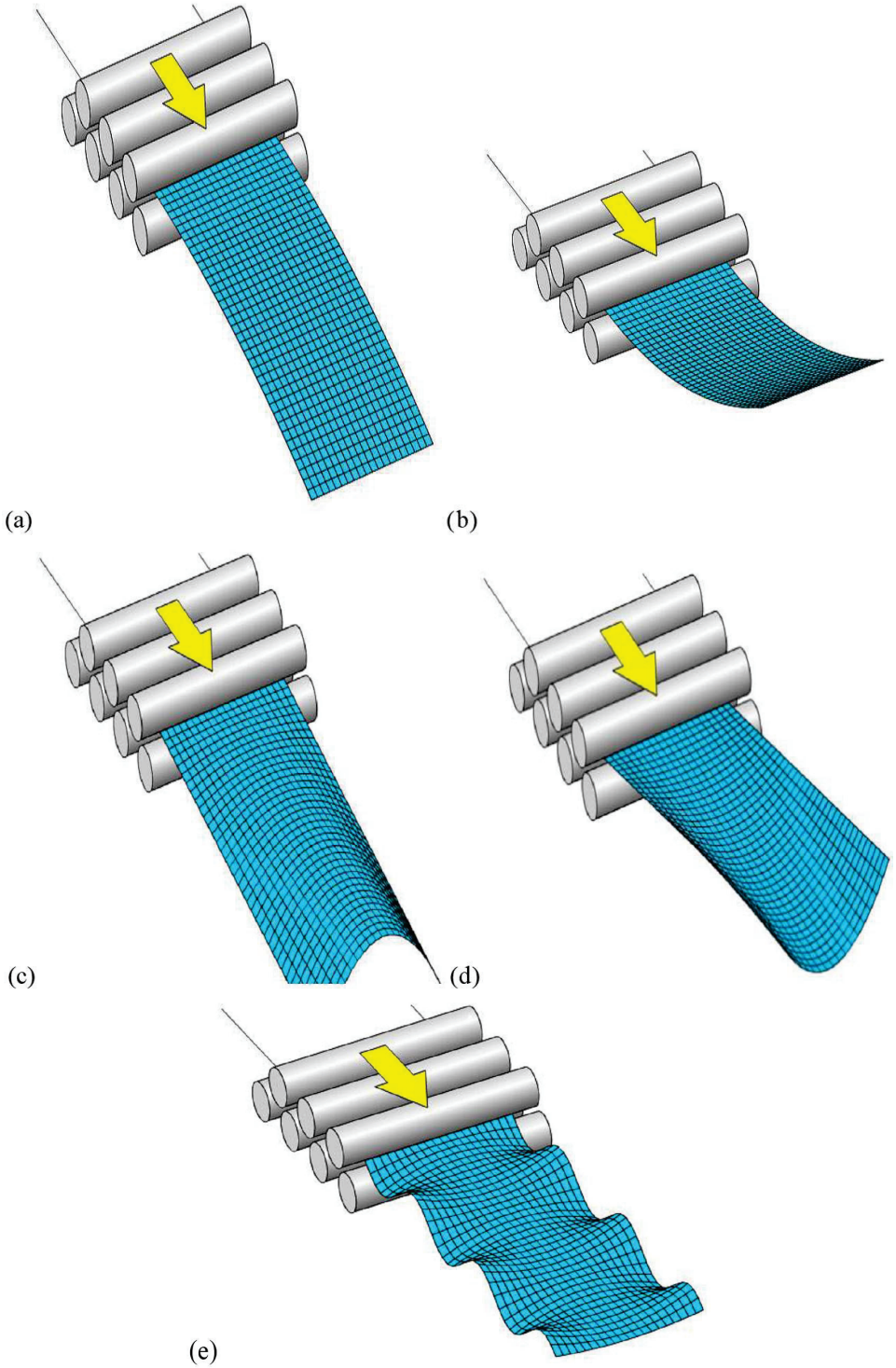


Figure 1. Schematic view of defects: (**a**,**b**) longitudinal defects in sheets—(**a**) downward bending direction—positive, (**b**) upward bending direction—negative; (**c**,**d**) transverse defects in sheets in the form of bending—(**c**) downward bending direction—positive, (**d**) upward bending direction—negative; (**e**) edge waviness in sheets. Own elaboration based on [7].

https://doi.org/10.3390/ma19061053

The characteristics of the technological process of producing flat products, particularly in the finishing rolling stage, are closely related to the non-uniform deformation occurring in the roll gap. At the exit of the rolling mill, the transverse contour of the strip is uneven, which is the main cause of residual stresses along its length. In the case of a convex contour, compressive stresses occur at the edges of the sheet, while tensile stresses develop in the center. If these stresses exceed the critical buckling strength of the strip, edge deformation may occur in the form of waviness or cyclic bulging in the central part of the strip, resulting from partial stress relaxation.

An additional source of stress during rolling is deformation caused by coiling and uncoiling of the strip, as well as by uneven cooling of the coiled sheet during hot rolling. As a result of all these technological processes [4,5,8], a complex residual stress state exists in the sheet strip, leading to shape deformations that must be removed to ensure the semi-finished product meets quality requirements [9,10].

Many authors [11–13] have studied the possibilities of using roller systems to reduce residual stresses. For particular note is the study [11], in which the authors used numerical tools to model straightening in multi-roller systems. This is important because such systems offer great flexibility for eliminating many types of defects. The defects shown in Figure 1 can be significantly reduced or even completely eliminated [14–16] through roller straightening, especially when combined with tension straightening. However, it is necessary to identify the type and magnitude of defects after uncoiling in order to choose the appropriate straightening methodology (in the case of a preliminary roller straightener—to determine the correct roller positions).

In addition to visible geometric defects, sheets also exhibit "hidden defects" in the form of residual stresses [17–19], which, when too high, can cause deformation—particularly during cutting. Such defects can be eliminated during the tensioning process. Their origin lies in non-uniform rolling conditions, and in the case of hot-rolled sheets, additional factors such as temperature non-uniformity further contribute to their formation. Uneven temperature distribution in the sheet leads to residual stresses, which often affect sheet geometry as well.

However, in order to apply the appropriate straightening method [20–22] (in the case of a roller straightener—proper roller positioning), it is necessary to determine the type and magnitude of defects after uncoiling.

Excellent results in process design, acceleration, and cost reduction in research can be achieved through the use of numerical tools, such as the finite element method (FEM). Many authors, including the authors of this paper, have used FEM-based tools to solve similar problems [23–25].

It is evident that internal stresses, which in the described case are a primary source of geometric defects, result from manufacturing processes. Many authors, in their works regarding stresses across various product groups, have described both their effects on properties or microstructure [26–28] and on defects, such as surface irregularities [29–31]. Another element to be considered in the field of internal stresses is their origin resulting from heat or thermomechanical treatment [32–34]. The observed effects—manifesting as changes in properties, microstructural non-homogeneity, delamination, and cracking—are unfavorable.

In industrial conditions, particularly on production lines dedicated to formatting sheet metal into sheets for further production, it is impossible to fully investigate stress distribution directions or determine their root causes. Therefore, it is crucial to develop solutions that allow for their reduction in a relatively universal manner. In this study, the authors focused on the analysis of such a production line; consequently, the origin of the stresses, regardless of its nature, was not the primary evaluation criterion. Among the most

https://doi.org/10.3390/ma19061053

commonly used industrial techniques for reducing internal stress states are technologies utilizing multi-roller systems. The research presented in this paper is part of a much larger project, the results of which led to significant positive outcomes, namely the reduction in geometric defects in metal sheets. The multi-roller system itself, while critical, was only one component of this solution, which constitutes the intellectual property of Serwistal and is legally protected; therefore, it is not possible to present all elements of the production line.

2. Research Material and Preliminary Tests

The material used for the study consisted of sheets uncoiled from coils made of structural steels S235JR + AR and S500MC. The selection of research materials was driven by the fact that these two steel grades account for a significant share of Serwistal's current production. Another important consideration was that both materials were subjected to similar finishing treatments. Both steels were in the hot-rolled condition and can be subjected to an annealing process after rolling; however, to reduce production costs, they are typically rolled into coils without additional heat treatment. During hot rolling, the rolls are cooled with water, and in most cases, the edges of the sheet cool faster than the central part, which may lead to differences in properties between the central and edge regions. Neither the microstructure nor the material texture was analyzed within this work or in the project (POIR.01.01.01-00-0477/18). Such analyses are not feasible under industrial conditions; furthermore, the material manufacturer is responsible for both the quality of the microstructure and the chemical composition. This work presents results that can be obtained quite quickly and easily in industrial conditions. The chemical composition of the tested steels, determined using spark spectroscopy, is presented in Table 1.

Table 1. Chemical composition (wt.%) of analysed materials.

	C	Si	Mn	P	S	Al	Fe
S235JR + AR	0.22	0.05	1.62	0.052	0.048	0.014	ball.
S500MC	0.11	0.45	1.55	0.021	0.010	0.012	ball.

As part of the first stage of the research, the anisotropy of the material properties was evaluated. The tests were carried out using Vickers hardness measurements with a Matsuzawa Via S hardness tester (Matsuzawa, Akita, Japan) and a static tensile test using an MTS E45.305 testing machine (MTS Systems, Eden Prairie, MN, USA).

Hardness test samples were taken from six areas of the coil—the beginning (b), middle (m), and end (e). Assuming symmetry of properties across the sheet width, the number of samples in the transverse direction was limited to two—one taken from the edge and one from the center of the strip. The areas from which hardness samples were taken covered the same zones of the beginning, middle and end of the coil that were examined later in the article. These locations were selected because the literature data, observations from sheet metal manufacturer Serwistal (Ełk, Poland), and preliminary studies indicated that these areas differ significantly in surface geometry. Additionally, as also presented in works [4,5], it was determined that these places are characterized by significant unevenness in internal stresses. Table 2 presents the sample identification and the corresponding area of the sheet (edge or center) from which each specimen was taken, while Tables 3 and 4 show the measured results obtained.

The obtained data indicate that the greatest differences in values were recorded at the beginning and end areas of the coil. These differences were observed regardless of the steel grade, which is closely related to the rolling process technology. Hot-rolled sheets

https://doi.org/10.3390/ma19061053

exhibited greater hardness non-uniformity across the strip width, with differences reaching up to 9.7%.

Table 2. Designation of samples for hardness testing.

Steel Grade	Sample Designation	Sampling Location
S235JR + AR	1 (b,m,e) 1_1 (b,m,e)	middle edge
S500MC/3	2 (b,m,e) 2_1 (b,m,e)	middle edge

Table 3. Hardness measurement results.

Des.	1	2	3	4	5	Mean	Std. Dev.	% Difference
1b	127.7	128.8	128.9	127.8	128.5	128.3	0.56	
1_1b	135.5	136.7	135.2	133.4	131.4	134.4	2.07	4.75
2b	229.8	226.4	226.3	229.4	227.1	227.8	1.68	
2_1b	232.9	235.7	234.5	237.6	233.9	234.9	1.81	3.13
1m	126.3	127.2	127.9	128.5	129.7	127.9	1.29	
1_1m	132.1	131.0	132.4	134.2	132.1	132.4	1.16	3.47
2m	228.9	225.3	226.5	224.7	225.1	226.1	1.70	
2_1m	229.6	230.1	231.2	234.6	237.9	232.7	3.51	2.91
1e	128.7	127.8	128.9	128.5	129.7	128.7	0.69	
1_1e	142.1	144.2	142.8	138.0	139.0	141.2	2.62	9.71
2e	231.8	234.4	233.4	236.1	234.1	234.0	1.56	
2_1e	239.9	238.7	237.9	238.5	239.4	238.9	0.78	2.10

Table 4. Anisotropy of the sheet made of S235JR + AR Steel.

					Average Across Width	Difference, %
Beginning of coil						
		Edge 1	Center	Edge 2		
	Ys, MPa	238	227	248	237.7	8.5
	UTS, MPa	364	353	375	364	5.9
Middle of coil						
		Edge 1	Center	Edge 2		
	Ys, MPa	231	226	234	230.3	3.4
	UTS, MPa	353	351	352	352.0	0.3
End of coil						
		Edge 1	Center	Edge 2		
	Ys, MPa	237	230	244	237.0	5.7
	UTS, MPa	365	346	381	364.0	9.2
Average along coil length	Ys, MPa	235	228	242	235.0	5.9
	UTS, MPa	361	350	369	360.0	5.1
	Ys, %	0.3	2.0	1.6		
	UTS, %	0.3	2.0	6.1		

The analysis of the anisotropy of mechanical properties aimed not only to investigate the hypothesis regarding significant differences between individual areas of the ring, but

also to determine the extent of these differences. Only this knowledge allowed for an assessment of the feasibility of numerical studies and the identification of necessary simplifications. This is particularly crucial because, while incorporating the actual geometry of an object into numerical tools is a relatively straightforward task, implementing significant anisotropy is essentially impossible or nearly so. The use of relatively simple tests, such as hardness and static tensile testing, served a dual purpose. Firstly, these tests are feasible under production conditions; secondly, they give a clear result. As will be explained further in this paper, the development of a tabular material model—as the most effective method for defining material anisotropy parameters—enabled its implementation in numerical research. Due to the fact that during the implementation of project POIR.01.01.01-00-0477/18, a sheet metal straightening system was designed and developed based on two components consisting of a preliminary multi-roller leveler and a final tension leveler, knowledge regarding the non-uniformity of mechanical properties in the longitudinal direction was essential. The multi-roller straightening system presented in this work served as a preliminary stress relief stage. Since this stage is important but not the primary factor, the research was simplified to focus solely on longitudinal properties. Consequently, it was possible to introduce a simplification by limiting the study to the investigation of properties in the longitudinal direction. By combining the roller system with the final tension stage, it is possible to orient the stresses and ultimately obtain high-quality products characterized by the absence of surface defects. Related studies [4,5] provide additional data on this project, specifically regarding stress states measured using the Barkhausen noise method.

Subsequently, tensile tests were carried out to determine the actual anisotropy of mechanical properties (Ys—yield strength; UTS—ultimate tensile strength). The samples used for testing at room temperature are shown in Figure 2.

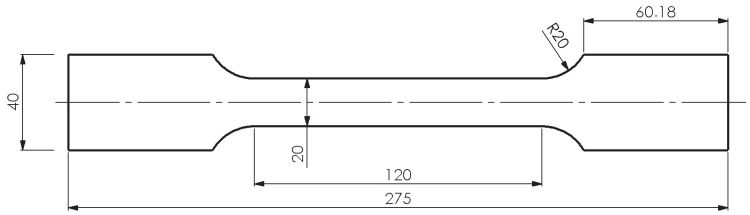


Figure 2. Dog-bone specimen used in the tests.

The sampling locations included the beginning, middle, and end of the coil—both from the central part of the sheet and near its side edges. Three samples were prepared from each location. The results are presented in Tables 4 and 5.

The data presented in Tables 4 and 5 show that the greatest differences in yield strength and tensile strength values—regardless of the steel grade—were observed across the sheet width at the beginning and end of the coil. This results from the rolling process technology. The differences across the width reached nearly 10%, while smaller variations, up to about 6%, were observed along the coil length.

For accurate numerical modeling, it was necessary to adopt a certain degree of data homogenization. To achieve this, the obtained values were averaged. Due to the significant number of samples intended for testing, dedicated computer software was developed to enable automatic numerical analysis of the collected data. The data, initially stored as text files, were processed into a structured table containing the essential parameters required to generate flow stress curves for each steel grade. Additionally, the results were averaged within each steel grade category.

Figure 3 presents examples of flow stress curves obtained for the selected steel grades, while Table 6 shows their averaged characteristics.

https://doi.org/10.3390/ma19061053

Table 5. Anisotropy of the sheet made of S500MC steel.

					Average Across Width	Difference, %
		Beginning of coil				
		Edge 1	Center	Edge 2		
	Ys, MPa	364	353	375	364.0	5.9
	UTS, MPa	520	499	535	518.0	6.7
		Middle of coil				
		Edge 1	Center	Edge 2		
	Ys, MPa	353	351	352	352.0	0.3
	UTS, MPa	510	500	506	505.3	1.2
		End of coil				
		Edge 1	Center	Edge 2		
	Ys, MPa	365	346	381	364.0	9.2
	UTS, MPa	506	489	516	503.7	5.2
Average along coil length	Ys, MPa	360.7	350.0	369.3	360.0	5.1
	UTS, MPa	512.0	496.0	519.0	509.0	4.4
	Ys, %	0.3	2.0	1.6		
	UTS, %	3.0	2.0	6.1		

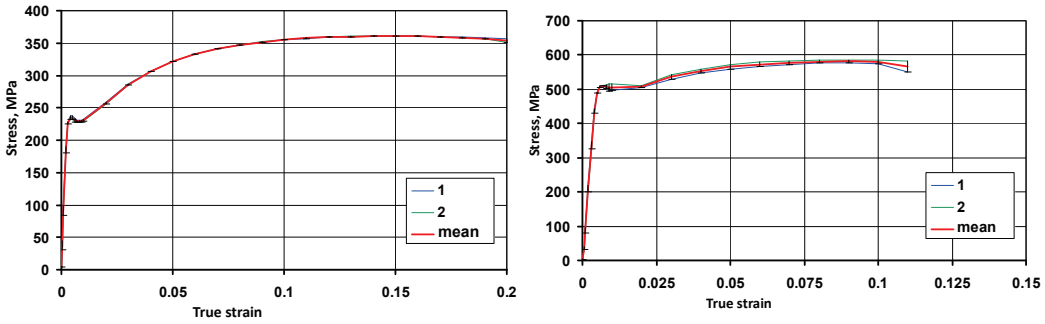


Figure 3. Averaged flow stress curves obtained from the results of the static tensile test: (**a**) S235JR + AR, (**b**) S500MC.

Table 6. Characteristics of averaged yield stress curves.

Steel Grade	Conventional Yield Strength Ys, MPa	Tensile Strength UTS, MPa	Young's Modulus E, GPa	Maximum Absolute Error Δ, MPa	Maximum Relative Error δ, %
S235JR + AR	234	360	181	±8.25	2.29
S500MC	509	582	169	±10.63	1.83

For the obtained curves, an exponential function was fitted using the developed computer program, as it most accurately represented the experimental data. An analysis of different forms of exponential functions, varying in the number of coefficients, showed that the four-parameter exponential function provided the best fit to the actual curve behavior. The function takes the following form:

https://doi.org/10.3390/ma19061053

$$\sigma_f = K \cdot \varepsilon^{m_1} \cdot exp^{\frac{m_2}{\varepsilon}} \cdot exp^{\varepsilon m_3}, [\text{MPa}] \quad (1)$$

The obtained flow stress curves were then subjected to numerical analysis using the developed software. A least-squares approximation was performed using a four-parameter quadratic exponential function dependent on strain, which made it possible to determine the coefficients of function (1): K, m_1, m_2, and m_3. The applied method for determining the function coefficients minimizes the deviation error between the fitted function and the actual flow stress curves. Table 3 presents the coefficients of function (1) for the selected steel grades.

The developed mathematical model of flow stress enables computer simulations of sheet behavior using a deformable body model in an elasto-plastic state. The elastic state is represented by Young's modulus, while the deformation range beyond the yield point is described by the flow stress function.

The final stage of the preliminary research involved analyzing the geometry of the selected sheets using 3D laser scanning. These tests were carried out with a Creaform MetraSCAN 3D optical-laser scanner (AMETEK Inc. Lévis, AC, Canada), used together with the C-Track tracking system, enables precise measurement of components. In combination with the HandyPROBE (AMETEK Inc. Lévis, QC, Canada) measuring device, sheet scanning within a range of 1 to 10 m is possible. An example view of the scanning process is shown in Figure 4, while the obtained sheet surface geometries are presented in Figures 5 and 6.



Figure 4. Sheet scanning using a 3D laser scanner. Own elaboration.

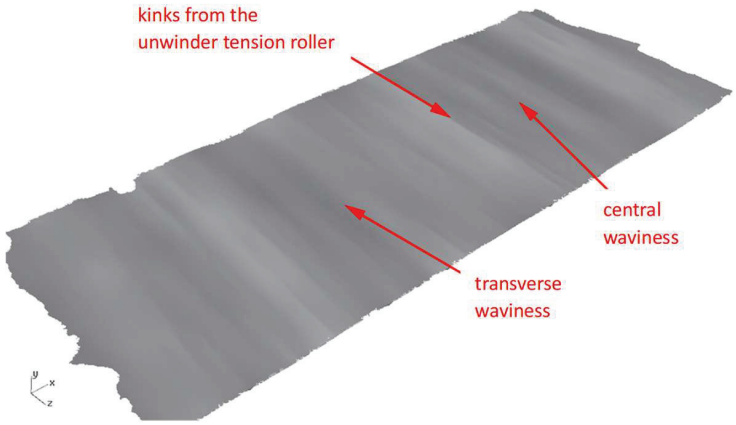


Figure 5. Sheet surface from the end of the coil obtained by 3D laser scanning for the steel grade S235JR + AR.

Based on the conducted scans, it was possible to determine the geometric parameters of the examined sheets and subsequently create the actual geometries to be used as input

material for FEM simulations. An example view of the prepared simulation file is shown in Figure 7.

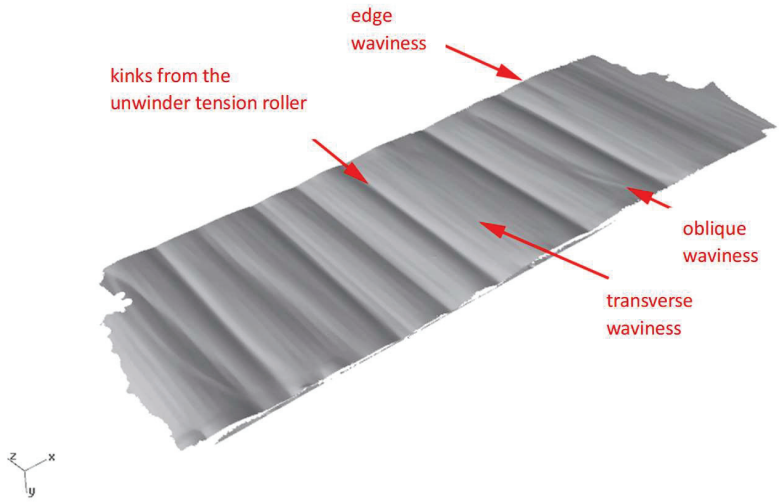
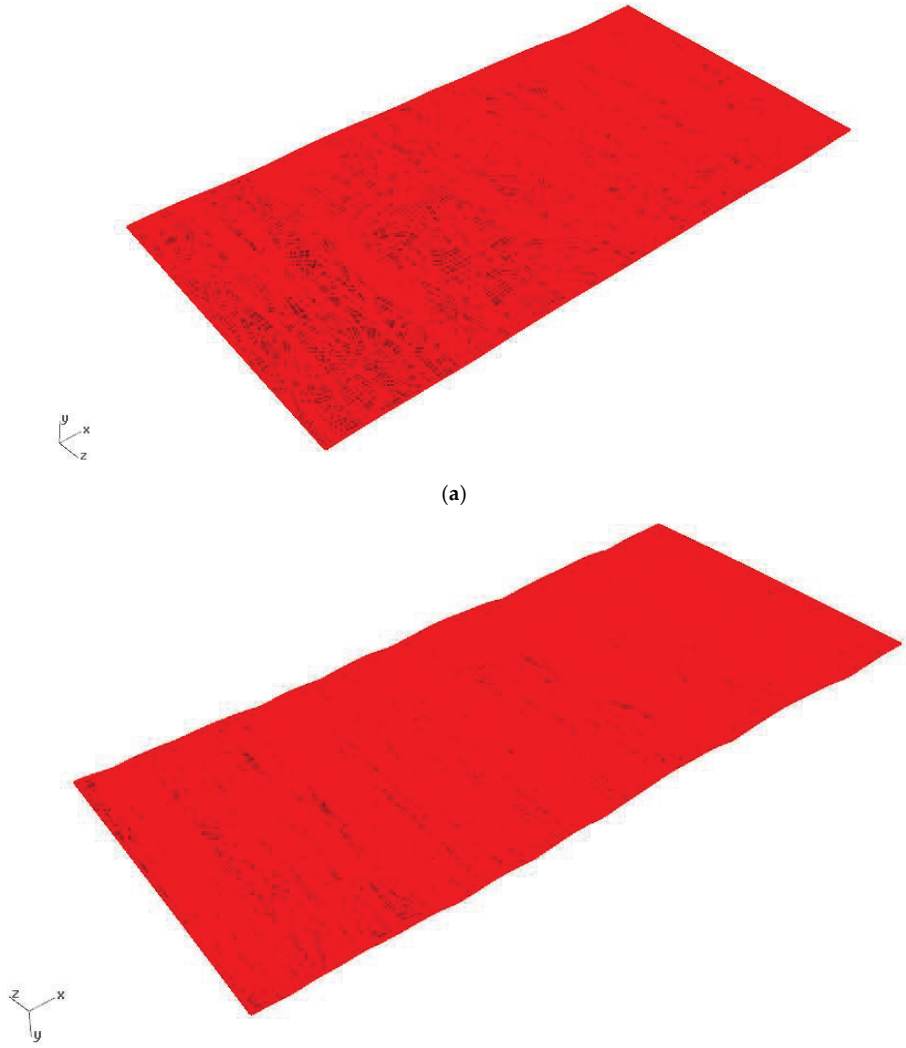


Figure 6. Sheet surface from the end of the coil obtained by 3D laser scanning for the steel grade S500MC.



(**a**)

(**b**)

Figure 7. Sheet surface from the end of the coil obtained by 3D laser scanning: (**a**) for steel grade S235JR + AR and (**b**) for steel grade S500MC.

https://doi.org/10.3390/ma19061053

3. Validation of the Mathematical Model of the Material Database

The mathematical model—material database—is one of the key elements for correctly performing numerical simulations [35–37]. Many authors point out that the accuracy of calculations based on plasticity curves is insufficient [36–38], and standard models are increasingly replaced with multi-parameter curves [29,39–41]; however, this approach is not always adequate. Therefore, as part of the work related to modeling the reduction in internal stresses and defects in uncoiled sheet metal, it was necessary to carry out validation of the obtained material model.

As part of the model verification, a comparison was made between the actual flow stress curves and those generated numerically based on Equation (1) and the coefficients listed in Table 7. Figure 8 presents an example of such a comparison for steel grade S235JR + AR. In Table 8 is presented the geometric parameters of the sheet waviness measurement for the selected steel grades using the 3D laser scanning method after uncoiling.

Table 7. Coefficients of Function (1) Defining the Flow Stress.

Steel Grade	K	m_1	m_2	m_3
S235JR + AR	483	0.18	0.001	1.8
S500MC	787	0.12	0.001	0.01

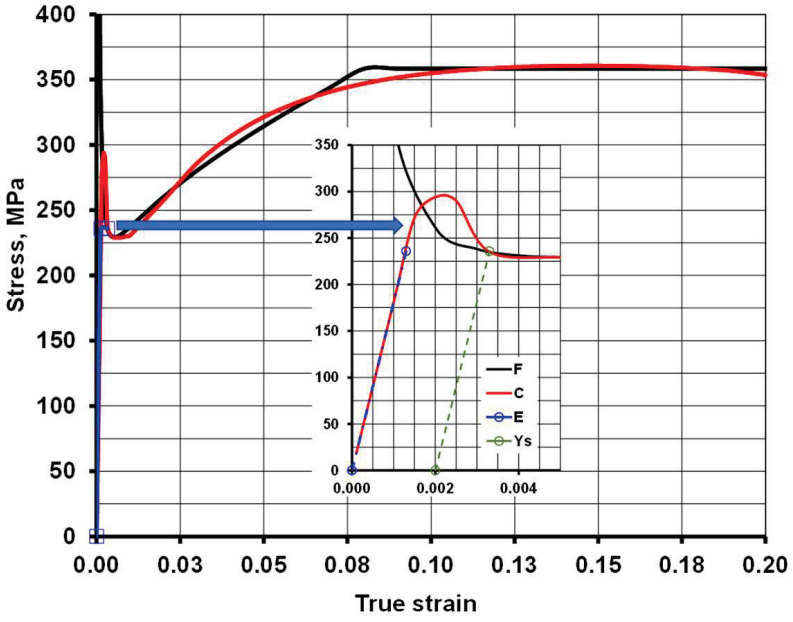


Figure 8. Graphical representation of the mathematical models of flow stress for the exemplary steel grade S235JR + AR (C—actual curve; E—Young's modulus; F—four-parameter stress function; Ys—flow stress).

Table 8. Geometric parameters of the sheet waviness measurement for the selected steel grades using the 3D laser scanning method after uncoiling.

Steel Grade	Sheet Thickness, mm	Sheet Width, mm	Average Waviness Height, mm		Waviness Wavelength, mm
			Center of the Coil	End of the Coil	
S235JR + AR	3	1500	15.2	21.5	Irregular
S500MC	3	1500	29.7	34.8	Irregular

https://doi.org/10.3390/ma19061053

By analyzing the course of stress changes as a function of strain, it can be observed that discrepancies occur between the curve determined during experimental tests and the curve obtained by approximating the results of static tensile tests. This is particularly noticeable in the region where the material transitions into the plastic state (the area marked with an arrow and enlarged). An imprecise mathematical description of the flow stress value (σ_f) may be one of the causes of significant numerical errors during tensile test simulations (determination of the range of plastic deformation). To reduce the discrepancies between the approximated and the actual results, it is necessary to introduce the flow stress values in a tabular form, without approximating the static tensile test results. When constructing such a table, it should be assumed that the accuracy of the flow stress values after approximation depends on the number of input data points for the actual strain and stress σ_f values. Reading the flow stress values for real strain increments equal to 0.05 may, in some strain ranges, result in underestimated σp values due to the adopted computational step size. Based on the obtained results of static tensile tests for individual steel grades, tabular forms of the flow stress were developed, as shown in Figure 9.

No	1	2	3	4	5	6	7	8	9	10
Strain	0.0001	0.0010	0.0015	0.0020	0.0025	0.0033	0.0050	0.0060	0.0070	0.0080
Stress, MPa	18.1	181.4	272.1	294.0	290.0	235.0	229.3	229.1	229.0	229.4

No	11	12	13	14	15	16	17	18	19	20
Strain	0.0090	0.0100	0.0200	0.0300	0.0400	0.0500	0.0600	0.0700	0.0800	0.0900
Stress, MPa	230.0	230.7	257.6	286.0	306.4	321.4	332.6	341.0	347.2	351.7

No	21	22	23	24	25	26	27	28	29	30
Strain	0.1000	0.1100	0.1200	0.1300	0.1400	0.1500	0.1600	0.1700	0.1800	0.2000
Stress, MPa	355.0	357.4	359.0	360.1	360.6	360.7	360.4	359.7	358.6	356.9

(**a**)

No	1	2	3	4	5	6	7	8	9	10
Strain	0.0001	0.0005	0.0010	0.0020	0.0030	0.0040	0.0050	0.0060	0.0070	0.0080
Stress, MPa	4.0	36.4	88.2	209.0	336.4	436.4	488.2	508.3	510.7	508.4

No	11	12	13	14	15	16	17	18	19	20
Strain	0.0090	0.0100	0.0200	0.0300	0.0400	0.0500	0.0600	0.0700	0.0800	0.0900
Stress, MPa	504.4	505.7	507.4	535.7	553.3	565.2	573.1	578.0	580.7	581.5

No	21	22	23	24	25	26	27	28	29	30
Strain	0.1000	0.1100	0.1200	0.1300	0.1400	0.1500	0.1600	0.1700	0.1800	0.2000
Stress, MPa	582.0	582.5	582.9	583.4	583.9	584.4	584.8	585.3	585.8	586.2

(**b**)

Figure 9. The flow stress value σ_f for temperatures 10–100 °C, strain rates 0.0001–100 s^{-1} and true strains in the range 0.0001–0.2 presented in tabular form: (**a**) steel S235JR + AR, (**b**) steel S500MC.

Based on the obtained data for the flow stress region, the differences between the experimental and simulation results were determined for two variants: one using the flow stress function and the other using the tabular form of the flow stress. The values of the relative percentage differences are presented in Table 9.

https://doi.org/10.3390/ma19061053

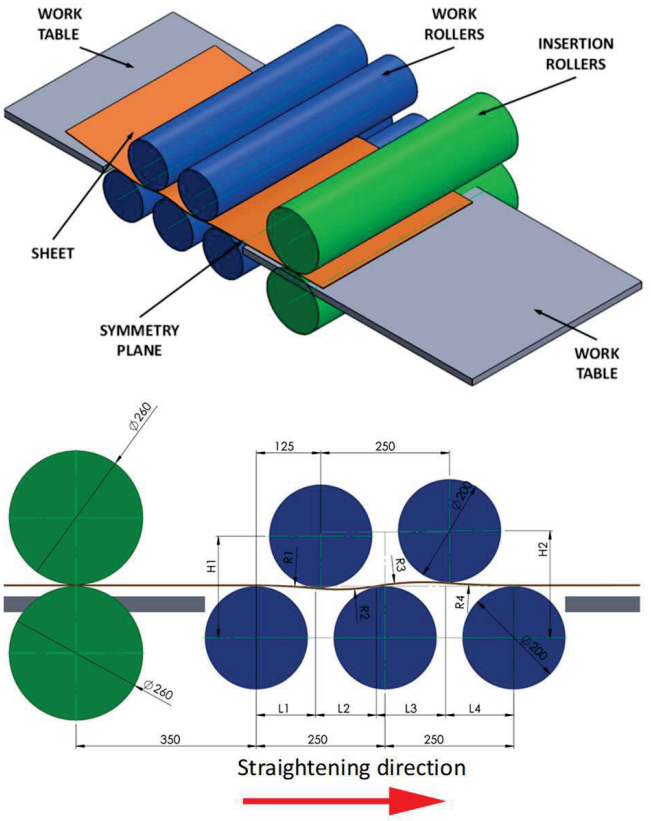
Table 9. The values of the relative percentage differences.

Steel Grade	Tensile Force F0.2 kN Experiment	Tensile Force F0.2 kN FEM Table	Tensile Force F0.2 kN FEM Function	Difference Experiment/FEM Table %	Difference Experiment/FEM Function %
S235JR + AR	13.964	13.903	12.389	−0.4	−4.2
S500MC	30.170	29.866	26.238	−1.0	−2.7

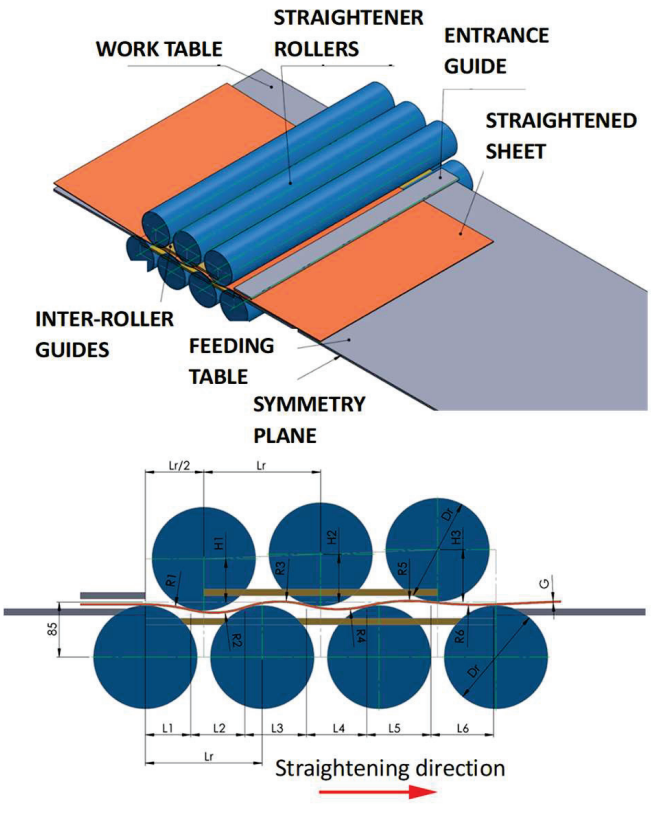
As can be observed, the obtained differences in stress values fall within the range of 0.63–2.35%, which indicates that the proposed testing procedure is highly accurate and can be applied to determine the range of forces and elongations. The developed mathematical model of flow stress enables computer simulation of the sheet metal using a model of the deformable object in the elastic–plastic state. The elastic state is represented by Young's modulus, while the deformation range beyond the yield point is implemented using the actual values taken from the table. This is particularly important when testing at ambient temperature. In such cases, models using approximation curves exhibit greater error in the area of elastic and small plastic strains.

4. Numerical Analysis of Sheet Straightening in a Roll Straightener

As part of the research continuing the work presented in [4], computer simulations of the straightening process were carried out using a roll straightener equipped with 5 rolls with a diameter of 200 mm, and 7 and 9 rolls with a diameter of 160 mm. The study was conducted using the software ForgeNxT®. The simulation used the rigid bodies model for the tools, this simplification was used because the aim of this research was the selection of roll pre-leveler parameters to ensure the removal of so-called "coil memory", reducing waviness (geometry defects). The 5-roll straightener is treated as the reference model. Numerical modeling of the sheet metal rolling process is a challenging task, primarily due to geometric factors—specifically the high width-to-thickness ratio. For the calculations, an elasto-plastic model of the deformed material was applied, disregarding the influence of strain rate. Material properties were determined based on tensile tests; the resulting tensile curves were converted into stress–strain curves and implemented as constitutive data. From the perspective of sheet straightening, properties in the longitudinal direction are of paramount importance. The strip geometry, obtained through 3D scanning, was introduced as a boundary condition. Contact between the material and the rollers was defined using the Coulomb friction model. Due to the unfavorable thickness-to-width ratio, the analysis of stress–strain states was performed using localized mesh refinement. These areas were kept small to allow for a finite element mesh dense enough to ensure sufficiently accurate results. The computer simulation of the leveling process was carried out with the use of an elastoplastic model in the triaxial state of strain by using the ForgeNxT® v2.1 Transvalor program, whereas the properties of the deformed material were described according to the Norton–Hoff [42,43] conservation law. The application of the computer program ForgeNxT® using the thermo-mechanical models that it contains requires the definition of boundary conditions, which are decisive to the correctness of numerical computation. The theoretical analysis was performed for the following conditions: friction coefficient, μ—0.15 (according to the ForgeNxT® v2.1 Transvalor database and [44]); sheet temperature—20 °C; Poisson coefficient—0.3, leveling velocity 45 m/min., number of elements 210,000; specific heat—480 J/(kg·K); density—7850 kg/m^3; conductivity—29.9 W/(m·K). Figure 10 presents the diagrams of the roll straighteners and the models used for the simulations.

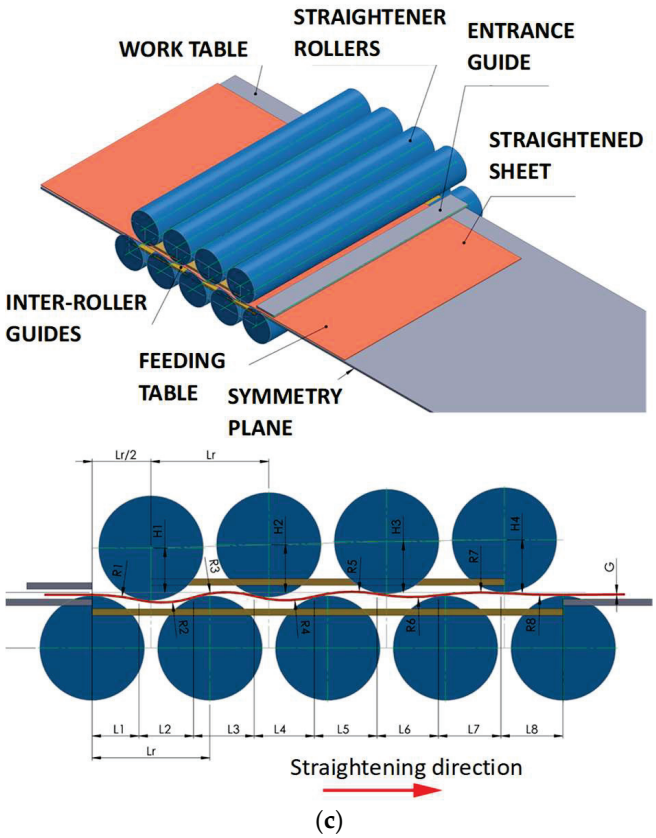


(**a**)



(**b**)

Figure 10. *Cont.*

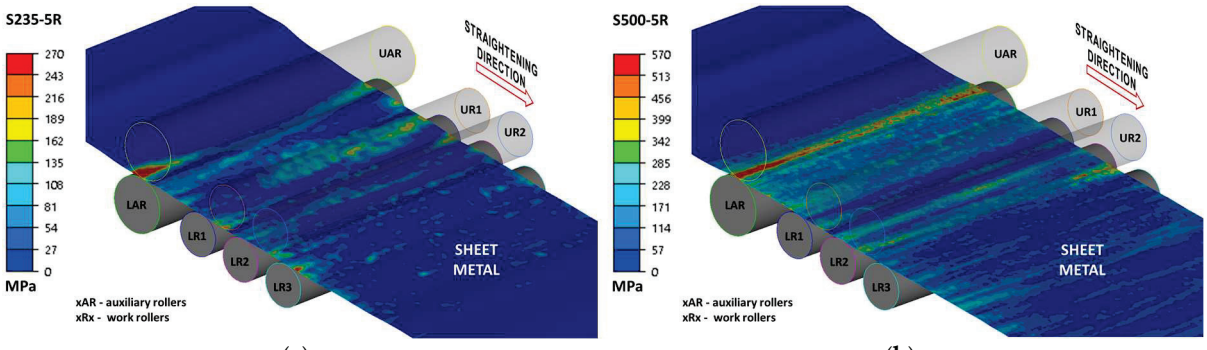


(**c**)

Figure 10. Diagram of the roll straightener and the models used for computer simulation of sheet straightening: (**a**) five-roll, (**b**) seven-roll, (**c**) nine-roll.

Due to the complexity of the results, the data are presented in two ways: as projections of stress intensity distributions (Figures 11–13) and as side views, which also allow for a better assessment of the cross-sectional geometry. Due to the fact that the present work was carried out as part of a larger project and some of the results were presented, among others, in [4], the authors will not duplicate the results.

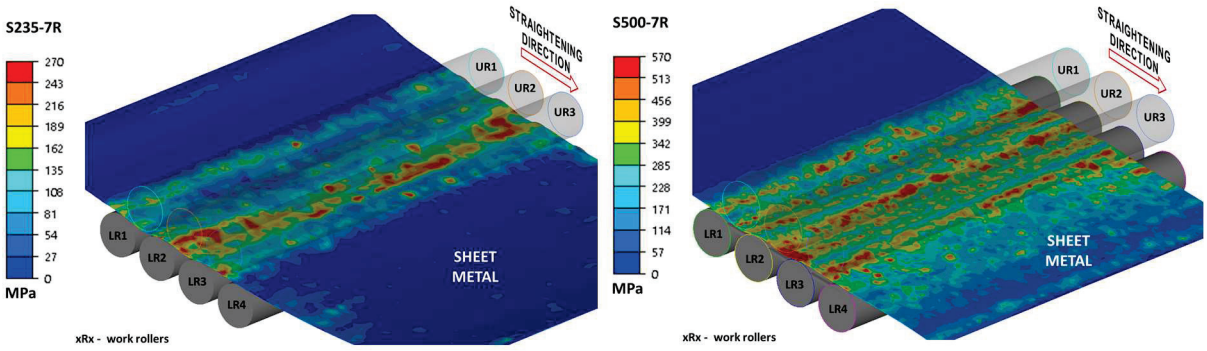
In the following part of the study, the results are presented in a side view. This approach also made it possible to evaluate the geometry of the strip. Figure 14 shows a view of the areas (measuring points) in which measurement data were collected. To limit the graphical data in this article, the results from the measurement points are presented in Table 10. The mesh was selected in such a way that when the box option was used, compaction occurred in the areas of contact with the rollers. This mesh densification approach not only accelerated calculations but, more importantly, improved their quality.



(**a**) (**b**)

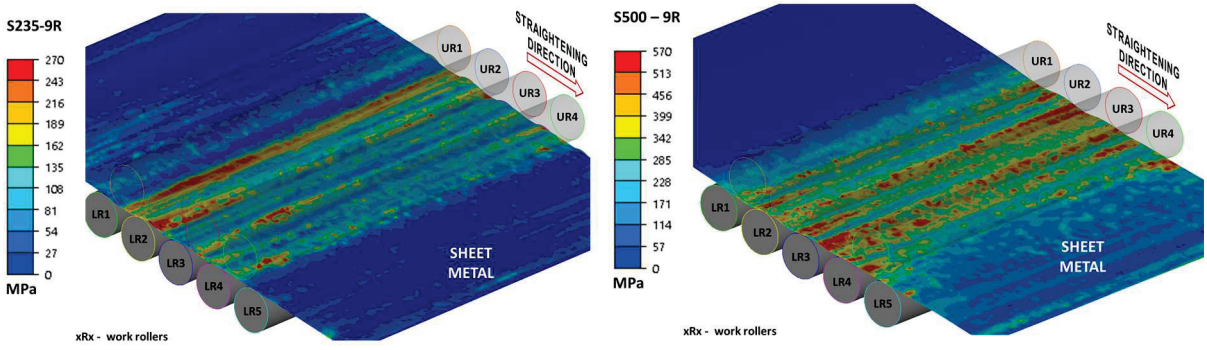
Figure 11. Equivalent stress distribution during sheet five-roll straightening: (**a**) steel S235 + AR, (**b**) steel S500MC.

https://doi.org/10.3390/ma19061053



(**a**) (**b**)

Figure 12. Equivalent stress distribution during sheet seven-roll straightening: (**a**) steel S235 + AR, (**b**) steel S500MC.



(**a**) (**b**)

Figure 13. Equivalent stress distribution during sheet nine-roll straightening: (**a**) steel S235 + AR, (**b**) steel S500MC.

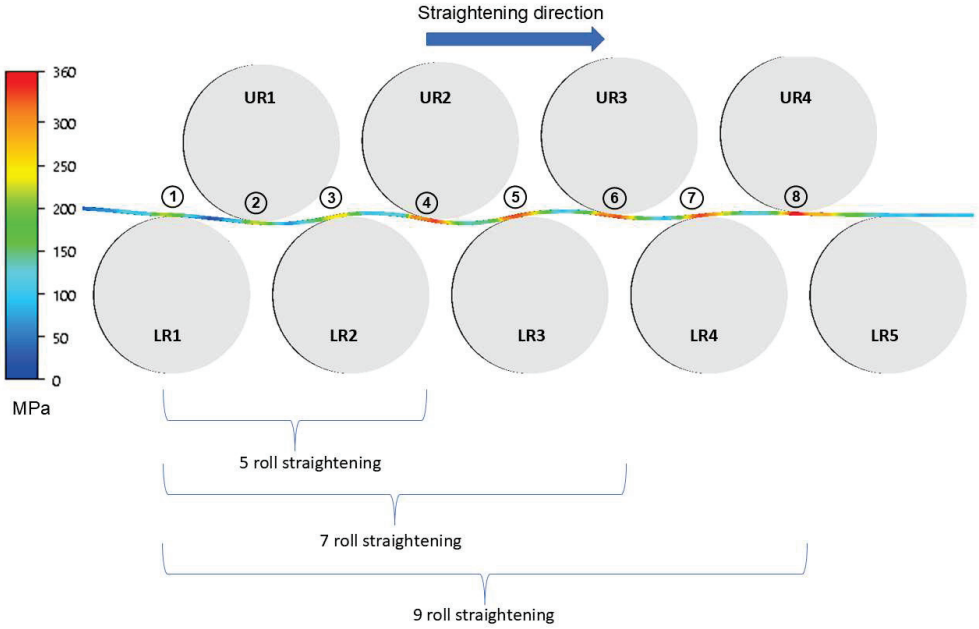


Figure 14. The view of the areas (measuring points) in which measurement data were collected.

Based on the data shown in Figure 14 and Table 10, it can be observed that the values of stress intensity and strain intensity, similarly to the seven-roll straightener, increase in the areas where the straightened sheet contacts the rolls, and then decrease in the free-forming regions of the sheet between consecutive rolls. However, when using the

https://doi.org/10.3390/ma19061053

nine-roll straightener, the increase in stress and strain within the straightened sheet is much more gradual—both compared to the currently used five-roll straightener and the newly designed seven-roll straightener. Analysis of the obtained numerical simulation results showed that for the remaining components of stress and strain, the distributions are similar to those obtained for the seven-roll straightener, but the nature of their variation becomes smoother due to the addition of an extra pair of rolls. An important observation is the increase in plastic deformation through the thickness of the straightened sheet as a result of adding more straightening rolls. Therefore, increasing the number of rolls in this case is fully justified. Interesting distributions were obtained for the elastic and plastic strain intensities. While the plastic strain intensity decreases as the sheet moves between subsequent rolls—which is a natural consequence of smaller deflections of the following rolls—the elastic strain intensity increases as the sheet passes through successive rolls. This indicates that the plastic deformation in the subsequent bending zones of the sheet has an increasingly smaller effect, and thus the sheet begins to deform mainly within the elastic range. A similar relationship was noted for the total strain in the straightened sheet, which is plastically deformed. However, in the case of the nine-roll straightener, plastic deformations are distributed over the first seven rolls, where the total strain reaches its highest and most intense values (as a sum of elastic and plastic strains), and then decreases sharply in the last two rolls, where the sheet is deformed only elastically.

Table 10. The results of stress and strain from the measurement points.

S235	Straightening	Roll								Sum	Upper Rolls Settings			
		1	2	3	4	5	6	7	8		UR1	UP2	UP3	UP4
Strain	5	0.0029	0.0066	0.0057	0.0042	x	x	x	x	0.0193	12.5	1.0	x	x
Stress	5	231.70	252.97	248.99	241.25	x	x	x	x					
Strain	7	0.0025	0.0063	0.0073	0.0074	0.0065	0.0056	x	x	0.0356	6.0	3.5	1.0	x
Stress	7	227.73	251.71	255.99	256.17	252.83	248.68	x	x					
Strain	9	0.0016	0.0043	0.0057	0.0062	0.0062	0.0060	0.0055	0.0050	0.0403	4.0	3.0	2.0	1.0
Stress	9	217.29	241.66	248.99	251.54	251.33	250.31	248.02	245.45					
S500MC	Straightening	Roll								Sum	Upper Rolls Settings			
		1	2	3	4	5	6	7	8		UR1	UP2	UP3	UP4
Strain	5	0.0033	0.0071	0.0063	0.0052	x	x	x	x	0.0219	13.0	2.5	x	x
Stress	5	501.06	517.00	514.57	510.42	x	x	x	x					
Strain	7	0.0027	0.0067	0.0077	0.0075	0.0071	0.0067	x	x	0.0385	6.5	3.5	2.5	x
Stress	7	454.44	515.82	518.44	518.13	516.97	515.82	x	x					
Strain	9	0.0020	0.0053	0.0068	0.0074	0.0072	0.0068	0.0064	0.0061	0.0479	5.0	4.0	2.5	2.0
Stress	9	340.76	510.85	516.08	517.76	517.04	515.86	514.63	513.61					

In summary, the results of the numerical calculations for the five-roll straightener and the seven- and nine-roll straighteners indicate that increasing the number of rolls positively affects the plasticization of the sheet. The plasticization process becomes smoother, and increasing the number of rolls to nine improves the straightness of the sheet and enhances the reduction in residual stresses—one of the main objectives of using a preliminary multi-roll straightener. Due to the fact that, based on numerical data, it was determined that the most effective system was one containing nine rollers for physical testing, such a system was selected. As mentioned, the research was conducted with an industrial partner, and therefore, one of the goals was to develop inspection tools suitable for such conditions. For this purpose, an original tool was developed in the form of a specially prepared laser-cut sheet of metal. A sample view is presented in Figure 15, and the results of measurements performed with commonly available engineering tools are presented in Table 11 and Figure 16.

https://doi.org/10.3390/ma19061053

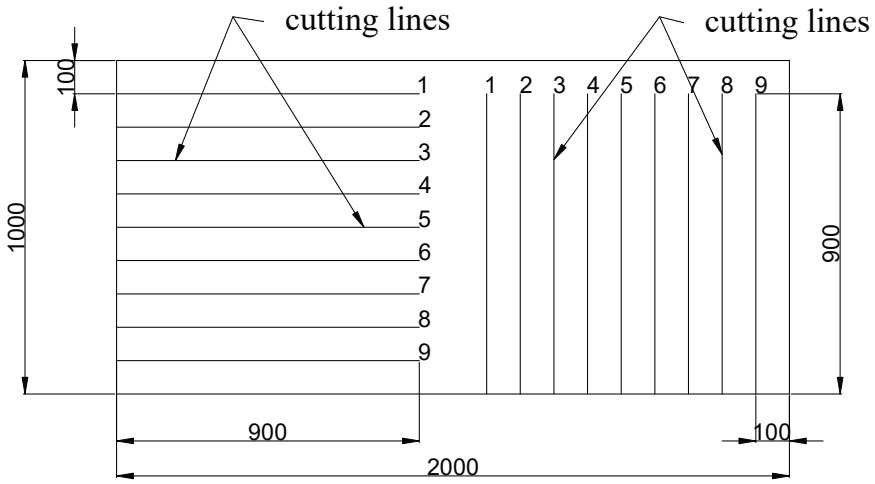


Figure 15. Sample preparation diagram for the author's method of assessing straightening effectiveness.

Table 11. Example measurement results for the tested materials.

Grade	Measurement Direction	Deflection Value, mm										Mean
		1	2	3	4	5	6	7	8	9	10	
S235JR	Along the straightening	1.82	1.15	0.95	1.23	1.06	0.86	1.32	1.26	1.46	1.48	1.26
	Across straightening	0.78	0.71	0.63	0.51	0.49	0.49	0.41	0.53	0.54	0.76	0.59
S500MC	Along the straightening	1.55	1.89	1.21	1.47	1.51	1.41	1.74	1.41	1.63	1.27	1.51
	Across straightening	0.99	0.84	0.72	0.68	0.79	0.57	0.71	0.73	0.81	0.61	0.75

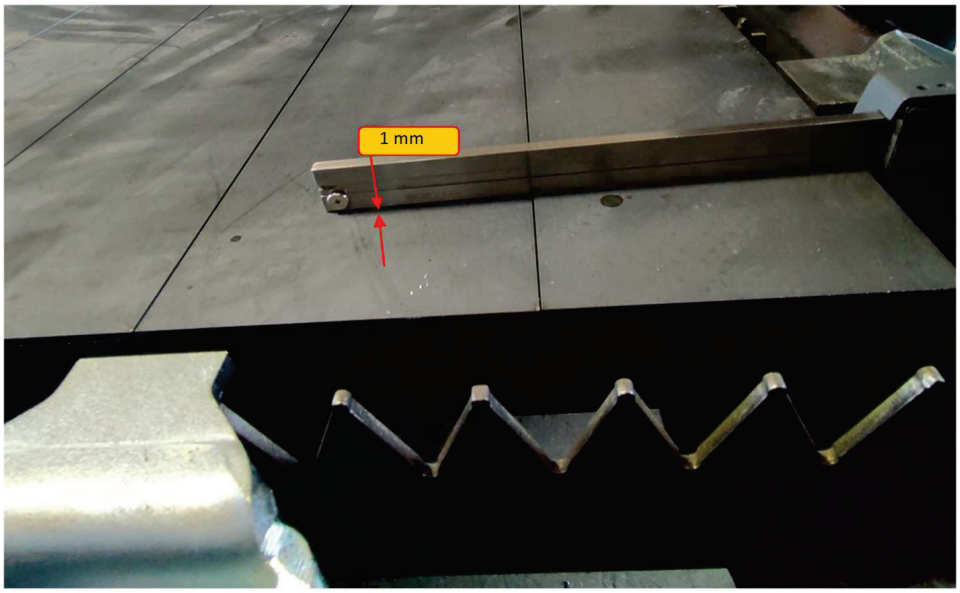


Figure 16. Example result of strip bending measurement for a 3 mm thick sheet of S235JR steel.

The choice of the method for assessing the state of internal stresses was based on the assumption that a material with trapped stresses in its volume will lead to their release and change in geometry. An easy and clear comparison result is the deflection measurement shown in the data in Table 10.

https://doi.org/10.3390/ma19061053

5. Conclusions

The numerical studies carried out demonstrated a high sensitivity of the input parameters to the obtained results. The validation of the mathematical model of the material database, combined with the integration of tabular data and real data from sheet surface scans, made it possible to achieve highly accurate results. Based on the obtained research findings, the following statements and conclusions can be formulated:

1. The anisotropy of the examined sheets, determined both by hardness measurements and static tensile tests, is evident. Therefore, for proper numerical analyses, it is essential to average the real material properties based on the obtained data.
2. To perform computer simulations with higher computational accuracy, it was necessary to transition from a material model based on the flow curve equation to a tabular form of data.
3. The incorporation of real sheet geometries, correlated with actual anisotropy properties, allowed for a high degree of accuracy in the obtained research results.
4. In the case of the nine-roll straightener, plastic deformations are distributed over the first seven rolls; total deformations reach their highest and most intense values (as a sum of elastic and plastic strains), and then decrease sharply in the last two rolls, where the sheet is deformed only within the elastic range.
5. On the base of numerical simulation it can be stated that use of a nine-roll configuration has a positive effect on the sheet straightening capability.
6. The proprietary method of analyzing the state of internal stresses enables a quick and rough assessment that can be applied in industrial conditions.
7. The measurements of real materials showed some differences between the tested steel grades and confirmed that the use of a nine-roll straightening system significantly reduces the stress on the material.

Author Contributions: Conceptualization, S.M., P.S., T.G. and G.S.; methodology, S.M., P.S. and J.G.; formal analysis, S.M., G.S. and R.G.; data curation, S.M., P.S. and G.S.; investigation, S.M., P.S., T.G., G.S., J.G. and R.G.; writing—original draft preparation, S.M., P.S. and T.G.; writing—review and editing, S.M., J.G. and R.G.; visualization, S.M., P.S. and G.S. All authors have read and agreed to the published version of the manuscript.

Funding: This work was financially supported by the National Center for Research and Development (NCBiR), grant no. POIR.01.01.01-00-0477/18.

Data Availability Statement: The raw data supporting the conclusions of this article will be made available by the authors on request.

Conflicts of Interest: Authors Jakub Gróbarczyk and Radosław Gryczkowski were employed by the company Serwistal Sp. z. o.o. The remaining authors declare that the research was conducted in the absence of any commercial or financial relationships that could be construed as a potential conflict of interest.

References

1. Hidveghy, J.; Michel, J.; Bursak, M. Residual Stress in Microaloyed Steel Sheet. *Metalurgija* **2003**, *42*, 103–106.
2. Abvabi, A. Effect of Residual Stresses in Roll Forming Process of Metal Sheets. Ph.D. Thesis, Deakin University, Melbourne, Australia, 2014.
3. Alhalaybeh, T.S.; Akhtar, H.; Chowdhury, A.I.; Lou, Y. Anisotropic Hardening of HC420 Steel Sheet: Experiments and Analytical Modeling. *Metals* **2025**, *15*, 149. [CrossRef]
4. Mróz, S.; Szota, P.; Garstka, T.; Stradomski, G.; Gróbarczyk, J.; Gryczkowski, R. The Selection of Leveler Parameters Using FEM Simulation. *Materials* **2024**, *17*, 52. [CrossRef] [PubMed]
5. Garstka, T.; Szota, P.; Mróz, S.; Stradomski, G.; Gróbarczyk, J.; Gryczkowski, R. Calibration Method of Measuring Heads for Testing Residual Stresses in Sheet Metal Using the Barkhausen Method. *Materials* **2024**, *17*, 4584. [CrossRef]

6. Jeon, Y.; Jeong, K.; Kim, G.-h.; Yoon, J. 1.5 GPa Grade High-Strength Steel Sheet Flattening by Roll Gap Adjustment Considering Pattern Roll Effects. *Materials* **2025**, *18*, 1702. [CrossRef] [PubMed]
7. Available online: https://www.arku.com/pl/blog/jak-wyeliminowac-defekty-w-blasze (accessed on 19 September 2025).
8. Dömling, F.; Paysan, F.; Breitbarth, E. Numerical Simulations of Stress Intensity Factors and Fatigue Life in L-Shaped Sheet Profiles. *Metals* **2024**, *14*, 1463. [CrossRef]
9. Mroziński, S.; Golański, G.; Jagielska-Wiaderek, K.; Szarek, A. Impact of Microstructural Anisotropy on the Low-Cycle Fatigue of S420M Steel. *Materials* **2025**, *18*, 2365. [CrossRef]
10. Roh, Y.-H.; Lee, D.; Lee, S.-E.; Kim, S.-G.; Lee, Y. Development and Validation of a Large Strain Flow Curve Model for High-Silicon Steel to Predict Roll Forces in Cold Rolling. *Machines* **2025**, *13*, 243. [CrossRef]
11. Perzynski, K.; Pyzynski, K.; Swierczynski, S.; Pidvysots'kyy, V.; Klis, J.; Madej, L. Influence of the roll leveler setup parameters on the quality of high-strength steel leveling operation. *Int. J. Adv. Manuf. Technol.* **2022**, *120*, 1203–1217. [CrossRef]
12. Liu, Z.; Luo, Y.; Wang, Y.; Liao, T.W. A new curvature analytical method in plate leveling process. *ISIJ Int.* **2018**, *58*, 1094–1101. [CrossRef]
13. Smith, R.P. The effect of the number of leveling rolls on the straightening process. *Iron Steel Technol.* **2007**, *4*, 57–68.
14. Keecheol, P.; Kyungsuk, O. Effect of the Leveling Conditions on Residual Stress Evolution of Hot Rolled High Strength Steels for Cold Forming. *J. Phys. Conf. Ser.* **2017**, *896*, 012117.
15. Brautigam, H.; Becker, S. *Leveling with Roller Levelers*; ARKU Maschinenbau GmbH: Baden-Baden, Germany, 2009.
16. Zhao, J.; Wang, X.; Yang, Q.; Wang, Q.; Wang, Y.; Li, W. Mechanism of lateral metal flow on residual stress distribution during hot strip rolling. *J. Mater. Process. Technol.* **2021**, *288*, 116838. [CrossRef]
17. Hu, Q.; Zhang, F.; Li, X.; Chen, J. Overview on the Prediction Models for Sheet Metal Forming Failure: Necking and Ductile Fracture. *Acta Mech. Solida Sin.* **2018**, *31*, 259–289. [CrossRef]
18. Cazacu, O. New Yield Criteria for Isotropic and Textured Metallic Materials. *Int. J. Solids Struct.* **2018**, *139–140*, 200–210. [CrossRef]
19. Richard, P.; Smith, J. Modeling Plastic Strain During Cold Leveling of Steel Plates. In Proceedings of the AISE Annual Conference, Pittsburgh, PA, USA, 10–12 May 1999.
20. Gruber, M.; Hirt, G. A strategy for the controlled setting of flatness and residual stress distribution in sheet metals via roller leveling. *Proc. Eng.* **2017**, *207*, 1332–1337. [CrossRef]
21. Behrens, B.-A.; El Nadi, T.; Krimm, R. Development of an analytical 3D-simulation model of the levelling process. *J. Mater. Process. Technol.* **2011**, *211*, 1060–1068. [CrossRef]
22. Widmark, M.; Melander, A.; Meurling, F. Low cycle constant amplitude fully reversed strain-controlled testing of low carbon and stainless sheet steels for simulation of straightening operations. *Int. J. Fatigue* **2000**, *22*, 307–317. [CrossRef]
23. Pietrzyk, M.; Madej, L.; Rauch, L.; Szeliga, D. *Computational Materials Engineering*; Elsevier: Amsterdam, The Netherlands, 2015. [CrossRef]
24. Frederick, C.O.; Armstrong, P.J. A mathematical representation of the multiaxial Bauschinger effect. *Mater. High Temp.* **2007**, *24*, 1–26. [CrossRef]
25. Lee, J.-B.; Kang, S.-S. Numerical modeling of roller leveler for thick plate leveling. *Int. J. Precis. Eng. Manuf.* **2018**, *19*, 425–430. [CrossRef]
26. Wiewiórowska, S.; Siemiński, M.; Śleboda, T.; Dyl, T.; Koczurkiewicz, B. Determination of Two-Stage Heat Treatment Parameters in Industrial Conditions in Order to Obtain a TRIP Structure in Low-Alloy Carbon Steel Wires. *Materials* **2022**, *15*, 8965. [CrossRef]
27. Rydz, D.; Dyja, H.; Berski, S. The prediction of curvature of bimetallic plate Al-Cu during asymmetrical cold rolling. *Metalurgija* **2003**, *42*, 261–264.
28. Stradomski, G.; Gzik, S.; Jakubus, A.; Nadolski, M. The assessment of resistance to thermal fatigue and thermal shock of cast iron used for glass moulds. *Arch. Foundry Eng.* **2018**, *18*, 173–178. [CrossRef]
29. Dyl, T.; Starosta, R.; Rydz, D.; Koczurkiewicz, B.; Kusmierska-Matyszczak, W. The experimental and numerical research for plastic working of nickel matrix composite coatings. *Materials* **2020**, *13*, 3177. [CrossRef]
30. Dyl, T.; Rydz, D.; Szarek, A.; Stradomski, G.; Fik, J.; Opydo, M. The Influence of Slide Burnishing on the Technological Quality of X2CrNiMo17-12-2 Steel. *Materials* **2024**, *17*, 3403. [CrossRef]
31. Garstka, T.; Dyl, T. Circumferential residual stresses in tubes estimated by means of deflection method. *Arch. Metall. Mater.* **2006**, *2*, 199–203.
32. Dembiczak, T.; Knapiński, M. Shaping microstructure and mechanical properties of high-carbon bainitic steel in hot-rolling and long-term low-temperature annealing. *Materials* **2021**, *14*, 384. [CrossRef]
33. Schindler, I.; Kawulok, R.; Opela, P.; Kawulok, P.; Rusz, S.; Sojka, J.; Sauer, M.; Navrátil, H.; Pindor, L. Effects of austenitization temperature and pre-deformation on CCT diagrams of 23MnNiCrMo5-3 steel. *Materials* **2020**, *13*, 5116. [CrossRef]
34. Dyl, T.; Starosta, R. Effect of the Ceramic Dispersion in the Nickel Matrix Composite Coatings on Corrosion Properties after Plastic Working. *Solid State Phenom.* **2012**, *183*, 43–48. [CrossRef]

35. Dyl, T.C.; Kuśmierska-Matyszczak, W. The Effect of the Burnishing Process on the Strain Rate and State Stress in Hollow Steel Tubes. *Metals* **2025**, *15*, 694. [CrossRef]
36. Stradomski, G.; Rydz, D.; Dyja, H. Bimetal plate St3S + Cu. *Metalurgija* **2005**, *44*, 147–150.
37. Transvalor, S.A. *FORGE® Reference Guide Release*; Parc de Haute Technologie: Sophia–Antipolis, France, 2024. Available online: https://www.transvalor.com/en/forge (accessed on 20 October 2025).
38. Banaszek, G.; Stefanik, A. Theoretical and laboratory modelling of the closure of metallurgical defects during forming of a forging. *J. Mater. Process. Technol.* **2006**, *177*, 238–242. [CrossRef]
39. Hartley, P.; Pillinger, I. Numerical simulation of the forging process. *Comput. Methods Appl. Mech. Eng.* **2006**, *195*, 6676–6690. [CrossRef]
40. Chen, K.; Yang, Y.; Shao, G.; Liu, K. Strain function analysis method for void closure in the forging process of the large−sized steel ingot. *Comput. Master. Sci.* **2012**, *51*, 72–77. [CrossRef]
41. Goh, C.-H.; Dachowicz, A.P.; Allen, J.K.; Mistree, F. A Computational Method for the Design of Materials Accounting for the Process–Structure–Property–Performance (PSPP) Relationship. In *Integrated Computational Materials Engineering (ICME) for Metals*; Horstemeyer, M.F., Ed.; John Wiley & Sons, Inc.: Hoboken, NJ, USA, 2018. [CrossRef]
42. Norton, F.H. *Creep of Steel at High Temperature*; McGraw Hill: New York, NY, USA, 1929.
43. Hoff, N.J. Approximate Analysis of Structures in the Presence of Moderately Large Steps Deformation. *Quart. Appl. Mech.* **1954**, *12*, 49–55.
44. Trzepieciński, T. A Study of the Coefficient of Friction in Steel Sheets Forming. *Metals* **2019**, *9*, 988. [CrossRef]

Disclaimer/Publisher's Note: The statements, opinions and data contained in all publications are solely those of the individual author(s) and contributor(s) and not of MDPI and/or the editor(s). MDPI and/or the editor(s) disclaim responsibility for any injury to people or property resulting from any ideas, methods, instructions or products referred to in the content.

materials

MDPI

Article

Tribological Properties of Eutectic White Cast Iron with Directional and Non-Directional Microstructure

Małgorzata Trepczyńska-Łent [1,*] and Jakub Wieczorek [2]

[1] Faculty of Mechanical Engineering, Bydgoszcz University of Science and Technology, Al. Prof. S. Kaliskiego 7, 85-796 Bydgoszcz, Poland
[2] Faculty of Materials Engineering, Silesian University of Technology, Krasińskiego 8 St., 40-019 Katowice, Poland; jakub.wieczorek@polsl.pl
* Correspondence: malgorzata.trepczynska-lent@pbs.edu.pl

Abstract

Tribological tests were conducted on eutectic white cast iron subjected to directional solidification (resulting in a directionally oriented microstructure) and, for comparison, on white cast iron with an equiaxed (non-directional) structure. The tests were performed under dry sliding conditions on a pin-on-block rig using Cu, AlSi12CuNiMg alloy, AlSi12CuNiMg + SiC composite, and steel grade 1.3505. The friction coefficient and wear rates of these materials were systematically compared. Quantitative and qualitative evaluations of the wear tracks formed on the test specimens were carried out using profilometry. The results demonstrate that the directionally solidified white cast iron exhibits improved friction coefficient stability and reduced wear in the specific tribological pairs. The oriented directional structure demonstrated more favourable interactions when paired with AlSi12CuNiMg + SiC composite and 1.3505 steel. These tribological combinations exhibited reduced roughness values across selected cross-sectional analyses, resulting in correspondingly lower Sa parameter measurements. This finding suggests a promising new application for inserts made of directionally structured white cast iron in structural components requiring enhanced wear resistance at elevated temperatures.

Keywords: eutectic white cast iron; directional solidified structure; tribological properties; coefficient of friction; wear

1. Introduction

Material strength and the complex of functional properties resulting from manufacturing technology and related to material surface characteristics are the decisive factors determining the operational lifespan of machines and equipment. The issues concerning surface condition changes and modifications of the surface layer in machine components are difficult to generalize. This complexity stems from the intricate nature of processes occurring at the material surface and their dependence on numerous variables [1–3]. Even more challenging is the unambiguous definition of friction and wear phenomena in relation to materials with multiphase structure. Among critical considerations is the determination of which microstructural features most significantly influence the tribological properties of a given material.

Foundry alloys have found extensive application in machine components that operate under friction conditions. There exists a continuous need for searching and investigating suitable materials for friction pairs. Multiphase materials such as cast iron, including

white cast iron, are also considered in this context. Over several decades, white cast irons have served as the primary materials for wear protection applications in mining and cement industries, as well as in road construction. Advanced wear-resistant metal matrix composites have been developed, incorporating hard particles such as carbides, borides, and nitrides within a metal matrix, designed with microstructures exhibiting superior properties. The selection of cast iron for friction pairs must consider its chemical composition, microstructure, and casting technology. The abrasive wear resistance of white cast iron depends primarily on the properties and proportion of individual phases and their mutual distribution. Extensive research has been conducted on the abrasive wear resistance of alloyed white cast iron [4–20].

The microstructure of high-chromium white cast iron often features a columnar zone where eutectic carbides align with the direction of heat dissipation, resulting in a distinctly anisotropic morphology. Research employing a pin abrasion test on specimens from this zone investigated the wear behaviour in directions both parallel (longitudinal) and perpendicular (transverse) to the primary axis of the carbides. The findings indicated that longitudinally oriented specimens exhibited a 27–67% lower volume loss compared to their transverse counterparts, with the exact reduction depending on the specific heat treatment applied [21]. The M_7C_3 carbide is a chromium-rich compound where M denotes various metals such as chromium, iron, vanadium, molybdenum, and tungsten. The relative proportions of these metallic elements within the carbide can vary depending on the specific alloy composition and the processing parameters applied [22]. The influence of M_7C_3 carbide orientation in high-chromium white cast irons was explored using high-stress pin-on-drum abrasion and single-scratch tests. This investigation concluded that orienting the long axes of the carbides perpendicular to the wear surface significantly compromises abrasion resistance. Conversely, superior wear resistance was achieved when the carbides were aligned parallel to the wear surface, with optimal performance observed when this parallel alignment was also oriented perpendicular to the direction of sliding [23]. In another study, two white cast iron alloys with differing chromium contents (13.81% and 24.41%) were unidirectionally solidified to produce oriented M_7C_3 carbides within a eutectic matrix. Pin-abrasion tests on specimens sectioned parallel and transverse to the solidification axis yielded contrasting results, revealing that the transverse sections demonstrated greater abrasion resistance. The authors attributed this behaviour to the fracture mechanics of M_7C_3 carbides, where cracks tend to propagate along their longest edge, which corresponds to the plane of lowest fracture toughness [24].

Unalloyed, eutectic white cast iron is characterized by the presence of transformed ledeburite in its microstructure. Such cast iron can be treated as an in situ composite. This composite consists of a eutectic mixture of cementite (iron carbide Fe_3C) in the form of layers (plates) and pearlite in the form of fibres (rods). Cementite hardness ranges from approximately 760–1340 HV [25], while pearlite hardness averages 180–220 HB. Hard cementite in this composite is responsible for load transfer, while pearlite provides plastic properties. Ledeburite hardness is approximately 450 HB.

Research has demonstrated that in carbon steel and white cast iron, the volumetric fraction of cementite significantly influences abrasive wear resistance. Nevertheless, since the cementite volume fraction in conventional steels and cast irons remains below 65%, the wear behaviour of Fe-C materials containing cementite volume fractions exceeding 65% remains largely unexplored [25]. Investigations have been conducted on abrasive wear behaviour using materials with varying cementite volume fractions [26].

Due to microstructural characteristics and properties, white cast iron is used to manufacture components resistant to abrasive wear, as well as artifacts requiring high resistance to high and low temperature effects (camshafts, extrusion dies, pipe couplings, flanges,

pump impellers, shot blast nozzles). The production of inserts (fragments) or surfaces and coatings made of white cast iron on structural elements of other metallic materials is also popular. Industrial applications frequently employ cladding techniques for specific surface areas exposed to severe wear conditions as a cost-effective solution for extending component service life. Among various surface coating protection and hardening techniques, hardfacing represents one of the most widely adopted approaches due to its economic advantages and operational simplicity [19,26–29].

The installation method of a given white cast iron insert may be significant depending on the operational mode of the structural element. In such cases, the possibility of using white cast iron with directional microstructure appears important. The mechanical properties of such cast iron depend on the working direction relative to directional solidification. The authors' previous studies [30–33] examined the microstructure, microhardness, and strength of directionally solidified eutectic white cast iron. Directional solidification involves the controlled removal of heat from the interface between the liquid and solid phases, as well as the controlled advancement of the melting or solidification front along the sample. This process enables the production of materials with precisely tailored properties. Building upon the author's research, investigating the abrasive wear resistance of eutectic white cast iron presents an interesting avenue. A hypothesis can be formulated regarding the beneficial influence of microstructure obtained through directional solidification of white cast iron on its tribological properties. It is important to compare, for example, the abrasion resistance of white cast iron having the same chemical composition, but differing microstructures obtained through different casting technologies. A directional structure can be achieved through directional solidification, for instance, using a Bridgman apparatus, whereas a non-directional structure results from casting methods where volumetric solidification occurs.

2. Material and Research Methodology

2.1. Directional Solidification of White Cast Iron

Directional solidification of cast iron was performed using a Bridgman apparatus with vertical temperature gradient (Faculty of Foundry Engineering, AGH, Krakow, Poland). Initially, Fe-C alloy ingots with a diameter of 12 mm were prepared in an argon atmosphere using a Balzers-type furnace, employing Armco iron and pressed graphite of spectral purity 99.99% C. Subsequently, cylindrical bars of the Fe-C alloy with a diameter of 5 mm were directionally solidified in a Bridgman apparatus using an alundum crucible under argon atmosphere. After maintaining the melt at 1450 °C for a homogenization period, the molten alloy was withdrawn downward from the heating zone directly into the cooling section at a constant withdrawal rate of 167 μm/s (equivalent to 600 mm/h), maintaining a steady temperature gradient of 33.5 K/mm [30–33]. Figure 1 shows a schematic illustration of experimental setup in the Bridgman apparatus.

The chemical composition of the eutectic cast iron used is presented in Table 1. The chemical composition was determined using a SPECTROMAXX spectrometer (Spectro Analytical Instruments, Kleve, Germany). Figure 2 shows the non-directional and directional microstructure of white cast iron, whose structural component is transformed ledeburite. In Figure 2a, a pronounced equiaxed dendritic growth of the ledeburite is visible. In contrast, Figure 2b shows alternating cementite plates and pearlite regions (within the transformed ledeburite), which are parallel to each other and to the axis of the sample (the pulled rod).

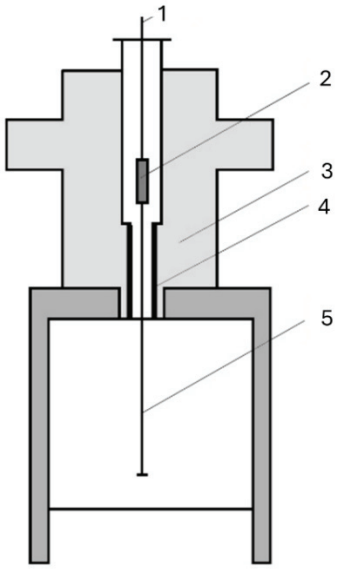
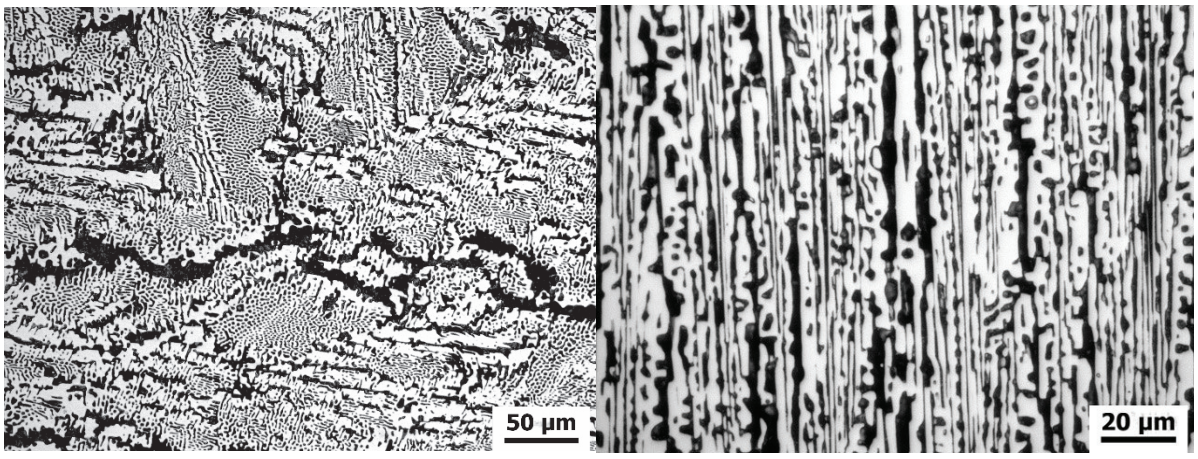


Figure 1. Schematic illustration of experimental setup in the Bridgman apparatus: 1-thermocouple, 2—sample, 3—heating furnace, 4—cooling system, 5—pulling system [30].

Table 1. Chemical composition, wt. %.

C	Si	Mn	P	S	Cr	Ni	Mo	Al	Cu
4.25	0.058	0.64	0.0079	0.021	0.033	0.0093	<0.0020	0.011	0.032
Co	**Ti**	**Nb**	**V**	**W**	**Pb**	**Mg**	**B**	**Sn**	**Zn**
0.0024	<0.001	<0.0040	0.0022	<0.010	<0.0030	<0.0010	0.0009	0.0061	<0.002
As	**Bi**	**Ca**	**Ce**	**Zr**	**La**	**Fe**			
0.0069	<0.002	0.0005	<0.0030	0.0043	0.0013	94.9			



(**a**) (**b**)

Figure 2. Microscopic images of: (**a**) non-directional structure; (**b**) directional structure white eutectic cast iron.

2.2. Tribological Investigations

Tribological investigations were conducted at the Faculty of Materials Engineering, Silesian University of Technology in Katowice. Testing of tribological properties, including determination of friction coefficient values and abrasive wear resistance, was performed at room temperature (25 ± 1 °C) under technically dry friction conditions using a specimen (block)—counter-sample (pin) configuration. A T-01 block-on-pin tribological tester

operating with reciprocating motion at 12 mm stroke was utilized for tribological property determination. The counter-specimen in the form of a pin with 5 mm diameter and 20 mm length was manufactured from eutectic white cast iron. Two pins were employed: one with directional structure (resulting from directional crystallization) and one with non-directional structure. Results were compared based on the applied white cast iron pin structure.

Four materials with varied mechanical properties (such as hardness, ductility, and tensile strength) were employed as blocks in friction pairs for tribological testing, paired with cast iron pins featuring non-directional and directional structures. The investigations were conducted using the following block materials (counter-specimens): electrolytic copper (ISO Cu-ETP [34], PN M1E), aluminum alloy AlSi12CuNiMg (EN AC-48000, [35]), composite based on AlSi12CuNiMg aluminum alloy (EN AC-48000 [35]) reinforced with SiC (reinforcing particle volume fraction 15%, diameter 15 μm), and bearing steel 1.3505 (100Cr6, [36]). The chemical composition of these materials is presented in Table 2. Composition of these alloys was tested by mass spectrometry (Foundry Master, Oxford Instruments—WAS, Abingdon, UK).

Table 2. Chemical composition, wt. %.

	C	Si	Cu	Mg	Ni	Mn	Ti	O	SiC	Al	Cr	Fe
Cu-ETP		-	≥99.9	-	-	-	-	≤0.04	-	-	-	-
AlSi12CuNiMg		12	1.0	1.0	0.9	0.2	0.05	-	-	bal.	-	-
AlSi12CuNiMg + SiC		11.5	2.0	2.0	0.9	0.2	0.05	-	15.0	bal.	-	-
1.3505	0.95	0.15	-	-	0.3	0.35	-	-	-	-	1.65	bal.

Block surfaces were ground using corundum abrasive papers to 500 grit. The prepared surfaces were subjected to abrasion. The experimental pin-on-block setup used in tribological tests is shown in Figure 3. A load of 0.5 MPa unit pressure was applied through the pins, the sliding speed was 0.5 m/s, and the friction distance was 200 m. During testing, continuous recording of friction coefficient value changes was performed. The wear trace formed on the block surfaces was subjected to profilometric analysis. Surface structure analysis after friction of blocks and cast iron pins was conducted based on profilometric measurements performed using an FRT MicroProf profilometer with WCL3000 aberration head (FRT GmbH, München, Germany). This measurement is contactless, completely eliminating the possibility of wear trace deformation during testing. Wear trace geometry investigations were conducted immediately after the friction process completion. The only surface preparation before measurement was cleaning with ethanol solution. Parameters of the conducted surface geometry measurements were:

- measurement field 6 × 10 mm,
- resolution 600 × 1000 measurement points,
- data acquisition and processing—MARK III v3.8.21 for windows software (FRT GmbH, München, Germany).

The analysis employed two- and three-dimensional images to evaluate basic surface characteristics such as: wear trace depth, roughness and waviness in the friction area, and wear trace volume loss. Macroscopic photographs of wear traces were taken using a Nikon 7000 digital camera (Tokyo, Japan).

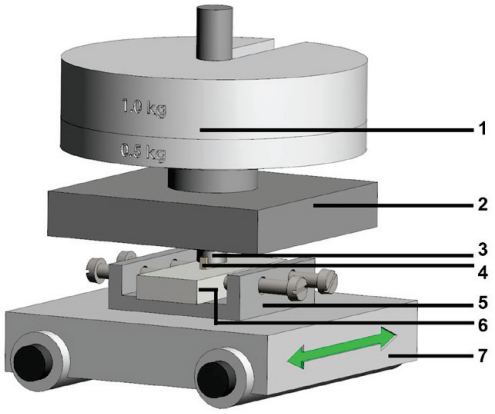


Figure 3. Schematic representation of the experimental setup used for tribological testing in pin-on-block configuration. The components are labelled as follows: 1—applied load, 2—strain gauge holder, 3—sample holder for the pin, 4—cast iron pin, 5—sample holder for the block, 6—sample, and 7—movable plate, green arrows—direction of sample movement [37].

3. Results and Analysis

3.1. Profilometry of Wear Tracks

Figure 4 presents images of sliding traces after tribological tests on blocks of four materials obtained after cooperation with cast iron pins having non-directional and directional structures.

Supplementary profilometric investigations facilitated both quantitative and qualitative evaluation of wear traces developed on the examined surfaces (Figure 5). Figure 5 shows the roughness profile curve and roughness (using a 0.25 mm Gaussian filter) at a representative location of the cross-section perpendicular to the friction direction.

In Figure 5, for the directional pin structure, the highest total abrasion depth was observed for AlSi12CuNiMg alloy at approximately 405 μm (Figure 5c). The smallest wear depth values were obtained for AlSi12CuNiMg + SiC composite (Figure 5e) and for 1.3505 steel (Figure 5g)—18.9 μm and 16 μm, respectively. This is confirmed by roughness distributions in the Gaussian filter, where for AlSi12CuNiMg + SiC composite—7.45 μm (Figure 5f), while for 1.3505 steel a value of 3.5 μm was obtained (Figure 5h).

Analysis of wear traces on matrix materials following interaction with cast iron pins revealed complex surface geometries. At the bottom of wear traces, discontinuous furrows were observed, interrupted by regions of significantly deformed material (Figure 5a,c,e,g). In Figure 5c, for directional pin structure, grooves at the bottom were uniformly distributed with evidence of transition to abrasive wear mechanisms.

In Figure 5e, for non-directional pin structure, the grinding surface appearance is characteristic of adhesive wear mechanisms. Large furrows created in the specimen were closed by deformed and displaced material during friction. In the upper portion of the wear trace, material was elevated above the primary surface. The total abrasion depth was 0.12 mm, including height above the primary surface (0.1 mm) and wear depth (0.02 mm).

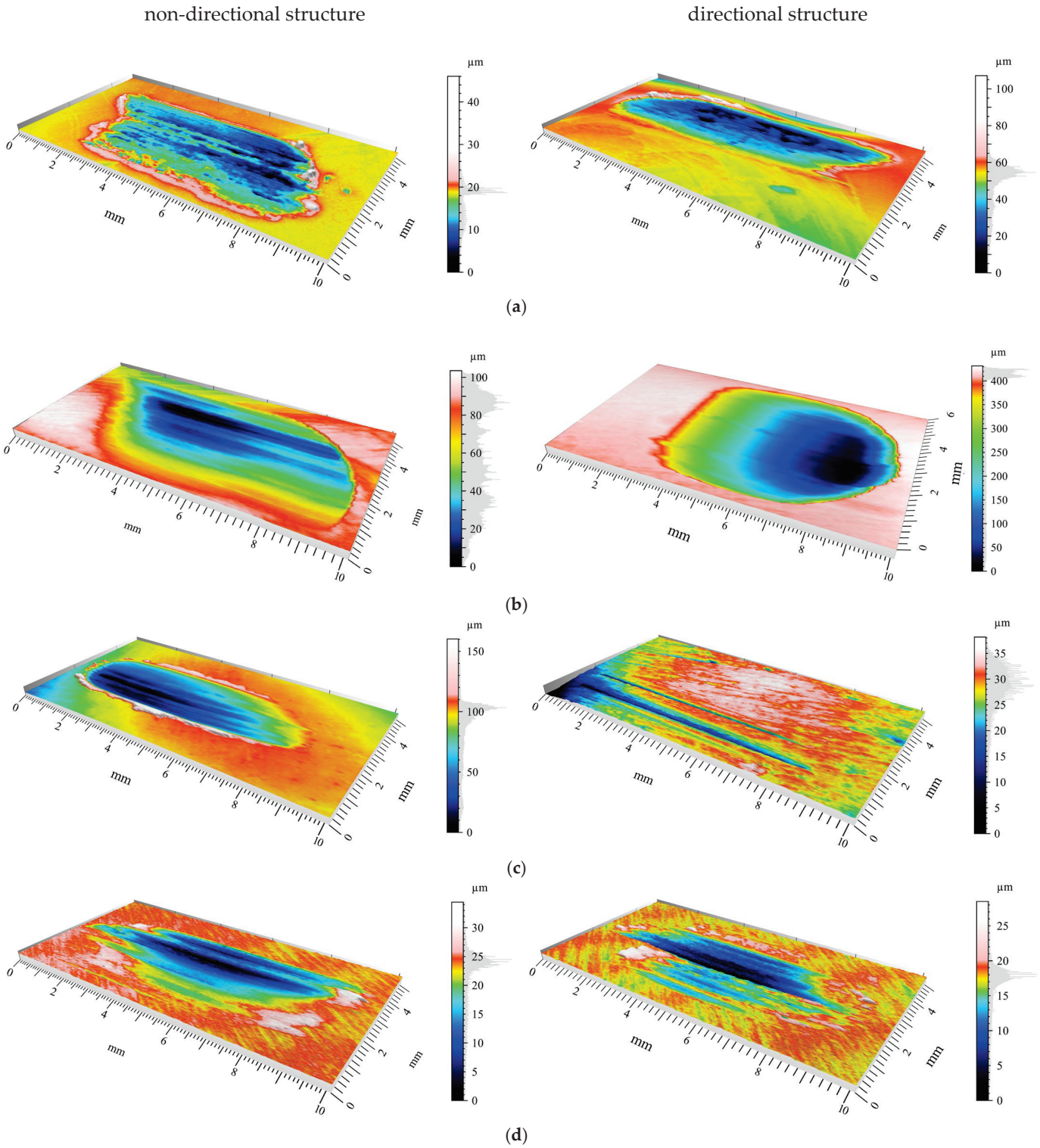


Figure 4. Three-dimensional surface topography images of wear tracks: (**a**) Cu-ETP; (**b**) AlSi12CuNiMg alloy; (**c**) AlSi12CuNiMg + SiC composite; (**d**) 1.3505 steel.

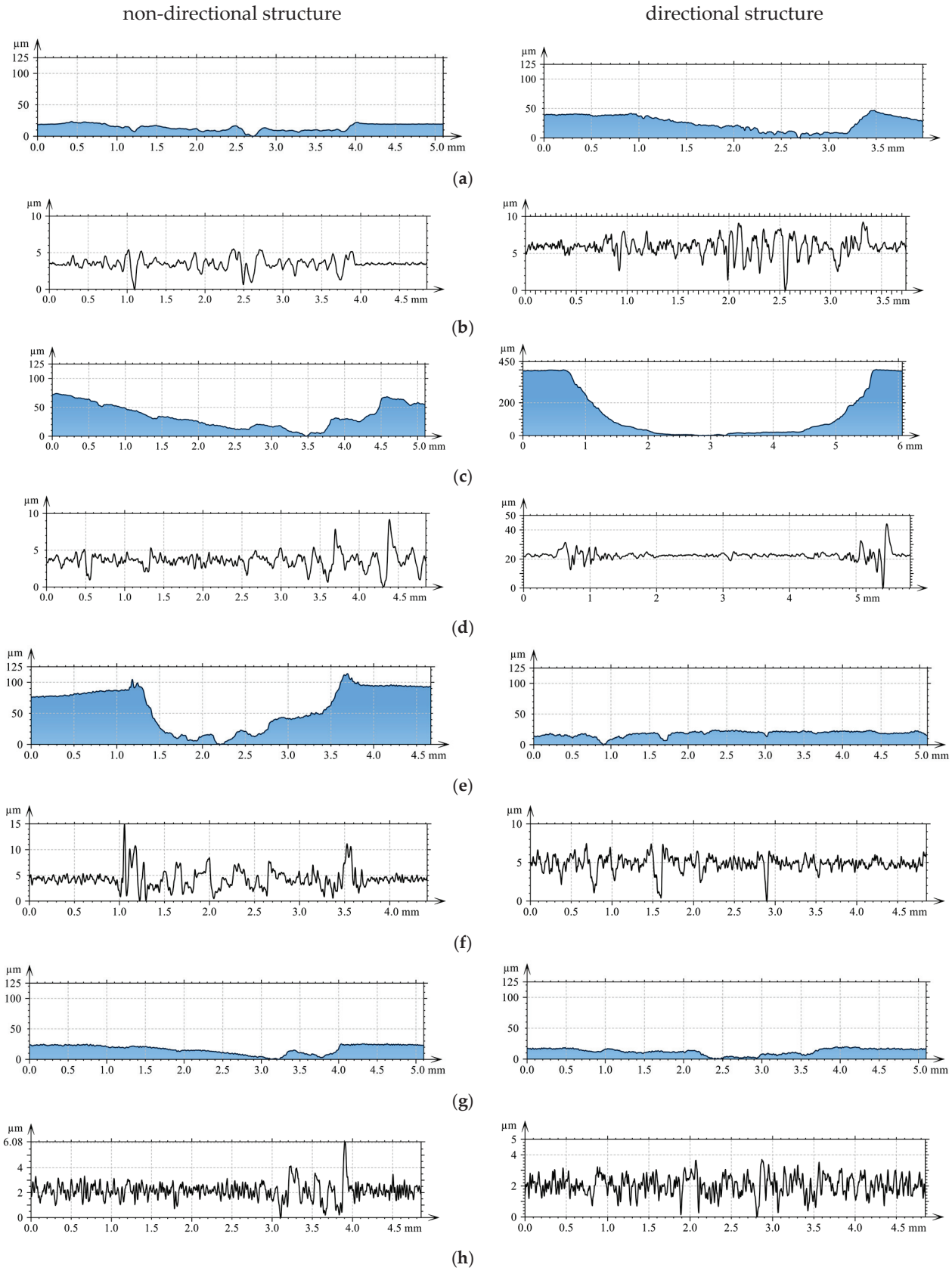
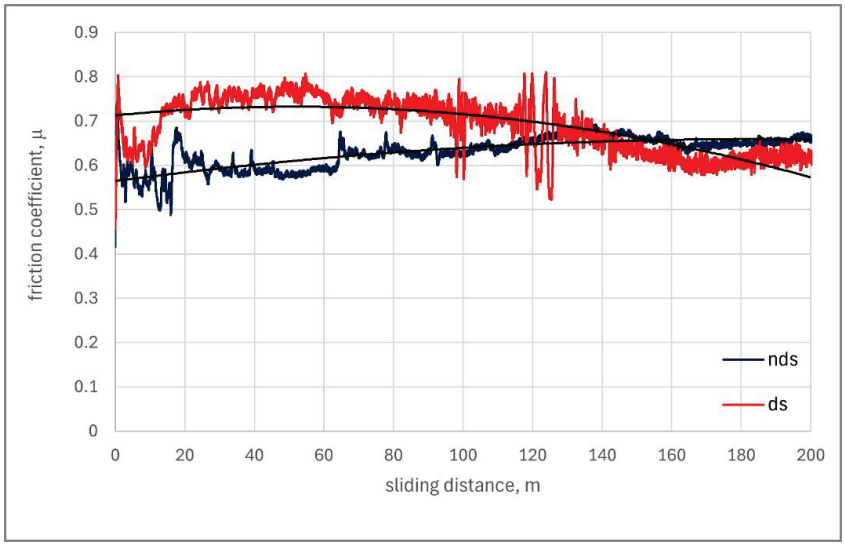


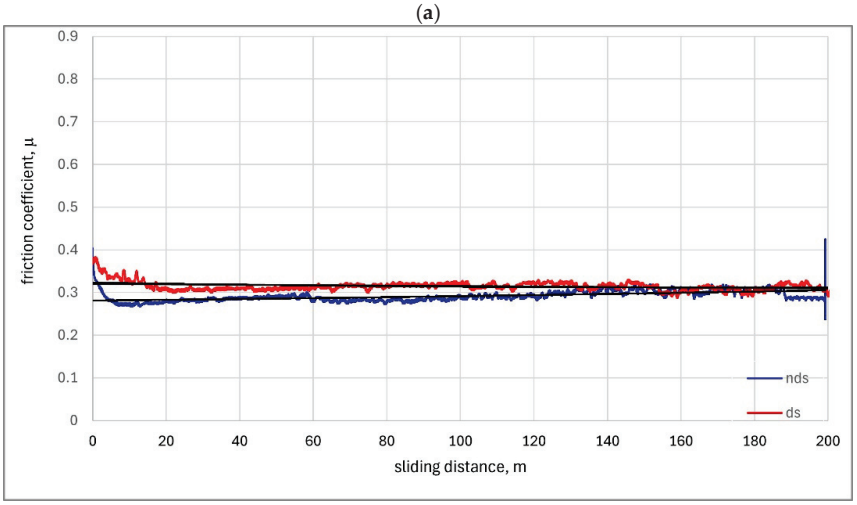
Figure 5. Surface roughness analysis of wear tracks: (**a**,**c**,**e**,**g**) roughness distribution in selected cross-sections perpendicular to friction direction for (**a**,**b**) Cu-ETP; (**c**,**d**) AlSi12CuNiMg alloy; (**e**,**f**) AlSi12CuNiMg + SiC composite; (**g**,**h**) 1.3505 steel; (**b**,**d**,**f**,**h**) roughness profiles (Gaussian filter, 0.25 mm cutoff).

3.2. Coefficient of Friction

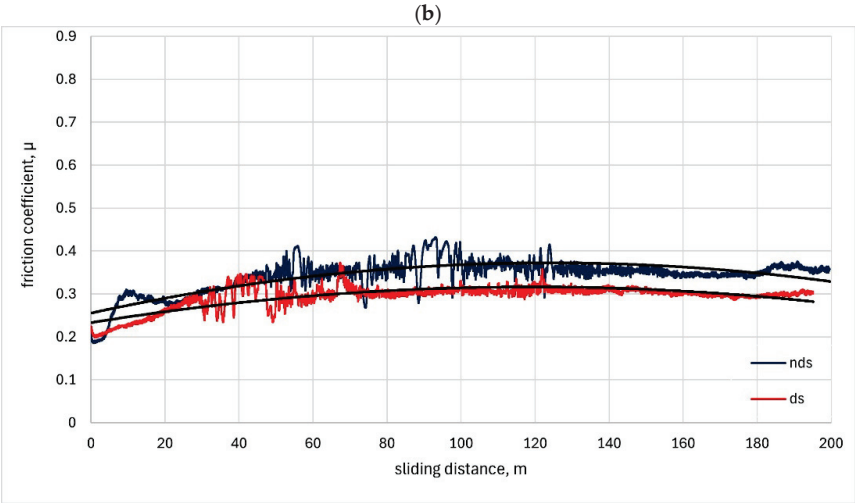
The coefficient of friction as a function of sliding distance for tested materials is shown in Figure 6. The compilation shows friction coefficient values recorded over distances from 0 to 200 m. The trend lines are marked with a solid black line.



(**a**)

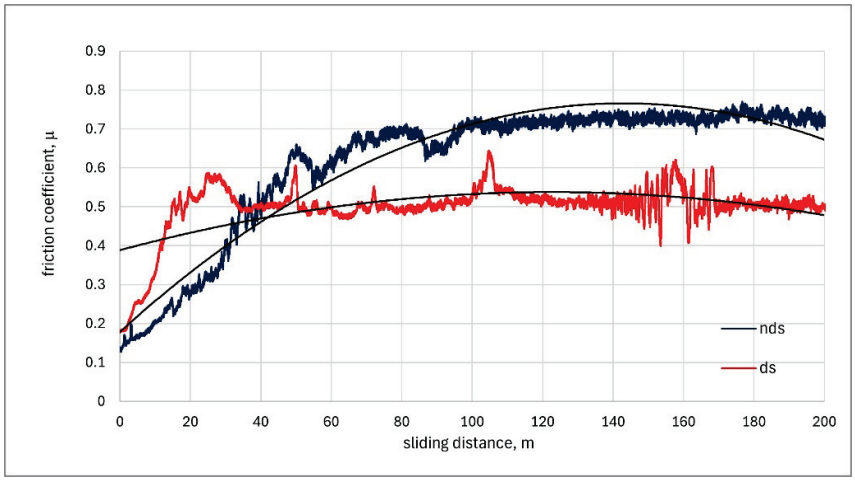


(**b**)



(**c**)

Figure 6. *Cont.*



(**d**)

Figure 6. Friction coefficient (μ) versus sliding distance for tested materials under dry sliding conditions: (**a**) Cu-ETP; (**b**) AlSi12CuNiMg alloy; (**c**) AlSi12CuNiMg + SiC composite; (**d**) 1.3505 steel, black line—trends lines.

For Cu-ETP (Figure 6a), friction coefficient changes were unstable for both directional and non-directional structure white cast iron, with average values exceeding 0.6 and 0.5, respectively. As observed, the friction coefficient value during the entire sliding distance for directional structure white cast iron changed from $\mu = 0.5$ to $\mu = 0.7$ and for non-directional structure from $\mu = 0.5$ to $\mu = 0.8$. Such high variation (equal to 0.2) is unacceptable. Up to sliding distance of approximately 150 m, friction coefficient values were lower for non-directional structure white cast iron, while above this distance values were higher than for directional structure white cast iron.

For AlSi12CuNiMg alloy as the block in the friction pair, friction coefficient changes were stable for both directional and non-directional structure white cast iron, with an average value of approximately $\mu = 0.3$ (Figure 6b). For non-directional structure white cast iron, values were slightly lower throughout the sliding distance from $\mu = 0.27$ to $\mu = 0.3$. Trend curves for both structures are very close to horizontal lines.

For the AlSi12CuNiMg + SiC composite (reinforced with SiC carbide) used as the friction pair block material (Figure 6c), friction coefficient values throughout the sliding distance were lower for directional structure and ranged from $\mu = 0.2$ to $\mu = 0.37$. For directional structure, similar unstable friction coefficient changes were observed up to 75 m sliding distance and for non-directional structure up to 125 m sliding distance. From 125 to 200 m, the friction coefficient achieved stability.

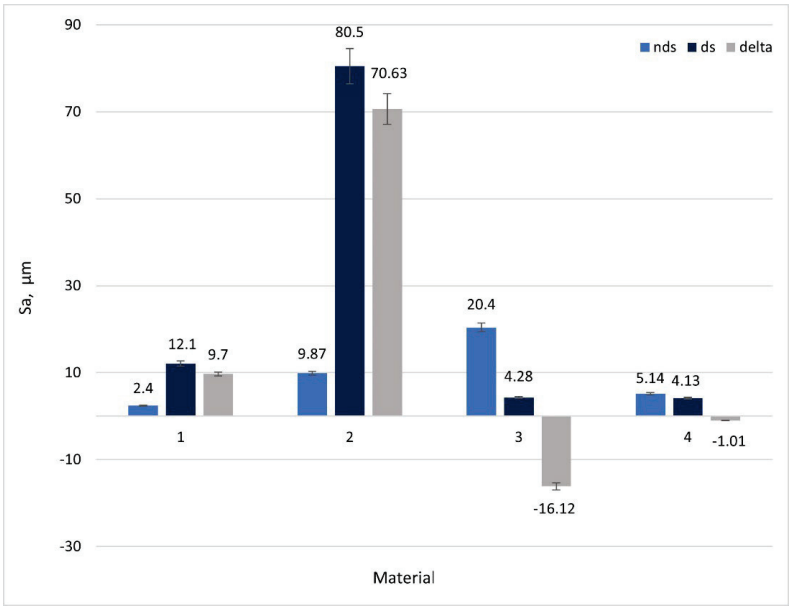
For steel 1.3505 (Figure 6d), the friction coefficient was lower for directional structure cast iron. A rapid increase from $\mu = 0.2$ to $\mu = 0.6$ was observed over a distance of up to 25 m. Subsequently, stabilization occurred at approximately $\mu = 0.5$ up to 200 m. For non-directional structure, a rapid increase from $\mu = 0.15$ to $\mu = 0.7$ was observed over a distance of up to 70 m and stabilization at $\mu = 0.7$, with increases and decreases in the range of $\mu = 0.4$ to $\mu = 0.65$.

The instability regions visible in the graphs (Figure 6a,d) showing friction coefficient variations (0.2 range) observed during interaction with directionally solidified cast iron pins occur after sliding distances exceeding 100 m. Considering the statistical analysis methodology applied to the experimental data, these anomalies indicate periodic phenomena occurring between the sliding surfaces. The working surface of the pin likely undergoes changes that subsequently disappear (similar to a running-in process) after approximately 10 m of sliding distance (roughly 850 cycles). Complete explanation of these friction-related

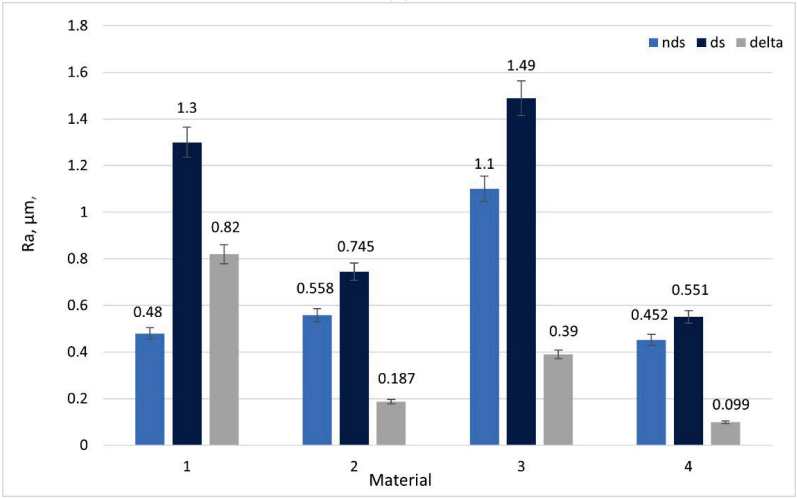
phenomena will be the subject of the authors' future investigations. Similar instabilities appearing in the initial stages of the friction process can be attributed to the running-in of mating surfaces, and this process shows minimal dependence on the types of sliding materials involved.

3.3. Roughness Parameters

Based on 3D images (Figure 4), it can be concluded that all tested materials exhibited abrasive wear mechanisms. However, significant differences in intensity were observed that can be compared using selected parameters. To evaluate surface geometry changes due to friction, basic roughness parameters were utilized, including (Sa)—arithmetical mean surface height (Figure 7a) and the arithmetical mean roughness value (Ra)—calculated as the arithmetical mean of absolute values of profile deviations from the mean line of the roughness profile (Figure 7b). Delta represents the parameter difference between directional and non-directional pin structures.



(**a**)



(**b**)

Figure 7. Surface roughness parameters: (**a**) Sa; (**b**) Ra values of wear tracks for tested materials: 1- Cu-ETP, 2—AlSi12CuNiMg alloy, 3—AlSi12CuNiMg + SiC composite, 4—1.3505 steel; nds—non-directional structure, ds—directional structure, delta—difference between ds-nds values.

For blocks manufactured from Cu-ETP and AlSi12CuNiMg alloy, the Sa parameter (Figure 7a) showed higher values for pins made with directional white cast iron structure. Differences between values for directional and non-directional structures were: ΔSa = 9.7 μm and ΔSa = 70.3 μm, respectively. For blocks made from AlSi12CuNiMg + SiC composite and steel 1.3505, Sa parameters showed higher values when cooperating with non-directional white cast iron structure pins. Differences between values for directional and non-directional structures were: ΔSa = −16.12 μm and ΔSa = −1.1 μm, for AlSi12CuNiMg+SiC composite and 1.3505 steel, respectively. The highest Sa parameter value for directional structure pins was observed for AlSi12CuNiMg alloy at Sa = 80.5 μm.

For all four materials used as blocks in friction pairs, higher Ra parameter values were observed for directional structure white cast iron pins (Figure 7b). The highest Ra = 1.49 μm value was obtained for AlSi12CuNiMg + SiC composite, followed by Cu-ETP, for which the parameter difference for directional and non-directional structures was greatest (ΔRa = 0.82 μm, Figure 7b). The smallest differences in ΔRa = 0.099 μm parameter value for directional and non-directional structure white cast iron were observed for the 1.3505 steel block.

The absence of statistically significant differences in surface geometry parameters Ra and Sa after friction, observed in the results obtained from friction testing of cast iron against the steel block, demonstrates the high wear resistance of steel relative to the other investigated friction pairs. Over the tested distance of 200 m (regardless of the white cast iron structure employed: directional or non-directional), the wear level measured by wear track depth (Figure 5g) and surface geometry parameters Ra and Sa (Figure 7) is markedly lower than that of copper and aluminum alloys and shows no dependence on the white cast iron structure used. It is possible that employing a longer friction distance would reveal differences, but this represents a research task requiring a separate series of investigations. Paired t-test analysis revealed that differences in Sa parameters between directional and non-directional pins were statistically significant for Cu-ETP ($p < 0.001$), AlSi12Mg ($p < 0.01$) and AlSi12Mg + SiC ($p < 0.001$). For steel 1.3505, the difference ΔSa = −1.1 μm did not achieve statistical significance ($p = 0.12$), indicating comparable surface heights for both structures. Statistical analyses were performed using OriginPro 2023 software.

4. Results Discussion

4.1. Comparison with Tribological Studies of White Cast Iron

The friction coefficients recorded in this study for directionally solidified cast iron, ranging from μ = 0.30 to 0.70, are in agreement with previously published values for metallic-cast iron tribological systems. For instance, investigations by Krawczyk [7] into mottled cast iron with varied chemical compositions documented friction coefficients between 0.29 and 0.40 during dry sliding, which is a close match to our findings for pairs involving AlSi12CuNiMg alloy and 1.3505 steel. The observed reduction in friction for the directional structure when paired with harder materials, such as the AlSi12CuNiMg + SiC composite and 1.3505 steel, is attributed to the improved load-bearing capacity of the aligned cementite plates. This aligns with observations made by Fashu and Trabadelo [8] in their work on high-chromium white cast irons exposed to wear-corrosive conditions.

Furthermore, the measured wear depths, which spanned from 16 to 405 μm, are comparable to those documented in the recent literature concerning directionally solidified cast materials. Purba et al. [9] in their study of three-body abrasive wear in multicomponent white cast irons, reported similar wear depth ranges, thereby reinforcing the conclusion that microstructural orientation is a significant factor in wear resistance. The superior performance of the directional structure with certain material pairings in our work lends support to the conclusions of González-Pociño et al. [10] who showed that controlled

microstructural alignment in white cast iron could diminish erosive wear by as much as 30% under ideal circumstances.

4.2. Dependence of Wear Mechanisms on Microstructure

The discrepancies in tribological behaviour between the directional and non-directional structures can be accounted for by the distinct wear mechanisms that operate within each material pairing. An analysis of the wear tracks, presented in Figure 5, reveals that abrasive wear is the dominant mechanism across all tested configurations. This observation is consistent with the findings of Barutçuoğlu et al. [11] for Ni-hard white cast irons alloyed with tungsten and boron.

In the case of the directional structure, the cementite plates within the ledeburite are aligned parallel to the direction of solidification, acting as reinforcing elements that enhance resistance to the penetration of abrasive particles. A similar reinforcement mechanism was reported by Zheng et al. [26] for cementite-iron composites, where they found that higher cementite volume fractions (>65%) markedly improved wear resistance by facilitating load transfer from the softer pearlite matrix to the hard cementite plates.

The microstructural advantage conferred by directional solidification is most evident when considering the composite nature of white cast iron. As demonstrated by Umemoto and Ohtsuka [25] the primary resistance to wear is provided by the hardness of the cementite (760–1340 HV), while the pearlite matrix (180–220 HB) contributes ductility. In directionally solidified structures, the continuous alignment of the cementite phase establishes preferential pathways for load distribution, which in turn reduces stress concentrations and minimizes the initiation and propagation of cracks.

4.3. Analysis of Performance Specific to Material Pairs

The superior performance of the directional structure when tested against the AlSi12CuNiMg + SiC composite and 1.3505 steel is a consequence of complementary hardness relationships and compatible wear mechanisms. With the AlSi12CuNiMg + SiC composite, the hard SiC particles (2500–3000 HV) induce a three-body abrasion scenario. In this context, the aligned cementite plates of the directional cast iron offer greater resistance to particle-induced gouging than randomly oriented structures. This outcome aligns with research by Jokari-Sheshdeh et al. [12] on Al-SiC composites, which demonstrated that wear resistance is enhanced when the alignment of the harder phase corresponds with the sliding direction. The 16.12 μm decrease in the Sa parameter for the directional structure (Figure 7a) signifies a more uniform wear distribution, suggesting that the oriented cementite plates are more effective at deflecting abrasive particles.

Conversely, the better performance of the non-directional structure with the softer Cu-ETP and AlSi12CuNiMg alloy (Cu: ~100 HB, AlSi12CuNiMg: ~80 HB) is attributable to the prevalence of adhesive wear mechanisms, as evidenced by the material transfer and surface deformation visible in Figure 5. The random orientation of cementite in the non-directional structure creates multiple points of resistance against the formation of adhesive junctions, a mechanism comparable to that reported by Sudhakar et al. [13] for high-chromium cast iron sliding against soft aluminum alloys. The contact pressure distribution between harder materials (1.3505 steel, AlSi12CuNiMg + SiC) and the cast iron establishes conditions where oriented carbides can effectively resist penetration. According to Jobayer Huq et al. [14], the critical element is the alignment of hard phases relative to the stress field, which explains why the directional structure excels with harder counterparts but performs poorly with softer materials where stress distributions differ.

4.4. Practical Implications and Limitations of the Study

The material-dependent performance of directional versus non-directional white cast iron structures carries significant implications for industrial applications. For bearing surfaces intended to operate against hard counterparts like steel or ceramic composites, directionally solidified white cast iron inserts could offer an extended service life due to lower friction and enhanced wear resistance. However, for applications involving softer metallic counterparts, conventional casting methods may prove more beneficial.

It is important to acknowledge several limitations of the present study. First, the tests were performed at an ambient temperature of 25 ± 1 °C, whereas numerous practical applications entail elevated temperatures where thermal effects can significantly alter microstructure and mechanical properties [15]. Second, the sliding distance of 200 m might not be sufficient to characterize long-term wear behaviour, especially for material systems known to exhibit transitional wear regimes. Finally, the specific directional solidification parameters used (withdrawal rate: 167 μm/s, temperature gradient: 33.5 K/mm) yield a particular microstructural scale and orientation that may not be optimal for all tribological contexts. Future work should therefore focus on investigating the effects of varying these solidification parameters on tribological performance under a wider array of operating conditions.

5. Conclusions

The tribological investigation conducted under dry friction conditions enabled the evaluation of material behaviour under extremely adverse operating conditions.

From the perspective of cast iron pin structure, directional structure orientation influences cooperation more favourably with blocks consisting of AlSi12CuNiMg + SiC composite and steel 1.3505. Smaller wear traces were observed compared to non-directional structure pins. Lower friction coefficient values were achieved: average values μ = 0.30 and μ = 0.40. Lower Sa parameter values were observed: Sa = 4.28 and Sa = 4.13. Roughness distribution in selected cross-sections was also characterized by smaller values: 18.9 μm and 16 μm, respectively. The smallest values were also obtained for wear profile curves for AlSi12CuNiMg + SiC composite and steel 1.3505 (18.9 μm and 16 μm, respectively).

For friction pairs: white cast iron pin—Cu-ETP block and AlSi12CuNiMg alloy—non-directional structure was more favourable from the pin structure perspective. This is confirmed by comparing obtained images of surface geometry after friction. The roughness parameters were also lower for Cu-ETP and AlSi12CuNiMg alloy (Sa = 2.4 and Sa = 9.87, respectively) than for directional structure pins. Roughness distribution was also lower for non-directional structure pins and amounted to 17.0 μm for Cu-ETP and 57.6 μm for AlSi12CuNiMg alloy.

Based on conducted investigations, it cannot be unambiguously stated that pins with directional white cast iron structure perform better in friction pairs than pins with non-directional structure. Research results indicate that the cooperating material in the friction pair is significant. In the conducted studies, two out of four applied block materials, namely AlSi12CuNiMg + SiC composite and steel 1.3505, produced more favourable effects for directional structure cast iron pins: lower friction coefficient μ and greater wear resistance.

Taking the above findings into account, further validation studies should be undertaken, including the use of additional block materials, in order to expand the understanding of the potential applications of directionally solidified pins made of eutectic white cast iron.

Author Contributions: Conceptualization, M.T.-Ł.; methodology, J.W.; software, J.W.; formal analysis, M.T.-Ł. and J.W.; investigation, J.W.; writing—original draft preparation, M.T.-Ł.; writing—review and editing M.T.-Ł.; supervision, M.T.-Ł. All authors have read and agreed to the published version of the manuscript.

Funding: This research received no external funding.

Institutional Review Board Statement: Not applicable.

Informed Consent Statement: Not applicable.

Data Availability Statement: The original contributions presented in this study are included in the article. Further inquiries can be directed to the corresponding author.

Conflicts of Interest: The authors declare no conflicts of interest.

References

1. Laird, M.; Gundlach, J.; Roehring, K. *Abrasion Resistant Cast Iron Handbook*; American Foundry Society: Schaumburg, IL, USA, 2000.
2. David, J.R. Cast Irons. In *ASM Specialty Handbook*; ASM International: Materials Park, OH, USA, 1996.
3. Azarhoushang, B.; Marinescu, I.D.; Rowe, W.B.; Dimitrov, B.; Ohmori, H. *Tribology and Fundamentals of Abrasive Machining Processes*, 3rd ed.; William Andrew: Norwich, NY, USA, 2022.
4. Gundlach, R.B. White Iron and High-Alloyed Iron Castings. In *Casting, ASM Handbook*; ASM International: Materials Park, OH, USA, 2008. [CrossRef]
5. Opapaiboon, J.; Inthidech, S.; Kaoru Yamamoto, K.; Matsubara, Y. *Effect of Carbon Balance on Structural Properties and Wear Resistance of Multi-Component White Cast Iron*; Inter Metalcast: Ochtrup, Germany, 2025. [CrossRef]
6. Purba, R.H.; Shimizu, K.; Kusumoto, K.; Gaqi, Y.; Huq, M.J. Tribological Characteristics of High-Chromium Based Multi-Component White Cast Irons. *Crystals* **2022**, *12*, 1488. [CrossRef]
7. Krawczyk, J. Microstructure and tribological properties of mottled cast iron with different chemical composition. *Arch. Mater. Sci. Eng.* **2011**, *51*, 5–15.
8. Fashu, S.; Trabadelo, V. Development and Performance of High Chromium White Cast Irons (HCWCIs) for Wear–Corrosive Environments: A Critical Review. *Metals* **2023**, *13*, 1831. [CrossRef]
9. Purba, R.H.; Shimizu, K.; Kusumoto, K.; Gaqi, Y.; Huq, M.J. A Study of the Three-Body Abrasive Wear Resistance of 5V/5Nb-5Cr-5Mo-5W-5Co-Fe Multicomponent Cast Alloys with Different Carbon Percentages. *Materials* **2023**, *16*, 3102. [CrossRef]
10. González-Pociño, A.; Asensio-Lozano, J.; Álvarez-Antolín, F.; García-Diez, A. Evaluation of hardness, sliding wear and strength of a hypoeutectic white iron with 25% Cr after heat treatments. *Metals* **2021**, *11*, 947. [CrossRef]
11. Barutçuoğlu, B.; Koç, F.G.; Erişir, E.; Karaarslan, G. The effect of tempering temperature on microstructure and wear behavior of tungsten and boron alloyed Ni-hard 4 white cast irons. *Int. J. Met.* **2024**, *19*, 480–495. [CrossRef]
12. Jokari-Sheshdeh, M.; Ali, Y.; Gallo, S.C.; Lin, W.; Gates, J.D. Comparing the abrasion performance of NiHard-4 and high-Cr-Mo white cast irons: The effects of chemical composition and microstructure. *Wear* **2022**, *492*, 204208. [CrossRef]
13. Sudhakar, A.N.; Markandeya, R.; Rao, B.S.; Pandey, A.K.; Kaushik, D. Effect of alloying elements on the dry sliding wear behavior of high chromium white cast iron and Ni-hard iron. *Mater. Today Proc.* **2022**, *60*, 1303–1309. [CrossRef]
14. Huq, M.J.; Shimizu, K.; Kusumoto, K. Abrasive Wear Characteristics of High-Cr Multicomponent White Cast Irons at Elevated Temperatures. *Crystals* **2025**, *15*, 113. [CrossRef]
15. Yoo, J.S.; Ko, S.J.; Kim, J.G. Effect of chromium on microstructure and corrosion behavior of High-Cr white cast irons used in coal-fired power plant desulfurization facilities. *Int. J. Met.* **2024**, *18*, 1664–1676. [CrossRef]
16. Bedolla-Jacuinde, A.; Guerra, F.V.; Guerrero-Pastran, A.J.; Sierra-Cetina, M.A.; Valdez-Medina, S. Microstructural effect and wear performance of high chromium white cast iron modified with high boron contents. *Wear* **2021**, *476*, 203675. [CrossRef]
17. Purba, R.H.; Shimizu, K.; Kusumoto, K.; Gaqi, Y.; Todaka, T. Effect of boron addition on three-body abrasive wear characteristics of high chromium based multi-component white cast iron. *Mater. Chem. Phys.* **2022**, *275*, 125232. [CrossRef]
18. Pasini, W.M.; Polkowski, W.; Dudziak, T.; dos Santos, C.A.; de Barcellos, V.K. Microstructure Formation and Dry Reciprocating Sliding Wear Response of High-Entropy Hypereutectic White Cast Irons. *Metals* **2025**, *15*, 4. [CrossRef]
19. Fortini, A.; Suman, A.; Vulpio, A.; Merlin, M.; Pinelli, M. Microstructural and Erosive Wear Characteristics of a High Chromium Cast Iron. *Coatings* **2021**, *11*, 490. [CrossRef]
20. Jain, A.-S.; Chang, H.; Tang, X.; Hinckley, B.; Zhang, M.-X. Refinement of primary carbides in hypereutectic high-chromium cast irons: A review. *J. Mater. Sci.* **2021**, *56*, 999–1038. [CrossRef]

21. Doğan, Ö.N.; Laird, G., II; Hawk, J.A. Abrasion resistance of the columnar zone in high Cr white cast irons. *Wear* **1995**, *181–183*, 342–349. [CrossRef]
22. Gong, B.; Zhou, R.; Li, L.; Lv, H.; Li, Y.; Bai, D.; Jiang, Y. Change in primary (Cr, Fe)7C3 carbides induced by electric current pulse modification of hypereutectic high chromium cast iron melt. *Materials* **2019**, *12*, 32. [CrossRef]
23. Doğan, Ö.N.; Hawk, J.A. Effect of carbide orientation on abrasion of high Cr white cast iron. *Wear* **1995**, *189*, 136–142. [CrossRef]
24. Coronado, J.J. Effect of $(Fe,Cr)_7C_3$ carbide orientation on abrasion wear resistance and fracture toughness. *Wear* **2011**, *270*, 287–293. [CrossRef]
25. Umemoto, M.; Ohtsuka, H. Mechanical Properties of Cementite. *ISIJ Int.* **2022**, *62*, 1313–1333. [CrossRef]
26. Zheng, B.; Huang, Z.; Xing, J.; Wang, Y.; Jian, Y.; Xiao, Y.; Fan, X. Three-Body Abrasive Behavior of Cementite-Iron Composite with Different Cementite Volume Fractions. *Tribol. Lett.* **2016**, *62*, 32. [CrossRef]
27. Fras, T.; Koenig, B.; Meyer, P.P.; Diop, I. Microstructural characteristics of a high-chromium cast iron hard-facing alloy. *Bull. Pol. Acad. Sci.-Tech. Sci.* **2025**, *73*, 151957. [CrossRef]
28. Wang, J.; Liu, T.; Xing, X.; Li, J.; Qi, X.; Yang, Q. Study of the wear resistance of Hypereutectic Fe-Cr-C Hardfacing Alloy reinforced with carbide particles. *Mater. Res. Express* **2022**, *9*, 106507. [CrossRef]
29. Jia, R.; Liu, S.; Luo, Z.; Ning, J.; Wang, H.; Luo, T.; Zhu, Y.; Yuan, X.; Wang, Z. Microstructure and wear resistance of WC and high chromium cast iron hardfacing layers. *Coatings* **2020**, *10*, 852. [CrossRef]
30. Trepczyńska-Łent, M.; Boroński, D.; Maćkowiak, P. Mechanical properties and microstructure of directionally solidified Fe-4.25%C eutectic alloy. *Mater. Sci. Eng. A* **2021**, *822*, 141644. [CrossRef]
31. Trepczyńska-Łent, M.; Seyda, J. Characteristics of ledeburite in EDS analyses of directionally solidified eutectic white cast iron. *Arch. Foundry Eng.* **2021**, *22*, 65–71. [CrossRef]
32. Trepczyńska-Łent, M. Characteristics of the growth of the directionally solidified Fe—4.25% C eutectic alloy. *Arch. Metall. Mater.* **2021**, *66*, 1179–1186. [CrossRef]
33. Trepczyńska-Łent, M.; Piątkowski, J. Study of directionally solidified Fe—4.25%C eutectic alloy using electron backscatter diffraction (EBSD) technique. *Metalurgija* **2020**, *59*, 347–350.
34. *Standard EN 1652:2000*; Copper and Copper Alloys—Plate, Sheet, Strip and Circles for General Purposes. European Commission: Brussels, Belgium, 2000.
35. *Standard EN 1676:2020*; Aluminium and Aluminium Alloys—Alloyed Ingots for Remelting—Specifications. European Commission: Brussels, Belgium, 2020.
36. *Standard ISO 683-17:2023*; Heat-Treated Steels, Alloy Steels and Free-Cutting Steels—Part 17: Ball and Roller Bearing Steels. International Organization for Standardization: Geneva, Switzerland, 2023.
37. Dolata, A.J.; Wieczorek, J.; Dyzia, M.; Starczewski, M. Assessment of the Tribological Properties of Aluminum Matrix Composites Intended for Cooperation with Piston Rings in Combustion Engines. *Materials* **2022**, *15*, 3806. [CrossRef] [PubMed]

Disclaimer/Publisher's Note: The statements, opinions and data contained in all publications are solely those of the individual author(s) and contributor(s) and not of MDPI and/or the editor(s). MDPI and/or the editor(s) disclaim responsibility for any injury to people or property resulting from any ideas, methods, instructions or products referred to in the content.

materials

MDPI

Article

Compound Castings for the Coke Industry

Tomasz Wróbel

Department of Foundry Engineering, Silesian University of Technology, 7 Towarowa Street, 44-100 Gliwice, Poland; tomasz.wrobel@polsl.pl

Abstract: In this paper, issues related to the technology of compound castings composed of two parts, i.e., the working layer and the supporting part, made of X46Cr13 high-chromium steel and EN-GJL-HB 255 grey cast iron, respectively, in a liquid–solid system by pre-installing a monolithic insert in the mould cavity are presented. As a part of the research, the mechanism of formation of transitional zones in the bonding area of the above-mentioned two alloys was identified and described. It was shown that the phenomenon that determines the formation of a permanent bond between the joined materials is the transport of C and heat from the "high-carbon and hot" material of the supporting part poured into the mould in the form of liquid cast iron to the "low-carbon and cold" material of the working layer placed in the form of a steel monolithic insert inside the mould cavity. In the paper, the suitability of the compound castings technology developed for use in the coke industry is also presented. Full-size high-chromium steel–grey cast iron compound casting plates designed for the coke quenching car lining were positively verified in real coke plant operating conditions.

Keywords: compound casting; steel; cast iron; coke

1. Introduction

In recent years, the demand for special-performance castings in various industries has been increasing, including those featuring high hardness, high resistance to abrasive wear, and corrosion resistance at room or elevated temperatures. Such parts are frequently made entirely of expensive, and hard-to-find materials, e.g., high-alloy steels and cast steels, alloys with Ni or Ti matrixes, and others [1]. In many cases, this is unnecessary because the high usable properties are often required not for the entire casting but only for its working surface. In such cases, the operating conditions of the casting result in wearing only one surface, the so-called working surface, which leads to its permissible dimensional tolerance being exceeded and forces the entire casting to be scrapped, which, taking into account the use of expensive materials, can be considered uneconomical.

Considering the above-mentioned factors, the technology of compound castings becomes particularly important. It can be used when, as described above, the high usable properties criterion is required only for the outside working layer of a casting, while its remaining part plays only the role of a supporting structure, not exposed to direct factors resulting in, e.g., corrosive or abrasive wear [2–20]. Furthermore, this technology is one of the most economical ways to improve the working surface of castings as it allows the production of compound components directly during the manufacturing process. As a result, for massive castings with simple geometry, it can be a significant technological alternative for the commonly used surfacing and thermal spraying or surface heat treatment. In addition, using the technology of compound casting, apart from its economic advantages and unlike the above-mentioned technologies of surfacing and surface heat treatment, does not involve the risk of cracking in the heat-affected zone resulting from the use of the above-mentioned methods [21–24].

The production of compound castings composed of two basic components, i.e., working part (layer) and supporting part, also referred to as bi-metal castings, is typically carried

out using three basic technologies, taking into account the state of matter in which the materials are at the time of bonding, i.e., in the following systems:

- liquid–liquid [2–5];
- solid–solid [6–9];
- liquid–solid [10–20].

For the first technology mentioned, both bi-metal parts consist of materials made exclusively by casting. An example of this technology is one in which two independent gating systems are made that guarantee two-stage filling of the sand mould cavity. According to this manufacturing method, the bimetallic elements of the hammer [2,3], lining of mills ball [4], or rolls [5] are cast in material configurations of the chromium cast iron working layer with a low-carbon cast steel supporting part.

In contrast, in solid–solid technology, it is possible to bond the previously produced cast alloys, i.e., grey cast iron with flake graphite with nodular cast iron [6] or cast alloys, with non-cast alloys, e.g., the chromium cast iron with carbon steel [7]. Moreover, with this technology, it is possible to obtain a bond between two steels, e.g., carbon steel and stainless steel, as the paper [8] presented. According to [6–9], solid–solid technology is limited to small elements with maximal contact surface between both components of approx. 200 mm^2 and 30 mm in thickness. Additionally, this technology needs an elevated temperature of approx. 1000 °C, pressure at the time of bonding of 1–10 MPa, and a vacuum at the time of bond creation [6–9].

Meanwhile, liquid–solid technology can use a combination of cast and non-cast alloys. In this manufacturing method, the element that enriches the surface of the casting is placed in the mould in the form of a granular [10–12] or monolithic [13–20] insert directly before the molten alloy is poured. With the use of granular inserts, compound castings were made in a material configuration working surface layer from WC [10], Al_2O_3 [11], or SiC [12] with an unalloyed cast steel or grey cast iron supporting part. This type of compound casting is characterized by a hard working surface layer that is resistant to abrasive wear, which is a decisive factor in its applicability in the mining industry. An example of a technology using the monolithic insert is compound castings in a configuration which comprises hard and resistant-to-abrasive-wear chromium cast iron connected with a weldable low-carbon steel plate [13,14]. Examples of small test castings manufactured with high-chromium or chromium–nickel stainless steel monolithic inserts using liquid–solid technology with grey cast iron are presented in papers [15–19]. It is possible to use 3D-printed elements as monolithic inserts, which was shown in paper [20] in compound casting in a configuration of pure Ti with grey cast iron.

Another division can be made by considering the nature of the bond of both bi-metal parts. It can be diffusion-based, adhesion-based, or mechanical. Considering the strength of the bond and the ability to dissipate heat, and therefore the service life of the compound casting, the most advantageous bond is obviously the diffusion-based one whose characteristic feature is the formation of a smaller or larger transition zone resulting from physical and chemical phenomena occurring at the layer border: working layer–supporting part. However, the phenomenon of diffusion does not occur for the adhesion-based bond, formed as a result of mutual intermolecular attraction. On the other hand, to obtain a mechanical bond by using the liquid–solid technology, it is necessary to make cuts, protrusions, or hooks in the poured component to connect it to the part formed after the solidification of a liquid alloy poured into the mould. This solution utilises the mechanical bond formed by the phenomenon of casting shrinkage that occurs in the cast-on part, as presented in papers [13,14].

As a result, in the paper the results of research on the compound casting technology in the liquid–solid system, based on the method of preparing the mould cavity by pre-installing the monolithic insert of high-chromium steel plate poured with grey cast iron, whose goal was to develop a completely novel and previously undescribed in the literature technologically useful bi-metal plates for use in lining a coke quenching car, are presented. Moreover, the studies aimed to describe the mechanism of the bond in analysed

compound castings in which the improvement in abrasive wear resistance is obtained by the application of high-chromium steel and, as a result, the creation of a hard microstructure containing Cr(Fe) carbides in a martensitic matrix, with a simultaneous improvement in corrosion resistance i.e., heat resistance and resistance to the corrosive effect of cooling water which is obtained by the creation of a passive surface layer with Cr oxides.

2. Materials and Methods

In reference to the aim of the paper, in general, the coke quenching car is lined with 376 plates with the following dimensions: width 520 mm, length 575 mm, and thickness 25 mm. They are used in the coke production cycle that includes the following steps:

- Discharging from the bank of coke-ovens onto the quenching car of between a few and more than ten tonnes of coke heated up to 900–1100 °C from a height ranging from 2 to 4 m (Figure 1a),
- Carrying heated coke to a quenching tower (Figure 1b),
- Quenching the coke using the dry method with neutral gases or using the wet method with water flowing in a closed circuit that contains lots of harmful corrosion-accelerating pollutants (Figure 1c,d),
- Dumping the cooled down coke from the quenching car surface onto a chute from where it is carried to the sorting plant.



Figure 1. A view of the coke production cycle process: discharging heated coke pushed out from the bank of coke-ovens onto the surface of a quenching car (**a**), carrying the heated coke from the discharge site to the quenching tower (**b**), and the car in the quenching tower (**c**) with a subsequent wet coke quenching process (**d**).

The above-presented coke production cycle is carried out from 50 to 150 times a day, resulting in the exposure of quenching car liner plates to high temperatures, thermal shocks, the corrosive effect of cooling water, and abrasive wear in the metal–coke system. As a result, there is a problem of unsatisfactory service life of the EN-GJN-HB 340 mottled cast iron plates with Cr $\leq$ 2 wt.% added used for the lining plates (Figure 2). Such cast iron provides a service life for the lining plates that does not exceed approx. 50% of the total service life designed for the quenching car. However, due to the difficulties encountered while dismantling the heavily corroded screw connections attaching the lining plates to the car surface and the resulting downtime, it is allowed—despite the damage—for them to continue their operation, at the same time creating conditions conducive to corrosive destruction of the remaining car structure.



Figure 2. A view of damaged cast iron casting plates used as a lining for a coke quenching car, still operated in spite of the destruction.

As a part of the experiment conducted and presented herein, compound castings were carried out using the following procedure: the type and arrangement of the casting gating system was developed using the liquid–solid system with a monolithic X46Cr13 steel insert (Table 1) 5 mm thick (solid/casting working layer) poured with grey cast iron (liquid/casting supporting part) grade EN-GJL-HB 255 (Table 1). Next, a wooden casting model was made, divided into a working layer and a supporting part with the dimensions of the compound casting plate used to line the coke quenching car: width 520 mm, length 575 mm and thickness 25 mm, and making a two-part mould of classic moulding sand with a quartz matrix with bentonite as a binder, with a division plane corresponding to the working layer contact surface with the supporting part. Then, the mould was dried at 180 °C. Subsequently, the monolithic insert contact surface was prepared by sandblasting and coating it with a flux–water solution of $Na_2B_4O_7$ and H_3BO_3, then drying at 120 °C for 1 h to remove H_2O. Finally, the mould was dismantled and the previously prepared monolithic insert placed inside its cavity (Figure 3).

In the next stage, the mould was assembled and prepared to pour with a liquid cast iron. Then, the metal charge was prepared, allowing us to obtain EN-GJL-HB 255 grey cast iron with flake graphite in a pearlite matrix. After this, the chemical composition of the liquid alloy was checked and corrected after melting the metal charge, if necessary. According to presented procedure, the castings of 8 compound casting plates were carried out; 4 moulds were poured with liquid cast iron at 1450 °C while 4 at 1550 °C. In all 8 cases, the temperature of the monolithic insert inside the mould before its filling was about 20 °C. For each test casting, free air cooling was applied in its mould after pouring. Once cooled down, the casting was knocked out of the mould and the components of the gating system were removed. In the next step, assessment of the quality of the plate compound casting

was carried out by visual inspection and non-destructive ultrasonic testing of the area where the working layer connects with the supporting part. The tests were conducted by using a DIO 1000 STARMANS ELECTRONICS flaw detector (STARMANS ELECTRONICS S.R.O., Prague, Czech Republic)with a flat-head PN10-4C, while the area showing proper, permanent bonding of the working layer with the supporting part was considered to be the area where the bottom echo was higher than the echo of the transition zone (the head applied from the side of the working layer (steel plate)).

Table 1. Chemical composition of the tested alloys.

Elements Concentration, wt.%										
C	**Mn**	**Si**	**Cr**	**Ni**	**Mo**	**Cu**	**Ti**	**V**	**S**	**P**
X46Cr13										
0.440	0.600	0.340	14.500	0.650	0.090	0.001	0.001	0.001	0.001	0.020
EN-GJL-HB 255										
3.18	0.50	2.10	0.62	0.05	0.01	0.15	0.01	0.01	0.06	0.10
EN-GJN-HB 340										
3.07	0.79	1.54	1.60	0.06	0.01	0.04	0.01	0.01	0.02	0.04

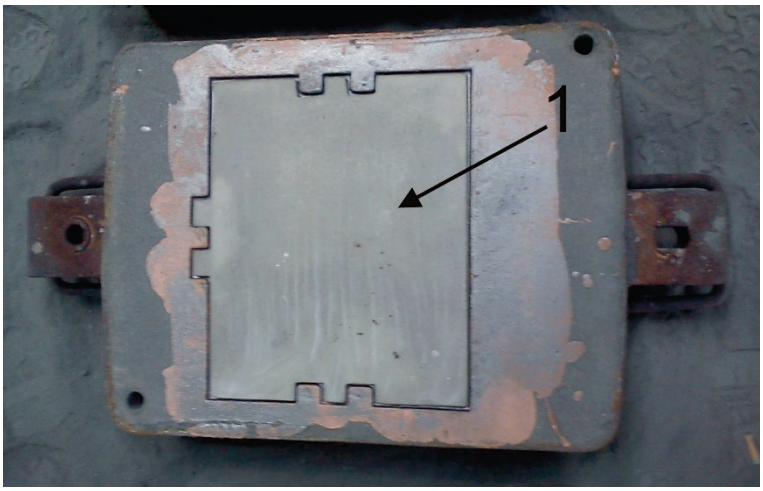


Figure 3. A view of the sand mould with a monolithic insert of X46Cr13 steel plate placed inside its cavity (1).

The scope of laboratory tests included, on the samples cut from the centre of the compound casting, testing of the chemical composition of steel X46Cr13 and grey cast iron by using a LECO GDS500A glow discharge spectrometer(LECO Corporation, St. Joseph, MI, USA). Moreover, in the case of C determination in grey cast iron, an IR analyser (infrared spectroscopy) LECO CS-125 (LECO Corporation, St. Joseph, MI, USA) was used. Additionally, for the samples cut from the centre of the compound casting metallographic testing was carried out using a NIKON Eclipse LV150N (NIKON Metrology Europe NV, Leuven, Belgium) (LOM) optical microscope, a scanning electron microscope (SEM) INSPECT F (FEI Technologies Inc., Hillsboro, OR, USA) with an energy X-ray dispersive spectrometer (EDS), and a transmission electron microscope (TEM) FEI TITAN 80–300 (FEI Technologies Inc., Hillsboro, OR, USA). Samples for LOM and SEM testing were prepared by cutting, grinding, and polishing with the water-based suspension of Al_2O_3 and electrolytic etching using LectroPol-5 STRUERS (STRUERS ApS, Ballerup, Denmark)and reagent with the following chemical composition: 3 g $FeCl_3$ + 10 cm^3 HCl + 90 cm^3 C_2H_5OH, with a voltage of 15 V and time of 15 s. Samples for the TEM testing were obtained using the FEI FIB Quanta 200i system (FEI Technologies Inc., Hillsboro, OR, USA)that made it possible to

collect lamellas with dimensions of 20 × 8 µm and a thickness of 50 nm using a convergent beam of gallium ions from SEM images. Metallographic tests were complemented by microhardness measurements at three points for each microstructure zone (the distance between points was 2 mm) using the Vickers hardness test with a FUTURE-TECH FM 700 tester (FUTURE-TECH CORP., Fujisaki, Japan) and a diamond indenter (right quadrangular pyramid with a vertex angle of 136°) loaded with a force of 4.9 N (µHV 0.5). Surface hardness measurements at nine points distributed on the samples cut from the centre, half-length, and near-edge areas of the working layer (three measurement points per sample) were made using the Vickers method with a universal SUNPOC SBRV-100 D hardness tester (Guizhou Sunpoc Tech Industry Co., Ltd., Guiyang, China) and a diamond indenter (right quadrangular pyramid with a vertex angle of 136°) loaded with a force of 50 N (HV5).

To determine suitability for industrial applications, i.e., for use of the compound casting plates made in the system as a lining for a coke quenching car, the working surface of the X46Cr13 high-chromium alloy steel and the supporting part made of EN-GJL-HB 255 grey cast iron, a series of tests was carried out covering the following activities:

- Installing 3 compound casting plates and 3 control plates of cast iron connected with EN-GJN-HB 340 low-alloy mottled cast iron with an average surface hardness of 350HV5 in a coke quenching car (Figure 4),
- Using plate castings in the operating conditions of a coke quenching car (Figure 5), including from 72 to 81 coke production cycles (discharge, transport, wet quenching, and dumping coke into a chute) per day, 7 days a week,
- Dismantling of plate castings after the completion of approx. 18,500 coke production cycles for 8 months.



(**a**) (**b**)

Figure 4. Installing 3 full-size compound castings of a X46Cr13 alloy steel working layer with a supporting part of EN-GJL-HB 255 (1) in a coke quenching car and 3 control EN-GJN-HB 340 mottled cast iron plates (2): (**a**) general view and (**b**) detailed view.

In turn, the scope of industrial tests included the following:

- Volumetric loss by measuring the thickness, with an accuracy of 0.1 mm, and weight loss by measuring the mass, with an accuracy of 0.1 kg, of the compound plates under the operating conditions of a coke quenching car and comparing the results with the damage of uniform EN-GJN-HB 340 mottled cast iron plates (Table 1) operated in the same conditions,
- Testing the microstructure of the compound casting plates after operation using LOM (the samples cut from the centre of compound casting),

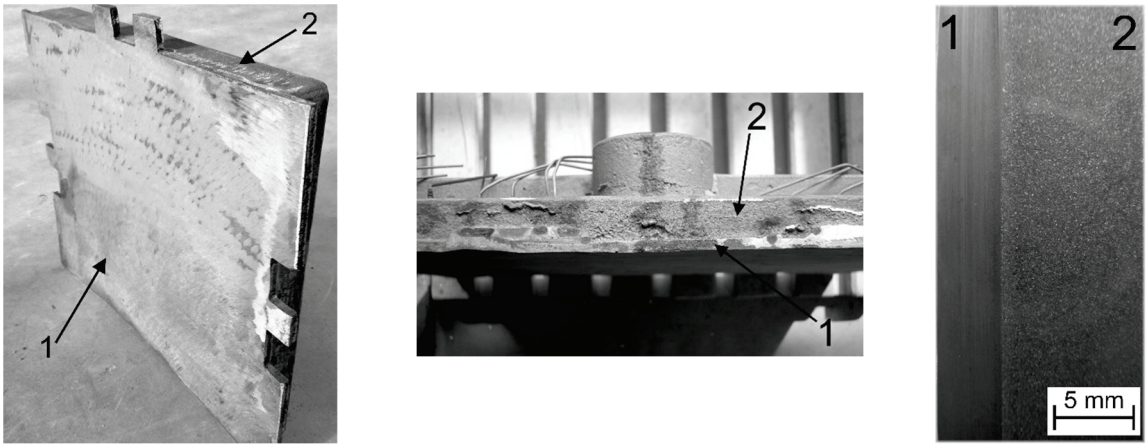
- Hardness tests after operation of the compound casting according to the above-mentioned procedure using the Vickers method.



Figure 5. A view of plate compound castings of a X46Cr13 alloy steel working layer with a supporting part of EN-GJL-HB 255 grey cast iron (1) during the operation of a coke quenching car.

3. Results and Discussion

Figure 6a,b present a view of an example compound casting plate in the following arrangement: working layer of X46Cr13 alloy steel and the supporting part made of EN-GJL-HB 255 grey cast iron. The conducted non-destructive ultrasonic tests show that, for the compound casting plates poured at 1450 °C ± 10 °C, a permanent bond of the high-chromium steel with the grey cast iron was obtained within a contact surface area ranging from about 60% to 80%. As a result, these four compound castings were recognised as technologically useless. However, at a pouring temperature of 1550 °C ± 10 °C, a permanent bonding of both component materials was achieved, covering the entire contact surface. Therefore, the remaining tests presented herein refer only to these compound casting plates. The permanent bond within the compound casting plate confirms the cross-section macrostructure, whose example, cut from the centre of the bi-metal, is presented in Figure 6c.



(**a**) (**b**) (**c**)

Figure 6. A view of a compound casting plate example of the system of X46Cr 13 (1) steel and EN-GJL-HB 255 (2) grey cast iron: (**a**) general view, (**b**) side view, (**c**) fragment of a macroscopic cross-section.

In turn, Figure 7 presents a microstructure of the bond area within the compound casting plate. The structure of the bi-metal bond area is formed as a result of diffusion, first of all of C in the direction from the supporting part to the working part and cooling down from the high temperature to which the monolithic insert is heated up, and whose source is the liquid cast iron poured into the mould.

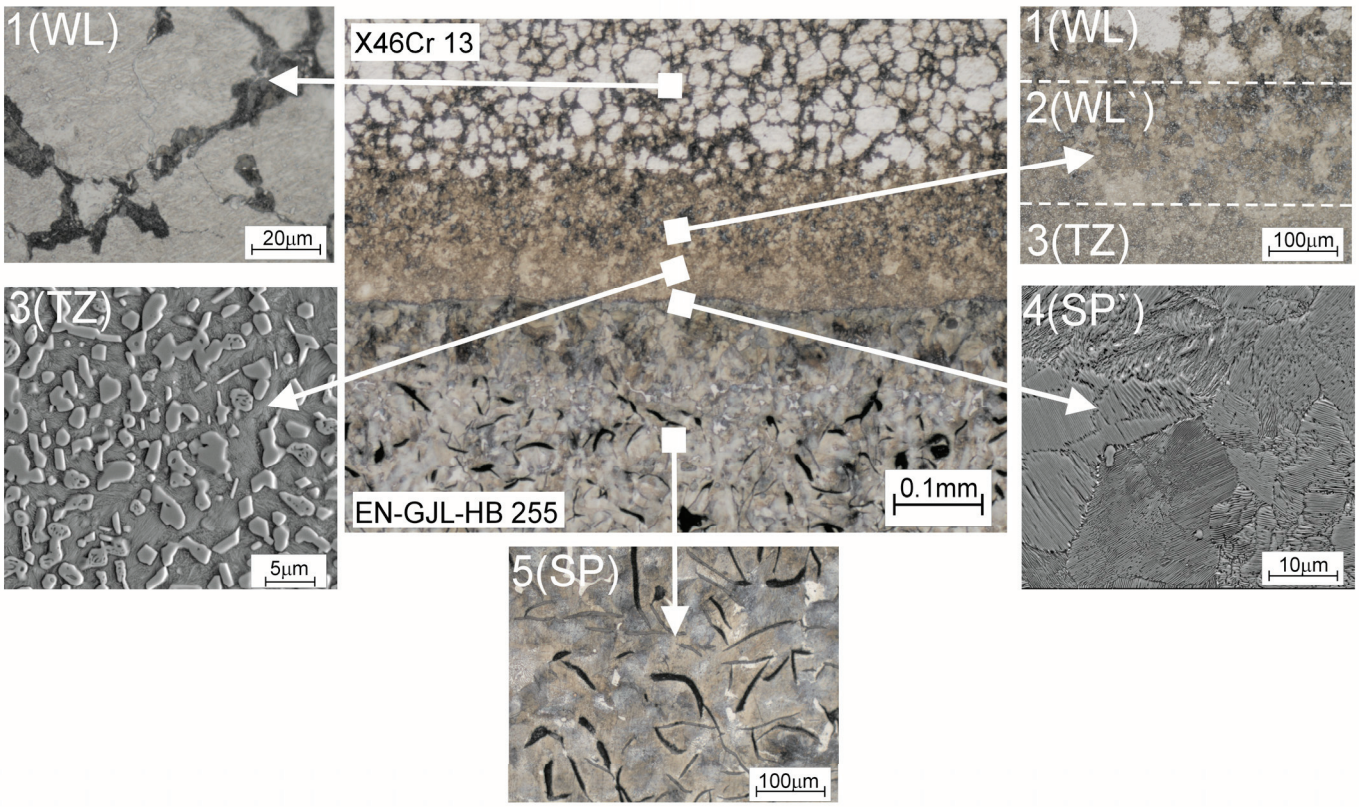


Figure 7. Microstructure of the bond area within the compound casting in the system: X46Cr13 steel working layer with the supporting part of EN-GJL-HB 255 grey cast iron.

In general, in the bonding area of X46Cr13 steel with grey cast iron, two classical zones in terms of microstructure typical for bonded materials, i.e., zone 1(WL) corresponding to the microstructure of X46Cr13 and zone 5(SP) corresponding to the microstructure of grey cast iron, can be distinguished. The area of zone 1(WL) because of the distance from the cast iron part, is not carburised but only heated to a high temperature, ranging from about 1000 to about 1150 °C, as demonstrated in another author's paper [19]. It should be noted that the mentioned temperature of the insert in zone 1(WL), i.e., exactly in the area from the bi-metal surface layer to the border with zone 2(WL') (whose microstructure is formed as a result of both high temperature and carburisation), is within the range typical for the austenitising temperature used in the classic heat treatment processes of X46Cr13 alloy steel [25,26]. Therefore, for the X46Cr13 alloy steel, which shows the phenomenon of self-hardening, heating up to the phase stability temperature γ combined with cooling in the sand mould with an average rate of about 0.1 °C/s [19] resulted in obtaining a working part microstructure different from the initial state before the mould pouring, i.e., the initial microstructure composed of $Cr(Fe)_{23}C_6$ carbides into the ferritic matrix (Figure 8a), with a hardness of 200 μHV0.5, transforms to form a final microstructure composed of $Cr(Fe)_{23}C_6$ carbides in a martensitic-pearlite matrix (Figure 8b), with a hardness of 460 μHV0.5 (Figure 9). The phase composition of the presented microstructures of X46Cr13 steel in various states is typical, as described in detail in the papers [26–28]. In turn, zone 5(SP) has a microstructure typical for EN-GJL-HB255 grey cast iron, i.e., flake graphite in a pearlite matrix.

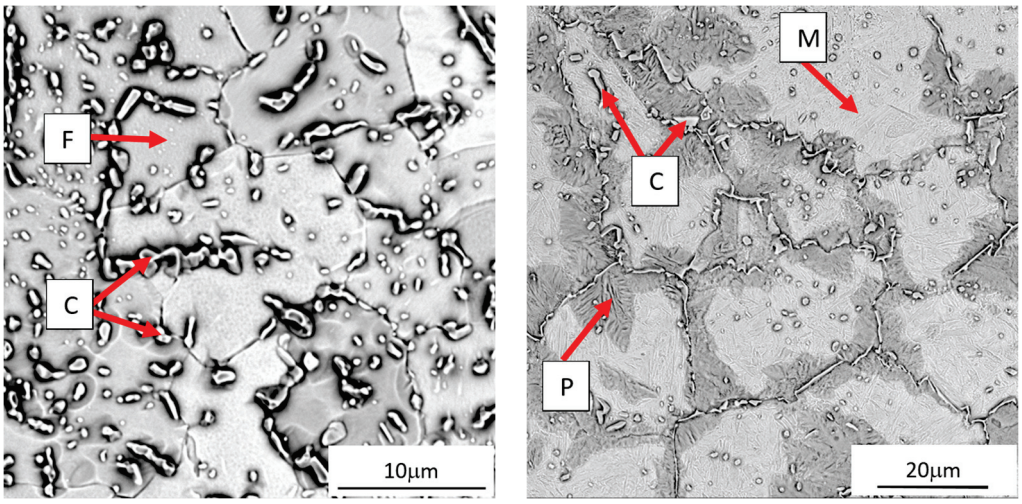


Figure 8. The microstructure of X46Cr13 steel (**a**) as-delivered monolithic insert (before the mould pouring) and (**b**) in the compound casting (after the pouring and cooling down of the mould); F—ferrite, C—Cr(Fe) carbides, P—pearlite, M—martensite.

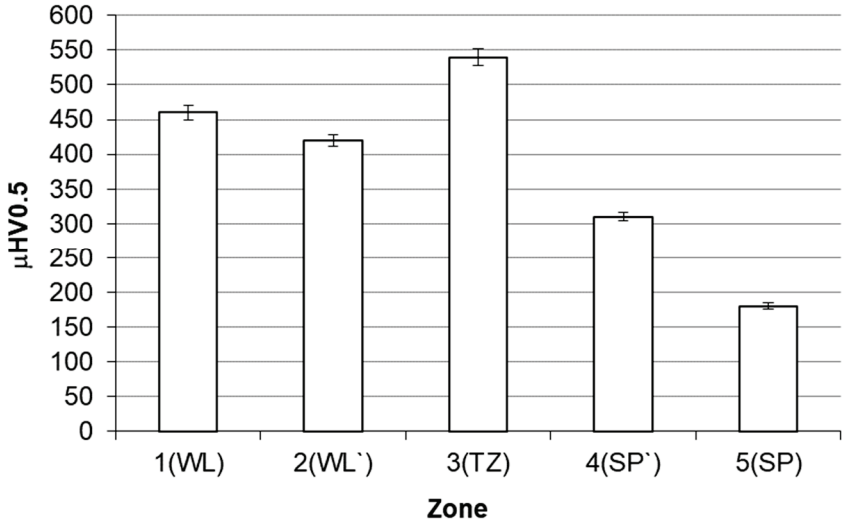


Figure 9. Distribution of hardness in individual zones of the compound casting: X46Cr13 steel–EN-GJL-HB 255 grey cast iron (zone marking as in Figure 7).

Between zones 1(WL) and 5(SP), there are three transition zones. As a result of carburising and cooling from a high temperature, at a moderate speed, i.e., the phase transformations take place in the solid state, the narrow zone 2(WL') is created. Since the cooling of the zone from a high temperature is carried out at a lower rate compared to the cooling rate for zone 1(WL), the dominating component of Cr(Fe) carbides is pearlite, which, in turn, results in reducing hardness to the level of 420 µHV0.5.

Another zone 3(TZ) is formed from the liquid phase as a result of the carburisation of the border area of the steel insert by the cast iron, which lowers its liquidus and solidus temperature, and next by melting of this area as a result of the impact of the high temperature of the liquid cast iron. The chemical composition formed in this zone determines the crystallization of the microstructure with a final hardness of 540 µHV, composed of large amount of Cr(Fe) carbides, mainly M_7C_3 in a pearlite matrix (Figures 10–12).

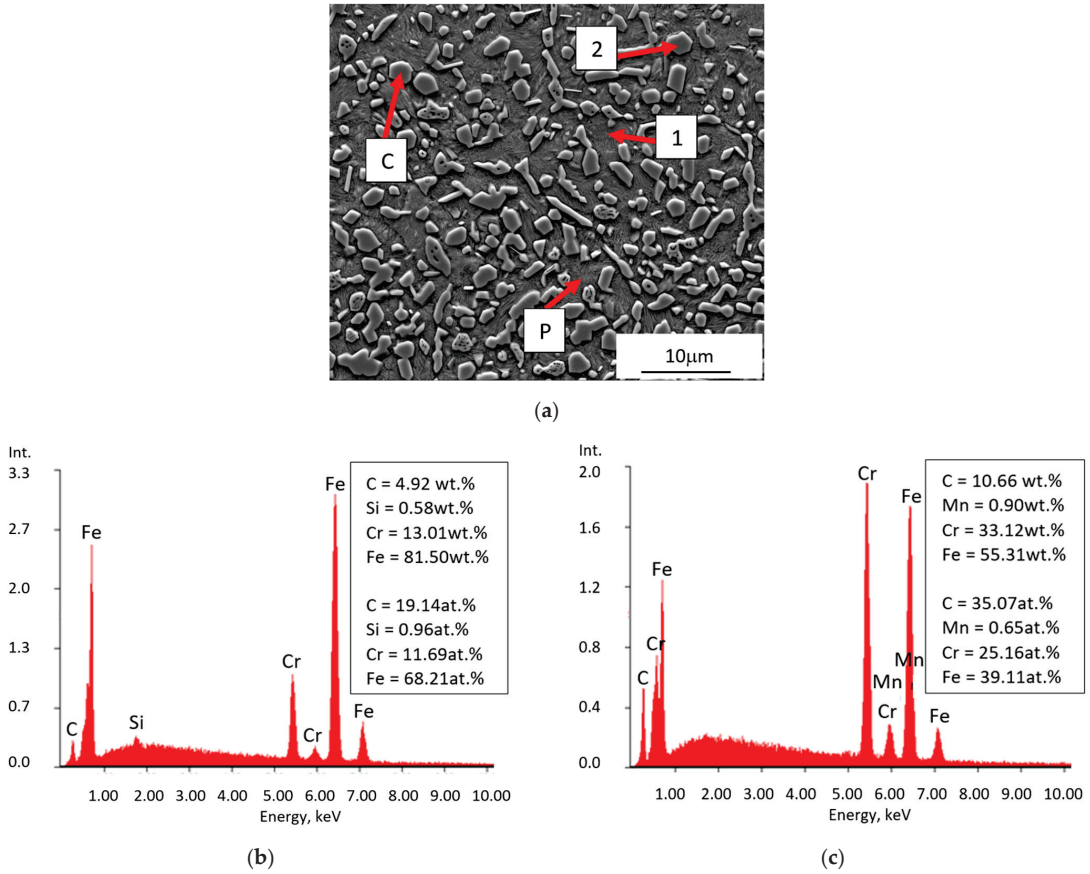


Figure 10. The microstructure of zone 3(TZ) in the compound casting of X46Cr13 steel–EN-GJL-HB 255 grey cast iron: (**a**) test area, (**b**) EDS results at point 1 from (**a**), (**c**) EDS results at point 2 from (**a**); P—pearlite, C—Cr(Fe) carbides.

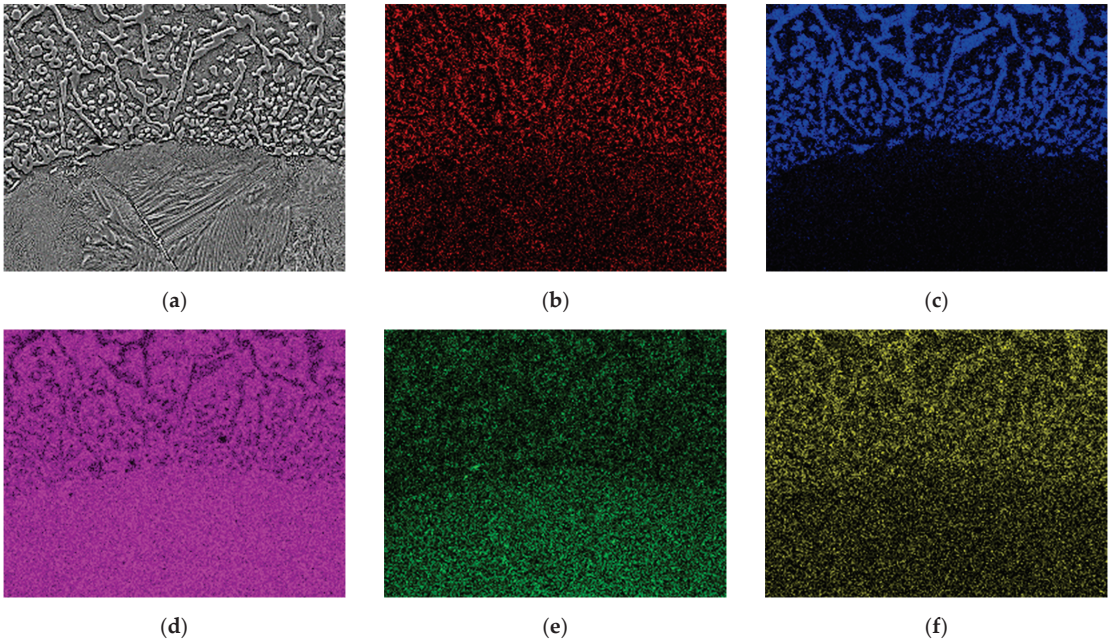


Figure 11. Surface distribution of elements on the border between zone 3(TZ) and 4(SP') in the compound casting of X46Cr13 steel–EN-GJL-HB 255 grey cast iron: (**a**) test area, (**b**) C, (**c**) Cr, (**d**) Fe, (**e**) Si, and (**f**) Mn.

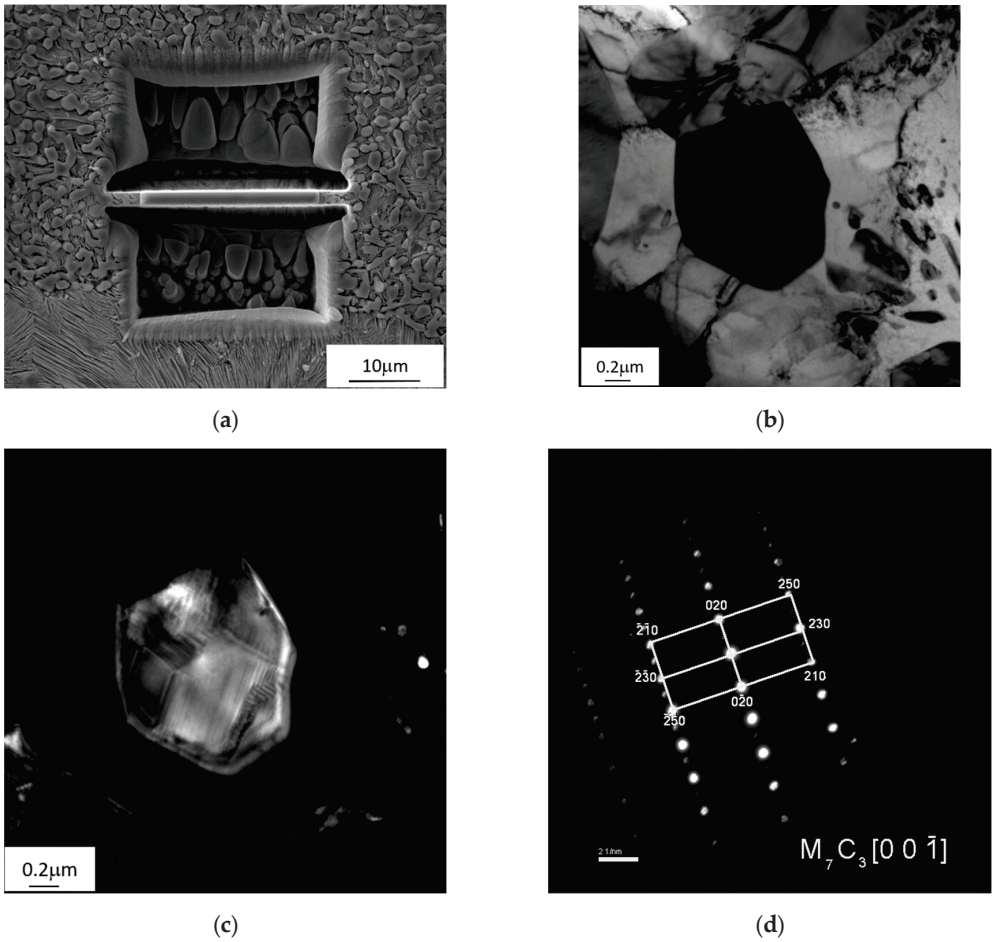


Figure 12. M_7C_3 carbide in pearlite in zone 3(TZ) in the compound casting of X46Cr13 steel–EN-GJL-HB 255 grey cast iron: (**a**) method of taking a lamella from zone 3(TZ) for TEM tests, (**b**) bright field, (**c**) dark field, and (**d**) selected area electron diffraction (SAD).

Then the pearlite zone 4(SP′) appears, representing decarburised microstructure of the casting supporting part (Figure 13).

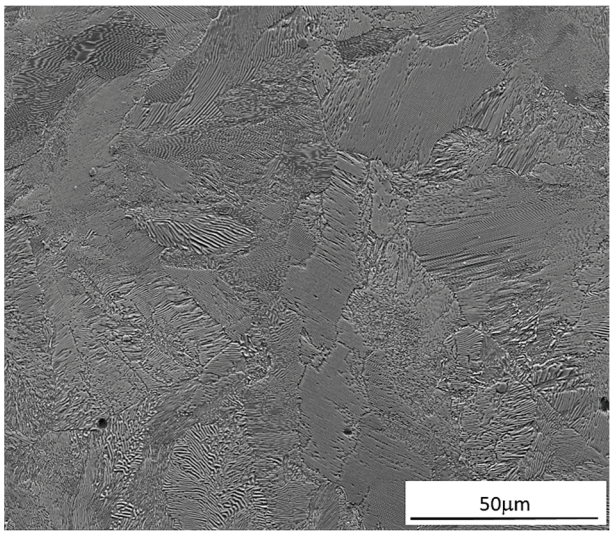


Figure 13. Pearlitic microstructure in zone 4(SP′) in the compound casting of X46Cr13 steel–EN-GJL-HB 255 grey cast iron.

Figure 14 presents a view of three bi-metal plates with an average surface hardness of 450 HV5 ± 12 HV5 after use under the operating conditions of a coke quenching car. For those plates and three mottled cast iron control plates with an average surface hardness of 350 HV5 ± 14 HV5, operated in the same conditions, their weight and thickness were measured. It was found that the bi-metal plates showed both volumetric and mass loss at a level comparable to plates made in whole of mottled cast iron (Figure 15).



Figure 14. A view of three bi-metal plate castings designed for coke quenching car lining after completing 18,500 coke production cycles.

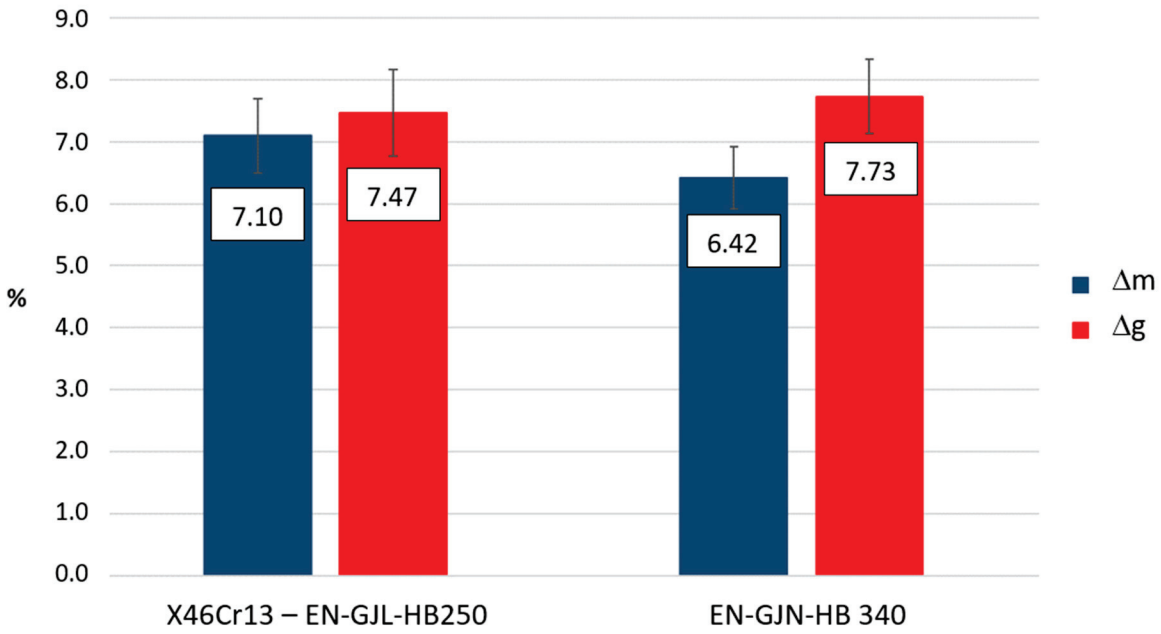
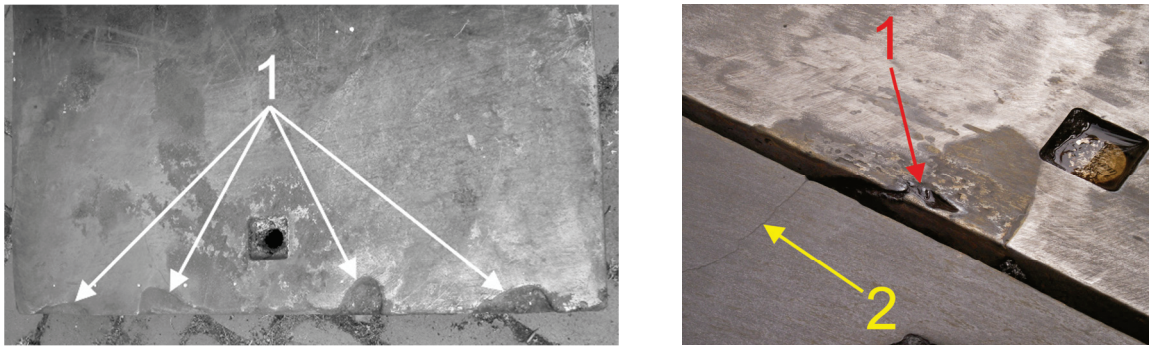


Figure 15. Average mass loss (Δm) and volumetric loss (Δg) of coke quenching car lining plates after completing 18,500 coke production cycles, carried out of compound castings of X46Cr13–EN-GJL-HB 255 and EN-GJN-HB 340 mottled cast iron.

More accurate observations showed that for compound castings, the highest-damage areas are located at the outer edges of the bi-metal working layer. For example, Figure 16 presents a view of a plate compound casting fragment after completing the operation cycle with visible, almost complete local loss of the X46Cr13 alloy steel working layer. The probable cause of the presented damage on the long edges of bi-metal plates is a local disconnection between the stainless steel and grey cast iron in a condition of multi-cycle thermal shock operation. This phenomenon generates an air gap between the working layer and the supporting part, increasing damage as a result of worsened heat conduction in the cyclically heated and cooled steel part and making it possible for water to ingress

into the gap, increasing corrosion. However, it should be noted that the average mass loss is at the level of approx. 7%, while maintaining the bonding stability on almost the entire contact surface in this type of compound casting plates of alloy steel–grey cast iron determines its suitability for further use as coke quenching car lining. Further suitability of lining plates for use is an extremely important factor from the point of view of coke quenching car overhauls. Removing the need to dismantle individual plates, typically carried out by mechanical cutting of heavily corroded mounting screws in the overhead position, allows operators to reduce the costs and time of overhauls.



(**a**) (**b**)

Figure 16. A view of the damage of a compound casting (1 in (**a**,**b**)) and a crack in an EN-GJN-HB 340 mottled cast iron casting (2 in (**b**)) lining plates after use under the operating conditions of a coke quenching car.

For mottled cast iron castings, the areas of increased damage occur locally, both in internal and external areas of the plate. In addition, despite the low average mass loss, not exceeding 6.5% on average, a crack was found in one of the plates under analysis (Figure 16). The cause of the presented damage by the thermal crack of a mottled cast iron plate is the non-uniform distribution of the carbon precipitations in the microstructure of the casting and the advantage in the amount of cementite (which increases the resistance on abrasive wear) to flake graphite (which increases heat conduction) in the pearlite matrix. The presence of a through-plate crack (Figure 17) makes it, unlike the remaining two, unsuitable for further use as a coke quenching car liner. It can be concluded that the through-plate crack of one of the three plates is a part of the trend that accompanies the use of this cast iron in coke quenching cars. According to our observations made during tests, between 30 and 40% of mottled cast iron plates are damaged by cracking before the entire car is withdrawn from service and sent for overhaul.



Figure 17. A view of a damaged test EN-GJN-HB 340 mottled cast iron test lining plate.

During the laboratory tests of coke quenching car lining plates, it was found that the coke production cycle resulted in slight carburising, sulphurising, and phosphating of the working layer of the bi-metal casting (Table 2). In addition, it was found that reducing the concentration of Cr by 0.2 wt.%, with the total concentration of this component exceeding 14 wt.%, can be considered negligible, e.g., from the point of bi-metal working layer corrosion resistance. Similarly, changes in the concentration of other components can be considered less significant.

Table 2. Chemical composition of the X46Cr13 steel working layer in the plate compound casting after use in a coke quenching car.

Elements Concentration, wt.%										
C	**Mn**	**Si**	**Cr**	**Ni**	**Mo**	**Cu**	**Ti**	**V**	**S**	**P**
0.514	0.560	0.359	14.300	0.535	0.080	0.001	0.001	0.001	0.020	0.030
Difference from the state before operation										
+0.074	−0.040	+0.019	−0.200	−0.115	−0.010	-	-	-	+0.019	+0.010

However, based on the conducted metallographic tests (Figure 18), it was found that the 18,500 completed coke production cycles practically did not cause any significant changes in the individual transition zones of the compound casting. Only when compared to the initial state before starting the operation did the microstructure of the bi-metal working layer (zone 1(WL)) show a slightly increased amount of pearlite at the expense of martensite. As a result, the hardness of the working layer, compared to the initial state before starting the operation, is slightly reduced by 30 HV5, i.e., to the level of 420 HV5 $\pm$ 9 HV5. However, the scope of changes in the microstructure of the working layer and its hardness might be as well considered negligibly small, especially considering the quantity of heating and cooling cycles the test castings were subjected to.

Summing up, the scope of the conducted tests covered the technology of creating compound castings composed of two parts, i.e., the working layer made of X46Cr13 high-chromium steel, and the supporting part made of EN-GJL-HB 255 grey cast iron, in a liquid–solid system by pre-installing a monolithic insert in the mould cavity.

The decisive impact of the C diffusion phenomenon, shown in the paper on forming the bond between the working layer and supporting layer materials, results obviously from the fact of easy transport of the component by an interstitial mechanism from one material to another, as opposed to the vacancy mechanism taking place, e.g., for Fe, Mn, Cr, Mo, or Ni. Omitting other components in the analysis, apart from C, present in the chemical composition of both the working layer and the supporting part is more justified, because despite the wide range of concentration variability, e.g., for chromium, the results of the conducted tests show no noticeable quantitative impact on the quality of bonding between both parts.

Considering this, it was found that the lasting diffusion bonding between the component materials of compound castings, made in the arrangement alloy steel working layer–grey cast iron supporting part, is created primarily as a result of the transport of C towards the lower concentration, i.e., from the supporting part to the working layer. Since the material of the supporting part, made in the presented technology, is poured into a mould where the working part material is already placed in a form of a steel plate, the transport of carbon is associated, in the first stage, with diffusion in the liquid–solid system, and after the solidification process is completed, with the mechanism of diffusion in the solid state. Of course, the above-mentioned diffusion processes are heat-activated, and therefore the C transport is preceded by heat transport in the same direction, i.e., from the "hot" liquid alloy poured into the mould to the "cold" monolithic insert. Therefore, obtaining a permanent diffusion bonding over the entire contact surface between the working layer and a supporting part requires using a suitably high pouring temperature of cast iron.

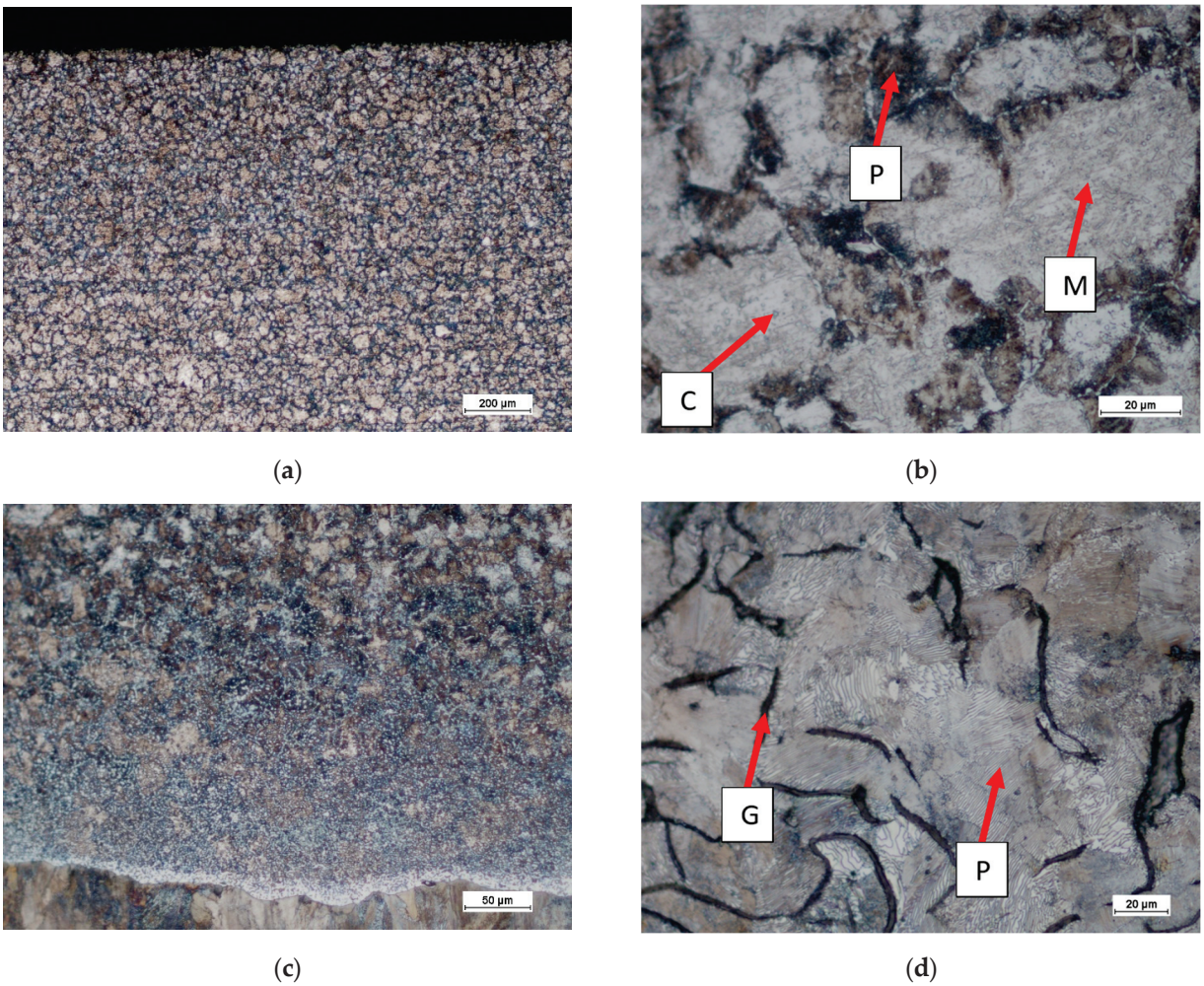


Figure 18. Microstructure of a lining plate compound casting of X46Cr 13–EN-GJL-HB 255 after use in a coke quenching car; (**a**,**b**) working layer (zone 1(WL); (**c**) area of bonding with diffusion transition zones 3(TS)—4(SP'); (**d**) supporting part (zone 5(SP); P—pearlite, M—martensite, C—Cr(Fe) carbides, G—flake graphite.

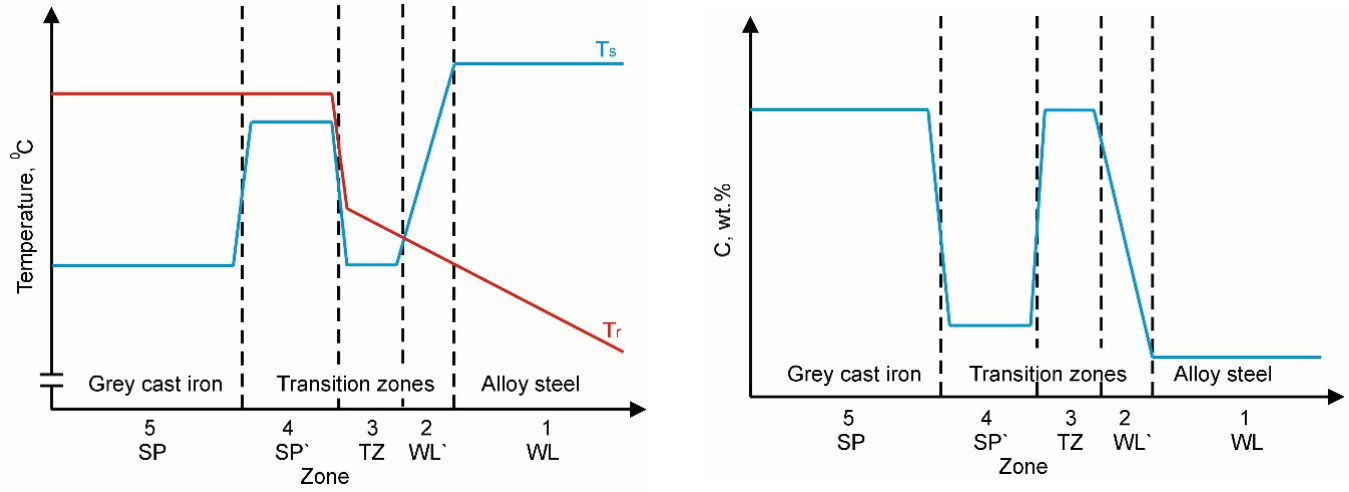
The course of the presented processes allows us to conclude that creating a permanent diffusion bonding in the compound castings under analysis takes place in four successive stages:

Stage I: Wetting the monolithic insert with liquid cast iron poured into the mould. At this stage, it is necessary to meet the condition $\theta < 90^{\circ}$ for the contact surface of the insert, where θ is the wetting angle formed by applying flux to the contact surfaces of the monolithic insert.

Stage II: Heat-activated C diffusion in the direction from the liquid cast iron to the steel monolithic insert. At this stage, we apply a temperature and concentration condition for the liquid alloy–insert system:

$$\begin{cases} T_{SP} > T_{WL} \\ C_{SP} > C_{WL} \end{cases} \quad (1)$$

Stage III: Melting a thin layer (up to several dozen µm) on the surface of the monolithic insert remaining in direct contact with the liquid alloy as a result of carburising that reduces the temperature of liquidus and solidus. Hypothetical temperature and carbon concentration distribution in the bi-metal system under analysis at this stage is presented illustratively in Figure 19.



(**a**) (**b**)

Figure 19. Hypothetical temperature (**a**) and C concentration (**b**) in individual zones of compound casting structure in the period corresponding to stage III: T_S—solidus temperature T_r—actual temperature of the bi-metal system under analysis.

Stage IV: Solid state C diffusion. At this stage, the structure of the compound casting, formed mainly during stage III, is consolidated and meets the following concentration condition:

$$\begin{cases} C_{SP} > C_{SP'}, C_{WL'}, C_{WL} \\ C_{WL} < C_{WL'}, C_{TZ}, C_{SP'}, C_{SP} \\ C_{SP} \approx C_{TZ} \end{cases} \quad (2)$$

The presented phenomena of transporting mass and heat determine the formation of compound castings, where for the material arrangement grey cast iron–high-chromium steel, five basic zones can be distinguished. Successively, in the direction from the supporting part to the working layer, there are the following:

- A zone (SP) appropriate for grey cast iron, used for the supporting part containing flake graphite in a pearlite matrix;
- A pearlite zone (SP′) formed in the near-border area of the supporting part, created as a result of decarburisation associated with the transport of C towards a lower concentration area, i.e., to the working layer;
- A transition zone (TZ) composed of a large amount of Cr(Fe) carbides, mainly M_7C_3 in a pearlite matrix, formed from the liquid phase as a result of carburising reducing the melting point for the working layer border area and then melting it by the high temperature, and obtained as part of the heat transport from liquid alloy to the monolithic insert;
- A zone (WL′) formed in the working layer in the solid phase by carburising (insufficient to significantly lower the melting point) and cooling from the high temperature (insufficient to melt this area), determining the occurrence of microstructure with Cr(Fe) carbides in a pearlite-martensitic matrix with a dominant amount of pearlite;
- A zone (WL) with a microstructure formed as a result of self-hardening of X46Cr13 steel i.e., Cr(Fe) carbides, mainly $M_{23}C_6$ in a martensitic-pearlite matrix with a dominant amount of martensite.

In addition, analysing the results of tests conducted under the real coking plant operating conditions shows the suitability of compound casting plates in the arrangement X46Cr13 alloy steel–EN-GJL-HB 255 grey cast iron for use as coke quenching car liners. Such bi-metal plates are characterised by the stability of their microstructure and, consequently, their performance in cyclically variable heating and cooling procedures, necessary in

the process of operating a coke quenching car. Considering this, thanks to their utility properties, such castings can successfully replace the plates used as liner plates for the coke quenching cars to date, made in whole of EN-GJN-HB 340 low-alloy mottled cast iron. It should be noted that the production cost, and consequently the purchase price, of bi-metal plate in the material arrangement under analysis is about 50% higher than for the full cast iron plate. The greatest impact on the cost of producing a bi-metal plate is the price of a 5 mm thick plate made of high-chromium steel and the cost of preparing a sand mould, considering the procedure for preparing a monolithic insert presented in the paper. However, this cost can be compensated by the higher service life of bi-metal plates compared to those made of cast iron, which results in no need to replace the damaged (cracked) plates. Thus, on one hand, savings are introduced due to the lack of the need to purchase a new plate to replace the damaged one, as already discussed, while on the other hand, it reduces the costs of coke quenching car overhauls as well.

4. Conclusions

Based on the analysis of test results, the following conclusions were elaborated:

1. The phenomena that determine the formation of permanent bonding between the two connected alloys, being component materials of a compound casting, include heat and C transport in the direction from the "hot and high-carbon" material of the supporting part poured into the mould to the "cold and low-carbon" material of the working layer, placed as a monolithic insert inside the mould cavity. Therefore, the process of forming a permanent bonding between the working layer and supporting part in the presented technology of compound casting takes place successively as a result of wetting the monolithic insert contact surface with liquid alloy poured into the mould and then by thermally activated C diffusion in the liquid alloy–insert system.
2. The most important aspect of forming a permanent diffusion bond between the two alloys in the presented compound cast iron technology was to create conditions for a transitional zone to emerge by carburising the material to reduce the temperature of the liquidus and solidus and then melting the thin layer of steel monolithic insert remaining in direct contact with the liquid cast iron poured into the mould.
3. Using the compound casting in the arrangement X46Cr13 alloy steel–EN-GJL-HB 255 grey cast iron to replace the EN-GJN-HB 340 mottled cast iron currently used to cast lining plates for coke quenching cars allows us to extend the service life of the components, primarily due to their higher resistance to cracking.

Funding: This publication was financed from the statutory subsidy of the Faculty of Mechanical Engineering of the Silesian University of Technology in 2023 and 2024; BK-278/RMT8/2024.

Institutional Review Board Statement: Not applicable.

Informed Consent Statement: Not applicable.

Data Availability Statement: Data are contained within the article.

Conflicts of Interest: The author declares no conflict of interest.

References

1. Campbell, J. *Complete Casting Handbook—Metal Casting Processes, Metallurgy, Techniques and Design*; Elsevier Ltd.: Oxford, UK, 2015.
2. Žic, S.; Džambas, I.; Konić, M. Possibilities of implementing bimetallic hammer castings in crushing industries. *Metal. Metall.* **2009**, *48*, 51–54.
3. Wie, N.; Wang, K.; Zhou, X.; Wang, Q.; Liu, Q.; He, J. Influence of cooling rate on the microstructure in HCCI/steel bimetal composite hammer. *Adv. Mat. Res.* **2012**, *538–541*, 1041–1044.
4. Xiao, X.; Ye, S.; Yin, W.; Xue, Q. HCWCI/carbon steel bimetal liner by liquid-liquid compound lost foam casting. *J. Iron Steel Res. Int.* **2012**, *19*, 13–19. [CrossRef]
5. Kiss, I.; Maksay, S. Bimetallic cast iron rolls—Some approaches to assure the exploitation properties. *Teh. Vjesn. Tech. Gazz.* **2010**, *17*, 173–178.

6. Özdemir, N.; Aksoy, M.; Orhan, N. Effect of graphite shape in vacuum-free diffusion bonding of nodular cast iron with gray cast iron. *J. Mater. Process Tech.* **2003**, *141*, 228–233. [CrossRef]
7. Gao, X.; Jiang, Z.; Wie, D.; Jiao, S.; Chen, D.; Xu, J.; Zhang, X.; Gong, D. Effects of temperature and strain rate on microstructure and mechanical properties of high chromium cast iron / low carbon steel bimetal prepared by hot diffusion-compresion bonding. *Mater. Design.* **2014**, *63*, 650–657. [CrossRef]
8. Vigraman, T.; Ravindran, D.; Narayanasamy, R. Diffusion bonding of AISI 304L steel to low-carbon steel with AISI 304L steel interlayer. *Mater. Design.* **2012**, *34*, 594–602. [CrossRef]
9. Lagos, M.; Retamal, C. An alternate theoretical approach to solid-state bonding. *Scripta Mater.* **2011**, *64*, 402–405. [CrossRef]
10. Duarte, L.; Lourenco, N.; Santos, H.; Santos, J.; Sá, C. Tungsten carbide powder inserts in ductile iron. *Mater. Sci. Forum.* **2004**, *455–456*, 267–270. [CrossRef]
11. Studnicki, A.; Dulska, A.; Szajnar, J. Reinforcing cast iron with composite insert. *Arch. Metall. Mater.* **2017**, *62*, 355–357.
12. Cholewa, M.; Wróbel, T.; Baron, C.; Morys, M. Surface phenomena at the interface between silicon carbide and iron alloy. *Materials.* **2021**, *14*, 6762. [CrossRef]
13. Studnicki, A.; Kilarski, J.; Przybył, M.; Suchoń, J. Technological experiments of production castings of chromium cast iron in the foundry. *Arch. Foundry Eng.* **2005**, *5*, 293–302.
14. Zhi, X.; Han, Y.; Liu, J.; Zhao, M.; Ma, S. Casting process optimization of a bimetal wear-resistant block using liquid–solid processing. *Int. J. Mater. Res.* **2014**, *105*, 953–960. [CrossRef]
15. Wróbel, T. Characterization of bimetallic castings with an austenitic working surface layer and an unalloyed cast steel base. *J. Mater. Eng. Perform.* **2014**, *23*, 1711–1717. [CrossRef]
16. Wróbel, T.; Wiedermann, J.; Skupień, P. Bimetallic castings in a chromium–nickel stainless steel working surface layer configuration with a grey cast iron base. *Trans. Indian Inst. Met.* **2015**, *68*, 571–580. [CrossRef]
17. Ramadan, M. Interface characterization of bimetallic casting with a 304 stainless steel surface layer and a gray cast iron base. *Adv. Mater. Res.* **2015**, *1120*, 993–998. [CrossRef]
18. Cingi, C.; Rauta, V.; Niani, E.; Orkas, J. Cast bonding of cast irons to ferritic stainless steel. *Mater. Sci. Forum.* **2010**, *654–656*, 2712–2715. [CrossRef]
19. Przyszlak, N.; Wróbel, T. Self-hardening of X46Cr13 steel integrated with base from grey cast iron in bimetallic system. *Arch. Foundry Eng.* **2019**, *19*, 29–34. [CrossRef]
20. Wróbel, T.; Przyszlak, N.; Dulska, A. Technology of alloy layers on surface of castings. *Int. J. Metalcast.* **2019**, *13*, 604–610. [CrossRef]
21. Ghaini, M.; Ebrahimnia, M.; Gholizade, S. Characteristics of cracks in heat affected zone of ductile cast iron in powder welding process. *Eng. Fail. Anal.* **2011**, *18*, 47–51. [CrossRef]
22. Yi, P.; Xu, P.; Fan, C.; Yang, G.; Liu, D.; Shi, Y. Microstructure formation and fracturing characteristics of grey cast iron repaired using laser. *Sci. World J.* **2014**, *2014*, 541569. [CrossRef]
23. Rudnev, V. Induction hardening of cast iron. *Therm. Process.* **2018**, *15*, 40–45.
24. Misaka, Y.; Kawasaki, K.J.; Shimizu, M. Fatigue strength of ferritic ductile cast iron hardened by super rapid induction heating and quenching. *Mater. Trans.* **2004**, *45*, 2930–2935. [CrossRef]
25. Börner, R.; Landgraf, P.; Kimme, S.; Titsch, C.; Lampke, T.; Schubert, A. Fundamental investigations in tool wear and characteristics of surface microstructure for ultrasonic vibration superimposed machining of heat-treated X46Cr13 steel using different cutting materials. *J. Manuf. Mater. Process.* **2021**, *5*, 27. [CrossRef]
26. Yang, Y.; Zhao, H.; Dong, H. Carbide evolution in high-carbon martensitic stainless cutlery steels during austenitizing. *J. Mater. Eng. Perform.* **2020**, *29*, 3868–3875. [CrossRef]
27. Garcia de Andre's, C.; Caruana, G.; Alvarez, L. Control of M23C6 carbides in 0.45C–13Cr martensitic stainless steel by means of three representative heat treatment parameters. *Mater. Sci. Eng.* **1998**, *A241*, 211–215. [CrossRef]
28. Alvarez, L.; Garcia, C.; Lopez, V. Continuous cooling transformations in martensitic stainless steels. *ISIJ Int.* **1994**, *34*, 516–521. [CrossRef]

Disclaimer/Publisher's Note: The statements, opinions and data contained in all publications are solely those of the individual author(s) and contributor(s) and not of MDPI and/or the editor(s). MDPI and/or the editor(s) disclaim responsibility for any injury to people or property resulting from any ideas, methods, instructions or products referred to in the content.

materials

MDPI

Article

Vari Morph Cast Iron—A High IQ Material—Structure, Properties, Ultrasonic Control, Technology and Industrial Application

Jerzy Stanisław Zych [1,*], Marcin Myszka [1], Janusz Postuła [2] and Sylwia Kobyłecka [2]

[1] Faculty of Foundry Engineering, AGH University of Krakow, Aleje Mickiewicza 30, 30-059 Krakow, Poland
[2] FANSULD Cast Iron Foundry, ul. Zielona 22, 26-700 Końskie, Poland
* Correspondence: jzych@agh.edu.pl

Abstract

Cast iron, whose structure simultaneously contains graphite precipitates in various forms, with controlled proportions of individual forms, has been named "Vari-Morph" (VM) cast iron by the authors. The authors have been researching the properties of such cast iron for many years, and the results are being published successively. This new type of cast iron, not included in national (Polish) or European standards, is intended as a material for special-purpose castings. These castings have unique requirements for a set of properties: physical, mechanical, and functional. VM cast iron is characterized by a set of properties that cannot be achieved when the graphite is uniform in shape. The desired properties of VM cast iron are achieved by controlling the morphology of graphite precipitates and the proportion of individual forms in the structure, rather than by changing the matrix. To quantitatively describe graphite precipitates, a proprietary method for determining the graphite shape indicator (f_K) was developed. Graphite precipitate analysis is performed by scanning a microscopic image of the metallographic specimen, and then using Tescan Imaging Software (Tescan ESSENCE™) Unified Control for Imaging and Analysis, each precipitate is described using surface metrology parameters. The final value of the graphite shape indicator (f_K) is calculated as a weighted average of all precipitates present in the analysis field. Empirical relationships between the f_K indicator and a selected group of physical, mechanical, and functional properties of VM cast iron were determined. Studies have demonstrated a very well-correlated relationship between the f_K indicator in VM cast iron and ultrasonic wave velocity (C_L). The relationship $C_L = f(f_k)$ is characterized by a very high correlation coefficient of $R > 0.90$. In previous publications, the authors presented the relationships between the f_K indicator and physical properties such as thermal conductivity (λ), specific density (ρ), strength (R_m), elongation (A5), index quality (IQ), and functional properties such as low-cycle mechanical fatigue resistance (Z_c), thermal fatigue resistance (N), and cast iron tightness (H) as functions of the f_K index. The study concerned VM cast iron with a ferritic matrix. This work contains new empirical relationships that extend previous studies. The newly developed relationships replace the f_k shape indicator with the velocity of the ultrasonic wave determined in cast iron with a specific f_K indicator value. This resulted in a number of practical dependencies, including: $\lambda = f(C_L)$; $\rho = f(C_L)$; $E_D = f(C_L)$; $R_m = f(C_L)$; $A5 = f(C_L)$; $IQ = f(C_L)$; $N = f(C_L)$; $Z_c = f(C_L)$; $H = f(C_L)$. These relationships allow us to measure the wave velocity in a Vari Morph iron casting (with various forms of graphite) and determine a number of characteristics and properties of the material/iron from which the casting was made. It is possible to assess the suitability of a casting with a specific structure for operation under selected conditions.

Keywords: cast iron; graphite shape; ultrasonic measurements; properties; physical; mechanical; functional

1. Introduction

Cast iron containing carbon in the form of graphite, known as gray iron, is the most commonly used material in global foundry production. Cast iron for castings, based on the form (morphology) of graphite precipitates, is produced in three groups (PN EN 1560): cast iron with flake graphite (from EN GJL-100 to EN GJL-350), cast iron with vermicular graphite (from EN GJV-300 to EN GJV-500), and cast iron with spheroidal graphite (from EN GJS-350-22 to EN GJS-900-2). Cast iron and castings are not produced with intentionally mixed forms of graphite. Only a very small percentage of graphite other than the intended form is permissible, e.g., up to 5.0% in ductile iron and up to 20% in vermicular iron. To achieve such uniform graphite structures, the production technologies for individual grades of cast iron have been adapted. In many cases, limiting and maintaining a uniform graphite morphology (flake (L), vermicular (V), or spheroidal (S)) significantly limits the ability to freely shape many of the cast iron's properties, both necessary and beneficial for casting applications. The form of graphite precipitates influences all cast iron properties and characteristics, including physical, mechanical, technological, functional, and operational properties. This limitation currently has no substantive justification.

The research conducted [1–12] indicates the possibility of producing cast iron with mixed graphite precipitate morphology and confirmed the possibility of controlling this morphology in a deliberate and predictable manner. Figure 1 presents the concept of cast iron with mixed graphite form, which has been given the name Vari Morph (VM) [1]. The EN ISO 945 standard specifies only three types of graphite form in raw castings that have not been heat treated [13,14]. The remaining types, crossed out in Figure 1a, cover the graphite precipitate forms in cast iron after heat treatment. VM cast iron encompasses both the group of graphite precipitate forms shown in Figure 1b,c. The idea of VM cast iron is a smooth transition of the graphite form from flake, through mixed: flake + vermicular and mixed vermicular + nodular, to fully nodular. This smooth transition in the form of graphite precipitates will also enable smooth shaping of a whole range of physical and mechanical properties. Within the range of standardized cast iron grades, property changes are gradual.

The research described in this article demonstrated the significant influence of graphite precipitate morphology on the entire group of cast iron properties and confirmed the possibility of controlling these properties. One of the most important results that can be achieved is the ability to produce gray cast iron characterized by relatively good strength (R_m—300–400 MPa) and simultaneously low hardness (HB—160–180). In traditional modified cast iron with homogeneous flake graphite (from EN GJL-250 to EN GJL-350), to achieve the described strength, the metal matrix is transformed into a purely pearlitic form, leading to an increase in hardness to HB—230–240. Modern casting machining methods using high-speed CNC machines are adapted to the processing of materials with reduced hardness. In the case of cast iron castings, hardness is expected to be maintained below 200 HB. If only the flake graphite form is retained, achieving these parameters (Rm and HB) is very difficult, and for higher Rm values, it is impossible. At hardnesses significantly above 200 HB, it is necessary to reduce the machining speed parameters of CNC machines, which is not conducive to economics. This was confirmed directly by research conducted as part of the project [8] at an iron foundry that uses CNC machining of its own castings. Cast iron quality is often measured by an index called Index Quality (IQ), which is defined as:

https://doi.org/10.3390/ma19061212

IQ = R_m/HB [15]. Gray cast iron has a relatively low IQ value of 1.0–1.4, while ductile iron ranges from 2.5–3.0. By controlling the graphite morphology and allowing the possibility of mixed forms in the casting structure, it is possible to continuously fill the IQ range and obtain values from 1.0 to 2.5. Vermicular cast iron partially falls between gray and ductile iron. However, the requirement of the European standard PN-EN 16079 (from EN-GJV-300 to EN GJV-500) to achieve 80% of vermicular graphite complicates the production technology on the one hand, and on the other limits the freedom in shaping many features of cast iron, including achieving a better IQ index and a number of other properties.

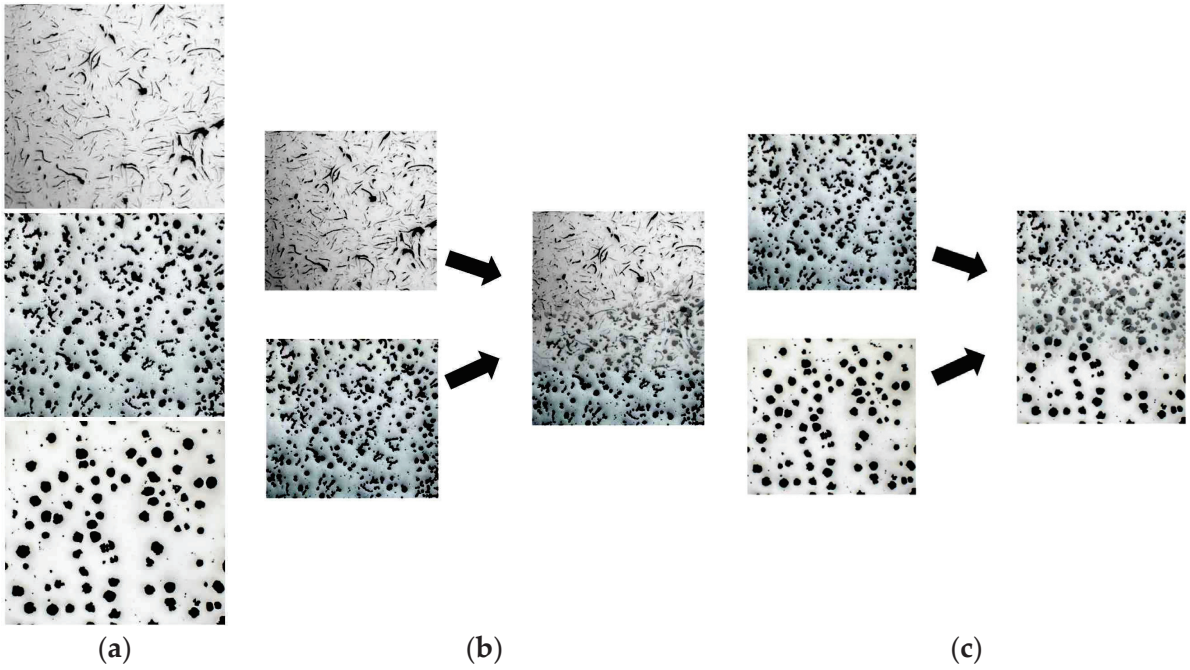


Figure 1. Types of graphite morphology: (**a**) flake, vermicular and spheroidal graphite; (**b**) cast iron with mixed forms of flake and vermicular; (**c**) cast iron with mixed forms of vermicular and spheroidal graphite.

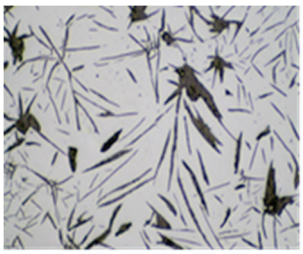
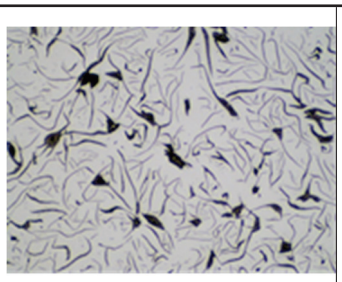
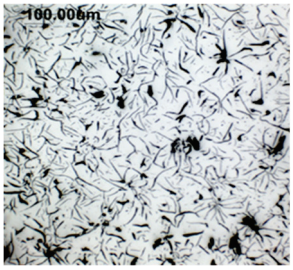
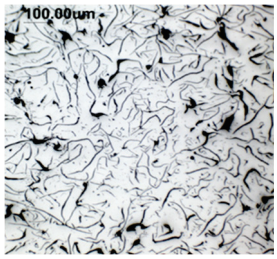
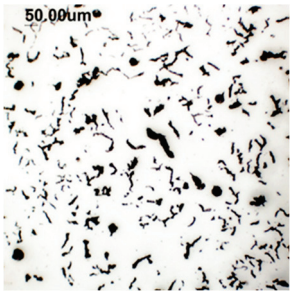
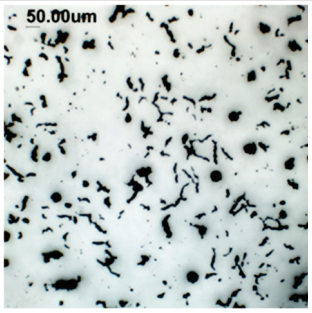
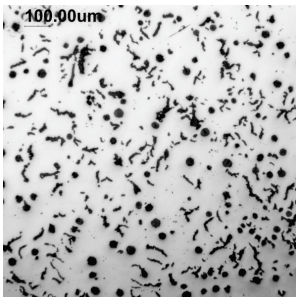
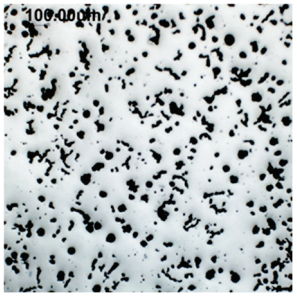
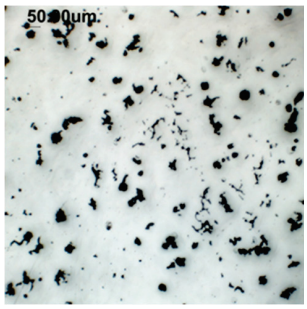
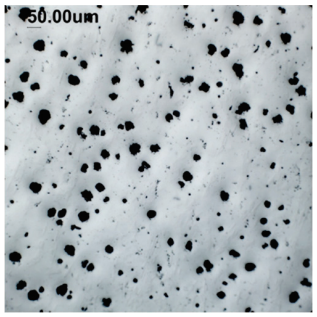
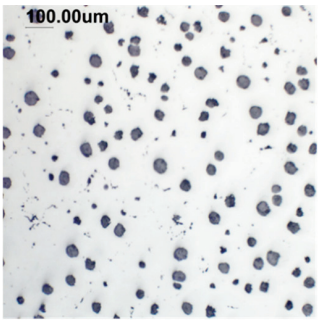
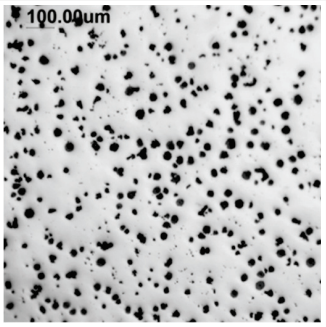
The production of cast iron in a form other than flake requires secondary treatment of the liquid metal, to which small amounts of additives (inoculants, cast iron spheroidizing mortars) are introduced. The possibility of controlling the graphite morphology over a wide range of changes has been confirmed, among others, in the works of the authors [1–12,16–18] and many others. The work concerned increasing the resistance of cast iron to thermal fatigue by controlling the morphology of graphite precipitates over a wide range, from flake to nodular [9–11]. Furthermore, as analytical work conducted so far has shown, cast iron in which the graphite is not homogeneous in terms of its morphology is characterized by above-standard properties that cannot be achieved with a uniform graphite form [12]. Examples of VM cast iron structures correlated with f_K shape indicator are shown in Table 1.

Studies on the influence of the graphite shape index f_K (or ξ index) on the resistance of cast iron to thermal fatigue also show that there are strict relationships that link other features and properties of cast iron with the shape index ξ, such as: R_m = f(ξ), A5 = f(ξ), E_D = f(ξ), α (vibration damping) = f(ξ), λ (thermal conductivity) = f(ξ); Index Quality IQ = f(ξ) [5,6]. The shape index is defined in many ways. For example, the ξ index is defined as the area of the surface occupied on a metallographic microsection by the graphite separation to its circumference when squared. The authors propose defining the graphite shape indicator "f_K" for VM cast iron as a weighted average of the values for the flake,

https://doi.org/10.3390/ma19061212

vermicular, and spheroidal precipitate forms, taking into account the contribution of each form to the overall set of precipitates visible on the metallographic specimen. Because most cast iron properties are determined as a function of the graphite shape indicator, correctly determining its value is crucial in describing the structure of Vari Morph (VM) cast iron.

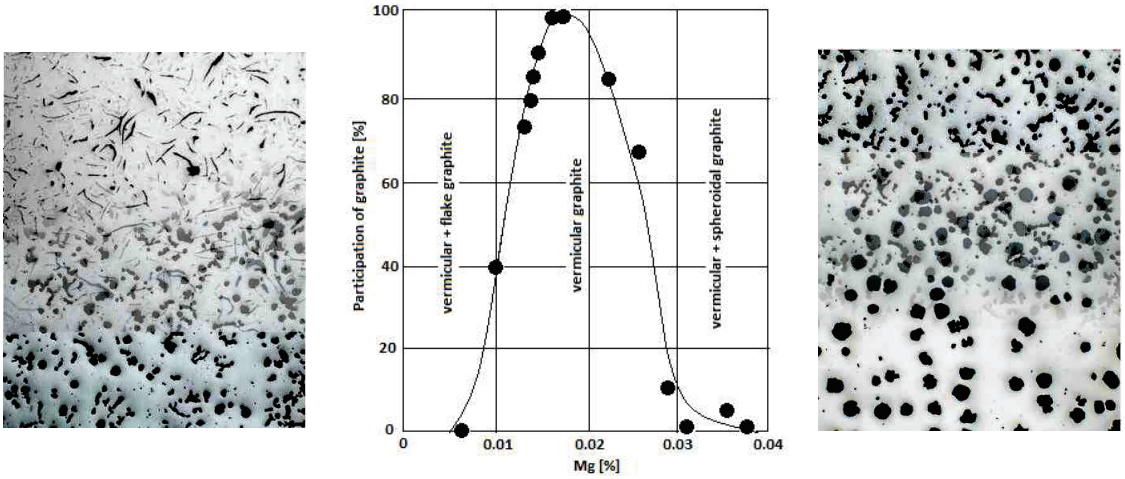
Table 1. Examples of graphite precipitate morphology for different values of the shape indicator f_K.

			
f_K = 0.28	f_K = 0.29	f_K = 0.31	f_K = 0.32
			
f_K = 0.42	f_K = 0.50	f_K = 0.59	f_K = 0.62
			
f_K = 0.63	f_K = 0.72	f_K = 0.78	f_K = 0.82

2. VM Manufacturing Technology—Method Selection

Technological standards do not provide for the production of mixed graphite cast iron. In 2018, the authors [1] named mixed graphite cast iron with controlled proportions of individual shapes "Vari-Morph" (VM). Cast iron with the proposed graphite precipitate structure could become an interesting material for castings with special applications and requirements for the combination of physical and mechanical properties. Since that year, the team has continued work on the technology, structure, and properties of this type of cast iron [1–11]. VM cast iron is characterized by a set of physical and mechanical properties that cannot be obtained when the graphite precipitates are uniform in shape. VM cast iron falls between cast iron with flake graphite (F) and vermicular graphite (V), and between cast iron with vermicular graphite (V) and spheroidal graphite (S). Figure 2 presents the idea of the existence of a mixed form of graphite in the structure of cast iron as a criterion for qualification to the group of Vari Morph cast iron grades.

https://doi.org/10.3390/ma19061212



"VM"—vermicular + flake graphite

Vermicular graphite

"VM"—vermicular + spheroidal graphite

Figure 2. Morphology of graphite precipitation in Vari Morph cast iron.

Cast irons with a L + V graphite mixture are characterized by good thermal conductivity and better plasticity and strength than gray cast iron. They can be used for structures and components subjected to rapid, cyclic heating, e.g., as a material for metal molds, slag ladles, ingot molds, etc. Of particular interest is cast iron with a mixed form of graphite: graphite (S) + graphite (V), with a high proportion of vermicular graphite. Such cast iron is characterized by high strength, good plasticity, and tightness. Furthermore, it has relatively good vibration damping properties and relatively good thermal conductivity, which are not found in ductile irons. In [1–5], it was demonstrated that such cast iron also has high resistance to thermal fatigue—higher than vermicular cast iron.

The authors' research work [1–12] conducted both on a laboratory and industrial scale indicates the technical possibility of producing VM cast iron with mixed graphite morphology and confirmed the technological ability to control graphite morphology in a deliberate and predictable manner as to the obtained assumed structure of graphite precipitates.

One of the most important results achieved by producing Vari Morph cast iron is the ability to produce gray cast iron characterized by relatively good strength (R_m—300–400 MPa) and simultaneously low hardness (HB—160–180). The graphite in such cast iron occurs in mixed, flake, and vermicular (F+V) forms. This cast iron has a ferritic or ferritic-pearlitic matrix. Traditional cast iron with only flake graphite (gray) has an almost purely pearlitic structure to achieve the described strength, reduced carbon content (low CE), and a hardness in the HB range of 230–240. Therefore, it has a reduced quality index (IQ), which in the case of cast iron is defined as the ratio of R_m strength to hardness ($IQ = R_m/HB$). Modern casting machining methods using high-speed CNC machines are designed to process materials with reduced and uniform hardness. In the case of cast iron, hardness below 200 HB is often required. If the graphite flake form is maintained, achieving these parameters (R_m and HB) for cast iron with a strength above 250 MPa is virtually impossible. Vari Morph cast iron offers this possibility and opportunity.

Producing any type of cast iron other than flake graphite requires secondary metallurgy of the metal/cast iron in its liquid state. Small amounts of master alloys/additives (cast iron spheroidizing mortars and inoculants) must be added. Several secondary metallurgy methods are known in industrial practice to modify the form of graphite precipitates and eliminate flake graphite from the structure. This group of methods includes:

- Magnesium addition (controlled amount)
- Simultaneous addition of magnesium and titanium

https://doi.org/10.3390/ma19061212

- Addition of "Michmetal" alloy.
- Simultaneous addition of magnesium, cerium, aluminum, and calcium (Mg-Ce-Al-Ca).
- PQ-CGI Inmold process
- Method using Sinter-Cast technology
- Elkem method (COMPACTMAG magnesium-cerium mortar).

As a result of many preliminary and verification tests conducted by the authors on the application of the above methods, it was concluded that the method of introducing a controlled amount of magnesium (Mg) into the molten metal (Figures 2 and 3) is the easiest technology. Furthermore, it is characterized by high repeatability of obtained results and simplicity of application. To date, this method has been widely used in the production of ductile and vermicular cast iron. With precisely defined (residual) magnesium contents remaining in the solidifying casting, mixed forms of graphite can be obtained in Vari Morph cast iron, as shown in Figures 2 and 3. Magnesium is introduced into the molten metal in the form of a low-magnesium FeSiMg mortar. The amount/content of magnesium introduced from the magnesium mortar into the cast iron and remaining as residual in the solidifying casting relative to the total amount of magnesium used in the spheroidization process is defined as the degree of magnesium assimilation. Its value ranges widely, from approximately 30% to over 80%. It depends on many technological factors, parameters, and the spheroidization technology/method. The authors tested three methods: the Tundish method using a tight-lid ladle, the PE method, and the in-mold spheroidization method—the Inmold process. The highest repeatability is achieved with the Inmold method, which allows for the precise and repeatable introduction of the planned amount of Mg into the cast iron. Using this method, it is possible to produce serial Vari Morph iron castings with any desired graphite precipitate morphology.

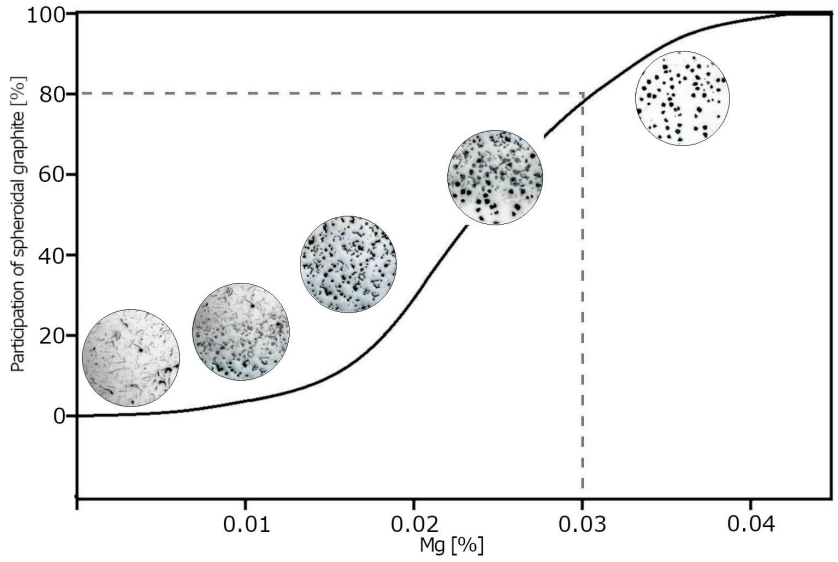


Figure 3. The influence of Mg content in cast iron on the share of nodular graphite in the structure.

Quantitative description of graphite precipitates in the metallographic structure of cast iron, when individual precipitates of different shapes occur side by side, requires the use of mathematical statistics. The shape of a single precipitate is described by a shape index, the degree to which the shape approximates a circular cross-section. The shape index "f" is most often defined as the ratio of the surface area of the precipitate visible on the metallographic micrograph to the area of the circle described by that precipitate. The value of the "f" index defined in this way falls within the following ranges:

➢ f = 0.00–0.34 for flake graphite,

https://doi.org/10.3390/ma19061212

- ➢ f = 0.35–0.64 for vermicular graphite,
- ➢ f = 0.65–1.00 for spheroidal graphite.

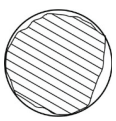
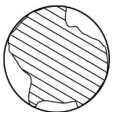
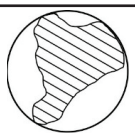
In their works, the authors [1–3,5] introduced a new concept of "averaged shape indicator of graphite precipitates" (f_K). In general, f_K is the weighted average of the shape indices of "all" graphite precipitates in the observed field of the metallographic cross-section. The methodology for determining the value of the f_K index is described later in the work.

To describe the effect of the morphology of graphite precipitates in VM cast iron on its broadly understood quality, empirical relationships were determined, in which the independent variable is the value of the average shape indicator of graphite precipitates f_K in connection with: mechanical properties ($R_m = f(f_K)$; $A5 = f(f_K)$; $IQ = f(f_K)$)); physical properties ($C_L = f(f_K)$; $\lambda = f(f_K)$; $\rho = f(f_K)$; and functional properties ($N = f(f_K)$, $Zc = f(f_K)$, cast iron tightness $H = f(f_K)$). In the light of the research results described below, the empirical relationships are relatively well correlated. This provides the basis for the thesis that a number of properties can be predicted based on the value of the average shape index f_K of VM cast iron. This is particularly important if the f_K indices are determined directly in the casting.

3. Research on the Structure of VM Cast Iron—Determination of the Graphite Shape Indicator

The main goal of research on VM cast iron is to determine the relationships between the broadly understood shape of graphite precipitates in the cast iron structure and its mechanical, physical, functional, and other properties. Therefore, developing a methodology for determining the graphite shape indicator is crucial. Defining the graphite shape indicator for a single precipitate is relatively easy. Several methods for determining it can be found in the relevant literature. Table 2 provides the mathematical definition of the shape indicator in three variants and the range of changes in its value as it transitions from flake-like to mixed (F + V), vermicular (V), mixed (V + S), and finally spheroidal.

Table 2. Graphite shape indicator values ξ, and "f" calculated according to various equations.

Graphite section	**Calculation formula**					
$\frac{\text{Graphite surface area}}{\text{Circle surface area}}$ %	$f = \frac{A_{graph.}}{A_{circle}} \cdot 100$	90.8	79.5	57.5	34.6	12.7
$\frac{\text{Graphite surface area}}{\text{Circle surface area}}$	$f = \frac{A_{graph}}{A_{circle}}$	0.91	0.80	0.58	0.35	0.13
$\frac{\text{Graphite surface area}}{\text{Grapfit diameter (P)2}}$	$\xi = \frac{A_{graph.}}{P^2}$	0.080	0.070	0.060	0.045	0.030

All variants of the shape indicator calculations use the relations between the parameters of the circle described on the graphite precipitate and its actual surface, as shown in Figure 4.

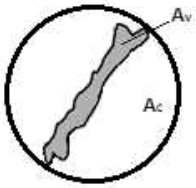
The graphite shape indicator f was determined for each precipitate, acc. to [19], in accordance with the equation (Figure 4 Equation (1)), where:

A_v—surface of the graphite precipitate [mm^2],

A_c—area of the circle of a diameter equal to the highest particle dimension [mm^2].

$$f = \frac{A_v}{A_c} \quad (1)$$

https://doi.org/10.3390/ma19061212



sketch

$$f = \frac{A_V}{A_c}$$

Equation formula (1)

Figure 4. Scheme of shapes of graphite precipitates cross-sections—sketch and formula of defining graphite shape indicator f.

It is important to remember that all attempts to describe the three-dimensional structure of cast iron, particularly the description of graphite precipitates based on a flat image of a metallographic microscope, are always a gross simplification. Table 3 compares an SEM image taken at a fracture of a cast iron sample with an optical microscope image obtained from a metallographic microscope. The images represent various forms of graphite.

To illustrate this degree of simplification, Table 3 presents fracture images obtained using SEM of three types of cast iron, alongside the appearance of the unetched metallographic microscope. In accordance with standards [13,14], the classification and structure description is based on the analysis of metallographic microscope sections using classical optical microscopy. For this reason, but with an awareness of the significant simplification, this work also uses the analysis of a flat image, which, with a plane, intersects the three-dimensional internal structure of the cast iron, as seen in the examples in Table 2.

It is rare for graphite precipitates of uniform shape to occur in the cast iron structure, particularly in grades containing vermicular or nodular graphite. In such a situation, to characterize the cast iron in terms of the shape of the graphite precipitates, an average value of the graphite shape factor must be determined. In this study, the average graphite shape indicator "f_K" was determined by calculating its value as a weighted average. This means that the precipitates observed in the microsections were counted in individual shape groups and size classes. Then, after assigning them a value of the "f" factor, the weighted average shape factor was calculated.

Counting and describing all graphite precipitates in the traditional manner is extremely labor-intensive, even in a simplified version. Therefore, computer software for image analysis and statistical data processing was used. The assessment of graphite precipitate morphology was performed with the support of the ImageJ program ver.1,52a. A new procedure was developed for determining the average value of the graphite shape indicator ("f_K") [2]. The starting point is a metallographic image of cast iron without etching and its electronic recording, shown in Figure 5a. The image is then processed using ImageJ, which provides its recording, as shown in Figure 5b. Particles with sizes d < 0.0785 μm for flake and vermicular graphite and d < 0.010 μm for spherical precipitates were software-rejected. Not all black dots on a metallographic specimen represent graphite precipitates; very small black areas represent micro-voids located at eutectic grain boundaries. Therefore, they were rejected and omitted from further calculations of the graphite shape indicator. ImageJ allows for the analysis of many image element parameters, including graphite precipitates in cast iron. Table 4 summarizes those used to describe and determine the graphite shape index value. As an example, they refer to the image shown in Figure 5b.

https://doi.org/10.3390/ma19061212

Table 3. Spatial and flat images of graphite precipitation in three types of cast iron.

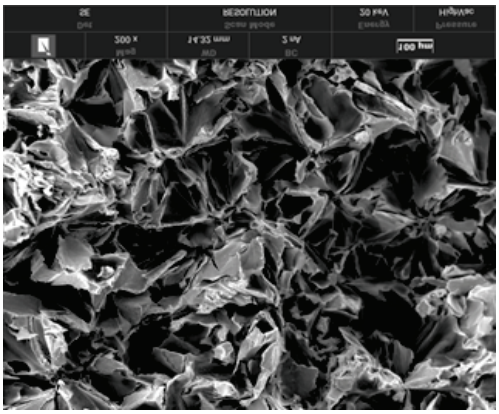
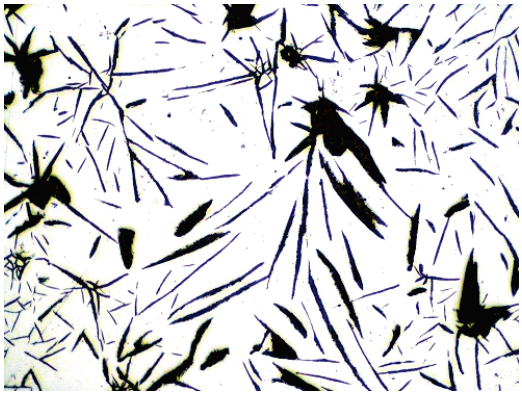
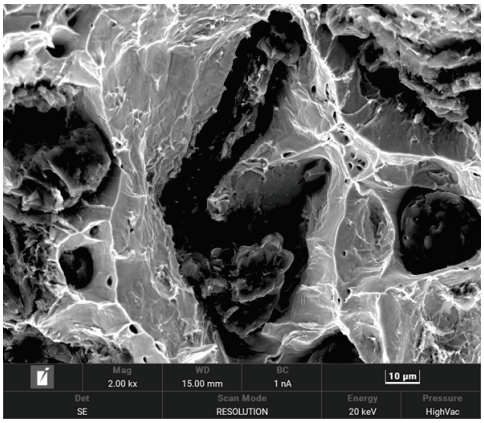
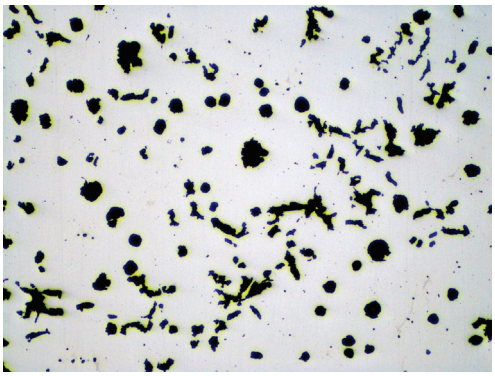
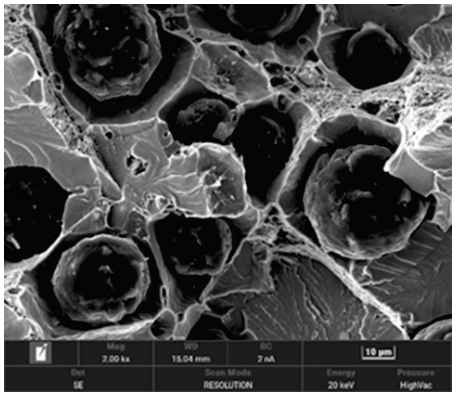
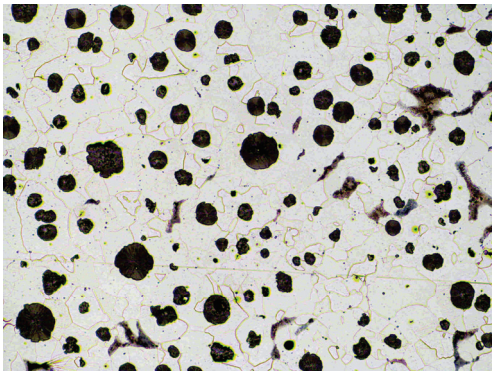
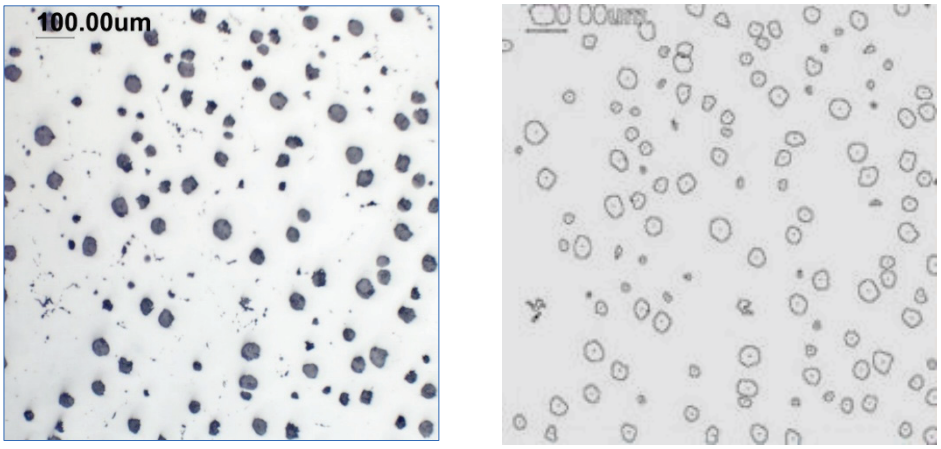
SEM Breakthrough Image	Image of a Metallographic Cross-Section
 a/	 b/
 c/	 d/
 e/	 f/

Table 4. Selected parameters of graphite precipitation in VM cast iron.

Parameter	Value
Average number of precipitates per mm^2	130
Total surface area occupied by graphite precipitates	10%
Average Feret diameter	0.03529440 mm
Average precipitate circumference	0.10759123 mm

https://doi.org/10.3390/ma19061212



(**a**) (**b**)

Figure 5. (**a**) Microstructure—optical microscope. (**b**) Precipitates with a diameter describing graphite d > 0.0785 μm.

The graph below presents the results of the graphite precipitate analysis per mm^2 of the tested surface/sample. Figure 6 shows the number of precipitates and their distribution across diameter classes, and Figure 7 shows the distribution of precipitates across surface size classes of individual graphite precipitates.

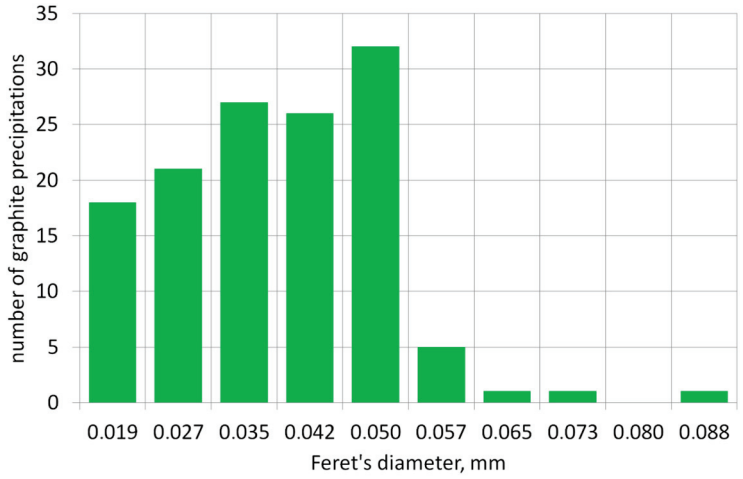


Figure 6. Number of graphite precipitates in Feret diameter size classes.

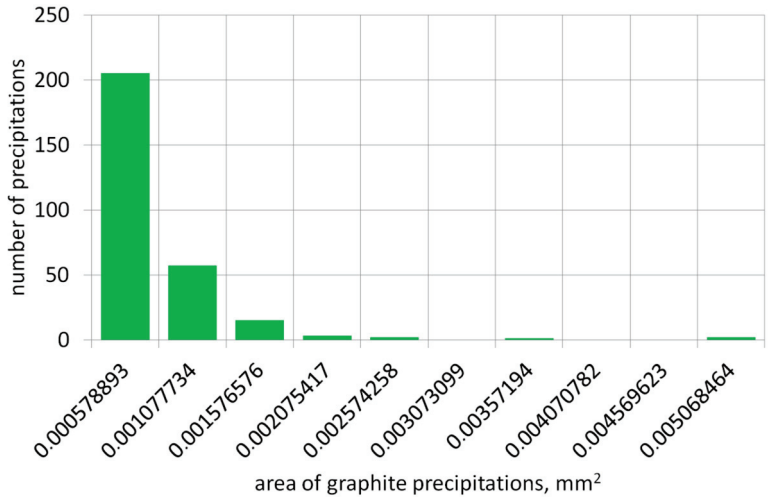


Figure 7. Number of graphite precipitates in surface size classes.

https://doi.org/10.3390/ma19061212

The further procedure for calculating the average value of the shape indicator f_K is performed in an Excel spreadsheet, based on the parameters obtained from ImageJ. For each precipitate, the surface area of the circle circumscribing the graphite precipitate was calculated based on its main dimension. The graphite shape indicator was determined from Equation (2).

$$f = \frac{A_v}{A_c} \tag{2}$$

where:

A_v—surface area of the precipitate,

A_c—surface area of a circle with a diameter equal to the largest dimension of the particle.

The "f" indicator is a number whose theoretical value varies from slightly above 0 to 1.0, but in practice ranges from 0.20 to 0.90. In the literature, characteristic values for uniform graphite morphology of each type of graphite are assumed [20]:

- 0.00–0.34—flake graphite
- 0.35–0.64—vermicular graphite
- 0.65–1.00—nodular graphite

For Vari Morph cast iron, in the methodology adopted by the authors for calculating the average value of the shape indicator f_K, graphite precipitates are grouped into three classes based on their shape, as shown in Table 5. Column 2 provides the number of graphite precipitates in each class, and column 3 provides the percentage share of the total number. Column 4 gives the average (arithmetic) values of graphite shape indices for each shape class calculated from Equation (3). Column 5 gives the average value, which is calculated as a weighted average, according to Equation (3). Equation (3) calculates the sum of the products of the values from column 3 multiplied by the value from column 4 and converted into a dimensionless value.

$$f_K = \frac{\Sigma(\text{participation } \%)\cdot \text{f}}{100} \tag{3}$$

Table 5. Analysis of the shape index "f" and calculation of the average value of the f_K index.

1	2	3	4	5
Graphite Type	Number of Precipitates	Percentage Share [%] (Degree of Spheroidization N)	the Average Value of the "f" Index in the Range	"f_K" Index (Weighted Average)
flake	3	2.4	0.18	0.78
vermicular	15	11.9	0.56	
spheroidal	108	85.7	0.83	
∑	126	100%		

Based on the calculation results summarized in Table 5, the average graphite shape indicator for this example is f = 0.78, which classifies the precipitates as spheroidal graphite. Since the percentage of graphite precipitates meeting the spheroidal shape criterion is 85.7%, the degree of spheroidization for this cast iron is N = 85.7%. Data from the selected example summarized in Table 5 are presented graphically in Figures 8 and 9.

https://doi.org/10.3390/ma19061212

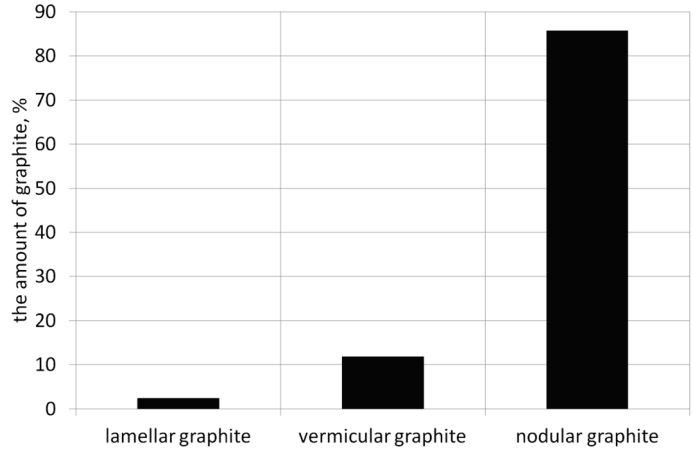


Figure 8. The share of individual types of graphite among all precipitates.

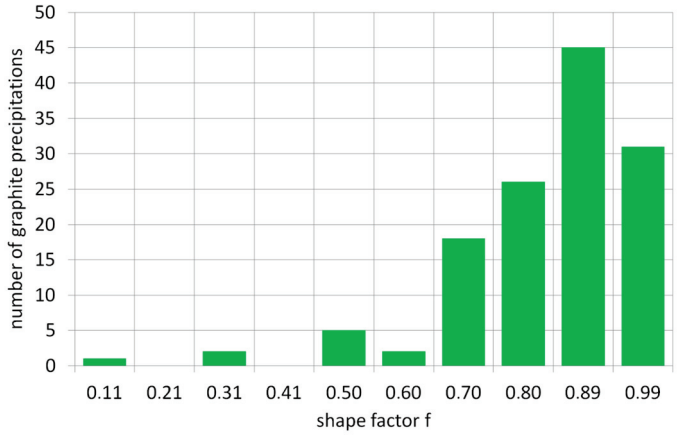


Figure 9. Number of graphite precipitates as a function of the aspect ratio.

ImageJ, as demonstrated by the conducted analysis, offers a wide range of possibilities for a comprehensive quantitative description of graphite precipitates, even when the degree of shape heterogeneity of the graphite precipitates is significant. It allows for the determination of graphite precipitate indices such as:

- the average (weighted average) shape index of graphite "f_K"
- the percentage of three graphite forms (Figure 8): flake, vermicular, and spherical.
- the distribution of graphite precipitate amounts by the "f" index value (Figure 9).
- the degree of spheroidization of cast iron "N," defined as the percentage of graphite precipitates with a shape close to a sphere ($f > 0.65$).

The described methodology and procedure for determining the average shape indicator of graphite precipitates in Vari Morph cast iron have been used in all studies conducted to date in this field [1–11]. It can be assumed that thanks to the application of ImageJ and its adaptation to the description, the image of the structure of graphite precipitates is multi-parameter and sufficient for the needs of scientific analyses as well as practical applications in the study of cast iron grades with a complex structure in terms of the graphite shape, including Vari Morph cast iron.

4. Vari Morph (VM) Cast Iron Production Technologies

The research results presented in this paper represent a synthesis of many years of work by the authors. The first work on developing the Vari Morph cast iron production technology was published in 2018 [1]. The research demonstrated that VM cast iron can be produced using several methods, similar to the production of vermicular or ductile iron [8].

https://doi.org/10.3390/ma19061212

The technologies for producing mixed graphite cast iron are similar to the technologies for vermicular/ductile iron. Based on the analysis of the preliminary research results, the VM cast iron production method was selected, which involves secondary furnace treatment with low-magnesium alloys (master alloys), FeSiMg. This is a variant of producing cast iron that initially contains a limited sulfur content (S < 0.01%) by introducing a strictly controlled amount of magnesium (Mg < 0.03%), shown in Figure 3. The introduction of a controlled amount of Mg was accomplished in three ways (three methods):

(a) PE rod method—using a flexible hose containing low-magnesium FeSiMg mortar introduced into a ladle with a lid.
(b) Using low-magnesium mortars dosed to the bottom of tightly closed ladles (slim ladles—Tundish method).
(c) Inmold technology, placing low-magnesium mortars in reaction chambers constructed in a casting mold.

4.1. Controlled Magnesium Content Method

Pure magnesium or a magnesium mortar is added to the molten metal in an amount smaller than necessary to obtain nodular graphite. In vermicular cast iron, the final Mg content ranges from 0.01 to 0.03%, shown in Figure 3. After adding magnesium, modification is performed, usually with ferrosilicon-based modifiers, as in the production of ductile iron. Obtaining vermicular cast iron is difficult in industrial practice because the range of magnesium content in the cast iron at which graphite crystallizes in the vermicular form is very narrow. To produce VM cast iron with flake + vermicular graphite, the magnesium content must be maintained below 0.02%. To obtain VM cast iron with vermicular + nodular graphite, the Mg content should be maintained within the range of Mg = 0.02–0.03%. The indicated Mg contents apply to cast iron with a low sulfur content (S < 0.01%), and no magnesium is used for desulfurization. Excess Mg (Mg > 0.03%) will result in the formation of nodular graphite, while too little Mg will result in flake graphite. Such cast iron is also more susceptible to vermicularization failure than cerium-treated cast iron.

4.2. Proprietary Technologies to Produce Vari Morph Cast Iron

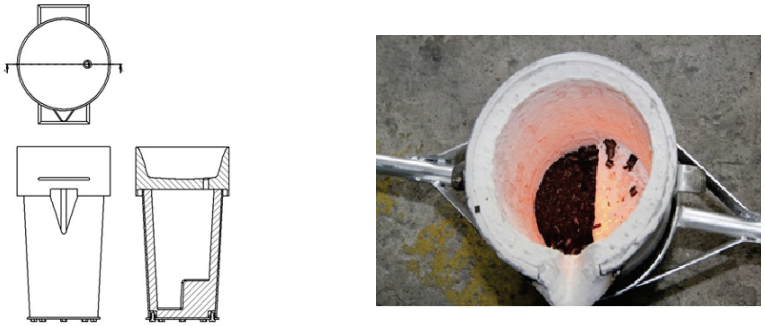
The research was initially conducted in the experimental foundry of the Faculty of Foundry Engineering at the AGH University of Science and Technology in Cracow, and then in a selected industrial foundry. The controlled Mg content method was chosen, and the spheroidization process was conducted using a ladle with a tight lid (Tundish technology) and the flexible conduit (PE) method. Inmold spheroidization was also performed under industrial conditions. Cast iron with a mixed graphite form (Vari Morph) is obtained using this technology by introducing a reduced amount of Mg compared to the amount in ductile iron. Therefore, the secondary metallurgy process, introducing Mg in a strictly controlled amount, can still be referred to as the spheroidization process of cast iron. This term is used throughout this paper. In the case of VM cast iron, spheroidization is incomplete, and the form of graphite precipitates varies widely across the three basic fractions in which it occurs in cast iron: flake (L), vermicular (V), and nodular (S).

Figures 10 and 11 show the experimental foundry layout, while Figures 12 and 13 show the industrial layout. Figure 10a shows a sketch of the experimental Tundish ladle, and Figure 10b shows the heated vat with magnesium solution.

In the second solution of the Vari Morph cast iron production technology, spheroidization of cast iron was performed using the PE (flexible core wire) method. The experimental setup is shown in Figure 11. The cast iron spheroidization process involves introducing a steel tube (thin-walled pipe) filled with FeSiMg mortar, typically containing 16–23%

https://doi.org/10.3390/ma19061212

magnesium, into the liquid metal. The process was carried out with full control of the rod immersion rate and the amount of mortar introduced, or more precisely, the amount of Mg introduced into the cast iron. The production of Vari Morph cast iron requires strict control of the amount of Mg introduced into the cast iron.



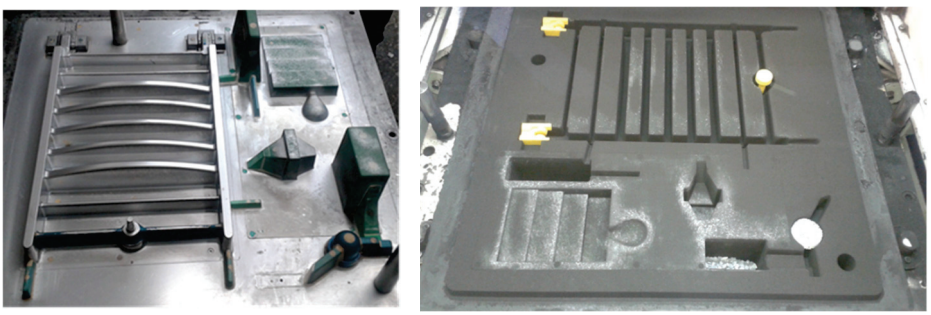
(**a**) (**b**)

Figure 10. Slim, tightly covered ladle (Tundish): (**a**) sketch of the ladle: (**b**) FeSiMg mortar in the pocket of the heated Tundish ladle.



(**a**) (**b**)

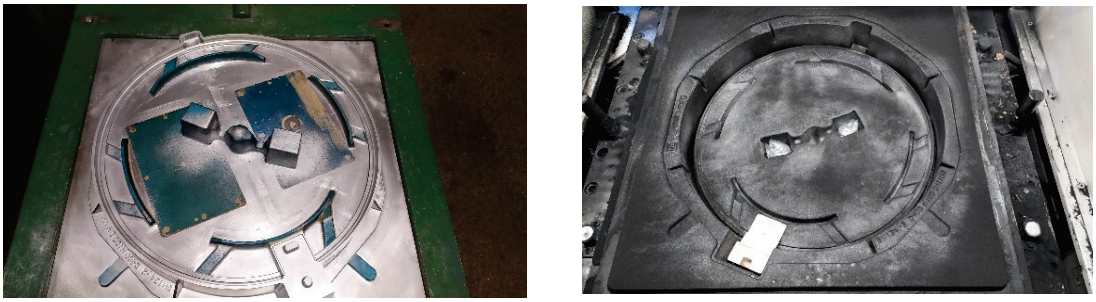
Figure 11. Experimental stand for spheroidization using the PE method (**a**) inserting the PE rod into the cast iron in the crucible with a cover. (**b**) metal in the crucible after spheroidization.



(**a**) (**b**)

Figure 12. Test technology of Vari Morph cast iron casting in the Inmold process on the FBO line: (**a**) lower pattern plate, (**b**) lower mold before assembly and pouring.

https://doi.org/10.3390/ma19061212



(**a**) (**b**)

Figure 13. Pattern plate and sand mold of the road manhole body made of Vari Morph cast iron using Inmold technology on the FBO line; (**a**) pattern plate, (**b**) lower sand mold.

Production trials of Vari Morph cast iron were also conducted under industrial conditions as part of NCBiR projects [8]. Test ingots and test castings were made in molds with a horizontal surface on an automatic FBO molding line (Figure 12). The production of a drainage grate for street sewage was tested. Tests of the casting before its release for serial production include a test of the structural strength of the casting, which is determined by the ultimate strength of the material itself (R_m, R_{02}) and the casting design. It can be produced from various grades of cast iron, including Vari Morph cast iron with a graphite structure: vertical + spheroidal. The technology was evaluated on ingots/samples visible on the pattern plate (Figure 13a) and on the mold image shown in Figure 13b. The amount of magnesium introduced into the cast iron to obtain Vari Morph cast iron was controlled by selecting/calculating the amount of FeSiMg6 mortar introduced into the reaction chamber (Figure 13b). Inmold technology is the most stable and repeatable technology, in which the degree of magnesium assimilation is the highest, as is the quality of the cast iron in the casting. The quality of the cast iron results from the short time between the process of introducing magnesium into the metal and the solidification of the cast iron.

Research conducted in both the experimental foundry and industrial settings aimed to assess the feasibility of producing Vari Morph cast iron in a repeatable manner, with the intended structure of graphite precipitates, as well as to assess the possibility of creating selected physical, mechanical, and functional characteristics and properties. Comparison of three cast iron spheroidization methods allowed us to verify their effectiveness in introducing magnesium from FeSiMg master alloys into cast iron. This indicator is called the Mg assimilation rate and is a measure of the effectiveness of each method. The highest Mg assimilation efficiency is achieved with the Inmold technology (65–75%), slightly lower with the Tundish ladle spheroidization technology (55–60%), and the lowest with the PE flexible hose technology (30–35%). The Mg assimilation rate in each case and technology depends on a number of factors, including the cast iron temperature, sulfur (S) content, and oxygen (O_2) content. However, the ranking of these technologies remains as indicated above.

This paper summarizes the results of research on unalloyed cast iron with a chemical composition close to the eutectic value (S_c~1.0; CE~4.30) and reduced manganese content (Mn < 0.25). In most cases, the cast iron had a ferritic matrix, which allowed for the assessment of the effect on physical and mechanical properties of the graphite precipitate form, rather than the matrix type. The results of this work allowed for the determination of a number of empirical relationships between the graphite shape index and selected properties.

The group of cast iron grades whose chemical composition oscillated near the eutectic value was subject to investigation (C = 3.3–3.6%, Si = 2.6–2.95%, Mn < 0.25; P < 0.02%; S < 0.01%; Mg = 0.005–0.040%).

https://doi.org/10.3390/ma19061212

5. Research Results

5.1. Preparation of Research Material

Research on Vari Morph cast iron, in the first period, aimed to determine empirical relationships between the graphite shape, described by the shape indicator f_K, and selected basic physical, mechanical, and functional properties [1–6]. In the second period, using and supplementing the earlier research, the aim was to determine similar relationships, but not so much as a function of the graphite shape indicator f_K, but as a function of the basic parameter of ultrasonic wave propagation, i.e., its velocity. The relationship between the shape of graphite precipitates and wave velocity is generally known from many studies: the more compact the shape of the precipitates, the higher the velocity, which for the entire range of graphite shape changes ranges from approximately 3700 to 5900 m/s. Wave velocity is clearly less dependent on the metallographic matrix: pearlitic or ferritic. For the same form and amount of graphite, differences in wave velocity are within several hundred meters (200–400 m/s) [9,10].

The research presented below involved ferritic cast iron with a composition of approximately eutectic CE~4.26. Table 6 provides the chemical composition of cast iron from several dozen melts carried out in experimental foundries and industrial foundries. The ferritic matrix was obtained by limiting the content of elements that promote the formation of a pearlitic structure, and the basic composition was limited to Mn content < 0.10%.

Table 6. Chemical composition of basic elements.

C [%]	Si [%]	Mn [%]	P [%]	S [%]	Mg [%]
3.3–3.6	2.6–2.95	<0.1	<0.02	<0.01	0.005–0.065

Cast iron was prepared in induction furnaces from a charge consisting of blast furnace pig iron and cast iron scrap in varying proportions, depending on the actual composition of the charge materials. Furthermore, carburizer and ferrosilicon were added to the metal bath to regulate the composition of the starting cast iron. In the final melting phase and after the spheroidization process, a modification and secondary modification process were performed to refine the grains. In the final melting phase, the metal was briefly superheated to 1500–1520 °C to achieve degassing and flush out impurities. The pouring temperature ranged from 1420–1450 °C.

The test ingots themselves, in accordance with the standards in force in this respect, are type Y2 ingots. The ingots were cast from furan resin-based sands. During each test run, samples were also collected for spectrometric analysis. In all tests, the cast iron composition was carefully selected (Table 6) to allow for comparison of the tested material regardless of the casting location and spheroidization method. Among several methods for producing cast iron with controlled graphite content, the method of controlled residual Mg content in cast iron was selected for this study. To achieve the full spectrum of graphite precipitation forms, the Mg content varied (was controlled) from 0.005% to over 0.065%.

5.2. Determination of Empirical Dependencies

As mentioned earlier, the aim of the research was to determine the empirical relationship between ultrasonic wave velocity in Vari Morph cast iron and its physical, mechanical, and functional properties. The goal is to enable future practice to predict selected properties of Vari Morph cast iron based on non-destructive ultrasonic testing of castings. The ultrasonic testing described below was performed using Unipan CT-3 ultrasonic material testers with 2.0 MHz transducers. Wave velocity was assessed on a Y2 sample ingot, from which test samples were subsequently prepared. Figure 14 shows the key relationship

https://doi.org/10.3390/ma19061212

obtained in the research: the relationship between the graphite shape index (f_K) and the velocity of the longitudinal ultrasonic wave (C_L). These two quantities, closely related to the shape of graphite precipitates, are well correlated. Wave velocity follows the spatial structure of the graphite precipitates, while the shape indicator is described by a flat image visible on the surface of the metallographic microsection. The more compact the graphite, the less dispersion of the propagating ultrasonic wave, resulting in its higher velocity. The greatest changes in wave velocity are observed in cast iron with a spatially expanded form, when the shape factor f_K reaches values below 0.50–0.60.

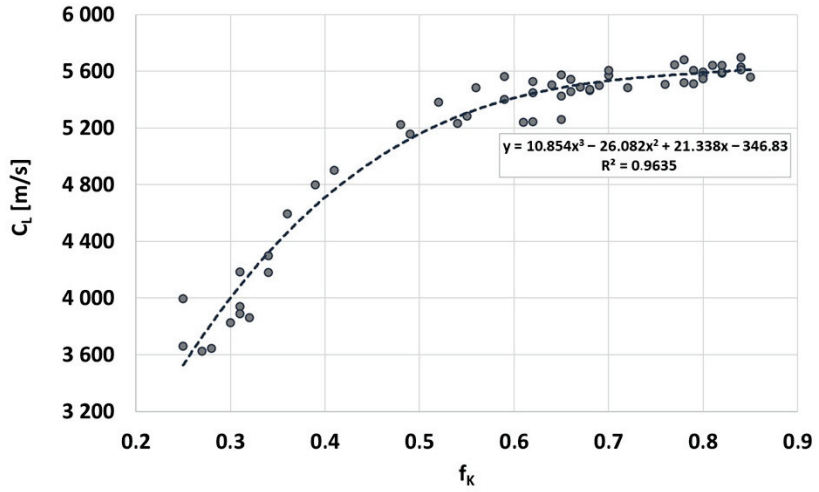


Figure 14. Relationship between the shape index of graphite precipitates f_K and the ultrasonic wave velocity in ferritic cast iron Vary Morph.

If the quantity measured in the sample/casting is the wave velocity, then on its basis and using the relationship in Figure 14, the value of the graphite shape indicator can be assessed, as shown in Figure 15. Measuring the ultrasonic wave velocity in a sample/casting made of Vari Morph cast iron, thanks to the connection with the graphite shape indicator f_K, allows for indirect determination of all physical and mechanical properties of cast iron that depend on this particular f_K indicator. These properties and their dependencies on the f_K indicator value are described in [5,6].

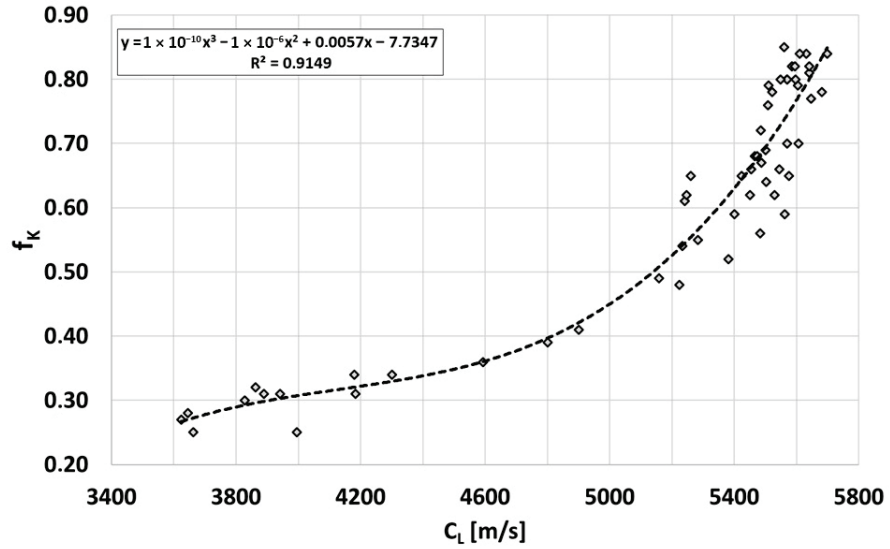


Figure 15. Relationship between the ultrasonic wave velocity and the shape indicator of graphite precipitates f_K in ferritic cast iron Vary Morph.

When only the form of graphite changes in cast iron and the matrix is ferritic, the relationship between wave propagation velocity, the f_K indicator, and specific density can be determined, as shown in Figure 16. Density depends on the form of graphite, but determining an averaged shape indicator is difficult. It is easier to determine the velocity of the ultrasonic wave. Therefore, the authors searched for relationships between wave velocity and a whole group of physical and mechanical properties, knowing that in reality, they depend on the form of graphite precipitates (f_K), as shown in Figure 16.

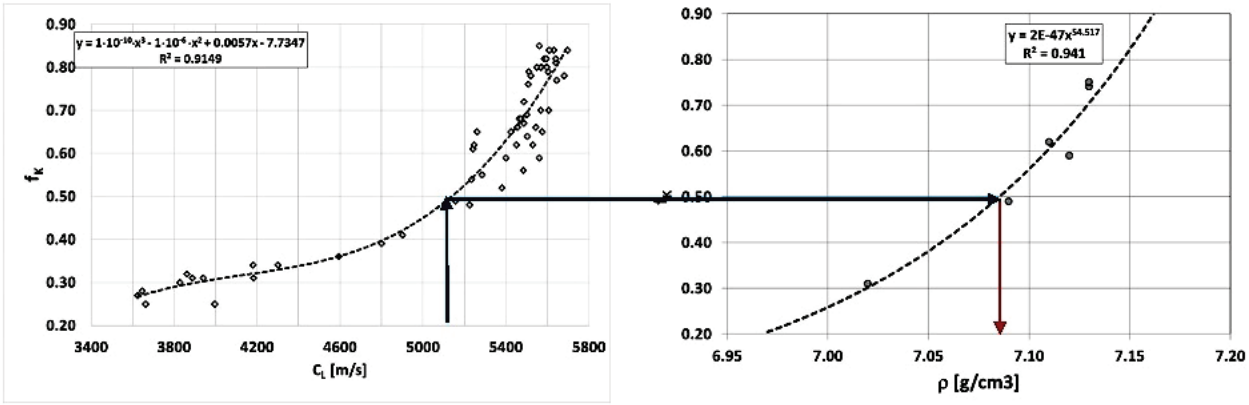


Figure 16. Interdependence of wave propagation velocity, averaged graphite shape index and specific density of ferritic Vari Morph cast iron.

Further descriptions of the test results will present direct relationships between wave velocity in Vari Morph cast iron and the selected feature/property of the cast iron. The density of the cast iron was determined gravimetrically by measuring the sample weight in air and ethyl alcohol [5,6]. In the case of density tests, the obtained relationship is as shown in Figure 17. Within the tested range of density variation, which depends on the amount of graphite, the relationship $\rho = f(C_L)$ is linear. The more compact the graphite form and the associated higher wave velocity, the higher the density.

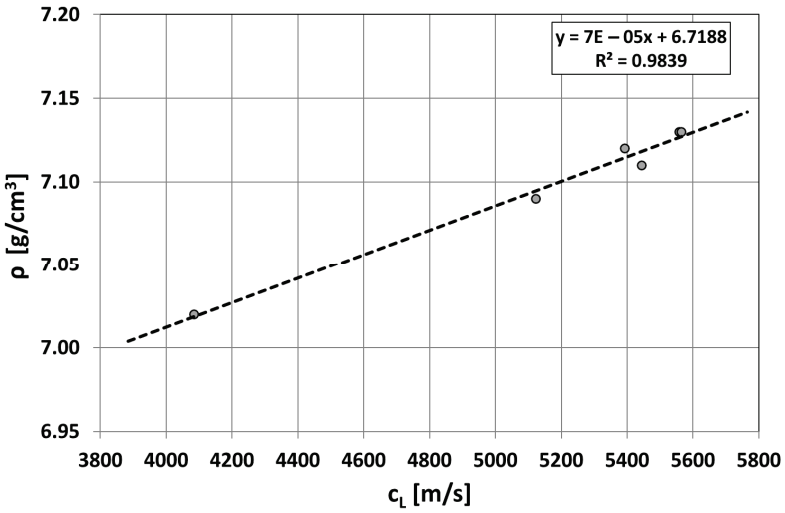


Figure 17. The relationship between the ultrasonic wave propagation velocity and the specific density of ferritic cast iron Vari Morph.

An important property and characteristic of Vari Morph cast iron is thermal conductivity (λ), which can vary widely with the shape of the graphite precipitates (f_K). Many structural elements or structures themselves require thermal conductivity of a specific value, either smaller or larger. This is the case for vehicle brake discs, combustion engine

https://doi.org/10.3390/ma19061212

housings, manifolds, and metallurgical equipment such as slag ladles and steel ingot molds, for which cast iron should be characterized by high thermal conductivity. The authors conducted research in this area, seeking an easy method for non-destructively determining the thermal conductivity of Vari Morph cast iron not only in test ingots but also in finished products/castings. The results of this work and the research methodology have been described in previous publications. The determined relationship of thermal conductivity (λ) as a function of longitudinal wave propagation velocity (C_L) is presented in Figure 18.

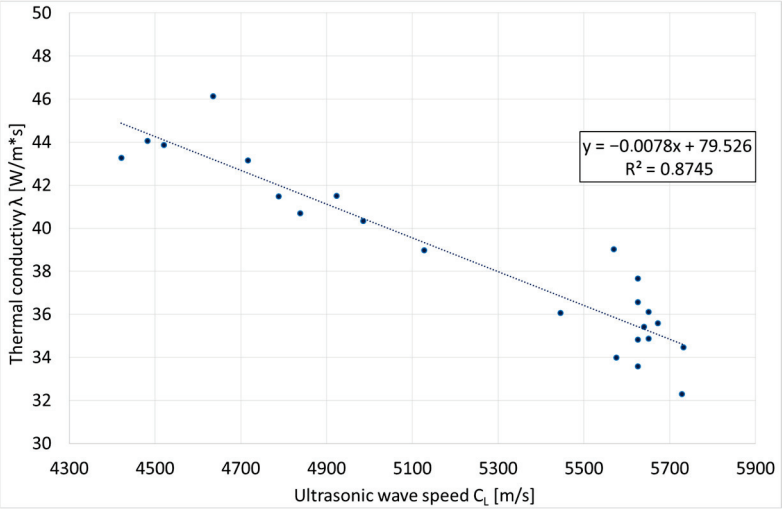


Figure 18. Relationship between ultrasonic wave propagation velocity (C_L) and thermal conductivity of ferritic Vari Morph cast iron [4].

Within the tested range of variability of Vari Morph cast iron, it is described by a linear equation. The expanded form of graphite promotes good thermal conductivity. For this reason, brake discs are manufactured from gray cast iron with a flake-like graphite form. Measuring thermal conductivity directly in castings has a significant advantage: the obtained results are averaged values. The metallographic structure on the cross-section of the wall of cast iron castings can vary widely. Averaging the conductivity values resulting from the measurement technique provides an image of the ability of heat to flow through the entire casting wall. This assesses the heat transfer capacity of the object/casting. In conventional thermal conductivity testing methods, thermal conductivity is most often performed on relatively small or very small samples (laser thermal diffusivity testing method). Translating from such a determined thermal conductivity to assessing the heat transfer capacity of a large object/casting is extremely difficult and often fraught with error.

The dynamic modulus of elasticity E_D, determined on the basis of a simplified equation using the measurement of wave velocity and specific density ($E_D = \rho \cdot (C_L)^2$) in Vari Morph cast iron varies within wide limits, along with the change in the average graphite shape index f_K, shown in Figure 19. The main changes in the modulus of elasticity are observed in cast iron with the shape index of graphite precipitates $f_k < 0.6$.

The form of graphite precipitates significantly affects both the strength (R_m) and ductility of cast iron (A5). The influence of the graphite shape index f_K on these properties in Vari Morph cast iron was described by the authors in previous works. Because graphite shape indexes and ultrasonic wave velocity are well correlated, the authors determined the following relationships for Vari Morph cast iron: $R_m = f(C_L)$ and $A5 = f(C_L)$, shown in Figures 20 and 21. These relationships apply to cast iron with a ferritic matrix. The ductility of cast iron measured by its elongation in a tensile test is characterized by a greater scatter of results and a lower correlation coefficient.

https://doi.org/10.3390/ma19061212

The IQ (Index Quality), defined for cast iron as the ratio of strength to hardness (IQ = R_m/HB), is generally a measure of cast iron quality. In the case of VM cast iron, it specifically describes its quality. Changes in form have virtually no effect on the HB of the cast iron, which is determined by the type of matrix. The IQ value of cast iron increases in ferritic VM cast iron in proportion to the increase in the graphite aspect ratio [2,5,6]. In ultrasonic inspection of Vari Morph cast iron, with increasing speed, the QI value increases progressively, shown in Figure 22. The definition of the IQ index suggests that an increase in its value indicates a greater increase in strength than in hardness, which is caused by changes in the metallographic structure. This tendency to increase R_m while maintaining a constant HB is particularly advantageous in the case of subtractive/finishing machining of cast iron castings. Ferritic matrix castings, despite the high strength obtained by increasing the graphite aspect ratio "f_K," can be very easily machined using CNC machine tools.

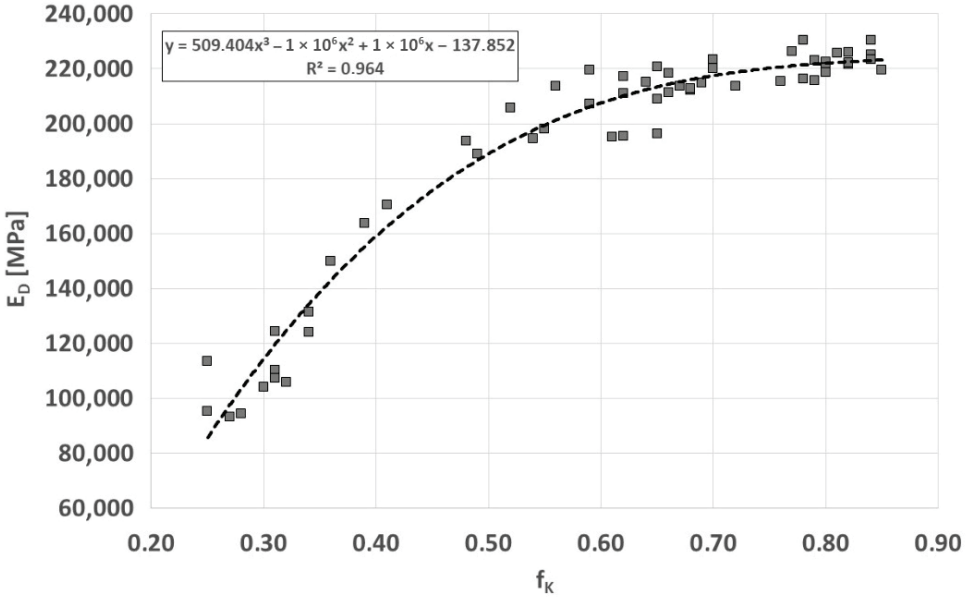


Figure 19. Relationship between the averaged shape index f_K of graphite and the dynamic modulus of elasticity of ferritic cast iron Vari Morph.

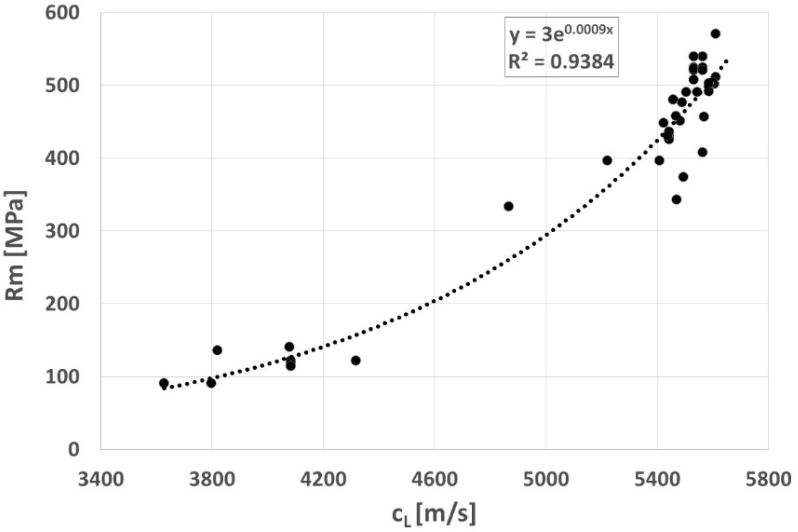


Figure 20. Relationship between ultrasonic wave velocity (C_L) and strength R_m of ferritic cast iron Vari Morph.

https://doi.org/10.3390/ma19061212

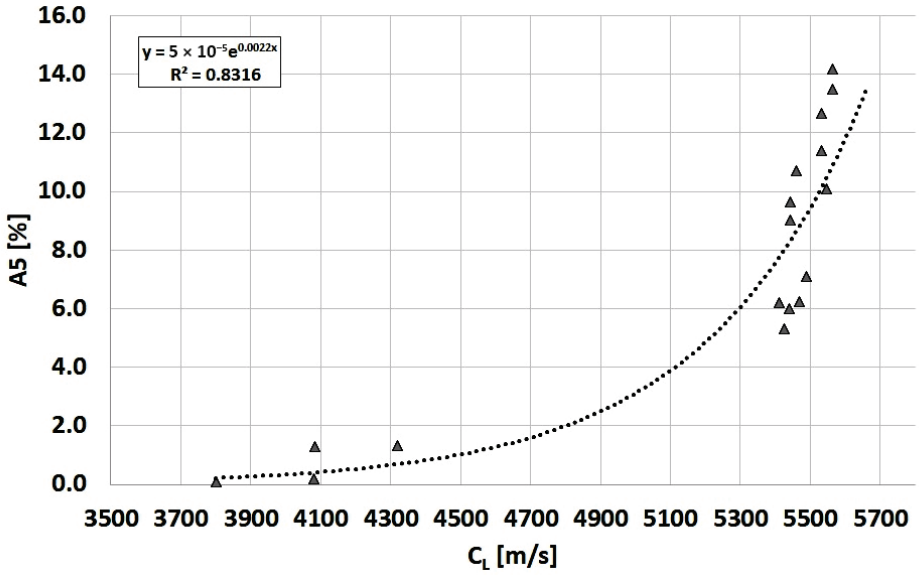


Figure 21. Relationship between ultrasonic wave velocity (C_L) and A5 elongation of ferritic Vari Morph cast iron.

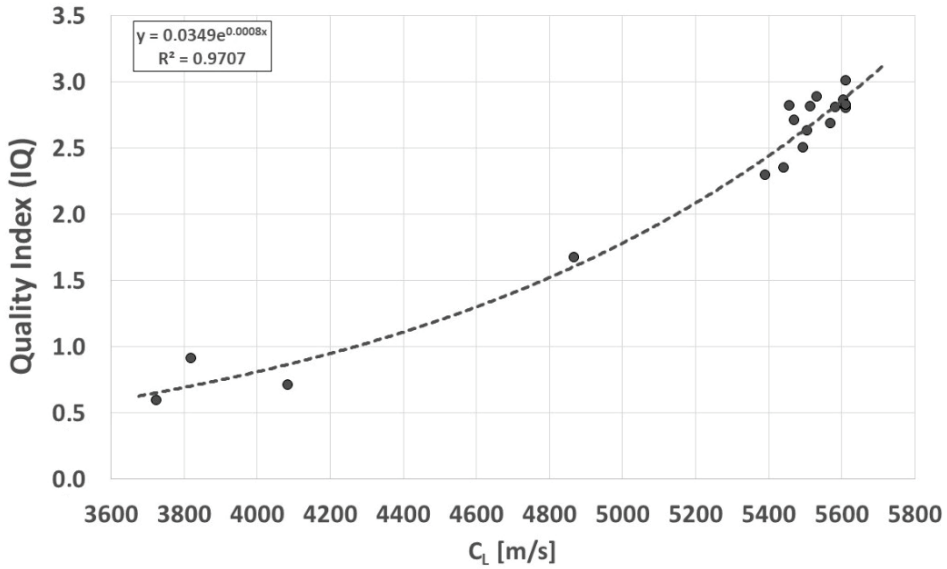


Figure 22. Relationship between ultrasonic wave velocity (C_L) and iron quality index (IQ) of ferritic Vari Morph cast iron.

Thermal fatigue resistance of metals is one of the most complex functional properties of metals, generally dependent on the metallographic structure of the alloy and the operating conditions of the component. The complexity of this property stems from the fact that it is linked to such physical and mechanical properties as thermal conductivity and expansion, elasticity, plasticity, and strength (including at elevated temperatures). Many methods exist for testing thermal fatigue resistance. This paper presents the results of thermal fatigue resistance tests obtained using resistance heating of rod-shaped samples (L.F. Coffin's method [10,11]). Vari Morph cast iron with a ferritic matrix was tested. An empirical relationship was determined between the thermal fatigue resistance of cast iron (the number of thermal cycles N to sample fracture) and the graphite shape indicator (f_K): $N = f(f_K)$, as well as a relationship in which the cast iron structure was assessed using ultrasonic testing: $N = f(C_L)$. Both relationships are power-law functions—as the graphite shape indicator increases, the thermal fatigue resistance of cast iron increases. Similarly, as the

https://doi.org/10.3390/ma19061212

wave velocity in the tested samples increases, their thermal fatigue resistance increases. The influence of the shape of graphite precipitates on thermal fatigue resistance is shown in Figure 23. The tests were conducted in the temperature range of the 200–650 °C cycle. Quantitatively, and at a slightly higher maximum temperature (200–700 °C range), the relationship shown in Figure 24 was obtained for ferritic cast iron. Therefore, based on the measurement of ultrasonic wave velocity, the behavior of cast iron (a part made of cast iron) under cyclic heating conditions can be predicted. Naturally, this is an estimate, as the actual resistance and durability of components operating under cyclic heating conditions depends on several other factors, including the degree of free thermal expansion of the heated component [12].

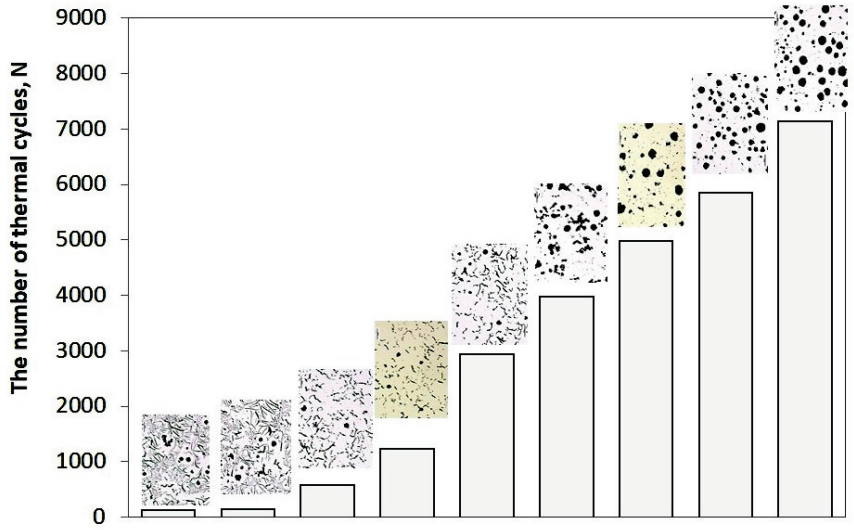


Figure 23. The influence of the form of graphite precipitations on the thermal fatigue resistance of cast iron determined using the L.F. Coffin method, T_{min} = 200 °C; T_{max} = 650 °C.

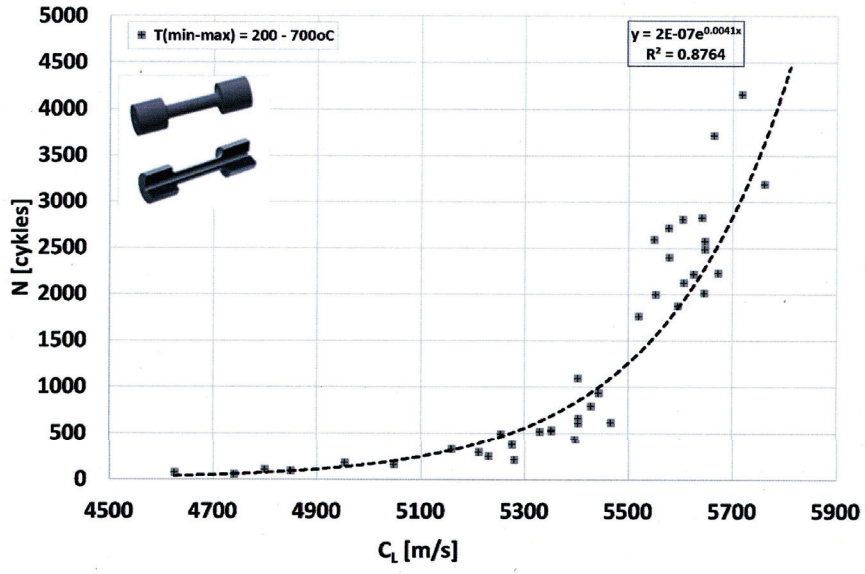


Figure 24. Relationship between ultrasonic wave velocity (C_L) and thermal fatigue resistance of ferritic Vari Morph cast iron. L.F. Coffin method, test parameters; T_{min} = 200 °C; T_{max} = 700 °C.

Low-cycle mechanical fatigue, the material's resistance to this type of loading in the case of cast iron, is primarily dependent on the form of graphite precipitates, the graphite shape indicator f_K. Mechanical fatigue tests were conducted under classical bending conditions on samples clamped unilaterally. Bilateral symmetrical bending was performed

https://doi.org/10.3390/ma19061212

at a frequency of 4 Hz and an amplitude of 2.0 mm. The tests were conducted on a prototype test stand shown in Figure 25a. The samples were designed so that the stress value along the entire length of the sample was approximately constant during bending, as shown in Figure 25b.

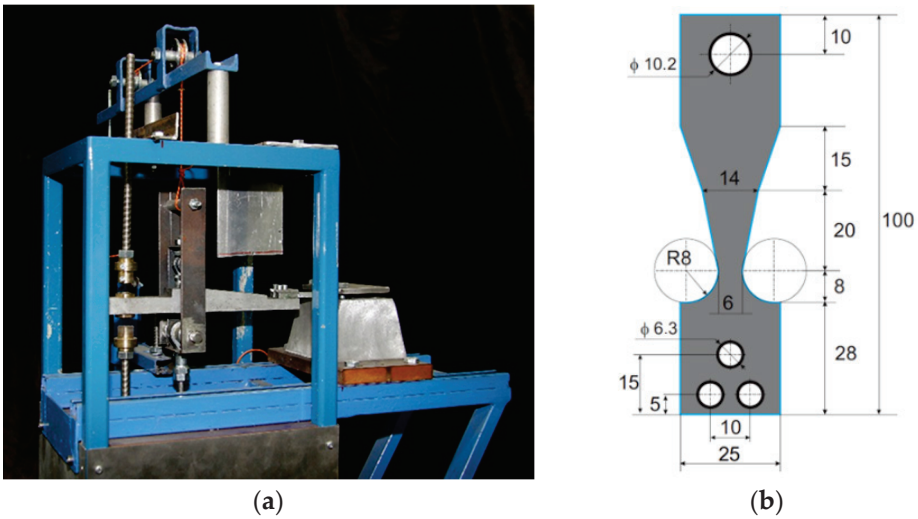


Figure 25. Appearance: (**a**) low-cycle fatigue test stand, (**b**) sample subjected to bending.

The aim of this study was to determine the relationship between the form of graphite precipitates, controlled indirectly by measuring the ultrasonic wave velocity (C_L), and the number of bending cycles (Z_c) that the sample endures before fracture. Figure 26 shows the obtained empirical relationship $Z_c = f(C_L)$. This relationship is of a power-law nature, confirming the significant influence of the graphite form on the low-cycle fatigue resistance of VM cast iron.

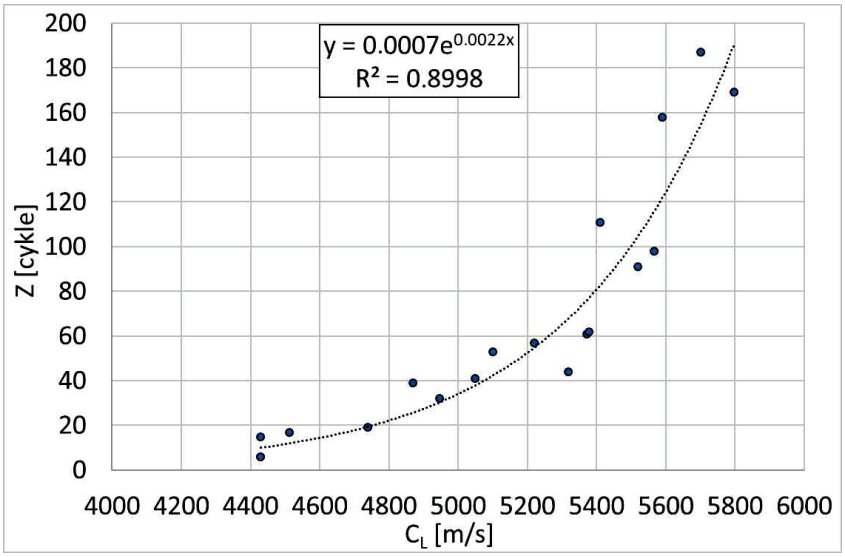


Figure 26. Relationship between ultrasonic wave velocity (C_L) and low-cycle mechanical fatigue (bending) resistance of ferritic Vari Morph cast iron.

Tightness is the ability of a wall to resist liquids and gases that exert a specific pressure on it and attempt to penetrate it. This material characteristic, in the case of cast iron castings, is of particular importance in many manufacturing sectors. This is primarily the automotive industry, the construction of electric motors, compressors, water and gas fittings, boilers, and radiators, where tightness is the primary criterion for assessing casting

https://doi.org/10.3390/ma19061212

quality. In research on the effect of graphite precipitate shape on the tightness of "Vari Morph" cast iron, with variable graphite form, an empirical relationship was sought between the cast iron's tightness index (e.g., time to penetration at constant pressure) as a function of the average shape index "f_K." The authors described the results of these studies in [12]. The tests were conducted on samples made from test ingots; the dimensions of the sample and test stand construction are given in Figure 27. A pressure of P = 20 MPa was applied to the sample in a measuring head filled with measuring liquid (technical kerosene), and the time required for the medium to penetrate the sample surface was determined. Vari Morph cast iron with various f_K index values was tested. The tightness measurement results as a function of the ultrasonic wave velocity characteristic for each sample are presented in Figure 28. Ultrasonic wave velocity in VM cast iron can be a good indicator of the predicted tightness of cast iron castings. Its measurement on finished iron products/castings can be helpful in assessing the suitability of these products for high-pressure operation—structures/die-castings. The higher the C_L velocity, the more compact the graphite (the higher the f_K index value) and the greater the tightness of the casting.

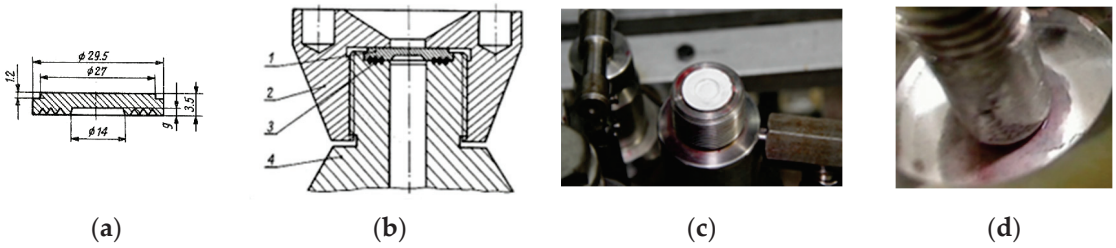


Figure 27. Sketches and photos of cast iron tightness sample and laboratory stand. (**a**) Cast iron leak test sample; (**b**) Sketch of the device head: 1-sample, 2-nut, 3-gasket, 4-head; (**c**) Placing the sample in the measuring head; (**d**) Medium permeation through the sample.

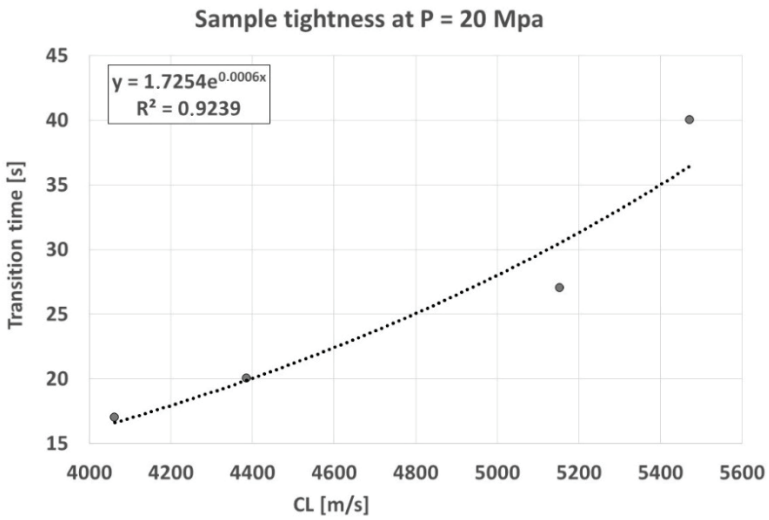


Figure 28. Relationship between ultrasonic wave velocity (C_L) and tightness of ferritic cast iron Vari Morph.

Summary: Work on the technology of production and application of cast iron with graphite in vermicular and compact form was carried out by many authors and is described, among others, in works [18–23]. The presented results of multidirectional research constitute a synthesis of several years of work by the authors on cast iron with a variable but intentionally controlled form of graphite precipitations in cast iron with a ferritic matrix. They complement the results described in [1–7,12]. This time, attention was focused on finding the relationship between ultrasonic wave propagation in Vari Morpf cast iron

https://doi.org/10.3390/ma19061212

and a group of physical, mechanical, and functional properties. The wave velocity, as shown in the work, is well correlated with the form of graphite precipitations, which is a leading factor for almost all (except HB) properties of cast iron. The following empirical relationships were determined: $C_L = f(f_K)$, density as a function of $\rho = f(C_L)$; modulus of elasticity $E_D = f(C_L)$; thermal conductivity $\lambda = f(C_L)$; tensile strength $R_m = f(C_L)$; elongation $A5 = f(C_L)$; cast iron quality index $IQ = f(C_L)$; thermal fatigue resistance $N = f(C_L)$; tightness of cast iron $H = f(C_L)$. The described relationships are relatively well correlated and can be used in practice to predict/forecast the properties in the walls of castings made of ferritic Vari Morph cast iron as well as to predict the behavior of structures/castings under specific operating conditions, e.g., when tightness of castings is required or when castings are subject to thermal fatigue.

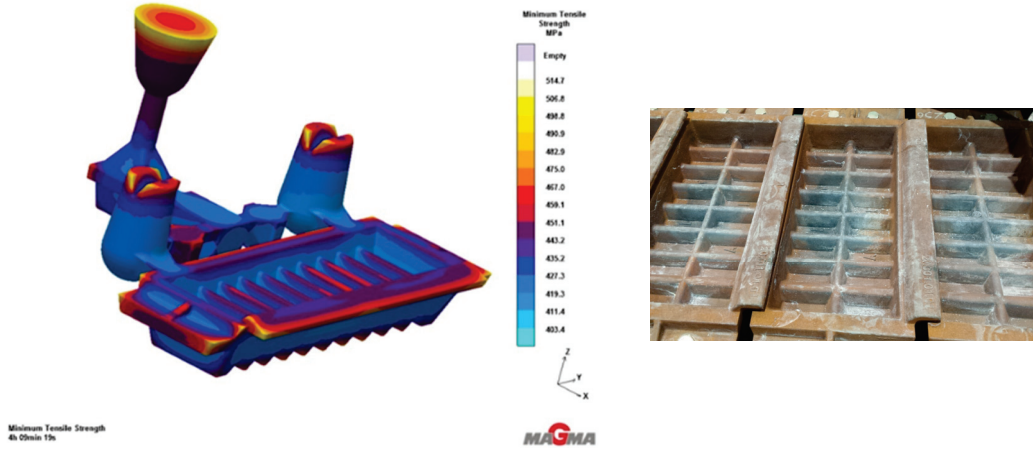
6. Examples of Mixed Graphite Iron Castings (Vari Morph)

In industrial applications, mixed graphite castings are very common, primarily in the production of vermicular or ductile iron. They can be incorporated into the casting structure, with different metal crystals in the wall. This occurs due to separate effects that can be caused by spheroidization and pouring momentum through the molds. Naturally, the diversified graphite structure applies to cast iron grades that are subject to an independent spheroidal casting method in the liquid state. However, the ruling notice should not be considered a classification as Vari Morph cast iron. VM is a grade of cast iron with mixed graphite, whose VM structure was intentionally created using the spheroidization process. The characteristics of cast iron obtained through the use of non-standard cast iron grades are available from the perspective of their practical application. Thanks to the new configuration of the graphite precipitates, it is possible to control properties such as resistance to temperature changes and thermal shocks, tightness of cast iron, extended range of quality IQ and higher efficiency at a comparable or additional R_m values.

A good example of the use of VM cast iron is all kinds of ingot molds, whose properties are a compromise between good thermal conductivity (Figure 18) and high resistance to thermal fatigue (Figure 24). Ductile iron (low thermal conductivity) does not meet these expectations, while vermicular cast iron (moderate resistance to thermal fatigue) is also not the best material to work in the conditions described. It would be advantageous to use VM cast iron with a graphite shape index f_K in the range of 0.60–0.75, which corresponds to the wave velocity range C_L = 5450–5550 m/s. An example of such a casting, an ingot mold for pouring aluminum, is shown in Figure 29 [21].

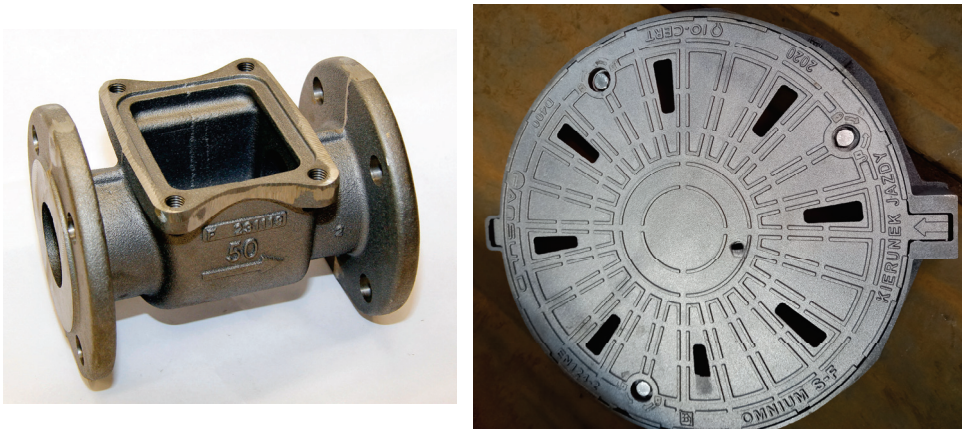
The group of castings tested from Vari Morph cast iron within the project [8] includes gas meter valve bodies, which are expected to be highly tight (Figure 30a), and castings dedicated to road sewers—manhole covers and sewer grates (Figure 30b). Valve bodies are currently made of EN GJL—250 cast iron; replacing it with Vari Morph cast iron allows for reducing the wall thickness by at least 10% while maintaining the required tightness. In the case of manhole covers, to maximize the weight of the castings, the covers are made of ductile cast iron EN GJS 500-7. Channel bodies in which mainly compressive stresses occur during operation can be made of VM cast iron, which in the Inmold technology is easily achieved by reducing the amount of FeSiMg mortar dosed into the reaction chamber. VM cast iron dampens vibrations more effectively, which helps extinguish them after a vehicle wheel passes through the hatch. This arrangement is recommended for micro-environment-friendly operation of the body and cover assembly (quiet operation). In Reference [5], the authors provide further examples of the use of Vari Morph cast iron in various technical and industrial sectors.

https://doi.org/10.3390/ma19061212



(**a**) (**b**)

Figure 29. Ingot molds for pouring Al-Si alloys made of vermicular cast iron and Vari Morpf—Inmold technology; (**a**) pouring and solidification simulation in Magma Soft 6.1-Cast Iron, (**b**) castings on the pouring line.



(**a**) (**b**)

Figure 30. Examples of applications of Vari Morph cast iron: (**a**) for castings with increased tightness—gas meter valve body; (**b**) for castings with increased strength and the ability to dampen vibrations (silence operation)—D400 manhole cover; ductile iron cover + VM cast iron body.

7. Conclusions

Research studies were conducted as a continuation of publications [1–12] on Vari Morph cast iron. Confirmation of the possibility of producing cast iron with graphite shapes in many forms, called Vari Morph, in a targeted and controlled manner was obtained. It was also claimed that it could be produced using several methods in experimental foundries, as well as in industrial foundries. Inmold technology ensures the production of this cast iron. The combination of the instantaneous introduction of Mg-protected graphite into the liquid cast iron and the moment of solidification in the mold cavity allows for the prediction of the amount of Mg required for the cast iron. In the case of spheroidization technology, magnesium evaporates during the spheroidization process until the moment of the control method. Industrial trials have been thoroughly verified.

Vari Morph cast iron has a number of properties characterized by high IQ quality indicators. It fills the area of a specific discontinuity in the isolated graphite compared to the definition of standardized cast iron grades with compatible graphite: flake, vermicular, or spheroidal. VM cast iron is an attractive material for structures and castings requiring above-standard properties that cannot be reused when graphite is functional. As demonstrated in this work, it is suitable for structures operating under conditions of rapid temperature

https://doi.org/10.3390/ma19061212

changes, leak-releasing emissions, easily machined castings, etc. Vari Morph cast iron is considered a future-proof application, filling a gap in the research offering cast iron grades.

Expanding on earlier work [1–11], the authors demonstrated that the properties of VM cast iron with a homogeneous ferritic matrix, previously described as a function of the graphite shape index, can be described by empirical relationships whose independent variable is the ultrasonic wave velocity. They therefore propose that the graphite form in VM cast iron be assessed and monitored non-destructively using ultrasonic techniques, commonly used in iron foundries. Ultrasonic testing of cast iron based on wave velocity is a very convenient inspection tool, previously used mainly for the inspection of ductile cast iron. It can be even more applicable to the study of the form of precipitates in VM graphite.

Within the entire range of ultrasonic wave velocity changes from gray cast iron with flake graphite to ductile cast iron with spherical graphite, wave velocity ranges characteristic for individual cast iron grades can be distinguished, as shown illustratively in Figure 3. And so, gray cast iron with a ferritic matrix—C_L < 4800–4900 m/s; VM cast iron with a mixture of flake and vermicular graphite C_L < 4800–5200 m/s; cast iron with vermicular graphite C_L < 5200–5350 m/s; VM cast iron with vermicular and nodular graphite: CL—5350–5500 m/s; ductile cast iron with nodular graphite; C_L > 5500 m/s. Naturally, these are approximate limits of the described ranges.

Investigations performed in this study allowed us to empirically determine dependencies existing between the ultrasonic wave velocity and the selected property, feature or functional property of VM cast iron. Like all empirical relationships, they are subject to some error, but they allow for a very quick and comprehensive assessment of cast iron with graphite, regardless of its form. Their use allows for the prediction of a whole group of properties and characteristics of cast iron in the finished product—a casting made from cast iron in which the matrix is purely ferritic or close to fully ferritic.

These are dependencies of:

- physical properties (graphite shape indicator f_K, specific density, thermal conductivity, ultrasound wave speed): $f_K = f(C_L)$; $\rho = f(C_L)$; $\lambda = f(C_L)$,
- mechanical properties (strength (Rm), A5, coefficient of elasticity E_D, quality index IQ): $Rm = f(C_L)$; $A5 = f(C_L)$, $E_D = f(C_L)$, $IQ = f(C_L)$,
- functional properties (heat fatigue resistance (N), low-cycle mechanical fatigue Z, cast iron tightness H): $N = f(C_L)$; $Z_c = f(C_L)$, $Z = f(C_L)$

Author Contributions: Conceptualization, J.S.Z. and M.M.; methodology, J.S.Z. and S.K.; software, J.P.; validation, J.S.Z., M.M., J.P. and S.K.; formal analysis, J.S.Z.; investigation J.S.Z., M.M., J.P. and S.K.; resources, J.S.Z. and J.P.; data curation, M.M. and S.K.; writing—original draft preparation, J.S.Z.; writing—review and editing, J.S.Z., M.M., J.P. and S.K.; visualization, M.M. and S.K.; supervision, J.S.Z.; project administration, J.S.Z. and J.P.; funding acquisition, J.S.Z. and J.P. All authors have read and agreed to the published version of the manuscript.

Funding: This research was conducted within the project of: POIR 01.01.-00-0042/17.

Data Availability Statement: The original contributions presented in this study are included in the article. Further inquiries can be directed to the corresponding author.

Conflicts of Interest: Author Janusz Postuła and Sylwia Kobyłecka were employed by the FANSULD Cast Iron Foundry. The remaining authors declare that the research was conducted in the absence of any commercial or financial relationships that could be construed as a potential conflict of interest.

References

1. Zych, J.; Postuła, J. Cast iron 'Vari-Morph' (VM) with Graphite of Several Forms—Material for Castings of Special Destinations. In *Proceedings of the 73rd World Foundry Congress "Creative Foundry", Krakow, Poland, 23–27 September 2018*; Foundry Trade Journal Winton House: Lyonshall, UK, 2018; pp. 149–150.
2. Zych, J.; Myszka, M.; Kaźnica, N. Control of Selected Properties of 'Vari-Morph' (VM) Cast Iron by Means of the Graphite Form Influence, Described by the Mean Shape Indicator. *Arch. Foundry Eng.* **2019**, *19*, 43–48. [CrossRef]
3. Zych, J.; Myszka, M.; Snopkiewicz, T. Thermal Conductivity of 'Vari-Morph' (VM) Cast Iron with Graphite of Several Forms. In Proceedings of the International Conference of Metals, Ceramics and Composites, Warna, Bulgaria, 25–27 September 2019; pp. 27–28.
4. Stanisław, Z.J.; Marcin, M.; Krzysztof, P. Determining the thermal conductivity in walls of cast iron castings by the ultrasound technique. *J. Mater. Sci. Eng. A* **2021**, *11*, 120–128. [CrossRef]
5. Jerzy, Z.; Marcin, M.; Janusz, P. Chapter: "Vari-Morph' (VM) Cast Iron with Several Forms of Graphite: Technology, Properties, Application". In *Casting Processes*; Intech Open: London, UK, 2022.
6. Marcin, M. Comprehensive Assessment of Cast Iron with Graphite in Many Forms Based on the Weighted Average Value of Its Shape Indicator. Doctoral Dissertation, AGH University of Kraków, Kraków, Poland, 2024.
7. Postuła, J. Production of Cast Iron with Variable Graphite Morphology. Evaluation of Solidification Process, Study of Microstructure and Selected Physical, Mechanical and Utility Properties. Master's Thesis, Department of Foundry, AGH University of Kraków, Kraków, Poland, 2017.
8. Project: POIR 01.01.-00-0042/17. Available online: https://www.gov.pl/web/ncbr-en (accessed on 18 September 2023).
9. Zych, J. The Impact of Some Selected Factors on Cast Iron Thermal Fatigue. *Sci. Noteb.-AGH Metal. I Odlew* **1989**, *15*, 131–145.
10. Zych, J. The role of graphite morphology in forming thermal fatigue resistance of cast iron. *Inżynieria Mater.* **2015**, 343–347.
11. Zych, J. Cast iron thermal fatigue resistance—Influence of graphite shape. *Seria Mech.* **2015**, 51–64.
12. Zych, J.; Mocek, J. Problem of tightness of casting alloys and castings made from them—New research methods. *Arch. Foundry Eng.* **2025**, *25*, 159–167. [CrossRef]
13. *ISO/TR 945-1*; Microstructure of Cast Irons—Part 1: Graphite Classification by Visual Analysis. ISO: Geneva, Switzerland, 2008.
14. *ISO/TR 945-2*; Microstructure of Cast Irons—Part 2: Graphite Classification by Image Analysis. ISO: Geneva, Switzerland, 2011.
15. Jura, S.; Jura, Z. Influence of Chemical Constitution and Graphite Spheroidization Grade on Mechanical Properties of Cast Iron. *Arch. Foundry Eng.* **2001**, *1*, 167–174.
16. Jura, S.; Jura, Z. Influence of Stereological Functional Parameters of Graphite on Ductile Cast Iron's Mechanical Properties. *Arch. Foundry Eng.* **2001**, *1*, 175–185.
17. Stawarz, M.; Jura, S. Stereological Parameters of Graphite and Chemical Constitution Determining Ductile Cast Iron's Mechanical Properties. *Arch. Foundry Eng.* **2002**, *2*, 446–453.
18. Patiero, V.; Tosto, S.; Natale, E. Microstructural characterization mechanical properties of various grades of nodularity in, S.G. iron. In Proceedings of the 44 International Foundry Congress, Florence, Italy, 11–14 September 1977; p. 4.
19. Walton, C.F.; Opar, T.J. *Iron Castings Handbook: Covering Data on Gray, Malleable, Ductile, White, Alloy and Compacted Graphite Irons*; Iron Castings Society: Columbus, OH, USA, 1981.
20. Podrzucki, C. *Cast Iron—Structure, Properties, Applications*; ZG STOP Publishing House: Kraków, Poland, 1991. (In Polish)
21. Żyrek, A. Obtaining Vermicular Cast Iron by the in-Mold Method Using Magnesium Mortars and Assessing Its Resistance to Thermal Fatigue. Doctoral Dissertation, AGH University of Kraków, Kraków, Poland, 2014.
22. Nachtelberger, E.; Puhr, H.; Nesselrode, J.B.; Nakajuasu, A. *Stand der Entwicklung von Gusseisen mit Vermiculagrahit—Herstellung, Eingenschaften und Anwendung*; Giesserei-Praxis: Berlin, Germany, 1982; pp. 359–372.
23. Guzik, E. *Cast Iron Refining Processes—Selected Issues*; Wydawnictwo Komisja Odlewnictwa PAN Katowice: Katowice, Poland, 2001. (In Polish)

Disclaimer/Publisher's Note: The statements, opinions and data contained in all publications are solely those of the individual author(s) and contributor(s) and not of MDPI and/or the editor(s). MDPI and/or the editor(s) disclaim responsibility for any injury to people or property resulting from any ideas, methods, instructions or products referred to in the content.

MDPI AG
Grosspeteranlage 5
4052 Basel
Switzerland
Tel.: +41 61 683 77 34

Materials Editorial Office
E-mail: materials@mdpi.com
www.mdpi.com/journal/materials



Disclaimer/Publisher's Note: The title and front matter of this reprint are at the discretion of the Guest Editors. The publisher is not responsible for their content or any associated concerns. The statements, opinions and data contained in all individual articles are solely those of the individual Editors and contributors and not of MDPI. MDPI disclaims responsibility for any injury to people or property resulting from any ideas, methods, instructions or products referred to in the content.





Academic Open
Access Publishing

mdpi.com

ISBN 978-3-7258-8532-9